

NORTH ATLANTIC TREATY ORGANIZATION



RESEARCH AND TECHNOLOGY ORGANIZATION

BP 25, 7 RUE ANCELLE, F-92201 NEUILLY-SUR-SEINE CEDEX, FRANCE

RTO MEETING PROCEEDINGS 14

Gas Turbine Engine Combustion, Emissions and Alternative Fuels

(la Combustion dans les turbomoteurs, les émissions et les
carburants de remplacement)

*Papers presented at the Applied Vehicle Technology Panel (AVT) Symposium (organized by
the former AGARD Propulsion and Energetics Panel (PEP)), held in Lisbon, Portugal,
12-16 October 1998.*

19990719 064



DISTRIBUTION STATEMENT A
Approved for Public Release
Distribution Unlimited

Reproduced From
Best Available Copy

Published June 1999

Distribution and Availability on Back Cover

AQT-99-10-1831

The Research and Technology Organization (RTO) of NATO

RTO is the single focus in NATO for Defence Research and Technology activities. Its mission is to conduct and promote cooperative research and information exchange. The objective is to support the development and effective use of national defence research and technology and to meet the military needs of the Alliance, to maintain a technological lead, and to provide advice to NATO and national decision makers. The RTO performs its mission with the support of an extensive network of national experts. It also ensures effective coordination with other NATO bodies involved in R&T activities.

RTO reports both to the Military Committee of NATO and to the Conference of National Armament Directors. It comprises a Research and Technology Board (RTB) as the highest level of national representation and the Research and Technology Agency (RTA), a dedicated staff with its headquarters in Neuilly, near Paris, France. In order to facilitate contacts with the military users and other NATO activities, a small part of the RTA staff is located in NATO Headquarters in Brussels. The Brussels staff also coordinates RTO's cooperation with nations in Middle and Eastern Europe, to which RTO attaches particular importance especially as working together in the field of research is one of the more promising areas of initial cooperation.

The total spectrum of R&T activities is covered by 7 Panels, dealing with:

- SAS Studies, Analysis and Simulation
- SCI Systems Concepts and Integration
- SET Sensors and Electronics Technology
- IST Information Systems Technology
- AVT Applied Vehicle Technology
- HFM Human Factors and Medicine
- NSPG NATO Simulation Policy Group (Modelling and Simulation)

These Panels are made up of national representatives as well as generally recognised 'world class' scientists. The Panels also provide a communication link to military users and other NATO bodies. RTO's scientific and technological work is carried out by Technical Teams, created for specific activities and with a specific duration. Such Technical Teams can organise workshops, symposia, field trials, lecture series and training courses. An important function of these Technical Teams is to ensure the continuity of the expert networks.

RTO builds upon earlier cooperation in defence research and technology as set-up under the Advisory Group for Aerospace Research and Development (AGARD) and the Defence Research Group (DRG). AGARD and the DRG share common roots in that they were both established at the initiative of Dr Theodore von Kármán, a leading aerospace scientist, who early on recognised the importance of scientific support for the Allied Armed Forces. RTO is capitalising on these common roots in order to provide the Alliance and the NATO nations with a strong scientific and technological basis that will guarantee a solid base for the future.

The content of this publication has been reproduced directly from material supplied by RTO or the authors.



Printed on recycled paper

Published June 1999

Copyright © RTO/NATO 1999
All Rights Reserved

ISBN 92-837-0009-0



*Printed by Canada Communication Group Inc.
(A St. Joseph Corporation Company)
45 Sacré-Cœur Blvd., Hull (Québec), Canada K1A 0S7*

Gas Turbine Engine Combustion, Emissions and Alternative Fuels

(RTO MP-14)

Executive Summary

NATO efficiency in the future will depend largely on air superiority, long range deployment capacity and rapid response both on land and at sea. The gas turbine engine will remain the power source of choice, and fuel efficiency, fuel availability and exhaust emissions will drive its design. The combustor is one of the crucial engine components and combustion system problems have traditionally contributed to well over half of the engine service problems in most air forces. The symposium focused on and addressed the key challenges for reducing fuel consumption, lowering emission levels and burning alternative fuels as requirements concurrent with improved performance and operation.

Widening the narrow standards of today's fuels offers a short term solution to scarcity but has detrimental effects on combustor life and emission levels. New fuels, such as liquid hydrogen and methane, offer some potential advantages but also pose new combustion problems. The contribution of military engines to emissions is of major concern today and will continue to be in the future. There are additional requirements for military engines such as higher combustion temperatures which are needed for superior efficiency but at the same time low exhaust temperatures and low exhaust volumes to reduce the infrared signature. Operability (blow-out stability and wind milling re-ignition, throttle response, etc.) must be enhanced as the aircraft flight envelope and manoeuvrability are expanded. Component durability must be maintained in an increasingly adverse environment. Combustor design, active control of flame stability, control performance and exhaust gas composition as well as operating procedure optimisation are the aims. Tools for combustion simulation and experimental validation are under continual elaboration to save on development and life cycle costs through better design.

Scientists and engineers met military and civil operators, and discussion concentrated on the customer's future needs and constraints. A review of current R&D activities and formulation of specific research resulted from the Symposium, for which there is no known competing event. Universities, government laboratories, industry and some agencies of the military services were represented and presented their knowledge and advice. The correct makeup of participants was indeed achieved. All papers presented were of good quality and covered new advances in many important areas.

Highlight topics for future AVT symposia in this field would seem to be as follows: gaseous and particulate emissions at altitude, optical diagnostics at elevated pressures in near-real combustors, and active combustion control all of which can crucially contribute to the military usefulness of engines.

La combustion dans les turbomoteurs, les émissions et les carburants de remplacement

(RTO MP-14)

Synthèse

L'efficacité des forces de l'OTAN à l'avenir dépendra largement de la supériorité aérienne, de la capacité de déploiement à grande distance et de l'intervention rapide terrestre et maritime. Le turbomoteur restera le propulseur de choix et sa conception sera guidée par des considérations d'émission de gaz polluants, ainsi que par des questions de rendement et de disponibilité du carburant. La chambre de combustion est l'un des composants clés du moteur et l'expérience montre que plus de la moitié des problèmes d'entretien des moteurs, rencontrés par la majorité des forces aériennes sont liés aux systèmes de combustion. Le symposium a privilégié les défis clés de la diminution de la consommation du carburant, l'atténuation des niveaux d'émission de gaz polluants et l'utilisation de carburants de remplacement en vue d'améliorer les performances et le fonctionnement des turbomoteurs.

Bien que l'assouplissement des normes restrictives qui s'appliquent aux carburants modernes offre une solution à court terme aux problèmes de pénurie, elle s'accompagne d'effets indésirables pour la durée de vie des chambres de combustion et les niveaux d'émission de gaz polluants. Les nouveaux carburants, tels que l'hydrogène liquide et le méthane, s'ils offrent quelques avantages possibles, posent en même temps des problèmes nouveaux de combustion. La contribution des moteurs militaires aux émissions polluantes est, et restera, un sujet de préoccupation majeur. En plus, les moteurs militaires ont des caractéristiques spécifiques, à savoir, des températures de combustion élevées, pour assurer une meilleure efficacité, avec en même temps des températures et des volumes de gaz d'échappement moindres, pour permettre de réduire la signature infrarouge. L'exploitabilité (stabilité en cas de suppression, réallumage en autorotation, réponse du moteur, etc.) doit être améliorée au fur et à mesure de l'augmentation de la maniabilité et de l'élargissement des domaines de vol. Il s'agit également de conserver la longévité des composants dans un environnement de plus en plus contraignant. La conception des chambres de combustion, le contrôle actif de la stabilité de la flamme, les performances en matière de contrôle, la composition des gaz d'échappement et l'optimisation de la procédure d'exploitation sont les objectifs en vue. Les outils de simulation et de validation expérimentale de la combustion sont en évolution permanente dans le but de réaliser des économies sur les coûts de développement et de possession par l'amélioration de la conception.

Les scientifiques et les ingénieurs qui ont assisté à la réunion ont pu rencontrer des exploitants militaires et civils et leurs discussions ont porté essentiellement sur les besoins futurs des clients et les contraintes qui leur sont imposées. Le symposium, qui est, à notre connaissance, unique en son genre, a permis de faire le point des activités de R&D actuelles et de formuler des projets de recherche spécifiques. Les universités, les laboratoires gouvernementaux, les industries et les agences militaires représentés ont exposé leurs connaissances et proposé des conseils. Du point de vue des participants, la répartition était équilibrée. Toutes les communications présentées ont été de bonne qualité, couvrant de nouvelles avancées dans bon nombre de domaines importants.

Les sujets présentant un intérêt particulier pour les futurs symposia AVT dans ce domaine pourraient être : les émissions particulières et gazeuses en altitude, le diagnostic optique aux pressions élevées dans des chambres de combustion quasi-réelles, et la combustion active, ces sujets pouvant faire l'objet de contributions déterminantes dans le domaine des moteurs militaires.

Contents

	Page
Executive Summary	iii
Synthèse	iv
Theme/Thème	ix
Recent Publications on Propulsion and Power Systems of the Former AGARD Propulsion and Energetics Panel and the RTO Applied Vehicle Technology Panel	x
Programme Committee	xii
	Reference
Technical Evaluation Report by G.J. Sturgess	T
Keynote Address by J.S. Lewis	K
SESSION I: GAS TURBINES IN LAND, SEA AND AIR APPLICATIONS	
Ground Vehicle Mobility Requirements. Meeting the Challenge with Electric Drives by G. Khalil and J. Hitchcock	1
Advances in a Gas Turbine System for Ship Propulsion by M.L. Parker, P.K. MacLeod and M. Coulson	2
Technical Challenges Associated with the Development of Advanced Combustion Systems by C.A. Van Erp and M.H. Richman	3
SESSION II: LOW EMISSION COMBUSTORS	
Paper 4 withdrawn	
Empirical and Anchored Methodologies for Controlling Combustion Dynamics by R.P. Pandalai, G.C. Hsiao and H.C. Mongia	5
Paper 6 withdrawn	
NO _x Reduction by Lean Premixed Prevaporized Combustion by Th. Ripplinger, N. Zarzalis, G. Meikis, C. Hassa and M. Brandt	7
Status of Catalytic Combustion R&D for the Department of Energy Advanced Turbine Systems Program by D. Fant, G. Jackson, H. Karim, D. Newbury, P. Dutta, K. Smith, D. Smith and R. Dibble	8
Measurement of Spray/Acoustic Coupling in Gas Turbine Fuel Injectors by T.J. Anderson, D.W. Kendrick, J.M. Cohen and T.J. Rosfjord	9

SESSION III: COMBUSTION MODELLING - PART 1

Soot and Radiation Modelling in Gas Turbine Combustion Chambers	10
by H.T. Brocklehurst, J.B. Moss, C.D. Hurley and C.H. Priddin	
A Novel Code for the Prediction of Transient Flow Field in a Gas Turbine Combustor Simulator	11
by N. Selçuk and O. Oymak	
Reduced Kinetic Mechanisms for Modelling LPP Combustion in Gas Turbines	12
by A. Liñán, M. Bollig, A.L. Sánchez and B. Lázaro	
Numerical Simulation of the Reactive Flow in a Tubular Chamber with Detailed Kinetic Effects	13
by B. Zamuner, B. Bourasseau, C. Berat and H. Niemann	
Kerosene Combustion Modelling using Detailed and Reduced Chemical Kinetic Mechanisms	14
by M. Cathonnet, D. Voisin, A. Etsouli, C. Sferdean, M. Reuillon, J.C. Boettner and P. Dagaut	
Modelling of a Lean Premixed Combustor	15
by P.J. Coelho and P. Salvada	

SESSION IV: OPTICAL MEASUREMENTS - PART 1

Validation and Application of a Droplet Evaporation Model for Real Aviation Fuel	16
by K. Prommersberger, G. Maier and S. Wittig	
Optical Diagnostics Applied to a Jet Diffusion Flame	17
by F. Grisch, B. Attal-Tretout, P. Bouchardy, V.R. Katta and W.M. Roquemore	
Experimental Investigation of an Axially Staged Combustor Sector with Optical Diagnostics at Realistic Operating Conditions	18
by C. Hassa, M. Carl, M. Frodermann, T. Behrendt, J. Heinze, I. Röhle, N. Brehm, Th. Schilling and Th. Doerr	

SESSION V: EMISSIONS

Measurement and Prediction of NO and NO₂ Emissions from Aero Engines	19
by T.J. Foster, C.W. Wilson, M. Pourkashanian and A. Williams	
Influence of Engine Performance on Emission Characteristics	20
by A. Döpelheuer and M. Lecht	
Modeling the Effects of Operating Conditions and Alternative Fuels on Gas Turbine Performance and Emissions	21
by W.P.J. Visser and S.C.A. Kluiters	
In-Flight Spectroscopic Aircraft Emission Measurements	22
by H.W. Jentink and J.J.F. van Veen	

SESSION VI: COMBUSTOR DESIGN - PART 1

The Design and Evaluation of a Piloted, Lean Burn, Premixed, Prevaporised Combustor	23
by M.I. Wedlock, J.R. Tilston and R.E. Seoud	

Advance Fuel Injection Strategies for High Performance Gas Turbine Engines by S. Samuelsen and V. McDonell	24
----------------------------------------------------------------------------------------------------------------------	-----------

Turbulent Structure of Generic LPP Gas Turbine Combustors by B. Lazaro, E. Gonzalez, J. Alfaro, P. Rodriguez and A. Lecuona	25
---------------------------------------------------------------------------------------------------------------------------------------	-----------

Paper 26 withdrawn

NO_x Reduction in a Fuel Staged Combustor by Optimisation of the Mixing Process and the Residence Time by N. Brehm, Th. Schilling, A. Mack and G. Kappler	27
-------------------------------------------------------------------------------------------------------------------------------------------------------------------------------	-----------

Paper 28 withdrawn

SESSION VII: IGNITION PROCESSES

A Novel Technique for Predicting the Ignition Performance of an Aero Gas Turbine Combustion Chamber by C.W. Wilson, C.G.W. Sheppard and H.C. Low	29
------------------------------------------------------------------------------------------------------------------------------------------------------------	-----------

Caractérisation des systèmes d'injection prémélangés en auto-inflammation et remontée de flamme (Characterisation of Autoignition and Flashback in Premixed Injection Systems) by C. Guin	30
--------------------------------------------------------------------------------------------------------------------------------------------------------------------------------------------------------	-----------

Ignition Diagrams and Bifurcation Maps by F.P. Di Maio, G. Barbieri and P.G. Lignola	31
------------------------------------------------------------------------------------------------	-----------

SESSION VIII: COMBUSTOR DESIGN - PART 2

On the Analysis of Combustion Performance in a LPP Combustor at Atmospheric Pressure by P.M. Anacleto and M.V. Heitor	32†
---------------------------------------------------------------------------------------------------------------------------------	------------

The Use of Fluidics in Gas Turbine Combustion Design by R.J. Woolhouse, J.R. Tippetts, M. Whiteman, K.J. Young, S.B.M. Beck and J. Swithenbank	33
----------------------------------------------------------------------------------------------------------------------------------------------------------	-----------

Fuel/Air Preparation in the Design of Low Emissions Gas Turbine Combustion Systems by M.K. Razdan	34
-------------------------------------------------------------------------------------------------------------	-----------

Experiments in a Small Gas-Turbine Combustor with Gas and Liquid Fuels by A.L. Heyes, D. Jelerčič and J.H. Whitelaw	35
-------------------------------------------------------------------------------------------------------------------------------	-----------

SESSION IX: ACTIVE COMBUSTION CONTROL

AGARD Workshops on Active Combustion Control for Propulsion Systems by V. Yang and K.C. Shadow	36
----------------------------------------------------------------------------------------------------------	-----------

Combustion Instabilities in Low NO_x Gas Turbines and Their Active Control by B.T. Zinn, T. Lieuwen and Y. Neumeier	37
-----------------------------------------------------------------------------------------------------------------------------------------	-----------

Active Control of Combustion Instability in a Liquid-Fueled, Low-NO_x Combustor by J.M. Cohen, N.M. Rey, C.A. Jacobson, T.J. Anderson and T.J. Rosfjord	38
-----------------------------------------------------------------------------------------------------------------------------------------------------------------------------	-----------

† Paper not available at time of printing

Adaptive Control of Aeroacoustic Instabilities with Application to Propulsion Systems by M. Mettenleiter, E. Haile and S. Candel	39
Application of Active Combustion Control to Siemens Heavy Duty Gas Turbines by S. Hoffmann, G. Weber, H. Judith, J. Hermann and A. Orthmann	40
Optimization of Active Control Systems for Suppressing Combustion Instability by J.G. Lee, B.-S. Hong, K. Kim, V. Yang and D. Santavicca	41

SESSION X: OPTICAL MEASUREMENTS - PART 2

Optical Measurements of Jet-Mixing in a Swirling Crossflow of a Combustion Chamber by B.H. Krautkremer, M.M. Blomeyer and D.K. Hennecke	42
Optical Measurements of Spray Combustion in a Single Sector Combustor from a Practical Fuel Injector at Higher Pressures by T. Behrendt, M. Frodermann, C. Hassa, J. Heinze, B. Lehmann and K. Stursberg	43
Combustion Characteristics of a Trapped Vortex Combustor by G.J. Sturgess and K.-Y. Hsu	44

SESSION XI: ALTERNATIVE FUELS

European Evaluation of JP8+100 Fuel and Its Impact on Engine/Fuel System Design by S.P. Bullock, A. Hobday and C. Lewis	45
Paper 46 withdrawn	
Catalytic Combustion Concepts for Industrial Gas Turbines From MicroWatt to MegaWatt by J.M. der Kinderen and R. van Yperen	47
Modification of the Fuel Control System of a Gas Turbine Engine from Kerosene to Hydrogen by D. Dini	48

SESSION XII: COMBUSTION MODELLING - PART 2

Numerical Predictions and Experimental Measurements of Radiative Heat Transfer in Gas Turbine Combustors by P. Di Martino and G. Cinque	49
Soot Formation Modelling in Turbulent Diffusion Flames by P. Di Martino and G. Cinque	50
Efficient Numerical Calculation of Evaporating Sprays in Combustion Chamber Flows by R. Schmehl, G. Klose, G. Maier and S. Wittig	51
Paper 52 withdrawn	
Pollutants Emission Prediction in Combustion in Inert Porous Media by I. Malico, X.Y. Zhou and J.C.F. Pereira	53

Theme

NATO efficiency in the future will depend largely on air superiority, long range deployment capacity and rapid response both on land and at sea. The gas turbine engine will remain the power source of choice, and fuel efficiency, fuel availability, and exhaust emissions will drive its design. The symposium will focus on the combustor as the crucial engine component, and will address the key challenges of reducing fuel consumption, lowering emission levels, and burning alternative fuels. Widening the narrow standards of today's fuels offers a short term solution to scarcity but has detrimental effects on combustor life and emission levels. New fuels, such as liquid hydrogen and methane, offer some potential advantages, but also pose new combustion problems. The use of these fuels will be considered, as will the contribution of military engines to exhaust emission levels, combustor design and operating procedures, and active control of flame stability. Development tools such as combustion simulation and experimental validation will also be discussed. Scientists and engineers will meet military and civil operators and discussion will concentrate on the customer's future needs and constraints. A review of current R&D activities and formulation of specific research may result from the Symposium, for which there is no known competing event.

Thème

L'efficacité, à terme, des forces de l'OTAN dépendra en grande partie de la supériorité aérienne, ainsi que des capacités de déploiement à grande distance et de réaction rapide sur terre et sur mer. Le turbomoteur restera le propulseur de choix et sa conception sera guidée par des considérations de rendement énergétique, de disponibilité de carburant, et d'émission de gaz polluants.

Ce symposium s'attachera à étudier la chambre de combustion en tant que composant propulsif fondamental et il examinera les défis décisifs représentés par la diminution de la consommation de carburant, l'abaissement des niveaux d'émission et les carburants de remplacement. Si l'augmentation des normes actuelles qui s'appliquent aux carburants peut fournir une solution à certains problèmes ponctuels de pénurie, elle a en revanche des effets contraires sur la durée de vie des chambres de combustion et sur les niveaux d'émission. Les nouveaux carburants, tels que l'hydrogène liquide et le méthane, offrent certes des avantages possibles, mais ils posent aussi de nouveaux problèmes de combustion.

L'utilisation de ces carburants sera étudiée, ainsi que l'apport des moteurs militaires aux problèmes des niveaux d'émission des gaz d'échappement, aux procédures de conception et d'exploitation et au contrôle actif de la stabilisation de flamme. Les outils de développement, tels que la simulation de la combustion et la validation expérimentale, seront également pris en compte. Des contacts seront établis entre scientifiques et ingénieurs d'une part, et militaires et exploitants civils d'autre part, avec des échanges de vues sur les attentes futures des utilisateurs et sur les contraintes qui leur sont imposées.

Le symposium, qui est le seul à être organisé sur ce sujet à l'heure actuelle, pourrait aboutir à une mise au point des activités courantes de recherche et développement dans ce domaine, ainsi qu'à la formulation de projets spécifiques de recherche.

Recent Publications on Propulsion and Power Systems of the Former AGARD Propulsion and Energetics Panel and the RTO Applied Vehicle Technology Panel

CONFERENCE PROCEEDINGS (CP)

Combustion and Fuels in Gas Turbine Engines

AGARD CP 422, June 1988

Engine Condition Monitoring — Technology and Experience

AGARD CP 448, October 1988

Application of Advanced Material for Turbomachinery and Rocket Propulsion

AGARD CP 449, March 1989

Combustion Instabilities in Liquid-Fuelled Propulsion Systems

AGARD CP 450, April 1989

Aircraft Fire Safety

AGARD CP 467, October 1989

Unsteady Aerodynamic Phenomena in Turbomachines

AGARD CP 468, February 1990

Secondary Flows in Turbomachines

AGARD CP 469, February 1990

Hypersonic Combined Cycle Propulsion

AGARD CP 479, December 1990

Low Temperature Environment Operations of Turboengines (Design and User's Problems)

AGARD CP 480, May 1991

CFD Techniques for Propulsion Applications

AGARD CP 510, February 1992

Insensitive Munitions

AGARD CP 511, July 1992

Combat Aircraft Noise

AGARD CP 512, April 1992

Airbreathing Propulsion for Missiles and Projectiles

AGARD CP 526, September 1992

Heat Transfer and Cooling in Gas Turbines

AGARD CP 527, February 1993

Fuels and Combustion Technology for Advanced Aircraft Engines

AGARD CP 536, September 1993

Technology Requirements for Small Gas Turbines

AGARD CP 537, March 1994

Erosion, Corrosion and Foreign Object Damage Effects in Gas Turbines

AGARD CP 558, February 1995

Environmental Aspects of Rocket and Gun Propulsion

AGARD CP 559, February 1995

Loss Mechanisms and Unsteady Flows in Turbomachines

AGARD CP 571, January 1996

Advanced Aero-Engine Concepts and Controls

AGARD CP 572, June 1996

Service Life of Solid Rocket Propellants

AGARD CP 586, May 1997

Aircraft Fire Safety

AGARD CP 587, September 1997

Future Aerospace Technology in the Service of the Alliance — Sustained Hypersonic Flight

AGARD CP 600, Volume 3, December 1997

Advanced Non-Intrusive Instrumentation for Propulsion Engines

AGARD CP 598, May 1998

MEETING PROCEEDINGS (MP)

Design Principles and Methods for Aircraft Gas Turbine Engines

RTA MP-8, February 1999

ADVISORY REPORTS (AR)

The Uniform Engine Test Programme (*Results of Working Group 15*)

AGARD AR 248, February 1990

Test Cases for Computation of Internal Flows in Aero Engine Components (*Results of Working Group 18*)

AGARD AR 275, July 1990

Test Cases for Engine Life Assessment Technology (*Results of Working Group 20*)

AGARD AR 308, September 1992

Terminology and Assessment Methods of Solid Propellant Rocket Exhaust Signatures (*Results of Working Group 21*)

AGARD AR 287, February 1993

Guide to the Measurement of the Transient Performance of Aircraft Turbine Engines and Components (*Results of Working Group 23*)

AGARD AR 320, March 1994

Experimental and Analytical Methods for the Determination of Connected — Pipe Ramjet and Ducted Rocket Internal Performance (*Results of Working Group 22*)

AGARD AR 323, July 1994

Recommended Practices for the Assessment of the Effects of Atmospheric Water Ingestion on the Performance and Operability of Gas Turbine Engines (*Results of Working Group 24*)

AGARD AR 332, September 1995

Structural Assessment of Solid Propellant Grains (*Results of Working Group 25*)

AGARD AR 350, December 1997

CFD Validation for Propulsion System Components (*Results of Working Group 26*)

AGARD AR 355, May 1998

LECTURE SERIES (LS)

Blading Design for Axial Turbomachines

AGARD LS 167, June 1989

Comparative Engine Performance Measurements

AGARD LS 169, May 1990

Combustion of Solid Propellants

AGARD LS 180, July 1991

Steady and Transient Performance Prediction of Gas Turbine Engines

AGARD LS 183, May 1992

Rocket Motor Plume Technology

AGARD LS 188, June 1993

Research and Development of Ram/Scramjets and Turboramjets in Russia

AGARD LS 194, December 1993

Turbomachinery Design Using CFD

AGARD LS 195, May 1994

Mathematical Models of Gas Turbine Engines and their Components

AGARD LS 198, December 1994

Integrated Multidisciplinary Design of High Pressure Multistage Compressor Systems (LS-211)

published as RTO EN 1, September 1998

AGARDOGRAPHS (AG)

Measurement Uncertainty within the Uniform Engine Test Programme

AGARD AG 307, May 1989

Hazard Studies for Solid Propellant Rocket Motors

AGARD AG 316, September 1990

Advanced Methods for Cascade Testing

AGARD AG 328, August 1993

REPORTS (R)

Application of Modified Loss and Deviation Correlations to Transonic Axial Compressors

AGARD R 745, June 1990

Rotorcraft Drivetrain Life Safety and Reliability

AGARD R 775, June 1990

Propulsion and Energy Issues for the 21st Century

AGARD R 824, March 1997

Impact Study on the use of JET A Fuel in Military Aircraft during Operations in Europe

AGARD R 801, January 1997

The Single Fuel Concept and Operation Desert Shield/Storm

AGARD R 810, January 1997 (*NATO Unclassified*)

Active Combustion Control for Propulsion Systems

AGARD R 820, September 1997

Programme Committee

Programme Committee Chairman
Prof. R. Evans
Department of Mechanical Engineering
University of British Columbia
2324 Main Mall
Vancouver, B.C. V6T 1W5
Canada

BELGIUM

Prof. R. Jacques
Ecole Royale Militaire
30 avenue de la Renaissance
1000 Bruxelles

CANADA

Mr. D. Rudnitski
Head, Engine Laboratory
Institute for Aerospace Research
National Research Council of Canada
Ottawa, Ontario K1A 0R6

GERMANY

Prof. D.K. Hennecke
Fachgebiet Gasturbinen und Flugantriebe
Technische Hochschule Darmstadt
Petersenstrasse 30
64287 Darmstadt

GREECE

Prof. Dr. P. Kotsiopoulos
Hellenic Air Force Academy
Chair of Propulsion Systems
Dekelia, Attiki

ITALY

Prof. G. Torella
Accademia Aeronautica
Dipartimento di Scienza e Applicate al Volo
80078 Pozzuoli (Napoli)

NETHERLANDS

Prof. W. De Wolf
National Aerospace Laboratory
P.O. Box 153
8300 AD Emmeloord

PORTUGAL

Prof. M.N.R. Nina
CTAMFUL
Instituto Superior Tecnico
Avenida Rovisco Pais
1096 Lisboa Codex

SPAIN

Prof. J. J. Salva Monfort
Dept. de Motorpropulsion y
Termofluidodinamica ETSIA
Plaza Cardenal Ciseros
28040 Madrid

TURKEY

Dr. T. Yaşar Katircioğlu
MSG ARGE D. Başkanlığı
06650 Yucetepe
Ankara

UNITED KINGDOM

Mr. R. Cottington
Research Manager
Propulsion Technology Department
DERA Pyestock
Farnborough, Hants, GU14 0LS

Prof. R.S. Fletcher
Deputy Vice Chancellor
Cranfield Institute of Technology
Cranfield, Bedford MK43 0AL

UNITED STATES

Prof. F. Culick
California Institute of Technology
205 Guggenheim
Mail Stop 205-45
Pasadena, CA 91125

Mr. R. Hill
Chief of Technology
WL/POT, Building 18
1950 Fifth Street
Wright Patterson Air Force Base, OH 45433-7251

Dr. C. Russo
Director of Aeronautics
NASA Lewis Research Center
MS 3-8
21000 Brookpark Road
Cleveland, Ohio 44135

Dr. K. Schadow
Head, Propulsion Research Section
Code 47420D, NAWC/WD
First Administration Circle, MS 104d
China Lake, CA 93555-6001

Technical Evaluation

by
Geoffrey J. Sturgess,
Innovative Scientific Solutions, Inc.,
2766, Indian Ripple Road,
Dayton, OH 45440-3638,
United States

Introduction:

The theme of the symposium may be paraphrased to "exploring NATO combat efficiency as influenced by the gas turbine engine combustor system and combustion process, with emphasis on future needs and constraints." The aircraft gas turbine engine remains the major powerplant for all types of military aircraft, and will for some time. For this engine, it's combustion system has been correctly identified as a system-critical component. The originators of practical aircraft gas turbine engines, Sir Frank Whittle and Dr. Hans von Ohain, both had serious difficulties in providing satisfactory combustion systems for their machines. These difficulties continued in later designs for many years. Combustion system problems have traditionally contributed to well over half of the engine unserviceability problems in most air forces. In recent times, considerable improvements have been made with conventional systems so that now the combustion system is usually the first engine component to reach initial maturity standards. However, the ever-present demands for improved thrust-to-weight ratio, specific thrust and power density, tax all engine components, but especially the combustion system. Higher temperature rise capability at high combustion efficiency with non-visible exhaust plumes in reduced burning volume are required, and operability (blowout stability and windmilling relight, throttle response, etc.) must be enhanced as the aircraft flight envelope and maneuverability are expanded. In addition, component durability must be maintained in an increasingly adverse

environment, using materials whose allowable working temperatures always seem to be lagging, and with cooling air that is at increased temperatures and which must be reduced in quantity. All of these exacting requirements must be achieved in an affordable and timely fashion. These latter two are additional constraints that require ingenious approaches.

Altogether, these are indeed severe challenges. The theme of the symposium is therefore, well-chosen.

To address the theme of the symposium in the correct manner requires the right forum. Special kinds of focus and participant make-up are necessary for success. Although the bottom line should always directed towards engine units in service, the theme should be addressed at all levels in order to provide the correct parameter-space for everyone. Researchers have to be able to perceive the problems and requirements of the manufacturers and users in order to bring focus to their work; manufacturers must on one hand, be aware of new ideas, techniques and possibilities in order to explore and exploit them in future designs, and on the other hand, must be able to determine that future designs will truly address the real needs of the users, and, users must be able to anticipate what technology is likely to become available so that they can plan on how to benefit best from it. These diverse needs demand a meeting that is very different than that normally provided through the national and international scientific, technical and engineering societies, good though they normally are. In fact, there are very few forums extant that provide the desired mix of participants while maintaining a tight focus. The former-AGARD meetings were virtually unique in this respect, and it would seem important to the general interest to preserve this important aspect in future AVT symposia.

In this particular meeting were representatives from, and presentations by, workers from universities, government laboratories, industry and some of the agencies of the military services. Therefore, the correct makeup of participants was indeed achieved. The focus on gas turbine combustion systems was strongly maintained throughout. Perhaps the balance could have been better had there been more user-papers. In general however, the symposium was well-formulated to adequately address it's theme.

It is always difficult to talk absolutely freely at international meetings, even amongst allies and friends and where attendance is by invitation only, about future work that is either in progress or is developing. The proprieties of national security, commercial sensitivities and competitive pressures must naturally be observed. Certain topics can even be proscribed from discussion entirely. Together, such inhibiting issues can make it rather difficult to clearly ascertain the future, which must always be seen "through a glass, darkly." However, from what is discussed, especially during break-periods, and sometimes from what is not discussed, it is possible, with perception, to ascertain general trends and potential roadblocks, albeit somewhat subjectively and perhaps imprecisely. The success of such technological forecasting, and hence satisfaction of the symposium theme, critically depends on having the catalysts of the right participants with common interests to serve.

The program for this meeting contained several papers directly concerned with combustion aspects in industrial gas turbine engines. The presence of such papers might initially be perceived as not being relevant to the theme of the symposium, which was exclusively directed towards military aircraft engines. It is essential to understand that the ideas, experiences and in certain circumstances even hardware and software developments, associated with industrial gas turbine combustion can indeed be relevant to military applications of the aircraft gas turbine engine. An example of this is concerned with fuel/air mixing. Good and rapid fuel/air mixing is an essential feature of the low emissions combustor designs of many industrial gas turbine engines; it is also a requisite for the high-rate combustion required in ultra-short combustors necessary for high thrust/weight ratio for military aero-gas turbines. Furthermore, well-mixed combustion systems are susceptible to the dynamic effects of combustion instabilities. Industrial gas turbine engines with low emissions combustors are already beginning to experience difficulties with combustion dynamics. The fundamental understanding of combustion dynamics, and its avoidance, amelioration and control, obtained in the industrial gas turbine could well prove to be invaluable to the military aircraft gas turbine in the near-future. These would be examples of reverse technology transfer.

Keynote Address:

The keynote address by Mr. Jerry Lewis, OBE., from Rolls-Royce plc., presented a manufacturer's view of the challenges facing combustion in the coming millenium. The address

provided a balanced picture of the many aspects that must be dealt with in translating research and technology into a practical and competitive product, and how these aspects are likely to be affected by the competitive times ahead.

Mr Lewis began by looking back to the 1993 symposium and its keynote address by Professor Schumann. He observed that the key technology objectives identified then by the Technical Evaluator George Opdike, have not really changed in form and might stand today; although, the absolute values associated with them then would need to be updated for a projection into the future from the viewpoint of today. To the 1993 list, Mr. Lewis added the key objective of low costs of research and development, product manufacture, and product ownership. He pointed out that low cost objectives are in conflict with advanced low emissions technologies which result in increased system complication.

In a comment concerning the new name of the panel organizing the symposium, it was suggested that future combustion challenges were as likely to come from stationary gas turbine engines as from aircraft or ground-based vehicular applications. The similarities due to fit, form and function between engine rotating machinery components for all applications were noted. However, the divergent needs result in a much wider range of solutions in combustion systems. It was speculated whether or not convergence might also take place in combustion systems at some time in the future.

For today's competitive world, the point was emphasized that the days of change for pure technology reasons are over, and that future change will only take place for sound business reasons. Emissions control was cited as a technological area where change would continue for regulatory and competitive-edge reasons, if not for environmental reasons alone. Gaseous and particulate emissions basics were reviewed.

For the important topic of design systems and methods, Mr. Lewis urged that computational fluid dynamics (CFD) be more closely and better integrated into the design system as more than a pure computational tool, but as an iterative design tool for producing fully-optimized designs. The conflicting needs of high CFD accuracy and low turn-around time were stressed as requiring resolution.

Product reliability is reflected in the cost of ownership. Regardless of the advanced component

technologies incorporated into an engine in order to achieve high performance, the user will expect the levels of engine reliability currently achieved to be maintained, if not improved upon. Methods of predicting component lives, especially of combustion components, are not yet all that could be desired, Mr. Lewis noted. Technology programs tend not to address reliability issues, he charged.

The topic of combustion-driven oscillations is one where clearly all the answers have yet to be uncovered. Finding a way around a particular problem does not constitute a generic solution, and much hardwork in this area will be necessary.

In closing, Mr. Lewis was of the opinion that despite demanding targets and support from industry and government agencies, suggested approaches to combustion challenges that he sees are often conventional and sometimes lack innovation.

Major Technical Categories:

In order to assess the overall technical issues explored in the symposium it is helpful to attempt to ascertain the major technical categories into which the presented papers might fall. Obviously, such a sorting process must inevitably be subjective to a certain degree. In many instances papers will unavoidably address several issues as their arguments are developed. For example, a paper on emissions might also include modeling discussions as well as advanced diagnostics for supporting experiments. In such cases the appropriate category for the paper might not be immediately clear. Under these circumstances the paper category has been based, wherever possible, on how the author verbally presented his material at the meeting. An example might be the paper of Visser (Paper 21) which addressed modeling aspects of engine emissions. The paper was presented as a piece of modeling work, and was therefore placed in the modeling category. Categorization in the manner described does not necessarily result in a sorting that corresponds to the session organization of the printed program.

The following major technical categories were identified as being representative of the symposium content:

1. Design and Development (5)
2. Catalytic Combustion (2)
3. Position Papers (2)
4. Optical Diagnostics (4)
5. Emissions (7)
6. Modeling (17)

7. Dynamics & Active Combustion Control (8)
8. Fuels (2)

Given in parentheses after each category are the number of papers assigned to that category. A total of 47 papers was presented at the meeting.

In order of numerical count, it can be seen that numerically, modeling topics formed the core of the meeting. This reflects the growing degrees of scientific understanding and discipline that are developing in the combustion field. Dynamics and Active Combustion Control was the second area of concentration. This is a relatively new field for the gas turbine that is assuming growing importance. The third thrust of the meeting was concerned with broad aspects of emissions issues. This is not surprising since the majority of combustion practical design and development efforts in recent years have been occupied with emissions. Design and Development papers followed closely behind. Such papers are difficult to write but provide important insight into how ideas are turned into working hardware. Although the number of papers falling into the Optical Diagnostics category was not large, all of the papers in this category were of high quality, addressed really challenging problems and broke new ground. The position papers provided essential user-background information against which technology developments may be assessed. Catalytic combustion continues to tantalize the combustion community with its potential. Fuels might appear to be a fairly mundane topic; however, since modern gas turbines place considerable demands on the fuel that they use, serious considerations have to be given to updating the fuel so that it continues to fulfill all of its required functions without introducing any problems.

The salient features of each of the major categories will be discussed below in the order of numerical paper count. At the beginning of each category an introductory passage is provided, and at the end of each category comments are given on the major points emerging from the topics discussed by the papers in the category. Inevitably of course, this will be colored somewhat by the reporter's own experiences.

Modeling:

The range of topics covered in the modeling category encompassed emissions, fuel sprays, radiation, soot, ignition and the kinetics of jet fuel. Not all of the approaches were mathematical modeling based, although the majority did involve CFD.

There were two ambitious papers concerned with soot. The first paper by Brocklehurst *et al.*, (Paper 10) attempted fully-coupled calculations for the spatial distribution of soot particle concentrations through an engine combustor, including the effects of radiation. The second paper by Martino & Cinque (Paper 50), together with its companion paper (Paper 49), examined the effects of the presence of soot on radiation, as influencing liner wall temperatures, also in an engine combustor. Given the only partially-understood chemical and thermo-physical complexities of soot formation and the subsequent burnup mechanisms, together with the length scales at which these processes take place, it is not surprising that the results of both studies were less than completely successful. What is extremely important is that such sophisticated calculations are presently being attempted. As much can be learned from the revealed short-comings of these calculations as from what they demonstrate is necessary. Such insights will assist in pointing out directions in which to proceed. One useful facet which does emerge from these studies is that the modelers are beginning to understand the important role of radiation in gas turbine combustors using aviation fuels.

The important topic of ignition was addressed in two papers. Di Maio *et al.*, (Paper 31) applied a classical approach based on bifurcation theory and continuation theory to the ignition problem. With this novel approach applied through the CHEMKIN computer program, they calculated ignition diagrams for zero-dimensional combustors with hydrogen as fuel and using a well-established kinetics model. The method gave satisfactory comparisons with experimental data and shows promise as a technique for exploring proposed reaction mechanisms. However, additional work is necessary to extend the techniques to one-dimensional combustors and to flamelets.

Calculation of ignition in an engine combustor was explored by Wilson *et al.*, (Paper 29). This clever piece of work followed the spark kernel as it develops on its trajectory through the primary zone. The criteria for flame existence were based on the Karlovitz Number and flammability limits, and these were evaluated on a cell-by-cell basis through the calculation domain of a converged CFD solution as a post-processing task. An empirically-based Karlovitz Number combined with unity Lewis Number, was used to assess whether flame quenching occurred or if propagation was possible. The spark kernel energy was represented by an impulsive conserved scalar introduced into the solution domain at the ignitor location, and its trajectory through that domain was tracked. The scalar concentration was related

to an arbitrary value representing minimum ignition energy. Along the calculated spark trajectory, on a volume-weighted basis, the limiting Karlovitz Numbers, kernel energy and flammability limits were compared to establish successful or unsuccessful ignition. The procedure was applied to an experimental combustor to assess the effects of ignitor position, ignitor type and combustor mass flow rate on ignition. Qualitative agreements were obtained. This work represents a promising approach that offers the prospect of generality, unlike some of the earlier approaches.

Calculation of the oxides of nitrogen produced in an engine afterburner system were presented by Foster *et al.*, (Paper 19). This is an important low-observables "stealth" issue, and is concerned with the production of so-called "yellow-smoke." The yellow-tinge is imparted to an engine exhaust plume under certain operating conditions by the yellowish/red-brown color of N_2O_4 and N_2O_5 , which tend to exist in equilibrium with NO_2 . Visibility can therefore be related to the plume diameter and NO_2 concentration. NO_2 comes from NO at temperature, but is reconverted to NO at really high temperatures; therefore, a "temperature window" for yellow smoke exists. Furthermore, an operating afterburner contains high quantities of unburned hydrocarbons, which also promote NO_2 production. The calculation therefore requires careful attention to the chemistry involved. For this reason the authors adopted a post-processing procedure to a CFD flowfield calculation. In this instance, the approach adopted was to uncouple thermal NO formation from the hydrocarbon combustion, together with the simplifying lean-mixture assumption for partial equilibrium of O atoms. To address the issue of super-equilibrium O atoms, the authors used data on O and OH concentrations from strained methane flames for the immediate reaction zone; also, the approximations for O and OH were improved by using partial-equilibrium assumptions for the fast-flame reactions. A joint pdf approach was used for thermal NO . The inlet boundary conditions for the afterburner were based on measured data. Comparisons of the calculations with measured data from the exit plane of the afterburner at several levels of augmentation showed acceptably good agreement for NO , NO_2 and NO_x .

Examples of CFD emissions modeling for lean prevaporized, premixed combustion were presented by Anacleto & Heitor (Paper 32), and Coelho & Selvada (Paper 15), who examined the effects of grid refinement and finite differencing on results for the eddy breakup combustion model within which the constants were also varied. Malico *et al.*, (Paper 53) discussed emissions

modeling for laminar combustion of methane in inert porous media with an integral heat exchanger, using a skeletal reaction mechanism.

Modeling of a different kind was covered by Visser & Kuiters (Paper 21). Almost all published engine emissions data were obtained under sea level, static operation, corrected to standard day conditions. With concerns over aircraft exhaust emissions now being extended from the near-airfield environs to altitude cruise, there is a need to assess emissions produced at altitude. Emissions measurements from engines in altitude chambers are few, as are in-flight measurements. Engine performance at cruise is considered to be competition-sensitive information, and is not readily forthcoming from the manufacturers. To fill these blanks, global engine performance models with integrated combustor emissions models are appearing. Such models allow optimization of flight mission profiles to minimize emissions and fuel consumption. The combustor model used by Visser & Kuiters in their performance model is relatively simple but does allow for a degree of generality. It consists of a stirred reactor network, the elements of which and their connectivity, represent global approximations of the real flow processes in an actual combustor. Rather simple kinetics are solved on the reactor network, with equilibrium assumptions and empirical sub-models being incorporated as computational shortcuts. Comparison of model results with data from the ICAO emissions databank up sea level engine operating lines was promising. However, the point was made that the approach is probably best used for sensitivity studies. Results were also presented to show the effects of alternative fuels in industrial gas turbines.

Work of similar content was presented by Doepeheuer & Lecht (Paper 20). In this case the combustor emissions were modeled using the simpler approach of scaling reference values. However, the overall model did incorporate aircraft performance also. Comparisons with emissions from the ICAO databank for three engines up sea level operating curves were presented, with satisfactory agreements. The modeling was then used to assess aspects of installed engine performance in simulated airplane missions for sensitivity studies.

Although reasonably well validated against sea level engine performance and fulfilling a real need, modeling procedures such as those described in Papers 21 and 20 are potentially dangerous until they can be calibrated against real altitude emissions data. For this

reason they should continue to be confined to sensitivity studies as described here.

Paper 51 by Schmehl *et al.*, presented CFD modeling of a dilute treatment of a polydisperse spray of liquid aviation fuel with evaporation, in which droplet secondary breakup was also modeled using empirical relationships for the different modes; droplet initial conditions were measured in a companion paper (Paper 16). The computational domain consisted of a segment of a premixing duct and the downstream combustor, although only results for the premixer were presented. A hybrid procedure was used, where an Eulerian approach with a coarse discretization of the spray was used to precondition the two-phase flow field to provide droplet sources for a conventional Lagrangian treatment in which a finer discretization of the spray is achieved and which contains the droplet secondary breakup calculations. This hybrid procedure combines the computational efficiency of Eulerian approaches with the high resolution of Lagrangian approaches, and results in a moderate reduction in solution time. However, time savings are case-dependent, and it is not immediately clear whether they are worth the additional complexity of the hybrid procedure.

Prommersberger *et al.*, presented a paper (Paper 16) on experimental measurements and CFD calculations of a liquid fuel spray, that is a companion paper to Paper 51. The spray measurements were performed in the premixing duct of a can-combustor at pressures up to 8 bar through a double-window system. A PDPA instrument was used at five axial stations in the duct, with off-axis collection of the signal. At each station the measurements included radial liquid volume fluxes, droplet mean velocities and SMD values. Visualization of the spray was provided by laser light sheet. LDV was used to characterize the premix duct air inlet conditions. The droplet portion of the calculations was based on a Lagrangian treatment of the spray. Within the Lagrangian calculation, a fractional distillation evaporation approach was incorporated to take account of the multi-component composition of real fuels. In this simulation, the droplet temperature profile was uniform in the assumed single-component liquid, which however, changed its thermophysical properties appropriately during evaporation. The droplet drag law used included the effects of evaporation. Droplet initial conditions for the calculation were taken from the first measurement station. The calculations were in qualitative agreement with the measured spray behavior; however, droplet sizes were over-estimated, and as a consequence, the volume flux distributions also. It was concluded that inclusion of droplet

secondary breakup was necessary to improve the agreements. Comparisons in the premixing duct of vapor concentrations for diesel fuel and tetradecane showed that the greater volatile content of diesel fuel resulted in higher vapor radial dispersion and greater vapor concentrations than for the tetradecane.

There is a need in many practical applications of CFD to gas turbine combustors to consider the effects of chemical kinetics in the combustion modeling. This involves two important steps: establishing suitable reaction mechanisms representing real fuels, and then radically simplifying these mechanisms for incorporation into CFD codes. Mechanism simplification is necessary for two reasons: First, the kinetic ordinary differential equations are mathematically stiff; and second, for each chemical specie in the mechanism a flow transport equation must be solved. While the former difficulty is being addressed by algorithm development, the latter is fundamental to CFD, and constitutes real solution time and convergence constraints, especially for recirculating flows. Two papers on modeling and reducing kinetic mechanisms for real fuels, methane and kerosine, were presented.

Paper 12 by Linan *et al.*, dealt with methane/air in lean premixed flames, with the intent of establishing good representations of the CO and NO_x produced, although the NO_x chemistry was not treated. The base reaction mechanism involved 195 elementary reactions and contained 34 species. Sensitivity calculations were performed with the base mechanism from 8.5 to 40 bars pressure and appropriate mixture initial temperatures, but mean equivalence ratios were confined to the range 0.45 - 0.60. From the sensitivity studies a reduced mechanism with 57 elemental reactions involving 17 species was produced. Steady-state approximations were then applied for 10 intermediate species. Two different, 4-step global mechanisms resulted from these simplifications; the first with CO, H₂ and H as intermediates, and the second with CO, H₂ and OH as intermediates. The rate constants for each of the global reactions depend on the several elementary steps that made-up the detailed chemistry. An important observation was that accounting for the CH₃ attack on HO₂ and OH was essential in this. Good descriptions were provided by both mechanisms, of laminar flame speed, flame structure, radical concentrations and strain effects. Using only the H-based mechanism, further studies established appropriate forward and reverse rate constants. Limit analyses then permitted a further reduction to a 2-step model. The 2-step model performance was examined by

considering one-dimensional flames and comparing the reduced model results for mole fractions against the detailed model results. The 2-step model satisfactorily described the one-dimensional flame structure, including profiles of relevant intermediates and gas temperature.

Establishing reaction mechanisms for kerosine-based fuels is a much more difficult task than it is for pure substances such as methane. Cathonnet *et al.*, (Paper 14), contributed to this effort.

The approach taken in Paper 14 was based on the experimental observation that in jet-stirred reactors and premixed flames, the combustion behavior of kerosine was very similar to that of n-decane. It was also experimentally observed that kerosine produces more aromatics as combustion products than does n-decane. Therefore, a detailed reaction mechanism for n-decane had added to it detailed mechanisms for oxidation of toluene and cyclohexane, and this formed the detailed mechanism simulating kerosine. The mechanism consisted of 692 reversible reactions involving 113 species. Jet A-1 was represented as 78% n-decane, 12.2% toluene and 9.8 % cyclohexane. The detailed behavior calculated by the mechanism for this surrogate fuel was compared with jet-stirred reactor results for Jet A-1/air combustion. Reasonable agreement for the major products was found at 10, 20 and 40 atm. pressure, for 0.5 and 1.5 equivalence ratios, and residence times of 0.5 to 2.0 seconds. The limited objective of a reduced mechanism based on the detailed mechanism, was established as predicting extinction limits to reasonable accuracy. Reduction was conducted in two steps: A sensitivity analysis was followed by steady-state assumptions for appropriate species. The first step gave a skeletal mechanism of 283 elemental reactions involving 78 species. Agreements on extinction temperatures at 1 and 40 atm. and, 600 and 900°K initial temperature, were excellent. The second step identified 30 fast intermediates, and with the steady-state assumption, gave acceptable agreements on extinction temperatures at 10 and 20 atm. for initial temperatures of 300 to 900°K.

Paper 13 by Zumuner *et al.*, applied detailed kinetics for methane to three-dimensional modeling of a relatively simple can combustor that contained the essential major features of a complete gas turbine combustor. Favre-averaged equations of motion and species conservation, were solved, together with a PDF-transport equation. For the latter equation a Monte Carlo Lagrangian solution was used. This was implemented in a hybrid fashion where first, complete Eulerian solutions for the mean flow were obtained

using the $k - \epsilon$ turbulence model and an algebraic fast-chemistry combustion model. The Lagrangian step was then executed using the Eulerian solution as initial values. Iteration between the Eulerian and Lagrangian steps was then conducted, but without the fast chemistry model. The methane/air chemistry used involved 35 species and 250 intermediate reactions, and this mechanism was solved using a low-order (2-D) manifold method. Unfortunately, experimental results from the subject combustor were not yet available for comparison with the calculations. The calculated results appeared to be realistic though. The solution times seem to be promising.

The modeling described above has all dealt with aspects of physical modeling. There was only one paper presented that addressed numerical methods explicitly. Paper 11 by Selcuk & Oymak, discussed a novel time-dependent DNS code based on the method of lines, that includes high-order accuracy, a parabolic algorithm for pressure and an elliptic grid generator using body-fitted co-ordinates. Although the code is presently two-dimensional, incompressible and single-phase, it offers the potential of accurate DNS simulations with reduced solution times for a given resolution.

Comments:

Numerical modeling has now become ubiquitous in the design and development of practical combustors for gas turbine engines. It would not be possible for engineering staffs today to satisfy the business demands of product timeliness and reduced development costs, without numerical modeling. In this respect, where component and engine testing is becoming too expensive and too time-consuming, the most significant contribution that numerical modeling currently makes is in the area of program risk-management, although this is frequently not recognized by the program managers who reluctantly pay for the calculations.

Given the structure of current CFD codes and the computing environment common in industry, design synthesis using numerical modeling is to not all easy. The cost-effectiveness balance means that CFD presently remains a better analysis tool than a design tool. While common-file structures are helping to change this situation by providing easy links to other analysis programs and CAD systems, there is still a long way to go to provide the ideal "What if?" tool.

CFD is still too expensive for many industrial needs, for example, implicit and detailed emissions calculations, and blowout and ignition. This is leading to some ingenious post-processing procedures that bring in other types of modeling as appropriate. Several examples of this have been described in the meeting, and useful contributions can be made through this approach. Part of the expense problem is that making sophisticated engineering calculations with a code still requires "expert guidance" if dangerous and misleading mistakes are to be avoided. This situation is unlikely to change in the near future; indeed, given the sophistication of modeling seen during the symposium, this situation is likely to become exacerbated in the future.

Even with the best physical modeling available, and in the industrial computing environment, for real situations the solution accuracy is still determined by the grid used (resolution) and the specification of the boundary conditions (calculation domain). Most engineers elect to use their available computing power to better resolve shear layers and/or to extend the calculation domain to directly include flow from the compressor and into the turbine (with an inlet guide vane simulation); they "get by" with just enough physical modeling to represent their flow situation. Making the appropriate decisions is one of the reasons why "expert guidance" is part of the task. For reasons of accuracy, attempts are being made, as was illustrated in the symposium, to "anchor" codes by comparison with experimental data. While this is an acceptable procedure for engineering purposes, it has an inherent danger in that thereafter, the code is "locked-in" to the models, algorithms, grids and calculation domains, used in the anchoring procedure. With time, this gets forgotten by the users, and subsequent "refinements" can take the code further from its anchoring without the user being aware of the danger. A prime example of this is the much-attacked but still used, two-equation $k - \epsilon$ turbulence model, the constants of which were numerically-optimized on 20×20 grids. If these dangers with anchoring are recognized and contained, there remains another insidious effect of anchoring. Since an anchored code cannot be used far from its anchoring, its use can lock designer thinking into what is known as incremental technology which can lead to non-competitive products. Calculations involving detailed kinetics in real combustor geometries and environments are also important. In addition to allowing for verification of the accuracy of advanced combustion modeling, they indicate the way for future calculations and allow exploration of the most economical implementations.

In view of these comments it might appear reasonable to question the need for some of the comprehensive physical modeling described in the papers presented. Exhaust soot is an example. The many individual chemical and thermophysical processes of soot production are poorly understood and are not well-modeled even individually in simple controlled experiments; soot burnup in engine combustors is in a similar position, and does not take place as a simple reduction in the diameter of a supposed spherical particle. However, it is extremely important that such calculations as soot production and burnup in a gas turbine combustor be attempted. *In situ* calculations of this kind suggest what is important and what is not in coupling effects, they reveal sensitivities, and they can indicate where additional research into fundamentals is needed. They also construct the computational framework for making the calculations when better physical modeling ultimately becomes available. Finally, such calculations can lead to interim pragmatic semi-empirical models that have immediate engineering utility.

Dynamics and Active Combustion Control:

Non-stationary combustion that acoustically couples with the combustion system and/or rotating machinery has appeared from time-to-time over the years on a variety of main combustor and afterburner systems. The results have sometimes been merely a cosmetic annoyance and at other times have resulted in catastrophic engine failures. Either way, expensive major redesigns have been needed to eliminate the problem. With the advent of low emissions combustion systems, the incidence of acoustically-coupled non-stationary combustion has dramatically increased, especially for LPP combustion systems. The design features for LPP combustion systems are such that the efficacy of passive control features are much reduced. Active combustion control is becoming of growing interest as a means of eliminating such problems.

Paper 6 by Pandalai *et al.*, provided a good review that typifies current industry operating experience and design philosophy as applied to industrialized versions of aircraft gas turbines for ground power generation, and having low emissions combustors. The state-of-the-art with respect to calculation of combustion instabilities is also briefly described. The methodology for control of combustion dynamics is largely empirically-based and relies on design experience. Great use is made of passive means of control such as Helmholtz and quarter-wave resonators, flow bleed, and creative fuel staging.

Modeling of combustion dynamics is playing a growing role. The wave equation is solved with incorporation of physical sub-component models for the entire combustion section for coupling with the combustor diffusion system. The combustion sub-model includes coupled unsteady heat-release. Realistic upstream and downstream boundary conditions are provided in terms of reflection coefficients for the turbomachinery. This modeling system is calibrated for ultra-low emissions designs against engine test data. Active control for these engines is provided by control of temperatures in the combustor dome via a feed-back loop that prevents local acoustic-driven blowouts through the injection of a small amount of fuel to enhance the lean blowout limit.

A passive means of control was described in Paper 9 by Anderson *et al.*, which outlined a novel and clever optical technique for assessing, and thereby *a priori* screening, the propensity of liquid fuel, airblast-atomizing injectors to spray/acoustic coupling. The technique relies on the ability of the aromatics and additives in jet fuels to fluoresce when excited by laser light at blue-green wavelengths. The fuel injectors were actively forced by an acoustic driver applied to the plenum chamber feeding atomizing air to the tested injector. A uniform laser sheet projected through the spray excited fluorescence that was proportional to the fuel mass within the light sheet. Continuous monitoring of the fluorescence intensity provided a temporal record of fuel mass and its fluctuations. The degree of interaction between the pulsed air supply and the spray was quantified through the coherence between the acoustic pressure signal and the fluorescence signal. High coherence indicates an injector that probably should not be incorporated in an engine. Additional analysis of the fluorescence signal revealed that the spray acts as a bandpass filter, only allowing significant interaction over a limited range of frequencies.

It was indicated above that passive control measures only have limited effectiveness, and that forms of active control for combustion dynamics are beginning to appear. Paper 36 by Yang & Schadow presented a review of two recent AGARD workshops on the subject that examined the state-of-the-art with respect to active combustion control for propulsion systems. These workshops considered additional propulsion systems other than gas turbines, and also took into account the experiences of the industrial power generation gas turbine. The workshops addressed possible applications in regard to future combustion requirements for advanced gas turbines, the current status, and the research and development needs. It was concluded that the relative priorities for active

combustion control were low for the aero-gas turbine, high for the industrial gas turbine, medium for air-breathing missiles, medium for solid fuel rockets, and low for liquid fuel rockets. It emerged that knowledge of appropriate scaling laws for successful translation of laboratory tests to full-scale application is relatively poor. It was felt that considerable research and development work, both experimentally and computationally, still remains to be done in order to achieve practical success and widespread application.

Some of the basics of combustion instabilities and their active control were eloquently discussed in Paper 37 by Zinn, Lieuwen & Neumeier. The example used to develop the major arguments was that of the lean-burn, premixed, gaseous fuel, low- NO_x gas turbine combustion system for industrial power generation. In this case it was demonstrated by means of time-dependent well-stirred reactor calculations that the dominant mechanism for instability was due to fluctuations in local equivalence ratio at the front of the combustor. These are driven by the unsteady combustion process, which causes pressure and velocity fluctuations near the fuel sources. Combustors of the example-type are extremely sensitive to equivalence ratio perturbations because operating close to the lean limit, as they do for low NO_x , spatial and temporal flame extinctions can be caused by the fluctuations. The mechanism for driving equivalence ratio fluctuations was described using a characteristic time analysis to address the role of convection in transporting equivalence ratio fluctuations. Although lacking damping effects, the described mechanism was applied to the experimental data of Straub & Richards, and showed good agreement with the measurements for instability regions. Comparison was also made to additional experimental data from a Georgia Tech. combustor, and again excellent agreement was obtained.

Understanding of the mechanism of this instability allowed passive control measures to be considered, and a successful example was mentioned. In general however, it was concluded that passive control approaches do not offer sufficient flexibility for all situations, and only work for single modes, whereas many modes are often excited; a supporting example was given. Active control offers an alternative way of suppressing these instabilities.

The Georgia Tech. active control system was described. It consists of a pressure transducer that senses all modes of significant amplitude, an observer that determines the unstable mode characteristics in near-real time, a controller that provides phase and gain (via a

lookup table based on separate open-loop experiments) for each identified mode, and an actuator that modulates a portion of the total fuel supplied to the combustor. Successful control experiments using this system were described.

An interesting elaboration of this discussion was offered by Lee *et al.*, in Paper 41, which was presented by co-author Santavicca. This paper offered a more detailed and certainly a thought-provoking, look into the flame phenomena during instability, how the flame phenomena are related to the combustor geometry and its operating conditions, and the effects of modulated fuel injection on these phenomena. Optical diagnostics applied to the Penn. State swirl-stabilized dump combustor with direct gaseous fuel injection were used to provide some clarification of this "phenomenology of instability." The observed instability in this combustor was a longitudinal mode at 480 Hz. The interest was in optimizing the secondary fuel injection to breakup the periodic heat release, and it was described how a simplified view of Rayleigh's criterion can be misleading with respect to optimizing an active control approach.

At atmospheric pressure it was observed that the size of the flames changed during an instability, giving a flame area that varied, and was in phase, with the pressure fluctuations. Flame area fluctuations and equivalence ratio fluctuations were about equal contributors to the total heat release fluctuation; furthermore, flame area fluctuations were better correlated with pressure fluctuations than were the equivalence ratio fluctuations. With increasing swirl it was noted that the instability shifted towards the lean blowout limit. The flame images indicated different behavior for swirled and non-swirled flames: Without swirl, flame remained in the centerbody region of the combustor and flame-vortex interactions appeared to be responsible for the instability. Whereas with swirl, flame appeared to leave the centerbody periodically. Distributions of Rayleigh Index had a maximum location where the flame interacted with the vortices for zero swirl, but for swirl, the Rayleigh Index distribution had a maximum removed to the position of flame shift from the centerbody.

For instability control the most effective approach was not to add out-of-phase heat as suggested by Rayleigh's criterion, but to attempt to disrupt the underlying mechanism causing the heat release fluctuations. The medical analogy was drawn to addressing the disease directly rather than treating the

symptoms. For control, a modulated supply of secondary fuel (which was additive to the main fuel) was injected by one of three locations, each of which resulted in a significantly different distribution of fuel in the combustor. For the case with swirl, the instability was suppressed when the secondary fuel was injected in the flame-separation region rather than at the location of maximum Rayleigh Index. For zero swirl, direct injection of secondary fuel into the regions of Rayleigh Index maximum suppressed the instability; injection elsewhere increased the amount of secondary fuel required for a given sound suppression by an order of magnitude. The amount of secondary fuel was only slightly dependent on the fuel modulation frequency.

Paper 38 by Cohen *et al.*, described an application of active combustion control to a careful rig simulation of an actual engine instability problem. The system was demonstrated in a single nozzle combustor using a full-scale fuel injector unit, and was operated at realistic engine conditions. The combustion system was of the lean, prevaporized, premixed type, and used liquid No. 2 Diesel fuel. The experimental simulation took appropriate account of the engine volumes and lengths for the upstream, combustion and shroud flow regions, and choked upstream and downstream boundary conditions were applied. The major instability mode was a bulk mode, and pressure fluctuations were coupled with heat release through their effect on airflow into the injector system. It was observed (as in Paper 41) that flame dynamics are important, even at high pressures where flames become more compact, and that equivalence ratio fluctuations (as described in Paper 37) cannot explain all of the observed behavior.

The active control system consisted of a condition sensor, a controller and an actuator. Measurements of combustor dynamic pressure (via pressure transducers) and heat release rate (via optical detection of CH and CO emissions) were both explored for sensing the instabilities, although the pressure transducers were finally used. Several control algorithms were available, and a simple threshold control was eventually used. This algorithm sent a signal to a solenoid valve that served as an actuator, when the sensor signal crossed a pre-specified threshold; the valve opened for positive-direction crossings and closed for negative-direction crossings. A time-delay was added for both openings and closings of the valve. The actuator was a solenoid valve controlling one-sixth of the nozzle total fuel flow. The active control system demonstrated strong reduction in the instability, and was self-tuning for 100-300 Hz; this suppression was achieved simultaneously with low NO_x .

Hoffmann *et al.*, in Paper 40, carried use of active combustion control one further step in describing application to actual engines. The engines were heavy duty industrial gas turbines for stationary power generation. The combustors were annular and used piloted, multi-fuel injectors that can operate in either diffusion, premixed or mixed, modes. Modulation of fuel flow was again used to provide the control, in this instance, of the pilot gas flow. This was achieved by mounting a robust, high-temperature Moog valve on each of the 24 injection units in the combustor, and tuning the delivery system to the acoustic field. The fluctuating pressure in the combustor was measured by upstream pressure transducers, and for one engine, by 12 high temperature piezo-electric transducers around the circumference of the combustor. In principle, each injection unit could be controlled independently from its own sensor. However, advantage was taken of the symmetry of the azimuthal modes to tailor the system to the particular harmonics excited. Thus, in one engine the number of sensors was reduced to 6, each serving 4 valves. In the other engine this was increased to 12, where each sensor served 2 valves. The Moog valves proved to be reliable and robust in the engines. The control algorithm worked in the frequency domain, and provided suppression of the two dominant frequencies. In the second of the engines the controller reliability was improved, and failure-detection features were added to it.

A demonstrator program showed that combustion instability could be dramatically reduced, the operational envelope extended, and NO_x emissions minimized using active combustion control. In engine application the active combustion control system provided instability control up the complete load-line to 102% base-load, and permitted smooth switch-over in burner operating modes. In addition, NO_x emission levels were decreased by more than 60%. However, it was an expensive system. Eventually, passive means were developed to eliminate the instability; however, the active control system provided the time necessary for the development of the passive means of control.

Aspects of adaptive control strategies for reducing longitudinal aeroacoustic instabilities in large, segmented, solid propellant rocket motors were described by Mettenleiter, Haile & Candel in Paper 39. A cold-flow, geometrically-simplified experimental study of the control of acoustically-driven vortex shedding from simulated inhibitors that are placed between grain segments in a rocket motor casing was described. The emphasis was on the dynamics of the controller and the system, and the study set out to

answer specific questions arising from the issue of control. Since combustion apparently plays only a minor role in the observed instability, this is an example of control of dynamics rather than active combustion control. A loudspeaker located at the base of the motor casing served as an actuator. Anti-noise and noise-source disruption control strategies were tried. A microphone and a hot-film placed in the casing wall at downstream locations served as sensors; finally however, a single microphone sensor was used due to flow turbulence effects on the hot-film resulting in a noisy error-signal. Sensors need to be as strongly correlated as possible to the noise to be controlled. An adaptive controller was able to reduce the pressure oscillations up to 40 dB, while automatically adjusting to changes in air mass flow rate in the casing. However, the controller efficiency fell off at higher mass flow rates. The feedback mechanism was less successful with broad-band and low amplitude frequency components than for discrete frequencies at peak amplitudes, since it involved forward extrapolation in time. The controller was found to act simultaneously on both the noise and its source, and typically, less than 50% of the acoustic power in the system had to be applied to achieve control.

Comments:

In the past, occurrences of acoustic coupling in the combustion system, and of the combustor with other engine components, were addressed entirely through avoidance by passive means. The most common approach used was to change the fuel injector design in order to modify the liquid fuel spray characteristics so as to establish benign burning behavior. Such "cut-and-try" *ad hoc* approaches were time-consuming and expensive. Design trends in the gas turbine combustion system, driven by the military for high engine thrust/weight ratios for liquid fuels and low- NO_x combustion for commercial aviation (liquid fuel) and industrial power generation (liquid and gaseous fuels), have resulted in well-mixed fuel/air combustion systems. As a consequence of the improved mixing, there are growing incidences of such combustion dynamics being encountered. The additional constraints on the combustor designs reduce the scope and efficacy of passive solutions for eliminating these combustion dynamics. Additionally, the present competitive and economic climates of the industry no longer permit the old approaches to solving the problem. Therefore, there is a growing effort to fully understand the problem, and to eliminate it by active control of the processes driving it.

Not surprisingly, passive solutions remain the preferred approach by industry, as was expressed by Paper 40 from Siemens where active control was used in the field **only** to buy time while a passive solution was found. Combinations of passive devices and avoidance procedures were described in Paper 6 from General Electric, and a clever fuel injector screening approach for minimizing the propensity to combustion dynamics was described by United Technologies Research Center in Paper 9. It is apparent that concerns over the reliability of sensors and actuators, especially the latter, together with system cost issues, presently dominate industrial thinking so far as deployment of active combustion control goes.

It is equally clear that active combustion control can effectively provide a solution to the combustion dynamics problem, as was convincingly demonstrated by Zinn *et al.* in Paper 37, Cohen *et al.* in Paper 38 and Lee *et al.* in Paper 41, as well as by Hoffman *et al.* in Paper 40. The preferred actuation is through modulation of fuel flow by means of secondary injection. Paper 40, where a very considerable number of megawatts was modulated, was particularly impressive in this respect.

It is also clear that the understanding of the phenomenon is by no means complete, as can be evidenced by comparing the discussions of Papers 37 and 41. Papers 41 and 38 both suggested that equivalence ratio fluctuations alone are a necessary but not sufficient cause of combustion dynamics, and that flame phenomena are also important. Several of the papers observed that it is better to work directly on the phenomenon as well as on disrupting its source. Despite this lack of a full understanding, effective and robust control can be obtained. However, to optimize systems, a much fuller understanding than is available now will be necessary. Some of the pragmatic procedures adopted by industry to get around this lack of complete understanding were described in the methodologies used at General Electric. A good summary of some of the issues associated with active combustion control was provided in Paper 36 from Yang & Schadow.

It is interesting that Papers 40 and 38 also showed that active combustion control, either directly or through conferring increased system operational robustness, could also be used to reduce NO_x emissions. This is a pro-active development that offers an exciting promise for the future. The idea of "intelligent engines" that sense present behavior and automatically change themselves accordingly to achieve

extended operating envelopes, lower emissions, extended durability and trouble-free operation, will assume growing importance, and is an area to be pursued.

Emissions:

The majority of the papers in the emissions category were concerned with NO_x , and dealt with ways of achieving low NO_x without sacrificing any of the other design requirements placed on combustors. Most of the papers were concerned with aero-engine applications.

Fuel-staging is a convenient way in which to separate combustor design functions into different burning zones, each of which may then be optimized on an individual basis. Since the number of functions required of each zone is reduced, low emissions designs for each separate zone may be produced without severe penalties on the major functions of the zone. Zone interactions then remain to be addressed.

Paper 27 by Brehm *et al.*, investigated zone interaction and overall optimization in an axially-staged annular combustor (ASC) for which a constant fuel split of 20/80 by mass for the pilot to main zones was maintained. Optimization was approached by (somewhat) systematic geometric changes to vary main zone combustion volume. CFD was used to evaluate the numerical effects on the planar averages of NO_x axial distributions, and gas outlet temperature distributions. These were compared against experimental data, described in a companion paper (Paper 18). In the calculations, the NO_x was obtained by post-processing the converged solutions; calculated NO_x levels agreed well with the measurements. In addition, contour plots of calculated mean dissipation rate, equivalence ratio, temperature and stoichiometric surfaces were compared on a quantitative basis. The measured temperature distributions represented as pattern factors (OTDF's) and profile factors (RTDF's) were always lower than those derived from the calculations. One possible explanation of this behavior is that the fuel/air mixing in reality is better than that in the calculations, for which the turbulent Prandtl and Schmidt Numbers were maintained constant at "standard values." Reducing the depth of the main zone (and hence, its volume and mean residence time) reduced the NO_x . However, it is not immediately clear how much of the effect is due to reduced main zone residence time and how much is due to the different interactions between zones as the pilot zone flow enters the main zone. There are also additional considerations in the main zone, where the inner liner contour changes with volume changes also result in different trajectories

for the inner liner combustion air jets, which in turn, modify their interaction with the main zone fuel sprays.

This paper illustrates the present difficulties referred to above in the previous section concerning utilization of CFD in its current form as a design tool to optimize a geometry for a given performance or emission level. Since one of the staged combustor configurations gave NO_x results essentially no different than an unstaged conventional annular combustor of similar volume, it also demonstrates the great care that must be exercised in implementing low emissions designs, and that some optimization work is always necessary.

The hybrid fuel injector with a pressure-atomizing primary and an airblast-atomizing secondary, is a convenient way to address some of the difficulties associated with poor atomization at low air pressure drops for pure airblast atomizers and, spray-cone collapse at high combustion pressures and poor atomization at secondary cut-in for dual-orifice pressure atomizers. However, hybrid fuel injectors can perform quite poorly if not correctly designed. Such poor performance can result in adverse exhaust emissions as well as other combustion problems. The issues associated with hybrid fuel injector design for low emissions were clearly discussed in Paper 34 by Razdan, who also covered aerodynamic influences on flashback and the role of droplet evaporation in autoignition in low equivalence ratio fuel/air mixers.

It was shown that the effects of air/liquid mass ratio on the atomization achieved by hybrid injectors is different depending on whether it is the liquid or the air mass flow rate that is varied. In addition, it was shown that air/liquid mass ratio is inadequate to characterize injector performance. It is well-known that a given injector may not fully utilize all of the atomizing air supplied to it. For this reason, Razdan advocated internally-mixed atomizers. Interaction of primary and secondary sprays can result in better atomization of the combined spray for a hybrid over wide ranges of fuel flow. If the hybrid fuel injector is used co-axially in combination with a main air swirler, the presence of the main swirler air can change this spray interaction. Therefore, careful optimization is necessary to avoid degradation in atomization in a combustor.

For flashback avoidance in a lean fuel/air premixer, conventional wisdom indicates that a flat profile of fuel concentration across the mixer is desirable. According to Razdan, it is necessary to tailor the fuel concentration profile to match the air velocity

profile at the maximum gas velocity axial station of the premixer. With respect to autoignition in premixers, Paper 34 indicates that a knowledge of the spray evaporation history is critical to estimating the ignition delay time. Fully prevaporized, lean premixed systems with liquid fuel will be limited to operating pressures of 40 - 50 atm. due to autoignition, even for separation-free and wake-free flow in the premixers.

Paper 23 by Wedlock, Tilston & Seoud, addressed some of the issues raised by Razdan in Paper 34 by exploring the design features of a lean burn, premixed, prevaporized combustor that utilized a pilot. The intent was to design for robustness in order to ameliorate the potential dangers of premixed combustion in aero-gas turbines.

A design study was conducted to determine the best distributions of fuel and air, and the arrangements of pilots, premix ducts and main combustion zones for the chosen engine operating conditions, which represented both supersonic and subsonic turbofan applications. No air was available for a conventional dilution zone to tailor gas outlet temperature distributions for the turbine. Almost half of the total air was used in the premix ducts, and that remaining for cooling was limited compared to conventional practice. The fuel mass flow rate splits between pilots and main zones for both applications was 50/50 at climbout, 30/70 at take-off and 27/73 at cruise; only half of the premix ducts were fueled at climbout. Significantly, only the pilots were fueled at ground idle, idle descent and approach power settings. Use of pilots-only during approach is manifestly unsafe in the event of a refused landing and go-around situation, and would probably not be allowed by certification authorities. The need for two staging points is noteworthy. Modular construction was used for the pilots, and 13% of the total air was utilized for cooling; fuel injection was by airblast atomization. The pilots and the premix ducts (also modular) bolted onto the main zone combustor bulkhead in a circumferentially-alternating arrangement, with 4 premixers between a pair of pilots. The premixers utilized a simple, pre-filming airblast-atomizer with a turbulence generator to assist fuel distribution. Measurements indicated that some liquid droplets were always present at the premixer exit, even at high air temperatures. Enhanced convective cooling of the premixer walls was used, with the spent cooling air being discharged axially as a wall air-film near the premixer exit. This is a desirable way to prevent flashback along the wall boundary layers. Flame was stabilized in the main zone in the dump recirculation regions formed on the simple bulkhead dome. Testing

revealed that flow into the pilots and premix ducts was distorted by the diffuser/dome flow field. This is a serious safety concern with all premix applications. For a variety of reasons the orientation of the premix ducts with the main zone dome had to be 90°, so that advantages of impinging the premix duct discharges could not be realized.

Sector-testing showed encouragingly low NO_x at pressures below 10 bar; however, the NO_x levels were not as low as was anticipated for premixed combustion, and revealed a pressure-dependency. This was attributed to the presence of the unevaporated liquid fuel exiting the premixers. At idle, idle-descent and approach power settings on the pilots alone, NO_x levels were comparable to a reference baseline; at climbout, take-off and subsonic cruise, the NO_x levels were 35%, 23% and 27% of the reference baseline respectively. High power smoke levels were very low, as expected, and idle combustion efficiency was "good;" however, altitude relight would have been unacceptable. No flashback or autoignition was encountered up to 17 bar and 857°K inlet temperature.

Although describing a well thought-out and carefully executed program, Paper 23 reveals the serious difficulties, as well as the low- NO_x potential, of translating the lean, premixed, prevaporized low emissions approach into a practical combustor that is safe while meeting all the operability requirements. The difficult environment and wide range of operating conditions of aircraft gas turbine engines severely challenge any low emissions concept. Much additional work would be necessary before such a combustor could be considered engine-worthy. Given the suggested pressure limits on premixed systems described in Paper 34, compared to today's and likely future engine operating conditions, one has to question the efficacy of the approach.

A relatively comprehensive experimental study of autoignition and flashback in premixing ducts for LPP combustors was described by Guin in Paper 30. Such work is exceedingly dangerous, and Dr. Guin's courage has to be respected. A variety of premixer configurations was tested, all involving swirl at either the premixer inlet or its exit, in conjunction with an exit cross-section that diverged. Airblast atomization of the liquid fuel was used for all concepts. A typical SMD for the sprays was about 37 μm , flat across the duct exit section. The tests were made with kerosene at air pressures up to 29 bar with inlet air temperatures to 900°K. The premixer walls carried a line of thermocouples and a line of fiber optic cables connected

to remote photo-electric cells. Autoignition was detected optically by a steady signal of several milliseconds duration that immediately saturated the photoelectric cells. Flashback was also detected optically by unsteady signals arising from local extinctions. Flashback interpretation was much more difficult than autoignition due to the several mechanisms that can result in, and terminate, flashback on a local basis in the wall boundary layers. Detection of an autoignition or flashback event triggered an automatic fuel shutdown to protect the rig and facility from damage. Mean and fluctuating velocity components at the premixer exit were measured by LDV at fixed operating conditions to characterize the premixer flowfields.

Autoignition was represented in Arrhenius form, with the global activation energy, pre-exponential rate constant and pressure exponent all being determined from the data. The pressure exponent was established as being 0.9 for these experiments. Data for three of the premixer configurations were well-correlated by this form. Flashback was observed for three of the configurations, and the behavior for the different configurations was complex. The rich limit for flashback was characterized by the pressure drop across the premixer for one of the concepts, but was independent of pressure drop once a minimum value was exceeded for another; for yet another configuration a combustion instability resulted from flashback.

Paper 30, although providing some possible encouragement with respect to autoignition, amplifies the concerns expressed following Paper 23 in connection with flashback. It clearly indicates that generalizations about flashback are extremely difficult and that every premixer has to be examined extremely carefully for its flashback propensity. Even the situation with respect to autoignition is not without concern for Paper 30 is in conflict with one of the standard publications on autoignition with respect to the important pressure exponent. Why this is must be resolved so that absolute limits for autoignition can be established with more certainty than at present.

Paper 7 by Ripplinger *et al.*, presented another implementation of a lean, premixed, prevaporized low emissions combustor. Again, the application was an aero-gas turbine. In this instance the premix ducts were similar to those of Paper 23, but their discharge instead of immediately entering the main zone through a bulkhead dome, entered at the main zone inner liner wall via a conical cyclone. The swirling flow in the cyclone provided flame stabilization in this pilot-less design. A prefilming airblast atomizer was used in each premix

duct, a number of which were disposed around the circumference of the annular main zone. Again, a large quantity of air, 43% of the total, entered the premix duct; 16% entered the cyclones and the remainder entered the main zones, in both cases as cooling air. Understanding of the flow behavior was obtained through a supporting CFD analysis, which revealed a pronounced recirculation zone in the cyclone. Tests of a single, rectangular segment of the design were conducted up to 20 bar pressure, with inlet temperatures up to 820°K. No autoignition or flashback was encountered, although the operating conditions were such that from the data in the literature, autoignition was to be expected. Tests of the premix duct alone indicated the evaporation history along the duct, as a function of pressure, as well as the dispersion of fuel normal to the flow direction. These tests allowed optimization of the premix duct. However, some wetting of the walls with liquid fuel did take place.

The NO_x results did show a pressure dependency, with an exponent from 0.25 to 0.5, typical of lean, well-mixed combustion. The NO_x levels were below those of a low NO_x diffusion-flame reference combustor. CO levels were on the high side, especially at lower equivalence ratios, and this might prove to be a problem. The high CO was attributed to reaction-quenching in the film cooling. Although adequate flame stability was claimed, the leanest mixture investigated was only 0.5 equivalence ratio at 6 bars, whereas a real engine would require at least 0.06 equivalence ratio lean blowout at 3 - 5 bars pressure. The authors recognized this and suggested a pilot and fuel-staging as necessary additions to the design. No dynamic instabilities were observed.

Samuelson & McDonell in Paper 24 discussed more fuel injection considerations for low NO_x combustors of the lean direct-injection type (LDI). The LDI approach recognizes the potential dangers of the LPP approach, and does not explicitly separate the complete fuel evaporation and initial mixing with air from the combustion process. It is therefore a lean, well-mixed, rather than a lean premixed, system. The lean-burn injector (LBI) described in Paper 24 had a fuel injector which was an internally-mixed airblast atomizer, as was advocated in Paper 34, that in conjunction with a main air swirler, is located just upstream of a quarl. The liquid fuel was sprayed radially into the injector internal airflow, and the mixture was then discharged radially from the injector body. All of the combustion air is introduced upstream of the quarl. The intent of the flow velocity acceleration associated with the quarl is to isolate the reaction zone from the

fuel injection and initial evaporation and mixing of fuel and air. Note however, that the fuel was introduced downstream of the plane at which the maximum air pressure drop across the combustor is established. The residence time of mixture upstream of the quarl was only 0.7 ms, which is insufficient to achieve 100% evaporation of liquid fuel, but which is well under the anticipated ignition delay time. Initial test results at 5 atm. indicated encouraging NO_x levels.

Optimization of the injector geometry is being attempted by an experimental parametric investigation, at elevated pressures, of the major influences on droplet size and dispersion. Dispersion of the fuel is optimal for air to liquid mass ratio of around 3. Droplet sizes are strongly determined by the crossflow velocity of the internal air. Although existing correlations for internally mixed airblast injectors describe the Sauter Mean Diameters well, the droplet size distributions are not well represented by existing correlations. The point is made that use of $D_{3,2}$ in evaporation calculations can be misleading since a significant population of smaller droplets will evaporate sooner, and could lead to premature autoignition. Interactions of the atomized fuel and atomizer air with the (swirling) crossflow, into which they are discharged, are also important. A liquid "nodule" can form on the downstream (relative to the crossflow) side of the injector exit orifices. This is undesirable in that it results in large droplets appearing in the spray into the combustor.

Paper 22 by Jentink & van Veen represented a change of pace by describing the development of instrumentation for inflight spectroscopy to directly measure engine emissions at altitude. This is an important topic since emissions are usually only measured on the ground, up a sea-level engine operating line. Only a few measurements exist for engines operating in altitude chambers, and these are not readily available. Direct gas sampling of an engine exhaust plume in flight at altitude by flying probes through the plume is hard on both the chase plane and its crew, and the measurements have an uncertainty introduced by dilution effects that necessitates some plume modeling. However, line-of-sight spectroscopic methods using both light-absorption and light-emission are now being explored. Installation of spectrometers in aircraft requires that they operate in an environment of vibration and pressure changes, which can cause optical alignment difficulties, and instrument modifications may therefore be necessary. The major challenge is light transmission from plume to instrument for emission spectroscopy, and for absorption spectroscopy, additionally from the light source to the plume. Fiber optics may be of help

at UV wavelengths, but not at IR wavelengths. Provisional evaluations in ground tests using commercially available spectrometers installed in a Cessna Citation II aircraft have shown good agreements with direct exhaust gas analysis for CO_2 , CO and NO measurements.

Comments:

LPP low emissions combustion systems are now standard for ground-based power generation gas turbines burning natural gas, and have been extremely successful for this purpose. However, they can be vulnerable to oil-leaks in the natural gas compression system. Also, it is fair to question if this solution will remain viable for the next generation of engines that will have higher pressure ratios and increased firing temperatures. LPP systems undoubtedly can give very low NO_x emissions. They have not yet appeared in aircraft gas turbine engines despite this. Some of the difficulties of applying LPP combustion to aircraft engines are to be seen in Papers 23 and 7, and in Paper 30. The aircraft gas turbine engine has such a wide range of operating conditions, is subject to so many flow distortion opportunities, and has to satisfy so many safety considerations, that the effort to produce successful LPP designs would be enormous. Even if achieved for the current generation of engines, how long a useful life would the concept have? Autoignition poses a fundamental chemical limit on premixing. Razdan in Paper 34 suggest 40 - 50 atm. as the maximum allowable compression pressure. Large commercial turbo-fan engines are already exceeding this lower limit. Logic suggests therefore, that LPP technology would be a poor investment for aircraft applications. It is apparent from the results presented and the conflicts revealed, that more work needs to be done on autoignition of liquid fuel sprays.

LDI concepts, such as that of Paper 24, appear to be more promising for aircraft applications, albeit at some debit in NO_x reduction potential. It remains to be seen if the implementation of the concept in real engines can hold the low NO_x emissions without resulting in a fuel distribution and injection system that is vulnerable to the problems of internal coke formation. Studies like that of Paper 23 are needed to explore the need for staging, suitable pilots, and the coking issues in LDI. Atomization and fuel dispersion are also of high importance in LDI systems. Papers 34 and 24 have indicated the advantages of internally-mixed airblast atomization fuel injectors, and this area should be aggressively pursued. Simple fuel staging alone, such as that described in Paper 27, can confer many all-

round advantages, but can only offer somewhat modest NO_x reductions. It was amply demonstrated by Paper 27 that careful optimization is an absolute necessity to achieve the maximum emissions reductions possible with staging.

The rich-burn, quick-quench, lean-burn (RQL) approach was not discussed at the symposium, which was unfortunate from a balance point of view. RQL can offer NO_x levels comparable to the LDI concept, but appears to have excessive output of particulates. The issue of particulates and aerosols, and their control, is likely to assume a growing importance for all combustors in the emissions field due to their potential in the atmosphere to act as condensation sites with subsequent heterogeneous chemical reactions of exhaust plume minor chemical species.

Military aircraft are not currently subject to exhaust emission regulation for environmental reasons. However, the need for low-observable profiles suggests that exhaust particulates and yellow smoke are stealth issues to be addressed. Paper 19 in the modeling category, touched upon yellow smoke concerns for afterburners. Paper 22 should also raise a warning flag to the military stealth community. Airborne spectroscopy in the UV for detecting NO_x , presently an emerging emissions research tool, could conceivably be developed in the future, into an aircraft detection and active weapons system. Future military aircraft gas turbines with high thrust/weight ratios requiring near-stoichiometric combustion could be large generators of NO_x , even in the supercruise mode, and so become highly vulnerable to such systems. Military gas turbines might then be faced with a need for low NO_x combustion systems.

Design and Development:

Papers dealing with the design and development of gas turbine combustion systems are difficult to write well since in general, a large amount of information has to be communicated in a clear and logical fashion, but in a restricted space while subject to proprietary constraints. Such papers therefore tend to fall into one of two classes: those describing in fairly general terms the many features of a complete system, and those dealing with a somewhat concentrated view of a single feature of a larger system. The information contained in papers of both classes also tends to be system-specific, and is therefore sometimes judged as being of limited utility and long-term value. Whilst these opinions can sometimes be valid, this is not always necessarily so to a discerning audience. In

addition to providing some solid engineering information that may well be useful in broader contexts than those presented, the approaches described in these papers and the tools used can reveal much about the design system, design practices and underlying philosophy of the originating group. Observed weaknesses and strengths can be compared to those of other organizations, and so lead to design system improvements that can provide better designs in a competitive fashion. Design and development papers also provide a snapshot of where real-world technology is at fixed period in time.

Paper 2 fell into the first class of papers, and provided an excellent description of the combustion system for a marine-propulsion adaptation of an aero-engine. Parker *et al.* did a magnificent job in reviewing the background, outlining the design drivers and constraints, and describing the combustor operational requirements. The design team's solutions to some of the problems encountered are presented, together with the performance achieved. Aspects of the development program were also covered. The effort highlighted the difficulties and limitations of working with fixed-geometry combustion systems.

There were four papers that fell into the second class. The first of these was Paper 35 by Heyes *et al.*, that described some atmospheric pressure tests in a small, reverse-flow (with and without the turn-around duct) combustor planar sector rig, comparing liquid fuel droplet distributions and gaseous fuel injection effects on the outlet fields of gas temperature and major species. Included were *in situ* measurements of mean liquid fuel droplet sizes showing the influences of overall fuel/air ratio and air inlet temperature.

Lazaro *et al.* in Paper 25 described some careful work conducted under cold flow and combustion conditions in two planar sector rigs representing a lean, premixed, prevaporized, piloted low emissions combustor that was similar in intent to the combustor of Paper 23, but used strong swirl-stabilization of flame in both pilot and main combustors, and as a means to enhance mixing rates. Although designed for operation at pressures up to 7 bars to simulate engine cruise conditions, only atmospheric pressure results were presented, except for a flame visualization at 2 bar pressure. The combustion rig was provided with optical access for flame observations and application of laser diagnostics. Gaseous propane was used as fuel in the reacting flow experiments. The purpose of the study was to ascertain the influence of the flow turbulence structure on LPP combustion.

The rigs were operated at atmospheric pressure to scaled cruise conditions. The scaling used attempted to match turbulent Damkohler and Karlovitz Numbers. On a Borghi plot the operating condition represented a distributed reaction zone. LDV was used to characterize the flow field and turbulence in the cold flow rig; PIV was used in the reacting flow rig. The cold rig mean flow field was dominated by recirculation zones produced by the swirling flows. Extremely high turbulence intensities exited the premixer, and the flow pulsed axially with an amplitude approximately 0.2 times the main combustor length. The pulsations were associated with the large main recirculation zone. Turbulence length scales in this region were dominated by the pulsation of the recirculation zone. The swirling flow from the main combustor entrained the pilot discharges due to the large velocity differences between them. On a Borghi plot the measured scales fell close to the scaling intent. Based on the cold flow measurements, the anticipated flame structure was modeled using a burning velocity approach. The estimated flame brush average thickness and average position agreed closely with flame visualization, including flame asymmetries, obtained from the combustion test at 2 bars pressure. The PIV results in the reacting flow at atmospheric pressure showed common trends with the cold LDV data for the mean flow. Attempts were made to relate the combustor blowouts to the turbulence structure.

Sturgess & Hsu in Paper 44 describe the lean blowout characteristics of an axisymmetric trapped-vortex combustor in which the cavity length was varied. It was found that for low cavity mass loadings flame at blowout was confined to the cavity, and blowouts were described by well-stirred reactor theory. For high cavity loadings the interfacial shear layer between cavity and mainstream became involved, and final blowout was from the shear layer. The shear layer burning had to be included in order to correlate blowout data, and the blowout equivalence ratios were greater than for cavity-contained blowouts. Cavity-contained lean blowouts were compared to blowouts for conventional swirl-stabilized combustors, and were found to be far superior. However, due to the need to contain burning to the cavity during blowout, it was suggested that the best use for a trapped-vortex combustor is to serve as a pilot arranged parallel to the main in a fuel-staged combustor.

Paper 2 dwelt on the difficulties imposed on designers by the fixed geometry combustor, and many other papers have referred to fuel-staged systems. The alternative variable geometry combustor, by air-staging, is rather difficult to implement in real combustors for

three major reasons: 1.) large quantities of air generally have to be moved from one part of a combustor to another, 2.) compensating air has to be moved to maintain near-constant pressure drop across the combustor, and 3.) the environment is not conducive to actuators involving sliding surfaces and air seals. However, pressure loss compensation is not always necessary. Most rotating machinery can tolerate the pressure drop changes associated with air modulation up to about 12 % of the combustor total, without undergoing re-matching. Quite interesting things can be done with such small amounts of air, provided that the air is directly involved in the combustion process.

Woolhouse *et al.* in Paper 33 developed some interesting ideas concerning the use of fluidics to modulate modest quantities of airflow in a combustor. One particular device described was a radial-inflow air-swirl chamber with a central, axial discharge; liquid fuel was introduced separately into the chamber. Depending on how and where the fuel is introduced into the device, the net airflow can be either increased with increasing fuel flow or decreased with increasing fuel flow. Fuel can be used to either reduce the air-swirl (counter-swirl; downstream introduction) and so increase the air effective area while reducing air-swirl, or, to increase the internal blockage (co-swirl; upstream introduction) and so reduce the air effective area while maintaining swirl. Since the control fuel is introduced into the air-swirl chamber, the device also serves as an internally-mixed airblast atomizer. Also, because the fuel and air are introduced into the combustor together from the swirl chamber, the effect of any air modulation on the combustion process is both immediate and can be dramatic.

Comments:

Despite the upsurge in mathematical modeling capabilities and the growing use of applications modeling, it is apparent that rig testing still plays a major role in combustor development. In the case of Paper 2 for example, it was surprising that extensive water analogy testing was used to provide flow visualization of the complicated flows around and into the combustor can, rather than using CFD which should have been quite capable of providing answers just as accurate and with infinitely more detail. The reasons given for this choice were a) greater confidence in the water analogy testing, and b) timeliness. There are perhaps surely important lessons here for the modelers. An equally possible reason could be associated with shortcomings in the way that CFD is presently managed and integrated into the design and development

process. Generally, physical modelers and code developers are not well-suited, motivated or adequately-staffed to handle day-to-day design/development case studies. CFD should have been much faster than designing, manufacturing, instrumenting, installing, calibrating and testing a water analogy rig, and should have been much less expensive. Paper 2 highlights an example of what appears to be a rather general industry failing.

With testing still of major importance in development work, despite its expense and long time-constant, it is important to do the testing right. Planar sectors for representation of annular combustors were featured in the work presented in Papers 35 and 25. Planar sector rigs are convenient and have their uses, but it is not for exploring outlet temperature distributions, as was the case in Paper 35, for example. The reason is the effects of circumferential wall curvature of the inner and outer combustor liners on the flow trajectories of transverse air jets, and on the mainstream flows around these jets. These are quite different between inner and outer liners of an annular combustor, and generally result in completely different outlet temperature distributions from those obtained in planar combustors. Although not containing transverse air jets, the combustor sector of Paper 25 might exhibit similar effects with respect to interaction of the pilots with mains, due to the relative entry angle between these two.

All combustor rigs, planar or otherwise, should have the correct exit boundary condition, and this is not an open exit. For the reverse flow combustor of Paper 35 for example, significant flame differences were noted with and without the turn-around duct in place. For straight-through combustors the correct exit boundary condition is the turbine entry guide vanes. Consider that for modern combustors, just a few centimeters downstream from the end of a primary zone recirculation where at the aft stagnation point the mean axial flow velocity is zero, the combustion gases and dilution air jets are accelerated up to about 0.8 Mach Number at the vane gauge points. With open-exit combustor rigs this tremendous acceleration and its effects on dilution air jets and mixing, are not represented. It should be noted that this comment also applies to many CFD simulations of combustors!

The convenience, low cost, and, easy optical access and exit-traverse capabilities of planar, open-exit combustor rigs has to be carefully weighted against the realism of the experiment and the validity of the resulting data.

With the overall pressure ratios of modern gas turbine engines becoming so high, the air capacities of test facilities are almost always exceeded for full-scale test hardware, even for reasonable sectors. Therefore, either parametric investigations with extrapolation, or scaling to simulated operating points have to be used. The former approach is attractive for many reasons but is very expensive and can be time-consuming. If scaling is used, a great deal of care has to be taken in selecting suitable scaling criteria. Paper 25 was a good example of defining a clear and limited objective, determining the right scaling for this single objective, and achieving it, for realistic testing of the phenomenon under investigation. (However, if Karlovitz Number is really important in the burning process, it would have been better to have also simulated in the experiment the acceleration associated with flow into the turbine.) With wide-ranging objectives, more than a single set of scaling parameters might have to be considered.

The use of fuel to provide modulation of modest amounts of combustor air, as described in Paper 33, appears as a clever way to avoid the control and reliability issues associated with mechanical actuation in a harsh environment. It represents out-of-the-box thinking that the Keynote Address charged was sometimes lacking today. The Turn-up Vortex Amplifier described is an intriguing device. However, much remains to be done to establish the efficacy of the device for engine use. A not-insignificant practical problem to be solved is that of connecting the combustor-mounted device to an engine fuel supply, while accommodating differential axial and radial thermal growths without allowing any fuel-spillage or backflow from the device. A second difficulty is matching the device characteristics to the desired combustion characteristics. For example, it was demonstrated that device airflow can be a maximum when the fuel flow becomes high, which is good; however, this is at the expense of swirl. Unfortunately, high swirl is needed when fuel flow and airflow are both high in order to stabilize the flame. An auxiliary swirl chamber mounted concentrically about the device, and unfueled, is perhaps a way to avoid this particular difficulty.

Similar devices to the Turn-up Vortex Amplifier have been evaluated previously. Although successful modulation of combustion air in the desired manner was eventually achieved in rigs, and many development problems were solved, including some mentioned in Paper 33, a practical way was not found in an engine to introduce the fuel to achieve the desired modulation in a safe fashion. Interior carbon build-up

led to external fuel spillage and engine destruction, resulting in eventual abandonment.

Optical Diagnostics:

In the recent past a tremendous amount of laboratory-scale work was conducted into the development of optical diagnostics as quantitative measurement techniques. This work demonstrated an enormous potential for learning so much more about reacting flows in a non-intrusive fashion. A few experiments, although not enough, were carried out in simplified representations of gas turbine combustors, even using real fuel injectors. This seemed to indicate that optical diagnostic techniques would become the tool of choice in future gas turbine development testing. This did not happen. The reasons were given as concerns over high pressure effects on some of the methods, the difficulties in providing good optical access, concerns over penetrating luminous flames, the taxing working environment, the requirement for specialized personnel, the program time delays, and above all, the cost. Some of these are valid concerns that have to be addressed. There also seemed to be a difficulty in knowing exactly how to usefully employ the detailed information to be gathered, other than for CFD validation. Fortunately, it appears as though the first tentative steps beyond these barriers, real and perceived, are now being taken.

Paper 17 by Grisch *et al.*, described application of optical diagnostics and CFD modeling to a laboratory-scale hydrogen/air buoyant diffusion flame at atmospheric pressure. The object was to investigate modeling findings concerning Lewis Number variations due to changes in local temperatures and species concentrations that result from compressions and stretchings as vortices interact with the flame. Vortex-flame interactions in the experiment were captured with good temporal and spatial resolutions using CARS, PLIF and DFWM optical diagnostic techniques for simultaneous measurements of temperature and, O and NO concentrations. The influence of argon and nitrogen diluents on the Lewis Number found from instantaneous temperature and concentration maps was in excellent agreement with the calculations.

Krautkremer *et al.*, with Paper 42 used optical diagnostics to explore the jet-mixing behavior in a simplified gas turbine annular combustor primary zone that was fuel-lean, but non-reacting. The intent was to explore the influence of swirl-field behavior at fixed Swirl Number on combustion air jet mixing. The rig was planar with an open exit, and had independently-

metered combustor and liner flows. Each liner wall introduced a single row of transverse air jets into the combustor, that were opposed to one another and positioned 3/4 of a dome height downstream from the dome. A bulkhead dome contained three swirl registers, and admitted the mainstream air which was heated to 325 °K compared to the 300 °K shroud air. Two types of swirler were used in the dome that resulted in swirling flow attaching to the dome in one case, and being detached in the other; for both swirler types the Swirl Number was 1.0. The center swirler of the three could be reversed so that co-rotating and counter-rotating swirl could be introduced. Jet to mainstream momentum ratios were maintained constant.

A five-hole pitot probe was used to provide a feel for local velocities in both attached and detached swirl cases, and wall static pressures were recorded by an array of static pressure tappings. A statistical mixing assessment was used based on measured temperatures, together with invoking Reynolds' analogy between heat and mass transfer. Again, an intrusive thermocouple was used to measure air temperatures. Mie-scattering from seed particles introduced into the appropriate flow was used to provide flow visualization, using the resulting concentration distributions. Analysis of the planar images was done qualitatively by assessing the mixing quality from the ratio of image mean light intensity to the standard deviation from the mean intensity.

It was observed that the presence of swirl had a profound effect on the transverse jet behavior and the mixing. For co-rotating swirl it was concluded that the flow with dome-attached swirl was not stable, and this was confirmed by time-resolved images of the mixing quality which showed large-scale lateral movements of the penetrating jets with time. Flow with dome-detached co-rotating swirl was also found to be unstable. Time-mean and time-resolved mixing was better with dome-attached swirl for both co-rotating and counter-rotating arrangements. Counter-rotating swirl however, resulted in the formation of counter-rotating vortex pairs that impaired mixing compared to co-rotating swirl.

Another level in complexity was reached in Paper 43 by Behrendt *et al.*, who conducted optical measurements in a single-sector combustor with reacting flows at pressures up to 9 bar and inlet temperatures to 473 °K using liquid Jet A-1 fuel. The fuel injector was an engine design, and had a measured Swirl Number of 1.23. The intent of the work was to understand the role of liquid fuel atomization in aero-engine combustion, particularly with respect to lean

blowout although this initial effort was devoted to exploring the effects of pressure and combustion on spray behavior. As the authors point out, this is a particularly difficult diagnostic task due to the high spray densities in the regions of interest. To address this difficulty, coupled planar and point techniques were used to relate global features to local, two-phase flow changes. Optical access to the combustor primary zone upstream of the opposed combustion air jets was provided. Conventional measurement methods were used for pressure, temperature and exhaust gas analysis; video recording was used to identify the flame position and detect any instabilities.

For isothermal flow at atmospheric pressure LDV and PDPA were used to measure gas and droplet velocities, and droplet diameters, in a separate primary zone model that represented the back-pressure effect of the combustion air jets by a cross-stream array of solid rods. PLIF images of OH and liquid Jet A, as well as OH line-of-sight chemiluminescence, were gathered in reacting flows at different pressures up to 9 bar with a fixed inlet temperature of 473 °K; care was taken to ensure that the effects of Jet A components were eliminated from the OH images. Some interesting effects of pressure and combustion on the spray were observed, and not all are presently fully explained. Some of the behavior was different to that observed in other, similar, experiments, and it was speculated that the internal details of the particular fuel injector design can strongly influence the downstream behavior. The spray evaporation region was found to be fuel-rich, and chemical reactions took place in the external group combustion mode. Increase in combustion pressure did not appear to change the droplet lifetimes or the evaporation rate. For this particular fuel injector design the droplet radial velocity component increased and the axial penetration was reduced as combustion pressure was increased. As the spray density was increased the spray angle and recirculation zone size both increased, which is surprising. The gas tangential velocity was unchanged by the presence of combustion, whereas the axial velocity was increased. This implies a change in effective swirl number. Attenuation of gas turbulence due to the presence of small liquid droplets was observed.

The degree of optical diagnostic difficulty was increased yet again by Hassa *et al.*, in Paper 18. In this case, a planar segment of an axially-staged (fuel) combustor was operated up to 6 bar pressure with up to 850 °K inlet temperature, although the capability to go to 20 bar exists. The operating conditions represent an engine part-power level, and therefore, results presented

were confined to the pilot zone. The sector consisted of three pilot fuel injectors, and two main zone fuel injectors, with the main zone injectors being staggered circumferentially in relation to the pilot zone injectors. For isothermal measurements good optical access through the pilot and main zone combustor liners was accommodated by means of extensive quartz panels containing the air ports. For reacting flows, smaller local windows, that could be placed in different regions of the liners as desired, were used in place of the larger windows. The combustor was confined within a pressure vessel whose optical windows carried the pressure loads while remaining relatively cool. The combustor design was identical to that of Paper 27, to which Paper 18 is a companion.

Doppler Global Velocimetry (DGV) was used to determine the three-component gas-phase flowfield by mapping of the entire combustor with a high resolution, and with careful validation to protect against dirty-windows effects. In reacting flow at atmospheric pressure, three-component PDPA was used with the combustor removed from its pressure vessel. The spray was interrogated by planar Mie-scattering, and good agreement with the PDPA results for spray angle was obtained. OH chemiluminescence was used as a flame zone marker, with the line-of-sight being across the entire width of the combustor. LDV was used for the reacting gas field velocities, with the seeding introduced in the diffuser upstream of the combustor to avoid biasing. Refractive index problems due to the multiple windows and window cooling were addressed; also, light-scattering from the liquid fuel droplets resulted in the velocities measured near the injector actually being combined gas/drop velocities. However, combining the PDPA and Mie scattering results in reacting flow provided a good appreciation of the spray behavior, especially when considered in comparison with the droplet flux and SMD profiles. The additional of OH chemiluminescence added information on the flame locations. To ensure correct boundary conditions, the center of the three pilot zone fuel injector was interrogated, and the anticipated problems of light transmission through the outer pilots did not materialize. All the diagnostic techniques were successful, and the preliminary results showed that the detailed fluid mechanics close to the fuel injectors were accessible, at least to 6 bar pressure. For example, the liquid fuel spray cone responded to changing operating conditions by increasing in angle from 1 to 6 bars, and in developing an asymmetry that was consistent with the pilot zone geometric radial confinement asymmetry. Flame was found to be stabilized by the outer recirculation zone for fuel-rich, unstaged operation at

low inlet temperatures, and by the central recirculation zone for fuel-lean, staged operation at high inlet temperatures.

Comments:

The optical diagnostics papers presented almost represented a microcosm of the historical spectrum of development for optical diagnostics, ranging from a classical laboratory experiment with gaseous fuel and no access difficulties operated at atmospheric pressure, to an almost-real combustor segment with liquid fuel and tremendous access problems being operated at elevated pressures. This segment of the symposium surely contained the most exciting and the greatest learning potential of all the interesting work presented: The tantalizing prospect offered was that of being able to "see" in detail what really goes on inside near-real combustors at close-to-real operating conditions!

A great deal of wise forethought has clearly gone into the joint DLR/German industry program, together with the kind of courage that was necessary to commit scarce fiscal and personnel resources to what is a long-term and high-risk effort. The overall objectives surely must have been broader than mere CFD validation, important and useful though that is. Despite the really encouraging start, it is by no means clear that the optical diagnostic techniques will continue to be as successful all the way up to 20 bar. If they are however, then much still will remain to be done for industry to truly benefit from the knowledge that could be discovered. From what has been revealed so far, answers must come to questions like: How do fuel injector internal details exert such a strong influence on the primary zone? Of these influences, what are "good" ones, and what are "bad" ones? How can the injector design be manipulated to eliminate the "bad" influences and enhance the "good" ones? In essence, what could emerge in the future is the chance for the combustion designer to learn how to directly manipulate the details, the small droplets and the eddy length scales, rather than indirectly by pushing somewhat blindly on the boundaries and trying to infer what happened by looking at the combustor exit.

If long-term success is achieved in this area, industry managers will be faced with some difficult decisions on how to best use the capability. The decisions that they will face will be similar in many respects to the decisions with which they had to deal when faced with CFD. One of the principal difficulties that may dictate the ultimate directions taken will be the

absolute requirement for specialized personnel to conduct the measurements and interpret the results.

Fuels:

In gas turbine engines the fuel has to do much more than provide energy to the working substance. Fuel is used to actuate valves, and as a sink for heat generated in the lubricating system, crew environmental system and some electronics. The heat sink demands in particular are increasing dramatically for modern engines and aircraft. At the same time, the environment within the engine that the fuel experiences is continually becoming more adverse. The resulting thermal stress on the fuel can result in unfortunate chemical changes that cause fuel system/fuel injector problems. The effects of such system degradation can have serious impacts on aircraft dispatch reliability, time between overhauls, engine down-time and spares inventories.

One of the methods being developed to combat the chemical changes in fuel is the use of small quantities of inexpensive additives that are designed to enhance the fuel thermal stability. Paper 45 by Bullock, Hobday & Lewis presented experiences with evaluation trials of one of these additive packages in JP-8, termed JP-8+100. The intent of JP-8+100 is to increase the allowable continuous use temperature of JP-8 from 325 °F to 425 °F at the fuel injector.

The evaluations in this case were carried out in an airframe/engine fuel system simulator, and looked at the impacts of thermal degradation on system operation. The program compared the stability behaviors of two JP-8 fuels produced by different refining processes, each with and without the additive package; a reference, high stability fuel JPTS, was also used for comparison. The results indicated that the +100 package improved the thermal stability of both JP-8 fuels, although the degree of improvement depended on the refining process used. Also, neither of the treated JP-8's achieved the stability performance of the referee fuel. A potential danger for field-use of JP-8+100 was discovered for systems that had been operated for periods of time on JP-8 and then were suddenly introduced to JP-8+100. The additive package contains surfactant/dispersant compounds that can clean previously fouled equipment, with a consequent danger of blocking downstream filters with displaced debris. Operational implementation of JP-8+100 therefore has to follow careful protocols to avoid such problems.

From time-to-time, alternative fuels to conventional hydrocarbons appear. One such fuel is

hydrogen, and Paper 48 by Dini outlined some experiences and advantages of considering gaseous hydrogen and mixtures of hydrogen and methane (hythane) as gas turbine fuels. It was shown that a gas turbine engine could be relatively easily modified to operate safely on gaseous hydrogen, and had the same thermal efficiency as for jet fuel. While combustion efficiency was high, so were NO_x emissions and combustor liner temperatures due to high flame temperatures. The fuel mixture hythane has produced low CO and unburned hydrocarbon emissions, and acceptable levels of NO_x . Difficulties of tankage for vehicular applications were discussed.

Comments:

The demands for fuel as a heat sink, particularly for military aircraft, will increase in the future so JP-8+100 can only be regarded as a successful first step. Future high thermal stability fuels will be required not to increase significantly in price. Therefore, the additive approach is clearly attractive. The challenge will be to find new additives that are effective and of low cost, to permit worthwhile increases in the allowable continuous-use temperature at the fuel injector. Such additives should not create biological or environmental hazards in the engine exhaust. With some of the projected future combustion systems designed for ultra-low NO_x emissions the fuel injection system can be highly distributed, resulting in extended runs of small internal diameter passages. Such systems can be highly vulnerable to the effects of thermal degradation of the fuel. Will additives be sufficient for such applications in advanced engines? Additives can only go so far. Eventually, another approach must be considered.

It is difficult to conceive of a better fuel for vehicular use than JP-8. Hydrogen burns "cleanly", but otherwise can be a difficult fuel. Embrittlement of metals, a high diffusion coefficient, an invisible flame that is a safety hazard, and a low calorific value that demands cryogenic tankage are all serious handling difficulties that have to be taken into consideration. For hydrogen ever to achieve widespread and extensive use as a fuel the supporting production and distribution infrastructure costs would be almost insupportable. The hythane concept is one that could perhaps be attractive under certain circumstances. One example might be when the hydrogen component is used in small quantities to extend lean blowout limits of methane in some stationary powerplant low emissions designs (not LPP however, due to auto-ignition/flashback concerns). This aspect might be worthy of further exploration.

Catalytic Combustion:

Catalytic combustion has long appeared as an attractive combustion strategy for achieving ultra-low NO_x emissions by extending lean blowout limits to extremely low levels and thereby resulting in very low flame temperatures. Many catalytic reactions are mass transfer-limited by physical diffusion of reactants to the catalytic surfaces, and by diffusion of reaction products away from the surfaces. For this reason, other than at engine starting, catalytic support of lean homogeneous reactions is the mechanism appropriate for most gas turbines. At this operating condition chemical equilibrium prevails on the catalytic surface, which operates very close to the local adiabatic flame temperature. The device is therefore temperature-limited rather than lean blowout limited. Stability becomes an issue of concern however, in terms of "breakthrough" when, due to high mass throughput, heat release in the front of the reactor bed does not compensate for heat losses due to convection, and gas-phase reactions are extinguished, causing the reactor bed to cool from front to rear. Also, operating close to adiabatic flame temperature, damage to the bed surfaces is sensitive to spatial variations in equivalence ratio, and this can lead to sintering of active catalysis sites or melting of the support structure. For the bed to become self-sustaining upon engine start, it is necessary to preheat the bed up to the catalyst ignition temperature in some way. The overall restrictions imply that catalytic reactors tend to be optimized as single operating point devices, whereas gas turbines have a wide range of operating conditions.

A comprehensive status report was given by Fant *et al.*, in Paper 8, of the U.S. Department of Energy-sponsored Advanced Turbine Systems catalytic combustion R&D effort. The work of multiple companies and university researchers was covered. While several approaches appear to be nearing engine-worthiness, it was conceded that much remains to be done in terms of configuration optimization to simultaneously satisfy low emissions and operability goals. The additional work also included fundamental understandings of the catalytic reaction process. Staged combustor configurations that isolate the catalytic section from an LPP pilot for engine starting, and then may, depending on engine pressure ratio, rely on an engine exhaust recuperator to preheat mixture entering the catalytic stage, address many of the operability problems referred to above. However, preheating the mixture entering the catalyst bed increases the NO_x produced there. Air modulation is used in one arrangement to address the "single operating point limitation of catalytic reactors."

Programs are generally divided into sub-scale tests to evaluate basic behavior, to be followed by full-scale testing for systems and integration evaluations. The sensitivity of the catalyst bed to fuel/air unmixing remains a fundamental issue. Efforts to develop low pressure drop fuel/air mixers were mentioned. Difficulties of a suitable catalyst remain. Palladium based systems have too high a vapor pressure for high temperature operation; however, they are needed for low temperature light-off. Difficulties of light-off at elevated pressures associated with the high partial pressure of oxygen on the catalyst surface have to be addressed as well. For this and other reasons research into the details of methane/air catalytic reactions on palladium/palladium oxide systems is proceeding, especially into troubling hysteresis effects where bed activity can be very much dependent on the previous history. Since palladium systems have maximum use temperatures that are far below the firing temperatures for advanced gas turbines, alternative catalytic systems are being sought. Modeling of catalytic combustion needs considerable improvement. A major part of the difficulty is lack of good combustion models for the heterogeneous reactions on the catalyst surface. Modeling of transient phenomena, such as light-off, breakthrough and non-stationary behavior is also needed.

A European view of catalytic combustion for industrial gas turbines using natural gas was described by der Kinderen & van Yperen in Paper 47, where again, the driver was the ultra-low NO_x potential of such an approach. In this study both experimental and modeling efforts were included, but the experiments were confined to the sub-scale and were designed to support the modeling. The modeling goal was to provide a tool to be used for scale-up and design studies. The experiments were to cover conditions up to 25 bar and 1600 °K combustor outlet temperature with methane as fuel.

The required features for catalytic-based combustion systems in gas turbine engines were first reviewed. In direct contrast to the U.S. Department of Energy program, this program concentrated exclusively on ceramic substrate materials. The suitability of washcoat materials for gas turbine use was experimentally investigated by examining their behavior in micro-reactors, and then evaluating their structural changes and remaining catalytic activity subsequent to the test exposure. It was found that the activity decrease was almost directly equal to the decrease in surface area due to sintering. Kinetic rate expressions were also developed by means of special near-isothermal tests.

An intermediate-scale test rig operating at near full-scale conditions was used to check partial scale-up, and to investigate the homogeneous gas-phase reactions of a hybrid system. This rig included a pre-burner and fuel/air mixers upstream of the catalytic section. Two monolithic catalyst sections were used in series. Noble metal low temperature catalysts and an undefined high temperature catalyst were investigated in separate tests. Model calculations agreed extremely well with measured gas temperatures for both types of catalyst, and agreed acceptably well with measured wall temperatures. The effects of boundary layer development and breakup due to monolith axial separation were well-shown. Most of the fuel conversion took place in the homogeneous gas-phase reactions, with only about 5 % conversion catalytically. However, the catalytic reactor portion only consisted of the two, relatively short axial length sections of monolith in series.

Comments:

On the surface, catalytic combustion for gas turbine engines does not appear to be any further advanced than the previous U.S. effort conducted in the 1970's. That would be a misleading conclusion however. A promising combustor configuration has emerged from Rolls Royce/Allison that, finally, looks feasible for gas turbine requirements. In addition, the understanding of catalytic reactions is being seriously probed, and the modeling capability is greatly improved. Despite this worthwhile progress, the problems remain the same as they were in the 1970's, and the potential answers appear just as uncertain. Serious questions remain concerning the suitability of noble-metal catalysts and metal substrates for advanced industrial gas turbine engine cycles. On the other hand, high-temperature catalysts and monolithic ceramic substrates have not been developed to the levels necessary for this application. It seems as though the dream of ultra-low NO_x by catalytic combustion is likely to remain just a dream for some further time.

Position Papers:

There were only two position papers. Paper 3 by Van Erp & Richman, examined technical challenges of advanced combustion systems from a U.S. Navy viewpoint, with an emphasis on engine thrust/weight ratio. The need for high thrust/weight ratio is driving up combustor exit temperatures.

The effects of near-stoichiometric operation on the make-up of chemical species exiting the combustor, and on the outlet temperature distributions, were

discussed. The implications of possible burning in the turbine airfoil cooling air, and apparent reductions in pattern factor, on turbine durability were described. A new parameter to characterize conditions at the combustor exit was introduced, the Fuel/Air Factor, FAF. The FAF in exit profiles, accommodates local values above the stoichiometric condition. The constraints to producing low exhaust emissions with near-stoichiometric combustion were discussed, and the need for new concepts was stressed. The role of high overall fuel/air ratio in reducing available air for dilution and liner cooling was discussed. It was described how, in turn, the combination of near-stoichiometric combustion and reduced cooling, together with higher cooling air temperatures associated with increased engine pressure ratios, create a combustor durability difficulty. Ceramic matrix composites were mentioned as promising candidates for liner material, but they do not yet have the required material-use temperature necessary.

Overall increasing temperatures in the engine have rapidly eaten away the available heat sinks, and work to further increase the heat sink capability of the fuel was briefly mentioned. Engine thrust/weight ratio is most strongly affected by length reductions. It was mentioned that reducing combustion length demands increased fuel/air mixing, and that a fully-integrated combustion section offers really worthwhile engine length reductions. It was hoped that solutions to these challenges will appear in the propulsion systems of the future.

Khalil & Hitchcock in Paper 1, made the only presentation to directly address the expanded role of the Applied Vehicle Technology Panel, in an interesting discussion on the possibilities of electric drives for military ground vehicles, especially armored fighting vehicles (AFV's). The mobility requirements of AFV's, and how the tractive forces necessary to satisfy them are delivered, were described. Provided that the vehicle engine can produce adequate power, current transmissions can certainly deliver all the necessary tractive forces. However, hybrid electric transmissions can provide faster acceleration and burst power capability, and have other advantages. The faster acceleration is due to the inherent characteristic of delivering maximum torque at zero speed of all electric motors, and the burst capability is provided by the necessary energy storage system. However, although successful demonstrators have been produced, there remain some technical challenges still to be overcome before widespread deployment can be considered.

Conclusions and Evaluation:

The papers presented at the meeting were all of good quality and addressed important issues. The material discussed covered new advances in many areas. The conference proceedings will therefore represent a useful contribution to the gas turbine literature.

The extensive section on physical modeling reflected the continued movement of applied combustion from being an "art" towards an engineering science. However, it is apparent that all the answers have not yet been provided. Design synthesis, using CFD as an optimization tool, remains a goal that is far from being reached. Development by testing remains an integral and essential part of achieving successful gas turbine combustor products, although at an ever-increasing cost. The growing expansion of knowledge from the application of CFD and optical diagnostics to the gas turbine combustor presents a considerable challenge to industry management who must learn how to best utilize both the knowledge and the tools to cut development costs. Modeling is expensive, but if used correctly it can reduce both risk and engine development time. CFD accuracy and capabilities must be expanded while containing costs. Optical diagnostics in real combustors at elevated pressures looks to be on the beginning of a similar learning curve.

The growing interest in combustion dynamics represents the return of an old enemy to the combustor designer. Active combustion control represents the appearance of a promising shield against this enemy. It also appears to offer the prospect of being able to provide combustion enhancements in the way of extended burning limits with lower NO_x. Although successful control has been demonstrated, at present there does not seem to be sufficient understanding of the phenomenon to achieve optimized control. Furthermore, the issues of engine cost and weight increases, uncertain sensor and actuator reliabilities, and systems integration, have to be addressed in engineering terms.

Emissions reduction appears to have reached a plateau, where the realities of engine operation constrain what can be achieved. Catalytically-supported combustion could represent the next stage for ultra-low NO_x in industrial gas turbines, but appears to be far from becoming a reality despite progress with combustor configurations. For commercial aircraft gas turbines interest is moving to altitude emissions; also, the interest in the troposphere seems to be shifting to the roles of particulates and aerosols on the climate change. However, while nothing in this area was

presented at this conference, it is possible that fuel additives may have a role to play here. For military aircraft engines it seems as though emissions could become extremely important in the future. Planned cycle developments could make future engines large NO_x producers, and this could raise stealth concerns through "yellow smoke" and the possible successful development of airborne spectroscopy to detect NO_x at altitude.

If the theme of the meeting is reviewed against these major conclusions, it would be fair to observe that in a larger sense, the meeting did adequately address its theme. Highlight topics for future AVT symposia would seem to be as follows: gaseous and particulate emissions at altitude, optical diagnostics at elevated pressures in near-real combustors, and active combustion control. While it was good to see participation in the present meeting from the other areas now part of the AVT Panels expanded mission, it is urged that care be taken when setting up future symposia, to preserve the tight focus achieved, and not lose it through dilution.

The Applied Vehicle Technology Panel Symposium on Gas Turbine Engine Combustion, Emissions and Alternative Fuels

12-16 October 1998, Lisbon, Portugal

Keynote Address

J.S. LEWIS

SINA - 9

WH35, Rolls-Royce plc

P.O. Box 3, Filton

Bristol, BS12 7QE

United Kingdom

THE COMBUSTION CHALLENGE IN THE 21 ST CENTURY

I would like to thank the members of the Applied Vehicle Technology Panel for this opportunity to present a keynote paper to this audience of International experts in the field of Combustion.

INTRODUCTION

In preparing a keynote address for this occasion I found it instructive to return to the report of a previous AGARD Symposium which had dealt with Combustion issues.

In 1993 (Reference 1) the keynote address by Professor Schumann provided "hard data about the impact of gas turbine emissions on various portions of the atmosphere". Here I quote the words used by George Opdyke in his Technical Evaluation Report on the Symposium - a most useful commentary. It was concluded that the bulk of the reduction of the harmful impact of aircraft emissions on the stratosphere was the responsibility of the gas turbine combustor designer.

An onerous responsibility to bear when expressed in those terms.

I believe that in the last five years our understanding of the impact of aviation on the atmosphere has moved on but there still seems to be a long way to go. Progress has been made in the application of new combustor technology but this too can take a considerable time to introduce into production particularly when the full implications have been identified and accounted for.

OBJECTIVES

In Reference 1, some of the key technology objectives for the future were identified as :-

- *Ultra Low NO_x
- *Combustor inlet temperature of 950K
- *Fuel bulk temperature at the injector upto 750K
- *Equivalence ratios from lean to near stoichiometric
- *Short, light, long life combustor liners with minimum cooling air and advanced materials
- *Little or no reduction in other performance requirements like cold day or high altitude ignition or combustor stability
- *Low pattern factor at turbine inlet

Few of those here today would have difficulty with identifying with those objectives for future applications in the aerospace field although the absolute values would change as a result of looking in the crystal ball.

The need to operate with even more efficient engine cycles to minimise fuel usage and therefore concomitantly carbon dioxide and other emittants will result in higher inlet temperatures to the combustor greater than 1000K at the higher pressure ratios associated with such cycles. Consequently ultra low NO_x technology will be required to minimise the potential increase in that emission.

The fuel bulk temperature at the injector of 750K remains a very challenging target.

The introduction of advanced materials into the core of aerospace production engines has, I suggest, been slower than anticipated but the need to minimise the inefficient use of cooling air remains as a critical design requirement for all gas turbines.

A key objective not identified at that time but now of equally high importance in military and civil aerospace and in land based engines is that of low cost. That is, in research and development, in manufacture and in operating cost. Every low emissions high performance combustor concept that I am aware of is potentially more expensive than today's systems.

APPLIED VEHICLE TECHNOLOGY

The gas turbine engine today is used as the power system for several types of vehicles as suggested by the name of the panel which is organising this symposium - the Applied Vehicle Technology Panel. However, it is clear from the papers to be presented that the application of combustion technology is not restricted to vehicles alone and that the challenge for today and for the future is as likely to come from stationary power generators as from subsonic or supersonic aircraft or ground based transport.

Figure 1 - Aerodynamic Blades

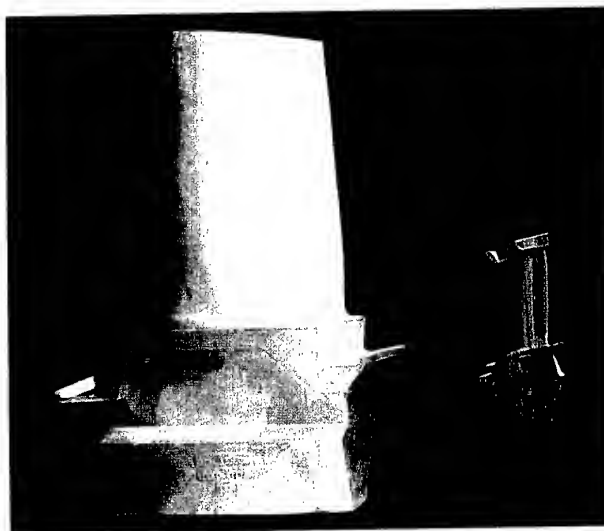
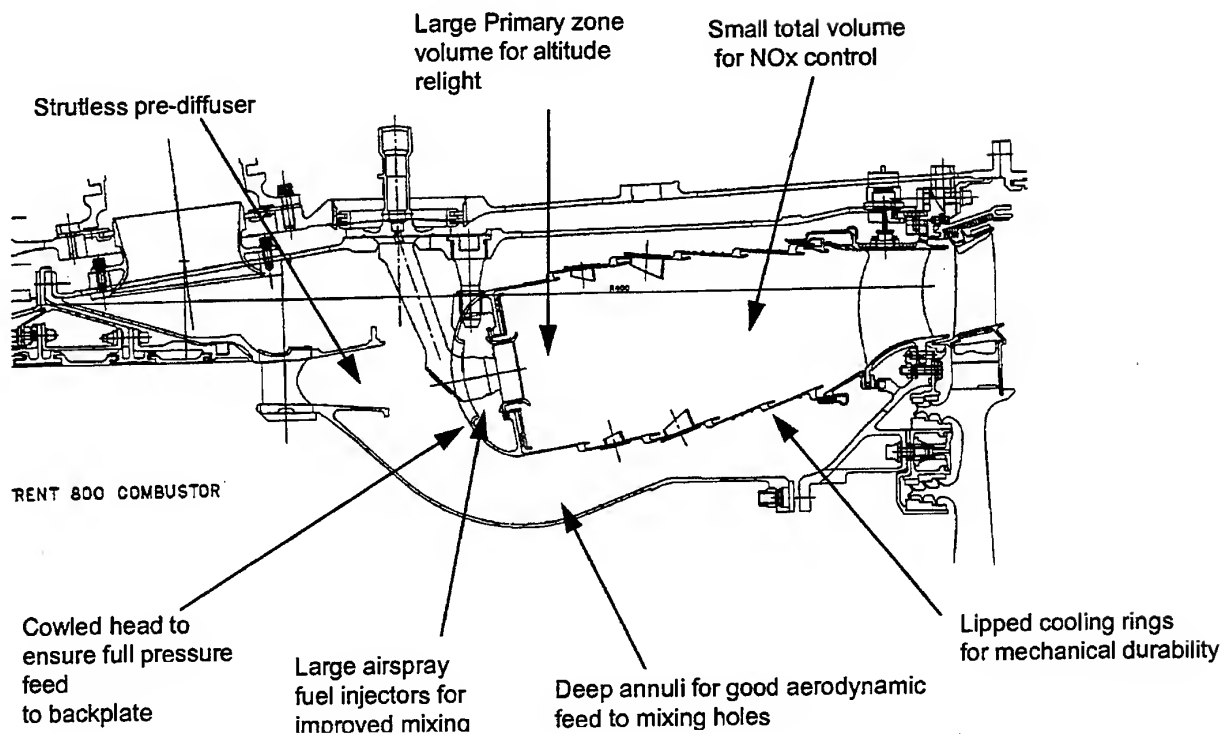


Figure 2 - Modern Aero Engine Single Annular Combustor



It is interesting to observe that the rotating parts of a modern gas turbine, that is the compression system and the expansion system have similar family likenesses for all applications, "an aerodynamic blade is an aerodynamic blade is an aerodynamic blade" as seen in Figure 1. The components of the combustion system show a similar family likeness when the technology has matured over a number of years to achieve a fully optimised solution, Figure 2 is a typical example. However, as the combustor designer strives to meet increasing demands a much wider range of solutions emerge. Compare modern single annular aero combustor designs with the designs used in stationary power generators, Figure 3 and the range of designs under consideration to meet future ultra low emissions requirements for subsonic and supersonic aero engines (Figure 4).

THE FUTURE

So what are the main drivers for the future?

It is quite clear that in the modern competitive world in which we operate, change will be brought about only for sound business reasons.

In the combustion area there is a strong link between reducing emissions for purely environmental reasons (ie a wish to protect the environment), for legislative reasons (ie in order to be able to sell a product) and for competitive reasons (ie to give the customer an edge in the market place and therefore the manufacturer).

GASEOUS EMISSIONS

I am sure that many of the participants in this conference will be familiar with the main emittants from a gas turbine engine. In detail these depend on the make up of the fuel used and the precise conditions under which it is combusted.

Ground based power systems are designed to meet legislation levels of emittants which in many cases are set by the Best Available Technology. Nitrogen Oxides (NO_x), Carbon Monoxide (CO), Volatile Organic Compounds (VOCs) and particulates are of most interest with the emphasis on "single digit NO_x" in recent times.

The emission levels for aircraft gas turbine engines are based on the recommendations from ICAO (International Civil Aviation Authority) which can then be introduced onto the statute of participating countries. Today's levels are based on the operating cycle of aircraft around airports covering NO_x, CO, Hydrocarbons (HC) and visible smoke particles.

The mandated levels for ground based installations differ considerably from those from aircraft. For example, the NO_x level is orders of magnitude less. The technology challenge may be equally severe for the two applications because of other and different restraints that are imposed.

Aircraft gas turbines uniquely deposit emittants at high altitude near to the tropopause (11kms) which is the typical cruise condition for the civil subsonic fleet. Supersonic aircraft cruise at much higher altitudes (18kms) in the stratosphere and are a much smaller fleet. The impact on the earth's climate of today's aircraft and of the future fleet has been studied for a number of years and will be the subject of a special report from the International Panel on Climate Change (IPCC) to be published in 1999.

Aircraft are a relatively small contributor to anthropogenic

predicted to continue at the current rate and therefore double in the next 15 years.

Carbon Dioxide and water are the main products from combusting hydrocarbon fuel. The latter impacts on the radiative forcing in the atmosphere in direct proportion to the percentage change regardless as to where it is injected. Water in the form of contrails has the potential to influence the forcing by changing the cloud cover and is purely an aircraft issue at altitude. The impact that the combustion system can have on the CO₂ and water level is very small as it is mainly a function of the fuel efficiency of the total power plant.

The use of hydrogen as a fuel would eliminate the production of CO₂ but the overall impact on the climate would require an environmentally and economically acceptable method of producing it.

The combustion designer can have the greatest impact on the level of NO_x, CO, VOC and smoke emitted by the engine. Technology acquisition programmes are in place with targets for NO_x set well below today's levels particularly in the aero gas turbine field (60-70% reduction).

The demand for increased fuel efficiency for power generation and vehicles implies a corresponding change to the operating regime of the combustor with increasing inlet temperature and pressure and a need to reduce the proportion of cooling air. At the same time the customer expectation is for reduced cost and greater reliability even though the drive for reduced emissions inevitably brings an increased complexity to the combustion system.

In power generation single digit NO_x will remain the target even for these more efficient cycles coupled with the use of a wide range of gaseous and liquid fuels.

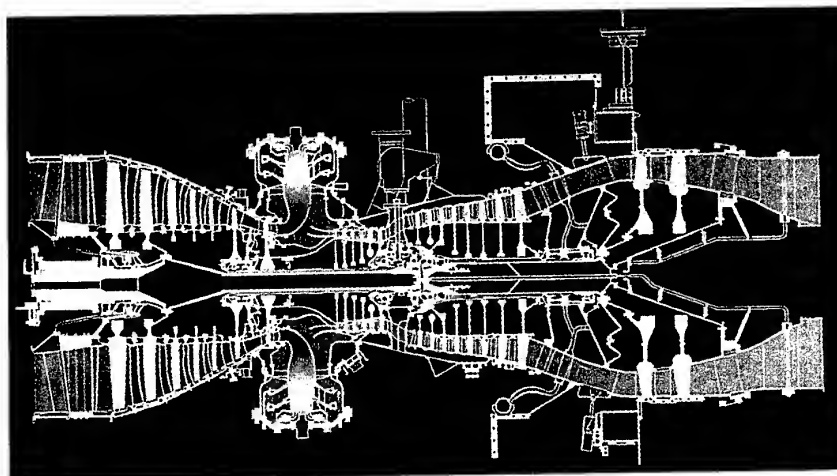
PARTICULATES

Low gaseous emissions will therefore continue to be a main driver as we go into the next century. It is also likely that a better understanding of particulates and their characteristics will be needed. In the military application, because of the contribution to the visibility of the engine plume, in the civil aero case where much work still needs to be done on the impact on the climate and in all cases where there is an increasing concern about the impact of very small particles on health. Any demands to control the distribution or range of particle size would present a severe challenge to the combustion engineer.

DESIGN METHODS

If we are to avoid the long and sometimes ad-hoc research and technology programmes the design methods of today must be validated for tomorrow's geometries and configurations.

This means that sufficient application of the advanced CFD codes be incorporated into the process taking full account of the need to achieve affordable analysis turn round times, the economical limits of experimental data collection and interpretation, the inability to obtain data at realistic conditions and then to adequately scale to more critical conditions, the ability to check the calculation, the link between aerodynamics, heat transfer, chemistry, material properties, time averaged and time dependent data, multi-phase flows, interacting pressure and thermal flow fields leading to, oscillations, etc, etc....

Figure 3 - Industrial Low Emissions Engine

If however, this coverage is too difficult then the range of the experimental programmes during the combustor development must be extended in a timely manner to be more representative of the working environment anticipated in the new advanced engines.

It is no longer sufficient to show pretty pictures of the three dimensional flow in and around a combustor. It is becoming even more important that the calculation produces data which can be used as an iterative design tool producing an optimised solution in a user friendly way.

INTEGRITY, RELIABILITY AND COST

The customers' expectations on reliability of the product continue to grow. A civil aircraft engine can stay on the wing for greater than 30000 hours, a military aircraft engine is expected to achieve more than 20000 severe cycles, an industrial power unit is expected to achieve greater than 16000 hours. These working lives will be expected even though the combustion system geometry may have become considerably more complex.

The theoretical prediction of the life of a combustion module, particularly of the combustor liners, relies on the ability to calculate the gas and then the material temperature distribution during transient operation as well as at steady conditions. Thermal loads are then calculated in conjunction with those related to gas pressure and other mechanical interfaces.

Conventional 3D stress analysis programmes are used to calculate these loads with some confidence, the greatest challenge comes from the definition of the material temperature.

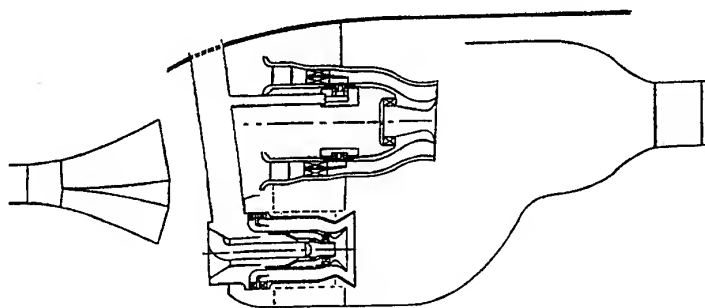
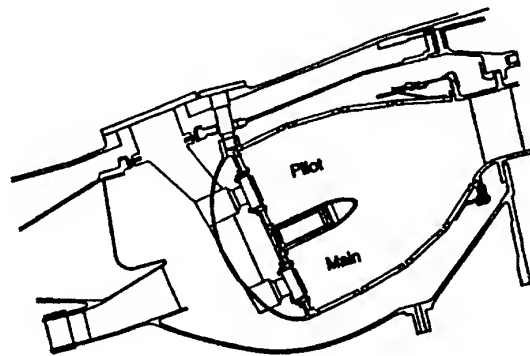
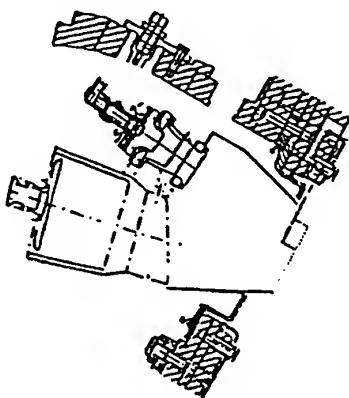
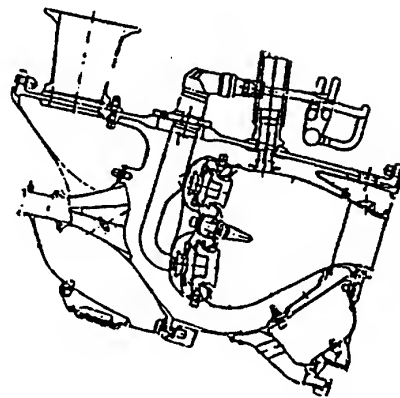
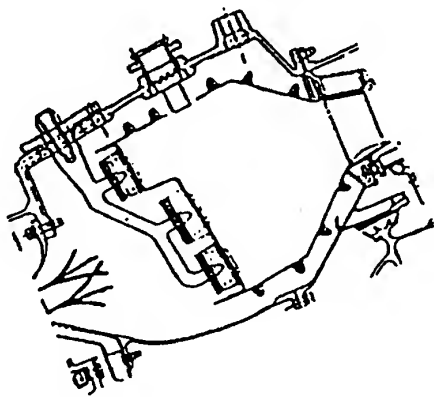
The process is currently based on a well instrumented engine test or a suitable rig test to validate the aerothermal and finite element stress programme. The read across to other steady state and transient conditions relies upon the ability of the codes and the available computing power. The life prediction is then based on empirical methods or upon more sophisticated models which for these structures are not yet mature.

The calculation of the various modes of vibration of the structure can be carried out with reasonable confidence. The amplitude of those modes has all the uncertainty associated with the steady and transient stress analysis.

All customers will expect a product that gives greater value for money, the engine supplier must therefore continually examine the processes used in the research, design and manufacture stages. In the combustion field, the technology changes that can be anticipated to meet the demands of reduced emissions are, I humbly suggest, far greater than in any other component of a gas turbine engine. The challenge to achieve the integrity, reliability and cost targets are therefore also far greater. The tools that are available to the designer in this area are still relatively immature and research and technology programmes do not always address the issues in question.

Much needs to be done in this area and I shall listen with interest to the forthcoming presentations to pick out those which contribute to advancements in this field of technology.

Figure 4 - Low Emissions Aero Engine Combustors



COMBUSTION DRIVEN OSCILLATIONS

I am quite sure that one aspect of integrity will be addressed at this conference and that is the problem of combustion driven oscillations. An excellent review paper was presented by Fred Cullick at an earlier panel meeting (Reference 2) and several workshops have been supported by this organisation.

Some of you may know that I started my combustion career working on Reheat Systems which have always been more prone to excitation in one or more of the many possible modes in the gas path. A combination of passive damping, empirical design methods derived from controlled experiments supported by an improving theoretical understanding, have enabled such systems to meet the operational requirements. However, in answer to the often asked question "have you cured the problem", the answer must be "no". I suggest that all combustion systems are capable of exhibiting the phenomenon and the researcher/ designer's job is to find ways of working round it. In this way the problem is similar to other vibration problems encountered in a gas turbine engine, compressor and turbine blade vibrations being just one example.

However, there may still be a significant difference which is that the geometry and concepts being employed by the various practitioners in low emissions combustors, differ so widely that generic or fundamental solutions will be harder to find.

SOFBALL

I have discussed the relative importance of research and development activity in support of the perceived future requirements of gas turbine combustion systems. The targets are demanding and justified and should attract the necessary support from Industry and from other sources such as government agencies. However, to me, the approach being taken is often conventional (perhaps rightly so) and sometimes lacks innovation.

I hope you can therefore understand my excitement in recently reading about SOFBALL.

SOFBALL stands for Structure Of Flame Balls At Low Lewis - number. These are premixed gas combustion experiments conducted during space flight on the Space Shuttle by NASA (Reference 3).

Earlier experiments on the Mir and the Space Shuttle (Reference 4) reported candle flames oscillating spontaneously !

ACKNOWLEDGEMENT

The author wishes to thank the Directors of Rolls-Royce plc for permission to give this address. All the opinions expressed are those of the author.

REFERENCES

1. Opdyke, G
Technical Evaluation Report, Fuels and Combustion Technology for Advanced Aircraft Engines. Propulsion and Energetics Panel 81st Symposium, Fiuggi, Italy, 10th-14th May 1993. AGARD-CP-536
2. Cullick, F.E. C.
Combustion instabilities in liquid - fueled propulsion systems - an overview. AGARD-CP-450
3. Romney et al, AIAA Journal Vol 36, No 8, August 1998.
4. King & Ross, AIAA Journal Vol 36, No 8, August 1998.

Ground Vehicle Mobility Requirements. *Meeting the Challenge with Electric Drives*

G. Khalil and Jennifer Hitchcock
U.S. Army Tank - Automotive and Armaments Command
AMSTA-TR-R
Building 212, Mail Stop 121
Warren, MI 48397-5000
United States

1. Abstract

Military ground vehicle requirements are defined by the terrains they traverse and the performance specifications defined by the users. While terrains have not changed much throughout the history of ground vehicles, the performance specifications have always evolved with the ever-changing technologies and the threats associated with them.

This paper contains a summary of current and future vehicle requirements, and the enabling technologies necessary for meeting them, including prime power sources which range from conventional engines to fuel cells.

Among the various technologies under consideration for future vehicle needs, electric drive stands out as a leading candidate. Therefore, a good portion of the paper is dedicated to electric drive systems and their impact on vehicle missions; particularly mobility.

2. Introduction

Military vehicles must have the capacity to operate anywhere in the world, under extreme environmental conditions, from the frigid temperatures of the arctic to the intense heat of the deserts, and from hard rocky and paved roads to hilly and soft soil. They must withstand the vibrations, shocks and violent twisting experienced during cross-country travel over rough terrain, and they must be able to operate for long periods of time with very little or no maintenance.

The above description was extracted from a handbook published by AMC in 1965. All of the conditions mentioned above are still valid today. However, there are additional requirements, which are changing the whole philosophy of vehicle design. The vehicles of the future must be lighter, faster, and more deployable but at the same time more lethal and more survivable. These constraints impose a departure from the traditional methods of making tanks. Therefore, new enabling

technologies have to be developed and implemented to meet the technical challenges of future vehicles. For survivability, electromagnetic armor must be developed to replace the thick armored plates. For lethality, higher speed projectiles with very high penetration capability must be introduced. For mobility, Active and semi active suspension systems must be considered to achieve greater cross-country speeds.

The above mentioned future vehicle needs require electric power that could be generated, stored and delivered to the different users in the vehicle within one integrated power management and distribution system. Thus an All Electric Combat Vehicle (AECV) is a concept whose time has arrived.

3.0 Mobility requirements

3.1 Mobility levels

There are three levels of mobility: Strategic, operational and tactical. Strategic mobility is the ability of the vehicle to move or be moved into the operational theatre. This implies that lighter and smaller vehicles have greater strategic mobility. Operational mobility is the ability of the vehicles to move by their own power at various speeds. Tactical mobility or battlefield mobility is the ability of

the vehicle to move over various terrains and obstacles such as ditches, trenches and streams.

The operational and tactical mobility requirements are extreme but necessary because the vehicle must be able to operate in various military environments. The most critical mobility requirements are:

- Vehicle top speed
- Vehicle top cross country speed
- Gradeability (60% max)
- Steering
- Acceleration
- Braking
-

3.2 Tractive forces

Some of the mobility requirements (steering, gradeability) are specified in terms of tractive effort to weight ratio (te/wt). Tractive effort being the tractive force needed to cause vehicle movement. For further clarification, the torque at the wheel or sprocket is the product of the tractive effort and the sprocket or tire radius.

Coincidentally, the te/wt for 60% grade and for pivot steer is approximately the same and is equal to 0.6, and a tracked vehicle traveling at 15 mph while turning on a 50 foot radius subjects its tracks to stresses comparable to climbing a 40% grade. The

cooling point is 0.7 te/wt ratio. That means the vehicle cooling system must be designed so that the drivetrain components can be continuously subjected to loads equivalent to 0.7 te/wt without exceeding their thermal limits. The maximum transient te/wt requirement for the total vehicle is 1.2, which is needed under certain severe operating conditions such as pulling out of deep and frozen mud. The most critical te/wt ratio is required for regenerative steering and it is 0.9 per side only, with 1.0 te/wt differential between the two sides. The rationale for the last requirement was specified for certain rare operating conditions where the vehicle's weight would be supported by one track only. Such conditions arise when one track is in a ditch or totally stuck in frozen mud or ice. Another situation is when one track is in a ditch to the extent that substantial earth movement is required. Under both of these situations the te/wt was calculated and found to be about 0.9 which must be achieved by the track that carries the weight of the vehicle. Fig 1. illustrates the different levels of te/wt ratio for the various conditions described above.

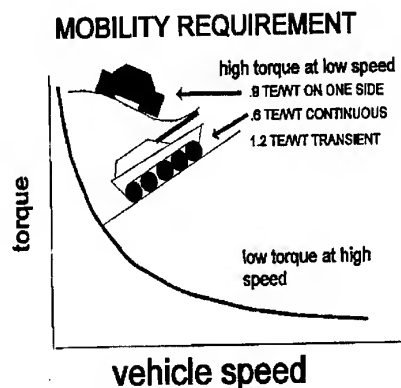


Fig 1

It should be noted that the te/wt values for the cooling point and the gradeability requirements are continuous. Whereas the maximum vehicle te/wt of 1.2 and the regenerative steering of 0.9 per side are transient values ranging from 0 to 60 seconds.

The governing equations for mobility are:

$$\begin{aligned} TE &= RRF + GRF + WRF \\ DBP &= TE - (RRF + GRF + WRF) \\ GRF &= GVW * \sin((\arctan(.01 * \% \text{GRADE}))) \\ WRF &= \frac{CD * FA * V^2}{418.5} \end{aligned}$$

Where:

RRF Rolling resistance i.e. force resisting vehicle's motion due to tire or track and road surface deflection and is also a function of the amount of sinkage of the track or tire in soft soil. Values range from 2% to 10% of the total vehicle weight.

GRF Slope resistance

WRF	Wind resistance
CD	Coefficient of drag
FA	Vehicle frontal area
V	Vehicle ground speed

3.2 Horsepower requirements

Requirements such as acceleration, top vehicle speed, steering at large radii and cross-country speed depend on the available horsepower originating from the prime mover and getting to the sprockets or wheels when needed for the various vehicle mobility conditions.

For all vehicles the power is transmitted from the prime mover to the wheels or sprockets through some type of transmission (mechanical, hydraulic or electrical) at different speeds and torques. The relationship of these parameters is defined by an operating envelope such as the one shown in Fig.2.

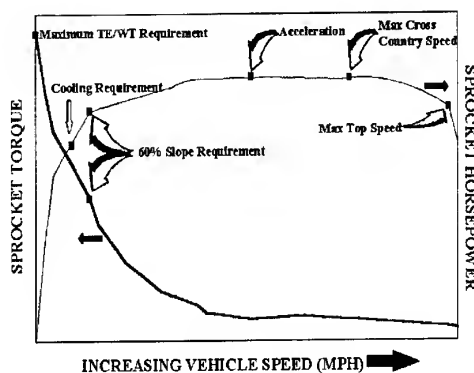


Fig.2 Operating envelope

For a combat vehicle each point shown on the operating envelope is a critical requirement. The top speed is required to enable the vehicle to move quickly into the operation zone. The top cross-country speed allows the vehicle to move at the highest possible speed in a battlefield environment, thus minimizing its exposure as a moving target. The 60% slope requirement, which requires about 0.6 te/wt at a speed of 10 kph, is needed for following the most strategic routes despite unfavorable terrain. Other transient conditions higher than 0.7 te/wt exist under some rare conditions as described in paragraph 3.2 (Tractive forces). Acceleration requirement is directly tied to survivability as it provides the vehicle the maximum dash capability and limits its exposure time from cover to cover.

State-of-the-art hydromechanical and hydrokinetic transmissions can meet all vehicle requirements described above; provided that an adequate power is delivered to the transmission from an engine. Electric transmissions in a hybrid electric drive system offers two advantages over their mechanical counterparts vis-à-vis the mobility requirements: Faster acceleration, and Burst power capability. The greater acceleration results from the peak torque at zero speed,

which is a characteristic of all electric motors. The burst power is provided from the energy storage system.

One important mobility operation; not shown on the operating envelope is steering. Some steering conditions for tracked vehicles require power at the outer track that exceed the engine horsepower by a factor of two.

The outer sprocket must be able to handle about 220% of the power delivered from the engine and the power absorbed at the inner sprocket may amount to 165% of the engine power, which can be regenerated to the outer track with a suitably designed transmission.

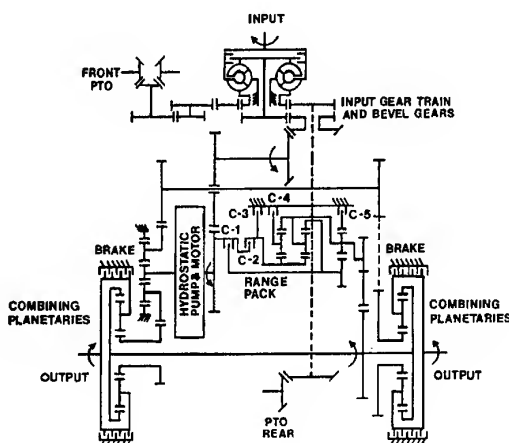


Fig.3 Hydrokinetic Transmission

Power regeneration can be achieved through clutch and gearing arrangement in the case of mechanical and hydraulic

transmissions as shown in Fig 3. and electrically in the case of electric drives.

The hp equation for the power needed at the vehicle sprocket is given by:

$$HP_{SP} = \frac{TE * V}{375}$$

Typically about 75% of the net power from the prime mover

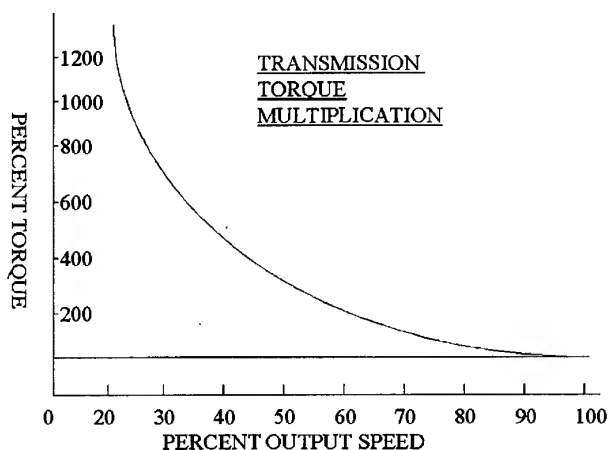


Fig. 4

reaches the sprocket over 10% to 100% of vehicle speed and The rest 15-20% of the engine power is wasted into frictional, spinning and heat losses. Fig 4 shows the speed and torque of a tracked vehicle over the speed range

4.0 Vehicle performance calculations

4.1 Mechanical drives

For a typical tracked vehicle with a hydraulic transmission (i.e either hydrokinetic, hydromechanical), as represented in Fig 5.

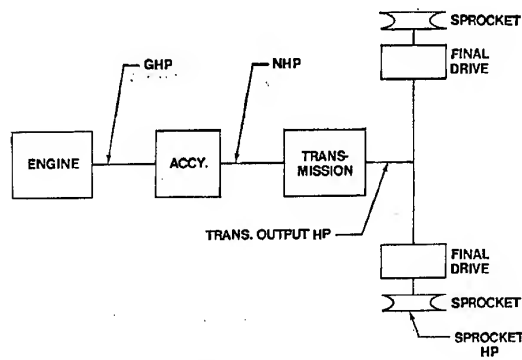


Fig.5

The approximate Losses can be broken down as follows:

Accessories	15%
85% efficiency	
Transmission	15%
85% efficiency	
Final Drive	3%
97% efficiency	

Thus the total driveline efficiency:

$$\text{Eff}_{\text{driveline}} = .85 \times .85 \times .97 = 70\%$$

The required engine gross horsepower is therefore the sprocket horsepower divided by the total driveline efficiency, or:

$$\text{Engine GHP} = \frac{\text{Sprocket hp}}{.70}$$

5.0 Electric Drives

There have been several attempts since the beginning of this century to power the automobile and heavy vehicles both industrial and military with electric drive. However, each attempt finished by identifying technical shortfalls that

forced the electric drive to remain a concept in the minds of engineers and scientists while allowing the conventional powertrains of IC engines and mechanical or hydraulic transmissions to advance. Two of the main shortfalls of the electric drive systems have been the battery range and the inefficient controls. Despite their shortfalls however, electric drives have been very successful where high power was needed, as is the case with locomotives, ships and mining equipment

It should be indicated that most of the reasons for considering electric drives have remained the same for the last sixty years. For commercial applications, the compelling reasons are fuel economy, reduced emissions, modular components and better performance. Similarly, the same reasons are driving electric drives for military applications; plus some very important benefits that are critical for military missions, such as silent watch, silent mobility, more electric power on-board the vehicle, better utilization of the under armor space claim and the design flexibility for either front drive or rear drive systems.

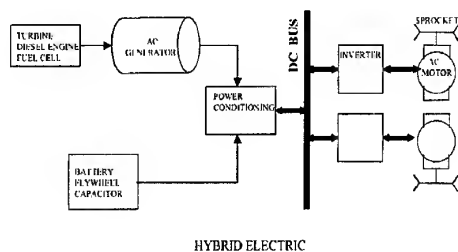


Fig.6 Electric drive schematic

Fig (6) shows a typical configuration of electric drives for military applications.

The schematic which is very generic shows a hybrid system having two sources of power, an engine (Turbine or diesel) driving a generator and an energy storage device (Flywheel or batteries). All the power generated from either or both sources are put into a DC bus and then transferred to the traction motors and other auxiliaries as needed to match the continuous and transient loads. The hybrid system has the advantages of using a small engine that can satisfy some of the continuous mobility requirements with less fuel and less emission levels than the bigger engine that would otherwise be required. All the transient requirements in a hybrid system are met from the stored energy. This also allows the vehicle integrator to size the components for burst power requirements such as accelerating or hill climbing.

The Hybrid system provides also the added capability of silent watch and silent mobility while operating on the battery power alone.

5.1 Performance calculations

Thus far the performance characteristics of the electric drives have been primarily based on projections and limited test data of prototypes. Therefore, all performance predictions in terms of total system efficiency over the speed range of the vehicle need to be verified through field testing and evaluation. However, the data obtained from component lab tests show that electric drive total losses are equivalent to those of the mechanical systems. A typical electric transmission shown in fig.6 consists of a generator/alternator, a rectifier, a DC bus, two traction motors and their inverters. For such a system, the losses are estimated to be:

Generator	4%
96% efficiency	
Rectifier	4%
96% efficiency	
Motors	5%
95% efficiency	
Inverter	5%
95% efficiency	

The accessory losses are similar to those of the mechanical drive system I.e. 15% and the final gear losses are 3%.

The total system efficiency:

$$EFF_{\text{driveline}} = .96 \cdot .96 \cdot .95 \cdot .95 \cdot .85 \cdot .97 = .69\%$$

The Prime power source(s) will have to deliver an output of :

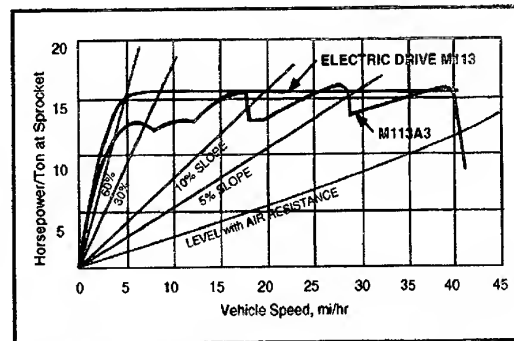
$$GHP = \frac{\text{Sprocket hp}}{.69}$$

5.2 Advantages

Some of the advantages of electric drives are listed in the previous paragraph. In order to understand the benefits of electric drives for military vehicles; we should evaluate their impact on the mobility criteria described in section 3.1.

5.2.1 Effect on vehicle speed and acceleration

Electric drives provide better agility than the mechanical system because of the inherent torque speed characteristic of all electric motors. Unlike mechanical and hydraulic transmissions, electric motors reach their peak torque at zero speed, which provides more power for acceleration at the low end of the power speed curve as shown in fig.7. In addition, since there is no gear shifting, electric drive act as continuously variable transmission where torque and speed are delivered to the traction motor to match its mobility needs on a continuous basis.



Comparison of available horsepower for the M113A3 and the Electric Drive M113 at same engine rating

Fig. 7

For cross country speed, electric drive systems provide sufficient power to incorporate active suspension which is needed to maintain stability of the platform on cross country terrain at high speeds

5.2.2 Effects on Gradeability

Electric drives have been successfully proven to meet the 60% grade with speeds equal to or higher than those achieved with mechanical drivetrains. In the case of a hybrid system, the energy storage on-board the vehicle can provide the burst power needed for hill climbing while keeping the engine at its constant speed.

5.2.3 Effects on steering

For wheeled vehicle, there is no difference between the steering systems used other than the fact that electric powered steering system is more readily integrable in electric drives. For tracklaying

vehicles however, steering with electric drives offers precise control by making one motor act as a generator to slow the inner track and speed the outer one. Although, it is the same principle for mechanical systems, the mechanism to achieve speed differential between the tracks is much simpler with electric drives.

5.2.4 Effects on braking

In the case of braking both traction motors are turned into generators to slow the vehicle and cause it to stop. A significant advantage in the electric braking is the capability of the system to capture the braking energy and store it back into the energy storage of the vehicle. Thus energy is regenerated and redirected into either a battery system or to other auxiliary users on the vehicle.

6. Challenges and enabling technologies

The most critical technical barrier for electric drive is the limiting operating temperature of the power semiconductors used in the motor and generator controllers. The power handling capability and reliability of state-of-the art silicon devices is limited by thermal performance. The operating temperature of Silicon devices is limited to approximately 150°C. Other parameters such as reliability, frequency, and power

handling capability of power semiconductors are also limited by the thermal characteristics of silicon.

The key challenge for electric drive is to develop power semiconductor switches that will provide system-level performance needed to meet vehicle requirements. However, the strategy should not strictly focus on the power switch. Advances in power converter circuit topology and control, thermal management, and improvements in other components, such as capacitors, bus bars, or inductors, may also yield significant system improvements.

Important system-level benefits for military applications are:

Higher reliability, longer life, high efficiency, improved fuel economy, lower cost, lower losses, smaller and lighter components, and reduced signature. At the switch level, the specific technical challenges for power semiconductors are: lower losses, higher reliability, higher operating temperature, lower thermal resistance, higher surge capability, and higher frequency operation at higher power levels.

The use of wide-bandgap semiconductors can have significant impact on electric drive application in a number of ways. Wide bandgap materials offer high temperature operation and much

higher electric fields. This leads to significant improvements in efficiency, cooling, and power density. Thus far, silicon carbide (SiC) is the most advanced of the wide band gap materials. The higher junction temperature possible with SiC allows effective cooling with higher temperature coolant, better surge capability, and higher power density. Silicon carbide thyristors have already demonstrated reliable operation at temperatures up to 500°C, much higher than what is possible with silicon devices.

Estimates suggest that SiC devices, probably diodes, may be commercially available as early as 2003. There are, however, significant problems to be addressed before the potential of the material is fully realized. Material defects, particularly killer defects called "micropipes", must be reduced. High quality, uniformly doped, low-defect epitaxial layers must be consistently produced. Processing and device fabrication techniques must be advanced.

Considerable effort is underway worldwide to produce useable SiC wafers for switching devices.

6. Prime Power

The prime power used so far for electric and hybrid electric drives have been conventional engines.

High speed diesel engines are currently being developed for hybrid electric cars and trucks. Fuel cells are being developed in the United States, Canada and Europe as an alternate prime power but they are not expected to replace the conventional engines any time soon.

6.1 Diesel engines

Most of the electric drive demonstrators to-date are powered with diesel engines. The main reasons for the diesel selection are its availability, and its high efficiency compared to other power plants. The diesel engine however has some disadvantages that need to be considered if it is to be used successfully in a hybrid electric system. First, the diesel is heavy, the hp/ton property of a diesel may be difficult to meet the desired metric of (20-25 hp/ton) due to its weight and the large cooling system it requires. Second the diesel engine has high levels of noise and smoke signatures. For a hybrid system there is an opportunity to reduce the weight and cooling burdens of the diesel by reducing the size of the engine which is made possible through the proper design and selection of the energy storage system.

6.2 Turbines

The turbine is ideally suited for electric and hybrid electric drives.

Its output speed matches that of the alternator it drives without the need of a gearbox. It is light with very low signature compared to a diesel engine and it runs cooler, therefore its cooling system is small and does not pose a design or integration problem. However, the turbine does have some disadvantages. The initial cost of the turbine is relatively high, it requires large amounts of intake air, which imposes air filtration burden, and it is not as efficient as diesel engines. Typically the specific fuel consumption (SFC) of a turbine is 0.45-.50 lbs./hp-hr as compared to 0.35 lbs/hp-hr for a diesel engine.

In a hybrid application, the efficiency of the turbine could be maintained at a comfortable level by running at a quasi steady state; which is possible with a hybrid electric since the ground speed is not dependent on the speed of the engine. This will prevent the turbine from cycling during varying vehicle speed, which is a primary cause for high fuel consumption.

Other desirable application of turbine engine in electric drives is the electrical turbo-compounding currently under investigation. This concept redirects the energy from the diesel exhaust to drive the turbine wheel of a small turbine and convert some of the

wastegated exhaust heat into electrical energy.

6.3 Fuel Cells

The fuel cells are still in their development stage. Their advantages are the claimed high efficiency associated with them. Efficiency numbers as high as 60% or more have been quoted for fuel cells by virtue of the direct conversion of chemical energy into electrical energy. Fuel cells have been demonstrated on a small scale for stationary power plant and for busses. However, for small commercial vehicles and for military vehicles, fuel cells have some disadvantages that require extensive development, which put them in the category of long term technologies. For commercial applications, fuel cells seem bulky and occupy large spaces, their configuration is not simple because of the complicated plumbing associated with them.

For military applications, fuel cells could not be considered unless they use the same fuels used for military vehicles. That implies that fuel cells would require reformers to extract the hydrogen from hydrocarbons before they could be accepted for military use. Adding a reformer would significantly reduce the efficiency of the fuel cell to make it almost the same as that of the diesel engine.

7. Summary

Military vehicle requirements are defined by mission scenarios over various terrains and environments anywhere in the world. These requirements dictate the design philosophy of the vehicles, which has evolved in the last eighty years according to the technological evolutions.

Future vehicles have new requirements, which could not be met with conventional methods. Therefore, new technologies have to be developed and applied to meet future vehicle needs. Electric drive is a prime candidate that is being considered worldwide for the XXI century. Its application will cover both the military and commercial markets even though the motives and benefits are not the same. Although electric and hybrid electric cars and trucks could be introduced for highway driving today, they are not yet applicable for the military due to the shortfalls of power electronics. Current development of wide band gap materials such as Silicon Carbide seem very promising for fielding electric vehicles in the next ten to fifteen years from now.

8. References

1. G. Khalil & R. Tuck, U.S Army Tank-automotive and Armaments Command. "The steering of tracklaying vehicles" 1996 SAE Convention, Detroit, Mich.
2. J. Hitchcock. U.S Army Tank-automotive and Armaments Command " Alternative Prime Power Sources for an All Electric Combat Vehicle" 1997 AECV conference proceedings, Dearborn, Mich

PAPER No. 1
Khalil & Hitchcock
(presenter: G. Khalil)

Question 1: R.L. Evans, University of British Columbia, Canada

You mentioned several prime movers, such as fuel cells and diesels. What do you see as the role of the gas turbine?

Answer:

The gas turbine is not popular in this application because of its poor fuel economy. However, a potentially good application for the gas turbine would be in a hybrid system. With a hybrid system the speed of the engine is not coupled to the speed of the drive-wheels or the sprockets. Therefore, the turbine does not have to be cycled during transients. It can be run steady-state at constant speed in its best operating mode. This would probably eliminate the fuel consumption penalty. Then, the gas turbine advantages could be capitalized upon, such as better matching with the generator, low noise, high power density, etc.

Advances in a Gas Turbine System for Ship Propulsion

M.L. Parker, P.K. MacLeod, M. Coulson
WR21 Project Office
Rolls-Royce Industrial & Marine Gas Turbines
Ansty, Coventry CV7 9JR, UK

INTRODUCTION

For thirty years, the obvious advantages of gas turbines in marine propulsion systems have been fully exploited by many of the world's navies. Conventional naval gas turbine propulsion systems utilise cruise engines (either a diesel or a gas turbine) to provide low speed fuel economy together with a boost gas turbine to provide the high power for top speeds. Fuel efficiency improvements in marine gas turbines have generally progressed in line with aero engine technology advancement.

The potential for substantial fuel savings in the future is available through the adoption of complex cycle engines.

An intercooled and recuperated (ICR) gas turbine, known as the RM60, went to sea in HMS Grey Goose (the world's first warship to rely entirely upon gas turbine propulsion) in 1953 and continued in service for over 4 years. The RM60, however was not viable for long term production due to its size and technical complexity.

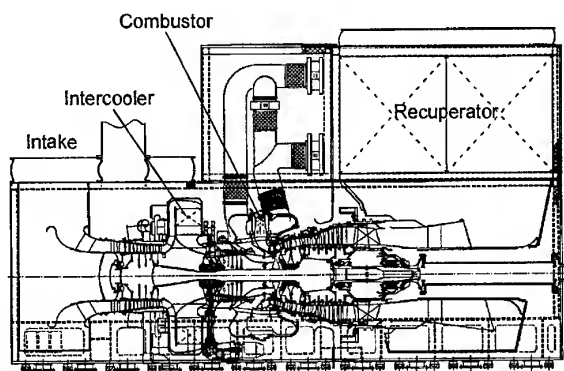


Figure 1 - WR-21 Cross Section

The only advanced cycle marine gas turbine currently in development is the intercooled and recuperated WR-21 (figure 1), the development of which is being funded by the United States Navy, the Royal Navy and the French Navy. The highly efficient WR-21, rated at 25.2 MW (ISO), is derived from the Rolls-Royce aero RB211 and latest Trent family of jet engines components being suitably adapted for the marine environment. In addition modifications are necessary to integrate the heat exchangers and hot-end variable geometry in an effective manner.

The imminent re-introduction of an advanced cycle marine gas turbine will radically improve fuel consumption by up to

30% when averaged over a typical naval duty cycle. This fuel saving, in conjunction with current condition-based maintenance techniques, engine modularisation and the potential for retrofit of an ultra-low emission combustion system should cause a re-examination of the dominance of the diesel in many commercial marine applications.

The combustion system requirements for the ICR cycle differ significantly from those of a conventional gas turbine, both in terms of the aerodynamic and thermal characteristics of the cycle and also the overall system architecture (figure 2).

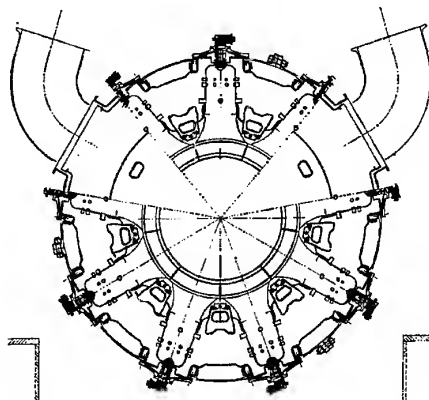


Figure 2 - WR-21 Combustion Design

This paper summarises the aerodynamic and mechanical design, rig verification and development engine experience on the WR21 Combustion System to the present time.

WR21 ENGINE CYCLE

The WR-21 achieves its significant fuel saving over existing simple-cycle engines through the use of heat exchangers to improve the part-power cycle efficiency.

The recuperator is used to recover heat from the exhaust and preheat the compressor delivery air. By returning this heat to the cycle, less temperature rise (and therefore fuel) is required by the combustors at any given power.

A Variable Area Nozzle (VAN) is used to optimise the recuperator performance across the power range by accurately controlling power turbine capacity (and hence engine air mass flow), which in turn maintains a high recuperator gas side inlet temperature and high recuperator effectiveness.

The intercooler reduces the work required to drive the HP compressor (which enables an overall improvement in specific power) but more importantly provides a low recuperator air side inlet temperature to permit maximum heat recovery in the

recuperator. Intercooling alone is inherently less efficient because heat is lost directly from the cycle, but the combination of the recuperator with the intercooler recovers the deficit and overall engine efficiency is improved through the reduction in compressor work.

By careful design of the engine and heat exchanger system, an excellent reduction in specific fuel consumption is achieved as shown in Figure 3.

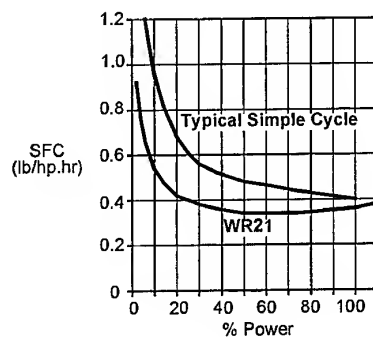


Figure 3 - ICR Fuel Savings versus Simple Cycle

A useful by-product of efficient exhaust heat recovery is low exhaust gas temperature, which is extremely valuable to a warship as it confers a reduced infra-red (IR) signature. Also of key importance in recuperated operation is low combustor smoke generation, since this further reduces IR signature and helps keep the recuperator operating efficiently without carbon fouling.

COMBUSTOR OPERATIONAL REQUIREMENTS

The ICR cycle is significantly different from that of a conventional engine, particularly when the warship requirement for high availability is considered.

In addition to normal ICR operation the WR21 is designed to operate with the recuperator bypassed only and with both the recuperator and intercooler bypassed together to ensure operability in the event of a system fault or battle damage. In the case of the recuperator this mode of operation may also be required for the purpose of cleaning carbon fouled gas washed surfaces. Cleaning of the recuperator is regarded as a normal in-service operation in order to recover cycle performance. Low power bypass operation with the VANs partially closed allows sufficiently high recuperator gas-washed surface temperatures to be obtained to burn off carbon and associated deposits.

Examination of all required cycles shows that the extreme boundaries of the combustor operating envelope are covered by the two regular modes of operation i.e. recuperator operative or bypassed but with the intercooler operating normally (Figure 4).

Recuperator operative mode is characterised by the near-constant and high value of combustor inlet temperature, maintained by controlling the VAN area. The benefit to the cycle of the recuperator is manifested by a reduction of fuel flow, particularly at low powers.

In recuperator bypass mode behaviour of the gas generator's compressors and turbines is largely unchanged from recuperated operation. However, the lower combustor inlet temperature requires greater temperature rise within the combustor, increasing fuel demand and reducing the air fuel ratio (AFR) significantly.

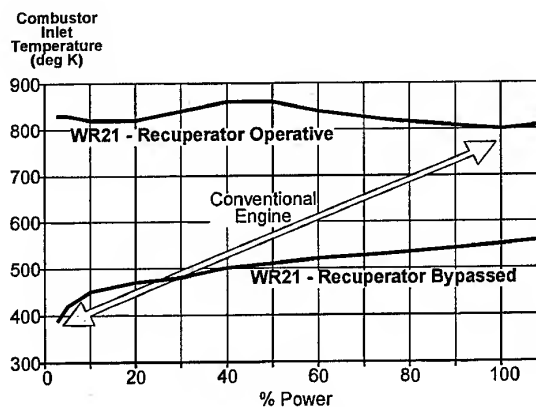


Figure 4 - WR-21 Combustor Operating Envelope

The four corner points of the operating envelope dictate the magnitude of the design task in terms of combustor operability and component life.

At idle with the recuperator bypassed and at maximum power with the recuperator operative the conditions of combustor inlet temperature and AFR are similar for the WR-21 and conventional gas turbines. However at most other engine conditions the combustor inlet temperature and AFR vary considerably from a typical simple cycle.

With gas generator operation governed by the VAN position, the combustor inlet non-dimensional flow function $W\sqrt{T}/P$ and correspondingly the combustor pressure loss (governed by its fixed flow area) varies somewhat over the operating range. As power is increased along the recuperator operative running line the combustor pressure loss reduces slightly. However, the lower combustion inlet temperature in bypass operation lowers the value of $W\sqrt{T}/P$ and hence pressure loss by a more significant amount. The lowest pressure loss to be catered for is therefore at maximum power with the recuperator bypassed. Since the High Pressure Nozzle Guide Vane (HP NGV) cooling is driven by the combustor wall pressure drop, this becomes the critical design point for that system.

Carbon deposition is frequently found in fuel-rich regions of combustors where the walls are cooler than 500 to 600°C (above which carbon will burn off if sufficient oxygen is present). Since the WR-21 combustor is designed to achieve

acceptable metal temperatures with the recuperator operative, the walls are over-cooled when the recuperator is bypassed. Regular operation in these conditions is limited to the minimum time necessary for cleaning of the recuperator (at low power conditions), nonetheless this mode of operation exposes the combustor to the risk of carbon deposition, and careful design is required to limit carbon growth on primary zone walls.

COMBUSTION SYSTEM CONFIGURATION

The ICR propulsion system package is designed to occupy the same footprint as existing powerplant installations and to deliver high levels of reliability, maintainability and component life. The design philosophy of WR-21 as an aero-derivative was to capitalise on the excellent in-service experience of the modular aero engine parent, thereby mitigating technical risk. Preservation of the proven aero RB211 HP and IP spool lengths, which are characterised as short, rigid high integrity structures, therefore became a principal design objective. The requirement to remove compressor delivery air and return recuperated air within the length constraint dictated that the annular RB211 combustor be replaced by a radially oriented tubo-annular system (Figure 5). Nine individual combustors provide the correct combustion volume at the increased radius of the radial location, and provide space between combustors for a suitable load-carrying structure.

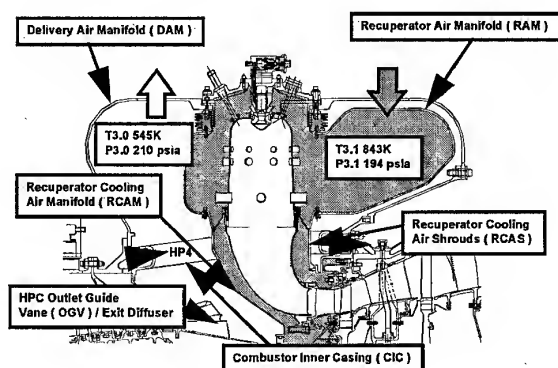


Figure 5 - Combustion Design

The radial mounting of the combustor, although unique to WR21, is not unlike the dry low emission (DLE) designs that feature in the latest Rolls Royce industrial family of engines. Future ultra-low emission liquid fuelled combustor designs drawing upon the gas fired DLE combustor experience should be easily retro-fitted if maritime emissions legislation becomes more stringent than currently proposed levels. In-situ removal of the combustor and burner is also a key feature of the WR-21 maintainability strategy. The design permits not only ease of life monitoring but also timely repair

or replacement of hardware (without engine removal) in the unlikely event of a premature failure.

The marine Spey SM1C combustor was adopted as the basis for the WR-21 combustor design. This combustor, although otherwise conventional in its construction, employs a Reflex Airspray Burner (RAB) method of fuel injection, developed specifically for the marine versions of the Spey engine. It achieves a controlled mixing of the fuel and air which allows a high burner exit AFR to be maintained with adequate flame stability. Based on previous experience, high (lean) AFR was considered an important factor in reducing visible smoke when burning diesel fuel.

The combustor and RAB assemblies are sited within a large annular chamber, the Return Air Manifold (RAM), which distributes recuperator return air at high pressure and high temperature from two recuperator return pipes (figure 2). To ease the thermal duty of the structure, the handling of pressure and temperature is separated through the use of a double skin arrangement. The nickel-based RAM forms a high-temperature lightweight insulated liner with minimal pressure load.

In order to achieve a compact arrangement, the RAM lies within a low temperature, high pressure casing which forms an annular chamber for compressor delivery air. This outer casing, the Delivery Air Manifold (DAM), is a 12% chrome steel fabrication that is detachable as three circumferential segments permitting in-situ discharge nozzle removal. To achieve a high level of cycle performance, significant attention is given to minimising heat loss from the RAM and to eliminating low temperature fluid leakage path into the RAM. The thermal expansion of the RAM inside the DAM is accommodated by a series of 9 flexible bellows assemblies located at each combustor position. Both the RAM and DAM are essentially isolated from the main engine casing loads which are transmitted by an inboard cooled spoke structure, running between the individual discharge nozzles, and connects the compressor and turbine casings.

COMBUSTOR DESIGN

Aerodynamics

The combustor is designed to have three rows of air entry ports. A single row of primary ports are used in conjunction with the RAB to establish the primary re-circulation (toroidal vortex) and stabilise the flame. Thereafter, secondary ports introduce a significant proportion of air to lean off the mixture and prevent smoke production with excess air used to consume smoke already generated in the primary zone. Finally, tertiary (or dilution) ports are arranged in a single row to generate vigorous downstream mixing and reduce peak gas temperatures to acceptable levels for turbine aerofoil integrity.

An aerodynamic study using water analogy techniques (and some basic Computational Fluid Dynamic (CFD) modelling) was used to establish the quality of the RAM flows. A linear 3/4 scale perspex model of the full RAM with the 2 recuperator feeds and all 9 combustors was used.

The feed into the RAM from the two return pipes is inherently asymmetric, although as anticipated, the flow in one half of the engine is the near mirror image of the other half. Figure 6 shows a developed view of the flow vector field observed within the RAM cavity.

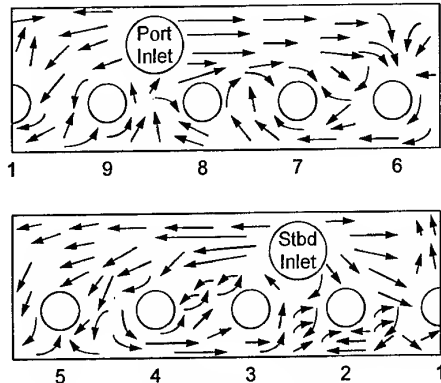


Figure 6 - Combustor External Aerodynamics

The flow does not feed combustors 3 and 8 directly but instead makes a loop around combustors 4 and 7. This produces tangential flows around these combustors which gives rise to non-uniform internal flow fields. Ideally to avoid uneven combustion behaviour the flow should be consistent for all the combustors irrespective of their location within the RAM. A single sector (one ninth) water analogy model was constructed at full size to facilitate a more detailed study of local flow effects at individual combustor locations. Using data from the 360° model test, and the CFD, flow inlet conditions were adjusted to simulate each of the nine positions. This model provided the means of developing an effective method of flow conditioning.

Externally chuted combustor ports were subsequently chosen to directly vector the direction of airflow into each combustor with negligible pressure loss.

Extensive testing on a single sector hot rig (simulating the variable RAM flow field) and subsequent engine tests have demonstrated that bell mouthed high aspect ratio ($L/D \approx 2$) chutes are highly effective in de-sensitising the non-uniform RAM flow effects from the overall combustor performance.

Ignition Performance

Unlike conventional axial turbo-annular systems, the large circumferential separation between adjacent combustors together with a desire for simple combustor removal precludes the use of interconnectors for light-round. It is necessary therefore to provide each combustor with its own ignition source. A duplicated high energy surface discharge igniter arrangement ensures start reliability in the event of a single igniter failure.

In common with the marine Spey, a separate pilot atomiser is provided in addition to the RAB to provide finely atomised fuel for good ignition.

Early rig tests demonstrated good ignition performance in plenum feed (encountered in engine combustor position 1), but revealed sensitivity to external flow conditions at other combustor locations.

Ignition was enhanced in position 4 where the external flow swirl opposes the combustor film cooling swirl ('contra-crossflow'), but in position 7 where the external flow swirl reinforces the combustor film cooling swirl ('Co-crossflow') ignition was worsened. The same general relationship with combustor position was found to extend to exit temperature traverse measurements, with high Overall Temperature Distribution Factor (OTDF) attributed to the co-crossflow positions.

In order to minimise the impact of the sensitivity to external flow conditions the first engine set of combustors were 'handed' such that the circumferential direction of film cooling was arranged to oppose the external (RAM) flows. Thus the direction of film cooling was reversed in combustors 2, 6, 7 & 8. Ignition performance achieved acceptable levels, with greatly reduced sensitivity to combustor position as shown in Figure 7

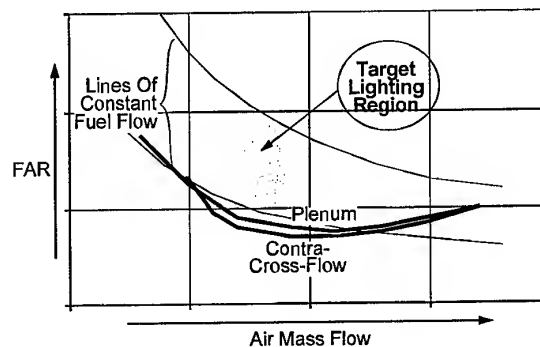


Figure 7 - Effect of RAM Aerodynamics on Ignition

Subsequent combustion chamber improvements including detail changes to primary port configuration are driving a re-assessment of the current system sensitivity to external aerodynamics. The ultimate objective being elimination of handed combustors and the consequent reduction in the customer's spares inventory.

Stability Efficiency and Noise

The WR-21 operation is like a conventional low pressure ratio gas turbine at recuperator bypassed idle conditions. Stability and efficiency in main burner operation are technically challenging as the low combustor inlet temperatures delay fuel evaporation and effectively weaken the zone of flame stabilisation. Whilst the RAB burner is an effective device for preserving stability at lean primary zone (PZ) conditions it was found that development of an effectively cooled primary zone barrel (by means of a higher proportion of cooling air than originally anticipated) led to insufficient stability margin

at very low powers and at cold-day conditions. The approach adopted to improve stability and efficiency and to eliminate noise was to operate the starting atomiser as a pilot fuel injector at low power conditions. This introduction of finely atomised, easily evaporated fuel was successful and operates in recuperator bypassed mode over the whole power range, but its proportion of fuel flow diminishes as power is increased.

Thermal Management

Fuel Injector

To cover the required engine power range in both recuperator operative and recuperator bypassed modes, the range of fuel flow (turndown ratio) of the WR-21 is significantly higher than in a simple cycle engine. Gas turbine fuel injectors commonly employ fixed orifices whose flow rate varies with the square-root of the injection pressure. In the WR-21 the wider ratio of injection pressures resulting from the high turndown ratio cannot be easily accommodated within an economic and reliable fuel system. Therefore, each fuel injector is fitted with a valve that reduces the range of fuel manifold pressures by varying the injector flow orifice sizes. The alternative methods of accommodating the high turndown ratio of a duplex system or the use of a more complex multi-orifice distribution unit both involve considerable additional complexity.

In modern aero gas turbines the propensity for fuel to degrade and deposit carbon in the internal passages of fuel injectors has become increasingly evident. At part power conditions with low fuel flows fuel temperature is raised by the use of fuel-cooled oil coolers to a level that encourages thermal breakdown. There is often a need to incorporate heat shields and insulation in fuel injectors to discourage the deposition of cracked fuel deposits which can lead to blockage of fuel injection orifices.

In the ICR cycle the problem is somewhat different to that of the aero parent. Fuel inlet temperatures are lower since oil cooling is not performed by the fuel. However, high combustor air inlet temperatures occur at idle power where the fuel flow is at its lowest level. Consequently effective heat management of the fuel injector is required to avoid high wetted wall temperatures. The problem is compounded by the fact that naval diesel, which often contains more complex aromatic compounds and a higher proportion of "cracked stock", are more susceptible to thermal breakdown.

Refinement of the WR-21 fuel injector design through extensive thermal modelling has resulted in predicted wall temperatures within target levels for acceptable rates of coking. Use of the RAB design provides additional benefit in this respect as it shields the fuel injector from combustor flame radiation. The WR-21 RAB and fuel injector are shown schematically in Figure 8.

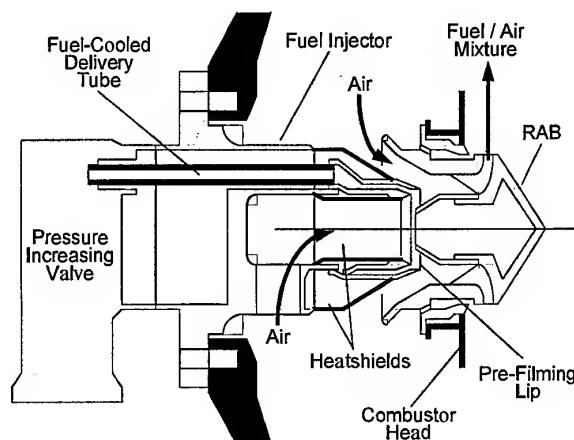


**Figure 8 – Fuel Injector and RAB Arrangement
RAB Endcap**

The burner endcap protects the fuel-cooled inner surface of the burner from carbon deposition and by its geometry encourages the formation of an effective primary recirculation. Thermal management of the burner endcap is one of the most difficult areas in the WR-21 combustor design. The geometry of the fuel/air passages within the burner limit the availability of cooling air to the endcap and furthermore the burner operates in a fuel rich zone at most powers (including cruise powers where combustor inlet temperature is at a maximum). In this regime, if cooling air is introduced into the rich region then it is possible to increase heat release local to the surface and negate the benefit of the cooling. Consequently, any cooling design must have a high cooling effectiveness. Furthermore, there is a propensity for carbon formation on the outer rim of the endcap, where the metal is fuel cooled and there is potential for local gas re-circulation, an effective airblast is necessary to maintain high local wall velocities and discourage carbon deposition.

Figure 9 shows the current development version of the RAB endcap cooling system. This design employs a combination of impingement cooling and extended surface heat exchange with air exiting at the periphery, away from the cooled surface and forming a clean air barrier against carbon deposition. The novel double skin design also controls differential thermal movements and limits stresses.

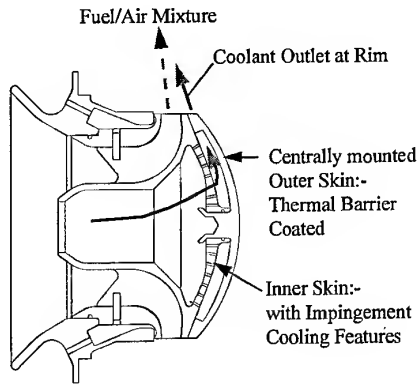


Figure 9 RAB Endcap Cooling

Combustor and Discharge Nozzle

The discharge nozzle of the WR-21 turns the flow into the axial direction to enter the turbine and is significantly larger than in a conventional engine (since the combustor can only be fed uniformly from the RAM if it is placed outside the spokes of the inner casing). Cooling flow for the discharge nozzle is therefore higher than in an aero-engine combustor. This reduces the air available for combustor barrel wall cooling or for exit temperature traverse (pattern factor) control (Figure 10). A further constraint on airflow usage is the higher than normal combustor wall cooling effectiveness required over the full power range in recuperated operation. A key feature of the WR-21 is the maximised use of the recuperator to achieve good fuel efficiency; the consequence is that over the entire power range combustor inlet temperature is maintained at constant high level.

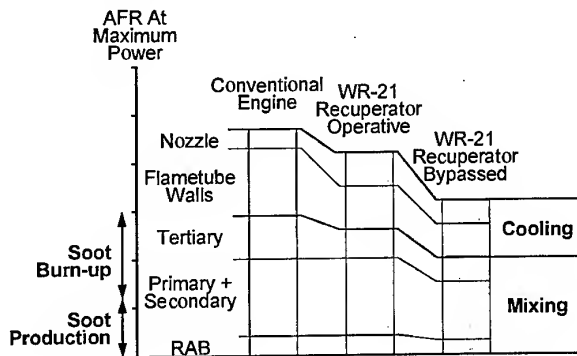


Figure 10 - Combustor Airflow Distribution

It is clear that if combustor inlet temperature is high, then a high cooling effectiveness will be required to achieve a satisfactory flametube metal temperature. Furthermore, at low powers the axial position of the maximum heat release translates upstream in the combustor as AFR increases. This

effect is illustrated by thermocouple measurements made at high and low power recuperated conditions (figure 11). This effect is not an issue in simple cycle engines as there is an accompanying reduction in combustor inlet temperature at low power.

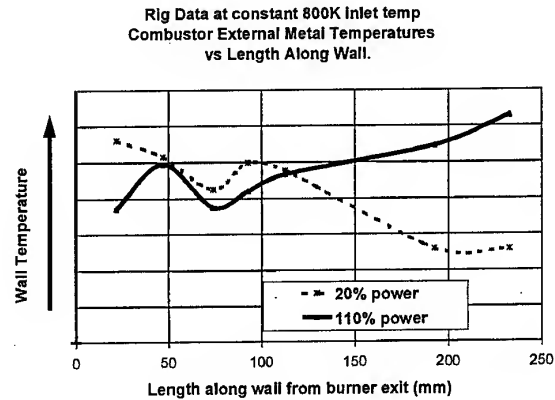


Figure 11 - Combustor Wall Temperatures

The ICR cycle therefore requires increased cooling (and therefore cooling flow) of upstream combustor walls compared to the simple cycle (Figure 12).

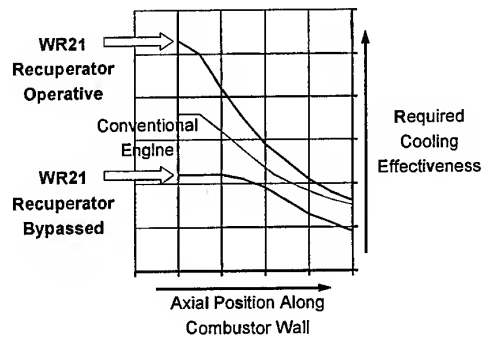


Figure 12 - WR-21 Combustor Cooling Effectiveness

High values of cooling effectiveness are achieved with complex wall cooling arrangements where the material is laminated, or where cast tiles employing pedestals or fins can be used. However, modern manufacturing methods such as laser or water-jet drilling now make large numbers of angled effusion cooling (AEC) holes an economic alternative to laminates or tiles. Angled effusion has comparable cooling effectiveness but gives improved lead-times and therefore greater flexibility in development. The angled effusion technique was selected for the WR-21 combustor since it offered the flexibility of treating hotspots quickly within a relatively short development programme whilst also maintaining a simple mechanical construction.

Thermal management in the head of the combustor has required special attention with distress observed on early development hardware. The careful optimisation of AEC by means of single sector hot-rig testing was a key factor in reducing absolute metal temperatures and thermal gradients and extending thermal fatigue and corrosion life.

Exit Temperature Traverse

Achieving combustor exit temperature distributions to satisfy the requirements of HP Turbine NGVs and rotor blades has required careful balance because of the difference in wall pressure drop in the extreme modes of recuperator operation. Traditional combustors rely on large dilution ports to add excess air after combustion is largely complete. These jets penetrate deeply into the combustor to mix with the gas to eliminate high peak temperatures. Furthermore, on an aero-style annular combustor the balance of inner and outer annulus air can be controlled to achieve the required radial position of peak temperature to ensure acceptable HP turbine rotor blade life.

In the case of WR-21 the most important objective is to ensure low peak gas temperatures in recuperated operation. In this mode maximum power temperature rise is similar to a simple cycle engine and although the amount of available flow to control traverse is less (due to the increased cooling flow demand) the wall pressure drop is a little higher than a conventional engine and so good mixing occurs and low peak temperatures result. This process is also facilitated by the long discharge nozzle which gives increased mixing time.

Traverse control is inherently worse at high power in recuperator bypassed mode as combustion is not complete by the plane of the dilution ports (due to rich AFR and poorer fuel evaporation). A consequent lower pressure drop also yields less jet momentum and therefore penetration and mixing. In addition, the combustor temperature rise is larger due to the cooler inlet air but with a similar combustor outlet temperature, will give rise to a fundamentally peakier traverse. The 90° bend in the discharge nozzle produces complex secondary duct flows and is another important factor to be considered in achieving an acceptable temperature profile. This flow behaviour results in an inboard shift in the radial position of peak gas temperature at recuperated conditions. The radial traverse profiles in the recuperator modes are shown in figure 13. The optimum height for the radial peak is at 50 to 60 % blade height since this avoids high rotor metal temperatures at the aerofoil critical stress section and avoids creep relaxation of the shroud interlocks required for vibration control. It can be seen that the recuperated temperature peak is a biased to the aerofoil root. However, the consequence of forcing it outboard would then hazard the integrity of the interlocks in recuperator bypass. The inboard bias is largely responsible for hot HP NGV inner platforms and local endwall treatment (trimming) of high gas temperatures has been necessary to keep metal temperatures within design limits. This objective was achieved by careful placement of trimmer coolant flows close to the discharge nozzle exit plane.

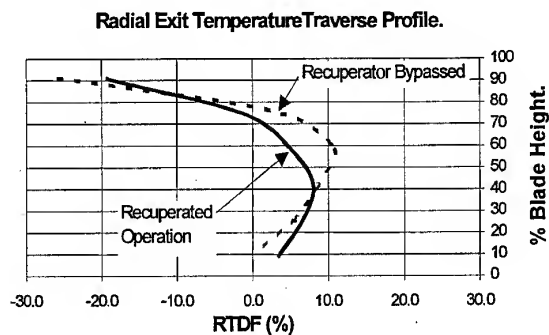


Figure 13 - Exit Temperature Traverse

Emissions

A key requirement for a naval marine engine is low IR detectability. The ICR contributes to this objective by having a low exhaust gas temperature due to recuperator heat recovery and therefore reduces the need for complex exhaust stack designs which dilute the exhaust gas with cold ambient air. In this way the recuperator reduces cost and space within the architecture of the ships upper decks. To ensure minimum visual detectability and further reduce IR signature there is a need to minimise visible exhaust emissions such as smoke and NO₂ (which gives brown smoke). The ICR cycle provides good conditions for clean combustion and smoke control. A smoke consumption zone is produced by controlled mixing of secondary port air.

Figure 14 shows the WR-21 engine smoke characteristic. The target level for invisibility is around 15 SAE and this target allows for the maximum anticipated diameter of exhaust stack (and therefore the maximum visual path length through the exhaust plume). With the minimum likely stack diameter (determined by back pressure and performance loss) the target level would be closer to 20 SAE.

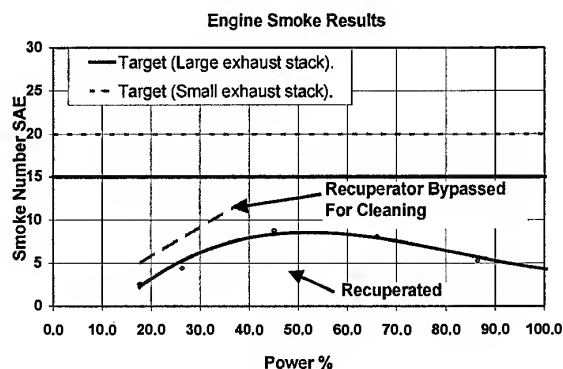


Figure 14 - Smoke Production

Marine legislation does not currently limit high levels of toxic pollutants such as CO or NO_x however the International Maritime Organisation (IMO) currently proposes legislation

aimed at reducing pollution from reciprocating diesel engines. This will put limits on oxides of nitrogen and sulphur (NO_x and SO_x) from after the year 2005 although the implementation date for this legislation is currently uncertain. Gas turbine emissions are not generally affected by this forthcoming legislation provided that they burn low sulphur fuels. The fundamental characteristic of continuous combustion in a gas turbine is that residence time at high flame temperatures. (which is the key cause of high NO_x) is capable of being controlled. This is not possible in a reciprocating diesel engine since combustion must be completed in a very short time at peak compression levels in order to give reasonable fuel consumption and prevent overheating of pistons.

The conventional combustor design utilised on WR-21 will meet all near term maritime requirements in recuperated operation with the exception of coastal legislation introduced in areas such as California where land based rules for NO_x and CO are extended into harbours and estuaries. With the ICR cycle flexibility it should be possible to avoid punitive charges by switching to recuperator bypassed operation at low powers for manoeuvring in these areas. The requirement for low smoke tends to increase NO_x production since the smoke consumption zone does not rapidly quench combustion temperatures to low NO_x production levels. However, the high combustor inlet temperatures over the power range in recuperated operation ensures complete combustion with extremely low levels of CO and unburned hydrocarbons (UHC). Figure 15 shows pollutant levels across the power range it can be seen that NO_x levels are high, consistent with low smoke across the power range. It is important to note that the proportion of NO_x present as NO_2 is very low and does not give rise to brown smoke.

The only way to overcome high NO_x would be to introduce staged Liquid Premixed, Prevapourised (LPP) Dry Low Emissions (DLE) technology that could be retro-fitted into the WR21 engine.

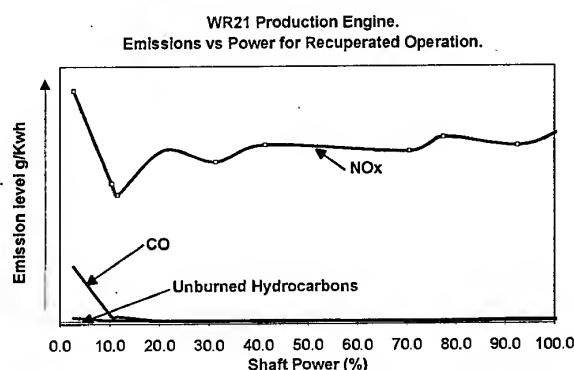


Figure 15 - Emission levels in recuperated operation.

COMPONENT VERIFICATION

Validation of combustion component operability makes extensive use of a single sector 'hot' rig facility in order to evaluate design modifications prior to engine embodiment. The rig permits a single combustor and discharge nozzle to be tested in a representative engine aerodynamic and thermal environment. Instrumentation is routinely installed for data acquisition relating to ignition, combustion stability, noise generation, metal temperatures, exit gas temperature traverse and emissions.

Around 20 hot rig tests (10 at low pressure ignition conditions and 10 at high pressure operation) were undertaken in the development of the first engine mark. Throughout the engine development programme a further six different aerodynamic standards progressively evolved. Thermal management has been the main area of testing in optimising the cooling in the head of the combustor and the chute wake regions. Thermal paint in conjunction with surface mounted thermocouple surveys have enabled a comprehensive map of wall temperatures across the operating envelope to be assembled. This data has enabled the validation of the stress analytical models which in turn influence design iterations. Concurrent development of the RAB endcap cooling has also been undertaken as part of the overall life enhancement programme. The radial combustion system of WR21 has provided development with the unique opportunity in executing a multiplicity of experiments using a single test vehicle. Most notably on the engine are the wall temperature measurements which has demonstrated excellent correlation with the rig measurements.

Engine testing has now surpassed 1400 hours (1100 hours recuperator operative) including a 500 hour endurance test. Stable operation has been achieved across the power range and in all operating modes. Future tests to complete validation concentrate on final optimisation modifications.

SUMMARY

The geometry of the WR-21 engine centre section includes a substantial redesign around the RB211 HP spool in order to allow removal and return of recuperator air. The thermal behaviour and sealing of the new RAM and DAM has required particular attention and understanding but the retention of the HP spool has significantly reduced the overall programme risk. The new arrangement of nine radial combustors also allows significantly improved maintenance access and offers invaluable opportunities for dedicated development engine tests. The development builds at the Pyestock test facility have consistently demonstrated that a full set of combustor assemblies can be successfully exchanged in-situ.

Combustor aerothermal development has identified several factors of special difficulty in the design of a fixed geometry combustion system for an ICR gas turbine. These arise principally from three constraints: limited supply of air for wall cooling and control of combustion processes; conflict of combustor design conditions across engine operating modes,

and variable combustor feed aerodynamics. Rig testing has been used extensively in the assessment of these risk areas and has been highly successful in mitigating the design risks prior to engine testing. In particular, the achievement of satisfactory wall temperatures and the elimination of aerodynamic variability have been crucial in overcoming the special difficulties of the ICR environment.

Significant lessons have been learned through the WR-21 engine development programme providing the foundation of knowledge of the design of combustors for future advance cycle gas turbines.

REFERENCES

Crissalli A J, Parker M L, "Overview of the WR-21 Intercooled Recuperated Gas Turbine Engine System - A Modern Engine For A Modern fleet", ASME 93-GT-231.

Hawkins W J, et al. "Systems development Test Programme For The WR-21 Intercooled Recuperated (ICR) Gas Turbine Engine System", ASME 94-GT-186.

PAPER No. 2 Parker, Macleod & Coulson (presenter: M. Parker)

Question 1: G.J. Sturgess, ISSI, U.S.

What decided the balance of the work split between the CFD calculations and the water analogy rig in the investigation of the complex flow fields around the combustor barrel and into the individual combustor air inlets?

Answer

The prime reason for preferring water analogy techniques over CFD analysis for investigating the flow fields was that greater confidence in the results existed with the former technique. We also believed that the results would be available earlier in the design process using the water analogy method. Two water analogy models were employed. The first investigated a 360° scaled-model of the total combustion system including all nine combustors. The second model was of a full-scale single combustor (i.e. 1/9th. of the total combustion system). The first model was used to investigate the flow distribution around the combustors. The second model was used to investigate the effectiveness of different modifications added to desensitize the combustors from the variable flow field features.

TECHNICAL CHALLENGES ASSOCIATED WITH THE DEVELOPMENT OF ADVANCED COMBUSTION SYSTEMS

Christopher A. Van Erp and Marcus H. Richman
 Naval Air Systems Command
 Bldg 106, Unit #4
 22195 Elmer Road
 Patuxent River, MD 20670-1534
 USA

INTRODUCTION

The U.S. Navy, as a participant in the United States' Integrated High Performance Turbine Engine Technology (IHPTET) initiative, is dedicated to increasing aircraft engine performance to satisfy the propulsion requirements of future Navy aircraft. This is accomplished by identifying the propulsion requirements, in terms of performance and total cost, for specific Navy aircraft. The required engine technology advances are then broken down into specific engine component technology objectives. Advanced technology is then developed on the component level. Once an appropriate level of readiness is reached, the components are then assembled into an engine for overall advanced propulsion system demonstration. Technologies from this demonstrator engine are then made available to development engine programs, such as the Joint Strike Fighter (JSF), for further development and eventual transition to production engine programs.

The figure of merit used to measure performance is engine thrust/weight ratio. The role of the combustor in this endeavor is to provide the necessary temperature rise to increase core engine output. This drives the combustor to operate at higher fuel/air ratios which in turn drives a larger portion of the combustor volume to operate at or near stoichiometric conditions. Combustor operation at these levels must be achieved with an eye to numerous other parameters such as durability, weight, cost and emissions. The technical challenges presented in attempting to meet these objectives simultaneously are the subject of this paper.

HIGH FUEL/AIR OPERATION

The most effective way to increase engine cycle output is to increase the energy generated by combustion of fuel. The temperature limitations of the component immediately downstream of the combustor, the turbine, limits the temperature exiting the combustor (T4). As advances are made in turbine material and cooling technology, the maximum allowable combustor exit temperature increases. To generate the higher temperatures desired, the fuel/air ratio of the combustor is increased (Figure 1).

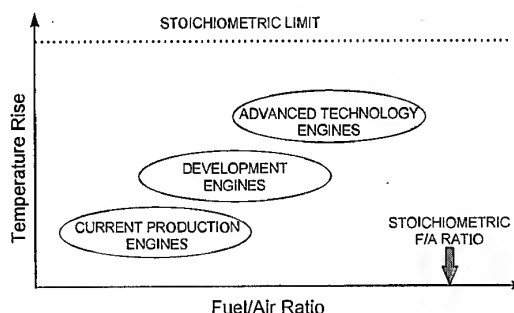


Figure 1

At fuel/air ratios below 0.04 combustor behavior is fairly well characterized. Instances of locally stoichiometric conditions are infrequent. As average fuel/air ratio (FAR) increases however, stoichiometric conditions become more prevalent. Although it is known that dissociation causes a reduction in temperature rise as stoichiometry is approached, the total influence of near stoichiometric conditions on combustion behavior is not well understood. The area of most concern is the characteristic of the molecular and atomic species at the combustor exit. If the gases exiting the combustor contain an appreciable amount of combustible species, reaction will occur in the turbine when these species are supplied with oxygen from turbine cooling air. A more complete understanding of the composition of the gases exiting the combustor at high fuel/air ratios is required.

COMBUSTOR EXIT FLOW CHARACTERIZATION

Combustor exit temperature is usually quoted as an average value which is appropriate for engine cycle performance applications. The turbine designer, however, is concerned not only with the average combustor exit temperature but also with the temperature profile of the gases exiting the combustor. The combustor exit temperature profile is characterized in two ways: the highest circumferential average temperature at a specific spanwise location (profile factor) and the maximum temperature at any location in the combustor exit flowpath (pattern factor).

The following equations provide numerical values for these parameters.

$$\text{Profile Factor} = \frac{T_{\max, \text{rad}} - T_{\text{avg}}}{T_{\text{avg}} - T_{\text{inlet}}} \quad (1)$$

$$\text{Pattern Factor} = \frac{T_{\max} - T_{\text{avg}}}{T_{\text{avg}} - T_{\text{inlet}}} \quad (2)$$

These equations help define the combustor exit temperature conditions for turbine durability consideration. Traditionally, lower numeric values for these parameters have been considered better for turbine durability because they represent lower maximum temperatures that the turbine must accept. More complete information is provided by a plot of these parameters over the span of the combustor exit flowpath (Figure 2).

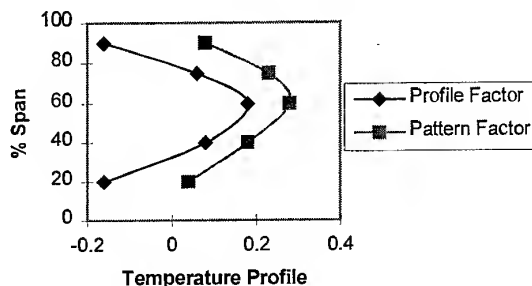


Figure 2

Plots such as these allow the turbine designer to accommodate the hottest portions of the combustor exit flow with increased turbine cooling air. As average combustor exit temperature increases two things occur: as mentioned before, the incidence of locally stoichiometric conditions increases and the average temperature rise increases. The locally stoichiometric condition determines the absolute maximum temperature in the combustor exit flowpath. Once this level has been reached, a higher local temperature is not possible. Therefore, the T_{\max} in the Pattern Factor equation [Equation 2] has reached its maximum value. The average temperature rise across the combustor however, can continue to increase. Because this is the denominator in the Pattern Factor equation, this causes the Pattern Factor value to decrease. This may generate a false sense of improvement in the combustor exit temperature profile and conceal a situation of concern for the turbine (Figure 3).

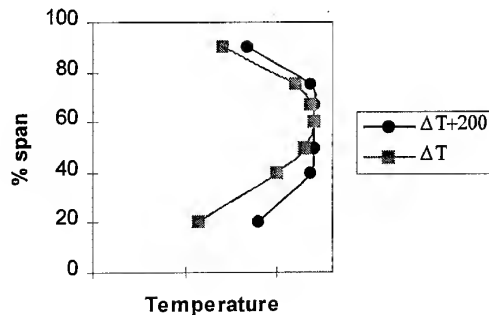


Figure 3

The temperature data for the right hand curve of Figure 3 converted into the Temperature Factor format defined in Equation 3 shows the same characteristic, as seen in Figure 4.

$$\text{Temperature Factor} = \frac{T_{\max} - T_{\text{avg}}}{T_{\text{avg}}} \quad (3)$$

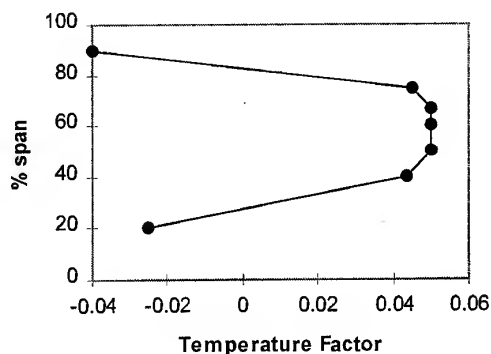


Figure 4

A parameter that better describes the conditions at the combustor exit for high FAR combustor designs is needed. The use of a Fuel/Air Factor (FAF) has been suggested by gas turbine engine manufacturers. This parameter is defined as follows:

$$\text{Fuel/Air Factor} = \frac{FAR_{\max} - FAR_{\text{avg}}}{FAR_{\text{avg}}} \quad (4)$$

This parameter accommodates fuel/air ratios above the stoichiometric value without flattening out as Temperature

Factor does as seen in Figure 5. For this reason, the Fuel/Air Factor characterizes the conditions at the combustor exit better than the Pattern Factor.

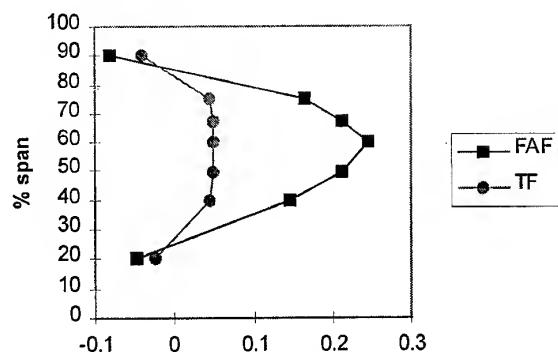


Figure 5

INSTRUMENTATION

The measurement of combustor exit gas temperatures has traditionally been accomplished using thermocouples. The highest temperature capability thermocouples (type B) are limited to measuring temperatures of approximately 3100°F (1700°C) with an accuracy of about 5°F. Durability is very limited at these conditions. Until recently, this capability has been sufficient for measuring combustor exit temperature but advanced technology engines have surpassed this value for engine T4. While thermocouples are still useful for measuring temperature rise in combustor rigs at ambient inlet conditions, gas sampling probes with higher maximum temperature capability are necessary for combustor development. The gas sampler measures molecular and atomic species in the combustor exhaust from which local fuel/air ratio and efficiency are determined. Temperature is then calculated based on this information, known inlet conditions and final pressure. The accuracy of temperature measurements taken by this method is difficult to verify because there is no other practicable method to measure these temperatures. An alternate method to measure combustor exit temperature and a means to verify the gas sampler reading are needed to accurately characterize advanced combustor designs.

EMISSIONS

Military engines have traditionally not been subject to the same emissions restrictions as civil aircraft engines. The only restriction observed has been the prevention of visible emissions for survivability reasons. This has allowed the military engine combustor designer to concentrate on performance and operability without compromise to reduce emissions. However, an environmental impact statement is

now necessary prior to deployment of new aircraft weapon systems. It is desirable to avoid an unfavorable report of this kind. As shown in Figure 6, NO_x production increases exponentially with the local flame temperature [ref. 1]. One of the major hurdles in minimizing NO_x production is keeping local flame temperature below 2700°F. With fuel/air ratios for advanced military engine combustors marching ever closer to the stoichiometric value it has become near impossible to meet this criteria with current designs.

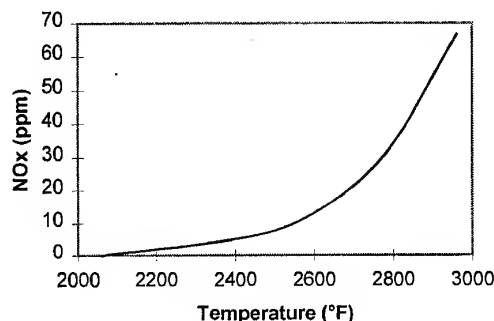


Figure 6

Improved mixing techniques developed for reduced length combustor designs have helped to eliminate locally rich zones in the combustor. This reduces NO_x production when these locally rich zones, or hot streaks, generated temperature excursions into the high NO_x production realm. Advanced military combustors are now operating in this realm on an average basis making these advanced mixing designs ineffective for NO_x reduction. Combustor concepts developed for civilian or industrial applications, such as lean direct injection and rich burn/quench/lean burn, have operational limitations that make them unacceptable for military engine applications. Innovative combustor designs that maintain NO_x emissions at reasonable levels with minimal impact on combustor stability, operability and weight are necessary to address this concern.

COMBUSTOR AIR FLOW DISTRIBUTION

High temperature rise in the combustor cannot be achieved simply by increasing fuel flow. Successful combustor designs are dependent upon effectively mixing fuel and air to maintain the high combustion efficiencies necessary for fuel efficient engines. More air will be required in the combustor front end to accommodate an increase in fuel flow. Since the portion of engine air flow allocated to the combustor is not likely to increase, the distribution of combustor air flow must be changed to accommodate a higher fuel flow. Air that in previous combustor designs had been used for combustor liner cooling or dilution of combustion products must be used

for combustion in high fuel/air ratio combustor designs [ref. 2] (Figure 7).

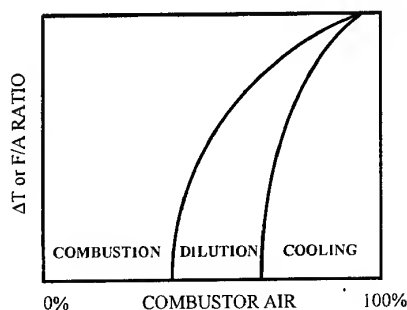


Figure 7

Bringing more fuel and more air into the combustor front end presents both a fuel/air mixing and a stability challenge to the combustor designer. The increased amount of fuel must be distributed evenly throughout the combustor volume which is leading to fuel injection designs other than the conventional fuel nozzle and swirler combination. The increase in combustor front end air flow makes it more difficult to stabilize combustion at lean operating conditions. Innovative flame stabilization techniques are being pursued to address this technical challenge.

COMBUSTOR LINER DURABILITY

Another technical challenge driven by high fuel/air operation is the need for increased combustor liner temperature capability. The temperatures generated by high fuel/air ratio combustors increase the heat load on the combustor liner. The portion of combustor air designated for liner cooling is not only decreasing, as described above, but the temperature of the cooling air is increasing. This is due to the higher pressure ratio compressors of advanced technology engines. Higher temperature cooling air reduces the effectiveness of any liner cooling design. Liner surface temperatures will surpass 2400°F (1300°C) under these conditions which far exceeds the capability of current thermal barrier coated metallic liners. Maintaining sufficient combustor liner life in this increasingly harsh environment is a significant technical challenge.

To address this challenge, advanced cooling technology and high temperature liner materials are being developed. The use of smaller, more numerous air passages is enabled by advances in manufacturing technology which has opened up a new world of creative cooling design possibilities. Advanced materials, such as ceramic matrix composites (CMCs) are being developed for combustor liner applications. Although CMCs have the potential to expand the liner material

temperature capability, current versions do not yet meet the 2400°F requirement. Current CMCs also have a low stress capability relative to metal. This presents limitations on the size and shape of any liner holes and on the size and shape of the liner itself. Although progress has been good with both cooling techniques and liner material development, there is still much to be accomplished. It is important to work material, manufacturing and cooling technologies simultaneously to ensure that the liner cooling technology is compatible with the liner material of choice.

HIGH TEMPERATURE FUEL

Cooling challenges for advanced technology engines are not limited to the combustor. The turbine component has always had an insatiable appetite for cooling air. The engines mechanical systems are also in constant need of cooling air. The pressure ratios of advanced technology engines are expected to be so high that the final stages of the compressor may have to be cooled. All of these cooling requirements, in addition to airframe requirements, have increased the demand for any possible heat sink the engine may have. One area that may not have been fully exploited is the fuel. The fuel temperature of current production combustors must be maintained below 300°F to avoid fuel thermal stability problems. Advanced technology programs are investigating the possibilities of fuel additives, dual phase (liquid and vapor) fuel systems, and supercritical/endothermic fuel systems to increase the fuel heat sink capacity. All of these efforts will raise the fuel temperature significantly beyond current levels.

The challenges presented by these systems are numerous. Although not specifically a combustor concern, compatibility of any additives with the fuel storage and delivery systems must be assured. This is especially important for aircraft carrier fuel supply systems where fuel purification and storage systems are more robust and more difficult to modify than land based supplies. The impact of dual phase fuels on the fuel injection system and combustor stability is another area that requires further investigation. Separate paths for liquid and vapor fuels increase the complexity (cost) and weight of the fuel delivery system, two areas where increases are all but forbidden in engine development programs. The injection of vaporized fuel into the combustor raises a stability concern that may manifest itself as an undesirable acoustic phenomena. The special fuels that may be necessary for the endothermic systems are subject to the same compatibility requirements as the additives described above.

There are significant advances possible in the area of high temperature fuels and there are significant technical challenges associated with these advances. Although these advances are not yet required, the demand for heat sink capacity may soon make them a necessity.

COMBUSTION SYSTEM LENGTH

The desire to minimize combustion system length is driven by the desire to reduce overall engine weight. A reduction in combustion system length not only reduces the weight of the combustor but also allows reductions in engine case and shaft length. Combustor burning length is determined by the fuel/air mixing characteristic of the combustor. This length is minimized while ensuring complete combustion at the exit. Improvements in mixing then, will not only provide benefits in exit temperature profile and efficiency but will also lead to shorter combustor designs. The other lengths that the combustor designer controls are those associated with the diffuser, fuel injection, and flame stabilization. Innovative designs that combine these functions into a single piece of hardware are currently being developed. Combustion system length reductions of greater than twenty five per cent are foreseeable but the designs are still in the early stages of development. The challenges are to satisfy the individual requirements of the diffuser, fuel injection system and flame stabilization method with an integrated design.

SUMMARY

The technical challenges associated with advanced combustor development are generated by a variety of factors. The primary driver is the need to operate at high fuel/air ratios in order to deliver the required temperature rise to maximize engine thrust. Effective mixing of fuel and air has always been a combustor design challenge and this trend will continue. Combustor liner cooling and material technology are essential to meeting the temperature rise requirement. Challenges driven by engine system requirements include combustor length reduction, the reduction of undesirable emissions, and the need to accommodate high temperature and possibly vaporized fuel. Improvements in combustor performance must be coupled with reductions in combustor cost and weight to ensure successful transition of combustor technology to development engine programs.

The ultimate challenge may be maintaining the pace of technical advances achieved to date. Military combustor designs have traditionally led their civilian brethren and their development has enjoyed funding levels that have made this possible. This trend seems to be diminishing. This has led to more cooperative efforts with the civilian propulsion sector which is a positive result. The goals of military and civilian propulsion and combustion systems remain different however.

These are the challenges that have been identified, there may be others that have yet to be uncovered. Combustor designers have successfully identified advanced technologies to address these challenges and hopefully, over the next few years, these technologies will transition to the propulsion systems of the future.

ACKNOWLEDGEMENTS

The authors appreciate the consultation and insight provided by the following individuals: Tyler Evans and Charles Graves of Pratt & Whitney, Tim Roesler of Allison, Dale Shouse of the United States Air Force Wright Laboratories, and Kenneth Barlow, James Zidzik, and Anthony Cifone of the United States Navy, Naval Air Systems Command.

REFERENCES

1. Lefebvre, A.H., Gas Turbine Combustion, Hemisphere Publishing Corporation, 1983.
2. Clouser, S.D. and Kamin, R.A, "Combustion Technology Needs for Advanced High Pressure Cycle Engines" AGARD Conference Proceedings 536, May 1993.

Empirical and Anchored Methodologies for Controlling Combustion Dynamics

Raghavan P. Pandalai[†], George C. Hsiao[§] and Hukam C. Mongia^{*}

GE Aircraft Engines, Combustion Center of Excellence

1 Neumann Way

Cincinnati, Ohio 45215, USA

ABSTRACT

This paper describes the empirical and anchored methodologies developed at General Electric Aircraft Engines (GEAE) to control combustion dynamics in aircraft and aero-derivative industrial turbine engine combustion systems. Combustion instability problems in aircraft and more recently in aero-derivative industrial engine combustors have been a serious problem during development, and in some production engines. The conventional approach to this problem has been based largely on empirical correlations and design experience. The advent of low emissions combustors for aircraft and industrial applications which incorporate several innovative technologies have put additional pressures to look at this problem from a more fundamental viewpoint so as to identify a dynamics 'fix' quickly based on root cause, and minimum testing to demonstrate the fix. To achieve this goal, a physics based combustion dynamics model is developed and described in this paper. The acoustic abatement technology that has made an optimum use of both the passive and active control techniques (hybrid control system) employed in GEAE's product lines consistent with customers' needs has also been integrated into this model.

The formulation of the dynamics model is based on the exact solution of the acoustic wave equation and is capable of incorporating several features unique to gas turbine combustors. The current approach is built on an acoustic based framework and the total combustion system from compressor exit to first stage turbine nozzle including fuel delivery system, fuel premixer and acoustic damping devices are incorporated into this model because of their impacts on overall dynamics. Engine test data obtained during the development phase of GEAE's ultra low emission industrial engine combustor development program was used to demonstrate the feasibility of the model and the anchored approach. The predicted trends not only agreed very well with test data, but also demonstrated the capability of the model to distinguish between acoustically active and inactive regimes of operation.

[†] Staff Engineer

[§] Lead Engineer

^{*} Manager

Copyright © 1998 by the author.

I. INTRODUCTION AND BACKGROUND

The design process for conventional compact high pressure aero and aero-derivative gas turbine engines includes careful and deliberate tradeoffs between often conflicting design requirements of low-emissions, low cost of ownership, performance, durability and operability. In order to meet the added challenge of achieving low NO_x, CO and HC emissions for a broad range of engine operation in aircraft applications, and also in industrial turbine applications without diluent (water/steam) injection (so called Dry Low Emissions, DLE), combustion systems rely on innovative techniques including ultra-lean combustion and flame stabilization devices operating over a narrow range with essentially premixed fuel/air mixtures.

Combustion instability (dynamics) problems encountered in industrial devices and liquid rocket engines[1-2] have been successfully solved through a combination of empirical design experience and simple models based on Rayleigh criteria for heat release. Usually, simple models based on the convective and chemical kinetic times have given us useful insight for solving dynamics problems in the conventional gas turbine combustors and afterburners. However, aircraft turbine engine combustors designed for low emissions and employing two stage burning (called Double Annular Combustors, DAC) have encountered combustion instability over a broader range of operation than conventional Single Annular Combustors (SAC), and therefore requires complicated engine control strategy for controlling pressure oscillations. The problem is much more acute in combustors designed for ultra low emission applications such as the GEAE LM6000 Industrial Aero-derivative (IAD) engines using DLE technology. Since the DLE combustor operates as close to lean flame stability limits as possible, the derivatives of chemical times to e.g., random mixture fraction variations are relatively larger than that of conventional diffusion flame combustors operating close to stoichiometric equivalence ratios. This coupled with the relatively sparse design and experience database of DLE combustion concepts has made the lean premix combustion dynamics problem a rather challenging one for the designers.

The basic approach to the problem of combustion instability is to design a combustion system to provide a stable flame with multiple fuel injection ports to release heat energy in a reasonable length and to meet the Rayleigh criterion. While it is relatively easy to design a combustion

system to meet the first requirement, axial heat release in a reasonable length is difficult to achieve in aircraft and aircraft-derivative combustors because of space limitations. It is reported in Reference [3] that a non-aero derivative gas turbine combustor design for power generation applications has incorporated features to inject fuel over an axial distance of about 9 inches presumably to alleviate the instability problem. The third requirement of meeting Rayleigh's criterion while easy to understand and interpret, is difficult to implement in practice for several reasons. Meeting this requirement involves an accurate knowledge of phasing relationship between fuel injection and heat release and also between heat release and dynamic pressure oscillations so that heat release can be accomplished when the acoustic pressure oscillations are low both in terms of time and spacial coordinates. While scattered information on this subject has been published in limited form by engine manufacturers, a well established design practice or guide lines to satisfy Rayleigh criterion in a practical system over the entire operating envelope of the gas turbine engine is virtually non-existent at this time. Currently established design practices are largely based on empirical correlations and design experience rather than on a well established theoretical framework encompassing the diverse areas of combustion, fluid mechanics, and acoustics. To alleviate this problem, the need for an analytical model capable of predicting resonant frequency, mode shape and amplitude has been felt for a long time. A comprehensive model development effort was therefore initiated 2 years ago at the GE Aircraft Engine to address the growing concerns identified during advanced engine development programs such as Advanced-Subsonic-Transport (AST), High-Speed-Civil-Transport (HSCT), and DLE, etc. In what follows, the traditional approach to solving dynamics problems in aircraft diffusion type combustors and the more recent ultra low emission industrial combustors are discussed, and the frame work of a physics based combustion dynamics model is described in detail.

II. EMPIRICAL METHODOLOGY FOR DIFFUSION FLAME COMBUSTORS

The dynamics characteristics of diffusion flame combustion systems depend primarily on chamber geometry, fuel-air equivalence ratio, and fuel spray characteristics. Typical cross section of an aircraft turbine engine combustor of the single annular design is shown in Figure 1. Key features of this design include 30 to 35% of total combustor airflow into the primary zone, approximately 30% of airflow for dilution and liner cooling, and the remainder for profile control and turbine cooling requirements. It is worth noting that liner cooling air which

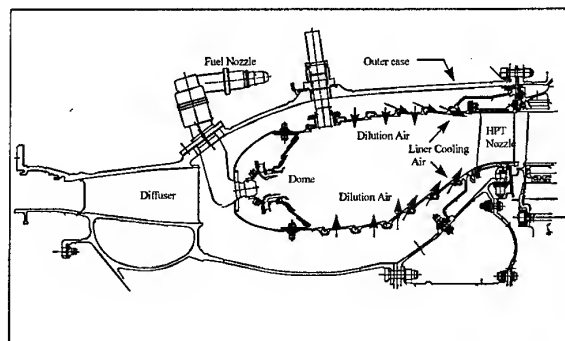


Figure 1 Typical Aircraft Engine Single Annular Combustor (SAC) Cross Section.

is ingested into the combustor acts as an effective attenuator of combustion generated noise over a broad range of operating conditions. These combustors typically experience high dynamics at comparatively low equivalence ratios during a transition involving burner mode changes, or during acceleration and deceleration along the operating line which may last only a few seconds. These instabilities are known by various names such as combustor buzz, growl, or howl depending on the specific frequency and source of its origin.

The traditional approach to solve combustion dynamics in diffusion flame combustors is illustrated in the block diagram of Figure 2. Once the source of instability is identified through engine testing, identification and final demonstration of a dynamics fix involved several levels of tests before production introduction into the appropriate product line. Three prime sources of combustion instability have been recognized in the past including fuel feed system coupling, external system instabilities, and instabilities arising from flame oscillations. These sources may exist either independently or in combination depending on the specific problem at hand. For example, external instabilities outside of the combustor may be amplified within the combustor and in turn could generate either flame instabilities or fuel line instabilities. Fuel feed system coupling with combustor pressure oscillations have been a major source of instability in many product lines. The solution technique for this situation invariably involved decoupling the fuel system by acoustically isolating them from the combustor by design modifications to the fuel delivery system. Installation of higher pressure drop fuel nozzles, eliminating fuel vapor from secondary passages, and improving the overall heat transfer characteristics within the fuel nozzle passages, have been employed in product lines with varying success.

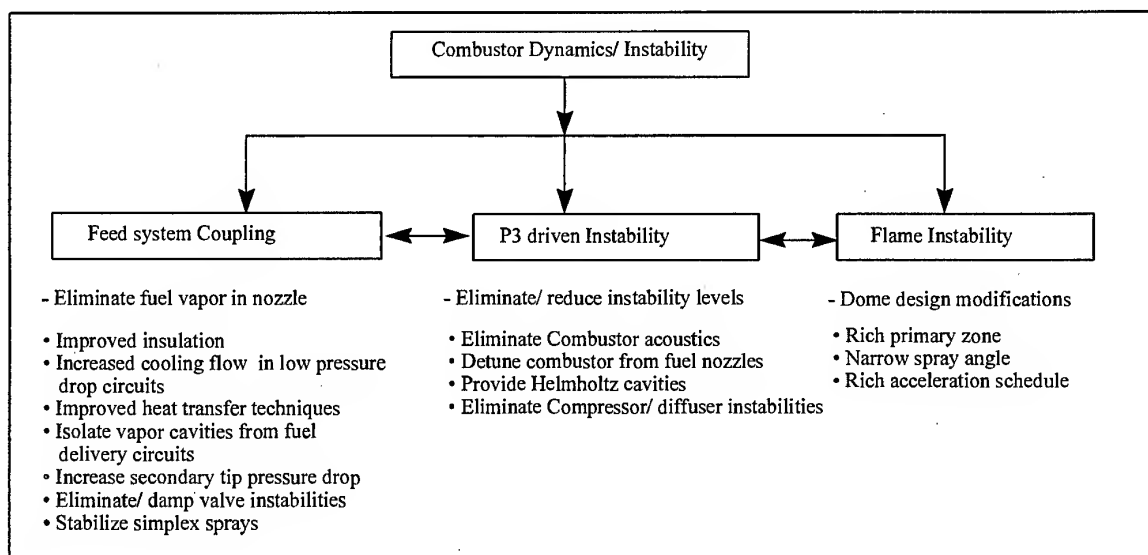


Figure 2. Control of Combustion Dynamics in Conventional Design

Combustion instabilities arising from sources external to the combustor such as from compressor and diffuser instabilities (due to flow separation, rotating stall, bleed extraction etc.) have been addressed through a variety of techniques including detuning devices, Helmholtz resonators, and flow path modifications to eliminate flow separation.

Flame instability in the form of pulsating flame and/ or unanchored flame is the third major source of combustor pressure oscillations, and can be eliminated by design changes to the fuel spray characteristics such as rich primary zone, narrow spray angle, rich acceleration schedules etc.

The empirical methodology although useful in many instances, has severe drawbacks because of their limited applications due to its product specific nature. Identification and demonstration of a dynamic fix on an engine has also been a time consuming process involving several component redesigns and tests using cut and trial techniques. In addition, finding a direct correlation between results from small scale sector tests and full scale component tests have been elusive and often not straight forward because of the inability to simulate acoustically sensitive features present in an engine environment. There has been a lack of basic understanding of the instability problem, driving mechanism and its interaction with design variables controlling emissions and performance. This lack of understanding has resulted in designs prone to high combustion oscillations and hardware failures with the consequence of escalating the cost and time for new engine

development as well as penalties associated with engine down time.

III. EMPIRICAL METHODOLOGY FOR ULTRA LOW EMISSION COMBUSTORS

The dynamics characteristics of combustion systems designed for ultra low emissions are significantly different from SAC. The GEAE LM6000 Industrial Aero-Derivative (IAD) combustor design which has evolved through a number of stages since the program was initiated in April 1990 incorporates several novel features unique to

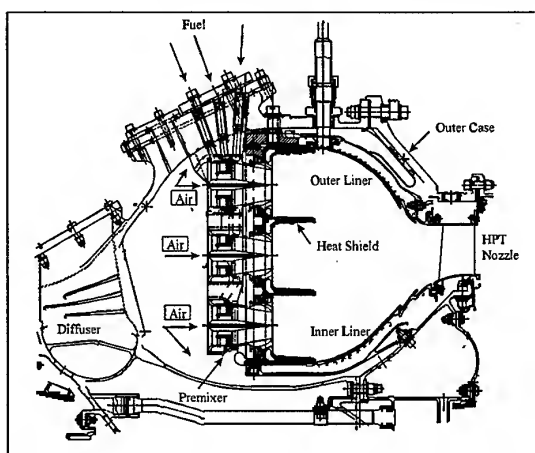


Figure 3 LM6000 Dry Low Emission (DLE) Combustor Cross Section.

an aero-derivative design[4-5]. The fundamental feature of this combustor is lean premixed combustion of fuel and air to obtain low NO_x levels. A typical cross sections of the LM6000 IAD combustor is shown in Figure 3. The current production IAD combustor is a triple annular design and is convectively cooled to minimize wall quenching of CO and for making available the maximum fraction of compressor air for combustion. Other significant differences between the DLE and SAC are in regard to 1) fuel/air mixing device, e.g., swirl cup in SAC versus dual annular counter-rotating axial swirlers w/ multiple natural gas (NG) injection points, 2) absence of any dilution and/ or liner cooling air ingested into the front end, and 3) the unique triple annular design for fuel staging and ultra-lean flame temperature levels. The middle annulus of the DLE design is comprised of 30 "pilot" premixers which are lit over the entire operating range; the outer and inner annuli contain an array of 30 and 15 premixers, respectively, which are lit, or "staged", in varying numbers to maintain combustor operation within a narrow flame temperature band. Staging may be accomplished in rings (radial) or individual zones within a ring (circumferential). Radial staging is preferred over circumferential staging because of the less likelihood for turbine blade excitation which is a real concern with circumferential staging.

It may be worth recognizing that even though dynamics in conventional diffusion flame combustors is not considered to be an issue of heightened concern now a days, we never-the-less do encounter dynamics at some critical points, and design guidelines allow acoustic activities up to 2.5 pounds per square inch (psi) RMS levels in conventional combustors. As we will see in the following paragraphs, since ultra low emission designs have features that could be more prone to dynamic excitations, we still restrict the acoustic activities to the same levels as allowed in the conventional combustors except that we may encounter the instability problems throughout the engine operating regime.

Several characteristic aerodynamic and geometric features of the DLE combustor contributing to increased levels of acoustic activity are noteworthy from an instability standpoint. A detailed description of these features can be found in Reference [6]. Among the significant features are: the minimal cooling flow ingested into the front end of the combustor, uniform fuel-air mixture required for low NO_x, geometric symmetry of the chamber configuration, concentrated heat release in a limited space, and the presence of external system instabilities inherently present in a commercial power generation environment. These factors contribute significantly to the overall instability of a lean premixed combustion system.

In addition, the DLE engine operation from no load to base load is achieved through a unique fuel staging scheme required to achieve low emissions throughout the load range. This staging scheme also has a significant impact on overall dynamics as explained below.

A pictorial representation of the different burning modes and the staging scheme of the LM6000DLE is illustrated in Figure 4. A detailed description of controlling engine power with compressor bleed variations is given in Reference [4]. Engine starting from ignition and up to core idle is essentially accomplished by burning fuel in the pilot (center or B ring) dome only, with no fuel injection from either the outer and/ or inner rings of the combustor. As the engine is accelerated from core idle to no load synchronous speed (NLS), when the generator in a commercial power plant would be engaged to the core engine, eight out of the fifteen additional burners of the inner ring is fueled to meet the power requirement. This would correspond to operation in the so called B+C/2 mode (not explicitly shown in Figure

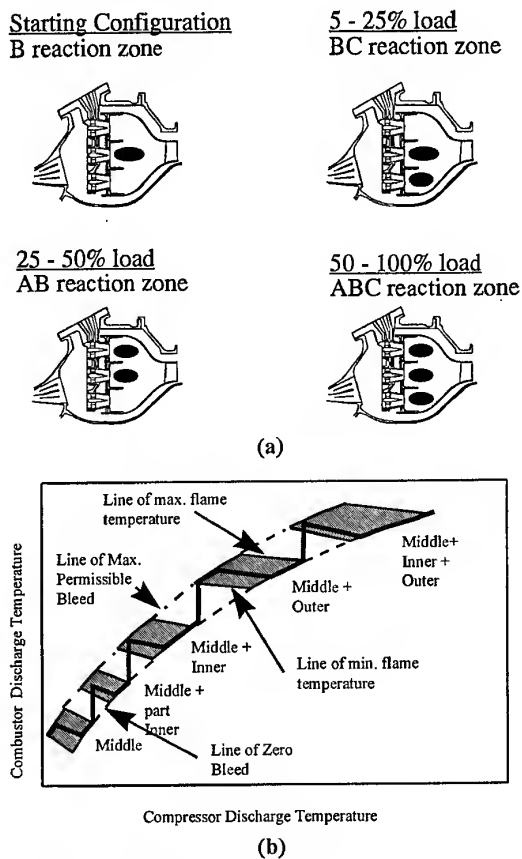


Figure 4 LM6000 DLE Combustor Burning Modes and Staging Scheme.

4). As the load is increased, additional fueling is initiated in the remaining cups of the inner ring (C dome) and subsequently in the outer ring (A dome) in a sequential manner so as to transition smoothly into the ABC mode when all the three rings take part in the combustion process.

Transition to three ring burning takes place around 40 to 50% power depending on ambient conditions. Two discrete frequencies have always been observed in this operating mode. In a given burner mode (BC, AB, or ABC), engine power is increased by decreasing the bleed and thereby pushing more air flow through the combustor proper. Additional fuel is injected in the appropriate rings to maintain the flame temperature at a pre-set level established during the mapping process. Once the maximum air flow through the combustor for a given mode is established, additional engine power is obtained by staging to the next higher ring and continuing the process previously described until full power is attained.

At the base load condition, the combustor burns fuel in all the three rings, with the amount of fuel in each of the three rings maintained at a pre-set level corresponding to stable operation consistent with acceptable dynamic pressure levels. Current production engines run with a temperature distribution where the pilot ring flame temperature is usually maintained at slightly higher levels than the inner and/ or outer rings for better flame stability. The particular temperature distribution currently scheduled into production engine control is based on several factors and tests conducted over the past two years during development

testing at various customer sites.

The magnitude of the dynamics problem with lean premixed combustion systems is considerably more complex and requires a different control approach than conventional diffusion combustors. The empirical methodology for dynamics control strategy leading to the current production control system is outlined in the block diagram of Figure 5. This has evolved through experience on the combustion system development activities on the full-scale annular rig, engine tests in the factory, as well as extensive tests at several customer sites. The specific approach involves a combination of passive and active control techniques in addition to incorporating conventional design features to provide for a stable flame, eliminating fuel feed system coupling with combustor, and minimizing system instabilities external to the combustor. This approach has worked very effectively and has become the basis for controlling dynamics in all current production engines.

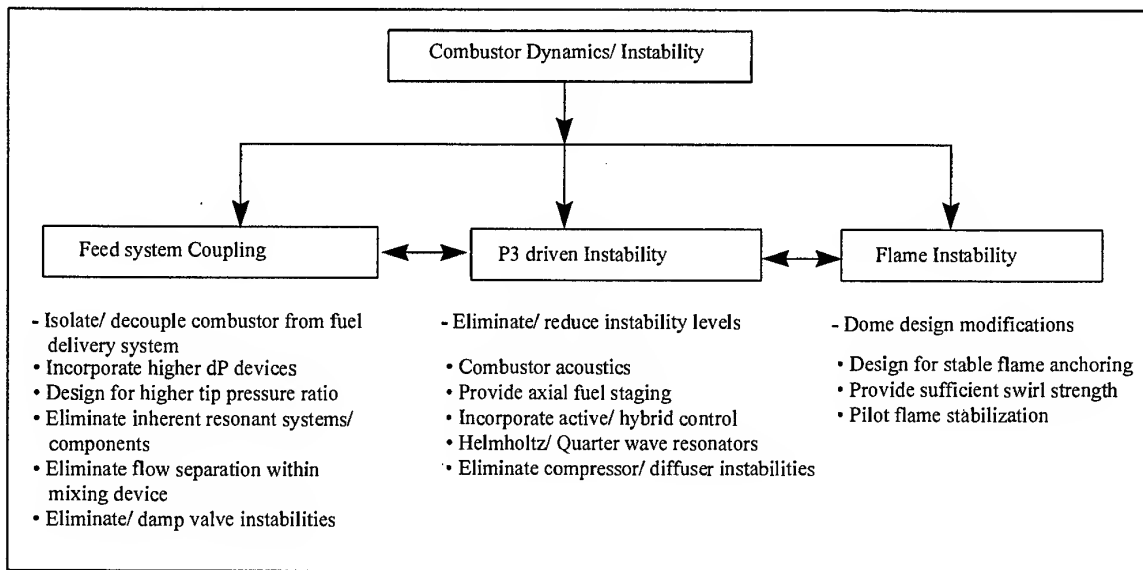


Figure 5 Control of Combustion Dynamics in Low and Ultralow Emission Designs.

IV. ANCHORED METHODOLOGY

The cornerstone of the anchored methodology at GEAE is a physics based combustion dynamics model for gas turbine engines and applicable to current and advanced designs. The formulation is based on the exact solution of the acoustic wave equation and is capable of incorporating physical models of sub-components in a relatively easy manner. The various components of the total combustion system from compressor exit to first stage turbine nozzle including fuel delivery system, fuel premixer and acoustic damping devices are incorporated into this model because of their impacts on overall dynamics. The theoretical framework for the current work is built on an acoustic approach to ensure easy integration of physical sub-models and fast turn around time for design analysis. In addition, future improvements in any of the sub-component models when available (based on improved physics and unique designs) can be easily incorporated into the current framework. The sub-models of the various components of a gas turbine combustion system is based on analytical formulations, semi-empirical correlations, or response functions correlated from a comprehensive unsteady CFD analysis.

Many features unique to gas turbine combustion systems were treated in the current model, including

1. Effect of mean flow Mach number;
2. Flow field non-uniformity in axial, radial, and circumferential directions;
3. Combined Axial and Circumferential Acoustic Modes;
4. Inclusion of frequency dependent generalized boundary conditions;
5. Coupling between diffuser and combustor;
6. Effect of passive damping devices such as acoustic quarter wave dampers;
7. Physical sub-model for unsteady heat release; and
8. Active combustion control using time unsteady fuel control.

To facilitate the analysis, the domain of interest, from compressor outlet guide vanes (OGV) to first stage turbine

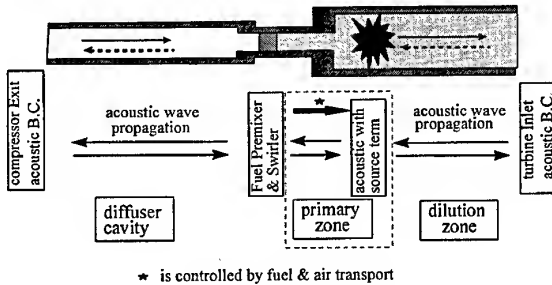


Figure 6 Schematic of Acoustic Wave Propagation in Gas Turbine Combustor

nozzle, is divided into three main sections or zones, namely diffuser cavity, primary zone, and dilution zone, respectively, as shown in Fig. 6. The fluid mechanic property variation (temperature, density, and flow Mach number) is introduced by dividing each of these three main zones into sub-sections in axial, circumferential, and radial directions. The continuous property variation can be replaced by a "stairstep" change in these properties and are further assumed to be uniform in each of these sub-cells. The length of each of these subsections is chosen such that the change in acoustic impedance between adjacent cells is relatively small.

In both diffuser cavity and dilution zone, the forcing functions on acoustic propagation are relatively weak compared to those in the primary zone. The acoustic field in these two sections of an annular combustor can be approximated using an unwrapped strip configuration and is best described by the solutions of classical wave equation in Cartesian coordinate system[7]

$$p'(x, y, z, t) = [A_1 e^{ik_x x} + A_2 e^{-ik_x x}] \cdot [A_3 e^{ik_y y} + A_4 e^{-ik_y y}] \cdot [A_5 e^{ik_z z} + A_6 e^{-ik_z z}] e^{-i\omega t} \quad (1)$$

$$\begin{aligned} \ddot{m}_z'(x, y, z, t) &= \rho u'(x, y, z, t) \\ &= \frac{1}{ck} [A_1 e^{ik_x x} + A_2 e^{-ik_x x}] \cdot [A_3 e^{ik_y y} + A_4 e^{-ik_y y}] \cdot \\ &\quad [-k_z^- A_5 e^{ik_z z} + k_z^+ A_6 e^{-ik_z z}] e^{-i\omega t} \end{aligned} \quad (2)$$

where A_i 's are complex wave coefficients. The wave numbers for pressure propagation in axial direction are denoted by k_z^\pm and the +/- signs correspond to forward and backward traveling waves. The wave numbers in radial and circumferential directions are represented by k_x and k_y , respectively.

Most of the fuel injected into the combustor is assumed to burn within the primary zone. The resulting energy release creates compression waves propagating away from the flame front. The acoustic waves induced by heat release serve as acoustic amplifiers which drive the unsteady motion in the combustion chamber. Following Chu's methodology[8], the acoustic field in the primary zone in frequency domain can be written as the left and right running pressure waves, respectively, using

$$p'_L = \frac{e^{ik_x x}}{2ik} \int_0^{L_b} S_0(\xi) e^{-ik_z \xi} d\xi \quad (3)$$

$$p'_R = \frac{e^{-ik_x x}}{2ik} \int_0^{L_b} S_0(\xi) e^{ik_z \xi} d\xi \quad (4)$$

where L_b is the length of primary zone, and S_0 is the forcing functions for the wave equation. This approach is capable of treating acoustic noise generation from the flame

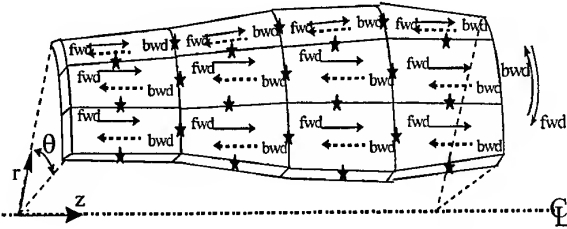


Figure 7 Wave Propagation in Acoustic Cells

zone with a finite thickness. For premixed gas turbine combustors, it is possible to assume further that the combustion occurs at a fixed axial plane in the primary zone. The effect of energy addition on acoustic wave generation can be expressed as pressure interaction indices of acoustic waves traveling with and against the flow direction, respectively[7]

$$N_f = N_b = \frac{\delta p / p}{p'_c / p_c} = \frac{\gamma(\sqrt{\psi} - 1) \frac{S_t}{c} K e^{-\alpha}}{1 + \tau_0 s} \quad (5)$$

where τ is the combustion time delay, $\psi = 1 + Q / C_p T_{st}$ and γ , c and S_t are the standard notations of fluid mechanics.

The acoustic field in each cell consists of forward and backward traveling waves, as shown in Fig 7. Calculation of the acoustic mode shape involves determining the wave coefficients (A_i 's in Eqs.(1)-(2)) in each cell. The correct solution for wave coefficients requires matching the acoustic pressure and mass flow at the interface between each sub-section and acoustic impedance at the compressor/diffuser and turbine/compressor boundaries. Figure 8 presents the coupling mechanism of combustion dynamics in a gas turbine combustion system. A forced oscillation with normalized magnitude set equal to one is specified as a forward-traveling wave at the swirler interface. The resulting fluctuation of chamber pressure

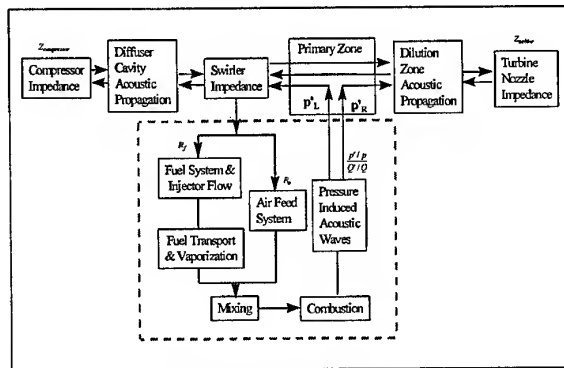


Figure 8 Block Diagram of Coupled Unsteady Heat Release Sub-Model

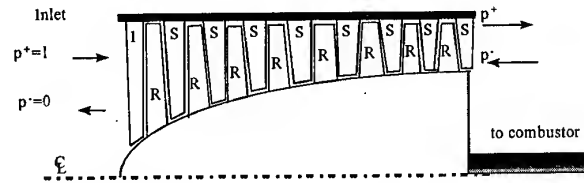


Figure 9 Schematic of Acoustic Wave Propagation in High Pressure Compressor.

alters the pressure drop across the fuel nozzle tip and induces a change of fuel flow to the combustor. The resulting variation in heat release can be associated with the change in fuel flow by a convection time delay τ . Two combustion induced acoustic waves are simultaneously generated and move away from the flame front in either direction. The forward traveling acoustic wave travels through the length of the combustor and is reflected back into the main cavity from the turbine nozzle. The backward traveling wave in conjunction with the reflected one, then propagates upstream against the flow and reaches the pre-mixer swirler vanes. Part of the acoustic energy is transmitted into the diffuser cavity through the pre-mixer passage, and the remainder is reflected back into the main combustion chamber. All the acoustic waves present in the combustion chamber, including combustion noise and reflected acoustic waves, are superimposed with each other using calculated phasing information based on mode shape analysis. The magnitude of the resulting dynamic pressure (when normalized) is called the stability index and is a measure of the relative intensity.

The interaction between combustor and its sub-systems is of critical importance in dynamics modeling since they are directly connected to each other. Any disturbance arising in one sub-system may propagate both upstream and downstream, and consequently affects the stability characteristics of the overall system. From the stability point of view, it is crucial to characterize the response of sub-systems to flow oscillations in the combustor. The response can be conveniently expressed as an acoustic admittance function or reflection coefficient at the appropriate boundary to simulate the real engine environment.

Compressor:

The acoustic reflection coefficient at the compressor-diffuser interface is calculated using the actuator disk theory[9]. This model was originally proposed to calculate pressure fluctuations resulting from the convection of temperature perturbations called entropy waves. The formulation is very general and is capable of predicting the reflection coefficient when an acoustic or vorticity wave impinges on the blade rows (stators and rotors) of a turbomachine. Figure 9 shows the schematic of a typical

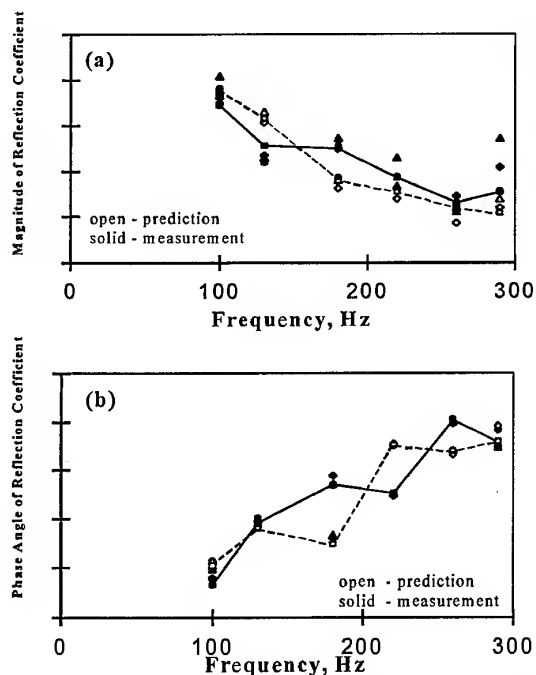


Figure 10 Validation of Actuator Disk Theory using Two-Stage Low Speed Compressor Rig, (a) Magnitude; (b) Phase Angle.

compressor flow path from inlet guide vanes (IGV) to outlet guide vanes (OGV). The reflection coefficient at OGV is calculated at the mid span location. The governing equations of this theory are based on the conservation laws of mass, energy and entropy of two adjacent blade rows, and assume no incident acoustic wave at the inlet. To evaluate the accuracy of this theory, acoustic data was taken from a two-stage low speed compressor test rig at GE Aircraft Engines[10]. Two adjacent arrays of pressure transducers consisting of a total of 36 sensors were installed in the test rig to characterize the forward and backward propagating waves. The excitation frequency was carefully selected to ensure that the acoustic mode of interest were "cut-on" at the measurement frequency. Figures 10(a) and (b) show comparisons of predicted versus measured reflection coefficient for the first order circumferential mode. The

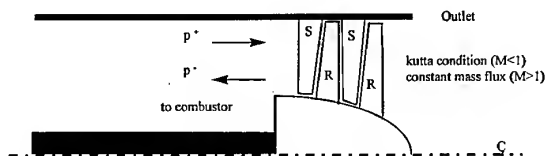


Figure 11 Schematic of Wave Propagation in Two-Stage High Pressure Turbine.

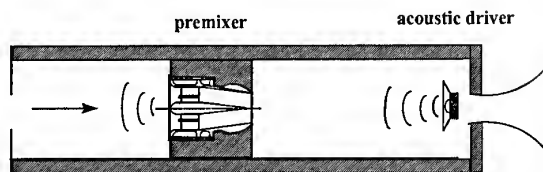


Figure 12 Schematic of LM6000 DLE Premixer in a Component Test Duct.

solid symbols and line are the measurement, and the open symbols and dashed line represent the prediction using the actuator disk theory. The results plotted in this figure clearly show that both the magnitude and phase angle of the acoustic reflection coefficient depend strongly on excitation frequency and agree reasonably well with measured data.

Turbine:

The frequency dependent reflection coefficient of high-pressure turbine interface is determined from a knowledge of the aerodynamic characteristics of the turbine cascades. Figure 11 presents the schematic of a two-stage high pressure turbine flow path similar to that on the DLE engines. Since the mass flow rate is fixed for a choked turbine nozzle, the boundary condition at the first stage nozzle can be assumed to correspond to an acoustic hard-wall at the mid span and can be written as

$$u'_{turbine} = 0 \quad \text{or} \quad Z_{turbine} = \infty \quad (6)$$

where $Z_{turbine}$ is the acoustic impedance. For an unchoked turbine nozzle, however, some acoustic energy will be transmitted past the turbine cascades. The reflection coefficient can therefore be calculated using the actuator disk theory and is defined by $R_f = p^- / p^+$ (forward traveling acoustic wave divided by backward traveling wave).

Swirler and Premixer:

The specification of the boundary conditions at the swirler/ premixer plane requires special consideration. The

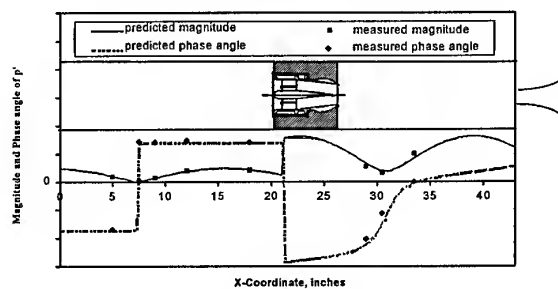


Figure 13 Acoustic Impedance Jump Across Fuel Premixer in Component Test Duct.

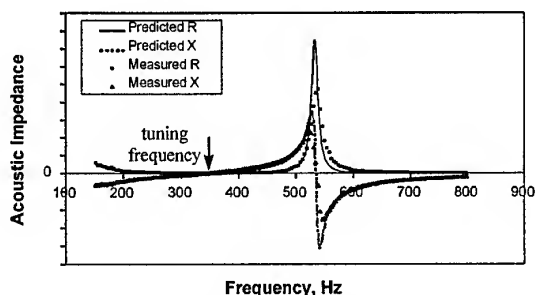


Figure 14 Comparison of Predicted Acoustic Impedance and Measurement for Quarter-Wave Damping Device.

impedance jump across the swirler presents a unique situation for gas turbine combustion systems. This device connects two acoustic cavities, namely diffuser and combustor, through a narrow air passage and therefore provides the coupling between combustion dynamics source and the diffuser cavity. Detailed investigation of the acoustic behavior of the swirler was conducted in a component test rig to investigate its characteristic features. Figure 12 shows the schematic of the test section consisting of a 3 x 4 inch rectangular cross section with an LM6000 DLE production B (middle) cup premixer assembly (with swirler) installed at 21 inches from the left end of the test duct. Acoustic speakers were placed on the right end of the duct to provide forced oscillations. Eight dynamic pressure sensors were installed in the test rig to measure the acoustic field at various axial stations. The square and diamond symbols in Figure 13 denote measured values (magnitude and phase angle, respectively) of the acoustic field in the test rig. The solid and dashed lines represent the predicted values based on one dimensional wave analysis[7]. The complex coefficients of the forward and backward propagating waves were obtained from a least square curve fit of the measured data. Results plotted on this figure clearly show an acoustic impedance jump across the premixer swirler.

Acoustic Damper Tubes:

Passive control devices such as acoustic damper tubes are increasingly being used to control dynamics and broaden the operating envelope in modern low emission gas turbine combustors for industrial applications. Functional integration of such devices into the dynamics model was therefore a prime objective of this work. Damper tubes of three different lengths are currently used in LM6000 DLE production engines. Since the diameter of these quarter-wave tubes is much smaller than the wave length of the resonant frequency of oscillation, a one-dimensional model has been found to be adequate to calculate the acoustic impedance. With the acoustic impedance at the hardwall

termination set equal to infinity, the acoustic impedance at the open end can be obtained by enforcing the continuity of acoustic pressure and mass flow at the interface of any two adjacent sections[7]. Figure 14 shows a comparison between predicted and measured acoustic impedance across the interface to the diffuser cavity. The acoustic resistance (R) is associated with dissipation of energy; while the reactance (X) is a function of the effective mass of the medium. The tuning frequency can be found where the acoustic reactance changes its sign. For the case presented in this plot, the tuning frequency was set at 350 Hz which is very consistent with the measurement.

V. CALIBRATION WITH ULTRALOW EMISSION DESIGNS

The key elements of the acoustic approach described in this paper include two major steps: (a) determination of the normal mode functions from a knowledge of the mean flow field and the correct (and realistic) boundary conditions at compressor and turbine interfaces, and (b) determination of acoustically active versus inactive regimes of operation based on the phasing information, and from a knowledge of acoustic wave propagation and feedback mechanism[7]. Engine test data obtained during the development phase of DLE combustor was selected for preliminary validation of the model. The data base from DLE tests covered multiple engines, different test sites, and extensive operation in the so-called ABC mode[6-7]. Two discrete frequencies, one at 450 Hz and the other from 600 to 650 Hz have always been observed in this operating mode. The exact frequencies at which these two modes appear depends on engine configuration and test conditions. The capability of the current model to predict these two observed frequencies from engine tests was a primary objective of this study. The procedure used to validate the current model is described below. The required properties of mean flow field for acoustic analysis was obtained from a steady state CFD simulation. A total of 69x73x51 grid cells were used to calculate the flow field of a 24-degree sector combustor burning in the ABC mode. The $k-\epsilon$ turbulence model and two-step eddy breakup combustion model were incorporated in the CFD simulation. The inlet turbulence kinetic energy, turbulence length scale, and velocity profile were obtained through anchoring process described in Reference [11]. The steady state energy release, and location of flame front were obtained by plotting the energy released from each ring as a function of axial location. An acoustic grid system consisting of 90x30x3 cells, and shown in Fig. 15, has been found to be adequate for detailed acoustic analysis for the full annular combustor geometry. The properties of each cell were obtained using linear interpolation as well as cell averaging in radial and circumferential direction based on CFD

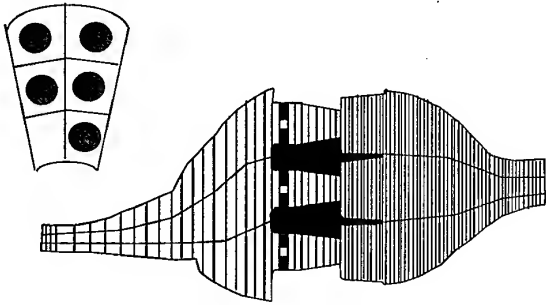


Figure 15 Grid System Schematic for Acoustic Analysis.

analysis. The coarse grid in radial and circumferential direction is designed to study the spectrum of stability index of each individual cup of this sector.

Figures 16(a) shows the comparison between measured and predicted dynamic response. The predicted response (shown by the thin line in figure) is compared with a line drawn through the individual peaks of the measured spectrum plot (shown by the thick line in figure). The predicted response is obtained by taking the maximum values of the individual responses from each ring, Figs (b)-(e), and normalizing with a reference value (peak value) from the measured spectrum plot. Results shown in Figs (b)-(d) are the predicted response of each individual cups of a 24 degree combustor sector. The circumferential temperature non-uniformity is taken into account by approximating the Eigen solution of the circumferential wave number using the unwrapped-strip technique[7]. The response characteristics of three different acoustic modes (plane wave, $m=1$, and $m=2$), are plotted in solid, dotted, and dashed lines, respectively, in these figures. Within the frequency range of interest, the model predicts two dominant frequencies, one at 500 Hz and the other at 600 Hz. These frequencies are reasonably close to those observed from engine tests at the specified operating condition. It is also seen from these figures that the 500 Hz mode is more active compared to the 600 Hz dynamics. The predicted resonance frequency of the 500 Hz mode is approximately 50 Hz higher than that observed from engine tests (Figure (a)). This deviation may be attributed to two possible sources of error which are inherently present in this computation. First, the accuracy of the predicted flame temperature is a critical factor because of its influence on speed of sound, and therefore contributes to errors in frequency prediction. Second, the uncertainty in estimating the location of the flame front (which is a required input into the model) by examining the steady state heat release contours could also be a factor contributing to the discrepancy in frequency calculation. The uncertainty in

calculating transport time τ associated with the unsteady heat release will induce different phase lag into the model and thus predicts a different resonance frequency. Based on the current analysis, the dynamic pressures response in the vicinity of 500 Hz is mainly contributed by the plane waves ($m=0$) from the middle and inner domes. On the other hand, the source of the 600 Hz acoustic mode appears to be the first order circumferential mode arising in the outer ring. This analysis did not indicate the presence of a second-order mode in LM6000 DLE combustor. In the high frequency region (above 1000 Hz) the current model over predicts the dynamic response probably due to the effect of neglecting viscosity in the governing equations.

The acoustic abatement for this family of engines is achieved through the following three technologies:

1. Active control of combustion dynamics through the incorporation of Acoustic Blowout Avoidance Logic (ABAL) which controls the dome flame temperature through a feedback loop;
2. Injection of a small amount of fuel called Enhanced Lean Blow-Out (ELBO) fuel to enhance lean blowout limit; and
3. Quarter-Wave acoustic damper tubes installed in the diffuser cavity to absorb combustion generated noise.

These three proven technologies have been very effective in controlling dynamics and have accumulated over 200,000 hours of engine operation in factory testing and commercial operation. A detailed description of the instability characteristics and control logic for LM6000 DLE combustion systems can be found in Reference [6]. It was observed during development testing that the optimum dome stoichiometry for minimal acoustics required maintaining the pilot (middle) ring at a relatively higher temperature (by approximately 150 to 200 degrees F) compared to the inner and outer rings. This operating condition in the ABC mode

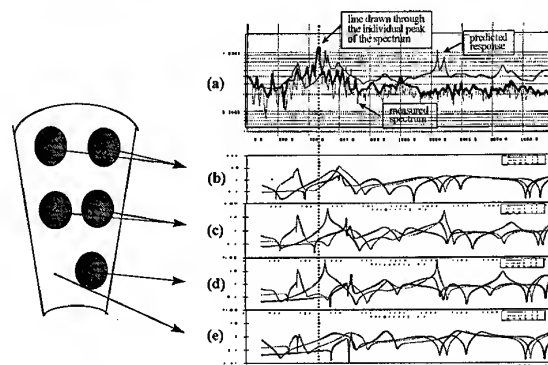


Figure 16 Typical Comparison of Predicted Stability Index versus Measured Frequency Spectrum for LM6000 DLE Combustor.

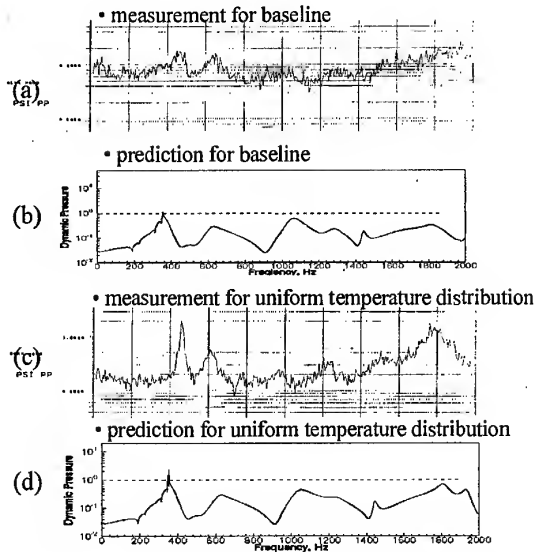


Figure 17 Effect of Radial Temperature Non-uniformity on Combustion Dynamics.

and the corresponding dome stoichiometry was chosen to be the baseline condition for the current anchoring and parametric studies reported in the following analysis.

The acoustic analyses of the baseline and a hypothetical uniform temperature distribution case were conducted to investigate the effect of radial temperature non-uniformity on combustion instability. The measured and predicted responses (using the approach described in Reference [7]) are shown in Figs. 17(a) and (b) respectively for baseline operation, and in Figs. 17(c) and (d) respectively for an operating condition with uniform

temperatures in all three domes. The measured spectra shown in these figures were based on dynamic pressure measurements from pressure sensors installed just downstream of the flame front in the DLE combustor. The predicted response is obtained by taking the maximum values of the individual responses from each of the three rings. Two distinct frequency peaks near 400 and 600 Hz were found from the analysis. These frequencies are reasonably close to those observed from engine tests at the specified operating condition. It is also seen from these figures that the 400 Hz mode is more active compared to the 600 Hz dynamics for both operating conditions. In addition, the measured amplitudes of the two acoustic modes at the baseline condition showed relatively low levels. The predicted stability indices for these two peaks were less than 1 and are both categorized as acoustically inactive. In contrast, an acoustically active mode near 400 Hz with a stability index of 3 is found for the operating condition with uniform flame temperatures in all three rings. This predicted trend agreed well with observed test data (qualitatively), and further demonstrates the capability of the current model to distinguish between acoustically active and inactive regimes of operation.

The methodology required to incorporate passive damping devices such as acoustic damper tubes used in GE Aircraft Engines' industrial aero-derivative DLE engines was a prime requirement in this modeling activity. These devices are quarter wave resonators installed in the cold section of the combustor just upstream of the premixers. The installation schematic of the damper tubes used in the formulation of this analysis is shown in Fig. 18. These devices act to detune the combustor by providing finite number of discontinuities at the locations where they are installed. The incident and reflected acoustic waves in the diffuser cavity are significantly altered to the extent that certain discrete oscillations are attenuated and therefore

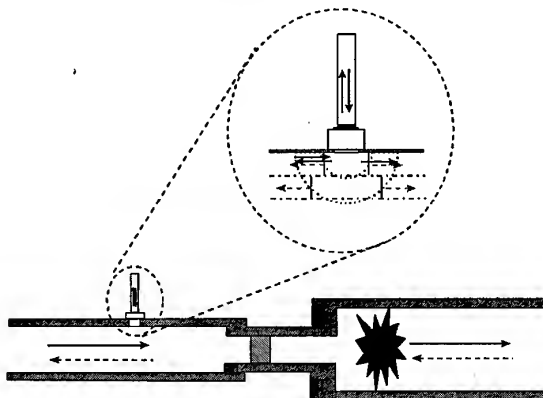


Figure 18 Schematic of Acoustic Damper Tube in Combustor.

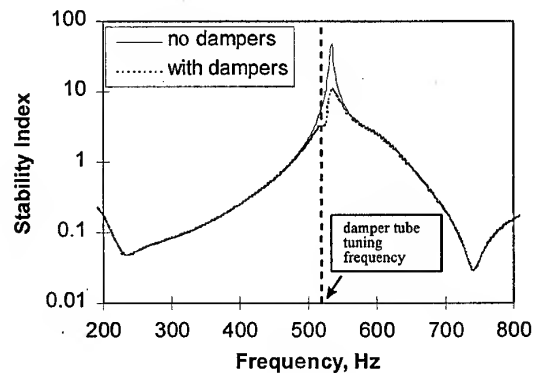


Figure 19 Effect of Damper Tubes on Pilot Ring Acoustic.

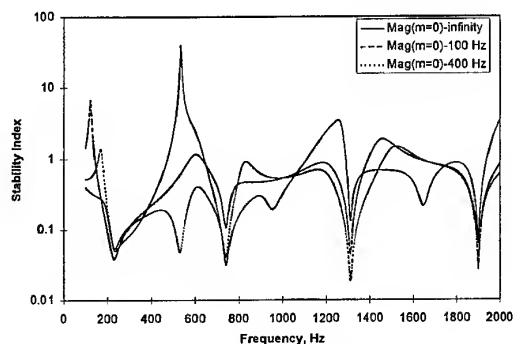


Figure 20 Effect of Fuel-Line Response on Combustion Dynamics.

become less destructive to the combustor. Since the mean flow Mach number in the air-column of these devices is very small (typically less than 0.05), the dynamic pressure and mass flow within the damper tubes can be represented by a one-dimensional analysis as presented in Reference [7]. The inclusion of acoustic damping devices into the current analysis is accomplished by treating each quarter-wave tube as a mono-pole acoustic source characterized by an acoustic impedance. The effect of damper tubes (tuned for 510 Hz) on combustion dynamics in the pilot (middle) ring is qualitatively shown in Fig. 19. A seven fold decrease in stability index at the tuning frequency of the damper tubes is predicted based on this analysis.

The effect of fuel line response is shown in Figure 20 where the stability index is plotted as a function of excitation frequency. A first-order model describing the effect of inertia in the fuel-line system was incorporated in this analysis. The fuel line response is characterized by what is called "break frequency" and is defined as the frequency at which the fuel flow fluctuation lags the dynamic pressure fluctuation in the combustor by 45 degrees. The detailed characterization of fuel line break frequency and its significance can be found in Reference [7]. The effects of three discrete break frequencies, including infinity, 100, and 400 Hz, marked by the solid, dashed and dotted lines, respectively are shown in this figure for a plane acoustic wave in the pilot ring. Results of this analysis show that at an excitation frequency of 500 Hz, the combustor with a fuel line break frequency of 400 Hz can be very stable; however, becomes highly unstable for a fuel system with infinite response (zero phase lag). In other words, the phase lag introduced by the fuel nozzle orifice inertia is a significant effect that must be considered by the designer. It is conceivable that this phase lag, together with the transport and combustion time delays, could tend to destabilize an otherwise stable system.

VI. SUMMARY

A comprehensive physics based combustion dynamics model development effort encompassing the diverse fields of combustion, fluid mechanics and acoustics was initiated to address the growing concerns identified during advanced engine development programs at GEAE. The basic approach to the problem of combustion instability in turbine engine combustors designed to meet lower emissions and high performance in both aircraft and industrial applications is a combined use of empirical design data base and anchored system based methodologies.

To achieve this objective, a physics based combustion dynamics model for gas turbine engines is developed to gain a better understanding of the instability phenomenon, its driving sources and methods of control. The theoretical formulation is based on the exact solution of the acoustic wave equation and is capable of incorporating several features unique to gas turbine combustors. The current approach is built on an acoustic based framework which allows incorporation of physical models and sub-component models in a relatively easy manner. The effect of mean flow non-uniformity is taken into account using results from steady state CFD analysis. The significance of the current approach is the inclusion of an unsteady heat release sub-model to predict relative amplitudes of the dynamic pressure oscillations. Engine test data obtained during the development phase of GEAE's ultra low emission industrial engine combustor development program was used to demonstrate the feasibility of the model and the anchored approach. The predicted trends not only agreed very well with test data, but also demonstrated the capability of the model to distinguish between acoustically active and inactive regimes of operation.

VII. FUTURE WORK

Although the feasibility of the current model to predict observed trends from engine tests have been demonstrated, the model needs to be extended to include higher temperature rise and high performance combustion systems currently under development. Comparison of anchored model prediction versus test data from multiple engines and partial burning modes is also required to extend the validity of the anchored methodology over a broader operating envelope. This work is currently underway at GE Aircraft Engines. Integration into the current methodology of refinements of combustion and turbulence models currently used in CFD calculation such as $k-\epsilon$ and eddy breakup models by the Large Eddy Simulation (LES) model is also planned to further anchor the model. Results obtained from the combined use of empirical data base and anchored methodology can not only be used to identify the driving mechanism of combustion dynamics in gas turbine engines,

but also provide a useful design tool to further extend the operating envelope of various combustors currently under development.

REFERENCES

- [1] Putnam, A.A., "Combustion- Driven Oscillations in Industry", Elsevier, New York, 1971
- [2] Yang, V et.al., "Liquid Rocket Engine Combustion Instability", Volume 169, Progress in Astronautics and Aeronautics, AIAA, 1995.
- [3] Sattelmayer, Th. et al., "Second Generation Low-Emission Combustor for ABB Gas Turbines: Burner Development and Tests at Atmospheric Pressure", ASME paper 90-GT-162, Paper presented at the Gas Turbine and Aeroengine Congress and Exposition, Brussels, Belgium, June, 1990.
- [4] Leonard, G., and Stegmaier, J., "Development of An Aero-Derivative Gas Turbine Dry Low Emissions Combustion System", ASME 93-GT-288, Paper presented at the IGTI conference in Cincinnati, June 1993
- [5] Joshi, N.J., Epstein, M., Durlak, S., Marakovits, S., and Sabla, P., " Development of a Fuel Air Premixer for Aero-Derivative Dry Low Emissions Combustors", ASME 94-GT-253, Paper presented at the IGTI Conference in The Hague, June 1994
- [6] Pandalai, R. P. and Mongia, H. C., "Combustion Instability Characteristics of Industrial Engine Dry Low Emission Combustion Systems, " Paper No. AIAA 98-3379, presented at the 34th AIAA/ASME/SAE/ASEE Joint Propulsion Conference & Exhibit, July 13-15, 1998
- [7] Hsiao, G. C., Pandalai, R. P., Hura, H. S., and Mongia, H. C., "Combustion Dynamic Modeling for Gas Turbine Engines, " Paper No. AIAA 98-3380, presented at the 34th AIAA/ASME/SAE/ASEE Joint Propulsion Conference & Exhibit, July 13-15, 1998.
- [8] Chu, B.T., "On the Generation of Pressure Waves at a Plane Flame Front, " The 4th International Symposium on Combustion, 1953, pp. 603-612.
- [9] Cumpsty, N. A. and Marble, F. E., "The Interaction of Entropy Fluctuations with Turbine Blade Rows; a Mechanism of Turbojet Engine Noise," Proceeding of Royal Society of London, 357, 1977, pp. 323-344.
- [10] Syed, A. A., " Acoustic Impedance Test of LM6000 DLE Premixer in a Flow Duct, " GE Aircraft Engine Internal Report, 1996.
- [11] Hura, H. S., Joshi, N. D., and Mongia, H. C., "Dry Low Emissions Premixer CCD Modeling and Validation," ASME TURBO EXPO Land, Sea & Air'98, Paper No. 98-GT-444, June 2-5, 1998.

PAPER No. 5
Pandalai, Hsiao & Mongia,
(presenter: H. Mongia)

Question 1: R.E. Seoud, DERA, U.K.

What was the extra solution cost associated with coupling the CFD and the wave equation?

Answer

Approximately three times the cost of a conventional steady-state CFD solution.

Question 2: D.K. Hennecke, Technische Hochschule Darmstadt, Germany

What modifications of the code are needed for application to turbines operating at pressure?

Answer

We are presently working on the forcing function; also, a time-dependent laminar flamelet model that is not ready yet either.

Question 3: S. Wittig, University Karlsruhe, Germany

What were the major findings revealed by a sensitivity analysis?

Answer

First, that the acoustic wave equation has to be implemented in fully three-dimensional form; second, that the details of the unsteady stirred reactor model are rather important.

NO_x Reduction by Lean Premixed Prevaporized Combustion

Th. Ripplinger*, N. Zarzalis, G. Meikis MTU München GmbH,
C. Hassa, M. Brandt DLR-Köln,

*MTU Motoren und Turbinen Union
München GmbH
Dachauer Strasse 665
D-80995 München
Germany

ABSTRACT

A low emission combustor working by lean combustion with premixing and prevaporizing of liquid fuel is presented for aero jet engine and power generation applications.

A model rectangular combustor was designed and manufactured as a portion from a full annular combustor and investigated in medium- and high-pressure tests at burner inlet temperatures up to 820 K and at operating pressures up to 20 bar. The design of the combustor was supported by 3D CFD calculations, which were conducted in order to optimise the flow field within the combustor, especially with a view to creating a sufficient recirculation zone for flame stabilization. In addition to the combustor tests, investigations were carried out with the two phase flow within the premixer by means of optical measuring techniques at the German Aerospace Research Establishment (DLR Cologne).

With the present design of the premixing duct and the airblast atomizer the liquid fuel can almost be completely evaporated within a premixing length of 150 mm, corresponding to a residence time of the fuel/air mixture in the premixer of 1.25 - 1.5 ms.

The model combustor was operated at burner inlet temperatures of up to 820 K and at operating pressures of up to 20 bar with no autoignition of the fuel/air mixture within the premixing duct or flash back of the flame into the premixer occurring.

The combustor combines very low NO_x emissions (up to 85 % less NO_x than a low NO_x diffusion combustor) with high combustion efficiencies (above 99 %) and a sufficient stability range ($\Phi_{\text{min,Primary}} = 0.5$).

Therefore, the present LPP concept provides a promising configuration for an ultra low NO_x combustor, both for aero engine and power generation applications.

NOMENCLATURE

CFD	Computer Fluid Dynamics
DLR	German Aerospace Research Establishment
RQL	Rich Quench Lean Combustion
LPP	Lean Premixed Prevaporized Combustion
NO _x	Nitrogen Oxides (NO and NO ₂)
CO	Carbon Monoxide
UHC	Unburned Hydrocarbons
C ₃ H ₈	Propane
N ₂	Nitrogen
O ₂	Oxygen
CO ₂	Carbon Dioxide
AFR	Overall Air to Fuel Mass Ratio
EI	Emission Index (g Species/kg Fuel)
T ₃	Burner Inlet Temperature
P ₃	Burner Inlet Pressure

c_{VVD}	Velocity in Premixing Channel
τ_{VVD}	Residence Time in Premixing Channel
$\Delta P_{134/P_{13}}$	Burner Pressure Loss
T_{Flame}	Flame Temperature
T_{Wall}	Wall Temperature
Φ	Equivalence Ratio
AFR_{Gas}	Air Fuel Ratio by Gas Analysis
$AFR_{\text{Perf.}}$	Air Fuel Ratio performed

INTRODUCTION

Endeavours to increase the efficiency of modern gas turbines, both in the field of power generation applications and aircraft jet engines, result in ever increasing compressor pressure ratios and turbine inlet temperatures and thus in higher operating pressures and temperatures in the combustors of these engines. At the same time, these gas turbines have to comply with the requirement for very low emissions in order to ensure their environmental acceptance.

Whereas the higher pressures and temperatures within the combustors in general improve the oxidation of the fuel, and thus reduce the emissions of carbon monoxide (CO) and unburned hydrocarbons (UHC), the formation of nitrogen oxides (NO_x) is accelerated by the higher operating conditions. Therefore, special low NO_x combustion concepts have to be used in order to meet the low emission limits, especially for power generation applications.

The low NO_x combustion concepts used are the rich quench lean combustion and the lean premixed prevaporized combustion, which both reduce NO_x production by controlling the stoichiometry, and thus the combustion temperatures, within the combustor.

In the field of aircraft jet engines a simplified RQL combustion concept, with application of conventional cooling techniques, is state-of-the-art, and LPP systems are the subject of several research programs. Due to the specific boundary conditions, application of the latter in aircraft jet engines can be expected in the long term future only.

For power generation applications driven by gaseous fuel the premixing concepts are state-of-the-art /1/, whereas for most engines operated with liquid fuel, water or steam injection has to be used in order to comply with the current emission regulations (e.g. TA-Luft in Germany /2/). Since water injection reduces the efficiency of the engine and increases the direct operating costs, many research activities are carried out on dry low NO_x combustion concepts.

The present paper describes an LPP system for liquid fuel applications, which was designed to produce very low NO_x emissions and allow reliable operation at burner inlet temperatures of up to 750 K and burner pressures of up to 20 bar.

LPP COMBUSTOR

The design of the present LPP concept is intended for an annular combustor application. However, in order to reduce the costs of both manufacturing the combustor and operating the test facilities, only a small part of a conceivable annular combustor, idealised as a rectangular combustor, was investigated under the present research program. Fig. 1 shows a schematic sketch of the derivation of the rectangular combustor from an annular combustor.

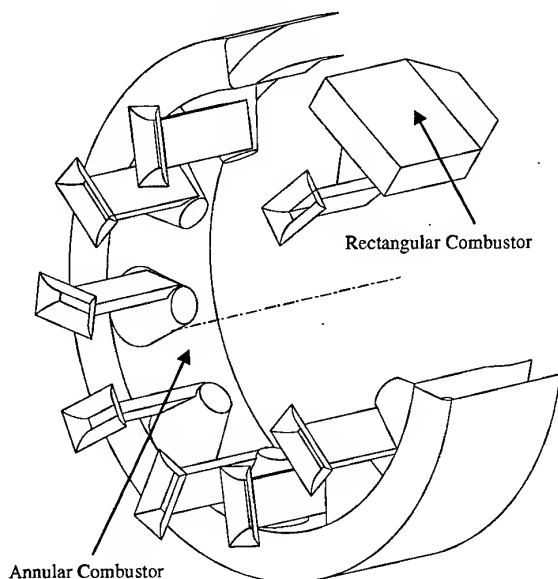


Fig. 1 LPP Annular Combustor

A more detailed view of the rectangular combustor is shown in Fig. 2.

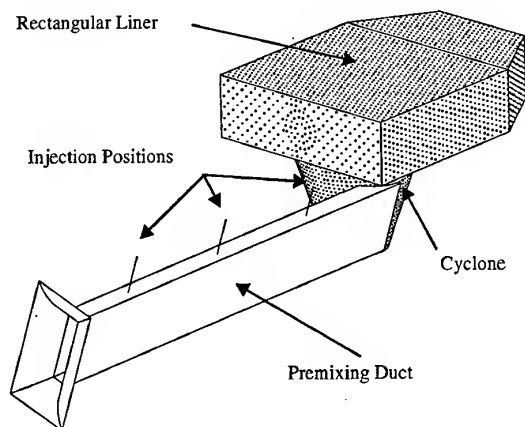


Fig. 2 LPP Rectangular Combustor

The LPP system consists of a premixing duct with constant area, rectangular cross section within which the liquid fuel is injected into the air with the help of a plain prefilmer airblast

atomizer (Fig. 3). The cross sectional area of the premixing duct is designed to produce an average air velocity of 100 to 120 m/s within the duct in order to produce a fine fuel spray by the airblast atomizer and to prevent flash back of the flame into the premixer. By installing the atomizer at different axial locations, the prevaporization time can be varied from 1.5 ms to 3.5 ms without changing other influencing parameters, such as the burner pressure drop or the atomization velocity around the airblast nozzle, for instance. The premixing duct is connected tangentially to a conical flame tube segment, the cyclone, in which primary combustion and flame stabilization take place. The tangential entry of the premixing flow into the cyclone produces a vortex flow which creates the necessary recirculation flow for flame stabilization. Downstream of the cyclone the combustion process continues in a rectangular liner. Both the cyclone and the rectangular liner are cooled by effusion cooling for ease of manufacturing.

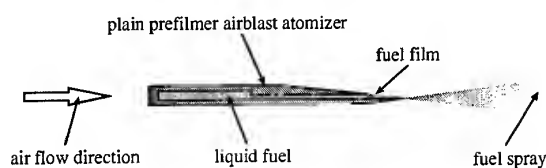


Fig. 3 Schematic View of Plain Prefilmer Airblast Atomizer

The key features of the concept are, first, the premixing duct, which is designed to prevent wall wetting with liquid fuel and to enable a flow pattern without any separations and with small boundary layer thickness, and second, the cyclone, which enables the creation of a recirculation flow without any metal parts exposed to the premixing flow. The latter characteristic protects the combustor from possible damage in the case of autoignition or flash back events.

The rectangular model combustor was designed to allow 43 % of the total air to flow through the premixer - used as primary combustion air -, 16 % of the air to enter the cyclone and the remaining 41 % of the air to flow into the rectangular flame tube. Both the cyclone and the main combustor air were used as effusion cooling air.

CFD ANALYSIS

The flow pattern in the area of the cyclone/liner interface has a major influence on the flame stability of the present combustor. A pronounced recirculation flow is needed in order to enable continuous ignition of the fresh mixture by recirculated hot and reactive radicals.

The design of the cyclone/liner interface was supported by isothermal 3D CFD calculations using a finite volume approach and k, ϵ turbulence modelling.

The recirculated fraction of the vortex flow was optimised by increasing the cone angle of the cyclone, which increases the value of the negative pressure gradient along the cone axis and thus promotes the tendency of the flow to recirculate. Fig. 4 and 5 show isolines of the velocity along the cyclone axis (w component of 3D vector) in a longitudinal and a normal plane

through the cyclone. Negative values of the w component indicate flow regions with recirculation into the cyclone.

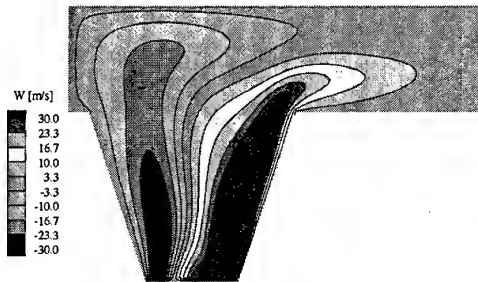


Fig. 4 Axial Velocity within Cyclone - Central Longitudinal Plane

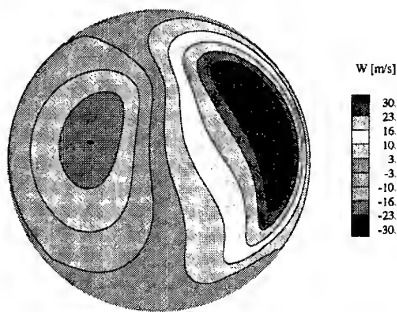


Fig. 5 Axial Velocity within Cyclone - Normal Plane at Cyclone Exit

It can be seen from the figures that a pronounced recirculation region, which enables an adequate flame stabilization, is located at the front end of the cyclone.

EXPERIMENTAL INVESTIGATION OF THE TWO PHASE FLOW WITHIN THE PREMIXING DUCT

One major requirement of LPP systems is that the liquid fuel should be atomized, evaporated and mixed homogeneously with the air in the premixing duct before it enters the reaction zone. The fuel/air mixture ideally has to enter the burning zone as a homogeneous gas in order to prevent chemical reactions from taking place under near stoichiometric conditions in the vicinity of droplet clouds with high NO production rates due to high temperatures. Therefore, the two phase flow within the premixing duct was investigated at the Institute for Propulsion Technology of the German Aerospace Research Establishment (DLR Cologne). Particle size distributions and liquid fuel concentrations were measured by means of Phase Doppler Anemometry. The distribution of the evaporated fuel was

described by extinction measurements of infrared and visible light along the line of sight of two laser beams.

Test Apparatus

The investigation of the premixing flow was carried out in a flow channel with rectangular cross section within which the liquid fuel was atomized by means of a plain prefilmer airblast atomizer. The test cell allowed optical access from three sides to the premixing duct through quartz glass windows. A sketch of the test cell is shown in Fig. 6, a more detailed description is given in [3].

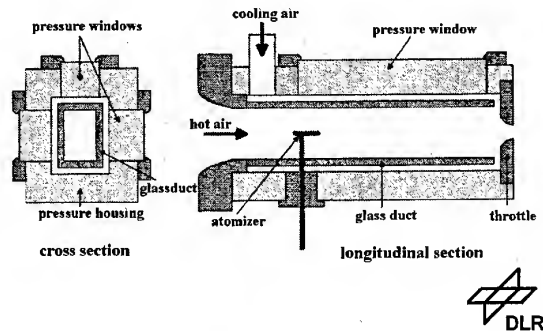


Fig. 6 Premixing Duct Test Cell

Evaporation Rate along the Premixer Length

The development of the evaporation rate along the premixer length is an important parameter in the design process of an LPP combustor. In order to achieve a homogeneous fuel/air mixture, a nearly 100 % evaporation rate at the exit of the premixing duct is preferable.

In Fig. 7 the evaporation rate of the present system, calculated from the integration of the local spray information, is shown along the premixer length for an inlet temperature of 750 K and an averaged air velocity of 120 m/s, with the operating pressure as a parameter. It can be seen from the figure that at pressures of 6 bar and above, a very high evaporation rate (> 95 %) can be achieved after 150 mm premixing length, corresponding to a residence time of 1.25 ms. The higher evaporation rates at higher pressures result from improved atomization due to the increased density of the air and a reduction of the surface tension of the fuel caused by increased heating of the fuel within the prefilmer [3].

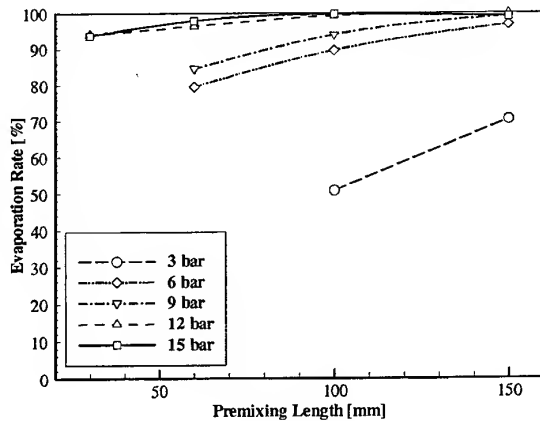


Fig. 7 Evaporation Rate along Premixer Length

Fuel Dispersion along the Premixer Length

In addition to the evaporation rate, the dispersion of the fuel within the air flow is another important parameter for a well operating premixer. The knowledge of the fuel dispersion characteristics, on the one hand, enables the designer to estimate the homogeneity of the fuel/air mixture at the exit of the premixing duct, and on the other hand, helps to design the premixer geometry for minimal fuel wetting of the wall.

Fig. 8 shows the fuel dispersion of the present system along the premixer length for an inlet temperature of 750 K and an averaged air velocity of 120 m/s, with the operating pressure as a parameter. It can be seen from the figure that the dispersion width of the fuel after a premixing length of 150 mm ranges between 13 and 15 mm, depending on the operating pressure.

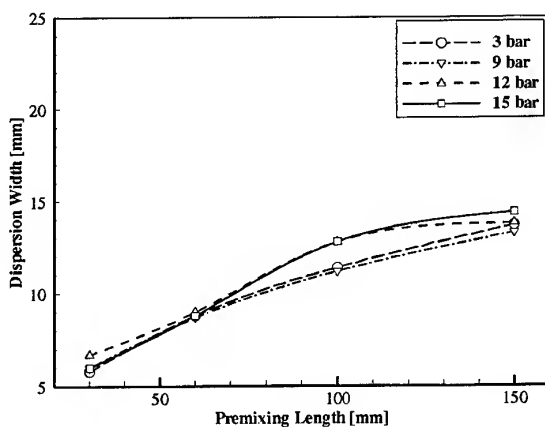


Fig. 8 Fuel Dispersion along Premixer Length

These results were taken into account during the design phase of the model combustor in order to obtain an optimal premixing duct with favourable premixing and prevaporization characteristics and minimal wetting of the premixer wall with liquid fuel.

COMBUSTION TESTS UNDER MEDIUM- AND HIGH-PRESSURE CONDITIONS

Test Facility

The rectangular combustor was investigated in combustor tests at burner pressures up to 6 bar at an MTU test facility and at burner pressures up to 20 bar at a DLR test facility. A schematic sketch of both test facilities, which are of similar design, is shown in Fig. 9, a more detailed description is given in /4/.

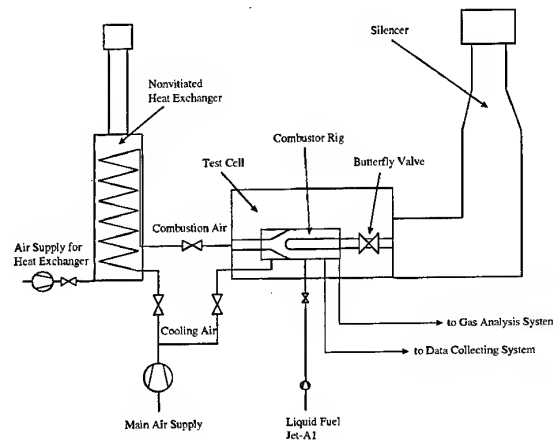


Fig. 9 Schematic View of Combustor Test Facility

Combustor Rig

The rectangular combustor was built in a tubular combustor rig (Fig. 10), which mainly acted as a pressure vessel and connection of the combustor to the main air supply and the butterfly valve. Upstream of the combustor rig an orifice plate was installed, which was used to determine the mass flow through the combustor. Immediately downstream of the liner an emission sampling probe, consisting of four individual probes with eight sampling orifices each, was installed, which was used to collect the emissions at the exit of the combustor.

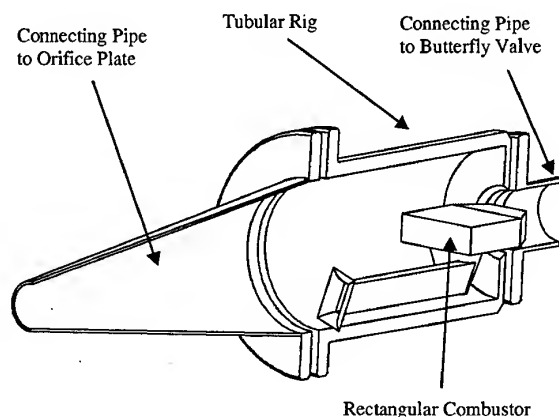


Fig. 10 Combustor Rig

Gas Analysis System

By means of a heated sampling line the emissions were transferred from the probe to the gas analysis instruments. A schematic view of the gas analysis system, which was set up in accordance with the ICAO recommendations [5,6], is shown in Fig. 11. With the help of this set-up the concentrations of CO_2 , CO , O_2 , UHC, NO_x and the smoke contained in the exhaust gas of the combustor could be determined.

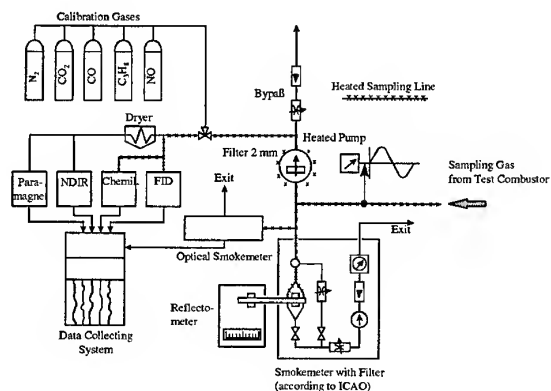


Fig. 11 Gas Analysis System

Instrumentation

In order to determine autoignition and/or flash back events, the premixing duct contained four static wall pressure taps and NiCr/Ni thermocouples evenly spaced along the premixer length. The cyclone and liner wall temperatures were measured by NiCr/Ni thermocouples connected to the outer surface of the walls.

Test Procedure - Medium-Pressure Tests

Medium-pressure tests were performed at operating pressures of 1, 3 and 6 bar and burner inlet temperatures of 650, 750 and 850 K. During these tests the velocity within the premixing duct was kept at a constant 100 m/s by adapting the burner flow parameter. By installing the airblast atomizer at different axial locations within the premixer, the residence time of the fuel/air mixture was varied between 1.5 ms and 3.5 ms. At constant burner inlet temperature and operating pressure the emissions at the exit of the combustor were measured from near stoichiometric primary zone conditions down to very lean mixtures close to the lean blow-out limit.

Jet-A fuel was used during all combustion tests both at medium- and high-pressure conditions.

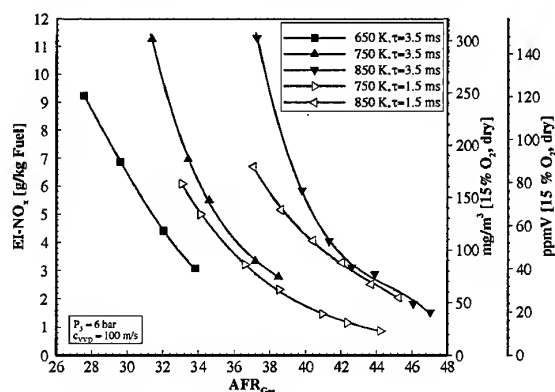
Test Results - Medium-Pressure Tests

Fig. 12 and 13 show the NO_x and CO emissions measured during the medium-pressure tests versus the measured air to fuel ratio at the combustor exit (overall AFR for the entire combustor). The burner inlet temperature and the residence time of the fuel/air mixture within the premixing duct are used as parameters in these diagrams, whereas the operating pressure and the air velocity within the premixer were kept at a constant 6 bar and 100 m/s, respectively.

Within the primary zone of the combustor, lean conditions, i.e. excess oxygen, prevailed over the whole operating range. NO_x production took place under these conditions almost exclusively by the thermal NO mechanism, which describes the NO formation through the reaction between molecular nitrogen and oxygen atoms [7,8]. Sufficient oxygen atoms with the necessary energy to split the relatively stable N_2 bond can only be found at very high reaction temperatures.

Consequently, the NO_x emissions decrease with increasing AFR at constant burner inlet temperature and with decreasing burner inlet temperature at constant AFR, as a result of the decreasing reaction temperatures.

At a burner inlet temperature of 850 K, NO_x emissions as low as 27 ppm (corrected to 15 % O_2 in dry exhaust) are attained, combined with a combustion efficiency of 99.5 %.

Fig. 12 NO_x Emissions - Medium-Pressure Tests

The CO emissions show the typical dependence on the AFR, i.e. a pronounced minimum at a specific AFR and increasing emissions both for higher and lower AFR's around the optimal AFR

(Fig. 13). The increasing CO emissions at higher than the optimal AFR result from the decreasing oxidation reaction rates at lower temperatures, the higher CO emissions at lower AFR's result from dissociation reactions taking place at extremely high temperatures. Hence, the conditions at which the minimal CO emissions were measured shift with higher burner inlet temperatures towards higher AFR values.

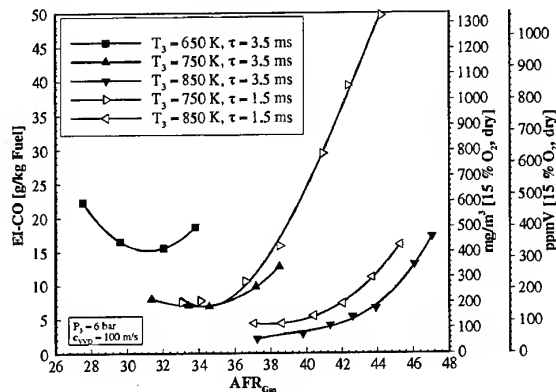


Fig. 13 CO Emissions - Medium-Pressure Tests

As a result of the dependence of the CO emissions on the AFR also the combustion efficiency shows pronounced optima at certain AFR's (Fig. 14). The general efficiency level is well above 99 %, apart from the results at a burner inlet temperature of 750 K and a residence time of the fuel/air mixture within the premixer of 1.5 ms, where the measurements were performed very close to the lean blow-out limit.

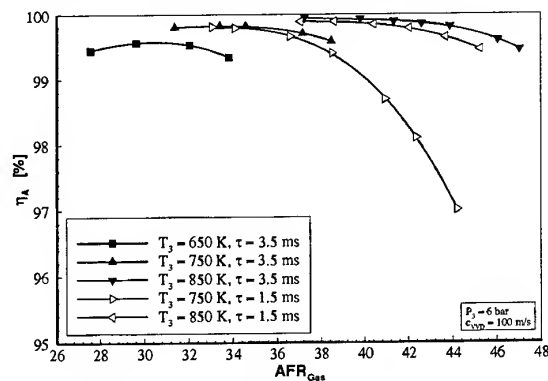


Fig. 14 Combustion Efficiency - Medium-Pressure Tests

The liner pressure loss varied between 3.1 and 3.8 % depending on the AFR. The decrease of the pressure loss with increasing AFR results from the reduced hot pressure loss at lower temperature increases (Fig. 15).

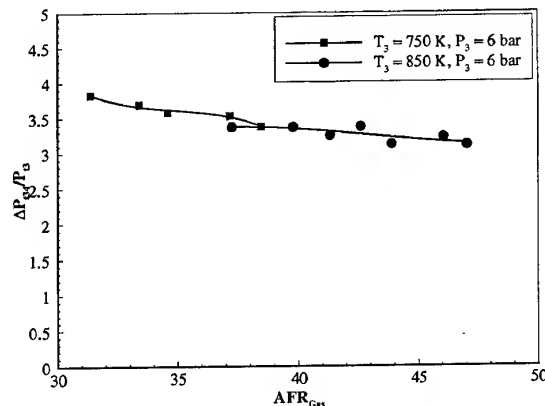


Fig. 15 Combustor Pressure Loss - Medium-Pressure Tests

Test Procedure - High-Pressure Tests

High-pressure tests were performed at operating pressures of 10, 15 and 20 bar and burner inlet temperatures of between 750 and 820 K. The air velocity within the premixing duct was kept at a constant 100 m/s again in order to achieve constant residence times of the fuel/air mixture within the premixer. In contrast to the medium-pressure tests, no variation of the axial injection position and thus of the residence time of the fuel/air mixture in the premixing duct took place. Only the shortest distance from the atomizer to the cyclone of 150 mm, corresponding to a residence time of 1.5 ms, was tested. The emissions of the combustor were measured over a wide range of AFR at constant operating pressure and burner inlet temperature.

Test Results - High-Pressure Tests

Fig. 16, 17 and 18 show the NO_x and CO emissions as well as the combustion efficiency against the AFR of the combustor for constant operating pressures and burner inlet temperatures. As a result of the small overall air mass flow, compared with the design value of the test facility (1.8 kg/s vs. 20 kg/s), the burner inlet temperature of 820 K could not be kept constant at an operating pressure of 20 bar. The burner inlet temperature decreased during adapting of the different AFR's; the individual values of the burner inlet temperature for the single measuring points are included in Fig. 16.

The general dependence of the emissions on the AFR and the operating conditions is in agreement with the medium-pressure test results. This means, increasing NO_x emissions both with increasing burner inlet temperatures and decreasing overall AFR's as well as increasing CO emissions with decreasing burner inlet temperatures and increasing AFR's.

At a burner inlet temperature of 788 K and an operating pressure of 20 bar, NO_x emissions as low as 35 ppm (corrected to 15 % O₂ in dry exhaust) could be attained at the leanest AFR (AFR = 54.1), combined with a combustion efficiency of 99 %.

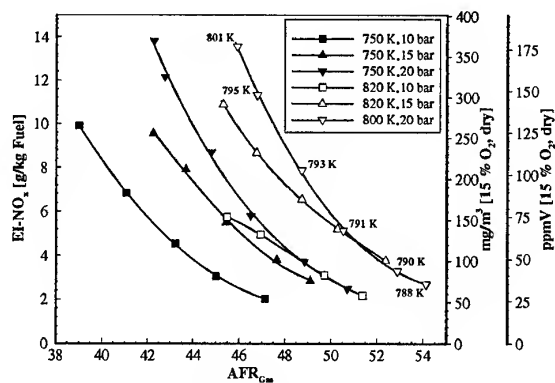
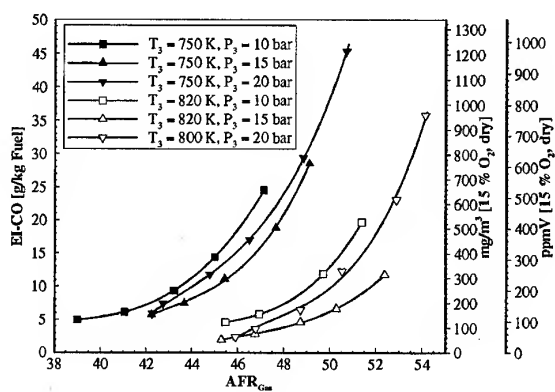
Fig. 16 NO_x Emissions - High-Pressure Tests

Fig. 17 CO Emissions - High-Pressure Tests

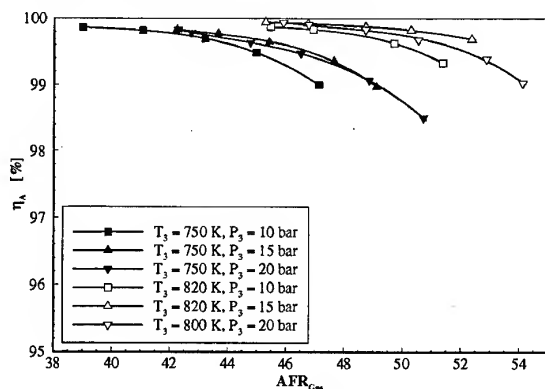


Fig. 18 Combustion Efficiency - High-Pressure Tests

During the standard high-pressure tests no autoignition of the fuel/air mixture within the premixing duct or flash back of the flame into the premixer occurred. Therefore, once the emission measurement had been completed, the burner flow parameter was reduced to half of the design value in order to provoke an autoignition or flash back event. But although the residence time of the fuel/air mixture within the premixing duct was doubled from 1.5 ms to 3 ms and the velocity of the mixture was halved from 100 m/s to 50 m/s, no autoignition or flash back event occurred. Thus, the described concept proved to be

very insensitive to off design operating conditions in terms of autoignition or flash back risks.

DISCUSSION

Residence Time within Premixer

The influence of the residence time of the fuel/air mixture within the premixer on the emissions can be seen from the emission results of the medium-pressure tests (Fig. 12, 13 and 14). Increasing the residence time of the fuel/air mixture within the premixing duct, achieved by installing the airblast atomizer further upstream, leads to higher NO_x emissions and slightly lower CO emissions. This behavior probably results from increased wetting of the premixer wall with fuel droplets in the case of the higher residence times. The collected liquid fuel flows along the premixer wall and locally, when entering into the cyclone, leads to richer conditions with higher temperatures and thus higher NO_x and lower CO emissions. This explanation is mainly based on the temperature measurements of the premixer wall, which are shown in Fig. 19.

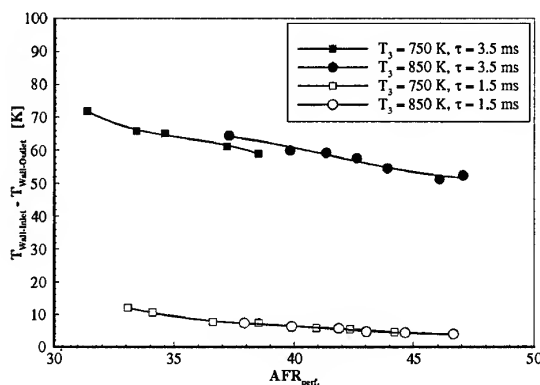


Fig. 19 Premixer Wall Temperature - Medium-Pressure Tests

In the case of the injection position located further upstream, the temperature decreases along the premixer length by about 60 to 70 K, which can only result from liquid fuel hitting and cooling the wall. In the case of the shorter injection position, the wall temperature decreases only by 4 to 10 K, which is close to the theoretical value which can be calculated from the heat balance of the evaporation process of the liquid fuel.

In addition, the results of the investigation of the two phase flow within the premixing duct at the German Research Establishment, especially the fuel dispersion results (Fig. 9), also back up this explanation.

The behavior of the present LPP system, which produces lower NO_x emissions with shorter residence times of the fuel/air mixture within the premixing duct, is favourable with a view to the high-pressure operating limit of the combustor. Consequently, the high-pressure tests were exclusively performed with the shortest residence time.

Burner Inlet Temperature

Increasing the burner inlet temperature increases the combustion temperatures at constant AFR and thus the production of thermal NO. However, for premixing combustors operated with

liquid fuel, increasing the burner inlet temperature also accelerates the evaporation process, which can result in an improved homogeneity of the fuel/air mixture and thus in less temperature peaks and thermal NO production in the primary combustion zone. The dependence of the NO_x emissions on the inlet temperature can be expressed in the formula

$$\frac{EI_{NO_x}}{EI_{NO_{x,0}}} = e^{\frac{T_3 - T_{3,0}}{C1}}$$

For lean stoichiometries, the factor C1 represents a measure of the homogeneity of the fuel/air mixture, where small C1 values signify more homogeneous mixtures. The C1 value of the present combustor amounts to 90 - 120 K, in the range of lean stoichiometries.

Operating Pressure

The influence of the operating pressure on the NO_x emissions is shown in Fig. 20.

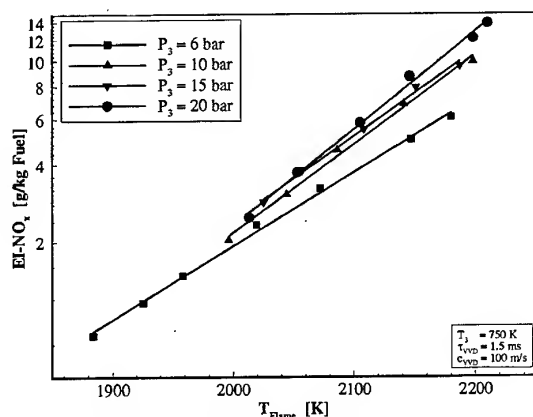


Fig. 20 Pressure Dependence of the NO_x Emissions

The dependence of the NO_x emissions on the operating pressure can be expressed in the formula

$$\frac{EI_{NO_x}}{EI_{NO_{x,0}}} = \left(\frac{P_{t3}}{P_{t3,0}} \right)^n$$

The pressure exponent *n*, determined for the present LPP combustor, ranges from 0.25 to 0.5, which is in agreement with theoretically expected values derived in chemical kinetic approaches. The steeper gradients at higher pressures result from more homogeneous fuel/air mixtures at higher pressures due to an improvement of the atomisation process under these conditions.

CO Emissions

The relatively high level of the minimal CO emissions, about 100 - 150 ppmV at T₃ = 750 K, as well as the distinct increase

of the CO emissions at leaner stoichiometries, can probably be attributed to quench effects in the area of the liner cooling films. Due to the relatively high cooling air flow fraction (60 %), the already low temperatures (lean stoichiometry) are cooled down further, which leads to a freezing of the CO oxidation reactions. The fact that the CO emissions are not attributable to insufficient combustion, but to quenching effects can also be seen from the dependence of the CO emissions on the operating pressure (Fig. 21).

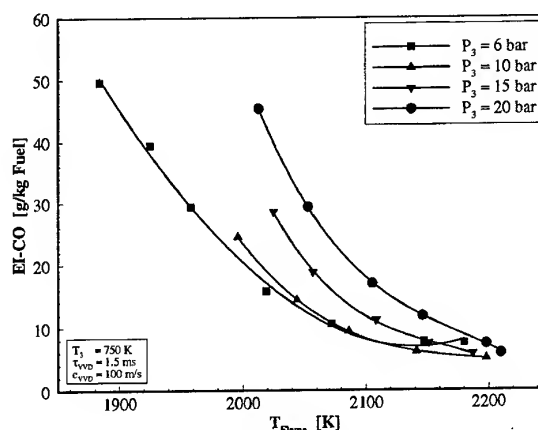


Fig. 21 Pressure Dependence of the CO Emissions

It can be seen from Fig. 20 that the CO emissions increase with increasing operating pressures at constant flame temperatures, although the CO oxidation reactions accelerate at higher pressures. A possible explanation for this behavior could be the improved mixture homogeneity at higher pressures accompanied by a reduction of temperature peaks, and thus a higher susceptibility to quenching effects.

Autoignition and Flash Back

The present configuration proved to be very insensitive to autoignition and flash back. During the whole test phase, in which about 50 operating hours were accumulated at different conditions, no indication of autoignition of the fuel/air mixture within the premixing duct or flash back of the flame into the premixer was observed. Fig. 22 shows the most critical operating conditions of the combustor compared with the autoignition correlation given by L.J. Spadaccini et al. for Jet-A fuel [9].

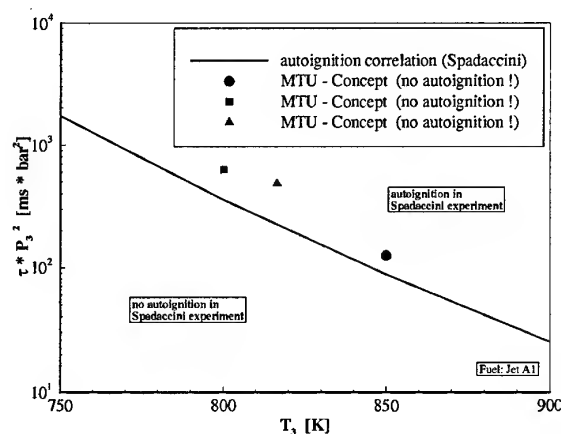


Fig. 22 Operating Conditions Compared with Autoignition Correlation

It can be seen from Fig. 22, where the product of the residence time of the fuel/air mixture within the premixing duct and the square of the operating pressure is plotted against the mixture inlet temperature, that the present combustor could be operated beyond the autoignition limit given by the Spadaccini correlation.

Comparison with Low NO_x Diffusion Combustor

A comparison of the NO_x emissions of the present LPP combustor with the NO_x emissions of a low NO_x diffusion combustor (lean airblast atomizer) is shown in Fig. 23. The NO_x emissions are plotted against the flame temperature for a constant burner operating pressure of 6 bar.

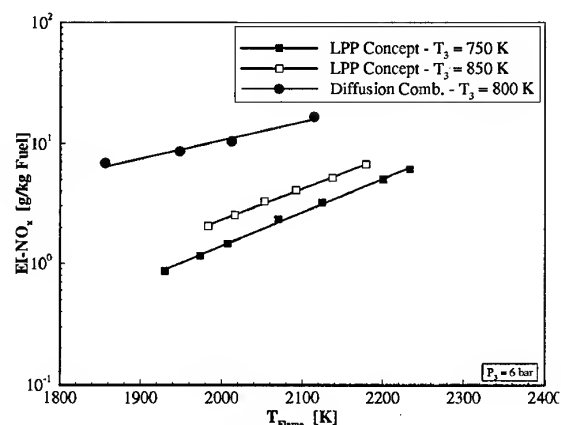


Fig. 23 Comparison with Low NO_x Diffusion Combustor

It can be seen from Fig. 23 that at a flame temperature of 1930 K the NO_x emissions of the LPP combustor are about 85 % lower than the emissions of the diffusion combustor. In addition to that, also the steeper gradients of the NO_x versus flame temperature lines indicate that the fuel/air mixture is more homogeneous with the LPP combustor.

CONCLUSIONS

An LPP combustor for liquid fuel applications was designed, manufactured and tested under medium- and high-pressure operating conditions.

The medium-pressure tests were performed at operating pressures of up to 6 bar and burner inlet temperatures of 650 - 850 K, whereas the residence time of the fuel/air mixture within the premixing duct was varied between 1.5 ms and 3.5 ms by installing the plain airblast atomizer at different axial locations within the premixer.

The high-pressure tests were performed at burner inlet temperatures of between 750 K and 820 K and operating pressures of up to 20 bar. During these tests, the residence time of the fuel/air mixture within the premixing duct was kept at a constant 1.5 ms. In addition to the combustion tests with the complete combustor, an investigation was conducted into the two phase flow within the premixer by means of optical measuring methods at the German Aerospace Research Establishment.

The results of the combustor tests and the experimental investigation of the two phase flow can be summarised as follows:

- At operating pressures above 6 bar and preheating temperatures in the range of 750 K, nearly 100 % of the liquid fuel can be evaporated within a premixing length of 150 mm corresponding to a residence time of 1.25 ms.
- The lowest NO_x emissions could be achieved with the shortest investigated residence times of the fuel/air mixtures (1.5 ms) within the premixing duct. At longer premixing lengths, the spray spreading leads to a wetting of the premixer wall with liquid fuel and consequently to local inhomogeneities at the exit of the premixer and thus to higher NO_x emissions.
- Operation of the combustor at operating pressures of up to 20 bar and burner inlet temperatures of 800 K is possible with no autoignition of the fuel/air mixture within the premixing duct or flash back of the flame into the premixer occurring. Even a reduction of the burner flow parameter to half the design value which leads to a doubling of the residence time and only half the velocity, could not provoke autoignition or flash back.
- Actual NO_x emissions, 35 ppmV at an operating pressure of 20 bar and a burner inlet temperature of 788 K or 27 ppmV at an operating pressure of 6 bar and a burner inlet temperature of 850 K, are very low.
- The CO emissions are slightly increased, probably due to quenching effects in the cooling film area.
- The combustion stability of the pure LPP combustor is sufficient. The leanest conditions resulted in a equivalence ratio for the primary zone (cyclone) of 0.5. Over the investigated operating range no combustion instabilities or pressure pulsations could be observed.
- Compared with a low NO_x diffusion combustor with an airblast atomizer, NO_x emissions are 85 % lower with the LPP combustor.

In summary, the present LPP concept proved to be a very promising configuration for an ultra low NO_x combustor for aero jet engine or power generation applications. In order to

cover the whole operating range of these turbines, it should preferably be combined with a diffusion combustor in a staged overall combustor design.

ACKNOWLEDGMENTS

This work was sponsored by the **bmb+f** (German Ministry of Research and Technology) within the framework of the AG-TURBO project under Contract No. 0326782D/215. The responsibility for the content of the paper is taken by the authors.

REFERENCES

- /1/ Aigner, M et al.
Second-Generation Low-Emission Combustors for ABB Gas Turbines; Tests under Full-Engine Conditions
ASME International Gas Turbine and Aeroengine Congress and Exposition, Brussels 1990
ASME Pap 90-GT-308
- /2/ Technische Anleitung zur Reinhaltung der Luft
TA-Luft vom 27. Februar 1986
Bundesumweltministerium, Bonn
- /3/ Brandt M., Hassa C., Rachner M.
Messung der Zwei-Phasenströmung
(Tropfengeschwindigkeit und -größe) in einer Ölvormischstrecke - Abschlußbericht April 1997
Förderkennzeichen Nr. 0326782D (TP 3.2.1.8)
- /4/ Kirschey G., Wagner R.
Full annular combustor test facility for high pressure/high temperature testing
AGARD Conference Proceedings No. 293
- /5/ International Standards and Recommended Practices
Environmental Protection
Annex 16 to the Convention on International Civil Aviation
ICAO, Second Edition 1993
- /6/ Huster G.
Schadstoffemission - Vorschriften und Schadstoffermittlung
LTH-Triebwerkstechnologie - MTU-M AT 34 000-01
17.07.1992
- /7/ Zeldovich Y. B., Sadovnikov P. Y., Frank-Kamenetskii D. A.
Oxidation of Nitrogen in Combustion
Academy of Sciences, U.S.S.R., Moscow-Leningrad, 1947
- /8/ Lefebvre A. W.
Gas Turbine Combustion
Mc Graw Hill, ISBN 0-07-037029-X
- /9/ Spadaccini L.J., TeVelde J.A.
Autoignition Characteristics of Aircraft-Type Fuels
Combustion and Flame 46, 1982, S. 283 -300

PAPER No. 7
Ripplinger & Hassa
(presenter: T. Ripplinger)

Question 1: G.J. Sturgess, ISSI, U.S.

Flashback behavior is governed by boundary layer development in the premixer. For a square or rectangular cross-section premixer, vorticity buildup in the sharp corners generates secondary flow vortex-pairs in each corner that would tend to increase the susceptibility to flashback. This would be especially so if inlet flow distortion was to be present when the vortex structures might be caused to leave the duct corners. Were any investigative tests with inlet flow distortion conducted to assess the robustness of the system to flashback in the premixer?

Answer

No, up to now no tests with inlet flow distortions have been conducted. It is planned to include these in the future development of the combustor:

Question 2: T. Rosfjord, UTRC, U.S.

What are the expected consequences of flashback in the premixer? Will flashback, and the consequences, happen in a real engine despite your present favorable rig results?

Answer:

The present concept exposes no uncooled premixer material to the flow downstream, of the fuel injectors in the premixer. Therefore, a flashback into the premixer should not lead to any damage of the premixer or combustor.

Question 3: T. Rosfjord, UTRC, U.S.

What is the combustor strategy for low inlet air temperatures less than 600 °K (i.e. at low engine power levels), when fuel evaporation rates in the premixer will be low?

Answer

The combustor presented here is a pure LPP combustor that would not be used as the only source of heat addition in an engine. In an engine design, the LPP combustor would be used as the main stage of a fuel-staged combustor. A diffusion flame combustor would be used as a pilot stage to cover the low power settings having the adverse operating conditions.

Question 4: M. Cathonnet, LCSR-CNRS, France

Due to the complex dependence of liquid fuel auto-ignition on fuel/air mixture temperature between 750 and 900 °K, and on pressure, there is no guarantee of the absence of autoignition at pressures higher than 20 atm. in an engine. It would be necessary to check this experimentally.

Answer

The authors agree. In order to be sure that there would be no autoignition of fuel/air mixture within the premixing duct at pressures higher than 20 bar, or for air inlet temperatures of 900 °K, specific tests would be needed to be made at these conditions.

Question 5: G.J. Sturgess, ISSI, U.S.

An extensive recirculation zone was shown occupying the forward half of the cyclone. With a high tangential inlet velocity of the fuel/air mixture from the premix tube into the cyclone, it is a little surprising to see the unsymmetric recirculation in the position shown. Could the general downstream flow velocity in the main combustor be responsible for this behavior by intruding into the cyclone and displacing the recirculation generated by the swirl?

Answer

The interference of the flow field from the main combustor with the cyclone flow certainly plays a role in the development of the cyclone flowfield. However, the location shown for the recirculation zone within the cyclone results more from the non-symmetric introduction of the high velocity flow from the premixer to one side of the cyclone.

Question 6: N. Brehm, BMW-RR, Germany

What is the percentage of cooling air used for the combustor?

Answer

For the LPP combustor as presented the amount of cooling air used came to 57 % of the total. This is certainly too high as some flame tube regions are clearly overcooled. The large amount of cooling air used is probably the reason for the slightly increased CO emissions measured, and this was discussed during the presentation. A reduction of the liner cooling air will be addressed in the future development of the concept.

STATUS OF CATALYTIC COMBUSTION R&D FOR THE DEPARTMENT OF ENERGY ADVANCED TURBINE SYSTEMS PROGRAM

D. Fant, South Carolina Energy R&D Center, AGTSR;
G. Jackson, University of Maryland;
H. Karim, Precision Combustion Inc.;
D. Newbury, Siemens Westinghouse;
P. Dutta and K. Smith, Solar Turbines Inc.;
D. Smith, Rolls-Royce Allison;
R. Dibble, University of California - Berkeley*

*386-2 College Avenue
Clemson, SC 29634-5180
United States

Key Words: Advanced Turbine Systems, Catalytic Combustion Technology, Ultra-Low NO_x Emissions, Palladium-Based Catalysts

1. SUMMARY

This paper discusses some of the advanced concepts and fundamental R&D needs associated with implementing catalytic combustion systems to achieve ultra-low NO_x emissions in the next generation of land-based gas turbine engines. In particular, the paper presents the development status and current design challenges being addressed by Siemens Westinghouse Power Corporation, Solar Turbines, and Rolls-Royce Allison, as part of the U.S. Department of Energy's (DOE) Advanced Turbine Systems (ATS) program. In addition, issues on catalytic combustion economics, durability and operability will be highlighted.

2. INTRODUCTION

One of the major goals for the DOE-ATS program is to demonstrate stable, quiet, ultra-low emission combustion systems for advanced land-based gas turbine engines. In this respect, two technology paths are being pursued by ATS: lean premixed combustion using natural gas is the primary path with an emissions target of less than 10 ppm for NO_x and less than 20 ppm for CO/UHC; the other path incorporates catalytic combustion and represents a growth ATS technology insertion with a step reduction in emissions, having a target goal of less than 5 ppm NO_x and less than 10 ppm for CO/UHC. This paper focuses on the second technology path and describes the status, approaches, and challenges of adapting catalytic combustion systems in advanced gas turbines.

2.1 Advantages and Challenges to Implementing Catalytic Combustion

The main advantage of catalytic combustion is that very little, less than 1 ppm, of nitric oxide is generated on the catalyst. A secondary advantage is that large pressure oscillations (at frequencies of 100 to 1000 Hz) that may occur in lean premixed combustors are highly suppressed in catalytic combustors.

The challenges for implementing reliable catalytic combustion systems in ultra-low emission gas turbines are being addressed at many different levels by catalyst/catalytic reactor companies, engine manufacturers, and academic researchers. Catalytic combustion development efforts in the U.S., including those under the Department of Energy's Advanced Turbine Systems program, are starting to produce

designs [e.g., Dutta 1997, Smith et al. 1997, Etemad et al. 1998] that are nearing engine worthiness. The various design approaches rely on a two stage combustion system, called a "hybrid" catalytic combustor. The hybrids include a first stage (front-end) catalytic reactor where fuel conversion raises the temperature to an intermediate temperature that is determined by the catalyst life properties. After the catalyst, a downstream second stage, called the 'homogeneous burnout zone' is where gas phase combustion completes the fuel conversion and raises the product temperature to that acceptable to the turbine rotor parts downstream. Unlike the catalyst first stage, the second stage gas phase combustion can generate NO and CO. In this respect, the less fraction of the fuel converted in the gas phase, the better; however, the catalyst can only convert so much before its self destruction limit is achieved. Many compromises are in progress; these new hybrid designs are far from optimized both in terms of operability and ultra-low emissions capability. To fully realize the potential of catalytic combustion, current efforts in materials development and characterization, as well as reactor design, and numerical model building, must expand. A schematic of a typical gas turbine, catalytic combustor system is provided in Figure 1.

Some of the outstanding issues in catalytic combustion can be introduced by Figure 2, which sketches out a typical operating window for a hybrid catalytic combustor in terms of combustor inlet temperature vs. equivalence ratio. The operating window is bounded by a low-temperature catalyst light-off limit (on the bottom), a minimum adiabatic combustion temperature (to the left) below which low CO emissions and flame stability are difficult to maintain, and a high-temperature catalyst limit (on the top), where catalyst overheating becomes very difficult to avoid. Figure 2 also indicates an approximate operating window for a typical dry-low-NO_x (DLN) combustion system. The figure suggests how the catalytic combustor offers advantages over DLN systems for operation at low adiabatic flame temperatures as well as at high adiabatic flame temperature where combustion acoustics can become problematic for the DLN systems. The potential to operate at lower adiabatic flame temperatures and to provide simultaneously NO_x and CO emissions below 5 and 10 ppm respectively, motivate the continual development efforts on catalytic combustion systems. Some key design challenges and recent fundamental and design efforts to

address those challenges are summarized in the sections that follow.

3. CATALYTIC COMBUSTOR DESIGN APPROACH AT ROLLS-ROYCE ALLISON

Given the potential NO_x emission benefits that could be derived from a catalytic combustion system, engine manufacturers have initiated efforts to integrate catalytic flame stabilization into future combustion systems. As mentioned, the fundamental understanding of the catalytic combustion system is incomplete at this time; however, other significant issues (system integration and engine operability) need to be addressed in addition to the fundamental topics for ultimate market acceptance of catalytic combustion systems. As a result, Rolls-Royce Allison has been moving forward with an engine demonstration program using a catalytic combustion system as a part of the U.S. DOE-ATS program.

Figure 3 shows a Rolls-Royce Allison combustor design for existing Pd/PdO catalytic technologies adapted to a modern industrial gas turbine engine designed to achieve high efficiency through a high pressure and temperature ratio simple cycle. This combustion system is designed to release heat in stages for emission control over a wide range of engine power conditions. The combustion system employs a catalytic combustor stage that is axially displaced from a downstream lean-premixed combustion stage. For engine operation, the lean-premixed stage is used during engine start up and low power running. As load is increased to about 50% power, fuel can be diverted to the catalytic stage as the compressor discharge air temperature is greater than the threshold activation limit of the catalyst. Once the catalytic reactor is activated, fuel is distributed between the catalytic combustion stage and the lean premixed stage to meet engine heat release requirements up to base load power demand.

This combustion system approach was selected to accommodate the unique requirements of a catalytic combustor within a high pressure ratio gas turbine engine. Catalyst light off limitations prevent the catalytic combustion stage from being operated at low engine power without preheating of the compressor discharge gases. This preheating creates undesirable NO_x as well as catalytic combustor inlet temperature variability that impacts the operating envelope, as shown in Figure 2. The combustion system arrangement shown in Figure 3 eliminates inlet temperature nonuniformity by only using the catalytic combustion stage at engine power settings that have sufficiently high compressor discharge temperatures.

The catalytic combustion stage operates by combusting only a portion of the incoming reactants in the reactor element. The balance of the heat release occurs aft of the catalytic reactor via gas phase reactions in a post-catalytic homogeneous combustion zone. The onset of the gas phase reactions must be displaced from the reactor element to avoid damage to the catalytic reactor. This delay time or displacement length necessary to accommodate a catalytic combustion system would create a system that would have increased length over that necessary in conventional lean premixed combustors. This is somewhat mitigated in the combustion system shown in Figure 3 as the catalytic combustor is displaced axially and

shares combustion volume with the aft located lean premixed combustion stage.

Given the current catalytic combustor knowledge base and design methodology limitations, the combustion system development approach is segmented into steps. The initial step is design and testing of small scale catalytic reactors. These reactors are evaluated at elevated pressures and temperatures in a long flame tube with perfectly mixed, uniform temperature reactants to assess post-catalytic gas phase reactions as well as internal reactor properties. The data accumulated from these subscale tests are used to evolve catalytic combustor design tools which are unverified for high pressure applications. These subscale tests also permit empirical examination of potential contaminants that would be present in either the gaseous fuel or turbine airflow in a typical gas turbine installation. This effort is necessary to identify and quantify special requirements for catalytic combustion systems as well as first order design verification.

The initial subscale testing provides the necessary foundation to proceed with the second step, the large scale combustor rig evaluation. Here, a large scale catalytic reactor element is tested in conjunction with an engine configured fuel-air premixer to study system performance. Recall that the catalyst has a defined and rather limited operating window with regard to variations of the incoming fuel-air mixture. If the fuel-air ratio is too high, local reactor distress will occur through overheating. For low fuel-air ratios, the gas phase reactions in the post catalyst reaction zone do not go to completion, resulting in inefficiency (high CO emissions). Any variation in fuel-air ratio due to unmixedness effectively narrows the catalyst operating window due to the fuel-air excursions beyond the mean value and thus concurrently reduces the power range over which the catalytic combustion stage can be utilized in the engine. Consequently, this step monitors and develops the appropriate approach conditions to the catalytic reactor. Once the combustor rig scale development of the catalytic combustor is completed, a rig scale, axially staged combustor will determine first order fuel flow distribution and operational strategies. The final step in the process is combustion system integration and development on a gas turbine engine where a range of dynamic and thermal loads will be present to influence catalytic combustion system performance over a range of steady state and transient operation.

4. CATALYTIC COMBUSTOR DEVELOPMENT AT SOLAR TURBINES

The Solar Turbine Mercury 50 ATS gas turbine is being developed to provide high thermal efficiency (>40%), ultra-low exhaust emissions, reduced electrical power costs, and high reliability and availability. The gas turbine is designed to meet increasing distributed power generation needs and combined heat and power (cogeneration) demands in local communities.

The Mercury 50 gas turbine uses a recuperated cycle in order to achieve high thermal efficiency goals. The configuration of the gas turbine, shown in Figure 4, is significantly different from conventional gas turbine layouts. Compressed air exits the compressor, travels through the recuperator, and enters the

combustor which is located at one end of the engine. This unique modular configuration of the Mercury 50 gas turbine, and the location of the combustor at one end of the engine, allows two combustion system options: the conventional low emissions approach incorporates an annular ultra-lean premixed (ULP) combustion system that is interchangeable with a future multi-can catalytic combustion system. The catalytic combustion system, when available, will achieve <5 ppmv NO_x and <10 ppmv CO and UHC (corrected to 15% O₂) over the 50-to-100% load range.

4.1 Development Status and Design Challenges at Solar Turbines

The development of the catalytic combustion system is divided into three phases:

- I. Subscale reactor (~10-12 cm dia.) testing at simulated engine conditions to obtain information on the performance and requirements of the catalyst;
- II. Evaluation of a system concept in a single-can full scale high pressure test rig; and,
- III. Multi-can hardware testing in high pressure rigs followed by demonstration on the Mercury 50 engine. The status of the catalytic combustor development process, and design challenges are summarized below.

Initial development of the catalytic combustion system was based on subscale testing of various Pd/PdO based catalytic reactor designs (designed and fabricated by Catalytica). Partial oxidation of the fuel is completed in the reactor, and the heat release is completed through homogeneous reactions in a post catalyst combustor. The catalyst substrate temperature is maintained at acceptable levels through a combination of preferential substrate coating and the unique thermodynamic characteristics of the Pd/PdO conversion at elevated pressures [Dalla Betta et al. 1993]. Results from the subscale testing program have been summarized in an earlier paper [Dutta 1997]. Testing showed that the fuel-air concentration needs to be very uniform at the catalyst inlet in order to avoid locally high or low temperatures in the catalyst substrate. Regions of high temperature lead to catalyst deactivation and damage, while areas of low temperature lead to high CO and UHC emissions in the exhaust. The development of low pressure drop fuel-air premixers capable of achieving less than 10% peak-to-peak variation in fuel concentration is critical to the success of catalytic combustion technology. The subscale tests also revealed the limited fuel-air turndown of the catalyst and the necessity of using air modulation to maintain catalyst performance at off-design load conditions. Based on the performance of the catalyst in the subscale tests, a concept for the Mercury 50 catalytic combustion system was established.

The catalyst design process is largely empirical, since sufficient information is not available to model heterogeneous reactions occurring at the catalyst surface. The operating window of the catalyst is typically optimized for a given engine cycle through high pressure rig tests. Chemical reactions downstream of the catalyst (using natural gas) can be modeled sufficiently accurately using one-dimensional formulations incorporating detailed chemical kinetic information.

The multi-can Mercury 50 catalytic combustion system concept follows the layout of Cowell and Roberts [1995]. Figure 5 shows a schematic of the combustor arrangement as tested in a single-can high pressure test rig. The system incorporates a start-up/part-load fuel injector located at the center of an annular catalyst, and a variable geometry valve that regulates the supply of air flow into the catalyst. The start-up/part-load injector is used to start the engine and operate it below 50% load. At 50% load, the combustor inlet temperature (recuperator discharge temperature) is sufficiently high for catalyst operation and the system transitions from part-load mode to catalyst operation mode. The Mercury 50 catalytic combustion system configuration has several operational benefits: a) The fuel flow bypasses the catalyst during engine light-off and initial acceleration, and avoids exposing the catalyst to non-optimum conditions; b) The catalyst operates between 50-and-100% without requiring a preburner. This allows the lowest levels of NO_x to be achieved; and, c) The temperature profile at the inlet to the catalyst is very uniform, since a preburner is not used in the system.

In order to investigate the viability of the concept, several engine operational parameters were studied in the single-can combustor: the ability of the system to light-off and meet simulated part-load operating conditions below 50% load using the central fuel injector, transition from part-load to catalyst operating mode at 50% load, and the use of variable geometry to modulate the air flow into the catalyst in order to meet <5 ppmv NO_x goals over the 50-to-100% load range. These engine operational requirements were demonstrated in the rig tests, and emissions goals were achieved over the 50-to-100% load range. Details of the design of the single-can catalytic combustor and results of rig tests are available elsewhere [Dutta, Cowell, Yee, Dalla Betta 1997, Dutta 1997].

The design and fabrication of the complete multi-can catalytic combustion system is currently in progress, with an engine demonstration planned for late 1999. The design of the combustion system has to address the following challenges: a) In addition to uniform fuel concentration at the catalyst inlet, uniform air flow distribution into each catalytic can is needed for combustor operation. Even slight variations in can-to-can air mass flow rates could lead to catalyst damage and high CO and UHC emissions; b) The presence of a variable geometry valve leads to significant changes in combustor aerodynamics, at different engine loads; and c) The engine control system is fairly complex in order to integrate the start-up system with catalyst operation.

In addition to issues related to engine operability, concerns such as long term catalyst durability, contamination, and mechanical integrity are also being addressed. Subscale catalyst tests at simulated engine conditions have shown no deterioration in catalyst performance over approximately 1000 hours. An accurate estimate of long term catalyst durability, however, will not be available until a field demonstration is performed. Potential contaminants/abrasives that have been identified include lube oil, turbine wash solutions, compressor coatings, fuel contaminants (e.g., Na, S, Cl), and air-borne contaminants (e.g., alumina, salt). Another area of concern is

the mechanical integrity of the catalyst containment structure at elevated temperature and when subjected to engine vibrations.

5. CATALYTIC COMBUSTOR DEVELOPMENT FOR THE SIEMENS WESTINGHOUSE ATS ENGINE

The Siemens Westinghouse Power Corporation (formerly Westinghouse Power Generation) ATS Engine shown in Figure 6 is a large, power generation combustion turbine containing sixteen can combustors located around the engine circumference. The hot gases from each combustor flow through steam cooled transition ducts prior to entering the turbine. In order to minimize the need for cooling air, the size of the combustion zone in the combustors has been reduced, and a significant fraction of the heat release takes place within the steam cooled transition ducts.

A major design goal of the catalytic combustor development program has been to incorporate catalytic combustion technology into combustors that are the same overall size as existing lean premixed combustor designs. This incorporation has been split into two programs: development of a catalytic pilot and development of a fully catalytic combustor.

5.1 Catalytic Pilot Development

The catalytic pilot consists of a radial inflow swirler with a catalytic centerbody. The pilot fuel and air are premixed upstream of the swirler and a small portion of each passes through the centerbody with the remainder passing through the swirler. The fuel/air and the hot combustion products of catalytic combustion exiting the centerbody assist in stabilizing the main fuel/air premixed flow in the surrounding combustor.

Initially the catalytic pilot was developed as a stand alone premixed burner at Precision Combustion Inc. This work involved CFD modeling, reactor modeling, and atmospheric testing of the burner with varying ratios of centerbody to swirler flows to determine the optimum performance. Once the stand alone design was proven, it was incorporated into an existing full scale, lean premixed combustor design and successfully tested at atmospheric pressure. Currently, the combustor is being prepared for rig testing at full engine conditions.

5.2 Fully Catalytic Combustor Development

The ability to construct a fully catalytic combustor to operate at ATS conditions has been largely dependent on the development of a suitable catalyst bed. The catalyst bed must operate at the relatively high fuel/air ratios required for ATS firing temperatures and provide enough reaction to stabilize the downstream burnout zone while still limiting the amount of reaction to prevent overheating and damage to the catalyst and substrate. Thus, significant emphasis has been placed on small scale catalyst bed design and testing, both at atmospheric and high pressure.

A suitable catalyst bed is selected and a block diagram of the full catalytic combustor design is shown in Figure 7. The combustor is designed without a preburner, so the catalyst modules will not be active below around 50% load for the ATS engine. To aid in starting and low load operation, the

combustor is equipped with a diffusion flame pilot. At high loads, when the catalyst modules become active, the diffusion flame will be shut off, and fuel will be premixed into the pilot air for minimum NO_x emissions. Once proven, the catalytic pilot discussed above may replace the pilot shown.

6. GENERIC R&D ISSUES, INCLUDING DURABILITY, OPERABILITY

This section highlights some of the important issues associated with low (Section 6.1) and high (Section 6.2) temperature catalysts needs, system integration and operability concerns, and the impact of modeling on catalytic combustion design and performance under actual gas turbine engine conditions. We conclude this section with suggested reading.

6.1 Low Temperature Light-Off Catalysts for Natural Gas

One of the outstanding issues in catalytic combustion as suggested in Figure 2 is the development of methane oxidation catalysts that maintain low light-off temperatures (say < 375°C) for several thousand hours. Low temperature light-off is critical for minimizing the need of complex preheating/start-up systems. Different approaches are used by various manufacturers.

In one design, a nonpremixed flame, called a 'preburner,' is ahead of the catalyst section (see Figure 1). This nonpremixed flame adds enough energy to the warm air leaving the compressor so that the temperature of the vitiated air mixture approaching the catalyst is above the 'light off' temperature of the catalyst. This nonpremixed flame may be used to start the engine and operate the engine at lowest loads. A drawback of this design is that the nonpremixed flame is responsible for about 3ppm NO_x emissions which result in relatively high overall emissions and thus loss of the key advantage of the catalytic combustor (e.g., [Dalla Betta, et al. 1994]).

For Rolls-Royce Allison, the ATS gas turbine engine has a pressure ratio near 25 to 30, and hence the air temperature leaving the compressor at maximum power is as high as 400 to 500°C, which is already above the catalyst light off temperature.

A third approach, used by Solar Turbines, has opted for the lower pressure ratio engine with heat exchange between the compressed air and the exhaust products leaving the turbine. These 'recuperated cycles' have inlet temperatures that may be quite a bit higher, up toward 600°C [Dutta et al 1997], well above the catalyst light off temperature.

A challenge of all three designs is that fuel has to be well mixed with the heated or vitiated air upstream of the catalyst [Schlegel et al. 1997].

The fuel for the second stage, homogeneous combustion, can be injected after the catalyst [e. g. Fujii, et al. 1996], or the catalyst may contain inactive channels that allow for some fuel and air to pass through the catalyst unreacted [e.g. Schlatter et al. 1997, Dalla Betta et al. 1996, Beebe et al. 1995]. This homogeneous zone is not unlike the 'afterburner' zone of a jet engine, and accordingly, the use of aerodynamic recirculation ('backmixing' on rearward facing steps or 'Vee' gutters) to stabilize a combustion zone may be incorporated.

The steady state inlet temperatures are designed to be above temperatures needed for palladium-based catalysts to maintain high activity for methane combustion. However, problems arise during low power conditions particularly for simple cycle engines where combustor inlet temperatures may drop below 375°C. At these low temperatures, the low surface reaction rates result in inadequate fuel conversion inside the catalyst bed. The product gases leaving the reactor are too cold to have significant homogeneous reaction in the second stage. Poor catalyst activity below 375°C also requires that catalytic combustion systems have an alternative means of combustion for engine start-up. Such systems have included variable geometry for switching from non-catalytic to catalytic modes of operation [Dutta et al. 1997] or downstream burners that must run relatively rich while the catalyst is not supplied with fuel [Smith et al. 1997]. Improved low-temperature catalysts would minimize the need for and complexity of the alternative combustion systems used for start-up and low-power conditions and thereby would improve the operability of catalytic combustors in general.

For the most part, supported palladium-based catalysts have been implemented for low-temperature light-off catalysts in natural gas combustors, and as of yet alternative non-precious metal catalysts such as perovskites and substituted hexaaluminates have not shown sustainable low temperature activity needed for natural gas combustor applications [Quinlin, Wise, McCarty 1989]. With palladium-based catalysts, the supports are generally in the form of high surface area 'washcoats', which provide a support base for sufficient dispersion of the palladium for low temperature light-off. However as the catalytic reactor heats up both spatially and temporally, the high surface area support becomes less critical because the increased rate of oxidation reactions at the exposed surface exceed the rate at which gas diffusion brings the reactants to the washcoat. (This is called the 'diffusion limited regime,' e.g. see text by Heck and Farrauto 1995). Research may still be done to provide guidelines for reducing precious metal loading through selective placement of high surface area supports without impacting reactor light-off or steady-state performance.

In the U.S., a significant amount of fundamental research, primarily using low-pressure (1 atm or lower), temperature-programmed reactors, has gone into understanding the behavior of supported palladium catalysts, particularly as it concerns methane oxidation. While no attempts will be made to summarize all of those studies here, some unique characteristics of palladium-based catalysts relevant to combustor design and operation will be pointed out. Firstly, even under reacting conditions, surface palladium molecules are for the most part in an oxidized state (PdO) below temperatures ranging from 600 to 900°C (depending primarily on oxygen partial pressure [Dalla Betta et al. 1993]). As the temperature increases, the palladium is reduced (PdO \Rightarrow Pd) and if temperatures rise high enough, the metal may undergo particle restructuring with loss of active surface area. As temperature falls, the palladium-based catalyst has a region of apparent negative activation energy that coincides with a loss of surface PdO which is more active to methane oxidation than the metal Pd. Thus, some have suggested that this region of negative activation energy can be used to control catalyst temperatures [Dalla Betta et al. 1993], i. e., if the temperature

is going to high, the PdO will revert to Pd and the reaction will slow down. However, even the reduced palladium (Pd) at higher temperatures still promotes methane oxidation (with a very high activation energy) and thus the methane oxidation reactions do not stop as PdO is converted to Pd, particularly at higher pressures [McCarty and Chang 1994]. All the same, the restructuring of the palladium catalysts at high temperatures will result in catalyst behavior which is very much dependent on past operating conditions. This hysteresis effect will be a distinct problem for combustor designers.

Much of our research understanding of Pd/PdO catalysts are from atmospheric pressure, or lower, test stands. This understanding is embedded into our models of the combustion process. However, there are features that will not be revealed until higher pressure tests are conducted and accordingly, our models of surface mitigated combustion at higher pressures is incomplete. A better understanding of the Pd/PdO system is needed at high pressures and at reacting conditions where surface oxides may be much more difficult to reduce than at low-pressure conditions of most micro-reactor studies. There is recent evidence suggesting that methane oxidation on Pd/PdO is promoted by CH₄ adsorption onto reduced Pd molecules with nearby PdO molecules promoting H-abstraction and subsequent CO₂ formation and desorption [Su, Carstens, and Bell 1998]. Assuming this new model is correct, it is not surprising that catalytic combustors have more difficulty lighting-off as pressure increases because the higher O₂ pressures will result in more complete oxygen coverage of the catalyst (perhaps more than one monolayer). The challenge for researchers and developers is to understand how Pd/PdO behaves under light-off and reacting conditions at higher pressures and then from that understanding to determine how to enhance the long-term durability of the necessary features which provide high catalyst activity at temperatures below 375°C. In particular, if it is critical to maintain some fraction of reduced Pd for good low temperature activity, efforts might focus on the potential of bimetallic palladium catalysts to sustain some reduced palladium at combustor light-off temperatures and pressures. The need for advanced processing techniques to ensure durable bimetallic catalysts will assist in that effort. As in all catalytic combustion studies, such an effort to hopefully improve low temperature catalyst light-off will require durability tests at conditions characteristic of actual combustors.

6.2 High Temperature Combustion Catalysts and Their Durability

Supported palladium-based catalysts which work well as low temperature catalysts have high temperature durability limits which may be driven by any of the following: loss of exposed catalyst due to surface sintering (sintering means loss of surface active area), change in surface chemical composition (e.g., formation of aluminates), or catalyst volatilization. (A good introduction to these considerations is presented in the recent text by Heck and Farrauto 1995). The sintering process, which is highly accelerated by water produced from the reactions, may involve recrystallization/ agglomeration of the supported precious metals as well as support phase (the washcoat) changes (such as from γ -Al₂O₃ to α -Al₂O₃) which may cause the precious metal to be covered by the washcoat.

To this end, washcoat stabilizers have been developed with rare-earth metals, which reduce the loss of surface area and thus exposed catalyst [Trimm 1993]. Researchers have looked at the effectiveness of more sintering resistant materials such as stabilized zirconia [Rodriguez et al. 1995] and low surface area α -Al₂O₃ [Lyubovsky, Weber and Pfefferle 1996] to provide consistent performance at higher temperatures.

Catalyst volatilization simply means that the vapor pressure of the metal, or its oxide, is becoming large enough that a significant loss of active catalyst is occurring merely by sublimation into the gas phase which is swept downstream. The 'restructuring' of precious metal catalysts at high temperatures as well as the metal volatilization both involve complex kinetic problems which are not well understood and thus difficult to control. Although palladium catalysts are generally agreed to be the least susceptible to catalyst volatilization of the precious metals, it is generally accepted that they only provide adequate resistance to temperatures of $1050 \pm 100^\circ\text{C}$ for long-term gas turbine applications. These temperatures are far below firing temperatures for advanced gas turbines, e. g. 1500°C , even for low-pressure ratio recuperative engines. Accordingly, there is a search for catalysts that will survive higher temperature. Many developers have investigated the use of non-precious metal, high-temperature catalysts, such as perovskites and substituted hexaaluminates. Material research on such materials has largely been performed outside the U.S. in Japan and Europe. Recent advances in substituted-hexaaluminate catalysts [Sadamori 1993] suggest that catalytic reactor exit temperatures as high as 1200°C may be achievable, but these catalysts are still prone to deactivation from high temperature excursions that may be caused by poor upstream fuel/air distribution. Schlegel et al. [1997] showed that low NO_x could be achieved, even if fuel-in-air distribution were temporally poor, but well mixed on the average.

Catalytic combustion systems presented thus far for ATS engines have not employed these alternative high temperature catalysts but have rather used precious metal catalysts and limited catalyst temperatures. Additional combustion occurs after the catalyst in the 'homogeneous' gas phase. Fuel for this additional combustion is injected after the catalyst [Fujii 1996], or passes directly through the catalyst by having passages that are not catalytically active [Schlatter 1997].

The absence of high temperature non-precious-metal catalysts in the U.S. for advanced gas turbines may in part be motivated by minimizing combustor pressure drop, but more likely the motivation stems from concerns about long-term durability of the catalytic reactor itself. Until high temperature catalysts can demonstrate durability for several 1000 hours with typical fluctuations in fuel/air ratios from premixers, engine manufacturers will restrain from their use. Fuel-air mixture preparation is a serious problem that will benefit from recent developments on diagnostics [Mongia et al. 1996, Mongia et al. 1998].

In general the issue of durability for high temperature catalysts is one of minimizing volatilization and sintering in the high temperature, steam-laden conditions of the

downstream region of the catalytic reactor. Thus, research aimed at high temperature catalyst development must clearly address this issue. Potential advantages of reduced NO_x emission from converting more of the fuel through the catalyst [Schlegel et al. 1994] should provide the motivation for continued materials development for high temperature combustion catalysts.

6.3 Catalytic Reactor Design and the Impact of Operating Conditions

Fundamental studies related to catalytic combustion should have an eye toward the actual implementation of concepts in combustor/reactor design. Consideration of reactor design and performance at actual operating conditions have been the focus of many scientists and engineers working on catalytic combustion issues for ATS gas turbine engines. The U.S. Patent literature has many proposed reactor designs oriented toward addressing some of the traditional problems associated with catalyst overheating; approaches include diffusion barrier coatings to reduce apparent activation energies, selective coatings to reduce mass transfer-limited catalyst temperatures [Dalla Betta et al. 1993, Chou, Kennelly, Farrauto 1992], and short segmented monoliths to increase mass transfer rates [Pfefferle et al. 1995]. Furthermore, metal substrates (e.g. inconel) are often preferred over ceramic since metals are less likely to break apart and be convected downstream where turbine damage is likely. Rather than enter into a lengthy discussion on the merits and challenges of the various approaches, a brief discussion will be presented here as to how operating conditions and scenarios impact the study of catalytic combustors and their design.

Catalytic combustors face system integration issues such as uneven air flow and fuel/air ratios from the upstream premixer [Schlegel et al. 1997]. A large effort in the ATS program has gone into the development of improved premixers both for dry-low NO_x as well as catalytic combustors [Mongia et al. 1996, Mongia et al. 1998, Mongia 1998]. Catalytic combustor design must include careful specifications of the limits in variation of fuel/air ratios and reactor velocities entering the catalytic monoliths. This is critical to avoid high temperature runaway or loss of long-term catalyst durability. One previous study looked at issues related to heat transfer in channels at different conditions [Worth 1993] but the model was not well suited for addressing critical issues related to high pressure catalytic combustors such as potential gas-phase ignition. Unlike heterogeneous reactors utilized in the chemical process industry, gas turbine catalytic combustors may operate at high throughput velocities consistent with relatively low pressure drop and low residence times. Accordingly, deep pore diffusion is not a typical property of a combustion catalyst. The high velocity throughputs reduce the risk of gas phase pre-ignition upstream and within the catalyst bed; this autoignition problem is exacerbated by higher pressures and temperatures [Warnatz et al. 1996]. The high velocities also reduce the catalysts' ability to light-off at low temperatures and to achieve adequate conversion.

Catalytic combustor developers must strike a balance in design between safe operation, reliable low temperature light-off, and overall reactor length (needed to achieve adequate fuel conversion within the catalyst). A point should be made

here that particularly for the high-pressure ratio ATS engines, velocities and pressures in the catalytic monoliths will likely lead to a transition to turbulent flow, from laminar flow, within the monolith. The transition to turbulent flow may pose the increased risk of flashback inside the catalyst due to the substantial increase in flame speeds caused by the turbulence, on the other hand, the increased mass transfer to the surface may serve to blunt autocatalytic reactions by radical recombination on the washcoat; more research is needed. The ways in which the high velocities impact catalytic combustor performance may be addressed to a large extent by improved computational models that combine fluid dynamics with gas phase chemistry and surface reactions. Such models are discussed in the next section.

One of the biggest challenges to implementing catalytic combustors for ATS gas turbine engines involves providing reliable/durable catalyst performance at the high operating pressures of these engines. Higher pressures increase the likelihood of gas-phase ignition due to the fact that ignition delay times and quenching distances for natural gas decrease approximately linearly with pressure [Schlegel et al. 1994, Dalla Betta et al. 1995, Warnatz, Maas, Dibble 1996]. Meanwhile the operating pressures of 25 to 30 atmospheres, characteristic of ATS engines, imply a likely transition to turbulence within the catalytic channels, which makes the system performance that much more difficult to characterize using less expensive low pressure tests. Furthermore, the catalytic reactions themselves may be influenced by the higher pressures since the higher pressures may result in increased oxygen coverage on the catalyst and changes in the active mechanism on palladium-based catalysts for methane oxidation. While low-pressure studies have indicated that methane oxidation on palladium catalysts is first order in CH_4 concentration and zeroth order in O_2 concentration [Fredrik 1997], it is not clear from simple Langmuir-Hinshelwood kinetic expressions whether or not the first order dependence on CH_4 will fall off as the pressure increases up to 30 atmospheres. Tests performed in high pressure rigs indicate that for a fixed bed length, conversion for a given velocity and inlet temperature does fall off with a $P^{-0.1}$ to $P^{-0.2}$ dependence which suggests that the conversion is controlled either by a mass transfer or chemistry process which increases by $P^{0.8-0.9}$ [Fredrik 1997]. It should be noted that this power dependence may not be operative over the entire pressure range and that light-off tests over these pressure ranges indicate an increase in light-off temperature as pressure increases. To improve our understanding of the applicability of simple scaling laws, improved computational models may play a significant role as discussed in the final section of the paper.

6.4 Potential for Modeling to Impact the Design Process

The expense and risk of testing catalytic combustion systems at actual engine conditions, and even more so in actual gas turbines, encourages the development of reliable and validated computational models for providing performance expectations and risk assessments of a given catalytic combustor design. Although several models have been presented in the literature as thoroughly reviewed in previous references [Cybulski and Moulin 1994, Kolaczowski 1995], these models for the most part are not well suited for simulating critical interactions between the catalyst and the

channel flows which dictate overall trends in catalyst/combustor performance. As implied in the previous section on reactor design, channel velocity profiles should play a large role in determining mass and heat transfer rates to and from the catalytic surfaces. The inability of previous models to simulate properly the velocity profiles inside catalytic monolith channels as well as the effects of complex surface chemistry suggests that these models have limited value in extrapolating catalytic reactor performance from controlled low-pressure experiments to the high-pressure conditions experienced in the engine. Thus, a challenge particularly for catalytic combustion research is to build computational models of catalytic channel flows which will adequately capture the coupling between heat release from the catalytic surface and the gas-phase velocity field (and gas-phase transport). Examples of such emerging models include Deutschmann et al. (1998), Warnatz et al. (1996), Bond et al. (1997), Coltrin, et al. (1990), Chou, C.P. et al. (1998). Where appropriate, large eddy simulations may be implemented to assist designers in understanding the impact of turbulent transitions inside catalytic channels on catalytic combustor performance at the high operating pressures associated with advanced gas turbine engines. The development of improved computational flow models for catalytic combustors may not only provide better prediction of conversion trends but also important information on the risk of preignition and fuel/air unmixedness [Mongia et al. 1996; Schlegel et al. 1997] for given combustor designs.

Another place where advanced modeling may play a critical role in improving the combustor design process involves the capturing of important transient phenomena, such as combustor light-off or oscillatory behavior in palladium-based catalyst systems. Such phenomena are generally driven by complex changes in surface chemistry and thus will only be understood as improved surface chemistry models are developed and incorporated into appropriate catalytic combustor models. For example, it is clear that palladium catalyst light-off is a complicated function of the palladium surface morphology and chemistry. Since low temperature activity is extremely important in determining the operability of a catalytic combustion system, developing validated transient models will improve our understanding of the driving mechanisms in catalytic combustor light-off and thus hopefully of critical design parameters for improving low temperature catalytic reactor light-off. Improved surface chemistry models particularly of Pd/PdO systems may also increase designer's capability to predict unwanted combustor oscillations as well as steady-state performance. Development of these models will require close collaboration between experimentalists, who have helped to build the large database on Pd-based catalyst behavior, and computational model builders. The potential cost benefits of using computer models to assess in advance the feasibility of a given catalytic combustor design for a high pressure engine should motivate a highly collaborative effort to build better surface chemistry models for critical catalyst compositions as well as improved flow models for catalytic monoliths in high temperature combustor applications.

Further reading: An introduction to the catalyst literature is the readable text by Heck and Farrauto (1995). Also, much

research progress is collected in the Proceedings for the International Workshop on Catalytic Combustion (IWCC) held at SRI, California (1991), Tokyo (1994), Amsterdam (1996), and San Diego (1999) - for details see McCarty (1999). Many of the presentations at these workshops later appear in a collective issue of *Catalysis Today*, e.g., the 2nd IWCC Workshop largely appeared in *Catalysis Today* vol. 26, 1995.

7. CONCLUSION

Although significant engineering and R&D challenges remain to successfully integrate and operate catalytic combustion systems in advanced gas turbines, the ATS OEM's are actively pursuing the technology and its long-term demonstration in full-scale engine tests. Results to date have been very encouraging, and once optimized, catalytic combustion has the potential to compete - from both an economic and emissions sense - with some of the latest after-treatment emissions reduction techniques. It is a viable technology that may be adapted and readily available in the near future to achieve ultra-low NO_x emissions in advanced power generation systems.

8. ACKNOWLEDGEMENT

This paper was written with partial support from the U.S. DOE-ATS program. The authors kindly recognize Ms. Abbie Layne and Dr. Norman Holcombe: ATS Product Manager and Contracting Officer Representative, respectively. The authors sincerely appreciate the paper invitation from RTA/NATO through Dr. Klaus Schadow of the Navy/China Lake, and coordination of the U.S. paper clearance process through Richard Hill of Wright-Patterson Air Force Base.

9. REFERENCES

- Beebe, K. W., Cutrone, M. B., Matthews, R. N., Dalla Betta, R. A., Schlatter, J. C., Furuse, Y., and Tsuchiya, T., (1995) 'Design and Test of a Catalytic Combustor for A Heavy Duty Industrial Gas Turbine' ASME 95-GT-137 Presented at TurboExpo95 Houston TX.
- Bond, T.C., Noguchi, R.A., Chou, C.P., Mongia, R.K., Dibble, R.W., J.-Y. Chen, J.-Y. "Catalytic Oxidation of Natural Gas Over Supported Platinum: Flow Reactor Experiments and Detailed Numerical Modeling," 26th Symposium (International) on Combustion/The Combustion Institute, pp. 1771-1778, 1997.
- Coltrin, M.E., Kee, R.J., and Ruply, F.M., (1990) "Surface Chemkin: A Fortran Package for Analyzing Heterogeneous Chemical Kinetics at a Solid-Surface--Gas-Phase Interface," Sandia Report SAND90-8003, (1990).
- Chou, C.P., Chen, J.Y., Evans, G.H., and Winters, W.S., (1998) "Numerical Studies of Methane Catalytic Combustion inside a Monolith Honeycomb Reactor using Multi-step Surface Reactions," submitted to *Combustion Science & Technology*, February 1998.
- Chou, T. C., Kennelly, T., and Farrauto, R. J., U.S. Patent No. 5,102,639 (1992).
- Cowell, L.H. and Roberts, P.B., US Patent No. 5,452,574 (1995).
- Cybulski, A. and Moulin, J.A., *Catal. Rev.-Sci. Eng.*, 36(2), 179-270 (1994).
- Dalla Betta, R.A., et al., U.S. Patent No. 5,183,401 (1993).
- Dalla Betta, R.A., et al., U.S. Patent No. 5,248,251 (1993).
- Dalla Betta, R.A., Schlatter, J.C., Nickolas, S.G., Yee, D.K., and Shoji, T., (1994) ASME Paper No. 94-GT-260.
- Dalla Betta et al. U.S. Patent No. 5,405,260 (1995).
- Dalla Betta, R. A., Schlatter, J. C., Nicolas S. G., Cutrone, M. B., Beebe, K. W., Furuse, Y., and Tsuchiya, T. (1996) 'Development of a Catalytic Combustor for a Heavy Duty Utility Gas Turbine' ASME paper 96-GT-485.
- Deuschmann, O., Gorablski, C. T. Schmidt, L. D., Raja, L. L., Kee, R. J., and Warnatz, J. (1998) 'Comparison of Navier -Stokes, Boundary-Layer, and Plug-Flow models for simulating flow in a catalytic-combustion honeycomb channel' Work In Progress Poster presented to 27th Symposium, International, on Combustion, 3 August 1998 (for copy contact Prof. R. J. Kee Engineering Division Colorado School of Mines, Golden CO 80401).
- Dutta, P., Cowell, L. H., Yee, D. K., and Dalla Betta, R. A., (1997), ASME Paper No. 97-GT-292.
- Dutta, P., Yee, D. K., and Dalla Betta, R. A., (1997), ASME Paper No. 97-GT-497.
- Dutta, P., (1997) Proceedings of the Quadrennial International Conference on Power Stations, Association des Ingenieurs de Montefiore, Liege, Belgium, pp. 267-272.
- Etemad, S., Karim, H., Smith, L. L., and Pfefferle, W.C., (1998) in press, *Catalysis Today*.
- Fredrik, A., Ahlstrom-Silversan, C., and Odenbrand, C., *Appl. Catal. A: General*, 157-175 (1997).
- Fujii, T., Ozawa, Y., Kikumoto, S., Sato, M., Yuasa, Y., and Inoue, H., (1996) 'High Pressure Test Results of a Catalytic Combustor for Gas Turbine' paper 96-GT-382 presented in Birmingham UK ASME TurboExpo96.
- Heck, R. M. and Farrauto, R. J. (1995) "Catalytic Air Pollution Control" text Van Nostrand Reinhold, and Chapman and Hall, ISBN 0-442-01782-0.

- Kolaczowski, S.T., *Trans. I. Chem. E.*, **73(A)**, 168-190 (1995).
- Lefebvre, A.H., *Gas Turbine Combustion*, Hemisphere, New York, ch. 7, 1983.
- Lyubovsky, M., Weber, R., and Pfefferle, L., *Twenty-Sixth Symp. (Intl.) on Combustion*, The Combustion Institute, Pittsburgh, 1996, pp. 1779-1787.
- McCarty, J.G. and Chang, Y., *Scripta Metallurgica et Materialia*, **31(8)**, 1115-1120 (1994).
- McCarty (1999) private communication: Dr. Jon McCarty, IWCC Chairman for 4th International Workshop on Catalytic Combustion to be held 14-16 April, 1999 in San Diego, Address: c/o Catalytica Combustion Systems, 430 Ferguson Drive, Mountain View, CA 94043-5272 USA, phone 650-940-6381 FAX650-960-0127, jmcarty@mv.catalytica-inc.com.
- Mongia, RK, Tomita, Hsu, F, Talbot L, and Dibble RW (1996), 'Use of an Optical Probe for time resolved in situ measurement of local air to fuel ratio and extent of fuel mixing with applications to low NOx emissions in premixed gas turbines.' 26th Symposium on Combustion The Combustion Institute, Pittsburgh, p2749.
- Mongia, RK, Dibble, RW, and Lovett, J (1998) 'Measure of air-fuel ration fluctuations caused by combustor driven oscillations' paper 98-GT-304 Presented at the ASME TurboExpo98; International Gas Turbine and Aeroengine Congress and Exhibition, Stockholm, Sweden, 2-5June 1998.
- Mongia 1998 Ph. D. Thesis, Department of Mechanical Engineering, University of California, Berkeley, CA 94720.
- Pfefferle, W. C. et al., U.S. Patent No. 5,453,003 (1995).
- Pfefferle, W. C. et al., U.S. Patent No. 5,601,426 (1995).
- Quinlan, M. A., Wise, H., and McCarty, J.G., (1989) GRI-Report-89/0141.
- Rodriguez, N.M., Oh, S.G., Dalla Betta, R.A., and Baker, R.T.K., (1995) *J. Catal.*, **157**, 676-686.
- Smith, D.A., Frey, S.F., Stansel, D.M., and Razdan, M.K., ASME Paper No. 97-GT-311 (1997).
- Su, S.C., Carstens, J.N., and Bell, A.T., *J. Catalysis*, **176**, 125-135 (1998).
- Sadamori, H. Tanioka, T., and Matuhisa, T., in *Proc. of Intl. Workshop on Catalytic Combustion*, ed. H. Arai, Catalysis Society of Japan, Tokyo, 158-161 (1993).
- Schlatter, J. C., Dalla Betta, R. A., Nickolas, S. G., Cutrone, M. B., Beebe, K. W., Tsuchiya, T., (1997) 'Single-Digit Emissions in a Full Scale Catalytic Combustor' ASME paper 97-GT-57 Presented at TurboExp97, Houston Tex.
- Schlegel, A., Buser, S., Benz, P., Bockhorn, H., and Mauss, F., (1994) *Twenty-Fifth Symp. (Intl.) on Combustion*, The Combustion Institute, Pittsburgh, 1994, pp. 1019-1026.
- Schlegel, A., Strichsbier, M., Mongia, R., and Dibble, R.W., "A Comparison of the Influence of Fuel/Air Unmixedness on NOx Emissions in Lean Premixed, Non-Catalytic and Catalytically Stabilized Combustion," Presented at the International Gas Turbine & Aeroengine Congress & Exhibition, Orlando, Florida, paper no. 97-GT-306, June 2-5, 1997.
- Spadaccini, L.J., Colket, M.B. III, *Prog. Energy Combust. Sci.*, **20** 431-460 (1994).
- Trimm, D.L., in *Proc. of Intl. Workshop on Catalytic Combustion*, ed. H. Arai, Catalysis Society of Japan, Tokyo, 46-55 (1993).
- Warnatz, J, Maas, U, Dibble, RW (1996) 'Combustion' Springer ISBN 3-540-60730-7.
- Worth, D.J., Kolaczowski, S.T., and Spence, A., *Chem. Eng. Res. Des.*, **71(A3)** 331-33 (1993).
- Winters, W.S "Swimming with the Current- An Interim User's Guide to the computer code CURRENT." Sandia National Laboratories at Livermore, 1992.

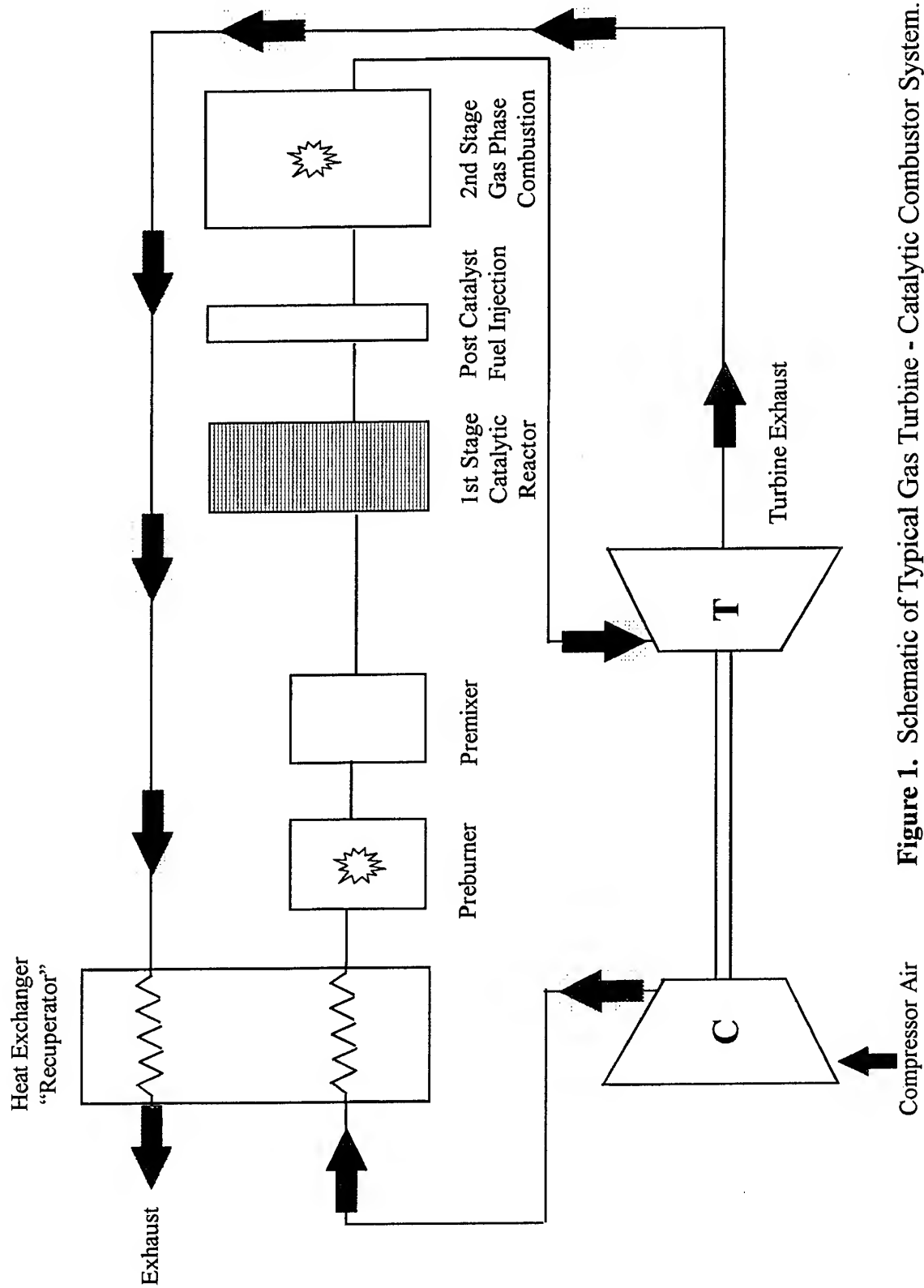


Figure 1. Schematic of Typical Gas Turbine - Catalytic Combustor System.

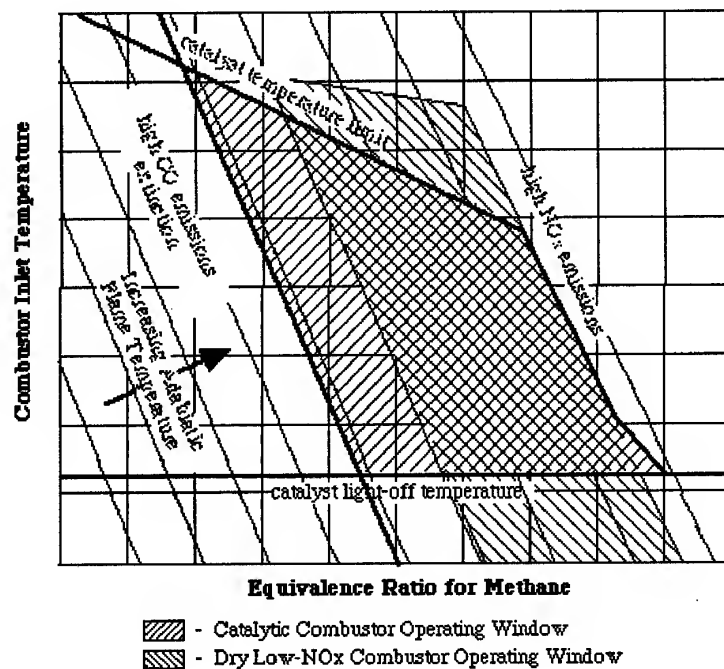


Figure 2. Sketch Showing Operating Windows of Representative Catalytic Combustion System and Dry Low NOx Combustion System.

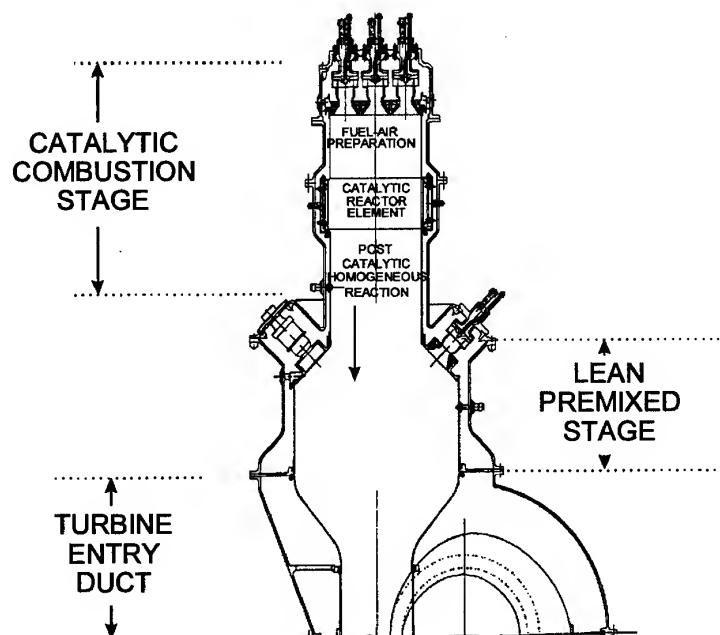


Figure 3. Rolls-Royce Allison ATS Catalytic Combustion System.

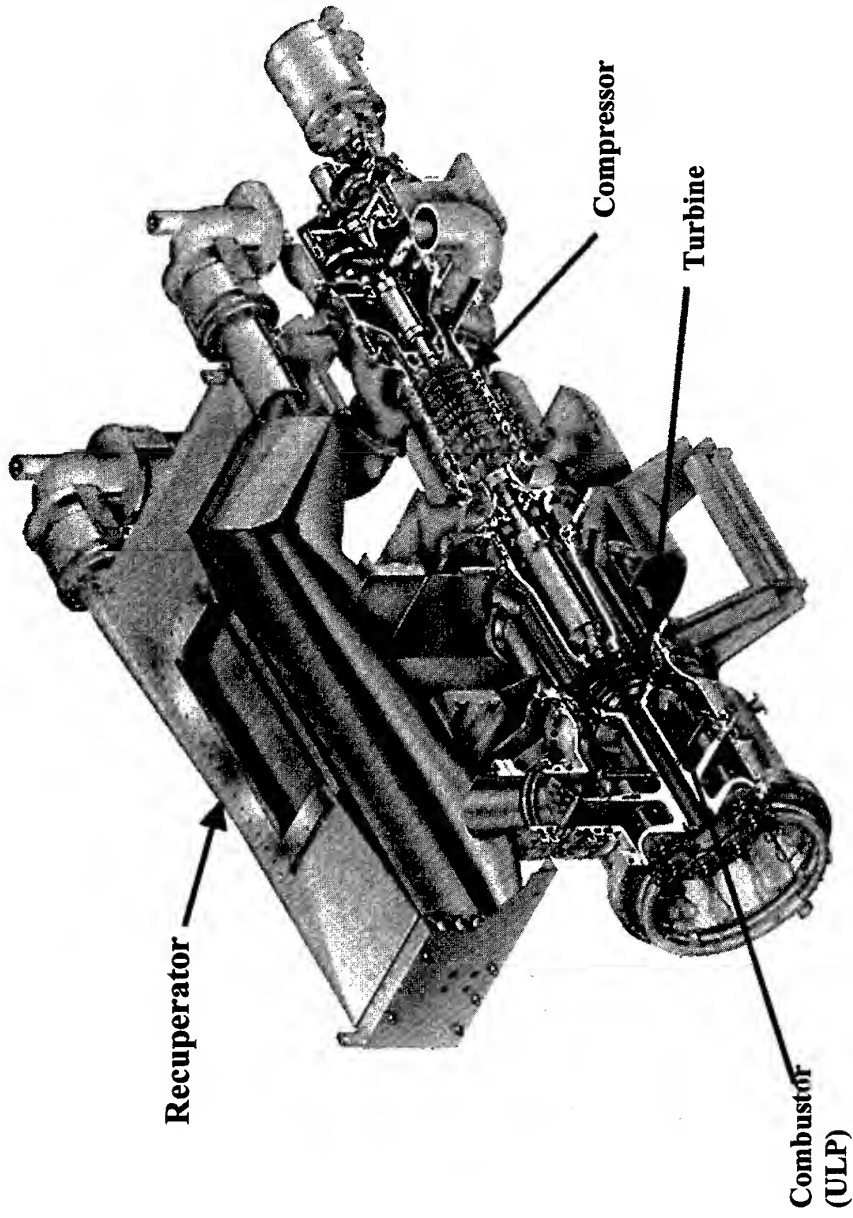


Figure 4: Mercury 50 Gas Turbine for Generator Applications.

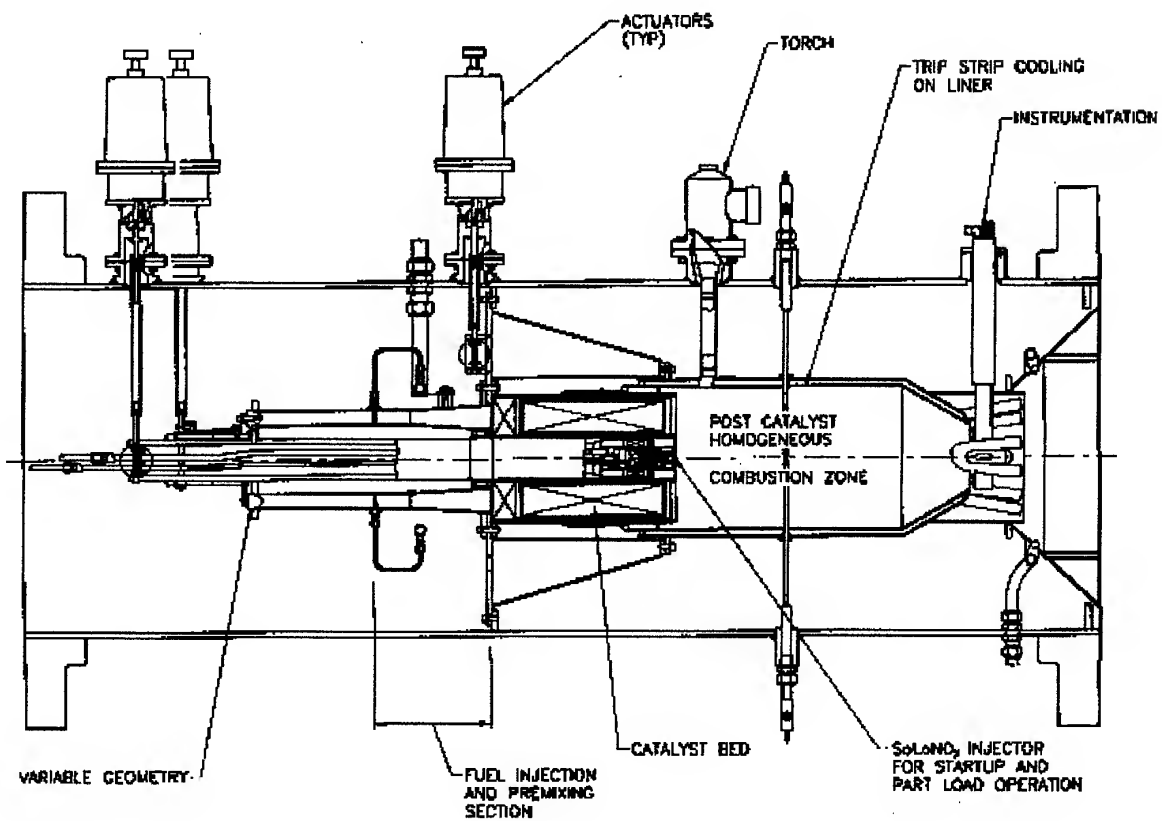


Figure 5: Solar Turbines' Catalytic Combustor Schematic.

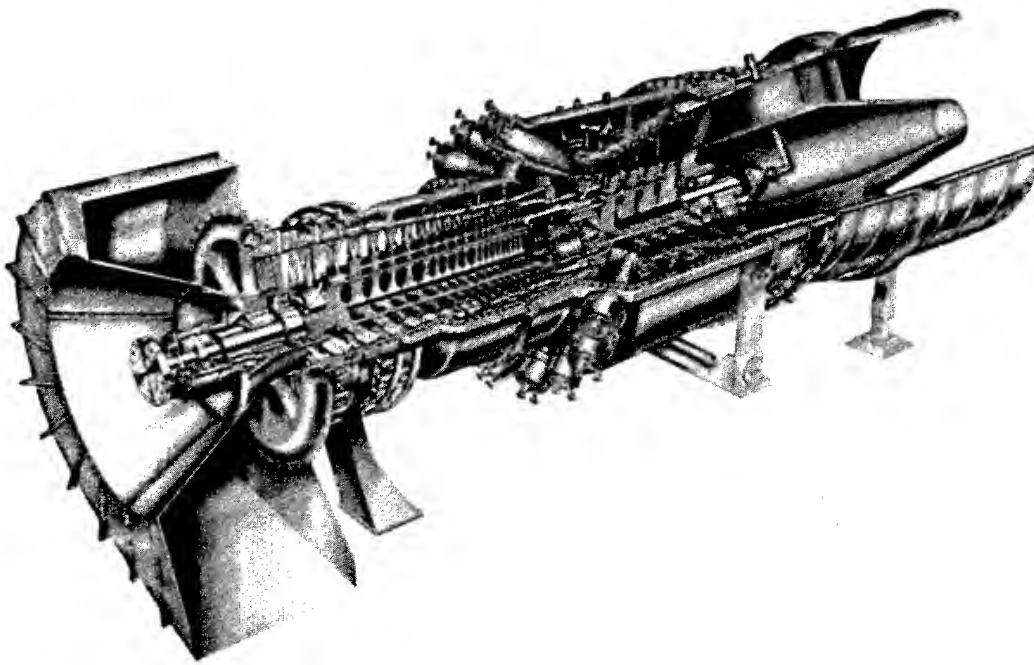


Figure 6. Siemens Westinghouse ATS Engine.

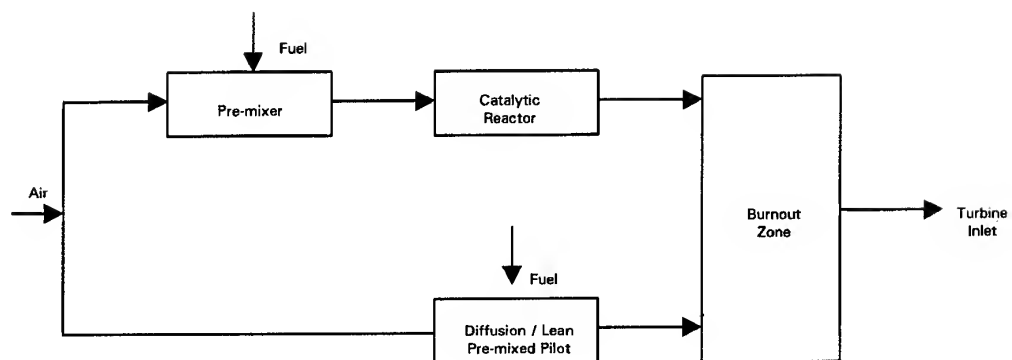


Figure 7. Block Diagram of the Siemens Westinghouse ATS Catalytic Combustor.

PAPER No. 8
Fant et. al
(presenter: D. Fant)

Question 1: T. Rosfjord, UTRC, U.S.

What level of fuel/air premixing is truly required for catalytic combustion systems, and what levels are currently actually achieved in practical systems?

Answer

The maximum fluctuations in fuel/air concentration allowable are plus or minus 3 % of the mean value. Rolls Royce - Allison (Dr. Mohan Razdan) has indicated that this premixing requirement has already been achieved in their designs.

Question 2: S. Hoffmann, Siemens A.G., Germany

If fuel/air premixing is better than plus or minus 3 % of the mean equivalence ratio has been achieved, why do you then need catalytic combustion since LPP would be more than satisfactory with such mixing levels?

Answer

Catalytic combustion suppresses the combustion dynamics that can arise with LPP combustion systems.

Question 3: M. Aigner, DZLR, Germany

In response to the previous question the author mentioned that he believes catalytic combustion suppresses acoustic instabilities. Why does he so believe?

Answer

It **may** be that the viscous boundary layers on the surfaces of the individual channels in the monolithic catalytic bed, and flow partitioning afforded by these channels, together provide sufficient damping to suppress these types of instabilities.

Measurement of Spray/Acoustic Coupling in Gas Turbine Fuel Injectors

Torger J. Anderson, Donald W. Kendrick, Jeffrey M. Cohen and Thomas J. Rosfjord

United Technologies Research Center
Aeromechanical, Chemical and Fluid Systems
411 Silver Lane
East Hartford, CT USA 06108

1. ABSTRACT

A diagnostic to measure the acoustic coupling of air flow with a fuel injector spray has been developed and tested. The instrument measures the mass of fuel within a plane of the spray using planar laser-induced fluorescence. The signal is monitored continuously to measure mass flow fluctuations during acoustic excitation of the flow. A comparison with the acoustic signal provides a measure of the response of the spray to acoustic excitation for a given nozzle design. This paper describes the approach to acquiring a planar-integrated time-dependent signal for response measurements. Results for several nozzle designs are also presented.

2. INTRODUCTION

In dealing with gas turbine combustion instability problems, the coupling between acoustic modes and other unsteady processes must be understood. One critical element may be the way in which the fuel spray formation process couples with the acoustics, creating time-varying fuel delivery to the combustion zone and leading to heat release oscillations. If these heat release oscillations are in phase with the acoustic pressure oscillations, a self-excited combustion instability will occur. A number of potential mechanisms may be involved in the atomization process, depending on the type of fuel injector used. An understanding of these mechanisms can be elusive; it is difficult to monitor what is happening within the small and complex injector assembly and fluctuations in the spray are hard to characterize.

UTRC has been studying combustion instabilities in order to develop injector designs which are less susceptible to spray/acoustic coupling. As an element in this effort, an instrument was built to measure the fluctuations of fuel flow through transverse planes of a fuel spray and to determine the level of coupling between an applied acoustic excitation and those fuel flow fluctuations. The instrument has been employed in a full-scale, single injector/air swirler fuel flow facility in which the air flow could be modulated at frequencies

from zero to 1 kHz using an electro-mechanical driver. The fluctuating air pressure upstream of the injector and fluorescence signal derived from the liquid fuel spray were continuously monitored to characterize the degree of correlation between them.

The instrument was then used to characterize four fuel injectors. In particular, the study was to ascertain whether injector response occurred within any preferred frequency ranges in which the motion of the atomized fuel spray could couple with the induced airflow pulsations, thereby providing a feedback mechanism leading to the formation of combustion instabilities. The acoustic resonance frequency of the subject combustor ranges between 200 and 700 Hz. The response of the different injectors within that range is of particular interest here.

This paper describes the details of the instrument and its operation. It will include a discussion of the results of the studies done thus far and the analysis procedures employed.

3. DIAGNOSTIC TECHNIQUE

The measurement technique takes advantage of the natural ability of typical jet fuels such as Jet A to fluoresce when excited by visible light in the blue/green region of the spectrum. The fluorescence was generated from additives and aromatic constituents (Arnold et. al, 1992). An atmospheric-pressure spray rig provided the framework in which this instrument was used. This facility provided the air and fuel flows necessary to operate a fuel nozzle, as shown in Figure 1. An acoustic driver was used to perturb the airflow over a range of frequencies so that the effects on the spray can be observed. An A.C.-coupled acoustic transducer located in the plenum chamber was employed to yield an accurate measure of the energy input to the system. The acoustic resonance frequencies of the plenum chamber were designed to be far above the range of interest (> 1 kHz). A uniform laser sheet, projected through such a spray, excited fluorescence proportional to the mass of the fuel within the sheet. Continuous monitoring of the fluorescence intensity with a single detector provided a temporal record of the mass and its fluctuations. Correlations of mass fluctuations with measurements of the acoustic pressure signal provided a means of examining the level of coupling. The laser sheet could be moved along the spray axis to determine the spatial nature of the coupling process.

Copyright © 1998 by United Technologies Research Center.
Published by The American Institute of Aeronautics and Astronautics, Inc. with permission.

In this instrument, an argon-ion laser, tuned to the 514.5 nm line, was used to excite the fluorescence. The fuel fluorescence was broadband in the visible spectrum and

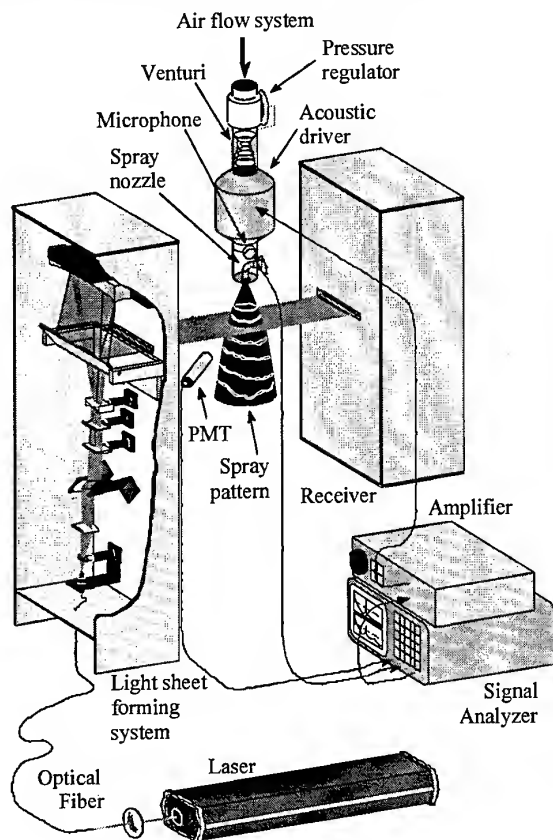


Figure 1. Test setup for fluorescence measurements of fuel mass flow fluctuations. The air flow system includes an acoustic driver which perturbs the flow. The microphone measures the acoustic forcing of the spray.

was easily isolated from the much stronger laser light with colored-glass long pass filters.

The laser sheet was projected through the spray pattern transverse to the flow axis. In order to make a practical continuous measurement of the mass represented by the fluorescence, it was necessary to acquire the signal on a single detector. Issues of uniform weighting of the measurement from fuel droplets in various regions of the spray were addressed. Four factors have been considered: (1) non-uniformities in the excitation laser sheet resulting from the beam intensity profile, (2) beam attenuation due to scattering as the sheet traverses the dense spray, (3) fluorescence signal attenuation due to scattering and (4) variation in distance from the detector (r^2 effects). While it is difficult to overcome the scattering issues, an initial assumption of

uniform and symmetric spray patterns was used. Variations in detector distance from the different portions of the spray have been dealt with by using low $f/\#$ detector optics and locating them a distance away from the spray.

In this instrument, a uniform laser sheet was produced in a novel way. A Gaussian beam of the form

$$\frac{I}{a} = e^{-\frac{1}{2}\left(\frac{R}{b}\right)^2} = e^{-\frac{1}{2}\left(\frac{\sqrt{x^2+y^2}}{b}\right)^2}$$

centered at the origin, was first collapsed in one dimension to create a sheet. (a and b are normalization constants for intensity and distance, respectively.) The integration of this profile in the y direction yields another Gaussian of the form

$$\frac{I}{a'} = e^{-\frac{1}{2}\left(\frac{x}{b}\right)^2}$$

The sheet was then split, overlapped with a proper spacing and recombined to produce a new beam profile dependent on the spacing of the two half-beams. The profile was split at the central axis and each half was shifted a distance, d/b , toward and across the axis as shown in Figure 2. Figure 3 is a series of profiles which result when various half-beam spacings, d/b , are used. Since uniform intensity was the goal, Figure 4 shows the intensity variation in each profile as a function of d/b based on the maximum and minimum

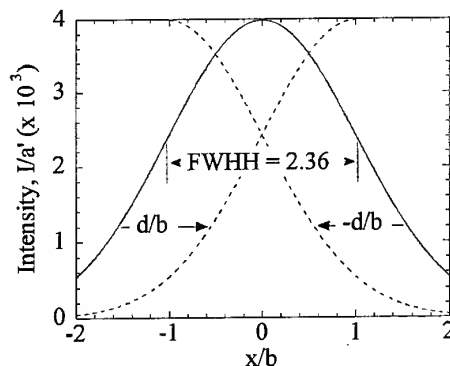


Figure 2. Gaussian beam profile is split and each half is shifted d/b to overlap.

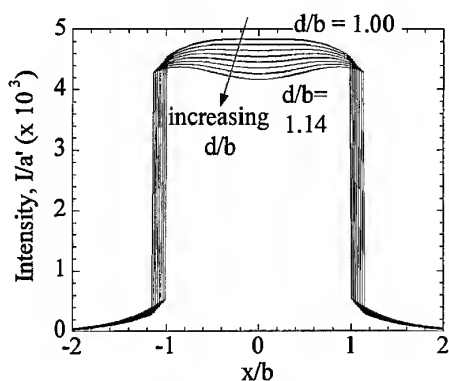


Figure 3. Intensity sums for split Gaussian's with varying overlap, d/b .

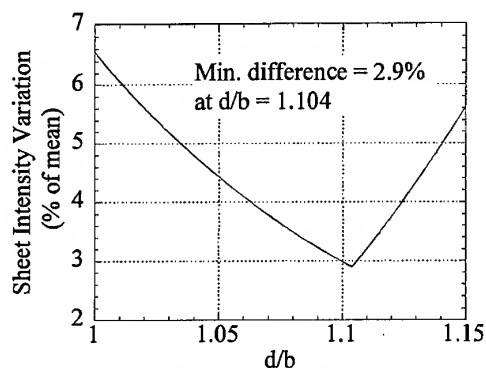


Figure 4. Intensity variation in the uniform part of the sheet for beams with different overlaps, d/b .

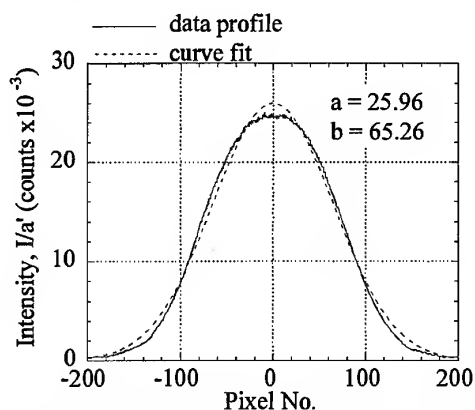


Figure 5. Actual "thick" sheet profile compared with a Gaussian curve fit.

difference in each profile. It shows a distinct minimum at $d/b=1.104$ where the sheet is uniform within approximately 3%. In reality, the beams are not exactly Gaussian as shown in Figure 5. Nonetheless, by varying the value of d/b , a nearly uniform beam profile can be produced.

This beam structure was generated with the optical configuration illustrated in Figure 6. The laser beam was transmitted to the instrument with an optical fiber of 65 μm dia. and 0.13 numeric aperture (n.a.). The beam was initially expanded into a thick sheet with the cylindrical telescope, L1/L2, and split at the centerline using a flat mirror, M1, at 45 deg. The reflected half of the beam was offset and reflected using M2 such that it overlapped and converged

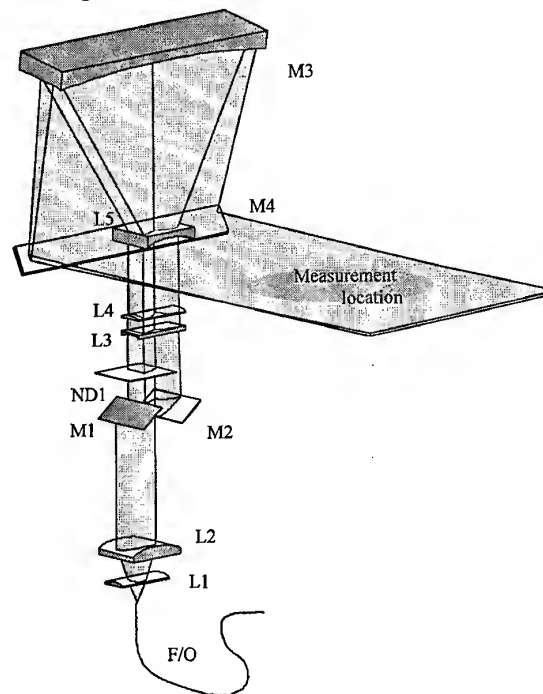


Figure 6. Optical configuration for creating a uniform sheet. Optics are cylindrical lenses L1 (13 mm f.l.), L2 (150 mm f.l.), L3 (-100 mm f.l.), L4 (200 mm f.l.), L5 (-150 mm f.l.), mirrors M1 (flat), M2 (flat), M3 (610 mm spherical mirror section), M4 (flat) and neutral density filter ND1 (~92% transmittance).

with the unaffected half beam at the measurement point. A glass plate attenuator, ND1, was placed in the unaffected half beam to reduce the intensity to the same degree as the reflected half beam. A telescope consisting of L3, L4 and M3 focused the beam into a thin sheet approximately 3 mm thick at the centerline of the measurement location. A further telescope (L5/M3) broadened the sheet to a parallel 200 mm width. A flat mirror (M4) directed the sheet through the spray as described earlier. Figure 7 is a measured beam intensity profile using this instrument and a CCD camera and

demonstrated an intensity variation of less than 5% across the sheet. It should be noted that the useable portion of the

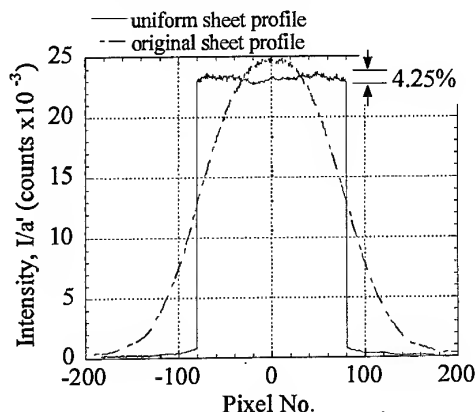


Figure 7. Most uniform beam was produced with $d/b = 1.24$ when the actual laser beam was split. Variation from the Gaussian prediction is due to the non-Gaussian profile. Additional intensity variation (4.25%) is due to laser and detector noise.

uniform sheet had 89% of the power in the Gaussian beam, the major loss being due to added optics. 98% of the final sheet energy is contained in the uniform portion of the sheet.

The laser sheet was collected with a similar planar mirror, concave mirror section and convex lens which focused it onto a photodiode so that the transmitted intensity could be monitored. This provided a measure of scattering occurring in the spray. All of the optics are incorporated into two boxes, one on either side of the spray rig. These can be moved up or down to examine the spray at varying downstream distances from the nozzle exit.

The fluorescence signal was acquired with a lens system and photomultiplier tube (PMT) mounted within the plane of the laser sheet at 45 deg. to the centerline. A 25 mm focal length lens ($f/1$) was used to generate a virtual image of the fluorescence centered at a distance of 500 mm. A mask at the image plane passed only light from the spray within the laser sheet. This light was acquired on the PMT after transmitting it through 3 mm of Schott OG590 colored glass which virtually eliminated all of the scattered 514.5 nm laser light. The PMT was a compact system produced by Hamamatsu which contained a signal amplifier and high voltage power supply. Alignment of the detector system was accomplished by placing a sheet of white paper at the centerline of the spray and adjusting the position of the detector while monitoring the fluorescence from the paper. Intensity errors resulting from the spatial distribution of the spray with respect to the detector were minimized by placing the detector at a relatively large distance (low $f/\#$) from the spray.

The above optical technique was used to characterize the dynamical signatures of four, aeroengine, airblast atomizers. They will be referred as injectors A through D, respectively. The injectors utilize the relative motion (Castleman, 1931) between a low-velocity sheet of liquid fuel and surrounding high-velocity air streams to effectively disrupt and break apart the liquid sheet into unstable ligaments and large droplets. The liquid fuel (Jet A) is injected onto a filming surface and is then atomized through the combined influences of inner and outer air flows having identical swirl directions.

4. CALIBRATION

An initial assessment of the technique was done in the form of a calibration. This entailed measuring the PMT signal for a variety of fuel flow rates. The air flow rate was regulated by a choked venturi and adjusted to yield a pressure drop of 2.5 psi across the air swirler, while the mass flow rate of fuel was varied between 0 and 250 lbm/hr. Both quantities encompassed the normal (scaled to atmospher-

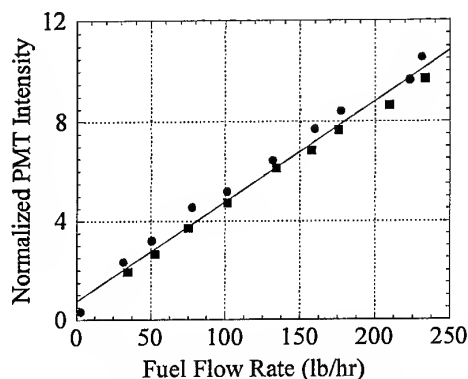


Figure 8. Calibration plot for injector A.

ic pressure) operating range of the device. For this series of tests, the laser sheet was located 4 inches from the exit plane of the injector. The results of the calibration are presented in Figure 8.

The measured PMT signal was non-dimensionalized by the incident laser intensity I_0 . Two data sets are shown with a linear curve fit to demonstrate the repeatability of the technique. The linearity of the curves is apparent: increasing the mass flow rate of fuel increased fluorescence intensity and consequently the PMT signal, as expected.

5.1 Forced Spray Results and Observations

A Ling Electro-Pneumatic driver (Model EPT-94B) was used to modulate the air flow driving the spray. This device is a high-capacity, high-response (up to 1 kHz) valve which was controlled by a sinusoidal voltage. A Hewlett-Packard (Model 35665A) signal analyzer provided an input to drive the valve

and recorded both the acoustic pressure measured in the air supply plenum and the PMT signal, representing the spray response.

5.2 Coherence Measurement

In order to quantify the degree of interaction between the pulsed air flow (forcing function) and the fuel spray (output), the coherence between the acoustic pressure signal and photomultiplier (PMT) signal signals was measured for a variety of flow conditions. Ideally, it is desirable to calculate the transfer function relating output to input. However, this assumes a linear relationship between the two. High coherence is essentially an indicator of linearity, and as such, represents a necessary condition for calculating the linear transfer function. Coherence is typically measured on a linear scale ranging from 0.0 (no coherence) to 1.0 (perfect coherence). The HP analyzer employed calculated the coherence from a series of averaged frequency response measurements. In simple terms, the coherence represents how much of a network's output is caused by its input. Perfect coherence at a frequency ν , for example, infers all of the output power at this frequency was caused by the system's input. Mathematically, the coherence, $\gamma_{xy}(\nu)$, is defined as the cross-power spectral densities between two random processes, x and y , divided by the square root of the product of their auto power spectral densities (Carter, 1985):

$$\gamma_{xy}(\nu) = \frac{G_{xy}(\nu)}{\sqrt{G_{xx}(\nu)G_{yy}(\nu)}}$$

The coherence is consequently complex. The magnitude-squared coherence which is displayed and plotted in the following plots is merely:

$$C_{xy}(\nu) = |\gamma_{xy}(\nu)|^2$$

$$0 \leq C_{xy}(\nu) \leq 1$$

By continuously varying the frequency of the forcing function, a map of the output's response was obtained detailing possible frequency bands in which interactions between the two signals could be seen. This measurement, therefore, yielded essential information on the dynamical behavior of prospective injectors. It should be noted, however, that the coherence is only a measure of the linearity of the relationship between the input (pressure) and the output (intensity) of the system and does not quantify the magnitude of that relationship.

The initial series of experiments was aimed at determining the coherence of the spray's response to the air-side forcing. The PMT signal derived from the fluorescence of the fuel

provided a measure of system output or degree of acoustic coupling. The A.C.-coupled acoustic transducer located in the plenum chamber was employed to yield an accurate measure of the energy input to the system. Using these two signals, coherence and swept-sine transfer function measurements were performed using the HP Signal Analyzer.

Figure 9 depicts the coherence measurements from injector A at several axial stations as the driver was forced at a variety of frequencies between 0-900 Hz. Examining the figure, there is a location at which the acoustic fluctuations have the greatest effect on the spray. This is consistent with the understanding of the evolution of the atomization process. As the liquid fuel issues from the injector, it is first atomized through the influences of the momentum flux ratio existing between the high velocity air flow and the slower moving liquid flow (Snyder et. al, 1996). After a primary atomization process where large, unstable ligaments and droplets are formed, a secondary atomization commences which further reduces the particles' size. This process is typically Weber number dependent (Hopfinger et. al, 1994). Only when the droplets have attained a unique size can they be more easily influenced by the surrounding air flow; if they are too large, prevailing forces are insufficient to accelerate them. This process generally relies on the governing Stokes number to be much less than unity. The Stokes number is typically defined as the particle's response time divided by the eddy turnover time or:

$$St = \frac{\tau_p}{\tau_e}$$

If particles are too large, they become centrifuged inside turbulent or large scale structures so their response to flowfield changes is negligible. As the particles are reduced in size with increasing axial distance, creation of an optimal axial location for forcing should occur. The reason for the drop in droplet response for greater axial positions (> 4 inches) is unclear, however. One possible explanation could be the attenuation of the acoustic energy over an increasingly larger area with subsequent downstream locations, thereby diminishing its influences on the liquid droplets. Another reason could simply be the damping of the spray's motion due to spreading and drag effects.

Also apparent is the strong coupling in the 300-700 Hz region at all axial distances. There are even tails on either side of the main peak hinting at other frequency bands of interaction. The increasing coherence near zero frequency is typical of zero frequency functions, which have very strong linear relationships, varying only by a gain factor (Cohen, et. al, 1997).

Figure 10 summarizes the coherence measurements for all four injectors taken at 4 inches from the exit plane. Except for injector D, all of the injectors exhibited spray/acoustic coupling within the frequency range of interest (350-700 Hz).

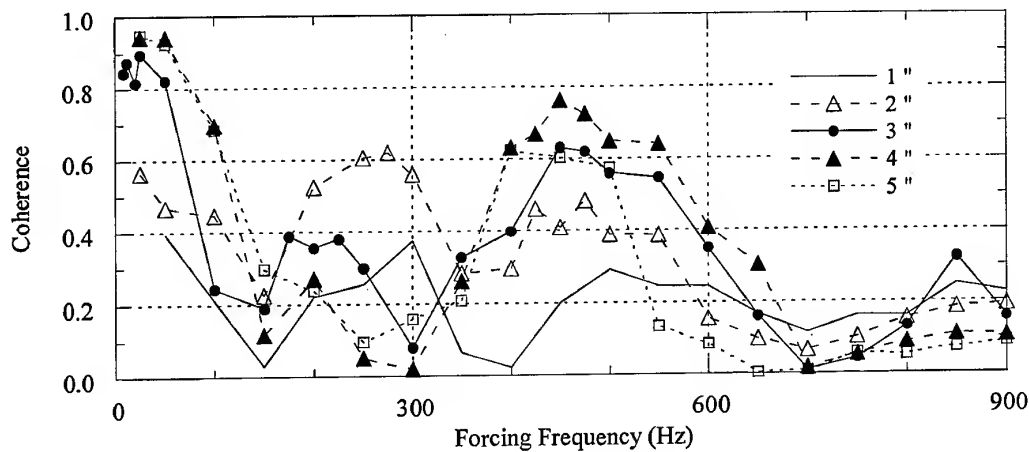


Figure 9. Coherence measurements for the injector A at several axial stations.

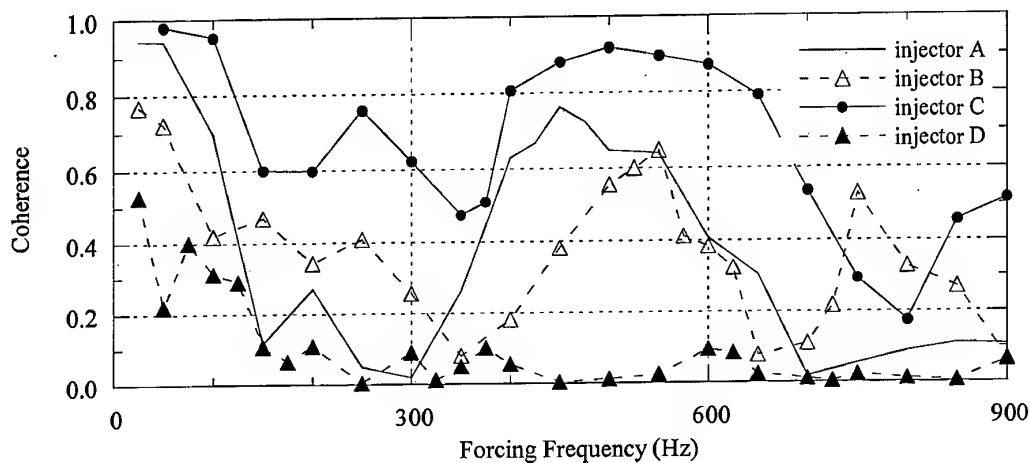


Figure 10. Summary of coherence measurements for all injector configurations, 4 inches from the exit plane.

This is important as it reflects the ability of the droplets to respond to the external excitation, thereby allowing for the possibility of a corresponding fluctuating heat release trace which could lead to unstable burning. Injector C exhibited the highest coherence over the frequency range of interest.

Between 400 to 650 Hz, the coherence remained at a fairly constant and high value of around 0.85 for this swirler. Even at lower frequencies (150-350 Hz), the coherence remained at fairly substantial values, even matching the highest coherence

measurements of injector A (compare the coherence of injector C at 250 Hz with the maximum coherence of injector A). The coherence plots also reveals injector B exhibited the most peaked coherence map, centering at approximately 550 Hz. It therefore has a narrower or more selective interaction region. Injector A, conversely, has a more intermediate region of interest when compared to the two above. Injector D would appear to be the more likely candidate for implementation in an engine, as acoustic forcing had negligible influence on the spray's behavior.

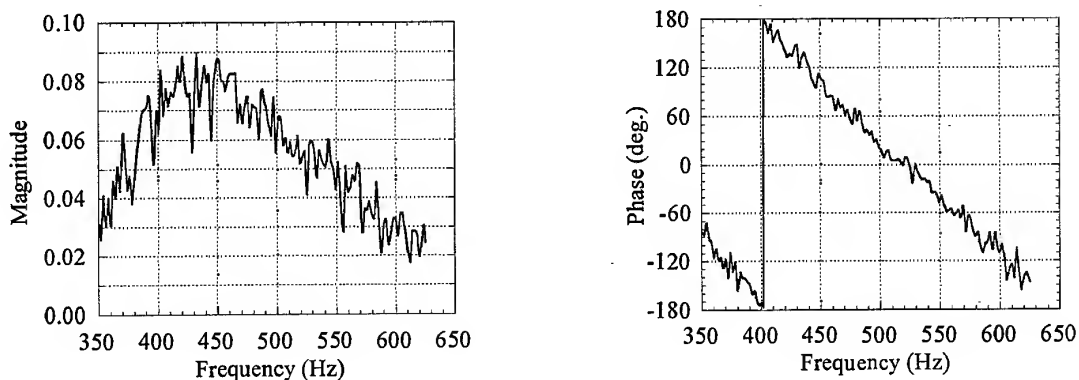


Figure 11. Magnitude and phase of the mass fluctuation/ p' transfer at a location 4 in. downstream of nozzle A. The mass fluctuation transfer function is derived from the mass/ p' transfer function (TF) by multiplying by frequency.

5.3 Swept-Sine Measurements

Further evaluation of the acoustic coupling was done through measurement of the spray mass flow / acoustic pressure transfer function, using the swept-sine feature of the HP Analyzer. Swept-sine data acquisition integrated the dynamic forcing and acquisition processes to allow for discrete tone excitation, and also for construction of a Bode plot (magnitude and phase vs. frequency) representing the spray mass flow/acoustic pressure relationship. The instrument was programmed to force the system in a series of discrete tones, collecting and averaging response data at each frequency. The frequency range of interest was set at 350-650 Hz, with resolution at 2 Hz intervals. This frequency range was chosen for injector A, based upon the high levels of coherence exhibited there.

Figure 11 shows the results of measurements of nozzle A in a plane 4 in. downstream of the nozzle exit. The plots show the transfer function for the mass fluctuations in this plane resulting from upstream acoustic pressure perturbations. The raw data representing time-dependent mass concentration were collected and stored by the analyzer in the frequency domain. The time derivative of mass in the measurement plane was derived in the frequency domain, so as to avoid amplifying noise in the signal. The results show the characteristics often found in bandpass-filtering devices. The fuel injector acts as a bandpass amplifier, only allowing significant interaction between the spray and the acoustics over a range of frequencies, peaking at approximately 450 Hz. Evaluation of this characteristic for an injector and comparison of this frequency range with the dominant acoustic modes of the combustion system will allow designers to address combustion instability problems earlier in the development process.

6. CONCLUSIONS

A novel optical technique has been devised to monitor the fuel flow fluctuations in an acoustically excited spray, using the fluorescence of additives and aromatic constituents in the

fuel. The technique was applied to four aeroengine fuel injectors and identified strong acoustic coupling between the pulsed air flow and the fuel spray mass flow in the 350 to 650 Hz range. Identification of such problematic frequency ranges is paramount in the better design of fuel injectors to help alleviate possible feedback mechanisms leading to unstable combustion. This instrument, therefore, represents a valuable tool in the screening of prospective fuel injector designs.

7. ACKNOWLEDGEMENTS

This project was funded by the Pratt and Whitney/United Technologies Research Center joint research program. The authors wish to thank the services of Joe Poplawski who was invaluable in the data collection.

8. REFERENCES

- Arnold, A., F. Dinkelacker, T. Heitzmann, P. Monkhouse, M. Schafer, V. Sick, and J. Wolfrum (1992), "DI Diesel Engine Combustion Visualized by Combined Laser Techniques," *Twenty-fourth Symposium (International) on Combustion*, pp. 1605-1609, The Combustion Institute.
- Carter, G. (1985) "Coherence and Time-Delay Estimation," IEEE Press.
- Castleman, R. A. (1931) "The Mechanism of the Atomisation of Liquids," *J. Res. Natl. Bur. Stand.*, Vol 6, No. 281, pp. 369-376.
- Cohen, J. and R. Hibshman (1996) "An Experimental Study of Combustor Air Swirler Acoustic and Fluid Dynamic Sensitivities," Presented at the *Propulsion Engineering Research Center 9th Annual Symposium on Propulsion*, October 1-2, 1997, Cleveland, OH.
- Eckbreth, A. (1988) "Laser Diagnostics for Combustion Temperature and Species," Abacus Press, Kent, United Kingdom.

Hopfinger, E. and J. Lasheras (1994) "Breakup of a Water Jet in High Velocity Co-flowing Air," *6th International Symposium on Liquid Atomization, Spray Systems*, pp. 110-117, Rouen, France, ICLASS.

Snyder, R., Herding, G., Rolon, C. and S. Candel (1996) "Analysis of Flame Patterns in Cryogenic Propellant Combustion," submitted and accepted to *Combustion, Science and Technology*.

PAPER No. 9
Anderson, Kendrick & Cohen
(presenter: T. Rosfjord)

Question 1: D. Santavicca, Penn. State University, U.S.

What was the magnitude of the pressure fluctuation that was produced in the fuel injector, and how did it compare to typical pressure fluctuations experienced in an engine combustor during unstable combustion?

Answer

The acoustic driver used varied the airblast injector airflow at the prescribed frequency using a high response rate valve. Consequently, high pressure perturbations, and not just pure acoustic waves, could be produced. The magnitude of the fluctuations was of the order of 1.0 psi.

Question 2: S. Hoffmann, Siemens A.G., Germany

Are the results obtained transferable to higher pressures and, what is the sensitivity to air mass flow rate?

Answer

This was a screening test for fuel injectors. Our experience was that fuel injectors indicated by this test as being susceptible to combustion pressure oscillations were found to be so in actual combustor tests at pressure, and those indicated as not being susceptible were found to be less sensitive in the combustion tests.

Question 3: G.J. Sturgess, ISSI, U.S.

Were the details of the sprays for Injectors A and D at 4 inches downstream, examined by means of high-speed photography, flow visualization and/or PDPA to ascertain the differences in spray characteristics between the two, and hence, the reasons for the susceptibility to combustion pressure waves?

Answer

We did perform some limited studies of this kind, but we are not presently able to share these results publically.

Question 4: N. Brehm, BMW-RR, Germany

What is more important for causing susceptibility to combustion pressure waves, is it perturbation of the fuel mass flow rate or is it the spray characteristics such as droplet size, spray cone angle, etc.?

Answer

The spray characteristics are a consequence of the spray formation response to pressure waves. It appears that pressure fluctuations cause fuel injector airflow fluctuations that then affect the spray formation. Spray mass flow fluctuations then follow as a consequence.

Soot and Radiation Modelling in Gas Turbine Combustion Chambers

H. T. Brocklehurst*, J. B. Moss**, C. D. Hurley***, C. H. Priddin*

* Rolls-Royce plc PO Box 31, Derby, DE24 8BJ UK

** Professor, School of Mechanical Engineering, Cranfield University, Cranfield, Beds, MK43 0AL, UK

*** Defence Evaluation and Research Agency, Farnborough, Hants, GU14 0LS, UK

1. SUMMARY

The processes of soot formation and burn-out in liquid-fuelled combustors at practically relevant operating conditions remain poorly understood despite their importance in relation to emissions and, through their influence on radiation, to liner durability and life. The development of simplified theoretical models, necessitated by the underlying physical and chemical complexity, incorporates substantial empiricism and is particularly sensitive to scaling and the calibration of model parameters. This is particularly evident in the application of these models to realistic geometries. Previous post processed soot calculations in gas turbine combustion chambers neglecting the effects of radiation have found that predicted soot levels are an order of magnitude too high in comparison to measurements at 6 bar. The situation is worse for full power conditions, where the increased pressure (over 40 bar) can lead to such large amounts of soot being produced, that more carbon is converted to soot than is available in the fuel. In addition, the soot models are not able to capture the measured level of oxidation between the primary zone and the combustor exit. This paper describes further developments in the modelling of the sooting processes, where the rate of oxidation is captured more accurately and the effects of radiation are treated more completely. The soot is modelled using a flamelet-based approach employing computations of a kerosene laminar counter-flow flame which incorporates detailed reaction kinetics, and radiation heat loss calculated using the Discrete Transfer Radiation Model. The effects of radiation on both the soot chemistry and the flow pattern (via density changes) are modelled by using a family of flamelets, each with a different amount of heat loss. The most appropriate flamelet is selected on the basis of the local computed enthalpy, including heat loss due to radiation. Comparisons are presented between model prediction and sampled measurements from a gas turbine combustor at 6 bar. Uncertainties remain in relation to the effective soot aerosol surface area and hence the rate of soot burn-out. Encouraging progress is reported on the coupling between soot production and radiation heat transfer for purposes of wall heat flux production

2. INTRODUCTION

In developing gas turbine combustion systems for a new application, there are many performance criteria which need to be achieved simultaneously. Some of these are becoming amenable to theoretical treatments but two of the most intractable are achieving design metal temperature limits (for adequate service life) and smoke emissions. Both of these require extensive (and expensive) high power test programmes to verify the effectiveness of proposed modifications. A comprehensive theoretical treatment which would enable combustor metal temperatures to be determined before test is a valuable goal. The largest single component in the heat flux balance at the wall is the incident radiation from the flame: the biggest single contributor to this is the local soot concentration. This is because soot emits as a black body across all wavelengths, and the higher the soot concentration, the higher the emitted radiation. Soot and radiation are therefore intimately

connected. They are also connected through the temperature, as the soot formation rate is strongly temperature dependent, and the local temperature is reduced by the presence of radiation. A sufficiently accurate representation of these processes and their interaction is needed for reliable predictions to be achieved.

Previous predictions in gas turbine geometries (Brocklehurst et al. [1]) used a post processed representation of soot formation, in which the interaction between the soot and radiation is represented only crudely. This study found that although the exit soot levels can be captured reasonably well through the use of an optically thin representation of the radiative heat loss, the evolution of the soot throughout the combustor is not, which has implications for predicting emissions and the radiative heat flux to the combustor walls. It was found that an accurate representation of the surface area of the soot aerosol is necessary for the burn out of soot to be captured. This paper describes a method of accounting for and coupling the effects of these processes.

3. NUMERICAL METHOD

The predictions were carried out with the Rolls-Royce CFD code, PACE, which has been widely applied to the prediction of the fully turbulent flow in gas turbine combustion systems (Priddin and Coupland, [2], and Coupland et al., [3]). Only a brief summary of key features will be given; see references cited above for more detail.

PACE uses a two-dimensional orthogonal mesh rotated to form a three-dimensional grid, which allows a fair degree of flexibility in the geometries that can be studied. The standard $k-\epsilon$ turbulence model is used in conjunction with the SIMPLE pressure correction method. A variety of differencing schemes are available, but in these calculations the Hybrid Linear Parabolic Algorithm, HLP (Jones, [4]) was used.

At the high inlet temperature and pressure conditions typical of gas turbine operation, combustion chemical kinetics are very fast compared to the mixing time scales. In the limit of fast chemistry the molecular species may be instantaneously related to the mixture fraction, ξ . To model the effects of turbulent interaction on the mean values, an additional transport equation for the mixture fraction variance is solved and a beta function presumed for the probability density function. The relationships between the thermochemical variables of interest and the mixture fraction are derived from a laminar flamelet calculation (Leung [5]).

4. SOOT MODEL

A cloud of soot particles may be characterised by the total mass of soot, expressed in terms of soot mass fraction c_m and the number density of the particles N (particles/kg of mixture). Since soot formation is strongly dependent on residence time, the volumetric source terms for nucleation, surface growth, coagulation and oxidation are related to the mixture fraction and additional transport equations for soot mass fraction and number

density terms are solved. Within these the following source terms accounting for the formation and destruction of soot are included.

$$\bar{\rho} \frac{d}{dt} (\tilde{N}) = \bar{\rho} \tilde{R}_{NU} - \bar{\rho} \tilde{R}_{CO} \tilde{N}^{2/2}$$

$$\bar{\rho} \frac{d}{dt} (\tilde{c}_m) = \bar{\rho} \tilde{R}_{SG} \tilde{N} + \bar{\rho} C_8 \tilde{R}_{NU} - \bar{\rho} \tilde{R}_{OX} \tilde{c}_m$$

where \tilde{R}_{NU} is the Favre averaged nucleation rate (particles/kg/s), \tilde{R}_{CO} is the coagulation rate (kg/s/particle), \tilde{R}_{SG} is the surface growth rate (kg/s/particle) and \tilde{R}_{OX} is the Favre averaged oxidation rate. C_8 (kg/particle) is a constant representing the mass of a nucleating particle. Note that in deriving the time averaged form of the equations all cross-correlation terms have been ignored implying the processes are independent. Such a decision is unavoidable given the difficulties that would be involved in deriving suitable models for all the correlations required.

The processes of nucleation, surface growth, coagulation and oxidation can be described either by using empirical models based on laminar flamelet measurements (Moss et al. [6]) or through detailed calculations of a laminar flamelet including detailed reaction kinetics and soot formation (Leung et al. [7]). Here the expressions of Leung [5] have been used since they have been found to capture more plausibly the soot oxidation rate within the geometry concerned (Brocklehurst et al. [1]). The detailed chemical composition of the flamelet is calculated, including soot concentrations. The soot formation is related to the concentration of the soot precursors acetylene and benzene as well as the temperature. To represent the approximate composition of kerosene, including the aromatic content which is key to soot formation, a mixture of 80% undecane and 20% benzene is used. This is described in more detail in Brocklehurst et al. [1] and the papers cited above. The oxidation model of Nagle and Strickland-Constable [8], based on O_2 has also been adopted.

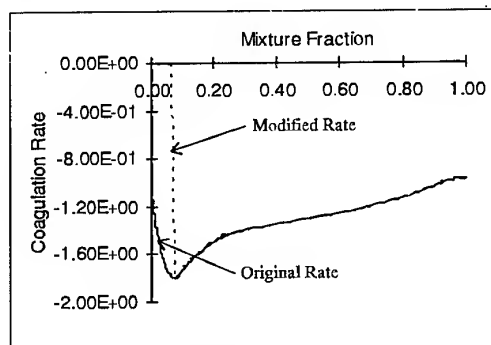


Figure 1 Modified Coagulation Rate

In the work of Leung et al. [7] the decrease in the number of soot particles due to coagulation is modelled using the square root dependence inferred from kinetic theory, given by

$$R_{CO} = -2C_a \left(\frac{6k_B T}{\rho C_8} \right)^{1/2}$$

where C_a is the agglomeration constant ($= 9$) and k_B the Boltzman constant ($1.38e-23$ J/K). This gave particles of the order of 30 nm. The work of Brocklehurst et al [1], however has

shown that although this did lead to increased oxidation compared to the model of Moss et al. [6], it still under predicted the overall oxidation rate. One feature which this model does not represent is the ageing of the soot particles and the influence that this has on the effective surface area. Old soot particles do not coalesce to produce single spherical particles as assumed in the coagulation model, rather they form loose agglomerates, leading to a very different surface area, close to that of the original particles. To mimic this effect the coagulation rate was curtailed at weak mixture fractions where there is no surface growth. In these regions, the soot is likely to be relatively old, since it would have been formed in regions richer than stoichiometric and transported to weaker mixtures. In addition, at weak mixture fractions there is no surface growth to overlay surface irregularities. The mixture fraction below which coagulation is prevented was selected from the point at which surface growth finishes. This limit is somewhat arbitrary, and it raises questions over the sensitivity of the model to the value selected. The resultant coagulation rate is shown in Figure 1.

5. RADIATION MODEL

Space does not permit us to detail here the relative merits of the various zone, discrete ordinates and other methods available for this purpose. The Discrete Transfer (DT) method of Lockwood and Shah [9] was selected principally because its accuracy can be improved as required by increasing the number of rays per point used and the ease with which it can be implemented. At each boundary node the hemisphere is split into a user specified number of areas through which it is assumed that the intensity is constant. A ray is fired from the centre of each of these regions and the intensity distribution along it is calculated by solving a discretised form of the radiative transfer equation. The incident heat flux is then calculated by summing the contributions from each of the rays, using a weighting set to account for the directional variation.

The transfer equation for thermal radiation of a grey gas along a ray including attenuation by absorption and emission from the cell, but assuming that the effect of scattering by sub-micron soot particles is negligible, is given by

$$\frac{dI}{ds} = -k_a I + \frac{k_a \sigma T_g^4}{\pi}$$

which can be integrated to give the variation in radiative intensity along a given ray in the following recurrence relationship;

$$I_{n+1} = \frac{\sigma T_g^4}{\pi} (1 - \exp(-k_a \Delta s)) + I_n \exp(-k_a \Delta s)$$

where

I_n = the ray intensity entering the volume

I_{n+1} = the ray intensity leaving the volume

Δs = the distance travelled along the ray

Given the variation in temperature and absorption coefficient in the medium and the initial intensity of a ray, the intensity at all intermediate points can be evaluated from this expression. In our implementation the ray is tracked until it strikes the opposite wall, then the recurrence relation given above is applied back down the ray starting with an assumed temperature at the far wall.

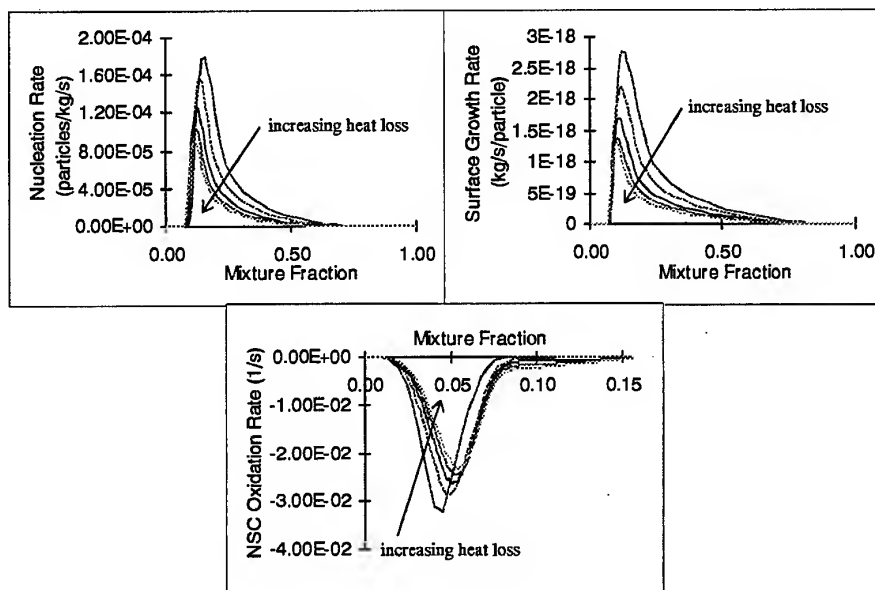


Figure 2 Family of Flamelets with Different Heat Loss

The absorption coefficient for the soot concentrations is calculated from the relationship of monochromatic absorption coefficient and soot volume fraction reported by Kent and Honnery [10]. The absorption coefficients of gaseous species are difficult to represent due to their spectral dependence, though in gas turbines where the radiation is due primarily to soot the radiation from the gas phase should be only a second order effect. Therefore, in these calculations the spectral behaviour of the gases is captured by using Leckner's [11] model which uses curve fits for the total absorptivity-emissivity of gas volumes for all wavelengths in homogeneous, isothermal media. This offers speed and accuracy within the limits of validity, summarised well by Modest [12].

In the coupled calculation, the DT contribution is summed over all rays to provide source term distributions cell by cell. These are then used in conjunction with a transport equation for the total mixture enthalpy, using the thermodynamic convention adopted by Gordon and McBride [13] that the enthalpy of formation of each species is chosen so that there is no net enthalpy change during reaction. The local enthalpy so calculated is used to obtain a suitable flamelet.

6. COUPLING SOOT, FLOW AND RADIATION

The coupling of the soot and radiation together with the flow field is a costly procedure, and as a result there are few examples in the literature. Kaplan et al. [14] have carried out a fully coupled calculation of a laminar, unsteady, ethylene jet flame. Sivathanu and Gore [15] report parabolic calculations of laminar, acetylene jet flames. However, in both these cases the laminar nature of the flow removed the need to model the interaction of chemistry and turbulence. In contrast, Bressloff et al. [16] carried out a fully coupled calculation of a turbulent, methane jet flame using the semi-empirical soot model approach of Moss et al. [6] together with the Eddy Dissipation Concept combustion model.

Radiation was modelled using the Discrete Transfer Radiation Model. To simulate the effect of turbulent fluctuations on chemistry they used a multiple flamelet approach in which families of soot source terms expressed as functions of mixture fraction are distinguished by the degree of radiative heat loss and averaged over the mixture fraction PDF. The most appropriate member of the flamelet family is then selected by comparing the integrated flamelet enthalpy values with the local enthalpy derived from the transport equation. The approach described by Bressloff et al. [16] has been adopted within this work, since it can be easily implemented within the laminar flamelet framework of the Rolls-Royce CFD code and it does offer a more accurate simulation of the interaction of soot, radiation and flow without prohibitive increase in computational costs.

The first step in implementing such an approach is to generate a family of flamelets with different amounts of heat loss. In this work the radiation is mainly from the soot. An 'optically thin' radiation calculation can be performed for each element in the flamelet using

$$q = C f_v T^5$$

where f_v is the soot volume fraction, C is a constant ($=2.77 \times 10^{-7}$) and T is the local gas temperature. This expression gives the maximum possible heat loss, since all the radiated heat is lost to the surroundings. To obtain the family of flamelets the soot volume fractions within the flamelet are altered, thus leading to a family of flamelets (Figure 2) with differing levels of heat loss.

At each point in the 3-D CFD calculation, where \tilde{h}_{trans} , the local enthalpy given by the transport equation, the mixture fraction statistics ξ , ξ'' and hence $P(\xi)$ are known, we can evaluate for each flamelet in the family

$$\tilde{h}_j = \int_0^1 P(\xi) h_j(\xi) d\xi$$

By linear interpolation the value r may be found which gives

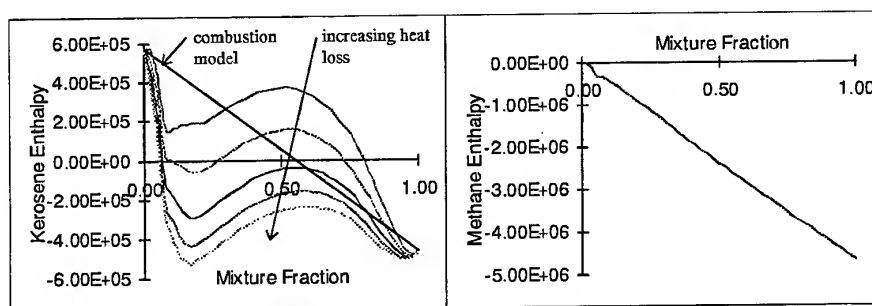


Figure 3 Mixture Fraction-Enthalpy Relationships (J/kg)

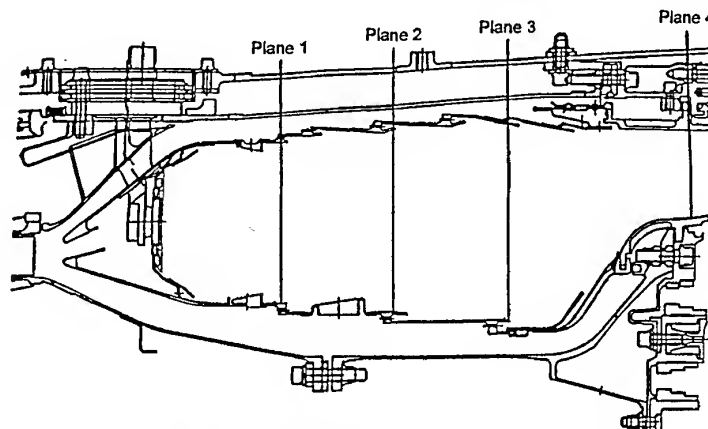


Figure 4 Combustor Geometry and Measurement Planes

$$\tilde{h}_{\text{trans}} = r\tilde{h}_{j-1} + (1-r)\tilde{h}_j$$

where j is chosen so that $\tilde{h}_j < \tilde{h}_{\text{trans}} < \tilde{h}_{j+1}$. This interpolated flamelet then matches the local mean enthalpy. All other required properties of the flamelet may then be computed from $\tilde{\phi} = r\tilde{\phi}_{j-1} + (1-r)\tilde{\phi}_j$ (including the new soot formation rates).

This procedure would be complete if the flamelet enthalpy were a simple function of fuel fraction, as might be expected from experience with simpler paraffins. However, as Figure 3 shows, in a kerosene flamelet the enthalpy profile is far from linear because of differential diffusion effects especially related to the presence of large molecules on the fuel rich side. For comparison purposes, Figure 3 also shows the equivalent plot for a simpler fuel (methane) in which an enthalpy profile close to linear is seen. In the CFD calculation turbulent mixing dominates and it is assumed that all species diffuse equally, so a linear mean enthalpy/fuel fraction relationship is implied. In the case of zero variance therefore, the situation would arise that the required enthalpy at a given fuel fraction without heat loss could not be achieved by any of the flamelets in the family. The previously described procedure has therefore been applied using the departure from adiabatic enthalpy in both cases, rather than the enthalpy itself. This procedure works well and is robust. An initial concern that in regions where significant absorption occurs, a flamelet with (effectively) negative heat loss might be required, it has not been found necessary since the situation has not arisen in any practical computation to date.

7. RESULTS FOR A GAS TURBINE COMBUSTOR

The phase 2 combustor used in the RB211-524 and -535 engines for B747 and 757 aircraft among others, has been extensively studied at DERA Pyestock. A four-fuel injector sector was built into a rig and tested at temperatures of 850K, representing take-off conditions but at a reduced pressure of 6 bar due to rig limitations. Engine take-off values of $M\sqrt{T}/P$ and AFR were maintained, and traverse sampling was completed on four planes inside the combustor, around the centre two sectors. All major species were measured, including the soot concentration (see Hurley [17]). Figure 5 shows the soot concentration on each of the four measured planes. It is apparent from the data that there are large quantities of soot in the combustor primary zone, but the vast majority is consumed by combustor exit to give an invisible exhaust. A factor of 10,000 is seen between the peak levels on planes 1 and 4. By way of an upper bound computation, Figure 6 shows the predicted soot concentrations from a post processed, adiabatic solution, including the original coagulation model.

The predictions used flow boundary conditions set to give the best overall flow field agreement, using annulus pressure data to derive flow splits. A value of 0.4 for the turbulent Prandtl (TPR) number gave best agreement with the combustor exit temperature distribution traverse, compensating for shortcomings in the description of the turbulent mixing but primary zone peak levels of fuel fraction were still too high compared with measurement. These could be reduced by further reducing the TPR to 0.2, but

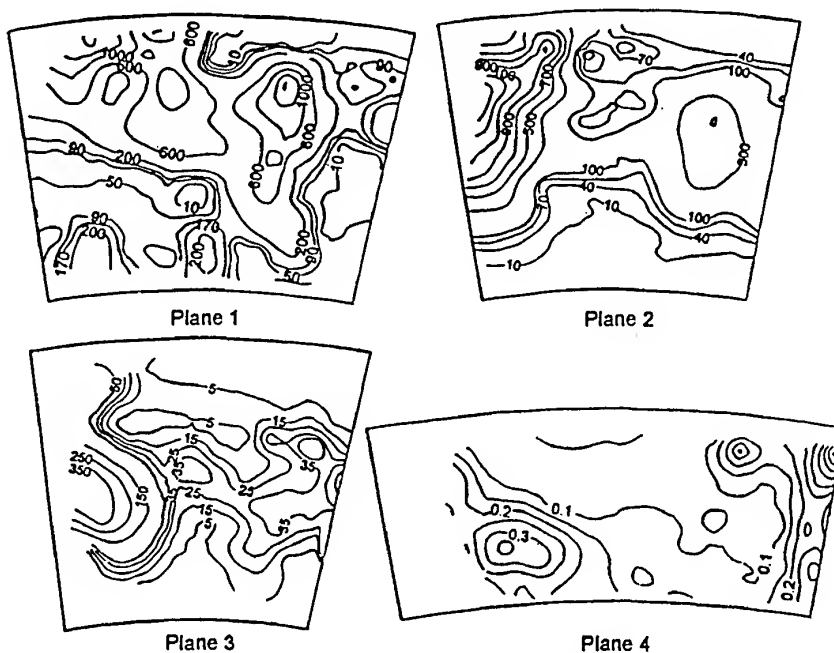


Figure 5 Measured Soot Concentration (mg/m^3)

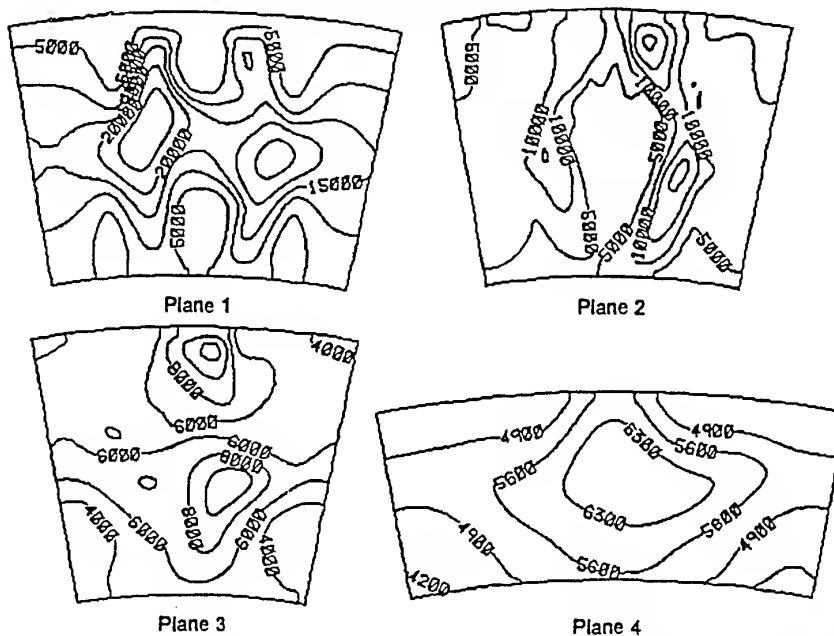


Figure 6 Predicted Soot Concentrations (mg/m^3) for the Adiabatic Solution with the Original Coagulation Model

the exit distribution was then too uniform. All subsequent calculations have been performed with $\text{TPR} = 0.4$.

The results of a calculation with an optically thin representation of the radiative heat loss and the modified coagulation model are shown in Figure 7. Here the concentration reduction, due largely to oxidation, between planes one and four is 4 orders of magnitude, close to that measured. It does suggest that the

alteration to the coagulation rate does improve the representation of the soot surface area, and should be employed in future calculations. In spite of the overall improvement in the predictions, the intermediate planes are not so well represented, as the soot destruction is spread throughout the combustor rather than concentrated between the last two planes as shown by the measurements. Hence, it is possible that this particular combination of models may not work as well in a different

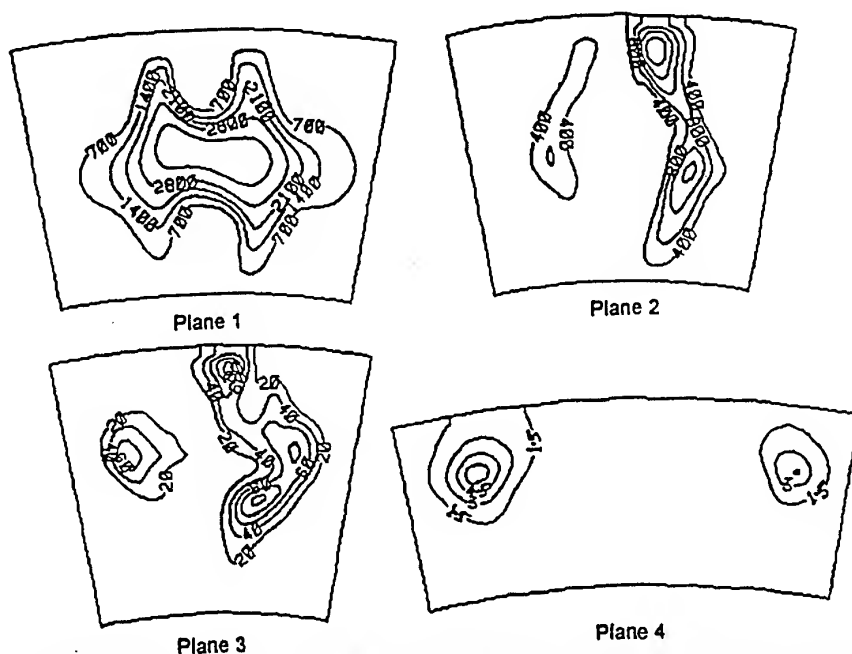


Figure 7 Predicted Soot Concentration (mg/m^3) with the Optically Thin Calculation and Modified Coagulation Rate

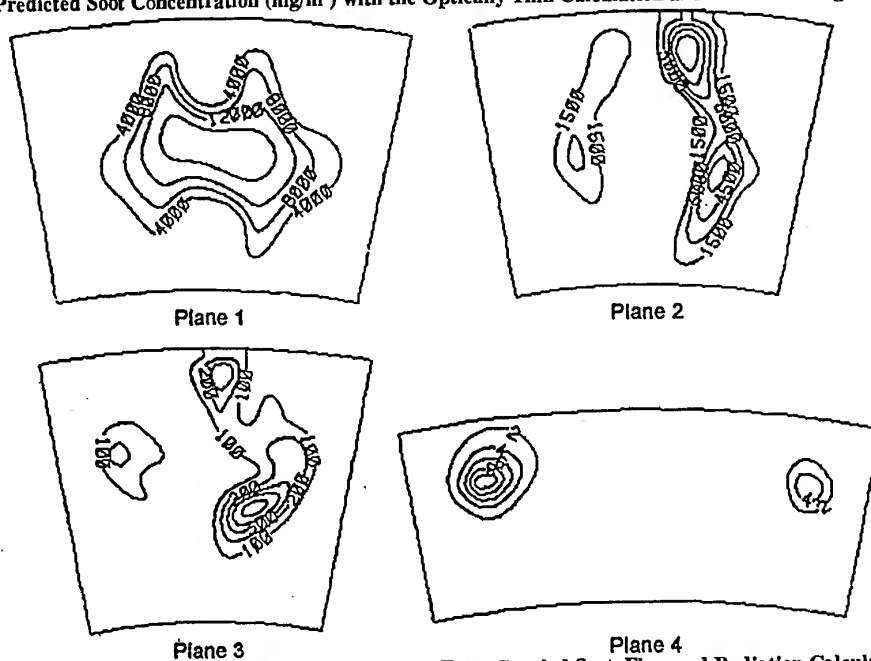


Figure 8 Predicted Soot Concentrations (mg/m^3) for Fully Coupled Soot, Flow and Radiation Calculation

combustor geometry or at different operating conditions. The global representation of radiation in the model may account for the discrepancies and this suggests that a more accurate approach is required if the soot distribution in the combustor is to be captured correctly.

When the fully coupled method described in section 6 which does offer a more complete representation of the processes

involved was used, the peak soot is significantly higher (Figure 8) than both the measurements and the optically thin calculation (Figure 7) even though it was reduced to ~80% of the adiabatic results. The discrepancy with the simple radiation model is perhaps not too surprising, given that the discrete transfer model allows for reabsorption by the soot which is neglected by the optically thin approximation. In downstream planes the soot concentration is increased slightly as the heat loss from the flame

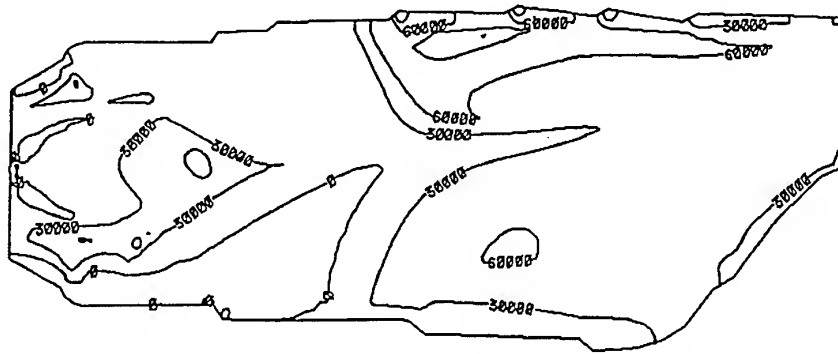


Figure 9 Enthalpy Drop Predicted with the Fully Coupled Model

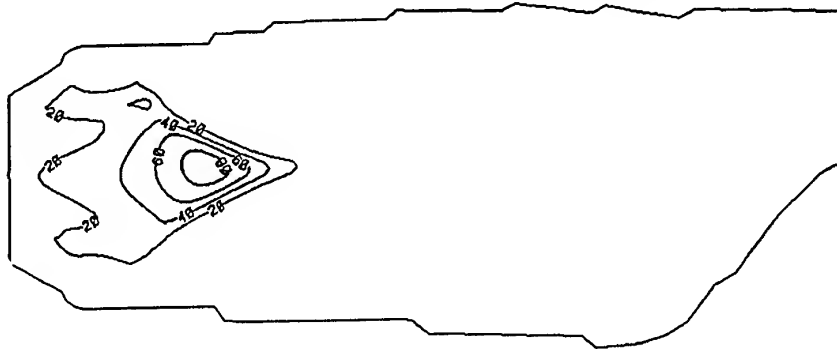


Figure 10 Predicted Soot Volume Fraction ($\times 10^7$) for the Fully Coupled Model

reduces the amount of oxidation. In contrast, the fully coupled simulations of Kaplan et al. [14], Sivathanu and Gore [15] and Bressloff et al. [16] have shown a dramatic reduction in the soot concentrations. This may be a function of the geometries concerned, with the mainly parabolic jet flames offering less opportunity for soot producing regions to be shielded by high soot concentrations hence resulting in a higher heat loss.

Figure 9 shows the departure from adiabatic enthalpy on the centreline of the combustor; a positive value corresponds to a reduction in enthalpy. The largest drop in enthalpy is around 7×10^4 J/kg, which is an order of magnitude lower than the inlet value of air and fuel (absolute values $\sim 4 \times 10^5$ J/kg). There is heat loss from the primary zone where the soot volume fraction is high (Figure 10) and the size and shape of the outer edge corresponds closely to that of the soot, although there is a 'tail' that stretches downstream into the region of maximum temperature (Figure 11). The maximum heat loss in the primary zone occurs where the temperature lies in the range 1500K to 1800K, which is relatively cool (see Figure 11). There is little heat loss in the early part of the primary zone where soot formation begins, in spite of finite soot concentrations. Here, the low temperature (< 1500 K) is likely to reduce radiation, though the region may also be shielded by the high soot concentrations that surround it. The initial stages of soot formation are thus little affected by radiation and will behave in a similar manner to the adiabatic solution. The heat loss downstream of the primary

jets is comparable to and in some areas exceeds the peak in the primary zone in spite of negligible soot concentrations. Here, emission is due only to the gaseous species, and is enhanced by temperatures which are higher than those in the region of peak heat loss in the primary zone (> 1800 K compared to 1500-1800K). These results suggest that there is some reabsorption by the soot in the primary zone leading to reduced heat loss and this accounts for the differences with the optically thin model.

That there is some reabsorption by the soot in the primary zone can be seen by comparing the adiabatic, optically thin and fully coupled temperature plots (Figure 11). There is no discernible difference in the adiabatic and fully coupled solutions in the primary zone, but the optically thin model shows a temperature drop of nearly 200K in the peak temperature, which is directly linked to the corresponding drop in soot concentration. Downstream of the jets there is noticeable heat loss in the fully coupled solution, but the optically thin solution shows an even bigger drop compared to adiabatic. These results suggest that the optically thin approach is inappropriate for this geometry. Conversely, the measured soot concentrations are at least an order of magnitude smaller than the optically thick limit found by Young [18] for a flame at similar operating conditions and of a similar size and this precludes the use of an optically thick approximation. The move towards a fully coupled prediction methodology is thus vindicated and the poor soot predictions must be due to neglecting some physical feature in the

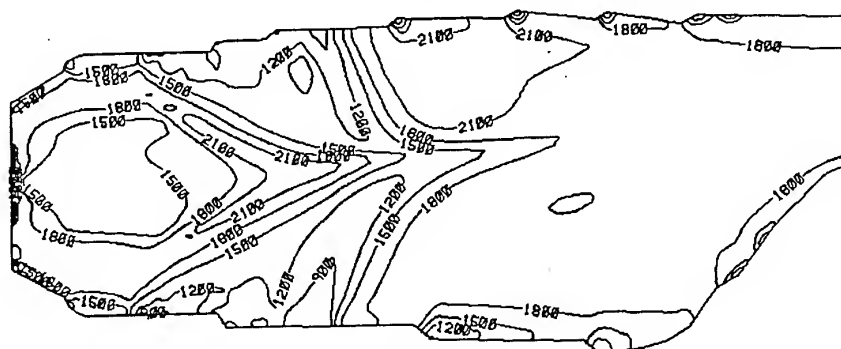
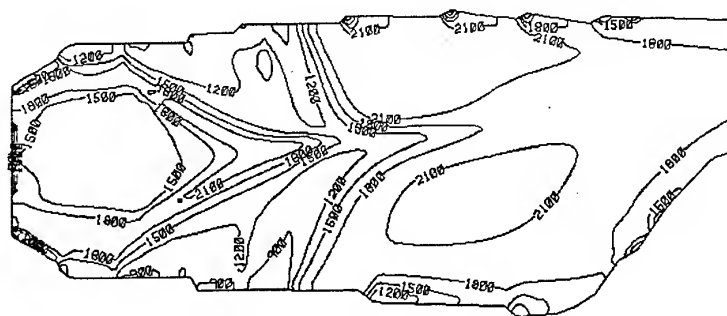
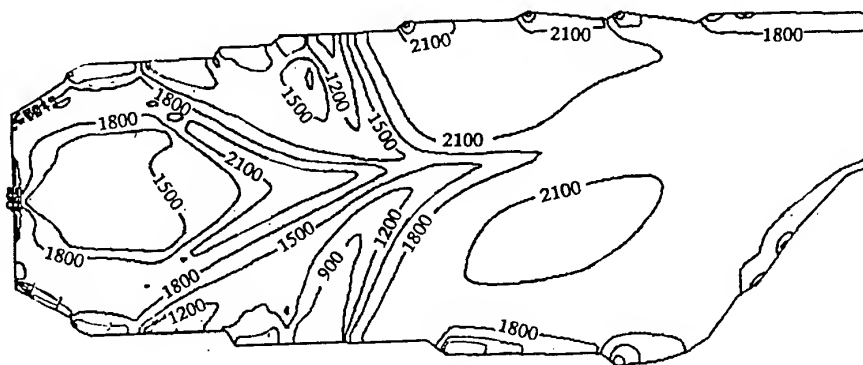


Figure 11 Comparison of Local Gas Temperature for Adiabatic, Optically Thin and Fully Coupled Solutions

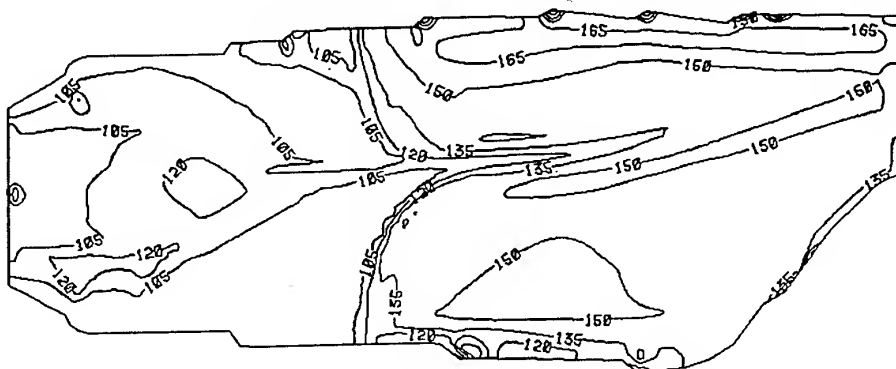


Figure 12 Flamelet Selected by the Fully Coupled Model ($\times 100$)

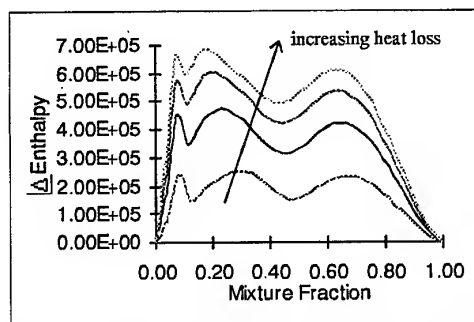


Figure 13 Δ Enthalpy-Mixture Fraction Relationships from the Laminar Flamelet Calculation for Kerosene

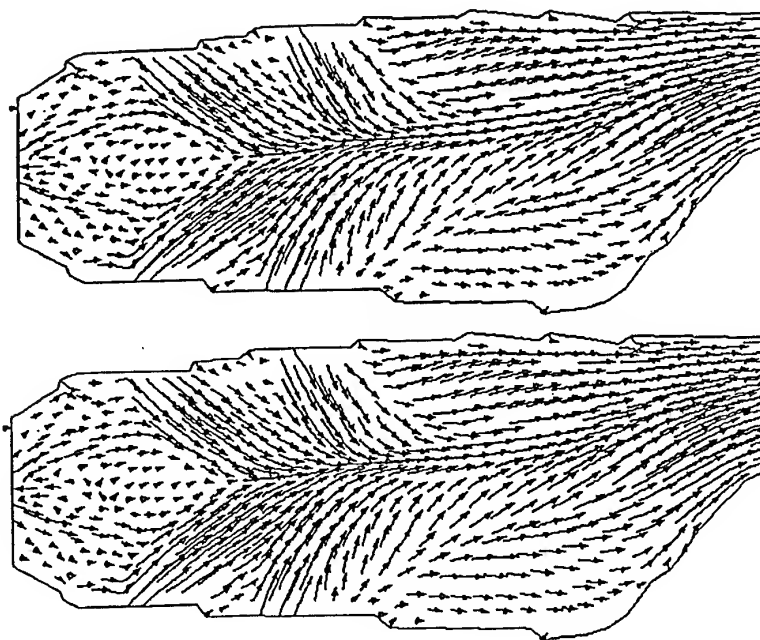


Figure 14 Streakline Plot for Adiabatic and Fully Coupled Solutions

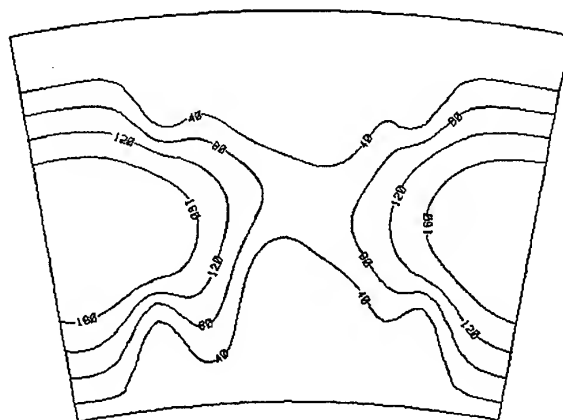


Figure 15 Soot Concentrations Predicted with Reduced Turbulent Prandtl Number (Plane 1 Only)

predictions. We must also consider the possibility that the methodology does not fully represent the physical process.

One area which may be introducing spurious effects is the selection of the most appropriate flamelet. Figure 12 shows the flamelet selected at each location in the field; a value of 1 corresponds to the adiabatic flamelet and a value of 5 to the maximum heat loss flamelet. In the primary zone the flamelets are very close to adiabatic at 1.2, whereas downstream of this the values range between 1.4 and 1.5 in spite of a similar heat loss. Referring to Figure 13, which shows the difference in enthalpy between each of the flamelets, the reason for this becomes clear. At rich mixture fractions, there is a much larger gap between the curves compared to weak mixture fractions, which will lead to the preferential selection of low heat loss flamelets.

The effect of radiative heat loss on the flow is negligible (see Figure 14), which is also in agreement with the predictions of Gore et al [19]. This would suggest that it is not necessary to model the interaction of the flow with the soot and the radiation, which would reduce the cost of soot calculations. This result should be treated with caution until the issues discussed above are resolved.

If the soot-radiation coupling methodology is not causing the current soot over prediction there must be some other effect which is not being represented. One concern is that the peak fuel fraction predicted is somewhat higher than measured (0.3 vs. 0.13,) and this may be responsible for the over prediction. To test this out, a calculation was performed with the TPR set to 0.2, a value which did reproduce the measured peak but at the expense of too uniform a pattern at the exit. The soot levels resulting are shown on Figure 15. The peaks have indeed reduced; unfortunately they are now a factor of 10 too low. This demonstrates just how sensitive the soot formation processes are

to local stoichiometry, and the importance of good modelling of the fuel/air mixing process.

8. WALL RADIATION FLUX RESULTS

The calculations performed above also yield values for the net wall heat flux. One issue which is of considerable importance in determining the computational cost of this method is the number of rays required to achieve sufficient accuracy. Figure 16 and Figure 17 show the effect of increasing ray density from 10 to 60 rays per points on both the internal enthalpy source terms and the incident wall heat flux. It transpires that less rays are needed to compute the internal source distribution than to achieve good wall heat flux - probably due to the number of rays that cross each cell and the smoothing effect of the CFD solution.

Are the wall flux values correct? We have no direct data to confirm this, but measurements in another rig, with different geometry, do at least show that the fluxes are of the right order. It is planned to take the flux information and perform FE calculations of the cooling devices to derive metal temperatures which can be compared with measured thermal point data but this has not yet been achieved.

9. CONCLUSIONS

A method has been devised and demonstrated to allow full coupling of flow field soot and radiation. However, the sensitivity of the soot chemistry to fuel/air ratio means that accurate modelling of the basic flow field and mixture strength will be required, such as may only be possible by Large Eddy Simulation methods.

It has been shown that radiation effects on the flow field are not large, and that a coarse representation of the radiant flux is appropriate for coupling purposes, however, more detail is required to accurately predict wall heat fluxes.

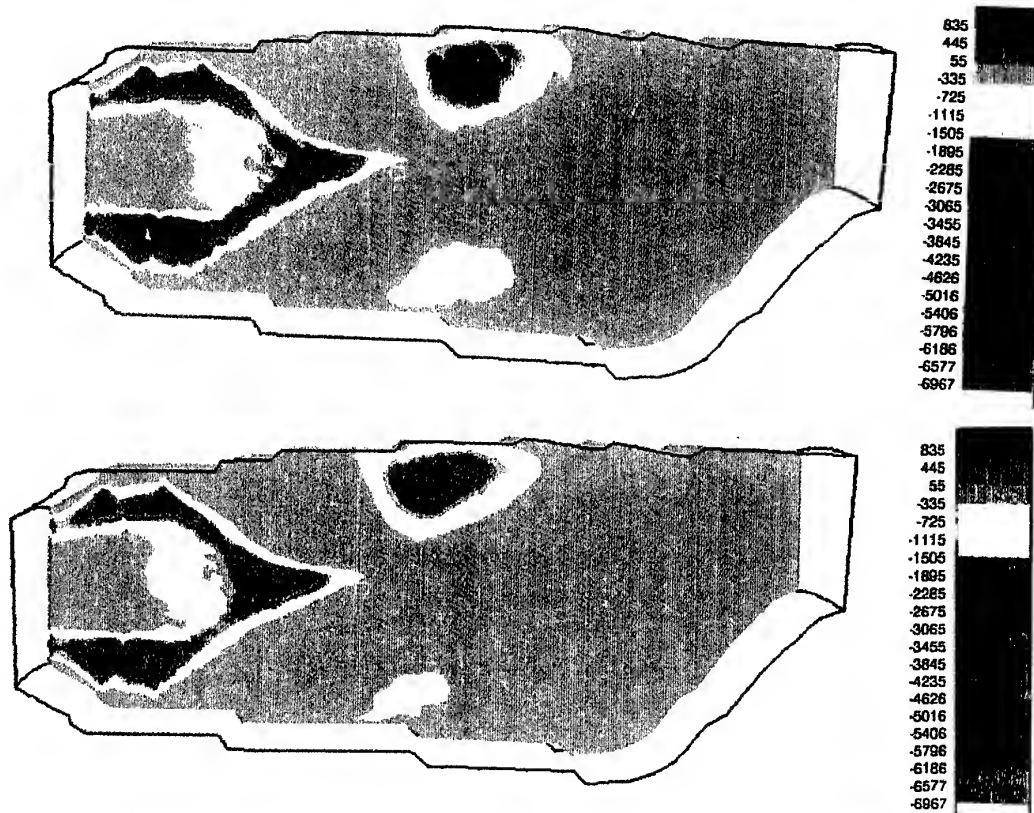


Figure 16 Effect of Increasing the Number of Rays Traced on Enthalpy Source Terms

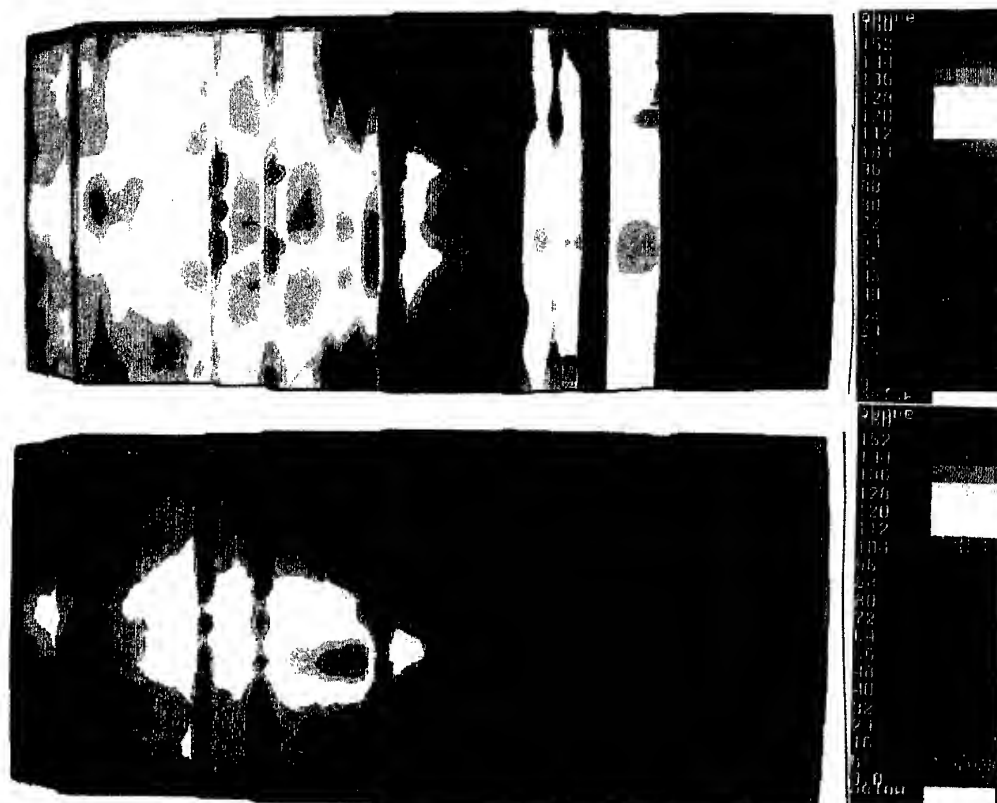


Figure 17 Effect of Increasing the Number of Rays Traced on the Incident Wall Heat Flux

The coupling of soot, radiation and the flow has reduced the over prediction of the soot concentrations, but there is still a significant difference compared to both the measurements and the predictions with the optically thin radiation model. The reasons for this have not been established, though a number of possibilities have been identified.

One possible reason for the limited effect of coupling soot and radiation could be the flamelet enthalpy profiles for kerosene, which are very different to the linear relationship assumed in the combustion model. This may be biasing the selection of the flamelet towards those with less overall heat loss, and hence may affect the soot concentrations predicted. Further work to investigate this is required.

10. REFERENCES

1. H. T. Brocklehurst, C. H. Priddin J. B. Moss 'Soot Predictions Within an Aero Gas Turbine Combustion Chamber', ASME-97-0148
2. Priddin, C. H. and Coupland, J. , 1988, Combustion, Science and Technology, Vol. 58, pp. 119
3. Coupland, J. , Fry, P. , and King, R. A. , 1991, Tenth International Symposium on Air Breathing Engines, Nottingham, U. K. , 2 - 6 September 1991.
4. Jones, W. P. , (1995), in *Turbulent Reacting Flows*, Academic Press, Libby and Williams
5. K. M. Leung, Kinetic Modelling of Hydrocarbon Flames Using Detailed and Systematically Reduced Chemistry PhD Thesis October (1996) Imperial College of Science, Technology and Medicine, Department of Mechanical Engineering
6. Moss, J. B., Stewart, C. D. & Syed, K. J. (1988) 22nd Symposium (International) on Combustion, The Combustion Institute, pp 413-423
7. Leung, K.M, Lindstedt, R.P. and Jones W. P., (1991), Comb & Flame 87:289-305 (1991)
8. J. Nagle and R. F. Strickland-Constable Proceedings of 5th Carbon Conference, Vol. 1, pp 154-164 (1962)
9. F. C. Lockwood and N. G. Shah, Eighteenth Symposium (International) on Combustion pp 1403-1413 (1981)
10. J. H. Kent and D. R. Honnery, Combustion and Flame 79: 287-298 (1990)
11. B. Leckner, Combustion and Flame 19: 33-48 (1972)
12. M. F. Modest Radiative Heat Transfer, McGraw-Hill Inc., USA, 1993
13. Gordon and McBride (1971), NASA-SP-273 (1971)
14. C. R. Kaplan, S. W. Baek, E. S. Oran and J. L. Ellzey Combustion and Flame 96: 1-21(1994)
15. Sivathanu, Y.R & Gore J.P (1994), Combustion and Flame 97:161-172 (1994)
16. N. W. Bressloff, J. B. Moss and P. A. Rubini Twenty-Sixth Symposium (International) on Combustion, 1996, pp 2379-2386
17. C. D. Hurley 'Smoke Measurements Inside a Gas Turbine Combustor', June 1993, 29th Joint Propulsion Conference
18. K. J. Young (1993) 'Soot Formation in Turbulent Vaporised Kerosine-Air Jet Flames at Elevated Pressures', PhD. Thesis, Cranfield Institute of Technology
19. Gore, J. P. and Faeth, G. M. (1986) 21st Symposium (International) on Combustion, pp 1521

PAPER No. 10
Brocklehurst, Moss, Hurley and Pridden
(presenter: C. Pridden)

Question 1: B. Zamuner, ONERA, France

Did you take into account fluctuations of temperature and composition in your radiation model? If yes, do you think that such fluctuations have a strong impact on the energy equation source term?

Answer

Yes, those fluctuations are described by the presumed beta-function pdf, so all the terms are integrated over the fluctuations. For example, the radiation sources are evaluated using \bar{T}^4 and not $(\bar{T})^4$ - there is a significant difference! (See H. Brocklehurst's Eng. D., thesis).

Question 2: N. Selcuk, Middle East Technical University, Turkey

This is a comment rather than a question. In a recent publication (*Intl. J. Heat & Mass Transfer*, 1997), we have shown that the Discrete Ordinate Method is more accurate and computationally more efficient, than the Discrete Transfer Method. As far as the accuracy of the Discrete Transfer Method in predicted source terms is concerned, an improved discrete transfer method appears in the Proc. ASME, 11th. Intl. Heat Transfer Conference, South Korea, 1998.

Answer

Thank you for your comments. We presently do not observe any problems with the source terms; perhaps this is because our flames are optically thick. We are working on Discrete Ordinate Methods with our Allison colleagues.

Question 3: G. Cinque, Alfa Romeo Avio S.A.P.A., Italy

Did you try to calculate wall temperatures with your method?

Answer

We have not attempted this yet; it will be the next step. Our present strategy is to use this method to compute incident wall heat flux only, then to transfer this data to a finite element model where more details of the cooling device geometry can be simulated.

A NOVEL CODE FOR THE PREDICTION OF TRANSIENT FLOW FIELD IN A GAS TURBINE COMBUSTOR SIMULATOR

Nevin Selçuk* and Olcay Oymak**

*Chemical Engineering Department,

Middle East Technical University, 06531 Ankara, Turkey,

Tel: + 90 (312) 210 2603, Fax: +90 (312) 210 1264

E-mail: selcuk@rorqual.cc.metu.edu.tr

**Babcock & Wilcox Gama Boiler Technology Inc.

Atatürk Bulvarı, 06650 Ankara, Turkey.

SUMMARY

In the present paper, numerical simulation of time-dependent two dimensional Navier-Stokes equations for incompressible separated internal flow was carried out by using the method-of-lines approach in conjunction with i) an intelligent higher-order spatial discretization scheme, ii) a parabolic algorithm for the computation of pressure, and iii) an elliptic grid generator using body-fitted curvilinear coordinate system for application to complex geometries. The proposed code was applied to predict the time development of turbulent, cold flow in a gas turbine combustor simulator. Predictions were found to be in reasonable agreement with measured data. The code provides an algorithm for future direct numerical simulation applications.

LIST OF SYMBOLS

D	Diameter, cm
f	Any function
J	Jacobian
\dot{m}	Mass flow, g s ⁻¹
M	Number of grid points in r direction
N	Number of grid points in z direction
p	Static pressure, g cm ⁻¹ s ⁻²
\hat{p}	z-dependent component of static pressure, g cm ⁻¹ s ⁻²
R	Radius, cm
r	Radial distance, cm
Re	Reynolds number
t	time, s
u	Instantaneous axial velocity, cm s ⁻¹
\bar{u}	Time-averaged axial velocity, cm s ⁻¹
U'	Coefficient defined by Equation (15), cm s ⁻¹
v	Instantaneous radial velocity, cm s ⁻¹
v'	Coefficient defined by Equation (17), cm s ⁻¹
V'	Coefficient defined by Equation (16), cm s ⁻¹
z	Axial distance, cm

Greek Letters

Δ	Macroscopic differential operator
η	axial distance in general curvilinear coordinate system
μ	dynamic viscosity, g cm ⁻¹ s ⁻¹
ν	Kinematic viscosity, cm ² s ⁻¹
ξ	radial distance in general curvilinear coordinate system

ρ Density, g cm⁻³

Superscripts

n	Index for time-level
+	Forward

Subscripts

cj	Center jet
i,j	Index for spatial coordinate of interest
in	Inlet
r	r-direction; first derivative in r-direction
rr	Second derivative in r-direction
o	Cross-section
sj	Side jet
z	z-direction; first derivative in z-direction
zz	Second derivative in z-direction
η	First-derivative in η -direction
$\eta\eta$	Second-derivative in η -direction
ξ	First-derivative in ξ -direction
$\xi\xi$	Second-derivative in ξ -direction

1. INTRODUCTION

Transient, turbulent, confined and separated flows are of great interest from the perspective of combustion engineering in aeronautical and industrial applications such as the design of new industrial burners for efficient combustion and minimum pollution, which are strongly affected by the transport of momentum in the separated, reattached and recirculating flows downstream of the expansions.

Existing studies on numerical solution techniques for turbulent flow can broadly be classified into three categories. The simplest and most practical approach in use at present is the solution of the time-averaged Navier-Stokes equations along with a turbulence model. The second level of sophistication includes the simulation of time-dependent, large-scale eddy motion, namely, large-eddy simulation (LES). In this approach, the effects of smaller scales are included by turbulence models. The third category includes the direct numerical simulation (DNS) of all important scales of turbulence. The second and third categories are presently in the infancy stage. One of the difficulties associated with these methods is the limitation of present day computers. However, with the advancements in computer technology, large-eddy and direct turbulent simulations seem possible within the next decade.

* The author to whom the correspondence should be addressed.

Due to the fact that a lot of grid points as well as time steps are needed for the direct simulation of turbulent flows, the computational effort is enormous. Use of efficient numerical methods can decrease the computation time considerably. This can only be achieved in two-ways; first way is to increase the order of the spatial discretization method, resulting in high accuracy with less grid points, and second way is to use not only a highly accurate but also a stable numerical algorithm for the time integration. The method-of-lines (MOL) that meets the latter requirement is an alternative approach for time dependent problems which does not involve the discretization of all variables. The proposed technique, the MOL, consists of converting the system of partial differential equations (PDEs) into an ODE initial value problem by discretizing the spatial derivatives together with the boundary conditions via Taylor series, or weighted residual techniques and integrating the resulting ODEs using a sophisticated ODE solver which takes the burden of time discretization and chooses the time steps in such a way that maintains the accuracy and stability of the evolving solution. The most important advantage of the MOL approach is that it has not only the simplicity of the explicit methods but also the superiority (stability advantage) of the implicit ones unless a poor numerical method for the solution of ODEs is employed. The advantages of the MOL approach are two-fold. First, it is possible to achieve higher-order approximations in the discretization of spatial derivatives without significant increases in computational complexity, and without additional difficulties with boundary conditions. Second, the use of highly efficient and reliable initial value ODE solvers means that comparable orders of accuracy can also be achieved in the time integration without using extremely small time steps.

Therefore, it was considered useful to develop a novel code based on the MOL in conjunction with i) a parabolic algorithm which removes the necessity of iterative solution on pressure and solution of a Poisson type equation for the pressure and ii) an intelligent higher-order multi-dimensional upwind scheme which chooses biased-upwind and biased-downwind discretization in a zone of dependence manner for the simulation of time-dependent incompressible separated internal flows in complex geometries using general curvilinear coordinate system.

This paper describes a novel code for the numerical simulation of transient, two-dimensional (2D), turbulent, incompressible flow of cold air in a gas turbine combustor simulator and its validation against measurements carried out in the Combustion Laboratory of National Research Council (NRC) in Ottawa, Canada within the framework of AGARD Project T51/PEP. Assessment of the code for the prediction of laminar flow field in a pipe with sudden expansion can be found elsewhere [1, 2].

2. GAS TURBINE COMBUSTOR SIMULATOR

The code was applied to and validated on a gas turbine combustor simulator (GTCS) which facilitates the verification of predictions by measurements. The GTCS is a cylindrical test combustor rig 43.2 cm in length (excluding exit cone length of 14.63 cm) and 10.16 cm in diameter. The chamber exit cone provided a 75 % blockage. The combustion chamber, shown schematically in Figure 1, was one of three main sections of the rig (air/fuel inlet, flow conditioning section and combustion chamber). Air was injected into the lowest section through four opposing inlets. The resulting turbulent air flow from the air

injection was reduced by a mixture of fine stainless steel mesh (200 grid), and an aluminum honey comb (10 cm in depth with 0.3 cm diameter channels) inserted in the settling chamber. The smoothed flow was pushed through a 4:1 contraction before flowing into the chamber. At the entrance to the chamber a bluff body of diameter 6.35 cm was set in an opening of 7.6 cm. The primary air stream was injected through a 0.845 cm diameter inlet in the center of the bluff body and the secondary air stream flowed through the annular gap formed by the outer edge of the bluff body and the chamber floor. The details of the test rig can be found in elsewhere [3].

Experiments were performed for center jet/annular flow velocity ratio of 1.63, and velocity measurements were carried out by using laser Doppler anemometer (LDA) in a test section of the rig between 6 and 32 cm.

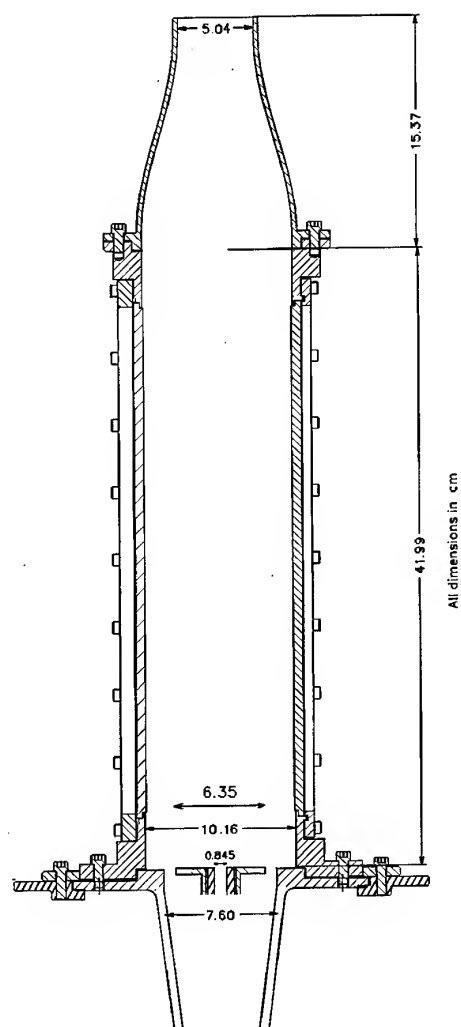


Figure 1. Schematic diagram of the gas turbine combustor simulator (GTCS).

3. GOVERNING EQUATIONS

Navier-Stokes equations for the simulation of transient, 2D, turbulent, incompressible cold flow of air in the GTCS can be written as follows

$$\frac{\partial u}{\partial t} = -u \frac{\partial u}{\partial z} - v \frac{\partial u}{\partial r} - \frac{1}{\rho} \frac{\partial p}{\partial z} + \nu \left(\frac{\partial^2 u}{\partial z^2} + \frac{1}{r} \frac{\partial u}{\partial r} + \frac{\partial^2 u}{\partial r^2} \right) \quad (1)$$

$$\frac{\partial v}{\partial t} = -u \frac{\partial v}{\partial z} - v \frac{\partial v}{\partial r} - \frac{1}{\rho} \frac{\partial p}{\partial r} + \nu \left(\frac{\partial^2 v}{\partial z^2} + \frac{1}{r} \frac{\partial v}{\partial r} + \frac{\partial^2 v}{\partial r^2} - \frac{v}{r^2} \right) \quad (2)$$

$$\frac{\partial u}{\partial z} + \frac{\partial v}{\partial r} + \frac{v}{r} = 0 \quad (3)$$

The initial and boundary conditions are

IC @ $t = 0, \forall r \wedge \forall z: v = 0, u = 0,$

BC1 @ $r = 0, \forall z \wedge \forall t: v = 0, \partial u / \partial r = 0,$

BC2 @ $r = R, \forall z \wedge \forall t: v = 0, u = 0,$

BC3 @ $z = 0, 0 \leq r < R_{cj} \wedge \forall t: v = 0, u = (u_{in})_{cj},$

@ $z = 0, R_{cj} \leq r \leq R_{sjb} \wedge \forall t: v = 0, u = 0,$

@ $z = 0, R_{sjb} < r < R_{sje} \wedge \forall t: v = 0, u = (u_{in})_{sje},$

@ $z = 0, R_{sje} \leq r \leq R \wedge \forall t: v = 0, u = 0,$

BC4 @ $z = L, \forall r \wedge \forall t: \partial^2 v / \partial z^2 = 0, \partial^2 u / \partial z^2 = 0.$

At the inlet, the axial component of the velocity is given as flat profile, and the radial component is set to zero. At the exit, the so-called soft boundary conditions are used. At the walls, no-slip and no-through flow boundary conditions are employed. At the centerline symmetry boundary conditions are utilized.

4. CODE

MOL Solution for Momentum Equations (MOLS4ME) is a general program for computing single-phase, transient, 2D,

incompressible, internal flows which may be laminar or turbulent in complex cylindrical geometries. The code uses body-fitted coordinate system. Therefore, the spacing of the computation grid in physical domain may be arbitrarily specified as uniform/non-uniform in regular/irregular geometries. The MOLS4ME embodies subroutines for solving the governing equations of fluid dynamics, i.e., equations of continuity and momentum. The modular structure of the code allows further conservation equations to be added with ease. In the same way, variables may be suppressed with similar ease. There is also a provision for computing both the Jacobian matrix and eigen values of the system of ODEs resulting from the spatial discretization. The programming language used is FORTRAN 77, and the code may be run on various computers. Because the program is teaching-oriented, and is not a black-box production code, the user must have some knowledge of, and experience with, CFD, before attempting to use or modify it. However, the program is written in a relatively straightforward form which is readily amenable to modification, and is easy to understand. Most subroutines are problem-independent and in many instances only minor modifications are required to the problem dependent subroutines when applications are made to a situation differing from that covered by the present version.

4.1. Code Structure

The structure of the MOLS4ME code is illustrated in Figure 2, wherein a line connecting two routines indicates that lower routine is called by the upper one. Overall control of the problem is exerted by the main driver routine Main_LCODE which performs the initial and final operations.

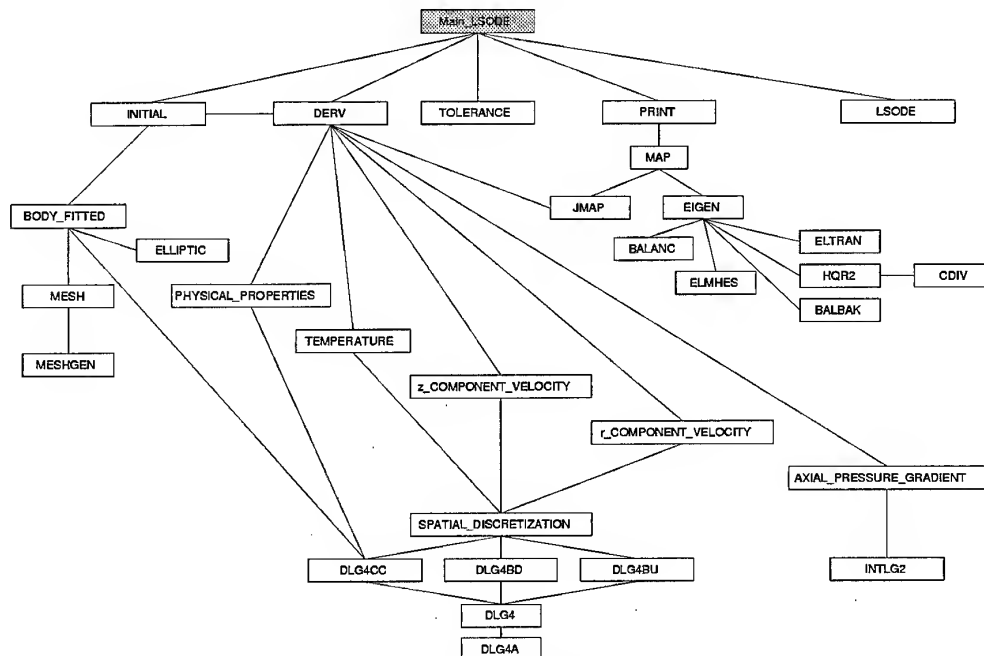


Figure 2. Structure of MOLS4ME code.

This main driver routine calls four subroutines, namely, INITIAL, DERV, PRINT, TOLERANCE to specify the initial conditions, model equations, printing instructions and user-specified tolerances respectively, and also calls subroutine LSODE to integrate the set of ODEs.

The code has been arranged as much as possible in a modular fashion, with different subprograms with different tasks. Hence the number of subprograms is fairly large. However, this feature aids in both understanding and, if necessary, modifying the code. Subroutines of MOLS4ME code can be categorized as i) main program (MAIN_LSODE), ii) initialization (INITIAL), iii) mesh generation (BODY_FITTED and its dependencies MESH, MESHGEN and ELLIPTIC), iv) spatial discretization (DLG4CC, DLG4BD, DLG4BU and their dependencies DLG4 and DLG4A), v) assemblage of the governing equations (DERV and its dependencies PHYSICAL_PROPERTIES, z_COMPONENT_VELOCITY, r_COMPONENT_VELOCITY and AXIAL_PRESSURE_GRADIENT and its dependence INTLG2), vi) time integration (LSODE and its dependencies INTDY, STODE, CCODE, PREPJ, SOLSY, EWSET, VNDORM, D1MACH, XERRWV, DGEFA, DGESL, DGBFA, DGBSL, DAXPY, DSCAL, DDOT and IDAMAX), vii) computation of the Jacobian map and eigenvalues of the coefficient matrix (MAP and its dependencies JMAP, EIGEN, and EISPACK routines BALANC, ELMHES, ELTRAN, HQR2, BALBAK and CDIV).

The subroutines composing these main parts can be classified as problem-independent and problem-dependent subroutines. The problem-independent ones are those appearing in the parts of spatial discretization, time integration, and computation of the Jacobian map and eigenvalues of the coefficient matrix.

The source code of LSODE and its dependencies can be obtained from the netlib, <http://www.netlib.org/odepack/>. The source code of EISPACK routines can also be obtained from the netlib, <http://www.netlib.org/eispack/>. A brief description of these EISPACK routines utilized in this study is available in literature [4].

4.1.1. Time Integration

The integration of the resulting ODEs derived from the discretization of the Navier-Stokes equations is carried out by an implicit algorithm (Backward Differentiation Formula (BDF)) embedded in the well-known ODE solver LSODES [5]. The elegance of the MOLS4ME is that it shares the advantages of both explicit and implicit methods. In the MOLS4ME the spatial derivatives and source terms are evaluated at the previous time level as applied in the explicit approach, so that no linearization problem arises. Furthermore, the solution of the resulting ODEs is carried out by one of the implicit methods, such as BDF or Adams-Moulton method [5]. Hence it is concluded that the MOLS4ME has the simplicity of the explicit approach and the power of the implicit one unless a poor algorithm for the solution of ODEs is adopted.

4.1.2. Higher-Order Spatial Discretization

Spatial derivatives of dependent variables are approximated by using five-point Lagrange interpolation polynomial which makes it

possible to investigate the solutions of the governing equations by a higher order discretization scheme on both uniform and non-uniform grid topology. When converting the PDE system into an ODE initial value problem by discretizing the spatial derivatives, the convective terms should be approximated in such a way that the resulting system of ODEs should be stable according to the linear stability theory [6, 7]. This is achieved by using a multidimensional intelligent scheme (scheme-adaptive method) [2] which is based on the choice of biased-upwind or biased-downwind stencils for the convective derivatives according to the sign of the coefficient of the concerned derivative.

4.1.3. Treatment of Pressure Gradient

The computation of pressure is the most difficult and time-consuming part of the overall solution of the Navier-Stokes equations and there are various pressure correction methods which are applicable to both stationary and time-dependent incompressible flow equations. Basically, most of them involve an iterative procedure between the velocity and pressure fields through the solution of Poisson-type equation for the pressure to satisfy the global mass flow constraint and the divergence-free condition for confined incompressible flows. Therefore in this paper a non-iterative procedure proposed recently [1] for the treatment of pressure gradients is applied.

4.1.4. Grid Generation

The spatial derivatives in the governing equations are converted from physical domain to computational domain using

$$f_r = J(z_\eta f_\xi - z_\xi f_\eta) \quad (4)$$

$$f_z = J(r_\xi f_\eta - r_\eta f_\xi) \quad (5)$$

for the first order derivatives and

$$f_{rr} + f_{zz} = J^2 (a f_{\xi\xi} - 2b f_{\xi\eta} + c f_{\eta\eta} + d f_\eta + e f_\xi) \quad (6)$$

where

$$a = r_\eta^2 + z_\eta^2 \quad (7)$$

$$b = r_\xi r_\eta + z_\xi z_\eta \quad (8)$$

$$c = r_\xi^2 + z_\xi^2 \quad (9)$$

$$d = J(z_\xi \alpha - r_\xi \beta) \quad (10)$$

$$e = J(r_\eta \beta - z_\eta \alpha) \quad (11)$$

and

$$\alpha = a r_{\xi\xi} - 2b r_{\xi\eta} + c r_{\eta\eta} \quad (12)$$

$$\beta = a z_{\xi\xi} - 2b z_{\xi\eta} + c z_{\eta\eta} \quad (13)$$

for the summation of second order derivatives on the right-hand-side of governing equations. Hence the z-momentum equation in the computational domain takes the following form

$$\frac{\partial u}{\partial t} + U' \frac{\partial u}{\partial \eta} + V' \frac{\partial u}{\partial \xi} = -\frac{1}{\rho} \frac{\partial \hat{p}}{\partial z} \quad (14)$$

$$+ vJ^2 \left[a \frac{\partial^2 u}{\partial \xi^2} - 2b \frac{\partial^2 u}{\partial \xi \partial \eta} + c \frac{\partial^2 u}{\partial \eta^2} \right]$$

where

$$U' = J(ur_{\xi} - v'z_{\xi}) - vJ^2d \quad (15)$$

$$V' = J(v'z_{\eta} - ur_{\eta}) - vJ^2e \quad (16)$$

where

$$v' = v - \frac{v}{r} \quad (17)$$

As is mentioned in [1] streamwise pressure gradient, $\partial \hat{p} / \partial z$, can be determined with the aid of global mass flow constraint combined with the discretized form of the z-momentum equation. Since the streamwise pressure gradient term can be regarded as a source term in the z-momentum equation, there is no need to convert the spatial derivative of \hat{p} from physical domain to computational domain as long as the grid point locations in the physical domain at each axial station are perpendicular to streamwise direction. Therefore, the same procedure in [1] is applied for computing the axial pressure gradient term to be used in the z-momentum equation transformed from physical domain to computational domain. For this purpose temporal derivative in Equation (14) is discretized as

$$\frac{u_{i,j}^{n+1} - u_{i,j}^n}{\Delta t} = -\frac{1}{\rho} \left(\frac{\partial \hat{p}}{\partial z} \right)_j^n - \left[U_{i,j}^n \left(\frac{\partial u}{\partial \eta} \right)_{i,j}^n + V_{i,j}^n \left(\frac{\partial u}{\partial \xi} \right)_{i,j}^n \right] \quad (18)$$

$$+ vJ^2 \left[a \left(\frac{\partial^2 u}{\partial \xi^2} \right)_{i,j}^n - 2b \left(\frac{\partial^2 u}{\partial \xi \partial \eta} \right)_{i,j}^n + c \left(\frac{\partial^2 u}{\partial \eta^2} \right)_{i,j}^n \right]$$

Rearranging the terms to solve for $u_{i,j}^{n+1}$ yields

$$u_{i,j}^{n+1} = \Phi_{i,j}^n + \left(\frac{\partial \hat{p}}{\partial z} \right)_j^n \Psi^n \quad (19)$$

where

$$\Phi_{i,j}^n = u_{i,j}^n - \Delta t \left\{ U_{i,j}^n \left(\frac{\partial u}{\partial \eta} \right)_{i,j}^n + V_{i,j}^n \left(\frac{\partial u}{\partial \xi} \right)_{i,j}^n \right. \quad (20)$$

$$\left. - vJ^2 \left[a \left(\frac{\partial^2 u}{\partial \xi^2} \right)_{i,j}^n - 2b \left(\frac{\partial^2 u}{\partial \xi \partial \eta} \right)_{i,j}^n + c \left(\frac{\partial^2 u}{\partial \eta^2} \right)_{i,j}^n \right] \right\}$$

and

$$\Psi^n = -\frac{\Delta t}{\rho^n} \quad (21)$$

Equation (19) is then multiplied by the density ρ^{n+1} and then integrated over the cross-sectional area perpendicular to the

streamwise direction. Thereafter the streamwise pressure gradient $\partial \hat{p} / \partial z$ is computed by the following equation

$$\left(\frac{\partial \hat{p}}{\partial z} \right)_j^n = \frac{2\pi \rho \int_0^{R_j} \Phi_{i,j}^n r dr - \dot{m}}{\pi R_j^2 \Delta t} \quad (22)$$

where R_j stands for radius of the curved wall which varies along the axis.

Transformation of Equation (33) in [1] for the r-component velocity to computational domain yields

$$v_{i+1,j}^n = \frac{r_{i,j}}{r_{i+1,j}} \left\{ v_{i,j}^n - \Delta r_{i,j}^* J \left[r_{\xi} \left(\frac{\partial u}{\partial \eta} \right)_{i,j}^n - r_{\eta} \left(\frac{\partial u}{\partial \xi} \right)_{i,j}^n \right] \right\} \quad (23)$$

where $i = 1, \dots, M-2$, $j = 2, \dots, N$, $\Delta r_{i,j}^* = r_{i+1,j} - r_{i,j}$

4.2. Mode of Operation

The general algorithm for the solution of governing equations of fluid dynamics by using the MOL approach is based on the evaluation of the derivative vector by which the solution is advanced from one time step to the next. Once the derivative vector has been obtained, the first step in solving the system of equations is to combine the dependent variables into a one-dimensional array. The evaluation of the derivative vector can be summarized as follows.

The velocity field satisfying the continuity equation is known a priori at the beginning of each cycle, either as a result of the previous cycle or from the prescribed initial conditions for the dependent variables. Once the spatial derivatives appearing in the governing equations have been evaluated using values of the present cycle, the radial component of the velocity is calculated by the direct utilization of the continuity equation, so that the divergence-free condition is ensured automatically. Then the corresponding pressure gradients along the axial direction are calculated to ensure that the mass flow is conserved. Once these calculations have been settled, the derivative vector is calculated over the spatial domain of interest, then it is sent to the ODE solver in the form of one-dimensional array to compute the dependent variables at the advanced time level. This completes the progression of the solution to the end of the new cycle having the new values of the velocity field. This cyclic procedure is then continued until the steady state is reached.

5. RESULTS and DISCUSSION

The code under consideration was run for the above-mentioned experiment and the steady-state predictions were compared with measurements. Experimental conditions for which the runs were carried out are listed in Table 1. Comparisons showed large discrepancies between the predicted and measured lengths of the recirculation zones. Several inlet velocity profiles for the center and co-annular flows have been tried in an attempt to remove the

discrepancies, but no improvement was obtained. The discrepancies were then considered to be due to the insufficient number of grid points employed. Considering that the code is based on DNS and that DNS requires number of grid points proportional to $Re^{3/2}$ for the present 2D application, the code was run for increasing number of grid points. It was found that the CPU time required increased exponentially with the number of grid points with insignificant improvement in accuracy. This was due to the fact that even the highest number of grid points utilized was very much smaller than that required by DNS. It was not possible to employ higher number of grid points due to the computer hardware limitations. Therefore, the problem was alleviated by referring to the classical approach i.e., employing artificial viscosity. The code was run for increasing viscosity and was found to produce predictions in good agreement with the measured data for an artificial viscosity of 100μ . This value was used for all the runs carried out on GTCS problem and resulted in approximately 8 hours of CPU time on an IBM RISC Sys/6000-590.

Table 1 Operating conditions and variables used in the numerical simulations and experiments.

	$\bar{u}_{sj}/\bar{u}_{cj} = 1.63$
Center jet flow, $\text{cm}^3 \text{s}^{-1}$	1066.7
Annular flow, $\text{cm}^3 \text{s}^{-1}$	42475
\bar{u} , cm s^{-1}	537.07
\bar{u}_{cj} , cm s^{-1}	1902.06
\bar{u}_{sj} , cm s^{-1}	3101.43
$Re = \bar{u} D/\nu$	34821
$Re = \bar{u}_{cj} D/\nu$	10256
$Re = \bar{u}_{sj} D/\nu$	24739

Figure 3 shows comparison between predicted and measured axial velocity components and the resulting streamline patterns at steady-state obtained with flat velocity profile at the inlet annular flow/center jet velocity ratio of 1.63. Measured and predicted mean velocities are illustrated in the upper and lower parts of the GTCS. As can be seen from the figure, reasonably good match is obtained for the length of the recirculation zone. Predicted streamlines follow the physically expected trends as the annular flow velocity is 1.63 times the center jet velocity. However, streamlines plotted from the measured data show recirculation zones at about the same radial location where high velocity jets are introduced.

In order to find out the reason behind the discrepancies within the recirculation zone area-averaged velocities were calculated from the point velocities and percentage errors were found using $(\bar{u} - u_o)/u_o$ where u_o denotes the cross-sectional velocity calculated from the measured mass flow rate supplied to the system. It was found that percentage errors in predicted area-averaged velocities at various axial locations for annular flow/center jet velocity ratio of 1.63 always satisfy the mass conservation.

In order to show the ability of the present code to predict transient solutions, time development of the streamline pattern for an impulsively started flow is exhibited in Figure 4. As can

be seen from the figure, as soon as the flow is started, vortices begin to form in the vicinity of the bluff-body and the corner. Thereafter the flow starts to separate downstream of the corner region, yielding two disconnected recirculating flow regions. As time progresses, the second vortex vanishes at the surface, while primary recirculating zone attached to the wall grows in size. The recirculating zone attached to the bluff-body also grows in size and takes its final form when steady-state is reached.

Although it was not possible to validate the transient predictions of the code owing to the absence of transient data in the open literature, the flow field predicted by using this code shows the expected trends.

6. CONCLUSIONS

The novel code developed in this study, MOLS4ME (method-of-lines solution for momentum equations), is a general program for computing single-phase, transient, two-dimensional, incompressible, internal flows which may be laminar or turbulent in complex cylindrical geometries. It was tested for accuracy by applying it to the prediction of transient, turbulent cold flow in a gas turbine combustor simulator and comparing its predictions with measurements.

Comparisons show that the predictions are in reasonable agreement with measurements. However, the success of the code for highly turbulent flows necessitates excessive number of grid points which can not be met by the present day computers.

The code developed in this study constitutes a major improvement to the previous codes employed in the prediction of transient, incompressible, separated internal flows and provides an algorithm for future DNS applications.

ACKNOWLEDGEMENTS

This study was performed as part of AGARD Project T51/PEP. The support is gratefully acknowledged. The authors wish to thank Dr. Ömer Lütfü Gülder, Dr. Ian Campell and Doug Logan of Combustion Laboratory of National Research Council of Canada in Ottawa for carrying out the measurements on the gas turbine combustor simulator reported in this paper.

REFERENCES

1. Oymak, O. and Selçuk, N., "Method of Lines Solution Time-Dependent Two-Dimensional Navier-Stokes Equations", *Int. J. Numer. Meth. Fluids*, Vol. 23, 1996, pp. 455-466.
2. Oymak, O. and Selçuk, N., "Transient Simulation of Internal Separated Flows Using an Intelligent Higher-Order Spatial Discretization Scheme", *Int. J. Numer. Meth. Fluids*, Vol. 24, 1997, pp. 759-769.
3. Oymak, O., "Method of Lines Solution Time-Dependent Two-Dimensional Navier-Stokes Equations for Incompressible Separated Internal Flows", Ph.D.

- Thesis, Chemical Engineering Department, METU, Turkey, 1997.
4. E. Anderson, Z. Bai, C. Bischof, J. Demmel, J. Dongarra, J. Du Croz, A. Greenbaum, S. Hammarling, A. McKenney, S. Ostrouchov and D. Sorensen, "LAPACK Users' Guide", 2nd ed., Society for Industrial and Applied Mathematics, Philadelphia, 1995.
 5. Hindmarsh, A.C., "ODEPACK: A Systematized Collection of ODE Solvers in Scientific Computing", North Holland Publishing Co., New York, 1983.
 6. Schiesser, W.E., "The Numerical Method of Lines: Integration of Partial Differential Equations", Academic, San Diego, CA, 1991.
 7. Hirsch, C., "Numerical Computation of Internal and External Flows, Volume 1: Fundamentals of Numerical Discretization", John Wiley & Sons, Chichester, 1988.

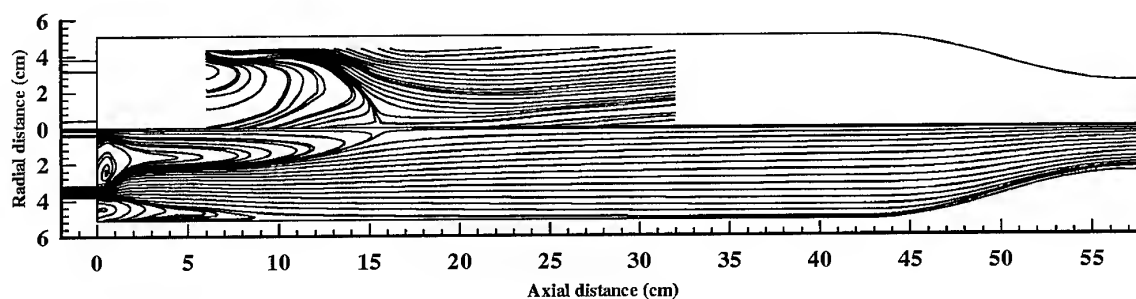


Figure 3. Streamline patterns obtained from the measured and predicted data for the velocity ratio of 1.63.

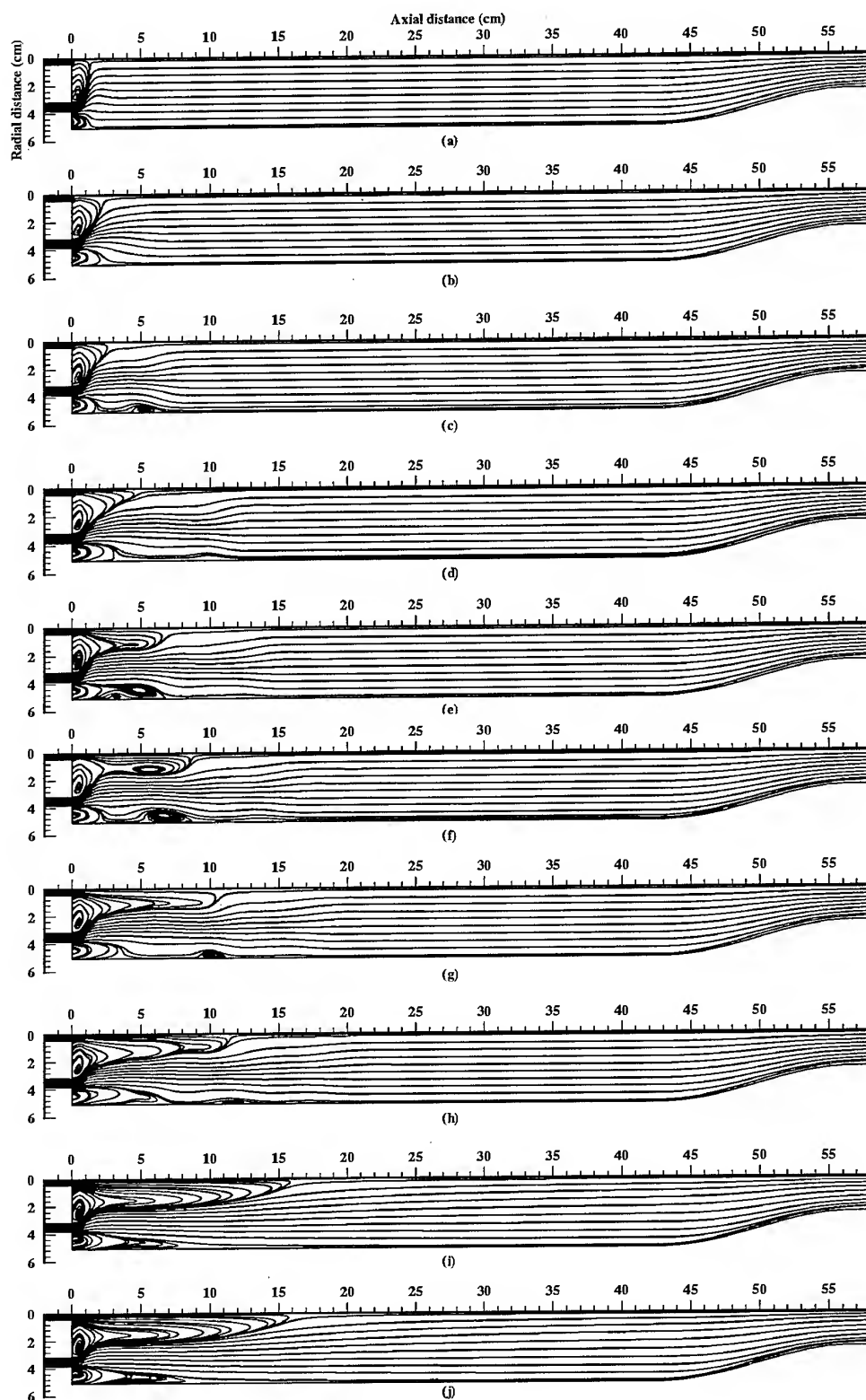


Figure 4. Time development of streamline for velocity ratio of 1.63. (a) @3 ms, (b) @9 ms, (c) @12 ms, (d) @18 ms, (e) @21 ms, (f) @24 ms, (g) @27 ms, (h) @30 ms, (i) @300 ms, (j) @steady-state.

PAPER No. 11
Selcuk & Oymak
(presenter: N. Selcuk)

Question 1: C. Pridden, RR, U.K.

In real turbulent flows there is always a three-dimensional component. Does it not limit the usefulness of your method that it is only set up for two-dimensional flows?

Answer

Yes, it does, but the present work is directed towards algorithm development. The code provides an accurate and efficient numerical algorithm for direct numerical solutions of two-dimensional flows in axisymmetrical cylindrical geometries. As the number of grid cells required by DNS changes with $[Re^{3/4}]^D$ where D represents the number of dimensions, fully three-dimensional turbulent flows require an excessive number of cells for Reynolds numbers of interest, and these cannot be accommodated by present-day computers. This is why we confined our study to two-dimensions. However, the extension of the algorithm to three-dimensions is under consideration.

Question 2: T Rosfjord, UTRC, U.S.

Your presentation described the prediction of a constant density flow. How are the conclusions altered for variable density flows such as those encountered in combustors? How will the code complexity and computer requirements change for extensions to variable density flows?

Answer:

The code containing the energy equation, in addition to the mass and momentum equations, (and called MOLS4MEE, the last E denoting the presence of the energy equation) was applied to the prediction of the transient velocity and temperature fields in a sudden expansion of a non-reacting, low temperature flow ($Re = 500$) contained in a pipe, the walls of which were kept at a higher temperature than that of the fluid. This was a variable density application, the results of which were published in *Advances in Computational Heat Transfer*, 1998. We found that the complexity was not affected due to the modular structure of the program, and that CPU time was not significantly increased. If combustion reactions were to be incorporated into the program, I expect that the CPU time would increase considerably.

Question 3: A. Sanchez, University Carlos III de Madrid, Spain

For the sudden expansion case that you mentioned, the Reynolds Number used was quite close to that for the instability limit for such flows. Therefore, I am surprised that a stationary solution was obtained.

Answer:

The ODE solver has to be stable. The eigen values for the Reynolds Number of 500 were examined to check for stability, and it was a stable solution.

Rebuttal:

The question was not directed to the numerical method used in the code, but to the physical flow that you were calculating. At the Reynolds Number used, stationary state solutions **should not** have been obtained.

In the interests of time, the Session Chairman terminated this discussion.

Reduced Kinetic Mechanisms for Modelling LPP Combustion in Gas Turbines

A. Liñán, M. Bollig
Universidad Politécnica de Madrid
Pza. Cardenal Cisneros 3, 28040 Madrid, Spain.

A. L. Sánchez
Universidad Carlos III
Butarque 15, 28911 Leganés, Spain.

B. Lázaro
SENER
Severo Ochoa 4, 28760 Tres Cantos, Spain.

1. SUMMARY

Lean premixed methane-air flames are investigated in an effort to facilitate the numerical description of CO and NO emissions in LPP (lean premixed prevaporized) combustion systems. Starting with a detailed chemistry description that includes 195 elementary steps, sensitivity procedures and steady-state approximations are introduced to obtain two different four-step reduced mechanisms, which employ either H or OH as the intermediate representing the radical-pool evolution. The resulting reduced mechanisms are especially well suited to describe high-pressure, lean premixed combustion. Based on the resulting flame structures, and following previous analyses, the mechanism is further simplified to give a two-step description, in which fuel is consumed and CO is produced according to the fast overall step $\text{CH}_4 + 3/2 \text{O}_2 \rightarrow \text{CO} + 2\text{H}_2\text{O}$, while CO is slowly oxidized according to the overall step $\text{CO} + 1/2 \text{O}_2 \rightarrow \text{CO}_2$. Because of its associated fast rate, fuel consumption takes place in thin layers, while CO oxidation occurs downstream in a distributed manner, in a region where CO is the only intermediate not in steady state. In this two-step description, the rate of fuel consumption is assigned a heuristic Arrhenius dependence that adequately reproduces laminar burning velocities, whereas the rate of CO oxidation is extracted from a reduced chemistry analysis. Preliminary results corresponding to one-dimensional unstrained flames indicate that the formulation reproduces well flame structures, including profiles of CO, temperature and radicals. The accuracy of the resulting profiles suggests that the proposed formulation can also be used to calculate NO emissions by appending the appropriate chemistry. Although methane is employed in the present study as a model fuel, the universal structure of the resulting CO oxidation region, independent of the fuel considered, enables the proposed formulation to be readily extended to other hydrocarbons.

2. REDUCED CHEMICAL KINETIC MECHANISMS

Four different test cases were selected for the present study. These test cases, which are shown in Table 1, are taken from the flight envelope definition of the E-engine cycle, the virtual gas turbine selected as representative during the EU research program LOWNOX-III.

As a preliminary step, a detailed chemical mechanism for methane oxidation was identified. The starting scheme contains 195 elementary reactions and 34 species, with

elementary rates largely taken from recent recommendations of the CEC [1]. This detailed mechanism contains in particular the C_2 chain of fuel oxidation. Extensive calculations with this chemistry set incorporated for the chemistry description were performed for the test cases outlined in Table 1. Both unstrained and strained flames were considered.

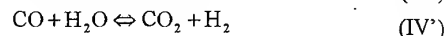
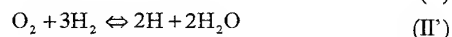
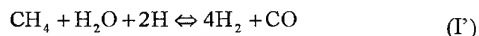
Previous analyses have shown that in these lean environments the C_1 chain of methane oxidation suffices to model flame structures [2]. Also, the contribution of the prompt mechanism to the NOx production is unimportant in high-pressure, lean premixed flames. As a result, the C_2 chain can be neglected when describing the combustion process in LPP combustion chambers.

Test-Case	p (Bar)	Φ	T_u (K)	Description
A	18	0.6	800	Cruise
B	40	0.6	900	Take-off
C	8.5	0.45	600	Approach
D	16	0.5	700	Descent

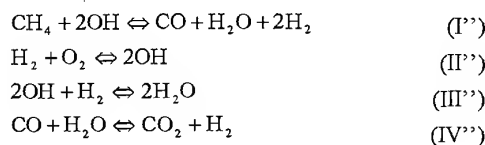
Table 1.- LOWNOX-III LPP combustor operating envelope. The columns correspond to the chamber pressure, and to the equivalence ratio and temperature of the fresh mixture.

Through reaction flux and sensitivity analyses a short mechanism with 57 elementary reactions and 17 species was identified. Further simplification was achieved by introducing steady state approximations for intermediates, providing two different four-step reduced kinetic schemes.

The first reduced description, with CO, H_2 , and H as intermediates not in steady state [2], results in the following four global reactions:



The second reduced description replaces H by OH, an alternative motivated by the relatively large OH concentrations observed in the computations, yielding the four overall reactions given below:



The above global steps represent the main chemical processes that occur during fuel oxidation. Thus, fuel consumption occurs according to the first step in a process that involves radical removal. The second step summarizes the hydrogen-oxygen chain branching reactions. The third reaction represents radical recombination, and the last step is the water-gas shift that converts the CO produced by the first step to CO_2 .

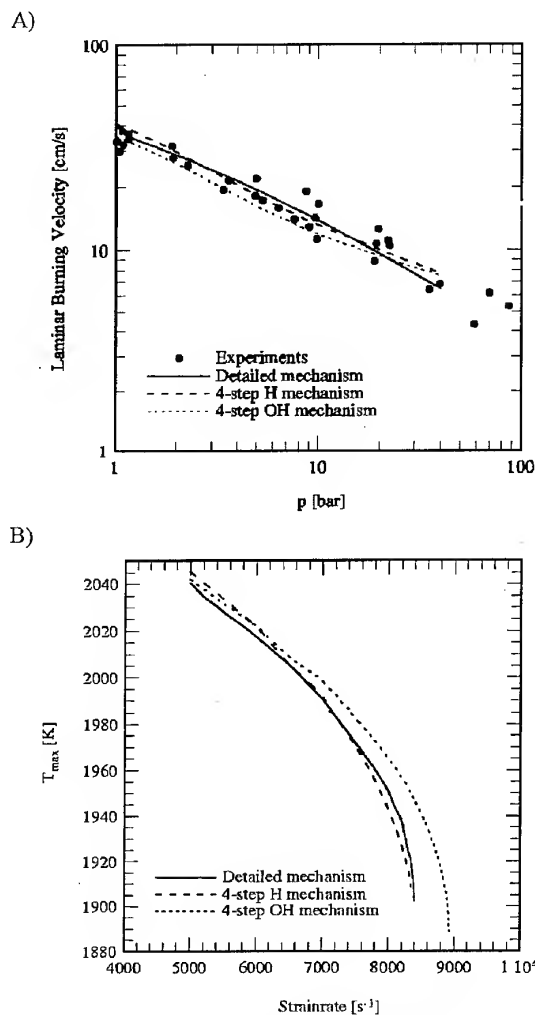


Figure 1: Laminar flame characteristics predicted by the two 4-step reduced schemes. A) Pressure dependence of the burning velocity for stoichiometric flames at $T_u=298$ K. B) Peak flame temperature under strained flow conditions (Test case A fresh mixture flowing against products at 1500 K)

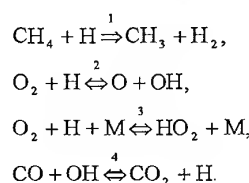
The rates of the above global reactions depend on the rates of several elementary steps that compose the detailed chemistry set. In particular, it was found that incorporating methyl attack by HO_2 and OH is critical to obtain accurate results at elevated pressures, a characteristic not seen in previous studies [2].

As can be seen in Figure 1, both reduced chemistry descriptions give excellent results. In particular, the resulting laminar burning velocities, flame structures and radical concentration levels are found to be very accurate. In addition, strain effects are adequately captured, with the H-atom based reduced mechanism giving somewhat better predictions for the strain rate at extinction.

Since both mechanisms are analogous and give similar results, further analysis can be based on either reduced description. In what follows we select reactions I' to IV' for further developments, and retain only the main contributor to each of the overall reactions, thereby giving global rates (moles per unit volume per unit time) of the form:

$$\begin{aligned}\omega_{\text{I}'} &= k_{\text{If}} [\text{CH}_4][\text{H}] \\ \omega_{\text{II}'} &= k_{2f} [\text{O}_2][\text{H}] - k_{2b} [\text{O}][\text{OH}] \\ \omega_{\text{III}'} &= k_{3f} [\text{M}][\text{O}_2][\text{H}] - k_{3b} [\text{M}][\text{HO}_2] \\ \omega_{\text{IV}'} &= k_{4f} [\text{CO}][\text{OH}] - k_{4b} [\text{CO}_2][\text{H}]\end{aligned} \quad (1)$$

where $[i]$ denotes the concentration of chemical species i , M representing a third body, and k_{If} and k_{3b} are the specific reaction-rate constants in the forward and backward directions for the elementary reactions:

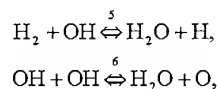


As explained below, if the reverse rate of reaction 3 were not included in the mechanism, then the resulting equilibrium concentrations of all intermediates would be zero, thereby potentially introducing significant errors in predictions of CO and NO formation. We therefore choose to retain this rate for increased accuracy.

Expressions for the different reaction-rate constants, with a third body efficiency equal to 0.4 introduced in computing $[\text{M}]$, are given below in cm³/mole/sec:

$$\begin{aligned}k_{\text{If}} &= 1.300 \cdot 10^4 T^{3.00} \exp(-4041/T), \\ k_{2f} &= 9.756 \cdot 10^{13} \exp(-7469/T), \\ k_{2b} &= 1.445 \cdot 10^{13} \exp(-352/T), \\ k_{3f}[\text{M}] &= 1.82 \cdot 10^{16} T^{-1.80} p, \\ k_{3b} &= 5.058 \cdot 10^{18} T^{0.80} \exp(-23574/T), \\ k_{4f} &= 4.400 \cdot 10^6 T^{1.50} \exp(373/T), \\ k_{4b} &= 1.270 \cdot 10^9 T^{1.50} \exp(-11872/T),\end{aligned}$$

where T and p are expressed in kelvins and atmospheres, respectively. Suitable simplified steady-state expressions for the concentrations of OH and O, necessary in evaluating Eq. 1 can be obtained by assuming partial equilibrium of reactions:



to give:

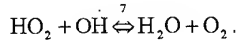
$$[\text{OH}] = K_5^{-1} [\text{H}_2\text{O}][\text{H}] / [\text{H}_2] \quad (2)$$

$$[\text{O}] = K_5^{-2} K_6 [\text{H}_2\text{O}][\text{H}]^2 / [\text{H}_2]^2 \quad (3)$$

Where $K_5 = 0.227 \exp(7614/T)$ and $K_6 = 0.0966 \exp(8573/T)$ are equilibrium constants. Similarly, the concentration of hydroperoxyl radicals needed to evaluate the backward rate of III' can be obtained from the truncated steady state expression:

$$[\text{HO}_2] = \frac{k_{3f} [\text{M}][\text{O}_2][\text{H}] + k_{7b} [\text{O}_2][\text{H}_2\text{O}]}{k_{3b} [\text{M}] + k_{7f} [\text{OH}]} \quad (4)$$

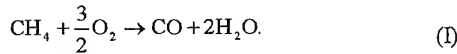
Where the rate constants $k_{7f} = 2.891 \cdot 10^{13} \exp(253/T)$ and $k_{7b} = 3.069 \cdot 10^{14} \exp(-36083/T)$ ($\text{cm}^3/\text{mole}/\text{sec}$) correspond to the reaction:



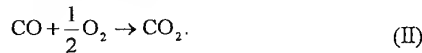
3. THE LIMIT OF SLOW CO OXIDATION

CO-oxidation is the slowest of the four chemical processes represented by I'-IV' [3]. To illustrate this, one can use Eq. 1 to give the characteristic chemical-time ratios $t_{\text{I'}/\text{IV'}} = k_{4f}/(k_{1f}K_5)$, $t_{\text{II'}/\text{IV'}} = k_{4f}/(k_{2f}K_5)$ and $t_{\text{III'}/\text{IV'}} = k_{4f}/(k_{3f}[\text{M}]K_5)$. Evaluating the above estimates at the temperatures and pressures typical of gas turbine combustion yields the scaling law $t_{\text{I'}/\text{IV'}} \sim t_{\text{II'}/\text{IV'}} \ll t_{\text{III'}/\text{IV'}}$ (for instance, at $T=1700$ K and $p=30$ atm, $t_{\text{I'}/\text{IV'}}=0.01$, $t_{\text{II'}/\text{IV'}}=0.016$, and $t_{\text{III'}/\text{IV'}}=0.022$). This scaling suggests that fuel consumption followed by radical branching and radical recombination occur in thin layers that exhibit small concentration of H_2 and radicals. CO oxidation is much slower, and consequently occurs in a distributed manner in a downstream region where in the first approximation $[\text{CH}_4]=0$ and H_2 and H maintain steady state [3]. Note in particular that fast radical removal through reaction I' causes all chemical activity to be frozen in the preheat zone upstream from the fuel-consumption layer [2].

The overall step describing the thin fuel-consumption layer can be obtained by eliminating H_2 and H by linear combination of I'-III' to give:



On the other hand, incorporating the steady states of H_2 and H into step IV' by linear combination with steps II' and III' provides the global CO-oxidation step:



The rate of reaction I, which is fundamental to determine the propagation velocity of the flame, is only extractable in terms of the rates of reactions I', II', and III' from a detailed study of the inner structure of the fuel-consumption layer, where both H and H_2 do not follow the steady-state approximation. Instead of further pursuing such an analysis, we choose to represent this rate by an Arrhenius law of the form

$$\omega_1 = B[\text{CH}_4] \exp\left(-\frac{E}{R^\circ T}\right) \quad (5)$$

where R° is the universal gas constant. The values of the activation energy E , and of the preexponential factor, B , must be chosen to adequately reproduce the steady flame propagation velocity. On the other hand, the rate of reaction II is given by:

$$\omega_{\text{II}} = \omega_{\text{IV'}} = k_{4f} [\text{CO}][\text{OH}] - k_{4b} [\text{CO}_2][\text{H}] \quad (6)$$

As shown below, with appropriate choices for E and B to reproduce the flame propagation velocity, the CO oxidation rate given in Eq. 6 describes accurately the nonequilibrium evolution of the CO concentration, as well as its associated radical pool (through appropriate steady-state expressions), downstream from the fuel-consumption layer. Failure of the proposed two-step model within the thin fuel-consumption layer has only a limited effect as shown below.

In the CO-oxidation region, the corresponding steady-state equations for H_2 and H with $[\text{CH}_4]=0$, $-3\omega_{\text{II'}} + \omega_{\text{III'}} + \omega_{\text{IV'}}=0$ and $2\omega_{\text{II'}} - 2\omega_{\text{III'}}=0$, can be solved to give the expression:

$$[\text{H}_2] = K_5^{-1} [\text{O}_2]^{-1} \alpha_1 \{ (K_6/K_2) [\text{OH}]^2 + \frac{1}{2} \left(\frac{k_{4f}}{k_{2f}} \right) [\text{CO}][\text{H}_2\text{O}] \} \quad (7)$$

together with the fourth-order polynomial:

$$a_4 [\text{OH}]^4 + a_3 [\text{OH}]^3 + a_2 [\text{OH}]^2 + a_1 [\text{OH}] + a_0 = 0 \quad (8)$$

where we have introduced the coefficients:

$$\begin{aligned} a_4 &= -(K_6 k_{7f}/K_2) [1 - \alpha_1 (1 - \gamma)] \\ a_3 &= -(K_6 k_{3b}/K_2) [1 - \alpha_1 [\text{M}]] \\ a_2 &= \frac{1}{2} \alpha_1 (k_{4f} k_{7f}/k_{2f}) (1 - \gamma) [\text{CO}][\text{H}_2\text{O}] \\ a_1 &= \frac{1}{2} \alpha_1 (k_{4f} k_{3b}/k_{2f}) [\text{M}][\text{CO}][\text{H}_2\text{O}] \\ a_0 &= \frac{1}{2} \alpha_1 (k_{3b} k_{7b}/k_{2f}) [\text{M}][\text{H}_2\text{O}]^2 [\text{O}_2] \end{aligned} \quad (10)$$

and the functions

$$\alpha_1 = \left(1 + \frac{1}{2} \frac{k_{4f}}{k_{2f}} \frac{[\text{CO}_2]}{[\text{O}_2]} \right)^{-1} \quad (10)$$

and

$$\gamma = k_{3f} [\text{M}] / k_{2f} \quad (11)$$

Once Eq. 8 is solved for $[\text{OH}]$, one can use Eq. 7 to compute $[\text{H}_2]$ and Eqs. 2 and 3 to calculate $[\text{H}]$ and $[\text{O}]$.

Note that, if the reverse of reaction III' is neglected in the formulation for simplicity, then Eqs. 7 and 8 reduce to the explicit expressions

$$[\text{H}_2] = \frac{1}{2} \frac{k_{4f} \alpha_2}{k_{3f} [\text{M}] K_5} \frac{[\text{H}_2\text{O}][\text{CO}]}{[\text{O}_2]} \quad (12)$$

and

$$[\text{OH}] = \left(\frac{1}{2} \frac{k_{4f} K_2 (1-\gamma) \alpha_2}{k_{3f} [M] K_6} \right)^{1/2} [\text{H}_2\text{O}]^{1/2} [\text{CO}]^{1/2} \quad (13)$$

where

$$\alpha_2 = \left(1 + \frac{1}{2} \frac{k_{4b}}{k_{3f} [M]} \frac{[\text{CO}_2]}{[\text{O}_2]} \right)^{-1} \quad (14)$$

Substituting then Eqs. 2, 12 and 13 into 6 yields

$$\omega_{\text{II}} = \left(\frac{k_{4f}^3 K_2 (1-\gamma) \alpha_2^3}{2 k_{3f} [M] K_6} \right)^{1/2} [\text{H}_2\text{O}]^{1/2} [\text{CO}]^{3/2} \quad (15)$$

as a simplified expression for the CO-oxidation rate corresponding to the limit of irreversible radical recombination.

4. CONSERVATION EQUATIONS

The conservation equations for the reactive species corresponding to the reproduced chemistry description I-II can be written as

$$\rho \frac{D}{Dt} (\Gamma_{\text{CH}_4}) - \nabla \cdot \left(\frac{\rho D_T}{L_{\text{CH}_4}} \nabla \Gamma_{\text{CH}_4} \right) = -\omega_{\text{I}}, \quad (16)$$

$$\rho \frac{D}{Dt} (\Gamma_{\text{CO}}) - \nabla \cdot \left(\frac{\rho D_T}{L_{\text{CO}}} \nabla \Gamma_{\text{CO}} \right) = \omega_{\text{I}} - \omega_{\text{II}}, \quad (17)$$

$$\rho \frac{D}{Dt} (\Gamma_{\text{CO}_2}) - \nabla \cdot \left(\frac{\rho D_T}{L_{\text{CO}_2}} \nabla \Gamma_{\text{CO}_2} \right) = \omega_{\text{II}}, \quad (18)$$

$$\rho \frac{D}{Dt} (\Gamma_{\text{H}_2\text{O}}) - \nabla \cdot \left(\frac{\rho D_T}{L_{\text{H}_2\text{O}}} \nabla \Gamma_{\text{H}_2\text{O}} \right) = 2\omega_{\text{I}}, \quad (19)$$

$$\rho \frac{D}{Dt} (\Gamma_{\text{O}_2}) - \nabla \cdot \left(\frac{\rho D_T}{L_{\text{O}_2}} \nabla \Gamma_{\text{O}_2} \right) = -\frac{3}{2}\omega_{\text{I}} - \frac{1}{2}\omega_{\text{II}}, \quad (20)$$

where use is made of the variable $\Gamma_i = Y_i/W_i = [i]/\rho$, with Y_i and W_i denoting the mass fraction and molecular weight for chemical species i , respectively, and ρ being the density. In the formulation, D/Dt is the substantial derivative and $D_T = \lambda/(\rho c_p)$ denotes the thermal diffusivity of the gas mixture, with λ and c_p representing its thermal conductivity and specific heat at constant pressure. A Fickian approximation is adopted here for the diffusion velocities, with $L_i = \lambda/(\rho c_p D_i)$ denoting the Lewis number of species i based on its diffusion coefficient D_i .

Similarly, the energy equation can be written for the thermal enthalpy $h_T = \int^T c_p \cdot dT$ as

$$\rho \frac{D}{Dt} (h_T) - \nabla \cdot (\rho D_T \nabla h_T) = q_{\text{I}} \omega_{\text{I}} + q_{\text{II}} \omega_{\text{II}} - 4\sigma T^4 l_p \quad (21)$$

where the overall heats of reaction are related to the enthalpies of formation per mole of species i , h_{fi} , by the equations $q_{\text{I}} = h_{\text{CO}}^0 + 2h_{\text{H}_2\text{O}}^0 - h_{\text{CH}_4}^0$, and $q_{\text{II}} = h_{\text{CO}_2}^0 - h_{\text{CO}}^0$. In writing Eq.

21, a low Mach number approximation has been employed, and unsteady pressure variations have been neglected along with the effect of the differences of the specific heat at constant pressure of each species from the mean c_p . The radiative heat loss corresponds to that of an optically thin gas with cold boundaries, with σ denoting the Stephan-Boltzmann constant and l_p being the Plank mean absorption length, a function of the partial pressure of H_2O and CO_2 that varies according to $l_p \propto (\alpha_{\text{CO}_2} \Gamma_{\text{CO}_2} + \alpha_{\text{H}_2\text{O}} \Gamma_{\text{H}_2\text{O}})$, where the coefficients α_{CO_2} and $\alpha_{\text{H}_2\text{O}}$ are temperature dependent. To completely describe the reacting flow field, Eqs. 16-21 must be integrated together with the continuity and momentum equations with appropriate boundary and initial conditions.

5. ONE DIMENSIONAL FLAME

For a preliminary assessment of the model performance, we first consider the case of a one-dimensional nonradiating flame propagating at velocity u_u , a configuration for which numerical computations with detailed transport and chemistry can be easily performed. This study provides in particular expressions for calculating the parameters B and E. Explicit values for these two parameters are, however, not provided here.

5.1 Problem Formulation

For the following description, it is convenient to utilize a reference frame attached to the flame with x denoting the distance across the flame. In the formulation, the subscript u and b denote, respectively, properties in the unburnt ($x \rightarrow -\infty$) and burnt ($x \rightarrow \infty$) sides of the flame. With this notation, the steady one-dimensional form of the continuity equation reduces to $\rho u = \rho_u u_u$, while the x -component of the momentum equation is replaced by $p = \text{constant}$, thereby simplifying the problem to that of integrating Eqs. 16 - 21 with the transport operator written in the form:

$$\rho \frac{D(\cdot)}{Dt} - \nabla \cdot \left(\frac{\rho D_T}{L_i} \nabla (\cdot) \right) = \rho_u u_u \frac{d(\cdot)}{dx} - \frac{d}{dx} \left[\frac{\rho D_T}{L_i} \frac{d(\cdot)}{dx} \right] \quad (22)$$

The boundary conditions for the problem become:

a) $x = -\infty$

$$\begin{aligned} \Gamma_{\text{CH}_4} &= \Gamma_{\text{CH}_4,u} \\ \Gamma_{\text{CO}} &= \Gamma_{\text{H}_2\text{O}} = \Gamma_{\text{CO}_2} = 0 \\ \Gamma_{\text{O}_2} &= \Gamma_{\text{O}_2,u} \\ h_T &= h_{T,u} \end{aligned}$$

b) $x = \infty$

$$\frac{d\Gamma_{\text{CH}_4}}{dx} = \frac{d\Gamma_{\text{CO}}}{dx} = \frac{d\Gamma_{\text{H}_2\text{O}}}{dx} = \frac{d\Gamma_{\text{CO}_2}}{dx} = \frac{d\Gamma_{\text{O}_2}}{dx} = \frac{dh_T}{dx} = 0$$

Introducing the variables:

$$\begin{aligned} y_{\text{CH}_4} &= \Gamma_{\text{CH}_4} / \Gamma_{\text{CH}_4,u} \\ y_{\text{CO}} &= \Gamma_{\text{CO}} / \Gamma_{\text{CH}_4,u} \\ y_{\text{H}_2\text{O}} &= \Gamma_{\text{H}_2\text{O}} / \Gamma_{\text{CH}_4,u} \end{aligned}$$

$$y_{\text{CO}_2} = \Gamma_{\text{CO}_2} / \Gamma_{\text{CH}_4, u},$$

$$y_{\text{O}_2} = (\Gamma_{\text{O}_2, u} - \Gamma_{\text{O}_2}) / \Gamma_{\text{CH}_4, u},$$

$$\theta = (h_T - h_{T,u}) / [(q_I + q_{II}) \Gamma_{\text{CH}_4, u}],$$

together with a new nondimensional coordinate $\eta = \int_0^x (u/D_T) dx'$, transform Eqs. 16-21 to

$$y'_{\text{CH}_4} - y''_{\text{CH}_4} / L_{\text{CH}_4} = -\varpi_I, \quad (23)$$

$$y'_{\text{CO}} - y''_{\text{CO}} / L_{\text{CO}} = \varpi_I - \varpi_{II}, \quad (24)$$

$$y'_{\text{CO}_2} - y''_{\text{CO}_2} / L_{\text{CO}_2} = \varpi_{II}, \quad (25)$$

$$y'_{\text{H}_2\text{O}} - y''_{\text{H}_2\text{O}} / L_{\text{H}_2\text{O}} = 2\varpi_{II}, \quad (26)$$

$$y'_{\text{O}_2} - y''_{\text{O}_2} / L_{\text{O}_2} = \frac{3}{2}\varpi_I + \frac{1}{2}\varpi_{II}, \quad (27)$$

$$\theta' - \theta'' = q_I \varpi_I + q_{II} \varpi_{II}, \quad (28)$$

where the prime denotes derivatives with respect to η . Also, the rates of fuel consumption and CO oxidation previously given in Eqs. 5 and 6 are scaled with $(\rho_u^2 u_u^2 \Gamma_{\text{CH}_4}) / (\rho D_T)$ to give the dimensionless rates ϖ_I and ϖ_{II} , and $\bar{q}_I = q_I / (q_I + q_{II}) = 0.6473$ and $\bar{q}_{II} = q_{II} / (q_I + q_{II}) = 0.3527$ represent the fractions of heat released through fuel consumption and CO oxidation. Equations 23-28 must be integrated with boundary conditions $y_{\text{CH}_4} - 1 = y_{\text{H}_2\text{O}} = y_{\text{CO}} = y_{\text{CO}_2} = y_{\text{O}_2} = \theta = 0$ at $\eta = -\infty$ and $y'_{\text{CH}_4} = y'_{\text{H}_2\text{O}} = y'_{\text{CO}} = y'_{\text{CO}_2} = y'_{\text{O}_2} = \theta' = 0$ at $\eta = +\infty$.

Further simplifications follow from assuming that the Lewis numbers appearing in Eqs. 23-27 are unity, enabling the integration of linear combinations Eqs. 25-28 with Eqs. 23 and 24 to give

$$y_{\text{CO}_2} + y_{\text{CO}} + y_{\text{CH}_4} = 1, \quad (29)$$

$$y_{\text{H}_2\text{O}} + 2y_{\text{CH}_4} = 2, \quad (30)$$

$$y_{\text{O}_2} + \frac{1}{2}y_{\text{CO}} + 2y_{\text{CH}_4} = 2, \quad (31)$$

and

$$\theta + \bar{q}_{II} y_{\text{CO}} - y_{\text{CH}_4} = 1, \quad (32)$$

as replacements for Eqs 25-28 in the following development.

5.2 The CO-oxidation region

As previously explained, reaction I is much faster than reaction II, and therefore takes place in a layer that is much thinner than the CO-oxidation region. Because of this relative scaling, for the analysis of this CO-oxidation region one can replace ϖ_I by a dirac-delta function located at the fuel consumption sheet. Also, due the translational invariance of the one dimensional problem, one can choose $\eta = 0$ as the location for the fuel-consumption sheet, thereby reducing the problem to that of integrating

$$y'_{\text{CH}_4} - y''_{\text{CH}_4} = -\delta(\eta) \quad (33)$$

and

$$y'_{\text{CO}} - y''_{\text{CO}} = \delta(\eta) - \varpi_{II} \quad (34)$$

supplemented by Eqs. 29-32. On the other hand, since the solution to Eq. 33 is simply $y_{\text{CH}_4} = 1 - \exp(\eta)$ for $\eta < 0$ and $y_{\text{CH}_4} = 0$ for $\eta > 0$, the problem further simplifies to that of integrating

$$y'_{\text{CO}} - y''_{\text{CO}} = -\varpi_{II} \quad (35)$$

with boundary conditions $y_{\text{CO}} - y'_{\text{CO}} = 1$ at $\eta = 0$ and $y'_{\text{CO}} = 0$ as $\eta \rightarrow \infty$. The dimensionless rate of CO oxidation is calculated from

$$\varpi_{II} = \left(\frac{\rho^2}{\rho_u^2} \right) \left(\frac{\rho \Gamma_{\text{CH}_4, u} k_{4f}}{u_u^2 / D_T} \right) \left(y_{\text{CO}} - \frac{K_5}{K_4} \frac{y_{\text{CO}_2} y_{\text{H}_2}}{y_{\text{H}_2\text{O}}} \right) y_{\text{OH}} \quad (36)$$

To integrate Eq. 35, use must be made of expressions $y_{\text{CO}_2} = 1 - y_{\text{CO}}$, $y_{\text{H}_2\text{O}} = 2$, $y_{\text{O}_2} = 2 - y_{\text{CO}}/2$ and $\theta = 1 - \bar{q}_{II} y_{\text{CO}}$, which follow from Eqs. 29-32 with $y_{\text{CH}_4} = 0$, and also of Eqs. 7 and 8 for the computation of the steady-state values of the variables $y_{\text{OH}} = \Gamma_{\text{OH}} / \Gamma_{\text{CH}_4, u}$ and $y_{\text{H}_2} = \Gamma_{\text{H}_2} / \Gamma_{\text{CH}_4, u}$.

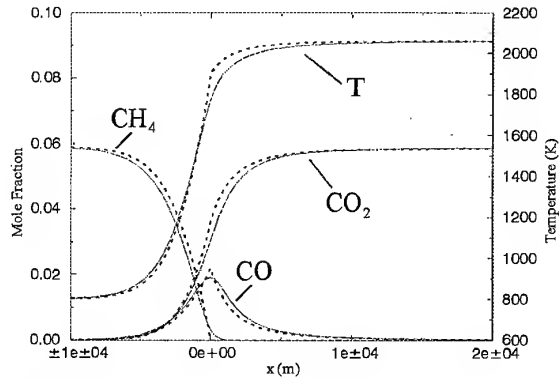


Figure 2: The variation of the temperature and of the CH_4 , CO and CO_2 mole fractions across the unstretched one-dimensional flame corresponding to test-case A., as obtained with detailed chemistry (solid lines), and with the two-step model with infinitely fast fuel consumption (dotted lines).

Integration of the autonomous Eq. 35 with the aforementioned boundary conditions can be easily performed with a simple shooting method. For simplicity in the calculations, constant values of $c_p = (c_p)_b$ and $\rho^2 D_T = (\rho^2 D_T)_b$ were assumed, and the variations of the density with composition were neglected, so that $\rho = \rho_b T_b / T$. The results for the simple model were compared with those of numerical integrations of the full conservation equations with detailed transport and chemistry (see [4] for a description of the chemical-kinetic mechanism employed). The "FlameMaster" code [5] previously used for instance in [6], is utilized in the detailed calculations. Conditions of test cases A and B were selected for the comparisons, namely, $T_u = 800$ K, $p = 18$ bar and $\phi = 0.6$, and $T_u = 900$ K, $p = 40$ bar and $\phi = 0.6$. In integrating Eq. 35 the function ϖ_{II} was evaluated with the value of u_u extracted from the detailed chemistry calculations.

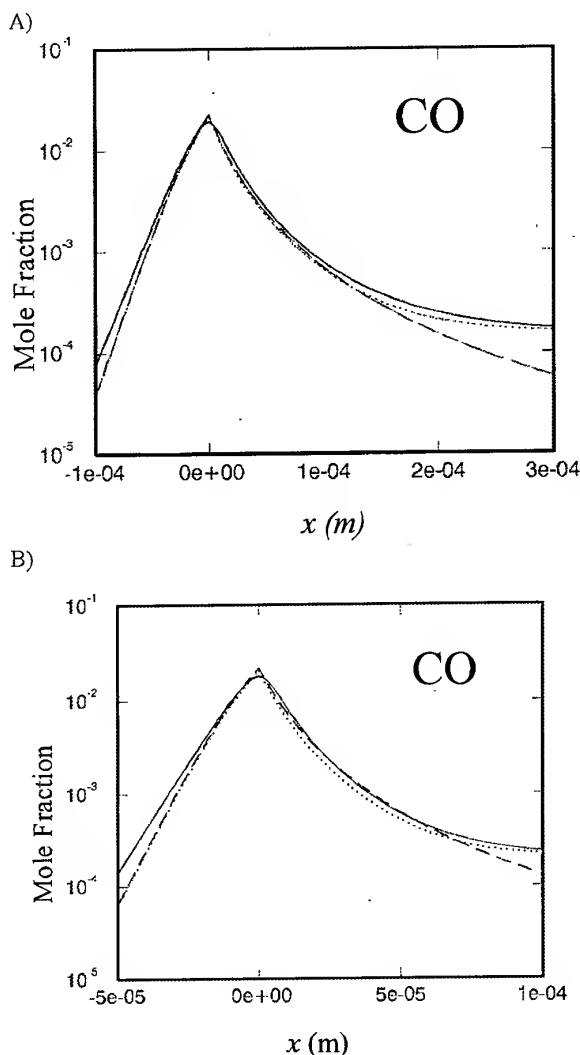


Figure 3: The variation of the CO mole fraction across the unstretched one-dimensional flame as obtained with detailed chemistry (solid lines), with the complete two-step model (dotted lines) and with two-step model with HO_2 recombination neglected (dashed lines). A) Test case A. B) Test case B.

The characteristic flame structure corresponding to the reduced two-step model is shown in Figure 2, along with the results of detailed chemistry calculations. Because of the infinitely fast fuel-consumption rate incorporated, the results of the two-step model exhibit an infinitely thin fuel-consumption layer across which the profiles of temperature, CH_4 and CO present discontinuities in derivatives, while the CO_2 whose rate of production is independent of ϖ_f , remains smooth. In the detailed calculations, however, the thin fuel-consumption layer remains of finite thickness. For the mutual comparison of the results of the two approaches, the point where the CO profile reaches its peak value is selected here as a suitable definition for the location of the fuel-consumption layer of the detailed calculations. Adoption of a different definition, e.g., point where the CH_4 concentration falls below an appropriate small threshold value, would result in a small relative translation of the different profiles by an amount of the order of the fuel-consumption layer thickness.

As can be seen, the two-step model adequately reproduces the shape and the peak value of the profile of CO mole fraction, with significant departures appearing only inside the fuel-consumption layer, where the detailed-chemistry profiles are rounded because of finite rate effects. To further illustrate this agreement, profiles of CO corresponding to the two sets of conditions previously mentioned are plotted in logarithmic scale in Figure 3. The resulting plots clearly show how the proposed formulation remains accurate as equilibrium is approached downstream from the flame, with the minimal departures in the final CO equilibrium values seen in Figure 3 being related to the truncated steady-state expression 4 utilized in the computations.

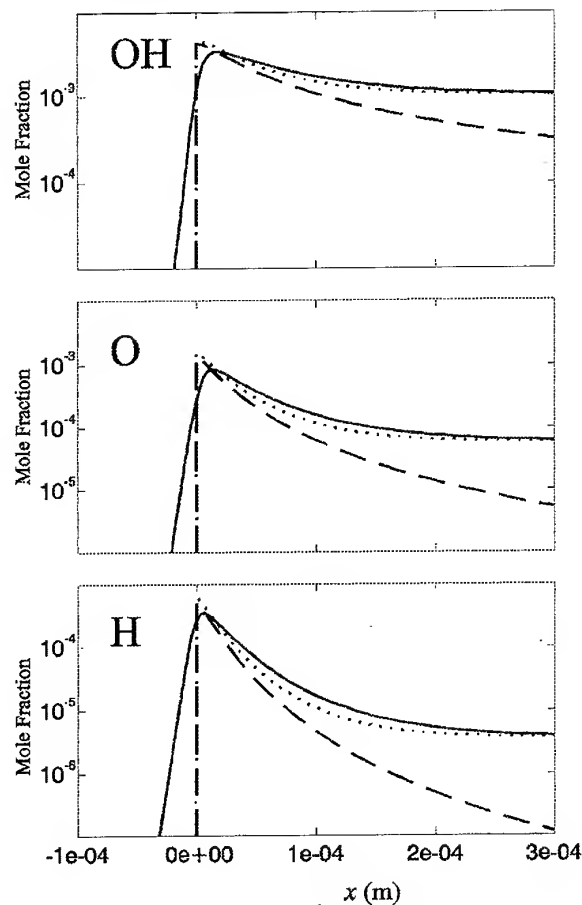


Figure 4: The variation of radical mole fractions across the unstretched one-dimensional flame as obtained with detailed chemistry (solid lines), with the complete two-step model (dotted lines) and with two-step model with HO_2 recombination neglected (dashed lines). Test case A.

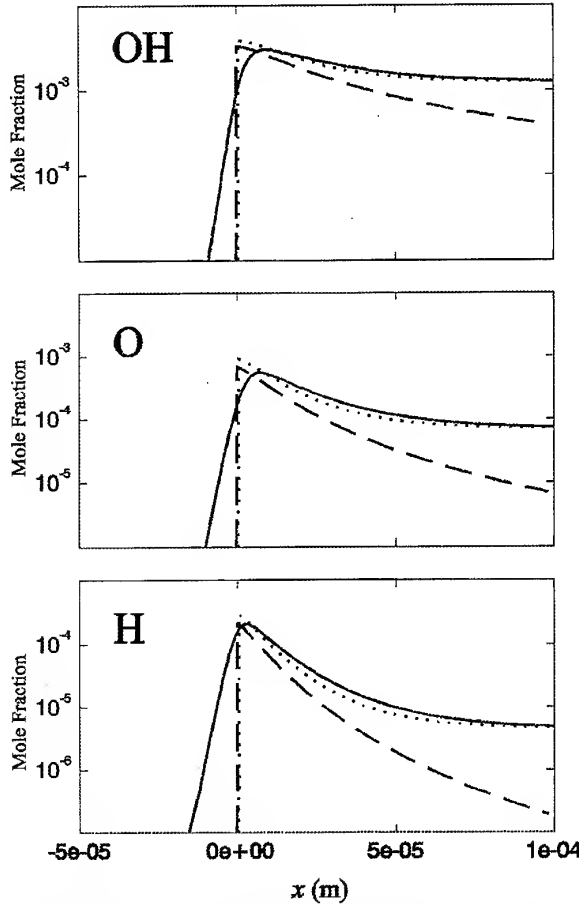


Figure 4 (cont.): The variation of radical mole fractions across the unstretched one-dimensional flame as obtained with detailed chemistry (solid lines), with the complete two-step model (dotted lines) and with two-step model with HO_2 recombination neglected (dashed lines). Test case B.

The proposed model also succeeds in predicting OH, O and H profiles across the flame, as can be seen in Figure 4, where radical mole fractions obtained from Eqs. 2, 3 and 8 are compared with results of detailed computations. The two-step model adequately describes both, the peak concentration and the profile evolution towards equilibrium. Because of fast radical depletion through fuel consumption, the radical concentrations of the detailed chemistry computations show very steep gradients upstream from the fuel consumption layer, rapidly approaching the zero value corresponding to the two-step model. It can also be seen that the radical profiles obtained with detailed chemistry peak slightly downstream from the location of maximum CO concentration, a characteristic not seen in the results of the two-step model that follows from the inner structure of the fuel-consumption layer [2].

5.3 The Limit of Irreversible Radical Recombination

Neglecting the reverse of the radical-recombination reaction III', a simplification adopted in previous asymptotic analyses [2, 3], leads to the reduced CO-oxidation rate previously given in Eq. 15. Since use of this more compact expression would somewhat reduce the effort required in computations, it is of interest to test the accuracy of the resulting approach.

Introducing Eq. 15 into Eq. 36 reduces the problem to that of integrating

$$y'_{\text{CO}} - y''_{\text{CO}} = -\Delta y_{\text{CO}}^{3/2} \quad (37)$$

with boundary conditions $y_{\text{CO}} - y'_{\text{CO}} = 1$ at $\eta = 0$ and $y'_{\text{CO}} = 0$ as $\eta \rightarrow \infty$. The Damköhler number

$$\Delta = \left(\frac{k_{4f}}{k_{3f}[M]} \frac{K_2(1-\gamma)\alpha_2^3}{K_6} \right)^{1/2} \left(\frac{\rho^2}{\rho_u^2} \right) \left(\frac{\rho \Gamma_{\text{CH}_4 u} k_{4f}}{u_u^2 / D_T} \right) \quad (38)$$

is a function of the temperature and, more weakly, of the mixture composition (through the function α_2) that usually takes fairly large values in the CO-oxidation region. For instance, evaluation of Eq. 38 at the equilibrium condition corresponding to the two test cases previously defined gives $\Delta = 9.36$ for $T_u = 800$ and $\Delta = 10.45$ for $T_u = 900$.

Results of integration of Eq. 37 with the aforementioned boundary conditions are included in Figures 3 and 4. As can be seen in the calculations, the reduced model adequately describes the CO profiles, including the peak values and the initial decrease due to CO oxidation. However, with irreversible radical recombination, the resulting description fails to reproduce the final equilibrium value, approaching instead a zero CO concentration far downstream from the flame. A similar behavior is found for the radical profiles, with significant departures appearing at somewhat smaller distances downstream. Since a detailed knowledge of the radical pool everywhere across the flame is fundamental to calculate NO emissions, the results in Figure 4 suggest that the complete model, including Eqs. 7 and 8 for calculating the concentrations of H_2 and OH, should be considered for increased accuracy in computations.

Despite the limitations exhibited, the reduced CO-oxidation ratio given in Eq. 15 describes the CO profile over about two orders of magnitude in CO mole fraction. To further investigate the resulting solution, use can be made of relatively large value of parameter Δ by considering the solution to Eq. 37 for $\Delta \gg 1$, an asymptotic limit also utilized in previous studies [3]. Since in this limiting case CO oxidation occurs in a region of thickness much smaller than that of the flame, we can neglect in the first approximation variations of Δ . The resulting solution is determined at leading order by a balance between diffusion and reaction as can be exposed by introducing the stretched variable $Y = \Delta^{2/5} y_{\text{CO}}$ and the associated stretched coordinate $\zeta = \Delta^{2/5} \eta$, thereby transforming the problem to that of integrating $\ddot{Y} - \Delta^{-2/5} \dot{Y} - Y^{3/2}$, with boundary conditions $\dot{Y} - \Delta^{-2/5} Y = -1$ at $\zeta = 0$ and $\dot{Y} = 0$ as $\zeta \rightarrow \infty$. Here, the dot denotes derivatives with respect to the coordinate ζ . Introducing the asymptotic expansions $Y = Y_0 + \Delta^{-2/5} Y_1 + \dots$ in the above equation and boundary conditions, and collecting terms in powers of Δ yields leading-order problem $\ddot{Y}_0 = Y_0^{3/2}$, $\dot{Y}_0(0) = -1$ and $\dot{Y}_0(\infty) = 0$, which can be readily integrated to give

$$Y_0 = \left(\frac{5}{4} \right)^{5/2} \left[1 + \frac{1}{4} \left(\frac{4}{5} \right)^{2/5} \zeta \right]^4 \quad (39)$$

Equation 39 determines the peak value of $y_{CO} = (5/4)^{5/2} \Delta^{-2/5}$ and also reveals a fast decay of the CO concentration according to $Y_0 \propto \zeta^{-4}$ as $\zeta \rightarrow \infty$. Because of the reaction-rate dependence on $y_{CO}^{3/2}$ appearing in Eq. 37 [7], the decaying rate changes downstream as the effect of convection becomes nonnegligible, which occurs at distances η of order unity ($\zeta \approx 0[\Delta^{2/5}]$) when the CO concentration y_{CO} reaches small values of order Δ^{-2} ($Y \approx 0[\Delta^{-5/8}]$), ushering in a convective-diffusive-reactive region whose structure is described in terms of the variable $y = \Delta^2 y_{CO}$ by integrating

$$y'' - y' = y^{3/2} \quad (40)$$

with leading-order boundary conditions $y \rightarrow \infty$ at $\eta=0$ and $y' \rightarrow 0$ as $\eta \rightarrow \infty$. The solution to this parameter-free problem, which is exhibited in Figure 5 for completeness, describes the evolution of the rate of decay of the CO mole fraction across this convective-diffusive-reactive region from the initial rate $y \propto \eta^{-4}$ of the diffusive-reactive region, to the slower rate $y \propto \eta^{-2}$ corresponding to the final convective-reactive balance that appears at distances $\eta \gg 1$. Clearly, this simplified analysis of irreversible radical recombination ceases being valid as the CO mole fraction emerging from Eq. 37 decreases to a value comparable to that of chemical equilibrium.

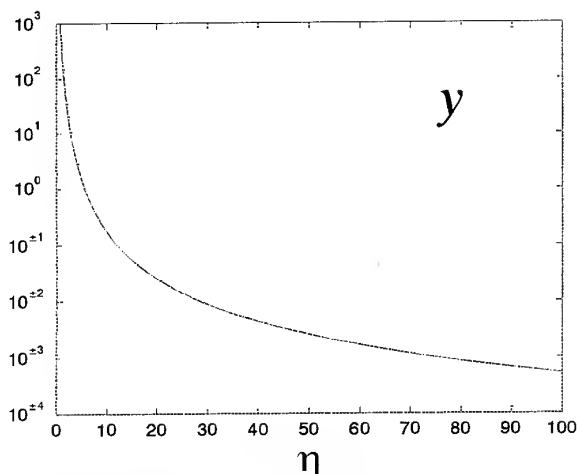


Figure 5: The variation of the function $y = \Delta^2 y_{CO}$ as obtained from integration of Eq. 40.

5.4 The Fuel-Consumption Layer

The previous asymptotic analysis $\Delta \gg 1$ yields in the first approximation $(y_{CO})_f = (5/4)^{5/2} \Delta^{-2/5}$ and $(y'_{CO})_f = -1$ as the peak value and slope of the CO concentration profile at the fuel-consumption layer, where the temperature, T_b is given in the first approximation by

$$\theta_f = \frac{T_f - T_u}{T_b - T_u} = 1 - (5/4)^{(5/2)} \bar{q}_I \Delta^{-2/5} \quad (41)$$

as follows from Eq. 32 with

$$T_b - T_u = \frac{(q_I + q_{II}) \Gamma_{CH_4 u}}{c_p} \quad (42)$$

These simplified results are useful in describing the inner structure of the fuel-consumption layer, which is studied below by activation energy asymptotics.

Owing to its small thickness, convection and CO-oxidation are negligible in the fuel-consumption layer, thereby enabling integration of a linear combination of Eqs. 23 and 28 to give

$$\theta - \theta_f = \frac{T - T_f}{T_b - T_u} = \bar{q}_I (\gamma \eta - y_{CH_4}) \quad (43)$$

where $\gamma = q_{II} / q_I = 0.5448$. Assuming that the modified Zeldovich number

$$\beta = \frac{E(T_b - T_u) \bar{q}_I}{R^\circ T_f^2} \quad (44)$$

is an asymptotically large quantity and introducing the rescaled variables $\phi = \beta y_{CH_4}$, and $\xi = \beta \eta$, reduces Eq. 23 to

$$\frac{d^2 \phi}{d\xi^2} = \frac{1}{2} \lambda \phi \exp(-\phi + \gamma \eta) \quad (45)$$

to be integrated with boundary conditions $\phi(-\infty) = -\xi$ and $\phi(\infty) = 0$. This canonical problem was previously encountered by Liñán [8] when studying the inner structure of diffusion flames in the premixed flame regime. In particular, he computed the value of the reduced Damköhler number

$$\lambda = 2 \frac{\rho^2 D_T}{\rho_u^2 u_u^2} \frac{B}{\beta^2} \exp[-E/(R^\circ T_f)] \quad (46)$$

as a function of the heat-loss parameter γ , obtaining $\lambda \approx 1.9$ for the particular value $\gamma = 0.5448$ of interest here. Incorporating this result enables the calculation of the flame velocity u_u from Eqs. 38, 41, 42, 44 and 46.

6. CONCLUSIONS

The main contribution of the present study is the development of a two-step reduced mechanism adequate for computation of premixed reacting flows under LPP combustion conditions. The analysis incorporates a fast fuel consumption step that produces CO, and a much slower CO-oxidation step. Results corresponding to one-dimensional flames indicate that the model describes satisfactorily the flame structure including profiles of all relevant intermediates and temperature. Furthermore, an Arrhenius rate with large activation energy is proposed here for the fuel consumption step. Equations relating the preexponential factor and the activation energy of the presumed rate with the laminar flame velocity, mixture composition, pressure, and upstream temperature are obtained through a rigorous asymptotic analysis of the resulting fuel consumption layer, thereby facilitating the selection of the reaction-rate parameters. Closure of the proposed two-step model through this selection and further testing are currently being performed.

7. ACKNOWLEDGEMENTS

This investigation was mainly supported by the European LOWNOX-III research project, contract BRPR-CT-95-0122, included in the EU sponsored Brite-Euram Aeronautics

program. Additional funding was obtained through the Spanish National Research and Technology Program, under grant CICYT-C95013002.

8. REFERENCES

- [1] Baulch, D., Cobos, C., Cox, R., Frank, P., Hayman, G., Just, Th., Kerr, J., Murrels, T., Pilling, M., Troe, J., Walker, R., Warnatz, J. *Combust. Flame* **98**, p. 59 (1994)
- [2] Peters, N. and Williams, F. A., *Combust. Flame* **68**, p.185 (1987).
- [3] Bui-Pham, M., Seshadri, K., and Williams, F. A., *Combust. Flame* **89**, p. 343 (1992).
- [4] Peters, N., in *Reduced Kinetic Mechanisms for Applications in Combustion Systems* (N. Peters, and B. Rogg, Eds.) *Lecture Notes in Physics* m15, Springer-Verlag, 1993, p. 3.
- [5] Pitsch, H., and Bolling, M.: "FlameMaster, A Computer Code for Homogeneous and One-Dimensional Laminar Flames Calculations". Institut für Technische Mechanik, RWTH-Aachen (1994).
- [6] Hewson, J., and Bolling, M., *Twenty-Sixth Symposium (International) on Combustion*, The Combustion Institute, Pittsburgh, PA, 1996, p. 2171.
- [7] Williams, F. A., *Combustion Theory*. Benjamin Cummings, Menlo Park, CA, 2nd editions, 1985, p. 162.
- [8] Liñán, A., *Acta Astronautica* **1**, p. 1007 (1974).

PAPER No. 12
Bollig, Linan, Lazaro & Sanchez
(presenter: A. Sanchez)

Question 1: M. Pourkashanian, University of Leeds, U.K.

Reduced reaction mechanisms like this should only be used for situations where they are validated. They tend to fail for diffusion flames. Was the mechanism reduced by examining the local Jacobians?

Answer:

We would agree with the comments. For reduction of the mechanism we did not examine the Jacobians, but rather used fluxes and sensitivities with respect to the flame velocities calculated.

Question 2: S. Wittig, University Karlsruhe, Germany

Did you analyze the predictions of Zeldovich NO_x made for the reduced mechanism? It appears as though the radical pool is not adequate and the concentrations not accurate enough to get nitric oxide correct.

Answer:

Yes, we did try, and you are right, the radical pool is inadequate so we over-predicted NO by 20%. However, the rates of both nitrous oxide production and the thermal mechanisms of NO prediction depend linearly on the O-atom concentration. Therefore, the departures found are not very significant, and are limited to the rate of NO production in the thin, fuel-consumption layer.

NUMERICAL SIMULATION OF THE REACTIVE FLOW IN A TUBULAR CHAMBER WITH DETAILED KINETIC EFFECTS

B. ZAMUNER, B. BOURASSEAU,
ONERA, BP 72, 92322 Châtillon Cedex, France

C. BERAT
TURBOMECA, 64511 Bordes Cedex, France

and

H. NIEMANN
University of Heidelberg, Germany

1. SUMMARY

Numerical simulation of turbulent flows in gas turbine combustors plays today a major role in the design of new concepts of combustion chambers. Indeed, the enforcement of strict environmental regulations urges gas turbine manufacturers to find out new solutions in order to reduce pollutants emissions. Lean premixed injection seems to be a promising way, but it poses the problem of flame stability induced by non extremely fast chemically controlled reaction rates.

In the present study, kinetic effects are incorporated in the turbulent CFD simulations of a methane/air tubular chamber developed at TURBOMECA by means of an original approach. First, a classical numerical code (DIAMANT), which solves the 3D Reynolds Averaged Navier Stokes (RANS) equations with an algebraic fast chemistry combustion model, is used to compute the main features of the mean flow. Then, a more sophisticated turbulent combustion model, called PEUL+ (Probabilistic Eulerian-Lagrangian) model, is coupled with the RANS solver in order to account for detailed kinetic effects. The PEUL+ model consists in solving the joint probability density function (PDF) transport equation by a Monte Carlo technique. This approach has the great advantage of directly taking into account, without modelling, chemical source terms coming from detailed kinetic mechanisms for fuel oxidation. To avoid CPU expensive computations, chemical source terms are evaluated, in this work, by an Intrinsic Low Dimensional Manifold (ILDM) technique, a new interesting tabulation method which keeps the complex behaviour of a detailed kinetic system, while describing its dynamics with only two or three progress variables.

The PEUL+ model with the ILDM table for methane-air mixture is applied to the tubular chamber at atmospheric pressure. Results are compared with infinitely fast combustion model simulations.

2. INTRODUCTION

Reactive flows in gas turbine combustors are characterized by a strong turbulence which enhances the mixing process between fuel and air, improves the combustion efficiency and eventually leads to shorter and more compact engines.

However, turbulent flows in combustion are difficult to study because they are by definition unsteady, and the coupling between the different physical phenomena is strongly non linear, making the use of simple analytic methods nearly impossible.

Solving the averaged balance equations in the framework of a numerical code is a good way to deal with this kind of complex flows. Indeed, the interest for numerical simulation of turbulent reactive flows in practical systems have been growing for the last decade due to the progress made in computer science and technology and the development of efficient numerical solvers which were specially optimized to be performant on supercomputers. Thanks to French Agency of Armament (DGA) fundings, we created, at ONERA, a three dimensional computational fluid dynamics (3D-CFD) code, called DIAMANT, and we obtained encouraging numerical results for the mean values of temperature, velocity and major species concentrations, in aircraft combustors configurations [1]. Today, this tool is widely used by french aeroengine companies in their design processes. The same type of approach is also currently employed in development departments of other gas turbines manufacturers [2-4].

The reason of this success may be explained by the enforcement of strict environmental regulations which urge aeroengines makers to better understand, and eventually, better control combustion mechanisms inside the engine and emission levels in the exhaust gases. Especially carbon monoxide (CO) and nitrogen oxides (NOx) are a real concern and will have to be further reduced in the future.

The need of more precise results concerning the main features of the flame and the hot products composition have considerably promoted the development of new models to describe the complexity of turbulent combustion. If conventional Mixed-Is-Burned models (chemistry is assumed infinitely fast) of Eddy-Break-Up type [5-6] were in the past sufficiently accurate to roughly predict the reactive zone location inside the combustor as well as the mean temperature profile in the exit plane, more sophisticated models must be implemented in 3D-CFD codes to improve the flame description and the pollutants prediction. However, incorporating a detailed chemistry mechanism to track the formation of several minor species with a turbulent

combustion model may lead to very huge computations, particularly in 3D geometries. We thus present in this paper the coupling between an advanced turbulent combustion model and an original low CPU-consuming approach to take into account detailed chemistry effects. This new tool is then applied to the prediction of the reactive flow in a tubular methane-air combustion chamber designed and tested at TURBOMECA.

3. BASIC EQUATIONS

As turbulent flows are truly unsteady, it is not possible, even numerically, to calculate all the instantaneous structures in a practical system. It is more convenient to define averaged quantities which can be computed in a relatively coarse mesh grid. When dealing with compressible flows, the Favre average procedure - noted $\bar{\cdot}$ - is commonly used. The averaged balance equations for a turbulent reactive flow then write :

mass balance

$$\frac{\partial}{\partial t} \bar{\rho} + \nabla \cdot \bar{\rho} \tilde{\mathbf{v}} = 0 \quad (1)$$

momentum balance

$$\frac{\partial}{\partial t} \bar{\rho} \tilde{\mathbf{v}} + \nabla \cdot (\bar{\rho} \tilde{\mathbf{v}} \tilde{\mathbf{v}}) = -\nabla \bar{p} - \nabla \cdot \bar{\rho} \tilde{\mathbf{v}}'' \tilde{\mathbf{v}}'' \quad (2)$$

energy balance

$$\frac{\partial}{\partial t} \bar{\rho} \tilde{h}' + \nabla \cdot (\bar{\rho} \tilde{\mathbf{v}} \tilde{h}') = \frac{\partial \bar{p}}{\partial t} - \nabla \cdot \bar{\rho} \tilde{\mathbf{v}}'' \tilde{h}'' + \bar{Q} \quad (3)$$

species balance

$$\frac{\partial}{\partial t} \bar{\rho} \tilde{Y}_k + \nabla \cdot (\bar{\rho} \tilde{\mathbf{v}} \tilde{Y}_k) = -\nabla \cdot \bar{\rho} \tilde{Y}_k'' \tilde{\mathbf{v}}'' + \bar{\rho} \tilde{W}_k \quad (4)$$

state law

$$p = \rho R T \sum_{k=1}^N \frac{Y_k}{\mathcal{M}_k} \quad (5)$$

In the above equations, \mathbf{v} is the velocity vector, ρ the density, p the static pressure, h' the total enthalpy - including heats of formation and kinetic energy -, Q the external heat source term, Y_k the mass fraction of species k , W_k the reaction rate of species k , \mathcal{M}_k the molar mass of species k and R the universal gas constant. Note that in equations (2), (3) and (4) the molecular diffusion terms have been omitted since they are negligible compared to the respective turbulent diffusion fluxes. A modelling is needed for the Reynolds stress tensor, the second term in the RHS of (2). The $k-\varepsilon$ model [7] is generally used, but more sophisticated approaches can be employed [8]. The turbulent transport terms in (3) and (4), which take the form of correlations between the fluctuating parts of the velocity and a scalar, are written with the classical gradient closure approach. Finally, the averaged reaction rates of each species must be expressed with an appropriate turbulent combustion model since the use of Arrhenius terms

with mean values of mass fractions and temperature would give very poor results. The modelling of \tilde{W}_k is a challenging task because the flame is usually very thin compared to the largest turbulent eddies and the interaction between a flame front and turbulent structures involves very complex physical phenomena. Theoretically, this term may be written in terms of a convolution between the local instantaneous chemical reaction rate and a multi-dimensional probability density function (PDF) $P(Y_i; \mathbf{x})$ as follows :

$$\bar{\rho} \tilde{W}_k(\mathbf{x}) = \int \rho W_k(Y_i) P(Y_i; \mathbf{x}) dY_i \quad (6)$$

In the above equation, it is possible to use the instantaneous reaction rate coming from the chemical kinetic mechanism. However, the multi-dimensional PDF which incorporates the whole statistics of the flow at the location \mathbf{x} , has generally a complex form and cannot be easily expressed.

4. THE TURBULENT COMBUSTION MODEL

An exact transport equation for the PDF function in the multi-dimensional space $(x_i; \psi_k)$ may be derived [9]. It follows :

$$\begin{aligned} \frac{\partial \bar{\rho} P}{\partial t} + \underbrace{\frac{\partial}{\partial x_j} [\bar{\rho} < v_j | \psi_i > P]}_{(I)} + \underbrace{\frac{\partial}{\partial \psi_k} [\bar{\rho} W_k P]}_{(II)} \\ + \underbrace{\frac{\partial}{\partial \psi_k} \left[\bar{\rho} < \frac{\partial}{\partial x_j} \left(\mathcal{D}_k \frac{\partial Y_k}{\partial x_j} \right) | \psi_i > P \right]}_{(III)} = 0 \end{aligned} \quad (7)$$

where ψ_k is the coordinate corresponding to the k th species in the multidimensional space and \mathcal{D}_k the molecular diffusion coefficient of the same species. The quantity noted $< \Phi | \psi_i >$ is the conditional mean of Φ , conditioned on the mass fractions values ψ_i . As the flow is highly turbulent, this kind of terms are often useful in order to analyse computational or experimental results. They actually represent the average value of Φ at a particular location \mathbf{x} when we only take into account the events for which the mass fractions (Y_i) are equal to the fixed vector (ψ_i). Conditional means appear in terms I and III of equation (7) and need to be modelled with particular closure assumptions. Term I accounts for the transport in the physical space by the mean flow - convection - and by turbulence effects - turbulent diffusion. Term III represents the transport in the composition space due to the micro-mixing, i.e., the mixing at small scales, and term II is related to the transport in the composition space due to chemical reactions. This last term can be easily computed with a given kinetic mechanism.

As mentioned in [9], the resolution of (7) with conventional approaches like finite-volume methods is very difficult to achieve, at least for a realistic thermochemical representation of the flow. The alternative is to solve (7) with Monte-Carlo techniques [10] which basically consist in constructing the discrete PDF $<P>$ from information given by a great number of lagrangian fluid particles that evolve in the physical and composition space. It can be shown that $<P>$ tends towards the solution of (7), P , when the number of tracked particles tends to infinity. The stochastic evolution of the particles is

governed by the following system of ordinary differential equations (ODE) :

$$\frac{dY_k}{dt} = \Xi_k + W_k \quad k=1, \dots, n+1 \quad (8)$$

$$\frac{dx_i}{dt} = \bar{v}_i + v_i'' \quad i=1, \dots, 3 \quad (9)$$

where Ξ_k is a stochastic term which accounts for the mixing at small scales and must obey to :

$$\langle \Xi_k | \psi_i \rangle = \left\langle \frac{\partial}{\partial x_j} \left(\mathcal{D}_k \frac{\partial Y_k}{\partial x_j} \right) | \psi_i \right\rangle \quad (10)$$

in order to get a consistent method. As n is the total number of species present in the mixture, the species $n+1$ is considered to be the enthalpy h , so it follows : $W_{n+1} = 0$. Obviously, equation (10) is not helpful to find a closure for the mixing term since it is nearly impossible to compute local gradients in the turbulent flame. We chose to use the simple IEM model (Interaction by Exchange with the Mean) [11], equivalent to the LMSE model (Linear Mean Square Estimation) [12]. Thus, it writes :

$$\Xi_k(Y_i) = \frac{\bar{Y}_k - Y_k}{C_a \tau_i} \quad (11)$$

where τ_i is a characteristic turbulent time - equal to k/ε - and C_a a constant of the model - taken equal to 2.0 in all our computations.

The fluctuating velocity v_i'' also needs to be modelled. Here, it is obtained from a stochastic procedure [13] which is constructed to respect both :

- i) the local cross-correlations of the fluctuating velocity components - the Reynolds stress tensor - directly evaluated from the $k-\varepsilon$ model
- ii) the lagrangian correlations which account for the relationship between the particle velocities computed at two neighbouring points on its trajectory. An isotropic Poisson law is retained here to simulate this stochastic process.

For steady problems on average, like it is often the case in aircraft combustors, the local number of particles injected through any inlet boundary is proportional to the local mass flow rate. Thus, the mean value of any quantity Y_k in the m th cell is then given by :

$$\bar{Y}_k = \frac{\sum_p \Delta t_p^m Y_k^p}{\sum_p \Delta t_p^m} \quad (12)$$

where Y_k^p is the lagrangian value of Y_k in the p^{th} particle which crossed the cell, and Δt_p^m the residence time of this particle in the cell. Mean reaction rates can also be calculated by the same way in order to evaluate the source-terms of the species balance equations. This type of hybrid method, mixing a conventional eulerian resolution of the flow and a Monte-Carlo lagrangian technique has been used at ONERA for many

years and it has served to build the so-called PEUL+ model (Probabilistic Eulerian Lagrangian Model) which was presented in detail and applied in several practical configurations [14-15].

In practice, the PEUL+ iteration procedure consists in firstly computing the mean flowfield by solving the balance equations (1) to (5) with a $k-\varepsilon$ model and an algebraic fast-chemistry turbulent combustion model, called CLE model [16] developed by SNECMA. This is done with the 3D-CFD numerical code DIAMANT which includes an implicit finite-volume solver with an upwind second-order numerical scheme. Then, the lagrangian step is performed by using the mean values of the first eulerian step as input data for the IEM model. Lagrangian mean values are evaluated by tracking several thousands of particles in the computational domain. A more accurate approximation of the mean reaction rates is then available and may be directly used as source -terms for equations (3). A new computation of the eulerian system can be performed without using the fast chemistry assumption. Three to four iterations, coupling eulerian and lagrangian calculations, are generally needed to converge [14].

5. THE ILDM METHOD FOR CHEMISTRY

When using the PEUL+ hybrid model, it is therefore possible to compute W_k in equations (8) with a detailed kinetic mechanism for fuel oxidation and pollutants formation. Up to forty species - with about 150 reaction steps - have already been tracked by this method [15], but computations become so huge that it is difficult to reach convergence in the iterative process. For methane oxidation at atmospheric pressure, several chemistry schemes have been recently developed and tested in laminar flames configurations [17-18]. They usually involve about 35 species and more than 250 reactions. Due to the broad range of chemical time scales associated with the elementary steps of a detailed chemical scheme, equations (8) can be very stiff, and an implicit ODE solver based on variable-step-size formulas must be employed. However, computational costs remain high and accurate PDF Monte-Carlo methods have been limited to a small number of degrees of freedom, typically less than ten. Moreover, reduced or global mechanisms are needed to simulate in this case the combustion process, but it turned out that this approach was not enough accurate everywhere in the composition space.

In order to improve the chemical description of the flow, a new method was recently proposed [19] to handle the chemistry in complex systems, the so-called Intrinsic Low-Dimensional Manifold (ILDM) method. This new tabulation technique has the great advantage of properly describing the dynamics of the chemical system with only two or three progress variables, while preserving the general behaviour of a detailed kinetic mechanism. The mathematical model has already been described in detail elsewhere [19], but it is interesting here to give some guiding principles. The fundamental idea is based upon the temporal analyses of the chemical evolution of a complex system. If we look, for instance, at the dynamics of a stoichiometric homogeneous methane-air mixture at atmospheric pressure, the maximum number of degrees of freedom is equal to n_s+1 , where n_s

corresponds to the total number of species involved in the kinetic mechanism - about 35 in this case. For adiabatic systems, some extra relationships between the principal variables may be written, exactly $n_s + 1$ where n_s is the number of independent elements - generally four to account for atomic conservations of C, O, H and N. Thus, the reaction space may be reduced to only $n_s + 1 - (n_e + 1) = n_s - n_e$ dimensions, which is still too large for turbulent flames computations. Figure 1 shows some examples of trajectories computed with a detailed mechanism and projected into the $\text{CO}_2\text{-H}_2\text{O}$ plane. Starting from different initial conditions in the $n_s\text{-}n_e$ -dimensional reaction space, the trajectories tend to bunch together and seem to follow a particular curve noted \mathcal{C} towards the equilibrium point. This curve may be regarded as a one-dimensional manifold since only one reaction progress variable is needed to determine the position of a particular point on the curve. The physical meaning of this observed behaviour lies on the fact that, before reaching the equilibrium point, the system has only one degree of freedom, most of the elementary reactions being in local equilibrium. Therefore, the 1D-ILDM method assumes that the relaxation of all trajectories towards the manifold, i.e. the curve \mathcal{C} , is infinitely fast. Thus, all thermochemical states are supposed to be located on the manifold and if the progress variable is known - Y_{CO_2} in our case - all the other mass fractions, the temperature and the CO_2 reaction rate are available. This information may be easily tabulated in order to be fastly retrieved in a typical computation involving a great number of chemical integration steps.

The improvement compared to conventional reduced mechanisms is also illustrated in Fig. 1. While mechanism reductions are mainly based upon *a priori* known partial equilibrium or quasi-steady state assumptions, the ILDM method provides an intrinsic estimation of the relaxation subspace which seems to be valid in a larger domain. Obviously, if fast time scales effects have to be represented in the simulation, the 1D-manifold assumption will not be valid any more, since chemical states of interest cannot be assumed to lie on curve \mathcal{C} . However, it is possible to show that a 2D-manifold, i.e. a curved surface in the 3D space, with two reaction progress variables, is able to improve the description of the system dynamics. For the stoichiometric methane-air mixture, events with time scales down to 5 μs can be simulated with a 2D-manifold method whereas 50 μs is the fastest time scale accessed by the 1D-ILDM technique. Higher dimensional manifolds can be generated to improve accuracy [20], but the costs for the table storage and the retrieval of information increase drastically.

For our specific application, we chose to use a 2D-ILDM table for methane-air combustion at atmospheric pressure. The mixture is supposed to be adiabatic with an initial temperature of 300 K for both fuel and air. The mixture fraction had to be added as a third principal variable in the table in order to deal with non-premixed flames commonly found in aircraft combustors. This table was previously assessed in perfectly stirred reactors and laminar flames configurations [20]. Preliminary tests in typical industrial applications also showed that the CPU total speed up factor compared to a skeletal

mechanism of 17 species and 71 reactions could increase up to 25.

6. THE TURBOMECA TUBULAR CHAMBER TEST CASE

As the PEUL+ILDM method was developed to allow computations in complex geometries, a numerical simulation of the reactive flow in a TURBOMECA tubular chamber was performed. The LESCALC chamber (Fig. 2) was specifically designed with the purpose of validating numerical codes regarding temperature profiles, pollutants emission and lean extinction limits. This combustor can operate at atmospheric pressure with liquid kerosene injection, but, here, we will only focus on a methane-air configuration with an overall mixture ratio of 0.025 ($\Phi = 0.42$), for which a stable combustion process has been experimentally observed. Gaseous fuel is injected (1) at 300 K through a swirling system that improves the mixing with air. The Reynolds number based on the injector diameter is approximately 45,000. The flow is therefore highly turbulent when it comes into the combustor. The local mixture, in this part of the chamber, is rich ($\Phi \approx 3.6$) but it rapidly mixes with air coming, at $T = 300$ K, from the multi-holes cooling (3) and the eight dilution holes (4). An air film (2), which is used to protect and cool the metallic shield, is also injected in the outer part of the combustor. To get a more precise idea of the different air inlets, the air mass flow rate distribution is given in table 1.

Injection Type	Mass flow rate (%)
Primary injection (1)	12.0 %
Shield film cooling (2)	6.4 %
Dilution holes (3)	36.4 %
Multi-holes cooling (4)	45.2 %

Table 1 : Distribution of the air mass flow rate between all the injection points

The third of the total mass flow rate comes from the dilution holes. It is three times higher than the air injected with the fuel mixture, leading to the formation of a large recirculation zone in the primary region of the chamber. The turbulent mixing between air, fuel and hot gases is therefore enhanced and the flame can ignite and stabilize in this intense stirred zone. Multi-holes cooling air promotes turbulence generation, but, above all, decreases the gas temperature and the overall equivalence ratio. The shield air film does not seem to have a strong influence on the internal aerodynamics, but it might influence combustion process since it is injected practically in the periphery of the flame stabilization zone.

The LESCALC chamber is being tested on TURBOMECA combustion facilities in order to investigate temperature profiles, mass fractions of major species and emission indices of CO and NOx with the help of thermocouples and sampling probes. However, experimental results concerning the configuration test presented above, are not yet available.

7. RESULTS AND DISCUSSION

Simulation with the fast chemistry model

For symmetry reasons, only one eighth of the chamber has to be discretized. The resulting structured grid mesh (Fig. 3) consists of 36,825 cells with 68 mesh points in the longitudinal direction - following x - 39 points in the radial direction and 16 in the azimuthal direction. We computed the turbulent reactive flow with the DIAMANT code and the fast chemistry turbulent combustion (CLE) model to get a first approximation of the flowfield. Mean streamlines, and the averaged fields of temperature and equivalence ratio, in the plane containing the axis and the dilution hole, are shown in figures 4 to 6.

First of all, the recirculation zone seems to be correctly captured by the numerical solver. The fuel coming into the chamber is pushed against the thermal shield by a mixture of air and hot products, which is transported against the main stream by the vortex strength. Combustion takes place approximately along the mean stoichiometric line as it is often the case with this type of modelling. For a fluid particle injected from the fuel inlet, temperature increases rapidly up to about 1750 K in the center of the recirculation zone. We also note that the air stream coming from the shield cooling strongly enhances the combustion process since it promotes the formation of a diffusion flame stabilized near the air film entrance plane. However, the high temperature levels observed in this region of the flow are likely overestimated due to the fast chemistry assumption. A turbulent combustion model with real chemistry effects will certainly improve the flow description and the prediction of the turbulent flame structure in this part of the combustor.

PEUL+/ILDM simulations

The lagrangian step, involving the PEUL+ model coupled with the ILDM method, was then performed by tracking the evolution of 20,000 fluid particles in the computational domain. Using this new technique to compute the chemical source terms, the CPU time decreased to one hour and half on a supercomputer Cray C94, compared to about 30 hours when integrating a skeletal mechanism of 17 species. One of the principal outcomes of the ILDM method lies on the fact that all the stiffness of the integration in the composition space is totally removed. Equation (8) is actually solved in its integrated form over a step size Δt and the corresponding chemical terms are directly given by a table look-up.

Computations were also carried out with 40,000 particles in order to evaluate the statistical errors effects. The differences between the two calculations regarding average values of temperature and mass fractions were so small that the first 20,000 particles computation was considered to accurately describe the main features of the reactive flow. Finally, with the purpose of reducing computational costs, mean velocity and turbulent fields were assumed to be correctly captured from the first eulerian (DIAMANT) step. Thus, no extra RANS iteration was performed as it should be the case in the usual PEUL+ iterative procedure. Obviously, this point should be investigated more precisely in future works, but some interesting results can be shown from now on, illustrating the

finite rate chemistry effects on the turbulent combustion process.

Mean temperature iso-lines are plotted in figure 7. We firstly observe that hot and cold zones are roughly distributed in a similar way compared to fast chemistry results. This is a well-known behaviour of conventional modelling. Mean temperature is often fairly predicted with these simplest approaches, at least where the combustion process is completed. However, the most noticeable chemistry effect appears in the slower temperature increase for the fluid coming from the fuel and the shield air film inlets. It seems that methane is first heated by primary mixing with hot gases, then burns when it enters the recirculation zone or when it reaches the shield film injection. Figure 8 confirms this hypothesis since it exhibits a poor combustion intensity near the axis of the chamber, within the stagnation plane region - where the axial velocity goes to zero due to counterflow effects (zone *a*). The diffusion-like flame is thus stabilized near the shield film injection which appears to play a major role in the combustion process. A large amount of methane is burned in the recirculation zone, though dilution air seems to complete fuel oxidation. Temperature in the center of the recirculation zone is higher for PEUL+ computations. It is likely caused by some effects of mixture fraction fluctuations since the exact PDF of Φ is evaluated by the Monte-Carlo method, while we use a presumed β -shaped PDF function in DIAMANT calculations.

Scatter plots of temperature in three different zones of the chamber are presented in figure 9. Zone *a* corresponds to the counterflow region near the axis, zone *b* is located very close to the shield air film injection, and zone *c* is placed near the center of the recirculation zone - where we observe the peak of CO. In zones *a* and *b*, many instantaneous values of the temperature reflect the mixing process, with no combustion effects. We may conclude that local extinctions or incomplete burning do occur in these regions of the flow. Such departures from equilibrium are often expected when turbulence effects strongly disturb the flame structure [21]. The discrepancy between the two computed mean values of temperature can be easily explained by this phenomenon. In the recirculation zone, extinction events are quite scarce, such that both models give very similar results - the difference with equilibrium value at the same equivalence ratio is probably due to mixture fraction fluctuations effects.

CO formation prediction

With the CLE model (Fig.10), mean concentration of CO is closely related to its equilibrium value at the appropriate mixture fraction. Therefore, CO formation is high in the bottom of the chamber, the richer region of the flow. The results of the PEUL+/ILDM simulation (Fig. 11) exhibit a completely different pattern. The peak of CO mass fraction is located in the recirculation zone, near the wall, while CO concentration vanishes near the shield, the fuel injection, and, of course, at the chamber exit. It is possible to explain this result if we focus our attention on the scatter values of Y_{CO} versus Φ in the characteristic zones of the flow (Fig. 12). As expected, we observe that the fast chemistry model always

predict an average CO concentration very close to its equilibrium value. However, in zones *a* and *b*, where many fluid particles remain unburned, scatter values and conditional mean clearly show that local extinctions have a strong influence on the final averaged result. The predicted mean CO mass fraction with the PEUL+ approach is rather comparable to the conditional mean value, one order of magnitude below the fast chemistry simulation.

The maximum of CO formation is observed where combustion is quite intense, around the stoichiometric iso-line. In this particular case (zone *c*), both predictions are nearly equivalent, even though fast chemistry assumption still leads to a slightly higher mean value. The fluid residence time in this region of the flow is relatively high, and chemical reactions have more time to evolve towards the equilibrium point. However, even in this case, mixture fraction fluctuations still have a strong impact on the final mean value due to the very steep slope of the equilibrium curve near stoichiometry.

We eventually obtained an emission index (*g* of CO in the exit plane per *kg* of fuel injected) of 4.0 with the PEUL+ simulation, value which seems to be in good agreement with the first experimental results. Unlike in the burning region, the CO index computed with the CLE model is five times smaller than the Monte Carlo value. It still illustrates the too strong dependency of this approach on equilibrium, since the fluid in this region is too lean to get correct CO levels from equilibrium assumption.

Even if the experimental data base is not already completely available, we may conclude that the PEUL+/ILDLM approach seems to improve significantly the numerical results concerning flame structure and CO formation in that case, without sacrificing CPU time.

8. CONCLUSIONS

Flame structures, combustion regimes and pollutants emission are often difficult to predict in aircraft combustors because they are closely related to the turbulent nature of the flow. Different types of combustion models with various complexity levels are available to deal with the challenging topic of turbulent reactive flows. Incorporating accurate chemistry effects in efficient models is usually prohibitive because of the huge amount of chemical computations needed to solve a practical problem. The Intrinsic Low Dimensional Manifold method, and more generally, all tabulation methods, offer a promising way to drastically reduce CPU costs. An application of the ILDM approach, coupled with a Monte-Carlo PDF transport method, to the flow prediction in an industrial 3D aircraft-type burner showed good trends, particularly concerning CO formation. It has been demonstrated that accurate prediction of this carbon oxide is related to the ability of representing precise turbulence-chemistry interaction phenomena, especially local extinctions. The PEUL+ model appears to be an interesting tool to capture, even partially, the physics of such a problem.

In order to improve the predicted values, a complete iterative procedure will be performed in the future. It will become possible to check finite rate chemistry effects on internal

aerodynamics. An other interesting issue is the prediction of lean extinction limits. The PEUL+/ILDLM approach is also planned to be applied on the same configuration in order to investigate this crucial problem which constitutes a real concern for aircraft turbine manufacturers.

9. ACKNOWLEDGMENTS

The main part of this work was performed at ONERA for the benefit of TURBOMECA under a contract from the French Agency of Armament (DGA/SPAé) which is gratefully acknowledged. The authors also thank Pr. J. Warnatz for permission to use and test the first version of the CH₄-air ILDM table.

10. REFERENCES

- [1] F. Pit, F. Dupoirieux, H. Tichtinsky, and F. Lacas, *Three dimensional numerical simulation for an aircraft engine type combustion chamber*, 9th ISABE, Athens, 1989
- [2] S. M. Correa, W. Shyy, *Computational Models and Methods for Continuous Gaseous Turbulent Combustion*, Prog. Energy Combust. Sci., Vol. 13, pp. 249-292, 1987
- [3] S. M. Correa, *A Review of NO_x Formation under Gas-Turbine Combustion Conditions*, Combust. Sci. and Tech., Vol. 87, pp. 329-362, 1992
- [4] H. Barths, N. Peters, N. Brehm, A. Mack, M. Pfitzner, and V. Smiljanovski, *Simulation of Pollutant Formation in a Gas Turbine Combustor Using Unsteady Flamelets*, Twenty-Seventh Symposium (International) on Combustion, Boulder, 1998
- [5] D. B. Spalding, *Concentration fluctuations in a round turbulent free jet*, Chem. Eng. Science, Vol. 26, 95, 1971.
- [6] B. F. Magnussen, H. Hjertager, *Sixteenth Symposium (International) on Combustion*, p. 719, 1976.
- [7] W. P. Jones and B. E. Launder, *Int. J. Heat. Mass Transfer*, Vol. 15, p. 301, 1972
- [8] J. P. H. Sanders, J. Y. Chen, and I. Gökalp, *Flamelet-Based Modeling of NO Formation in Turbulent Hydrogen Jet Diffusion Flames*, Combust. Flame, Vol. 111, pp. 1-15, 1997
- [9] S. B. Pope, *PDF methods for turbulent reactive flows*, Prog. in Energy Comb. Science, Vol. 11, pp. 119-192, 1985.
- [10] S. B. Pope, *Comb. Sci. and Tech.*, Vol. 25, pp. 159-174, 1981
- [11] C. Aubry, J. Villermaux, *Représentation d'un mélange de deux courants de réactifs dans un réacteur agité continu*. Chemical Engineering Ser., Vol. 30, pp. 457-464, 1975.

- [12] C. Dopazo, E. O'Brien, *An approach to the autoignition of a turbulent mixture*, Acta Astronautica,, Vol 1, 1239-1266, 1974
- [13] A. Ormancey, J. Martinon, *Simulation numérique du comptement de particules dans un écoulement turbulent*, La Recherche Aéronautique, pp. 353-362, n° 1983-5.
- [14] P. Caillaud, *Modélisation et simulation de la combustion turbulente par une approche Probabiliste Eulérienne Lagrangienne*, Thèse de Doctorat de l'Université de Rouen, 1994.
- [15] E. Varin, *Etude et développement du modèle de combustion turbulente PEUL. Application à la prédiction de la formation des suies dans les foyers aéronautiques*, Thèse de Doctorat de l'Université de Rouen, 1998
- [16] F. Ravet, L. Vervisch, *Modeling non-premixed turbulent combustion in aeronautical engines using PDF-generator*, AIAA paper n°98-1027, 1998
- [17] M. Frenklach, H. Wang, H. Goldenberg, G. P. Smith, D. M. Golden, C. T. Bowman, R. K. Hanson, W. C. Gardiner, V. Lissianski, *Gas Research Institute Technical report No GRI-95/0058*, November 1, 1995
- [18] C. Chevalier, PhD Thesis, Institut für Technische Verbrennung, Stuttgart University, 1993
- [19] U. Maas, S. B. Pope, *Symplifying Chemical Kinetics : Intrinsic Low-Dimensional manifolds in Composition Space*, Combust. Flame, Vol 88, pp. 239-264, 1992
- [20] D. Schmidt, J. Segatz, U. Riedel, J. Warnatz, and U. Maas, *Simulation of laminar Methane-Air Flames using Automatically Simplified Chemical Kinetics*, Combust. Sci. Tech., Vol 113-114, pp. 3-16, 1996
- [21] A. R. Masri, R. W. Bilger, and R. W. Dibble, *Turbulent Nonpremixed Flames of Methane Near Extinction : Probability Density Functions*, Combust. Flame, Vol 73, pp. 261-285, 1988

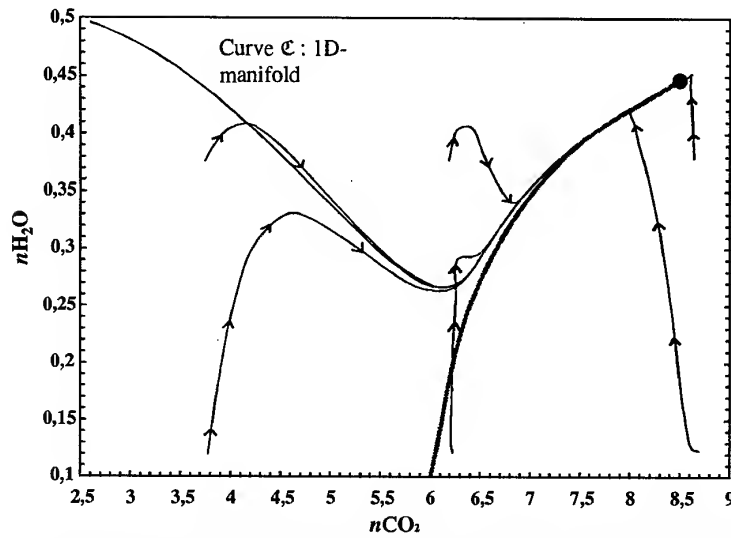


Fig.1 : Examples of trajectories in the $\text{CO}_2\text{-H}_2\text{O}$ concentrations plane computed with a detailed mechanism for a stoichiometric methane-air mixture at atmospheric pressure (grey thick line : conventional reduced mechanism)

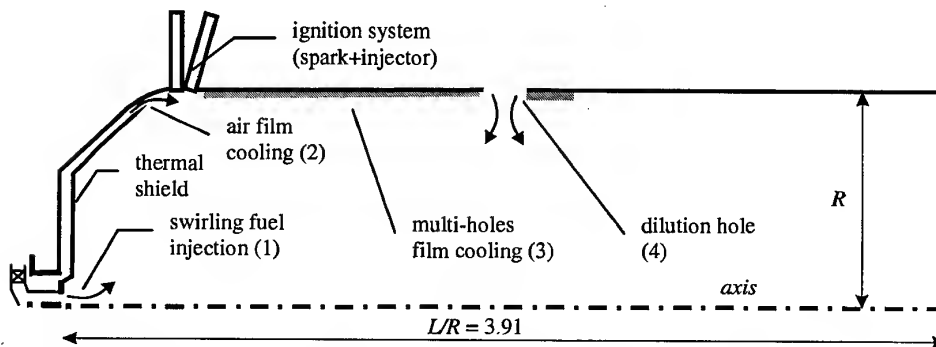


Fig. 2 : Sketch of the TURBOMECA tubular chamber LESALC

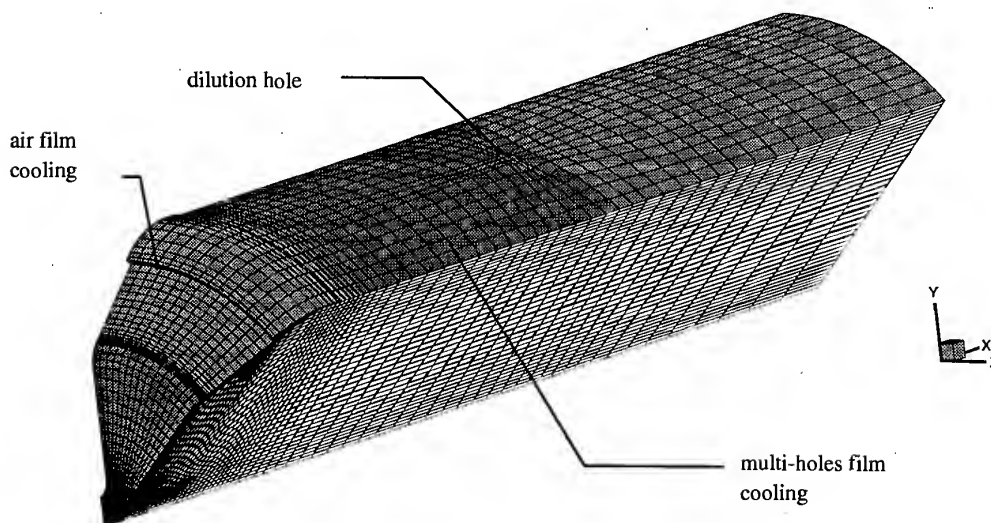


Fig 3. Three dimensional view of the grid mesh representing 1/8th of the combustor (36,825 cells)

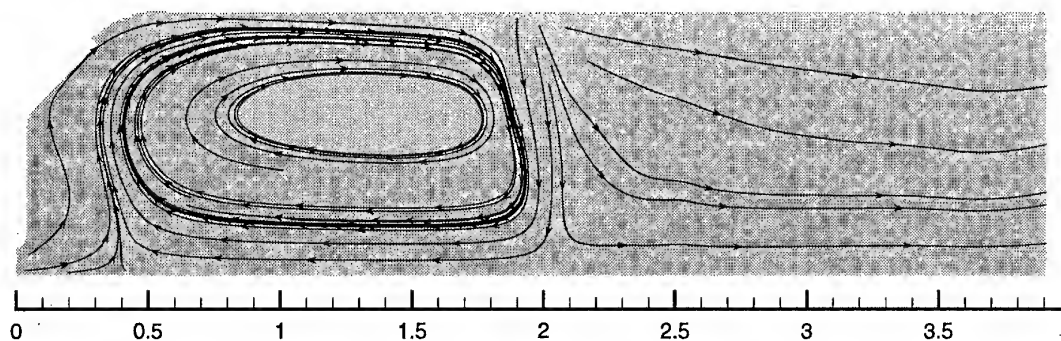


Fig 4 : Mean streamlines in the plane containing the axis and the dilution hole

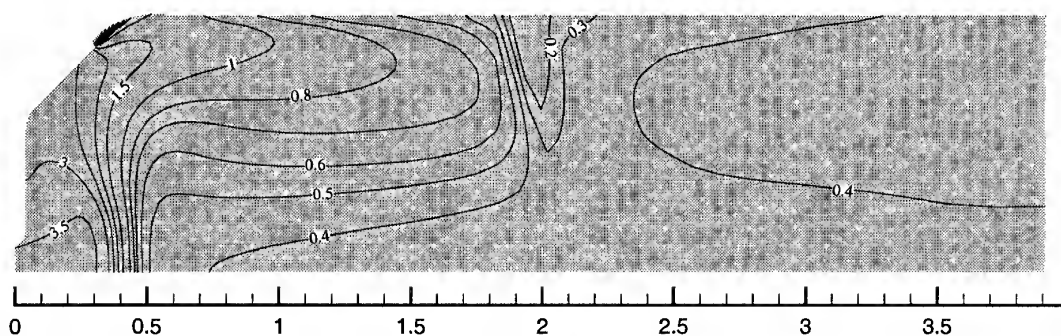


Fig 5 : Mean equivalence ratio computed with the RANS code (DIAMANT)

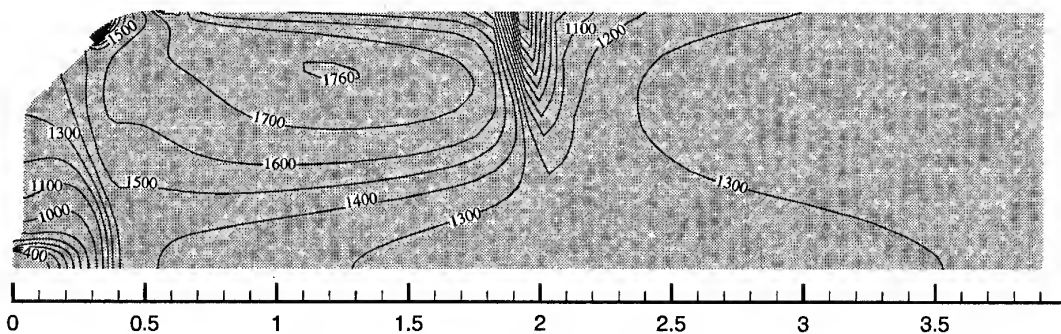


Fig 6 : Mean temperature iso-lines with the fast chemistry turbulent combustion model (values are in Kelvin)

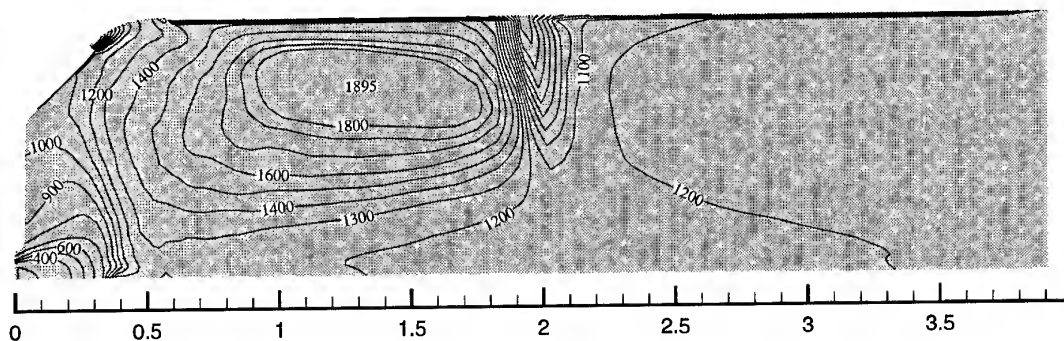


Fig 7 : Mean temperature iso-lines (in K) computed with the Monte-Carlo method (PEUL+ model)

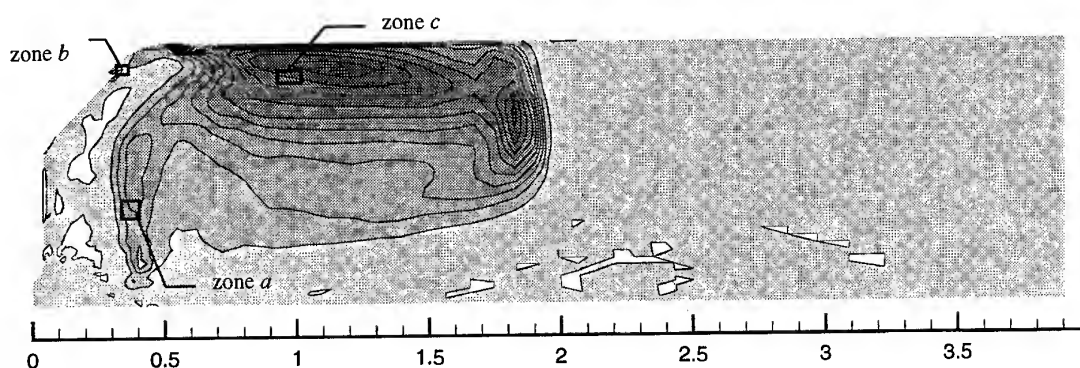


Fig 8 : Heat release rate computed with the Monte-Carlo method (combustion intensity is proportional to darkness ; rectangles show three regions of the flow *a, b, c* where detailed analyses were performed)

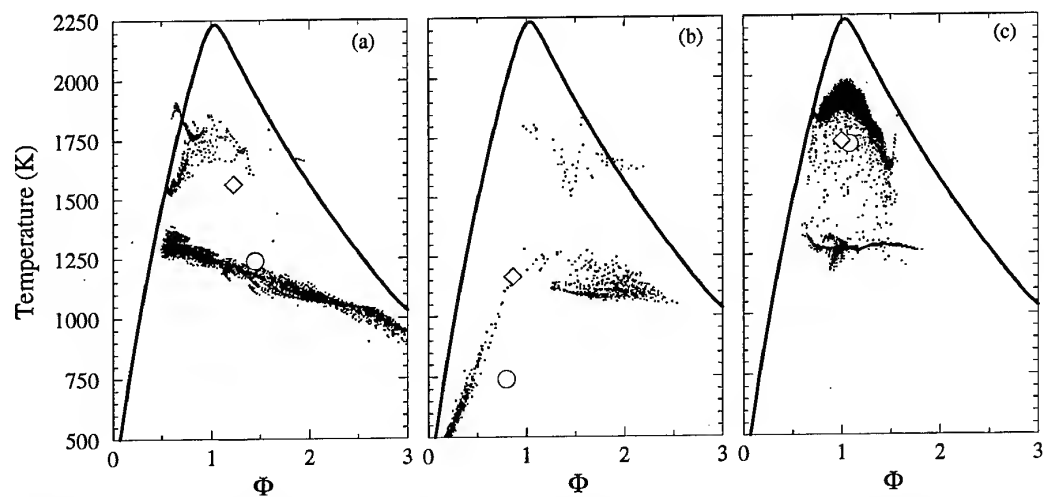


Fig 9: Temperature analyses in three different zones of the flame (black dots : lagrangian instantaneous values ; solid line : equilibrium curve ; diamond : fast chemistry mean value ; circle : PEUL+/ILDM mean value)

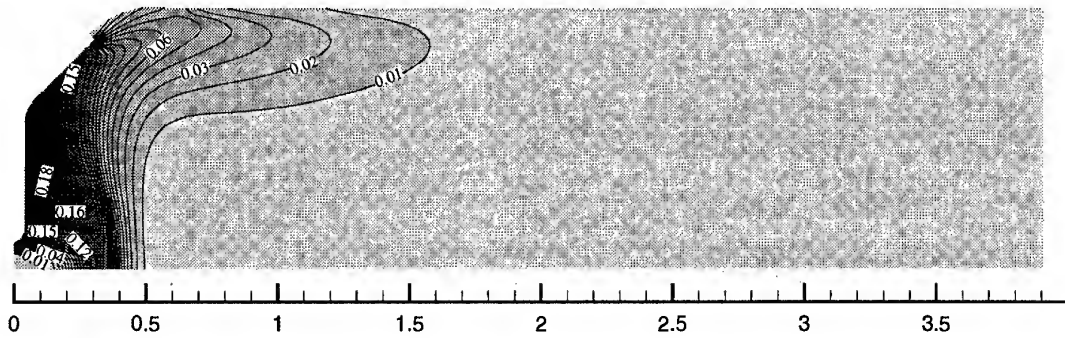


Fig 10 : CO mass fraction with fast chemistry and equilibrium assumptions (CLE model)

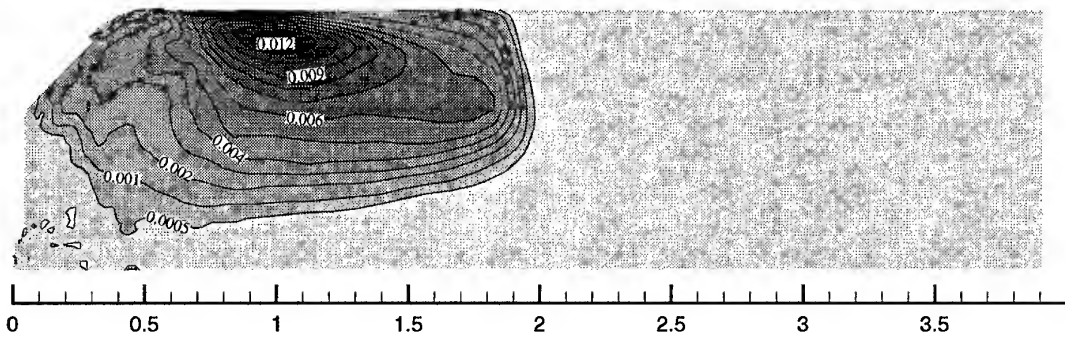


Fig 11 : CO mass fraction obtained from the PEUL+/ILDM method

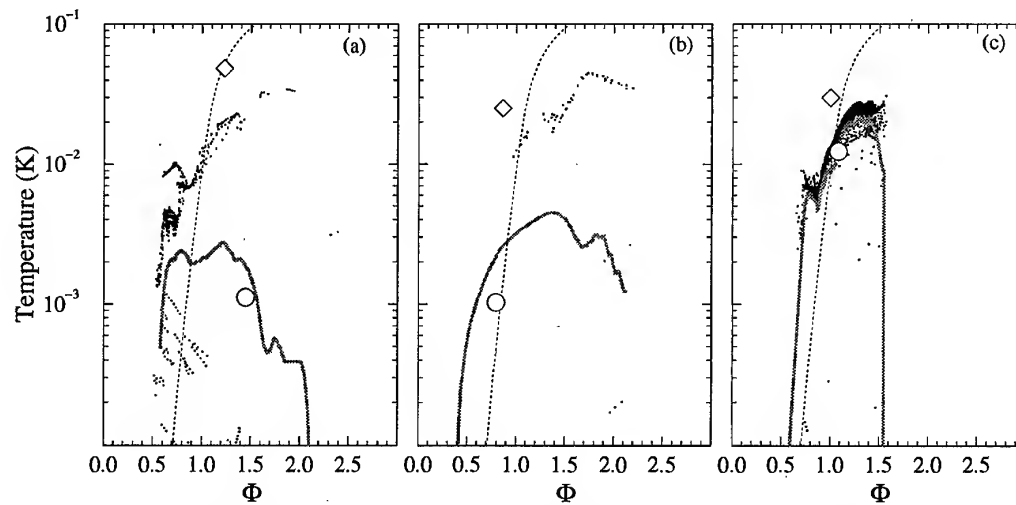


Fig 12: CO mass fraction analyses in three different zones of the flame (black dots : lagrangian instantaneous values ; dotted line : equilibrium curve ; grey solid line : conditional mean of CO ; diamond : fast chemistry mean value ; circle : PEUL+/ILDM mean value)

PAPER No. 13
Zamuner & Bourasseau
(presenter: B. Zamuner)

Question 1: C. Priddin, RR, U.K.

Why did not any of the particles presented in the temperature scatter-plot reach equilibrium?

Answer:

The problem lies with mixture fraction fluctuations around the mean values. The particles do not have time therefore, to evolve to equilibrium. This is essentially an unsteady effect.

Question 2: M. Razdan, RR-Allison, U.S.

A comment: At Allison, we have explored these methods using controlled experiments. What was found was that conventional methods over-predict temperature significantly.

Answer:

Yes, the look-up tables in the computations are adiabatic, whereas actual experiments have non-adiabatic effects.

Kerosene Combustion Modelling Using Detailed and Reduced Chemical Kinetic Mechanisms

M. Cathomet, D. Voisin, A. Etsouli, C. Sferdean, M. Renillon, J.C. Boettner and P. Dagaut
 Laboratoire de Combustion et Systèmes Réactifs - CNRS
 1C Avenue de la Recherche Scientifique
 45071 Orléans Cédex 2
 France

1. INTRODUCTION

The growing cost of experimental tests in aircraft combustors and the efforts to reduce development time, lead combustor designers to develop computer programs in order to predict the performances of the combustors. The contribution made by these calculation methods has become all the more important, given that the increase in severity in military engine cycle and requirements for reducing pollution in civil aircrafts needed different types of combustor structure to be designed.

In many of these combustion models, chemical kinetics is reduced to a single-step empirical expression or to global multistep schemes. However, a better knowledge of the chemistry of combustion is essential for the quality of the prediction of many important phenomena like ignition delays, flame speed, blow-out, engine efficiency and pollutant emissions. Therefore, several studies in the field of chemical kinetics have been devoted to the conception of reaction mechanisms with growing complexity for the representation of kerosene oxidation.

In a previous study [1] on kerosene oxidation in a jet-stirred reactor at atmospheric pressure, a quasi-global model was proposed to reproduce the concentration profiles of the major chemical species. Unfortunately, quasi-global mechanisms cannot be used in the whole range of operating conditions of a combustion chamber. In fact, the validity domain of chemical kinetic schemes in terms of temperature, pressure and equivalence ratio has to be large enough in order to include the wide range of operating conditions of modern combustors. This is particularly true for the prediction of carbon monoxide and unburned hydrocarbons which are intermediate products of combustion mainly at low ratings, or for the prediction of nitrogen oxides which are mostly produced at high temperature and pressure.

Because of the superiority of detailed chemical kinetic mechanisms to predict combustion chemistry features, we have begun to develop detailed mechanisms for the oxidation of higher hydrocarbons in a wide range of temperatures. However, very large mechanisms cannot be introduced into complex multi-dimensional fluid dynamics codes for the modelling of the combustion of practical fuels. For this reason, we have also used reduction methods for the simplification of large mechanisms in order to keep the essential features of the chemistry in realistic combustor configurations.

Previous studies in jet-stirred reactors [1,2] and in premixed flames [3,4] have shown similar combustion behaviours between kerosene and n-decane, concerning the nature of the products and the reactivity. For this reason, a detailed reaction mechanism for the oxidation of n-decane has been used to describe the combustion of kerosene in a jet-stirred

reactor up to 40 atm, and a good prediction of the experimental concentration profiles of the major species has been obtained [1].

This mechanism has been recently updated, and a general improvement of the predictions was obtained, especially for unburned hydrocarbons. In addition, a reduced mechanism was developed. However, in the conditions of our experiments, several aromatics have been found in significant amounts among the products of kerosene oxidation [2], whereas the oxidation of n-decane yields much less aromatics [2,5]. This is due to the presence of mono-aromatics in kerosene, these compounds being the main source of benzene, toluene and xylene formed in kerosene combustion.

Naphthenes are another class of compounds constituting kerosene. To take into account the presence of these different families in kerosene, we have added to the mechanism of n-decane oxidation, the detailed mechanisms of the oxidation of toluene and cyclohexane.

2. EXPERIMENTAL STUDY OF THE OXIDATION OF KEROSENE

2.1 Experimental device

The experimental set-up has been described previously [1,2]. It includes a fused silica jet-stirred reactor enclosed in a stainless steel pressure resistant jacket filled with insulating material. A regulated nitrogen flow in the outer part of the reactor balances the pressure inside the reaction cell, allowing operation at pressures as high as 40 atm. The reactor is heated by a regulated electrical resistance system.

The liquid fuel is prevaporized in a heated vaporizer, the vapours are mixed with a preheated nitrogen and oxygen flow at the entrance of the injectors. The fuel is delivered at a precise flow rate into the vaporizer by a liquid pump, and the flow rates of the gases are measured and regulated by mass flow controllers. Because of the high dilution of the fuel (0.1% or less by volume), no flame occurs in the reactor and operation at steady state is possible.

The temperature of the gases inside the reactor is measured by moving an uncoated chromel-alumel thermocouple of 0.16 mm diameter, along a whole diameter of the reactor. Gas samples are collected at low pressure (20-30 Torr) through a sonic quartz probe. In this study, in order to follow the fuel oxidation from low to high conversion, the temperature of the gases in the reactor was varied stepwise at a constant mean residence time. Several gas chromatographs equipped with capillary columns and a GC/MS system were used for the analyses of the samples.

2.2 Experimental results

The oxidation of TR0 kerosene (Jet A1 aviation fuel) was studied in the temperature range 550-1200K between 10 and 40 atm, for an initial fuel concentration ranging from 0.025% to 0.1% at equivalence ratios extending from 0.5 to 1.5. The concentration profiles of stable species were obtained for different mean residence times in the reactor (0.5s to 2s), corresponding to reaction yields ranging from low conversion to the formation of the final products.

The concentrations of more than 30 species have been monitored [2]. Among them, the major products are :

- carbon dioxide, carbon monoxide and hydrogen
- C_4 to C_9 alkenes
- smaller unsaturates (alkenes, dienes, alkynes)
- lower alkanes (methane, ethane and propane)
- monoaromatics
- oxygenates (aldehydes, cetones, ethylene oxide)

As shown previously [2], in the temperature range of this study, the oxidation of kerosene follows different regimes :

1. At temperatures lower than 750K, the formation of several oxygenated compound, and the existence of a negative temperature coefficient, are characteristic of the cool flame regime already observed in similar experiments on n-heptane and n-decane oxidation [6,5].
2. At temperatures higher than 750K the major oxygenated intermediate detected is formaldehyde. Other main products are carbon oxides, hydrogen, alkenes, lower alkanes, acetylene, and C_6 - C_9 monoaromatics. These products of the high temperature oxidation regime have also been found in premixed kerosene flames [3,4].

3. KINETIC MODELLING OF THE OXIDATION OF KEROSENE IN A JET-STIRRED REACTOR

In this study, the detailed mechanism of n-decane oxidation [1] has been updated and completed by those of cyclohexane and toluene, to model the oxidation of kerosene.

3.1. Detailed mechanism for the oxidation of n-decane

The main sequences of reactions occurring in the high temperature oxidation and ignition of higher alkanes in the intermediate and high temperature ranges have been described in several papers [7,8,9]. The present mechanism includes the following steps :

- a. initiation by thermal decomposition or through reaction between the fuel and molecular oxygen,
- b. abstraction of H atoms from the fuel by reactions with small radicals. These reaction steps form different n-decyl radicals depending on the site of the abstracted H atom,
- c. thermal decomposition or isomerization of n-decyl radicals,
- d. reactions of smaller intermediates (alkyl radicals and olefins) formed by the reactions of n-decane and n-decyl radicals, yielding small alkanes, diolefins, alkynes and carbon monoxide 'through the production of aldehydes).

Because many small hydrocarbons are formed as intermediate products, the proposed detailed chemical kinetic reaction mechanism has a hierarchical structure. It has been validated by extensive comparison between experiments and simulation not only for the oxidation of n-decane itself, but also for the combustion of smaller intermediate hydrocarbons studied separately. This mechanism has been recently updated following the same procedure.

3.2. Detailed mechanism for the oxidation of cyclohexane
Reactions of cyclic compounds (naphtenic and aromatics) are less well known than those of alkanes because of the complexity introduced by the reactions steps involving a carbon cycle. During the oxidation process of naphtenic hydrocarbons, once the carbon cycle is broken, the reactions of the fragments (radicals or molecules) belong to the submodels of smaller hydrocarbons oxidation which has been established before. However, the chemical processes occurring before the rupture of the cycle are more speculative.

For the modelling of cyclohexane oxidation, these steps have been added to the reactions of hydrocarbons issued from the cycle rupture, and their elementary mechanisms and rate constants have been taken or estimated from existing data in the literature. The resulting mechanism has been validated by an experimental study of cyclohexane oxidation at 10 atm in the jet-stirred reactor. This mechanism predicts with reasonable accuracy the experimental concentration profiles of the fuel and the oxidation products.

3.3 Detailed mechanism for the oxidation of toluene

The mechanism for the oxidation of toluene has been built by adding to a previous mechanism developed in the laboratory [10], which includes the formation of benzene and its reactions, the reactions of toluene from the mechanism of Emdee et al [11]. The benzene oxidation mechanism has been updated and validated by new experimental data obtained at 10 atm in a jet-stirred reactor.

3.4 Comparison with experiments

Kerosene is represented by a surrogate model comprising 78% n-decane, 9.8% cyclohexane and 12.2% toluene by volume. Examples of comparisons between experimental and computed concentration profiles, using the described mechanism for, are given in figures 1-4 corresponding to different pressures and equivalence ratios. Reasonable agreement is found between computed and experimental profiles for major products. Although some discrepancies remain between computations and experiments, the overall predictive capabilities of the new mechanism are better than those of the previous one. The main improvements regarding the computation of the concentrations of several intermediates are :

- benzene concentration is, in most conditions, predicted within a factor of 1.5 (whereas benzene formation according to the pure n-decane mechanism used before was much lower than observed experimentally),
- the prediction of the concentrations of C_4 to C_9 alkenes, which was within several order of magnitudes with the previous model, has been greatly improved,
- the prediction of lower hydrocarbons concentrations has also been generally improved.

3.5 Discussion

The improvements obtained with the new mechanism for the prediction of intermediates in jet A kerosene oxidation is encouraging. This study shows that a commercial fuel can be represented, by a surrogate model comprising several pure hydrocarbons. A more realistic representation of the aromatic fraction will be used, in the future, to predict not only benzene, but also other aromatic products (toluene and xylenes).

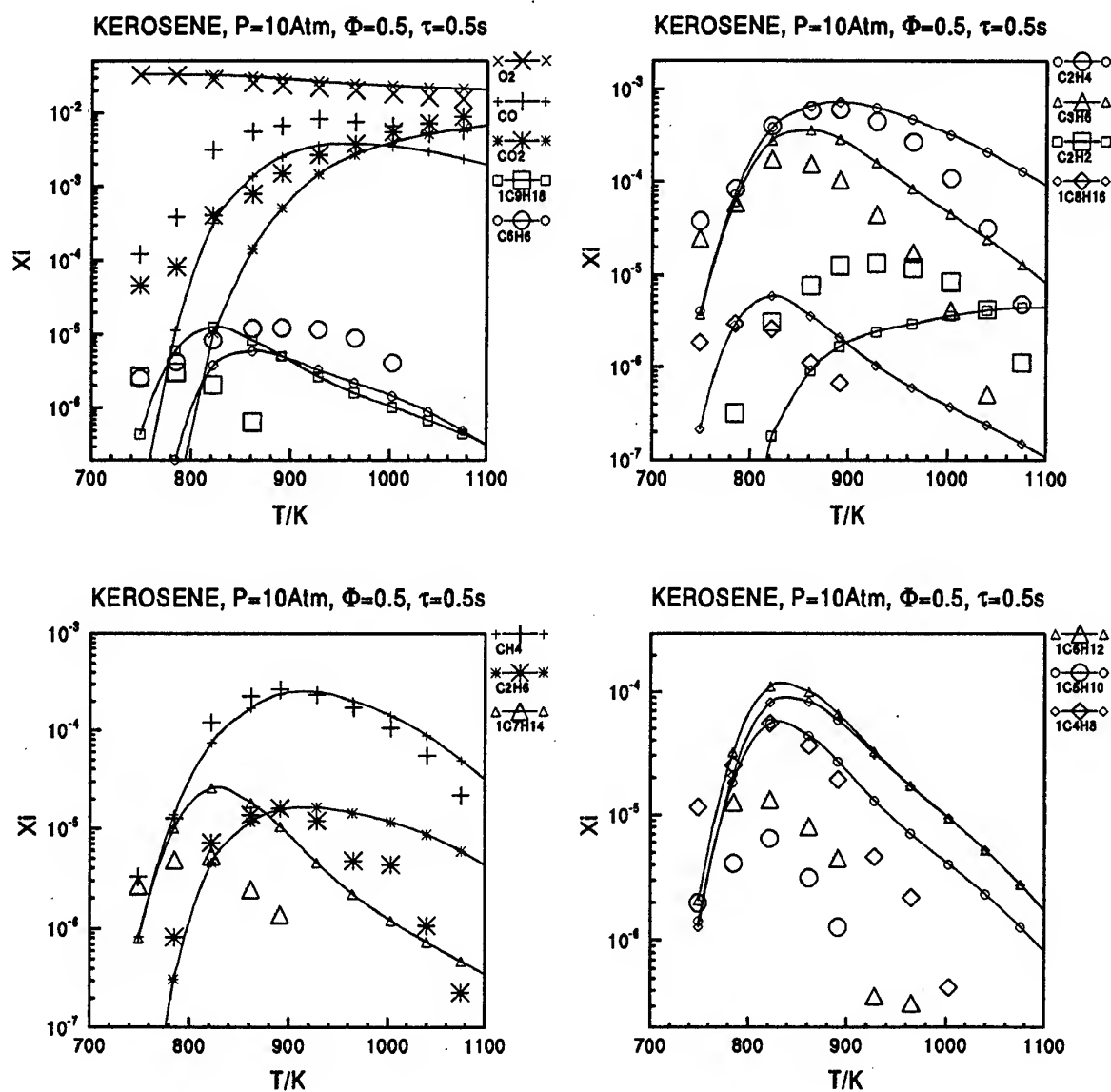


Figure 1 : Comparison between computed (lines and small symbols) and experimental (large symbols) concentration profiles in the jet stirred-reactor at 10 atm. Equivalence ratio = 0.5. Initial mole fraction = 10^{-3}

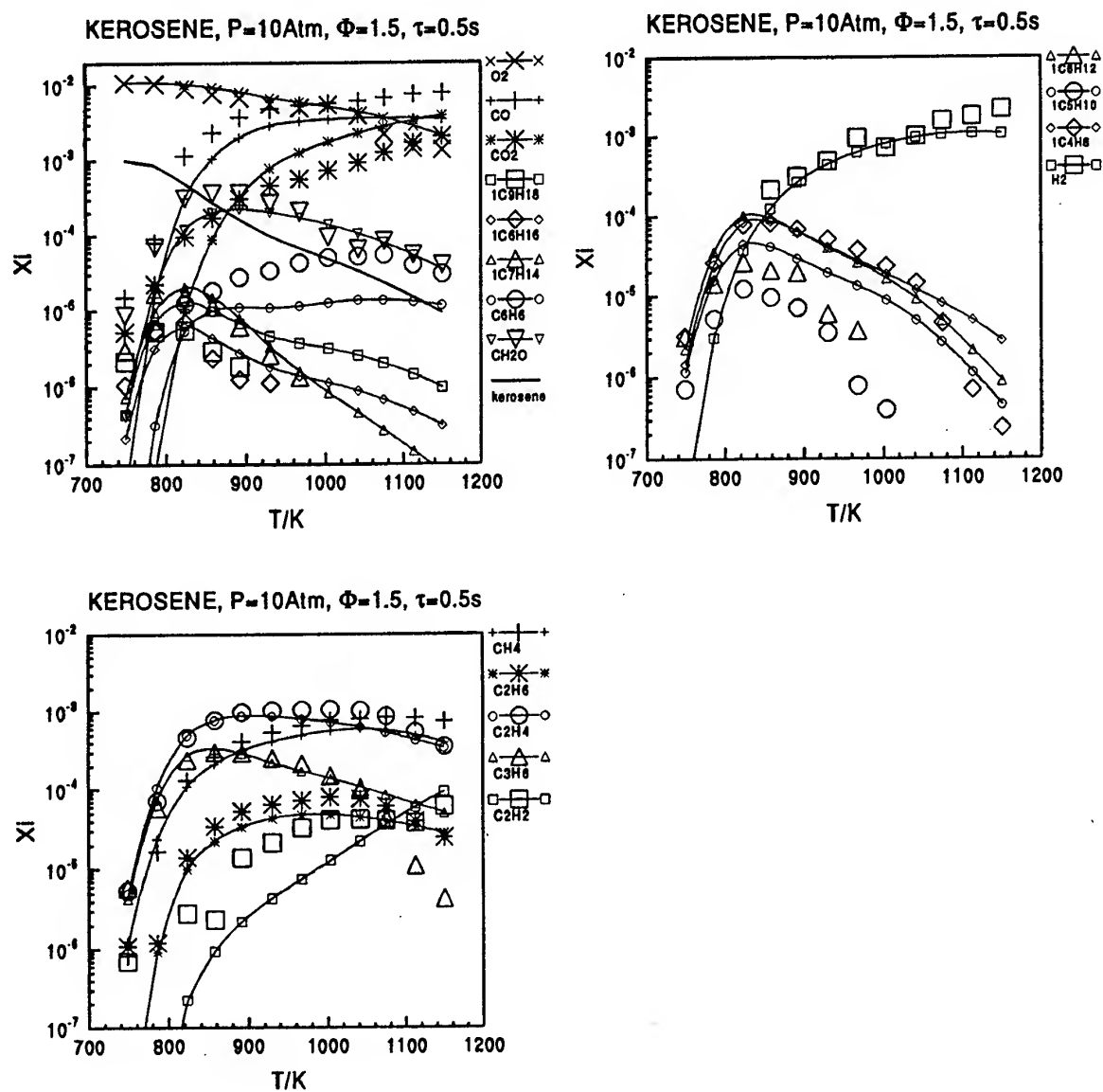


Figure 2 : Comparison between computed (lines and small symbols) and experimental (large symbols) concentration profiles in the jet stirred-reactor at 10 atm. Equivalence ratio = 1.5. Initial mole fraction = 10^{-3}

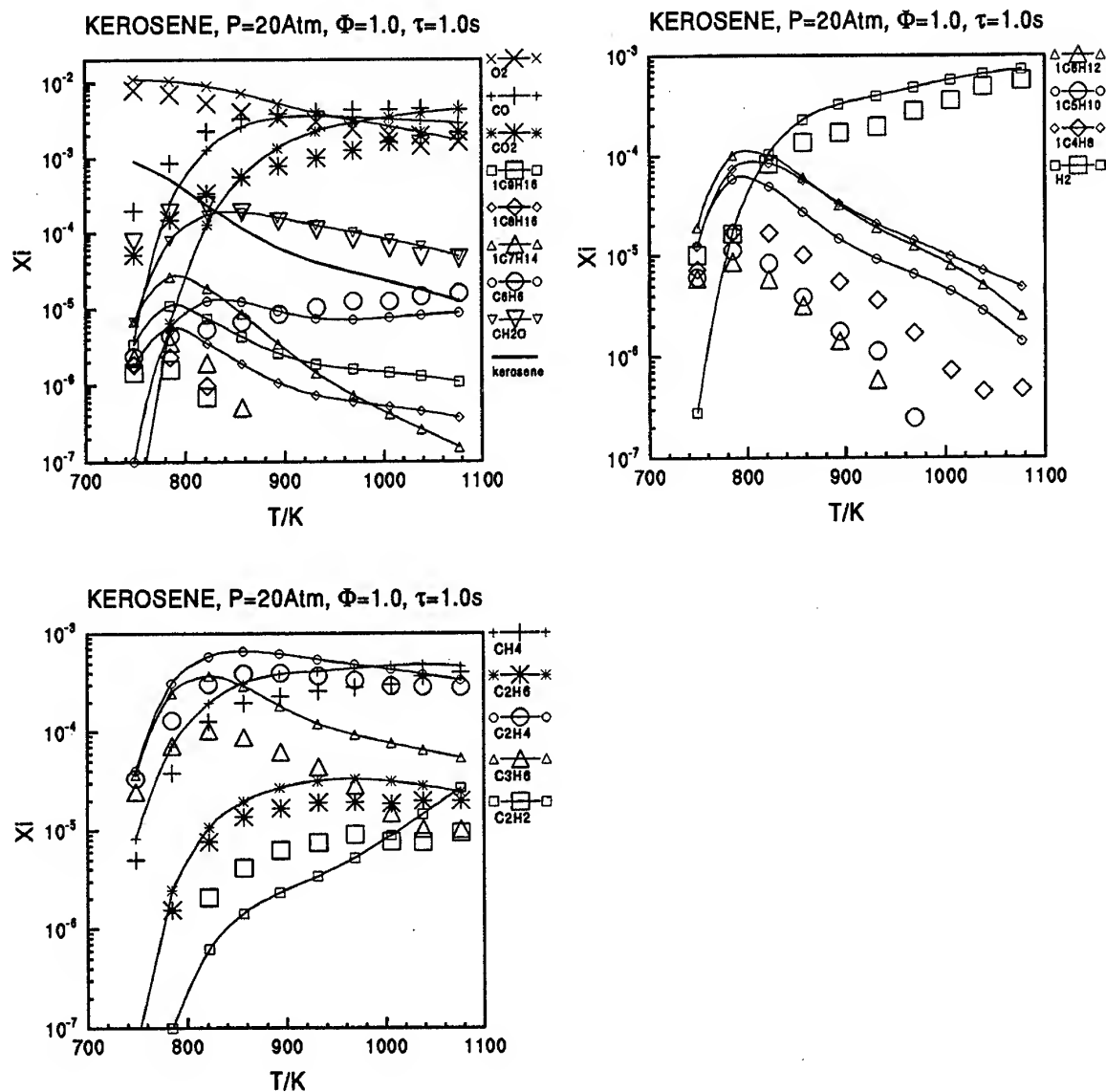


Figure 3 : Comparison between computed (lines and small symbols) and experimental (large symbols) concentration profiles in the jet stirred-reactor at 20 atm. Equivalence ratio = 1. Initial mole fraction = 10^{-3}

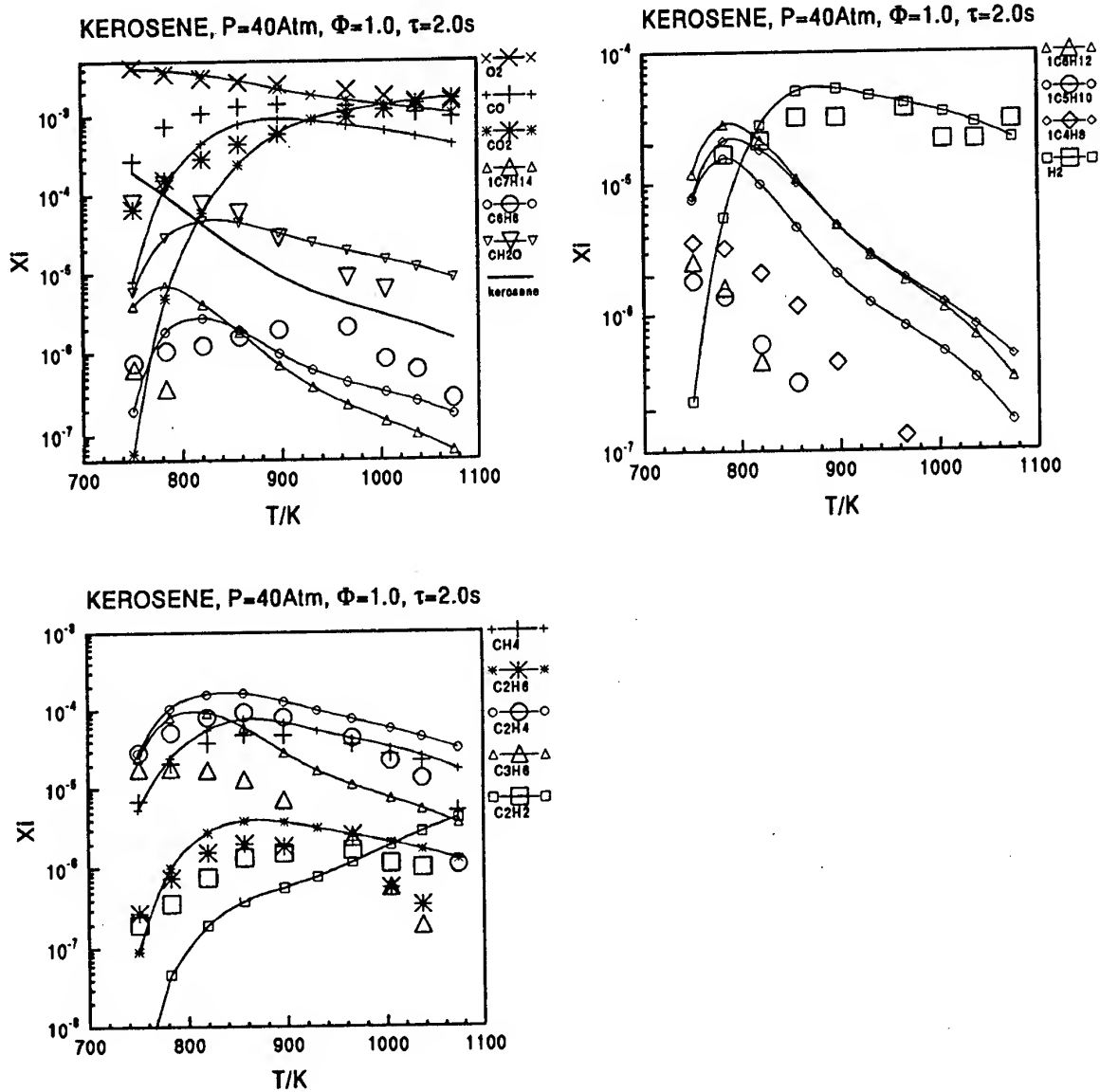


Figure 4 : Comparison between computed (lines and small symbols) and experimental (large symbols) concentration profiles in the jet stirred-reactor at 40 atm. Equivalence ratio = 1. Initial mole fraction = 0.25×10^{-3}

4. REDUCTION OF THE MECHANISM FOR THE OXIDATION OF N-DECANE

4.1 Objective of the study

The development of large comprehensive mechanisms is necessary to understand the essential details of the chemistry of combustion, however, because of their size, they cannot be used in industrial computer codes. To address practical problems, simplified mechanism, firmly based on detailed mechanisms, are needed.

Our intention, in this study, was to reduce the detailed mechanism of n-decane oxidation which represents the main part of kerosene combustion scheme. The mechanism of n-decane oxidation includes 113 chemical species involved in 692 reversible reactions. It has been validated on experimental concentration profiles in a jet-stirred reactor ; it can also be used for the computation of the conditions of flame blow-out or ignition.

The objective assigned to the reduced mechanism, was to predict with reasonable accuracy the extinction limits in the combustion of n-decane in air in an adiabatic perfectly-stirred reactor. The conditions chosen in the reactor were the followings :

- entrance temperature between 300K and 1500K
- Pressure between 1atm and 40atm
- equivalence ratios between 0.3 and 2.5

4.2 Reduction method

The reduction method involves the following steps :

a Elaboration of a skeletal mechanism :

A reduction of the number of reactions is obtained by the reaction rate analysis method : reactions having a net rate lower than a threshold value in the entire range of investigation are identified and removed from the detailed mechanism.

b Identification of species being at quasi-steady-state :

A further simplification of the system can be obtained by application of the quasi-steady-state approximation (QSSA). Fast intermediate species at quasi-steady-state are identified and their concentrations are expressed algebraically in terms of other species.

4.3 Description of the reduced mechanism obtained

Fixing to 0.5% of the sum of all reactions, the threshold value for the rate of non important reactions, reduces the number of reactions in the mechanism from 692 to 283. This operation also reduces the number of chemical species involved from 113 to 78.

Application of QSSA to this skeletal mechanism leads to identify 38 fast intermediate species in the whole range of investigations. The concentrations of these species are then obtained from the concentrations of the other 40 species by explicit algebraic expressions.

Examples of comparisons between extinction temperatures obtained with the detailed and the skeletal mechanism at 1 and 40 atm are shown in figures 5. Table 1 and 2 report extinction temperatures computed at 10 and 20 atm after application of QSSA to 38 species.

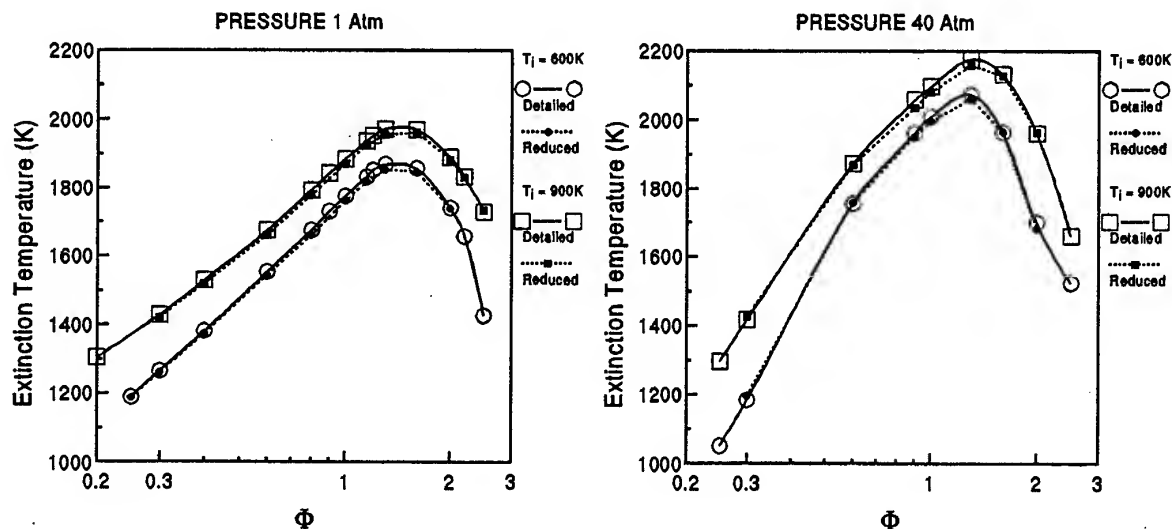


Figure 5 : Computed extinction temperatures using the detailed mechanism (full lines and large symbols) and the skeletal mechanism (dotted lines and small symbols).

TABLE 1 : Computed extinction temperatures (in K) at 10 atm

Entrance Temperature (K)	Equivalence ratio	Detailed mechanism	Skeletal mechanism	QQSA
300	0.4	1218	1212	1214
300	1.0	1796	1786	1796
300	2.0	1509	1495	—
600	0.3	1264	1274	1278
600	1.0	1872	1860	1874
600	2.0	1755	1786	—
900	0.3	1487	1484	1510
900	1.0	1958	1948	1957
900	2.0	1931	1923	1929

TABLE 2 : Computed extinction temperatures (in K) at 20 atm

Entrance Temperature (K)	Equivalence ratio	Detailed mechanism	Skeletal mechanism	QQSA
300	0.4	1192	1187	1206
300	1.0	1877	1869	1860
300	2.0	1523	1518	—
600	0.3	1199	1204	1215
600	1.0	1982	1966	1962
600	2.0	1711	1725	—
900	0.3	1414	1432	1466
900	1.0	2057	2063	2059
900	2.0	1966	1959	—

5. CONCLUSION

The predictions of experimental data obtained for kerosene oxidation in a jet-stirred reactor up to 40 atm have been improved by using a new detailed chemical kinetic mechanism. This new mechanism addresses the multi-component nature of kerosene via a lumping procedure where single species represents chemical families : cyclohexane for the naphthenes and toluene for the aromatics.

The reduction of the mechanism for n-decane oxidation yields a skeletal mechanism involving 283 reactions instead of 692, and 78 chemical species instead of 113. A further simplification of the mechanism is introduced by applying quasi-stationary-state approximation to 30 intermediate species. The simplified mechanism reproduces, with sufficient accuracy, the extinction limits predicted in an adiabatic perfectly-stirred reactor by the detailed mechanism.

Acknowledgements :

Financial support from DRET is gratefully acknowledged.

REFERENCES

1. C. Guéret, M. Cathonnet, J.C. Boettner and F. Gaillard : Twenty-Third Symposium (International) on Combustion, The Combustion Institute, 1990, p. 211.

- P. Dagaut, M. Reuillon, M. Cathonnet and D. Voisin : *J. Chim. Phys.*, 1995, 92, 47.
- C. Vovelle, J.L. Delfau, M. Reuillon, R. Akkrich, M. Bouhria, and O. Sanogo : 202nd ACS National Meeting, American Chemical Society, 1991, 36, 1456.
- C. Douté, J.L. Delfau, R. Akkrich, and C. Vovelle : *Combust. Sci. and Tech.*, 1995, 106, 327.
- P. Dagaut, M. Reuillon, M. Cathonnet and D. Voisin : *Combust. Sci. Tech.*, 1994, 95, 233.
- P. Dagaut, M. Reuillon, and M. Cathonnet : *Combust. Sci. and Tech.*, 1994, 103, 349.
- A. Chakir, M. Bellimam, J.C. Boettner and M. Cathonnet : *Combust. Sci. and Tech.*, 1991, 77, 239.
- Chakir, A., Bellimam, M., Boettner, J.C., and Cathonnet, M. : *Int. J. Chem. Kinet.*, 24:385 (1992).
- M. Cathonnet, C. Balès-Guérét, A. Chakir, P. Dagaut, J.C. Boettner, and J.L. Schultz : Third European Propulsion Forum, Association Astronautique et Aéronautique de France, Paris, 1991, p. 313.
- Y. Tan, P. Dagaut, M. Cathonnet and J.-C. Boettner : *Combust. Sci. and Tech.*, 1994, 102, 21.
- J.L. Emdee, K. Brezinsky, I. Glassman : *J. Phys. Chem.*, 1992, 96, 2151.

PAPER No. 14
Voisin, Boettner, Dragnet, Roscillon & Cathonnet
(presenter: M. Cathonnet)

Question 1: M. Pourkashanian, University of Leeds, U.K.

Could you please comment on the accuracy of the CO concentration predicted by using your reduced kerosene reaction mechanism? It seems that most of the detailed kerosene reaction mechanisms available either under-predict or over-predict CO concentrations significantly. Could you comment on possible reasons for this?

Answer:

Figures 1-4 of the paper show that our approximate mechanism under-predicts CO concentrations, mostly in lean mixture oxidation (Fig. 1), and we are trying to improve on this. For example, toluene presently represents all of the aromatics present in the fuel, and obviously, more would be better. However, for all equivalence ratios and pressures there is an important and systematic under-prediction not only of CO, but also of CO₂ for initial temperatures less than 800 °K. We believe that this is due to the occurrence of the low temperature oxidation reactions, which are not included in our chemical mechanism.

Modelling of a Lean Premixed Combustor

P. J. Coelho* and P. Salvada**

* Instituto Superior Técnico,
Technical University of Lisbon
Mechanical Engineering Department
Av. Rovisco Pais, 1096 Lisboa Codex
Portugal

** Academia da Força Aérea
Granja do Marquês, 2710 Sintra, Portugal

SUMMARY

A mathematical model of a fuel lean premixed axisymmetric combustor is presented and applied to an experimental facility. The combustor is constituted by a pre-chamber where propane is injected and mixed with the oxidant, and the combustion chamber where most of the reactions take place. The mathematical model is based on the numerical solution of the equations governing conservation of mass, momentum and energy, and transport equations for scalar quantities. The k- ϵ model, the eddy break-up or the eddy dissipation models, and the discrete ordinates model are used to simulate turbulence, combustion and radiation, respectively. The results are compared with experimental data. The grid size and the discretization scheme are shown to have a significant influence on the results, demonstrating the need for error estimation in practical engineering computations. The influence of the constants of the combustion model and the role of the radiation model are examined. The influence of the equivalence ratio and the inlet air temperature are also investigated.

NOMENCLATURE

A : Area
A₁, A₂ : Pre-exponential factors
A_{mix} : Constant of the eddy-dissipation model
C_D : Constant of the scalar dissipation rate
C_{EBU} : Constant of the eddy-dissipation model
C_p : Specific heat at constant pressure
C _{μ} : Constant of the turbulence model
C₁, C₂ : Constants of the turbulence model
E : Activation energy
G : Production of turbulent kinetic energy
h : Specific enthalpy
h^o : Specific enthalpy at standard state
I : Radiation intensity
k : Turbulent kinetic energy
M : Molar mass
p : Pressure
r : Radial coordinate
R : Gas constant; combustion rate
R_o : Universal gas constant
s : Coordinate direction of propagation of a radiation beam

s₁ : Stoichiometric ratio of fuel mass to oxygen mass
s₂ : Stoichiometric ratio of CO mass to oxygen mass
S : Source term
T : Temperature
T^o : Temperature at standard state
u : Velocity component in axial direction
v : Velocity component in radial direction
V : Volume
w : Velocity component in tangential direction; quadrature weight
x : Axial coordinate
Y : Species mass fraction

Greek symbols

α : Geometric coefficient
 ϵ : Dissipation rate of turbulent kinetic energy
 ζ : Direction cosine
 η : Direction cosine
 κ : Absorption coefficient
 μ : Dynamic viscosity; direction cosine
 ρ : Density
 σ_t : Constant of the turbulence model
 $\sigma_K, \sigma_\epsilon$: Constants of the turbulence model
 Ψ : Azimuthal angle

Subscripts

b : Blackbody
ef : Effective
fu : Fuel
i : Direction
N,S,E,W : North, south, east, west
P : Grid node
t : Turbulent

Superscripts

o : Standard state
(\rightarrow) : Vector
(\cdot)^{''} : Favre fluctuation
($\overline{\quad}$) : Reynolds average
(\sim) : Favre average

1. INTRODUCTION

The design of advanced gas turbine combustors remains a challenge to the combustion engineer. The need to comply with current and projected pollutants emission regulations and the effects of alternative fuels on gas turbine combustor performance are two of the key issues requiring further research [1]. But many other problems must be addressed, namely the requirements of high combustion efficiency, reliable and smooth ignition, wide stability limits, freedom from pressure pulsations, low pressure loss, small pattern factor, minimum cost, ease of maintenance and durability [2]. In the case of combustors for propulsion systems, the combustor length, size and weight, as well as the ratio of the engine thrust to the weight are also of paramount importance. Other important aspects in the combustor design include liner cooling, diffuser configuration, fuel injection, advanced combustor concepts and materials [3].

The use of accumulated experience and empirical correlations, though historically fairly successful in developing combustors based on proved design concepts, is unable to face all the challenges mentioned above. In fact, as pointed out in [4], empirically based methods have shown severe limitations in scaling combustors, and the empirical correlations are generally inadequate if novel concepts or jumps in the technology, e.g., combustor temperature rise, are required. Therefore, it is not surprising that the developments in the computers technology, and the consequent emergence of computational fluid dynamics, have given rise to the increased use of computational models in combustor design.

Since the early seventies, when the well known SIMPLE algorithm [5] and the $k-\epsilon$ model [6] appeared, the application of these methods to model gas turbine combustors has begun. Common to these earliest models [7-9] is the solution of the governing equations in Cartesian or cylindrical coordinates using a finite volume method and the SIMPLE algorithm. Turbulence was modelled using the standard $k-\epsilon$ model, and combustion was generally dealt with using a conserved scalar approach. The modelling of liquid-fuel combustors was also carried out, as reported, for example, in [10-12], and radiation was included in some of the works [13-15]. A survey of the physical models and numerical solution techniques employed in computational models for gaseous turbulent combustion up to 1987 is given in [16], while representative papers of the state of the art at that time are compiled in [17]. Many of these physical models and numerical techniques are still used nowadays. The comparison of the predictions with experimental data has shown the potential of these models, but also their limitations, specially regarding the CO and pollutants emission.

Significant progress in different aspects of the models has been achieved since then. Turbulence closure using the

$k-\epsilon$ model is known to poorly predict swirling and recirculating flows. The advantages of second order moment closures has been investigated by several authors, and an example of application to a gas turbine combustor is given in [18]. Combustion modelling has also been the subject of continuous research, and advanced combustion models have been applied to gas turbine combustors, including stretched laminar flamelets [19], and Monte Carlo [20] methods. Much attention has been given to the pollutants formation and emission [21], specially NOx [22]. As far as the numerical solution techniques are concerned, body-fitted coordinates [23, 24], zonal methods high order discretization schemes and multigrid solvers [25] have been used. The assessment of the numerical solution accuracy is a key issue in any CFD code, and has been addressed, e.g., in [26].

Current concerns regarding acid rain and depletion of stratospheric ozone have motivated the development of low NOx combustors. Two main lines of development have been pursued [1], one through various minor modifications to conventional designs, and the other by means of advanced concepts. The most promising advanced concepts are the variable geometry, the staged combustion, e.g., the rich burn-quick quench-lean burn concept, the lean premixed prevaporized combustion and the catalytic oxidation.

The present work deals with an experimental lean premixed combustor. In this kind of combustor there is a pre-chamber where the fuel is injected, vaporized and mixed with the air, yielding ideally a vaporized, uniform, lean fuel-air mixture. In the combustion chamber the flame is stabilized by the creation of a recirculation zone, and the overall fuel lean conditions guarantee mean temperatures well below the temperature at stoichiometric conditions, resulting in low NO production. The remaining intermediate hydrocarbons and CO are oxidized in the post-flame region.

In this work an axisymmetric lean premixed combustor was modelled and the predictions were compared against experimental data. The mathematical model is described in the next section. Then, the results obtained are presented and discussed, and the concluding remarks are given in the last section.

2. THE MATHEMATICAL MODEL

The density-weighted averaged form of the continuity and momentum equations for an axisymmetric swirling flow in steady state may be written as:

$$\frac{\partial}{\partial x}(\bar{\rho} \bar{u}) + \frac{1}{r} \frac{\partial}{\partial r}(r \bar{\rho} \bar{v}) = 0 \quad (1)$$

$$\begin{aligned} \frac{\partial}{\partial x}(\bar{\rho} \bar{u} \bar{u}) + \frac{1}{r} \frac{\partial}{\partial r}(r \bar{\rho} \bar{v} \bar{u}) = & -\frac{\partial p}{\partial x} + \frac{\partial}{\partial x} \left(\mu \frac{\partial \bar{u}}{\partial x} - \bar{\rho} \bar{u}'' \bar{u}'' \right) + \\ & + \frac{1}{r} \frac{\partial}{\partial r} \left(r \left(\mu \frac{\partial \bar{u}}{\partial r} - \bar{\rho} \bar{v}'' \bar{u}'' \right) \right) + \\ & + \frac{\partial}{\partial x} \left(\mu \frac{\partial \bar{u}}{\partial x} \right) + \frac{1}{r} \frac{\partial}{\partial r} \left(r \mu \frac{\partial \bar{u}}{\partial r} \right) - \frac{\partial}{\partial x} \left(\frac{2}{3} \mu \nabla \cdot \bar{v} \right) \end{aligned} \quad (2)$$

$$\begin{aligned} \frac{\partial}{\partial x}(\bar{\rho} \bar{u} \bar{v}) + \frac{1}{r} \frac{\partial}{\partial r}(r \bar{\rho} \bar{v} \bar{v}) = & -\frac{\partial p}{\partial r} + \frac{\partial}{\partial x} \left(\mu \frac{\partial \bar{v}}{\partial x} - \bar{\rho} \bar{u}'' \bar{v}'' \right) + \\ & + \frac{1}{r} \frac{\partial}{\partial r} \left(r \left(\mu \frac{\partial \bar{v}}{\partial r} - \bar{\rho} \bar{v}'' \bar{v}'' \right) \right) + \\ & + \frac{\partial}{\partial x} \left(\mu \frac{\partial \bar{u}}{\partial r} \right) + \frac{1}{r} \frac{\partial}{\partial r} \left(r \mu \frac{\partial \bar{v}}{\partial r} \right) - 2\mu \frac{\bar{v}}{r^2} + \frac{1}{r} (\bar{\rho} \bar{w} \bar{w} + \bar{\rho} \bar{w}'' \bar{w}'') \\ & - \frac{1}{r} \frac{\partial}{\partial r} \left(\frac{2}{3} \mu r \nabla \cdot \bar{v} \right) + \frac{2}{3} \frac{\mu}{r} \nabla \cdot \bar{v} \end{aligned} \quad (3)$$

$$\begin{aligned} \frac{\partial}{\partial x}(\bar{\rho} \bar{u} \bar{w}) + \frac{1}{r} \frac{\partial}{\partial r}(r \bar{\rho} \bar{v} \bar{w}) = & \frac{\partial}{\partial x} \left(\mu \frac{\partial \bar{w}}{\partial x} - \bar{\rho} \bar{u}'' \bar{w}'' \right) + \\ & + \frac{1}{r} \frac{\partial}{\partial r} \left(r \mu \frac{\partial \bar{w}}{\partial r} - \bar{\rho} \bar{v}'' \bar{w}'' \right) - \\ & - \frac{1}{r} (\bar{\rho} \bar{v} \bar{w} + \bar{\rho} \bar{v}'' \bar{w}'') - \frac{\bar{w}}{r^2} \frac{\partial}{\partial r}(r \mu) \end{aligned} \quad (4)$$

Closure of these equations was achieved using the standard k-ε model. Hence, the Reynolds stresses are computed as follows:

$$-\rho \bar{u}'' \bar{u}'' = \mu_t \left(2 \frac{\partial \bar{u}}{\partial x} \right) - \frac{2}{3} (\mu_t \nabla \cdot \bar{v} + \rho k) \quad (5a)$$

$$-\rho \bar{v}'' \bar{v}'' = \mu_t \left(2 \frac{\partial \bar{v}}{\partial r} \right) - \frac{2}{3} (\mu_t \nabla \cdot \bar{v} + \rho k) \quad (5b)$$

$$-\rho \bar{w}'' \bar{w}'' = \mu_t \left(2 \frac{\bar{v}}{r} \right) - \frac{2}{3} (\mu_t \nabla \cdot \bar{v} + \rho k) \quad (5c)$$

$$-\rho \bar{u}'' \bar{v}'' = \mu_t \left(\frac{\partial \bar{u}}{\partial r} + \frac{\partial \bar{v}}{\partial x} \right) \quad (5d)$$

$$-\rho \bar{v}'' \bar{w}'' = \mu_t \left(\frac{\partial \bar{w}}{\partial r} - \frac{\bar{w}}{r} \right) \quad (5e)$$

$$-\rho \bar{u}'' \bar{w}'' = \mu_t \frac{\partial \bar{w}}{\partial x} \quad (5f)$$

Introducing these relations into the momentum equations (2) - (4) results:

$$\begin{aligned} \frac{\partial}{\partial x}(\bar{\rho} \bar{u} \bar{u}) + \frac{1}{r} \frac{\partial}{\partial r}(r \bar{\rho} \bar{v} \bar{u}) = & -\frac{\partial p}{\partial x} + \frac{\partial}{\partial x} \left(\mu_{ef} \left(\frac{\partial \bar{u}}{\partial x} + \frac{\partial \bar{u}}{\partial x} \right) \right) + \\ & + \frac{1}{r} \frac{\partial}{\partial r} \left(r \mu_{ef} \left(\frac{\partial \bar{u}}{\partial r} + \frac{\partial \bar{v}}{\partial x} \right) \right) - \frac{\partial}{\partial x} \left(\frac{2}{3} \mu_{ef} \nabla \cdot \bar{v} \right) \end{aligned} \quad (6)$$

$$\begin{aligned} \frac{\partial}{\partial x}(\bar{\rho} \bar{u} \bar{v}) + \frac{1}{r} \frac{\partial}{\partial r}(r \bar{\rho} \bar{v} \bar{v}) = & -\frac{\partial p}{\partial r} + \frac{\partial}{\partial x} \left(\mu_{ef} \left(\frac{\partial \bar{v}}{\partial x} + \frac{\partial \bar{u}}{\partial r} \right) \right) + \\ & + \frac{1}{r} \frac{\partial}{\partial r} \left(r \mu_{ef} \left(\frac{\partial \bar{v}}{\partial r} + \frac{\partial \bar{v}}{\partial r} \right) \right) - 2\mu_{ef} \frac{\bar{v}}{r^2} + \frac{\bar{\rho} \bar{w} \bar{w}}{r} - \\ & \frac{1}{r} \frac{\partial}{\partial r} \left(\frac{2}{3} \mu_{ef} r \nabla \cdot \bar{v} \right) + \frac{2}{3} \frac{\mu_{ef}}{r} \nabla \cdot \bar{v} \end{aligned} \quad (7)$$

$$\begin{aligned} \frac{\partial}{\partial x}(\bar{\rho} \bar{u} \bar{w}) + \frac{1}{r} \frac{\partial}{\partial r}(r \bar{\rho} \bar{v} \bar{w}) = & \frac{\partial}{\partial x} \left(\mu_{ef} \frac{\partial \bar{w}}{\partial x} \right) + \\ & \frac{1}{r} \frac{\partial}{\partial r} \left(r \mu_{ef} \frac{\partial \bar{w}}{\partial r} \right) - \frac{\bar{\rho} \bar{v} \bar{w}}{r} - \frac{\bar{w}}{r^2} \frac{\partial}{\partial r}(r \mu_{ef}) \end{aligned} \quad (8)$$

The turbulent and the effective viscosity are calculated as

$$\mu_t = C_\mu \rho k^2 / \varepsilon \quad (9)$$

$$\mu_{ef} = \mu_t + \mu \quad (10)$$

while the turbulent kinetic energy, k, and its dissipation rate, ε, are obtained from the solution of the transport equations which may be written as

$$\begin{aligned} \frac{\partial}{\partial x}(\bar{\rho} \bar{u} k) + \frac{1}{r} \frac{\partial}{\partial r}(r \bar{\rho} \bar{v} k) = & \frac{\partial}{\partial x} \left(\frac{\mu_{ef}}{\sigma_k} \frac{\partial k}{\partial x} \right) + \\ & \frac{1}{r} \frac{\partial}{\partial r} \left(r \frac{\mu_{ef}}{\sigma_k} \frac{\partial k}{\partial r} \right) - \frac{\mu_t}{\rho^2} \left(\frac{\partial \bar{\rho}}{\partial x} \frac{\partial \bar{p}}{\partial x} + \frac{\partial \bar{\rho}}{\partial r} \frac{\partial \bar{p}}{\partial r} \right) + G - \bar{\rho} \varepsilon \end{aligned} \quad (11)$$

$$\begin{aligned} \frac{\partial}{\partial x}(\bar{\rho} \bar{u} \varepsilon) + \frac{1}{r} \frac{\partial}{\partial r}(r \bar{\rho} \bar{v} \varepsilon) = & \frac{\partial}{\partial x} \left(\frac{\mu_{ef}}{\sigma_\varepsilon} \frac{\partial \varepsilon}{\partial x} \right) + \\ & \frac{1}{r} \frac{\partial}{\partial r} \left(r \frac{\mu_{ef}}{\sigma_\varepsilon} \frac{\partial \varepsilon}{\partial r} \right) + C_1 \frac{\varepsilon}{k} \left(G - \frac{\mu_t}{\rho^2} \left(\frac{\partial \bar{\rho}}{\partial x} \frac{\partial \bar{p}}{\partial x} + \frac{\partial \bar{\rho}}{\partial r} \frac{\partial \bar{p}}{\partial r} \right) \right) - \\ & C_2 \bar{\rho} \frac{\varepsilon^2}{k} \end{aligned} \quad (12)$$

The production rate of turbulent kinetic energy, G, is computed as follows:

$$G = \mu_t \left\{ 2 \left[\left(\frac{\partial \tilde{u}}{\partial x} \right)^2 + \left(\frac{\partial \tilde{v}}{\partial r} \right)^2 + \left(\frac{\tilde{v}}{r} \right)^2 \right] + \left[r \frac{\partial}{\partial r} \left(\frac{\tilde{w}}{r} \right) \right]^2 + \left(\frac{\partial \tilde{v}}{\partial x} + \frac{\partial \tilde{u}}{\partial r} \right)^2 + \left(\frac{\partial \tilde{w}}{\partial x} \right)^2 \right\} \quad (13)$$

The constants of the model are $C_\mu=0.09$, $C_1=1.44$, $C_2=1.92$, $\sigma_k=1.0$ and, $\sigma_\epsilon=1.3$ [6].

Two combustion models have been used: the eddy-break-up [27] and the eddy-dissipation [28] models. The eddy-break-up model is an empirical model for the mean reaction rate in the case of fast chemistry which is given by

$$\tilde{S}_{fu} = C_{EBU} \rho \frac{\epsilon}{k} \sqrt{\tilde{Y}_{fu}^2} \quad (14)$$

where CEBU is a constant of the model which was set to 0.35.

If the rate of combustion is controlled by the kinetics, then the reaction rate is:

$$\tilde{S}_{fu} = A_1 \rho Y_{fu} Y_{O_2} \exp(-E/RT) \quad (15)$$

The source term of the transport equation for fuel mass fraction is taken as the minimum of the rates given by equations (14) and (15), using mean values in equation (15). The first rate prevails if the kinetic time scale is smaller than the turbulence time scale, while the last is appropriate in the opposite case.

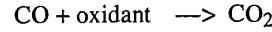
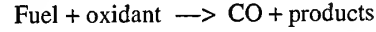
The mean and variance of fuel mass fraction are obtained from the solution of the following equations:

$$\frac{\partial}{\partial x} (\bar{\rho} \tilde{u} \tilde{Y}_{fu}) + \frac{1}{r} \frac{\partial}{\partial r} (r \bar{\rho} \tilde{v} \tilde{Y}_{fu}) = \frac{\partial}{\partial x} \left(\frac{\mu_{ef}}{\sigma_t} \frac{\partial \tilde{Y}_{fu}}{\partial x} \right) + \frac{1}{r} \frac{\partial}{\partial r} \left(r \frac{\mu_{ef}}{\sigma_t} \frac{\partial \tilde{Y}_{fu}}{\partial r} \right) - \tilde{S}_{fu} \quad (16)$$

$$\begin{aligned} \frac{\partial}{\partial x} (\bar{\rho} \tilde{u} \tilde{Y}_{fu}^2) + \frac{1}{r} \frac{\partial}{\partial r} (r \bar{\rho} \tilde{v} \tilde{Y}_{fu}^2) &= \frac{\partial}{\partial x} \left(\frac{\mu_{ef}}{\sigma_t} \frac{\partial \tilde{Y}_{fu}^2}{\partial x} \right) + \\ &+ \frac{1}{r} \frac{\partial}{\partial r} \left(r \frac{\mu_{ef}}{\sigma_t} \frac{\partial \tilde{Y}_{fu}^2}{\partial r} \right) + 2 \frac{\mu_t}{\sigma_t} \left[\left(\frac{\partial \tilde{Y}_{fu}}{\partial x} \right)^2 + \left(\frac{\partial \tilde{Y}_{fu}}{\partial r} \right)^2 \right] \\ &- C_D \bar{\rho} \frac{\epsilon}{k} \tilde{Y}_{fu}^2 \end{aligned} \quad (17)$$

In addition, a transport equation for a conservative scalar, taken as the mixture fraction, is solved. The concentrations of the chemical species are obtained from the mixture fraction by assuming a single global reaction, and taking the fuel mass fraction computed from equation (16).

The eddy-dissipation model was used assuming that combustion takes place in the two following steps:



The combustion rate of the fuel is determined as

$$\tilde{R}_{fu} = A_{mix} \frac{\epsilon}{k} \bar{\rho} \min \left\{ \tilde{Y}_{fu}, \frac{\tilde{Y}_{O_2}}{s_1 + s_2 \tilde{Y}_{CO} / \tilde{Y}_{fu}} \right\} \quad (18)$$

while the combustion rate of CO may be either kinetically or mixed controlled, and is obtained as the minimum of the two following rates [29-30]:

$$\begin{aligned} \tilde{R}_{CO} &= A_2 \bar{\rho}^2 \tilde{Y}_{CO} \left[\left(\tilde{Y}_{O_2} / M_{O_2} \right) \left(\tilde{Y}_{H_2O} / M_{H_2O} \right) \right]^{1/2} * \\ &\exp(-E/RT) \end{aligned} \quad (19)$$

$$\tilde{R}_{CO} = A_{mix} \frac{\epsilon}{k} \bar{\rho} \min \left\{ \tilde{Y}_{CO}, \frac{\tilde{Y}_{O_2}}{s_2 + s_1 \tilde{Y}_{fu} / \tilde{Y}_{CO}} \right\} \quad (20)$$

A_{mix} is a constant of the model which was set equal to 4.0.

The mass fractions of fuel, O_2 , CO, CO_2 , H_2O and N_2 are obtained from the solution of transport equations whose source terms are related to the combustion rates of fuel and CO (see [29-30] for details).

The enthalpy of the reactive mixture is defined as

$$h = \sum_j Y_j \left(h_j^\circ + \int_{T^\circ}^T C_{p,j}(T) dT \right) \quad (21)$$

where the index j runs over all the chemical species. The enthalpy is determined from the solution of the energy equation which may be written in a form similar to equation (16), with the radiation source substituted for the reaction rate of fuel. The temperature is calculated from the enthalpy using equation (21) and the density is computed from the ideal gas law:

$$p = \rho R_o T \sum (Y_j / M_j) \quad (22)$$

The discrete ordinates method [31-32] was used to calculate the radiative heat transfer. In the case of a grey non-scattering medium the radiative transfer equation (RTE) may be written as

$$\frac{dI}{ds} = -\kappa I + \kappa I_b \quad (23)$$

In the discrete ordinates method this equation is solved for a set of $n(n+2)$ directions yielding the so-called S_n approximation. These directions span the total solid angle of 4π around a point in space. Along a direction \bar{s}_i the RTE reads as

$$\frac{\mu_i}{r} \frac{\partial(rI_i)}{\partial r} - \frac{1}{r} \frac{\partial(\eta_i I_i)}{\partial \psi} + \zeta_i \frac{\partial I_i}{\partial x} = -\kappa I + \kappa I_b \quad (24)$$

where μ_i , η_i and ζ_i are the direction cosines of direction i . If this equation is discretized using the finite volume approach, a relationship between the volume average radiation intensity, $I_{p,i}$, and the radiation intensities at the control volume faces is obtained [33]:

$$\begin{aligned} \mu_i (A_N I_{N_i} - A_S I_{S_i}) + \zeta_i (A_E I_{E_i} - A_W I_{W_i}) - (A_N - A_S) * \\ \frac{\alpha_{i+1/2} I_{i+1/2} - \alpha_{i-1/2} I_{i-1/2}}{w_i} = -\kappa V I_{p,i} + \kappa V I_b \end{aligned} \quad (25)$$

and

$$\alpha_{i+1/2} - \alpha_{i-1/2} = w_i \mu_i \quad (26)$$

The incoming and the outgoing radiation intensities are related to the volume average radiation intensity according to the discretization scheme employed. The step scheme was used in the present work, along with the S_4 approximation and a level symmetric quadrature satisfying sequential odd moments [34]. Additional details of the method, including the derivation of the equations given above, the boundary conditions treatment and the solution algorithm may be found in [31-34]. The absorption coefficient of the medium was calculated using the weighted sum of grey gases model.

The governing equations were discretized over a non-staggered grid using a finite volume/finite difference method. The central differences discretization scheme was used, except for the convective terms which were discretized using either the hybrid central differences/upwind or the MUSCL [35] schemes. In the last case, the normalized variable and space formulation

methodology [36] was employed, and a diagonally dominant matrix of coefficients was enforced using the deferred correction technique [37]. Pressure-velocity coupling was accomplished by means of the SIMPLE algorithm, and the interpolation technique of Rhie and Chow [38] was used to calculate the velocities at the cell faces. The algebraic sets of discretized equations were solved using the Gauss-Seidel line-by-line iterative procedure except the pressure correction equation which was solved using a preconditioned conjugate gradient method. The code is fully parallelized using the domain decomposition strategy and the MPI message passage library. Details of the parallelization technique may be found in [39-40]. However, the present results were obtained in a sequential computer.

The radiative calculations were performed every 50 iterations of the fluid flow algorithm. The convergence criterion demands that the sum over all the control volumes of the normalized residuals of mass, velocity components and enthalpy decrease below 10^{-3} .

3. RESULTS AND DISCUSSION

The combustion chamber modelled in the present work is schematically shown in Fig. 1. It is constituted by a pre-chamber where the fuel is premixed with the air, and the combustion chamber itself where the reactions take place. The air is introduced radially in the pre-chamber through openings which impart swirl to the air flow. The fuel (propane) flows in an axial pipe and is injected radially in the pre-chamber, downstream of the air inlet, through four holes. These are approximated as an annular inlet that preserves the mass flow rate and the inlet velocity. A bluff body of conical shape placed at the exit of the pre-chamber provides flame stabilization.

The air mass flow rate for the conditions under investigation is $0.025 \text{ m}^3/\text{s}$, and the overall equivalence ratio is 0.6. The temperature of the air and fuel is 300K. Measurements of mean temperature and concentrations of main chemical species were obtained using digitally compensated thermocouples and a water cooled probe, respectively [41]. One major drawback of these measurements is the lack of velocity data. In particular, the swirl number is not known. Therefore, the comparison between the measurements and the predictions presented below should be regarded with caution, due to the uncertainty about the boundary conditions, in particular the inlet conditions. The calculations were repeated using three different tangential velocities, namely 1m/s, 3m/s and 6m/s. The velocity field changes a little, but the temperature profiles remain very similar. The results presented below were obtained for a tangential velocity equal to 1 m/s.

Calculations were made using two different grids comprising 75×40 and 130×80 grid nodes. The grid lines are denser in the vicinity of the bluff body and expand towards the combustor exit, and upstream up to the fuel

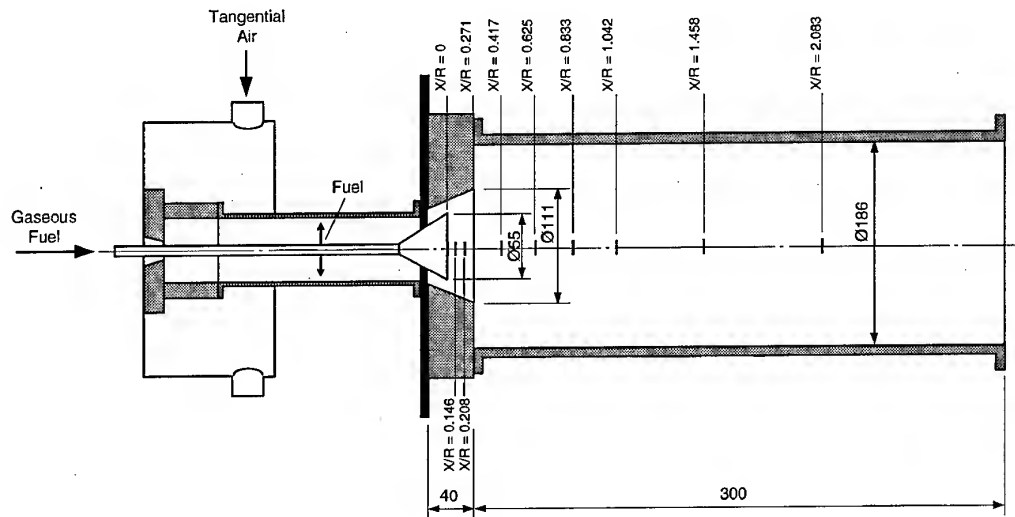


Figure 1 - Schematic of the combustor.

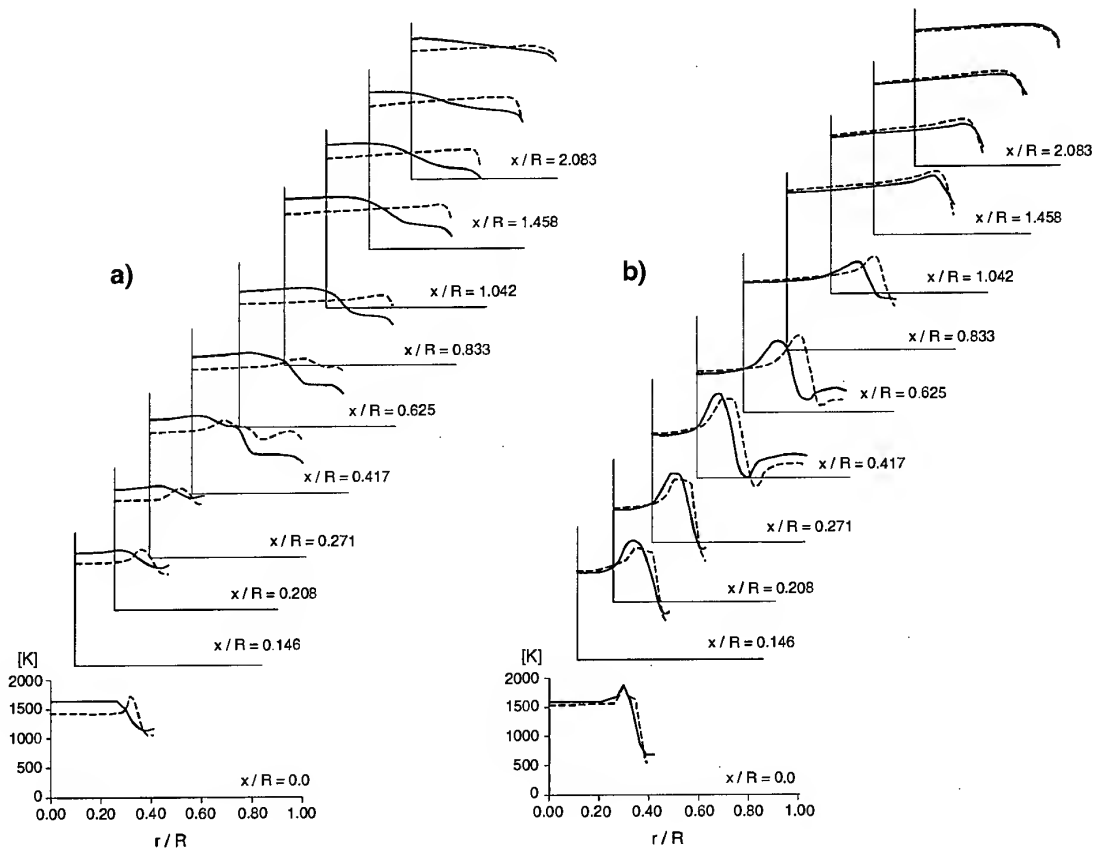


Figure 2a)- Predicted mean temperature profiles using the hybrid scheme (solid line: coarse grid; dashed line: fine grid).

Figure 2b) - Predicted mean temperature profiles using the MUSCL scheme (solid line: coarse grid; dashed line: fine grid).

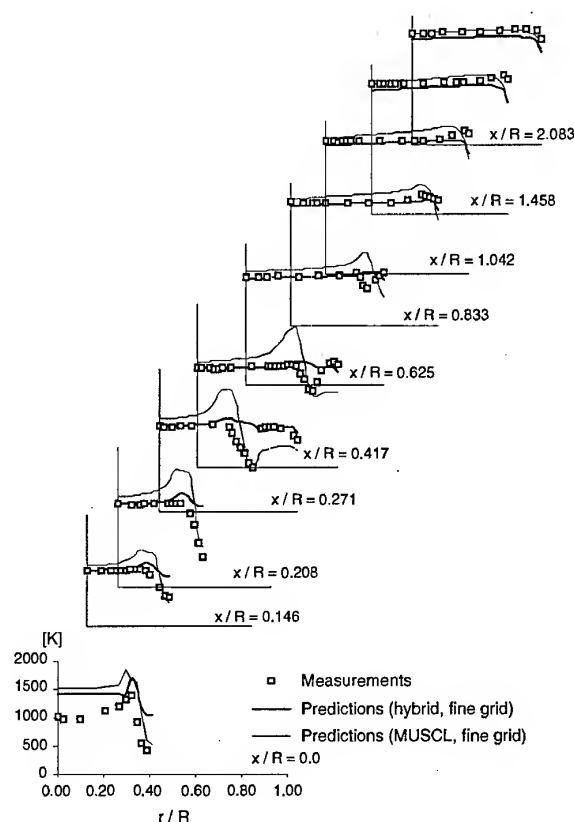


Figure 3 - Predicted and measured mean temperature profiles.

injection section. The predicted radial profiles of mean temperature at several stations where measurements are available are plotted in Fig. 2. These results were obtained using the eddy dissipation model. In Fig. 2 the x coordinate is measured along the axis, starting just downstream of the bluff body surface normal to the axis. At the stations displayed in Fig. 2 the x coordinate is normalized by the internal radius of the combustor, R .

The results in Fig. 2a) were obtained using the hybrid discretization scheme, and show a great dependence on the grid size. In the quarl the temperature profiles are qualitatively different for the two grids. A peak is observed for the finer grid, but not for the coarser one. Farther downstream, the profiles computed using the finer grid are almost flat, except close to the wall, while those calculated using the coarser grid exhibit a negative temperature gradient which is attenuated very slowly towards the exit. If the MUSCL scheme is employed, the results computed for the two grids are closer to each other, as observed in Fig. 2b). The profiles displayed in this figure are qualitatively similar for the two grids, but

there is still a noticeable grid effect near the quarl exit, namely at $x/R=0.217$, 0.417 and 0.625 . The sensitivity of the results to the grid size and discretization scheme highlight the well known, but often overlooked, need to assess the numerical accuracy of the predictions. It would be desirable to further refine the grid, but this was not done due to the long run times, and disk space limitations in the multiusers computer used in the present calculations.

The predicted mean temperature profiles along with the measurements are shown in Fig. 3 for the finer grid and for both discretization schemes. The temperature profiles predicted by the two different schemes still exhibit quite large differences, particularly in the quarl and in its vicinity. It is expected that the results obtained with the MUSCL scheme are more accurate, since the hybrid scheme is known to be much more diffusive. Moreover, the results previously shown in Fig. 2 reveal a much higher sensitivity on the grid size for the hybrid scheme. Therefore, the following analysis is based on the MUSCL scheme predictions.

Just downstream of the bluff body, at $x/R=0.$, the predicted profile is in qualitative agreement with the measured one, but the temperature in the central region is overestimated, and the predicted temperature peak is slightly displaced from the measured one. This peak remains well pronounced up to $x/R=0.833$. The experimental data, however, suggest a rapid disappearance of this peak. This may be due to the turbulent fluctuations which are not properly accounted for in the model. The shear region where combustion takes place is reasonably well predicted, as well as the minimum temperatures corresponding to the unburnt mixture. The temperature of the combustion products in the recirculation zone close to the combustor wall is underestimated. Farther downstream the predicted and the measured profiles are in very good agreement, except close to the wall where the predicted temperature drops markedly. This may be due to the uncertainty about the wall temperature or the role of the laws of the wall in the predictions. If the hybrid scheme is used, then the temperature profile rapidly becomes flat and does not reproduce the measured temperature gradients in the reaction zone.

Measurements and predictions (MUSCL scheme, finer grid) of O_2 and CO_2 molar fraction profiles on a dry basis are shown in Fig. 4. The predictions are in very good agreement with the measurements in the core region of the combustor, and downstream of the reaction zone where the profiles are almost uniform. However, significant discrepancies are found in the reaction zone and in the annular recirculation region downstream of the quarl. These are not surprising regarding the disagreement already found in the temperature profiles.

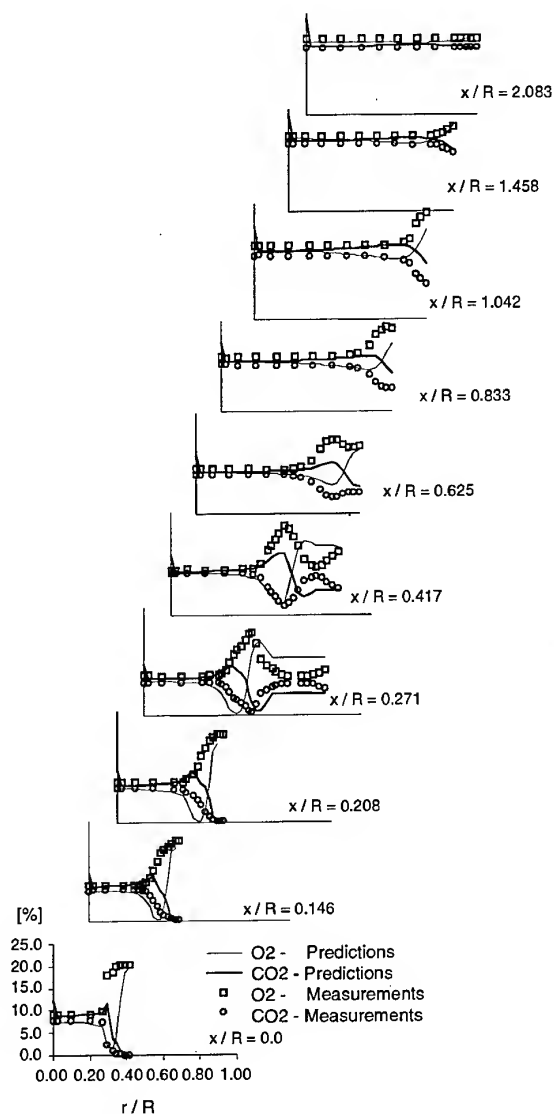


Figure 4 - Predicted and measured molar fractions of O_2 and CO_2 on a dry basis.

It is not possible to ascertain the ultimate reason for the observed discrepancies. It was already observed that the present results are not grid independent, but it is expected from the similarity of the profiles displayed in Fig. 2b) that this effect is of secondary importance for the finer grid and the MUSCL scheme. The lack of velocity data, including the inlet profiles, prevents the assessment of the turbulent model. It is known that the $k-\epsilon$ model is inadequate to simulate swirling flows, but it is uncertain how important is the role that it is playing in the present case. The influence of the radiation and combustion models is investigated below.

Figure 5 shows predicted temperature profiles, with and without accounting for the radiative transfer, along with the measurements. These predictions were obtained using the hybrid scheme and the coarser grid. This choice is dictated by the lower computational requirements and was also used in the next calculations reported below. Although it has already been found that such results are strongly influenced by the grid size and discretization scheme, this choice is acceptable since our present aim is just to find out how the predictions are affected by the radiation or the combustion model. The results displayed in Fig. 5 reveal that the effect of the radiation model is negligible. Only a small decrease of the predicted temperatures is visible at the stations closer to the combustor exit.

Figure 6 shows the influence of the constant A_{mix} which appears in the calculation of the reaction rate using the eddy dissipation model. Besides the standard value $A_{mix} = 4.0$, results are also presented for $A_{mix} = 3.1$. No convergence was achieved for smaller values of A_{mix} . Higher values were not tried since the reaction rate would be larger and the predictions would depart further from the measurements. Fig. 6 reveals that the influence of A_{mix} on the predicted temperature is very small, and restricted to the reaction zone in the quarl. The temperature slightly decreases if A_{mix} is smaller, but the profiles remain similar.

If the eddy-break-up model is used instead of the eddy dissipation model, the predicted temperature profiles remain similar, as shown in Fig. 7. A low value of the constant, $C_{EBU}=0.1$, slightly improves the predictions in the quarl region, but underestimates the temperatures downstream of the reaction zone. On the contrary, if a high value of the constant is used ($C_{EBU}=1.0$), the predictions are very close to those obtained using the eddy dissipation model. The constant C_{EBU} influences the temperature level, but not the shape of the profiles.

Finally, the influence of the overall equivalence ratio and the air temperature is investigated. The results obtained using the finer grid are displayed in Fig. 8 along with the experimental data. If the equivalence ratio increases from 0.6 to 0.7, then the measured temperatures are slightly higher and the temperature gradients in the reaction zone are smaller. However, the radial temperature profiles are qualitatively similar. The predictions obtained using the MUSCL scheme exhibit a smaller temperature peak than in the case of smaller equivalence ratio. Hence, they become closer to the experimental data. Nevertheless, the predicted peak remains up to $x/R=0.833$, while according to the data it only appears very close to the bluff body. The results obtained using the hybrid scheme are much less satisfactory, since it yields a too fast attenuation of the temperature gradients in the reaction zone. If the inlet air

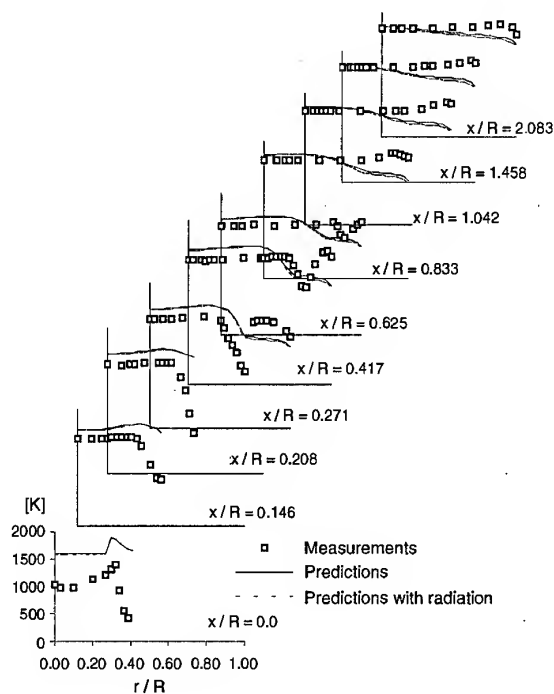


Figure 5 - Influence of the radiative transfer on the predicted mean temperature profiles (symbols: measurements; solid line: without radiation; dashed line: with radiation).

temperature increases from 300K to 450K the measured temperature profiles are both qualitatively and quantitatively similar to those obtained in the previous situation when the equivalence ratio was increased. The shortcomings of the predictions mentioned above also apply to these operating conditions.

4. CONCLUDING REMARKS

A fuel lean premixed axisymmetric combustor was modelled using the $k-\epsilon$ turbulence model and the eddy dissipation or the eddy-break-up combustion models. Calculations performed using two different grids and two different discretization schemes, the hybrid and the MUSCL schemes, yielded significantly different predictions, specially if the hybrid scheme is used. This proves the need for assessment of numerical accuracy in practical engineering computations. Comparison of the predictions based on the finer grid and on the MUSCL scheme with the experimental data has shown some limitations. In particular, a temperature peak in the quail which extends into the combustion chamber suggests that

the temperature fluctuations were not adequately accounted for. It was concluded that the radiation plays a minor role in this combustor, and that the two combustion models employed yield similar results. These are qualitatively influenced by the constants of the models, but the shape of the temperature profiles remains unchanged. The increase of the equivalence ratio, as well as the increase of the inlet air temperature, results in an increase of the temperature level in the combustor, and a reduction of the temperature gradients in the reaction zone. In the former case the predicted results are in reasonable agreement with the experiments, but the temperature peak mentioned above still remains.

REFERENCES

1. Gupta, A.K. and Lilley, D.G., "Combustion and Environmental Challenges for Gas turbines in the 1990s", *Journal of Propulsion and Power*, Vol. 10, No. 2, pp. 137-147 (1994).
2. Lefebvre, A.H. "Gas Turbine Combustion", McGraw-Hill, New York (1983).
3. Peters, J.E., "Current Gas Turbine Combustion and Fuels Research and Development", *Journal of Propulsion and Power*, Vol. 4, No. 3, pp. 193-206 (1988).
4. Mongia, H.C., Reynolds, R.S. and Srinivasan, R., "Multidimensional Gas Turbine Combustion Modeling: Applications and Limitations", *AIAA J.*, Vol. 24, No. 6, pp. 890-904 (1986).
5. Patankar, S.V., "Numerical Heat Transfer and Fluid Flow", Hemisphere Publishing Corp., Washington (1980).
6. Launder, B.E., and Spalding, D.B., "The Numerical Computation of Turbulent Flows", *Computer Methods in Applied Mechanics and Engineering*, Vol. 3, pp. 269-289 (1974).
7. Jones, W.P., Clifford, W.C., Priddin, C.H. and de Chair, R., "A Comparison between Predicted and Measured Species Concentrations and Velocities in a Research Combustor", *AGARD CP-229*, paper 40 (1978).
8. Serag-Eldin, M.A. and Spalding, D.B., "Computations of Three-dimensional Gas Turbine Combustion Chamber Flows", *ASME J. Engineering for Power*, Vol. 101, pp. 326-336 (1979).

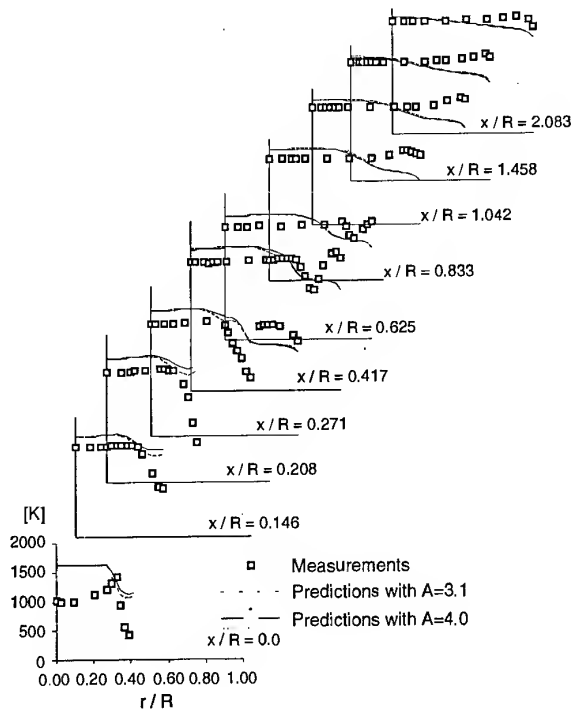


Figure 6 - Influence of A_{mix} (eddy dissipation model) on the predicted mean temperature profiles.

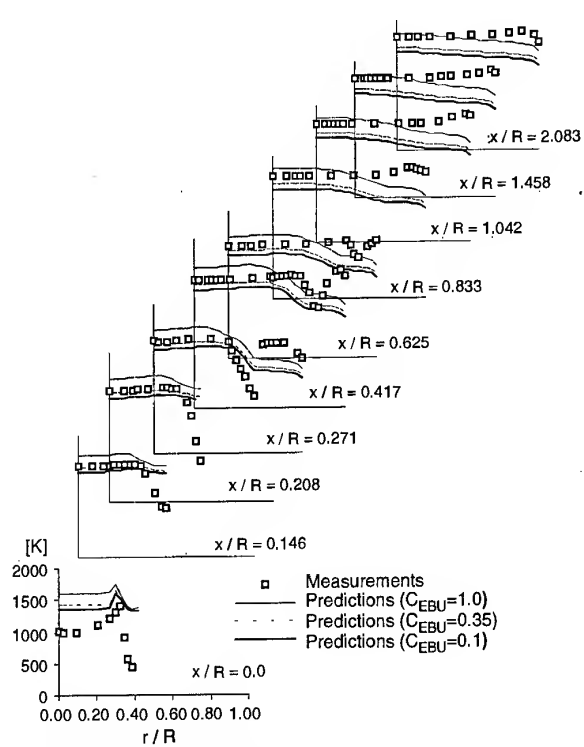


Figure 7 - Influence of C_{EBU} (eddy-break-up model) on the predicted mean temperature profiles.

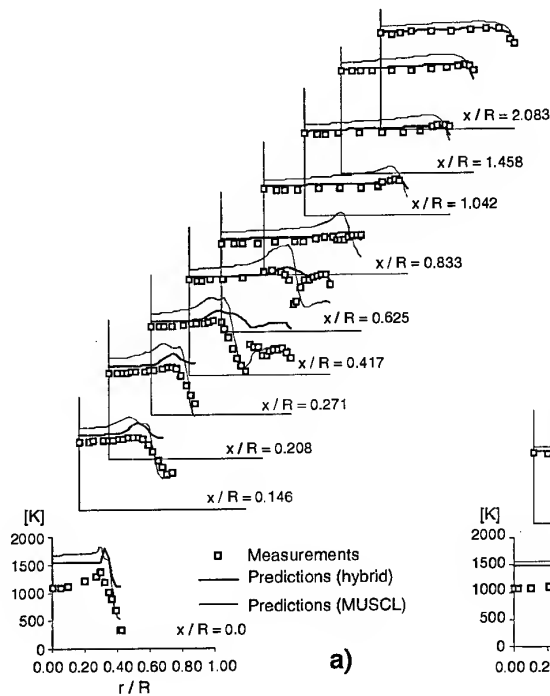


Figure 8a) - Mean temperature profiles for an equivalence ratio equal to 0.7.

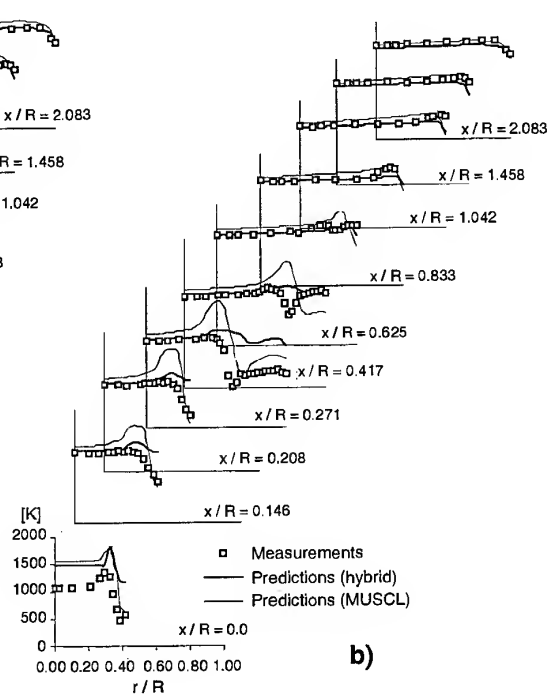


Figure 8b) - Mean temperature profiles for an inlet air temperature equal to 450K.

9. Jones, W.P. and McGuirk, J.J., "Mathematical Modelling of Gas Turbine Combustion Chambers", AGARD CP-275, paper 4 (1980).
10. Jones, W.P. and Priddin, C.H., "Prediction of the Flow Field and Local Gas Combustion in Gas Turbine Combustors", 17th Symposium (Int.) on Combustion, The Combustion Institute, pp. 399-409 (1979).
11. Boysan, F., Ayers, W. H., Swithenbank, J. and Pan, Z., "Three-dimensional Model of Spray Combustion in Gas Turbine Combustors", J. Energy, Vol. 6, pp. 368-375 (1981).
12. Sampath, S., Ganesan, V., "Numerical Prediction of Flow and Combustion in Three-dimensional Gas Turbine Combustors", J. Institute of Energy, pp. 15-28 (1987).
13. Lockwood, F.C., McGuirk, J.J. and Shah, N.G., "Radiation Transfer in Gas Turbine Combustors", AIAA paper No. 83-1506 (1983).
14. Carvalho, M.G., Durão, D. and Lockwood, F.C., "Computation of Thermal Radiation for Gas Turbine Conditions", AGARD CP-390, Paper No. 20 (1985).
15. Carvalho, M.G. and Coelho, P.J., "Heat Transfer in Gas Turbine Combustors", J. Thermophysics and Heat Transfer, Vol. 3, No. 2, pp. 123-131 (1989).
16. Correa, S.M. and Shyy, W., "Computational Models and Methods for Continuous Gaseous Turbulent Combustion", Progress in Energy and Combustion Science, Vol. 13, pp. 249-292 (1987).
17. AGARD CP-422, "Combustion and Fuels in Gas Turbine Engines" (1987).
18. Lin, C.A. and Lu, C.M., "Modeling Three-dimensional Gas-Turbine Combustor Model Flow using Second-Moment Closure", AIAA J., Vol. 32, No. 7, pp. 1416-1422 (1994).
19. Bai, X.-S. and Fuchs, L., "Sensitivity Study of Turbulent Reacting Flow Modeling in Gas Turbine Combustors", AIAA J., Vol. 33, No. 10, pp. 1857-1864 (1995).
20. Tolpadi, A., Correa, S., Burners, D. and Mongia, H.C., "Monte Carlo Probability Density Function Method for Gas Turbine Combustor Flowfield Predictions", J. Propulsion and Power, Vol. 13, No. 2, pp. 218-225 (1997).
21. Rizk, N.K. and Mongia, H.C., "A Semi-analytical Emission Model for Diffusion Flame, Rich/Lean and Premixed Lean Combustors", J. Engineering for Gas Turbines and Power, Vol. 117, pp. 290-301 (1995).
22. Correa, S.M., "A Review of NO_x Formation Under Gas-Turbine Combustion Conditions", Combustion Science and Technology, Vol. 87, pp. 329-362 (1992).
23. Coupland, J. and Priddin, C.H., "Modeling the Flow and Combustion in a Production Gas Turbine Combustor", 5th Symposium on Turbulent Shear Flows, pp. 10.1-10.6, Cornell University, Ithaca, NY, August 7-9 (1985).
24. Kandamby, N.H. and Lockwood, F.C., "On the Aero-Thermal Characteristics of Gasifier-Fuelled Gas Turbine Combustors with Complex Geometries", 25th Symposium (Int.) on Combustion, The Combustion Institute, pp. 251-259 (1994).
25. Shyy, W., Braaten, M.E. and Burrus, D.L., "Study of Three-dimensional Gas-Turbine Combustor Flows", Int. J. Heat and Mass Transfer, Vol. 32, No. 6, pp. 1155-1164 (1989).
26. McGuirk, J. and Palma, J., "The Influence of Numerical Parameters in the Calculation of Gas Turbine Combustor Flows", Computer Methods in Applied Mechanics and Engineering, Vol. 96, pp. 65-92 (1992).
27. Spalding, D.B., "Mixing and Chemical Reaction in Steady, Confined Turbulent Flames", 13th Symposium (Int.) on Combustion, The Combustion Institute, pp. 649-657 (1971).
28. Magnussen, B.F. and Hjertager, B.H., "On Mathematical Modeling of Turbulent Combustion with Special Emphasis on Soot Formation and Combustion", 16th Symposium (Int.) on Combustion, The Combustion Institute, pp. 719-729 (1977).
29. Jessee, J.P. and Fiveland, W.A., "A Non-orthogonal Combustion Model for Natural Gas Flames", Proc. 3rd Int. Conference on Combustion Technologies for a Clean Environment, paper 21.2, Lisbon, Portugal, 3-6 July (1995).
30. Peters, A.A.F. and Weber, R., "Mathematical Modeling of a 2.25 MWt Swirling Natural Gas Flame. Part 1: Eddy Break-up Concept for Turbulent Combustion; Probability Density Function Approach for Nitric Oxide Formation", Combustion Science and Technology, Vol. 110-111, pp. 67-101 (1995).

31. Carlson, B.G. and Lathrop, K.D., "Transport Theory - The Method of Discrete Ordinates", in "Computers in Reactor Physics", Gordon & Breach, New York (1968).
32. Fiveland, W.A., "A Discrete Ordinates Method for Predicting Radiative Heat Transfer in Axisymmetric Enclosures", ASME Paper 82-HT-20 (1982).
33. Jamaluddin, A.S. and Smith, P.J., "Predicting Radiative Heat Transfer in Axisymmetric Cylindrical Enclosures Using the Discrete Ordinates Method", Combustion Science and Technology, Vol. 62, pp. 173-186 (1988).
34. Fiveland, W.A., "The Selection of Discrete Ordinate Quadrature Sets for Anisotropic Scattering", in "Fundamentals of Radiation Heat Transfer, Vol. HTD-160, ASME, pp. 89-96 (1991).
35. Van Leer, B., "Towards the Ultimate Conservative Difference Scheme.V. A Second-Order Sequel to Godunov's Method", J. Computational Physics, Vol. 32, pp. 101-136 (1979).
36. Darwish, M.S. and Moukalled, F.H., "Normalized Variable and Space Formulation for High-Resolution Schemes", Numerical Heat Transfer, Part B, Vol. 26, pp. 79-96 (1994).
37. Khosla, P.K. and Rubin, S.G., "A Diagonally Dominant Second-Order Accurate Implicit Scheme", Computers and Fluids, Vol. 1, pp. 207-209 (1974).
38. Rhie, C.M. and Chow, W.L., "Numerical Study of the Turbulent Flow past an Airfoil with Trailing Edge Separation", AIAA J., Vol. 21, pp. 1525-1532 (1983).
39. Gonçalves, J. and Coelho, P. J., "Parallelization of the Discrete Ordinates Method", Numerical Heat Transfer, Part B, Vol. 32, pp. 151-173 (1997).
40. Coelho, P.J., Novo, P.A. and Carvalho, M.G., "Modelling of a Utility Boiler Using Parallel Computing", The Journal of Supercomputing, in press.
41. Anacleto, P., "Análise Experimental de uma Câmara de Combustão Axissimétrica com Pré-Vaporização e Pré-Mistura de Regentes" (in Portuguese), M. Sc. Thesis, Instituto Superior Técnico (1993).

PAPER No. 15
Coelho & Salvada
(presenter: P. Salvada)

Question 1: R. Schmeilm University Karlsruhe, Germany

Using a "mixed is burned" combustion model as you did in your calculations, why did you not show flame upstream in the premixed region?

Answer:

In fact, we have verified that the flame was actually ignited in the premixed zone. No results are shown for this region since no experimental measurements were made there. The measured data immediately downstream of the bluff-body suggest that the actual ignition occurs later than in the calculations, and this may be one of the reasons for the observed discrepancies between calculations and measurements in the downstream region of the combustor.

Question 2: M. Razdan, RR-Allison, U.S.

Once the fuel/air mixing limitation is removed (as in lean premixed systems), we have shown that fast chemistry or the eddy breakup combustion model assumptions do not work well, particularly for temperature and NO_x. This may be the reason that your temperature predictions particularly, in the early stages of combustion, are over-predicted. This, of course, has significant implications if one is interested in estimating NO_x emissions. Would you care to comment?

Answer:

We agree with your comments. The eddy breakup and eddy dissipation models have recognized limitations, although they are widely employed due to their simplicity, especially in commercial CFD codes and in engineering computations. In order to try to improve the predictions we have used the eddy dissipation model with two steps, and we have also checked the sensitivity of the solutions to the values of the constants. It turned out that no significant improvements were achieved. Therefore, we intend to include in the future, a more advanced combustion model such as the Bray-Libby-Moss model, or a laminae flamelet model based on the solution of the G-equation.

Question 3: G. Cinque, Alfa-Romeo A.G., Italy

Did you apply the hybrid and MUSCL convective discretization schemes to all of the equations, or only to the momentum equations? Also, what were the wall boundary conditions for the temperature calculations?

Answer:

The hybrid and MUSCL schemes for the convective terms were applied to all of the partial differential equations. The boundedness of both discretization schemes ensures that no over- or under-shoots will occur, and so they were applied without any problems, to all of the equations. The temperature of the boundary wall was prescribed as 650 °K. We have performed other runs with the wall temperature between 500 °K and 800 °K, but the results were very similar.

Validation and Application of a Droplet Evaporation Model for Real Aviation Fuel

K. Prommersberger, G. Maier, S. Wittig

Lehrstuhl und Institut für Thermische Strömungsmaschinen
Universität Karlsruhe (T.H.)
Kaiserstrasse 12
76128 Karlsruhe, Germany

1 SUMMARY

Fuel droplet dispersion and evaporation within the premix duct of a Lean Premixed Prevaporized (LPP) combustor is investigated both experimentally and numerically with a two phase flow code. Mean droplet velocity and diameter distributions have been measured in different axial planes with a Phase Doppler Particle Analyzer. The data of the droplet and gas flow measurements near the nozzle is used to establish the boundary conditions for the simulation. The two phase flow is calculated using a Lagrangian type particle tracking method. For the first time an evaporating fuel spray is simulated by the Distillation Curve evaporation model. Based on fuel property data, this model allows the consideration of the multicomponent behavior of aviation fuels. Downstream measurements of droplet size, volume flux and velocity are compared with the numerical results.

The objective of the study is to present the simulation of a fuel spray evaporation process inside a LPP duct with reasonable computational effort. The numerical calculation of spray propagation and evaporation demonstrates, that the Distillation Curve evaporation model is able to cover typical multicomponent behavior of aviation fuels under realistic operating conditions. The comparison with the experimental data shows that for the given high relative velocities between gas phase and droplets secondary droplet breakup has to be taken into account (as discussed in the paper of Schmehl et. al. presented at this conference).

2 NOMENCLATURE

B_m	-	Spalding mass transport number
B_T	-	Spalding heat transport number
c_p	J/(kg K)	heat capacity
d	m	droplet diameter
D	m ² /s	diffusion coefficient
F	-	Stefan flow correction
Le	-	Lewis number
\dot{m}	kg/s	mass flow
Nu	-	Nusselt number
p	bar	total pressure
Pe	-	Peclet number
Pr	-	Prandtl number
Q_{in}	J/s	heat flux
Re	-	Reynolds number
Sc	-	Schmidt number
Sh	-	Sherwood number
t	s	time
T	K	temperature
Y	-	mass fraction

Greek letters

λ	W/(mK)	thermal conductivity
ρ	kg/m ³	density
σ	-	standard deviation
ω	-	evaporated droplet mass fraction

Subscripts

d	droplet
f	fuel, fuel vapor
g	gas phase
$Pe=0$	Peclet number is 0
$Pe=\infty$	Peclet number is infinite
$Pe=0 \rightarrow \infty$	Peclet number rises from 0 to ∞ within the iteration timestep
ref	gas phase reference value
$start$	start condition
s	droplet surface
∞	free stream condition
0	without Stefan flow
$*$	with Stefan flow

3 INTRODUCTION

In the framework of the development of low emission jet engines, the numerical simulation of the combustion of gas turbine fuels is an important subject. Since the combustion process substantially depends on the fuel atomization, evaporation and air-fuel mixing, the physical properties of different types of aviation fuels have to be considered. Especially for LPP combustors, the interaction of the generation of a lean homogenous mixture and low emission levels is evident. The extensive test rig measurements, which are currently used for the design process, can be reduced using numerical simulation codes as demonstrated in this paper.

The recent enhancements of computer technology in terms of CPU speed and memory space makes a combustor design based on computational fluid dynamics feasible. For the simulation of the two phase flow within a LPP duct at least 20.000 droplet trajectories have to be calculated. The necessary CPU time is in the order of about 10 hours. A major problem with the simulation of the combustor internal flow is still the realistic calculation of fuel evaporation. The evaporation models, which are currently used in commercial CFD codes, cannot account for the multicomponent nature of fuel, because the fuel is represented by a single hydrocarbon. Since aviation fuels are complex mixtures of hundreds of different species with different volatilities, they show a wide boiling range. Important aspects of gas turbine operation like cold

start behavior or autoignition within a LPP duct cannot be calculated correctly with those simplifications. Studies with a two component evaporation code, in which the diffusional mass transport within the droplet is considered, the Diffusion Limit model, showed very good agreement with experimental data. Because the Diffusion Limit Model (DLM) utilizes a discretisation scheme for every single droplet, the computing time required for spray simulation exceeds reasonable limits for engineering purposes. Therefore, only studies concerning single evaporating droplets have been conducted with the DLM so far (Stengle et. al., 1997, 1998).

To provide a physically correct, but still time efficient simulation, an evaporation model has been developed, which is capable to simulate multicomponent fuels without time consuming droplet discretisation. This is possible by a calculation method proposed by Chin (1994), which makes use of the ASTM distillation curves of gas turbine fuels. The thermophysical property of the droplet varies its thermophysical property according to its distillation curve during evaporation. Fuel vapor pressure and the molar mass is determined as a function of the diffusion resistance within the droplet. Convective heat and mass transfer calculations of the gaseous

phase are based on the common methods considering the Stefan flow effect (Abramzon et. al., 1989).

The evaporation model has been implemented as a module for spray calculation into the in-house CFD code EPOS / LADROP. It has been for the first time applied to a combustor fuel spray investigation. The results of the numerical predictions, i.e. droplet mean velocity profiles or spatial distributions of droplet diameter are compared to experimental data of fuel spray collected by PDPA measurements within a model LPP combustor.

4 EXPERIMENTS

The experimental investigation of the air flow field and the measurement of droplet velocity and size distributions is carried out in order to determine the effect of the air fuel mixing on the emissions of a LPP combustor. The main focus of the present study is on the numerical simulation of the two phase flow inside the premix duct, only the experimental results concerning this part of the combustor are presented here. Experimental results concerning the pollutant emission measurements are described by Layher et. al., 1998.

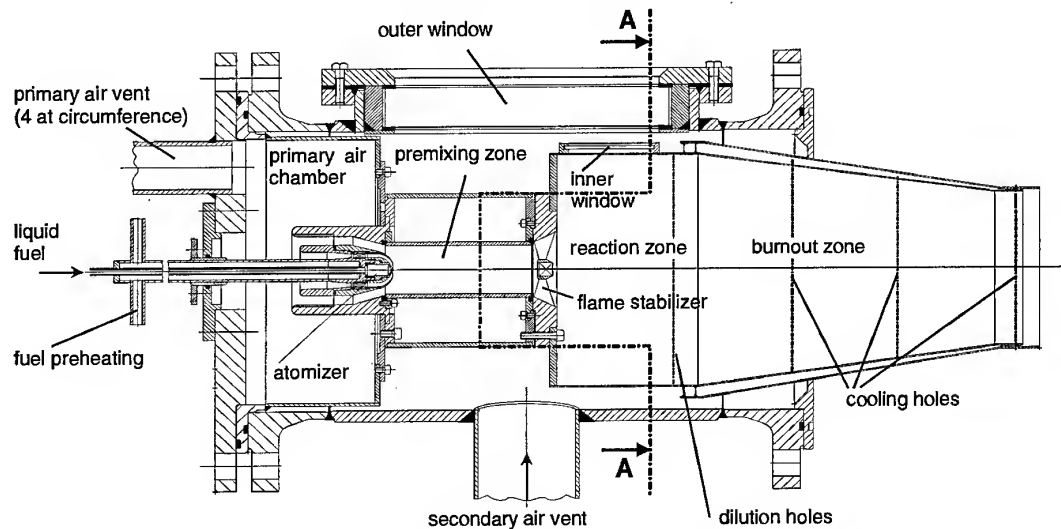


Fig. 1: Longitudinal section of the experimental premix combustor with optical access for PDPA measurements

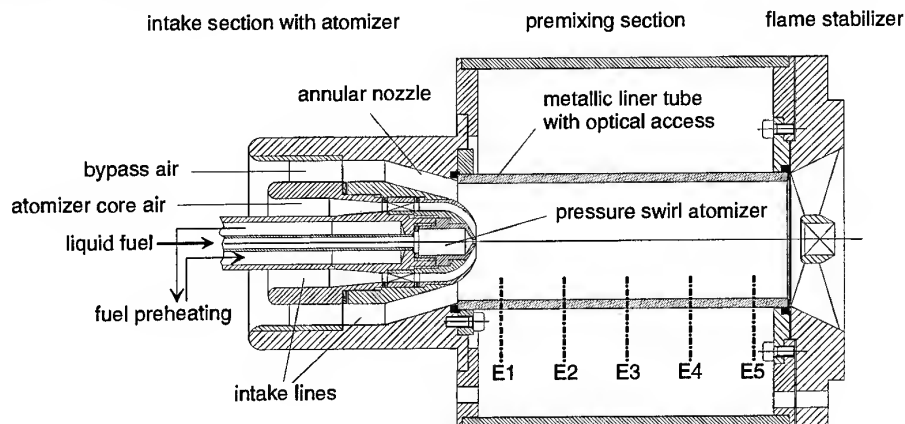


Fig. 2: Atomizer and premix duct in detail. The distance of the measurement planes E1 – E5 from the nozzle orifice are: E1 = 20 mm, E2 = 25 mm, E3 = 55mm, E4 = 70 mm, E5 = 90mm.

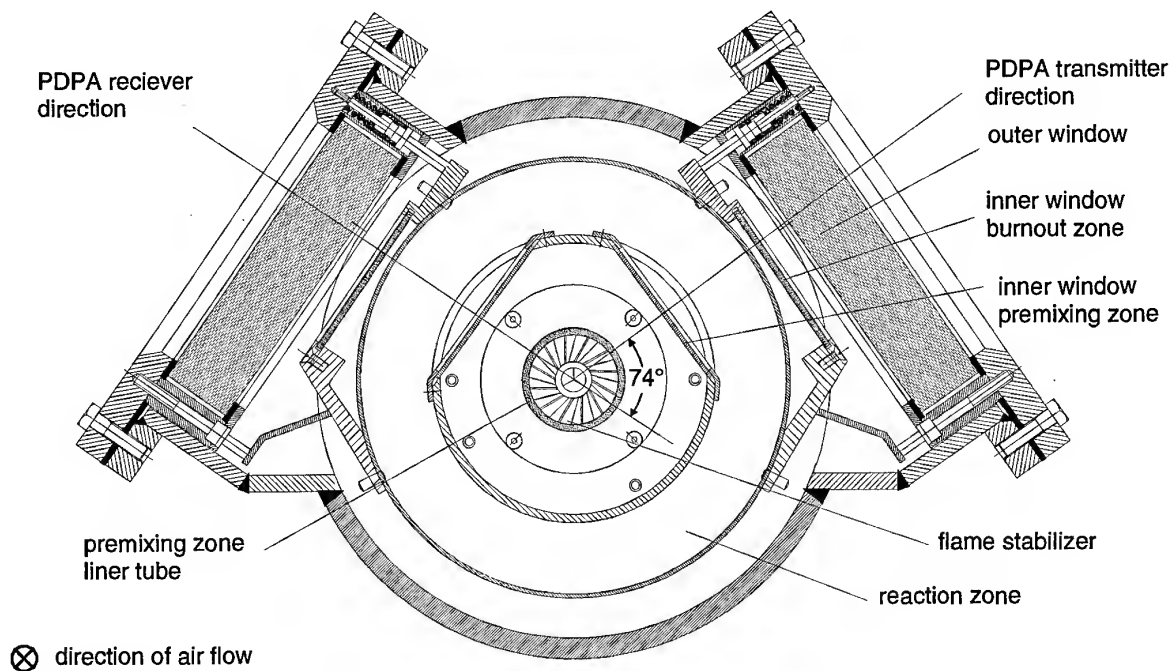


Fig. 3: Cross section along A-A in Fig. 1 of the LPP model combustor: Optical access for Phase Doppler Anemometry

4.1 Experimental Set-Up

Fig. 1 shows a cross section of the model LPP combustor: The primary air is guided by four uniform radial arranged tubes into the primary air chamber, which is used as tranquilizing volume. The flow through the atomizer is divided into two coannular streams. The inner air flow is accelerated and hits the spray cone of the pressure swirl atomizer with an angle of 80° relative to the spray axis. The outer stream shields the spray in the premix duct to avoid droplet wall interactions. The flow inside the premixing zone is free of swirl in order to avoid wall film buildup caused by centrifuged fuel droplets. Flame stabilization is realized by an axial swirler at the exit of the premix duct.

A cylindrical geometry is chosen for the premix duct in order to provide convenient optical access for laser measurement techniques. The attached combustor section is similar to a jet engine tubular combustor. Consequently this setup can be regarded as a combination of an experimental premix duct and a combustor with realistic geometry. This allows the analysis of the fuel preparation in terms of grade of evaporation and degree of unmixedness and its effect on the combustor emissions.

The premix duct has a diameter of 44,6mm and a length of 124mm. In order to provide optical access for the PDPA-measurements five different ducts are used with each a slit at different axial positions (E1 .. E5 in Fig. 2). For visualization techniques a quartz glass tube with the same dimensions is used instead of the metal ducts.

The main part of the combustion chamber is the air assisted pressure swirl atomizer ("Simplex Air Assist"), as shown in Fig. 2. The atomization process is based upon the aerodynamic

interaction between fuel and air by intended induction of an atomizing air stream towards the liquid sheet of a pressure swirl atomizer. This principle can be regarded as a combination of pressure and airblast atomization, which was developed and thoroughly investigated at the Institut für Thermische Strömungsmaschinen (Maier, 1998).

4.2 Measurement Technique

Droplet diameter, axial and radial velocity distributions are measured by a Phase Doppler Particle Analyzer (PDPA) at five axial locations. Consequently all plots concerning the planes E1 ... E5 are results of many single punctual measurements along the radius. An off axis angle of 74 degrees is chosen for the experimental setup, because the dominant light scattering mode is independent from the droplet temperature. The achieved intensity of the scattered light is high with this configuration (Maier, 1995).

Additional measurements of the air flow at several radial points in the primary air chamber at the front of the inlet of the atomizer duct are conducted. This measurement are carried out with a two dimensional Laser Doppler anemometry system. This additional data is used for the validation of the calculation results of the gas flow field.

5 NUMERICAL INVESTIGATION

As illustrated in Fig. 6, the two phase CFD code used for the calculations is composed of two separate modules:

- **EPOS:** a 3D Finite Volume code for predicting the turbulent gas flow.
- **LADROP:** a 3D particle tracking code for the spray computation including spray / wall and spray / film interaction.

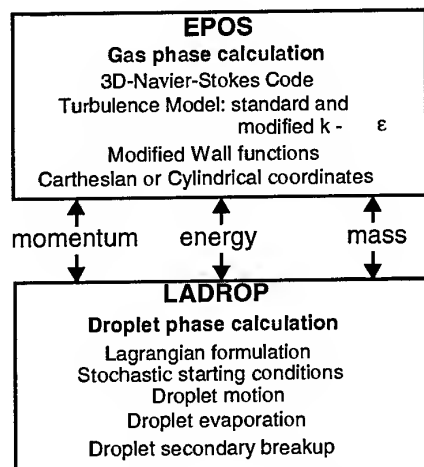


Fig. 4: Interaction of gas phase and droplet liquid phase model

Initially, a gas phase calculation with the EPOS module is performed. The results are validated by the experimental data of the Laser Doppler Anemometry measurements. Based on the resulting gas flow field, the droplet motion and evaporation calculation is carried out by one iteration with LADROP, which determines the source terms for momentum, heat and mass transfer between the liquid and the gas phase. These source terms are coupled into a second gas phase calculation in order to determine the effect of droplets and fuel vapor on the flow field. The coupled calculations of gaseous and liquid phase are repeated until convergence is reached. A more detailed explanation of the coupling procedure is provided by Schmehl et. al., 1998b and Roßkamp, 1997. All following explanations concern the LADROP module alone, in which the Distillation Curve Model is implemented as an additional droplet evaporation model.

5.1 Basics of Droplet Evaporation Modeling

As illustrated in Fig. 5 the evaporation process of a multicomponent droplet can be separated into three domains for the heat and mass transfer model:

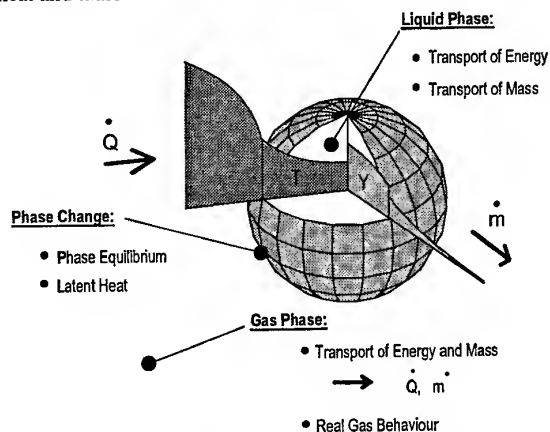


Fig. 5: Profiles of temperature and concentration within the droplet and the surrounding gas phase

Droplet liquid:

Heat conduction and mass transport by diffusion and radial equilibrium flux. Since the most volatile droplet component evaporates first, mass diffusion is induced causing a variation of the liquid consistency during droplet lifetime.

Droplet surface:

Coupling of liquid and gaseous phase by phase equilibrium equation (vapor pressure equation)

Surrounding gas:

Heat and mass flux from droplet surface into surrounding gas phase

For the numerical calculation of the evaporation process some assumptions and simplifications must be considered. Fig. 6 gives a comparison of three different evaporation models and their individual assumptions.




Model	Rapid-Mixing Model (RMM)	Thin-Skin Model (TSM)	Diffusion-Limit-Model (DLM)
liquid phase	rapid diffusion no gradients of temperature and concentration	no diffusion of components, composition unchanged	diffusive, onedimensional heat- and mass transport
gas phase	integral formulation of surrounding gas phase		
discret.-scheme	 no discretisation	 no discretisation	 1-dim. discretisation (min. 20 nodes)
	medium effort, restricted validity	medium effort, restricted validity	very high effort, in common correct calculation

Fig. 6: Multicomponent evaporation models

Rapid Mixing Model:

This model assumes equilibrium evaporation of the droplet comparable with a batch distillation process. The diffusion resistance within the droplet is zero. The model delivers reasonable results for slow evaporation processes, when droplet internal heat conduction and diffusion has not a major effect on the internal temperature and concentration profiles.

Thin Skin Model:

The droplet fluid temperature and consistency is unchanged during evaporation assuming a infinite diffusion resistance. Only a thin layer on the droplet surface is heated and evaporated. The validity of the model is limited to cases when the droplet reaches its boiling temperature immediately after the start of the evaporation process.

Diffusion Limit Model:

The temperature and concentration distribution inside the droplet are determined using a discretisation scheme to solve the equations of heat conduction and mass diffusion. In comparison with experiments, the Diffusion Limit Model (DLM) was found to be the most accurate multicomponent evaporation model (Stengle, 1998). It proved reliability even for supercritical gas phase conditions. The major disadvantage of this model is the enormous computational effort. In addition as only binary diffusion coefficients are known, the DLM is limited to bicomponent droplets.

5.2 The Distillation Curve Model

In order to combine the efficiency of single component evaporation models with the possibility to calculate real aviation fuel spray evaporation, the Distillation Curve Model was developed. The Distillation Curve Model assumes an uniform temperature profile inside the droplet. The determination of fuel vapor pressure and molar weight during evaporation is based on the distillation curve as pointed out in Bardon (1986).

Further simplifications are:

- The droplet consists of a single component liquid, which changes its thermophysical properties during evaporation in order to simulate the multicomponent nature of aviation fuel.
- The droplet evaporates in an inert atmosphere. The interface between liquid and gas phase is assumed to be in thermodynamic equilibrium.
- Radiative heat transfer is neglected (Lage, 1992).
- Fick's law is used to calculate mass diffusion. Dufour and Soret effects are not considered.
- The evaporation process is assumed to be spherically symmetric, the asymmetric convective effects on the evaporation process are included implicitly in the correlation of Ranz and Marshall (1952).

Liquid Phase and Phase Equilibrium Equations

At the beginning of the evaporation of fuel droplet the most volatile fractions evaporate. The heavy species remain in the droplet resulting in a rising liquid density. Thus, assuming a constant temperature level, the vapor pressure on the droplet surface decreases. Only in the case of equilibrium evaporation, this process can be described by vapor pressure correlations. If the droplet temperature is very high, the droplet lifetime is shorter than the significant time of mass diffusion. Therefore the lighter fractions of the droplet center cannot reach the surface, so that the resulting vapor pressure is different from the equilibrium case. The influence of diffusion resistance on the evaporation can be quantified by the liquid Peclet number, which is defined as the ratio of surface regression rate and the diffusion coefficient (Makino, 1988).

$$Pe = \frac{\dot{m}}{2\pi d D_f \rho_f} \quad (5-1)$$

A Peclet number ≈ 0 describes equilibrium evaporation following the fuel distillation curve. For $Pe \rightarrow \infty$ the diffusion within the droplet is suppressed or the evaporation is very fast, leaving the droplet composition unchanged. In the latter case also the vapor pressure is constant and meets the mean vapor pressure of the droplet liquid. For Peclet numbers between both limits the vapor pressure and the molar weight is calculated by an exponential interpolation equation:

$$p_{fs} = p_{Pe=\infty} + (p_{Pe=0} - p_{Pe=\infty}) e^{-cPe} \quad (5-2)$$

Variable c is a function of the evaporated droplet fraction, which was determined by Chin from Diffusion Limit Model calculations of Law (1977), Makino (1988) and Kneer (1993).

$$c = 0.305\omega - 0.35\omega^2 + 0.14\omega^3 \quad (5-3)$$

The effect of the Peclet number on the vapor pressure at the droplet surface during evaporation is shown in Fig. 7.

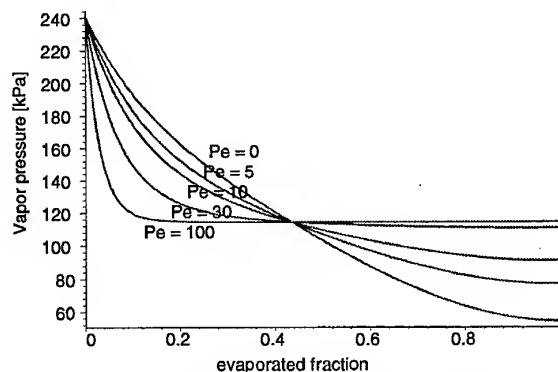


Fig. 7: Vapor pressure during evaporation as function of the liquid Peclet number. Jet-A1, $T_{fuel}=500$ K

Although this function should be adapted individually to each type of fuel, the results with Eq. 5-3 for the fuels illustrated in Fig. 10 showed good agreement with experimental results.

In a similar manner, the molar weight of the fuel vapor is also influenced by the liquid Peclet number. The variable c is again defined by Eq. 5-3.

$$M_{fv} = M_{fv,Pe=\infty} + (M_{fv,Pe=0} - M_{fv,Pe=\infty}) e^{-cPe} \quad (5-4)$$

Fig. 8 illustrates the influence of the Peclet number on the molar weight of the fuel vapor near the droplet surface.

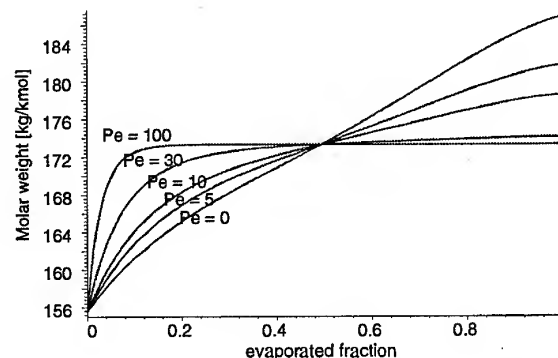


Fig. 8: Molar weight of the vapor pressure during evaporation as function of the liquid Peclet number. Jet-A1, $T_{fuel}=500$ K

The latter calculation method is only valid for constant droplet temperature a Peclet number. In reality the liquid Peclet number increases during the droplet evaporation with the evaporation rate caused by the droplet heatup from 0.3 at the beginning to about 18.

To implement Eq. 5-4 also for variable Peclet numbers, the equation has to be modified in that way, that the upper and lower limit of the molar weight and vapor pressure have to be calculated dependent from the droplet history. This procedure is broadly explained by Chin (1994), and is applied without modifications.

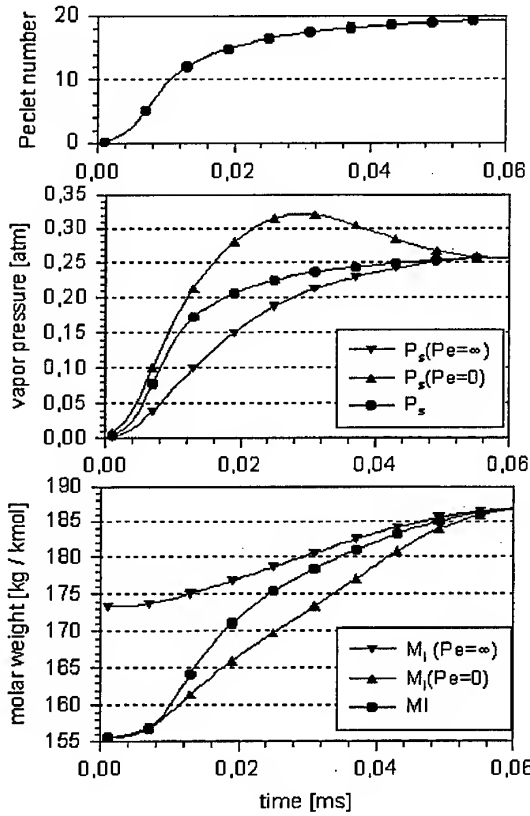


Fig. 9: Peclet number, vapor pressure and molar weight of JET-A during evaporation process. $T_\infty=800$ K, $p_\infty=1$ bar, $d_0=100\mu\text{m}$, stagnant atmosphere

As a result Fig. 9 shows the vapor pressure and the molar weight of an evaporating 100 micron JET-A droplet during its lifetime. The vapor pressure reaches its maximum at half of the droplet lifetime. At this point the heatup process is nearly in equilibrium causing the high vapor pressure. Because the Peclet number is still comparatively low, most of the high volatile droplet species leave the droplet due to mass diffusion effects. Therefore the vapor pressure decreases during the second half of droplet lifetime.

Gas Phase Equations

For the application of the Distillation Curve Model the gas phase is assumed to be quasi-steady. Delplanque (1993) proved that this assumption is valid for typical high pressure spray application, since the characteristic timescale of the flow around the droplet is significantly shorter than the droplet lifetime. Applying the integral solution of the governing equations (Hubbard, 1975) and the extended film theory of Abramzon (1989), the evaporating mass flow of the droplet and the heat transfer from the hot environment towards the droplet are calculated as follows:

The convective effects on the heat and mass transfer of the evaporating droplet are determined by modified Nusselt and Sherwood numbers following equations 5-5 and 5-6.

$$\text{Nu}^* = 2 + \frac{\text{Nu}_0 - 2}{F(B_T)} \quad (5-5)$$

$$\text{Sh}^* = 2 + \frac{\text{Sh}_0 - 2}{F(B_m)} \quad (5-6)$$

The radially outward directed flow of the evaporating droplet mass for heat and mass transfer is described by the terms $F(B_T)$ and $F(B_m)$.

$$F(B_T) = (1 + B_T)^{0.7} \frac{\ln(1 + B_T)}{B_T} \quad (5-7)$$

$$F(B_m) = (1 + B_m)^{0.7} \frac{\ln(1 + B_m)}{B_m} \quad (5-8)$$

To calculate the Nusselt and Sherwood numbers Nu_0 and Sh_0 , the correlations of Ranz and Marshall (1952) are used in equations 5-5 and 5-6.

$$\text{Nu}_0 = 2 + 0.6\sqrt{\text{Re}_d} \text{Pr}^{1/3} \quad (5-9)$$

$$\text{Sh}_0 = 2 + 0.6\sqrt{\text{Re}_d} \text{Sc}^{1/3} \quad (5-10)$$

By the integration of the quasi-steady energy and mass equations the evaporating mass flow of the droplet is obtained.

$$\dot{m}_{\text{vap}} = 2\pi r_d \frac{\lambda_{g,\text{ref}}}{c_{p,g,\text{ref}}} \text{Nu}^* \ln(1 + B_T) \quad (5-11)$$

$$\dot{m}_{\text{vap}} = 2\pi r_d \rho_{g,\text{ref}} D_{g,\text{ref}} \text{Sh}^* \ln(1 + B_m) \quad (5-12)$$

where B_T and B_m are the Spalding heat and mass transfer numbers.

$$B_T = \frac{\dot{m}_{\text{vap}} c_{p,g,\text{ref}} (T_{g,\infty} - T_{g,s})}{\dot{Q}_{\text{tot}}} \quad (5-13)$$

$$B_m = \frac{Y_{f,s} - Y_{f,\infty}}{1 - Y_{f,s}} \quad (5-14)$$

The necessary thermophysical properties are obtained following the 1/3-rule of Renksizbulut (1983). The only exception is the gas density of the Reynolds number, which is calculated at free stream conditions (Yuen, 1976). Combining equations 5-11 and 5-12 the following relationship is obtained.

$$B_T = (1 + B_m) \frac{1}{\text{Le}_g} \frac{\text{Sh}^*}{\text{Nu}^*} - 1 \quad (5-15)$$

The calculation procedure starts from equation 5-11 where the evaporating mass flow of the liquid fuel is calculated. From this, B_T is determined by equation 5-13. This has to be done by iteration. Furthermore, the total heat transfer from the surrounding gas towards the droplet is calculated using equation 5-15.

For the calculation of the droplet motion, the drag coefficient is determined by a correlation of Renksizbulut (1983), where the flow of the evaporating fuel radially outward is included. The Reynolds number is calculated again with the free stream density (Yuen, 1976).

$$c_w(1+B_m)^{0.2} = 0.36 + 5.48 \cdot \text{Re}_d^{-0.573} + \frac{24}{\text{Re}_d} \quad (5-16)$$

5.3 Effect of Fuel Type on Droplet Evaporation

As an example the Distillation Curve Model is applied on 100 micron droplets exposed to a stagnant hot atmosphere. The results of the calculation for different fuel types are presented in Fig. 10.

The droplet lifetimes for different fuels vary remarkable due to their different volatility. The volatility is reverse proportional to the molar weight and the normal boiling temperature of the fuels as shown in Tab. 1.

	molar weight [kg/kmol]	boiling temperature [K]	evaporation time [s]
JP4	124.0 *	416.0 *	0.052
Decane	142.5	447.3	0.054
JetA-1	173.0 *	489.0 *	0.063
Diesel fuel	215.0 *	537.0 *	0.072

* mean values

Tab. 1: Thermophysical properties of different fuel types

Furthermore, the droplet temperature at the end of the droplet lifetime is also dependent on the boiling temperature of the fuel. A significant difference is revealed if the droplet temperature charts of real fuels are compared with the chart of decane. The temperature chart of decane in Fig. 10 indicates a plateau in the latter half of the droplet lifetime, whereas the heatup of the real fuel droplets is continued until full evaporation. The JP4 droplet for example is far from thermal equilibrium at the end of droplet lifetime with a still steep increase of the droplet temperature.

Because the fuel volatility extensively affects the current evaporation rate, the realistic formulation of the thermophysical data of the droplet liquid is an essential condition for the exact evaporation simulation. Since the resulting fuel vapor concentration field is a result of a superposition of numerous evaporating droplets, the correct prediction of the evaporation rate in any point of the droplet lifetime is necessary. The correct prediction of the evaporation time, which is widely considered as an quality criterion for evaporation models, is not sufficient.

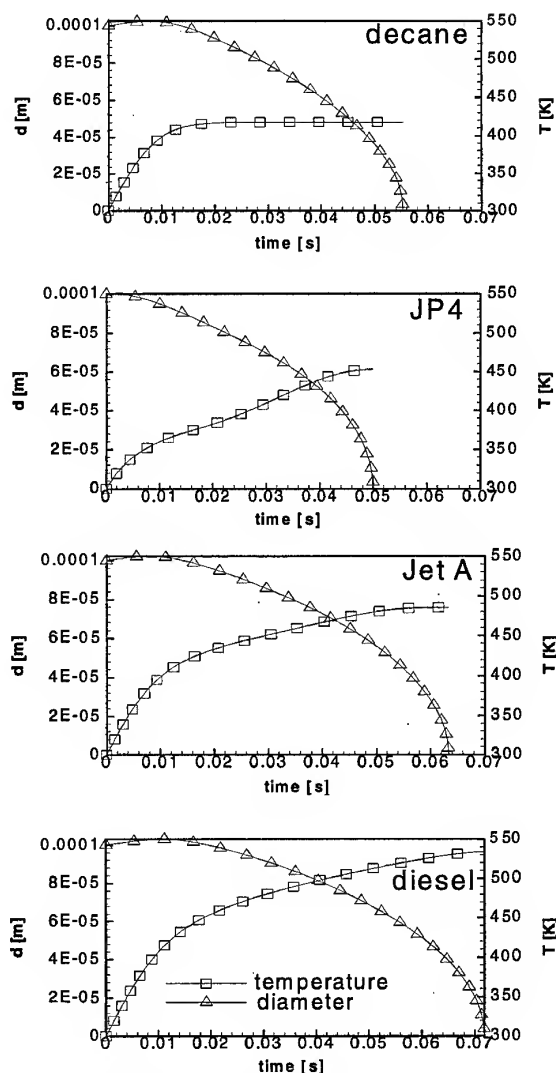


Fig. 10: Droplet diameters and temperature during evaporation for different fuel types: ambient pressure $p_\infty = 1$ bar; initial droplet diameter $d_0 = 100 \mu\text{m}$; ambient temperature $T_\infty = 800$ K, Distillation Curve Model calculation

6 EXPERIMENTAL RESULTS

In the first step a laser sheet visualization of the spray inside the premix duct is performed in order to get an information about the overall flow field. A typical light sheet picture is illustrated in Fig. 11. In the periphery region of the spray cone a cumulation of larger droplets is discovered, which results from the disintegration of the light sheet. In the center of the spray significantly smaller droplets are found. They appear in light sheet pictures only as a grey layer because of the limited resolution of the camera system. The small droplets follow the inward directed air flow very well resulting in a minimum of the characteristic droplet diameter at the spray axis. An inhomogeneity of the spray structure, which is induced by aerodynamic wake effects, is clearly observable in the visualizations. The local distance of the dense spray portions is found to be proportional to the gas flow velocity.

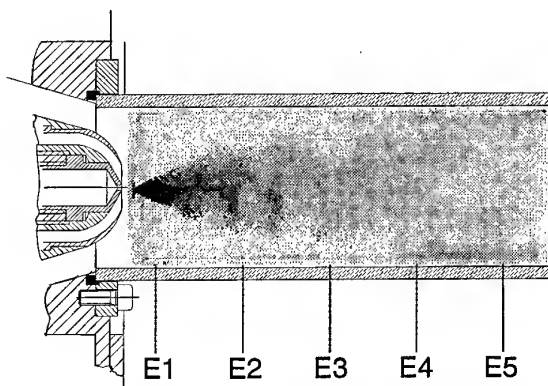


Fig. 11: Laser light sheet visualization of the fuel spray within the premix duct

The thickness of the light sheet is 2+3 mm. Therefore with increasing radial expansion of the spray the amount of droplets within the illuminated volume decreases. This should not be interpreted as an effect of droplet evaporation. In fact, only a partial evaporation of the fuel is observed.

Fig. 12 shows the radial distribution of the normalized local volume flux distribution. This quantity is defined as the volume flux passing the area of a coaxial ring of 1 mm width and the radius of interest. Because this quantity is normalized, only the radial spray dispersion can be seen in this chart.

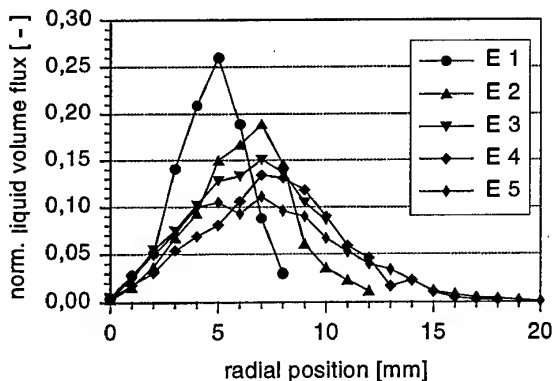


Fig. 12: Measured radial liquid volume flux distribution of the droplet phase

Near the nozzle orifice the radial distribution of the fuel is clearly peaked due to the hollow cone character of the atomizer. Downstream the volume flux maximum shifts as expected radially outward while lowering its maximum value due to evaporation and dispersion.

The interaction between gas phase and droplets is illustrated by the chart of the measured droplet axial velocity in Fig. 13. For the plane E1 nearest the atomizer the axial velocity of the droplets decreases in radial direction. This is caused by the wake region of the atomizer air channels. Downstream the droplets accelerate gradually to the velocity level of the gas phase. The radial velocity profile is mainly influenced by the fast bypass air stream. At the last two measurement planes E4 and E5 nearest the exit of the premix duct the droplets reach almost the free stream velocity.

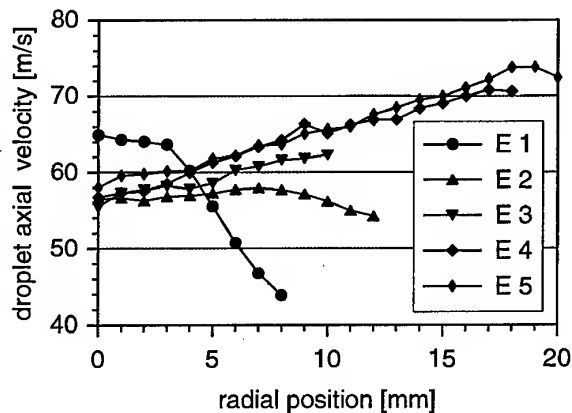


Fig. 13: Mean velocity of the droplets at the axial positions indicated in Fig. 2

The radial distribution of the Sauter mean diameter (D_{32}) shows again the hollow cone character of the fuel spray in the measurement plane E1. A mean diameter of 45 microns is measured at the spray axis. At 8 mm radial flow position a maximum value of 70 microns is detected. In the measurement plane E2 the point where maximum diameters occur is located further away from the axis.

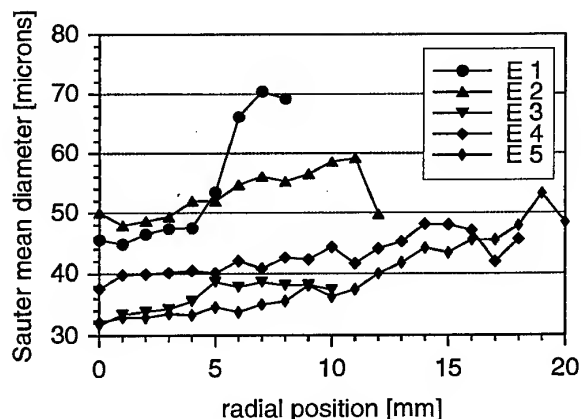


Fig. 14: Sauter mean diameter at different axial positions

The significant decrease of the droplet diameters between plane E2 and E3 cannot be explained by droplet dispersion and evaporation. The residence time and consequently the droplet heating time of the droplets in this region is too short for a fuel evaporation of this extent. Furthermore the high relative velocity of air and fuel droplets causes secondary droplet breakup within the region of plane E2. The Weber number of about 20 and the Ohnesorge number of 0.05 the characteristic breakup criterion is considerably exceeded at this point (Samenfinck, 1994). The droplets are deformed into a bubble and break into several secondary droplets. In this region the secondary atomization affects the PDPA measurements with higher occurrence of phase errors caused by irregularities of the droplet shape.

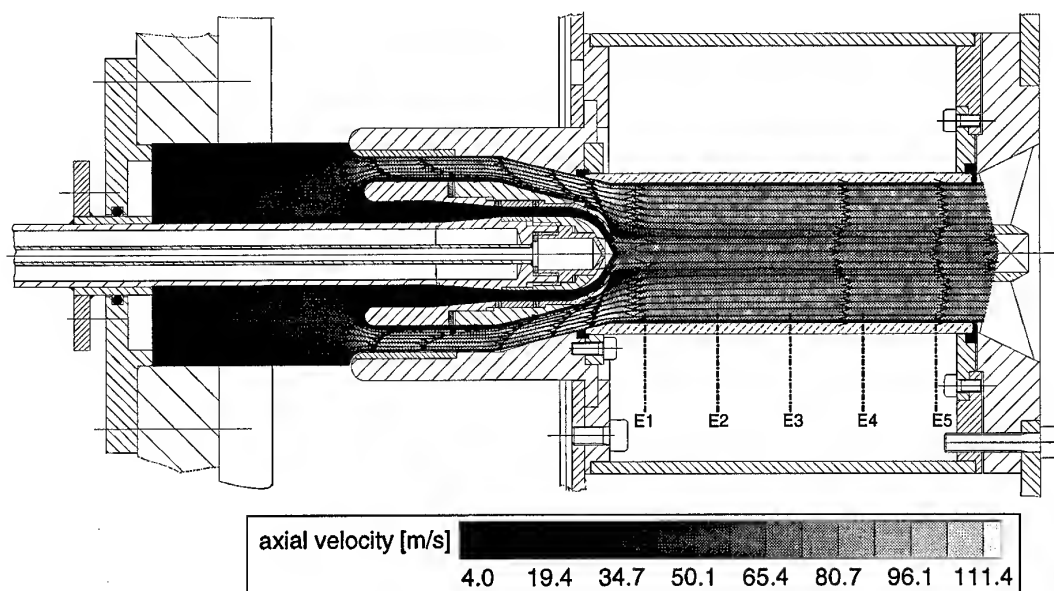


Fig. 15: Calculation of gas phase velocity: axial velocity field and streamlines in the atomizer region

7 TWO PHASE FLOW SIMULATION

In order to achieve thorough boundary conditions for the calculation of the gas phase flow field within the evaporation duct, the complete flow path is considered. This includes the atomizer and bypass air stream from the primary air chamber to the flame holder at the exit of the premix duct. All boundary conditions used for the calculations are listed in Tab. 2.

droplets	
fuel massflow	6 g/s
temperature	350 K
absolute velocity	30 m/s
gas phase	
temperature	753 K
pressure	4.0E5 Pa
turbulence level	15 %
air mass flow	213 g/s

Tab. 2: Boundary conditions for two phase flow calculation

7.1 Gas Phase Calculation

At the entrance of the primary air chamber an uniform air velocity field assumed for the gas phase calculations. As illustrated in Fig. 15, the resulting axial velocity of the atomizer air is significantly lower than the bypass air because of the convergent contour of the channel. At the nozzle orifice the inward directed air streams of the atomizer impinge resulting in a fast axial air streak at the spray axis. Its velocity reaches the level of the bypass air inside the premix duct. Only in the wake of the atomizer body a domain of slower air occurs.

7.2 Droplet Initial Conditions

The droplet initial conditions are determined in order to match the light sheet visualizations and the PDPA measurements of the first measurement plane satisfactorily.

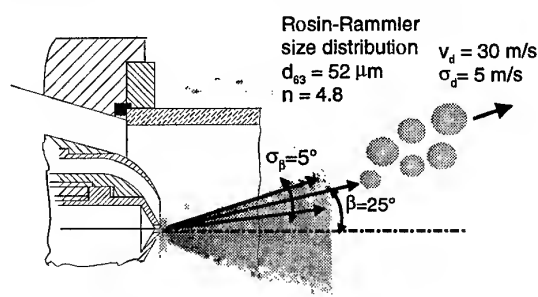


Fig. 16: Determination of the droplet initial conditions

The location of the droplet source is assumed to be near the location of the liquid sheet disintegration. The droplet diameter distribution is fitted by means of the widely used Rosin-Rammler function. Fluctuations of the droplet injection angle and velocity are simulated by the use of random processors.

7.3 Calculation Results

Fig. 17 presents the results of the normalized local volume flux distribution. This quantity is defined as the volume flux passing the area of a coaxial ring of 1 mm width and the radius of interest. The first measurement plane is used for the formulation of the droplet initial conditions. Therefore the accordance between measurements and calculation is nearly perfect at this point. Downstream the radial dispersion of the spray is clearly overestimated, which results from the secondary atomization of the larger droplets. Secondary droplet break-up takes place up to

50 mm downstream the nozzle, as shown by Schmehl (1998b). As the main focus of this study is on the evaporation model, secondary atomization effects are not considered here. Consequently all subsequent results are influenced by the negligence of this phenomenon.

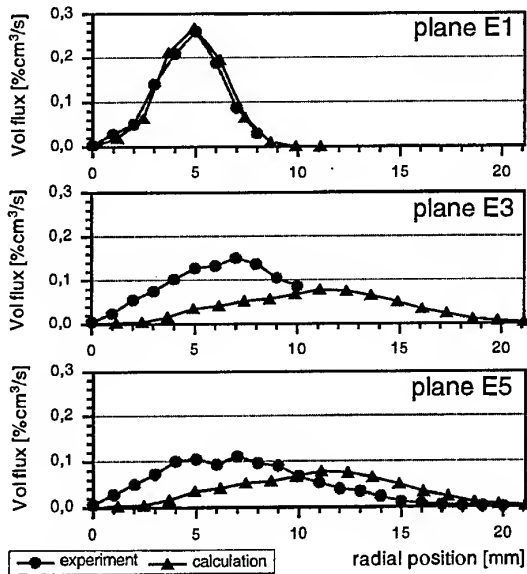


Fig. 17: Radial distribution of the liquid volume flux at different axial positions

Because the inertia of larger droplets is significantly higher, the radial spray propagation is overestimated. The maximum value of the radial volume flux distribution in for measurement planes E3 and E5 in Fig. 17 is therefore flatter in comparison to the measurement and its location is shifted towards the duct wall.

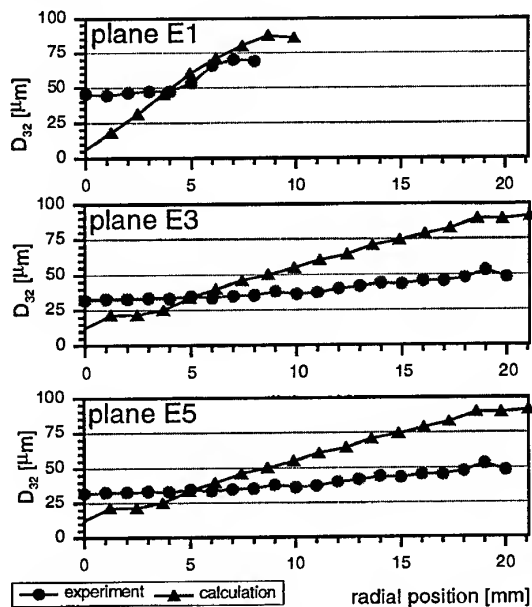


Fig. 18: Sauter mean diameter distribution

Of course, the deficiency of the correct simulation of the secondary atomization affects also the predicted droplet diameter distribution shown in Fig. 18. In the measurement plane E1 the calculated droplet diameters near the spray center are too small, which results from the assumed droplet initial conditions. With an off-axis angle of 25 degrees for the mean droplet trajectory and a standard deviation of 5 degrees as illustrated in Fig. 16, too less large droplets remain in the spray core resulting in a decline of the droplet mean diameter. At the downstream locations E3 and E5 again an overestimation of the droplet diameter inside the spray is obvious.

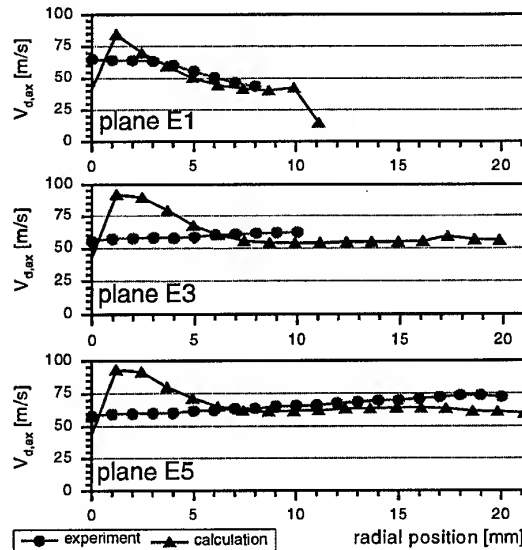


Fig. 19: Radial profiles of droplet mean axial velocity

As illustrated in Fig. 19, the calculated axial droplet velocities are also affected by the inexact droplet diameter calculation. Especially in the spray core, where too small droplets are assumed, the calculation predicts velocities which exceed the measurement results in all axial positions. From the droplet diameters at the exit of the premix duct an evaporated fuel mass ratio of 33% is determined.

To make sure that the deviations from the experimental data are not caused by the new evaporation model, an additional calculation with the standard Uniform Temperature Model has been carried out. As shown in Fig. 20, the resulting droplet diameter distributions are nearly identical. With the use of an additional secondary atomization module, the quality of the numerical prediction can be raised substantially as demonstrated by Schmehl (1998b).

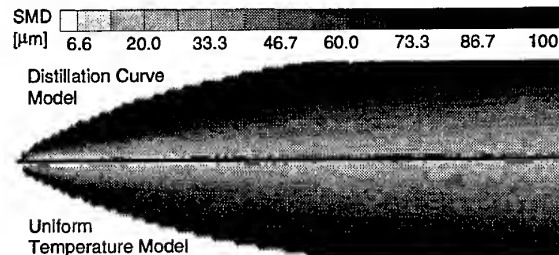


Fig. 20: Comparison of calculated Sauter mean diameters: Distillation Curve Model (above) and Uniform Temperature Model (below)

The resulting fuel vapor concentration inside the premix duct is presented in Fig. 21. Due to the absence of any swirl, the vapor concentration at the exit of the premix duct is far from uniform. At the spray axis a high vapor concentration is determined. This can be explained by the relatively small droplets in the spray core.

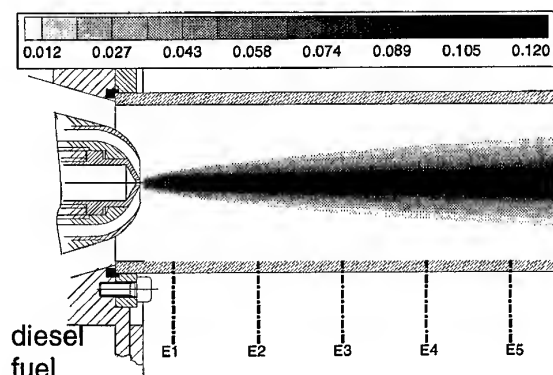


Fig. 21: Fuel vapor concentrations inside premix duct for diesel oil

In Fig. 22 the calculation with the same boundary conditions is shown for tetradecane as liquid phase. For this simulation the Uniform-Temperature-Model is used. Compared with the diesel case, the maximum concentration of vapor is lower and the vapor phase propagation is far less extended.

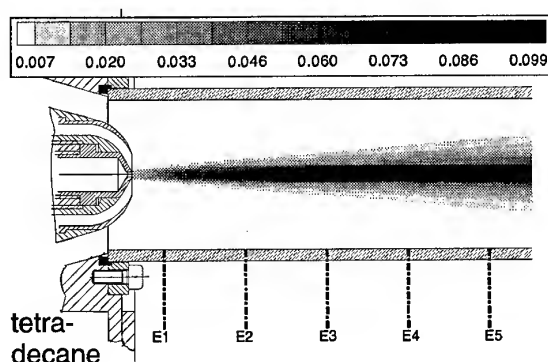


Fig. 22: Vapor concentration profile for tetradecane

This difference results from a multicomponent effect on the aviation fuel evaporation. According to its ASTM boiling curve, diesel fuel contains more volatile fractions than tetradecane. These volatile fuel fractions leave the droplet surface instantly when exposed to a hot environment. Thus the evaporation rate of a diesel droplet rises faster than the evaporation rate of its tetradecane counterpart.

This behavior is most significant for large droplets due to their long heat up period. In Fig. 23 the calculated droplet diameter and temperature charts of a 96 micron droplet passing the premix duct is shown for both diesel fuel and tetradecane.

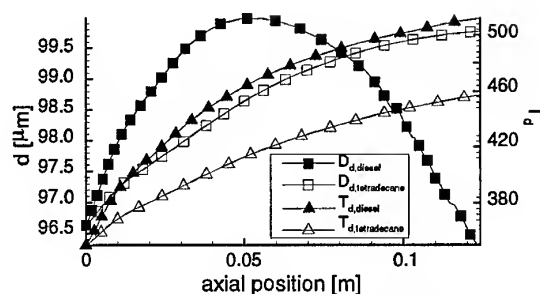


Fig. 23: Diameter and temperature of a large droplet passing the LPP premix duct. Comparison of tetradecane and diesel fuel.

The droplet diameter of the diesel droplet decreases significantly in the second half of the flow path, whereas the tetradecane droplet permanently increases its diameter due to thermal expansion. The evaporation rate of the diesel droplet is higher in the first stages of its evaporation model than for a tetradecane droplet. Consequently the resulting vapor concentration in the gas phase will be higher with a diesel fuel spray, if only a part of the droplet fluid is evaporated within the volume of interest.

8 CONCLUSIONS

The Distillation Curve evaporation model is applied for the first time to the simulation of an evaporating fuel spray. The two phase flow inside the premix duct of a lean premixed prevaporized combustor is calculated with consideration of the multicomponent character of fuel. The fuel property data is derived from the ASTM distillation curve. The boundary conditions for the calculations are taken from experimental data of Phase Doppler Particle Analyzer measurements.

In accordance with the experiments, only a partial evaporation of the fuel spray is predicted by the Distillation Curve evaporation model. The high air flow velocity inside the premix duct causes secondary droplet breakup, which influences the droplet diameter and velocity distributions. These secondary atomization phenomena are not considered by the evaporation model. Therefore, the calculation overestimates the droplet sizes and, in consequence, the volume flux distribution. The comparison with an additional calculation of the droplet diameter distributions using the Uniform Temperature Model proved that the observed deviations are not caused by the evaporation model itself.

In comparison with tetradecane, the Distillation Curve Model predicts a higher fuel vapor concentration, according to the higher volatility of diesel fuel at the beginning of the evaporation process. The vapor concentration profile is more dispersed than in the Uniform Temperature Model result, proving the capability of the Distillation Curve Model to account correctly for multicomponent effects.

With further extensions of the Distillation Curve Model concerning secondary atomization and droplet wall interactions, the presented model offers a practical and efficient tool for the calculation of fuel preparation.

9 ACKNOWLEDGEMENT

The present work was supported by the SFB 167 (high intensity combustors) of the Deutsche Forschungsgemeinschaft, which is gratefully acknowledged.

10 REFERENCES

- Abramzon W. A., Sirignano, 1989, "Droplet vaporization model for spray combustion calculations", *Int. J. Heat Mass Transfer*, Vol. 32, pp. 1605 - 1618
- Bardon, M. F., Rao, V. K., Vaivads, R., Evans, R., 1986, "Measured and predicted Effect of the Extent of Evaporation on Gasoline Vapor Pressure", *Journal of the Institute of Energy*, pp. 216-221
- Chin, J. S., 1994, "An Engineering Calculation Method for Multi-Component Stagnant Droplet Evaporation with Finite Diffusivity", ASME-94-GT-440
- Delplanque, P., 1993, "Liquid-oxygen droplet vaporization and combustion: analysis of transcritical behavior and application to liquid-rocket combustion instability", Ph.D. Thesis, University of California, Irvine
- Hallmann, M., Scheurlen M., Wittig, S., 1993, "Computation of turbulent evaporating sprays: Eulerian versus Lagrangian approach", ASME-93-GT-333
- Hubbard, L., Denny V. E., and Mills, A. F., 1975, "Droplet evaporation: effects of transient and variable properties", *Int. J. Heat Mass Transfer*, Vol. 18, pp. 1003 - 1008
- Kneer, R., Schneider, M., Noll, B., Wittig, S., 1993, "Effects of Variable Liquid Properties on Multicomponent Droplet Vaporization, *Journal for Engineering of Gas Turbines and Power*, Vol. 115, pp. 467 - 472
- Kurreck, M., Willmann, M. and Wittig, S., 1996, "Prediction of the three-dimensional reacting two-phase flow within a jet-stabilized combustion", ASME-96-GT-468
- Lage, L. C. and Rangel, R. H., 1993, "Single droplet vaporization including thermal radiation absorption", *J. of Thermophysics and Heat Transfer*, Vol. 7, pp. 502 - 509
- Law, C. K., Prakash, S. und Sirignano, W. A., 1977, "Theory of Convective, Transient, Multicomponent Droplet Vaporization", *Proc. 16th Symp. Int. on Combustion*, pp. 605 - 617
- Layher, W., Maier, G., Wittig, S., 1998, "Gemischaußbereitung und Emissionsverhalten einer druckbeaufschlagten Vormischbrennkammer", DGLR Jahrestagung 1998
- Makino, A., Law, C. K., 1988, "On the controlling parameter in the gasification behavior of multicomponent droplets", *Combustion and Flame*, Vol. 73, pp. 331 - 336
- Maier, G., Bauer, H.J., Wittig, S., 1995, "In situ-Charakterisierung des Sprühstrahls einer druckbeaufschlagten Gasturbinenbrennkammer - Einfluß von Druck und Luftmassenstrom", 11. Tecflam Seminar, Heidelberg
- Maier, G., Willmann, M., Wittig, S., 1997, "Development and Optimization of Advanced Atomizers for Application in Premix Ducts", ASME-Paper 97-GT-56
- Maier, G., Wittig, S., 1998, "Effects of Liquid Properties on the Operating Performance of Air-Assisted Pressure Swirl Atomizers", ILASS, 14th International Conference of Liquid Atomization and Spray Systems, Manchester England
- Prommersberger, K., Willmann, M., Wittig, S., 1997, "Modellierung des Verdunstungsverhaltens von Gasturbinenbrennstoffen auf Grundlage ihrer Siedekurve und variabler tropfeninterner Diffusion", *Spray '97*, Lampoldshausen, Germany
- Ranz, E., Marshall, W. R., 1952, *Evaporation from drops: part I + II*, *Chem. Eng. Progress*, Vol. 48, pp. 141 - 146, pp. 173 - 180
- Renksizbulut, Yuen, M. C. 1983, "Experimental study of droplet evaporation in a high temperature air stream", *J. Heat Transfer*, Vol. 105, pp. 384 - 388
- Roßkamp, H., Willmann, M., Wittig, S., 1997, "Computation of Two-Phase Flows in Low-NOx Combustor Premix Ducts Utilizing Fuel Film Evaporation" ASME-97-GT-226
- Samenink, W., Hallmann, M., Elsässer, A., Wittig S., 1994, "Secondary Break-Up of Liquid Droplets: Experimental Investigation for a Numerical Description", *Proceedings of ICLASS '94*
- Schmehl, R., Roßkamp, H. Willmann, M., Wittig, S., 1998a, "CFD Analysis of Spray Propagation and Evaporation Including Wall Film Formation and Spray / Film Interactions", Presented at the 14th ILASS-Europe Conference, Manchester, UK
- Schmehl, R., Klose, G., Maier, G., Wittig, S., 1998b, "Efficient Numerical Calculation of Evaporating Sprays in Combustion Chamber Flows", 92nd Symp. on Gas Turbine Engine Combustion, Emissions and Alternative Fuels, Lisbon Portugal, 1998
- Stengele, J., Bauer, H.-J., Wittig, S., 1996, Numerical study of bicomponent droplet vaporization in a high pressure environment, ASME-96-GT-442
- Stengele, J., Willmann, M. and Wittig, S., 1997, Experimental and theoretical study of droplet vaporization in a high pressure environment, ASME-97-GT-151
- Stengele, J., Prommersberger, K., Willmann, M., Wittig, S., 1998, "Experimental and theoretical study of one- and two-component droplet vaporization in a high pressure environment", accepted for publication in *Int. J. Heat Mass Transfer*
- Wittig, S., Klausmann, W., Noll, B., Himmelsbach, J., 1988, "Evaporation of fuel droplets in turbulent combustor flow", ASME-88-GT-107
- Yuen, C., Chen, L. W., 1976, "On drag of evaporating liquid droplets", *Combustion Science and Technology*, Vol. 14, pp. 147 - 154

PAPER No. 16
Prommersberger, Maier & Wittig
(presenter: K. Prommersberger)

Question 1: T. Ripplinger, MTU, Germany

What was the experimentally-measured fuel residence time in the premix duct?

Answer:

The residence time was 8 ms.

Question 2: V. McDonnell, University of California, Irvine, U.S.

Can you say how the fuel vapor concentration levels at the E5 plane centerline compare to the expected saturation level for the conditions of the experiment? Some of the fuel remains in the liquid state at the flame stabilizer. How will you address this fractal application?

Answer:

The vapor concentration at this point is significantly below the saturation level. A quantitative determination is difficult because of the variable velocity of the fuel. We estimate that it is about one-half of the saturation level. We measured an evaporated mass fraction of 35 % at the exit plane of the premixer duct. The remaining unvaporized large droplets in particular, impinge on the flame stabilizer. However, I presently cannot give information concerning the effect of this on the emissions. We observed no flashback into the premix duct.

Question 3: C. Berat, Turbomeca, France

Do you think that using a Rosin-Rammler size distribution for the droplet initial conditions is the best way to achieve the correct SMD distribution in Plane E1 (Fig. 18), especially in the outer region of the duct? A discrete size could be used at the first plane.

Answer:

In my opinion, the Rosin-Rammler size distribution matches, in general, the droplet initial conditions for a pressure swirl atomizer quite well. In the current configuration the droplet sizes in measurement plane E1 are influenced by secondary droplet breakup. Therefore, the PDPA measurements suffer from errors due to droplet shape irregularities, especially in the spray periphery where the volume flux is rather low.

Question 4: B. Zamuner, ONERA, France

I agree with you concerning the strong influence of secondary atomization effects on the two-phase flow patterns. What kind of turbulent dispersion model was used for the droplet equation of motion, and were fluctuating velocities used when calculating droplet drag? Did you validate the model on a classical flow case, such as a round jet?

Answer:

We used the Gaussian distribution Gosman-Ioannides dispersion model for turbulence effects on the droplets. We checked the model against the classical experiment of Synder & Lumley that used corn pollen and hollow glass particles dispersing in a decaying turbulent flow. The correspondance of the experiment and the appropriate calculation was excellent.

OPTICAL DIAGNOSTICS APPLIED TO A JET DIFFUSION FLAME

F. GRISCH, B. ATTAL-TRETOUT, P. BOUCHARDY

Office National d'Etudes et de Recherches Aéronautiques
Département Mesures Physiques
Fort de Palaiseau, 91761 Palaiseau Cedex, France

V. R. KATTA

Innovative Scientific Solutions, Inc
2766 Indian Ripple Road
Dayton, OH 45440-3638, USA

W. M. ROQUEMORE

Air Force Research Laboratory
Wright-Patterson Air Force Base, OH 45433, USA

1. SUMMARY

An experimental study was conducted on low speed hydrogen-air buoyant diffusion flames to investigate the vortex-flame interaction and the effect of the Lewis number on the flame structure. Simultaneous single shot measurements of temperature, pollutant nitric oxide (NO) and atomic oxygen (O) have been obtained using a combination of Coherent anti-Stokes Raman spectroscopy, laser-induced fluorescence and degenerate four-wave mixing. Temperature and molar fraction of NO and O are presented in two-dimensional maps and are compared with theoretical predictions. It was found that temperature and NO concentration increase - with later being more significantly - in the compressed region of the flame whereas high concentration of oxygen atoms is located in the stretched region of the flame. Good agreement was found between the simulated and measured data.

2. INTRODUCTION

A few years ago, experimental studies have been undertaken in a buoyant hydrogen jet diffusion flame in which vortex-flame interactions are significant. Numerical studies of Katta *et al.* [1,2] have shown that significant changes occur in local temperature and species concentration during the vortex-flame-interaction processes. To accurately compare the measured quantity to the predicted ones, the vortex-flame interaction has to be captured both spatially and temporally with a good resolution. We accomplished this by using different single shot measurement techniques to investigate the temporal and spatial evolution of these coherent structures. Namely, coherent anti-Stokes Raman scattering (CARS) was used for temperature measurements in combination with both degenerate four-wave mixing (DFWM) and laser-Induced fluorescence (LIF) for concentration measurements. Preliminary results presenting dual measurements of temperature and NO concentration in the flame have been presented [3]. In this paper, we enlarge the experimental database by recording concentrations of several other species important for understanding the flame chemistry. One of the most important specie is the atomic oxygen, which plays a major role in ignition and pollutants formation in this flame.

This paper presents the results of simultaneous measurements of temperature, O and NO concentrations during a vortex-flame interaction. The experimental results are compared to predictions. Measurements were made with three different optical diagnostic techniques. The cross comparison of the different detection channel was used for accurate calibration of absolute concentration. We investigated the interaction of an outside vortex with a low speed hydrogen/air jet diffusion flame at two location downstream from the jet nozzle (i.e., 50 mm and 135 mm) and for two diluents, nitrogen and argon. The measurements, which were phase locked to the vortex motion, were made in one millisecond time steps. The radial location of temperature, NO and O peak concentrations in and around the flame bulge are identified. The positions of these peaks correspond to the stretched and compressed regions of the flame as predicted by Katta *et al.* [1,2]. The results are presented as space-time maps, enhancing the temperature and concentration gradient through the vortices. Additional numerical simulations for some of the cases studied will be presented in a future paper. Predictions of the flame dynamics are outlined in the first section. Experimental description is given in the second section. Results and discussion are presented in the last section.

3. DYNAMIC FLAME STRUCTURE

The structural changes that occur in jet diffusion flames during the laminar to turbulent transition have been the subject of several studies [4-6]. A typical instantaneous image of a high-Damköhler-number H₂/air diffusion flame, similar to the one studied here is shown in figure 1. The fuel jet emerges from a contoured nozzle having a flat, low velocity profile at the exit and is surrounded by a low-speed coflowing airstream. The potential core of the flame is laminar whereas large coherent vortices are observed outer the flame surface. They are generated by an absolute instability resulting the natural convection, buoyancy-driven shear layer. The outer vortices are responsible for flame flicker as defined by the separation of the flame tip from the main body of the flame or by the natural low frequency oscillation of the flame surface. The 15 Hz frequency of the outer vortex is

nearly independent of jet characteristics such as fuel exit velocity, nozzle diameter and fuel type.



Fig.1 - Reactive Mie Scattering Image of low-speed dynamic H_2 /air flame

Predictions of the dynamic structure of the H_2/N_2 diffusion flame in Fig.1 were recently made by Katta et al. [1, 2]. As the outer vortices rotate, they entrain air, which is preheated by mixing with combustion products picked up from the flame surface. The vortex dynamics, referred to as a vortex-flame interaction, creates locally stretched and compressed flamelets along the flame surface. It was found that preferential diffusion, non-unity Lewis number, and curvature effects influence the temperature of the flame. The local temperature was predicted to increase in the compressed regions of the flame and decreases in the stretched regions as shown in Fig.2. Preferential diffusion, non-unity Lewis number, and flame curvature not only affect the temperature but also the species concentration. Specifically, species with lower mass diffusion coefficients than that of the fuel,

tend to disappear whereas, species with higher mass-diffusion coefficients tend to become rich. In particular, O tends to peak in the squeeze region and NO peaks in the bulge region as noted in Fig.2. Experimental support of these unusual predictions is given in Refs 3, 19. This paper is a continuation of the investigation of the dynamic characteristics associated with the vortex-hydrogen flame interaction.

4. EXPERIMENTAL APPROACH

4.1. Set-up

The schematic diagram of the experimental set-up is shown in Fig. 3. A special diagnostic system was developed that allows simultaneous trace species analysis and CARS thermometry. The laser system is composed of two benches mounted on a single table. The first bench comprises a frequency-double injection-seeded Nd:YAG laser and a broadband dye laser that generates the pump and Stokes beams required for the multiplex CARS temperature measurement. The Stokes beam is centered at 607 nm to probe the nitrogen Raman Q branches and has a bandwidth of 60 cm^{-1} (Full Width at Half Maximum). The output energies are about 70 mJ for the pump beam and 5 mJ for the Stokes beam.

The second laser used to measure the NO and the O concentrations with DFWM and LIF techniques consists of a tunable narrow-band dye laser pumped by a multi-mode Nd:YAG laser. The dye laser is operated with Coumarin 460 and provides pulses of 10 ns duration and up to 15 mJ pulse energy at 452 nm. The frequency is doubled in a BBO crystal to produce UV pulses with energy up to 3 mJ with a linewidth of 0.12 cm^{-1} (FWHM) at 226 nm. The two laser systems are synchronized within a temporal jitter less than 2 ns and operate at a repetition rate of 10 Hz.

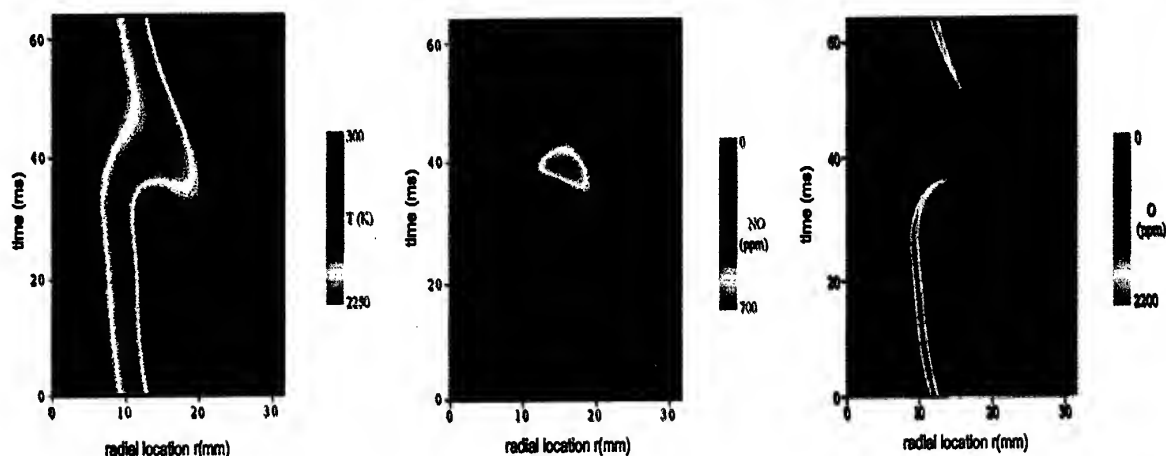


Fig.2 - Evolution of temperature, NO and O concentrations of dynamic flame at downstream location of 135 mm from nozzle exit

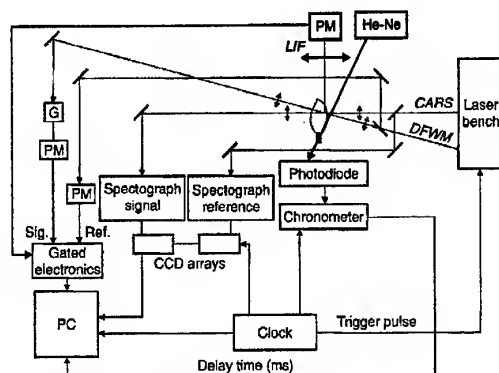


Fig.3 - Schematic diagram of the experimental setup

A planar BOXCARS arrangement is used for the CARS system in which referencing and non-resonant background cancellation are applied systematically [7]. Referencing is performed by first focusing the laser beams in a flow of argon at atmospheric pressure, then splitting off the non-resonant CARS signal using a dichroic plate and then refocusing the laser beams in the flame. The CARS beams are focused in the flame using a 300 mm focal length yielding a 3 mm long, 100 μm diameter probe volume. The available energies in the probe volume are 35 mJ and 2.5 mJ at 532 nm and 607 nm respectively. Both signals are recollimated before the entrance of the spectrographs. Reference and sample CARS spectra are dispersed in separate spectrographs and detected by means of two 512 diode arrays. The spectral dispersion and resolution (FWHM) are 0.125 $\text{cm}^{-1}/\text{pixel}$ and 0.8 cm^{-1} respectively.

The UV beam is split into three beams in a folded BOXCARS arrangement [8]. The pump beam P_1 is vertically polarized whereas the P_2 pump and the probe beam P_r are horizontally polarized. This arrangement was demonstrated to provide optimal signal to noise ratio in forward DFWM involving one photon resonances [9]. The three beams are focused at the same probe volume using a 900 mm focal length lens. With a beam separation of 22 mm, the DFWM probe volume is 10 mm long and 200 μm in diameter. The beams are then recollimated using collection lens. Spatial filtering and a dichroic polarizer are used on the signal path. Detection of the DFWM signal is performed by a UV photomultiplier tube (RTC, XP2020 Q).

The fluorescence signals are collected at $f/2$ by a fused-silica lens and focused into a 1 mm-inner diameter optical fiber. The sample volume in the flame is a cylinder of 1-mm long and 200 μm in diameter. A combination of 7-mm BG24 and 2-mm UG5 Schott glass filtering are used in front of the photomultiplier (RTC, XP2018 B) to isolate the NO fluorescence signal between 226 and 300 nm. For O-fluorescence, colored filters (Schott, 3-mm RG780 and 3-mm RG 665) and a narrow-band interference filter centered at 860 nm are

used with a red-sensitive photomultiplier (RTC, XP 2237 B) to separate the fluorescence emission from the scattered laser light and the water vapor flame emission. Noise rejection is further discussed in last section.

The angle between the UV and the CARS beam axes is 5° . The superposition of the UV and the CARS probe volumes is adjusted using a 200 μm -diameter pinhole mounted on translation stages. Part of the UV beam is also detected on a reference channel to monitor the laser power fluctuations. The signals from the different detection channels are gated, integrated by an electronic device and processed by a PC computer. Single-shot processing consists in temperature derivation from the CARS spectra analysis and pretreatment of DFWM and LIF signals including background noise subtraction. The noise level varies linearly with laser power in the LIF and DFWM detection channels. This relationship is first calibrated for each detection path in the useful power range corresponding to either O or NO excitation. Then, this value is subtracted from single-shot DFWM and LIF signals using the laser intensity measured simultaneously on the reference channel.

These noises mainly originate from stray light diffusion of the pump P_1 UV beam in DFWM whereas a small contribution from the flame emission add to laser light diffusion from both YAG and UV beams in LIF. The sensitivity of the concentration measurements is notably improved using this procedure especially for low NO and O trace regions. Further processing of the data is described thoroughly in section 4.3.

4.2 Burner and synchronization

The burner is a concentric jet assembly in which a fuel jet nozzle is located at the center of a coaxial annular flow. The annular flow with a 150 mm diameter is designed with a divergent section and a flow straightener (honeycomb and fine mesh screens), providing uniform and low turbulence flows surrounding the central jet. A short tapered contour nozzle of 10 mm-inner diameter was used as a fuel jet. The fuel was a mixture of hydrogen with nitrogen or argon with a volumetric ratio of 3.5. The flow velocities for the fuel and air jets are equal to 3.55 m/s and 37.9 cm/s respectively, resulting in the generation of torroidal outer vortices at a frequency of 14.8 Hz.

The frequency of the outer vortices is monitored by passing a He-Ne laser beam through the outer part of the flame and by detecting the beam wandering using a PIN photodiode. The phase angles, on which single shot measurements are performed, are obtained by measuring the delay between the laser pulses and the periodic signal generated by the PIN photodiode using a chronometer (Hewlett Packard, 5345 A).

The measurement sequence is provided by the PC computer which controls the photodiode arrays, the electronic device and the chronometer and processes the

data at 5 Hz. Measurements were taken in the flame by translating the burner to the axial (h) and radial (r) positions of interest. The radial position is changed in coarse steps of 1 mm. For each position, measurements are recorded in real time over successive cycles of the buoyant vortices. Typically, sequences of 500 laser shots are recorded. The laser repetition rate is adjusted at 9.8 Hz in order to obtain a temporal sampling of ~1 ms.

4.3 Diagnostic procedure

4.3.1 Temperature

The multiplex N₂ CARS thermometry has been used to perform single-shot measurements of temperature with a good spatial resolution. The temperature information is obtained by fitting the experimental spectral shape of the N₂ Q-branch CARS spectra, which display the population of rotational and vibrational N₂ states with a library of theoretical ones [10]. The accuracy of the temperature measurements obtained in stable conditions is about 10 K at room temperature and 30 K at 2000K with a standard deviation of 5 % and 2 % respectively.

4.3.2. Concentration

NO molecule - The NO concentration measurements are performed by Degenerate four Wave mixing (DFWM) and by Laser Induced Fluorescence (LIF). For both techniques, the excitation frequency is tuned to the Q₁(21.5)+S₂₁(10.5) set of transitions of the A² Σ⁺-X² Π (0,0) band of the γ system. These lines are well isolated from the O₂ Schumann-Runge transitions also present in this spectral range and yield good signal strength over a wide range of temperatures.

DFWM

A detailed description of the theoretical basis of the technique has been previously given [9]. Only the salient features of the method are repeated here. Using one-photon resonances in NO, it was shown that optimum sensitivity is achieved with a pump beam lying just at the level of the saturation threshold ($S = \Omega^2 / \gamma_{\text{coll}}^2$) of the stronger rotational line under study. Ω and γ_{coll} are the Rabi frequency and the collisional linewidth respectively. The DFWM signal intensity S^{DFWM} can be written as

$$S^{\text{DFWM}} \propto \mathcal{N}^2(T) \mathcal{F}^{\text{DFWM}}(T, S, \gamma_{\text{coll}}(T))$$

where N is the number density. The \mathcal{F} function is calculated for each of the temperatures involved in the CARS library according to the evolution of the collisional linewidths with temperature and using a model of saturation adapted to the range of energy used. For the present experiments, the energies at the sample volume for the pump beams have been fixed at 23 μJ which is about half the saturation intensity of NO [11]. The collisional linewidths for NO measured by Di Rosa et al. [12] and by Chang et al. [13] have been used in the calculation.

LIF

The measurement of the local NO concentration with laser-induced fluorescence relies upon a proportionality between the fluorescence intensity and the concentration of the NO molecule. Using a linear excitation, (i.e ; laser energy at the probe volume lower than 10 μJ), the fluorescence intensity is independent of the energy transfer in the ground state. This proportionality can be expressed in terms of the fluorescence yield in the upper state. This quantity reflects the fraction of molecules promoted to the excited states which undergo radiative decay back to the ground state. In a general way, the observed signal intensity S^{LIF} is then related to the number density N by

$$S^{\text{LIF}} \propto \mathcal{N}(T) \mathcal{F}^{\text{LIF}}(T, \gamma_{\text{coll}}(T))$$

The function \mathcal{F}^{LIF} summarizes the influence of the rates for spontaneous emission and the collisional energy transfer processes as quenching, vibrational energy transfer (VET) and rotational energy transfer (RET), and the line broadening. For the NO case, the VET which is slow in comparison with the quenching rate [14] and the RET which does not influence the quenching cross section with rotational level [15], have both been neglected in the \mathcal{F}^{LIF} function evaluation. The calculation of the Boltzmann fraction and corrections for quenching and line broadening were also included. The total quenching rate has been estimated for two conditions of flame (lean and rich flames) using the data of Paul et al. [16] and compositions of gas and temperature taken from adiabatic equilibrium calculations.

O atom - Oxygen atoms are excited to the 3p³P state by two-photon absorption of 226 nm radiation. The processes originating from J=2 are probed preferentially. The experiments are performed by exciting the J' = 0, 1, 2 triplet components of the excited state. The O-atom fluorescence is monitored at 844.6 nm from the 3p³P excited state down to the 3s³S intermediate state. In opposition to the NO excitation, the energy of the pump beam is set at 900 μJ which is far below the saturation intensity of the two-photon process in the atmospheric pressure flame conditions.

4.3.3. Absolute calibration

NO molecule - Since the DFWM and LIF signals are temperature-dependent, the absolute number density of NO have been calibrated in a flame in which NO concentration, temperature and pressure are well-known. For both optical techniques, the calibration of the signals is performed in a laminar premixed H₂/air flame with an equivalence ratio of 0.43 and a temperature of 1350 K. The flame was doped with a small amount of NO (280 ppm). In this procedure, it is assumed that the doped NO does not react through the flame, and that the amount of natural NO is small compared to the doped amount. The former assumption is supported by computer modeling performed using the CHEMKIN II and PREMIX codes [17, 18]. These calculations indicate that in burnt gases,

the NO concentration is equal to the doped NO concentration to within 2 %. Moreover, we have checked that the variation of LIF (and DFWM) signals versus input NO is linear (quadratic) in a large range of concentrations (Fig. 4). The relative accuracy of the NO concentration measurements is estimated to be about 5 % from the standard deviation measured on a 300 laser shots sequence.

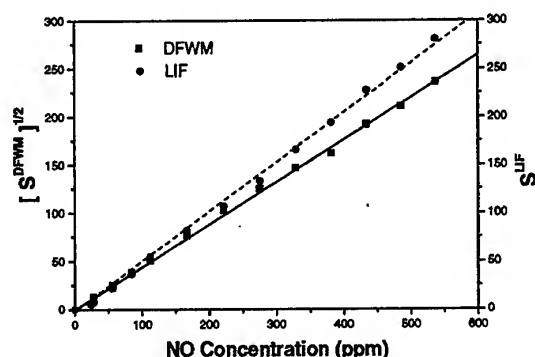


Fig.4 - LIF and DFWM signals as a function of doped NO concentration

O atom - Due to their high reactivity, the presence of O atoms is found only in high temperature regions (i.e., between 1800 and 2300 K), assuming thus that the fluorescence of O is insensitive to the temperature. Correction for temperature changes of the fluorescence signal therefore becomes negligible and the conversion of the O fluorescence signal to the number density is simply obtained using the following expression

$$N_f = N_{cal} \frac{S_f}{S_{cal}} \frac{R_{cal}^2}{R_f^2}$$

where N, S and R are the number density, the fluorescence signal and the energy of the laser beam; the subscripts *f* and *cal* denote the sample flame and the calibration flame.

The absolute calibration of the O signals is performed in a laminar H₂/air premixed flame with an equivalence ratio of 0.9 by recording the fluorescence intensity of O as a function of the height above the porous surface. This curve gives the relative O concentration along the flame axis. The absolute calibration was performed by comparing the experimental and theoretical profiles for the same flame conditions. As previously described, the flame has been modeled as one-dimensional using the CHEMKIN and PREMIX computer codes. However, for additional accuracy, the experimental temperature profile directly measured by CARS at the above axial locations has been introduced as input data in order to avoid the resolution of the energy equation. Such a procedure makes it possible to account for heat losses from the flame. As shown in Fig. 5, the behavior of the two profiles are quite comparable and the rescaling procedure thus provide an absolute value at peak concentration of 2000 ppm which is used to calibrate the measurements in

the buoyant flame. The latter value is responsible for the final uncertainty of our measurements of O concentration. We assume the absolute accuracy to be at maximum a factor of 2. About the relative accuracy, it is also important to outline that O concentration measurements using LIF in the calibration flame exhibit large shot to shot fluctuations. The latter are due to several effects including : (1) the real time, fast variation of the O concentration in the reaction zone ; (2) shot to shot fluctuations of the LIF signals due to the low number of photoelectrons collected in this detection channel ; (3) and the squared dependence of two-photon LIF signals versus laser energy. Therefore, we estimated our relative accuracy to be about 20 %.

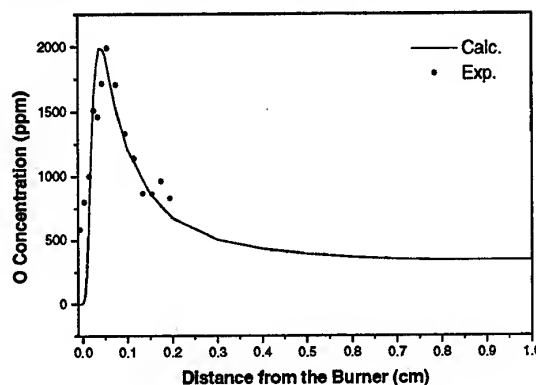


Fig.5 - O concentration as a function of height above the burner. The symbols are the experimental results; the solid line is calculated from PREMIX code [17, 18].

5. RESULTS AND DISCUSSION

5.1 Time profiles

Variation in temperature and molar concentration of NO were recorded as a function of time over the 66 ms period of the vortices. In a first step, NO was measured, simultaneously with temperature, by DFWM and LIF on two different detection channels in order to test the accuracy of the measurements. For instance, a typical time-dependent profile of the stably oscillating flame is shown in Fig. 6 at axial and radial locations of 135 and 15.5 mm respectively. Absolute number density of NO is measured by subtracting the noises from the LIF and DFWM signals. Signal dependence versus temperature and collisional linewidths are taken into account as explained previously to correct the measurements. The resulting concentrations obtained from LIF and DFWM techniques are in quiet good agreement further supporting the accuracy of the calibration procedure. It is important to note that this profile is representative of the vortex-flame interaction at the bulge center where the maximum occurs. A well reproducible two peaks structure is observed which correspond to the stretched and compressed flamelets [3]. The two techniques are found to have slightly different sensitivity limit as shown in the right wings of the NO profiles (Fig.6). The DFWM sensitivity is lower in this limit. Below 10 ppm, we can

see that the higher sensitivity of LIF allows one to probe NO traces found in the far boundaries of the buoyancy-induced vortices. Predicted temperature and NO concentration time profile were found to correctly represent the observed ones in this flame [3].

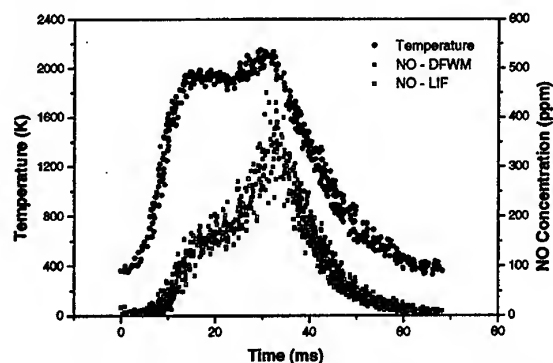


Fig.6 - Time-profiles of temperature and NO mole fraction in the H_2/N_2 /Air diffusion flame at $r=15.5$ mm and $h=135$ mm

5.2 Two-dimensional maps

Two-dimensional maps are constructed from the individual time profiles obtained at 32 radial locations. About 10 single-shot measurements are averaged for each temporal position, i.e. every ms and every mm on the flame radius. The temperature and the number densities of NO and O are shown in Fig.7 at downstream locations of 50 and 135 mm. First, we note that islands of high temperature and NO concentration contours develop in the compressed region of the flame bulge with the NO peaks being slightly right shifted by few mm compared to the radial location of the high temperature region. Maximum concentration contours of O are well reproducibly found in the stretched and hot regions of the flame. At the height of 50 mm, these regions are mainly located up and down on the time scale of Fig.7, i.e. close to the steeper temperature gradients at $r=11$ mm. At the height of 135 mm, the larger O concentrations are found along the steep temperature gradient at $r=12$ mm, i.e. left shifted compared to the radial location of the high temperature region. Let us note that O and NO maxima are located on each side of this high temperature island, thus corresponding to the stretched and compressed region respectively. As discussed by Katta et al. [1,2], these different peaks locations of O and NO in the hot region are attributed to the preferential diffusion mechanisms in hydrogen diffusion flames.

The comparison of the experimental temperature, O and NO peak concentrations to the calculated ones is performed to determine the effect of the vortex-flame interaction in the flame. Good agreement is found between the calculated and measured temperatures both on relative and absolute scales (Figs.2 and 7). The ratio of NO peak concentration between 135 mm and 50 mm

is about 1.2 in both calculated and experimental maps. However, the ratio of O peak concentration between 135 mm and 50 mm is about 1.5 experimentally whereas the calculated ratio is 1. This discrepancy cannot be explained by a simple temperature-driven O production. At 135 mm, the temperature in the O peak region is lower than at 50 mm whereas the effect of vortex-flame interaction is more pronounced. The O concentration results from these two opposite effects. The large amount of O atom measured at 135 mm proves that the O production is driven by vortex-flame interaction. In particular, partial equilibrium, existing between O and OH, might be influenced by these effects. This could lead to an enhanced O production. More elaborated chemistry might be necessary to resolve that uncertainty.

The agreement between the theory and the experiment is quite good as previously explained but it is important to note that absolute concentrations differ. Experimental NO and O peak values are lower than the theoretical ones by 30 % and a factor of 3, respectively. We have confidence in the calibration procedure of NO since the latter has been carefully reproduced several times using different techniques. However, the O calibration procedure requires a calculated result with a probable large uncertainty. We believe the discrepancies between the measured and predicted concentrations of O are too large to be explained by the uncertainty in the measurements.

5.3 Radial profiles

At the location of 135 mm, temperature, NO and O concentrations are plotted as function of the radial distance in Figs 8a and 8b. They display the data obtained respectively at the time positions of 5ms and 39 ms. As observed in the previous numerical studies, the temperature exhibits a narrow profile in Fig.8a since this stretch region results from the increase of the reactant fluxes in the flame zone. By contrast, the decrease of these fluxes broadens the temperature profile of Fig.8b. The temperature profile exhibits two peaks with a temperature difference of only 100 K. As already seen in Fig.6, these maxima are located in the rich side of the flame ($r=10$ mm) and in the bulge region ($r=16$ mm).

In the stretched region of Fig.8a, the O concentration profile is narrow and slightly right shifted toward the lean side of the flame. In Fig.8b, the O concentration profile exhibits a peak value at the local temperature maxima characterizing the stretched region of the flame. In the bulge region, O seems to vanish despite high local temperature. Comparison between the O concentration profiles of Figs 8a and 8b shows an increase of 30 % of the peak concentrations mainly due to the elevation of the temperature.

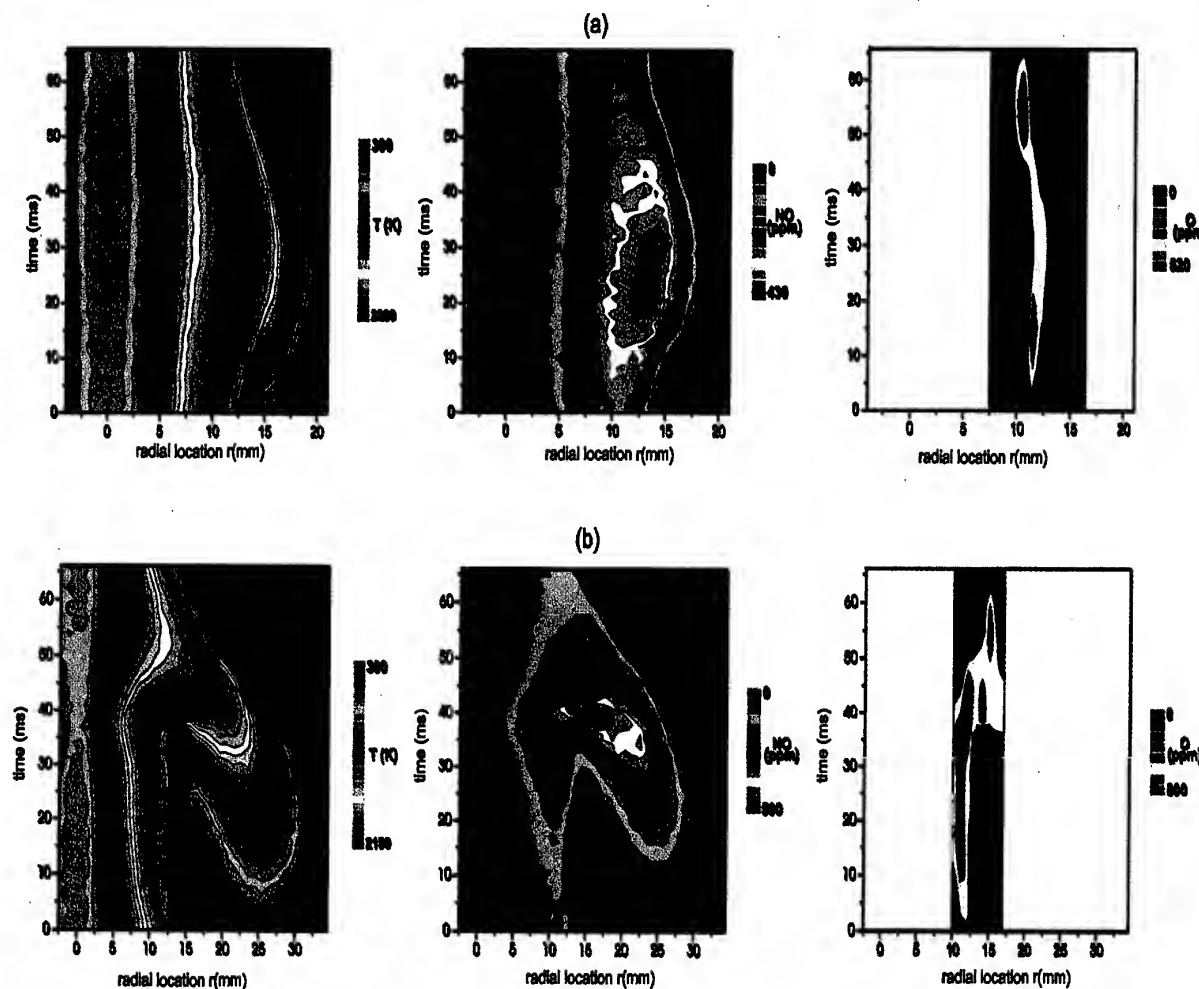


Fig.7 - Experimental two-dimensional maps of temperature, NO and O concentrations as a function of time and radial location r . a) $h=50$ mm, b) $h=135$ mm.

In these radial profiles, NO concentration closely follow the temperature with NO peak located in the bulge region as expected from calculation (Fig.2). It is interesting to note that the large NO concentration in the compressed flame is only due to the transport of the NO created in the stretched flame at $r=10$ mm. The concomitant decrease of O and increase of NO in the bulge region illustrates quite clearly the validity of the Zeldovich mechanism governing the NO production. In particular, O may react with nitrogen present in large excess in this zone to form NO.

5.4 Diluent effect

Time dependent measurements of temperature and NO concentration were recorded using a different diluent, namely argon. The volumetric ratio between H_2 and diluent being constant, the observed temperature, NO and O concentrations are increased. For example, the effect of argon increases significantly the NO concentration up to 630 ppm whereas temperature is only

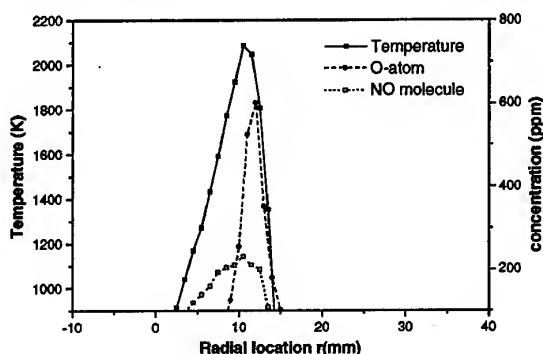
slightly different (about 100 K) as shown in Fig. 9. This effect is resulting from the change in Lewis number and drives the NO generation on the fuel side on the flame surface.

The O production ratio between 135 mm and 50 mm is found experimentally 1.5 larger than the calculated one.

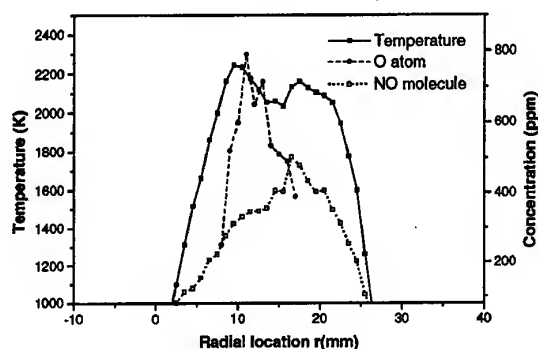
This trend is therefore similar than the one observed in nitrogen (see § 5.2) indicating that analog vortex-flame interaction takes place whatever the Lewis number.

The effect of the Lewis number is clearly evidenced by comparing the change in NO and O concentrations between argon and nitrogen dilution. Experimental observation has shown an increase in concentration by a factor 1.2 and 1.1 for NO and O respectively. Good agreement is found with the flame calculation which predicts an increase of NO and O concentrations by a factor of 1.24 and 1.11 respectively. Moreover, the

experimental O concentration ratio between argon and nitrogen is independent of the vertical location in the flame, the relative variation between 135 and 50 mm being less than 5 %.



(a)



(b)

Fig.8 - Flame structure at (a) $t=5$ ms and (b) $t=39$ ms. Radial distributions of temperature and mole fractions of O and NO are plotted.

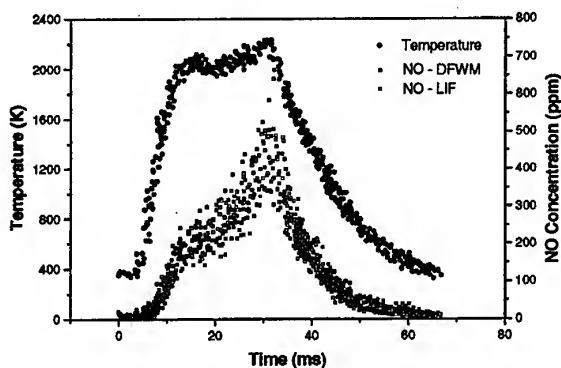


Fig.9 - Time-profiles of temperature and NO mole fraction in the $H_2/Ar/Air$ diffusion flame at $r=15.5$ mm and $h=135$ mm.

All these results provide additional information that confirms the good reproducibility of our measurements and provide a better insight into the chemistry of the flame code.

6. CONCLUSION

An experimental study was conducted in a high Damköhler number H_2 /air jet diffusion flame in which temperature, NO and O concentrations change rapidly during flame-vortex interaction. The influence of diluent on the Lewis number was observed on instantaneous temperature and concentration maps obtained by CARS, LIF and DFWM. The agreement between the predicted and the measured data is excellent. The measurements of absolute concentrations of radicals and molecules presented here will greatly expand our capability to identify important chemical steps for a variety of processes in this H_2 /air diffusion flame. It should be possible to evaluate directly the currently proposed strategies for determining precise mechanical processes appropriate for combustion.

7. ACKNOWLEDGMENTS

This work was supported in part by Direction des Recherches, Etudes et techniques. We would like to thank C. Rolon and N. Darrabia from Ecole Centrale Paris for providing us with some calibration flame calculations.

8. REFERENCES

1. Katta V.R., Roquemore W.M., *Combust. Flame* 96, 60 (1994)
2. Katta V.R., Roquemore W.M., *Combust. Flame* 100, 61 (1995)
3. Grisch F., Attal-Tretout B., Bouchardy P., Katta V.R., Roquemore W.M., *J.N.O.P.M.*, 5, 505 (1996)
4. Yule A.J., Chigier N.A., Ralph, S., Boulderstone R., Ventura, J., *AIAA J.*, 19, 752 (1981)
5. Buckmaster J., Peters N., Twenty first Symposium (International) on Combustion, The Combustion Ins. Pittsburgh, PA, 1829-1836 (1986)
6. Chen L.D., Seaba J.P., Roquemore W.M., Goss L.P., Twenty-second Symposium (International) on Combustion, The Combustion Ins. Pittsburgh, PA, 677-684 (1988)
7. Druet S., Taran J.P., *Prog.Quant. Electronics* 7, 1 (1981)
8. Prior Y., *Appl. Opt.*, 19, 1741 (1980)
9. Bervas H., Le Boiteux S., Labrunie L., Attal-Tretout B., *Molecular Physics*, 79, 911 (1993)
10. Pealat M., Magre P., Bouchardy P., Collin G., *J. Appl. Opt.*, 30, 1263 (1991)
11. G.N. Robertson, K. Kohse-Höinghaus, S. Le Boiteux, F. Aguerre, B. Attal-Tretout, *JQSRT*, 55, 71 (1996)
12. Di Rosa M.D., Hanson R.K., *JQSRT*, 52, 515 (1994)
13. Chang A.Y., Di Rosa M.D., Hanson R.K., *JQSRT*, 47, 375 (1992)
14. Cattolica R.J., Mataga T.G., Cavolowsky J.A., *JQSRT* 42, 499 (1989)
15. Drake M.C., Ratcliffe J.W., *J. chem. Phys.*, 92, 5211 (1990)
16. Paul P.H., Gray J.A., Durant J.W., Thoman J.W., *AIAA J.*, 32, 1670 (1994)

17. Kee R.J., Rupley F.M., Miller J.A., Sandia National Lab. Rep. SAND89-8009 (1989)
18. Kee R.J., Gear J.F., Smooke M.D., Miller J.A., Sandia National Lab. Rep. SAND85-8240 (1985)
19. Carter C.D. et al., Joint Technical Meeting, Central and Western States (USA) Sections and Mexican National Section of the International Combustion Institute, p. 429 (1995)

Experimental Investigation of an Axially Staged Combustor Sector with Optical Diagnostics at Realistic Operating Conditions

C. Hassa*, M. Carl, M. Frodermann, T. Behrendt, J. Heinze, I. Röhle DLR Köln,
N. Brehm, Th. Schilling, Th. Doerr BMW-RR

*DLR Deutsche Zentrum für Luft
und Raumfahrt e.v.
Inst. for Propulsion Technology
Linder Höhe
51147 Köln, Germany

1 SUMMARY

A rectangular sector of an axially staged combustor built by BMW-RR was investigated with optical diagnostics in a newly built experimental facility at DLR Cologne. The goal of the investigation was to acquire data on the combustor flow field of a practical combustor at realistic operating conditions to aid the design and validate results achieved with computational fluid dynamics (CFD). The rig is capable of operating at pressures up to 20 bar, preheat temperatures of 850K and air mass flows of 10 kg/s. The combustor is optically accessible through the side windows and the combustor liners, which allows the use of planar imaging techniques.

The measurement techniques applied so far are Doppler Global Velocimetry (DGV) for the isothermal flow, Laser Doppler Anemometry (LDA) for the gas velocity of the combustor flow, Phase Doppler Anemometry (PDA) for size and velocity of fuel droplets and Mie scattering of Kerosene for the imaging of the liquid fuel concentration. The reaction zone was investigated with measurements of the spontaneous OH emission. The paper reports results and experiences from those measurements at 1 and 6 bar. Application of CARS and OH-LIF for the in situ measurement of temperature and the extension of the application to 20 bar are planned for the immediate future.

2 NOMENCLATURE

CARS	Coherent Anti-Stokes Raman Scattering Spectroscopy
CCD	Charge Coupled Device
CFD	Computational Fluid Dynamics
DGV	Doppler Global Velocimetry
FWHM	Full Width at Half-Maximum
J	Flow Momentum Ratio
LDA	Laser Doppler Anemometry
LIF	Laser Induced Fluorescence
OH	Hydroxide
PDA	Phase Doppler Anemometry
SMD	Sauter Mean Diameter
UV	Ultraviolet

3 INTRODUCTION

The application of optical diagnostics in combustor flows has obvious advantages: light rays can't burn away and they do not obstruct the flow. Hence with almost every optical flow

measuring technique invented with the advent of the laser came after some time the note that it had also been applied to combustor flows [1] - [4]. Already some twenty years ago, the field seemed promising enough to bring together combustor technologists and instrumentation specialists in a workshop [5] to identify "the different sorts of instrumentation likely to be useful at the various levels of combustor design, from the basic phenomenology to the real engines". To that effect, the development engineer, the combustor researcher and the fundamental combustion scientist were set apart to define their respective diagnostic needs in the concluding review [6]. Whereas the designer would like to know fuel spray pattern and penetration, size and position of recirculation zones, dilution jet trajectories and local equivalence ratio distribution throughout the combustor, the combustion scientist was interested in basic experiments about turbulent mixing with reaction, hydrocarbon and pollutant kinetics, spray combustion and interaction of acoustic waves with combustion. At the time, the developer had to rely on probe measurements, whereas laser diagnostics were held capable to measure the steady state quantities of the fundamental experiments. Although 2-D and 3-D CFD of combustors was in its very beginnings, it was recommended to integrate the measurements into an analytical model of the overall combustor flow and to strengthen the dialogue between measurement and combustor specialist.

Some of the cited statements seem surprisingly up to date, prompting the question about the progress made since that time. The answer is, that there is not so much fundamentally new, but both CFD and optical combustion diagnostics have matured considerably. CFD is now capable of modeling complex combustor geometries, and its application has already shortened the combustor development process. Combustion diagnostics have moved away from the breadboard to "hardened" and "mobile" systems, allowing their use in practical combustion systems [7].

Then it was only with simplified (2-D) research combustors retaining some key elements of the actual hardware, that the bridging of the gap between development combustors and fundamental processes was possible. At the conception stage of the research programme described in this contribution, it was thought that the time had come to try and leave out the intermediate step of the simplified research combustor and find out, what the most mature measurement techniques could do in a real combustor geometry at realistic operating conditions. Hence a rectangular combustor sector was built and made optically accessible for pressures up to 20 bar, covering

the cruise and scaled take-off conditions of modern civil aircraft.

The advantages of this approach are:

- For the first time, the designer would be able to see the features he is specifically interested in without the geometrical and thermodynamic approximations of research combustors. If the measurements are trustworthy, there are no more doubts about the relevance of the results. Furthermore, the results can act as a guidance for the conception of future research combustors, by showing how good the approximations of previous research combustors have been.
- CFD validation in the real environment becomes possible.
 - Given the risks they have to take, designers have to be notoriously distrustful of CFD results, such that comparisons of CFD and experiment made here are more than a formal milestone which could have been obtained cheaper in "validation geometries" and are crucial to build up confidence in CFD.
 - The CFD code applied has to incorporate a lot of submodels to cover the effects which are held to be important. Validation within the complexity of a real case might guide CFD development to some extent by identifying which of the effects of physical models are masked by the faults of others, thus not being of immediate concern.
- The combustor can act as a demonstrator for measurement techniques.
 - For some techniques, it may come to light that and why they will never work in the real environment, thus saving the resources of further development.
 - For the others, in conjunction with the CFD validation effort, it may be shown if they provide the answers to the right questions, or if they give answers to questions nobody really ever asked.

The disadvantages of the approach are:

- Although looking into a real design, the results are not going to help the development engineer during the current development effort, because scientific understanding will always be too slow to beat engineering intuition.
- The demonstrator rig is a very expensive validation experiment. Combustion modelers will have to forward the argument that the money is more efficiently spent on more and simpler validation experiments for submodels, because it is part of their expertise to know which effects are important and which are not. Hence, to spend so much on an experiment just to know things for sure which were believed to be evident by the knowing is a waste of resources.
- It is with great risks that "ultimate" demonstrations of measuring capabilities are undertaken. In case of a technique having proved its too limited capabilities, a success oriented R&D management operating in a lean environment might be tempted to streamline the attached resources away instead of authorizing the search for alternative routes.

The remainder of the paper will be devoted to the description of the research programme, the experimental facilities, the combustor, the measuring techniques and procedures and the results achieved so far. Although the actual results might be very specific, the contribution to the community might be to share the experience gathered with the described strategy,

exemplified on the current combustor, such that the reader can build his own judgement on the enumerated pros and cons.

4 THE RESEARCH PROGRAMME

The research programme carried out with the optical sector combustor rig is divided into two separate cooperations between BMW-RR or MTU respectively and DLR. The preparation of the experimental means was effected in a trilateral cooperation between BMW-RR, MTU and DLR. All activities are connected to the larger framework of the German aeronautics research programme. In this contribution, only the work done by BMW-RR and DLR will be reported. The worksplit here was as follows: BMW-RR realized the optically accessible combustor, whereas DLR modified the test stand formerly used within the German Sanger programme for hydrogen combustor-thrust nozzle tests to a kerosene combustor test facility for higher pressure. At the same time, the candidate measurement techniques were further developed by DLR and tested in laboratory scale experiments with respect to their usefulness for higher pressure.

The optical accessible combustor sector is a rectangular version of the combustor described in more detail in [8]. The experimental programme on the combustor is determined by agreement upon discussion of mutual interests and applicability and availability of measuring techniques. The evaluation of the results is also carried out collaboratively and is supported by parallel CFD activities of both parties.

The workprogramme was divided into a preceding isothermal investigation of the gas phase flow field and the actual investigation of the combustor flow field. The latter was again subdivided into three parts at 1, 6 and 20 bar. The isothermal and the 1 bar investigation were carried out during the manufacturing phase of pressure vessel and exhaust valve. The same pressure levels were chosen for both cooperations to approximate part load and cruise conditions as well as the inlet temperature at takeoff and to make the results of the respective combustors comparable. So far, experiments at 1 and 6 bar have been made. Since these pressure levels correspond best with part load conditions of the combustor, the results that will be presented in this contribution will focus mainly on the pilot zone with a special emphasis on the aspects of interest to the community, i.e. a preliminary evaluation of the experience gained with the experimental techniques.

5 EXPERIMENTAL FACILITIES

As the test rig was planned and designed specifically for optical investigations on combustor sectors, two modifications were made in the design of the liner in the interest of better applicability of optical techniques: The sector was not curved but rectangular, allowing techniques which require access along a line of sight for the laser beams and the optical signal like e.g. CARS. On the outboard and the inboard of the flametube, there are panels where small quartz windows can be placed with approximate dimensions of 15 x 90 mm at the top and 20 x 65 mm at the bottom with the long side in the main flow direction. Variable positions of these panels are possible. The window panels together with windows on the side of the combustor are used for imaging techniques working with Laser light sheets. The side windows have dimen-

sions of 80 x 120 mm and can be inserted at three different positions thus covering the whole length of the liner. An axial-radial cross section of the combustor in its casing is depicted in Fig. 1. For the purpose of demonstration, the figure shows both the pilot and the main burner, although they are circumferentially staged. Two large windows on the outboard side on top of the main zone liner and on the inboard side below the pilot zone give access through the casing to the quartz panels in the liner walls.

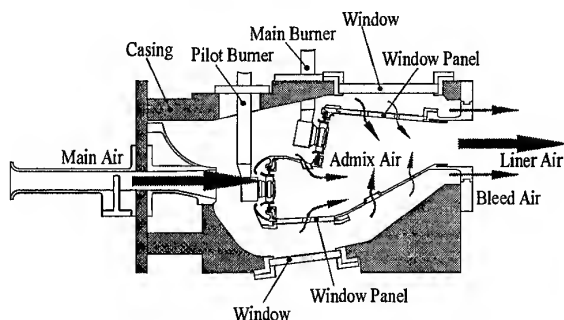


Fig. 1 Axial Radial Cross Section of Combustor and Casing

In Fig. 2, a cross section in the radial and circumferential direction through the combustor and the pressure vessel is presented. Here the central position of the liner window panels is shown with the cross section cutting the inboard panel through a liner hole. In this representation, it can be seen, that the side windows cover the entire height of the liner and the casing windows enough of the central section to check the deviations from periodicity that the specific combustors will exhibit. The pressure vessel is designed for pressures up to 20 bar. Its dimensions are 436 mm i.d. and 800 mm length. It has four window flanges with the windows in front of the casing windows. The diameter of the side windows is 170 mm, and 115 mm for the upper and lower window. The latter are mounted eccentrically in a rotatable metal plate to accommodate the different light sheet positions. The windows shown in the figure are mounted for the measurements at 6 bar.

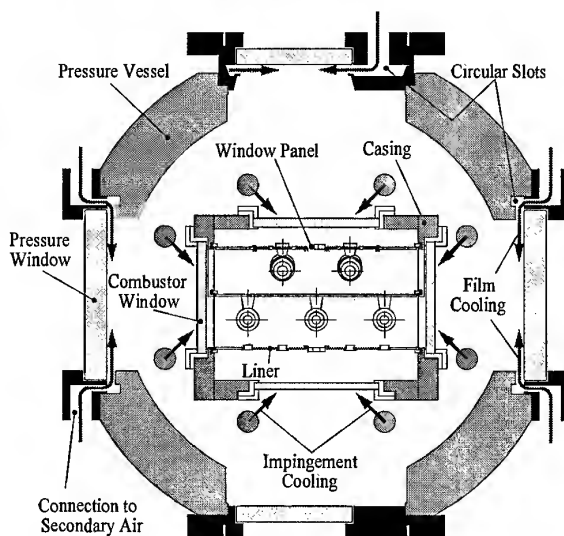


Fig. 2 Radial Circumferential Cross Section of Combustor and Pressure Vessel

The axial radial cross section of the combustor mounted in the pressure vessel is seen in Fig. 3. The combustor casing is mounted to spacers, that produce a shift between casing and pressure windows. That shift enables to place the desired part of the casing in front of the pressure windows. A coordinate table with a board size of 1500 x 500 mm spans below the pressure vessel. It can be traversed with 0.1 mm precision by stepping motors.

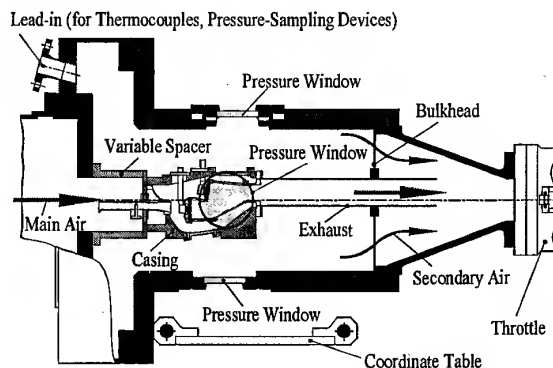


Fig. 3 Axial Radial Cross Section of Combustor and Pressure Vessel

Fig. 4 gives a schematic representation of the pressure vessel within the test plant. The pressure vessel is uncoupled from the bottom of the test stand by a supporting structure. The bottom itself supports the coordinate table. The main air entering the combustor through the diffuser is preheated by the fuel oil heat exchanger for the tests at higher pressures. The maximum condition is a preheat temperature of 850 K at 20 bar and 10 Kg/s mass flow. For the atmospheric experiments, an electrical preheater was used.

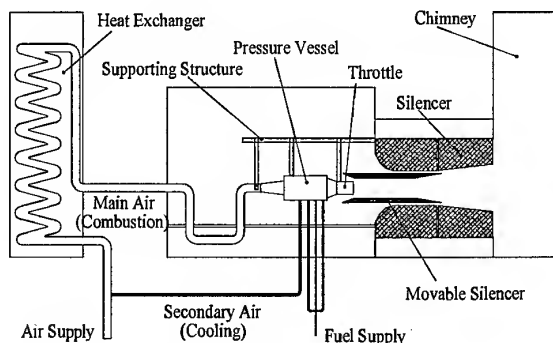


Fig. 4 Schematic View of Test Plant

Unheated secondary air enters the pressure vessel through three separately controllable lines, one for the internal film cooling of the pressure windows, another for the outer impingement cooling of the combustor and casing windows through the tubes seen in Fig. 2 and the third near the lead-ins as purge air for the pressure vessel. The outer cooling air flows into the transition piece to the throttle through the exit holes of the bulkhead which thus maintains a positive pressure difference to the combustor. A maximum cooling air flow of 3 Kg/s is available.

A movable silencer connects the throttle to the main silencer and chimney. Kerosene Jet A1 fuel is used so far throughout the tests, which is conveyed by a pump from the central storage tank of the center to the test plant. The maximum supplied quantity is 450 Kg/h. After the pump, the line is divided into three ducts, which are separately regulated providing flexibility for fuel staging and exact metering at different levels of fuel flow. A nitrogen purge for the pipeline and the burners was also installed. The whole test plant control system is integrated into a memory controllable test unit, enabling the operation of the test stand from one computer.

6 ISOTHERMAL VELOCITY MEASUREMENT

As a first step of the CFD validation, the measurement of the isothermal gas flow was undertaken by Doppler Global Velocimetry (DGV). The technique as applied enables simultaneous 2-D acquisition of time averaged three component velocity data. The measurement principle, the development status as well as some applications are described in [9]. Here only the features of the set-up which are specific to the combustor measurement will be described.

As shown in Fig. 5, the combustor liner was equipped with glass windows instead of window panels at the bottom of the pilot and at the top of the main zone. For the measurement, the light sheets were introduced from either side as well as from the top or bottom of the chamber. A mirror was placed

downstream of the combustion chamber exit, such that the camera used for the data acquisition was not directly exposed to the flow. The entire DGV equipment, camera and light sheet devices, were mounted on the coordinate table, such that the interior flowfield could be mapped in a tomographic manner at increments of $\Delta x = 2$ mm. Up to 50 adjacent planes were recorded in this manner resulting in volumetric data sets containing up to $120 \times 60 \times 50$ distinct data points at a spacing of $1 \times 1 \times 2$ mm³.

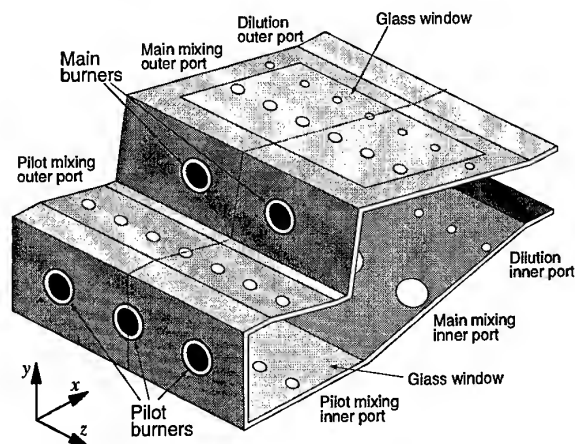


Fig. 5 Combustor with Windows used in DGV Measurements

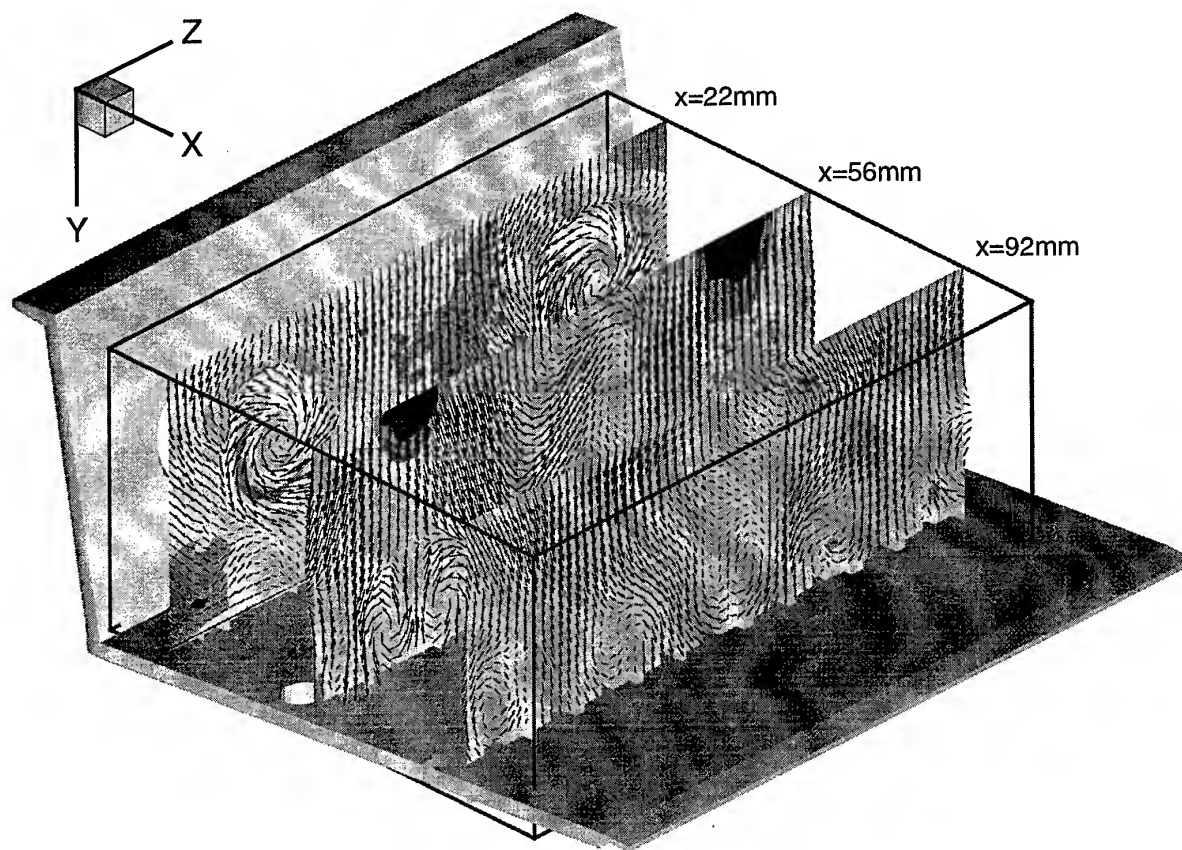


Fig. 6 Y-Z Cross Sections through the Main Zone (The representation is turned about 180°)

Fig. 6 shows Y-Z cross sections of the combustion chamber. Here, the view is through the main zone onto the outboard wall. The depicted velocity planes are placed behind the burners, the first and the second jet row. Radial and tangential velocity components are depicted by the vectorplot, axial velocities by the grey scale. The swirling main burner flow is clearly visible as well as the large scale vortical structures associated with the jet mixing, e.g. in the lower left corner of the $x = 56$ measuring plane. Looking at the picture, it has to be borne in mind, that this is a CFD related exercise and conclusions about the combustor flow structure should only be drawn when the similarity of the jet to mainstream flow momentum ratio J is given, which is not the case here, because of the differing densities in the combustor case. For a discussion of the potential of isothermal mixing studies see e.g. [10].

Another example of the results is given in Fig. 7, which shows the X-Y plane intersecting the axis of the middle pilot burner. At the top wall, the contour of the igniter and a modified pilot zone chute can be seen. The velocity measurement shows, that the recirculation of the burner is limited by the air entering through the igniter hole and that the burner near field is not symmetric to the burner axis but is quickly deflected to the bottom of the pilot zone. Although for the sake of lighting the combustor, the igniter position in the middle sector is clearly preferential, it was decided, that the modification of the flow in that sector was too big to obtain representative results and hence the igniter position was modified between the atmospheric and 6 bar tests without tangible difference in ignition behaviour.

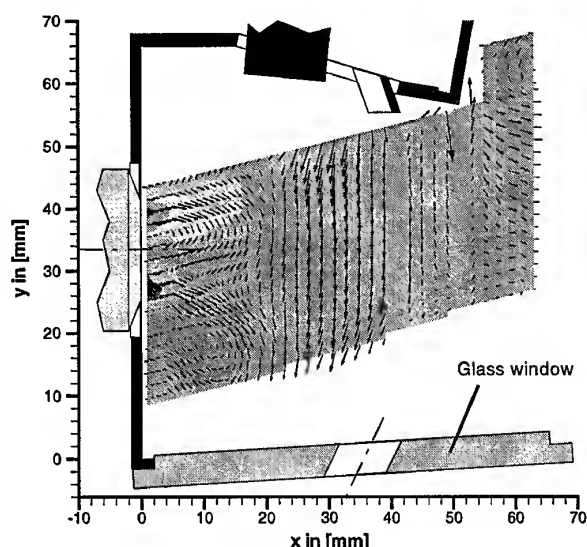


Fig. 7 X-Y Plane through the Axis of the middle Pilot Burner

Data validation in the recovered DGV velocity images is often necessary especially near flow bounding walls and other scattering surfaces. Frequently nonuniformities in the light sheet caused by deposits or obstructions on facility windows introduce a banded disturbance pattern in the velocity component data resulting in a velocity bias aligned with the light sheet disturbance. Hence, validation schemes which are sensitive to the respective light sheet directions have to be applied. Time averaging DGV's accuracy is limited by the

remaining jitter of the frequency stabilized Ar⁺ laser of about 1 MHz resulting in a velocity resolution of about 1 to 2 m/s. For low velocity regions like recirculation boundaries this means considerable relative errors, however as apparent from Fig. 6 at $x = 92$ mm, even the mixing patterns resulting from the small holes are very clearly resolved, such that the technique presents itself as a viable tool to understand the global flow patterns and guide the application of LDA if necessary. A comparison between DGV and LDA on a Swirler nozzle is presented in [11].

Currently an effort is underway towards developing DGV for application in flames. For this purpose, a long-pulse, tuneable frequency doubled ND:YAG laser was developed in collaboration with the Laser Zentrum Hannover, which reduces the Fourier limited bandwidth to the order of 1 MHz.

7 COMBUSTION DIAGNOSTICS

So far, planar Mie scattering, OH chemiluminescence as well as Laser-Doppler and Phase-Doppler Anemometry have been applied in the combustor flow and hence will be described in that order.

7.1 Optical Diagnostic Systems

7.1.1 Planar Mie Scattering

The distribution of the liquid kerosene in the near field of the nozzle was measured by planar Mie-scattering. In order to obtain time and spatially resolved two-dimensional information about the distribution of the spray droplets within a plane, the light of a pulsed, frequency tripled Nd:YAG laser (15 mJ at 355nm within 8 ns) was formed to a planar light sheet by a multiple lens optic. This optic produced a laser sheet having dimensions of 50×0.2 mm. The scattered light was detected perpendicular to the laser beam by a UV-grade photo lens attached to an intensified CCD-camera having an image format of 384×286 pixels. Due to the short exposure time of typically 20 ns, only the scattered laser light was detected. In addition an appropriate band pass filter was implemented into the imaging optic to minimise the influence of the remaining radiation of the flame and other laser induced processes.

7.1.2 OH* Chemiluminescence

The radiation of the electronically excited OH* radical (310 nm) was used as a marker for the flame reaction zone in space and time. The excited OH* radical is most likely due to the reaction $\text{CH} + \text{O}_2 \rightarrow \text{CO} + \text{OH}^*$, that directly forms OH* and, in contrast to ground state OH, is present only near the reaction zone [4]. In this experiment, the chemiluminescence was spectrally filtered using an interference filter centred at 310 nm (FWHM: 10 nm) and detected by the intensified CCD camera. The exposure time of the CCD camera was 10 μs for a single image and 1 ms for an averaged image. Due to the camera position perpendicular to the side window, the detected OH* fluorescence was integrated over the entire width of the rectangular combustor.

7.1.3 Velocity and Particle Size Measurement

The velocity distribution in the reacting flowfield was measured with a Laser Doppler Anemometer (LDA). It is a standard method whose principle and application is described e.g. in [12]. The LDA measurements at the pressure conditions

were conducted with a two component LDA built by DANTEC. It was powered by an Argon Ion Laser running at about 3W. A near forward scattering angle of 12° was used. The Gaussian beam diameter of the measuring volume was $320\text{ }\mu\text{m}$ and the length was about 3 mm. The bursts were analyzed via Fast Fourier Transform (FFT), giving the capability to process signals with a poor signal to noise ratio down to -6 dB. The processing error for single particles is about 1% of the bandwidth.

One important prerequisite for LDA measurements is seeding the air flow with scattering particles. The requirement of a sufficient amount of particles with detectable scattering cross sections evenly distributed throughout the combustor usually stands against the requirement to operate for longer time periods without being able to clean the windows. To obtain an optimum seeding, several types of particles and particle feeds were investigated. In the result SiO_2 particles of $0.5\text{ }\mu\text{m}$ diameter were conveyed by a fluidized bed generator. The chosen feed arm ended in front of the inlet diffuser, thus seeding all sectors, which avoids particle bias in the mixing zones of the combustion chamber. At each measuring location 20000 particles were collected or the measurement was aborted after two minutes. The two velocity components measured are the axial and the radial velocity.

The diameter of a spherical droplet and its velocity can be measured with a Phase Doppler Anemometer (PDA). For a discussion of the measurement principle see e.g. [13].

Due to the better optical access of the combustor when operated without the pressure vessel, the PDA measurements under atmospheric conditions were made with a three component PDA. The specific instrument used was a dual PDA built by DANTEC [14]. The dual mode concept is an extension of the conventional (standard) PDA with the capability of rejecting incorrect size measurements caused by effects, which are probable to occur if the particle diameter is not small against the diameter of the measuring volume. The Gaussian beam diameter of the measuring volume was $160\text{ }\mu\text{m}$ and the length was about 1 mm. In Fig. 8 the optical set-up of the 3D PDA is shown in top view for measurements in the pilot zone. The centerlines of the pilot fuel nozzles and the mixing holes are indicated. The tangential velocity is obtained by a velocity transformation.

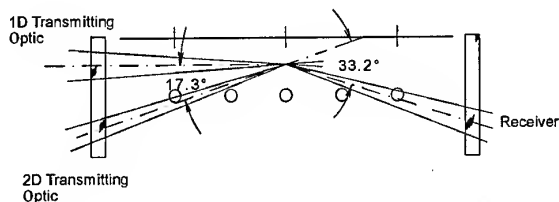


Fig. 8 Optical Set-up of 3D PDA

The Doppler-frequencies and the phase-shift were determined with a covariance-processor. The processing errors for single droplet velocity is about 1% and 4% for the particle diameter. The signals were processed if the signal to noise ratio of every burst of a particle was +2 dB or better. At each measuring location 50000 droplets were collected or the measurement was aborted after four minutes. Measurements of mass flux can be made with an accuracy of 10% for thin, isothermal sprays as recently shown [15].

From the LDA measurements at 6 bar, the following preliminary conclusions concerning the application of the measuring technique can be drawn. Although LDA has proven to be a suitable measuring technique for combustion, some limitations occurred for this specific application:

The shear layer between the cold (ambient temperature) window cooling air and the hot combustion gases causes strong turbulent fluctuations of the gas density and hence the refractive index. These fluctuations deflect the laser beams and reduce the intersection volume. If the beam diameter is too small the beams would not overlap at all or only seldom. A poor overlap reduces the signal to noise ratio because of low signal intensity and poor modulation depth. The effect of the density fluctuations was even more pronounced because of the distance between the shear layer and the measuring plane. To reduce the influence of the sidewalls on the flowfield, the center fuel nozzle of a row was investigated. In consequence the optical set-up was changed and the beam diameter increased leading to the larger measuring volume diameter for the 6 bar investigations. But increasing the beam diameter reduced the spatial resolution and light intensity per unit area. Hence much higher laser power was needed to discriminate the scattered light against the soot luminescence.

In regions of high spray density, measurements on tracer particles only could not be made. The surface area of the fuel droplets is up to 2 orders of magnitude larger than the area of the SiO_2 particles. The high voltage of the photomultipliers had to be reduced to avoid damages by the large amount of scattered light in the dense spray. This reduced the probability of detecting a small particle even if it was travelling through the middle of the measuring volume, where the light intensity is the highest. In the interpretation of the results, one has to keep in mind that the velocity distribution close to the nozzle exit not only represents the gas velocity but also the spray velocity.

The comparison of the images of the Mie scattering of the kerosene with the results of the PDA measurements under atmospheric conditions (Fig. 9) reveals a very good agreement. The angle of the spray cone as measured by PDA is approximately 57° against 60° by the Mie scattering.

The combination of the techniques delivers complementary insight into the combustor flow. The fast light sheet technique gives qualitative information on the fuel placement over large areas. The slower PDA gives quantitative information on droplet diameter and velocities.

8 RESULTS

8.1 Atmospheric Combustion

All measurements shown in this section were taken at an unstaged operating condition with 550 K preheat. For this measurement, the light sheet was placed in the central region of one fuel spray nozzle of the main or pilot zone, perpendicular to the nozzle exit plane. 100 - 200 single pulse images were taken to determine the averaged kerosene spray cone (Figs. 9, 13 and 14). Due to the small kerosene flow of atmospheric combustion, which is below the normal operating envelope of the combustor, the kerosene distribution strongly fluctuates from pulse to pulse (Fig. 10).

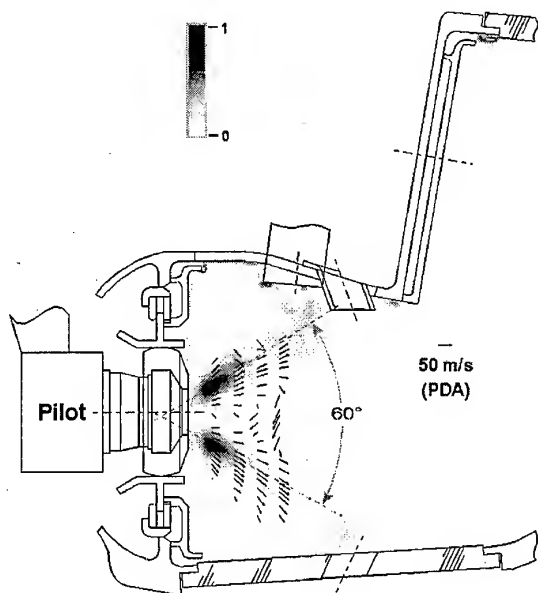


Fig. 9 Kerosene Spray Distribution in an Atmospheric Spray Flame in the Pilot Zone (The image is measured by Mie scattering and averaged about 200 laser pulses. In addition, the PDA velocity field of droplets smaller $7 \mu\text{m}$ is presented.)

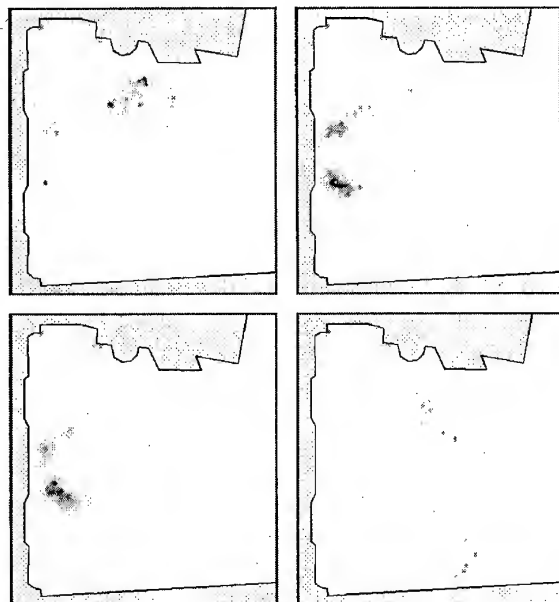


Fig. 10 Example of 4 Single Pulse Images of the Kerosene Distribution in the Pilot Zone (The images are measured by Mie scattering under same experimental conditions as in Fig. 9.)

In Fig 9, the angle of the spray cone is approximated from the Mie scattering image with the dotted line, measured in front of the middle fuel spray nozzle of the pilot zone. The velocity vectors of the droplets with smaller than $7 \mu\text{m}$ diameter along the dotted line point in the same direction. Consistent to this observation are the profiles of Sauter diameter and droplet

flux at 5 and 20 mm behind the nozzle in Fig. 11. For the sake of representation, the profiles which are both measured at the outboard side of the nozzle axis are depicted as mirror image on the right and left side of the figure. Although the Sauter diameter is smaller at the inner edge of the spray, in the region of high mass flux, the Sauter diameter remains almost constant. This differs from results obtained with the same nozzle in isothermal, unconfined spray tests, where a clear radial separation of particle diameters in the spray cone could be observed. There, the big $50 \mu\text{m}$ droplets follow the same 30° half angle as in the combustor, however the gas flow expands only with a 20° angle.

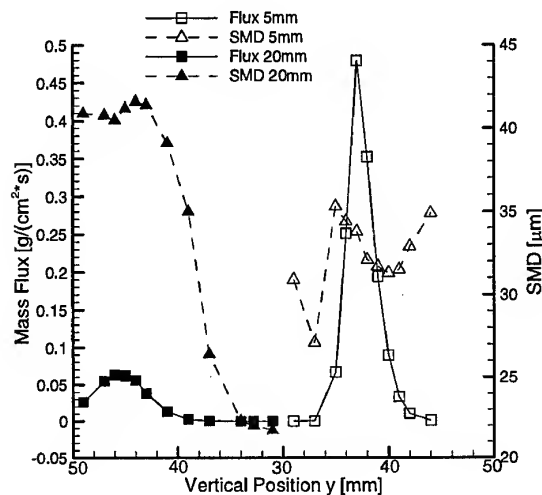


Fig. 11 Droplet Flux and SMD behind the Pilot Nozzle (The profiles are measured by PDA 5 mm and 20 mm behind the nozzle. The nozzle axis is at $y = 33.4 \text{ mm}$.)

The following explanation is proposed to explain those differences: The gas flow changes in the combustor because of the presence of the 1st jet row, providing a positive pressure gradient and partially filling the recirculation zone, which both contributes to a quicker expansion compared with the free isothermal case. The behaviour of the big droplets is unchanged, because the velocity field near the nozzle during early acceleration is similar in both cases and the droplets are nearly ballistic once the acceleration is finished. Hence in this case the changes in gas flow compensate the usual radial separation and the gas flow can be said to follow the droplets. Two conclusions might be drawn from this comparison: Spray angles measured in isothermal nozzle flow have to be interpreted with care and calculations of the spray which can build upon spray initial conditions measured near the nozzle should perform better in the task of predicting the fuel placement in the combustor, see e.g. [16].

The evaporation history can be seen in Fig. 12, where the mass averaged SMD and the measured liquid mass flux integrated over the y-traverse are depicted. At 5 mm, the spray is too dense to be fully captured by the single particle counting PDA. According to the measurement, half of the liquid is evaporated 15 mm behind the nozzle, and according to the Mie scattering, evaporation is almost complete at 40 mm behind the nozzle. The Sauter diameter shows the well known tendency to increase along the evaporation pathlength. The

effect exists only in polydisperse sprays, when vanishing small droplets overcompensate the diameter reduction of the larger drops. Depending on drops size distribution and gas temperature history encountered by the spray, a different behaviour is possible, e.g. for prevaporization of a small SMD spray, constant SMD's have been observed [17], whereas for an airblast atomized sprayflame without preheat, a small increase during evaporation was noted [18]. Supposing that the drops size distribution effects are the same for sprays which can be reasonably described by Rosin-Rammler distributions, as was the case in the noted examples, the general tendency for the SMD to increase with higher gas temperatures and wider drops size distributions can be formulated.

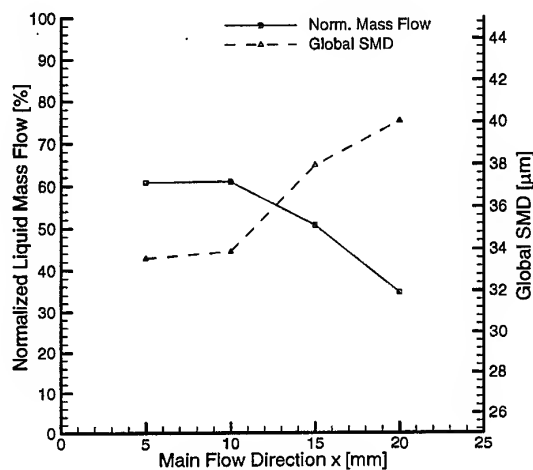


Fig. 12 Mass Averaged SMD and Liquid Mass Flux (The profiles are measured by PDA.)

8.2 Combustion at 6 bar

a) Spray Distribution

The angle of the spray cone, measured in front of the middle fuel spray nozzle of the pilot zone shows a different behaviour in both groups of test cases, at atmospheric pressure it is about 60° , while it amounts to around 76° in the cases at 6 bar presented here in Figs. 13 and 14. Since the pilot zone airflow distribution was modified after the atmospheric tests, it is not useful at this stage to perform a detailed comparison between the 1 and 6 bar results. However it is interesting to state the unsymmetry of the spray cone angle at 6 bar. The upper half angle measures 33° and the lower 42° . This asymmetry reflects the asymmetry of the pilot zone confinement. The ratio of the distance between the injector axis and the upper or lower liner respectively at the pilot zone exit turns out to be about the same as that of the sines of the upper and lower spray cone. Although the latter agreement seems to be rather incidental, the observation underlines the strong interaction between spray burner aerodynamics and confinement, which makes the optical access to the real geometry even more attractive.

For these test cases, the components of velocity field are determined by LDA measurements too. In Figs. 13 and 14 the velocity field vectors are represented together with the Mie scattered light from liquid kerosene.

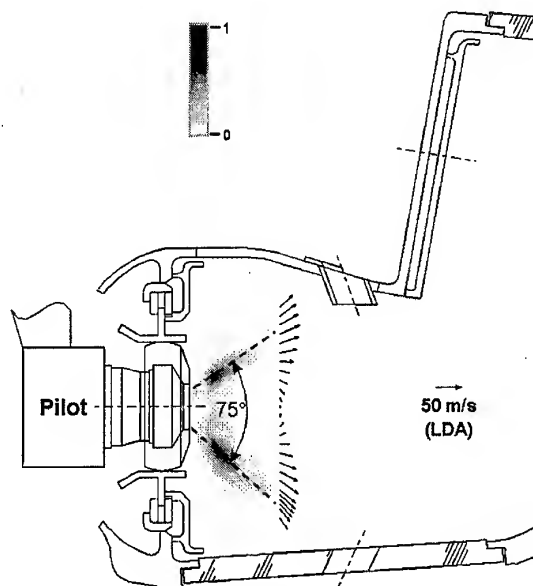


Fig. 13 Kerosene Spray Distribution in a rich Fuel / low Air Temperature Flame at 6 bar (The image is measured by Mie scattering and averaged about 100 laser pulses. In addition, the LDA velocity field is presented.)

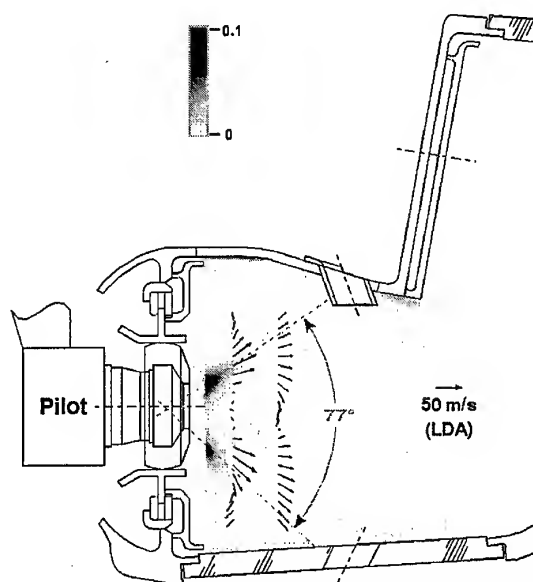


Fig. 14 Kerosene Spray Distribution in a lean Fuel / high Air Temperature Flame at 6 bar (The image is measured by Mie scattering and averaged about 100 laser pulses. In addition, the LDA velocity field is presented.)

b) Flame Stabilization

The distribution of the OH^* chemiluminescence indicates the reaction zone and points to the location where the flame is stabilized. Fig. 15 and Fig. 16 show the OH^* distribution of an unstaged test case of rich fuel and low preheat (666 K) and of a staged case of lean fuel and high preheat temperature (850 K) respectively. Also the iso-lines of the fuel distribution measured by Mie scattering are represented.

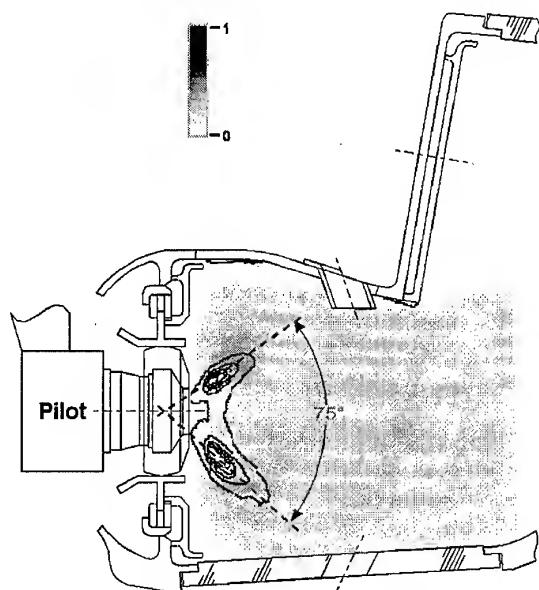


Fig. 15 Flame Zone in a rich Fuel / low Air Temperature Flame at 6 bar (The image is measured by OH* chemiluminescence. To indicate the liquid kerosene distribution, iso-lines of the Mie scattering intensity of Fig. 13 are added.)

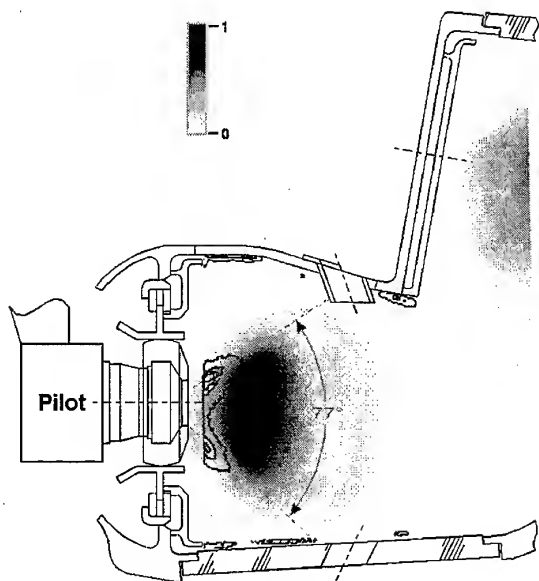


Fig. 16 Flame Zone in a lean Fuel / high Air Temperature Flame at 6 bar (The image is measured by OH* chemiluminescence. To indicate the liquid kerosene distribution, iso-lines of the Mie scattering intensity of Fig. 14 are added.)

In the test case of rich fuel and low air temperature, the flame stabilized to the outer recirculation zone. In the case of lean fuel and high air temperature, the flame stabilized to the inner recirculation zone. This difference is also reflected in the comparison of the axial velocity profiles at 20 mm distance from the nozzle in Fig. 17. In this figure, the velocities are normalized for better comparison with the velocity resulting from the pressure head across the liner. For the unstaged test

case, the velocity field indicates no inner recirculation zone, but due to the higher heat addition also higher peak velocities. The comparison of the Mie scattering images shows the spray to be much faster evaporated in the staged case. According to the picture, the evaporation where the Mie signal reaches 10% of its max. intensity is at $x_s = 8.5$ mm for the staged and $x_u = 17$ mm for the unstaged case. Since the staged case has the higher preheat, early evaporation will be able to produce a stoichiometric zone around the recirculation boundary which is nearest to the atomizer lip, which in this case is the inner recirculation zone. However, even for the staged case, it can be seen in Fig. 14, that due to the high confinement, the radial extent of the recirculation zone already diminishes from the first to the second measurement plane. Hence with the spray transporting the source of gaseous fuel continuously away from the centerline, if a stoichiometric zone is not reached within about 10 mm, it is only in the outer recirculation where conditions needed to anchor the flame can be established. Once combustion is stabilized there, the outer recirculation will expand due to the temperature gradient and the inner recirculation will be restricted even more, such that as shown in Fig. 17 for the unstaged case, the recirculation is already finished at $x = 20$ mm, cf. [18].

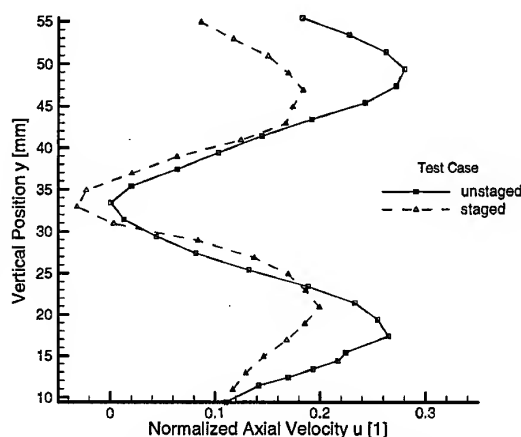


Fig. 17 Axial Velocity Profiles 20 mm behind the Pilot Nozzle (The profiles are measured by LDA. The nozzle axis is at $y = 33.4$ mm.)

9 FUTURE PLANS

The work on the BMW-RR axially staged combustor will be continued with measurements at 6 bar using PDA, LIF on OH and CARS. Especially with the temperature measurements planned, it is hoped to gain a more complete insight into the combustion process. With the measurements at 6 bar finished, decisions will be made on the measurement techniques to be used in the 20 bar campaigns. Parallel to that, calculations on a rectangular 5 nozzle sector with sidewalls have begun at BMW-RR in order to interpret the measured results with a calculation, that replicates the flow features arising from the deviations of the rectangular from a periodic sector.

10 CONCLUSIONS

The programme on which has been reported in this contribution clearly is a multiyear effort, and final judgement about its achievements and effectiveness is still some time away, nevertheless, a few preliminary conclusions can be drawn:

The aim to build a sector combustor realizing wide optical access for the inlet temperature and pressure range corresponding to cruise and scaled take-off conditions of modern engines has been reached. As e.g. Figs. 11-14 show, the detailed fluid mechanics of the jet mixing and the burner nearfield are accessible, for the main zone not shown here in the same way as for the pilot zone. However, a full scan of the combustor volume for one technique is connected with multiple dismantling and remounting of pressure vessel and casing, such that careful attention has to be given to the right choice of measurement planes etc. Clearly, efficient communication between measurement and modeling on the base of CFD prediction is a decisive factor for the fruitfulness of the whole approach.

So far all measurement techniques that have been tried have been successful in generating the kind of data that were expected including those depending on coherence of Laser beams. Partly because of the success in the application of the measurement techniques, presentation, reduction and interpretation of data has caused more effort than expected, even more so as it has turned out, that because of the adverse conditions, state of the art correction and processing techniques have to be employed that can only be successfully handled by experienced specialists.

The kind of data generated shows, that this rig can be used to understand the way combustor components work and interact in the real environment and it can be made a viable tool in the realization of the potential that staged combustors might have through optimization of their components cf. [8]. The results also show how to judge the validity of data generated in research configurations or what problems should receive a closer look in simplified configurations. As one example it should be useful to look into the change of flame stabilization mode of the pilot combustor with AFR and temperature in a can or single sector combustor enabling better optical access to the zone of flame stabilization.

Last but not least, the collaboration of industry and research with a "true" industry configuration can be successful in converging the respective views of priorities in the development of research tools. As the industry partner carries a substantial part of the financial burden and commits nonnegligible manpower to the joint definition of measurement campaigns and the CFD-based evaluation of results, the involvement is too deep to tolerate a nice to have view on the effort. Instead, in view of the hard choices to make, both partners are forced to come up with a clear view about the usefulness of the different techniques and methods employed.

11 ACKNOWLEDGEMENT

The project underlying to this report was supported with means of the German Federal Minister for Research and Technology (BMBF) under supporting sign 20T9403A. The responsibility for the contents of this publication is controlled by the author.

12 REFERENCES

- [1] Baker R.J., Bourke P.J., Whitelaw J.H.
The Application of Laser Anemometry to the Measurement of Flow Properties in industrial Burner Flames, Proc. 14th Combustion Symposium, 1973
- [2] Lapp M.
Flame Temperatures from vibrational Raman Scattering in Laser Raman Gas Diagnostics, p 107, eds M. Lapp, C.M. Penney, Plenum Press, N.Y. 1974
- [3] Moya F., Caumartin S.A.J., Taran J.P.E.
Gas Spectroscopy and Temperature Measurement by Coherent Raman Anti-Stokes Scattering, Optics Communications 13, 169, 1975
- [4] Dyer M.J., Crosley D.R.
Two Dimensional Imaging of OH⁺ Laser-Induced Fluorescence in a Flame, Optics Letters 7, 382-384, 1982
- [5] Goulard R.
Combustion Measurements in Jet Propulsion Systems, Hemisphere 1976
- [6] Goulard R., Mellor A.M., Bilger R.W.
Review and Suggested Experiments, p 419-462, in [5]
- [7] Lückcrath R., Bergmann V., Stricker W.
Characterization of Gas Turbine Combustion Chambers with Single Pulse CARS Thermometry, Paper 14, AGARD CPP 598, May 1998
- [8] Brehm N., Schilling Th., Mack A., Kappler G.
NO_x Reduction in a Fuel Staged Combustor by Optimization of the Mixing Process and the Residence Time, Paper 27 AVT Symposium on Gas Turbine Engine Combustion, Emissions and Alternative Fuels, Lisbon 12-16 October 1998
- [9] Röhle I., Schodl R.
Applications of three dimensional Doppler Global Velocimetry to turbo machinery and wind tunnel flows, Paper 52, see [15]
- [10] Hassa C., Migueis C.E., Voigt P.
Design principles for the quench zone of rich-quench-lean combustors, Paper 18, 1st. AVT-PPS Symposium on Design Principles and Methods for Aircraft Gas Turbine Engines, Toulouse, 11-15 May 1998
- [11] Lehmann B., Röhle I.
A comparison of velocity-field data behind a double swirl nozzle measured by means of a Doppler-Global and conventional three component LDA techniques, Paper 33-2, Proc. 9th. Int. Symp. On Appl. of Laser Techniques to Fluid Mechanics, Lisbon 1998
- [12] Durst F., Melling A., Whitelaw H.
Principles and Practice of Laser-Doppler-Anemometry, Academic Press, 1981

- [13] Bachalo W.D., Houser M.J.
Phase Doppler Spray Analyser for Simultaneous Measurements of Drop Size and Velocity Distributions, Optical Engineering, V 23, pp 583-590, 1984
- [14] Dual PDA Manual
DANTEC/invent measurement technology, 1996
- [15] Behrendt T., Hassa C.
Investigation of the spray dynamics of aeroengine fuel injectors under atmospheric and simulated pressure conditions, AGARD CP 598, Paper 5, 1997
- [16] Rachner M., Schmitz G., Hassa C., Schütz H., Eickhoff H.
Numerische Untersuchung in einer Modellbrennkammer, 4. Workshop Spray, Essen, 13.-14.10. 1998
- [17] Brandt M., Gugel K.O., Hassa C.
Experimental Investigation of Liquid Fuel Evaporation in a Premix Duct for Lean Premixed and Pre-vaporized Combustion, ASME J. Eng. Gas Turbines and Power, V 119, 815-821, 1997
- [18] Hassa C., Deick A., Eickhoff H.
Investigation of the Flow in a Research Combustor under Reacting and Non-Reacting Conditions, AGARD CPP 536, Paper 41, 1993

PAPER No. 18

**Carl, Hassa, Rohle, Behrendt, Heinze, Frodermann, Brehm, Schilling &
Doerr
(presenter: M. Carl)**

Question 1: G. J. Sturgess, ISSI, U.S.

Were all three of the pilot fuel injectors fuelled and operating during the optical measurements, and if so, were any difficulties encountered with beam steering and signal/noise ratio for measurements at the central injector?

Answer:

Yes, all three injectors were operating with jet-fuel. There were some problems, but they were relatively insignificant.

Measurement and Prediction of NO and NO₂ Emissions from Aero Engines

T J Foster and C W Wilson*

Combustion and Emissions Section, Propulsion Department
170 Building, DERA, DERA Pyestock
Farnborough, United Kingdom, GU14 0LS

M Pourkashanian and A Williams,

Department of Fuel and Energy, University of Leeds, Leeds, United Kingdom. LS2 9JT.

Abstract

Aircraft fitted with afterburner systems for increased thrust have been observed to have NO_x emissions with a higher proportion of nitrogen dioxide (NO₂) than non-augmented aircraft. These emissions are generally characterised by a brown plume and has implications for aircraft visibility and stealth as well as environmental considerations. This paper describes the CFD modelling of NO_x emissions from a modern afterburner system.

A commercial CFD code, Fluent, was used to develop and solve a three dimensional model of a "burn then mix" afterburner system under investigation. A post processor package has been developed and was used to calculate both NO and NO₂ concentrations. Four reheat settings were investigated; minimum, 25%, 50% and maximum reheat. For all conditions investigated the bulk of NO_x emission was found in the core, stemming from the vitiated combustor air flow. NO_x was also formed in the bypass stream, the production zone was found to be close to the fuel sprayers and flame stabiliser at minimum reheat, but moved downstream towards the exit nozzle as reheat power was increased. The model showed that for all the conditions under investigation, over 90% of the NO_x produced in the reheat system was formed via the thermal-NO route.

The model has been compared with centre-line traverse data measured at the exit nozzle of the engine on a sea-level static test bed. The predicted NO_x emissions agreed quantitatively with the experimental measurements to within $\pm 5\%$.

Introduction

The requirement of a modern gas turbine aero-engine is for reduced emissions of pollutants to meet both civil legislation and military aircraft plume invisibility needs. Recent advances in gas turbine combustor technology have lead to a progressive reduction in the emissions of black carbonaceous smoke from aircraft engines. However, these improvements; increased efficiency and consequently higher combustion temperatures, have lead to increased combustor exit emissions of nitrogen oxides (NO_x), mainly in the form of nitric oxide (NO). If conditions are favourable NO can be rapidly converted to nitrogen dioxide (NO₂) in the engine jet pipe and near-field plume, giving rise to a yellow/brown plume. It has been observed that rapid conversion of NO to NO₂ can occur especially in reheat systems operating at low power where the average gas temperature and the presence of large concentrations of unburnt hydrocarbons favour NO₂ production.

In order to quantify and understand the effect of operating cycle on aircraft emissions measurements need to be made. A number of authors have made emissions measurements from aero-engines in flight (Fahey *et al.* 1995, Schulte and Schlager, 1996), although these measurements are expensive to make and give little information on the emissions at the exit plane of the engine. In order to understand these near-field plume effects measurements need to be made from engines installed on test beds. Such measurements have been made on military engines by a number of authors (Seto and Lyon, 1994, Foster and Wilson, 1997, Brundish *et al.*, 1997), all of which reported that high NO to NO₂ in the near-field plume of the engine under investigation especially at low reheat power levels.

Experimental measurements highlight the problem of nitrogen dioxide formation in the near-field plume and to understand the exact conditions leading to NO₂ formation computer modelling can be utilised. Generally computer models fall into two categories. The first is the detailed kinetic modelling approach, where a detailed understanding of the aerodynamics is sacrificed for a better knowledge of the reaction chemistry occurring (Foster and Wilson, 1997). The second is to use a Computational Fluid Dynamics (CFD) code to accurately predict the flow-field and through simplified reaction schemes, predict the temperature and emissions. CFD calculations have been used to aid understanding and to identify problems in a number of industrial applications such as power stations (Amin *et al.*, 1996) and furnaces (Al-Fawaz *et al.*, 1994).

In this paper we have taken experimental measurements from the exit plane of a reheated gas turbine engine and compared them to a CFD model at a number of power settings. The CFD model was also used to highlight regions of NO formation within the afterburner system with respect to potential NO to NO₂ conversion in the jet pipe and near-field plume.

NO_x FORMATION

NO_x is the collective name given to the oxides of nitrogen; these being Nitric Oxide (NO), Nitrogen Dioxide (NO₂) and Nitrous Oxide (N₂O). In general NO_x is emitted from fossil fuel combustion in the form of NO, where upon it is oxidised to NO₂ in the atmosphere, although certain conditions can favour the production of NO₂ and N₂O leading to significant emissions (Miller and Bowman, 1989).

Thermal NO

The formation of thermal NO is determined by highly temperature dependent chemical reactions known as the extended Zeldovich mechanism. The three principal reactions

governing the formation of thermal NO from molecular nitrogen are:



The third reaction which has been shown to contribute particularly at near stoichiometric and fuel-rich zones:



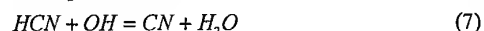
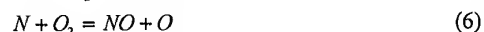
The rate constant for these reactions have been measured in numerous experimental studies (Flower *et al.*, 1975, Blauwens *et al.*, 1977, Monat *et al.*, 1979) and the data obtained from these studies has been critically evaluated by Baulch *et al.* (1973) and Hanson and Salamian (1984). The expressions for the rate coefficients for reactions (1-3) used in the current thermal NOx model are based on Hanson and Salamian (1984), and therefore the net rate of formation of NO via reactions (1-3) is given by;

$$\frac{d[NO]_r}{dt} = k_1[O][N_2] + k_2[N][O_2] + k_3[N][OH] - k_{-1}[N][NO] + k_{-2}[O][NO] + k_{-3}[H][NO] \quad (4)$$

In order to calculate the formation rates of NO and N, the concentrations of O, H, and OH are required. The rate of formation of NO is significant only at high temperatures, greater than 1800K, as formation of nitrogen requires the breaking of the strong N₂ triple bond (dissociation energy of 941 kJ/mol). This effect is represented by the high activation energy of reaction (1), which makes this the rate limiting step of the extended Zeldovich mechanism. However, the activation energy for oxidation of the N atom is small and, providing there is sufficient oxygen, the rate of consumption of free nitrogen atoms becomes equal to the rate of formation and therefore a quasi-steady state can be established. This assumption is valid for most combustion cases except for extremely fuel rich zones.

Prompt-NO

The pathway for the formation and destruction of NO in combustion systems is complex and not fully understood. It can be shown that during the combustion of hydrocarbon fuels the NO formation rate can exceed that predicted by the thermal route alone and must be accounted for by another mechanism. The presence of this mechanism was first identified by Fenimore (1971) and was termed as "prompt" NO. In flames where successful NO abatement measures have been used, often the total NO emissions can be dominated by prompt NO. Furthermore, there is substantial evidence that prompt NO can be formed in significant quantities in some combustion environments such as in the low-temperature, fuel-rich zones found in staged burners and gas turbines. Prompt NO is more predominant in rich flames and the actual formation involves a complex series of reactions and many possible intermediate species. The most valid route now accepted is as follows;



A number of species, which result from fuel fragmentation, have been suggested as a main source of prompt NO in hydrocarbon flames, i.e., CH, CH₂, C, C₂H, etc. However, reaction (5) is of primary importance. Recent studies (Schefer *et al.*, 1991) have shown that comparison of probability density distribution for the location of the peak NO with those obtained for the peak CH shows a close correspondence. This suggests that the majority of the NO at the flame base is prompt NO and therefore, assuming that reaction (5) controls the prompt NO formation rate;

$$\frac{d[NO]_p}{dt} = k_7[CH][N_2] \quad (9)$$

However, there are uncertainties about the rate data for the reaction (5) and from reactions (5-8) it can be concluded that the prediction of prompt NO formation within the flame requires coupling of the NO kinetics to the hydrocarbon combustion mechanism. Hydrocarbon combustion mechanisms involve a large number of steps, which can become very complex to solve and have a catastrophic effect on computer-processing time. In the present NO model, a global kinetic parameter derived by DeSoete (1975) and modified (Missaghi *et al.*, 1991) was used.

$$\frac{d[NO]_p}{dt} = K_p[O_2]^a[N_2][Fuel]\exp\left(\frac{-E_a}{RT}\right) \quad s^{-1} \quad (10)$$

It was found that the rate of prompt NO formation was first order with respect to nitrogen and fuel concentration, but the oxygen reaction order depends on experimental conditions. The De-Soete model was modified by using available experimental data from Backmier *et al.* (1973) and the effects of fuel type, (i.e. the number of carbon atoms) and air-fuel ratio were incorporated in a correction factor (f) applicable for aliphatic hydrocarbon fuels (Missaghi *et al.*, 1991) and hence;

$$\frac{d[NO]_p}{dt} = f k_p[O_2]^a[N_2][Fuel]\exp\left(\frac{-E_a}{RT}\right) \quad s^{-1} \quad (11)$$

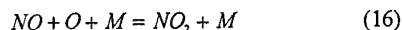
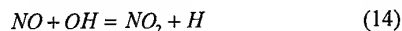
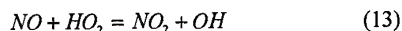
$$\text{where } f = 4.75 + C_1n - C_2\phi + C_3\phi^2 - C_4\phi^3 \quad (12)$$

C₁ to C₄ are constants, n is the number of carbon atoms of hydrocarbon fuel and ϕ is the equivalence ratio. In the model the values for C₁ to C₄ were 8.19 x 10⁻², 23.2, 32 and 12.2 respectively. These values are applicable for aliphatic alkane hydrocarbon fuels and for air/fuel ratios of 0.6-1.6. It is important to remember that oxygen reaction order (a) will depend on experimental condition. For example, at high flame temperatures, (a) will approach unity, but at low flame temperature the oxygen reaction order will approach zero. In order to obtain a realistic prediction of prompt NO, the oxygen reaction order should be calculated from composition data.

Aviation kerosene contains little fuel bound nitrogen, therefore the Fuel-NO is not considered here and although additional NO can be formed by the nitrous oxide route it is only an important contributor to the total NO at lower temperature regimes than the work presented here. (Miller and Bowman, 1989, Michaud *et al.*, 1992, Johnsson *et al.*, 1992).

Nitrogen Dioxide

Nitrogen dioxide is formed by the reversible reactions of NO with HO₂, OH, O and O₂ via;



At high temperatures, found in the flame zone, NO₂ is rapidly converted back to NO. However NO₂ conversion is favoured in the lower temperature regions where the combustion products have been rapidly cooled and high concentrations of the radical HO₂ can occur. Such conditions can be found in gas turbine engines where bleed flows cool the combustor exhaust gases before entering the turbine stages and in afterburner systems (Seto and Lyon, 1994), and also in probe sampling from fuel lean combustion products (Bromley *et al.*, 1988). Under these low temperature conditions the reaction of HO₂ with other species is generally slow, with the exception of NO, reaction (13), and itself. The conversion of NO to NO₂ is enhanced strongly by the presence of any unburnt hydrocarbons and work by Hori *et al.* (1992) showed that trace amounts of hydrocarbons could enhance the rate of conversion as shown in the following order; H₂<CH₄<C₂H₆<C₃H₈<i>i</i>-C₄H₁₀<n-C₄H₁₀. Under most conditions nitrogen dioxide formation proceeds mainly via the reaction of nitric oxide with the HO₂ radical. Higher order hydrocarbons, those with a high carbon number, decompose faster to form intermediary radicals such as C₂H₃, C₂H₅, n-C₃H₇, i-C₃H₇. These radicals can then react with oxygen to form HO₂, which will rapidly react with NO (Bromley *et al.*, 1988, Hori *et al.*, 1992)

CFD Modelling Technique

In this study, CFD is demonstrated as an engineering tool and a commercially available code, FLUENT, was used to solve the reacting fluid-flow and a post-processing package was then linked to the output to obtain distributions of NO concentrations. This code uses a moment method approach to solve the transport equations in finite-volume form. Turbulence closure for the turbulent convective fluxes has been achieved with the k-ε model. The source terms are evaluated using the slower of either the laminar reaction rates or the mixing rates determined by the eddy-break-up model (Magnussen and Hjertager, 1977). The flow field solution is subsequently used to solve the transport equation for the NO species. In order to solve equation (4), the concentration of quasi-steady species N, stable species (O₂ and N₂ etc.) the concentration of O atoms as well as free radical OH are required. Following a suggestion by Zeldovich, the thermal-NO formation mechanism can be decoupled from the main combustion process, by assuming equilibrium values for temperature, stable species, O atoms and OH radicals. However, an error may be involved by this approximation. The effect of super equilibrium O atom concentrations on NO formation rates has been investigated (Missaghi *et al.*, 1990) during CH₄/air combustion and the results indicated that the levels of NO emissions can be under-predicted by as much as 28% in the flame zone by assuming equilibrium O atom concentrations.

In order to overcome this inaccuracy two approaches can be used. Firstly the extended Zeldovich mechanism can be coupled with actual hydrocarbon combustion mechanisms. Miller *et al.* (1985) has used this approach but high computer processing times has made these models unattractive for practical problems. Instead a more simplified approach can be used where the thermal NO formation process can often be decoupled from the main combustion reaction mechanism and NO formation rate can be calculated by assuming equilibration of the combustion reactions. Using this approach, the calculation of thermal NO formation rate is therefore considerably simplified. The assumption of equilibrium can be justified by the reducing importance of radical overshoots at higher flame temperatures (Drake *et al.*, 1987). The partial equilibrium for O atom concentration can be obtained from expression;

$$[O] = K_p (O_2)^{\frac{1}{2}} \quad (17)$$

and assuming that for the combustion of lean fuel-air mixtures;

$$k_2[O]_{eq} \gg k_3[OH]_{eq} \quad (18)$$

Therefore reaction (3) can be neglected and equation (4) becomes;

$$\frac{d[NO]_r}{dt} = 2k_1[O][N_2] \left\{ \frac{1 - [NO]^2 / K[O_2][N_2]}{1 + k_{-1}[NO] / (k_2[O_2] + k_3[OH])} \right\} \quad (19)$$

Where, $K = (k_1/k_{-1})(k_2/k_{-2})$ and is the equilibrium constant for the reaction between N₂ and O₂. This approach can only be valid in fuel lean air mixtures and/or high flame temperature conditions.

Under certain conditions thermal NO formation rates can be strongly affected by super equilibrium O atom and OH radical formation, which exceed equilibrium values. Although the super equilibrium overshoot of O atom and OH radicals have been studied in detail in laminar flames (Fenimore, 1964), there is lack of detailed information of radical concentration in industrial turbulent flames. Theoretical studies of methane/air flames using detailed chemical kinetics and realistic transport parameters carried out by Dixon-Lewis (1980) have provided the concentration of super equilibrium O atoms and other free radicals at various strain rates, but at present there is no definitive conclusion on the effect of super equilibrium on NO formation rates in turbulent flames. Peters and Donnerhak (1981) suggest that super-equilibrium radicals can account for no more than a 25% increase in thermal NO while fluid dynamics can have a dominant effect on NO formation rates. Bilger and Beck (1975), however, suggest that in turbulent diffusion flames the effect of O atom overshoot on NO formation rate is very important. In this study two different techniques were adopted for prediction of O atom and OH radical concentrations. Allowance for super-equilibrium concentration of radicals in and near the primary reaction zone were made by imposing the data given by Dixon-Lewis (1980) on O and OH concentrations in methane/air flames at different strain rates. The rate of strain of the flame is related to the turbulent intensity of the combustion process. In addition an improved approximation

of the O atoms and OH radicals is derived from the concentration of the stable species by use of the partial equilibrium assumption for the fast-flame reactions.

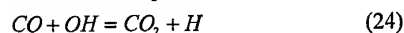
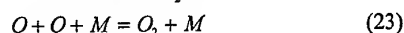
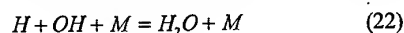
The oxygen concentration can be obtained from;

$$[O] = K_o [O_2] [CO] / [CO_2] \quad (20)$$

and the hydroxyl concentration from;

$$[OH] = K_h ([O_2] [CO] [H_2O] / [CO_2])^{1/2} \quad (21)$$

The equations (20) and (21) are derived from the partial equilibrium model by introducing the recombination rate of molecules. The recombination reactions considered are;



It should be noted, however, that this approach could only be employed if the concentration of CO is predicted properly in the flow-field calculations.

To predict the NO scalar field, the conservation equation has been solved subsequently to solving the flow field. The source term ω_{NO} is evaluated using a PDF approach. Thermal NO formation depends critically on the mean O radical concentration with allowance for non-equilibrium radical concentrations. The prompt NO concentration field in turn depends critically on the CH radical concentration and temperature. Therefore, the turbulent model used in the present investigation is improved by using a two depended variable system for which the first moments are obtained from the solution of the transport equations. The mean turbulent reaction rate ω_{NO} can be described in terms of the instantaneous rate ω and a joint PDF of various variables;

$$\omega = \int \omega(v_1, v_2, \dots) p(v_1, v_2, \dots) dv_1 dv_2 \dots \quad (25)$$

Where v_1, v_2, \dots are temperature and species concentration and therefore for a two variable joint PDF;

$$\omega_{NO} = \int \omega_{NO}(v_1, v_2) p(v_1, v_2) dv_1 dv_2 \quad (26)$$

where ω_{NO} is the mean turbulent rate of production of NO, ω_{NO} is the instantaneous rate of production given by equation (11) and (19), and $p(v_1, v_2)$ is the joint PDF of the variables v_1 and v_2 . If it is further assumed that the variables v_1 and v_2 are statistically independent;

$$p(v_1, v_2) \neq p_1(v_1) p_2(v_2) \quad (27)$$

Where p_1 and p_2 are assumed here to be two moment beta functions, the equation for the beta function is the second moment v^2 was assumed to be related to the first by;

$$v^2 = s(v(1-v)) \quad (28)$$

Where s is a coefficient to be selected to represent the intensity of fluctuation and the term in the brackets is the top limit of the second moment. Higher values correspond to higher Dahmkohler numbers, representing wrinkled laminar flame regimes, while lower values represent distributed combustion regimes.

In order to limit the computational time, each beta function was evaluated at 10 points on a histogram basis. A sensitivity analysis prior to the detailed computation was carried out for the beta functions, so that when V_1 or V_2 were near their extreme values, the associated beta function was replaced by a delta function and the instantaneous rate of production was directly incorporated.

The code is written so that the variable V_1 and V_2 can be selected depending on the type of NO formation in question. For example, for thermal NO, V_1 was temperature and V_2 was O radical mass fraction while for prompt NO they were temperature and CH mean mass fraction, respectively. At each step during two interactions, the extreme limits of V_1 and V_2 were calculated and the integration in equation (26) was obtained over the whole range of V_1 and V_2 at the interaction step in question.

Experimental Measurements

Combined temperature and emissions measurements were taken at the exit nozzle of a reheated gas turbine engine, fitted with a burn and mix reheat system, installed on a sea level static test bed at DERA Pyestock. The sampling probe was capable of traversing the engine diameter in both horizontal and vertical planes and was made stainless steel and is shown in Figure 1. High pressure hot water was used both to cool the probe and condition the gas sample. The sampling probe was connected to the analysers by ca. 15m of 6mm i.d. insulated stainless steel tubing, maintained at $150 \pm 15^\circ\text{C}$. A chemiluminescent analyser was used to measure NO and NOx. Carbon monoxide and dioxide were measured by NDIR analysers and total unburnt hydrocarbons were measured using a FID. Gas temperature was measured using a shielded platinum/platinum-rhodium thermocouple, located 10mm above the gas sampling orifice.

During the test programme gas temperature and emissions measurements were made across the centre line of the exhaust nozzle with the engine at idle, maximum continuous and a number of reheat power settings.

Results and Discussion

NOx, NO and NO₂ emission measurements for the engine running at maximum continuous and reheat conditions are shown in Figures 2, 3 and 4 respectively. for all the results shown the emissions values have been non-dimensionalised by dividing the respective point measurement by the maximum NOx concentration measured during the whole experimental trial. The results in Figure 2 show that at low afterburner settings there is a net reduction in NOx emissions compared to the non reheated, maximum continuous, condition. This reduction is probably due to a reburning effect, as the temperature and poor reheat combustion efficiency, and consequently high unburnt hydrocarbon levels, would favour reburning of the NO formed in the combustor at these conditions. NOx destroying reactions within the probe were ruled out as a separate test was performed in order to

investigate probe induced reactions and no loss of NOx was observed. As power is further augmented NOx emissions increase reaching a maximum in the order of 200 ppmv. The NOx results at 50% and maximum reheat show two distinct emission peaks in the traverse corresponding to the location of the bypass sprayers and the method of fuelling the afterburner system. At these conditions the bypass stream is running close to stoichiometric combustion conditions and consequently forming NO via the thermal route, as highlighted in the experimental and NO measurements in Figure 3 and the CFD NOx predictions shown in Figures 8 and 9.

Figure 4 shows measured NO₂ concentrations at the engine exit plane. When compared to the NO results in Figure 3 it can be seen that at dry operation the NOx emission is predominantly NO, however, at low reheat power settings, NO₂ makes up a large proportion, approximately 80%, of the total NOx emission. Probe effects were again investigated and it was found that at these inefficient reheat conditions NO to NO₂ conversion is accelerated within the probe tip by the reaction with HO₂ radicals. The true proportion of NO₂ was approximately 30% of the total NOx at the centre point of the traverse although further conversion within the test house detuner gave rise to a visible brown/yellow plume at the detuner exit. At 50% reheat and above it can be seen that the nitrogen dioxide results in Figure 4 shows that NO₂ formation occurs mainly at the edge of the exhaust jet as relatively cold air, from jet pipe cooling and some entrained ambient air, interact with the hot combusting jet leading to conditions favouring NO₂ formation. This trend can also be seen at lower afterburner powers although it is somewhat swamped by probe effects.

In order to clarify the experimental observations a CFD model, based on a single sector of the reheat system, was used and is outlined in Figure 5. In this paper full CFD predictions are only shown for maximum reheat. Figures 6 and 7 show temperature predictions for the sector and full engine respectively, NOx predictions are shown in Figures 8 and 9. From the temperature predictions it can be seen that there is little mixing between the core and bypass streams within the jet pipe. The predicted temperature field shows a slight increase in the core gas temperature, reaching a maximum around 1600K, with the flame anchored by the gutters. Combustion in the bypass stream is initiated and stabilised by the fuel from colander, which in turn ignites the fuel from the bypass sprayers. A peak exit plane temperature of 2200K is predicted, although combustion will continue downstream of the exit plane. The results also show that the cooling air film is maintained down the length of the jet pipe.

From the NOx predictions it can be seen that the reheat system does not produce huge quantities of NOx. A small amount of NOx is formed in the core stream in the flames stabilised by the gutters, although at lower reheat powers some NOx formed in the combustor is destroyed in this region via the reverse of the reactions in the CFD code. At maximum reheat there is some NOx formed within the bypass stream, via the thermal-NO route, corresponding to the high temperature regions. However, very short residence times prohibit the formation of vast quantities of NO within the reheat system. A comparison of experimental and predicted NOx at a number of reheat settings is shown in Figure 10. It can be seen that the results compare favourably, both in absolute value and in the trends across the traverse. There is a slight discrepancy at minimum

reheat as the CFD model under-predicts the combustion intensity, and consequently the temperature and NOx. But despite the complexity of the problem being modelled the influence of features, such as the bypass sprayers on the exit profile, are being successfully predicted.

Conclusions

The aim of this work was to make a series of experimental measurements in the exit plane of a reheated gas turbine engine and compare them to predictions from a CFD model. The system to be modelled was complicated, involving high flowrates, multi-point fuel injection and vitiated air, but the results reported in this paper show good agreement between the two techniques both qualitatively and quantitatively. The CFD model showed where NOx is produced and, in the future, where NO to NO₂ conversion occurs within the reheat system allowing the development of smart fuelling systems that minimise the production of NO and prevent the formation of visible emissions. The work also highlights problems associated with probe induced reactions in making measurements of NO and NO₂ in fuel rich regions, such as those found at minimum reheat, and needs to be addressed to validate the CFD predictions.

References

- Al-Fawaz, A. Dearden, L. M., Hedley, J. T., Pourkashanian, M., Williams, A. and Yap, L. NOx Formation in Geometrically Scaled Gas Fired Industrial Burners. *25th Symposium (International) on Combustion*. The Combustion Institute p. 1027. (1994).
- Amin, E. M., Andrews, G. E., Pourkashanian, M., Williams, A. and Yetter, R. A Comparison Study of Pressure Effects on Pollutant Generation in Gas Turbine Combustors. *Journal of engineering for Gas Turbines and Power*. 118. p 773. (1996).
- Backmier, E., Eberius, K.H. and Just I. *Combustion Science and Technology*, Vol. 7. p. 77. (1973).
- Baulch, D.L., Dysdall, D.D., Home, D.G., and Lloyd, A.C., "Evaluated Kinetic Data For High Temperature Reaction", Vol. 1,2,3, Butterworth. (1973).
- Bilger, R.W. and Beck, R.E., *15th Symposium (International) on Combustion*. The Combustion Institute. p. 541. (1975).
- Blauwens, J., Smets, B., and Peters, B. *16th Symposium (International) on Combustion*. The Combustion Institute. p. 1055. (1977).
- Bromley, J. H., Barnes, F. J. and Little, L. H. The Effects of Low Concentrations of CO, H₂ and Hydrocarbons on NO₂/NO Ratios in Heated Gases. *Journal of the Institute of Energy*. 61. pp. 89-97. (1988).
- DeSoete, G. G. Overall Reaction Rates of NO and N₂ Formation From Fuel Nitrogen. *15th Symposium (International) on Combustion*. The Combustion Institute. pp. 1093-1102. (1975).
- Dixon-Lewis, G. Private Communications. Leeds University, Leeds. (1980).
- Drake, M.C., Correa, S.M., Pitz, R.W., Shyy, W. and Fenimore, C.P. *Combustion and Flame*. 69. p. 347. (1987).
- Fahey, D. W et al. In Situ Observations in Aircraft Exhaust Plumes in the Lower Stratosphere at Mid-latitudes. *Journal of Geophysical Research*. 100. pp. 3065-3074. (1995).
- Fenimore, C.P. *13th Symposium (International) on Combustion*. The Combustion Institute. p. 373. (1971).

Fenimore, C.P. *Chemistry of Premixed Flames* MacMillan, New York. (1964).

Flower, W.L. Manson, R.K. and Kruger, C.H. *15th Symposium (International) on Combustion*. The Combustion Institute. p. 823. (1975).

Foster, T.J. and Wilson, C.W. Detailed Chemical Modelling Predictions of Emissions from a Reheated Gas Turbine Engine with Application to Future Subsonic Aircraft ASME PAPER GT-97- (1997).

Hanson, R.K., and Saliman, S. Survey of Rate Constants in H/N/O System. p. 361. *Combustion Chemistry*, (Ed. W.C. Gardiner). (1984).

Hori, H., Matsunaga, N., Malte, P. C. and Marinov, N. M. The Effect of Low Concentration Fuels on the Conversion of NO to NO₂. *24th Symposium (International) on Combustion*. The Combustion Institute. pp. 909-916. (1992).

Johnsson, J. E., Glarborg, P. and Dan-Johansen, K. Thermal Dissociation of Nitrous Oxide at Medium Temperatures. *24th Symposium (International) on Combustion*. The Combustion Institute. pp. 917-923. (1992).

Magnussen, B.F. and Hjertager, B.H. *16th Symposium (International) on Combustion*. The Combustion Institute. p. 719. (1977).

Michaud, M. G., Westmoreland, P. R. and Feitelberg, A. S. Chemical Mechanisms of NO_x Formation for Gas Turbine Conditions. *24th Symposium (International) on Combustion*. The Combustion Institute. pp. 879-889. (1992).

Miller, J. A. and Bowman, C. T. Mechanism and Modelling of Nitrogen Chemistry in Combustion *Progress in Energy and Combustion Science*. 15. pp. 287-338. (1989).

Miller, J.A., Branch, M.C., McLean, W.J., Chandler, D.W., Smooke, M.D. and Kee, R.J. *20th Symposium (International) on Combustion*. The Combustion Institute. p. 673. (1985).

Missaghi, M., Pourkashanian, M., Williams, A. and Yap, L. Proceedings of American Flame Days Conference. USA. (1990).

Missaghi, M., Pourkashanian, M., Williams, A., Yap, T.L. Predictions of NO_x Emissions from Oxygen-Enriched low NO_x Burners. *Proceedings of the International Conference on Environmental Control of Combustion*. Honolulu, Hawaii, AFRC. (1991).

Monat, J.P., Hanson, R.K., and Kruger, C.H. *17th Symposium (International) on Combustion*. The Combustion Institute. p. 543. (1979).

Peters, N. and Donnerhack, S. *18th Symposium (International) on Combustion*. The Combustion Institute. p. 33. (1981).

Schefer, R.W., Namazian, M. and Kelly, I. Combustion Research Facility News, Sandia National Laboratories. Vol 3., No. 4, (1991).

Schulte, P. and Schlager, H. In-flight measurements of cruise altitude nitric oxide emission indices of commercial jet aircraft. *Geophys. Res. Lett.* 23, pp. 165-168. (1996).

Seto, S. P. and Lyon, T. F. Nitrogen Oxide Emissions Characteristics of Augmented Turbofan Engines. *Journal of Engineering for Gas Turbines and Power*. 116. pp. 478-482. (1994).

Brundish, K. D., Monciet, J., Wilson, C. W. and Wootton, A. DIAL Measurements on a Gas Turbine Exhaust. AGARD Fall Meeting (1997).

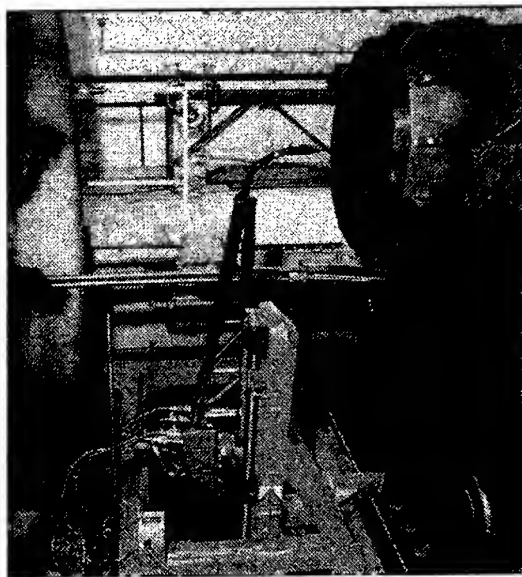


Figure 1. Photograph showing the traversing gas sampling probe insitu.

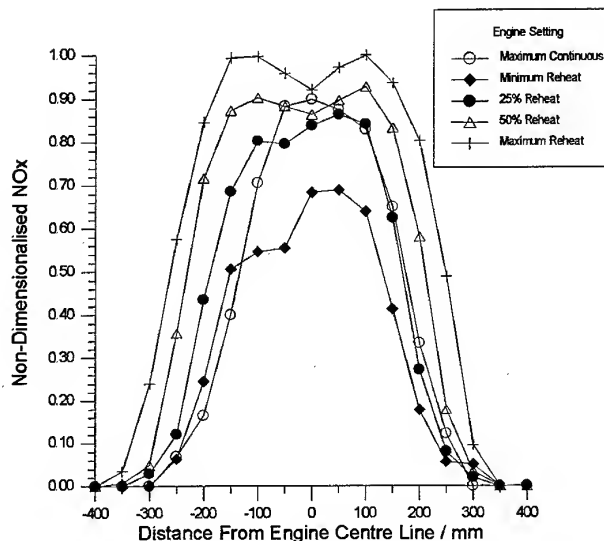


Figure 2. Engine exit centre line NO_x measurements at maximum continuous and reheat conditions.

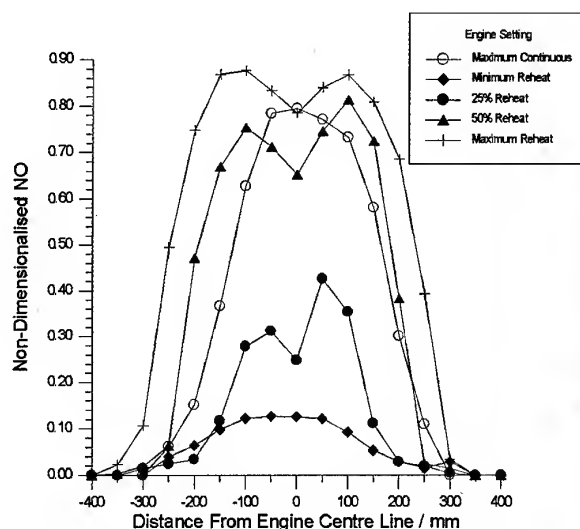


Figure 3. Engine exit centre line NO measurements at maximum continuous and reheat conditions.

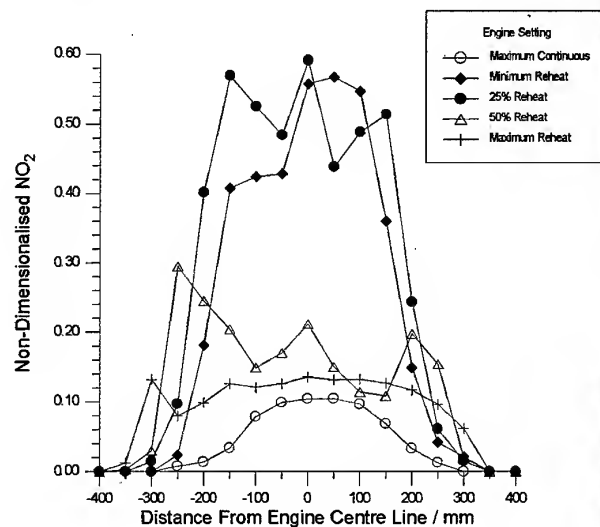


Figure 4. Engine exit centre line NO₂ measurements at maximum continuous and reheat conditions.

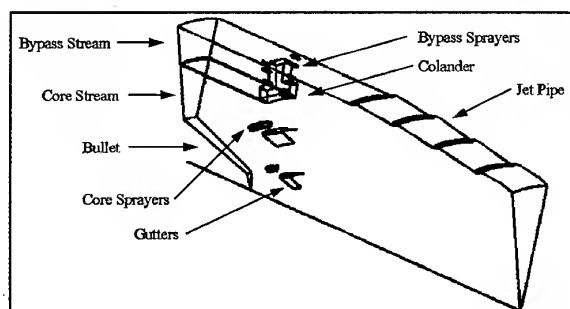


Figure 5. CFD model outline of the reheat section.

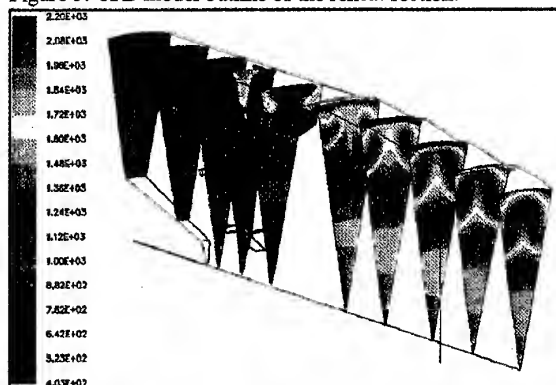


Figure 6. CFD Temperature prediction at various planes in the reheat section.

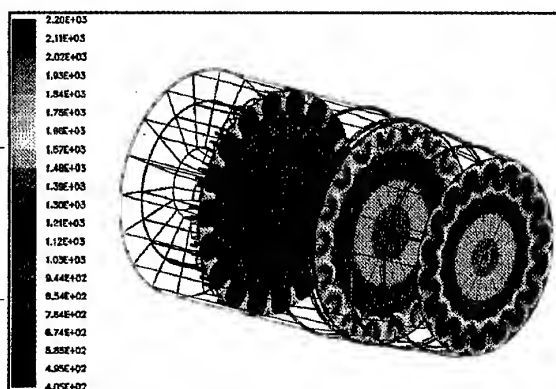


Figure 7. CFD Temperature prediction shown for the complete engine at various planes down the reheat system.

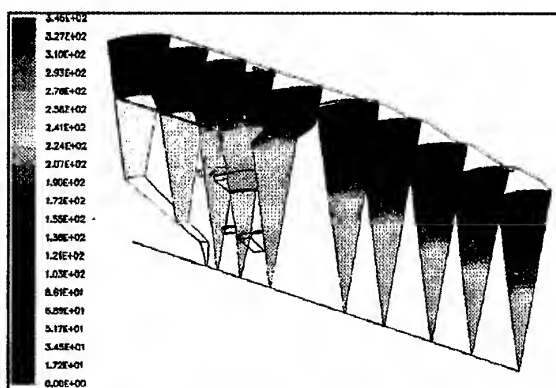


Figure 8. CFD NO_x prediction at various planes in the reheat section.

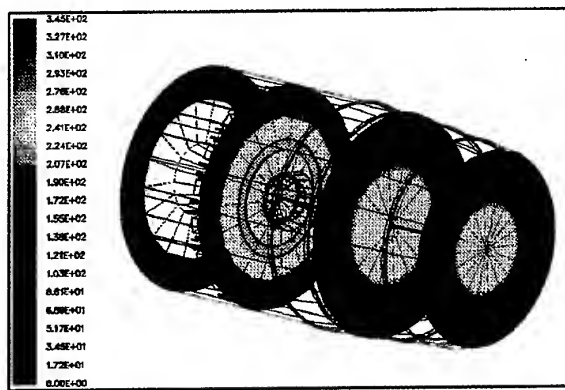


Figure 9. CFD NOx prediction shown for the complete engine at various planes down the reheat system.

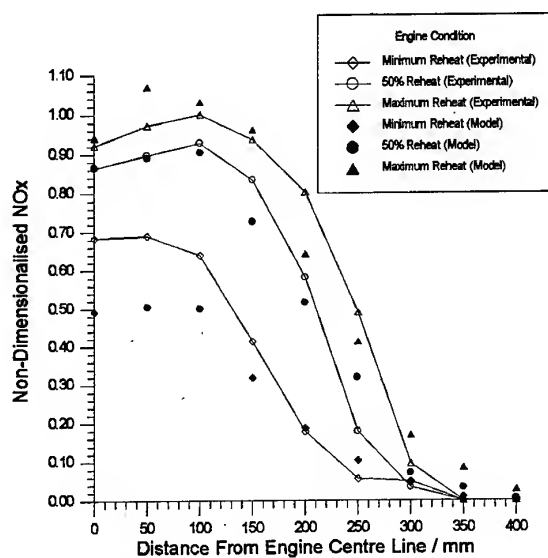


Figure 10. Comparison of NOx concentrations made by experimental measurement and CFD predictions at a number of conditions.

PAPER No. 19
Pourkashanian, Williams, Foster & Wilson
(presenter: M. Pourkashian)

Question 1: G.J. Sturgess, ISSI, U.S.

What was the upstream boundary condition for NO and NO₂ for the afterburner calculations? At high afterburner temperature rises, NO₂ goes back to NO through reverse reactions. However, as the exhaust plume cools downstream of the afterburner exit, more NO₂ should be produced. Have the calculations been extended downstream into the exhaust plume, or is such an extension planned? What visibility criteria were used for visibility of the plume due to the presence of the NO₂?

Answer:

The upstream boundary conditions for all of the species NO, NO₂, CO, CO₂ and unburned hydrocarbons, were measured values at maximum continuous power. For NO_x, this can be seen as less than 240 ppmV in Figure 8. No, the calculations were stopped at the engine afterburner exit plane. Calculations in the plume are of great importance, and work is planned within the BRITE/EURAM Framework 5 program. The visibility criterion is an interesting question. The angle of view of the plume, the NO₂ concentration and the eyesight of the individual all come into play. We have previously published papers showing the NO₂ can be detected as parts per billion¹. However, by eye, the visibility criterion is more likely to be in the range around 50 ppmV/meter plume thickness.

1. Brundish, K.D., Moncreet, J., Wilson, C.W. and Wooton, A., "DIAL Measurements on a Gas Turbine Exhaust," AGARD Fall Meeting, 1997.

INFLUENCE OF ENGINE PERFORMANCE ON EMISSION CHARACTERISTICS

A. Döpelheuer, M. Lecht

DLR
German Aerospace Center
Institute of Propulsion Technology
Engine Systems
Linder Höhe
D-51147 Köln / Cologne
Germany

ABSTRACT

This paper concentrates on the results of different investigations on aircraft engine emissions. In a first step semi-empirical emission correlation methods to predict the sum of nitric oxide and nitrogen dioxide (NO_x), carbon monoxide (CO), hydrocarbons (HC) and soot are introduced. They all are of a „variable“ reference type meaning, that published sea level static (SLS) measurements will be used as a reference. To calculate the amount of emissions for altitude operating conditions, the actual parameters involved like the fuel flow (for the NO_x correlation method), the reciprocal value of the combustor loading parameter (for the CO and HC correlation methods) and the combustor inlet temperature and pressure, the flame temperature and the equivalence ratio (for the soot correlation method) are set into relation to the respective reference ground values.

The necessary internal engine parameters are received from a thermodynamic engine modelling program shortly described in this paper. Because of the fact, that the engine thermodynamic state is mainly determined by the thrust demand of the aircraft and the ambient conditions, not only engines, but also aircraft engine combinations on different flight missions had to be looked at. Therefore a flight performance module is presented, which allows - in combination with the engine modelling program and the emission calculation methods - detailed simulations and investigations of flight missions on the entire route.

As a result not only the effects of engine performance modes and parameters (like bypass ratio in combination with overall pressure ratio) but also the effects of ambient conditions (like wind and ambient temperature) and flight profile (like cruise altitude, step climb, take off weight and payload factor) on the fuel burned and the emissions produced by different engines and aircraft in use are investigated. Finally the results of a comparison between a subsonic and a supersonic mission and a comparison between a jet aircraft of the first generation and a modern type are given.

G_0	take off weight	[kg]
H	altitude	[m]
HC	hydrocarbons	[-]
IAS	indicated air speed	[kn]
ICAO	International Civil Aviation Organisation	[-]
ISA	International Standard Atmosphere	[-]
Ma	Mach Number	[-]
N	atomic nitrogen	[-]
N_2	nitrogen	[-]
NO	nitric oxide	[-]
NO_x	sum of nitric oxide and nitrogen dioxide	[-]
O	atomic oxygen	[-]
O_2	oxygen	[-]
OPR	overall pressure ratio	[-]
p	pressure	[bar]
p_∞	ambient pressure	[bar]
p_3	combustor inlet pressure	[bar]
pass	passengers	[-]
$p_{t,1}$	total pressure at engine inlet	[bar]
r	weighting factor for flame temperature	[-]
R	universal constant of gas, 8.314	[J/mol/K]
ref	reference	[-]
SFC	specific fuel consumption	[kg/(daN h)]
SLS	sea level static	[-]
SMD	Sauter mean Diameter	[μm]
SN	Smoke Number	[-]
t	time	[s]
t_E	evaporation time	[s]
T_∞	ambient temperature	[K]
T_3	combustor inlet temperature	[K]
T_4	combustor outlet temperature	[K]
T_n	flame temperature	[K]
T_{ISA}	temperature derived from ISA	[K]
T_{PZ}	temperature in primary zone	[K]
T_{stoich}	stoichiometric temperature	[K]
$T_{t,1}$	total temperature at engine inlet	[K]
V_C	volume of combustor	[m^3]
w	mass flow	[kg/s]

LIST OF SYMBOLS AND ABBREVIATIONS

a, b, c	constant values	[-]
C	concentration	[mg/ m^3]
CO	carbon monoxide	[-]
corr	corrected	[-]
E	activation energy	[J/mol]
El	emission index	[g/kg]
FL	flight level	[100 ft]
δ_t	$p_{t,1} / 1.013 \text{ bar}$	[-]
Φ	equivalence ratio	[-]
η_C	combustion efficiency	[%]
μ	bypass ratio	[-]
π	pressure ratio	[-]
θ_t	$T_{t,1} / 288.15 \text{ K}$	[-]
Θ	simplified air loading parameter	[$\text{bar}^{1.8} \text{ m}^3 \text{ s} / \text{kg}$]
Ω	reciprocal value of Θ	[kg / ($\text{bar}^{1.8} \text{ m}^3 \text{ s}$)]

1. INTRODUCTION

The environmental aspect of airtraffic continues to be an important objective within the atmospheric sciences. Aircraft engines emit their combustion products in a sensitive area of the atmosphere within and above the tropopause. Furthermore the airtraffic is expected to grow substantially in the next decades. It is still an open question whether - and how - aircraft engine emissions now or in the future may influence the climatic balance of the earth.

Many research programs have been established to investigate these open questions. In some cases detailed aircraft engine emission data are needed. This paper deals with information about methods evaluated to determine these data. Due to the fact, that the emission characteristics of aircraft engines are highly influenced by the engine performance and the engine operating conditions, this paper concentrates on these different influences.

2. EVALUATION OF EMISSION INDICES

All methods explained in this paper to calculate the amount of emissions from aircraft engines are so called „variable reference methods“. They have the following principle in common: The sea level static measurements for 7, 30, 85 and 100 % thrust published in [ICAO, 1995] are used to evaluate a reference function of the form „emission index versus typical parameters“. With this function the typical behaviour of the investigated engine caused by constant characteristics like the evaporation system and the geometry of the combustor is considered. This leads to a nearly exact emission calculation on the ground.

Proceeding from this reference function for altitude conditions the emission indices are evaluated by setting the dominating actual parameters into relation to the reference ground parameters. This will be shown in more detail in chapters 2.1 to 2.3.

2.1. NO_x

The production of thermal NO_x in a combustor of an aircraft engine is coupled with the chemical reaction process within the hot flame region of the primary combustion zone and the residence time of the reacting species. The dominating reaction with respect to this time is the formation of nitric oxide (NO) and atomic nitrogen (N) out of atomic oxygen (O) and nitrogen (N₂) as prescribed by the first equation of the extended Zeldovich mechanism [Heywood, 1973]. The mole concentration of NO_x developed during a time t (x_{NO_x}) can generally be expressed by

$$\text{Eq. 1)} \quad x_{\text{NO}_x} = \text{const} \cdot \left(\frac{p}{T_{\text{PZ}}} \right)^{0.5} \cdot e^{\frac{E}{8RT_{\text{PZ}}}} \cdot t$$

with E being the activation energy (315600 J/mol) for the above mentioned reaction.

While the pressure p can be well taken as the pressure at the combustor inlet p_3 , the temperature T_{PZ} is an average more allocated to an average density within the primary combustion zone and T_{fl} is the flame temperature ruling the chemical reaction process.

The emission index of NO_x can then be expressed by its definition as mass NO_x per mass of fuel burned, if the following assumptions are made:

- a) the residence time t being proportional to

$$(w_{\text{air}} / (p_3 / T_{\text{PZ}}))^{-1}$$

- b) the airflow w_{air} into and through the combustor being proportional to

$$p_3 / \sqrt{T_3} \quad \text{and} \quad p_3 / \sqrt{T_4}$$

- c) from the heat balance of the combustor and with assumption b) the fuel weight flow w_{fuel} could then be proportional to

$$p_3 \times \sqrt{T_3}$$

Using these assumptions leads to an expression for the emission index (EI) NO_x of the following format:

$$\text{Eq. 2)} \quad EINO_x = \text{const} \cdot \left(\frac{p_3}{T_3} \right)^{0.5} \cdot T_{\text{PZ}}^{-1.5} \cdot e^{-\frac{38000}{T_{\text{fl}}}}$$

This formula can only be applied in a reference type correlation mode, because the value of the constant may not really be known. Therefore a correlation formula with respect to a reference condition (index: ref) may be a useful tool based on theoretical considerations:

Eq. 3)

$$\frac{EINO_x}{EINO_{x, \text{ref}}} = \left(\frac{p_3}{p_{3, \text{ref}}} \right)^{0.5} \left(\frac{T_{3, \text{ref}}}{T_3} \right)^{0.5} \left(\frac{T_{\text{PZ, ref}}}{T_{\text{PZ}}} \right)^{1.5} e^{\frac{38000}{T_{\text{fl, ref}}} - \frac{1}{T_{\text{fl}}}}$$

To analyse Eq. 3 it is necessary to describe the thermodynamic situation within an engine. This is not a special problem considering the combustor inlet pressure p_3 and temperature T_3 . In contrary the temperatures within the primary zone of the combustor may allow some more space for an interpretation of T_{PZ} and T_{fl} . Within this analysis the following assumptions developed in [Stöppler, 1992] have been made to give an average of these quantities.

$$\text{Eq. 4)} \quad T_{\text{PZ}} = 0.5 \cdot (T_{\text{fl}} + T_3)$$

$$\text{Eq. 5)} \quad T_{\text{fl}} = r \cdot T(\Phi) + (1 - r) \cdot T_{\text{stoich}}$$

Herein T_{stoich} is the temperature reached by a homogeneous stoichiometric fuel/air mixture in the primary zone i.e. an equivalence ratio of $\Phi = 1$, while $T(\Phi)$ is the temperature at a "homogeneous equivalence ratio" of Φ in the primary zone.

In the non-homogeneous mixture of a real combustor the hotter flame zones contribute more to the total NO_x-production than the cooler flame zones. This effect has been approximated in [Stöppler, 1992] by introducing a weighted flame temperature according to Eq. 5. The weighting factor r changes with the specific combustor design; an evaluation of ICAO-emissions data shows, that a weighting factor of $r = 0.25$ is a good average value for most engines.

As an example a modern high bypass fan engine has been evaluated on this basis using a 100 % rated output thrust as a point of reference. Quantitative values of the internal engine data at the reference operating condition and at a single part load performance have been calculated by the thermodynamic 1-dimensional engine simulation model described in chapter 3.1 [Deidewig, 1993] and given in Table 1.

Quantity	Reference Values	Part Load Values
P_3 (kPa)	3000	1570
T_3 (K)	818	670
Φ (-)	1	0.82
T_{stoch} (K)	2629	2533
T_{fl} (K)	2629	2490
T_{PZ} (K)	1723	1580
W_{fuel} (kg/s)	2.353	1.07
EI NO _x (g/kg)	28.06	***** 11.4 *****

Table 1: Data to calculate the NO_x emission index for an off-reference operating condition

The temperature $T(\Phi)$ has been determined in approximation with a special code, used for chemical reactions of a fuel/air mixture [Pratt, 1976]. The evaluation of Eq. 3 with respect to its various terms from these data is shown in Table 2.

1	2	3	4	5
$\left(\frac{P_3}{P_{3,ref}}\right)^{0.5}$	$\left(\frac{T_{3,ref}}{T_3}\right)^{0.5}$	$\left(\frac{T_{PZ,ref}}{T_{PZ}}\right)^{1.5}$	$e^{X_{ref}-X}$	$\frac{EINOx}{EINOx_{ref}}$
0.7234	1.1049	1.1388	0.4462	0.4061

Table 2: Influence of the different contributing terms of Eq. 3

That term with the highest uncertainty (column 4) from its modelling aspect as well reveals the highest sensitivity. Therefore measured values have to be included as far as possible to support the theoretical analysis. Figure 1 shows how the above theory would fit into a scale of measured values at SLS.

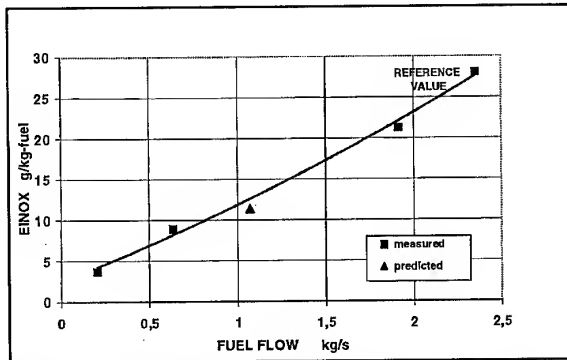


Figure 1: Comparison of measured and predicted NO_x emission index (CF6-80C2 type engine at SLS)

For practical applications equations such as Eq. 2, which have been deduced from the theory, have been modified by further

simplifying approximations. Therefore the following version can be found in the literature [Sullivan, 1975]

$$\text{Eq. 6) } EINOx = \text{const} \cdot p_3^a \cdot e^{bT_3}$$

On the one hand the problem has been reduced to a function of the combustor inlet pressure and temperature only by this type of correlation formula, on the other hand these thermodynamic data are considered a proprietary and sensitive status by the engine manufacturer. Therefore methods have been looked at, which do not even need p_3 and T_3 .

One method found is based on correlating the EI NO_x with fuel flow. For this a reference function of the emission index versus engine fuel flow has to be established by measurements under reference inlet conditions. This could for instance be done by choosing the four data points from certification measurements for an engine (see Figure 1), which represent different thrust settings at sea level static and international standard atmospheric (ISA) conditions and which have been published in the ICAO engine emissions data bank [ICAO, 1995].

The basic idea now is, if an engine is running at other than ISA SLS conditions all pressures p_3 and temperatures T_3 at the combustor inlet taken versus fuel flow will line up to one function if pressures, temperatures and fuel flow are corrected to reference engine inlet conditions by the following equations:

$$\text{Eq. 7) } T_{3,corr} = T_3 / \theta_t \quad \text{with} \quad \theta_t = T_{t,1} / 288.15K$$

$$\text{Eq. 8) } p_{3,corr} = p_3 / \delta_t \quad \text{with} \quad \delta_t = p_{t,1} / 101.3kPa$$

$$\text{Eq. 9) } w_{fuel,corr} = \frac{w_{fuel}}{\delta_t \cdot \sqrt{\theta_t}}$$

Some idealisation has been made here in assuming, that for a real similarity the compressor polytropic efficiency and the combustion efficiency is constant. Another approximation using an EI NO_x correlation formula has to be made in avoiding T_3 to appear in the exponent like in Eq. 6.

Therefore the following simplification has been used:

$$\text{Eq. 10) } EINOx = \text{const} \cdot p_3^a \cdot T_3^b$$

In combination with Eq. 7 and Eq. 8 the following relationship can be established:

$$\text{Eq. 11) } \frac{EINOx}{EINOx_{corr}} = \frac{EINOx}{EINOx_{ref}} = \delta_t^a \cdot \theta_t^b$$

Since at ISA and SLS engine inlet conditions $\delta_t = \theta_t = 1$ is given, the EI NO_x then represents the corrected i.e. the reference value. To gain the exponents a and b it has been considered, that from the theory $a = 0.5$ would be the value of choice, but in reality observed from measurements for the CF6 engine family an exponent of $a = 0.4$ might rather be expected [Bahr, 1991].

The evaluation of Eq. 3 for the given example shows, that for a pressure exponent in the range of 0.4 to 0.5 a temperature

exponent of about $b = 3$ would be well in line with the theory. Thus the exponents of a first choice were: $a = 0.4$ and $b = 3$.

An application of this simplified method of EI NO_x versus fuel flow correlation is shown in Figure 2 and Figure 3. The analysis of different engine inlet operating conditions reveals the collapse of values by correcting with respect to the ISA SLS reference condition. Although the actual EI NO_x during flight operation were calculated from a more sophisticated prediction method similar to Eq. 3 [Deidewig, 1996], the application of the fuel flow method shows the expected effect.

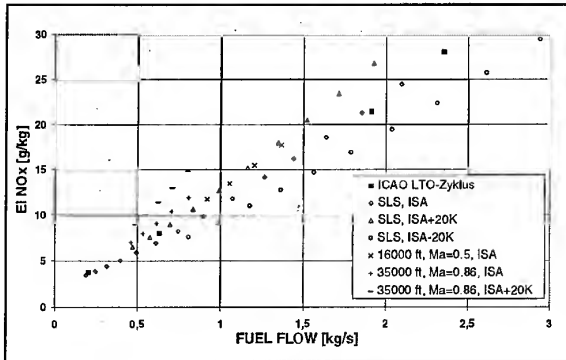


Figure 2: EI NO_x versus fuel flow for CF6-80C2B1F

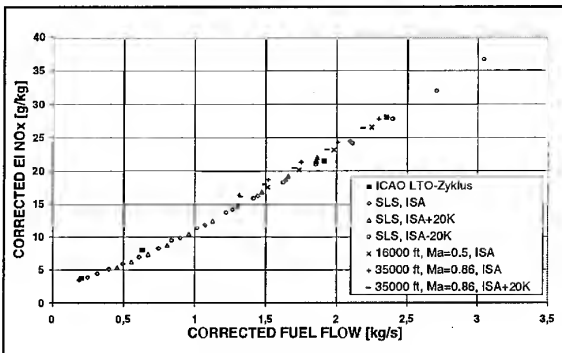


Figure 3: Corrected values for CF6-80C2B1F

2.2 CO and HC

Carbon monoxide and the hydrocarbons are products of an incomplete combustion of a fossil fuel. Therefore they are directly coupled with the combustion efficiency η_c . If one sets the lower heat value of the unburned hydrocarbons equal to the lower heat value of the kerosene, one can derive the following equation [Dodds, 1990]:

$$\text{Eq. 12)} \quad \eta_c = 100 - 0.1 \cdot \text{EI HC} - 0.02334 \cdot \text{EI CO} [\%]$$

This equation has been applied to the ICAO SLS data of engines developed in different decades, see Figure 4.

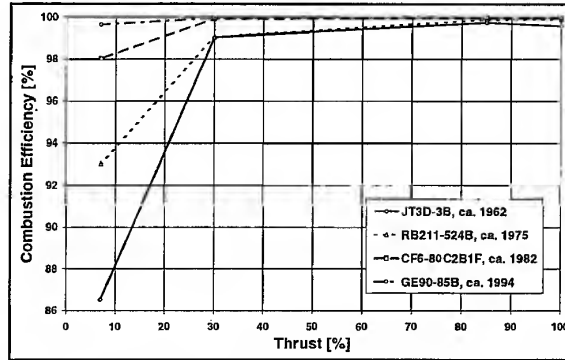


Figure 4: Calculated combustion efficiencies versus thrust at SLS following [ICAO, 1995] and Eq. 12

Even the JT3D developed in the sixties reaches combustion efficiencies above 99.5 % at high power settings. But especially at the lower power settings the huge progress in combustor and injection technology gets obvious: While the combustion efficiency of the JT3D drops to about 86.5 % at 7 % SLS thrust, the GE90 reaches about 99.6 % at the same power setting.

The combustion efficiency of an aircraft engine can be correlated with a parameter called Ω , which is the reciprocal value of the simplified combustor loading parameter Θ (see for example [Münzberg, 1977] and [Lefebvre, 1983]).

$$\text{Eq. 13)} \quad \Omega = \frac{w_{\text{Air}}}{V_c \cdot p_3^{1.8} \cdot e^{T_3/300K}}$$

The idea of the emission correlation explained here is to use Ω as the reference function for CO and HC. Due to the fact, that the volume of the combustor V_c is unknown in most cases but a constant value, the parameter $(\Omega \cdot V_c)$ has been introduced. This leads to emission correlations of the following form:

$$\text{Eq. 14)} \quad \text{EI CO, EI HC} = f(\Omega \cdot V_c) = f\left(\frac{w_{\text{Air}}}{p_3^{1.8} \cdot e^{T_3/300K}}\right)$$

Figure 5 shows the CO and HC SLS emission indices for the CF6-50C2 published in [ICAO, 1995] versus $(\Omega \cdot V_c)$ used as reference function.

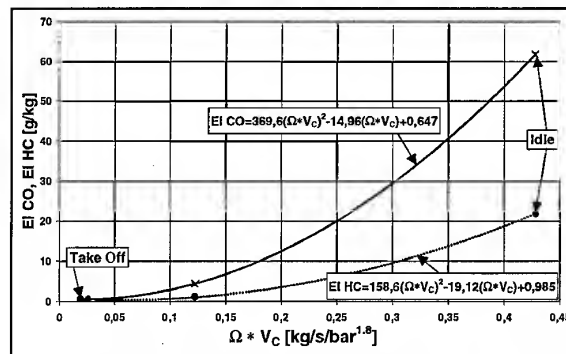


Figure 5: Measured EI CO and EI HC versus $(\Omega \cdot V_c)$ for CF6-50C2

At very high altitudes the evaporation properties of aircraft engines may change due to lower temperatures and pressures in the combustion chamber and lower mass flows of fuel and air through the injection system. Therefore a correction concerning the evaporation time t_E based on the changing Sauter mean diameter SMD in comparison to a reference value at SLS (ref) has been developed [Döpelheuer, 1997]. This finally leads to correlations of the form:

Eq. 15)

$$EI_{CO}, EI_{HC} = f \left(\frac{W_{Air}}{P_3^{1.8} \cdot e^{T_3/300K}} \right) \cdot \left\{ \frac{T_3}{T_{3,ref}} \cdot \frac{P_{3,ref}}{P_3} \right\}^c$$

The correlations have been validated with P&W 305 data, which were measured within the national research program „Pollution from Airtraffic“ in the altitude test facility at the university of Stuttgart as share of MTU. The results are shown in Figure 6. Open symbols represent uncorrected data (Eq. 14), filled symbols represent data correlated with the correction term concerning the evaporation time (Eq. 15). For the P&W 305 the value for the constant c resulting from the experiments is 0.4.

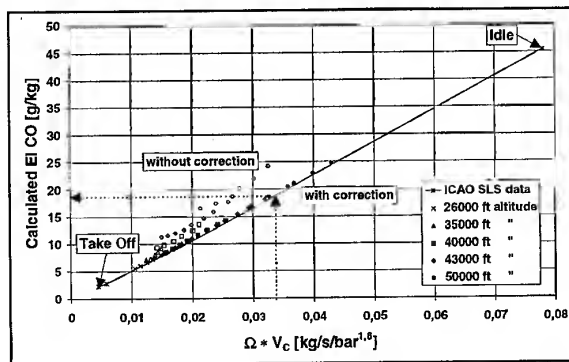


Figure 6: Calculated EI CO versus $(\Omega \cdot V_c)$ for P&W 305

Up to an altitude of 35000 ft the data correlated with Eq. 14 (uncorrected, open symbols) lie on a line directly determined from the SLS data and used as reference function. But for altitudes above 35000 ft the values are higher than the expected values due to evaporation properties getting worse.

The values correlated with Eq. 15 (corrected, filled symbols) all lie on the SLS reference function. The altitude emission index of CO for the P&W 305 can thereby be determined by evaluating the altitude value of $(\Omega \cdot V_c)$ with Eq. 13 and finding the corresponding SLS reference value of EI CO (see arrows in Figure 6). By this method an easy way has been found to determine altitude emission indices out of altitude combustor inlet conditions in combination with ground measurements.

2.3 Soot

The soot production and oxidation mechanism is very complex and not well known. Especially the non-homogeneous flow and temperature fields in the combustion chamber, the different influences of the injection systems and combustor technologies, the influence of the type of fuel burned and the rare measurements make it difficult to calculate the amount of soot emitted by aircraft engines. Furthermore neither a soot emission index nor a soot

concentration, but only the Smoke Number SN is measured for the ICAO certification process, see Figure 7.

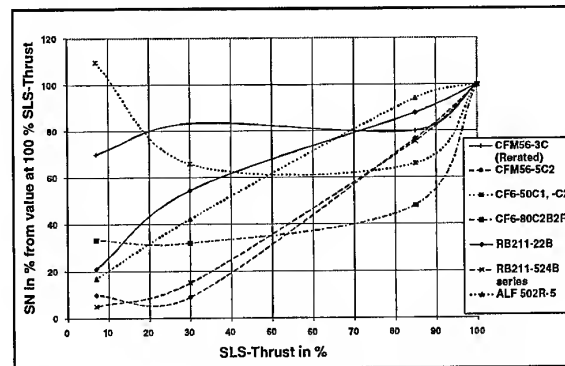


Figure 7: SN versus SLS-thrust in percentage terms for several engines [ICAO, 1995]

Figure 7 shows the extremely different behaviour of some engines concerning the emitted soot. Furthermore the absolute values of the SN not shown in this Figure differ widely. A semi-empirical soot correlation with variable reference values has been developed to cope with these problems [Döpelheuer, 1997]. The different variable reference functions for every investigated engine taken from ground measurements consider the special properties of the combustor and injection system, the actual operating condition is taken into account by thermodynamic combustor data.

As a first step the soot concentration values C_{soot} at SLS have to be determined out of the ICAO SN measurements. Some measured functions of soot concentration versus SN for different engines have been published, see Figure 8.

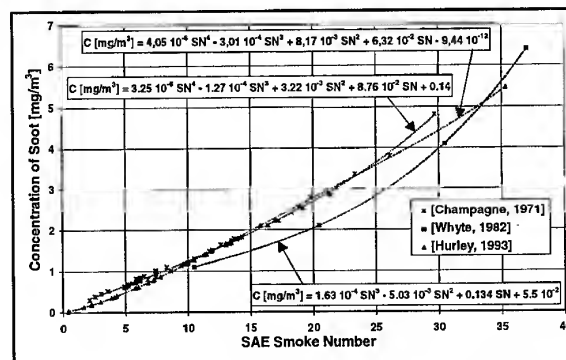


Figure 8: Soot concentration versus Smoke Number, comparison between different authors

There is no direct connection between C_{soot} and the SN, this connection depends on the soot properties (especially the particle size distribution) of the engine looked at. A combination of the results of [Champagne, 1971] and [Hurley, 1993] has been used for concentrations up to 6 mg/m³, for higher concentrations the function of [Whyte, 1982] has been applied. The necessary reference function for the soot correlation introduced here is of the form C_{soot} versus T_3 for SLS conditions, as shown in Figure 9 for the RB211-22B and the CFM56-5C2.

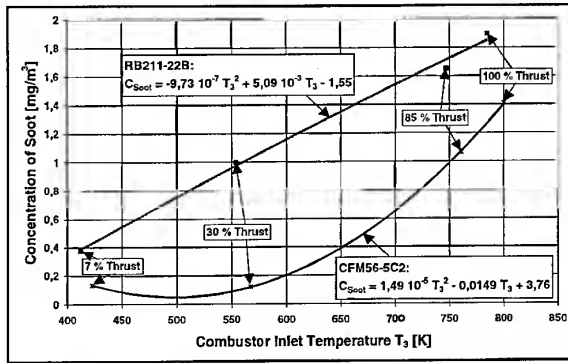


Figure 9: Concentration of soot versus combustor inlet temperature for CFM56-5C2 and RB211-22B at SLS

Both, the amount of produced soot and the development of the concentration with lower power settings is very different for these two engines. This can be explained by the different injection systems and combustor technologies leading to different evaporation properties (the RB211 was developed much earlier than the CFM56) and is the main reason, why a soot correlation on the basis of a variable reference function will be used.

The emission index of soot for other than sea level static conditions is calculated with the help of these reference functions and actual thermodynamic data effecting the soot production. These are the combustor inlet pressure p_3 , the flame temperature T_f and the equivalence ratio Φ as parameter considering the actual ratio of atomic carbon to atomic oxygen C/O. Measured results of model flames and combustor tests have been combined to determine a soot correlation of the following form:

Eq. 16)

$$C_{Soot} = C_{Soot, ref} \cdot \left(\frac{\Phi}{\Phi_{ref}} \right)^{2.5} \cdot \left(\frac{p_3}{p_{3, ref}} \right)^{1.35} \cdot \frac{e^{(-20000/T_f)}}{e^{(-20000/T_{f, ref})}} \text{ mg / m}^3$$

The reference variables (ref) are the SLS values at the same combustor inlet temperature T_3 as the operating condition looked at. The other variables are the actual values obtained from the investigated operating condition. The competing influences of the thermodynamic parameters Φ , p_3 and T_f on the soot production and oxidation are all combined in one term each.

3. NECESSARY TOOLS

3.1 Engine Model

The basic tool to predict any aircraft engine emissions during operation is an off-design performance simulation code based on a given design point. In this investigation a more general thermodynamic description of a two spool bypass engine has been used without detailed compressor or turbine performance mapping. Once the design point has been chosen with respect to thrust, fan pressure ratio and the internal engine heat cycle data, and after matching the design with public available data, the off-design will be modelled by balancing the power on the low and high pressure spool, by matching engine and nozzle pressure ratios as well as turbine and nozzle air mass flows in the hot and cold flow path [Deidewig, 1998].

The engine simulation code contains a high pressure turbine cooling model and can - if necessary - as well address a change of off-design component efficiencies. Figure 10 shows - as an example - the prediction of fuel flow versus thrust for a high bypass turbo fan engine - the JT9D-7R4G2 - taking the maximum rate output from ground tests as a design point for modelling. Under various off-design conditions for sea level static and in flight operating conditions a good agreement with the measurements and manufacturers predictions can be reached.

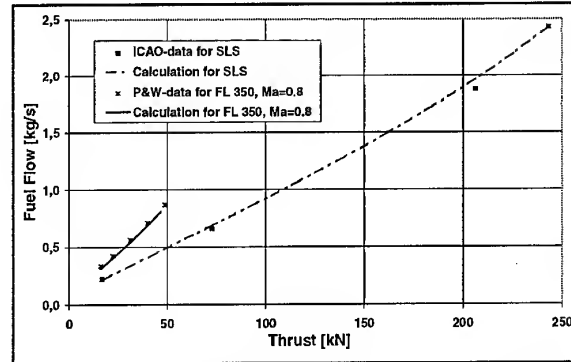


Figure 10: Comparison between measured and calculated fuel flow values for JT9D-7R4G2

3.2 Flight Performance Calculation

The flight performance program described in more detail in [Deidewig, 1996] is divided into the flight phases taxi out, take off, climb, cruise, optional step climb and second cruise, descent including approach and taxi in. All phases except taxi out and taxi in are once again divided into different segments and interpolated between the points of calculation.

During steady cruising phases the thrust demand of an aircraft only is connected with the ambient conditions, the actual weight and the actual lift over drag value. Additional thrust must be delivered by the engines in cases of take off and climb modes, less thrust is required in descent modes.

The necessary information about the different aircraft like wing area, maximum take off weight and maximum payload have to be taken out of published reports and books like [Jane's, 1994] and others.

The aerodynamic properties of each aircraft are described by an overall parabolic lift over drag polar, which can be generated by only 2 characteristic values: The vertex of the polar and the point of best aerodynamic efficiency. This rough polar has to be seen as a combination of the different lift over drag functions for every single flap configuration of an aircraft assuming, that the pilot always flies at optimum flap setting.

The segments for the cruise phase are calculated with the Breguet formula and a range dependent correction leading to slightly higher fuel consumption values on long range flights.

3.3 Program „Mission“

The main program „MISSION“ combines and controls the thermodynamic engine calculation and emission determination carried out by the program „VARCYCLE“ and the flight performance calculation, which is done within a program called „BLOCKF“. The main tasks of „MISSION“ are to

balance the aerodynamic, inertial and engine forces and to sum up main flight values like flown distance, trip time, burned fuel and produced emissions. The main structure of the program system can be seen in Figure 11.

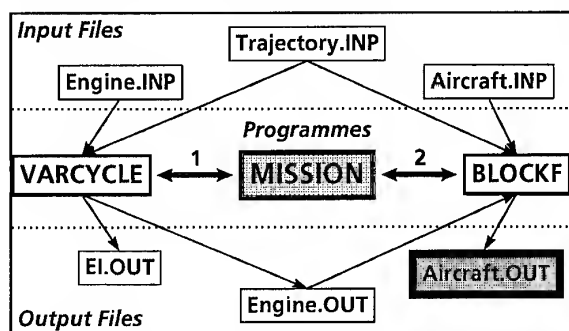


Figure 11: Scheme of flight mission calculation

In a first step „MISSION“ starts „VARCYCLE“, which uses the engine and trajectory data of the input files „Engine.INP“ and „Trajectory.INP“ and generates the output files „EI.OUT“ and „Engine.OUT“. The engine internal thermodynamic status and main data like thrust, fuel flow and emission indices are determined at any operating condition set in „Trajectory.INP“. These main data are saved in the file „Engine.OUT“, which also is an input file for the second step, the start of the flight performance program „BLOCKF“. Furthermore „BLOCKF“ uses the input files „Aircraft.INP“ describing the properties and aerodynamic behaviour of the investigated aircraft and also „Trajectory.INP“ to generate the main output file „Aircraft.OUT“. This most important file contains all the information about the engine and the aircraft during all segments of any flight phase and the total mission values.

These total mission values have been compared to results of Lufthansa and Swissair for detailed flight missions. It turned out, that in all cases a good agreement between the obtained data could be reached.

4. APPLICATIONS AND OBTAINED RESULTS

4.1 Investigations on Engines

As an application of the described engine model the following engine investigation has been carried out: A CF6-80C2B1F engine with a bypass ratio μ of 5.1 has been compared with simulated engines of same technology (same component efficiencies and combustor technology) but different bypass ratios. The design condition for all simulated engines was the thrust at a cruise altitude of 35000 ft (FL 350) and a Mach Number Ma of 0.86. The fan pressure ratio was optimised by finding the minimum specific fuel consumption for every bypass ratio. The overall pressure ratio OPR was taken from 26 for $\mu = 1$ to 45 for $\mu = 20$. In this first rough investigation installation effects and other losses due to the growing engine size have been neglected. Figure 12 shows the results in comparison to the reference engine CF6-80C2B1F (100 %).

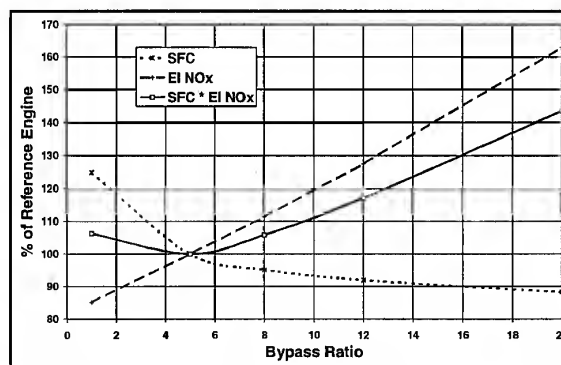


Figure 12: Results of engine investigation for FL 350 and Mach Number 0.86, comparison of different bypass ratios

The specific fuel consumption SFC decreases with increasing bypass ratio due to gains in thermal and propulsive efficiency. But the small profits at very high bypass ratios may be lost due to the installation effects neglected in this investigation. The emission index for NO_x increases more than linear with increasing μ , but the increase for the cruise conditions shown in Figure 12 is not as big as the increase for sea level static conditions. For engine pressure ratios higher than 45 a nearly exponential increase of EI NO_x for the same combustor technology can be expected.

A strong value to compare the NO_x production rates of aircraft engines at the same thrust is the parameter SFC times EI NO_x. It can be seen from Figure 12, that this parameter decreases to its minimum at bypass ratios of 4 to 6 and then increases again. The increase of EI NO_x with the bypass ratio overcompensates the decreasing specific fuel consumption.

4.2 Investigations on Aircraft

Several investigations on aircraft have been performed to demonstrate the big ability of the program system „Mission“. In a first step only the ambient conditions are changed, in a second step the influences of the flight profile and the type of aircraft are investigated. It will be shown, that the change of each parameter has many effects on both, the engine and the aircraft performance. The influence on the total mission values always is a combination of these different effects.

4.2.1 Influences of Ambient Conditions

Wind:

The wind has one of the most dominant influences on the fuel consumption and the emission production of a given flight mission. But due to the fact, that he only affects the ground speed at given true air speed and thereby the flight time and effective flown distance through the air, the influence of the wind can roughly be determined by introducing an „effective distance“. The following example will explain the procedure:

A calculated 6400-km-mission with a B747 at the cruise altitude 11875 m with a Mach Number of 0.86 including take off, climb, cruise and descent without wind sums up to about 434 min or 7.23 h (see Table 5). If one has to determine the influence of a tailwind component with a constant strength of for example 50 km/h in all altitudes, the „effective distance“ for this mission will be reduced by 7.23 h times 50 km/h which is equal to 361.5 km. The 6400-km-mission with a

constant tailwind of 50 km/h is thereby equivalent to a 6038.5-km-mission without wind.

Of course one would never find a constant wind over the whole flight path in reality. Therefore the flight profile has to be divided into several sections with a constant wind component to consider the wind influence in more detail.

Ambient air temperature:

A much more complicated influence on the fuel burned and the emissions produced has the ambient air temperature. Among others it affects the specific fuel consumption of the engine, the lift to drag ratio of the aircraft, the emission indices and the air speed at constant Mach Number (and thereby the trip time). The consequence of the influence of ambient air temperature is a combination of all these effects.

Figure 13 shows the main results of two 8000-km-missions of a B747 powered by RB211-524D4 with ambient air temperatures of T_{ISA} plus 5 and T_{ISA} minus 5 degrees Celsius at all altitudes in comparison to a mission with temperatures derived from international standard atmosphere T_{ISA} (100 %). The Mach Number during the cruise in 11875 m, that corresponds to FL 390, is kept constant at 0.86, the landing weight is set to 230 to.

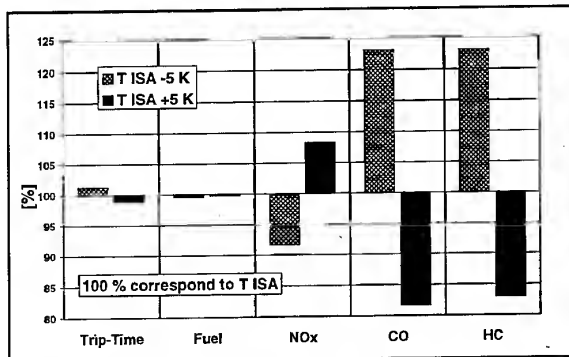


Figure 13: Influence of ambient air temperature, B747 powered by RB211-524D4, 8000 km

Although the necessary turbine entry temperature to balance the drag of the aircraft changes (in this example from 1255 K at T_{ISA} minus 5 degrees to 1315 K at T_{ISA} plus 5 degrees at the middle of cruise), the effect on the total fuel consumption is relatively small. The reasons for this are the competing influences of a higher specific fuel consumption at reduced trip time due to constant cruise Mach Number on a warm day and vice versa for a cold day.

The influence on the calculated emissions is much bigger. A warm day increases the produced NO_x due to higher temperatures at combustor inlet, primary zone and turbine entry, but decreases the total amounts of CO and HC (the products of incomplete combustion) due to increased combustion efficiencies. The influences of a cold day are vice versa.

4.2.2 Influences of Flight Profile and Mission

Cruise altitude:

The effect of a changing cruise altitude on total mission values is very complex due to different temperatures and pressures

and their influences on the engine parameters and on the aerodynamic coefficients of the aircraft. Figure 14 and Figure 15 show the changes of fuel consumption and NO_x and soot production in percentage terms due to 1000 ft lower and 1000 ft higher cruise altitude in comparison to the typical cruise altitude. All percentage changes correspond to values at the middle of cruise, the investigated aircraft are a B747-400 with CF6-80C2B1F (compared with cruise at FL 390), a DC10-30 with CF6-50C2 and a MD11 with PW4460 (both compared with cruise at FL 350).

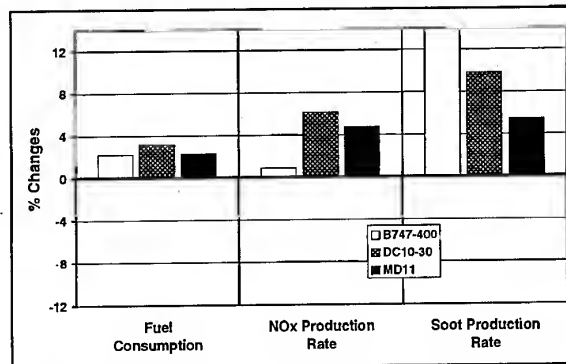


Figure 14: Changes in fuel consumption and emission production due to 1000 ft decrease in cruise altitude

Figure 14 shows clearly the rising amounts of fuel and emissions with decreasing cruise altitudes for all aircraft engine combinations. Again a combination of effects on the engine and the aircraft performance is responsible for this behaviour. The fuel consumption is determined by the competing influences of a decreasing SFC and an increasing drag and therefore increasing thrust demand of the aircraft to balance the forces.

The higher combustor inlet and exit temperatures in combination with higher combustor inlet pressures lead to a higher EI NO_x and in combination with the increasing fuel consumption to more produced NO_x . The soot production is mainly influenced by the higher combustor inlet pressures, but also by the different sensitivity to changes in combustor inlet temperatures (see Figure 9).

The results for an increasing cruise altitude shown in Figure 15 are mainly conversely to the results for a decreasing cruise altitude. It is interesting, that the production of NO_x is nearly unaffected, which means, that the competing influences described above are of the same magnitude.

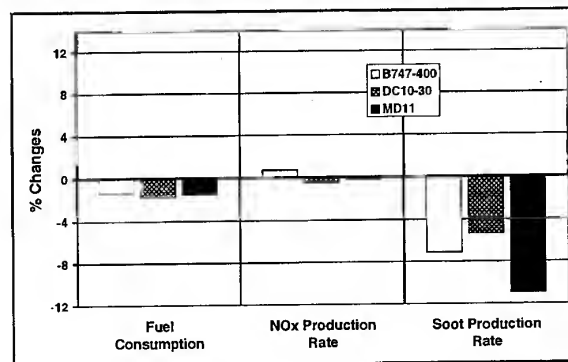


Figure 15: Changes in fuel consumption and emission production due to 1000 ft increase in cruise altitude

A welcome minor matter is the decreasing soot production by increasing the cruise altitude mainly due to the lower absolute pressures in the combustion chamber.

The fuel consumption of all aircraft engine combinations decreases with increasing altitude, which explains the wish of the airlines to fly as high as possible with the actual weight. That would mean a slow, but continuous increase in altitude during the cruise due to the reduction of weight from the burned kerosene. This is impossible due to air traffic control reasons, which leads to frequently seen step climbs dealt with in the following investigation.

Step climb:

The former investigation described the influence of changing altitudes on the values at the middle of cruise. In this investigation the influence of the position of the step climb on the total mission values is looked at.

As an example the results for mission fuel and total NO_x amount of an A340-300 powered by CFM56-5C2 engines on a 8200-km-mission with a cruise Mach Number of 0.82 and a take off weight of 240 to are shown in Figure 16. A step climb from 10670 to 11875 m (FL 350 to FL 390) has been inserted at different positions (step climb at 0 km means immediate climb to FL 390, step climb at 8000 km means no step climb at all).

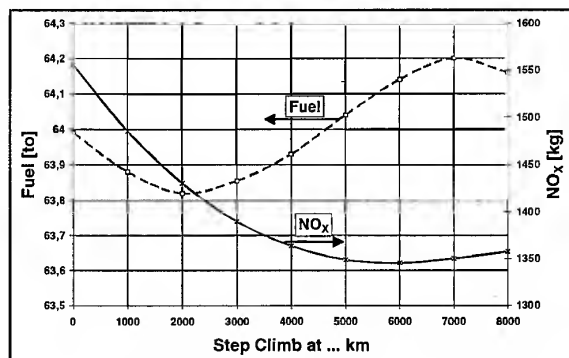


Figure 16: Influence of step climb-position on total mission fuel and NO_x

If the step climb is done at 2000 km, the total fuel amount reaches its minimum. This optimal step climb position shifts to larger values for heavier aircraft on longer distant flights. A very late step climb (at 7000 km) is worse than no step climb at all (at 8000 km). In this case the savings of kerosene due to flying at higher cruise altitude for about 1000 km are overcompensated by the higher fuel consumption during the step climb.

Regarding the produced NO_x amount, the optimal step climb position is located at about 6000 km. If one wants to optimize the total fuel burned, one would climb very early, if the total NO_x amount is more important, a late step climb would be recommendable.

Take off weight:

The effect of a changing take off weight G_0 is addressed for two different aircraft, a B747 with CF6-80C2B1F and a B737 with CFM56-3B2. A short and a longer range mission at their

typical cruise altitudes and Mach Numbers have been calculated (see Table 3). Shown are the fuel and NO_x changes in percentage terms per 1 % increased take off weight.

Aircraft	B747		B737	
Engines	CF6-80C2B1F		CFM56-3B2	
Cruise Ma	0.86		0.77	
Cruise H [m]	11875		10670	
Distance [km]	8000	1000	2000	500
Fuel change [%]	0.83	0.61	0.73	0.74
NO _x change [%]	1.50	0.99	1.23	1.03

Table 3: Percentage increase of fuel and NO_x per 1% increased take off weight

For all missions the calculated percentage increase in fuel consumption is smaller than the increase in take off weight. For the short range missions the increase in total NO_x is as big as the increase in take off weight, for the longer range missions the increase in NO_x is even bigger than the increase in take off weight.

Due to the competing influences of the increased fuel consumption and the increased combustion efficiency and thereby decreased amount of products of incomplete combustion, the total amounts of CO and HC are nearly unaffected.

Payload-factor:

The payload factor has another important effect on fuel consumption and emission production. For these comparisons of 2000-km-missions the landing weight of the A310 with CF6-80C2A2 is set to empty weight of the aircraft (80.4 to) plus reserve plus payload in percentage terms (100 % payload factor for the A310 is equal to about 32 to). The increase of the payload factor also influences the take off weight, which leads to the consequences discussed in the investigation above. The results in Figure 17 are shown in kilograms of fuel and grams of emissions per kg of payload versus the payload factor in %.

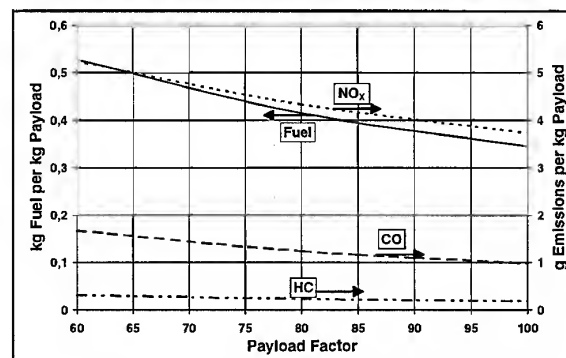


Figure 17: Investigations on payload factor (A310 with CF6-80C2A2, 2000 km)

The total amounts of fuel burned and emissions produced increase with increasing payload factors due to the growing take off weight (see investigation before), but it can be seen in Figure 17, that an increasing payload factor decreases all specific values. For a 2000-km-mission with the A310 and 100 % payload factor about 0.34 kg fuel per kg payload are needed. On the same mission every kilogram of payload

causes about 3.7 grams of NO_x , 1 gram of CO and 0.2 grams of HC in total.

4.2.3 Other Investigations on Flight Missions

Missions in detail:

In Table 4 some values for a 8000-km-mission of an A300 with CF6-50C2 divided into flight phases and in total are given.

	Takeoff	Climb	Cruise	Descent	Total
kg Fuel	215.60	3565.80	44029.90	507.30	48318.60
kg NO_x	7.76	116.60	594.80	1.57	720.73
kg CO	0.10	1.65	51.95	27.71	81.42
kg HC	0.17	2.31	20.88	8.58	31.93
kg Soot	0.01	0.05	0.30	0.02	0.38

Table 4: Burned fuel and produced emissions in all flight phases for an A300 with CF6-50C2 on 8000-km-mission

For this long range mission the take off phase only plays a minor role, during cruise most of the fuel is burned and most of the emissions are produced. During the climb phase noticeable amounts of NO_x are produced due to higher temperatures at the combustor inlet and the turbine entry, during the descent phase the produced CO and HC amounts are considerable due to worse combustion efficiencies. In all phases the produced soot amount of the A300 with CF6-50C2 is very small. The average emission index of soot for the whole mission is about 0.008 g/kg.

Figure 18 shows an example of a detailed flight mission of an A340-300 powered by CFM56-5C2 with taxi in and out, a step climb from 10060 to 11280 m (FL 330 to FL 370) and reserve included. The amount of reserve kerosene is evaluated from Alternate (100 nm in 10000 ft with 330 kn IAS), Hold (30 min in 15000 ft with 250 kn IAS) and 5 % trip fuel and sums up to about 6.4 to.

The flight profile and the development of the emission index of soot are given in Figure 18. The range is 4000 km with a cruise Mach Number of 0.82 and a payload factor of 80 %.

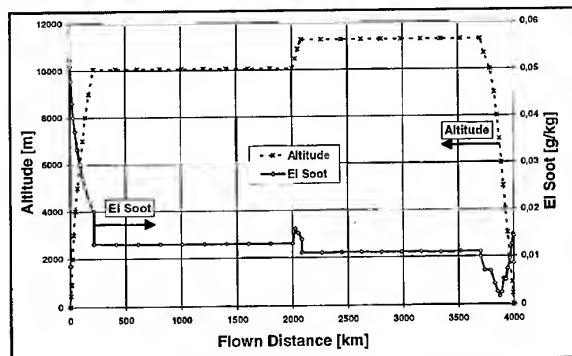


Figure 18: Example of detailed mission investigation, A340-300, CFM56-5C2, 4000 km, $\text{Ma}_{\text{Cruise}} = 0.82$, 80 % payload factor

The value of the emission index of soot is below 0.01 g/kg during taxi out, increases to its maximum of well above 0.05 during take off and decreases continuously during the climb

phase. The main parameter to cause this behaviour is the decreasing combustor inlet pressure.

While reaching the first cruise altitude of 33000 ft the power setting is suddenly set to lower values only balancing the drag of the A340. This also causes a decreasing combustor inlet pressure and thereby the EI soot decreases from about 0.02 to a first cruise value of about 0.012 g/kg. During cruise this value decreases very slowly due to lower thrust requirements of the aircraft getting lighter.

The emission index of soot increases during the step climb and drops in the second cruise phase to values well below the first cruise due to lower pressure values in the combustion chamber. During the descent the EI soot first decreases due to the lower power settings of flight idle and finally increases due to slightly higher power settings in the approach phase. For taxi out as well as for taxi in the soot emission index is below 0.01 g/kg.

Comparison of subsonic and supersonic mission:

The program system „Mission“ also has the potential to describe supersonic flight missions [Döpelheuer, 1994]. Table 5 shows results of the only supersonic passenger jet, the Concorde, in comparison to a modern subsonic passenger jet, the Boeing B747-400, on a 6400-km-mission.

Aircraft	B747-400	Concorde
Engines	CF6-80C2B1F	Olympus 593
Passengers	370	110
Cruise Values:		
Ma	0.86	2.0
Altitude [m]	11875	16500
SFC [kg/(daN h)]	0.61	1.25
EI NO_x [g/kg]	13.4	12.1
Trip Values:		
Time [min]	434	205
Fuel [to]	67.5	77.1
NO_x [kg]	942	921
kg Fuel / (pass. 100 km)	2.85	10.95
kg NO_x / (pass. 100 km)	0.04	0.13

Table 5: Comparison between B747-400 and Concorde on 6400-km-mission

Table 5 clearly shows the advantages and the disadvantages of supersonic transport. The trip time of the Concorde is less than half the value of the B747. But despite the fact, that the total trip values of fuel and NO_x are comparable, the specific values per passenger and 100 km differ strongly. The Concorde consumes nearly 4 times more kerosene per passenger and 100 km and the specific NO_x production is about 3 times higher.

Aircraft technology:

The results of another important investigation are shown in Figure 19. Compared are three different aircraft on 4000-km-missions with technologies from the 50's (B707), from the 70' (A300) and from the 80's (B767). The numbers written in the figure are given in grams per passenger and flown kilometer, the bars show the values of g / (pass. km) in percentage terms of the B707.

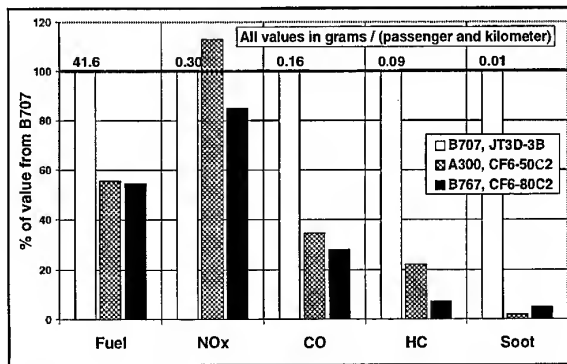


Figure 19: Comparison of aircraft technology, 4000 km flown distance

It becomes obvious, that the specific values of the fuel consumption and the production of CO, HC and soot have been reduced drastically. Improvements concerning the NO_x production are suffering from increasing combustor inlet temperatures and pressures of modern engine heat cycles.

All improvements are combinations of changing engine and aircraft technologies. High bypass engines with better thermal and propulsive efficiencies have been introduced, the aircraft gained higher aerodynamic efficiencies and better weight to payload ratios.

5. CONCLUSIONS

It has been shown, that the combination of thermodynamic engine modelling, semi-empirical emission correlation with variable reference values and rough flight performance calculation described in this paper is a powerful tool to investigate aircraft engine emissions in all situations and for all purposes. All explained calculation procedures have been validated with measured data. Emphasis was laid on methods to determine the emissions in all flight phases including whole flight missions and on the sensitivity of the emissions to changing engine performance and operating conditions.

Investigations concerning

- the bypass ratio of an engine in combination with the overall pressure ratio,
- changing ambient conditions and
- different flight profiles

have been performed. Every single parameter changed has many different and sometimes competing influences on the fuel consumption and the amount of emissions produced. The result of the combination of these different influences is the main aspect looked at in this paper.

REFERENCES

- Bahr D. W. (1991) Aircraft engine NO_x emissions abatement progress and prospects, 10. ISABE, Nottingham, paper 91-7022
- Champagne, D. L. (1971) Standard Measurement of Aircraft Gas Turbine Engine Exhaust Smoke, ASME, 71-GT-88
- Deidewig, F. (1993) Thermodynamische Teillastrechnungen gemischter und ungemischter ZTL-Triebwerke bei Berücksichtigung variabler Geometrien, Institut für Antriebstechnik der DLR, IB-325-04-93
- Deidewig, F., Döpelheuer, A., Lecht, M. (1996) Methods to Assess Aircraft Engine Emissions in Flight, ICAS-96-4.1.2
- Deidewig, F. (1998) Ermittlung der Schadstoffemissionen im Unter- und Überschallflug, Institut für Antriebstechnik, DLR Forschungsbericht 98-10
- Dodds, W. J., Bahr, D. W. (1990) Combustion System Design, Chapter 4 in [Mellor, 1990]
- Döpelheuer, A. (1994) Abschätzung des Brennstoffverbrauchs und der NO_x-Emissionen von Überschallverkehrsflugzeugen, IB-325-13-94, DLR, Institut für Antriebstechnik
- Döpelheuer, A. (1997) Berechnung der Produkte unvollständiger Verbrennung aus Luftfahrttriebwerken, IB-325-09-97, DLR, Institut für Antriebstechnik
- Heywood, J. B., Mikus, T. (1973) Parameters controlling Nitric Oxide Emissions from Gas Turbine Combustors, AGARD-CP-125 (Atmospheric Pollution by Aircraft Engines), Paper 21, London
- Hurley, C. D. (1993) Smoke Measurements Inside a Gas Turbine Combustor, AIAA 93-2070, 29th Joint Propulsion Conference and Exhibit, Monterey
- ICAO (1995) Engine Exhaust Emissions Data Bank, First Edition, Doc 9646-AN/943
- Jane's (1994) All the World's Aircraft, Jane's Information Group, Sentinel House, 163 Brighton Road, Coulsdon, Surrey CR5 2NH, UK
- Lefebvre, A. H. (1983) Gas Turbine Combustion, Mc Graw-Hill, New York, ISBN 0-07-037029-X
- Mellor, A. M. (1990) Design of Modern Turbine Combustors, Academic Press Limited, London
- Münzberg, H. G.; Kurzke, J. T. (1977) Gasturbinen - Betriebsverhalten und Optimierung, Springer-Verlag, Berlin/Heidelberg/New York
- Pratt, D. T., Wormeck, J. J. (1976) CREK, a computer program for calculation of combustion reaction equilibrium and kinetics in laminar or turbulent flow, Report WSU-ME-TEL-76-1
- Stöppler, B. (1992) Entwicklung einer verbesserten Korrelation für die Stickoxidemission von Flugtriebwerken, IB-325-08-92, DLR, Institut für Antriebstechnik
- Whyte, R. B. (1982) AGARD Advisory Report No. 181, Alternative Jet Engine Fuels, Vol. 2

PAPER No. 20
Doppelheuer & Lecht
(presenter: A. Doppelheuer)

Question 1: T. Ripplinger, MTU, Germany

Do you have an explanation for the big difference in optimal step-climb position in terms of NOx and fuel consumption?

Answer:

Even when using a so-called fuel flow correlation, the emission index of NOx is not directly proportional to the actual fuel flow. The highest amounts of NOx are produced when climbing steeply to 39,000 ft., and may be explained by the emission index increasing due to increased temperatures in the combustion chamber. This is especially the case for the first 3,000 - 4,000 km of the flight when the aircraft is relatively heavy and the climb thrust demand is therefore high. Things may change for more typical operations, for example, a step-climb from 31,000 to 35,000 ft.

Question 2: N. Brehm, BMW-RR, Germany

Did you take drag and nacelle weight into account in your bypass ratio study? If not, would not they make the trade-off between NOx and SFC even worse?

Answer:

No, I did not take these into account. The drag and installation weight penalties that are neglected in this study would probably decrease the gains in SFC with increasing bypass ratio.

Modeling the Effects of Operating Conditions and Alternative Fuels on Gas Turbine Performance and Emissions

W.P.J. Visser (wvisser@nlr.nl)
National Aerospace Laboratory
NLR VH Department
P.O. Box 90502
1059 CM Amsterdam
The Netherlands

S.C.A. Kluiters
Faculty of Aerospace Engineering /
Laboratory for Thermal Power Engineering
Delft University of Technology
Mekelweg 2, P.O. Box 5037
2600 GA Delft, The Netherlands

1. SUMMARY

With the increasing attention to gas turbine exhaust gas pollution, a need has emerged to assess effects of a variety of operational variables on the emission levels. An effective approach to address this need is to integrate combustor emission models in gas turbine performance models.

NLR's generic gas turbine performance simulation environment (GSP) has therefore been extended with a number of features for accurate analysis of these effects on the major exhaust gas emissions NO_x , CO, UHC and Smoke. First, GSP's gas model has been extended to include a detailed description of gas composition including the particular emission species. Second, a new generic multi-reactor combustor model has been developed for detailed modeling of the processes in a combustor. The combustor model is set up by defining a number of reactors modeling combustion, mixing, steam/water-injection and their effects on emission formation using semi-empirical models for the reaction kinetics. Fuel properties and composition can be specified in detail, enabling analysis of effects of alternative fuels on gas turbine engine performance and emissions.

Preliminary validation results with the multi-reactor combustion model corresponded with measured emission data and with expected operating condition effects on emissions. With the NO_x model best accuracy was obtained. The accuracy of particularly the CO, UHC and Smoke formation models may be improved by adapting the multi-reactor model to allow for modeling of effects such as film cooling and other effects not covered by a one-dimensional model.

The current generic multi-reactor combustor module will be used for easy implementation of improved emission models in the future. This work will also involve extensive validation using detailed engine, combustor and emission data.

2. NOMENCLATURE

ϕ	equivalence ratio	
EI	Emission Index	
ETA	η , efficiency	
GSP	NLR Gas turbine Simulation Program	
LCV	Low Calorific Value fuel	
LH_2	liquefied hydrogen	
LNG	liquefied natural gas	
LPP	Lean Premixed Pre-evaporated combustion	
Ma	Mach number	
p	pressure	
P_{netc}	Net (fuel compression corrected) power output	
ppm	parts per million	
RQL	Rich Quick-quench Lean combustion	
S	Soot formation concentration	[mg/kg gas]
SN	Smoke number	
T	Temperature	[K]
UHC	Unburnt HydroCarbons	
X	mole fraction	
[X]	mole (volume) concentration	[kmole/m ³]
W	mass flow rate	[kg/s]
Wf	Fuel mass flow rate	[kg/s]
ω	Specific surface oxidation rate	[g/cm ² /s]

indices

CH	hydrocarbon
eq	(chemical) equilibrium
f	fuel
ox	oxidant
pz	primary zone
stoich	stoichiometric (fuel-air ratio)

3. INTRODUCTION

With the increasing attention to gas turbine exhaust gas pollution, a need has emerged to predict gas turbine exhaust gas emission levels at varying operating conditions. On the manufacturers side, the processes in the combustor are modeled in detail (i.e. with CFD) in order to develop new technologies to reduce emissions, such as LPP and RQL combustion (e.g. Schumann [33]). On the operational side, there is interest in how to minimize emissions by optimizing operating conditions such as engine condition, aircraft flight procedures, fuel type and water/steam injection. The latter two variables mainly relate to ground based gas turbines, using LNG, LH_2 or fuel obtained from gasification of coal or biomass. However, it must be noted that LNG and LH_2 fuels for aircraft are already being considered (Pohl [28]).

NLR contributes to several programs directed at more accurate assessment of gas turbine exhaust gas emissions and their effects on the environment, using test-bed and in-flight measurements (Jentink [16]) and prediction with models. For developing accurate models to predict emissions at deviating operating conditions, accurate measurement methods are required for validation.

An effective approach to analyze operating conditions effects on emissions is to integrate emission models in gas turbine performance models like NLR's Gas turbine Simulation Program GSP [37]. A lot of work has already been performed modeling the processes in the combustor in order to predict emissions, ranging from simple relations between engine performance parameters and emission levels (0-dim parametric models, Kretschmer [19] and Rizk [30]) to complex CFD computations (e.g. Maidhof [23]). Especially the more simple, often empirical, models require some sort of calibration to a reference condition before they can be used for sensitivity analysis, so they can be referred to as "off-design" or "ratio" models (Schumann [34]). For accurate direct prediction of emissions without any reference data, CFD calculations will be required. It must be noted that best results with combustion CFD modeling still are "suffering" from inaccuracies in the order of 10-30%.

Ratio models can easily be implemented in an engine performance model in order to provide a tool to directly relate operating condition (via combustor operating condition) to emission level. However, the potential of the single equation ratio models to analyze a large variety of effects is very limited.

In order to obtain better insight in effects of using other fuels, deviating air properties, water injection etc. a more detailed model is required. Yet, integration of CFD computations in GSP was not considered feasible due to the disproportional

complexity and computing power requirement of CFD in relation to the 0-dimensional GSP model.

A compromise between the CFD models and the simple empirical models are multi-reactor models, which apply a limited degree of spatial differentiation inside the combustor. Multi-reactor models usually include separate flow and chemical models and offer a means to calculate a number of intermediate temperatures along the combustion process such as primary and dilution zone temperatures.

The simplest *combustor flow models* employ "well-stirred" reactors, assuming immediate mixing of separate user defined reactant flows. Explicit modeling of the distribution of cooling flows and the mixing processes involves a significant increase in complexity (e.g. multi-dimensional models).

Simple *chemical models* assume complete combustion in each reactor (no dissociation). Higher fidelity is obtained when calculating chemical equilibrium and best 1-dimensional detail is obtained when calculating chemical kinetics (Rodriguez [31]; Bozza [5]).

A considerable number of publications suggest the value of multi-reactor models for prediction of especially NO_x emissions (Botros [4]; Bozza [5]). These models include detailed fuel and gas composition data and NO_x formation kinetics.

This approach was considered as the best trade-off between model fidelity, complexity and computing power requirements, and has been employed in the work described below. An important presumption was that the model would primarily be used to calculate deviations of emissions from predefined reference values at reference engine conditions.

4. NLR GAS TURBINE SIMULATION PROGRAM GSP

NLR's primary tool for gas turbine engine performance analysis is the "Gas turbine Simulation Program" (GSP) [37]. Both steady-state and transient simulation of any kind of gas turbine configuration can be performed by establishing a specific arrangement of engine component modules. GSP is a powerful tool for analysis of effects of ambient and flight conditions, installation losses, deterioration and malfunctions of control- and other subsystems on performance.

During continuous development at NLR, GSP has been extended and improved with new features for specific applications. A significant improvement has been the conversion (from mainframe) to the Windows95/NT platform, enabling execution on PC's which currently offer sufficient power to perform the extensive thermodynamic calculations.¹ GSP is now implemented in the Borland Delphi object oriented development environment, offering excellent means to maintain and extend the program.

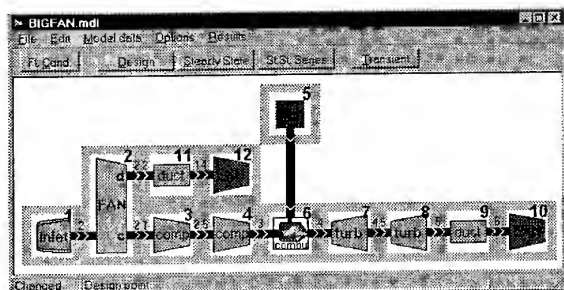


Figure 1 GSP model window with simple turbofan model

With Windows95/NT, GSP has a user friendly drag&drop graphical user interface, allowing quick implementation of

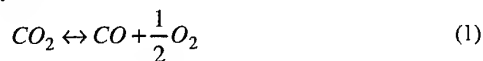
new engine models and quick analysis of complex problems. In section 9, examples of GSP output are shown.

The current object oriented structure offers excellent opportunity to implement new developed models of subsystems, such as combustor/emission models. Where necessary for particular analysis problems, new or modified component models can easily be derived from existing ones using inheritance.

5. GAS MODEL

A first improvement necessary to be able to calculate the combustion process in more detail is a gas model including detailed accounting of gas composition, and the implementation of the equations for chemical equilibrium to calculate dissociation effects and effects of evaporation of injected water. This, combined with a detailed specification of fuel composition provides a means to calculate effects of fuel and gas composition and water or steam injection on gas turbine performance.

The resulting "global" gas model is now used throughout the entire engine cycle calculation and currently includes the following species: CO₂, CO, O₂, Ar, H₂O(gas), H₂O(liquid), H₂, CH₄, C₂H₆, C₂H₄, C₃H₈, C₄H₁₀, O, H, OH, NO, N₂O, N₂. Chemical equilibrium is calculated for the CO₂-CO-O₂-H₂O-H₂ system:



For water, also the vapor-liquid equilibrium is calculated.

In the combustor, a more detailed gas model is used, calculating equilibrium for CO₂, CO, O₂, O, H₂O, H₂, H, OH, NO, N₂O, N₂.

An efficient algorithm was developed to calculate the equilibrium using the equilibrium constants method (Kuo [20], Glassman [10]) thereby avoiding explicit solution of the Gibb's equations like in the NASA CEA program (Gordon, McBride [11, 24]).

6. FUEL SPECIFICATION

In order to maintain proper bookkeeping of the composition downstream of the combustor, also specification of fuel composition is required. Therefore GSP was extended with a flexible user interface module for fuel properties with either:

- specification of hydrogen/carbon (H/C) ratio and heating value, or,
- explicit specification of composition.

For fuels with many different species like jet fuels, specification of all specie concentrations is unpractical and the H/C ratio option is used with the heating value specified. This option also allows for easy specification of other fuels whose composition is unknown or complex. The resulting combustion gas composition is calculated using the H/C ratio.

For fuels with a limited number of species, the composition can be specified explicitly (per specie) and the heat release can directly be calculated from the heat of reaction (changes in formation enthalpies) and the enthalpies of the reactants, using the NASA CEA program data [11, 24]. This option enables the user to specify exotic fuels such as those generated with bio-mass gasification and allows for detailed analysis of effects of alternative fuels on performance and emissions, taking the effects of deviations in combustion gas properties fully into account.

Other fuel properties to be specified include pressure and temperature and data to calculate fuel pump compression power.

¹ A demo copy of GSP can be downloaded from <http://www.nlr.nl/public/facilities/f141-01/index.html>

7. COMBUSTOR MODEL

For gas turbine performance analysis, the combustor model must accurately calculate both heat release and combustor exit gas composition. Heat release is calculated assuming the combustion ends with chemical equilibrium, as calculated with the gas model described in section 5.

If the chemical equilibrium equations include terms for NO_x , CO, and UHC emission species, then the equilibrium emission values in a combustion process can be calculated. However, due to the rapid variation of gas conditions (temperatures etc.) in the combustion process, the formation of these emissions is highly subject to chemical kinetics, resulting in emissions significantly deviating from equilibrium, like "frozen" NO_x after rapid cooling of hot gas. Thus, the model should include kinetics to calculate the emission reaction rates.

In order to account for different reaction rates in the different combustor zones, the multi-reactor approach is required.

7.1 Generic multi-reactor model

A generic reactor model was developed, allowing the calculation of both chemical equilibrium and kinetics between reactor entry and exit (see fig. 2). The reactor receives the gas from a preceding reactor and exits into a successive reactor (the first and the last reactors will usually connect to compressor discharge and turbine entry instead, like in figure 3). A second reactor entry permits the injection of fuel, cooling air, gas, water or other matter to be mixed or combusted in the reactor.

By stacking a number of reactors, a multi-reactor model is obtained simulating the subsequent processes of flow-dividing, combustion, secondary combustion, mixing and, if desired, the injection of other species such as water or steam.

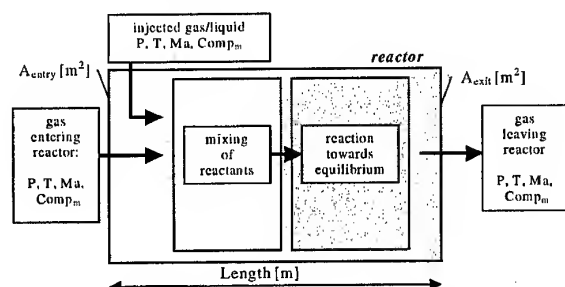


Figure 2 Generic 1-dim reactor model

Any number of reactors, each with specific characteristics, can be specified. For a conventional combustor the first reactor would represent the primary combustion zone followed by one or two reactors for the secondary or tertiary (mixing) zones (see the two-reactor model in figure 3). For detailed analysis of emissions or for multi-stage combustors, more reactors can be added.

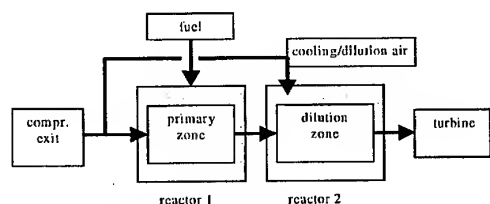


Figure 3 Simple multi-reactor configuration for a conventional combustor

7.2 Flow model

The flow model represents the distribution of the flows over the different reactors defined for the combustor. Mixing is assumed to occur instantaneously (i.e. well stirred reactors). The detailed combustor data necessary to determine flow distribution often are hard to obtain. For a fixed operating point of a conventional combustor model, a reasonable estimate can be made of the portion of total compressor air flow entering the primary combustion zone (i.e. the first reactor), which determines the primary zone equivalence ratio. However, to predict how this ratio will change with changes in power setting or other operating conditions, is difficult unless CFD flow models are used. It is therefore decided to use fixed user defined ratios for the moment. Future research will be directed at an attempt to find relatively simple 1-dim models for this effect using parametric models of the aerodynamics of the cooling flows (e.g. using equations suggested by Lefebvre [22]).

The limitation of user defined fixed flow ratios implies that validity of the model may well degrade with large deviations from the reference operating point (especially deviating total airflow rate).

7.3 Chemical model

The chemical model calculates chemical equilibrium (for heat release) and a kinetic scheme for emissions.

Heat release calculation

The combustion heat release is calculated assuming instantaneous attainment of chemical equilibrium. This can be justified by the fact that hydrocarbon reactions generally are rapid (see for example Sturgess [35]). Justification for this assumption can also be found in Hammond [12], who compared application of kinetic schemes with an equilibrium model. Conclusions were that for the exact determination of the composition, an equilibrium model could not be used, but the completeness of combustion and the temperature (i.e. heat release) could be fairly well approximated with the equilibrium assumption.

Emission calculations

The formation of all four emissions of interest (NO_x , CO, UHC and Smoke) is modeled using the same generic approach, assuming two separate mechanisms. The first mechanism is "prompt" emission formation in a flame in an infinitely short time. The second mechanism is the subsequent change in emission concentrations due to chemical reactions during the flow through the successive reactors. This way of modeling reaction kinetics (the kinetic scheme) implies the integration of reaction rates, calculated at the reactor intersections. The reaction rates are calculated depending on the type of emission.

Kinetic schemes

An approach was chosen using average reaction rates at the reactor entry and exit planes. By (trapezium rule) integration of these rates across the reactors, a 1-dim kinetics model is obtained.

For a number of species, relations between reaction rate, gas composition and conditions can be derived. With known gas conditions, flow rates at the reactor intersections and reactor lengths, reactor residence times can be calculated and used for integration.

The kinetic scheme reaction rates are functions of temperature and concentrations of species (including radicals) participating in the reaction. Kinetics of radical formation are neglected and equilibrium radical concentrations are assumed. Due to the rapid radical reaction rates relative to residence times in the combustion zones of interest, this is expected to be a good approximation.

Heat release is assumed not to be affected by emission formation itself. Normally, this is a good approximation because exhaust gas emission concentrations are very low.

The generic reactor model algorithm allows easy implementation and adaptation of equations for reaction rates of any specie. For the current multi-reactor model, kinetics calculations are only applied to the emission species NO_x , CO , C_xH_y and Soot (smoke). All other species are assumed to correspond with the chemical equilibrium composition.

Overall emission concentrations result from integration over the reactors.

7.4 NO_x

A NO_x prediction method is used similar to Bozza [5], Fletcher [9] and Barrère [3], and extended with extra chemical reactions and equations.

NO_x concentration is defined as the sum of NO and NO_2 . NO_2 , if existent, easily reacts to NO at high temperatures. In the flame zone, a portion of NO_2 may remain as a result of sudden chilling (Glassman [10]; Miller [25]). In a combustor dilution zone, NO_2 may also be formed due to a shift of the equilibrium towards NO_2 . However, in most cases, the portion of NO_2 is relatively small. Therefore, the sum of NO and NO_2 concentrations is represented by a single NO concentration in the chemical and kinetics models.

N_2O concentration is calculated as an intermediate specie in the NO formation reactions. At the end of the combustor N_2O is only present in very small (calculated equilibrium) concentrations.

All four significant NO_x formation pathways are modeled: prompt, fuel and thermal NO_x and formation via N_2O . Fuel and prompt NO_x formation is assumed instantaneous in the flame zone because both mechanisms are very rapid and involve radicals that are only present in the main fuel reaction zone. This is consistent with the assumption that the combustion process reaches equilibrium instantaneously (see section 7.3).

Prompt NO_x

An equation for prompt NO_x mole concentration is used suggested by Toof [36]:

$$[\text{NO}]_{\text{prompt}} = X_{\text{CH}} f(\phi) \sqrt{p} [\text{NO}]_{\text{eq.stoich}} \quad (3)$$

where:

X_{CH} = mole fraction of hydrocarbon species in fuel,

$f(\phi)$ = a function of ϕ ,

p = static pressure (bar).

$[\text{NO}]_{\text{eq.stoich}}$ = stoichiometric equilibrium NO concentration.

The empirical equation predicts prompt NO_x formation at combustion of hydrocarbon fuels according to the following reactions:



The radicals formed by reactions (4) through (7) may subsequently oxidize to NO_x .

Prompt NO_x formation via the Zeldovich mechanism with super-equilibrium O and OH radical concentrations and the N_2O mechanism is neglected. This is a good approximation because in flames, super-equilibrium O and OH concentrations are usually only present at temperatures too low for the Zeldovich mechanism (Miller [25]).

The contribution of the N_2O mechanism to prompt NO_x formation is also neglected because it only becomes significant at conditions where total NO_x emissions are very low (Glassman [10]). An empirical function $f(\phi)$ (figure 4) is determined using measurement data described in Bachmaier [2] and assumes negligible prompt NO_x formation at equivalence ratios below 0.6 and above 1.65.

However, with gasoline or fuels with significant amounts of ethylene and acetylene in very rich mixtures (i.e. $\phi > 1.65$), significant prompt NO_x may well be formed and then equation (3) will underestimate prompt NO_x .

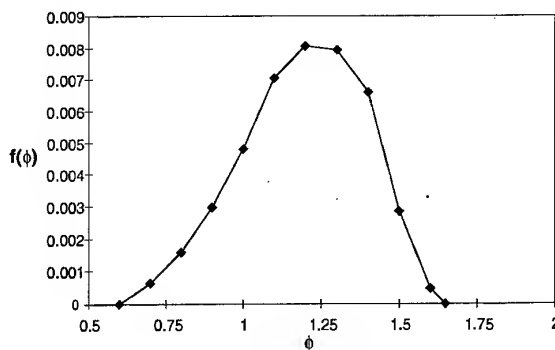


Figure 4 Prompt NO_x factor function

Fuel NO_x

Fuel NO_x formation is specified with the *conversion fraction*, i.e. the fraction of total fuel bound nitrogen that is actually converted to NO_x . Glassman [10] and Fenimore [8] indicate that the conversion fraction seems independent of the way nitrogen is chemically bound in the fuel, but it strongly depends on the combustion environment (e.g. equivalence ratio and fuel composition). Experiments by Kelsall [18], Sato [32], Nakata [27] and Fenimore [8] indicate large differences in conversion fractions depending on many different factors. It was therefore decided to apply a user specified conversion fraction for the model at this stage. The fraction of fuel-bound nitrogen in the fuel is also user-specified.

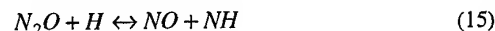
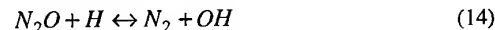
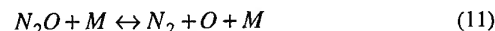
Thermal NO_x

For both the thermal and N_2O mechanisms, a reaction scheme is used to derive an equation for NO formation rate, required for integration across the subsequent reactors. Thermal NO_x formation rate is predicted according to the extended Zeldovich mechanism:



N_2O mechanism

For the N_2O mechanism's contribution to the NO_x formation rate the following reactions are included:



The NO_x formation rate equation is derived according to Barrère [3] although more reactions are included. All the

species are assumed to be in equilibrium, except for NO, N₂O and N.

"One-way equilibrium reaction rates" (Fletcher [9]) represent the forward and backward reaction rates of reactions 8 through 16 when equilibrium is assumed. For reaction *r*, with on the left of the reaction equation, *n* species with concentrations [X₁] to [X_n], the (one way) equilibrium reaction rate is:

$$R_r = k_f \prod_{i=1}^{i=n} [X_i]_{eq} \quad (17)$$

k_f is the forward specific reaction rate constant (Arrhenius law):

$$k = AT^B e^{-\frac{E_a}{RT}} \quad (18)$$

A, B are constants, *E_a* is the activation energy and R is the gas constant. The equilibrium reaction rate *R_r* can also be calculated using the concentrations on the right of the equation and the backward specific reaction rate constant.

The factors α, β and γ represent the deviation from equilibrium of the actual NO, N and N₂O concentrations at a time *t* during integration:

$$\alpha = \frac{[NO]}{[NO]_{eq}} \quad (19)$$

$$\beta = \frac{[N]}{[N]_{eq}} \quad (20)$$

$$\gamma = \frac{[N_2O]}{[N_2O]_{eq}} \quad (21)$$

From the above equations then the following equations for the reaction rates can be derived:

$$\frac{d[NO]}{dt} = R_8 + \beta(R_9 + R_{10}) + \gamma(2R_{13} + R_{15} + R_{16}) - \alpha(\beta R_8 + R_9 + R_{10} + 2\alpha R_{13} + R_{15} + R_{16}) \quad (22)$$

$$\frac{d[N]}{dt} = R_8 + \alpha(R_9 + R_{10}) - \beta(\alpha R_8 + R_9 + R_{10}) \quad (23)$$

$$\frac{d[N_2O]}{dt} = R_{11} + R_{12} + R_{14} + \alpha(\alpha R_{13} + R_{15} + R_{16}) - \gamma(R_{11} + R_{12} + R_{13} + R_{14} + R_{15} + R_{16}) \quad (24)$$

The N and N₂O concentrations may well assumed to be in steady state (Lavoie [21] and Botros [4]). With this assumption, the left-hand sides of equations (23) and (24) are zero, and β and γ are found as a function of α and the relevant one-way equilibrium reaction rates. After substitution of β and γ in equation (22), the following equation is found for the NO formation rate:

$$\frac{d[NO]}{dt} = 2(1 - \alpha^2) \left\{ \frac{R_8}{1 + \alpha \frac{R_8}{R_9 + R_{10}}} + \frac{R_{13} + \frac{R_{15} + R_{16}}{2(1 + \alpha)} \left(1 + \frac{\alpha R_{13}}{R_{11} + R_{12} + R_{14}} \right)}{1 + \frac{R_{13} + R_{15} + R_{16}}{R_{11} + R_{12} + R_{14}}} \right\} \quad (25)$$

Equation (25) can directly be used in the integration in the reactor model. The one-way equilibrium reaction rates can directly be calculated from gas conditions and equilibrium composition, and α results from the actual NO concentration as calculated in the previous integration step.

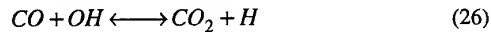
The first term between the curly brackets represents thermal NO_x formation, while the second term relates to the N₂O mechanism.

Because the one-way equilibrium reaction rates can be calculated using either the forward or backward reaction, the number of equilibrium concentrations to be calculated can be limited to only the NO and N₂O equilibrium concentrations.

7.5 CO

For the carbon monoxide emission calculation, the assumption is made that during combustion, fuel first reacts to all CO and water. After this initial and instantaneous step, CO further reacts to CO₂ depending on reaction rates calculated in the reactor models. This approach is based on the fact that oxidation to CO is very rapid relative to oxidation from CO to CO₂, (Sturgess [35], Hammond [12] and Westenberg [38]). The reaction scheme is used for CO emission calculation only and does not affect heat release. Also the CO formation rate still depends on equilibrium temperature level.

The reaction to CO₂ is assumed to take place according to the dominant mechanism at CO oxidation (Westenberg [38]; Dryer [7]):



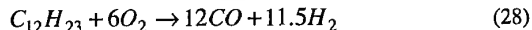
Chleboun [6] proposes the following equation for the rate of carbon monoxide oxidation assuming H and OH equilibrium concentrations and a separate conservation of carbon atoms for this mechanism:

$$\frac{d[CO]}{dt} = -k_{26f} [OH]_{eq} \left\{ 1 + \frac{[CO]_{eq}}{[CO_2]_{eq}} \right\} ([CO] - [CO]_{eq}) \quad (27)$$

In this equation, the *k_{26f}* is the specific forward reaction rate constant of equation (26). The equation is integrated across the combustion chamber reactors similar to the method for NO_x. Equation (27) is able to model the effect of rapid reaction down towards equilibrium CO concentrations at relatively high temperatures and also to simulate the effect of frozen high CO concentrations due to sudden quenching. In the latter case, the reaction rate constant will suddenly decrease to a very low value, thereby preventing further rapid CO oxidation.

7.6 UHC

To predict the emission levels of unburned hydrocarbons, reaction rates are integrated starting at an initial concentration corresponding with the fuel flow entering the reactor. Two different reactions are used. Jet-A fuel may well be represented by $C_{12}H_{23}$ (NASA publications: Gordon [11]; McBride [24]) which initially reacts according to:



Other jet and diesel fuels are assumed to react according to this reaction also. In Pratt [29], the following equation is proposed for the rate of this reaction:

$$\frac{d[C_{12}H_{23}]}{dt} = -10^{11.5} \left(\frac{p}{p_0} \right)^{-0.815} * e^{\left(\frac{12200}{T} \right)} \left[\frac{9T}{10^4} - \frac{1}{2} \right] \sqrt{[C_{12}H_{23}][O_2]} \quad (29)$$

For natural gas and other hydrocarbon gas fuels, the flow of hydrocarbons entering the combustion chamber is converted to a concentration of methane assuming that the molar mass of the hydrocarbons is the same as the methane molar mass. The burning rate of methane is taken from Dryer [7]:

$$\frac{d[CH_4]}{dt} = -10^{10.2} e^{\left(\frac{-48400}{RT} \right)} [CH_4]^{0.7} [O_2]^{0.8} \quad (30)$$

The UHC level is found by integrating either equation (29) or (30) depending on the fuel type.

7.7 Smoke

The smoke emission model is based on a number of properties described by Appleton [1]. It appears that the soot formed in flames only weakly depends on the conditions where it is formed. For example, the soot formation is hardly affected by the type of flame (premixed or diffusion). Soot primarily contains carbon, although also hydrogen and oxygen can be present. Concerning structure, soot particles are roughly spherical and grouped together in a "necklace-like" fashion. The smoke model again utilizes the assumption of instantaneous formation followed by subsequent oxidation according to the kinetics mechanism in the generic reactors. The formation model is derived from an empirical equation taken from Rizk [30] predicting both formation and oxidation. The equation's term for oxidation is omitted resulting in the following equation:

$$S = 0.0145 \cdot \frac{\phi \cdot FAR_{stoich} p_3^2}{W_{ox} T} (18 - H)^{1.5} \quad (31)$$

p_3 = burner pressure (kPa), W_{ox} = oxidant mass flow (kg/s), T reaction end temperature (K), H = fuel hydrogen mass percentage. The term for fuel air ratio has been replaced by the equivalence ratio multiplied with the stoichiometric fuel air ratio. This results in a more generic representation of the fuel air ratio relative to a stoichiometric mixture and allows for oxidants and fuels other than pure air and jet fuel. Equation (31) is based on measurements in diffusion flame combustion chambers and because the soot formation process is relatively poorly understood, it can only be roughly predicted with this equation.

The soot oxidation process is much better understood and can be modeled using equations for the overall specific surface

reaction rate developed by Nagle and Strickland-Constable [26]:

$$\omega = 12x \left[\frac{k_A p_{O_2}}{1 + k_Z p_{O_2}} \right] + k_B p_{O_2} (1 - x) \quad (32)$$

with:

$$x = \frac{1}{1 + \frac{k_T}{p_{O_2} k_B}} \quad (33)$$

$$k_A = 20 e^{\left(\frac{30}{RT} \right)} \quad (34)$$

$$k_B = 4.46 \cdot 10^{-3} e^{\left(\frac{15.2}{RT} \right)} \quad (35)$$

$$k_T = 1.51 \cdot 10^5 e^{\left(\frac{97}{RT} \right)} \quad (36)$$

$$k_Z = 213 e^{\left(\frac{4.1}{RT} \right)} \quad (37)$$

ω is Specific surface oxidation rate (g/cm²/s), p_{O_2} is partial pressure (atmospheres) of O_2 . For validation and explanation of these semi-empirical equations refer to Appleton [1].

The smoke calculation procedure is as follows. First, the smoke (mass) formation calculated with equation (31) is converted into a number of spherical smoke particles per unit of combustion gas. This number depends on a user specified initial radius of the spheres, which usually should be around 40 nm. The smoke particles are then oxidized in the subsequent reactors. The smoke surface oxidation rate is calculated using equation (32). Applying a constant average soot density of 1800 (kg/m³), this surface oxidation rate is converted into a rate of radius change. At the end of the combustion chamber the number of spherical particles and their radii are used to find the "particulate mass loading" (for the smoke number). In the case where new particles are emitted in subsequent combustion stages (e.g. in multi-stage combustors), particles with different radii would exist. In that case, a weighted averaged radius is used to continue calculation.

8. CONSIDERATIONS FOR BUILDING A MODEL

For application of GSP's new combustor model to predict emissions the following issues need to be considered:

- In general, it is best to use the model corresponding to GSP's general way of use: i.e. as a sensitivity analysis tool instead of a direct prediction tool. Accurate analysis can be made of effects of a large variety of operating conditions on emission levels.
- For off-design analysis, reference emission data are required as well as combustor data.
- The emission model can be tuned to the reference data using unknowns like geometric reactor data (determining residence times), flow distribution factors and a number of other parameters depending on the emission type.
- At this stage, flow distribution is specified with constant factors. Until a combustor operating condition dependent flow distribution model is available, the implications of this limitation must be considered for large deviations from the reference combustor flow conditions.

- CO, UHC and Smoke emissions are to a large extent caused by effects that cannot be easily simulated with one-dimensional models (e.g. combustor liner cooling, atomization etc.). Therefore "temperature tuning factors" have been added to represent deviations from equilibrium temperatures at the reactor intersections. These factors will typically be used to represent effects like cooling flow films on average temperatures. Temperature factors may be set for all emission types at every reactor intersection and can also be used for NO_x. A temperature factor of 1 indicates unmodified equilibrium temperature is used.
- Specific attention must be paid to the multi-reactor configuration. With only two reactors, the combustor processes can only be simulated to a very limited extent. With a large number of reactors, several effects like varying dilution ratios, residence times, temperatures etc. can be calculated accurately.
- Direct prediction of emissions is possible if limited (geometric) combustor data are available but will only provide reasonable estimates for NO_x emission levels.
- Accurate simulation of combustor operating conditions is required for deriving the correct relation between engine operating conditions and emissions. This requires a validated GSP thermodynamic model.
- The model may be particularly valuable for coupling detailed CFD calculation results to general gas turbine performance models. In this case combustor CFD results must be transformed into an accurately tuned GSP multi-reactor model.

9. RESULTS

Extensive validation of the models will be the subject of future work, requiring the acquirement and analysis of detailed gas turbine data. However, the new model has been applied to a number of gas turbine engines to demonstrate the analysis of a variety of problems.

First, the ability of the model to predict emissions of a large turbofan engine (GE CF6-80C2) was tested. Emission data from the ICAO databank [15] and (especially low power setting) test bed measurement data were used for validation. The combustor was modeled with three reactors (figure 5). The data required at the intersections are given in table 1.

Initial soot radius was set to 50 nm. Little was known about the flow distribution within the combustor and therefore stoichiometric primary zone (first reactor) fuel-air ratio was assumed for the design point (sea level static rated thrust) at this stage. Limited tuning with temperature factors (see section 8) was applied for the NO_x and UHC emissions.

Figure 5 shows fuel-air ratio (FAR), temperature, emission concentrations and soot radius as calculated at the 4 intersections along the axial in the design (reference) operating point.

In figure 6 emissions calculation results are presented for standard conditions (solid curves) and for the case of a deteriorated high-pressure turbine (dashed line) to demonstrate typical use of the model. Turbine deterioration is represented by a 4% lower isentropic efficiency combined with a 2% increase in flow. The solid lines should correspond with data from the ICAO databank (★) and with test-bed measured data (☆, for the low power settings). The NO_x prediction matches the data along the operating range. UHC emissions only become significant in a narrow low power range, which is well predicted by the model. Significant CO emissions are predicted to occur at slightly higher power settings than those of the reference data. The single smoke number (SN6) value that was available could accurately be matched.

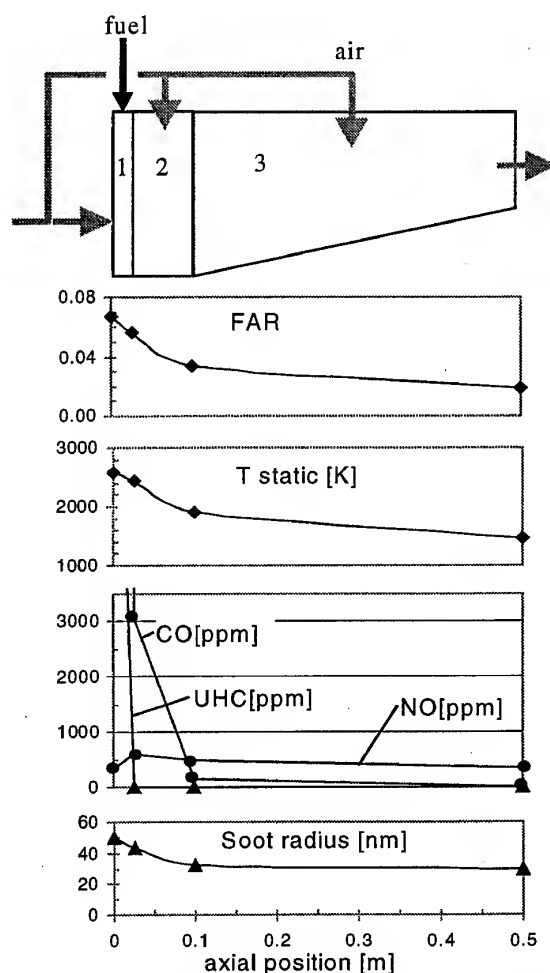


Figure 5 CF6-80C2 3-reactor combustor model and design point results

Zone	Flow area (m ²)	reactor length (m)	Air inflow fraction
Flame front	0.360		0.28
Primary	0.360	0.025	0.05
Secondary	0.360	0.074	0.22
Dilution	0.1653	0.4	0.45

Table 1 CF6-80C2 combustor model data

The effects of turbine deterioration are as expected: due to higher combustor temperature levels, higher NO_x and lower CO and UHC emissions. Note that at high power setting, the NO_x increase becomes smaller due to the richer primary zone with a deteriorated turbine. Other results with rich (instead of stoichiometric) primary zone mixtures (in the design point) even indicated a fall in NO_x with turbine deterioration, resulting from the then dominant effect of decreasing combustion temperatures with equivalence ratios increasing beyond 1. Smoke number values could only be validated against the take-off power value (i.e. 7.1) from the ICAO databank [15].

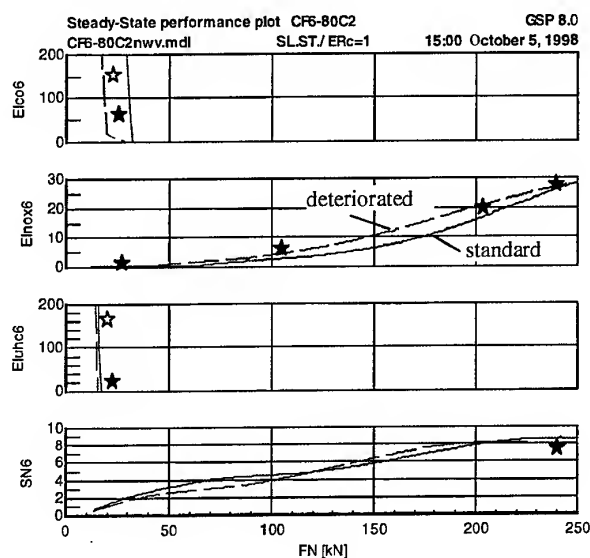


Figure 6 CF6-80C2 emission results and deterioration effects

A second application is the analysis of the effect of low calorific fuel (LCV, 15.6% CO₂, 8.8% CO, 24% steam, 7.4% H₂, 5.2% CH₄, 0.3% C₂H₆, 1.1% C₂H₄, 37.6% N₂) obtained from a bio-mass gasifier at Delft University of Technology (Hoppesteyn [14]; de Jong [17]), if used for a GE-LM2500 class LNG-fuel turboshaft engine.

The gasified fuel heating value is only about 1/10 of the LNG heating value, delivery pressure is 5 bar and temperature is 1073 K. Separate compressors are assumed to compress the gasifier air and fuel gas for injection into the combustor. With the large amount of (hot) fuel gas this requires a considerable quantity of power to be taken from the power turbine drive shaft, leaving P_{netc} as net power output².

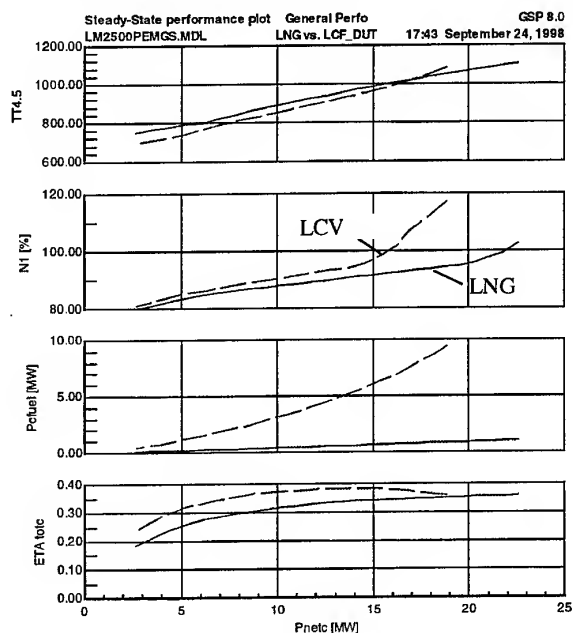


Figure 7 Effects on general performance of LCV

² This case may not represent an optimal configuration but only serves to demonstrate the potential of the model.

The effect on both thermodynamic performance and emissions was calculated (LCV=dashed curves) and compared to normal operation with LNG (solid curves). In figure 7 the effect on performance is presented with net power output P_{netc} on the X-axis. The third graph shows the high LCV fuel compression power P_{cfuel}. The TT4.5 power turbine entry temperature curves indicate similar turbine temperature levels for both fuels.

An important outcome is that nominal power cannot be obtained without exceeding the compressor speed (N1) limit. This is due to the mismatch between compressor and HP turbine power resulting from the large fuel mass flow injected into the combustor. Unless compressor load is increased (e.g. by taking compressor bleed air to feed to the gasifier) or major hardware modifications are applied (turbine flow capacity), lower net power output must be accepted. It should be noted that with a fixed power turbine (i.e. a single shaft engine) this problem will not occur; but then stall-margin problems are likely to emerge instead.

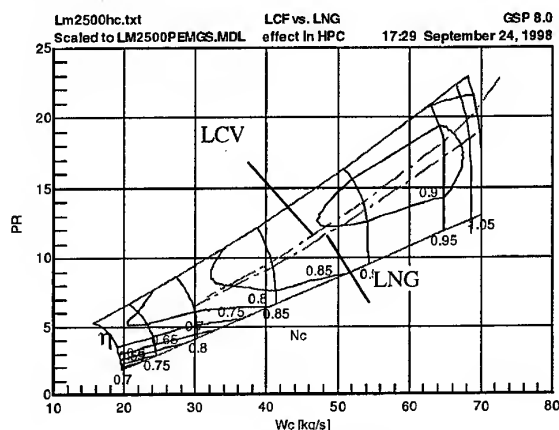


Figure 8 LCV vs. LNG fuel HPC operating lines

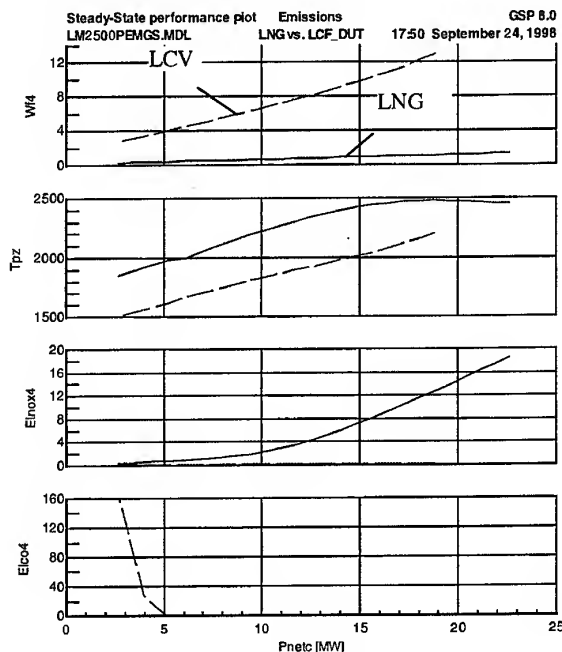


Figure 9 LCV vs. LNG fuel exhaust gas emissions

Total efficiency (ETA_{totc}, corrected for required fuel compression power) shows favorable values at partial power levels, but this may well have to be corrected with extra power required for the gasifier.

A major concern will be how the compressor operating line will be affected. Figure 8 shows the expected shift towards the surge line, possibly resulting in implications with regard to (turbine) hardware modifications.

Finally, the effects on emission levels are predicted using the multi-reactor emission model with similar characteristics as those of the above-mentioned CF6-80C2 model, assuming a similar global combustor geometry.

The top graph in figure 9 shows the large LCV fuel mass flow WF₄ (to be multiplied with the EI indices for total emission output by mass). The next graph shows the much lower primary zone temperature T_{p2}, causing virtually no (thermal) NO_x emission with LCV at equal power levels (as compared to LNG fuel, 3rd graph in figure 9).

The lower T_{p2} values with LCV fuel are due to the large portions of N₂, CO₂ and H₂O in the LCV fuel "cooling" the combustion process, resulting in a low adiabatic flame temperature.

Finally, the high CO emission at low power (4th graph in figure 9), only with LCV, is due to the low CO reaction rate at lower temperatures.

10. CONCLUSIONS

The GSP gas turbine simulation environment, after being extended with a detailed composition specific gas model, is a powerful tool to predict effects of alternative fuels on performance and emissions.

The new multi-reactor combustor model is a generic structure in which 1-dim kinetic models can be implemented for formation of various species including the major exhaust gas emissions.

For NO_x, CO, UHC and Smoke, models have been developed for instantaneous formation in the flame zone and subsequent formation or reaction according to multi-reactor kinetics schemes.

It should be noted that in general these models are best used as sensitivity analysis tools, i.e. to calculate effects on performance and emission parameters relative to reference values.

A useful application of the new gas model has been demonstrated in the analysis of the effect of low calorific gas from a bio-mass gasifier on various performance parameters and emissions. This type of performance analysis may well be used to support decisions concerning engine hardware modifications.

The emission models have also been demonstrated on a large turbofan engine. The results corresponded with measured emission data and with expected operating condition effects on emissions. With the NO_x model best accuracy was obtained. The accuracy of particularly the CO, UHC and Smoke formation models may be improved by adapting the multi-reactor model to allow for modeling of effects such as film cooling and other effects not covered by a one-dimensional model. In particular, a flow distribution model depending on a variety of conditions in the combustor must be developed to allow for large deviations from the reference conditions.

More work needs to be done to validate results using detailed combustor data of a variety of engines and operating conditions. The generic set-up of the model allows easy implementation of improved emission models.

Interesting future applications include performance analysis of LH₂ and LNG fueled aero-engines and a variety of alternative fuel solutions for land based gas turbines.

11. REFERENCES

- 1) Appleton, J.P., 'Soot oxidation kinetics at combustion temperatures', *Atmospheric Pollution by Aircraft Engines, AGARD-Conference Proceedings-125*, paper 20. Neuilly Sur Seine: AGARD, 1973.
- 2) Bachmaier, F., Eberius, K.H., Just, Th., 'The formation of Nitric Oxide and the detection of HCN', *Combustion Science and Technology*, vol.7, p.77. New York: Gordon and Breach Science Publishers Ltd., 1973.
- 3) Barrère, M., 'Modélisation des foyers de turboréacteur en vue de l'étude de la pollution', *Atmospheric Pollution by Aircraft Engines, AGARD-Conference Proceedings-125*, paper 27. Neuilly Sur Seine: AGARD, 1973. (in French)
- 4) Botros, M.J., et al., 'One-dimensional predictive emission monitoring model for gas turbine combustors', ASME Paper 97-GT-414, *ASME Technical Papers*, New York: ASME, 1997.
- 5) Bozza, F., Tuccillo, R., Fontana, G., 'Performance and Emission Levels in Gas Turbine Plants', *Journal of Engineering for Gas Turbines and Power*, vol.116, p.53-62. New York: ASME, 1994.
- 6) Chleboun, P.V., Hubbert, K.P., Sheppard, C.G.W., 'Modelling of CO Oxidation in Dilution Jet Flows', *Combustion and Fuels in Gas Turbine Engines, AGARD-Conference Proceedings-422*, paper 38. Neuilly Sur Seine: AGARD, 1988.
- 7) Dryer, F.L., Glassman, I., 'High-Temperature oxidation of CO and CH₄', *Pollutant Formation and Destruction in flames, 14th Symposium (Int.) on Combustion*, p.987-1003. Pittsburgh: The Combustion Institute, 1973.
- 8) Fenimore, C.P., 'Formation of Nitric Oxide from Fuel Nitrogen in Ethylene Flames', *Combustion and Flame*, vol.19, p.289-297. New York: American Elsevier Publishing Company Inc., 1972.
- 9) Fletcher, R.S., Heywood, J.B., 'A model for nitric oxide emissions from aircraft gas turbine engines', AIAA Paper 71-123, *AIAA Technical Papers*. New York: AIAA, 1971.
- 10) Glassman, I., *Combustion*. Princeton NJ, USA: Academic Press, 1996.
- 11) Gordon, S., McBride, B.J., *Computer Program for Calculation of Complex Chemical Equilibrium Compositions and Applications. I. Analysis*. NASA Reference Publication 1311. Ohio, National Aeronautics and Space Administration, Lewis Research Center, 1994.
- 12) Hammond, D.C. JR., Mellor, A.M., 'Analytical Calculations for the Performance and Pollutant Emissions of Gas Turbine Combustors', *Combustion Science and Technology*, vol.4, p.101-112. New York: Gordon and Breach Science Publishers Ltd., 1971.
- 13) Holderness, F.H., Macfarlane, J.J., 'Soot Formation in Rich Kerosine Flames at High Pressure', *Atmospheric Pollution by Aircraft Engines, AGARD Conference Proceedings-125*, paper 18. Neuilly Sur Seine: AGARD, 1973.
- 14) Hoppesteyn, P.D.J., Andries, J., Hein, K.R.G., 'Biomass/coal derived gas utilization in a gas turbine combustor', ASME Paper 98-GT-160, *ASME Technical Papers*. New York: ASME, 1998.
- 15) 'ICAO Engine Exhaust Emissions Data Bank', issue 1, 1993, Appendix C, data for CF6-80C2B1F, page C-41.
- 16) Jentink, H.W., Veen, J.J.F. van, 'In flight spectroscopic aircraft emission measurements'. To be published in the proceedings of this symposium *Gas Turbine Engine Combustion, Emissions and Alternative fuels*. Neuilly Sur Seine: RTO, 1998.
- 17) Jong, W. de, Andries, J., Hein, K.R.G., 'Coal-biomass gasification in a pressurized fluidized bed gasifier', ASME Paper 98-GT-159, *ASME Technical Papers*. New York: ASME, 1998.

- 18) Kelsall, G.J., et al., 'Combustion of LCV Coal Derived Fuel Gas for High Temperature, Low Emissions Gas Turbines in the British Coal Topping Cycle', ASME Paper 91-GT-384, *ASME Technical Papers*. New York: ASME, 1991.
- 19) Kretschmer, D., Odgers, J., 'The characterization of combustion by fuel composition - measurements in a small conventional combustor', *Combustion and Fuels in Gas Turbine Engines, AGARD-Conference Proceedings-422*, paper 10. Neuilly Sur Seine: AGARD, 1988.
- 20) Kuo, K.K., *Principles of Combustion*. New York: John Wiley & Sons, 1986.
- 21) Lavoie, G.A., Heywood, J.B., Keck, J.C., 'Experimental and Theoretical Study of Nitric Oxide formation in Internal Combustion Engines', *Combustion Science and Technology*, vol.1, p.313-326. New York: Gordon and Breach Science Publishers Ltd., 1970.
- 22) Lefebvre, A.W., *Gas Turbine Combustion*. Washington: Hemisphere Publishing Corporation, 1983.
- 23) Maidhof, S., Janicka, J., 'Numerical modelling of turbine combustion chambers', *Fuels and Combustion Technology for Advanced Aircraft Engines, AGARD-Conference Proceedings-536*, paper 10. Neuilly Sur Seine: AGARD, 1993.
- 24) McBride, B.J., Gordon, S., *Computer Program for Calculation of Complex Chemical Equilibrium Compositions and Applications. II. Users Manual and Program Description*. NASA Reference Publication 1311. Ohio, National Aeronautics and Space Administration, Lewis Research Center, 1996.
- 25) Miller, J.A., Bowman, C.T., 'Mechanism and modelling of nitrogen chemistry in combustion', *Progress in Energy and Combustion Science*, vol.15, p.287-338. Oxford: Pergamon Press plc., 1989.
- 26) Nagle, J., Strickland-Constable, R.F., 'Oxidation of carbon between 1000°C-2000°C', *Proceedings 5th Conference on Carbon*, page 154, Pergamon, 1961.
- 27) Nakata, T., et al., 'Experimental Evaluation of a Low NO_x LBG Combustor Using Bypass Air', ASME Paper 90-GT-380, *ASME Technical Papers*. New York: ASME, 1990.
- 28) Pohl, H.W., (editor) *Hydrogen and Other Alternative fuels for Air and Ground Transportation*. Chichester, UK: John Wiley & Sons Ltd., 1995.
- 29) Pratt, D.T., 'Coalescence/Dispersion Modelling of Gas Turbine Combustors', *Combustor Modelling, AGARD-Conference Proceedings-275*, paper 15. Neuilly Sur Seine: AGARD, 1980.
- 30) Rizk, N.K., Mongia, H.C., 'Emissions Predictions of Different Gas Turbine Combustors', AIAA Paper 94-118, *AIAA Technical Papers*. New York: AIAA, 1994.
- 31) Rodriguez, C.G., O'Brien, W.F., 'Unsteady, finite-rate model for application in the design of complete gas-turbine combustor configurations', *Design principles and methods for aircraft gas turbine engines, AGARD Conference Proceedings*. Neuilly Sur Seine: RTO, 1998.
- 32) Sato, M., et al., 'Coal Gaseous Fueled, Low Fuel-NO_x Gas Turbine Combustor', ASME Paper 90-GT-381, *ASME Technical Papers*. New York: ASME, 1990.
- 33) Schumann, U., (editor) *Lecture Notes in Engineering. Air Traffic and the Environment-Background, Tendencies and Potential Global Atmospheric Effects*. Berlin: Springer-Verlag, 1990.
- 34) Schumann, U., AERONOX, *The impact of NO_x Emissions from Aircraft Upon the Atmosphere at Flight Altitudes 8-15 km, EC-DLR Publication on research related to aeronautics and environment*. DLR, Germany, 1995.
- 35) Sturgess, G.J., McKinney, R., Morford, S., 'Modification of Combustor Stoichiometry Distribution for Reduced NO_x Emission From Aircraft Engines', ASME Paper 92-GT-108, *ASME Technical Papers*. New York: ASME, 1992.
- 36) Toof, J.L., 'A Model for the Prediction of Thermal, Prompt, and Fuel NO_x Emissions From Combustion Turbines', ASME Paper 85-GT-29, *ASME Technical Papers*. New York: ASME, 1985.
- 37) Visser, W.P.J., 'Gas Turbine Simulation at NLR', 'Making it REAL', *CEAS Symposium on Simulation Technology* (paper MOD05), Delft, the Netherlands, 1995.
- 38) Westenberg, A.A., 'Kinetics of NO and CO in Lean, Premixed Hydrocarbon-Air Flames', *Combustion Science and Technology*, vol.4, p.59-64. New York: Gordon and Breach Science Publishers Ltd., 1971.

PAPER No. 21
Visser
(presenter: W.P.J. Visser)

Question 1: M Cathonnet, LCSR-CNRS, France

How can your model predict the effect of air/fuel ratio? I think this effect cannot be properly represented by the empirical relationship used. Air/fuel ratio affects the soot and hydrocarbon kinetics; unburned hydrocarbons are **not** fuel molecules, but are intermediate hydrocarbon species.

Answer:

The answer addresses the unburned hydrocarbons (UHC) model. The UHC emission model is a relatively simple one at this stage, with only empirical relations for burning rate and without intermediate species being involved; however, the hydrocarbon and oxygen concentrations are included. These, in effect, represent fuel/air ratio. The author is aware of the UHC model's limitations, and future updates may well employ physical relations including intermediate HC species.

Question 2: N. Brehm, BMW-RR, Germany

How do you address the modeling of different combustor designs, for example, stoichiometric primary zones or rich-lean low NO_x strategies? Features such as these have an important effect on emissions, and design details are usually confidential.

Answer:

Indeed! Combustion design data **are** hard to obtain. However, geometric data can be used to determine reactor dimensions. Further, the unknown parameters can be used for tuning the model. An example would be primary zone fuel-air ratio. It should be noted that for industrial gas turbines, combustion data are easier to obtain.

Question 3: G.J. Sturgess, ISSI, U.S.

This is a comment. Fuel distribution and film cooling, as well as reaction kinetics, will determine the UHC's in a gas turbine combustor. To represent these effects adequately it might be necessary to utilize a simple network array of series and parallel reactors in your combustor model.

Answer:

Yes, we have thought about doing this.

In-flight spectroscopic aircraft emission measurements

H.W. Jentink

National Aerospace Laboratory NLR,
Instrumentation Department, PO Box 90502, 1006 BM Amsterdam, The Netherlands

J.J.F. van Veen

Netherlands Organisation for Applied Scientific Research TNO,
Sensor Technology Department, PO Box 6011, 2600 JA Delft, The Netherlands

1. Summary

Aircraft emit their exhaust gases for the larger part during cruise conditions. The knowledge about the emissions in these conditions is limited because adequate in situ measurement methods are not available. In this presentation the complications encountered measuring exhaust gases in flight are addressed. The potential of spectroscopic measurement methods for this application is discussed. Experimental data gathered on ground are used to support the argumentation.

2. Introduction

Up to now the primary reason for the interest in the gaseous emissions of aircraft has been their impact on the environment around airports. This is reflected in current certification requirements for civil aircraft engines where the emissions during the landing, during taxiing and during take-off (the LTO cycle) are regulated¹. These emissions have a direct impact on the atmosphere around airports and therefore on the health of citizens. The impact of cruise emissions is much more indirect and long term. However, the amount of gas being emitted during the cruise phase of a typical flight is much larger than the gaseous emissions in the LTO cycle. Attention for the cruise emissions is growing as investigations show that the recovery of nature and the influence on health is much less straightforward for these impacts.

A quite different reason for interest in gaseous emissions of aircraft engines is the potential of detecting stealthy aircraft through gas detection². The exhaust gases are a potential omission in the stealthiness of aircraft where detection of military aircraft with traditional methods is increasingly being prevented.

An alternative to the measurement of gaseous emissions is the calculation of emissions. Carbon, hydrogen and sulphur are emitted almost completely as CO₂, H₂O and SO₂ molecules. The emission of these gases can be derived from the consumption of fuel and the composition of fuel, with some corrections for emissions of carbon, hydrogen and sulphur in other molecules. These molecules, as well as the important nitrogen oxides, can either be measured or calculated with models. Models of thermodynamic conditions in the engine, combined with chemical predictions of the production of exhaust gases, have been developed. With these models the emissions at cruise

altitude can be calculated (e.g. ref. 3). Models have been validated with results of measurements in test rigs, whereas the validation in-flight is still in an early stage. In-flight measurements are required for the ultimate validation of these and future models, resulting in a demand for instrumentation.

In the future it is very likely that regulations with respect to aircraft emissions are expanded to include the gaseous emissions in cruise conditions. In the International Civil Aviation Organisation (ICAO) the Committee on Aviation Environmental Protection (CAEP), workgroup 3, dealing with gaseous emissions at altitude, has expressed the need for the development of methods to measure the gaseous emissions in flight conditions.

The need for validation of models for the calculation of gaseous engine emissions, together with the need for future certification methods initiated in the Netherlands the evaluation and development of measurement methodology for the in-flight gaseous emissions of aircraft engines. The approach for the development of the technique is presented and other activities on this field are referenced.

The work was supported by the Dutch Ministry of Housing, Physical Planning and Environment (VROM) and the Netherlands Agency for Aerospace Programmes (NIVR).

3. Measurement techniques

Standard measurement techniques on the ground are based on sampling exhaust gases and leading the samples to analysers analysing the concentrations of gases¹. The method is not feasible for in-flight application, because the installation of a sampling rake behind an engine would be a major effort, and, moreover, proving that the sampling rake is deriving a representative sample from the total exhaust gases being emitted is not trivial at all. Leading the gases through a heated tube (heated to prevent the water in the exhaust gas from condensing) from the engine to analysers is not simple either.

Trailing an aircraft engine under investigation with another aircraft equipped with gas sampling and gas analysis instrumentation is an option⁴ where the installation of equipment on the aircraft under investigation is not necessary. Installation of a broad range of instruments in the trailing aircraft is manageable. However, in the measurement results the dilution of emissions in the

environment has to be eliminated which introduces a considerable uncertainty in measurements.

Open-path spectroscopic measurements close behind the exhaust of engines have been introduced for test rigs and ground tests to avoid the installation of gas-sample systems^{5, 6, 7}. These are also being developed for in flight tests⁸. The remote sensing of gases with spectroscopy requires a manageable installation effort on the aircraft and is therefore investigated for the application.

4. Spectroscopic measurement techniques

Several spectroscopic techniques are available for the measurements. Spectroscopic detection is based on the excitation of electrons in molecules or the excitation of vibrational or rotational modes of molecules. Electron excitation is in the ultraviolet (UV) and for some molecules partly in the visible light wavelengths (the brown colour of NO₂). Vibrational and rotational modes are excited at infrared (IR) wavelengths.

A feasibility study of NLR and TNO showed that spectroscopy applied in light absorption as well as in light-emission mode can give relevant information. In the light-emission mode the radiation of molecules is detected and analysed. The emission intensity is dependent on number of molecules in the gas, on the emissivity of the gas, but also very much on the temperature of the gas. Accurate knowledge about the temperature of the gases is essential for accurate gas concentration measurements in this mode. Light emission at infrared wavelengths is intense enough for detection at temperatures of the exhaust gases, i.e. below 1000 degree Celsius. Emission spectroscopy is not feasible at UV wavelengths.

Absorption spectroscopy needs an external light source. A light path is created from source to detector through the exhaust gas under investigation. Photons with wavelengths corresponding to excitation modes of molecules are absorbed, leading to a decreased intensity in the spectrum of transmitted light. The dependence of the transmission characteristics of gases on the temperature is much less than the dependence of emission characteristics on temperature. Information on the exact temperature of the gas is therefore less crucial for absorption measurements. Absorption spectroscopy at IR and UV wavelengths can be applied.

In the feasibility study both sensitivity and selectivity of spectroscopic techniques appeared to be crucial parameters. The sensitivity has to be sufficient for detection of gas components in the concentration range found in exhaust gases. The selectivity, detecting a gas component in a matrix of other gases, is also a critical parameter for obtaining accurate results.

Spectroscopic measurements are taken along a light beam. Information about the density of gas molecules in the light beam is derived. Gas velocity information and information on the spatial distribution of gases is necessary to calculate total emissions of exhaust gases. Approximations are commonly made to simplify the measurements. A simplification can be achieved by assuming that each of exhaust gases has the same spatial distribution in the plume, which is likely at the exhaust. Now contemplate the

carbon atoms. By measuring the carbon density, which is primarily equal to measuring the CO₂ density, the amount of fuel, burnt to produce the sample of exhaust gas being probed, can be traced back. Gaseous carbon production is related to the fuel consumption and the fuel consumption can be measured easily. The total mass of emitted gas species can be calculated in this case from the fuel consumption, the carbon density and the densities of other gas species in the probed volume⁸.

More advanced methods have been developed modelling the exhaust gas plume in layers with homogeneous conditions. Contributions from the different layers to the spectrum are estimated.

5. Installation on aircraft

Spectrometers to be installed on an aircraft should perform in an environment with vibrations and pressure changes. Special design or modification of instruments may be necessary for these requirements, but no basic problems are to be expected in this respect. The installation of optical components inside the cabin of aircraft imposes less severe requirements on the components than outside the cabin and may therefore be the favourable option. The primary design challenge is the light transmission from the exhaust gases to the spectrometer and, for absorption spectroscopy additionally, from the light source to the exhaust gas. For some aircraft the exhaust can be seen from the cabin through a cabin window or a modified cabin window and in this case the installation of the spectrometer in the cabin and open-path light transmission is a good option. The best spectrometer installation may also be in the cabin for aircraft with the engine exhaust out of sight from cabin windows, using fibre optics for light transmission. However, this is not simple at IR wavelengths, because of the poor transmission properties and the brittleness of commercially available fibres.

For an absorption spectrometer the installation of a retroreflector on the engine exhaust may be considered anyhow, enabling easy alignment of source and detector and enabling the installation of both the source and the detector inside the cabin.

6. Towards in-flight measurements

A co-operation between NLR and TNO was set up to develop a spectrometer for the in-flight measurement. On the road towards in-flight spectroscopy it was decided to start with the evaluation of the capabilities of available spectrometers in ground tests. Spectrometers developed for other environmental applications, such as the measurement of emissions from chimneys, were considered as a good starting point for the development. Spectrometers were installed next to the NLR research aircraft in a test run facility. An engine of a NLR research aircraft, the Cessna Citation II, was run at several thrust settings. Exhaust gases from the engine were sampled simultaneously with the spectroscopic measurements. Gas samples were analysed as a reference for the spectroscopic measurements, which should lead to a validation of the measurement method for low altitudes. The method for the sample analysis was based on standard ICAO procedures¹, with some simplifications to keep instrumentation and the engine run time limited. In fig. 1 the test set-up is shown.



Fig. 1 Set-up for evaluating spectrometers. Gas samples are taken from the perforated tube installed behind the exhaust of the engine and led to gas analysers. A retroreflector is visible behind the tail of the aircraft

Several spectrometers available on the market have been evaluated. FTIR spectrometry in light emission mode was demonstrated to give good results for CO_2 , CO and NO measurements. This is in accordance with results reported earlier ^{6, 7, 8}. First results for UV absorption with the Differential Optical Absorption Spectroscopy (DOAS) techniques were obtained detecting NO. This technique is expected also to have potential for NO_2 measurements, but this has not been demonstrated yet. The potential for this type of measurements is in accordance with results reported in test rigs ⁵. Further research on the reproducibility and accuracy of measurements is needed for definite selection of the spectrometer.

Once that the best spectrometer will have been selected, the next phase of the development will be the installation of a spectrometer in another NLR research aircraft, a Fairchild Metro II. This aircraft has good testing options for spectrometry as the spectrometer can be installed in the aircraft cabin where light can be transmitted and received through inserts in a dummy window (fig. 2). For absorption measurements a small retroreflector can be installed on the exhaust.

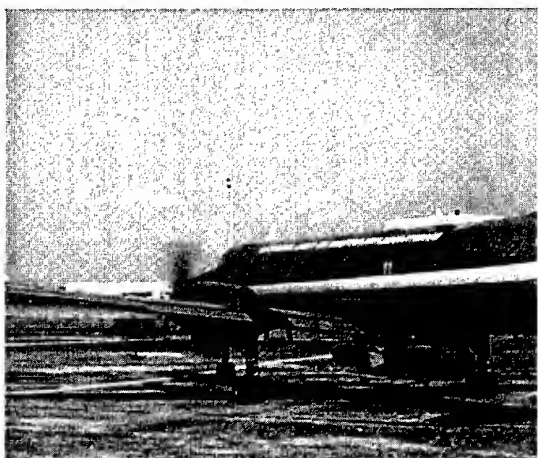


Fig. 2 The Fairchild Metro II research aircraft. This aircraft has the exhaust in sight of cabin windows, enabling easy installation of open-path spectrometers

7. Conclusion

The in-flight measurement of gas emissions of aircraft engines is demanded for several reasons. The remote spectroscopic methodology has considerable potential for achieving this. Characteristics of the application are listed and a strategy towards in-flight measurements is drafted. Commercially available instruments are being evaluated for this application, showing good prospects.

8. References

1. ICAO "Environmental Protection, International Standards and Recommended Practices", Annex 16, vol. II, "Aircraft Emissions", Second Edition (1993)
2. Wilson C., Brundish K., Moncrieff J.T.M., Wootton A.G., "DIAL Measurements on a Gas Turbine Exhaust", AGARD CP 598, paper 9, 90th PEP Symposium "Advanced Non-Intrusive Instrumentation for Propulsion Engines", Brussels, Belgium, 20-24 October 1997
3. Visser W.P.J., Kluiters S.C.A., "Modeling the Effects of Operating Conditions and Alternative Fuels on Gas Turbine Performance and Emissions", RTO-AVT Symposium "Gas Turbine Engine Combustion, Emissions and Alternative fuels", Lisbon, Portugal, 12-16 October 1998, paper 21
4. Schulte P., Schlager H., "In-flight measurements of cruise altitude nitric oxide emission indices of commercial jet aircraft", Geophysical Res. Letters, vol. 23, p.165 (1996)
5. Howard R.P., "Experimental Characterization of Gas Turbine Emissions at Simulated flight Altitude Conditions," AEDC-TR-96-3 (1996)
6. Bittner H., et. al., "Optical Remote Sensing of Aircraft Emissions with the K300", IEEE Trans. Geosc. and Remote Sensing vol. 31, p. 1 (1993)
7. Heland J., Schäfer K., "Analysis of aircraft exhausts with Fourier-transform infrared emission spectroscopy", Applied Optics vol. 36, p. 4922 (1997)
8. Haschberger P., Lindermeir E., "Spectrometric inflight Measurement of Aircraft Exhaust Emissions: First results of the June 1995 Campaign", J. of Geophys. Research vol. 101, p. 25995 (1996)

PAPER No. 22
Jentink
(presenter: H. W. Jentink)

Question 1: C.W. Wilson, DERA, U.K.

In your talk you identified the concern that the spectroscopic technique measures a column density while the important measurement for atmospheric effects is the mass of emissions. You then described a method that will derive a mass flux using plume calculations and engine performance data also. Have you performed an error analysis on the technique? If so, what error do you expect to have in the emission mass flux? How will this compare with the 2 % of full-scale required by ICAO for emissions measurement, or the 2 % of reading adopted by most engine manufacturers? If you have not yet performed an error analysis, what is your current target for the measurement accuracy?

Answer:

We did not make a detailed assessment of the accuracies for total gas mass emissions. We expect accuracies between 10 % and 20 % for the instrument under consideration. By achieving these accuracies and by developing measurement procedures, we shall meet the objectives of the present development. Developing measurement methods and procedures to result in a tool for unambiguous assessment of gaseous emissions is important for possible future inflight certification, in my view.

Question 2: W. de Wolfe, National Aerospace Laboratory, Netherlands

Which of the three methods that you described is your preferred approach, and which is the closest to success?

Answer:

The answer depends a little on the objective of the measurements. Taking the current emphasis on NO_x emissions into account, the UV-absorption technique is the most promising.

THE DESIGN AND EVALUATION OF A PILOTED, LEAN BURN, PREMIXED, PREVAPORISED COMBUSTOR

MI Wedlock, J R Tilston & R E Seoud
Propulsion Dept.
170 Building, DERA
Pyestock, Farnborough
Hants, GU14 0LS, UK

1. SUMMARY

A piloted, lean burn, premixed, prevaporised combustor was designed to significantly reduce NO_x levels. The combustor performance was evaluated over a range of conditions typical of a future large subsonic turbofan. The results showed NO_x reductions in the range of 70-80%.

The work was carried out as part of the CEC BRITE EURAM LOWNOX II programme. (Contract No AER2-CT92-0036, Project No AERO-2019)

2. INTRODUCTION

The emissions of NO_x from commercial aircraft gas turbine combustors have been a topic of intense scrutiny in recent years. Environmental impact studies indicate that NO_x emissions introduced into the upper troposphere and lower stratosphere may result in the formation of ozone at these altitudes. The resulting ozone may, in turn, be a contributing factor in causing global warming. Subsonic aircraft typically cruise at these altitudes.

Other studies indicate that NO_x emissions introduced at higher altitudes in the stratosphere can contribute to the depletion of the stratospheric ozone layer. The optimum cruise altitudes of supersonic aircraft are generally at the altitudes where the ozone layer is located.

Because of these concerns, extensive efforts are underway to develop low NO_x combustors for use in both subsonic and supersonic civil aircraft engines.

International legislation has sought to control aircraft gas turbine NO_x emissions, but the reductions required so far have been met by the application of conventional combustor technology. Also, these standards are expressly designed to regulate emission quantities that can be discharged in and around airports. However, the regulatory agencies are now reviewing existing legislation in the light of the long term effects of atmospheric pollution. For the first time, consideration is being given to requirements for the reduction of emissions generated by aircraft at cruising altitudes.

As an important part of the efforts to assess the environmental acceptability of a fleet of new SST aircraft, extensive studies were conducted by NASA and others to determine the impact of such aircraft fleets on the stratospheric ozone layer. Based on the findings, a NO_x emission index of 5 grams per kilogram of fuel at supersonic cruise conditions was established by NASA as a goal for future SST engines. This cruise target represented about a 90% reduction from that of a conventional combustor prior to the introduction of existing legislative NO_x controls.

Reductions as large as 90% in NO_x levels may only be achieved in aircraft gas turbine engines by the use of advanced combustion technologies, e.g. lean premixed/prevaporised combustion, or rich burn/quick quench/lean burn combustion.

In February 1990 a CEC BRITE EURAM programme (LOWNOX) started that was designed look at the reduction potentials of these ultra-low NO_x technologies. The programme was designed to run in three phases, culminating in a testing of a full scale combustor demonstrator. This report describes work carried out in Phase II of the programme to demonstrate the NO_x reduction potential of a lean premixed prevaporised (LPP) combustor for a future SST or subsonic civil aircraft engine.

3. DESIGN PHILOSOPHY

In preliminary meetings with other programme partners, it was agreed that a staged multiple zone combustor architecture would be needed to attempt to meet all the engine operating conditions.

It was clear that any practical LPP combustor for large engines would have to incorporate a pilot zone to provide adequate stability and turn-down ratio. There was likely to be interaction between the pilot and LPP zones, so their early evaluation within a prototype combustor was seen as essential.

A double or treble annular combustor of the arrangement of the type shown in Figure 1 would have produced the optimum combustor architecture.

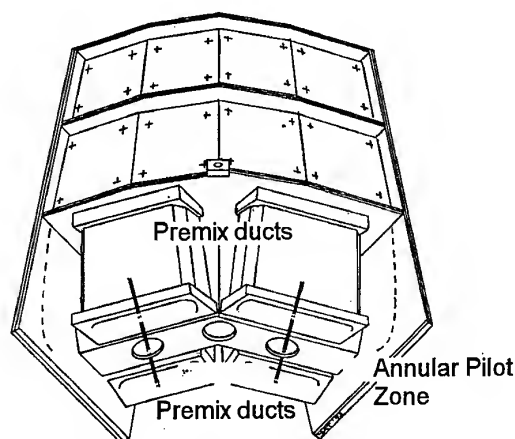


Figure 1 Treble annular LPP combustor configuration

However the available sector rig pressure casing was not deep enough to accommodate four sectors of a double/treble annular combustor. Because of this an alternative combustor

layout was adopted that consisted of radially aligned pilot modules interspersed with premix ducts (see Figure 2).

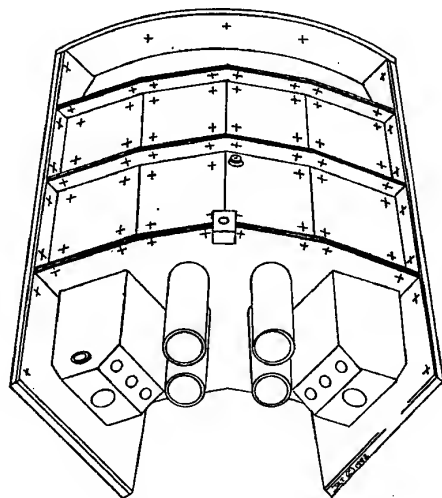


Figure 2 Four sector LPP configuration

An interactive study¹ was undertaken in parallel with the engineering design to identify a combination of airflow split and fuel distribution that would offer the prospect of satisfactory performance at all engine cycle conditions. Preliminary estimates were made of premix duct length with the objective of achieving a compromise between residence time (ignition delay time) and an adequate evaporation time.

The volume provided for the main combustion zone was also estimated, taking into account the relatively low reaction rate expected in weak, premixed combustion.

Initially, in the interests of realism, the pilot combustor volume was sized to achieve relight at 10,000 metres. However, it quickly became evident that NO_x production in this large, long residence time zone would be unacceptable. As a result the design emphasis was then placed on providing the minimum pilot zone volume necessary to meet idling emissions targets but minimising the NO_x production at higher power conditions. Indications were that at high power conditions the fuel split would be approximately 75:25 (LPP to Pilot), so the pilot zone would have to achieve substantial NO_x reductions. If the LPP combustion produced a 95% NO_x reduction, then the pilot zone would have to achieve a 75% NO_x reduction for there to be an overall 90% NO_x reduction.

Because of the proposed modular layout of the piloted LPP combustor, it was possible to optimise the design of the pilot zone in some preparatory low pressure 2-sector rig tests at 1 to 5 bar - see Section 7.

4. DESIGN CONDITIONS

The LOWNOX programme had already agreed specimen operating conditions for a large engine, subsonic cycle and a supersonic transport cycle. These are shown in Table 1 & Table 2.

Condition	Thrust	Combustor Inlet Conditions			Combustor AFR	Combustor Exit Temperature K	Fuel Flow kg/s
		Temperature K	Pressure bar	Air Flow kg/s			
Take-off	100%	917	47.6	157.2	36.88	1792	4.262
Climb out	85%	878	41.09	140.3	40.83	1683	3.436
Approach	30%	709	18.17	73.1	68.57	1232	1.066
Idle	7%	551	7.01	33.3	115.11	886	0.2893
Cruise		846	17.58	60.3	39.91	1672	1.511

Table 1 Subsonic turbofan performance data, ISA SLS rated take-off thrust 459 kN

Condition	Thrust	Combustor Inlet Conditions			Combustor AFR	Combustor Exit Temperature K	Fuel Flow kg/s
		Temperature K	Pressure bar	Air Flow kg/s			
Take-off	100%	734.9	16.224	120.8	36.2	1650	3.338
Climb out	85%	645.7	11.727	96.81	49.67	1352	1.949
Approach	30%	565.4	7.703	70.39	68.61	1103	1.026
Descent	15%	496.2	4.876	48.47	88.451	929	0.548
Idle	7%	452.5	3.427	35.43	99.8	844	0.355
Cruise		917	7.875	57.28	41.39	1701	1.384

Table 2 Supersonic turbofan performance, ISA SLS rated take-off thrust 208.9 kN

5 KEY COMBUSTOR DIMENSIONS

Because of test plant limitations, the combustor air mass flow was scaled to suit the available air mass flow from the rig compressor. There was insufficient rig pressure capability to achieve the full range of subsonic engine conditions, so these conditions were to be tested at a constant combustor flow function ($M\sqrt{T/P}$).

The dimensions of the four sector combustor were maximised by increasing the mean radius to take the best advantage of the pressure vessel dimensions.

Some key component details were as follows:-

- each pilot zone volume 0.415 litre;
- total main combustion zone volume 5.600 litre;
- combustor exit nozzle volume 1.470 litre
- pilot zone length 100 mm;
- main zone annulus height 100 mm;
- premix duct length 100 mm;
- main combustion zone length 140 mm;
- combustion exit nozzle length 70 mm;
- total angle of 4 sectors 83.04°.

6 AIR & FUEL FLOW DISTRIBUTIONS

The general design objective was to achieve zonal stoichiometries that would give combustion gas temperatures in the range 1700K to 2100K over the entire engine operating envelope. It was assumed that the 1700K limit would be close to weak extinction or to an unacceptably low reaction rate. The upper limit of 2100K was set to limit the production of thermal NO_x .

A spreadsheet program was used to investigate the effects of a range of different air flow splits to the pilot zone, the premix ducts and the main zone cooling. The fuel split between the pilot zone and the premix ducts was also varied. The combustion gas temperature objectives could not be met at all the engine conditions, so a compromise had to be made. It was decided that it was important to meet the objectives for take-off and cruise. Figure 3 shows the nominal air flow splits for the key components of the piloted LPP combustor.

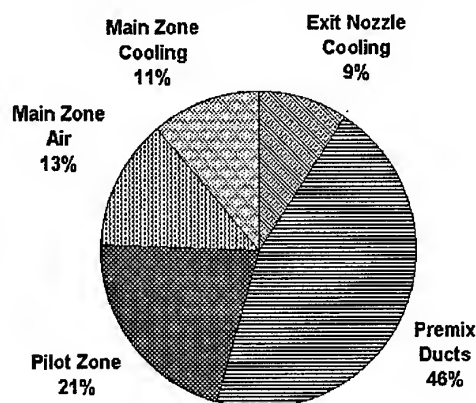


Figure 3 Combustor air flow splits

It is interesting to note that nearly 50% of the combustor air passed through the premix ducts, and only 20% of the air was used in cooling films on the main zone and exit nozzle. The cooling air used on the pilot zone, premix ducts and main zone headplate totalled 13%, but was subsequently used in the combustion zone. Significantly there was no air available for a conventional dilution system that is often used to adjust the combustor exit traverse.

Figure 4 and Figure 5 show the approximate flame temperatures for the pilot and premix zones. It can be seen that the subsonic engine is run on the pilot zones only for idle and approach. The SST engine additionally runs on the pilot zones only for the descent power setting.

The target gas temperature range 1700 to 2100K for the premix zones was met with the exception of the climb out condition for the subsonic turbofan.

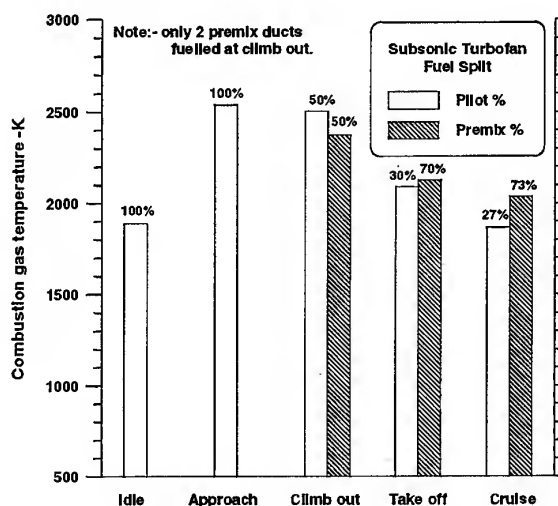


Figure 4 Zonal gas temperatures - subsonic turbofan

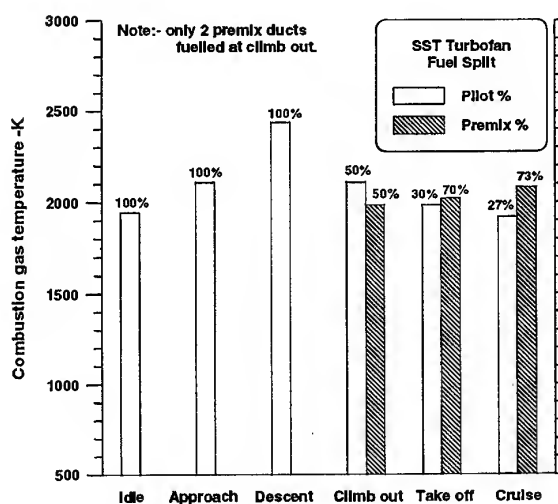


Figure 5 Zonal gas temperatures - SST turbofan

It was possible that the fuel split for this condition could have been changed to 30% pilot/70% premix with all 4 premix ducts fuelled. However this significantly reduced the flame temperatures in both pilot and premix zones, and it was felt that the combustion efficiency/stability might be unacceptable.

The other observation was that the subsonic engine approach NO_x levels could be a problem. The engine was fuelled on the pilot zone only and the combustor burning zone fuel/air ratio was calculated to be close to stoichiometric.

7 PILOT ZONE DESIGN & DEVELOPMENT

The pilot zone was designed as a modular sub-assembly that could be bolted to the main combustor head plate. It was constructed from an outer metal box lined with metal cooling tiles. Figure 6 shows a general external view of a pilot zone complete with airspray fuel injector. Figure 7 is an internal view to show the cooling tile arrangements.

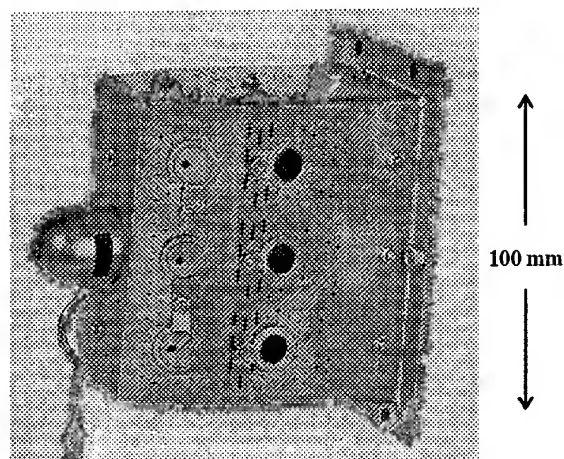


Figure 6 General view of pilot zone

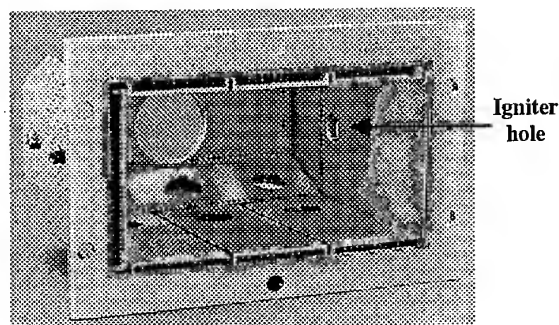


Figure 7 Internal view of pilot zone

The outer box was fitted with a total of 12 combustion holes (6 per side), although only 6 were used at any one time. Blanks were fitted to those not required, and plunged inserts to the rest. The three holes closest to the airspray were blanked in Figure 6. Each blank had a small hole for cooling air to enter. This air then passed into the main tile cooling flow. By using different insert positions, the interaction between the air jets and the airspray flows could be altered, thus changing the local residence times. Also, the local stoichiometry could be changed slightly by varying the size of

the plunged inserts. Three different atomiser designs were evaluated during pilot zone development rig trials at 1 to 5 bar.

Also visible on the outside are the small air feed holes and slots for the internal metal cooling tiles. A small diameter (8 mm) high energy igniter was fitted to each pilot zone.

Some pilot zone optimisation testing was carried out at low pressures (1 to 5 bar). A 2-sector rig build (1 pilot + 1 premix) was used. The one premix sector was in fact two half sectors. The premix sector was not fuelled, but representative air flows were simulated either side of the pilot zone. These tests² produced a pilot zone design with the following performance:-

- 4% pressure loss;
- 97.5% SST idle combustion efficiency;
- 99.8% subsonic idle combustion efficiency
- 68% NO_x reduction at SST cruise (estimated);
- < 7 SN smoke at all conditions;
- good ignition characteristics;
- acceptable metal temperatures.

8 PREMIX DUCT DESIGN

The premix ducts were designed as straight-through, low loss ducts with the full combustor pressure loss (4%) applied across them. The resulting high flow velocity - in excess of 100 m/s - was intended to keep boundary layers thin and to be much greater than any possible flame speed to prevent flashback events. An additional advantage was that the velocity was sufficiently high for the fuel injector to be a simple prefilming surface immersed in the flow at the entry to the duct.

The ducts were designed with convectively-cooled walls featuring heat transfer enhancement devices. This wall cooling flow was exhausted into the premix duct just upstream of the duct exit. This was intended to break the continuity of the duct boundary layer with clean air to prevent the possibility of flashback up the duct boundary layer. Initially, premix designs of circular cross section had been considered, but they were modified to an ob-round section. This would suppress possible vortex flow in the ducts. Figure 8 is a cross-section schematic view of a premix duct and prefilmer. The wing-shaped fuel prefilmer delivered a thin sheet of fuel from one side of its trailing edge.

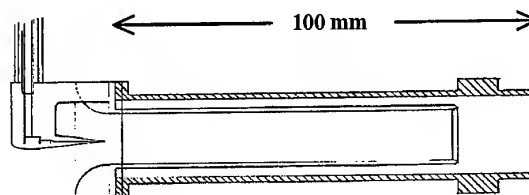


Figure 8 Premix duct

Initial 3D CFD calculations by SNECMA indicated a fuel distribution problem. Although the fuel was being broken into small droplets, the fuel was not being distributed across the vertical plane of the duct. This was confirmed by some atmospheric tests at DERA. Discussions with the partners CERT/ONERA, DLR and SNECMA, resulted in the addition of a simple turbulence generator close to the trailing edge of

the prefilmer - see Figure 9. Atmospheric tests showed a big improvement in fuel distribution at the duct exit plane.

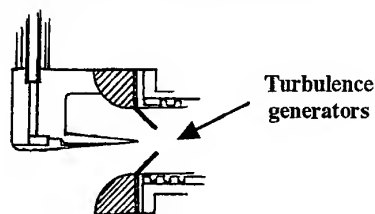


Figure 9 Premix duct turbulence generators

SNECMA modified their CFD model to include these turbulence generators. The 3D calculations³ showed a dramatic improvement in the fuel distribution and evaporation rate. Figure 10 shows the CFD droplet trajectory results, and confirmed that a good vertical spread of fuel would be achievable. It was also important that there seemed to be no droplet impingement on the walls. Figure 11 is a photograph showing the various parts of the premix duct/preflimer assembly.

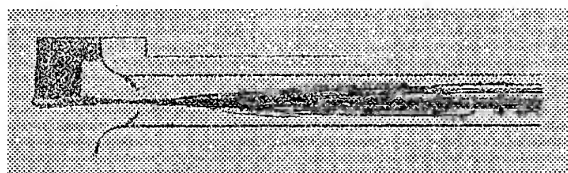


Figure 10 Droplet trajectories (Courtesy of SNECMA)

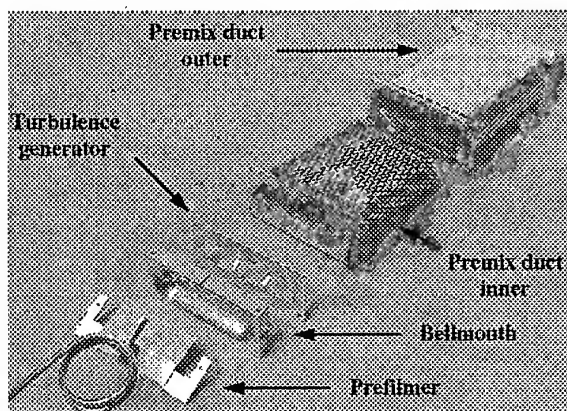


Figure 11 Premix duct/preflimer sub-assemblies

Because the premix flame stabilisation in the main combustor zone relied on dump combustor principles, two ducts were used per sector. This increased the dump shear layer area and minimised the mixing length in the main combustor zone.

The initial design layout was schemed with the two premix ducts set an angle to improve mixing in the main combustion zone (see Figure 12). This arrangement also aligned the premix ducts inlets with the flow from the diffuser exit. This alignment was considered to be important because a large

percentage of the air ($\approx 46\%$) has to travel from the diffuser to the premix ducts with minimal turning losses.

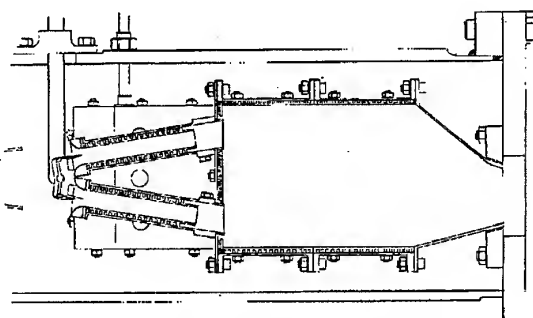


Figure 12 Initial arrangement of premix ducts

However during the pilot zone tests it was discovered that the air flow around the head of the combustor was badly distorted. The inlet diffuser design had been based on the requirements for a 'conventional' combustor - air holes distributed more evenly than a pilot LPP combustor. As a result, the inlet diffuser was replaced by a plenum fed chamber to eliminate the flow field distortion into the pilot zone air holes and the premix ducts.

During the atmospheric tests of the 4-sector combustor it was noticed that the premix duct flow was impinging onto the main zone walls. There were indications that the main zone tiles would be too hot during the 15 bar tests. A 3D CFD study⁴ was carried out to investigate alternative dispositions of the premix ducts. The CFD model was 2 sectors wide to allow the possible interactions between the pilot zone and the premix ducts to be studied. The full 3D model was run at SST cruise conditions under iso-thermal conditions with the various duct arrangements. Subsequent combustor flow calculations using a gaseous methane chemistry model were only applied to the premix ducts. Figure 13 indicates the grid structure of the CFD model.

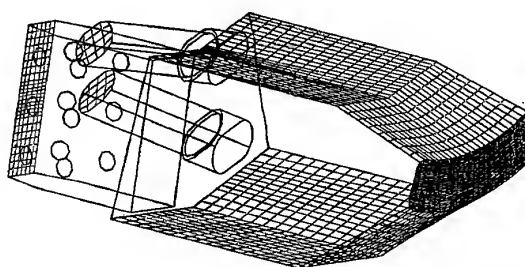


Figure 13 Two sector CFD model (FLUENT)

The possible alternative layouts for the premix ducts were restricted by existing components. However, the ducts could be arranged to be parallel to each other, or produce converging jets within the main combustion zone. These alternatives are shown schematically in Figure 14.

The results of the isothermal model with the divergent ducts confirmed the observations made during the atmospheric tests. The flow exiting the premix ducts did not expand very much in the plane normal to the duct. It also showed that the high

velocity premix duct flows induced transverse flow from the pilot zone. This was also confirmed by the atmospheric tests, and helped to explain the excellent light-across characteristics during these trials.

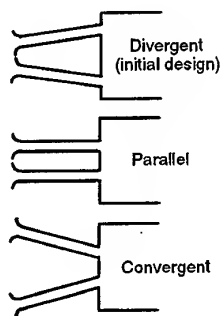


Figure 14 Layout options for premix ducts

The CFD calculations showed that the optimum arrangement was the convergent layout. The convergent flows produced improved mixing within the main combustion zone. The temperature distribution at the combustor exit plane was much improved. At large convergence angles the premix combustion zone spread laterally and mixed well with the flow from the adjacent pilot zones. Thus, there was scope to be able to adjust exit temperature profiles by changing the angle of convergence of the ducts. Typical temperature profiles within the main combustor volume are shown in Figure 15 for the parallel and convergent premix duct configurations

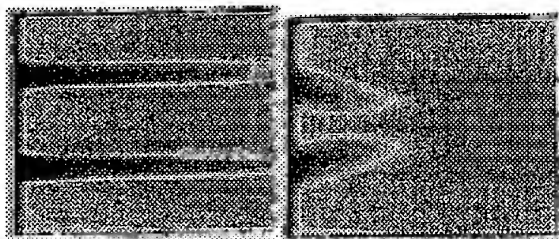


Figure 15 Parallel & convergent combustor flows

Unfortunately, practical constraints severely limited the convergence angle that could be applied to the ducts. As a consequence, the premix ducts were mounted parallel to each other.

9 LIF MEASUREMENTS ON PREMIX DUCT

The achievement of the evaporation of the fuel and good fuel/air mixing in a premix duct is crucial for NO_x reduction. Volvo Aero Corporation, with the assistance of Lund Institute of Technology used optical methods to visualise the degree of the fuel vaporisation at the premix duct exit plane. The tests⁵ were done at atmospheric pressure with air inlet temperatures in the range 500 to 900K.

To visualise the degree of vaporisation Laser-Induced Fluorescence (LIF) and a scattering (Mie) method was used. With a split-mirror arrangement and a CCD camera it was possible to capture two images of the flow. With different

optical filters in the two image channels, it was possible to capture LIF from the UV (266 nm) beam and elastic (Mie) scattering from the 532 nm beam. The images captured by the technique showed that although there was a good degree of fuel vaporisation at high air inlet temperatures (take off & cruise), there were still some kerosene droplets. At SST climb out (645K) conditions, the rate of fuel vaporisation was much worse, and there were significant numbers of fuel droplets.

10 PREMIX DUCT AUTOIGNITION & FLASHBACK TESTS

It is recognised that the most significant problem in developing LPP technology will be the design of a suitable premix duct. The most obvious threats to the integrity of an LPP combustor are autoignition in, or flashback into the premix duct. A series of tests⁶ was conducted by ONERA on a single premix duct to determine the susceptibility of the design to autoignition and flashback. Inlet conditions were in the range 600 to 850K and 7 to 24 bar. No flashbacks or autoignition phenomena were observed before the limits of the rig were reached. The premix duct design had a residence time of approx. 0.8 ms at subsonic take-off conditions. At 24 bar and 750K the premix duct flow was reduced by 40% without mishap.

The ONERA rig was also equipped to take gas analysis measurements. Two single point gas analysis probes were positioned about 230 mm behind the exit from the premix duct. The NO_x results from the probe that gave a closer calculated gas analysis air/fuel ratio match with the rig metered value are shown in Figure 16.

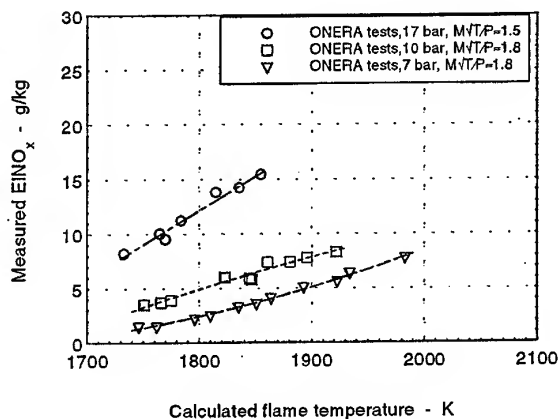


Figure 16 Premix duct NO_x values (Courtesy of ONERA)

These NO_x results were encouraging, but they indicated that the fuel was not being perfectly premixed and prevaporised before the combustion zone for two reasons:-

- NO_x levels were not as low as expected;
- NO_x levels affected by pressure.

It should be noted that the tests at 17 bar were done at an airflow that was about 15% below the design value. This may explain why these NO_x results are particularly high - poorer fuel atomisation and increased combustion zone residence time.

11 4-SECTOR COMBUSTOR BUILD

The 4-sector combustor was assembled with two pilot zones and four premix ducts. The disposition of the pilot zones and premix ducts may be seen on Figure 17. It was decided to position the premix ducts on the two central sectors since it was felt that this would more closely resemble an axially staged combustor. The pilot zones would have one combustor sidewall, and one side of each premix zone would be next to the efflux from a pilot zone.

Figure 18 is an internal view of the combustor that shows the positions of the premix ducts relative to the pilot zones. It also shows that some of the cooling air from the pilot zone cooling tiles exited into the main combustion zone. The air from the main zone cooling tiles entered the boundary layer via multiple rows of angled effusion holes on the trailing edge of each tile.

Figure 19 is a photograph of the combustor main zone and the combustor exit nozzle. The combustor was mounted in the casing using the 'smile-shaped' flange on the exit nozzle. The exit nozzle was constructed using Transply.

The effective areas of the main combustor components were measured during a series of cold flow air tests at atmospheric pressure. These values were used to update the spreadsheet program (see Section 6), so that the pilot and premix zone stoichiometries could be set more accurately during the 15 bar tests.

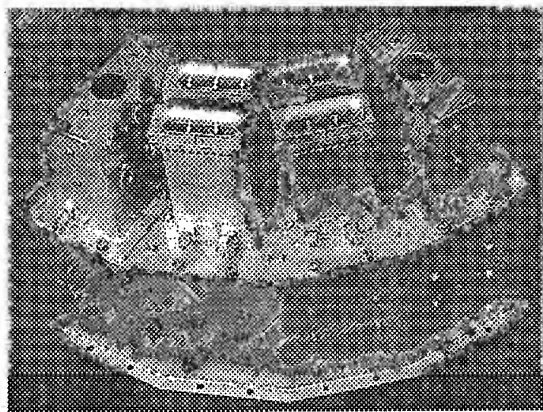


Figure 17 External view of 4-sector combustor

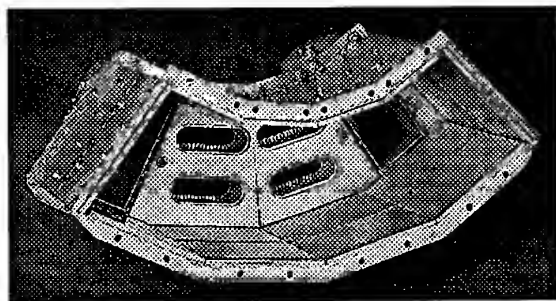


Figure 18 Internal view - looking upstream

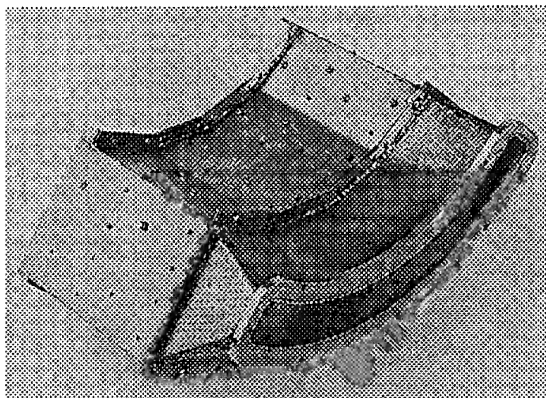


Figure 19 Combustor main zone & exit nozzle

12 16 BAR RIG FACILITY

The combustor rig facility was capable of operating over the following conditions:-

- combustor inlet air pressure up to 16 bar;
- combustor inlet air temperature up to 875K.
- combustor inlet air flow up to 5 kg/s.

The 16 bar rig was equipped with a 5-point gas sampling rake that could be traversed around all four sectors of the combustor. The five individual sampling points of the rake were positioned at centres of equal area at the combustor exit plane. A five channel gas analysis system conforming to ICAO regulations⁷ allowed a 5 by 42 point traverse to be completed in about 50 minutes.

This gas analysis traverse data could be presented as a contour plot, or 'mass averaged'⁸ to produce a single figure for each condition. There was also an 'EPA' averaging rake position downstream of the rig exhaust back-pressurising valve. Measurements could only be made from this averaging rake at low conditions since high pressure water was sprayed just downstream of the combustor exhaust at high power conditions.

The rig fuel system permitted the individual control of the fuel flow to each of the pilot zone and premix duct fuel injectors. If any of the fuel injectors were turned off during the tests, the trapped fuel could be purged using high pressure N₂.

The rig was equipped with calibrated air and fuel flow meters. Other instrumentation measured the combustor inlet pressure, temperature and the combustor wall pressure drop.

13 4-SECTOR RIG TESTS

The 4-sector combustor and its outer casing were mounted inside a circular water-cooled pressure casing and installed on the 16 bar combustion rig facility.

Some of the engine test conditions were limited by the maximum available pressure of 15 bar and 875K inlet temperature. The combustor was however run at the correct $M\sqrt{T/P}$ flow function.

Initially the combustor was run at all the simulated engine conditions (see Table 1 and Table 2) with only the pilot zones fuelled. This was necessary to try to quantify the relative NO_x contributions from the pilot and premix zones when both zones were fuelled. It was suspected that it would be difficult to separate the NO_x contributions from the combustor exit traverse data. The gas analysis results for these tests are shown in Table 3.

	Combustion efficiency %	EINO _x h=ref g/kg	Smoke SN
SST idle	96.5	2.7	0.1
SST descent	99	4.0	1.8
SST approach	99.9	8.1	4.4
SST climb out	99.9	6.9	5.2
SST take off	99.99	9.5	8.5
SST cruise	99.95	12.5	0.3
Subsonic idle	98.5	4.2	6.5
Sub. descent	99.99	7.3	3.6
Sub. approach	99.99	16.3	2.0
Sub. climb out	99.95	29.7	4.3
Sub. take off	99.93	16.9	7.5
Sub. cruise	99.95	14.0	2.3

Table 3 4-sector pilot only results

As expected the NO_x levels at subsonic climb out were particularly high. To put the measured NO_x levels for the pilot zone into context, comparisons were made with standard aero gas turbine levels. The reference baseline for NO_x levels was taken from the correlation of gas turbine emissions data reported by Lipfert⁹. In this correlation the data related to emissions measurements made on engines with conventional combustor technology, i.e. without any deliberate NO_x reduction features. It was found that all the available engine NO_x data could be correlated against combustor inlet temperature after corrections for differences in ambient humidity had been made.

Although the choice of this early correlation may appear strange at first sight, it is a simple baseline that may be used without detailed information of the combustor. It also represents the *status quo* for all aero gas turbine engines before the application of emission control technology. The NASA SST cruise EINO_x target of 5 g/kg represents about a 90% reduction from 'Lipfert levels' (see Section 2).

A baseline reference NO_x level was determined for each of the rig inlet temperatures. Corrections were made for the differences in combustor inlet pressure between the rig tests and those from the Lipfert engine data. Since the Lipfert report did not contain combustor inlet pressure data, values were calculated for each combustor inlet temperature assuming an adiabatic compressor efficiency of 87%. It is widely accepted that NO_x levels in conventional combustors may be corrected for differences in pressure using p^{Const} . The value of the constant is usually¹⁰ in the range from 0.4 to 0.5. A value of 0.4 was used since this had improved the correlation of the NO_x results during the pilot zone development tests.

The results of this comparison for the engine conditions run on the pilot fuel only are shown in Figure 20. Only the subsonic idle and descent conditions show large reductions in NO_x levels, but fortunately the current ICAO NO_x parameter is dominated by the contributions from take-off and climb out.

Figure 21 shows a similar comparison for the pilot zone NO_x levels at the other conditions of climb out, take-off and cruise. These levels looked encouraging since large reductions would be required to ensure that the low NO_x benefits of the LPP combustion were realised.

The pilot zones showed good combustion efficiency levels at all power conditions with the exception of SST idle- see Figure 22. The SST idle efficiency of 96.5% was slightly lower than that achieved in the earlier pilot zone development trials, though it is felt that this could be improved if required.

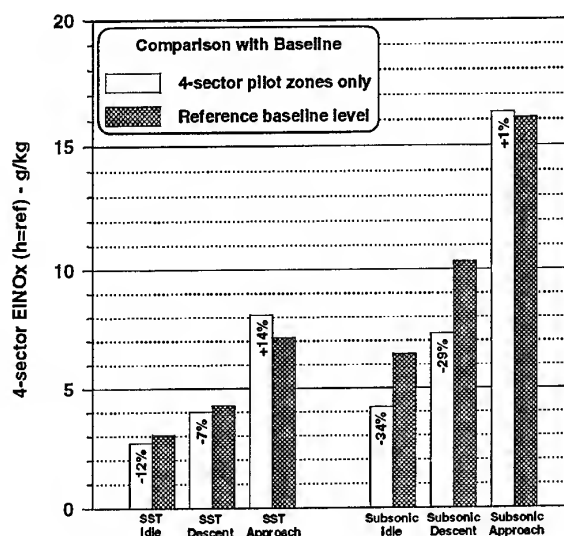


Figure 20 EINO_x at idle, descent & approach

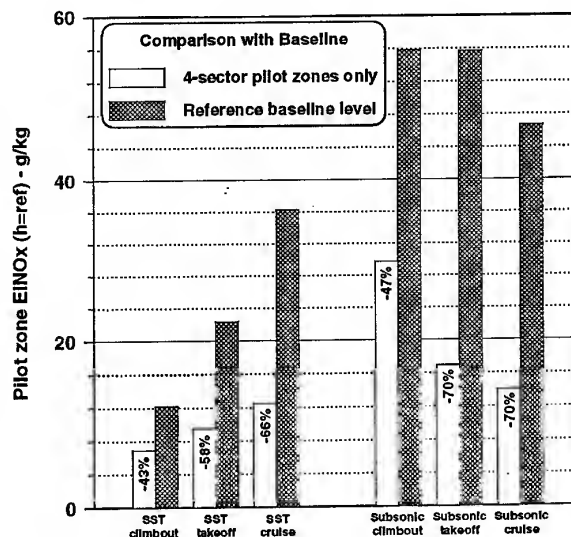


Figure 21 Pilot EINO_x at climbout, take-off & cruise

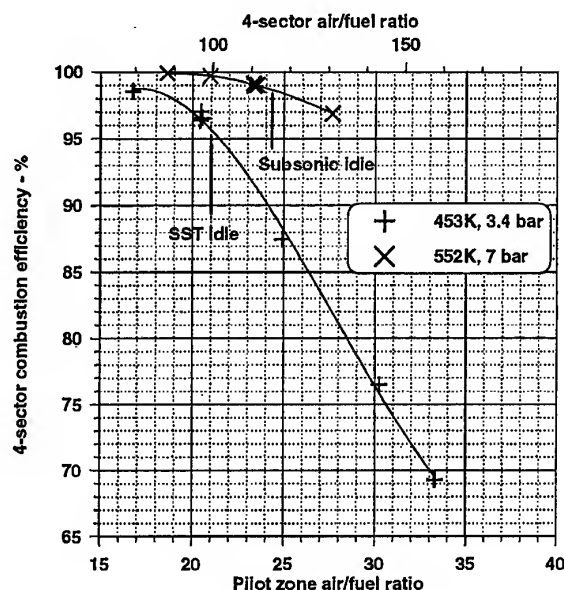
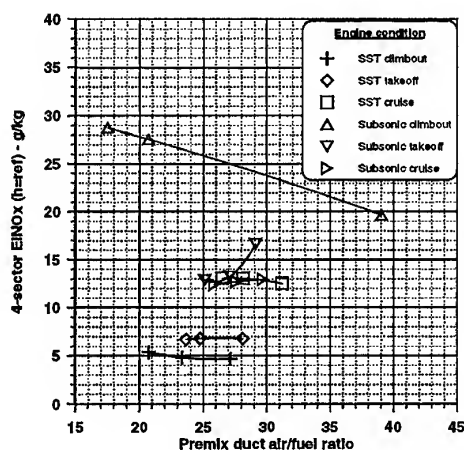


Figure 22 Idle combustion efficiencies

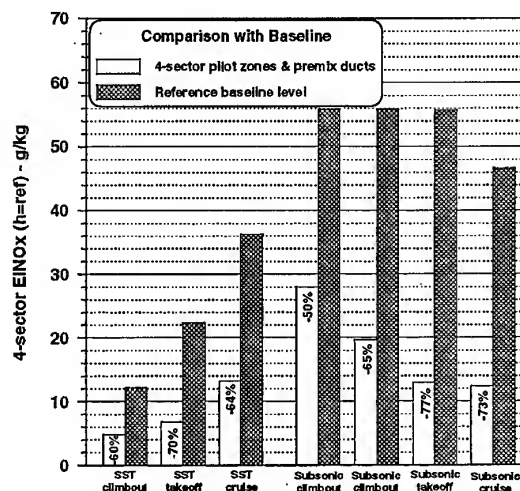
The 4-sector combustor was then run over the simulated engine conditions of climbout, take-off and cruise with both the pilot and premix ducts fuelled. At each condition a complete 5x42 point gas analysis traverse (see Section 12) was completed at the nominal design pilot/premix fuel split. The fuel split was then varied slightly either side of the design value and the gas analysis traverse repeated. The data for each condition was then interpolated precisely at the design fuel split. For example the $EINO_x$ data was plotted against the calculated premix duct air/fuel ratio - see Figure 23. The interpolated data for climbout, take-off and cruise is shown in Table 4. Detailed smoke measurements were only taken at one of the premixed-fuelled conditions since there was only a single smoke meter available. These measurements confirmed that LPP combustion produces very low smoke.

Figure 23 4-Sector $EINO_x$ results

	Combustion efficiency %	$EINO_x$ h=ref g/kg	Smoke SN
SST climbout	95.3	4.8	-
SST take-off	97.4	6.8	-
SST cruise	97.6	13.2	-
Subsonic climbout 4 ducts fuelled	94.8	19.7	-
Subsonic climbout 2 ducts fuelled	99.9	28.0	-
Subsonic take-off	99.8	12.9	-
Subsonic cruise	99.5	12.4	1.2

Table 4 4-Sector results at climbout, take-off & cruise

Comparisons with the reference baseline NO_x levels were again made and are shown in Figure 24. There were significant NO_x reductions at all the conditions, though the subsonic climbout condition showed the least reduction. It had been recognised that the calculated premix flame temperature could not be kept within the 1700-2100K band whilst maintaining an efficient pilot zone. Figure 4 shows that the premix flame temperature would be approximately 2400K with only two ducts fuelled. If the same total premix fuel was supplied by four ducts the premix flame temperature dropped to about 1750K. This was done and Figure 24 shows that the overall NO_x reduction improved from 50% to 65%. However, the combustion efficiency dropped from 99.9% to 94.8%. Although not tested, the solution would have been to divide the fuel 30% to the two pilot zones and 70% to the four premix ducts. This would have given a flame temperature of approximately 2000K for both pilot and premix zones. The subsonic cruise fuel split gave similar zonal temperatures and the test results gave an acceptable combustion efficiency with a 73% NO_x reduction.

Figure 24 $EINO_x$ at climbout, take-off & cruise

The combustion efficiency levels for the SST climbout, take-off and cruise were too low. Figure 25 shows the 4-sector combustion efficiency results for climbout, takeoff and cruise plotted against a calculated premix flame temperature. It shows that a zonal flame temperature of 2000K did not necessarily produce a high combustion efficiency. Work by other partners (see Sections 8 & 9) suggested that the premix duct performance needed to be improved. The SNECMA CFD calculations said that only 75% of the fuel was evaporated by the exit of the duct at SST cruise conditions. The LIF measurements by Volvo confirmed the presence of fuel droplets at the duct exit even at high inlet air temperatures. At air inlet temperatures below 700K the LIF measurements showed poor rates of fuel evaporation.

However gas analysis measurements made by ONERA on a single premix duct gave combustion efficiencies between 99.7% and 99.9%. The test conditions covered pressures of 7bar to 17bar and flame temperatures of 1750K to 2000K. An examination of the combustion efficiency contour plots at the exit of the 4-sector combustor showed that at least one of the four premix ducts had an uneven fuel distribution.

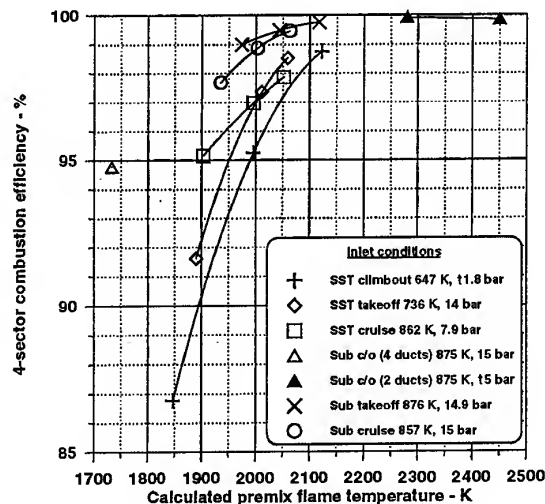


Figure 25 4-sector combustion efficiency

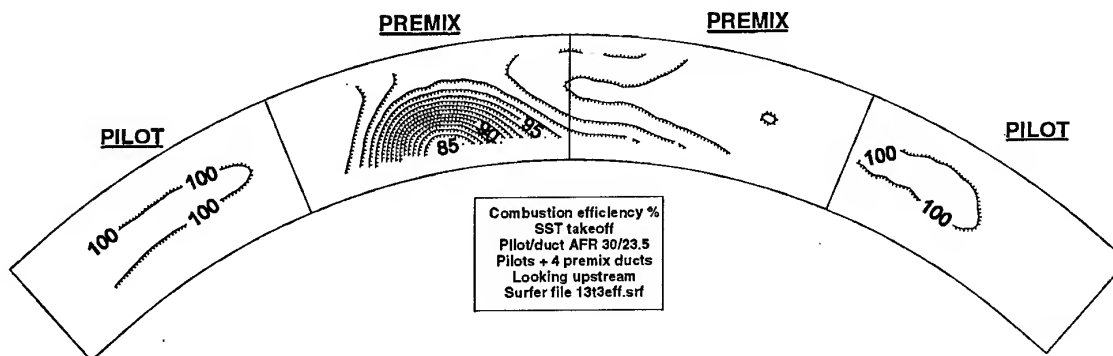


Figure 26 Combustion efficiency at SST takeoff

From Figure 26 it can be seen that the poor combustion efficiency was confined to the lower half of the left-hand premix sector, i.e. down-stream of one premix duct. The design of the prefilmer had proved difficult to make, and there had been previous problems of partial blockage of internal fuel feed holes.

It is therefore assumed that the low combustion efficiencies at SST take-off and cruise were due to a problem with one of the prefilers. At SST climbout the prefilmer with the poor fuel distribution was not being used since only the two outer premix ducts were fuelled. Therefore the low combustion efficiency was due to the relatively poor fuel vaporisation performance of the design at low air inlet temperatures (<645K). This poor fuel vaporisation at low inlet temperatures had been noted during the LIF measurements by Volvo.

14 SUMMARY

This work has demonstrated that it is possible to reduce combustor NO_x levels by about 75% at takeoff, climbout and cruise conditions using a piloted LPP system. These NO_x reductions may be achieved whilst maintaining very low smoke levels and good levels of combustion efficiency.

Using a straight-through, low loss premix duct design, no problems of autoignition or flashback were experienced during the testing. However, the fuel prefilmer design was susceptible to internal fuel feed blockage resulting in poor fuel distribution. The prefilmer/premix duct design also needs improved fuel vaporisation performance at air inlet temperatures below 700K.

The staging of the main premix duct fuel was achieved without any apparent significant combustion delay.

The 'conventional' pilot zone almost achieved the required NO_x reductions at take-off, climbout and cruise, but the design would not have given sufficient altitude reight performance. Further development work is required to produce a practical 'low NO_x ' pilot zone.

It proved difficult to produce a piloted LPP combustor that could operate successfully across the engine operating envelope without at least two fuel staging points. Even then, the stoichiometry to achieve ultra-low NO_x levels was compromised. Therefore it is thought that some form of air staging will be required to achieve stable, efficient, low NO_x performance of the complete engine power range.

15 ACKNOWLEDGEMENTS

This paper was based on work carried out during the CEC funded BRITE EURAM LOWNOX II programme. The authors are grateful for permission from the Commission to publish this paper. The authors are also grateful for the valuable work contributions made by SNECMA, VOLVO, Lund University and ONERA during the work programme.

© British Crown Copyright 1998/DERA
Published with the permission of the controller of Her
Britannic Majesty's Stationery Office

REFERENCES

- 1 Tilston J R, "Rig and combustor definition", DERA Report DRA/AS/AP/PTD/CR/94017, Feb 1994.
- 2 Wedlock M I and Tilston J R "Pilot zone development", DERA Report, DRA/AS/AP/CR/93016/1, December 1993
- 3 Aubert S., "3D CFD calculation of premixed duct flow", SNECMA Report YKC No 7195/YKC/94, December 1994.
- 4 Seoud R.E., "CFD assessment of lean premixed prevaporised ducts configuration to improve combustor durability", DERA Report DRA/AS/PTD/WP/95186/1, July 1995.
- 5 Kaaling H & Löfström C, "LIF measurement of premix duct performance", Volvo Report 9979-1093, November 1994.
- 6 Guin C, "Adaptation of Volvo & DRA premix ducts on the tubular combustor of ONERA and combustion tests", ONERA Report, RT 63/1629 EY.
- 7 ICAO, Annexe 16 Volume II Aircraft engine emissions, First Edition 1981.
- 8 Tilston J R, "The averaging of gas analysis data allowing for density and velocity weighting", RAE Tech Memo P1213, August 1991
- 9 Lipfert F W, "Correlation of gas turbine emissions data", ASME 72-GT-60, March 1972.
- 10 Sarli V J, Eiler D C, & Marshall R I, "Effects of operating variables on gaseous emissions", APCA Conference on Air Pollution Measurement Accuracy, New Orleans, Oct 1975.

PAPER No. 23
Wedlock & Tilston
(presenter: J. Tilston)

Question 1: I. Gokalp, LCSR-CNRS, France

Do you have an explanation for the increase in NOx emissions index with pressure? Would it be possible that the strong decrease of the fuel vaporization rate with increasing pressure plays a role? The dependency has been demonstrated both experimentally and numerically at the LCSR.

Answer:

We know that fuel/air unmixedness and fuel evaporation quality were not very good in the present tests from the atmospheric pressure LIF and MIE-scattering work done at 650 °K for us separately at Lund University. It seems likely that both unmixedness and evaporation would improve markedly at 16 bar and 900 °K. The pressure dependency almost certainly shows that these parameters were not as good as we had hoped.

Question 2: N. Brehm, BMW-RR, Germany

Was the relight capability of the pilot zone tested at sub-atmospheric conditions, or checked by correlations? How do you think that good altitude relight and low NOx can both be met?

Answer:

The relight capability was estimated from existing correlations. It was not demonstrated experimentally because this aspect had not been a feature of the original programme plan - we had tacitly assumed that both relight and NOx objectives could be met in the same combustor. Although the calculations indicated that the pilot volume was independent, there is at least a reasonable chance that the relight target could be met because the pilot combustion process was found to continue into the main LPP combustion volume. How much additional heat release can be achieved (for engine acceleration) in the main zone from this carry-over really needs to be measured experimentally at low pressure. I think that the combustor architecture could be adjusted to improve relight, but this would require a dedicated research activity. The relight capability therefore, remains unproven.

Question 3: M. Razdan, RR-Allison

The test pressure was reduced compared to actual engine conditions. Can the concept work safely at engine overall pressure ratios of say, 50:1?

Answer:

Yes, this a real concern. ONERA has tested premix ducts to 22 bar pressure without autoignition, but for high pressures we really do not know.

Question 4: G.J. Sturgess, ISSI, U.S.

In your design study, and in the emissions measurements that you presented, it was assumed that the combustor would be operating on the pilots only at the approach power condition. From a safety point of view, in the event of a refused landing and a go-around, this is dangerous because a main-stage light-off would be necessary for the go-around. It is doubtful of a certification agency would permit this. Operating at approach power with both combustor stages fueled and burning would increase all of the gaseous emissions.

Answer:

I agree.

Advance Fuel Injection Strategies for High Performance Gas Turbine Engines

Scott Samuelson

Vince McDonell

UCI Combustion Laboratory

University of California

Irvine, CA 92697-3550 USA

1. SUMMARY

Advanced gas turbine combustion systems will demand fuel injection strategies that are efficient in the rapid mixing of fuel and air, sophisticated in the ability to control the spatial distribution of the fuel, and both sufficiently flexible and intelligent to accommodate change over the duty cycle of the engine. The paper reports performance of a candidate injector and strategies, through mechanistic studies with advanced diagnostics, to optimize the system.

2. MOTIVATION

One of the major challenges to gas turbine engineering today is the requirement to reduce pollutant emissions, especially oxides of nitrogen (NO_x), from next-generation aeroengines (Prather, et al. 1992; Stolarski, et al. 1995). One strategy is to operate the combustor lean overall with little or no wall jet injection of primary or secondary air. While a number of lean burn, low NO_x , gas turbine combustor concepts have been demonstrated using only gaseous fuel, there is a need to develop and demonstrate a design that uses liquid aviation fuel (Tacina 1990).

Conventional gas turbines have less than complete mixing because the fuel and air are separately introduced into the primary reaction (dome) zone. To be successful, the injection is accomplished such that the fuel and air are well mixed prior to reaction. Furthermore, the fuel-to-air ratio of this mixture is lean relative to conventional combustors, and all the combustion air enters through the injector. As a result, the reaction temperature is lower than that of conventional combustors. Lower reaction temperatures result, in principle, in a direct reduction of thermal oxides of nitrogen (Zeldovich 1946).

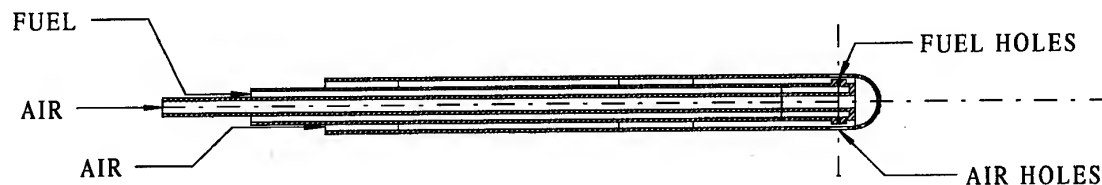
Since a key strategy to meeting the goals for advanced fuel injector concepts involves tailoring of the fuel air mixture, diagnostic methods amenable to characterization of the mixture are needed in order to successfully evaluate any injection concept developed. As a result, the objectives of the current effort are:

- Develop and evaluate a candidate injector concept for advanced liquid fired gas turbine combustors.
- Develop and apply diagnostics to characterize fuel/air mixing for liquid fuel injectors.
- Apply the diagnostics to develop mechanistic understanding of the candidate injector concept to guide optimization of the design.

3. ADVANCED LIQUID FUEL INJECTOR CONCEPT

An injector design designated as the Lean Burn Injector (LBI) has been developed for use in advanced gas turbine engine concepts (Samuelson, et al., 1995). The LBI has two main components, the injector and a mixing region dubbed the "quarl." The quarl defines the dome geometry, and utilizes a design similar to a "swirl cup" (Wang, et al. 1994) with an internal venturi contour.

The LBI design was tested at both atmospheric and elevated pressures. The goal of the atmospheric pressure testing was to develop the LBI concept into a simple, low cost, reasonably sized, and low maintenance injector with a relatively uniform reaction. The goal of the elevated pressure testing, which followed the atmospheric pressure testing, was to evaluate the emission performance of the final LBI design at inlet conditions which were representative of practical gas turbine engine applications.



CROSS SECTIONAL VIEW

Figure 1. LBI injector Cross Section (Shaffar and Samuelsen, 1998).

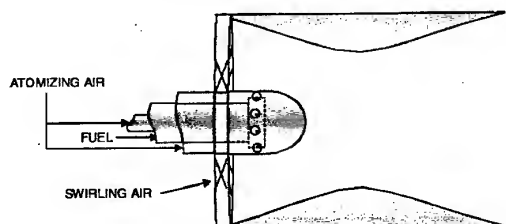


Figure 2. LBI Quarl Design.

Atmospheric pressure tests were utilized to develop the LBI design for four reasons, (1) to provide optical access for expeditious qualitative evaluation of the reaction, (2) to allow quick hardware changes, (3) to rule out poor designs because in general, poor performance at atmospheric pressure conditions is a good indicator of similar performance at elevated pressure conditions, and (3) to reduce the development cost since atmospheric pressure testing is significantly less expensive than elevated pressure testing.

3.1 Liquid Injector Development

The performance of the injector can have a major impact on the performance of the combustor in terms of the emissions of oxides of nitrogen. The combustion parameters that are influenced or determined by the injector design include (1) the atomization quality, (2) the initial dispersion of the droplets, (3) the time required for vaporization, and (4) the unmixedness of the fuel and air prior to reaction.

Most current gas turbine combustors have fuel injectors that utilize an axial spray direction. This method of fuel injection results in a partially mixed (fuel and air) reaction zone. This unmixedness can result in significant levels of NO_x emissions (Lyons, 1981, Fric 1993). The LBI injector design departs from conventional design by changing the primary injection direction of the fuel from axial to radial with the goal of inducing enhanced mixing of the fuel and air prior to reaction. The design uses eight radial injection points for improved spatial mixing.

A number of radial injected, lean burn combustors have been designed and demonstrated using gaseous fuels (Alkabie, and Andrews 1990; Alkabie, Andrews, and Ahmad 1988; Matsuzaki, et al. 1992; Smith 1992). It is important to note, however, that the design developed in this work utilizes liquid aviation gas turbine fuel (Jet A). The development of a liquid fueled combustor is more challenging than a gaseous fueled combustor due to the additional steps associated with atomization and vaporization.

The LBI incorporates a plain jet, airblast injector. An airblast injector was selected for a number of reasons including (1) simplicity of manufacture, (2) durability, (3) knowledge regarding atomization performance, and (4) suitability for gas turbine engine application (Lefebvre 1989).

The LBI injector is constructed using three concentric tubes, as illustrated in Figure 1. Fuel flows in the middle tube, and air flows in the inside and outside tubes. The fuel exits the middle tube through eight radial holes. Between this middle tube and the outside tube, the air and fuel interact. As the atomization air exits the eight air holes in the outer tube it accelerates, creating a shear force between the air, and the liquid jet. In addition to contributing to the total atomization air, the airflow exiting the inner tube provides cooling to the nose of the injector. The nozzle air and fuel hole diameters are 2.235 mm, and 0.343 mm respectively. This critical aspect of the injector is worthy of additional investigation which is described in Section 5.

3.2 Quarl Geometry

The quarl assembly includes the swirler, and an internal venturi contour as illustrated in Figure 2. The contracting volume between the swirler and the throat of the venturi acts as a fuel and air-mixing zone.

In the LBI design, all of the combustion air is sent through the swirler. This feature eliminates the need to inject additional air downstream to complete the reaction. The overall length and total weight, therefore, of this design can be significantly less than a conventional combustor.

A conventional dome geometry, without the venturi, was tested using the LBI injector design. In this configuration, the reaction extended upstream to the LBI injector. This is undesirable due to the heat loading on the injector and the residual unmixedness in the fuel/air charge. Test results with this conventional dome geometry revealed high pollutant emissions, and poor stability. The venturi, therefore, is required to (1) prevent hot products from extending to the injector, and igniting the fuel at the injector, and (2) provide a region for mixing prior to reaction.

In the present application, the quarl outside diameter is 80.0 mm, and the quarl length is 57.15 mm. The throat diameter, and other dimensional information are given in Table I. The quarl configurations for the atmospheric and elevated pressure testing were slightly different due to the significantly different

flow conditions, which are illustrated in Table II.

3.3 Autoignition and Flashback

The residence time of the fuel droplets inside the quarl determines the amount of droplet evaporation prior to reaction. (The quarl residence time is herein defined as the time for a fuel droplet to travel a path from the exit port of the atomizer to the throat of the venturi.) In the elevated pressure reacting experiment the quarl residence time was approximately 0.7 msec.

Autoignition will occur if the residence time of the flammable mixture exceeds the autoignition delay time. The autoignition delay time was estimated from Lefebvre, Freeman and Cowell (1986) as being on the order of 10-100 msec. Since the residence time was only 0.7 msec, autoignition was neither

TABLE I. LBI QUARL DIMENSIONS

Test Pressure (atm)	Quarl Length (mm)	Quarl Throat Diameter (mm)	Quarl Inlet Diameter (mm)	Quarl Contraction Angle	Quarl Expansion Angle
1	57.15	38.10	63.50	18.4°	45°
5	57.15	44.45	76.20	21.0°	45°

TABLE II. LBI TEST CONFIGURATION AND CONDITIONS

Parameter	Atmospheric Pressure Test Value	Elevated Pressure Test Value
Fuel type	Jet A (liquid)	Jet A (liquid)
Injector type	UCI LBI 8 jet, air-blast nozzle with venturi quarl	UCI LBI 8 jet, air-blast nozzle with venturi quarl
Combustor inside diameter	76 mm	74 mm
Combustor material	Tubular quartz	Hastalloy-X, lined with refractory
Pressure	1 atm	5 atm
Inlet air temperature	444 K	700 K
Fuel mass flow rate	2.6 - 3.9 kg/hr	17.9 - 29.1 kg/hr
Total air mass flow rate	76 kg/hr	653 kg/hr
Reference velocity	5.5 m/s	17.0 m/s
Combustor Air Pressure Loss	5.3 %	4.8 %

expected, nor encountered in the tests conducted.

Flashback is another concern in any design that mixes the fuel and air prior to reaction. The design of the venturi was intended to eliminate any possible separation within the quarl. During both the atmospheric and elevated pressure testing, flashback was not observed.

3.4 Combustion Performance Tests

Testing was conducted in the UCICL elevated pressure facility to assess the performance of the baseline configuration. The NO_x emissions were of particular interest. The results obtained are presented in Figure 3. The results appear very encouraging, falling within the optimal performance of a lean premixed prevaporized system according to Tacina (1990). While the design process developed for the LBI concept appears successful (Shaffar and Samuelsen, 1998), the physics of the processes occurring within the injector are not delineated. As a result, it is possible that additional improvement in performance can be realized by optimization of the injector configurations.

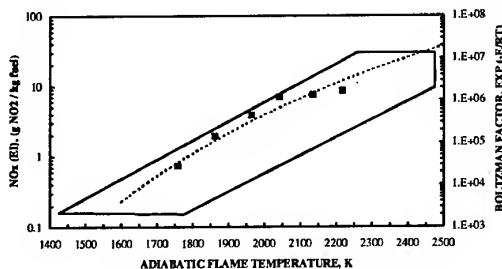


Figure 3. NO_x emissions at 5 atm.

While this could be accomplished to some extent through "in/out" measurements and trial and error, it is desirable to understand, from a more fundamental view, the processes occurring in the LBI device. Detailed measurements offer this possibility and the strategy for this approach is described in the next section.

4. DIAGNOSTICS FOR MECHANISTIC UNDERSTANDING

Experimental methodologies for the characterization of liquid sprays have evolved considerably over the past decade (Bachalo, 1994). In order to be effective for characterizing advance fuel injection systems, several attributes are desirable. In particular, the mass distribution of fuel is of great interest as the uniformity (or lack of) may be directly related to combustion performance. While the mass distribution is of interest, additional critical information relative to combustion performance is the size and velocity (or momentum) of the droplets)

4.1 Planar Methods for Sprays

While intrusive, mechanical devices characteristics have been developed into fairly sophisticated, automated devices (e.g., McVey, et al., 1987). Optical methods such as Planar Laser Induced Fluorescence offers an opportunity to obtain similar information but in a non-intrusive fashion (e.g., Melton and Verdick, 1984). In recent years, several examples of application of planar methods for characterizing the distribution of fuel produced by injection systems have appeared (Talley et al., 1996, Allen et al., 1995, Bazile and Stepowski, 1995).

The most basic approach for the planar method is illustrated in Figure 4. A laser sheet is formed by some combination of cylindrical and spherical optics. A digital camera is convenient for imaging the energy of interest. Depending upon the information desired, either continuous or pulsed lasers can be employed. Continuous lasers offer a more convenient means of illuminating the spray since standard video protocols can be utilized. In particular, if time averaged information is desired, a continuous light source is adequate. If instantaneous information is required, a pulsed laser offers more flexibility.

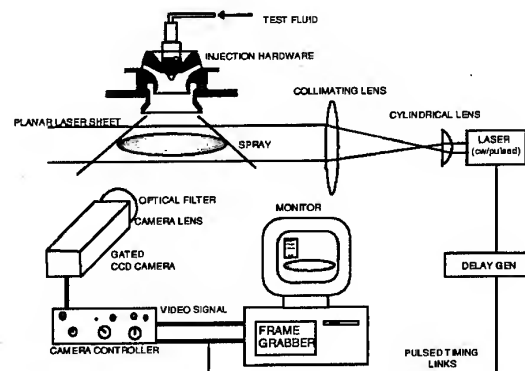


Figure 4. General Setup.

4.1.1 Light Scattering

For purpose of assessing the distribution of material, several approaches are possible. In the most basic case, elastic light scattering can be utilized. In this case, a filter may not even be required. Scattering has been widely employed as a qualitative visualization tool and is effective in capturing the basic structure of sprays. Elastic light scattering is approximately proportional to the diameter of the droplets squared, and, in principle, can be used to gain information regarding drop size. Unfortunately, scattering is dependent upon a variety of optical parameters, including particle size, refractive index, wavelength, and viewing angle. Despite the issues associated with using scattering for quantitative

results, light scattering is a powerful means of visualizing spray structure, and, in a quality control situation where a reference image can be compared to images of interest, may be adequate (e.g. Wang, et al., 1997).

4.1.2 Fluorescence

If a suitable light source is selected in conjunction with a suitable test fluid, fluorescence can be induced. Fluorescence is dependent upon the concentration of the fluorescing molecules. If a molecule which can be made to fluoresce is present within the test fluid in a homogenous fashion, then the fluorescence can be related to the volume of material. Some materials may fluoresce naturally (e.g., ringed hydrocarbons), while others may not (e.g., octanes, alcohols, water). In a laboratory situation, it may be desired to utilize safe test fluids. In this case, a suitable dye can be added to the fluid (e.g., rhodamine, fluorescein). If a dye is added, it can be selected such that its absorption spectra conveniently overlaps common laser wavelengths (e.g., Ar⁺).

The basic approach for the application of fluorescence can be described by Equation 1:

$$I_f = I_o \alpha \int n_i D^3 dn \quad (1)$$

where

I_o = incident light intensity

α = quenching factor

n_i = number of drops of size D_i

To illustrate the basic response of a common dye and laser selection, Figure 5 illustrates the spectra of with fluorescein dissolved in methanol.

In the case of fluorescence, the goal is to image the fluorescence rather than elastic light scattering. As a result, some means of blocking out the elastic scattering is required. An optical filter is one option and a filter suitable for the fluorescein/488 nm system is shown in Figure 5 as an example. In this case, the fluorescence is well red-shifted from the excitation and a filter to cut the scattering is readily available.

While the application of planar laser based techniques to sprays provides information in an efficient, non-intrusive manner, the degree to which the information is quantitative is dependent upon the ability to account for a wide variety of factors including: (1) secondary scattering, (2) extinction of the incident light and signal, (3) laser sheet intensity variation in space and time, (4) perspective

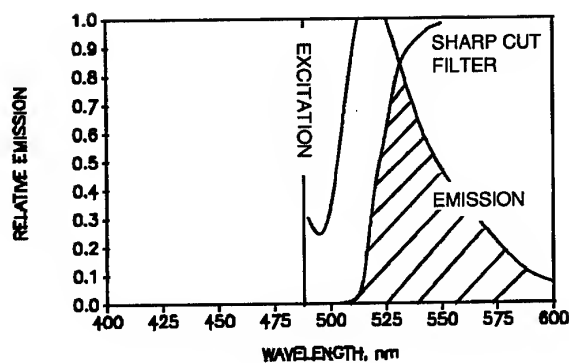


Figure 5. Emission Characteristics of Fluorescein in Methanol Excited at 488 nm and Spectral Response of Color Sharp Cut Filter.

corrections, and (5) electronic transfer function uncertainties. These issues and some potential solutions are described in Talley et al. (1996).

4.1.3 Size

In addition to planar measurement of the mass distribution, the potential for planar method for measurement of the local Sauter mean diameter has also been demonstrated (Sankar, et al., 1996). This approach has not yet been widely applied.

4.2 Droplet Size and Velocity

In the absence of a suitable planar method for particle size, line-of-sight methods such as laser diffraction are potentially useful, but have limited spatial resolution. Phase Doppler interferometry offers the ability to provide highly detailed information at a point. While time consuming to apply, PDI offers by far the most information from the spray--temporally resolved measurements of droplet size and multiple components of velocity at a point.

For the purpose of the present effort, laser light scattering, optical patterning of the mass distribution and phase Doppler interferometry appear well suited for obtaining the required information about the spray injection process.

5. MECHANISTIC STUDIES

Since the radial airblast injection process is at the heart of the LBI concept, mechanistic studies have been conducted to understand how various parameters influence the size and dispersion of the droplets. To this end, a test facility has been developed to isolate the effect of the radial injector and the cross flow within the LBI quarl. Through the mechanistic understanding provided by these results, the strategy for further optimizing the LBI performance can be developed.

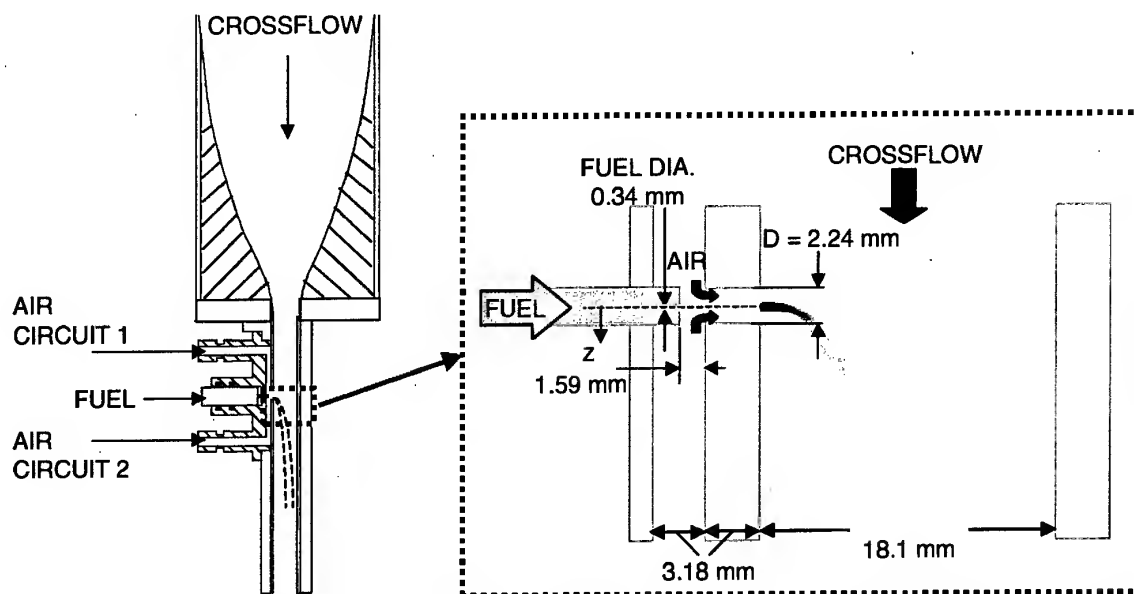


Figure 6. Experimental Setup for Mechanistic Study of Single Radial Fuel Injection Point.

Figure 6 illustrates the basic approach utilized which essentially isolates one of the 8 injection points and allows the detailed characterization of the two-phase flow to be conducted using the optical diagnostics described in Section 4 to be applied. The mechanistic study facility allows the key aspects of the LBI concept to be retained, including the inclusion of the counterflowing airblast air, the injection of the liquid in an intact thin rod of material. The crossflow can be varied in terms of both velocity magnitude and profile in order to evaluate precisely what is occurring within the LBI. The facility can also be placed within the UCI high pressure facility to allow the effects of crossflow pressure and temperature to be studied using the same optical diagnostics employed for the atmospheric facility. The setup is illustrated in Figure 7.

5.1 Atmospheric Studies

Under atmospheric conditions, initial studies were conducted to establish the effect of basic operating conditions on the fuel distribution and droplet characteristics using both PLIF and PDI.

Figure 8 presents results from an atmospheric study using PLIF to evaluate the fuel distribution at a plane 10 mm downstream of the injection point and PDI to characterize the droplet sizes produced as a function of the atomizing air pressure drop. This result allows understanding of the importance of the atomizing air relative to the penetration and dispersion of the droplets.

Figure 8 presents four processed PLLIF images and corresponding PDI data for variations in the air-to-liquid ratio (ALR). For the PLLIF images, the view

is that of the mainstream air approaching the fuel injection hole, with the left axis representing the wind tunnel wall (i.e., injector panel). This top view presents the jet penetrating from the y-axis out into the crossflow of air in the x direction. A 10-level gray scale is employed to represent contours of fuel mass fraction from 0 to 1.0. A value of 0 (white in color) denotes a zero concentration of fuel and

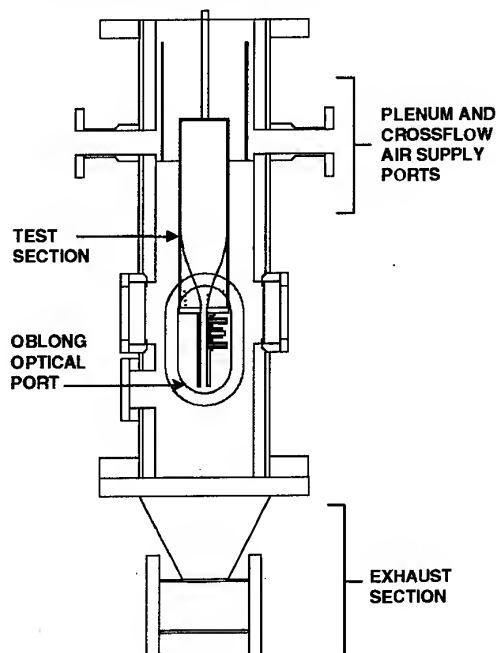


Figure 7. Installation of the Mechanistic Study Test Rig in the UCICL High Pressure Facility

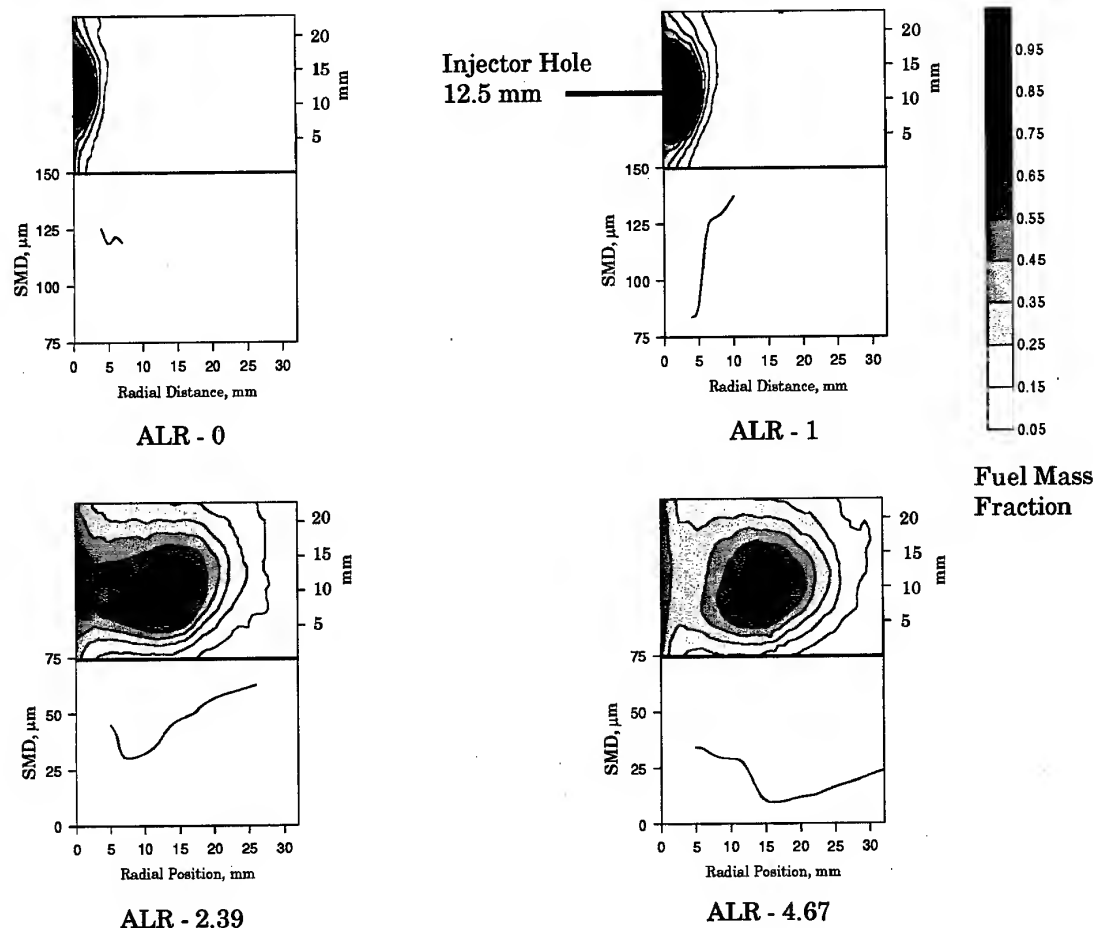


Figure 8. PLIF measurements of fuel Mass Dispersion and Droplet Size along the axis of the injector.

therefore can be considered pure mainstream flow. For convenience, the highest fuel mass fraction (0.95 - 1.0) is depicted as black in Figure 8. These images are overlaid onto PDI data taken in the plane of the jet. All images and PDI data presented are at a plane located 10 mm downstream of the injector hole. Due to clipping on the receiver, no data could be acquired closer than 5 mm from the injector panel. Additionally, the radial distance outward is limited by the number of drops present. Occasionally the PDI data extends past what appears to be the edge of the PLLIF image. In these areas, some drops are present but are not in large enough numbers to be detected by the PLLIF system.

A substantial change in both penetration and spray area can be observed as the air-to-liquid ratio is increased from 0 to 4.67. The mass flow of fuel was held constant for these four plots at 0.146 g/sec.

For the ALR-0 case, no atomizing air is introduced. As seen in the figure, the fuel is only able to penetrate into the mainstream a maximum distance of approximately 7 mm. The majority of the fuel is confined to the boundary layer and, when running at this condition, fuel drips down the tunnel wall. This

condition yields poor dispersion and mixing of the fuel. The atomization of the liquid jet is also very poor at this condition. The SMD remained fairly constant at a value of approximately 120 microns for all radial locations. For the ALR-0.947 case, not much improvement is attained. Although the small amount of atomizing air (0.139 g/sec) provides sufficient momentum to push the fuel further into the crossflow, it is still not capable of distributing the fuel uniformly. The PDI data demonstrates that the atomizing air is pushing the fuel outward. Smaller SMD drops are found very near the wall. The SMD then rises steeply when moving out directly under the fuel jet.

A profound improvement in penetration and spray area is evidenced when operating at the ALR-2.39 case. For this condition the air flow is increased to 0.349 g/sec. The fuel penetrates out approximately 28 mm into the crossflow and is distributed more uniformly. A noticeable improvement in atomization is also observed at this condition. The maximum SMD detected is 60 microns, with the largest drops penetrating further into the crossflow.

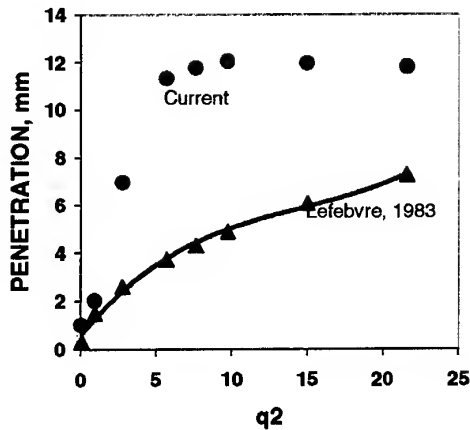


Figure 9. Penetration for the Two-Phase Spray.

Only a slight improvement in penetration and spray area is evidenced when increasing the air further to the ALR-4.67 case (0.684 g/sec air). The maximum concentration of the fuel is reduced one level down to the 0.75 - 0.85 band, but the penetration is essentially the same. The atomization for this condition is dramatically reduced. A reasonably uniform SMD profile was attained, with most drops below 25 microns.

The leveling off in penetration experienced between ALR-2.39 and ALR-4.67 is more clearly seen in Figure 9. This plot presents penetration of the center of mass of the spray versus momentum flux ratio which is defined in Equation 2 for the two-phase jet:

$$q_2 = \frac{(\rho V^2 A)_{\text{airblast}} + (\rho V^2 A)_{\text{liquid}}}{(\rho V^2)_{\text{crossflow}}} \quad (2)$$

Included in Figure 9 is an empirical prediction of jet penetration based on data for air jet penetration through a combustor liner (Lefebvre, 1983). In general, the equation underpredicts the jet penetration. This is a result of the increased momentum associated with the liquid which allows the jet fluid to penetrate farther into the cross stream compared to a single phase jet. The equation is also not capable of predicting the leveling off in penetration for higher jet momenta. An unknown amount of kinetic energy from the atomizing air is consumed in stripping, atomizing, and mixing the liquid. The PDI data demonstrates this with the steadily decreasing SMD's as ALR is increased. Because the equation uses the *initial* jet momentum to predict penetration, it excludes additional energy sinks associated with the atomization and transport of the liquid. Therefore, pure air, or liquid (Reinecke, 1978), jet in crossflow predictions are not sufficient for describing the phenomenon seen here.

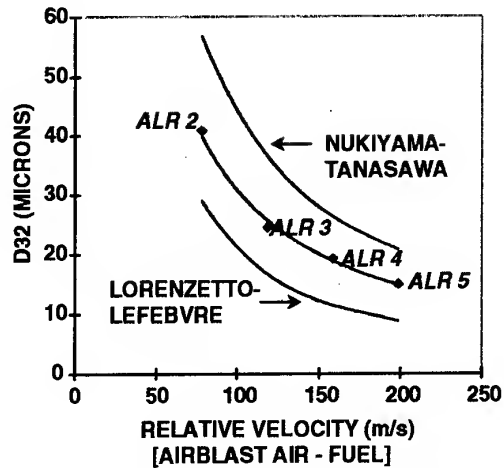


Figure 10. Comparison of Measured and Predicted Drop Sizes for the Radial Air-Blast Injector.

The results illustrate that the dispersion of the fuel reaches an optimal level around an ALR of 3. As a result, this information can be used in the LBI concept to guide the design of the effective area of the atomizing air holes.

In addition to the penetration, the droplet size is also of interest since this will play a role in determining penetration, autoignition characteristics, and vaporization characteristics of the LBI. Since the system appears as an internally mixed air-blast device, it might be expected that the droplet sizes can be described by well known correlations for these devices. However, in the present case, the crossflow velocity is also a potentially important source of momentum which can aid in the atomization. To evaluate this, measurements of the droplet size obtained via PDI are integrated over a plane to generate an average size as a function of operating condition. Figure 10 shows the results from the measured values and the predicted values based on two existing empirical expressions. The results reveal that the atomization process in the present case is well described by existing correlations. However, these correlations do not adequately describe the distribution of the droplet sizes. This is very significant, because even if average sizes meet certain criteria relative to autoignition, the minimum size present can still lead to rapid vaporization possibly giving rise to autoignition. Likewise, despite a sufficiently fine average drop size, the largest droplet sizes present may still survive the mixer region and lead to diffusion flame burning in local regions of the combustor which can lead to an increase in NO_x and CO emissions. That the current combustion tests found reasonable levels of NO_x and CO attests to the fact that the droplet size distribution must not possess extremely long "tails" on the large end.

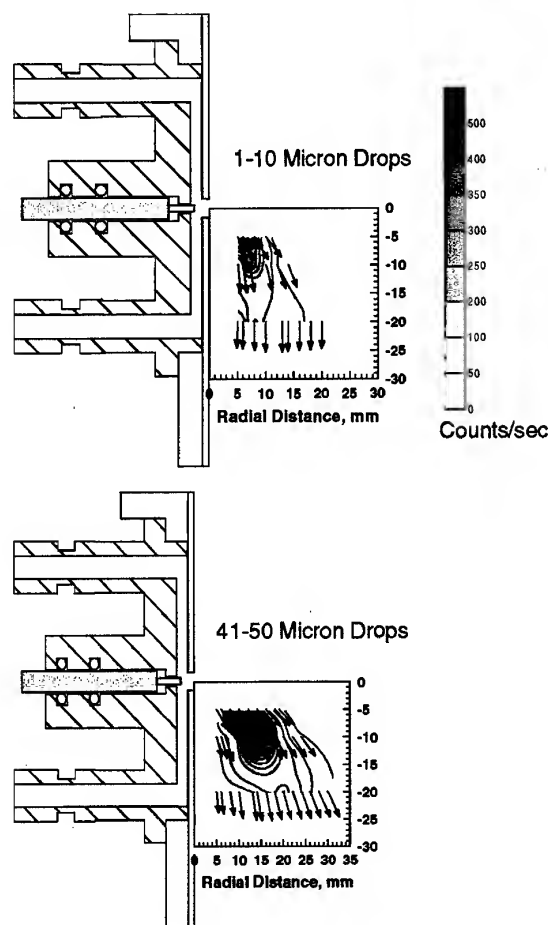


Figure 11. Relative Penetration and Population of Two Droplet Size Classes.

Returning to the mechanistic facility allows some conclusions to be drawn relative to the role of drop size in the penetration of the fuel. It is expected that larger droplets will penetrate farther, but by applying PDI to the problem, the degree to which they penetrate relative to smaller drops can be quantified. Figure 11 presents such information for two size classes of drops. The data rate, in counts/sec, is also overlaid on these plots. The data presented in this figure is for the ALR 2.39 case. This air flow was capable of atomizing the liquid jet into drops in the size range of 1-10 microns. However, at this condition, the airblast was not as great as to prevent the presence of larger drops (70-90 microns). Therefore this case was selected to examine the trajectory of various drop sizes within the crossflow region.

The 1-10 micron drops are immediately forced down at the injector panel wall by the crossflow air. As seen in Figure 11, no drops of this size range are capable of penetrating further than approximately 8 mm from the injector wall. In the near wall region

(<6 mm), the smallest droplets are moving almost directly downward. The 41-50 micron drops are centralized at a radial distance of 8-20 mm from the wall. Additionally, the trajectory of these drops is much less vertical and appears to be dominated by the injector air. Although data for larger drop sizes are not presented here, a similar trend to that demonstrated by the 41-50 micron drops is observed.

The results also reveal that using average sizes in the design process may be misleading. In the case of the LBI, the population of droplets below the average size can lead to rapid vaporization and the possibility of autoignition. If the mass associated with the fine drops is small enough this may not be an issue. At the other end of the spectrum, if many larger drops are present, they can survive the available mixing time and provide locally rich pockets of fuel that can lead to high temperatures, high NO_x, and possibly high CO levels. As a result, using a mean diameter in the process should be done so with care.

With the information provided by PDI, it is possible to determine the optimal droplet size distribution to give the most uniform fuel distribution. From here, methodologies for generating such a size distribution may be developed using existing or, more likely, new design approaches.

5.2 Elevated Pressure Studies

Thus far, results have been presented for atmospheric pressures. The role of ambient pressure is also of great interest for gas turbine applications.

To this end, visualization and PDI measurements of the droplets were obtained within the setup illustrated in Figure 7. These results are shown in Figure 12.

The introduction of airblast air into the system increases spray atomization, as observed in the set of images shown in Fig. 12. Images are presented at each ambient pressure case for three groups of atomizing air pressure drop ranges: a 1.2-1.5% range, a 2.0-2.3% range, and a 2.9-3.3% range. For the purpose of this comparison, these three groups will be referred to as the 1%, 2%, and 3% ranges, respectively. For each image, the ALR and the pressure drop are noted.

The airblast air also has a significant effect in atomizing the liquid, as evidenced by the increase in spray width between the $\Delta P = 0\%$ and 1% cases for the 1-atm case. For the 3- and 5-atm cases, the spray width also increases, but it is unclear to what extent this increase in atomization is attributable to the atomizing air or to the crossflow. The fact that the atomizing air increases liquid jet penetration and exposes more jet surface area to the crossflow air makes the crossflow a potential contributing factor to spray atomization for the 3- and 5-atm cases.

As the atomizing air pressure drop is increased further, however, the airblast air begins to atomize the liquid before it is injected into the crossflow. The 2% group of cases shows an atomized jet leaving the exit plane of the orifice. Increasing the airblast air pressure drop to 3% yields an overly-atomized spray at the orifice exit plane. A nodule of liquid occurs at the trailing edge of the orifice, and is thought to form because of a separation-induced, internal flow pattern in the injector panel orifice.

From these observations, three distinct jet shapes occur for similar atomizing air pressure drops at the different ambient pressure cases. The first regime, which occurs for airblast pressure drops less than 2%, yields an intact jet structure at the orifice exit plane. The second regime, occurring for airblast pressure drops between 2-3%, forms an atomized spray across the orifice exit plane. The third regime accounts for air pressure drops greater than 3%, which produce a fully-atomized spray across the exit plane with the appearance of a liquid nodule at the trailing edge of the jet orifice. The presence of this liquid nodule is undesirable since this condition has been observed to lead to the formation of larger droplets near the injector wall in an otherwise well-atomized field of small droplets.

Note the large sizes present near the wall in the atmospheric results shown in Figure 8. This is attributed to the nodule associated with some internal flow characteristics within the airblast passage.

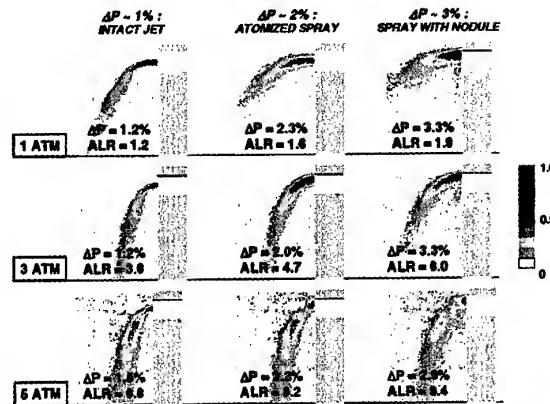


Figure 12. Effect of Ambient Pressure on Two-Phase Spray Injected into a Uniform Crossflow)

The results obtained for high pressure conditions suggest that the findings from atmospheric studies may be difficult to apply. The regimes shown and the conditions where transitions occur have yet to be fully correlated. At this point, development of correlations for the upper and lower surface of the spray jet are being developed in order to provide guidance to the design of an optimized LBI injector (i.e., it will be possible to identify improvements in the hole sizes).

The results are shown using the definition of momentum flux ratio defined in Equation 2 in Figure 13 and appear encouraging. Additional terms

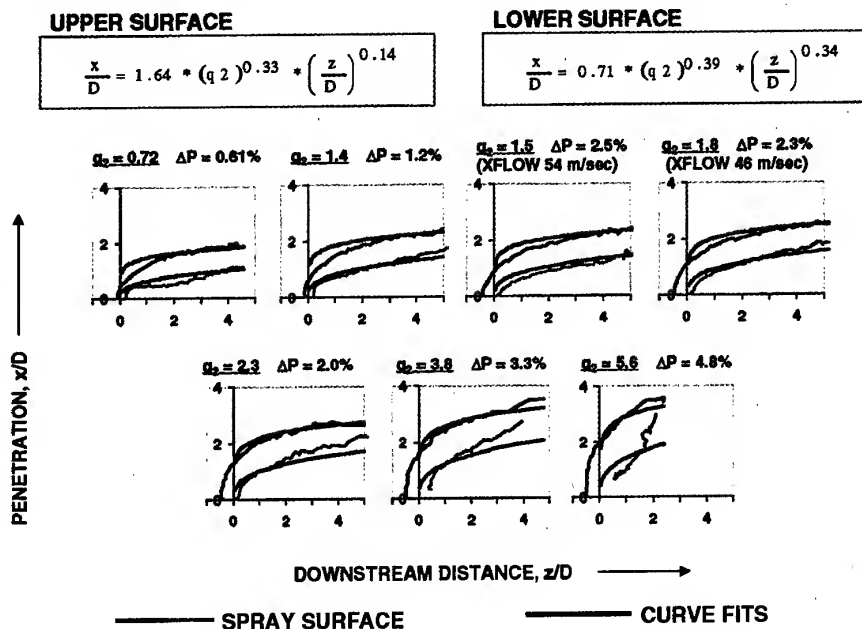


Figure 13. Development of Dispersion Correlations as Function of Operating Conditions at 3 atm.

are currently being added to the correlation terms to account for particle size and evaporation effects.

6. SUMMARY

An advanced liquid fuel injector fuel injector concept for application to gas turbine combustion has been presented. An initial design concept is discussed and good combustion performance is illustrated. To optimize the design and to bring in physics associated with the process, a test facility to provide mechanistic understanding was developed. Recent advances in non-intrusive measurement methods allow for detailed investigation of the processes occurring. The results allow for mechanistic understanding of the basic processes and provide guidance for the optimization of the injector. Figure 14 summarizes the basic mechanisms occurring.

7. REFERENCES

- Alkabbie, H. S., and G. E. Andrews. 1990. Radial Swirlers with Peripheral Fuel Injection for Ultra-Low NO_x Emissions. ASME paper 90-GT-102.
- Alkabbie, H. S., G. E. Andrews, and N. T. Ahmad. 1988. Lean Low NO_x Primary zones Using Radial Swirlers. ASME paper 88-GT-245.
- Allen, M.G., McManus, K.R. Sonnenfroh, D.M., and Paul, P.H. (1995). Planar Laser Induced Fluorescence Imaging Measurements of OH and Hydrocarbon Fuel Fragments in High-Pressure Spray-Flame Combustion, *Applied Optics*, Vol. 34, pp. 6287-6300.
- Bachalo, W.D. 1994, Experimental Methods in Multiphase Flows, *International Journal of Multiphase Flows*, Vol. 20, Supplement, pp. 261-295.
- Bazile, R. and Stepowski, D. (1995) Measurements of Vaporized and Liquid Fuel Concentration Fields in a Burning Spray Jet of Acetone using Planar Laser Induced Fluorescence, *Experiments in Fluids*, Vol 20, pp. 1-9.
- Fric, T.F., "Effects of Fuel-Air Unmixedness on NO_x Emissions," *Journal of Propulsion and Power*, Vol. 9, No. 5, 1993, 708-713.
- Lefebvre, A.H., Freeman, W., and Cowell, L. (1986). Spontaneous Ignition Delay Characteristics of Hydrocarbon Fuel/Air Mixtures, NASA CR 175064.
- Lyons, V.J., "Fuel/Air Nonuniformity—Effect on Nitric Oxide Emissions," *AIAA Journal*, Vol. 20, No. 5, 1981, 660-665.
- Lefebvre, A.H., *Gas Turbine Combustion*, Hemisphere Publishing Corporation, 1983.
- Leong, M.Y., McDonnell, V.G., and Samuelsen, G.S. (1998). Effect of Ambient Pressure on an Airblast Spray Injected into a Crossflow, Paper AIAA-98-3903, Joint Propulsion Conference, July, 1998.
- Lefebvre, A. H. 1989. *Atomization and Sprays*. New York: Hemisphere Publishing.
- Lorenzetto, G.E. and Lefebvre, A.H. (1977).

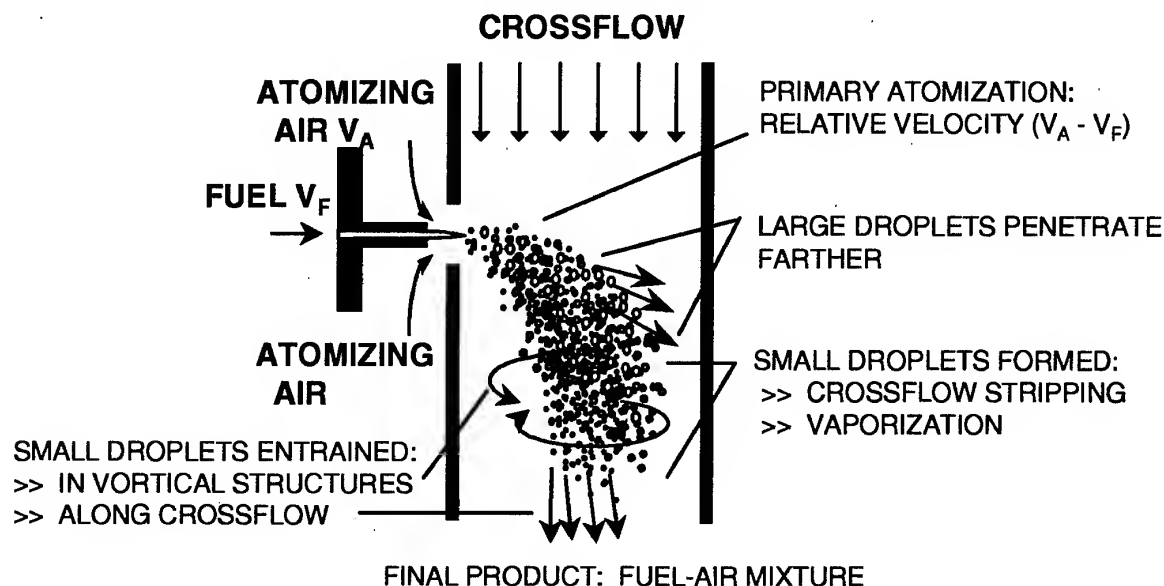


Figure 14. Mechanist Description of the Radial Air-Blast Atomization Process.

- "Measurements of Drop Size on a Plain Jet Airblast Atomizer," *AIAA Journal*, 15(7): 1006-1010.
- Matsuzaki, H., I. Fukue, S. Mandai, S. Tanimura, and M. Inada. 1992. Investigation of Combustion Structure Inside Low NO_x Combustors for a 1500°C-class Gas Turbine. ASME paper 92-GT-123.
- Melton, L.A. and Verdick, J.F. (1984). Vapor/Liquid Visualization in Fuel Sprays, *Twentieth Symposium (International) on Combustion*, The Combustion Institute, Pittsburgh, PA, 1283-1290.
- McVey, J.B, Russell, S., and Kennedy, J.B. (1987). Characterization of Fuel Sprays Using a High Resolution Patternator, *J. Prop. and Power*, Vol., 3, pp. 202-209.
- Nukiyama, S. and Tanasawa, Y. (1939). "Experiments on Atomization of Liquids in an Airstream." *Trans. Soc. Mech. Eng. Jpn.*, 5: 68-75.
- Prather, M. J., et. al. 1992. The Atmospheric Effects of Stratospheric Aircraft: A first Program Report. NASA RP 1272.
- Samuelsen, G.S., Sowa, W.A., and Shaffar, S.W., (1995). "Lean Burn Injector for Gas Turbine Combustor," Patent No. 5,477,685.
- Sankar, S.V., Bachalo, W.D., and Robart, D.M. (1996). ILASS-Americas, 9th Annual Conference, May, San Francisco, CA.
- Shaffar, S.W. and Samuelsen, G.S. (1998). A Liquid Fueled, Lean Burn, Gas Turbine Combustor Injector, to appear, *Combustion Science and Technology*.
- Stolarski, R. S., et al. 1995. Scientific Assessment of the Atmospheric Effects of Stratospheric Aircraft. NASA RP 1381.
- Tacina, R. R. 1990. Low NO_x Potential of Gas Turbine Engines. Presented at the Twenty-Eighth Aerospace Sciences Meeting, Reno, Nevada, January. AIAA-90-0550.
- Tally, D.G., Thamban, A.T.S., McDonell, V.G., and Samuelsen, G.S. (1996). Laser Sheet Visualization of Spray Structure, in *Recent Advances in Spray Combustion: Volume II: Spray Combustion Measurements and Model Simulation*, Ken Kuo, ed., Volume 171, *Progress in Astronautics and Aeronautics*, Chapter 5, pp 113-142.
- Reinecke, W.G., "Drop Breakup and Liquid Jet Penetration", *AIAA Journal*, Vol. 16, No. 6, 1978.
- Wang, G, Delijouravesh, R., Sellens, R.W., Olesen, M.J., and Bardon, M.F. (1997). An Optical Spray Pattern Analyzer, *Proceedings, ILASS-Americas '97*, Ottawa, ON, Canada, May, pp. 261-265.
- Wang, H.Y., V.G. McDonell, W.A. Sowa, and G.S. Samuelsen. 1994. Experimental Study of a Model Gas Turbine Combustor Swirl Cup, Part I: Two-Phase Characterization. *AIAA Journal of Propulsion and Power* 10, no. 4: 441-445.
- Zeldovich, J. 1946. The Oxidation of Nitrogen in Combustion and Explosions. *Acta Physicochimica* 21, no. 4: 577-628.

PAPER No. 24
Samuelson & McDonnell
(presenter: V. McDonnell)

Question 1: D. Santavicca, Penn. State University, U.S.

This is an interesting paper but, if you have already perfectly premixed fuel and air, as was illustrated for your device, how can you further hope to improve NO_x by optimization?

Answer:

We need to optimize the device for things other than NO_x; for example, its operability.

Question 2: T. Rosfjord, UTRC, U.S.

The LBI concept uses swirling, accelerating airflow to achieve its high level of mixing. The fuel injection studies, performed with non-swirling, constant velocity cross-flows, concluded that injectant momentum ratio and spray structure were important to fuel preparation. Are the swirling, accelerating airflow features important to these conclusions? In particular, can you assess swirl without centrifuging droplets excessively?

Answer:

We plan to extend the current study to encompass some of the features you mention. In particular, we have already started to examine how the conclusions are affected by variations in the crossflow velocity profile by introducing controlled gradients into the crossflow stream. In addition, the experimental apparatus can incorporate "vanes" upstream of the fuel injection to study the effect of vane wakes and flow structures on the spray behavior. Relative to the swirling flow centrifuging droplets, this effect will depend on the velocity profile associated with the swirler used in the LBI, and the droplet lifetime compared to the radial acceleration due to swirl. The response of the droplets to swirl can be estimated from a Stokes Number based on the centrifugal force and droplet inertia (e.g. Dring, R. & Suo, M., *J. Energy*, Vol.2, 1967, pp. 232-237.). This response can also be estimated from the response of the droplets to the axial velocity. In the case of both axial and swirling velocities, the droplet size is a critical factor. As a result, it is essential to incorporate the effects of vaporization and droplet lifetimes to provide a more complete understanding. This is also being done as part of the current study through the use of preheated crossflow and PLIF measurements with acetone and Jet-A vapor.

Question 3: T. Ripplinger, MTU, Germany

Do you have any combustion efficiency data corresponding to the NO_x emissions that you showed?

Answer:

These results are to be discussed in detail in a forthcoming *Combustion Science & Technology* paper. For the 5 atm. data presented, the combustion efficiency exceeded 99.8 % in all cases, based on Goodyear (*Combustion Calculations*, MacMillan Press, New York, 1977.):

$$\eta_{comb} = 1 - \frac{[\dot{m}_{C/CO} (\Delta H_{C/CO_2} - \Delta H_{C/CO})]}{\dot{m}_{fuel} CV_{fuel}}$$

where,

- $\dot{m}_{C/CO}$ = mass rate of C reacting to CO
- \dot{m}_{fuel} = mass rate of fuel supplied
- $\Delta H_{C/CO_2}$ = enthalpy of C reacting to CO_2
- $\Delta H_{C/CO}$ = enthalpy of C reacting to CO
- CV_{fuel} = heating value of fuel

Question 4: N. Brehm, BMW-RR, Germany

Lean direct injection systems usually work well at low pressures, showing good NOx reduction, where the NOx reaction rate is low. However, they tend not to be so good at high pressures. Have you made investigations of how the LBI concept performs at realistic higher pressures?

Answer:

We have made studies at higher pressures. The initial experiments have been conducted up to 10 atm, and reveal performance, both in terms of NOx and efficiency, consistent with premixed data compiled from the literature. Additional experiments are planned and these early data need to be repeated, and acquired over a variation in loading. From this platform of data, we will introduce the results from the optimization and mechanistic studies with the goal of improving the overall LBI performance.

Question 5: B.T. Zinn, Georgia Tech., U.S.

The measured NOx appeared to level off with increasing temperature. Do you know why?

Answer:

No.

Turbulent Structure of Generic LPP Gas Turbine Combustors

B. Lazaro

SENER

Severo Ochoa 4, 28760 Tres Cantos, Spain

E. Gonzalez

Universidad Politecnica de Madrid

Pza. Cardenal Cisneros 3, 28040 Madrid, Spain

J. Alfaro, P. Rodriguez, A. Lecuona

Universidad Carlos III

Butarque 15, 28911 Leganes, Spain

1. SUMMARY

An experimental investigation has been carried out aimed at increasing the knowledge of the turbulent flow features that characterize lean premixed prevaporized combustors for aircraft gas turbine applications. Taking into account constraints imposed by the available facilities, the design of the experimental rigs was performed to reproduce the combustor geometry and conditions being investigated under the EU sponsored LOWNOX-III program. Two different facilities were built, allowing both isothermal and reacting flow characterizations. Flow visualization, and two-component LDA and PIV systems were used as experimental techniques. Initial characterizations are presented and discussed in relation to technological relevant aspects such as combustor stability, efficiency and pollutant generation behavior.

2. INTRODUCTION

Recently, much attention is being paid to the development of gas turbine combustors that can offer substantial reductions in the levels of pollutants being discharged to the atmosphere [1]. For commercial aircraft applications, NOx abatement is considered a mayor target in this effort. Its relevance stems from the high percentage of the engine cycle that is spent in the lower stratosphere, where deposition of nitric oxide can be particularly harmful to the ozone layer. Due to their higher operating altitude, NOx control will also be a mayor concern in the development of combustors for high-speed civil aircrafts [2].

Different technologies are being considered to control NOx production in aircraft gas turbine combustors. Noticing the mayor impact that high temperature levels have on the formation of this pollutant, all of them strive to keep low the flame temperature. One of the most promising methods that follow this approach is the lean premixed prevaporized (LPP) combustor, where fuel and air are thoroughly mixed prior to entering the flame zone, which operates in a lean mode to ensure low temperatures in the product gases [3].

Among currently investigated methods, LPP technology offers the highest potential in NOx reduction, but its implementation poses important technological challenges. One of the most critical for aircraft applications is combustor stability and relight issues, prompted by the low flame temperatures and combustor entrance stoichiometries. Resulting from these operating conditions, LPP combustors can be particularly

sensible to perturbations introduced to the incoming flow and in the combustor exit plane.

For a given design point, the combustor stability characteristics are directly related to the turbulence field which develops in the combustion chamber. Specifically, the flow features characterizing the flame-anchoring region play a key role in the combustor stability response. In a majority of current aircraft combustor designs, flame holding occurs in the stagnation region formed between a highly turbulent swirling jet and its associated recirculation bubble. Detailed knowledge of its dynamics is thus critical to ensure appropriate combustor stability response.

Another important aspect that gas turbine LPP combustor designers have to face is the NOx/CO production balance. The low flame temperatures characterizing these systems lead to large CO conversion characteristic times, which can be of the order of the flow residence time in the burning chamber. The dilution flow used to condition the exit temperature to turbine entrance acceptable levels not only stops NOx production, but also inhibits CO conversion to CO₂. Therefore, decreases in the combustor efficiency and high levels of the undesired pollutant CO can be present in some operating ranges. As it occurred in the stability response, the turbulent structure of the flow developing in the combustion chamber plays a central role in the NOx/CO production balance. In particular, the residence times of the flow particles in the different combustor regions and the mixing process of combustion products and dilution flow are directly linked to the final levels of efficiency and pollutant formation obtained in a given design.

Detailed investigation of the turbulent flow characterizing LPP systems is therefore key to optimize the combustor design in terms of stability, efficiency, and pollutant generation. With presently available diagnostics, experimental studies can be performed with a much higher level of detail in isothermal systems. On the other hand, flow modifications due to heat release effects indicate the need to complement the isothermal characterizations with reacting flow campaigns.

Based on the above discussion, the main objective of the present study is to gain understanding in the turbulent flow features that characterize gas turbine LPP combustion systems for aircraft applications. Both isothermal and reacting flow characterizations are contemplated. The design of the experimental rigs was carried out trying to reproduce as close as possible the conditions found in the real combustor. State of the art, non-intrusive anemometry diagnostics were used to

characterize the turbulent flow field developing in these systems. Preliminary results obtained were post-processed and used to better assess the combustor response in terms of stability, efficiency, and pollutant generation performance.

3. GENERIC LPP COMBUSTOR GEOMETRY AND FACILITY DESIGN

The selection of the LPP combustor geometry and the experimental conditions used in the investigation was steered by the activities carried out in the ongoing European program LOWNOX-III. The program includes the construction of two different low NO_x combustors whose main unit is based in LPP technology. A virtual engine cycle has been identified to define the combustor operating range. The cruise condition of this engine was chosen to guide the facility scaling process. The main operating parameters that define the combustor operation are given in Table 1.

OPERATING PARAMETER	CRUISE VALUE
Inlet mixture temperature	850 K
Chamber pressure	18 Bar
Combustor flow function ($m \sqrt{T_{\text{entrance}}/p}$)	100 Kg \cdot K $\sqrt{K}/(s \cdot \text{Bar})$
Premixed flow stoichiometry	0.55
Flame adiabatic temperature	2000 K
Number of main/pilot combustion domes	24/24
Main premixed/total combustor flow	0.47
Pilot premixed/total combustor flow	0.20
Cooling/total combustor flow	0.33
Combustor flow per main dome	2.5 Kg/s

Table 1: Operating parameters for the target LPP combustor.

A generic LPP combustor geometry was defined using the combustor length (0.14 m) as characteristic to obtain non-dimensional magnitudes. The geometrical description was simplified to retain only the combustor features having a significant impact in the combustor flow. The combustor has equal number of main and pilot domes that operate in an LPP configuration. The pilot burning occurs upstream of the main combustion chamber. The pilot and main premixing tubes are geometrically similar. Strong mixing within the tube is achieved by using two counter-rotating swirl air streams that are brought into contact at the end of a splitter lip. Fuel injection takes place at this point, quickly mixing with the incoming stream in the shear layer that forms at the lip. Both the outer and inner swirlers are characterized by flow passages inclined 45° with respect to the axial direction. There is a 5:1 flow ratio between the inner and outer swirling streams. As a result, the outer swirl prevails at the flow exiting the tube, which also maintains a high turbulence level. The strong rotation that characterizes the premixed mixture is meant to generate recirculation bubbles in both pilot and main combustion chambers, thus providing appropriate flame holding conditions. The cold-flow rig was designed to reproduce a combustor sector composed by 3 pilot and main domes, with characterizations being performed only in the central main burning region.

The isothermal tests were conducted at ambient pressure and temperature. The facility scaling implied determining its characteristic length and velocity. The two parameters were fixed to match as close as possible the Reynolds and Mach numbers in the real combustor flame region. The matching process need to pay attention to length constraints imposed by the LDV probe geometry. The final cold flow rig scale and

entrance flow velocity was respectively 1.6 and 0.8 times those characterizing the real combustor operation. With these ratios, the cold flow facility Reynolds and Mach number are within 20% of the real combustor figures.

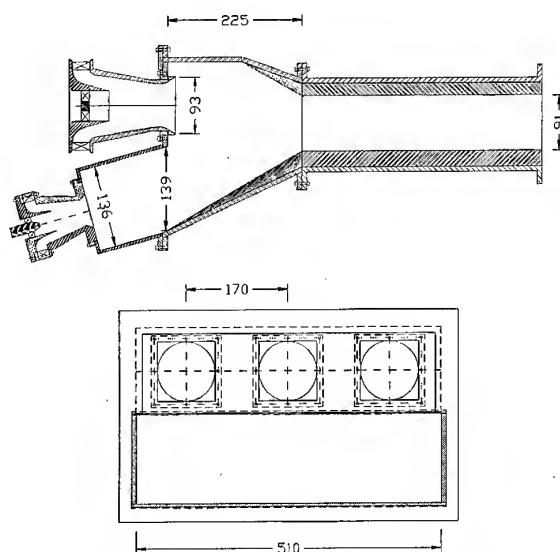


Figure 1: Schematic views of the cold flow experimental rig. A) Longitudinal cut. B) Cross-flow cut at the main combustor inlet plane. Dimensions in mm.

Figure 1 displays schematic views of the obtained cold flow facility, which operates in suction, open return mode. Downstream from the test section there is a flow tranquilization section followed by a contraction and a diffuser that interfaces to a 10 Kw centrifugal blower. Two additional blowing units working in series are placed at the end of 20 m exhaust conduit system. Different mass flow rates passing through the combustor model can be obtained by simply switching on different blowers. The flow generation system is able to provide a mass flow rate of 2 Kg/s with a maximum 5.5 % pressure drop. The test section is made of Perspex material to allow optical access. Key geometrical parameters such as the main chamber acceleration ramp or the premixing tube incidence angles can be easily changed. A perspective view of the built cold-flow facility appears in Figure 2.

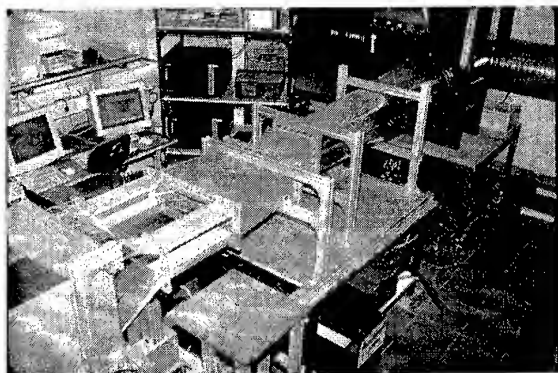


Figure 2: Experimental set-up for cold flow studies.

The reacting flow facility scaling process was conditioned by the available limited compressor air supply, which imposed constraints in the maximum pressure, mass flow rate, and inlet temperature. Specifically,

$$\begin{aligned} (T_{\text{inlet}})_{\text{max}} &= 800 \text{ K} \\ (p)_{\text{max}} &= 7 \text{ Bar} \\ (\dot{m})_{\text{max}} &= 0.7 \text{ Kg/s.} \end{aligned} \quad (1)$$

With these constraints, two scaling parameters were to be determined, namely, the combustor characteristic size and velocity. Noticing the mass flow rate limitation, the number of pilot and main domes in the reacting flow facility was set equal to one. The rationale followed to fix the scaling parameters was to reproduce as much as possible the real burner turbulent combustion regime. The latter is determined by the value of the turbulent Damköhler (Da_t) and Karlovitz (Ka) numbers [4]:

$$\begin{aligned} Da_t &= \frac{t_t}{t_L} = \frac{l_t}{l_L} \left(\frac{v_t}{v_L} \right)^{-1} \\ Ka &= \frac{t_L}{t_K} = \left(\frac{l_t}{l_L} \right)^{-1/2} \left(\frac{v_t}{v_L} \right)^{3/2} \end{aligned} \quad (2)$$

The turbulent Damköhler is constructed as the ratio between the turbulent integral time scale (t_t) and the premixed laminar flame time scale (t_L). In turn, the Karlovitz number specifies the ratio between the time scale of the laminar flame and the Kolmogorov time scale (t_K), i.e., the turnover time of the smallest eddies present in the turbulent field. It is customary to represent the combustion regime as a function of the ratio between turbulent integral length and velocity scales to their corresponding laminar flame scales (l_t/l_L and v_t/v_L respectively). It is possible to obtain an estimate of the values that these ratios will have in the real combustor. The laminar flame scales can be computed using laminar one-dimensional flame calculations with detailed chemical kinetics. For cruise conditions, they become $v_L = 0.40$ m/s and $l_L = 5 \cdot 10^{-5}$ m [5]. The turbulent integral scales in the flame region are determined by the flow exiting the premixed tube and the dynamics of the recirculation bubble. The integral length scale is given by the large-scale movement of the recirculation region, and can be estimated as 1/10 of its size, i.e., 1/10 of the premixing tube diameter. Due to the strong turbulence levels characterizing the inlet flow, the turbulent velocity scale in the flame region will be taken as 1/3 of the averaged inlet flow velocity. The real combustor turbulent regime is then characterized by:

$$\frac{l_t}{l_L} \approx 10^2; \quad \frac{v_t}{v_L} \approx 70 \quad (3)$$

The combustor operation corresponding to cruise conditions is represented in Figure 3. The point is located in the upper portion of the distributed reaction regime. A line representing the operation of the reacting flow facility as given by constraints (1) is also shown in Figure 3. In addition, the graph depicts the lines characterized by Karlovitz and turbulent Damköhler numbers equal to the ones obtained in the real combustor cruise operation.

The scaling of the reacting flow facility is selected then as the point along its operation line closer to the point representing the real combustor cruise condition. Notice that this choice represents a compromise to obtain Ka and Da_t similar to the ones found in the real engine combustor. The obtained

reacting flow facility length and velocity scales are respectively 0.85 and 1.03 of those found in the real engine combustor. With this choice, the Mach, turbulent Damköhler and Karlovitz numbers of the reacting flow facility are within 20% of the ones characterizing the real LPP combustor, whereas the Reynolds number is about 1/3 of the one found in the E-engine cruise condition.

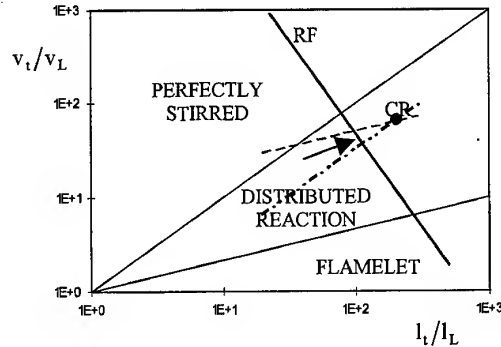


Figure 3: Turbulent combustion diagram for the E-engine cruise (CR point) and reacting flow facility operation (RF line). Also shown are the lines having Ka and Da_t equal to the E-engine cruise condition. The reacting flow facility scaling is selected where the arrow points.

A schematic view of the reacting flow facility test section appears in Figure 4. The combustion chamber is plenum fed by the compressor flow. Prior to entering the inlet plenum, the incoming air stream can be heated to 700 K through a two staged heating unit. The geometry of the premixing tubes, pilot, and main domes is similar to the isothermal hardware. Film cooling is used in the pilot and main domes. The pilot dome is located in the cylinder enclosing the upstream plenum. Optical access to the main combustion chamber is achieved through quartz windows. A rectangular cross-section pressure vessel having 20 mm thick Pyrex windows allows the chamber to be pressurized up to 7 Bars.

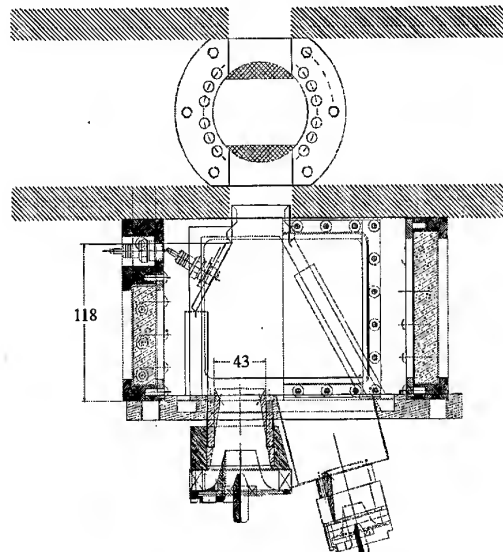


Figure 4: Schematic longitudinal cut of the reacting flow facility. Test section detail.

Flow elements downstream from the test section include a ball valve to control the reacting rig operating pressure and a water spray driven exhaust gases cooling system.

The facility operates with propane as fuel supply. The fuel is vaporized in an external, 10 m³ deposit. Fuel delivery into the premixed tubes is performed in the outer stream side of the premixing tube separating lip, and is achieved through 5.1 mm diameter holes (see Figure 5).

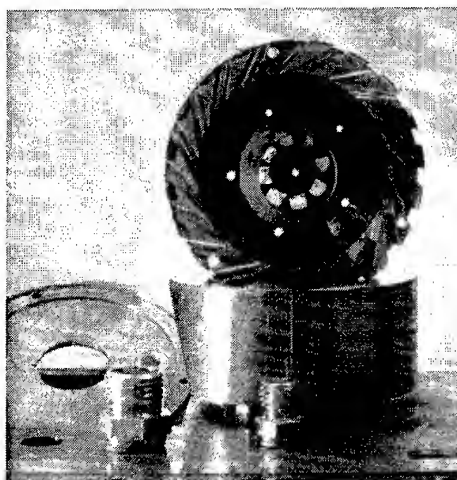


Figure 5: Parts composing the main premixing tube. The outer (radial) and inner (axial) swirlers, and the separating streams lip assembly stands over the tube body. Fuel delivery holes are also visible in the photograph.

A close-up look to the reacting rig test section is shown in Figure 6. The external pressure vessel is not mounted to better observe the main combustion chamber elements.



Figure 6: Perspective view of the reacting rig test section.

4. EXPERIMENTAL TECHNIQUES

The turbulent structure characterization in the cold flow facility was achieved through two-component LDV anemometry. The processor used is a Dantec enhanced BSA 57N20/57N21 system, using FFT signal processing to extract the velocity information. The Doppler signal was collected in

a backscatter mode. The processor is able to handle signal to noise ratios down to 3 dB. The LDV probe made use of an optical fiber arrangement to separate the laser and the receiving photomultipliers from the probe location. The selected optical configuration generated a 120 μ m diameter cylindrical measurement volume with a 100 μ m height. A Coherent 4 W Argon-Ion laser was used as light source. The acquisition software program was an in-house developed program running under Windows NT 4.0 and making use of the LabView programming environment. It has routines to automatically optimize, in each measurement point, the LDV processor central frequency and bandwidth. This feature proved to be critical to allow acquiring the large amount of experimental data in reasonable times. The acquisition suite provides also automatic control of an ISEL 3 axis positioning system. Post-processing of the acquired raw-data was done using transient time statistics. Seeding was achieved using submicron polyethylene-glycol particles, which were produced by controlled, electrical heated seeding units. Two different seeders were placed to allow independent seeding of main and pilot flows. The seeders were adjusted to produce similar average interparticle distance in their seeded streams.

In the reacting flow facility, turbulence characterization was achieved through PIV measurements. A fluidized bed seeder was placed to deliver 4 μ m alumina particles in the plenum located upstream from the test section. The PIV equipment is composed by two pulse Nd-Yag lasers generating 200 mJ laser pulses with 8 ns duration at a repetition rate of 10 Hz. A cylindrical lens was located between the laser head and the combustion chamber, generating a 2 mm thick laser sheet which illuminated the main combustor plane of symmetry ($z=0$). A Pulnix DoubleImage 700 intensified CCD camera with a 768x484 pixel resolution was placed normal to the laser plane to image the burner plane of symmetry. Image post-processing was obtained using a commercial processor (Dantec PIV 2000) and cross-correlation software (Dantec's FlowManager V1.0). In addition, the combustion chamber was characterized for lean blow-out behavior by calibrated diaphragm measurement of the main premixed tube air and fuel mass flow rates.

5. COLD FLOW RESULTS

Three dimensional anemometry measurements were performed in the main combustion chamber, resolving mean velocities and turbulent Reynolds stresses.

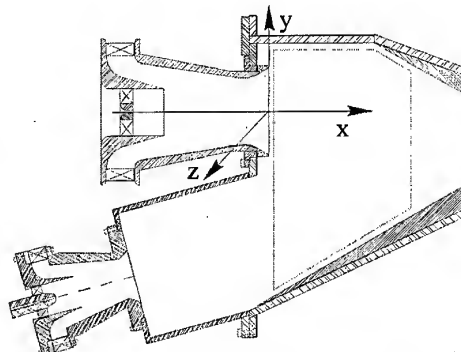


Figure 7: Coordinate axis system used for the cold and reacting flow characterizations. The broken line inside the main combustion chamber represents a projected view of the characterization region.

Figure 7 schematizes the coordinate axis used in the study. The x and y axis are located within the longitudinal combustor plane, the x axis being aligned with the main premixing tube axis. The coordinate system origin is located at the center of the premixing tube outlet. Results will be presented in non-dimensional form. The characteristic length and velocity scales used are, respectively, the main combustor chamber length (0.225 m) and the average main premixed tube outflow velocity (46 m/s). The resulting characteristic time is 5 msec.

Mean velocity profiles at the main premixing tube outlet have been displayed in Figure 8.

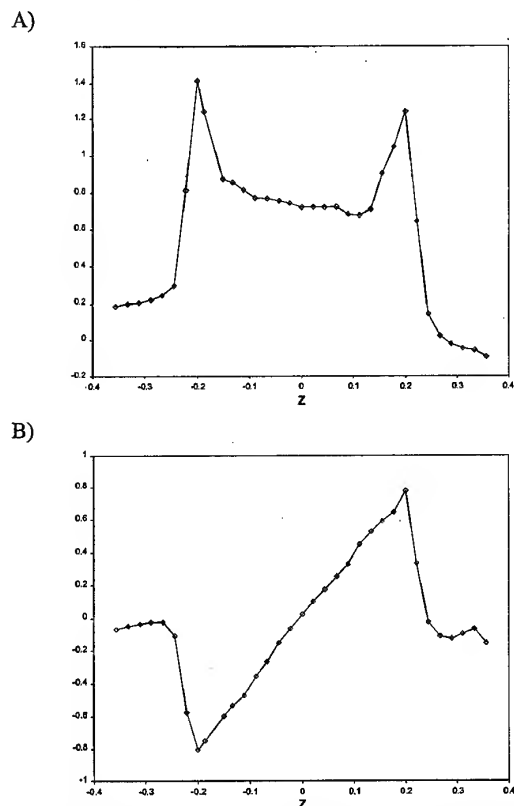


Figure 8: Mean velocity at the main premixing tube outlet. A) Axial velocity profile. B) Tangential velocity profile.

The axial velocity shows a uniform profile through most of the premixing tube outlet area. The external radial positions are characterized by higher axial velocity profiles values. This effect is due to the presence of a main recirculation zone (MRZ) downstream from the tube outlet, which decelerates the tube core flow. There is a small asymmetry in the axial velocity profile, which, as will be seen later, is connected to the MRZ axis not being aligned in the x direction.

The tangential velocity shows a solid body rotation profile with levels that are of the order of the axial velocity values. The resulting swirl number is:

$$S = \frac{\int_0^R U W r^2 dr}{R \int_0^R U^2 r dr} = 0.51. \quad (4)$$

This value is obtained at the premixing tube outlet, which has a divergent shape. A higher, more representative swirl number would be that obtained at the tube throat. Therefore, the premixing tubes generate strong swirling jets. The resulting swirl value together with the divergence angle that characterizes the tube outlet contributes to create the MRZ. Existence of this recirculation zone is confirmed by the axial velocity profile obtained along the x coordinate axis (Figure 9), which exhibits a region with negative axial velocity.

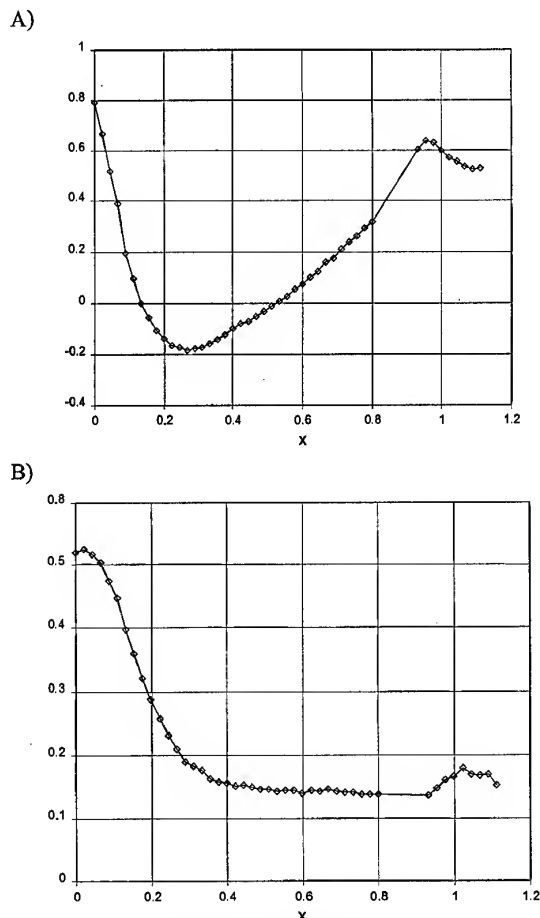


Figure 9: Axial velocity evolution along the x coordinate axis. A) Mean velocity. B) RMS turbulent velocity.

The recirculation bubble is seen to intersect the axial coordinate at $x=0.15$ and $x=0.5$. Downstream from the MRZ, the flow accelerates towards the combustor exit. Notice the high levels of turbulent RMS velocity that characterizes the flow issuing from the premixing tube, with turbulence intensity close to 0.7. As the flow decelerates and enters the MRZ, turbulence is highly damped. However, the most upstream locations within the main recirculation zone still show significant turbulent activity. Finally, the flow acceleration towards the combustor exit is seen to proceed with a decrease in the relative turbulent intensities.

A better understanding of the mean flow features can be obtained by analyzing velocity vectors and pseudo streamlines of the velocity field projected along selected combustor planes.

Projected mean velocity maps in the central dome streamwise plane of symmetry ($z=0$), and in the streamwise plane located between two premixing tubes ($z=0.35$) are shown in Figure 10.

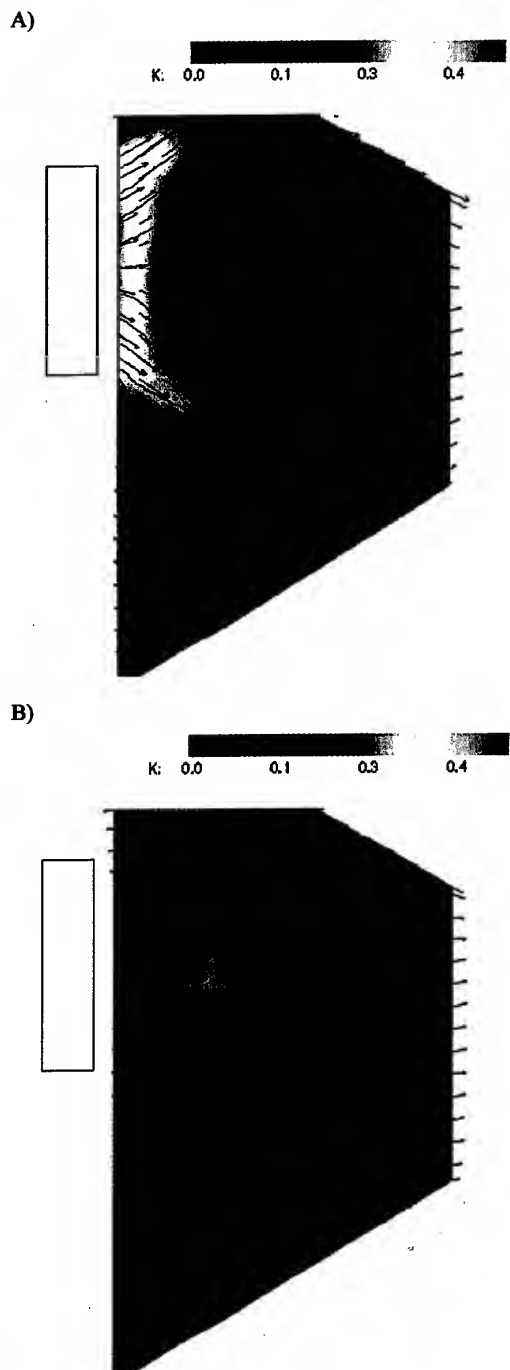


Figure 10: Streamwise anemometry results in the main combustion chamber. A) Longitudinal cut through $z=0$. B) Longitudinal cut through $z=0.35$. Pseudocolor represents non-dimensional turbulent kinetic energy.

Additional information on the mean velocity field is obtained from cross-stream plane maps corresponding to the premixing tube outlet ($x=0$) and two more downstream locations ($x=0.175$ and $x=0.35$), which are shown in Figure 11.

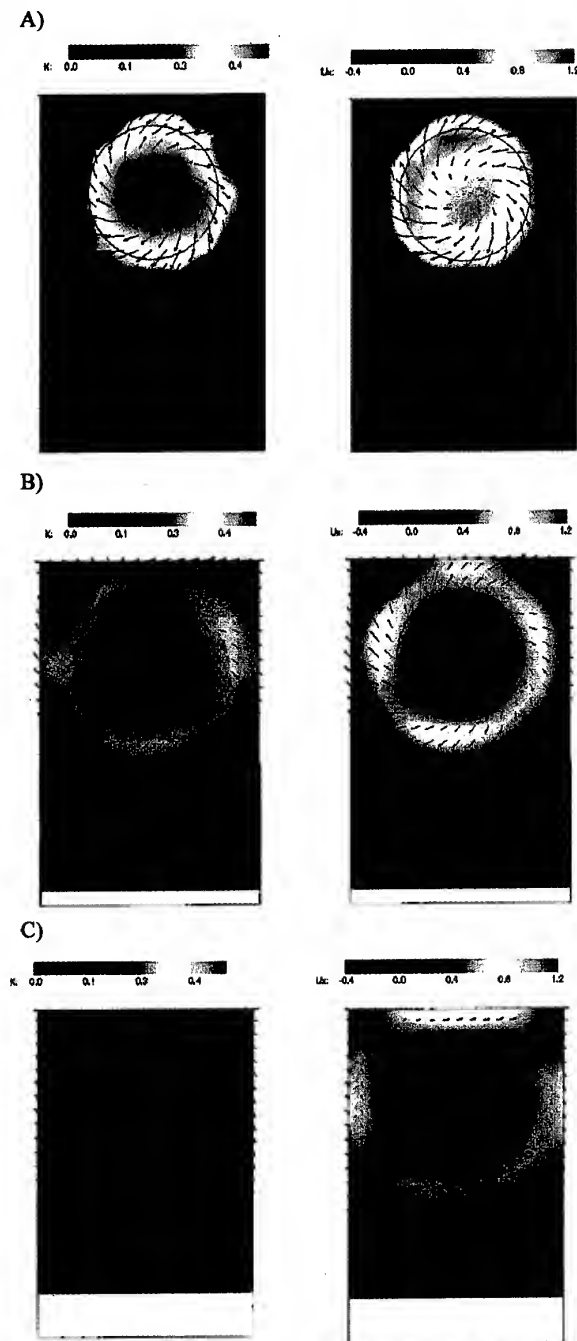


Figure 11: Cross-stream anemometry results in the main combustion chamber. A) Cross cut through $x=0$. B) Cross cut through $x=0.175$. C) Cross-cut through $x=0.53$. Pseudocolor in left hand side graphs represents non-dimensional turbulent kinetic energy, whereas right hand side images display axial velocity as pseudocolor.

The streamwise anemometry map through $z=0$ shows major distinctive features of the turbulent field, namely, the main recirculation zone (MRZ) associated to the vortex breakdown of the swirling flow issuing from the main premixing tube. This flow is so intense that creates a lower recirculation zone (LRZ) similar to the pattern characterizing a sudden expansion flow. This flow recirculation forms a blockage barrier to the

pilot chamber efflux, which is forced to enter the main combustion chamber through the cross-stream region located between consecutive premixing tubes (Figure 10B). In these regions, it is possible to still track the LRZ presence, suggesting that the lower recirculations are connected in the different main chamber domes. Figure 10A also shows the intense turbulent kinetic energy that characterizes the flow exiting the main premixing tube, whose turbulent intensity is of order one. As a result, one has to expect severe deviations of the instantaneous velocity field with respect to the averaged maps. The turbulence level quickly decreases first when, as a result of the strong initial swirl, the flow diverges. Further turbulence decrease is achieved as the flow accelerates towards the main chamber outlet. The low turbulent kinetic energy levels that prevail at the outlet region also characterize the levels found in the MRZ and LRZ cores.

The cross-stream anemometry results at the main combustion chamber inlet (Figure 11A) demonstrate the high turbulence levels that characterize the main premixing tube outflow. The axial velocity defect that occurs in the premixing tube center is also visible in Figure 11A, a consequence of the strong flow divergence that the swirling jet is experiencing. The pilot chamber efflux does not exhibit any significant memory of its initial swirl. In fact, the main premixing jet entrainment dominates the pilot efflux and the LRZ flow cross-stream velocities.

The cross-stream anemometry results at $x=0.175$ and $x=0.35$ show the evolution of the main premixing tube swirling jet and MRZ as flow divergence occurs. The highest turbulent kinetic levels correspond to the swirling jet, and they correlate well with high axial velocity values. The turbulence memory from the premixing tube thus dominates the flow in most of the combustion chamber volume. The presence of the upper wall and adjacent premixing tubes flows are seen to interfere the swirling jet expansion, creating high axial velocity pockets. In addition, the upper wall interference creates turbulence damping through flow stretching, an effect that is most apparent in the $x=0.35$ map. On the contrary, the interference with the lateral and pilot efflux is seen to increase the turbulence activity. This effect can be best observed by comparing the turbulence levels present along the y, z coordinate axis with those found at directions forming 45° with respect to them. The wall turbulence damping can be observed already in the $x=0.175$ downstream location and it will create differences with respect to the flow developing in a single dome sector.

The main swirling jet is seen to entrain pilot efflux. The latter also contributes to close the LRZ. Close inspection of Figure 11 shows how the LRZ cross-stream extension (region with negative axial velocity) is reduced in the vertical direction and spread out along the z axis as the downstream distance is increased. The LRZ shape is complex and asymmetric with respect to the $z=0$ plane. Its topology is influenced by the adjacent flows, and in particular by the relative rotation of consecutive main swirling premixed flows.

The obtained 3D experimental database can be further post-processed to give insight in the turbulent flow field characterizing the generic LPP combustor. Figure 12 shows streamlines constructed from the mean velocity field for fluid particles released at selected positions. The streamline generated at the upper premixing tube periphery can be taken as representative of a fluid particle corresponding to the main fresh mixture. The fluid pocket is seen to fly over the

recirculation bubble. The swirl motion induces on the fluid particle an azimuthal rotation close to 180° during its flight along the main combustor chamber, without interacting much with the pilot efflux. A fluid particle released in the main premixing tube core flow gets entrained in the recirculation bubble. After spending a complete flow bubble cycle, the fluid particle is again entrained by the main swirling jet flow.

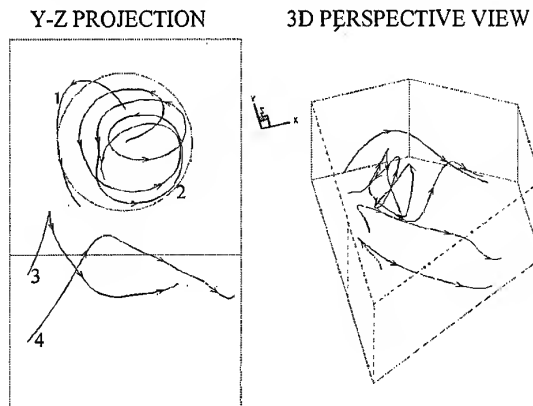
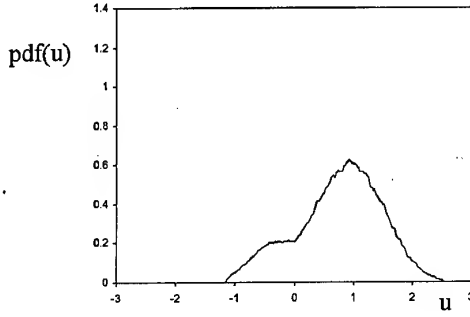


Figure 12: Mean velocity based 3D streamlines in the cold flow main combustion chamber. Line 1: Main premixing tube periphery flow. Line 2: Main premixing core flow. Line 3: Pilot efflux upper flow. Line 4: Pilot efflux lower flow.

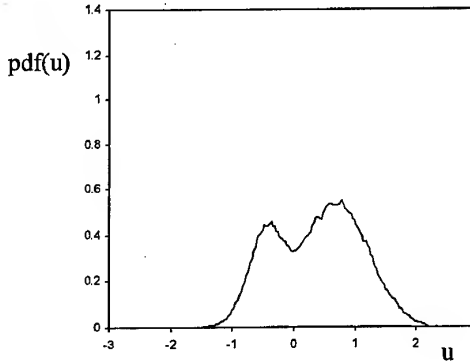
Fluid particles released in the pilot efflux are quickly entrained by the main premixing tube flow. This effect can be understood in the grounds of the large velocity difference characterizing both flows. Recall that, due to the flow blockage caused by the main swirling jet expansion, the pilot efflux enters the main combustion chamber in the regions between main premixing tube outlets. A fluid particle released in the pilot efflux zone close to the main swirling jet flow is rapidly incorporated to main stream. For fluid particles released in the pilot efflux zone most distant from the swirling jet flow, the effect is similar, although the downstream distance in which it is captured by the main swirling jet flow is increased. Therefore, a strong interaction occurs between the lower main premixing tube flow and the pilot efflux. As result, it is expected that the pilot efflux will have an influence in the main combustor stability behavior.

Detailed study of the flow characteristics close to the main premixing tube outlet is relevant to better understand the flame anchoring and stability process. The flow along the premixing tube axis and close to the MRZ upstream stagnation point shows indications that the recirculation bubble performs large scale motions in, at least, the axial direction. Figure 13 displays probability density functions of the axial velocity in the above mentioned region. The axial velocity pdf close to the main premixing tube outlet clearly shows a bimodal character, indicating axial flow pulsation. The characteristic velocity of this pulsation can be assessed from the pdf data in the stagnation point. Assuming that a gaussian random function and a coherent sinusoidal pulsation compose the turbulent motion, one half of the pdf local maxima separation gives the velocity associated to the latter. Thus, a velocity close to $1/2$ of the average axial flow velocity at the premixing tube outlet is seen to characterize the axial pulsation.

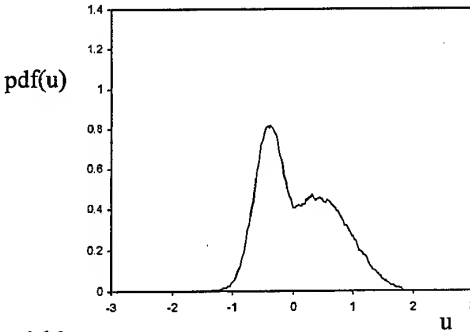
x=0.04



x=0.08



x=0.12



x=0.16

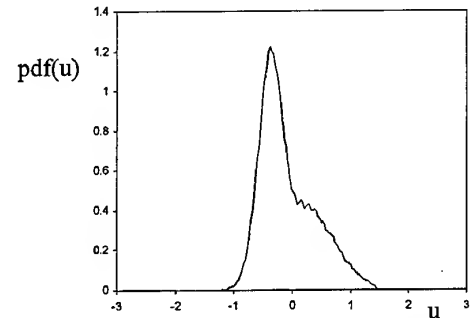
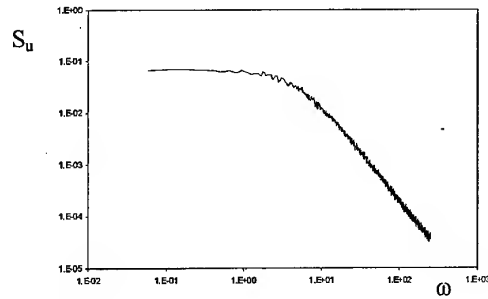


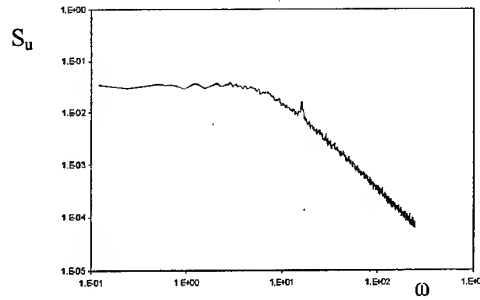
Figure 13: Probability density function of the axial velocity along the main premixing tube axis. Measurements close to the tube outlet.

Also, the downstream distance corresponding to the maximum separation between the bimodal pdf peaks can be taken to assess the axial pulsation center. The experimental evidence presented in Figure 13 indicates that the pulsation is centered close to the MRZ upstream stagnation point.

x=0.1; y=0.0



x=0.1; y=0.1.



x=0.3; y=0.3.

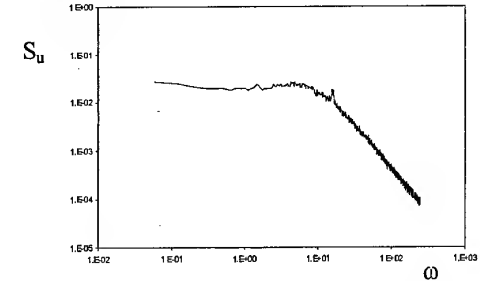


Figure 14: Velocity (u-component) power spectra density in the $z=0$ plane. Measurements in the main premixing tube outlet region.

Further insight on the flow characteristics can be obtained from measurements of the velocity power spectral density (x-component) $S_u(\omega)$, defined as the Fourier transform of the autocorrelation function $C_{uu}(\tau)$ (13):

$$C_{uu}(\tau) = \frac{\overline{u'(t)u'(t+\tau)}}{u'^2}$$

$$S_u(\omega) = \frac{1}{2\pi} \int_{-\infty}^{\infty} e^{-i\tau\omega} C_{uu}(\tau) d\tau. \quad (5)$$

Power spectral density results are presented in Figure 14. The flow region investigated is the $z=0$ plane in the neighborhood of the MRZ upstream stagnation point. Here, the velocity z-component closely reproduces the main swirling jet azimuthal velocity.

All the spectral data exhibit the characteristic low frequency plateau and approximate the $-5/3$ decay in the high frequency end. In the premixing tube axis ($x=0.1, y=0, z=0$) there is no clear evidence of any flow coherence. At the same downstream position but going away from the axis ($x=0.1,$

$y=0.1, z=0$) there is a distinctive coherent peak located at the non-dimensional circular frequency close to $\omega=15$ and an enhanced spectral content around $\omega=10$. The existence of the coherent peak can have its origin in the shear layer created between the main swirling jet and the MRZ flow. The enhanced spectral content can be associated to the MRZ large scale pulsation. Using its associated frequency and taking into account the axial pulsation velocity estimation given before, the large-scale pulsation should have an amplitude close to $2/10$ of the main combustor length. With the pulsation characteristic frequency, it is also possible to estimate the effect of the MRZ pulsation on the flame. This can be achieved by obtaining the Damköhler Da_p formed between the large scale motion and the laminar flame characteristic times. For cruise conditions, it results:

$$Da_p = \frac{t_p}{t_L} \cong 10 \quad (6)$$

Therefore, the pulsation should not affect the flame structure. The turbulent integral time scale in different locations within the main combustion chamber can be obtained from the velocity spectral density measurements. Specifically:

$$t_w = \pi \cdot S_u(0). \quad (7)$$

It is possible to obtain the integral time scale of the turbulence motion that filters out the coherent pulsation. However, the coherent spectral contents are only a few percent, so that spectral density filtering will not be performed. After knowing the integral time scale, turbulent integral lengths are readily determined:

$$l_w = t_w \cdot u'. \quad (8)$$

Table 2 presents the turbulent scale results as obtained in different measurement locations located around the MRZ and selected to represent points close to the expected flame location.

POINT	(x,y)	t_w	u'	l_w
P1	(0.09,0)	0.22	0.50	0.11
P2	(0.09,0.09)	0.13	0.56	0.056
P3	(0.18,0.18)	0.10	0.52	0.066
P4	(0.27,0.27)	0.073	0.42	0.031

Table 2: Turbulent integral scales in the $z=0$ plane. Flow region close to the main premixing tube outlet.

It is seen that, at the flame anchoring region, the integral time and length scales are large. The integral length scales in the MRZ forward stagnation point (P1) are dominated by the bubble pulsation. The scales, therefore, can be taken as representatives of this motion. The swirling jet flow flying over the MRZ (points P2 to P4) progressively decreases its integral time scale. Its rms level is seen to reach a maximum value at P2, and latter decreases as the turbulent field is stretched by the average flow.

Determination of the flame region turbulent integral scales allows positioning the expected combustor operation within the turbulent combustion diagram. The result is shown in Figure 15.

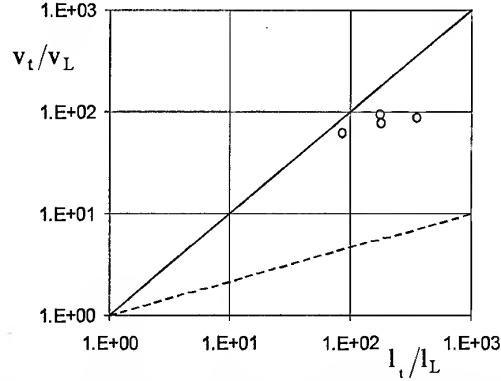


Figure 15: Turbulent combustion regime of the generic LPP combustor estimated from the cold flow turbulence characterizations.

As already anticipated the main LPP burner is placed in the distributed reaction regime. Therefore, the flame turbulent Damköhler is greater than unity. As a result, one should expect turbulent flame velocities closely following the local turbulence intensity levels. On the other hand, the smaller turbulent scales may disturb the slowest processes in the internal flame structure. This will occur, for example, with the CO oxidation layer which, in lean premixed combustion, is much thicker than the fuel consumption layer [6].

Knowledge of the turbulent integral flow scales allows an estimation of the flame front position within the combustor. To this end, the assumption is made that, in the region close to the premixing tube outlet, the turbulent structure of the highly energetic main swirling jet will not be significantly disturbed by the flame presence. The average flame front position will be computed calculating the upstream envelope of flame kernels propagating with the local mean fluid velocity U and a modelled turbulent burning speed $v_{FF}(v_{FFx}, v_{FFy}, v_{FFz})$:

$$\mathbf{v}_{FF} = U + v_{FFx} \mathbf{n}_x + v_{FFy} \mathbf{n}_y + v_{FFz} \mathbf{n}_z. \quad (9)$$

where $\mathbf{n}(n_x, n_y, n_z)$ represents an arbitrary unit vector used in the envelope determining process. Each component of the turbulent burning velocity will be modelled introducing its dependence with the turbulent Damköhler number [7]:

$$\frac{v_{FFi}}{v_L} = 1 + \frac{v'_i}{v_L} \frac{1}{(1 + Da_{ti}^{-2})^{0.25}} \quad (10)$$

In order to start the calculation, it is necessary to identify a flame front point. This can taken as the one where the flame will be anchored, i.e., the location along the streamline passing through the MRZ upstream stagnation point whose velocity matches the turbulent flame burning velocity.

The result of this computation is shown in Figure 16. The flame front propagates from the anchoring location into the incoming swirling jet stream. As the flame front advances from the anchoring location the flow axial velocity increases while, simultaneously, the turbulent intensity decays. This decrease, in turn, generates smaller flame burning speeds, and causes the flame front to bend in the downstream direction. Figure 16 also shows the estimated flame brush thickness, obtained with a correlation similar to that introduced in expression (10).

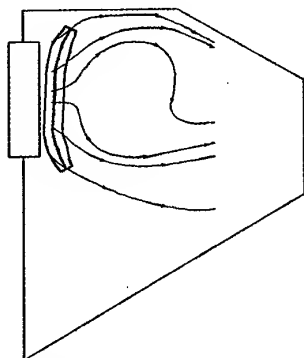


Figure 16: Estimation of the turbulent flame front average position and of the flame brush thickness obtained from the cold flow anemometry data.

6. REACTING FLOW CHARACTERIZATIONS

A flow visualization of the reacting flow facility main combustor is shown in Figure 17. Fuel is being supplied to both pilot and main premixing tubes. The main and pilot stoichiometries are 0.6 and 0.7 respectively. The chamber pressure is 2 Bar, whereas the incoming flow temperature is 500K. The flame surface can be identified with the blue color region. As it can be seen, the pilot combustion occurs upstream of the main chamber, with no significant flame radiation being present in the pilot efflux. A substantial amount of red and yellow radiation can be observed coming from the upper and back chamber walls.

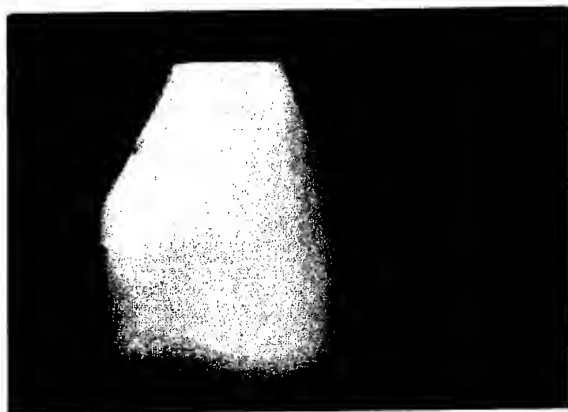


Figure 17 Flow visualization of the reacting flow main combustor chamber with pilot and main combustion enabled.

The experimental flame obtained in Figure 17 can be compared to the flame front estimation displayed in Figure 16. The x coordinate in the burner displayed in Figure 17 runs along the vertical page direction. In spite that, for this flow visualization, the cross-flame temperature ratio was higher than the one characterizing the real combustor operation, the flame front estimation obtained before closely reproduces the experimental mean flame surface. Some flame surface asymmetry can be detected in Figure 17, the result of the main dome velocity field, which exhibits higher velocity in the dome region close to the walls, and the pilot efflux entrainment by the main swirling jet. The flame front

asymmetry is also captured in the cold flow estimation (Figure 16). Also visible in Figure 17 is the lower recirculation zone created by the swirling jet radial expansion, and which can be linked to the dark region in the right portion of the photograph. The envelope of this dark zone resembles the lower recirculation zone geometry obtained in the cold flow velocimetry maps as seen, for example, in the downstream location of the main swirling jet lower wall impingement.

Preliminary quantitative studies of the combustor characteristics were performed at atmospheric pressure. The stability behavior was investigated maintaining the pilot combustor operation at a fixed premixed flow stoichiometric ratio of 0.7, and fixing the inlet flow temperature and total mass flow rate. The main premixed flow stoichiometry was then decreased from a starting value of 0.7 until extinction was achieved. The result of the stability behavior experiment is shown in Figure 18.

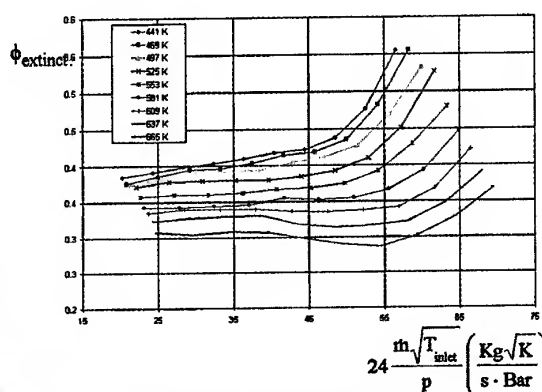


Figure 18: Stability behavior of the main combustion zone. Atmospheric pressure operation with constant pilot zone premixed flow stoichiometry ($\Phi_p=0.7$).

For a given inlet flow temperature all the curves show similar behavior, namely, an almost constant extinction stoichiometry for low incoming flow, and an increase in the minimum stable stoichiometry ratio as the incoming mass flow rate is increased. The increase in incoming flow temperature results in an extended region of stable operation. Also, the entrance temperature is seen to increase the threshold mass flow rate for which the extinction stoichiometry starts to increase from its low flow value. As the incoming flow rate is a measure of the flame Damköhler number, the described behavior can be understood as the progressive decrease of this non-dimensional parameter for increasing entrance flow rates. The mechanisms by which the flame is extinguished are linked to different phenomena taking place in the flame, which can be characterized by different Damköhler numbers. Thus, the characteristic time of the flow in the MRZ upstream stagnation point, the main residence time over the MRZ and in the recirculation bubble, and the characteristic turbulent time in the flame region can be selected to help understanding the combustor extinction response. Of these, the Damköhler constructed with the turbulent integral time and the residence time over the MRZ is most probably linked to the increase in the extinction stoichiometry that occurs for high values of the combustor incoming flow rate.

The characterization of the mean velocity field in the main burner dome was performed using PIV techniques (Figure 19).

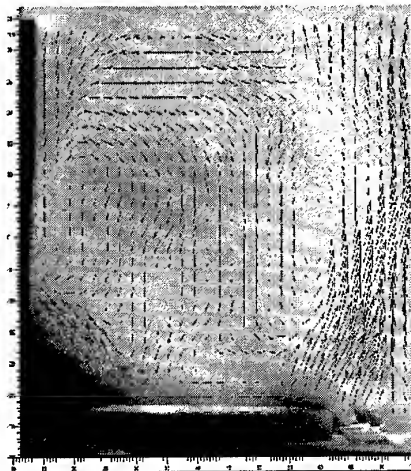


Figure 19: PIV x-y velocimetry map of main burner dome zone in the reacting facility ($z=0$ plane). Atmospheric burning conditions with pilot and main premixed flow stoichiometry of 0.65 and inlet flow temperature of 500 K.

The common trends between this anemometry data and the equivalent map obtained in the cold flow facility (Figure 10A) are evident. In particular, the MRZ geometry including the flows around the upstream and downstream stagnation points, the main swirling jet expansion, and the exhaust flow streamline pattern can be seen to exhibit very similar characteristics. This similitude is supported by the relatively modest flame temperature jump and the dominant role played by the main swirling jet and its associated turbulent structure, so that flame induced turbulence cannot introduce significant modifications in the turbulence flow features. Finally, the expansion effects caused by temperature increases are heavily constrained by the imposed geometry. All these aspects contribute to enhance the similarities between the major flow characteristics found in the cold and reacting facilities. This gives support to extend the turbulent structure findings obtained in the cold flow studies to the reacting flow condition.

7. CONCLUSIONS

The turbulent characteristics of low emission gas turbine combustors based in the lean premixed prevaporized concept have been experimentally investigated. Both cold flow and reacting flow studies were performed, using flame visualization and non-intrusive anemometry to characterize the flow. Initial efforts were directed to define a generic LPP combustor geometry taking into account the restrictions imposed by the existing facilities. The selected geometry had a pilot and a main combustion dome, both of them based on the LPP principle, and was inspired by designs currently being considered in the EU LOWNOX-III initiative. The cold flow test-rig scaling was selected to reproduce as close as possible the turbulent structure found in the real combustor flame region. The reacting flow facility scaling process was achieved trying to place its operation in the same region of the turbulent combustion diagram as the one characterizing the real burner.

The cold flow anemometry results demonstrate that the swirling jet issuing from the main premixing tube dominates the flow within the main combustion chamber. The strong swirl imposed in the jet promotes its radial expansion at the tube outlet, and generates a recirculation bubble in the main

burner dome. The expansion of the swirling jet creates a blockage to the pilot burner efflux, which is forced to exit in the space between consecutive main premixing tubes. The velocity difference between the main swirling jet and the pilot efflux promotes the latter rapid entrainment. The strong turbulence levels present at the main swirling jet outlet plane dominate the turbulence characteristics in the main flame zone, which is characterized by large scale pulsation of the recirculation bubble. Spectral density measurements demonstrate that this pulsation should not affect the flame structure. The integral scales that characterize the flame region turbulence allow locating the LPP main burner within the distributed reaction zone. Based on this finding, burning speed models are used to determine the average flame front position. The distinctive features found in the cold flow studies are also obtained when investigating the reacting flow facility. Flow visualization and mean anemometry characterizations performed in the main flame region indicate similar trends to those obtained in the cold flow studies. Finally, the combustor stability response can be discussed in terms of the incoming flow characteristics and the turbulent structure developing in the main combustion zone.

8. ACKNOWLEDGEMENTS

This investigation was mainly supported by the European LOWNOX-III research project, contract BRPR-CT-95-0122, included in the EU sponsored Brite-Euram Aeronautics program. Additional funding was obtained through the Spanish National Research and Technology Program, under grant CICYT-C95013002.

9. REFERENCES

- [1] Schumann, U. On the Effect of Emissions from Aircraft Engines on the State of the Atmosphere. AGARD CP536 (1993).
- [2] Brasseur, G.; Amanatidis, G.; Angeletti, G. European Assessment of the Atmospheric Effects of Aircraft Emissions. *Atmospheric Environment* **32**, No. 13 (1998).
- [3] Lefebvre, A. The Role of Fuel Preparation in Low Emission Combustion. *Journal of Engineering for Gas Turbines and Power* **117** (1995).
- [4] Borghi, R. On the Structure and Morphology of Turbulent Premixed Flames. *Recent Advances in Aerospace Science*, E. Casci, Ed. (1985).
- [5] Bollig, M.; Liñan, A.; Sanchez, A.; Lazaro, B. Reduced Kinetic Mechanisms for Modelling LPP Combustion in Gas Turbines. AGARD Conference on Gas Turbine Engine Combustion, Emissions and Alternative Fuels (1998).
- [6] Mahalingam, S.; Chen, J.; Vervisch, L. Finite-rate Chemistry Effects in Direct Numerical Simulations of Turbulent Premixed Flames. *Combustion and Flame* **102**, No. 3 (1995).
- [7] Pocheau, A. Scale Invariance in Turbulent Front Propagation. *Physical Review E* **49**, No. 2 (1994).

PAPER No. 25
Lazaro, Lecuona, Rodriguez, Alfaro & Gonzalez
 (presenter: A. Lecuona)

Question 1: D. Santavicca, Penn. State University, U.S.

How do the implications of your experimental results relate to your modeling effort?

Answer:

Yes, they do relate and the implications could be important. They could perhaps provide some simplifying assumptions for the modeling.

Question 2: H.B. Weyer, DLR, Germany

With respect to the PIV and LDA flow results, did you consider the effect of seeding particle size, which you mentioned to be around 4 microns, on whether or not the flow trajectories were actually followed?

Answer:

The LDV experiments were performed with submicron polyethylene-glycol particles that had excellent response to the flow in the frequency range under study. To give an approximation to the frequency response of the particles used for the PIV, the method for spherical particles described in "Motion of Discrete Particles in a Turbulent Fluid Flow," *Appl. Sci. Res.* Vol. 16, 1966, pp. 149-161, by Hjelmfel & Mickros, were applied. The particular use of particles of 4 microns was studied. The amplitude and phase of such particles is depicted in the attached figures for atmospheric conditions and for a pressure of 7 bar at 800 °K respectively. Not that these figures depict the maximum values at the inlet conditions stated; for the higher temperature of the flame, the accompanying increase in the gas kinematic viscosity more than offsets the density increase.

The described macro-scale at w of 10 - 15, is within a good measurement range in any case. Most of the higher frequency features are lost for the atmospheric case, but if this case is of interest the seeding material could be changed. On the other hand, at the temperatures that require alumina for a seeding material, the measurements are of good quality up to a non-dimensional frequency ω of 100. The PIV measurement technique is radically different to LDV. In the present work, no attempt has been made to cross-calibrate each other, other than checking for the global topology of the flow.

There are two figures for which I do not have reproducible copies

NOX REDUCTION IN A FUEL STAGED COMBUSTOR BY OPTIMISATION OF THE MIXING PROCESS AND THE RESIDENCE TIME

N. Brehm, Th. Schilling, A. Mack, G. Kappler

BMW Rolls-Royce AeroEngines GmbH

Eschenweg 11, D-15827 Dahlewitz

Abstract

The paper deals with research work for NOx reduction carried out on an axially staged combustor. The combustor is operated with airblast atomizers and the combustion process is controlled by turbulent diffusion, like today's single annular combustors. Therefore the NOx formation is mainly defined by the time the combustion products spend at high temperatures. The objective of the work presented here was the reduction of NOx by the optimisation of the mixing process, combined with a reduction of the overall residence time.

Three concepts were first investigated by computational fluid dynamics (CFD). The special emphasis was to distinguish differences in the mixing process, which indicate an improvement for NOx reduction. Based on this, the different configurations were tested in a high pressure sector rig under realistic engine conditions. A systematic NOx reduction was achieved by optimisation of the combustor geometry, leading to a more enforced, fast combustion process.

Nomenclature

AFR	air fuel ratio
χ	scalar dissipation rate
CFD	Computational Fluid Dynamics
CO ₂	carbondioxide
D _t	turbulent diffusion coefficient
EI	emission index
ϵ	turbulent energy dissipation rate
f	mixture fraction
g	mixture fraction variance
k	turbulent kinetic energy
l	fluidynamical lengthscale
L	combustor length
LDV	Laser Doppler Velocimetry
ν_t	turbulent viscosity
NOx	nitrogenoxide
OTDF	overall temperature distribution factor
PDF	probability density function
PDPA	Phase Doppler Particle Anemometer
P ₃₀	combustor inlet pressure
RTDF	radial temperature distribution factor
SAC	single annular combustor
SC	Schmidt number
τ_{mean}	mean residence time
τ	turbulent time scale
Φ	equivalence ratio
T ₃₀	combustor inlet temperature
V	volume

\dot{V}	volumetric flow rate
x	spatial distance
\sim	Favre average
—	Reynolds average
"	fluctuations around the Favre average
'	fluctuations around the Reynolds average

1. INTRODUCTION

With the increasing world wide air traffic the environmental aspects of aircraft pollutants in the upper atmosphere are the motivation for research work on the possible impact from aviation on climatic changes. Recent research results [1] indicate an increase in NOx concentration of up to 30% by aviation leading to a zonal ozone enhancement of up to 8%. Both, increased ozone and carbon dioxide emissions (CO₂), emitted from the combustion process, tend to increase the global mean surface temperature. Although the current contribution by aviation compared to other traffic source is considered to be small, the aero-engine industry is working on low emission combustor technologies as a precautionary principle and to cope with the predicted increase in air traffic. The requirement from the atmospheric researchers consists in a reduction in both, the CO₂ and NOx emissions. The specific fuel consumption and by this, the CO₂ emissions, can be reduced by higher thermal efficiencies of gas turbines, i.e. higher pressure ratios and combustor exit temperatures. High outlet temperatures at a given inlet temperature are directly linked to a high overall fuel-air-ratio which potentially may increase smoke emissions. Therefore low NOx/low smoke combustor technology is required to cope with the more adverse combustor inlet conditions of current and expected future aero-engines designs.

Combustor design has to cope with requirements which leads to a contradictory aerothermal design. For example, to ensure a wide altitude windmill relight envelope with a sufficient pull-away characteristic to accelerate the engine to idle, adequate residence time in the combustor is required, which on the other hand leads to increased NOx emissions at high power. Therefore local stoichiometry and residence times are carefully matched to meet all requirements in a combustor development program. Low NOx technology with a fuel rich primary zone and a subsequent quick transition to the lean stoichiometry can lead to increased smoke emissions caused by high soot production and reduced consumption in the colder combustor secondary zone. Usually engine manufactures develop various variants of an engine type with different cycle data (i.e. T₃₀, P₃₀, AFR), which

makes the optimisation process for low NOx/low smoke even more challenging [2], [3].

A functional separation of the requirements would allow for more freedom in the optimisation process. Therefore a fuel-staged combustor with two independent burning zones provides in principle advantages against a single stage combustor [4]. The pilot zone is fuelled over the entire operating range whereas the main zone operates in high and intermediate power settings only. By a variable fuel split between both zones the stoichiometry of the individual zones can be adjusted to be suitable to the various engine operating conditions. Therefore the pilot zone can be optimised for low power emissions, altitude relight and stability whereas the main zone has not to deal with these requirements and can now be designed for low NOx emissions. In the staged mode the pilot zone is operating lean and stabilises the main zone at the staging point after its ignition. The lean overall stoichiometry of the pilot zone reduces thermal NOx production, and furthermore, by a small proportion of fuel burned in the pilot zone compared to the main zone, the total specific NOx emissions can be reduced. A constraining factor is the shift of the exit temperature profile when varying the fuel split.

The present work comprises an investigation on the effect of the combustor volume and mixing on NOx emissions in an axially staged combustor. A research program, covering sector tests supported by CFD analysis was established. It is part of a technology program funded by the German Ministry of Research and Technology, which comprises all combustion and fuel/controls system aspects with a final demonstration in a core engine.

2. COMBUSTOR DESIGN

2.1 Mixing considerations

The combustion chamber of all modern aeroengines function to the same principle. A spray of liquid fuel is generated and burned in an annular flame tube. The mixture at the combustor exit becomes lean by controlled addition of air. In this non premixed combustion process the fuel always has to pass the stoichiometric condition. The amount of NOx formed is therefore defined by the mixing process, i.e. by the mean temperature and the residence time of hot products at temperatures above 2000K. A reduction of NOx can be achieved, if this transition from a rich to a lean mixture can be accelerated.

The mixing process of fuel with air is described by the transport equation for the scalar mixture fraction $f(x,t)$. In the Favre averaged form, this leads to two equations, one for the average \bar{f} and one for its variance \tilde{f} :

$$(eq. 1) \quad \bar{\rho} \frac{\partial \bar{f}}{\partial t} + \bar{\rho} \tilde{v} \nabla \bar{f} = \nabla (\bar{\rho} D_t \nabla \bar{f})$$

$$(eq. 2) \quad \bar{\rho} \frac{\partial \tilde{f}}{\partial t} + \bar{\rho} \tilde{v} \nabla \tilde{f} = \nabla (\bar{\rho} D_t \nabla \tilde{f}) + 2\bar{\rho} D_t (\nabla \bar{f})^2 - \bar{\rho} \tilde{\chi}$$

$$\text{with } \tilde{\chi} = 2D(\nabla \tilde{f})^2$$

Here the molecular diffusion is neglected.

In the Eulerian coordinate system, the left hand side contains the convective transport, which is defined by the mean values of the flow field. The right hand side of the equations contains the turbulent mixing terms, depending on the turbulent diffusion coefficient and the scalar dissipation rate, which have to be modeled.

A perfectly stirred reactor (PSR) is defined by $f \neq f(\tilde{x}, t)$ which leads to:

$$\tilde{f} \neq \bar{f}(\tilde{x}, t) \quad \text{and} \quad \tilde{g} \neq \bar{g}(\tilde{x}, t) = 0$$

The value of the probability density function of such a mixture is simply the Dirac δ function.

A perfect mixing process can be defined by the requirement to achieve a PSR within an infinite short time, i.e. an infinite high mixing rate.

In the κ , ϵ -model, the turbulent diffusion coefficient is expressed by:

$$(eq. 3) \quad D_t = \frac{v_t}{Sc} = \frac{\kappa^2}{\epsilon}$$

with the turbulent length scale being defined as

$$(eq. 4) \quad \tilde{l} = \frac{\kappa^{\frac{3}{2}}}{\epsilon}$$

The effect of the turbulent diffusion in the mixing process is the homogenisation of f and g in the mixing volume.

The mean scalar dissipation rate is the only source term in equation (2), where the variance is dissipated and not just distributed. The mean scalar dissipation rate can be modeled [5], [6] as:

$$(eq. 5) \quad \tilde{\chi} = c_\chi (\tilde{\epsilon}/\kappa) \tilde{g}$$

The turbulent time scale τ is related to κ and ϵ as:

$$(eq. 6) \quad \tau = \frac{\kappa}{\epsilon}$$

The turbulent mixing process is balanced between the turbulent diffusion rate and the scalar dissipation rate. The scalar dissipation rate is rate determining, and the diffusion rate defines the length scale of the mixing volume.

This leads to the conclusion, that the perfect mixing process, i.e. an infinite quick achievement of a PSR, can only be approximated in a small mixing volume, e.g. in a shear layer, where the scalar dissipation rate is high and the turbulent diffusion rate defines the depth of the volume, which can be mixed out.

The mixing rate in a combustor is dependent on the convective transport of the mean value of the mixture fraction and

its variance, sometimes called macromixing [7], and the overlaid turbulent mixing process. The convective transport is defined by the mean velocity field. For a perfect mixing process the flow field needs to be configured in such a way, that fuel and air are transported in small scales to each location in the volume, homogeneously. These flow scales are defined by the geometric scales of the combustor and the boundary conditions. This small scale macroscopic mixing defines the scale for the turbulent mixing structure, which requires a turbulent length scale, proportional to the length scale of the turbulent mixing depth.

2.2 Mean residence time

A mean residence time in the combustor is defined by:

$$(eq. 7) \quad \tau_{mean} = \frac{V}{\dot{V}}$$

For a given mass flow, the mean residence time in the combustor depends on the volume and the mean gas density.

A volume change leads to a proportional change of the mean residence time, if the mean density does not change by a changed location of heat release within the combustor.

For the interesting range of flame conditions and residence times, the thermal NO_x production is nearly proportional to the residence time. Therefore a reduction of the mean residence time should lead to a proportional reduction of NO_x emissions, if the mixing rate changes accordingly. A distinction between the effect of a volume change on NO_x production achieved by a change of the residence time or the mixing process is therefore not reasonable, except for the impractical case of cutting off a hot streak by shortening the combustor.

2.3 Combustor volume reduction

A higher scalar dissipation rate in the diffusion type combustion process, which leads to lower peak temperatures, and a quicker mixing process between the hot products and the air, are measures to reduce the NO_x emissions of a combustor. An appropriate approach is an increased number of shear layers, i.e. a smaller convective, macroscopic scale, and an intensified turbulent mixing by smaller turbulent scales [8].

In the described work, a more homogeneous macroscopic mixing is intended by a change of the combustor liner geometry to diminish poorly mixed regions. The turbulent mixing should be enhanced by the reduction of the turbulent time scales in a smaller volume. Therefore the depth of the main zone of an axially staged combustor was systematically reduced, to study the effect on NO_x emissions. A reduction in combustor depth leads to a higher transport velocity and to thinner turbulent mixing layers assuming to first order a constant turbulent diffusion rate. The scalar dissipation rate is increased in the mixing layers due to higher shear stresses.

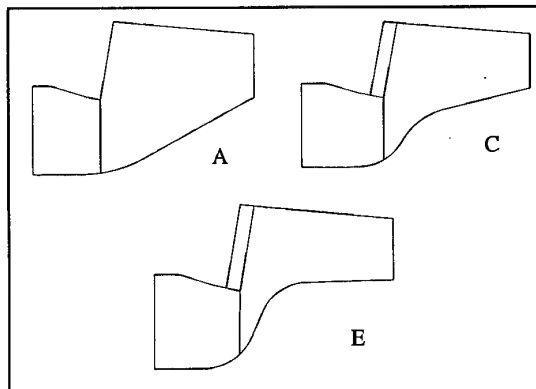


Figure 1 Staged Combustor Configurations

Three basic configurations of an axially staged combustor were designed (fig.1). The first flame tube, nominated A-can, has the datum volume. The second one, nominated C-can, has a main zone volume, reduced by 10%. The main zone volume of the so called E-can is 18% smaller than the datum can. The smaller main zone should make it possible to confine the mixing to a better controlled volume in the primary zone and the jet mixing area, which defines the end of the primary zone. This should lead to a more efficient usage of air in the rich lean transition region. The boundary conditions, i.e. the number and characteristics of the fuel injectors, and the mixing jet configuration are kept unchanged. The pilot and main fuel injectors are circumstantially staggered. The magnitude of the volume reduction was designed in such a way, that at low power acceptable emissions performance could have been expected.

The flow field, the mixing process and the NO_x production were analysed in a CFD study, and the emissions and the temperature traverse were determined in sector tests.

3. CFD-ANALYSIS

3.1 Code description and boundary conditions

For this study the commercially available code CFD-ACE [9] was used. Its main numerical features are:

- block structured grids
- finite volumes-second order spatial differencing
- pressure correction/SimpleC algorithm
- logarithmic wall functions
- fully implicit discretization
- Lagrangian treatment of droplets

The physical models used for the simulations are:

- κ-ε turbulence model
- f, g combustion model with presumed pdf
- liquid fuel C₁₂H₂₃
- NO_x production model based on oxygen-equilibrium.

The CFD-ACE code solved the gas equations in Eulerian form whereas the droplets were treated in a Lagrangian formulation with discrete trajectories. The spherical droplets evaporated according to the Uniform Temperature Model [10] and interchanged enthalpy, mass, and momentum with the gas phase and vice versa. The mean local gas temperature was calculated along the lines of the assumed PDF approach (f-g model) [6] by weighting the mixture fraction dependent thermodynamic equilibrium temperature with an assumed probability function. This 2-parameter function solely depended on the local average of the mixture fraction and its variance and was assumed to be a β -function.

The negligible effect of the thermal NO_x production on the local density allows the decoupling of the computation of the main flow field and the NO_x field. Therefore the computation of the thermal NO_x field was performed as a postprocessing step whereas the velocity, enthalpy, k , ϵ , f , and g distribution were kept constant. This required just the computation of a single transport equation with a β -PDF averaged source term for the NO_x source term.

The mass flow boundary conditions for the air inlets at dilution, mixing, and cooling holes were taken from the effective area and static and total pressure measurements around the combustor cans. Detailed atmospheric high resolution LDV velocity profiles at the exit of pilot and main fuel injector were taken as inlet profiles for the 3D combustor simulations. The droplet size and velocity distribution for the fully established dilute spray was based on detailed PDPA measurements and approximated by a Rosin-Rammler distribution function. The chosen boundary conditions represented the reduced take off case with

$$P_{30} = 20 \text{ kPa}, T_{30} = 846 \text{ K}.$$

Four different fuel staged 18° sector combustor configurations (A, A2, C, E) were computed and all except the factious A-can were compared with combustor exit EINO_x and OTDF/RTDF from rig tests. The fuel injectors were identical in all of the simulations.

The grid for a 3-D combustor simulation had up to 400,000 hexahedral cells. Typical computation times on a R10000 SGI workstation were 30 hours.

3.2 CFD predictions

The macroscopic mixture is predicted to be defined by the mean flow field and the boundary conditions. The mixing - and by this the combustion- is concentrated to small scales around the macroscopic structures. Therefore for each configuration, the macroscopic distribution of all scalars, which describe the mixing, looks similar. Experimentally, mixing was studied by different research labs at universities and gas turbine companies. The main emphasis was put on macro-mixing in the past, e.g. [11], [12]. Everson et al. [13] tried to apply optical methods and an entropy principle to get more insight into local mixing rates.

The design requirement for the low NO_x combustor was a high mixing rate around the stoichiometric condition. This is equivalent to the requirement for a high heat release rate on the fast chemistry limit. Considering, for example, a

model according to Bilger for non premixed combustion [6], the mixing rate is mainly controlled by the scalar dissipation rate χ . The mixedness is defined by the distribution of the mixture fraction f and its variance g . With the infinite rate combustion model and an assumed PDF the temperature is directly related to f and g .

Two configurations were studied for the combustor with the largest volume, i.e. the A-can with the same boundary conditions as the C- and the E-can, and the A2-can, with a different mixing jet arrangement. The distribution of χ , Φ , T and the iso-plot of the A-can are shown in fig.2. The iso-plot at an equivalence ratio of $\Phi=1$ is added for clarification of the 3-D structure of the combustion process. The contours for the mean mixture fraction between 0.9 and 1.1 are indicated on top of the χ distribution. In the A-can the mixing in the main plane is as intended, i.e. high values of χ around the stoichiometric mixture fraction, and a steep gradient of Φ . The temperature in the main plane stays below 2350 K. In contrast the pilot plane is poorly mixed. The scalar dissipation rate in the stoichiometric regions is low, which leads to low gradients in the Φ distribution. Large hot volumes above 2350 K are the consequence.

In the A2-can (fig.3), with a changed mixing jet arrangement, the mixing is restricted circumferentially to a volume close of the fuel injector. The areas between and radially inward to the fuel injectors are almost completely unused for mixing. High scalar dissipation rates are still visible downstream of the mixing jets, which should be avoided, and low scalar dissipation rates are visible around stoichiometric conditions. This indicates insufficient mixing activities in these areas. A strong hot streak is fed into the secondary zone due to incomplete, slow mixing. Between the fuel injectors a large hot area is present at the outer barrel together with a large cold area at the inner side of the combustor.

The basic mixing jet arrangement was optimised for the combustor shape of the C-can. The two planes of the C can are shown in fig.4 together with the iso-plot. In the main plane of the C-can, the distribution of χ is very similar to the A-can. It is high around the stoichiometric mixture fraction and takes a larger portion of the primary zone. In general, the χ distribution in the pilot plane looks similar to the one of the A-can, but with the improvement, that the size of this non-optimum mixing area is reduced. The gradients in Φ are increased against the A-can, and the areas with temperatures above 2350 K are very much reduced. Although better than the A-can, the macroscopic mixing is still not optimum and the available air is not used efficiently. The iso-plots show, that compared to the A-can the C-can has an improved jet mixing zone with less strong hot streaks downstream of the jets.

The change from C- to E-can was, like for the A-can, done without any optimisation of the mixing jet arrangement. In the main plane the E-can shows similar distributions of χ , Φ and T (fig.5) as the C-can. In the pilot plane the amount of fuel is further reduced with very low mixing activities. The mixing process is even more concentrated to the fuel injector region. More fuel escapes through the mixing jets than in the C-can, and a somewhat longer hot streak is formed. A

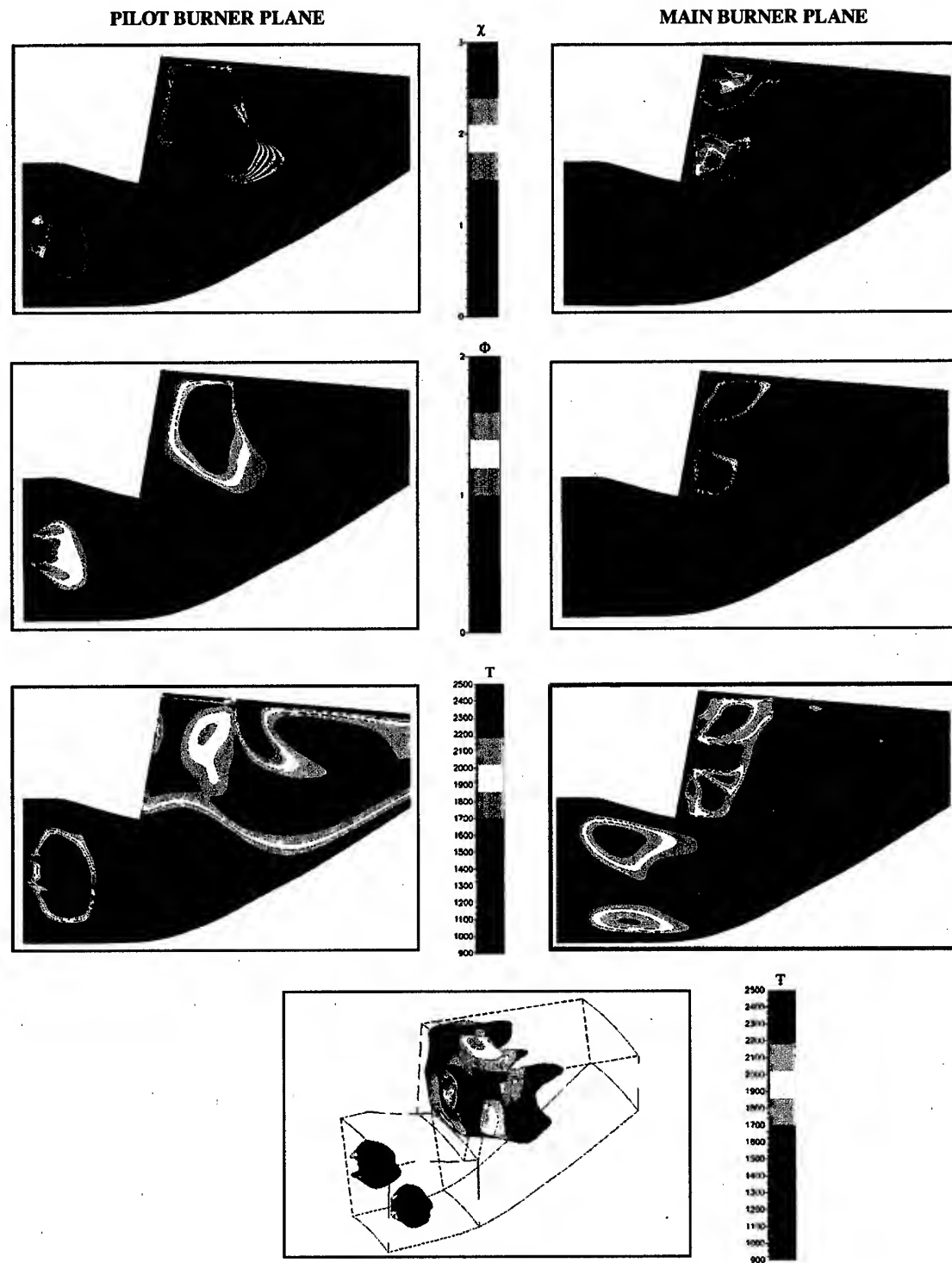


Figure 2 Distribution of mean dissipation rate, equivalence ratio, temperature and stoichiometric surface of A-Can

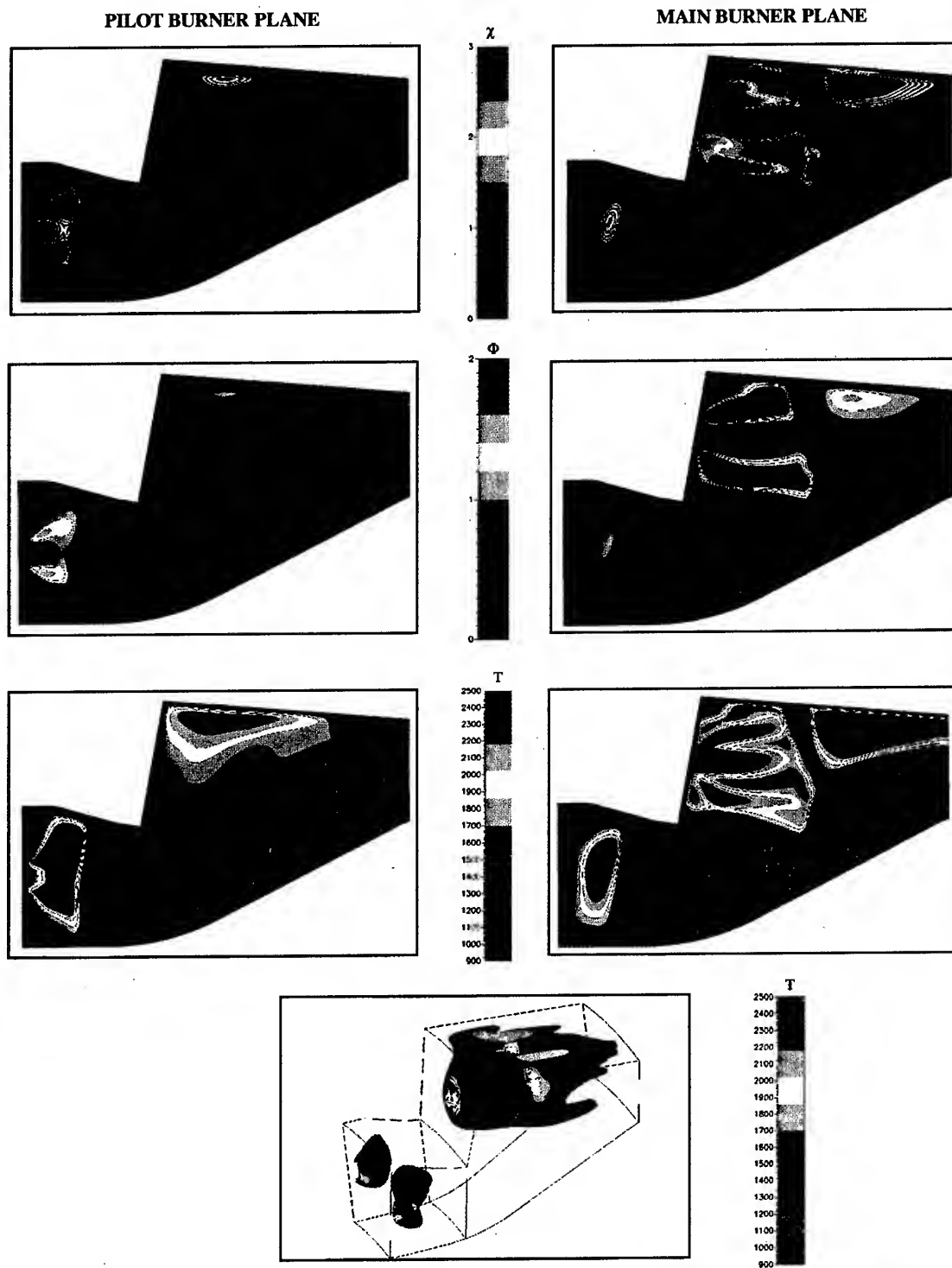


Figure 3 Distribution of mean dissipation rate, equivalence ratio, temperature and stoichiometric surface of A2-Can

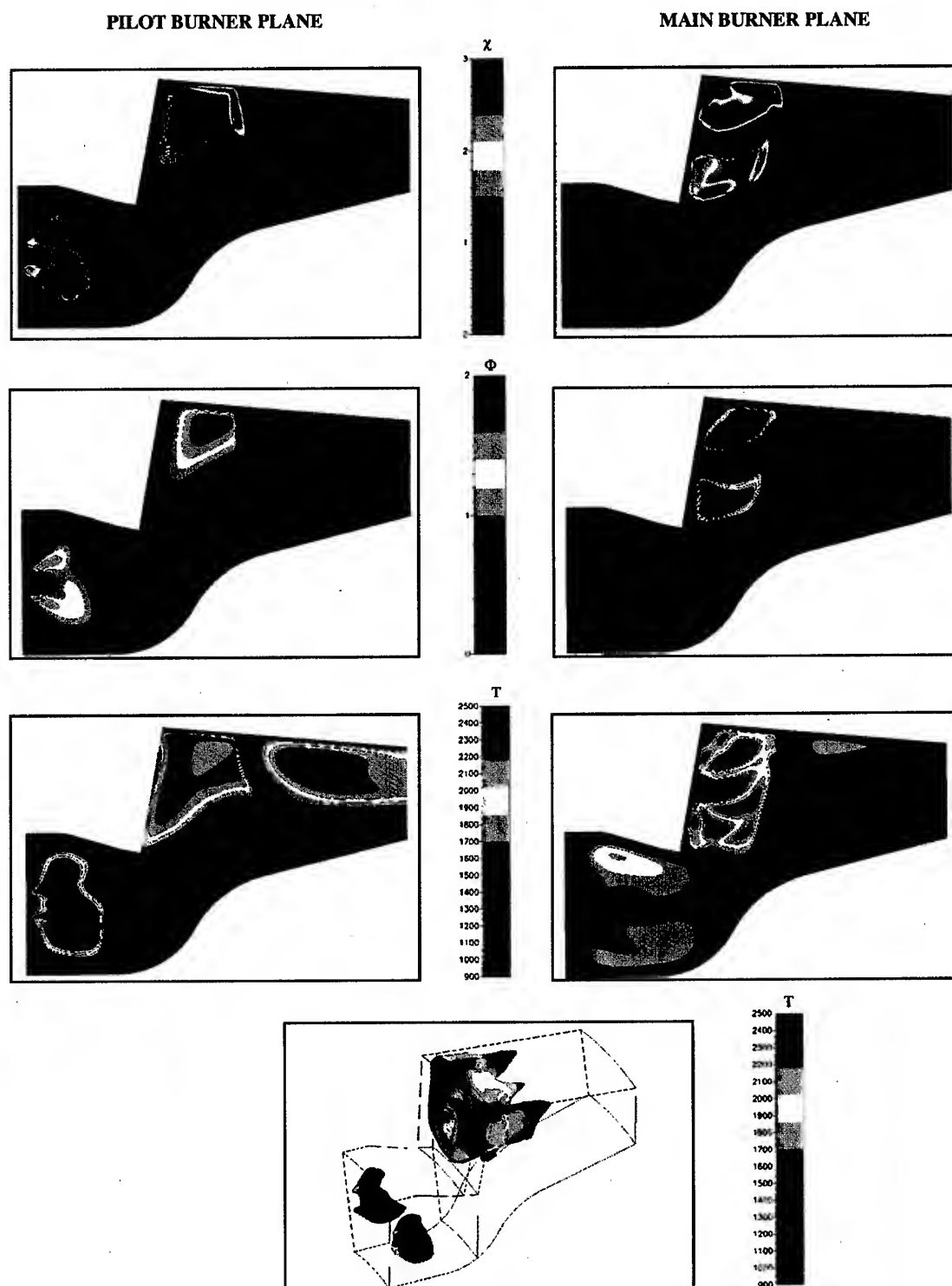


Figure 4 Distribution of mean dissipation rate, equivalence ratio, temperature and stoichiometric surface of C-Can

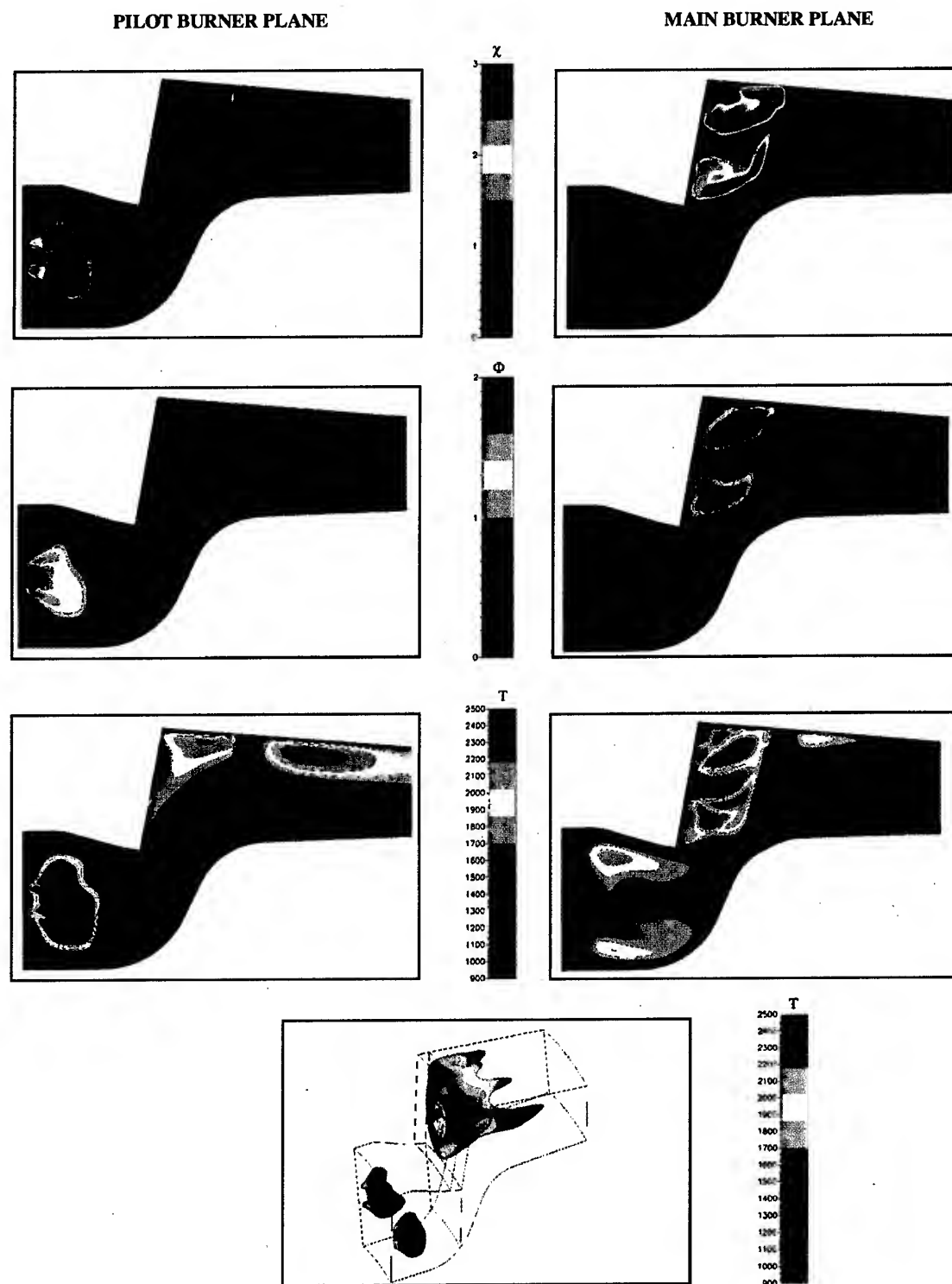


Figure 5 Distribution of mean dissipation rate, equivalence ratio, temperature and stoichiometric surface of E-Can

possible explanation for this is, that the thickness of the turbulent dissipation zone around the jets is thinner due to the increased shear stresses. The locally strong but thin mixing layers in conjunction with the higher axial velocity lead to an increased mixing length. The temperature distribution in fig.5 indicates a changed location of heat release in the narrower combustor compared to the C-can in fig.4. An optimisation of the mixing jet configuration would therefore be possible. The circumferentially inhomogeneous mixing performance indicates a non optimum fuel placement, which could be improved by an adaption of the fuel injector spacing to the combustor depth.

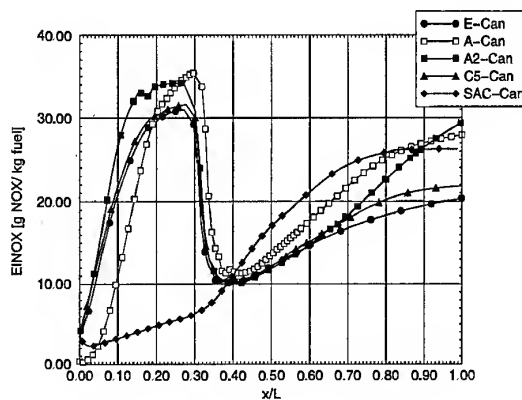


Figure 6 Computed EI-NOx along combustor axis

Finally, the interesting item is the effect of the volume change on the combustor NOx-emissions. Fig.6 shows the mean spatially averaged NOx emissions index along the combustor axis. Dry inlet air is assumed. The step down in the EI-NOx at the primary zone exit is due to the additional fuel from the main injectors. The curves are compared to the latest low NOx single annular technology. The A-can and the A2-can produce higher levels of NOx emissions than the single annular one, according to the CFD simulations. The EI-NOx of the C-can is predicted to be reduced by 25% compared to the A-can. The NOx production rate approaches to zero due to the short hot streaks in the secondary zone. The E-can is predicted to have the lowest level, with an EI-NOx of 20g/kg at the given conditions.

4. EXPERIMENTS

4.1 Experimental set up

The experiments were carried out in a 90°-sector combustor rig using the test facility of DLR Köln. Inlet pressure P_{30} is restricted to 2000 kPa whereas inlet temperature T_{30} and air-fuel ratio (AFR) represented realistic engine conditions. The AFR measured by gas analysis was within 10% of the value adjusted on the rig. Dry unvitiated air was used. A sampling probe was located in the combustor exit plane measuring gas concentrations in 5 radial positions. The rake was traversed in a circumferential direction averaging the gas concentration in a 54° center of the sector combustor. This reduced the side wall effects on the emissions measurement. 40 measured points were taken during the traverse.

The test conditions represent various sea-level-static engine cycle data.



Fig. 7 90° Staged Combustor Rig

Figure 7 shows the 90° staged combustor sector with 5 pilot and 4 main sectors. The fuel flow for the pilot and main bank is adjusted and measured individually. By this, different pilot to main fuel flow ratios were established for various power settings. The inlet of the rig was represented by a prediffuser to provide a representative flowfield in the annuli of the combustor. The rig was instrumented with total pressure rakes, static pressure tappings and thermocouples for monitoring the inlet conditions. Turbine bleed was simulated by appropriate orifices at the combustor exit without interfering with the gas sampling. During light-up and establishing the test conditions the rake was moved outside the combustor exit flow area to avoid any contamination of the rake and the sampling lines. Emissions measurement equipment and calculation procedure is according to SAE Aerospace Recommended Practice 1256. For calculating the mean emission-indices of the gaseous species, all 5 radial lines of the sampling rake were linked together. To gain the temperature exit profile of the combustor, the 5 lines of the rake were analysed separately and by means of balancing the enthalpy, the exit temperature for individual positions were deduced.

4.2 Experimental results

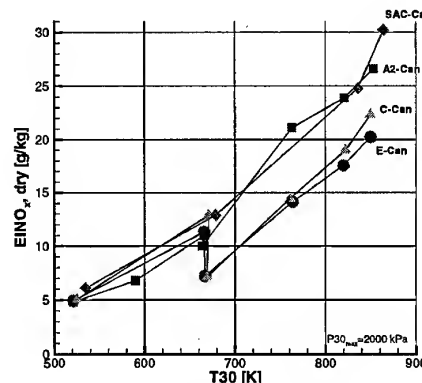


Fig 8 EI-NOx versus T30

Figure 8 compares the measured dry NO_x-emissions for the three staged combustor standards and a single stage combustor (SAC) versus T30.

When comparing the A2-Standard of the staged combustor with the SAC it is obvious that the staged combustor concept by itself does not lead to reduced NO_x emissions. The A2-Standard provides only a very limited NO_x reduction when the fuel is distributed to both zones, although the mean local AFR's are changed drastically. This shows the importance of the 3-D mixing process. The C- and E-Standard shows the typical EINO_x-T30 characteristic [4] with EINO_x drop at staging. By this, high power emissions are reduced by 19% and 26% for C- and E-Standard respectively compared with the SAC.

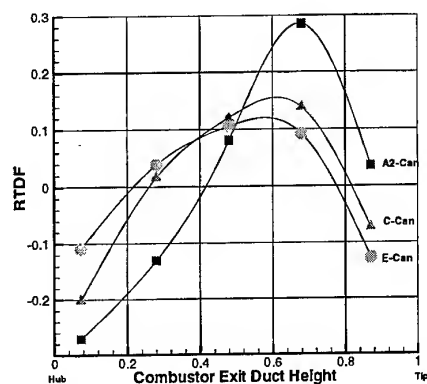


Fig 9 RTDF measured

Combustor	OTDF measured	OTDF computed
A2	0.5181	1.051
C	0.3545	0.587
E	0.4072	0.877

Tab. 1 Measured and computed OTDF

Figure 9 shows the temperature profile at combustor exit at simulated max. take-off condition for the three staged combustor standards expressed as RTDF profile versus normalised exit duct height. The symbols in the diagram correspond to the 5 radial position of the gas sampling rake. The fuel split ratio between pilot and main zone is fixed to 20% pilot fuel flow, 80% main fuel flow for all three standards. The profile of the A2-standard indicates a fundamentally different mixing process compared to C- and E-standard. The A2-Standard temperature profile peaks outboard with low temperatures near the hub. The C- and E-Standard are more even, with lower tip and higher hub tem-

peratures. For comparison, the computed RTDF of the different combustors are shown in fig. 10,

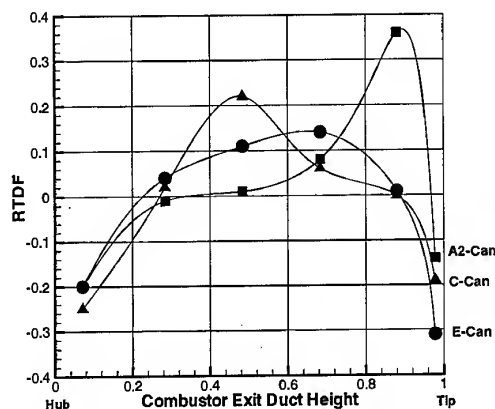


Fig 10 RTDF computed

A general observation is, that the mixedness at the combustor exit expressed by the temperature traverse is better in the experiment than predicted in the CFD simulations. For example, the hot streak predicted in the pilot plane of the E-can (fig.5) is not measurable at the exit. This is an often observed phenomenon, which is assumed to be related to the known deficiencies of the κ - ϵ -turbulence model. The underestimation of the mixing is also visible from a comparison between the measured and computed RTDF value, Figs. 9, 10. Table 1 shows that the measured OTDF values are always lower than the computed ones.

5. CONCLUSIONS

The agreement for the EI-NO_x between CFD prediction and measurement is reasonable. Especially, the relative improvements between the combustor concepts were predicted correctly. One of the objectives of this study was to show that it is possible to reproduce the trend in NO_x reduction based on major combustor design changes which were visible in the sector tests. The main emphasis was put on keeping the models, e.g. the constants (Prandtl, Schmidt numbers) unchanged and not on trying to fit the combustor exit profiles to measured profiles. This investigation shows that CFD in this application field is a valuable tool in supporting the design process in an early stage and also very useful for the interpretation of the experimental results.

The reduction of the depth of the main zone leads to a reduced residence time and an improved mixing process, as indicated by the CFD analysis. The design intention to reduce the NO_x emissions by a volume reduction was demonstrated by high pressure rig testing. Further improvements within the given geometry are possible by optimisation of the fuel injection spacing and the mixing jet configuration. Radical reductions in the geometrical dimensions of the combustor, the fuel injector and the jet mixing spacing are needed to approach the perfect mixing process and to reduce

the NO_x emissions substantially. This leads to the lean direct injection concept, which is a measure for further NO_x reduction for future high pressure ratio engines.

Acknowledgement

The authors would like to acknowledge the financial support of the German Ministry of Research and Technology BMBF sponsored E3E program. Special thanks to the BMW Rolls-Royce measurement department for performing the rig tests. The detailed LDV and PDA measurements taken by DLR Cologne and Berlin were also greatly appreciated. Finally, this work would have not been possible without the continuous support from the entire BMW Rolls-Royce combustion department.

Literature

- 1 Schadstoffe in der Luftfahrt, 1998 Abschlußkolloquium des BMBF-Verbundprogramms, 31.3.1998, Köln, Germany
- 2 Brehm N., Baker S.J., Jones S.P., 1997 "A Three Step NO_x Reduction Programme: Achievements with the Single Annular Low-NO_x Combustor for the BR 700 Engine Family" ASME 97-GT-145, 2.-5. June, Orlando Florida
- 3 Brehm N., Kau H.P., Jones S.P., 1997 "The BR 710, an environmentally friendly engine" CASI-Annual Conference 97, 28. - 30. April, Toronto
- 4 I. Segalman, R.G. McKinney, G.J. Sturgess and L.-M. Huang, 1993 "Reduction of NO_x by Fuel-Staging in Gas Turbine Engines - A commitment to the future" AGARD Conference Proceedings 536, Fuels and Combustion Technology for Advanced Aircraft Engines, proc. Propulsion and Energetics Panel 81st Symposium, Fiuggi, Italy
- 5 Spalding D.B., 1971 "Concentration fluctuations in a round turbulent free jet", Chemical Engineering science Vol.13, 3-25
- 6 Libby, P.A., Williams, F. A., 1994 "Turbulent Reacting Flows", Academic Press
- 7 Tonouchi J.H., Held T.J., Mongia H. C., 1997 "A Semi-Analytical Finite Rate Two-Reactor Model for Gas Turbine Combustors", ASME 97-GT-126, 2.-5 June, Orlando Florida
- 8 G.J. Sturgess, 1996 "Combustor Design Trends For Aircraft Gas Turbine Engines", ASME 96-TA-29, Turbo Asia Conference, Jakarta
- 9 CFD Research Corporation, 1998 "CFD-ACE Users Manual"
- 10 Faeth G. M., 1983 "Evaporation and Combustion of Sprays", Prog. in Energy and Combustion Sci., Vol. 9, pp. 1-76
- 11 Doerr Th., Blomeyer M., Hennecke D. K., 1997 "Optimization of Multiple Jets Mixing with a Confined Crossflow", J. of Eng. for Gas Turbines and Power, Vol. 119, No. 2, pp. 315-321
- 12 Migueis, C.E., 1996 "Untersuchungen zur Optimierung der Mischzone einer fett-mager gestuften Ringbrennkammer", DLR-Forschungsbericht 96-33
- 13 Everson R., Manin D., Sirovich L., 1998 "Quantification of mixing and Mixing Rate from Experimental Observations", AIAA Journal, Vol. 36, No. 2, pp. 121-127

PAPER NO. 27
Brehm, Schilling, Mack & Kappler
 (presenter: N. Brehm)

Question 1: M. Pourkashanian, University of Leeds, U.K.

In your post-processing of the CFD solutions for NO_x using O-equilibrium, how did you deal with the CH-steps?

Answer:

We only accounted for O and OH, there was no account of the CH-steps. The good agreement of the calculations with the companion measurements (Paper No. 18) was therefore surprising.

Question 2: G.J. Sturgess, ISSI, U.S.

First a comment: Congratulations to BMW for this fine computational paper, and also to your colleagues at DLR who provided the remarkable companion measurements (Paper 18); altogether an excellent program!

The CFD results reveal that, by apparent design philosophy, there is little direct action between the pilot and main stages of this combustor. Other implementations of the ASC low emissions concept (Segalman *et al.*, "Reduction of NO_x by Fuel-Staging in Gas Turbine Engines - A Commitment to the Future," Paper No. 29, AGARD Conference Proc. No. 536, Fuiggi, Italy, 10 - 14th. May, 1993; Segalman *et al.*, "Engine Demonstration of NO_x Reductions with a Fuel-Staged Gas Turbine Combustor," AIAA Paper No. 94-2712, 30th. Joint Propulsion Conference, Indianapolis, 27 - 29 June, 1994.) have used more direct interaction, indeed, such interactions have been viewed as essential for good combustion efficiency of the main at staging. Could you comment on your thoughts with respect to stage interactions? Most staged combustors have suffered from an efficiency penalty around the staging point. To what extent do you think that the staging combustion efficiency difficulties are due to stage interactions or the lack thereof? Recent observations of staging at 13 bar conducted at the Air Force Research Laboratory, have revealed just how difficult it actually is to achieve satisfactory stage interactions.

Have you an explanation for the experimental failure that you reported, of one of the staged combustor configurations, with respect to NO_x, to behave like a staged combustor, even though your CFD calculations indicated that it did so behave?

Answer:

A strong interaction between the pilot and main stages is a design intention for NO_x reduction. CFD analysis and optical measurements revealed only a weak interaction near the main zone fuel injectors. The mixing between the two stages was much improved by the geometrical changes from the A- to the E-can. A trade-off against low power efficiency has to be taken into account. Measurements in our overall programme revealed that a strong interaction between the two stages is positive for NO_x reduction, but leads to a penalty in efficiency at the staging point.

We have at present, no satisfactory explanation for the anomalous behavior with respect to NO_x characteristics, of one of the combustor configurations, where experimentally, it did not behave like a staged combustor.

Question 3: S.N.B. Murthy, Purdue University, U.S.

This question is in response to the remarks made by Dr. Sturgess in his questions, on the manner in which flames from independent sources, including one being ignited by the other, apparently like to remain independent of each other, except in rare situations when the flames are or become identical in a variety of ways, including flame structure, chemical reactions, and propagation characteristics. This is a fundamental question, and in general, it is very difficult to get flames to interact, although they may intermingle to some extent. Is this what Dr. Sturgess was referring to?

Answer (Dr. Sturgess):

I agree that flame interactions are issues of both interest and practical importance. When an array of simple gas-jet flames is brought closer together by decreasing the spacing between the jets, the flames adjust their size accordingly, and do not co-mingle until the spacing between them reaches a critical distance that is quite small. When they do co-mingle, the resulting combined flame is different in appearance than the individual jet-flames, even just before they merge. I have observed similar behavior in different practical engine combustors employing both axial staging (as in the BMW combustor) and parallel staging, with liquid Jet-A fuel, at atmospheric pressure and at pressures in excess of 10 bar (with commensurate air inlet temperatures). In these conditions it has proved surprisingly difficult to light off a main stage, even when the fine fuel spray of the main stage is completely surrounded by visible flame from the pilot stage. When ignition of the main stage does occur, initially separate mainstage flames are established and the pilot stage flames appear to exist as distinct envelope flames around the main stage flames. Such behavior can be independent of either pilot or main stage equivalence ratios, or absolute fuel mass flow rates. I have seen a case where some design "tweaking" did result in rapid main stage light-off with no loss in combustion efficiency around the staging point; it was difficult to comment on the flame states from simple visual observations. There is no immediate and satisfactory explanation for this improvement. The behavior described is clearly of major significance for practical fuel-staged combustors, (see my question to Tilston, Paper No. 23), and is deserving of some intellectual research.

A Novel Technique for Predicting The Ignition Performance of an Aero Gas Turbine Combustion Chamber

C W Wilson * Technology Leader Combustion & Emissions
Propulsion Dept., 170 Building, DERA Pyestock
Farnborough, Hants, GU14 0LS, UK

C G W Sheppard
University of Leeds, Woodhouse Lane
Leeds, Yorkshire, LS2 9JT, UK

H C Low
Combustion Engineering
Rolls Royce plc, P.O. Box 31
Derby, DE24 8BJ, UK

Summary

The work reported in this report is directed towards improvements in the ignition of gas turbine combustors. Currently available design rules are incapable of predicting the improved performance obtained with different ignition systems or igniter placement. Work has been carried out to address the inadequacies, in the current ignition prediction techniques, using Computational Fluid Dynamics (CFD).

A preliminary validation of the CFD ignition prediction technique was performed using ignition results from a fully annular research combustor. Qualitatively, the effect of igniter position, igniter type and combustor mass flow rate on ignition performance have been predicted, by inspection of the Karlovitz number encountered by a tracer, used to model a developing ignition kernel.

Introduction

For an aircraft gas turbine engine, the ignition performance is usually expressed in terms of the range of flight conditions over which combustion can be established. Once lit there is no guarantee that the gas turbine combustor will stay lit. In flight flameout of gas turbine engines may be caused by a variety of circumstances. For example, transient changes in engine airflow during aircraft manoeuvres, exhaust gas ingestion following the release of ordnance and severe ingestion of ice, water or dust can all terminate combustion. Whatever the cause, it may then prove necessary to fly the aircraft to a lower altitude for relight; whether the mission is military or civil, the result is obviously undesirable.

The size of an aircraft gas turbine combustion chamber is predominantly dictated by its altitude relight performance. Existing empirical design rules are used to indicate the volume required to give adequate primary zone airflow loading for acceptable altitude relight capacity. These empirical design rules indicate the conditions that have generally been found to work in practice in broadly similar temperature, pressure, and fluid dynamic regimes. The rules do not lead to any appreciable understanding of the mechanisms involved, nor do they prove that substantial improvements could not be achieved if understanding of the process were improved.

Altitude relight requirements have been a matter of concern from the earliest days of gas turbine development. If relight performance could be improved, combustion chambers could be made more compact with direct weight and cost reduction benefits. Much larger weight savings would also be achieved as a result of shorter shafts, connecting turbines and compressors, and smaller diameter engine casings. Reduction

in combustor size will result in performance benefits particularly in reduced NO_x emissions.

The most obvious assumption would be that the ignition performance is directly, and solely proportional to the total amount of energy released in the spark. However, the amount of energy delivered is typically orders of magnitude in excess of the minimum ignition energies for static fuel-air mixtures similar to those used in engines. Moreover doubling the delivered spark energy rarely has any perceptible effect on practical ignition limits. Even for fast flowing fuel-air mixtures, the energies used in practice are well above measured minima, Ballal and Lefebvre (1977).

Computational Fluid Dynamic (CFD) computer codes are now used extensively throughout the gas turbine industry. The way in which the combustion process is modelled varies considerably, from the assumption of chemical equilibrium to attempts to model the kinetic process by limited step chemical reactions. Although modelling of the ignition process should ideally include solution of the chemical kinetics, a simple approach for approximating ignition performance may be achieved by post processing converged CFD solutions and evaluating local characteristic times.

The method outlined in this paper enables combustion engineers to evaluate ignition limits by inspection of the trajectory of a developing ignition kernel. The method is based on evolution off the Karlovitz Flame Stretch Factor, a non-dimensional correlating parameter relating characteristic chemical and turbulent eddy lifetimes.

In order to validate the prediction capabilities, extensive testing is required. Preliminary, partial validation has been carried out using a modern research combustion chamber. This is reported here.

Experimental Programme

Test facility

A fully annular, vaporiser fuelled, research combustion chamber, shown in cross section in Figure 1, was installed in the Rolls Royce - Bristol, altitude test facility, Test Plant 123 (RJ4), Gypsy Patch North. The combustor was fitted with pressure jet atomisers to aid ignition performance. A fully annular ring carrying thermocouples was installed just downstream of the combustor exit to give an indication of successful ignition. These thermocouples were monitored using an IRRIS data logger; this was also used to record the inlet total pressure, air mass flow, vaporiser fuel flow and inlet temperature.

* Previously employed as Combustion Research Specialist at Rolls Royce plc, Filton, Bristol, U.K.

Two types of igniter were used; a standard Smiths Industries surface discharge igniter and a FDI06-2 focused discharge igniter. Both igniters were used in conjunction with a Marrelli AA63A/B 6 Joule high energy ignition unit. The spark rate for each igniter was timed at 135 sparks/min..

The combustion chamber outer casing had two groups of three bosses positioned either side of bottom dead centre which permitted location of the primers and igniters in various configurations, Figure 2. The igniter and primer were both located in the combustor head. The igniter was positioned circumferentially inline with the inlet to the vaporiser fuel injector and the primer was positioned between adjacent vaporisers. Holes were provided in the flame tube to allow the igniter and primer to enter the combustor. These holes were total pressure fed by air scoops to ensure that no combustion gases could escape from the combustion chamber into the feed annuli.

An alternative of the igniter/primer configuration was also tested, for the surface discharge igniter. This involved moving the igniter into the barrel position (firing through an air admission port in the primary zone) while the primer was placed through the hole in the head circumferentially on the vaporiser inlet.

Test procedure

The inlet pressure was set at the required level and maintained constant to within $\pm 3\%$ throughout each test. The combustor air mass flow was then established at the desired value and the fuel was introduced to achieve the required fuel to air ratio (FAR). The ignition unit was switched on and the period required to obtain light up of the combustor recorded. A successful light was indicated by a sudden and rapid increase in downstream temperature. The selection of test points was guided by the results and a matrix of test points was generated to define the relight loop.

A combustion stability loop was established for the combustor by lighting the combustor and then increasing/decreasing the air mass flow and fuel flow incrementally until the flame was extinguished. The results obtained allowed an envelope to be produced defining the lean extinction, rich extinction and blow-out limits.

Results from annular combustor testing

Combustion stability implies "smooth" burning and the ability to maintain burning over a wide operating range. The stability loop established for the research combustor can be seen in Figure 3. The range of fuel/air ratio between the rich and weak limits can be seen to reduce as the air velocity inside the combustor increases. The air mass flow at the point of extinction has been termed the "blow out mass flow rate" and all measurements are given relative to this.

An ignition loop generally has limits similar to those shown for stability. The ignition loop, however, lies within the stability loop since it is more difficult to establish combustion under "cold" conditions than to maintain an existing combustion process. However, the ignition loops obtained from the focused discharge igniter and surface discharge igniters, shown in Figure 4, proved to be well inside the stability loop for this combustor, suggesting that large improvements in ignition performance should be possible. The focused discharge igniter shows an improvement over the datum igniter due to an increase in chemical activity in the early stages of ignition (Wilson et. al. 1989).

A problem associated with existing ignition correlation parameters is that they do not allow for the location of the ignition device. The importance of the latter on ignition performance is shown in Figure 5, where it can be seen that the 1st configuration permitted relight with a 20% higher combustor mass flow.

Ignition Modelling technique

The ideal way to model the ignition process would be via a comprehensive computer programme, which could model both the liberated spark energy and then the processes governing the propagation of the spark kernel towards successful combustion. This would involve solving the aerodynamic flowfield, combined with chemical kinetic reaction schemes for the initial spark kernel and subsequent transition to turbulent flame propagation. However, the eventual aim of this work must be to produce a method capable of being used in the design process for combustion chambers, fuelled by kerosene. Given the complex composition of kerosene the required chemical kinetic scheme would be very large; such schemes are currently unavailable.

Odgers and Kretschmer (1985) reviewed the "state of the art" relating to the ignition of gas turbine combustors. The papers reviewed were described as representative rather than comprehensive and they concluded that the modelling of gas turbine combustor ignition was difficult and recommended an empirical or semi-empirical approach.

Plee and Mellor (1979) and Peters and Mellor (1982) have developed "characteristic time" based models for several gas turbine combustor operating parameters; including both ignition and stability. Their approach for ignition relies on characteristic times for evaporation and turbulent mixing.

Such characteristic time models rely on estimations of various fluid flow and chemical parameters. For example, it is generally accepted that the local turbulence levels within a combustor can be estimated from the pressure drop across the combustor wall, since the loss in pressure energy is converted into turbulent kinetic energy, Swithenbank (1974). The "chemical times" normally rely on empirically developed correlations for hydrocarbon reaction rates and evaporation times.

A common failing of the empirical correlation methods, e.g. the characteristic time approach of Plee and Mellor, is that the position of the igniter and the local characteristics affecting the developing kernel, both fluidic and chemical, are not considered. The experimental results set out in Figure 5 clearly show that the position of the igniter has a dramatic effect on ignition performance; this could not be predicted using either of the above methods empirical.

Rizk & Mongia (1986), Mongia and Smith (1978) and Mongia et.al. (1986) have demonstrated the use of semi-empirical techniques for determining a number of combustor performance parameters. They took existing correlations and applied them to each cell of a converged Computational Fluid Dynamic (CFD) solution for the combustor under evaluation. This allowed some of the assumptions normally made on a macro scale to be eliminated, with CFD being used to predict values (such as turbulent velocity, local equivalence ratio etc.) which normally had to be assumed for a given combustion chamber.

One parameter which has been used to predict ignition performance and subsequent flame propagation is the Karlovitz

stretch factor, K , Abdel Gayed et al. 1989. This parameter, described by Chomiak and Jarosinski (1982) and given by:-

$$K = \frac{u' \delta_l}{\lambda SL} \quad (1)$$

where $\frac{u'}{\lambda}$ can be regarded as either a strain rate or an eddy life time obtained by dividing the turbulent velocity fluctuation (u') by the Taylor microscale of turbulence (λ)

and $\frac{\delta_l}{SL}$ can be regarded as a chemical lifetime or a reciprocal chemical strain rate.

The laminar flame thickness δ_l can be estimated, Gaydon and Wolfhard (1970), by:-

$$\delta_l = \frac{\nu}{SL} \quad (2)$$

where ν is the kinematic viscosity and SL the laminar burning velocity.

For isotropic turbulence the Taylor turbulence microscale, λ , can be obtained (Hinze, 1959) by:-

$$\frac{\lambda^2}{L} = \frac{A}{u'} \quad (3)$$

where A is a constant assigned a value of 40.4 by Abdel-Gayed and Bradley (1981) and L is the integral length scale of turbulence.

Since the value of turbulent Reynolds number, Re , is given by:

$$Re = \frac{u' L}{\nu} \quad (4)$$

Substituting for λ and δ_l into Equation 1 and using Re gives:

$$K = 0.153(u'/u_l)^2 Re^{-0.5} \quad (5)$$

If it can be assumed that the flow within each cell of a CFD model is homogeneous and isotropic, then it is possible to adopt an approach, similar to that of Rizk & Mongia (1986) to obtain a semi-empirical solution to the ignition problem. In this the CFD solution is used in evaluating the Karlovitz parameter for each cell in the combustor domain.

PACE Description

The Rolls Royce suite of computer codes known as PACE (Prediction and Analysis of Combustion Emissions) was used for the CFD calculations. A history of the development of PACE has been given by Chlebon (1987). The main computer code, used to produce the work presented in this paper, is based on a variant of that described by Jones and Priddin (1978) and Jones et al. (1978). The version of the code used here solved equations for the finite difference representations of mass continuity, scalar conservation, momentum, turbulence energy generation and dissipation. The

finite difference formulations include a $k-\epsilon$ turbulence sub-model, after Launder and Spalding (1974), to accommodate the fluctuating turbulent velocities. The PACE system has been developed so that full combustion systems may be analysed, by joining together internal and external flows, Mannors (1988). However, in the current study only the flows internal to the flamentube have been considered.

For a combustor employing vaporiser fuel injectors two of the boundary edges usually represent planes, or axes, of symmetry. In these cases the velocity component normal to the boundary is set equal to zero, and all other variables have a zero gradient applied across the boundary. This is commonly referred to as mirror boundary conditions.

When modelling the vaporiser fuel injector the physical shape of the vaporiser is "blocked" out of the mesh. The blockages then take on the same properties as a solid wall. The exit of the vaporiser has a velocity calculated from empirical relationships and PACE grid area written on to it. The flow is assumed to have a flat velocity profile, containing no gradients or swirl.

KARL computer code

A computer code, KARL, was written to calculate variables not available as standard output from PACE. The PACE output database was interrogated for the standard solution data, along with information describing the type of solution obtained. The required variable was calculated within each cell of the solution domain and also stored on the PACE database.

Assuming the flow field within each cell to be isotropic ($u'=v'=w'$), the variable u' was obtained from the PACE calculated value of turbulent kinetic energy, Ke , by:

$$u' = \sqrt{\frac{2}{3} Ke} \quad (6)$$

The value of L was then be obtained from:

$$L = \frac{C_D Ke^{3/2}}{\epsilon} \quad (7)$$

where ϵ is the turbulence dissipation rate and the value of the constant C_D was set as 0.202, as suggested by Abdalla et. al. (1981).

Data for the laminar burning velocity of real fuel such as kerosene are sparse in the literature. Polymeropoulos (1975) produced a mathematical model for calculating the laminar burning velocity of kerosene sprays. Data from this model was used, in curve fitted form, to derive an equation for laminar burning velocity as a function of local equivalence ratio.

$$SL = C_0 + C_1 \times \phi + C_2 \times \phi^2 + C_3 \times \phi^3 \quad (8)$$

For a fuel other than kerosene an alternative set of polynomial coefficients (C_0 , C_1 , C_2 and C_3) are required.

The local value of Karlovitz number at each point in the solution domain was then calculated using Equation 5.

Post Processing of solutions

The ignition performance was predicted by first obtaining a converged PACE solution. Following convergence, the computer program KARL was run to calculate local values of additional variables, such as u' and K . A conserved tracer was then introduced to simulate the movement of an ignition kernel. This kernel was convected within the solution domain via a transient, time marching, formulation of the Navier-Stokes equations [Marquis (1986)]. The value of the tracer was then stored at set time intervals to enable its time history to be investigated. The ignition kernel was modelled as an "impulse function". The typical duration for a standard high energy surface discharge igniter is 100 μ s. Compared to a typical combustor residence time of 20 ms this is short. Therefore, in modelling the ignition kernel, the energy, in the form of a conserved scalar, was applied for a number of iterations depending on the time step used. Consequently, the energy density obtained at any point in the combustor varied with time.

TRACE computer code

A computer code which enabled detailed evaluation of the movement of the simulated kernel within the combustion chamber was written. It starts by reading the PACE database, to obtain the steady state (converged) solution data, and then calculates (from the sum of all the individual cell volumes) a total volume for the combustor. An iteration loop was then initiated by the computer program. Each time through the loop the file containing the kernel concentration, at a given time, was read. The volume of the solution contained between predetermined upper and lower limits of kernel concentration was calculated. The distribution of any PACE variable, within the kernel, was then evaluated. When all the time steps were completed, and the kernel convected out of the solution domain, plots relating to the history of the kernel were evaluated.

Modelled Combustor

The research combustor was modelled using PACE. The solution was evaluated for two separate igniter positions and two igniter types.

The full annular combustor had twenty six fuel injector outlets. Thus, the smallest repeatable circumferential section that could be used to model the flow was $1/26^{\text{th}}$ of the annular combustor (13.85°). This was achieved by employing mirror symmetry boundary conditions for each circumferential end plane. The computational grid used, shown in Figure 6, was 73 nodes in the axial direction, 37 in the radial direction and 21 in the circumferential direction. The solution domain extended from the centreline of the vaporiser inlet to a plane midway between vaporiser outlets. The inclusion of the vaporiser fuel injectors into the solution domain was achieved by blocking out cells within the mesh. This resulted in a castellated edge rather than a smooth surface to the vaporiser.

Mass flows were investigated for two conditions one either side of the ignition boundary, based on the experimental results shown in Figure 4. For the case where the combustor mass flow was below the limiting value for ignition, a combustor mass flow of 35% of blowout mass flow was chosen. To investigate the effect of combustor aerodynamics on the ignition process a second condition was modelled, at a mass flow of 80% of blowout mass flow. This may seem a high mass flow but is still within the boundary of combustor

stability, Figure 3, and both ignition and stable combustion should be possible. The overall fuel air ratio for each case was 0.02.

The inlet temperature and pressure from the altitude test facility, along with the mass flow described above were used to define overall combustor conditions. An empirical 1-D airflow analysis program was utilised to predict the proportion of total mass, and mean flow injection angles, through each of the various air inlet features.

The boundary conditions for turbulent energy were calculated using a turbulence intensity of 5% of the mean velocity through each feature; the dissipation rate was calculated using a length scale based on a characteristic length for each feature.

The PACE code uses chemical equilibrium to calculate the local species concentration, and hence the local density at a point. Hence the usual density - fuel fraction relationship used within PACE was not valid for ignition calculations. Instead, a relationship between fuel fraction and mixture density, assuming that both air and gaseous kerosene behaved as ideal gases, was derived from the equation of state and the respective relative molecular masses. Since the experimental ignition results were generated using liquid kerosene, the work reported here could only be used to validate the effect of increased mass flow on ignition performance.

The ignition performance was calculated from the CFD prediction using the techniques described previously. The two igniter locations investigated in the experimental programme were analysed; one where the igniter was fired into the combustor from the head of the combustor and an alternative position where the igniter was co-located with the primary zone port. A further igniter position was analysed after inspection of the PACE data; this position was recommended for improved ignition performance.

Computational results

Flow field

Streak-line plots, for the theta plane passing through vaporiser exit are shown in Figures 7 and 8, respectively. The same tracking time has been used for each combustor. The flow field patterns for each proved to be essentially the same. The primary zone port flows in each solution impinge downstream of the vaporiser exit, at approximately mid combustor height. The difference in streak line lengths between the two figures is associated with the higher mass flow, for the case where the combustor failed to ignite. The outer primary port flow appears to be dominant. Particle tracking calculations for this solution suggest that the outer primary port flow acts as a pump, rapidly moving flow out of the combustor, with the inner primary port providing the recirculation necessary for good relight performance.

Predicted Karlovitz number

The Karlovitz number, K , was used to assess whether flame propagation or quench would occur at individual points in the flowfield. The limiting value of Karlovitz adopted employed a correlation based on the work of Abdel-Gayed and Bradley (1985). Subsequent work by Abdel-Gayed et al. (1989) identified three different regimes of combustion in turbulent explosion flames. These regimes also showed a dependence upon the values of Lewis number, Le , as well as Karlovitz number. With increasing flame stretch; one moves from a continuous flame sheet regime into one of partial and,

eventually, complete quenching. As the product of the Karlovitz and Lewis numbers (KLe) reaches a value about 0.15, break up of the flame sheets was noted by Abdel-Gayed et al. At values of KLe greater than 0.3, partial quenching was observed in a fragmented reaction zone, prior to complete flame quenching. Complete flame quenching occurred when:

$$K(R_L)^{-0.5} > 0.079 \quad \text{for } R_L < 300 \quad (9)$$

$$KLe > 1.5 \quad \text{for } R_L > 300 \quad (10)$$

More recent correlations by Bradley et al. (1992) show that a flame can develop at KLe values greater than 1.5 without complete flame quench occurring. For the work reported here, the Lewis number has been set to unity and the relationships given in Equations 9 and 10 were adopted.

When the PACE solution for the research combustor was interrogated for R_L , the values found were generally above 300, suggesting the use of Equation 10. However, in some parts of the combustor, especially for the case inside the ignition loop, R_L values as low as 100 were obtained, where Equation 9 is more appropriate. For ease of discussion (and since only small regions of the developing kernel encounter low R_L values) quench was assumed for all regions of the flow where $K > 1.5$.

The predicted Karlovitz numbers, for the high and low mass flow conditions are shown in Figures 9 and 10 respectively. These data are displayed on mesh k-planes moving down the combustor, from left to right. The k-planes shown correspond to 10, 37, 57, 63 and 73. The left most k-plane, 10, shows the vaporiser outlet in the centre of the plane. The value of K would suggest that a flame could be supported here. However, this is an erroneous result associated with the blocked out cells method used to model the vaporiser, which have a zero default value of Karlovitz number. The inlet for the vaporiser is on the constant theta plane (J), furthest into the page. This is better seen in Figure 11 where two circular patches can be seen on k-plane=10. The contours are plotted for all values of Karlovitz number between 0 and 25. The grey regions show where the value of Karlovitz is in excess of 25.

Low mass flow case

For the case where the modelled conditions fall within the experimental ignition boundary, a large region of low Karlovitz number can be seen on the outer portion of the k-plane=37. There are also several other significant regions of low Karlovitz number; one around the vaporiser inlet and the other in the recirculation region downstream of the primary zone port and one in the plane between vaporiser outlets. The region around the vaporiser inlet is important because of its proximity to the wall and the fact that an ignition kernel could be confidently placed in this region, from which the combustor would be expected to light. This would not be the case for the region of low Karlovitz number found on the k=10 plane, in the plane between vaporiser outlets, since the high velocity flows in this region would convect the developing kernel away from the zone. The low value of Karlovitz number found in the lee of the inner primary zone port demonstrates the mixing ability of the air flow from this port and highlights the necessity to provide sheltered regions for ignition and stability.

High mass flow case

For the case with an air mass flow rate outside the known ignition boundary of the combustor, the value of Karlovitz number is generally higher than for the lower mass flow case. Most of the regions with Karlovitz number below 1.5 have disappeared from the primary zone. The only large region with Karlovitz number lower than 1.5 is in the downstream wake of the inner primary zone port.

The increase in Karlovitz number is associated with the increase in u' between the two conditions, as shown in Figures 11 and 12. The high combustor mass flow results in high mean velocities. These high velocities are generated by a higher pressure drop across the combustor wall, with the loss in pressure energy being converted into turbulent kinetic energy.

Ignition kernel calculations.

The qualitative assessment of ignition performance, described above, can be used to postulate why one combustor will light and the other will not. However, in order to assess the combustor ignition performance and rank the effect of igniter position and type; it was necessary to establish the ignition kernel trajectory, within the combustor. This determines whether the flame kernel is entrained into the primary zone, is swept out of the primary zone to the exhaust or is just strained into extinction.

In this paper the kernel has been modelled as an "impulse function" conserved scalar, being present at a value of 1.00 for the first time step only. The volume within which the ignition kernel tracer was set, combined with the igniter energy, was used to calculate a tracer concentration that equated with the minimum ignition energy of kerosene. The minimum ignition energy used for this work was taken as 10mJ; this is fairly arbitrary since in reality the value will depend on a range of parameters including the equivalence ratio, fuel droplet size and local air velocity.

As the tracer was convected within the solution domain by turbulent transport, the values of Karlovitz number, and other PACE derived variables seen by the developing kernel were evaluated. The results obtained using this technique are discussed in the following sections.

Effect of combustor operating condition

The time history of volume weighted Karlovitz number is shown in Figures 13 and 14 for the high and low mass flow conditions. For neither case is the mean Karlovitz number below 1.5. The value of Karlovitz number has been calculated for a proportion of the tracer volume, as shown in Figures 15 and 16 for each case. This demonstrates that the kernel is being moved around the primary zone and reaching points where the equivalence ratio is such that a flame cannot exist. In such regions, outside the flammability limits, the value of Karlovitz number was set to a high value ($9.0E+9$). Shown in Figure 16 is the effect of the higher combustor mass flow, for the condition outside the ignition boundary where, in less than 4 milliseconds, the ignition kernel "energy" tracer has been reduced to a level below the minimum igniter energy. The steep rise and fall in the percentage of the tracer are associated with this rapid reduction in ignition energy with time. In contrast, to this reduction in minimum ignition energy, for the case with a flow rate inside the ignition boundary, the energy density within the ignition kernel is still above the minimum ignition energy after 12 milliseconds have elapsed.

If the distribution of Karlovitz number (at various times) is inspected for each case, it can be seen that there are only a few very large Karlovitz numbers which produce the high mean value.

For Karlovitz number < 100 the distributions shown in Figure 17 are produced. These distributions demonstrate that the amount of mixing generated in the high mass flow case is high, since a much shorter time-step is required to obtain the same amount of tracer dissipation.

However, since the criterion for successful ignition was a Karlovitz number less than 1.5, a further evaluation of the data was undertaken. This showed for the high mass flow condition, the value of K within the tracer volume never fell below the critical value of 1.5. However, within the ignition boundary more than 15% of the kernel volume encounters values of Karlovitz number < 1.5 , as shown in Figures 18 and 19. The long time delay experienced between the igniter being fired and the kernel finding a region that could support flame propagation has been experienced experimentally in gas turbine combustors. Shown in Figure 20 is such an event, taken from ignition testing of a Spey cannular combustor at DERA Pyestock [Tilston(1982)]. The photograph in the top left frame of the series, shows the initial firing of the igniter. The visible emission from the spark decays over the next three frames and the combustor appears to have failed to ignite. Some eleven frames later a small glimmer of kernel is evident before, within the next 20 frames, the combustor is fully ignited and stabilised; proving that the spark kernel can tolerate reduced energy per unit volume and travel through regions of adverse conditions before finding satisfactory conditions to allow it to ignite the mixture.

Effect of igniter position

The contour plots of Karlovitz number, shown in Figure 9, would suggest that placing the igniter through the primary port would be beneficial to ignition if the kernel could migrate into the regions of low Karlovitz number surrounding the region of the outer primary port flow. The kernel trace calculation is shown in Figure 21. The delay between the igniter being fired and the kernel finding conditions suitable for ignition has increased relative to the datum condition. The percentage of the kernel which has found acceptable conditions is shown in Figure 22. This is also lower than for the datum condition.

The experimental effect of igniter location between the datum, Position 1, and the alternative, Position 2, is shown in Figure 5. The actual change in performance is a reduction in limiting mass flow, from 50% to 40% of blowout mass flow. Although the calculation suggests that the datum condition is better, the relative amount of improvement is difficult to assess. It will probably be necessary to model several combustors, with known ignition performance, to produce a robust and acceptable correlation.

Effect of igniter type

In an attempt to model the change in igniter type, measurements of flame propagation using schlieren imaging were consulted. These showed that the initial volume of the kernel was larger for the Focused Discharge Igniter (FDI) than standard Surface Discharge Igniter (SDI) igniters. Therefore, to model the change in igniter a new conserved scalar was established, by utilising a larger initial volume for the "impulse function" ignition event.

The results for the new tracer are shown in Figure 23. The time to ignition, measured from the start of the time marching solution to when the kernel first finds conditions which will support a flame, has reduced relative to the datum igniter. This indicates improved ignition performance. The amount of kernel convected into the regions suitable for combustion has also increased by approximately 50%, Figure 24. The results set out in Figure 4, in which the performance of the two igniters are compared, shows that FDI had a limiting mass flow $\approx 58\%$ of blowout mass flow, while the SDI has a lower limiting mass flow of 50% of blowout mass flow. The model quantitatively predicts this improvement. However, a somewhat larger data base is required to confirm this.

Recommended igniter position

Shown in Figure 25 are contours of Karlovitz number for the theta plane through a vaporiser inlet ($J=1$). The contours are shown in such a way that apart from those shown grey, any colour contour should support a flame. There is a large region above the vaporiser inlet that looks promising as an area in which to initiate combustion. A conserved scalar was therefore set up in the combustor head location, but positioned circumferentially in line with the vaporiser inlet plane. For this condition it is clear that the developing kernel now enters into the combustor and immediately experiences favourable conditions of low K , Figure 25. Further, the low Karlovitz number is seen by a very large proportion of the kernel, Figure 26. This recommended igniter location has not been evaluated experimentally.

Conclusions

1. CFD calculations have been used to determine maps of Karlovitz number within a gas turbine combustor for two operating conditions.
2. A conserved scalar tracing technique has been employed to produce a "pseudo" ignition kernel.
3. Qualitatively, the effect of (a) igniter position, (b) igniter type and (c) combustor mass flow rate on ignition performance were predicted.
4. The value of Karlovitz > 1.5 for quench has been used to identify successful ignition.
5. More work is necessary to obtain wider correlation of CFD and experimental ignition for greater confidence in the theoretical method to be developed.

References

1. Abdalla, A.Y., Ali, B.B., Bradley, D., and Chin, S.B., "Stratified combustion in recirculating flow", *Comb. & Flame* vol 43: pp131-143, 1981.
2. Abdel-Gayed, R.G., and Bradley, D., "A two eddy theory of premixed turbulent flame propagation.", *Phil. Trans. R. Soc. Lond. A* 301, pp 1-25, 1981.
3. Abdel-Gayed, R.G., and Bradley, D., "Criteria for the turbulent propagation limits of premixed flames", *Comb. & Flame* vol 62, pp 61-68, 1985.
4. Abdel-Gayed, R.G., Bradley, D., and Lung, F.K., "Combustion regimes and the straining of turbulent premixed flames", *Comb. & Flame*, Vol 76, pp. 213-216, 1989.
5. Ballal, D. R., and Lefebvre, A. H., "Ignition and flame quenching in flowing gaseous mixtures", *Proc. Roy. Soc. Lond. A* 357, pp 163-181, 1977.

6. Bradley, D., Lau, A.K.C. and Lawes, M., "Flame stretch rate as a determinant of turbulent burning velocity", *Phil. Trans. R. Soc. Lond. A* 338, pp 359-387, 1992.
7. Chleiboun, P.V., "Mathematical modelling relevant to gas turbine combustion", PhD thesis, Mech. Eng. Dept., University of Leeds, 1987.
8. Hinze J. O., "Turbulence an introduction to its mechanism and theory.", McGraw Hill, New York, 1959
9. Jones, W.P., Clifford, W.C., de Chair, R., and Priddin, C.H., "A comparison between predicted and measured species concentrations and velocities in a research combustor." *High Temperature Problems in Gas Turbine Engines. AGARD Conf. Proc.* 229, 1978
10. Jones, W.P. and Priddin, C.H., "Prediction of the flowfield and local gas composition gas turbine combustors", 17th Symposium (International) on Combustion. 1978
11. Launder, B.E., and Spalding, D.B., "The numerical computation of turbulent flows.", *Comp.Meth. Appl. Mech. Eng.* 3, pp 269-289.
12. Manners, A.P., "The calculation of flows in gas turbine systems", PhD thesis, University of London, 1988.
13. Mongia, H.C. and Smith, K.F., "An empirical/analytical design methodology for gas turbine combustor", *AIAA Paper* 78-998, 1978
14. Mongia, H.C., Reynolds, R.S., and Srinivasan, R., "Multidimensional gas turbine combustion modelling applications and limitations", *AIAA journal*, 1986
15. Odgers, J., and Kretschmer, D., "Problems of ignition correlations - an assessment of applications to real combustors", *ISABE paper* 85-7092, 1985
16. Polymeropoulos, C.E., "Ignition and propagation rates for flames in a fuel mist", *FAA-RD-75-155*, 1975.
17. Tilston, J.R., Unreported work on a Spey combustion chamber, NGTE Run number 19, 1982
18. Peters, J.E. and Mellor, A.M., "A spark ignition model for liquid fuel sprays applied to gas turbine engines", *Journal of Energy* 6(4), 272, 1982.
19. Plee, S.L., and Mellor, A.M., "Characteristic time correlation for lean blowoff of bluff-body-stabilized flames", *Comb. & Flame*, Vol 35: pp. 61-80, 1979
20. Rizk, N.K., and Mongia, H.C., "Gas turbine design methodology", *AIAA Paper*, 1986
21. Sotheran, A., "The Rolls Royce annular vaporiser combustor", *ASME Paper* 83-GT-49, 1983
22. Swithenbank, J., "Flame stabilization in high velocity flow", *Combustion Technology- some modern developments*, Academic Press Inc. 1974.
23. Wilson, C.W., Low, H.C., Abdel-Gayed, R.G. and Bradley, D., "Evaluation of Novel Igniters in a Turbulent Bomb Facility and a Turbo-Annular Gas Turbine Combustor", *AIAA Joint Propulsion Conference*, Monterey, June 1989.

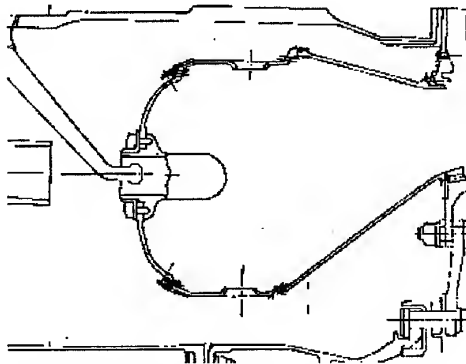


Figure 1 Research combustion chamber cross section

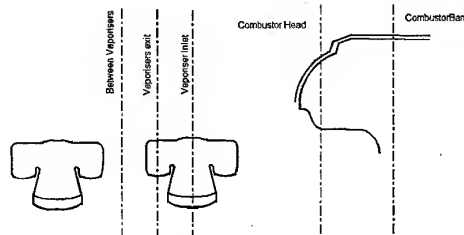


Figure 2 Igniter and primer location in the research combustor

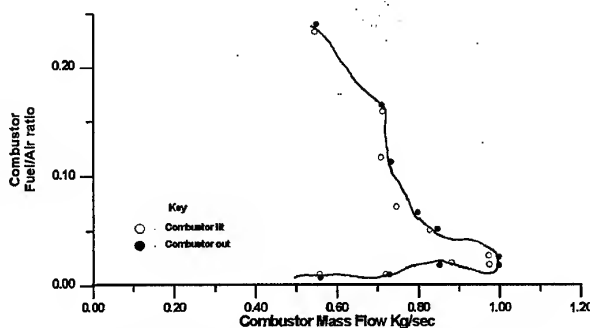


Figure 3 Experimental stability loop for research combustor at 55 kPa

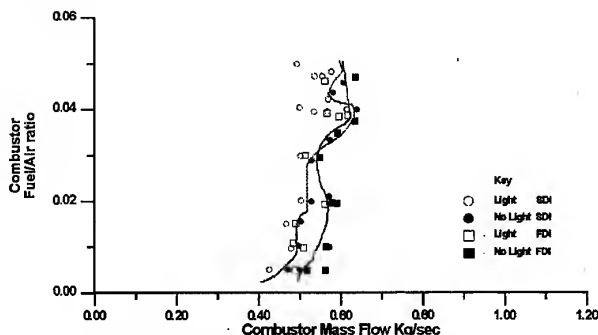


Figure 4 Research combustor ignition loop

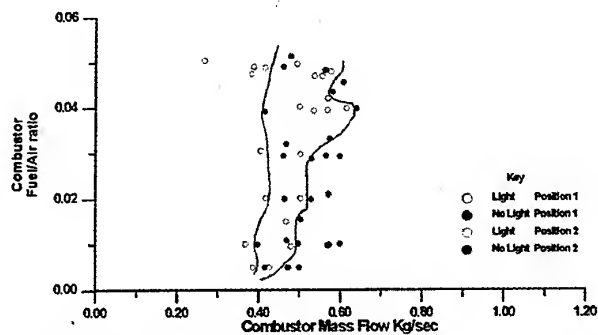


Figure 5 effect of igniter position on ignition loop.

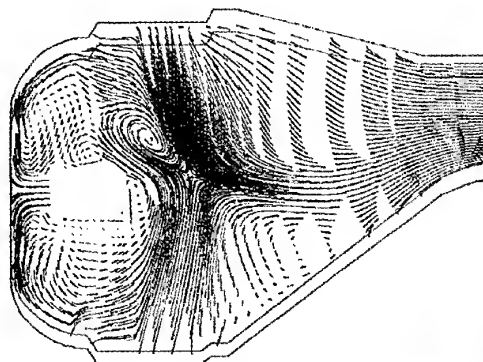


Figure 8 Streakline plot for the high mass flow condition.

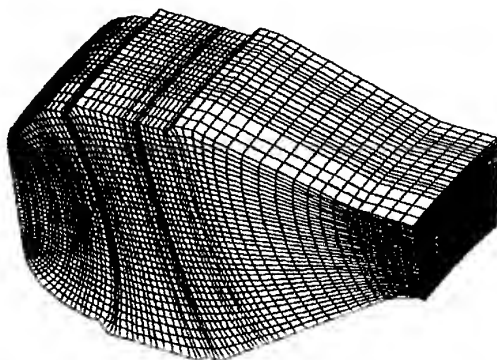


Figure 6 Rotated Orthogonal mesh



Figure 9 Predicted Karlovitz number for the low mass flow condition.

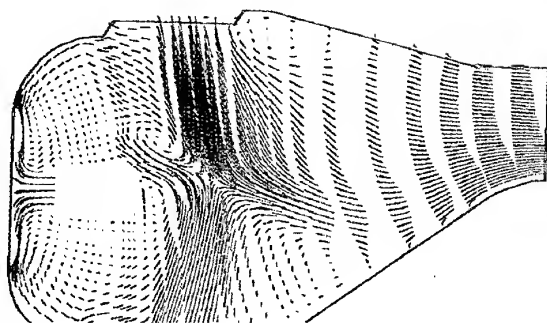


Figure 7 Streakline plot for the low mass flow condition.



Figure 10 Predicted Karlovitz number for the high mass flow condition.



Figure 11 u' predicted for the low mass flow condition.

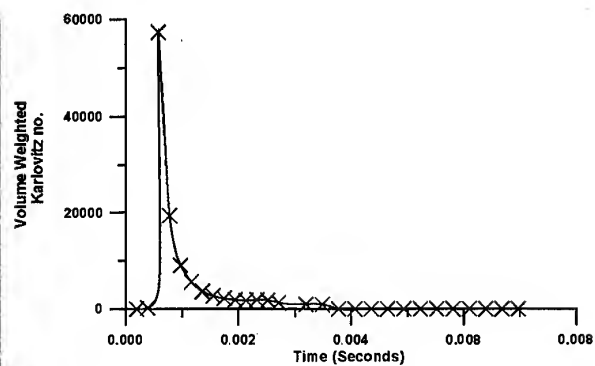


Figure 14 Karlovitz number seen by the developing kernel (High mass flow case).

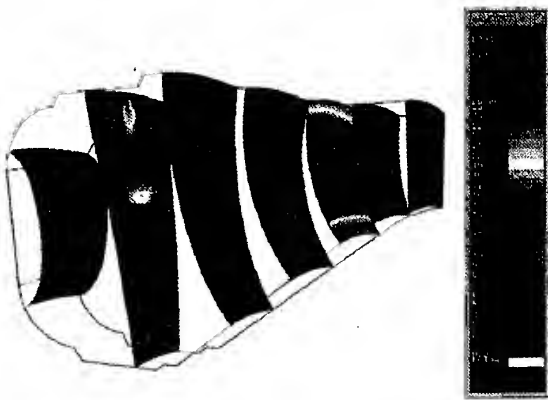


Figure 12 u' predicted for the high mass flow condition.

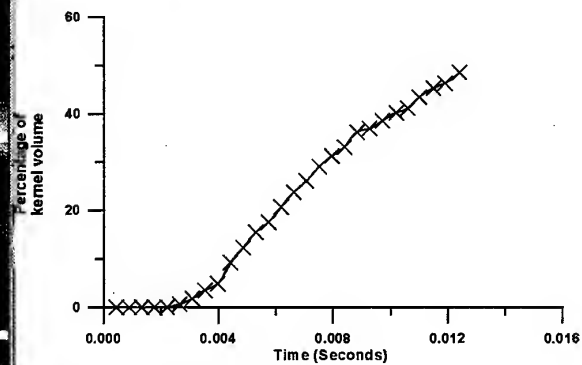


Figure 15 Percentage of kernel volume seeing Karlovitz number below $9.E+09$

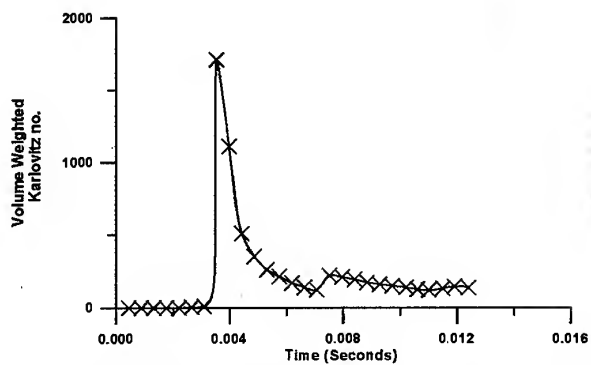


Figure 13 Karlovitz number seen by the developing kernel (low mass flow case)

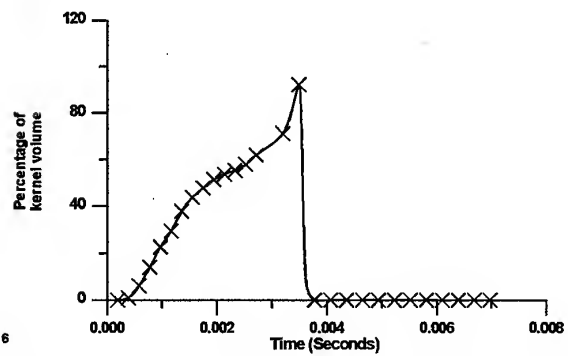


Figure 16 Percentage of kernel volume seeing Karlovitz number below $9.E+09$

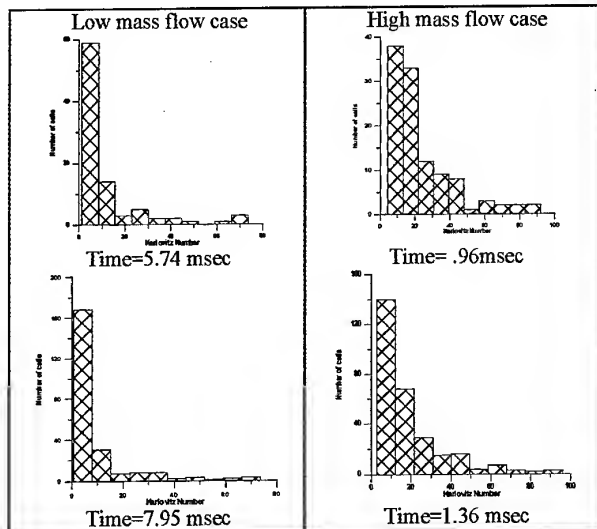


Figure 17 Distribution of Karlovitz number experienced by the developing kernel

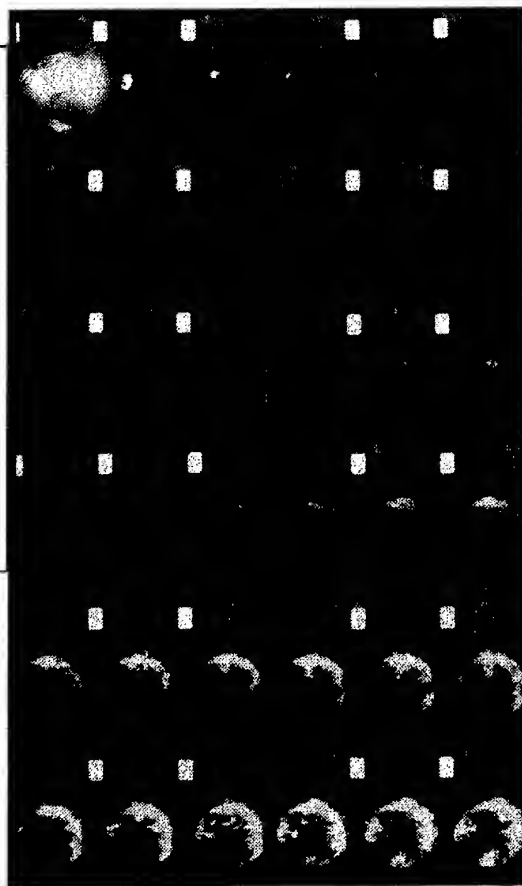


Figure 20 Gas turbine atmospheric ignition test after Filston (1982)

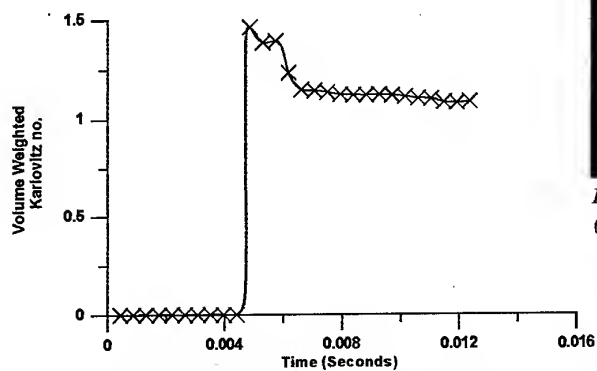


Figure 18 Volume weighted Karlovitz number, below 1.5, within the developing kernel for the standard igniter location.

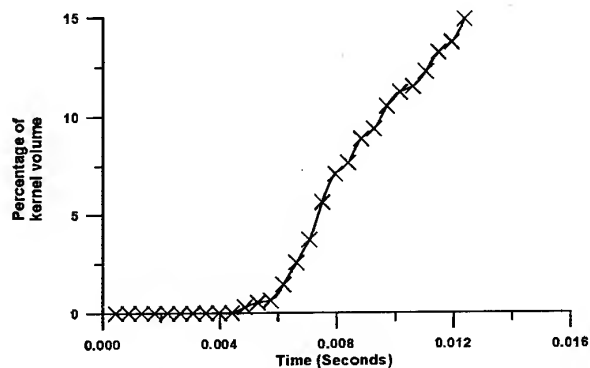


Figure 19 Percentage of the kernel volume experiencing Karlovitz number below 1.5

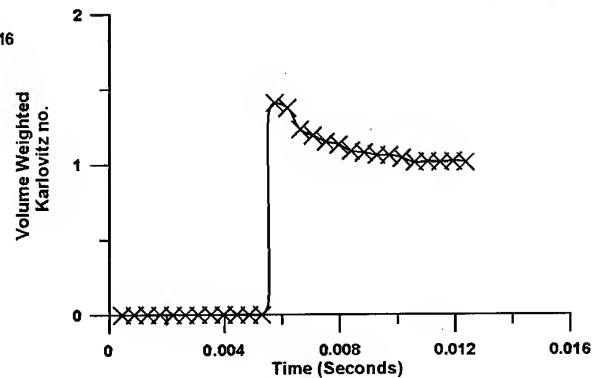


Figure 21 Volume weighted Karlovitz number, below 1.5, within the developing kernel, for the alternative igniter location

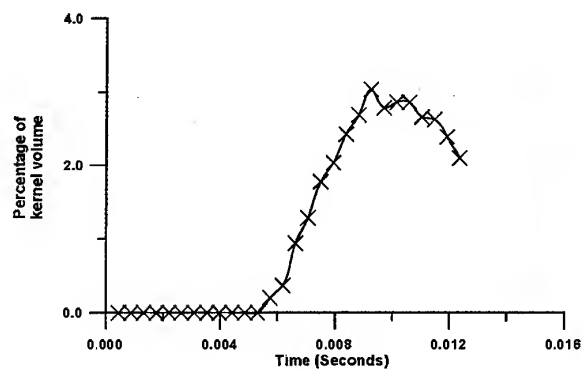


Figure 22 Percentage of the kernel volume seeing Karlovitz number below 1.5, for the alternative igniter location

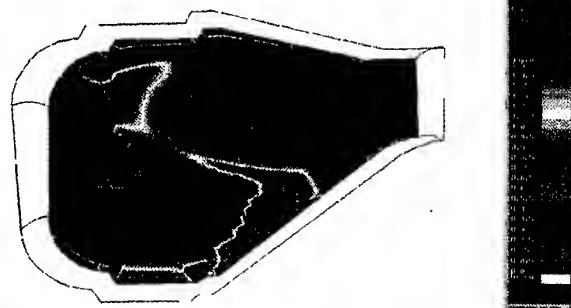


Figure 25 Karlovitz numbers below 1.5 for the plane passing through vaporiser inlet.

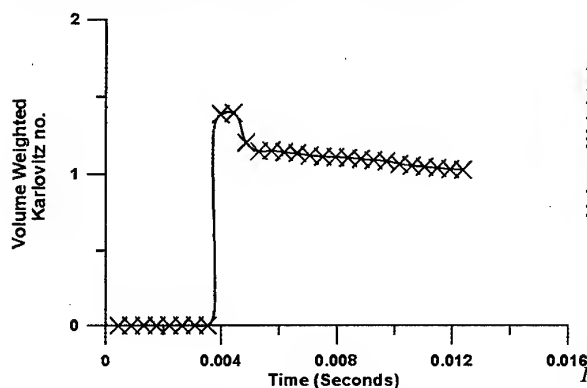


Figure 23 Volume weighted Karlovitz number, below 1.5, within the developing kernel for the FDI igniter.

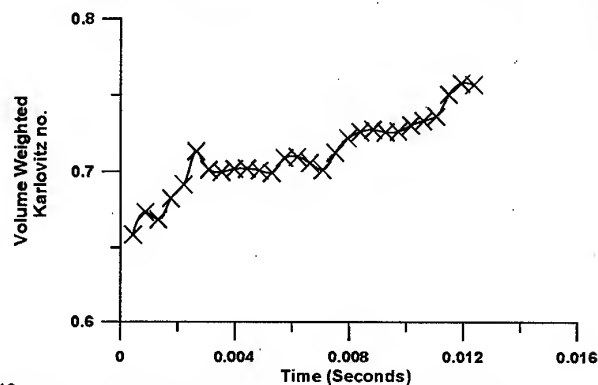


Figure 26 Volume weighted Karlovitz number, below 1.5, within the developing kernel for the proposed igniter location.

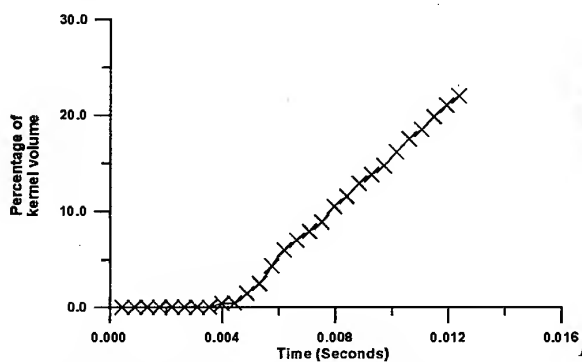


Figure 24 Percentage of the kernel volume experiencing Karlovitz number below 1.5, for the FDI igniter.

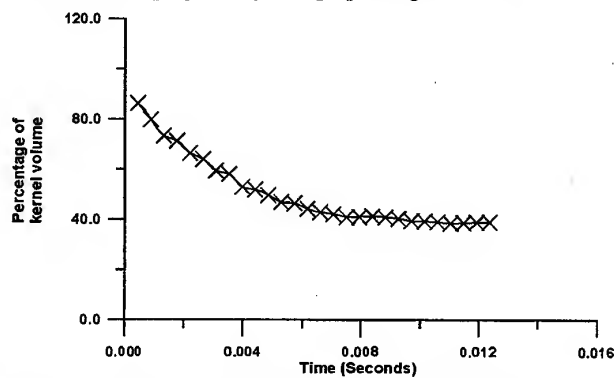


Figure 27 Percentage of the kernel volume experiencing Karlovitz number below 1.5, for proposed igniter location.

PAPER NO. 29
Wilson & Sheppard
(presenter: C.W. Wilson)

Question 1: G.J. Sturgess, ISSI, U.S.

The energy delivered to the spark plug can be measured. Have you accounted for the proportion of this energy that is dissipated in the spark shock wave?

Answer:

In this work we have not. However, if you understand the mechanism and can then calculate the energy dissipated in the shock, it is a simple modification to allow for this. The work described here was performed with a 12 joule exciter box, and assumes that 3 joules are present in the spark.

CARACTERISATION DES SYSTEMES D'INJECTION
PREMELANGES EN AUTO-INFLAMMATION ET REMONTEE DE FLAMME
C. GUIN ONERA / DEFA
BP n° 72 92322 CHATILLON CEDEX France

SOMMAIRE

Les chambres de combustion à prémélange pauvre sont un concept très performant pour réduire les émissions d'oxydes d'azote mais qui est pénalisé par des problèmes d'auto-inflammation et de remontée de flamme, en particulier pour les moteurs fortement comprimés. Aussi, dans le cadre du programme européen Brite Euram, l'ONERA a développé un banc d'essais spécifique pour caractériser les systèmes de prémélange vis à vis de ces phénomènes dans des conditions opérationnelles et indépendamment du foyer. Le montage expérimental autorise une surveillance continue de l'écoulement au sein même du tube de mélange par un système optique et permet de discerner l'auto-inflammation de la remontée de flamme.

Plusieurs concepts développés par les industriels TURBOMECA, VOLVO, BMW, ROLLS-ROYCE, SNECMA y ont été testés et pour chacun d'entre eux les limites de fonctionnement sans risque ont été établies.

Cette publication décrit le moyen d'essais, la procédure utilisée et les mesures effectuées. Les principaux paramètres qui gouvernent les phénomènes sont présentés et une loi définissant les conditions d'auto-inflammation est établie. Quelques exemples d'enregistrements de mesures sont utilisés pour expliciter la manière d'interpréter les résultats.

NOMENCLATURE

D_{32}	diamètre moyen de Sauter des gouttelettes
E	énergie d'activation
ER ou PHI	richesse
$FF = mT^{0.5} / P$	débit réduit
L	longueur du tube de mélange
m	débit d'air
M	nombre de Mach en sortie du tube de mélange
P_{12}	pression au niveau du tube de mélange
P_{div}	perte de charge au travers du système en %
R	constante des gaz parfaits
t	délai d'auto-inflammation et temps de séjour
T_{12}	température d'air au niveau du tube de mélange
U	vitesse axiale du flux d'air
U'	fluctuation de vitesse axiale
V_t	vitesse de flamme turbulente
ρ	masse volumique de l'air

1. INTRODUCTION

Une des principales difficultés à résoudre pour l'aéronautique civile dans les 20 prochaines années sera d'accroître selon les prédictions, le transport aérien sans en aggraver les effets sur l'environnement. Or, si l'optimisation des chambres de combustion des moteurs actuels a permis de réduire considérablement les émissions d'imbrûlés (monoxyde de carbone et hydrocarbures) il en va autrement des émissions d'oxydes d'azote pour lesquelles les techniques mises en oeuvre permettent à peine de compenser l'effet défavorable dû à l'augmentation des taux de compression des moteurs modernes.

De plus à très haute altitude, dans le cas des vols supersoniques, ce polluant pourrait agir sur la destruction de la couche d'ozone.

C'est dire si les oxydes d'azote sont un polluant sur lequel doit porter l'effort des motoristes. Aussi, au sein du programme européen BRITE EURAM, 9 industriels supportés par 15 établissements de recherches et universitaires se sont associés afin d'évaluer les potentialités et les difficultés de différents concepts de chambre de combustion qui permettent d'obtenir d'importantes réductions sur les émissions d'oxydes d'azote (chambre à 2 têtes, RQL, LPP).

Les travaux réalisés au cours des 2 premières phases de ce programme ont montré que le concept LPP, qui consiste à réaliser un mélange homogène gazeux dans un tube avant pénétration dans la chambre, était le plus performant. Des réductions d'émissions supérieures à 80 % ont été atteintes.

Cependant ce concept est pénalisé par une stabilité insuffisante et présente l'inconvénient des risques d'auto-inflammation et de remontée de flamme dans le tube de prémélange.

La 3^{ème} phase de ce programme, qui se poursuit actuellement, devrait aboutir aux essais de secteurs de chambre intégrant cette technologie.

Dans ce contexte, l'ONERA qui est un des partenaires de ce programme, a développé un banc d'essais spécifique afin de caractériser les systèmes de prémélange vis à vis des risques d'auto-inflammation et de remontée de flamme dans des conditions opérationnelles mais indépendamment du foyer.

Le montage expérimental autorise une surveillance continue de l'écoulement au sein même du tube de prémélange par un système optique. Il permet ainsi de rechercher les limites de fonctionnement possible des tubes de prémélange jusqu'à des pressions de 30 bar et des températures d'air de 900 K et d'analyser les phénomènes rencontrés, en particulier de discerner l'auto-inflammation de la remontée de flamme.

Sa modulabilité rend également possible l'étude de l'écoulement diphasique à hautes pressions et hautes températures en sortie du tube de prémélange afin de relier la nature du mélange aux conditions d'apparition des phénomènes.

Le présent article a pour objet d'illustrer les possibilités de ce moyen d'essais à l'aide des résultats les plus significatifs obtenus sur diverses configurations industrielles de systèmes de prémélange. Aussi, après une description du banc d'essais et des moyens de mesures utilisés, il est explicité comment interpréter les phénomènes rencontrés sur chaque configuration essayée.

2. DESCRIPTION DU BANC D'ESSAIS ET PROCEDURE DES ESSAIS

Le montage d'essais, schématisé sur la figure 1, est alimenté par 2 sources d'air différentes :

- des compresseurs aux pressions inférieures à 12 bar
- un stockage haute pression (20 tonnes d'air sous 250 bar) aux pressions supérieures

Le débit maximal est de 3 kg/s sous une pression de 30 bar. Ce flux d'air peut être réchauffé jusqu'à une température de 900 K dans un échangeur. Le flux chaud de l'échangeur provient d'un foyer air / kérosène également alimenté par les compresseurs. La double distribution d'air du montage d'essais permet de n'utiliser le stockage haute pression que durant la phase utile de l'expérimentation, la phase de mise en régime thermique de l'installation s'effectuant à basse pression.

Quand l'installation a atteint la température souhaitée, les 2 sources d'air sont progressivement commutées à une pression inférieure à 12 bar. Puis les 2 flux d'air de l'échangeur sont simultanément augmentés jusqu'à l'obtention des niveaux de débit et de pression souhaités dans le montage d'essais.

Le circuit d'alimentation en kérosène est muni d'un surpresseur délivrant une pression d'injection de 80 bar. Les débits de kérosène, tant pour la maquette d'essais que pour le foyer de l'échangeur, sont régulés en richesse au moyen d'un ordinateur qui pilote des servovannes.

Le montage d'essais est pourvu d'une chambre de combustion modulable qui autorise, à moindre coût, l'adaptation de différents types de système de prémélange. Pour cela, elle est réalisée en 2 parties séparées par une plaque interchangeable sur laquelle se fixe le tube de prémélange. Cette plaque, spécifique à chaque système, est refroidie soit à l'eau soit par effet d'impact afin d'éviter un écoulement d'air de refroidissement en fond de chambre qui pourrait perturber l'écoulement principal.

La première partie se compose d'une enveloppe cylindrique qui reçoit le système d'alimentation en kérosène et dans laquelle est placé le tube de prémélange. Elle permet également le passage vers l'extérieur des mesures effectuées sur ce tube.

La seconde partie se compose d'une enveloppe cylindrique à double paroi refroidie à l'eau dans laquelle se développe la combustion. Elle forme avec le tube de prémélange un "dump combustor" allumé par une torche air/hydrogène. L'épaisseur de la paroi interne est de 15 mm afin d'obtenir,

pour une température d'eau n'excédant pas 80°C, une température de paroi interne proche de celle d'une chambre multiperforée.

La chambre de combustion se termine par un col sonique à section variable afin d'ajuster en continu la pression.

Entre le système de prémélange et le venturi de mesure du débit d'air, un circuit de prélèvement d'air permet de faire varier le débit de la chambre tout en conservant des conditions de débit et de température constantes au niveau de l'échangeur. A cet effet, un autre col sonique à section variable, piloté par ordinateur, ajuste en continu le débit dans la chambre de combustion.

La présence d'une flamme au sein du système de prémélange est détectée par 4 à 8 thermocouples et par 4 à 8 cellules photo-électriques (détection entre 0,35 et 1,1 μm). Ces dernières sont reliées au tube de prémélange par des fibres optiques guidées à leur extrémité par des petits canons soudés sur le tube. Ainsi l'angle solide de visée de la fibre est très étroit et permet de localiser la position du point de départ de la flamme.

Des passages étanches permettent la traversée des thermocouples et des fibres optiques au travers de l'enveloppe externe.

Pour la sécurité, des seuils préprogrammés d'intensité lumineuse et de température de paroi donnent un ordre automatique de fermeture à la servovanne du circuit de kérosène. Cette dernière est placée à proximité de la chambre de combustion et se ferme en moins de 0,1 seconde.

Les instabilités de pression au niveau du système de prémélange sont mesurées par un capteur piezo électrique. La fréquence d'échantillonnage du signal est de 10 khertz mais afin d'éviter des perturbations, par repliement du spectre dans l'analyse des fréquences, le signal est filtré à 5 khertz.

Les signaux des cellules photo-électriques et du capteur piezo électrique sont enregistrés sur un ordinateur spécifique. La fréquence d'acquisition pour chaque voie de mesure est de 100 khertz pour une capacité d'acquisition de 5 Méga octets. Un top de synchronisation permet de synchroniser ces mesures avec l'enregistrement des paramètres thermodynamiques et des températures de paroi enregistrés à plus faible fréquence sur l'ordinateur central. Le traitement du signal instationnaire s'effectue sur 1024 points, soit une fenêtre de temps de 0,1024 seconde, par transformée de Fourier.

La procédure d'essais consiste, après avoir établi les conditions thermodynamiques souhaitées (température, débit et pression d'air) à augmenter progressivement le temps de séjour et corrélativement à réduire la vitesse d'écoulement dans le système de prémélange jusqu'à la détection d'une flamme au sein de ce dernier. Ceci est obtenu par le pilotage simultané de la pression, qui est maintenue constante, et du débit d'air dans le foyer qui décroît. L'analyse ultérieure des signaux lumineux et des instabilités de combustion permet de distinguer s'il s'agit d'auto-inflammation ou de remontée de flamme.

L'introduction d'une virole optique équipée de 2 hublots en silice entre la plaque support du système de prémélange et le foyer refroidi, tel que schématisé sur la figure 2, permet également d'étudier l'écoulement diphasique en sortie du tube de prémélange.

Par ailleurs, une sonde de prélèvement de gaz multi-points, placée entre la chambre de combustion et le col sonique, permet d'analyser en continu les émissions de polluants afin de caractériser les systèmes de prémélange en performance de combustion. Toutefois, cette caractérisation est indépendante de celle des phénomènes d'auto-inflammation ou de remontée de flamme et donc les résultats ne sont pas présentés dans cet article.

3. CONCEPTS DE SYSTEME DE PREMELANGE ETUDIES

Les phénomènes à l'origine de l'auto-inflammation ou de la remontée de flamme, rencontrés sur les systèmes de prémélange étudiés, peuvent être décrits par les résultats obtenus sur 4 concepts différents. Ces concepts, schématisés sur la figure 3, sont proposés par les industriels TURBOMECA, ROLLS ROYCE, BMW, SNECMA et se différencient par :

- leurs vrilles d'entrée d'air (1 ou 2, co ou contra-rotatives, axiales ou radiales)
- l'injection du combustible (centrale ou multi points répartis autour du tube)
- le nombre de Mach de sortie de l'écoulement
- la convergence ou non du tube de mélange et de vaporisation
- le temps de séjour moyen de l'écoulement dans le tube.

concept n°1

C'est un simple tube équipé d'une vrille axiale à son entrée et d'une petite marche suivie d'un court divergent à sa sortie.

L'injection du kérosène est centrale avec pulvérisation aérodynamique.

Aux conditions nominales de fonctionnement correspondant à une perte de charge de 4 %, le nombre de Mach de sortie est d'environ 0,1.

concept n° 2

Il utilise le tube de vaporisation et le système d'injection à pulvérisation aérodynamique du concept n° 1 mais l'arrivée d'air est réalisée, à l'amont, par de simples orifices répartis autour du système d'injection et, à l'aval au niveau du divergent, par une vrille centripète traversée par 20% du débit d'air. Le nombre de Mach de sortie est 0,16.

concept n° 3

Ce système de prémélange se compose de 2 vrilles radiales équipées chacune d'un venturi conique. Les 2 écoulements centripètes ainsi créés débouchent dans un tube de mélange et de vaporisation également conique qui se termine par un bol très divergent. Le nombre de Mach à l'extrémité du cône est de 0,15.

L'injection du combustible est au centre de la première vrille dite "vrille interne".

Deux versions sont possibles selon le montage des vrilles qui peuvent être co ou contra-rotatives.

concept n° 4

Dans ce concept, l'écoulement d'air annulaire est alimenté par 2 vrilles axiales contra-rotatives.

L'injection du combustible s'effectue par des petits orifices répartis tout autour de la paroi interne du système de prémélange. Les jets de combustible impactent sur une lèvre de séparation des vrilles.

Un corps central est alimenté par 10 % du débit d'air par l'intermédiaire d'une vrille radiale. L'écoulement annulaire converge au niveau du corps central ; 2 convergences sont proposées qui conduisent à des nombres de Mach de sortie sensiblement différents : $M = 0,15$ et $M = 0,17$.

4 RESULTATS OBTENUS EN AUTO-INFLAMMATION ET REMONTEE DE FLAMME

Sur le domaine opérationnel de chaque système de prémélange (pression, température d'air, richesse) les conditions minimales de débit d'air pour lesquelles apparaît une flamme dans le tube de mélange ont été établies. Ce débit minimum correspond soit à un temps de séjour suffisant pour qu'il puisse y avoir auto-inflammation du mélange carburé soit à une perte de charge suffisamment faible pour qu'une remontée de flamme soit possible. Aussi, l'auto-inflammation n'est obtenue que si un phénomène de remontée de flamme n'est pas rencontré préalablement et inversement.

Comme le montrent les figures 5, 6, 7, l'aspect des signaux lumineux renseigne sur le phénomène rencontré.

L'auto-inflammation correspond à des signaux stables avec une saturation immédiate des cellules photo-électriques (concept n° 1 et 2) alors que la remontée de flamme correspond à des signaux plutôt instables qui peuvent :

- soit avoir des départs décalés de quelques millisecondes (concept n°1 - figure 7)
- soit ne concerner que les fibres optiques les plus à l'aval du tube de mélange avec des allumages-extinctions à fréquence assez régulière (concept n°3 - figure 6).

En fait, il faut distinguer plusieurs types de remontée de flamme. Car si d'une façon pratique c'est toujours le paramètre de perte de charge minimum qui caractérise l'apparition de la remontée de flamme, les causes de déclenchement rencontrées sont multiples :

- remontée de flamme par les couches limites
- remontée de flamme due aux instabilités de combustion
- remontée de flamme due à une zone de recirculation

L'analyse des instabilités de combustion et les caractéristiques de l'écoulement diphasique en sortie du système de prémélange sont des éléments aidant à l'identification du phénomène.

4.1 Interprétation des phénomènes d'auto-inflammation

L'auto-inflammation a été observée sur les systèmes 1, 2 et 4 (un seul point sur le concept n°4 en configuration M=0,17 aux pressions et températures maximales du banc d'essais).

Ce phénomène apparaît dès que le temps de séjour du mélange carburé est équivalent au délai nécessaire à son inflammation. Le temps de séjour moyen dans le tube est défini comme le rapport entre la longueur du tube, à partir du point d'injection, et la vitesse moyenne de l'écoulement. Il peut aisément être calculé à partir des paramètres thermodynamiques de pilotage de l'essai (température d'air T_2 et débit réduit FF).

$$t = L / U = V 10^8 / R * T^{0.5} * FF$$

avec t exprimé en ms, V en m^3 et FF en $kg / s.K^{0.5}$

Les résultats obtenus à $T_2 = 760 K$, reportés sur la figure 8, montrent une dépendance du délai d'inflammation inversement proportionnelle à $P^{0.9}$. L'ensemble des points, toutes températures d'air et configurations confondues, peut être représenté par une même loi exponentielle de la température d'air (figure 9).

$$t_{auto} = \frac{0.508 e^{(3377/T_2)}}{P_{i2}^{0.9}}$$

Cette loi est du même type que celle issue des travaux fondamentaux de SPADACCINI [1] et la dépendance exponentielle vis à vis de la température est en accord avec les travaux théoriques [2] qui relient le délai d'auto-inflammation à l'énergie d'activation du combustible par une loi du type :

$$\ln t = \frac{E}{R * T} + A$$

ou E est l'énergie d'activation et T la température locale qui peut être approximativement considérée comme la température de l'air.

Un effet de la richesse dans le tube n'a pas réellement été mis en évidence sur le délai d'auto-inflammation. Toutefois la plage explorée était limitée entre $0.7 \leq ER \leq 1$.

D'un point de vue pratique, ces résultats montrent que pour les conditions opérationnelles des moteurs actuels le dimensionnement du système de prémélange doit être tel que le temps de séjour du mélange carburé soit inférieur à :

$$t_{max} = \frac{30}{P_{max}^{0.9}}$$

4.2 Interprétation des phénomènes de remontée de flamme

Des remontées de flamme ont été observées sur les concepts n° 1, 3 et 4. Elles se caractérisent par une perte de charge minimum en deçà de laquelle le phénomène apparaît. Avec le concept n°1 la perte de charge minimum dépend de la richesse du foyer ($P_{div} = 5\%$ à $PHI = 0,4$ et $P_{div} = 9\%$ à $PHI = 0,7$) alors qu'elle est indépendante de ce paramètre avec le concept n° 3. Pour ce dernier, des signaux lumineux

aléatoires commencent à apparaître dans le tube de mélange lorsque P_{div} est compris entre 4 et 5 %, selon le niveau de pression et la configuration co ou contra rotative (la perte de charge minimum est plus faible lorsque la pression décroît et pour la configuration contra rotative). Avec le concept n° 4, l'apparition d'une flamme dans le tube, aux environs de $P_{div} = 3\%$, semble être corrélée avec l'amplification d'une instabilité de combustion et varier sensiblement avec la richesse et la température d'air. La possibilité ou non de l'amplification de l'instabilité de combustion dépend cependant de la géométrie de la chambre. Ainsi, avec un rapport $d/D = 0,575$ (diamètre de sortie du tube de mélange sur diamètre du foyer) il y a amplification de l'instabilité, lorsqu'on réduit la perte de charge au travers du système de prémélange, alors qu'avec un rapport $d/D = 0,39$ ce phénomène n'a pas lieu.

Ces exemples montrent qu'il faut distinguer plusieurs causes de déclenchement à la remontée de flamme.

Remontée de flamme par la couche limite

De nombreux auteurs ont démontré que la vitesse de propagation d'une flamme turbulente était liée à l'énergie cinétique de la turbulence [3] $V_t = \alpha * k^{0.5}$ où :

- k est l'énergie cinétique turbulente $= 3 U'^2 / 2$
- α est un facteur de proportionnalité qui varie de 0,6 à 2 selon les auteurs.

Il apparaît donc qu'une remontée de flamme n'est possible qu'avec un niveau de turbulence $lu = U'/U$ au moins égale à 40 %. Aussi, pour les vitesses débitantes rencontrées dans les systèmes de prémélange, la remontée de flamme loin des parois n'est pas possible. Par contre, près des parois où la vitesse d'écoulement devient petite la remontée de flamme est plus probable.

LEWIS et ELBE ont démontré que ce retour de flamme par les parois ne se produit que si le gradient de vitesse à la paroi est plus petit que le rapport entre la vitesse théorique de flamme et la distance de coïncement $g_f \leq V_t/d_p$. Cette distance de coïncement est une zone où les pertes thermiques à la paroi sont telles que la vitesse de flamme s'annule. Il existe donc un gradient critique en dessous duquel il y aura remontée de flamme. Ce gradient critique, qui correspond au débit minimum qu'il faut assurer afin que la flamme ne remonte pas, dépend de la richesse du mélange.

Ainsi, avec le concept n° 1, le fait de pouvoir corréler le phénomène observé à la fois à des conditions de perte de charge et de richesse peut indiquer que nous avons à faire à des remontées de flamme par les couches limites. Les signaux optiques observés (figure 7) ne contredisent pas cette hypothèse, l'ordre et le déphasage des départs pouvant correspondre au délai nécessaire à la propagation de la flamme. Enfin, les mesures effectuées immédiatement en sortie du système de prémélange par vélocimétrie 3D ($x = 0.5$ mm) et par analyseur de particules à phase Doppler PDPA ($x = 10$ mm) confirment l'hypothèse (figures 11 et 12). En effet, elles montrent que dans le sillage de la paroi :

- le niveau de turbulence du flux d'air est très élevé puisque la fluctuation de vitesse axiale est du même ordre de grandeur que la composante axiale du vecteur vitesse
- la vitesse axiale des gouttelettes est également du même ordre de grandeur que sa fluctuation et le flux

volumique de combustible y est important du fait de la centrifugation.

- **remontée de flamme due à une instabilité de combustion**

Si l'amplitude des oscillations de pression dues à la combustion dépasse la valeur de la pression dynamique de l'écoulement $\rho U^2/2$, cela doit logiquement conduire à un retournement du flux pendant une partie du cycle. Une remontée de flamme est donc induite périodiquement. L'aspect des signaux optiques, enregistrés sur le concept n°4 (figure 6) semble s'apparenter à ce phénomène.

L'analyse du spectre de fréquences des instabilités de combustion correspondantes, présentée en figure 13, montre qu'une oscillation de pression d'une fréquence de 1500 Hz s'amplifie progressivement lorsqu'on réduit la perte de charge au travers du système de prémélange. L'amplitude de l'oscillation croît jusqu'à 1.3 % du niveau de pression dans le foyer. Cette amplitude est obtenue pour une perte de charge de 2.9 %. A partir de cette valeur, si on continue de réduire le débit d'air, l'oscillation disparaît et est remplacée par une oscillation de faible amplitude d'une fréquence de 300 Hz. La figure 14, qui présente la corrélation en temps des instabilités de combustion et des signaux optiques, montre que l'instant du changement de fréquence des oscillations de pression est celui de l'apparition d'une remontée de flamme dans le tube de mélange. Cependant, la fréquence élevée de l'instabilité ne peut pas être à l'origine d'une réelle remontée de flamme. On peut donc imaginer qu'une petite pénétration de la flamme dans le tube de mélange initie des remontées périodiques de la combustion dans la couche limite, à plus basse fréquence (300 Hz).

- **remontée de flamme due à une zone de recirculation**

Le phénomène rencontré sur le concept n° 3 se différencie des précédents par le fait que l'apparition d'un flux lumineux dans le tube de mélange ne s'accompagne pas d'une augmentation de la température de paroi. D'autre part, il ne peut pas être corrélé à des instabilités de combustion et ne dépend pas de la richesse dans le tube mais plutôt du niveau de pression.

Sur la figure 15 sont reportées, à la fréquence de 0,1 seconde, les intensités lumineuses et les températures de paroi en fonction de la perte de charge lors d'une diminution progressive du débit d'air du foyer. On constate, qu'aux conditions choisies ($P_2 = 24$ bar, $T_{i2} = 890$ K, $ER = 0.5$) :

- à partir de 5 % de perte de charge, les premiers "flashes" lumineux apparaissent dans le tube de mélange puis, si l'on continue de diminuer la perte de charge, l'intensité et la fréquence de ces "flashes" augmentent. Dans le même temps, la température de paroi du tube reste constante à une valeur proche de la température de l'écoulement d'air
- à partir de 2,5 % de perte de charge, l'intensité lumineuse sature les cellules photo-électriques et la flamme est en permanence présente dans le tube. La paroi commence à s'échauffer légèrement
- en deçà de 2,5 %, la température de paroi s'équilibre à une valeur d'autant plus élevée que la perte de charge diminue sans cependant devenir dangereuse pour le

système de prémélange. De simples visualisations effectuées en sortie du système de prémélange montrent que l'éclatement tourbillonnaire crée en son centre une petite zone de recirculation. On peut donc penser que les flux lumineux détectés sont ceux d'une flamme installée dans cette zone de recirculation qui peut remonter comme un dard dans le centre du tube. Plus la perte de charge est faible et la pression élevée plus ce dard pénètre dans l'axe du tube. Cette zone de flamme n'est pas dangereuse pour la tenue thermique du tube puisqu'elle est entourée d'un flux d'air carburé froid.

5 CONCLUSION

L'ONERA a développé un banc d'essais pour caractériser en auto-inflammation et remontée de flamme les systèmes d'injection à prémélange pauvre. Il est équipé de systèmes automatiques de pilotage des conditions d'essais et d'arrêt de la combustion lui permettant une conduite précise et en sécurité de ce type d'essais. Il dispose d'une chambre de combustion modulaire sur laquelle il est aisé d'adapter différents concepts de prémélange et d'effectuer des mesures optiques de qualification de l'écoulement diphasique.

Dans le cadre des études européennes sur les chambres de combustion à basses émissions d'oxydes d'azote (programme Brite Euram) plusieurs concepts définis par les industriels TURBOMECA, VOLVO, BMW, ROLLS-ROYCE, SNECMA y ont été testés jusqu'à une pression de 30 bar et une température d'air de 900 K sans aucun dommage pour ces systèmes de prémélange.

La présence de la flamme dans le tube de mélange est détectée par des cellules photo-électriques. Il a été montré que la nature des signaux optiques permettait d'identifier le phénomène rencontré et en particulier de discerner l'auto-inflammation de la remontée de flamme.

Le temps de séjour maximum du mélange carburé dans le système d'injection pour éviter son auto-inflammation a été établi en fonction de la pression et de la température d'air. Il est défini par la loi :

$$t_{\text{auto}} = \frac{0.508 e^{(3377/T_{i2})}}{P_{i2}^{0.9}}$$

Pour chaque concept, un débit réduit limite ($m \cdot T_{i2}^{0.5}/P_{i2}$), en deçà duquel une remontée de flamme devient probable, a été trouvé. Il correspond à une perte de charge minimum au travers du système de prémélange. L'analyse des signaux optiques, des instabilités de combustion et de l'écoulement diphasique ont permis d'identifier les causes de déclenchement des remontées de flamme. Trois causes ont été identifiées :

- remontée de flamme par la couche limite lorsque le taux de turbulence à la paroi est élevé
- remontée de flamme provoquée par l'amplification d'une instabilité de combustion
- remontée de flamme par une zone de recirculation en sortie du tube de mélange.

Les défauts de chacun de ces systèmes de prémélange sont maintenant identifiés et leurs limites de fonctionnement établies. Ces renseignements sont

précieux pour optimiser ces dispositifs avant leur intégration dans un secteur de chambre complexe et coûteux.

REMERCIEMENTS

Ce travail a été réalisé avec le soutien financier de la Commission Européenne et du service officiel français DGAC dans le cadre du programme européen "Low Emission Combustor Technology LOW NOX III" aero CT 95-0122. L'auteur exprime ses remerciements à ces organismes ainsi qu'aux Industriels qui ont fait confiance à l'ONERA et qui ont autorisé cette publication.

REFERENCES :

- [1] SPADACCINI. L.J, Autoignition characteristics of hydrocarbon fuels at elevated temperatures and pressures - Journal of Engineering for Power. January 1977.
- [2] MULLINS. B.P, Studies on spontaneous ignition of fuels injected into a hot airstream - Part. I to III, Fuel, Vol. 32 - 1953.
- [3] THIBAUT. D, Etude de la remontée de flamme dans les foyers prémélangés prévaporisés. Synthèse bibliographique CNRS, Ecole Centrale Paris, Avril 1994.

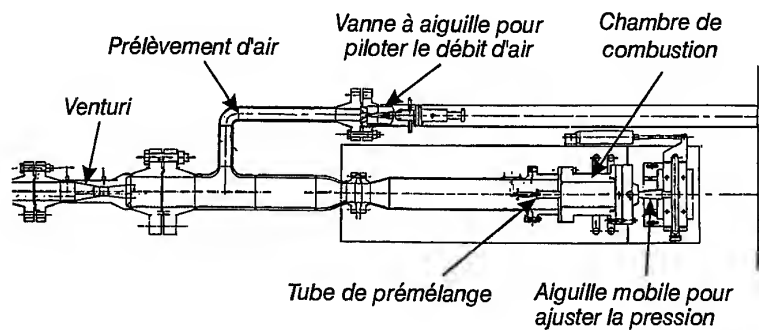


Fig. 1 - Distribution d'air sur le banc d'auto-inflammation et de remontée de flamme

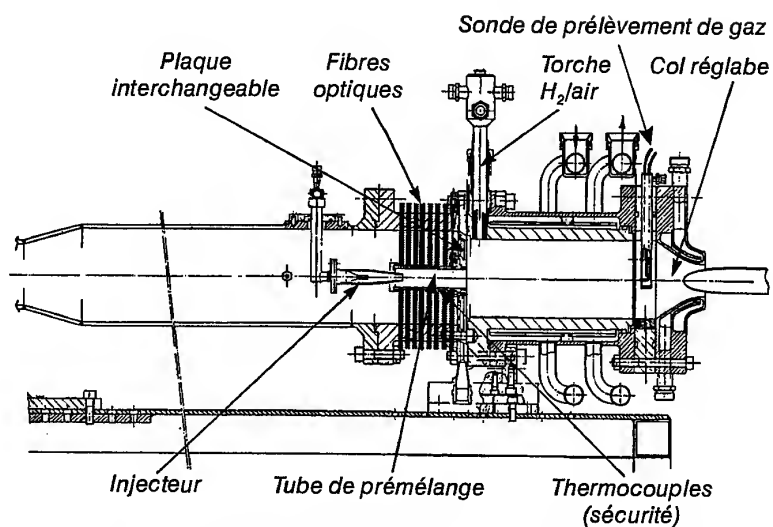


Fig. 2 - Dispositif d'essais d'auto-inflammation et de remontée de flamme

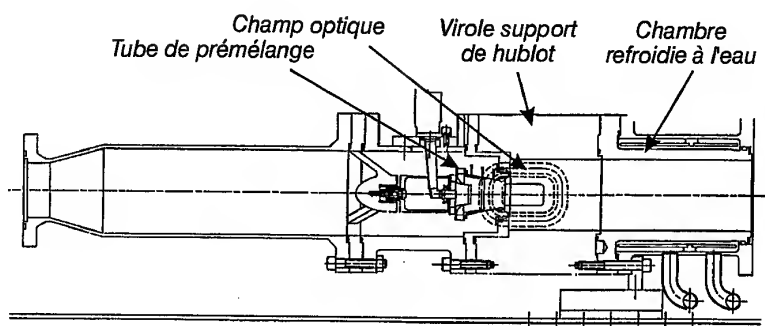


Fig. 3 - Adaptation du dispositif d'essais d'auto-inflammation aux mesures de PDPA et de LDV

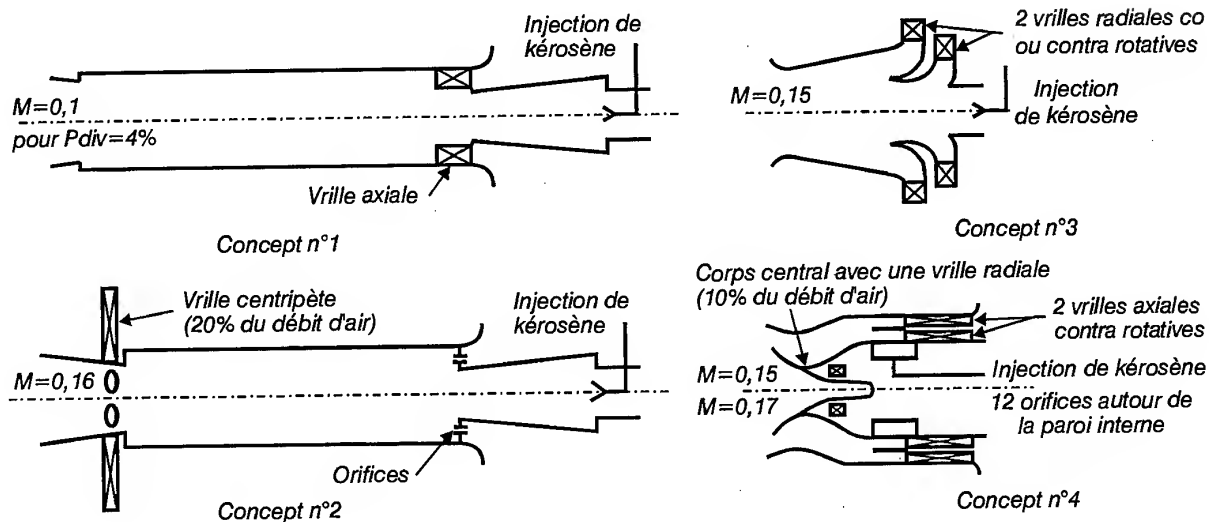


Fig. 4 - Concepts étudiés

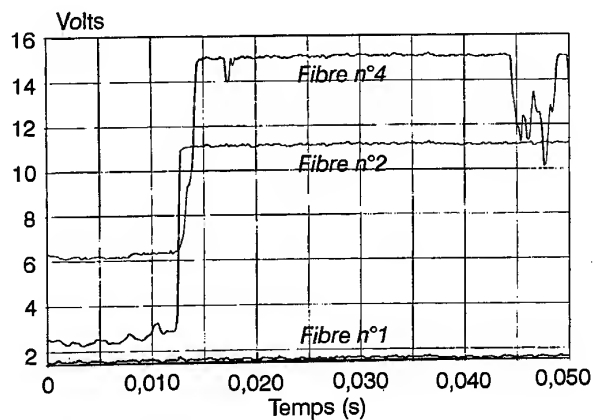


Fig. 5 - Exemple de signaux optiques pour une auto-inflammation

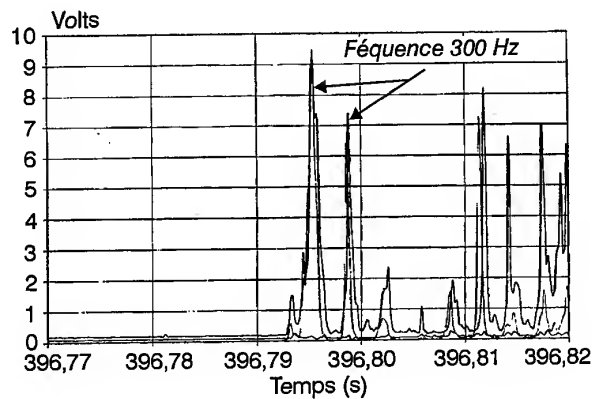


Fig. 6 - Exemple de signaux optiques pour une remontée de flamme

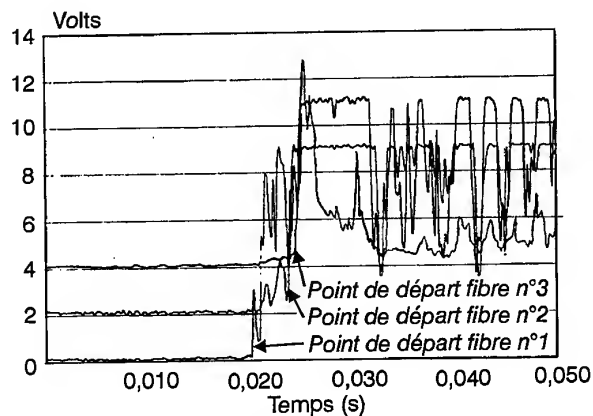


Fig. 7 - Exemple de signaux optiques pour une remontée de flamme

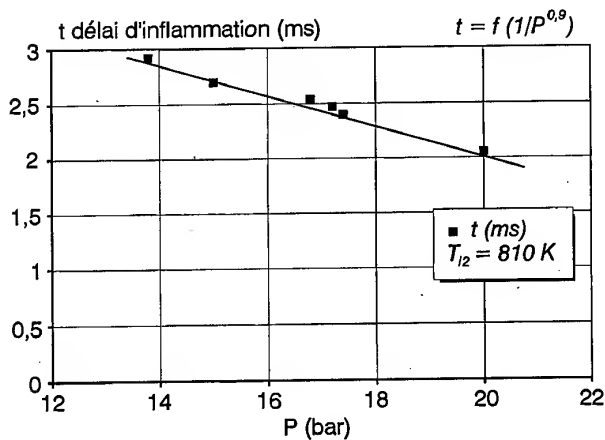


Fig. 8 - Effet de la pression sur le délai d'inflammation

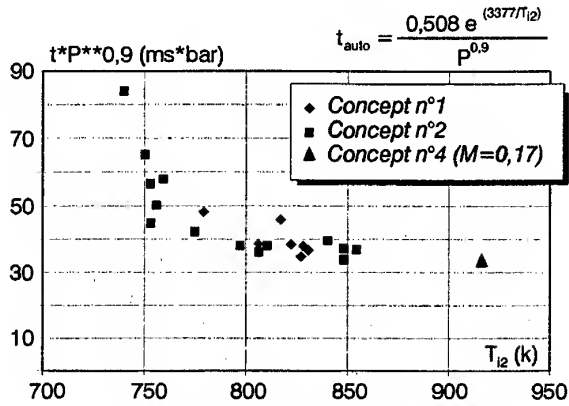


Fig. 9 - Loi d'auto-inflammation

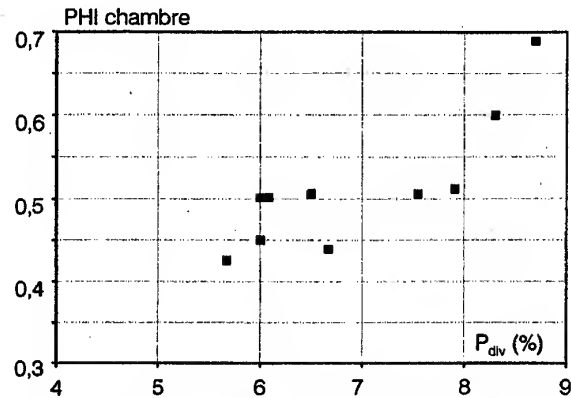


Fig. 10 - Richesse limite de remontée de flamme fonction de la perte de charge. Concept n°1

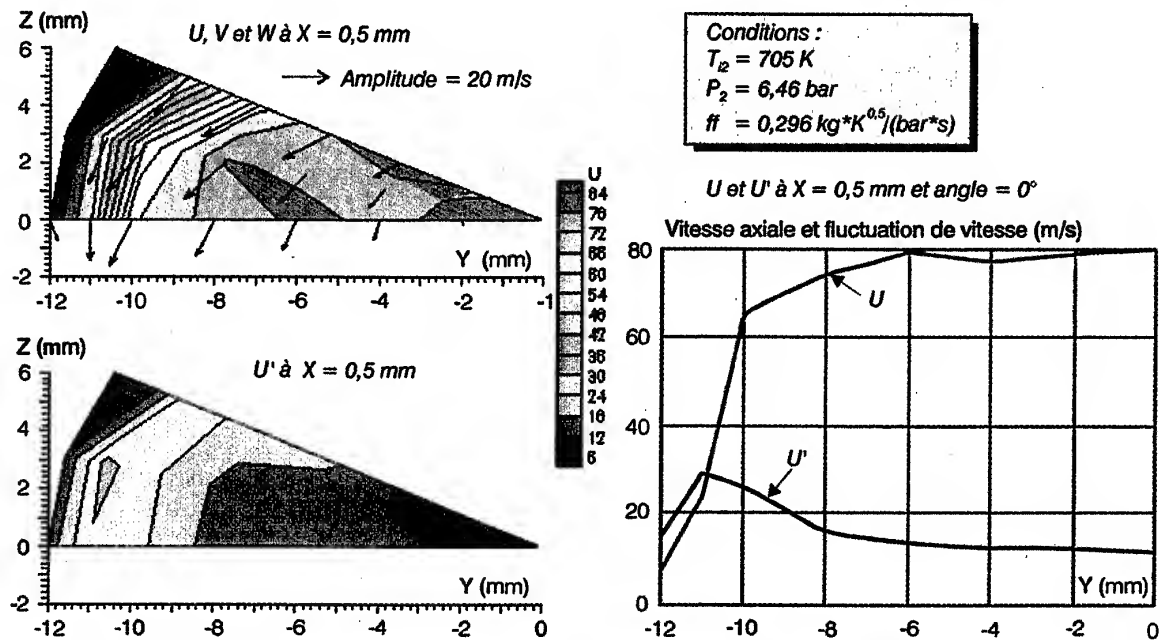


Fig. 11 - Mesures LDV. Champ de vitesses 3D en sortie de tube

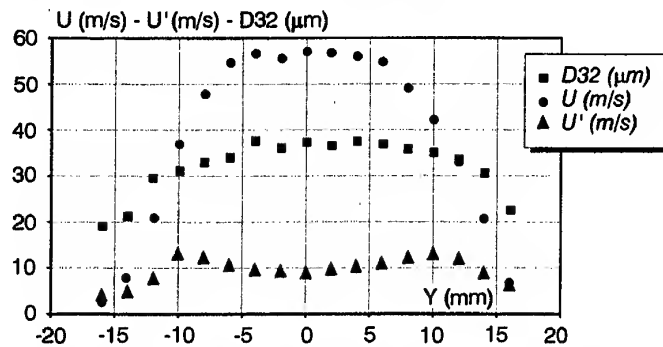


Fig. 12 - Vitesse, fluctuation de vitesse, taille de gouttes,
 en fonction de la position radiale (axe horizontal).
 $P_{\text{div}} = 4,7\%$ $T_{\text{air}} = 606 \text{ K}$ $P = 6 \text{ bar}$ mesures à 10 mm
 Concept n°1

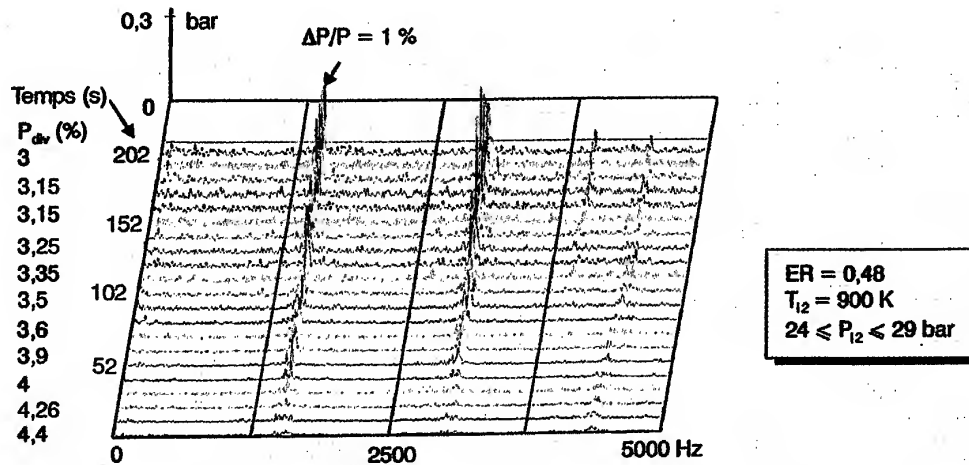


Fig. 13 - Spectre de fréquences des fluctuations de pression fonction de la perte de charge au travers du tube. Concept n°4

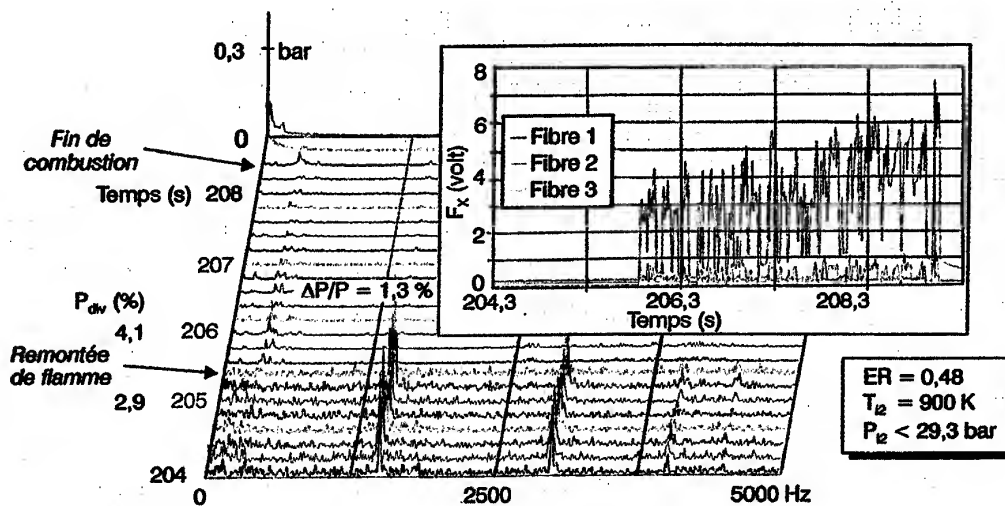


Fig. 14 - Spectre de fréquences des fluctuations de pression Corrélation avec les signaux optiques. Concept n°4

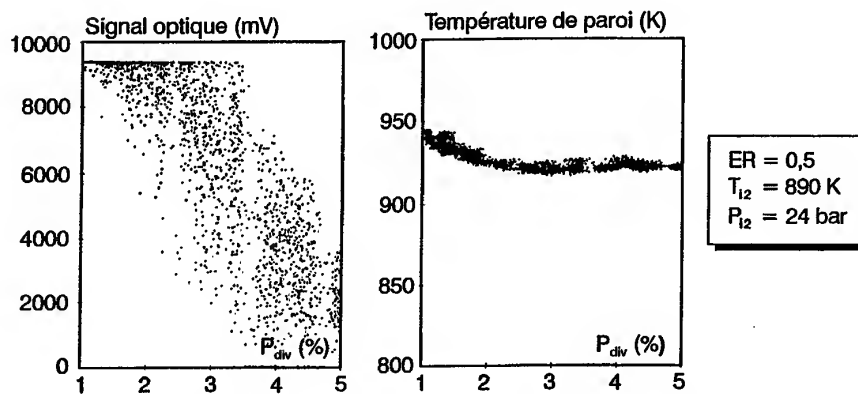


Fig. 15 - Signal optique et température de paroi en fonction de la perte de charge. Concept n°3

CHARACTERISATION OF AUTOIGNITION AND FLASHBACK IN PREMIXED INJECTION SYSTEMS

C. GUIN, ONERA / DEFA

BP 72, 92322 CHATILLON CEDEX France

SUMMARY

Lean premixed combustors are very performing for reducing NOx emissions, but the concept is penalised by problems of autoignition and flashback, especially in motors with a high pressure ratio. In the framework of the Brite Euram programme, ONERA has therefore developed a special test facility for characterising these phenomena in premixed systems under operational conditions and independently of the combustor.

The test rig allows continuous monitoring of the flow within the mixing duct by an optical system able to detect autoignition and flashback.

Several concepts developed for the manufacturers Turbomeca, Volvo, BMW, Rolls-Royce and Snecma were tested in the facility. The safe operating limits for each concept were determined.

This paper describes the test facility, the procedure used and the measurements made. The main parameters governing the phenomena are described and a law defining the autoignition conditions is established. A few examples of measurement records are used to explain how the results are interpreted.

NOMENCLATURE

D_{32}	Average Sauter diameter of the droplets
E	Activation energy
ER or PHI	Equivalence ratio
$FF = mT^{0.5}/P$	Reduced flow rate
L	Mixing duct length
m	Air flow rate
M	Mach number at the mixing duct outlet
P_{12}	Pressure in the mixing duct
P_{div}	Pressure loss through the system as a percentage
R	Perfect gas constant
T_{12}	Air temperature in the mixing duct
U	Axial velocity of the air flow
U'	Axial velocity variation
V_t	Turbulent flame velocity
ρ	Air density

1. INTRODUCTION

One of the main difficulties facing the aeronautical industry in the next 20 years will be to cater for the forecasted increase in air traffic without aggravating the environmental impact. Although combustors have been optimised as regards unburnt product emissions (carbon monoxide and hydrocarbons), this is far from true for NOx emissions for which the techniques implemented barely compensate for

the adverse effect due to the increased pressure ratio of modern engines.

In addition, at the very high altitudes where supersonic aircraft fly, this pollutant could contribute to destroy the ozone layer.

Engine manufacturers therefore need to do everything possible to reduce NOx emissions. In the European Brite Euram programme, nine manufacturers, supported by 15 research organisms and universities, are co-operating on evaluating the potential and the problems inherent in new combustor concepts which greatly reduce NOx emissions (two-head chambers, RQL, LPP).

The work conducted during the first two stages of this programme showed that the LPP concept, which consists of making a homogeneous gas mixture in a duct before penetrating the combustor, was the most performing. Emissions were reduced by more than 80 percent.

However, this concept is penalised by insufficient stability and has the drawback of risks of autoignition and flashback in the premixing duct.

The third stage of this programme, which is currently in progress, should lead to testing of combustor sectors integrating this technology.

In this context, ONERA, one of the partners on this programme, has developed a special test facility for characterising premixed systems under operational conditions, but independently of the combustor, as regards the risks of autoignition and flashback.

The test rig continuously monitors the flow within the premixing duct by an optical system. It therefore enables investigation of the possible operating limits of the premixing ducts up to pressures of 30 bar and air temperatures of 900 K and analysis of the phenomena occurring, in particular by detection of autoignition and flashback.

As the facility is modular, it also allows investigation of the two-phase high-temperature/high-pressure flow at the premixing duct outlet, in order to relate the nature of the mixture to the conditions under which certain phenomena occur.

This paper illustrates the capabilities of the test facility through significant results obtained on various industrial premixed system configurations. After a description of the test facility and the measuring instruments used, interpretation of the phenomena encountered for each configuration tested is explained.

2. DESCRIPTION OF THE TEST FACILITY AND TEST PROCEDURE

The test facility schematically illustrated in Figure 1 is supplied by two different air sources :

- compressors with pressures below 12 bars ;
- HP storage tank (20 tonnes of air at 250 bars) for higher pressures.

The maximum throughput is 3 kg/s at a pressure of 30 bar. This air flow can be reheated up to 900 K in an exchanger. The hot flow of the exchanger is from an air/kerosene combustor supplied from the compressors. The dual air system of the facility makes it possible to use the HP storage tank only during the useful part of the experiment, but to set up the required temperature conditions at low pressure.

When the facility has reached the required temperature, the two air sources are gradually switched to a pressure below 12 bar. Then the two air flows through the exchanger are gradually increased until obtaining the required flow rate and pressure levels in the test facility.

The kerosene supply line is fitted with a pressure booster providing an injection pressure of 80 bar. The equivalence ratios of the kerosene flow rates for the test set-up and the exchanger combustor are regulated by computer-controlled servo-valves.

The test rig is provided with a modular combustor on which different premixed systems can be fitted at a reasonable cost. It is made in two sections, separated by an interchangeable plate on which is mounted the premixing duct. This plate, specific to each system, is cooled by water or by impact to avoid a cooling air flow in the bottom of the combustor, which could disturb the main flow.

The first section is a cylindrical shell fitted with the kerosene feed system and housing the premixing duct. It also sends out the measurements made on the duct.

The second section is a water-cooled double wall cylindrical shell where combustion takes place. Together with the premixing duct, it forms a dump combustor ignited by an air/hydrogen torch. The internal wall is 15 mm thick to obtain an internal wall temperature close to that of a multiperforated combustor for a water temperature not exceeding 80°C.

The combustor ends with a variable section sonic throat in order to be able to continuously adjust the pressure.

An air sampling circuit is located between the premixed system and the air flow measurement venturi to vary the flow through the combustor while preserving a constant flow rate and temperature in the exchanger. For this purpose, another computer-controlled variable section sonic throat continuously adjusts the flow rate in the combustor.

The presence of a flame in the premixed system is detected by four to eight thermocouples and four to eight photoelectric cells (detection between 0.35 and 1.1 μm). The photocells are connected to the premixing duct by optical fibres whose ends are guided by small guns welded

to the duct. The solid fibre aiming angle is therefore very narrow to be able to pinpoint the flame starting point.

Sealed passages are provided through the outer shell for crossing of the thermocouples and optical fibres.

For safety, programmed luminous intensity and wall temperature thresholds automatically close the kerosene feed servo-valve. This servo-valve is located near the combustor and closes in less than 0.1 second.

Pressure instabilities in the premixed system are measured by a piezoelectric transducer. The signal sampling frequency is 10 kilohertz, but the signal is filtered at 5 kHz to avoid aliasing.

The signals from the photoelectric cells and transducer are recorded on a special computer. Each channel has an acquisition frequency of 100 kHz for an acquisition capacity of 5 MB. A pulse synchronises these measurements with the thermodynamic parameter and wall temperature measurements, recorded at lower frequency on the principal computer. The unsteady signals are processed on 1024 points, i.e. a time window of 0.0124 seconds, by Fourier transform.

Once the required thermodynamic conditions have been established (air pressure, temperature and flow rate), the test procedure consists of gradually increasing the residence time and correlatively decreasing the flow velocity in the premixed system until detecting a flame in the duct. This is achieved by simultaneously controlling the combustor air pressure, held constant, and flow rate, which decreases. Subsequent analysis of the optical signals and combustion instabilities allows us to distinguish between autoignition and flashback.

The introduction of an optical sleeve equipped with two silica windows between the premixed system support plate and the cooled combustor, illustrated in Figure 2, also allows investigation of the two-phase flow on the premixing duct outlet.

In addition, a multipoint gas sampling probe was placed between the combustor and the sonic throat to have a continuous analysis of pollutant emission in order to characterize the combustion performance of the premixed systems. However, since this characterization is independent of the autoignition and flashback phenomena, the results are not presented herein.

3. PREMIXED SYSTEM CONCEPTS ANALYZED

The phenomena at the origin of autoignition or flashback occurring in the premixed systems studied can be described by the results obtained for four different concepts. These concepts, proposed by the manufacturers Turbomeca, Rolls Royce, BMW and Snecma and schematically illustrated in Figure 3, differ by :

- their air intake swirlers (one or two, co- or contrarotating, axial or radial) ;
- the fuel injection system (central or multipoint, distributed around the duct) ;

- the flow exit Mach number ;
- convergence or not of the mixing and vaporization duct ;
- the average residence time of the flow in the duct.

Concept 1

This concept is a simple duct whose inlet is equipped with an axial swirler and a small step followed by a short divergent on the outlet.

Kerosene is injected centrally with aerodynamic atomization.

Under the nominal operating conditions corresponding to a pressure loss of four percent, the exit Mach number is approximately 0.1.

Concept 2

This concept uses the vaporization duct and aerodynamic atomization injection system of concept 1, but the air intake upstream is by small holes distributed around the injection system and downstream, in the location of the divergent, by a centripetal swirler crossed by 20 percent of the air flow ; the exit Mach number is 0.16.

Concept 3

This premixed system consists of two radial swirlers each equipped with a conical venturi. The two centripetal flows thus created are fed into a mixing and vaporization duct which is also conical, ending in a highly divergent bowl. The Mach number at the exit of the cone is 0.15

Fuel injection is in the centre of the first swirler, called "internal swirler".

Two versions are possible, according to installation of the swirlers, which can be co- or contrarotating.

Concept 4

In this concept, the annular air flow is supplied by two contra-rotating axial swirlers.

Fuel is injected through small holes distributed all around the inner wall of the premixed system. The fuel jets impinge on a swirler separation lip.

A central body is supplied with 10 percent of the air flow via a radial swirler. The annular flow converges on the central body. Two convergences are proposed, leading to substantially different exit Mach numbers: $M = 0.15$ and $M = 0.17$.

4. AUTOIGNITION AND FLASHBACK RESULTS

Over the operating range of each premixed system (pressure, air temperature, equivalence ratio), the minimum air flow conditions at which a flame appears in the mixing duct were determined. This minimum flow rate corresponds either to a sufficient residence time for autoignition of the carburetted mixture to occur or to a sufficiently small

pressure loss for flashback to occur. Therefore, autoignition occurs only if flashback does not occur first and vice versa.

As shown in Figures 5, 6 and 7, the form of the optical signals gives information on the phenomena which occurred.

Autoignition corresponds to stable signals with immediate saturation of the photoelectric cells (concepts 1 and 2), whereas flashback corresponds to relatively unstable signals, which can :

- have starting points offset by a few milliseconds (concept 1, Figure 7), or
- concern only the optical fibres farthest downstream in the mixing duct with relatively regular ignition/quench sequences (concept 3, Figure 6).

It is actually necessary to distinguish between several types of flashback. Although the occurrence of flashback is generally characterized by the pressure loss parameter, it can have many causes :

- flashback by the boundary layers ;
- flashback due to combustion instabilities ;
- flashback due to a recirculation region.

The analysis of the combustion instabilities and two-phase flow characteristics at the outlet of the premixed system helps to identify the phenomenon.

4.1 Interpretation of autoignition phenomena

Autoignition was observed on systems 1, 2 and 4 (a single point on concept 4 in $M=0.17$ configuration at the maximum pressure and temperature of the test facility).

This phenomenon occurs whenever the residence time of the carburetted mixture is equivalent to the time necessary for its ignition. The average residence time in the duct is defined as the ratio between the duct length after the injection point and the average flow velocity. It can easily be calculated from the thermodynamic parameters governing the test (air temperature T_{i2} and reduced flow rate FF).

$$t = L / U = V / 10^8 / R * T^{0.5} * FF$$

where t is in ms, V in m^3 and FF in $kg/s.K^{0.5}$.

The results obtained at $T_{i2} = 810$ K, illustrated in Figure 8, show that the ignition time is inversely proportional to $P^{0.9}$. The set of points at all air temperatures and in all configurations can be represented by an exponential law of the air temperature (Fig. 9).

$$t_{\text{auto}} = \frac{0.508 e^{(3377/T_{i2})}}{P_{i2}^{0.9}}$$

This law is of the same type as that resulting from Spadaccini's basic work [1] and the exponential dependency on the temperature agrees with the theoretical work [2]

relating the time to autoignition to the fuel activation energy by a law of the type :

$$\ln t = \frac{E}{R * T} + A$$

Where E is the activation energy and T is the local temperature, which can be considered as the air temperature to simplify.

It was not effectively demonstrated that the equivalence ratio had any effect on the time to autoignition in the duct. However, the range investigated was only between $0.7 \leq ER \leq 1$.

From a practical standpoint, these results show that for the operational conditions of current engines, the premixed system must be dimensioned so that the residence time of the carburetted mixture is less than:

$$t_{\max} = \frac{30}{P_{\max}^{0.9}}$$

4.2 Interpretation of flashback phenomena

Flashback was observed for concepts 1, 3 and 4. It is characterized by a minimum pressure loss below which the phenomenon occurs. For concept 1, the minimum pressure loss depends on the combustor equivalence ratio ($P_{\text{div}} = 5\%$ at $ER = 0.4$ and $P_{\text{div}} = 9\%$ at $ER = 0.7$) whereas for concept 3, it is independent of this parameter. For concept 3, random optical signals began to appear in the mixing duct when P_{div} was between 4% and 5%, depending on the pressure level and the co- or contrarotating configuration (the minimum pressure loss was lower when the pressure decreased and for the contrarotating configuration). With concept 4, the appearance of a flame in the duct, at around $P_{\text{div}} = 3\%$, seems to be correlated with the amplification of a combustion instability and to vary substantially with the equivalence ratio and air temperature. Whether or not combustion instability is amplified depends on the combustor geometry. For instance, with a ratio $d/D = 0.575$ (mixing duct outlet diameter to combustor diameter), the instability was amplified when the pressure loss through the premixed system decreased, whereas this was not the case for a ratio $d/D = 0.39$.

These examples show that a distinction must be made between several causes of initiation of flashback.

Flashback by boundary layer

Many authors have shown that the propagation velocity of a turbulent flame was related to the kinetic energy of turbulence [3] $V_t = \alpha * k^{0.5}$, where :

- k is the turbulent kinetic energy $= 3 U'^2 / 2$;
- α is a proportionality factor which varies from 0.6 to 2, depending on the author.

Flashback therefore appears to be possible only for a turbulence level $I_u = U'/U$ at least equal to 40 percent. For the mass flow velocities encountered in premixed systems, flashback far from the walls is not possible. However, near the wall, where the flow velocity is low, flashback is more probable.

Lewis and Elbe demonstrated that flashback by the walls occurred only if the velocity gradient on the wall was smaller than the ratio between the theoretical flame velocity and the quenching distance $g_f \leq V_t/d_p$. The quenching distance is a region where the heat losses on the wall are such that the flame velocity vanishes. There exists a critical gradient below which flashback occurs. This critical gradient, which corresponds to the minimum flow rate to be ensured to prevent flashback, depends on the equivalence ratio.

Thus, for concept 1, the fact that we were able to correlate the phenomenon observed with both the pressure loss and the equivalence ratio may mean that flashback occurred by the boundary layer. The optical signals observed (Fig. 7) do not contradict this hypothesis. The order and phase shift of the starting points may correspond to the time required for the flame to propagate. Finally, the measurements made right at the outlet of the premixed system by Laser Doppler Velocimetry (LDV) ($x = 0.5$ mm) and by Phase Doppler Particle Analyser (PDPA) ($x = 10$ mm) confirm this hypothesis (Figs. 11 and 12), because they show that in the wake of the wall :

- the air flow turbulence level is very high, since the axial velocity fluctuation is of the same order of magnitude as the axial component of the velocity vector ;
- the axial velocity of the droplets is also of the same order of magnitude as its fluctuation and the mass flow rate of the fuel is high because of centrifuging.

Flashback due to combustion instability

If the amplitude of the pressure oscillations due to combustion exceeds the dynamic pressure of the flow $\rho U^2/2$, this should logically lead to a return flow during part of the cycle. Flashback is therefore induced periodically. The appearance of the optical signals recorded for concept 4 (Fig. 6) seems to be related to this phenomenon.

The analysis of the frequency spectrum of the corresponding combustion instabilities, given in Figure 13, shows that a 1500 Hz pressure oscillation is gradually amplified as the pressure loss through the premixed system decreases. The oscillation amplitude increases up to 1.3 percent of the pressure level in the combustor. This amplitude is reached for a pressure loss of 2.9 percent. Above that value, if the air flow rate continues to decrease, the oscillation disappears and is replaced by a low amplitude oscillation at 300 Hz. It can be seen from Figure 14, which shows the correlation in time of the combustion instabilities and optical signals, that the change in frequency of the pressure oscillations occurs at the same time as flashback in the mixing duct. However, flashback cannot be due to the instability, because the frequency is too high. It can therefore be surmised that a slight flame penetration in the mixing duct initiates periodic

flashback in the boundary layer, where the frequency is lower (300 Hz).

Flashback due to a recirculation region

The phenomenon encountered for concept 3 differs from the above in that the appearance of an optical flow in the mixing duct is not accompanied by an increase in wall temperature. In addition, it cannot be correlated with combustion instabilities and seems to depend on the pressure level rather than on the equivalence ratio in the mixing duct.

Figure 15 shows the luminous intensities and wall temperatures versus the pressure loss at 0.1 s intervals during a gradual decrease in the air flow rate through the combustor. The following can be observed under the conditions selected ($P_2 = 24$ bars, $T_{i2} = 890$ K, $ER = 0.5$).

- At a pressure loss of 5%, the first luminous flashes appear in the mixing duct; then, if the pressure loss continues to decrease, the intensity and frequency of the flashes increase. At the same time, the duct wall temperature remains constant at a value close to the air flow temperature.
- At a pressure loss of 2.5%, the luminous intensity saturates the photoelectric cells and the flame is continuously present in the duct. The wall begins to heat up slightly.
- Below 2.5%, the wall temperature stabilizes at a value which increases as the pressure loss decreases, without however becoming dangerous for the premixed system. Simple visualisations made at the outlet of the premixed system show that vortex shedding creates a small recirculation region in the centre. It can therefore be concluded that the luminous flows detected correspond to the presence of a flame in this recirculation region which may shoot back into the centre of the duct. The lower the pressure loss and the higher the pressure, the farther the flame shoots back into the centre of the duct. This flame region is not dangerous for the thermal resistance of the duct, since it is surrounded by a cold carburetted air flow.

5. CONCLUSION

ONERA has developed a test facility for characterizing autoignition and flashback of lean premixed injection systems. It is equipped with automatic systems for controlling the test conditions and stopping combustion, allowing accurate safe control of this type of test. It includes a modular combustor which can easily be fitted with different premixing concepts and on which optical measurements are made for qualifying the two-phase flow.

In the framework of European research on low NOx emission combustors (Brite Euram programme), several concepts developed by the manufacturers Turbomeca, Volvo, BMW, Rolls-Royce and Snecma were tested up to a pressure of 30 bar and an air temperature of 900 K with no damage to these premixed systems.

The presence of a flame in the premixing duct is detected by photoelectric cells. It was demonstrated that the nature of the optical signals allowed identification of the phenomenon encountered and in particular a distinction between autoignition and flashback.

The limit on the carburetted mixture residence time in the injection system to prevent autoignition was established according to the pressure and air temperature. It is defined by the equation :

$$t_{\text{auto}} = \frac{0.508 e^{(3377/T_{i2})}}{P_{i2}^{0.9}}$$

A reduced minimum flow rate ($m \cdot T_{i2}^{0.5}/P_2$) below which flashback becomes probable was found for each concept. It corresponds to a minimum pressure loss through the premixed system. The analysis of the optical signals, the combustion instabilities and the two-phase flow allowed us to identify the causes of flashback. Three causes were identified :

- flashback by the boundary layer when wall turbulence is high ;
- flashback caused by amplification of a combustion instability ;
- flashback caused by a recirculation region at the outlet of the premixing duct.

The shortcomings of each of these premixing concepts have now been identified and their operating limits have been established. This information is very valuable for optimizing these systems before their integration in a complex, costly combustor.

ACKNOWLEDGEMENTS

This work was accomplished with funding from the European Commission and the French civil aviation authority DGAC in the framework of the European "Low Emission Combustor Technology Low NOx III" Aero CT 95-0122 programme. The author wishes to thank these organisations as well as the manufacturers who demonstrated their confidence in ONERA and authorized publication of this paper.

REFERENCES

- [1] SPADACCINI. L.J, Autoignition characteristics of hydrocarbon fuels at elevated temperatures and pressures - Journal of Engineering for Power. January 1977.
- [2] MULLINS. B.P, Studies on spontaneous ignition of fuels injected into a hot airstream - Part. I to III, Fuel, Vol. 32 - 1953.
- [3] THIBAUT. D, Etude de la remontée de flamme dans les foyers prémélangés prévaporisés. Synthèse bibliographique CNRS, Ecole Centrale Paris, Avril 1994.

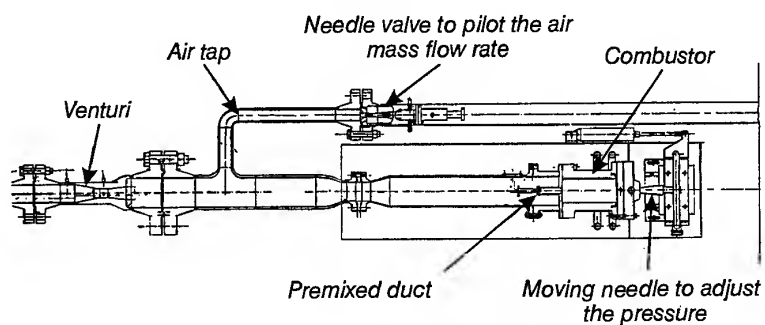


Fig. 1 - Air supply on the autoignition and flashback test rig

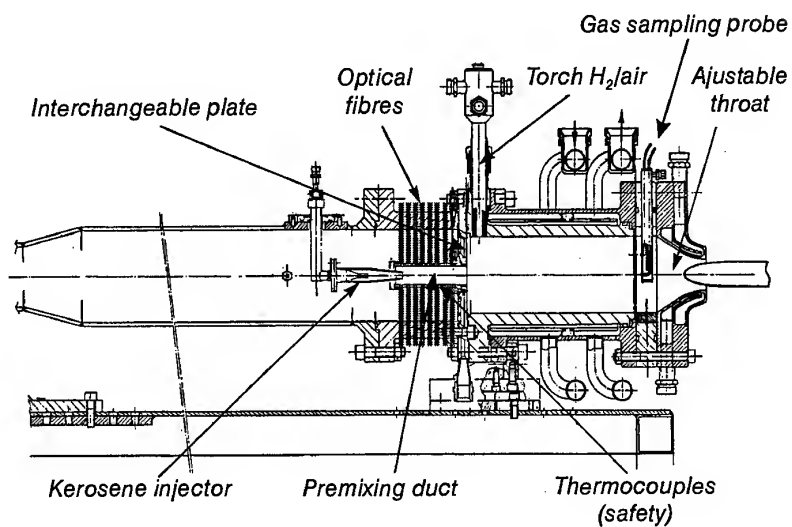


Fig. 2 - Autoignition and flashback test apparatus

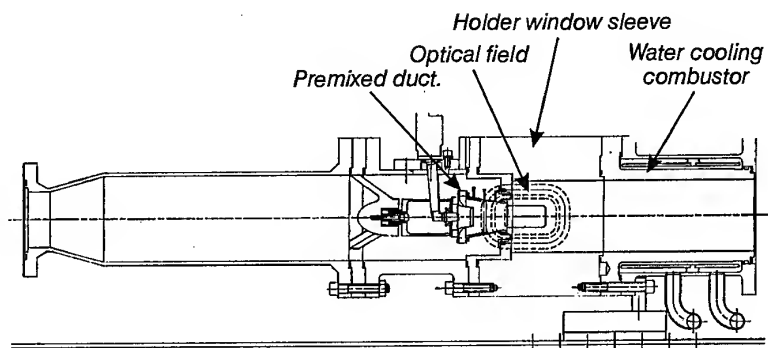
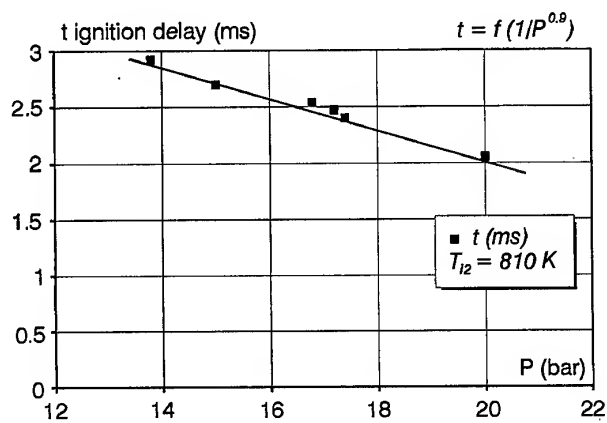
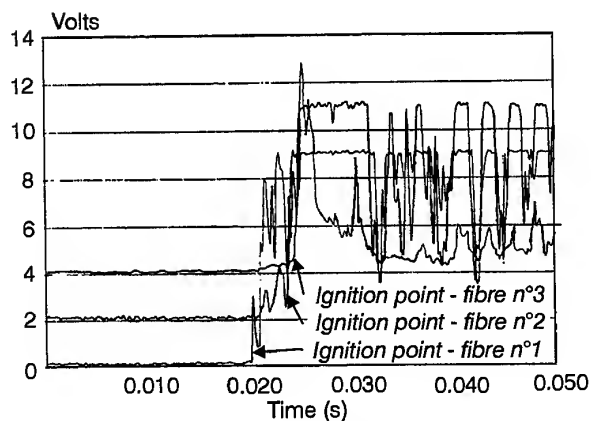
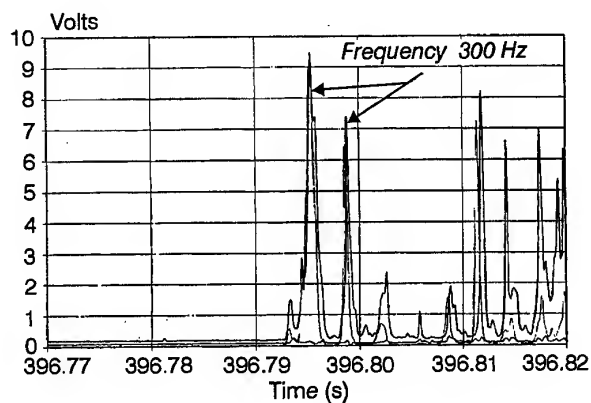
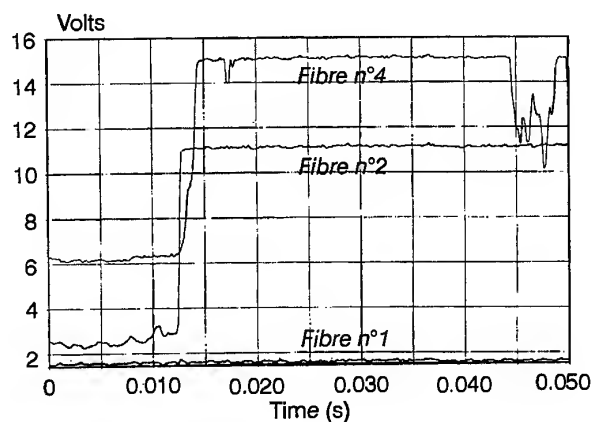
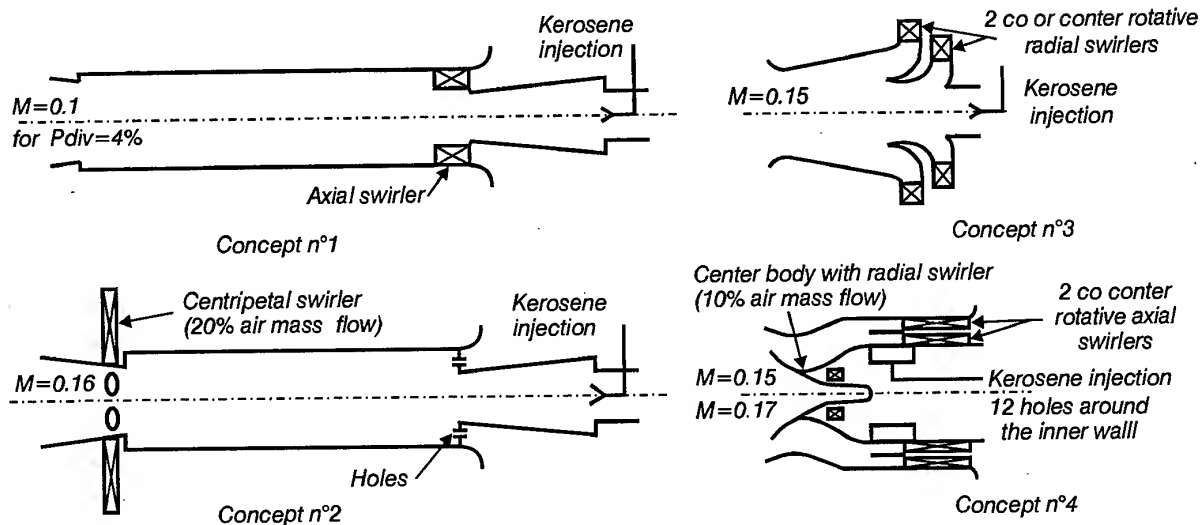


Fig. 3 - Adaptation of the autoignition test apparatus for PDA and LDV measurements



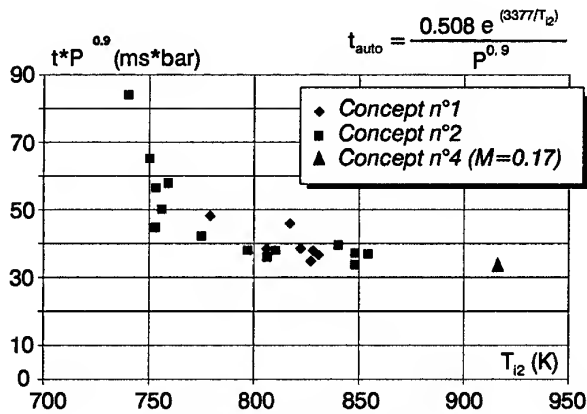


Fig. 9 - Autoignition law

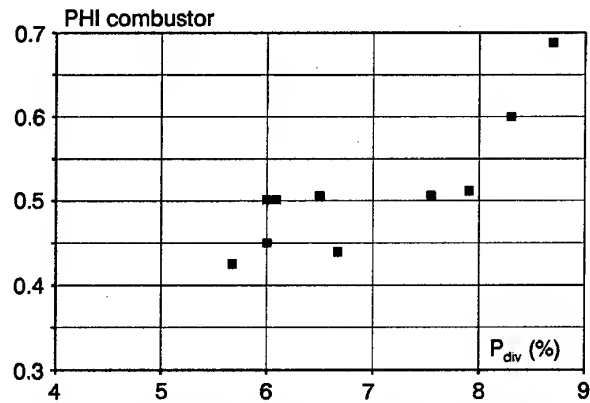


Fig. 10 - Equivalence ratio limit for flashback versus pressure drop. Concept n°1

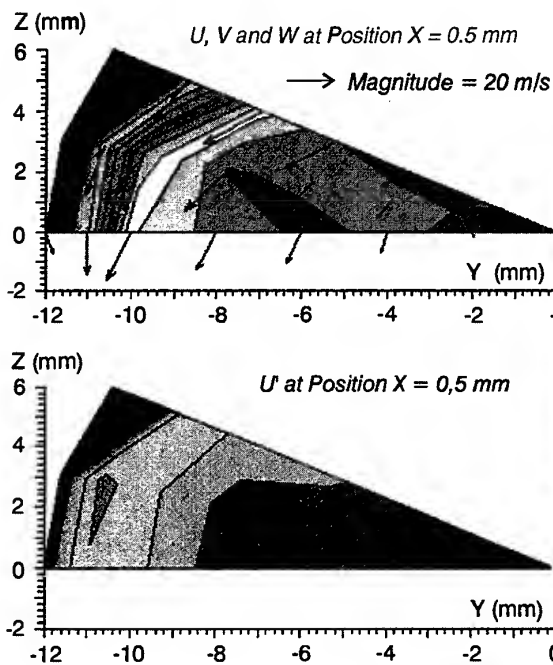


Fig. 11 - LDV measurements - 3D velocity field at duct outlet

Conditions :

$T_{i2} = 705 \text{ K}$
 $P_2 = 6.46 \text{ bar}$
 $f = 0.296 \text{ kg} \cdot \text{K}^{0.5} / (\text{bar} \cdot \text{s})$

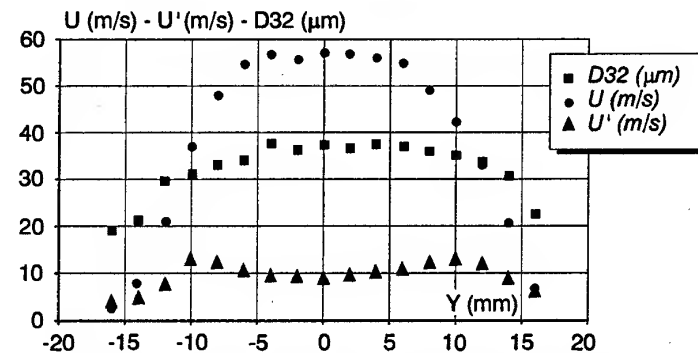
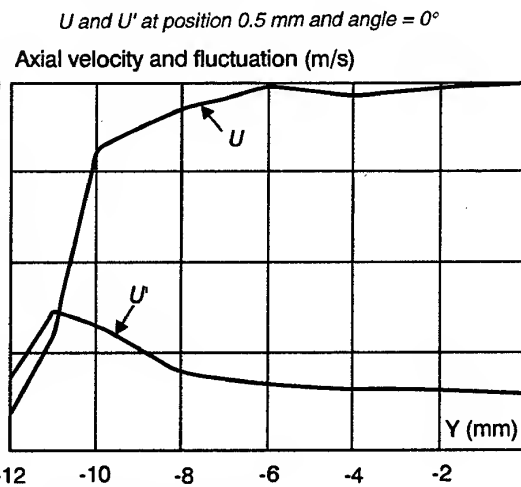


Fig. 12 - Velocity, velocity fluctuation, droplet size versus position (horizontal axis)

$P_{\text{div}} = 4.7\%$, $T_{\text{air}} = 606 \text{ K}$, $P = 6 \text{ bar}$
 mesured at 10 mm from the duct outlet. Concept n°1

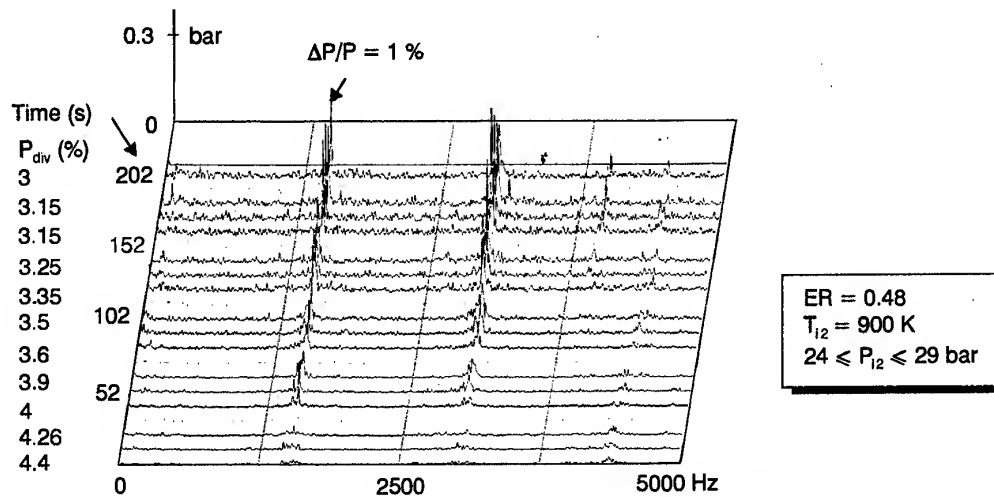


Fig. 13 - Pressure fluctuation frequency spectrum versus pressure loss through duct.
Concept n°4

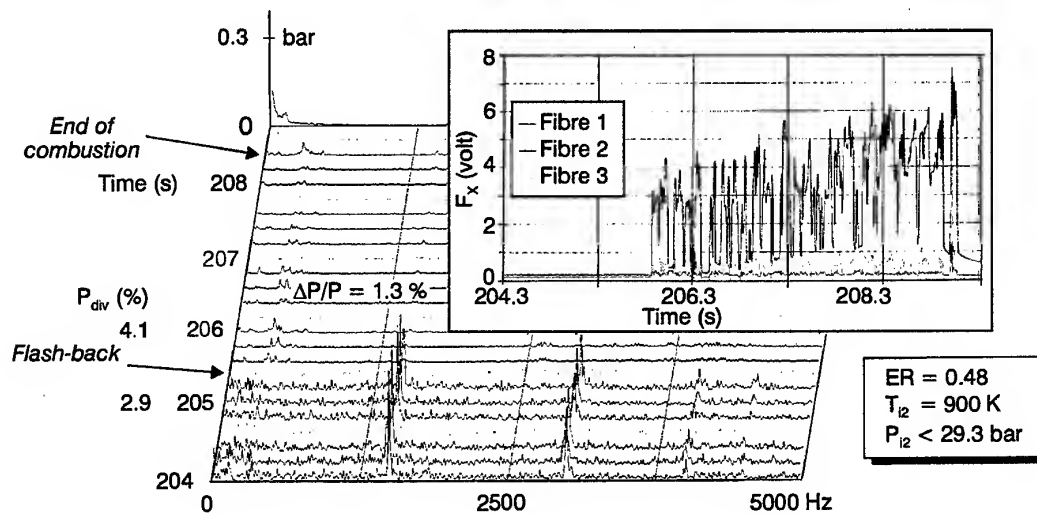


Fig. 14 - Pressure fluctuation frequency spectrum
Correlation with optical signals. Concept n°4

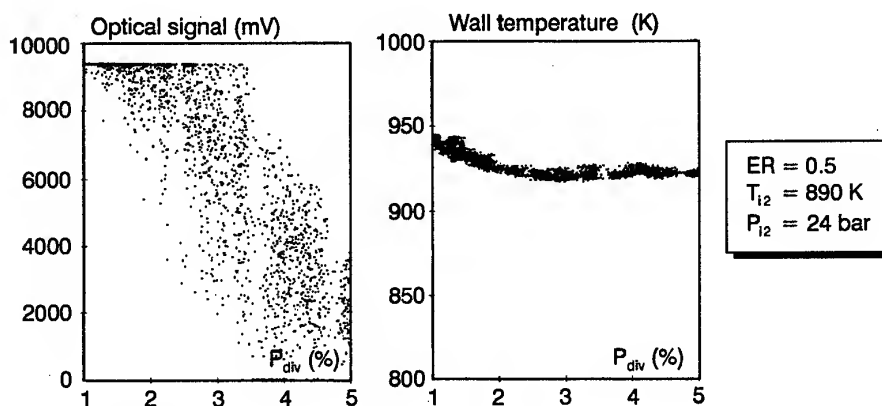


Fig. 15 - Optical signal and wall temperature versus pressure drop.
Concept n°3

PAPER No. 30
Guin
(presenter: C. Guin)

Question 1: P.G. Lignola, Second University of Naples, Italy

When you encountered a flashback incident, did you ever inhibit the automatic fuel cut-off to see if flame was stabilized in the premix duct, and if so, did the presence of the stabilized flame change the duct airflow?

Answer:

For safety, the fuel was automatically cut-off by means of a threshold level of wall temperature. Nevertheless, sometimes we had a few seconds of time between the flashback detection and the fuel valve closing. Even so, it was difficult to ascertain if the flashback flame was sustained in the flow.

Question 2: J. Tilston, DERA, U.K.

Were you able to associate the oscillation frequencies that you observed, with any dimension associated with the premix tube, combustor or rig?

Answer:

Yes, with the combustor dimensions. The 1500 hertz frequency corresponds to the first longitudinal mode for the combustor. The amplitude of this frequency did not always increase when the flow function was decreased, as it depended on the air inlet temperature and pressure, and on the ratio of the premixer outlet diameter to the combustor diameter. The 300 hertz frequency was often encountered, but it did not correspond to an acoustic mode for the combustor; I cannot verify if this frequency corresponded to an acoustic frequency of the rig. However, this particular oscillation was not encountered unless combustion was present.

Question 3: R. Jacques, Ecole Royale Militaire, Belgium

What determines the length of the premix duct?

Answer:

The length of the premix duct is determined by the engine maximum power condition. However, at off-design conditions the fuel evaporation for example, falls. Therefore, optimization is required, and this is subject to autoignition and flashback constraints. The premix duct design problem (length) is more difficult for smaller engines because the operating conditions and pressures are generally lower.

Ignition Diagrams and Bifurcation Maps

F.P. Di Maio

Dept. of Aerospace Engineering
Second University of Naples
Real Casa dell'Annunziata
via Roma 29
81031 (CE) Aversa, Italy

G. Barbieri

Institute of Research on Membrane and Modelling of Chemical Reactors,
C.N.R.
87036 Rende (CS)

P.G. Lignola

Department of Aerospace Engineering
THE SECOND UNIVERSITY OF NAPLES
81031 Aversa (CE)

Italy

1. SUMMARY

In this work a method is presented for the analysis of models of combustion processes. The method, based on the theory of bifurcation and on that of continuation, permits the calculation of ignition diagrams for combustion systems reacting in zero dimensional combustion devices. The method is applied to combustion of hydrogen and the results are encouraging. Selected residence times have been investigated. A rich variety of dynamic behaviours has been detected, as experimentally observed.

2. INTRODUCTION

Combustion processes are known to evolve by means of complex kinetics. In particular, hydrocarbon combustion processes are known to proceed according to branched radical chain mechanisms which involve tens of species in hundreds or thousands of elementary reaction steps. The assessment of the kinetic mechanism for each reacting system of interest is the objective of a specific field of research in combustion. The mechanism must be capable of predicting the evolution of the combustion process in the large existing variety of combustion devices, if the appropriate model equations are solved.

Experiments in combustion span from flame analysis to shock tubes, to bombs and to well characterised reactors, such as the plug flow reactor and the CSTR (Continuous Stirred Tank Reactor). Among these experimental set-ups, it is opinion of the authors, that the CSTR has played an important role in the analysis of combustion processes.

Indeed the CSTR experimental technique provides a reaction volume with no gradients in a flow system, where very fast combustion processes can be studied even at steady state conditions. Moreover the dynamic nature of the steady states can give precious informations on the ability of the models to predict the experimental results.

As compared to other flow operating conditions, such as flames or plug flow reactors which can be modelled by means

of partial differential equations, the CSTR offers the advantage of being modelled as a lumped parameter system, i.e. ordinary differential equations are used instead of partial differential equations.

For the aim of this work, it must be remarked that because of the flow operation ignitions and cool flames in a CSTR do occur in periodic fashion. On one hand the periodicity permits the continuous experimental observation of phenomena that in a closed system occur in a very short time, on the other hand the comparison of frequency analysis of model results with those of the experiments, provide new constraints for model validation.

This work describes the method the authors developed for obtaining more constraints in the validation of models of combustion processes, by applying the bifurcation theory and the continuation theory to the field of combustion.

3. BACKGROUND

The presentation of the mathematical theories of bifurcation and of continuation is beyond the scope of this paper. The reader is referred to specific literature (1-7).

It is sufficient here to say that a combustion process in a CSTR can be modelled by the following set of ordinary non-linear differential equations:

$$\dot{x} = f(x, \lambda), \quad x \in \mathbb{R}^n, \quad \lambda \in \mathbb{R}^k \quad (1)$$

The set consists of $n-1$ equations for species conservation and 1 equation for energy conservation. λ is the set of k natural parameters of the system. There are several parameters of interest, among them the attention can be focused to pressure (P), temperature (T), residence time (τ) and fuel/air ratio. However only two parameters can be studied at one time, the remaining ones are kept constant. Of course the role of constant and variable parameters can be changed.

The bifurcation analysis of such system consists of finding values of parameters for which the stationary solutions of the dynamical system described by zeroing the right hand side of the set (1), change their nature, i.e. the set starts having multiple solutions, the solutions become periodic, the solutions become stable or unstable.

In the case of two parameters bifurcation, it can be demonstrated that the set of possible types of solutions is limited and moreover that there exist contact equivalent polynomial forms which embed the properties of each type of solutions, i.e. one can define a diffeomorphism which transforms the problem under study in a canonical form (7). A bifurcation diagram is the graph of a state variable against the parameter on which the dependence of the system is studied, e.g. reaction temperature against inlet temperature.

In the frame of this work it is sufficient to report only the main bifurcation varieties, which have been experimentally detected in combustion processes (8). Namely the limit points LP, which are defined as the points belonging to a bifurcation diagram where the graph presents a vertical tangent and the Hopf bifurcations (HB) where the solution of the set of equations becomes oscillatory.

Whereas the LP bifurcation is the simplest bifurcation variety, the Hopf bifurcation is less widely known by combustion researchers, not specifically interested in the field of non-linear dynamic systems. In Fig. 1 a sketch of HB occurrence in a system is shown.

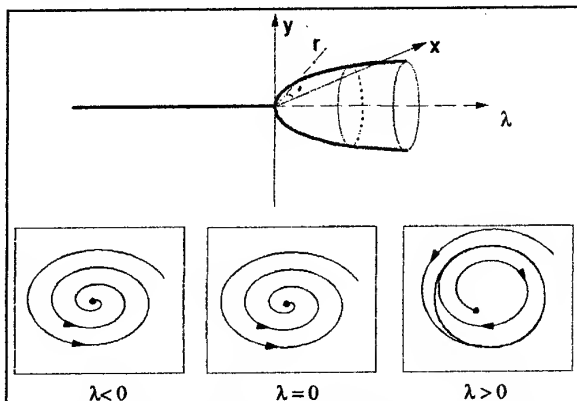


Figure 1 - The Hopf bifurcation. The graph shows that trajectories in the phase plane change their nature from spirals (damped oscillations in the time domain) to a closed curve (purely periodic oscillations) by varying the parameter λ : i.e. a limit cycle appears.

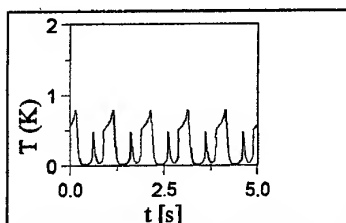


Figure 2. Complex wave form oscillations, showing that Period doubling bifurcation occurred in the system.

In the oscillatory branch one can identify the period doubling bifurcation (PD), where the period of oscillations is halved and the time dependent graph of a state variable, e.g. the reaction temperature, shows the so called complex wave form

oscillatory behaviour (8), as Fig. 2 shows.

The PD bifurcation is shown in Fig. 3.

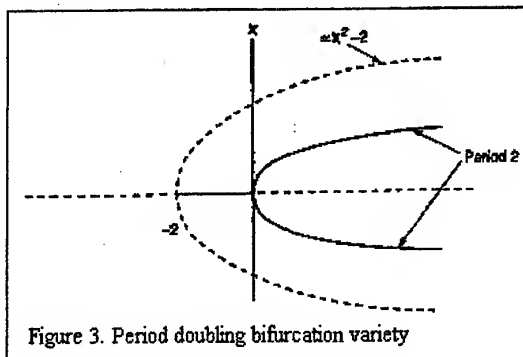


Figure 3. Period doubling bifurcation variety

A bifurcation map is a diagram on which the loci of values of parameters for which a definite type of bifurcation occurs in the system. Experimentally in combustion a typical bifurcation map is the ignition diagram, generally, but not necessarily, in the pressure - temperature plane. In the ignition diagram of a combustion system, e.g. CH_4/air , the plane is divided into regions by pressure vs temperature curves, in each of which a specific behaviour occurs; i.e. one can define a parametric region in which slow combustion occurs, one can define another region in which ignitions occur, one can define another region in which cool flames occur (9) and so on. If the combustion process occurs in a CSTR, ignitions and cool flames appear as oscillatory phenomena, as already reported.

The continuation theory can be used in order to detect the bifurcation points. A naive form of continuation is generally adopted by those who try to solve numerically a set of non-linear equations and assume the solution at a certain value of the independent variable as a first approximation of the solution at a new value of the independent variable, very close to the previous one. Indeed behind this naive approach a solid mathematical theory exists and several methods of continuation have been developed under rigorous mathematical principles (5, 10).

Several computer programs have been developed for the application of continuation theory. Among them the authors adopted the AUTO program (11).

On the basis of the above mentioned background the author developed a method for the analysis of combustion processes, with the aim at defining the bifurcation maps of the models, whatever complex, in order to have more constraints for their validation against experimental data. The method has been applied to a simplified model of acetaldehyde combustion (12), to hydrogen combustion (13) and work is in progress on methane combustion.

In practice the method consists of:

- detecting the most complex bifurcation diagram for a combustion process, i.e. the diagram which presents the largest number of bifurcation varieties, for a selected set of $n-1$ constant parameters;
- detecting by means of the continuation theory limit points, Hopf bifurcations and period doubling;

- applying the two parameter continuation in order to construct the bifurcation map.
- comparing the calculated bifurcation map with the experimental one.

4. THE H₂/O₂ SYSTEM

4.1. Introduction

Whereas for the acetaldehyde and methane combustion in CSTR several experimental results there exist, for the combustion of hydrogen in CSTR only few results are available and the state of the art has been reported elsewhere (13). However the kinetic model of hydrogen oxidation is well established and is reported in Table 1. The kinetic scheme consists of 33 elementary reactions with 12 chemical species.

CHEMKIN is kinetic solver for complex kinetics (14). Since few years it became a standard for kinetics in combustion schemes. In order to compare simulation results with those appearing in the literature the adoption of CHEMKIN for the integration of the set of ordinary differential equations was considered. Moreover the use of its thermodynamic library allows any interested reader to repeat the numerical experiments with the same data.

The CSTR model in the CHEMKIN format is the following:

$$\frac{dy_i}{dt} = K_f(y_i^0 - y_i) + \frac{\omega_i W_i}{\rho} \quad (i = 1, \dots, NSPE)$$

$$C_p \frac{dT}{dt} = K_f \sum_{i=1}^{NSPE} y_i^0 [H_i^0 - H_i] - \frac{1}{\rho} \sum_{i=1}^{NSPE} H_i \omega_i W_i - \frac{UA}{V\rho} (T - T_0)$$

definition of symbols is reported at the end of the paper.

In the case under study the ODE set consists of 13 equations (12 for species conservation and 1 for energy conservation). Constant parameters are: $U = 13 \text{ W m}^{-2} \text{ K}^{-1}$, $V = 550 \text{ cm}^3$ and the molar feed ratio $\text{H}_2/\text{O}_2 = 2$. Moreover the following assumptions have been made for each numerical experiment: pressure is considered constant and equal to feed pressure, the feed temperature equals the ambient temperature, i.e. simulation assumes that gases are preheated at the temperature of the furnace inside which the CSTR is virtually located.

Bifurcation parameters used for the study were: pressure (P), inlet temperature (T_0) and residence time (τ). Since numerical methods are available only for two parameters continuation, analysis was performed at selected residence times and pressure - inlet temperature bifurcation maps were obtained at each residence time.

Numerical experiments were performed with the following procedure:

- at a constant set of parameters, as reported above, for a selected pressure and inlet temperature a system steady state is calculated by means of CHEMKIN code
- the calculated steady state is used as a starting point for bifurcation analysis by means of the continuation AUTO code
- the calculated bifurcation diagram (reacting system temperature T against inlet temperature) shows the bifurcation points
- Hopf bifurcation points were continued whenever possible in order to seek period doubling bifurcations

- finally, starting from each singular point detected in the bifurcation diagram, the bifurcation map (pressure against inlet temperature) is obtained by means of two parameters continuation.

The first results obtained in the analysis of hydrogen combustion have been already published (13). In this paper more results are presented.

4.2. Residence time $\tau = 4 \text{ s}$

For $T_0 = 820 \text{ K}$ and $P = 0.10 \text{ atm}$, with all the other parameters kept constant as described, the steady state reached by the system is:

State variable	Value (K or mass fraction)
T	920.61
O ₂	$9.4652 \cdot 10^{-3}$
H ₂	$8.2871 \cdot 10^{-4}$
OH	$4.8203 \cdot 10^{-3}$
HO ₂	$4.9930 \cdot 10^{-6}$
H ₂ O	$9.8557 \cdot 10^{-1}$
H ₂ O ₂	$4.6673 \cdot 10^{-8}$
O	$1.4755 \cdot 10^{-5}$
H	$1.2924 \cdot 10^{-5}$
H _{inert}	$6.1785 \cdot 10^{-4}$
O _{inert}	$7.0719 \cdot 10^{-4}$
OH _{inert}	$2.3145 \cdot 10^{-3}$
HO ₂ inert	$2.3944 \cdot 10^{-4}$

The steady state has been calculated by means of continuation of the steady state obtained by CHEMKIN, because the accuracy of the continuation code AUTO is higher than that of

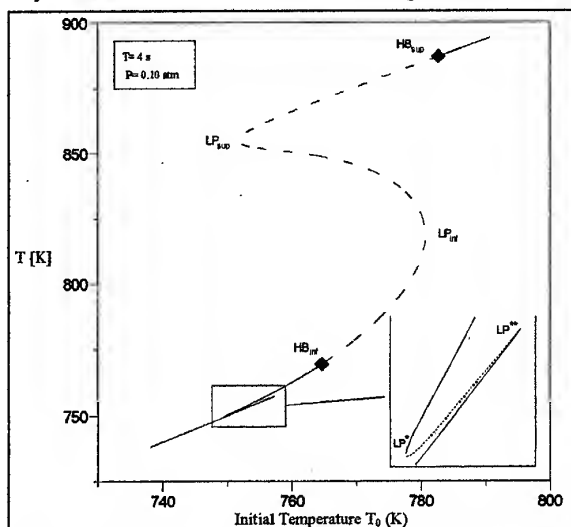


Figure 4. The bifurcation map for $\tau = 4 \text{ s}$. The inset shows an enlargement of the graph where two limit points occur.

CHEMKIN. The reason of this procedure is that owing to the large parameter sensitivity of the bifurcation points, the higher the accuracy the easier to detect singular points.

Starting from the above steady state the bifurcation diagram was obtained by continuation for the T_0 parameter. Figure 4 shows the T against T_0 plot. Of course any other state variable can be plotted, but T appears to be the most significant.

On the graph two Hopf bifurcation and four limit points can be observed. Dotted lines mark unstable states.

Table 1. Kinetic mechanism of hydrogen oxidation. $K = A T^n \exp (E_a / RT)$ parameters $\text{cm}^3 \text{mole cal K}$							
N	Reaction				A	n	E _a
1)	H ₂	+O ₂	→ HO ₂ +H		5.50E+13	0.0	5.782E+04
2)	H ₂	+OH	→ H ₂ O +H		2.20E+13	0.0	5.146E+03
3)	H	+O ₂	→ OH +O		2.20E+14	0.0	1.679E+04
4)	H ₂	+O	→ OH +H		1.37E+13	0.0	8.901E+03
5)	H	+O ₂	+M	→ HO ₂ +M	5.10E+15	0.0	-9.93E+02
6)	H	→ Hinert			1.20E+01	0.0	0.000E+00
7)	O	→ Oinert			1.20E+01	0.0	0.000E+00
8)	OH	→ Ohinert			1.20E+01	0.0	0.000E+00
9)	HO ₂	→ HO ₂ inert			1.20E+01	0.0	0.000E+00
10)	HO ₂	+HO ₂	→ H ₂ O ₂ +O ₂		2.00E+12	0.0	0.000E+00
11)	HO ₂	+H	→ 2OH		2.50E+14	0.0	1.888E+03
12)	HO ₂	+H	→ H ₂ O +O		3.00E+14	0.0	3.974E+03
13)	HO ₂	+H ₂	→ H ₂ O ₂ +H		7.30E+11	0.0	1.868E+04
14)	HO ₂	+H	→ H ₂ + O ₂		2.50E+13	0.0	6.954E+02
15)	H ₂ O ₂	+M	→ 2OH +M		1.20E+17	0.0	3.974E+04
16)	H ₂ O ₂	+H	→ H ₂ +HO ₂		1.70E+12	0.0	3.775E+03
17)	H ₂ O ₂	+H	→ H ₂ O +OH		1.00E+13	0.0	3.596E+03
18)	H ₂ O ₂	+OH	→ H ₂ O +HO ₂		1.00E+13	0.0	1.808E+03
19)	H ₂ O ₂	+O	→ OH +HO ₂		2.80E+13	0.0	6.406E+03
20)	H ₂ O ₂	+O	→ 2OH		6.80E+13	0.0	1.892E+04
21)	H ₂ O ₂	+H	→ H ₂ +OH		9.30E+13	0.0	2.037E+04
22)	OH	+O	→ O ₂ +H		1.30E+13	0.0	0.000E+00
23)	OH	+H	→ H ₂ +O		6.22E+12	0.0	6.954E+03
24)	OH	+OH	→ H ₂ O +O		6.30E+12	0.0	1.093E+03
25)	H	+OH	+M	→ H ₂ O +M	2.49E+17	0.0	0.000E+00
26)	H	+O	+M	→ OH +M	1.26E+16	0.0	0.000E+00
27)	H	+H	+M	→ H ₂ +M	1.03E+15	0.0	0.000E+00
28)	OH	+OH	+M	→ H ₂ O ₂ +M	9.10E+11	0.0	-5.06E+00
29)	O	+O	+M	→ O ₂ +M	5.00E+14	0.0	0.000E+00
30)	HO ₂	+OH	→ H ₂ O + O ₂		6.00E+12	0.0	0.000E+00
31)	H ₂ O	+M	→ H +OH +M		2.20E+16	0.0	1.039E+05
32)	H ₂	+M	→ H +H +M		2.20E+14	0.0	9.607E+04
33)	O ₂	+M	→ O +O +M		1.20E+14	0.0	1.078E+05

As mentioned above, continuation from Hopf bifurcations can give more information about the structure of bifurcation diagram. In the case under study, however, continuation from HB is mandatory since no stable states exist between HB_{inf} and HB_{sup} . The available codes not always are successful in continuing oscillatory solutions, since in most cases the oscillatory branch is practically vertical. With a fatiguing procedure based on piece wise calculations, the oscillatory branch was plotted (Fig. 5).

Curves represent the amplitude of oscillations. As can be seen the oscillatory branch consists of a stable and of an unstable part: i.e. stable and unstable limit cycles exist. OLP_{inf} marks a limit point in the oscillatory branch. The bifurcation diagram presents two regions of multiple states. That at lower temperature is very small, the other at higher temperature includes the oscillatory branch.

From the bifurcation diagram one can observe that hydrogen combustion process in a CSTR at the conditions of simulation starting at $T_0 = 820 \text{ K}$ with increasing T_0 proceeds following the bifurcation diagram until LP^{**} is reached, where a small jump to the upper steady branch occurs, then the system moves to HB_{inf} , from which large amplitude oscillations can be observed. Oscillations decrease in amplitude with increasing T_0 , until HB_{sup} is reached, where the system follows

again a non-oscillatory branch. If from a stable state of this last branch T_0 is lowered, the system follows the same path

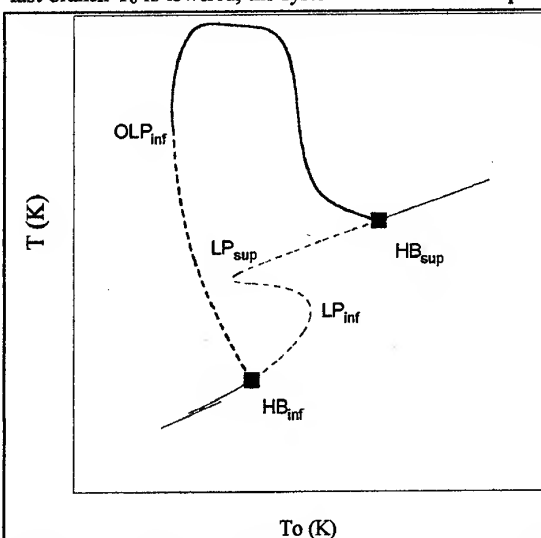


Figure 5. Oscillatory branch. Dotted lines are unstable states.

along the bifurcation diagram, but at OLP_{inf} , from where it jumps to the lower branch of the graph.

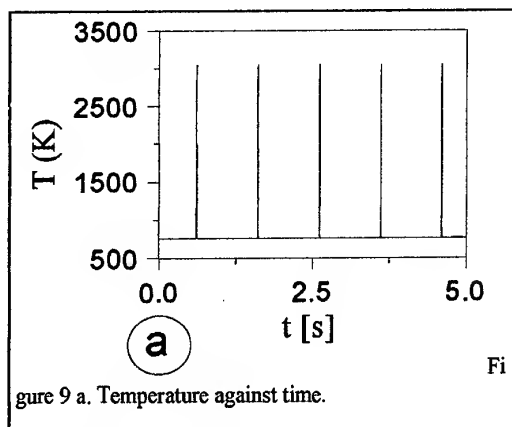
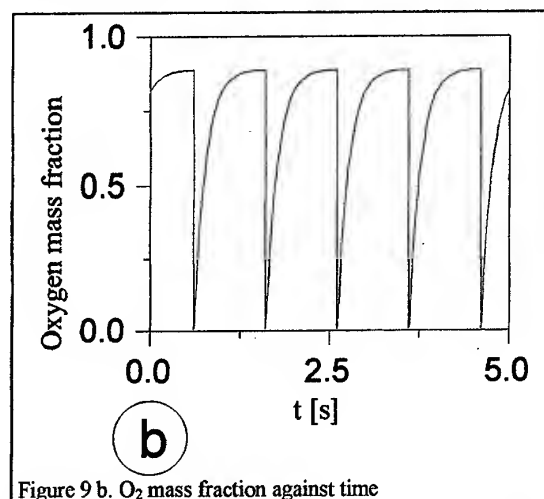


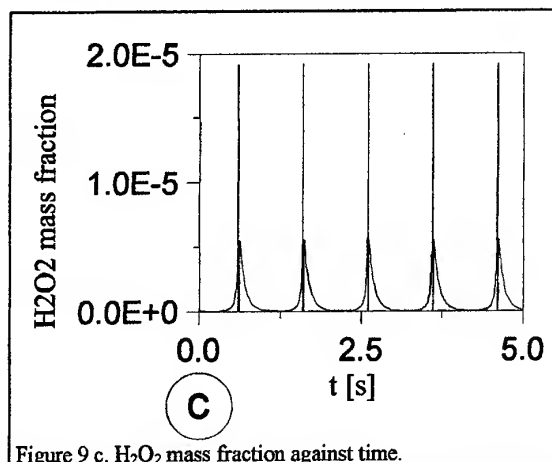
Figure 9 a. Temperature against time.

Several other residence times have been investigated up to 10 s with the same procedure. One can observe with in-

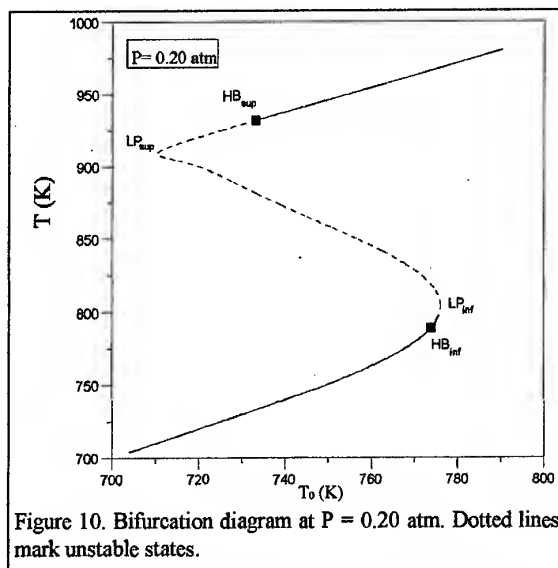
Figure 9 b. O₂ mass fraction against time

creasing τ that:

- HB_{sup} and HB_{inf} move to higher T_0 with increasing pressure
- the region between LP_{sup} and LP_{inf} shrinks
- LP^* and LP^{**} exist only at higher pressures

Figure 9 c. H₂O₂ mass fraction against time.

More residence times will be investigated since, in fact, the next goal of the research group is to calculate bifurcation maps in three dimensional parametric space: T_0 , P , τ .

Figure 10. Bifurcation diagram at $P = 0.20$ atm. Dotted lines mark unstable states.

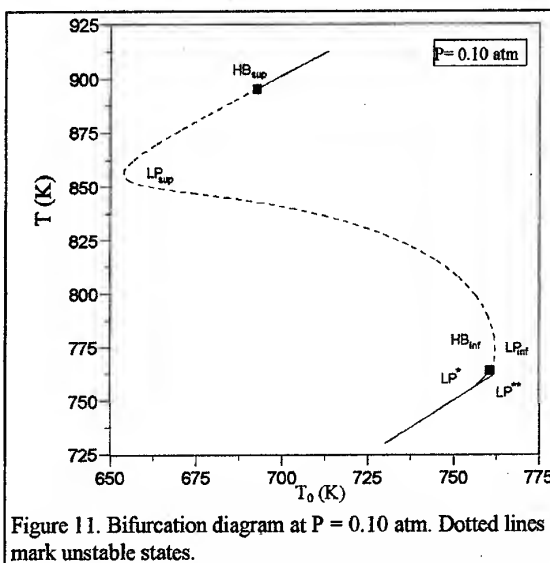
In this paper it appears more interesting to show that continuation has been used also to derive steady states at different residence times and that oscillatory continuation was also successful in one case. This last remark must be considered in the frame of difficulties encountered for continuation of oscillatory branches already discussed.

4.3 Residence time $\tau = 2$ s

The starting stationary state has been obtained by residence time continuation from the steady state calculated at $\tau = 4$ s, $T_0 = 820$ K and $P = 0.10$ atm.

According to the described procedure the bifurcation diagram for $P = 0.10$ atm has been calculated (Fig. 11).

The main difference of the bifurcation diagram of Fig. 11 in comparison with those already discussed is the different

Figure 11. Bifurcation diagram at $P = 0.10$ atm. Dotted lines mark unstable states.

relative position of HB_{inf} and HB_{sup} . This consideration implies that:

- the oscillatory solutions are unstable if no multiplicity region is present in the same T_0 range.
- a multiplicity range exists between LP^{**} and HB_{sup} varieties.

The bifurcation map has been calculated by means of two parameters continuation and it is reported in Fig. 12.

The bifurcation map of Fig. 12 is more difficult to read because of overlapping of parametric regions. However the calculated trends are those one could expect: from the previous analysis. In this case it seems even more important to show some bifurcation diagrams at selected pressures

In Figure 13 the bifurcation diagram for $P = 0.02$ atm is reported.

The bifurcation diagram is more simple than the previous ones. One can observe that only HB_{sup} is present. In this case not only continuation of oscillatory branch was successful, but also it was possible to calculate branches departing from PD varieties.

In Fig. 14 the oscillatory branch stemming from HB_{sup} has been plotted.

The bifurcation diagram of the oscillatory branch, as in the previous case presented shows that LP^{**} is reached by critically slowing down: i.e. the system from the oscillatory branch moves to the non-oscillatory one with oscillations of infinite period. Also in this case there are two PD bifurcations. However the calculation of the branches departing from PD was successful. The bifurcation diagram is reported in Fig. 15

The graph of Fig. 15 is plotted in a very small range of temperatures (1 K). Because of the scale the slope appears larger than that of Fig. 15, of which this last graph is a detail. The new branch departing from the lower PD at $T_0 = 744.8291$ K (number of figures depends on the accuracy required by the method) joins the main one at higher PD at $T_0 = 744.0692$ K. Two more PD appears in coincidence of loss or gain of stability.

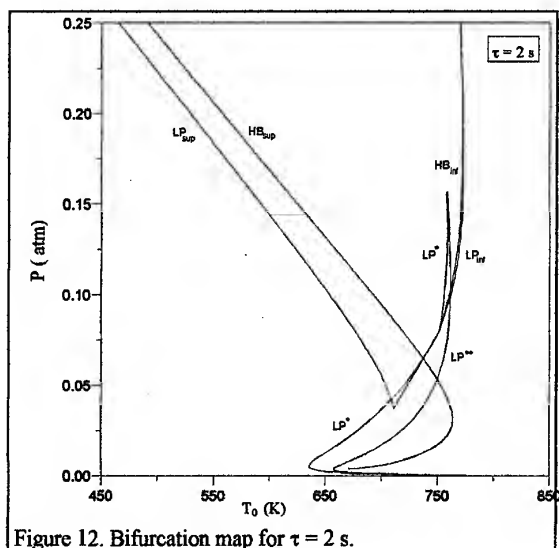


Figure 12. Bifurcation map for $\tau = 2$ s.

The bifurcation diagram for $\tau = 2$ s and $P = 0.20$ atm is reported in Fig. 16.

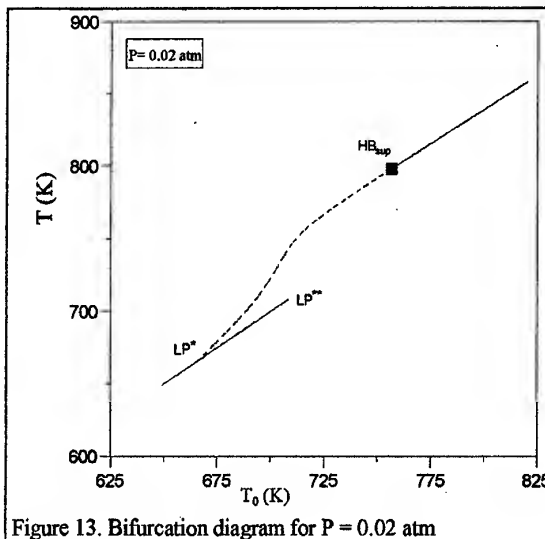


Figure 13. Bifurcation diagram for $P = 0.02$ atm

From the graph of Fig. 16 one can observe that LP_{inf} and HB_{inf} are so close each other to be nearly indistinct. One can observe a multiplicity region, the extension of which is outside the calculated range. The oscillatory branch has not yet been calculated.

5. CONCLUSIONS

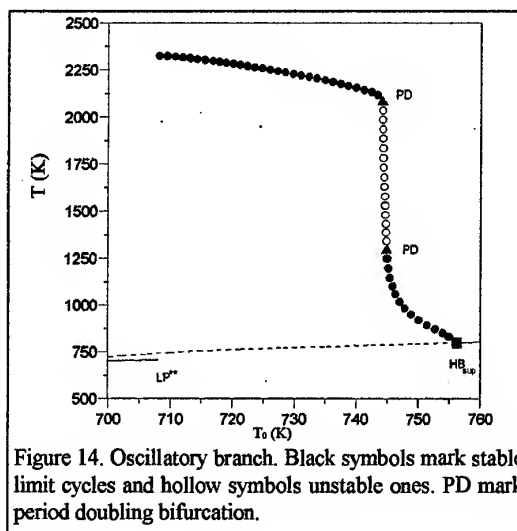


Figure 14. Oscillatory branch. Black symbols mark stable limit cycles and hollow symbols unstable ones. PD mark period doubling bifurcation.

The developed method is very encouraging. Comparison with experiments, reported elsewhere (13) is also satisfactory. The method provides a formidable tool for validation of models of combustion processes. Of course experiments must be performed according to the CSTR technique, which however is now used by several research groups. Infinite dimensions bifurcation has been also studied (15) but it seems that continuation methods and codes such as AUTO are not yet available. If they were, the present method could be applied to distributed parameters models, such as flames and PFR.

The difficulties encountered in calculating the oscillatory branches depend on the form of the branch itself. In par-

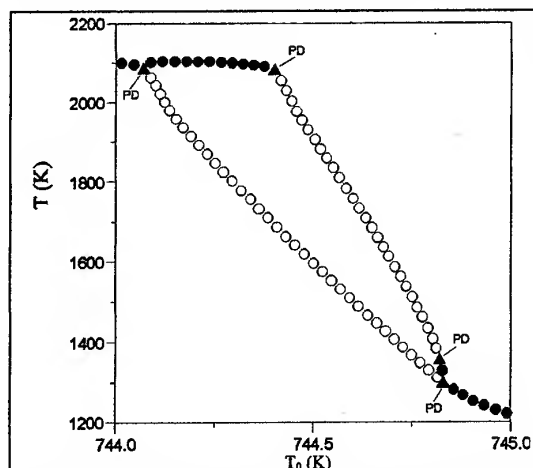


Figure 15. Oscillatory bifurcation diagram. Black symbols mark stable limit cycles and hollow symbols unstable ones. PD mark period doubling bifurcation.

ticular if it is vertical the algorithm fails. The authors are studying how to circumvent this.

To the best of authors knowledge their work in developing the present method appears to be the first application of bifurcation and continuation theory to combustion processes. They hope that other researchers will follow this road, as it happened to the CSTR technique in which they trusted.

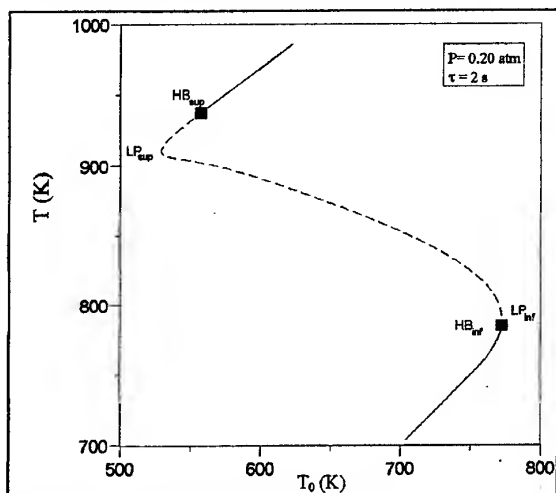


Figure 16. Bifurcation diagram for $\tau = 2$ s and $P = 0.20$ atm. Dotted lines mark unstable states.

Work is in progress for application of the method to methane combustion process.

6. REFERENCES

- 1 - Keller, H.B. Numerical solution of bifurcation and non-linear eigenvalue problems in application of bifurcation theory. P.H. Rabinovitz ed., Academic Press.
- 2 - Carr, J. *Application of center manifold theory*. Springer Verlag (1981)

- 3 - Guckenheimer, J. and Holmes, P.J. *Non linear oscillations, dynamical systems and bifurcations of vector fields*. Springer Verlag (1983)
- 4 - Kubicek, M. and Marek, M. *Computational methods in bifurcation theory and dissipative structures*. Springer Verlag.
- 5 - Troger, H. and Steindl, A. *Non linear stability and bifurcation theory*. Springer Verlag (1991)
- 6 - Doedel, E., Keller, H.B. and Kernevez, J.P. *Numerical analysis and control of bifurcation problems. (I) Bifurcation in finite dimensions*. Int. J. of Bifurcation and Chaos, 1, nr. 3, 493. (1991)
- 7 - Continillo, G., Crescitelli, S. and Lignola P.G. *Analysis, simulation, dynamics of Chemical Reactors*. CUEN, Naples (1995).
- 8 - Gray, P., Griffiths, J.F., Hasko, S.M. and Lignola P.G. *Novel, multiple stage ignitions in the spontaneous combustion of acetaldehyde*. Combust & Flame, 43, 175 (1981)
- 9 - Lignola P.G., Reverchon E. *Cool flames* Progress in Energy and Combustion Science, 13, 75-96 (1987).
- 10 - Holodniok, M and Kubicek, M. *DERPER: an algorithm for the continuation of periodic solutions in ordinary differential equations*. J. Comp. Phys., 55, 254 (1984).
- 11 - Doedel, E and Kernevez, J.P. *AUTO: Software for continuation and bifurcation problems in ordinary differential equations*. Applied mathematical report. California Institute of technology (1986)
- 12 - Cundari, A., Di Maio, F.P. and Lignola, P.G. *Bifurcation analysis of chemical reacting systems*. In Chaos and fractals in chemical engineering, Biardi, G., Giona, M and Giona, A.R. ed., World Scientific, Singapore (1996)
- 13 - Di Maio, F.P., Barbieri, G. and Lignola P.G. *Combustion processes in CSTR- Bifurcation analysis of the H_2O_2 system*. J. Chem. Soc., Faraday Trans., 92, 2989 (1996)
- 14 - Baulch, D.L., Griffiths, J. F., Pappin, A.J. and Sykes, A.F. *Stationary state and oscillatory combustion of hydrogen in a well stirred reactor*. Combust & Flame, 73, 163, (1988).
- 15 - Doedel, E., Keller, H.B. and Kernevez, J.P. *Numerical analysis and control of bifurcation problems. (II) Bifurcation in infinite dimensions*. Int. J. of Bifurcation and Chaos, 1, nr. 4, 745 (1991)

7. SYMBOLS

A	= heat transfer area (cm^2)
C_p	= heat capacity at constant pressure ($\text{erg g}^{-1} \text{K}^{-1}$)
H_i	= enthalpy of species i (erg g^{-1})
HB	= Hopf bifurcation point
K_f	= space velocity (s^{-1})
LP	= limit (turning) point bifurcation
NSPE	= number of chemical species
P	= pressure (atm)
PD	= period doubling bifurcation
ρ	= average mixture density (g cm^{-3})
τ	= residence time (s)
T	= reaction temperature (K)
T_0	= inlet temperature (K)
U	= overall heat transfer coeff. ($\text{erg cm}^{-2} \text{s}^{-1} \text{K}^{-1}$)
V	= reactor volume (cm^3)
ω_i	= reaction rate of formation of species i ($\text{moles s}^{-1} \text{cm}^{-3}$)
W_i	= molecular weight of species i

y_i = mass fraction of species i
 subscript
 inf = lower branch bifurcation
 sup = upper branch bifurcation

Acknowledgement

The work has been partially funded by Ministry of University and of Scientific and Technological Research of Italy in the frame of national interest research projects and by CNR. The work of ing. Giuseppe Siciliano, who performed additional numerical runs, during the preparation of his Laurea thesis in Chemical engineering at University of Calabria, is gratefully acknowledged.

Note added in proof

The authors learned by a kind letter of August 14th 1998 of Prof. D. G. Vlachos - University of Massachusetts (USA) - that independently, nearly at same time, also the group of Prof. Vlachos started applications of bifurcation and continuation theory to combustion processes.

PAPER No. 31 Di Maio & Lignola (presenter: Di Maio)

Question 1: R. Jacques, Ecole Royale Militaire, Belgium

Can you relate this work to Dr. Guin's work (Paper 30)?

Answer

Yes, although any experiments must be conducted very carefully otherwise it is extremely difficult because these systems are divergent.

Question 2: S.N.B. Murthy, Purdue University

Is it now possible to identify the one or more, first-order reactions that control the existence of bifurcation regimes? Has the analysis been extended to high convection situations, i.e. high Mach Number flow conditions?

Answer:

Yes. To this end we developed a computer code, named RIA (**R**elative **I**mportance **A**nalysis) that can provide at bifurcation points, the role of each elementary step for each reaction intermediate, which in addition to phase-space analysis, permits one to know the kinetic causes for bifurcation. In answer to your second question, no, not yet, although we have started to study H_2/O_2 combustion in the supersonic regime in order to get the first results to work on.

The Use of Fluidics in Gas Turbine Combustion Design

R.J. Woolhouse, J.R. Tippetts, M. Whiteman*, K.J. Young[#], S.B.M. Beck⁺
and J. Swithenbank

University of Sheffield
Department of Chemical and Process Engineering
Newcastle Street
Sheffield
England
S1 3JD

⁺ Department of Mechanical Engineering, Sheffield

[#] Now at Rolls Royce, Derby

^{*} Now at DERA, Pyestock

1. SUMMARY

Current legislation demands clean combustion in gas turbines. One line of work concerning this objective at the University of Sheffield uses no-moving-part fluidic techniques to modulate flow in the combustor. Schemes described include BLC swirl vanes, a multi-inlet "modulated swirl combustor", a switched vortex valve to provide "fluidic VAD" and multiple ejector systems to recover mixing energy from the fuel supply. A brief description is given of a recently-started project which uses a so-called "turn-up vortex valve" as a fuel injection device to modulate the throughflow and the flowfield thereby achieving a form of variable air distribution.

2. INTRODUCTION

Following an increased understanding of the impact of certain chemical species on the atmosphere, legislation has been implemented to reduce these emissions. Gas turbine engines (both aero and industrial) have been included, due to their NO_x, CO and hydrocarbon (UHC's and smoke) releases.

Modern combustion chambers tend to be fully annular, and operate in severe conditions [1] with temperatures in excess of 850K (inlet) and 10 bar with air entering the chamber through the injector, primary air ports, dilution holes and cooling slots.

Future engine cycles are tending towards the use of both higher temperature and pressures - risking higher NO_x production. One potential solution is to use lean combustion at high power, however this leads to problems when the power level decreases and the primary zone becomes leaner and leaner - eventually leading to flame extinction, and a curtailed engine operating range.

Combustor designs such as dual annular units, axial fuel staging and lean prevaporised premixing combustors (LPP) and rich burn - rapid quench have been developed [2, 3, 4] to control primary zone AFR and thus avoid blow-out. All these technologies add to both the weight and complexity of the engine.

An alternative solution is to reduce the airflow into the primary zone at low power using some form of variable

area fuel injector, the air being diverted elsewhere in the engine. This primary zone airflow reduction has two benefits [5] both of which aid stability. These are to reduce airflow to that zone (maintaining primary zone AFR) and also reduce the bulk forward velocity both of which aid stability. Previous attempts have concentrated on mechanical devices [6] which due to the extreme conditions are prone to wear and seizure [1].

Fluidic technology has been proven in, amongst others, the nuclear industry and provides a method of controlling the airflow with no moving parts. Sheffield has, historically, been involved with a number of projects and is currently investigating a form of the Vortex Amplifier device.

3. PREVIOUS WORK

To paraphrase Lenin: if you eat fluidics, drink fluidics and dream fluidics for 30 years, then you must eventually achieve fluidics. Cynics and optimists can play with this theme, however the conjunction of no-moving-part flow control and combustion aerodynamics in jet engines seemed the perfect match if only a way could be found for consummation. The perfect match was the motivation that kept two of the authors [Swithenbank and Tippetts] busy in spasms of discussion, research-funding, no-funding, experimentation, hubris and bathos etc. for soon-to-be 30 years. We knew that it would not be easy so our current projects are conditioned by this knowledge, but we are convinced that somehow a practical fluidically modulated combustor can be made. The evidence comes from previous projects: Initial ideas [7] related to afterburners. Cascades of bistable flame-holders would permit low-drag throughflow for normal operation but would introduce more recirculation (but possibly drag) during afterburn. These remained ideas but more concrete schemes related to the primary zone in the heart of the combustor.

BLC (Boundary Layer Control) Swirl Vanes

One system [8] used a fluidically modulated swirler to modify the flow field in the primary zone of a cylindrical combustor (styled like one from a Lycoming helicopter

control flow. The need for injected flow can be avoided by controlling the VA with a fluidic flow diverter forming what is sometimes called a "coanda-switched vortex valve". In a 3-month project an attempt was made to use the switched-vortex valve concept to control the airflow into the primary zone(s) of an annular combustor. These combustors have "can"-like zones downstream of each injector so the cold flow test scheme used an essentially rectangular cross-section "sector" representing one such zone. A novel "multi-switched vortex valve" having 14 flow diverters ranged round a single vortex chamber was used to control the airflow to the primary zone. The objective was to get the potential flow turndown (five-fold) of established coanda-switched vortex valves but within a greatly restricted diameter. Unfortunately geometry and time-deadlines defeated the promising but slow trend of fluid dynamics. A flow turndown of 1.7 was achieved but no chance for development or optimisation had been available. Hence the (justifiable) conclusion that here was no "quick fix". However, the concept still lives in a form using an axisymmetric switched vortex valve as described by Brundish et al [12]

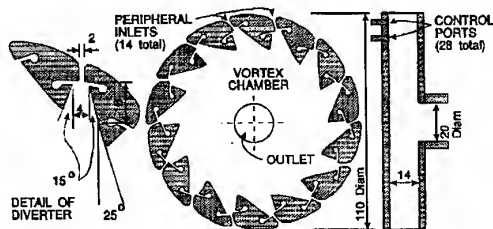


Fig 3: 14-fluidic-diverter-switched vortex valve

4. COANDA EJECTOR

Mixing power is normally provided in a gas turbine from the compressor, with up to four percent of the compressor delivery pressure being used to provide adequate mixing [13]. Thermodynamic calculations show that this is a loss of two percent in the specific thrust of a gas turbine [14]. Even if the pressure loss were reduced to two percent to allow for wall cooling a one percent gain in thrust could still be achieved

As a rather long-term concept it was thought that if pressurised liquid fuel heated by hot gases from the combustor could be used to provide a high pressure source this could be then used to replace the mixing power provided by the compressor. As a step in this direction a novel gas turbine combustion chamber was therefore developed incorporating a system of ejectors initially using high pressure gaseous fuel as the primary fluid supply, to replace the mixing power provided by the compressor. The use of gaseous fuel-driven ejectors would be feasible for ground based gas turbines, but obviously would be inappropriate for liquid fuels.

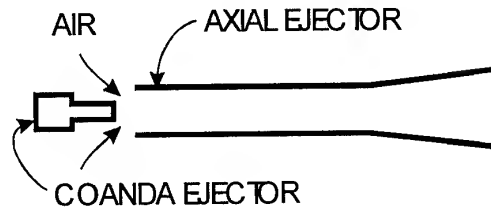


Fig 4: Diagram of a Hybrid Burner

The hybrid burner developed consisted of two ejectors in series forming a 2-stage unit, as shown in Fig 4. The first-stage ejector was a Coanda-type (parietal wall-jet type) which provided most of the mixing, entraining a volumetric ratio of 15.6:1 air to propane fuel. This was followed by an axial ejector that entrained the remaining air into the combustor.

The Coanda ejector was used for the first stage because its driving nozzle area could easily be adjusted (being an annular slot) Coanda ejectors also incorporate a shorter mixing length than axial types. Coanda ejectors can also operate optimally over a wide range of primary pressures, unlike axial ejectors which have a more restricted range for primary fluid pressure [15].

With this system it was possible to obtain volumetric entrainment ratios up to 37:1, with no pressure loss (or gain) across the complete system. This implies no mixing pressure loss or potentially a very slight pressure gain since the necessary volumetric stoichiometric air flow ratio (to propane) is 25.8. Pressure gain would accrue if the outflow from the combustor were slightly restricted to reduce the entrainment from the no-gain figure of 37 to the stoichiometric ratio.

This configuration was run under both fuel lean and fuel rich conditions, with exit emission measurements being taken under both conditions. Detailed inflame measurements were also taken for the burner operating under fuel rich conditions [16]. All measurements were at ambient temperature and pressure.

The development of this burner involved considerable iteration of design, construction, CFD modelling and redesign etc. Two basic Coanda ejectors were built with reference to design methods given [14, 19]. Notably amongst these methods, Fricker [15] treats the Coanda nozzle as an equivalent axial nozzle, ESDU, [18] uses mass and momentum balances across a control volume, Ameri [18] develops models from empirical data, and CFD implemented by the Fluent code [14] produces simulation results useful for design

It was found that the "best" (but not good quantitatively) approach was that of ESDU (control volume method) as it consistently underestimated the actual entrainment of the device. Once the main dimensions were obtained then the Coanda ejector could be modelled by CFD to optimise the design.

A summary of the actual and predicted results in terms of zero-pressure-drop entrainment ratios are given in the table.

Further work on this topic would be justified in view of the promising results from the project.

	Coanda 1	Coanda 2
Experiment	4.1	15.6
Fricker	16.3	22.9
Ameri	13.14	18.13
Control Volume	2.25	10.41
Fluent (CFD)	5.5	19

Volumetric Entrainment Ratios

5. THE VORTEX AMPLIFIER (VA)

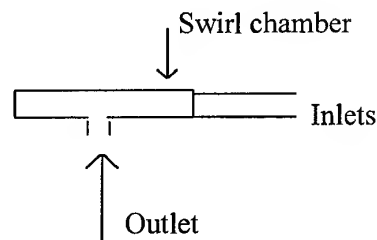
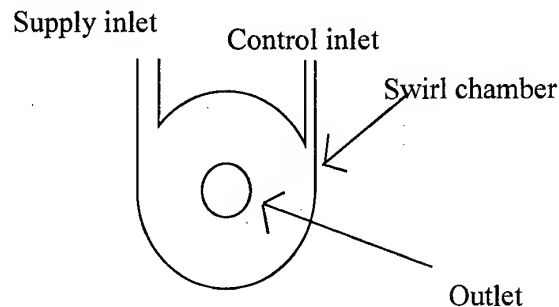
The use of the VA has been previously reported [5] and potentially has attractive flow control properties. Its usual form consists of a vortex or "swirl chamber" having radial and tangential inlets, and an axial outlet. Radial flow in the absence of control flow passes through essentially unimpeded. Control flow however, causes a strong vortex which may eventually stop the radial flow. The penalty for this control mode is that the control flow must come from a higher pressure than the main (radial) flow.

The TuVA

The severity of this requirement can be greatly diminished by using the vortex principle in the so called "Turn-up Vortex Amplifier" (TuVA). Its mode of operation is complementary to that of the usual VA in which control flow turns down the main flow. As shown in Fig 5 the TuVA has a tangential supply inlet and an opposed tangential control inlet.

Supply flow enters the chamber setting up a strong vortex flow field. At this condition the pressure drop resulting from the centrifugal force (vortex motion) is greater than that caused by the two orifices (supply and outlet). Adding control flow decreases the amount of swirl and hence the overall flow resistance of the device thereby tending to turn up the supply flow.

Fig 5: 'Basic' TuVA



There are many designs of TuVA to suit different purposes. Designs and applications related to high flow gain tend to have small control nozzles and a very strong distinction between "supply" and "control" flows. Other designs, for such applications as level control in separators, [20] make virtually no distinction between control and supply. Their controlling influence is entirely concerned with the outflow. In an extreme form of design (the symmetrical TuVA) the two inlets are identical. The characteristics show the degree to which the "higher control pressure" penalty can be alleviated. A convenient test on a TuVA is to maintain the supply flow constant while varying the control flow and plotting the supply and control pressures (relative to the outlet). The results can be nondimensionalised in terms of the supply flow (for flows) and the value of the supply pressure in the vortex state (i.e. with $q_c = 0$). Typically, both pressures drop to a minimum as the control flow increases. Importantly in a symmetrical TuVA the control pressure is less than the supply pressure for nearly all of the control range. Depending on symmetry, and some other factors, the control pressure and supply pressure are virtually identical at the zero-swirl maximum flow state.

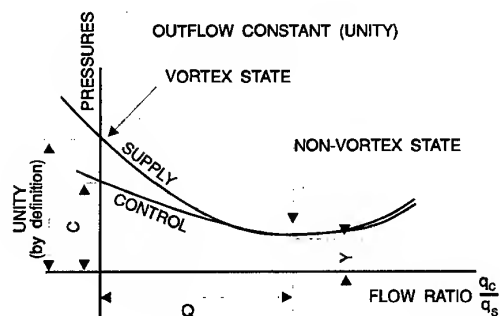


Fig 6: Schematic Non Dimensional Characteristics of a Turn-up Vortex Amplifier (Symmetric type)

The performance can be quantified in terms of non-dimensional parameters :

C the ratio of control/supply pressure at $q_c = 0$

Q the ratio of control/supply flow at the zero-swirl point

Y supply pressure at the zero swirl point/supply pressure at $q_c = 0$

In the extreme case of the symmetrical TuVA values of these can be

$$C = 0.98, \quad Q = 1.0 \quad \text{and} \quad Y = 0.07$$

These imply a strong form of flow control (which can be expressed as a "flow turn-up ratio" of circa 7.5) with almost zero excess control pressure.

In adapting this device for primary zone airflow control, air enters through the supply and the fuel is used for control purposes (this is necessary as no air flow of higher pressure than the compressor outlet is available). Given that the device effectively replaces the injector, it also provides fuel air mixing, further aiding combustion stability. At high power, fuel flow is high, and hence the degree of swirl low. Low power operation requires little fuel and so the degree of swirl is high resulting in a small effective area for the injector. Gas turbine combustors can be simply considered to be a set of parallel holes, so as the area of one hole is reduced (via the TuVA) air is diverted from the primary zone to other areas of the combustion chamber.

Addition of fuel droplets to the system was thought to present a flow problem i.e. when the droplets hit the wall, how do they leave the system? This was hopefully solved by designing a series of TuVA devices (fig 5, 7) with dished top and centre sections but maintaining the same outer dimensions as the basic TuVA. Droplets impinging on the walls would flow down the 'cone' and hence into the exit as in the ubiquitous cyclone separator.

Fig 7a: 'Cyclone' TuVA

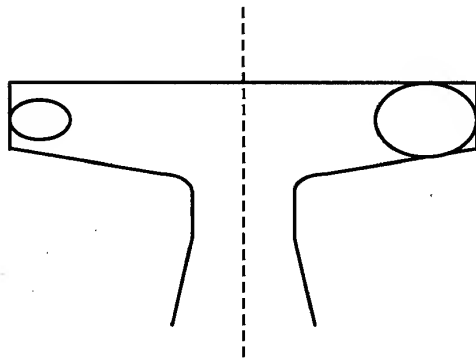
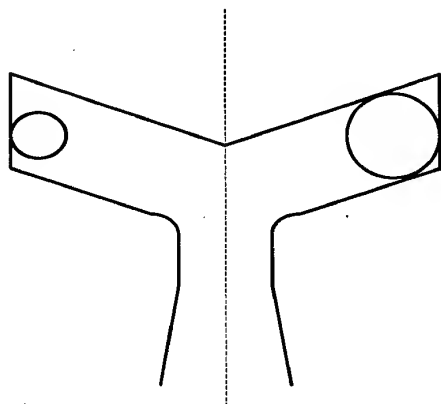


Fig 7b: 'Dished' TuVA



6. DEVICE SELECTION

Device selection criteria included the theoretical ability for the fuel drops to leave the system after contacting the walls and, most importantly, that the device effective area was sufficiently large for the purpose; whilst the physical size was suitable for use as a gas turbine injector.

Initial tests were completed using air as both the supply and control flows. Air flowrate was obtained by passing the supply and control airflows through rotameters, with pressure tapings fitted at the device inlets and compared to atmospheric pressure via either a 'U tube' or inclined manometer depending upon the pressure drop. Later tests utilised the Furness Controls FC016 digital manometer, for improved accuracy at the zero swirl case (minimum supply flow pressure drop). Supply flow for the tests was significantly lower than for the actual turbine injector, and concerns were expressed regarding Reynolds Number effects.

The test models were constructed of perspex and in a modular form of top, middle and outlet nozzle (top 0° and 20°; middle 0°, 5° and 20°; outlet nozzle small and large: thus the dished device is referred to as 20 20 L in figure 7 and the cyclone unit, small nozzle, is defined as 0 5 S).

Effective area calculations were carried out using equation 3, itself derived from 1 and 2.

$$\Delta P = \frac{1}{2} \rho v^2 \quad 1$$

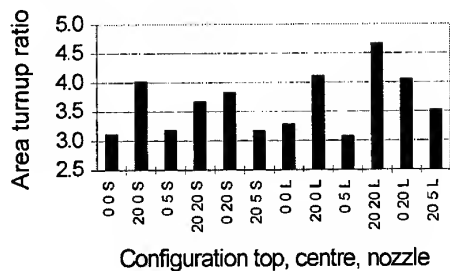
$$\dot{m} = \rho v A \quad 2$$

$$A_{eff} = \frac{\dot{m}_s}{\sqrt{2 \rho \Delta P_s}} \quad 3$$

For the purpose of the gas turbine the control pressure is largely irrelevant (liquid can be pumped to high pressures for little power cost) and so the effective area of the device is found with respect to the supply flow - i.e. the area is what the device presents to the air flow within the combustion chamber.

The device characteristics were all found to match the required performance criteria in terms of area turn-up however it was clear that the small nozzle gave insufficient effective area at the zero swirl condition (approximately 0.6 compared to 1.0 for the theoretical high power condition) and was thus discarded. Theoretical pressure loss increases corresponding to the idle case are approximately 75% higher than those at the high power condition (device designed to have minimal flow resistance at this operating point) and are low enough not to cause problems with the compressor.

Fig 8: Effects of device configuration of turn-up performance.



Further examination of the results showed the conventional VA to be less effective (and problems were anticipated with liquid hold up). This criterion also eliminated the other case to use the flat centre section. Previous work [8] has shown the 'cyclone' style VA to be less effective, although it was not seen in the current work. Of the remaining devices the dished unit gave the best performance (fig 8) and was thus selected for further study. The improved performance of the dished device was thought to result from the ease in which the vortex was able to move down the slope (to be confirmed by CFD work), and the fact that the actual chamber diameter is slightly bigger than the conventional unit (by 6% - $1/\cos 20^\circ$), also possibly explaining the lack of lost performance in the 'cyclone' TuVA.

7. EXPERIMENTAL / THEORETICAL

Comparing the results obtained from the global combustion model [5] with those obtained by experimental techniques (figs 9 and 10) gave a good correlation of effective area trends.

Fig 9: Theoretical Device Effective area

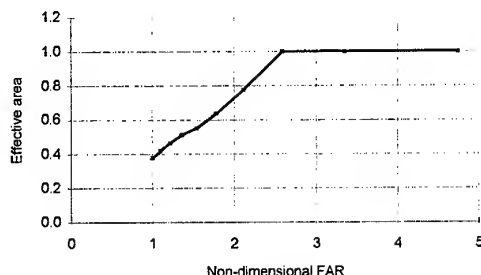
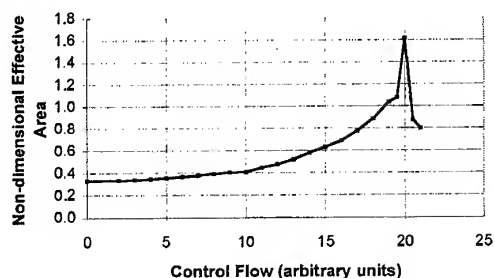


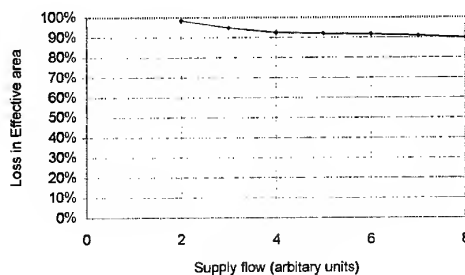
Fig 10: Experimental effective area (20 20 L) - non dimensional wrt full power



As can be seen although the trends are similar the actual control flow/FAR values are different. This is the result of insufficient momentum being delivered into the control stream (the control port was too large).

Current device testing was carried out at atmospheric conditions, thus an effect caused by an increased Reynolds Number was expected (actual operating conditions being considerably hotter and at higher pressure). To confirm this the full swirl case was examined. Reynolds Number was calculated at the outlet nozzle throat and the supply flow adjusted accordingly to vary Re, with the device effective area being calculated at each point.

Figure 11: Reynolds Number effect



Examining the data shows that approximately 5% of the full swirl effective area will be lost, and it can be assumed that a similar loss will occur at the zero swirl state.

The experimental results also showed that the effective area at zero swirl was significantly larger than that required by the theoretical model. When in operation within the gas turbine engine the zero swirl point would never be approached for stability reasons. This larger than desired effective area thus allows scope to make the device smaller (and more than compensates for the Reynolds effect), if required and also provides 'spare' performance where zero swirl (and thus full device operating range) is not permitted.

Area turn up criteria were exceeded by the initial tests, modelling shows that a value of around 2.6:1 is necessary whereas the experimental value was found to

be around 4.5:1. Again this higher than required value allows a certain leeway with the point of minimal swirl necessary for combustion.

7. FUTURE WORK (TuVA)

The improvement of the initial design is the subject of further research at the University of Sheffield and is concerned with the matching of the device operating curve to that of an engine. For this to be accomplished another degree of control freedom may be required.

The work reported thus far only deals with the addition of a gaseous fuel (e.g. natural gas) and will require testing and modifications to allow the use of a liquid fuel (e.g. kerosine - although water and air will be used experimentally).

CFD modelling of the various TuVA devices is required to explain the improved performance of the dish unit, and to examine the flowfield found at the device exit.

8. CONCLUSIONS

A range of fluidic techniques applied to gas turbine combustors has been described. In no case is there an easy route to success but several promising schemes have emerged.

The work leading to the successful gas fuelled zero-pressure-loss hybrid ejector (Coanda plus axial) burners has shown that this is a line worth further development. A notable feature was the volumetric air/fuel entrainment ratio of circa 30. Useful generic design techniques have been developed and validated. The "control-volume" ejector design method followed by optimisation using CFD was a useful technique.

In the VAD schemes a great deal depends on the criteria that must be met. For example, the fuel-controlled TuVA VAD project is attractive because even a relatively small flow gain (turn-up ratio of circa 2.5) by fluidic standards would give a useful result. In principle the gain should be easily achievable but the frontier of knowledge here is the implementation using fuel as the control medium, and in retaining a compact unit analogous to an existing injector.

The switched vortex valve offers another method of potentially strong VAD controllable by extracted flow. The current status of this project is at the point of testing realistically sized cold flow devices to see if originally adequate performance has been sacrificed too much in "shoe-horning" the device to fit into a realistic combustor.

The near future should see progress in both of these vortex-controlled VAD schemes. Recent results for the TuVA yielding an effective area modulation by a factor of 4.5 using cold gaseous flows is particularly encouraging. This, together with the very low control pressure necessary should give scope to accommodate the unknown demands of control by liquid fuel.

9. ACKNOWLEDGEMENTS

The authors wish to thank Delavan Inc. for their aid in this project as well as C.W. Wilson and K.D. Brundish of the Combustion and Emissions Group, DERA Pyestock for their technical assistance.

10. REFERENCES

1. Brundish, K.D., Foster, T.J., Gray, C.R., Seoud, R.E., and Wilson, C.W., 1997, 'The Use of Axially Fuel Staged Combustion in Gas Turbine Combustors', Fourth International Conference on Technologies and Combustion for a Clean Environment (Lisbon, Portugal).
2. Lefebvre A.H., 1983, 'Gas Turbine Combustion', Taylor and Francis
3. Lefebvre A.H., 1997, Lectures given at the Gas Turbine Combustion Course, Cranfield University
4. Mellor A.M. (ed), 1990, 'Design of Modern Turbine Combustors', Academic Press
5. Woolhouse R.J., Young K.J., Tippetts J.R., Beck S.B.M., 1998, 'Mixture Ratio Control For the Next Generation of Gas Turbines', Proceedings of the IChemE Research Event, ISBN 0-85295-400-X
6. Dodds W.J., 1987, 'A Variable Geometry Combustor for Broadened Properties of Fuels', AIAA-87-1832
7. Swithenbank J., 1970, Presented at the USAF contractors meeting, Department of Chemical Engineering and Fuel Technology, University of Sheffield
8. Tippetts J.R., 1975, 'Experiments on Aerodynamically Modulated Combustors', Departmental Report, HIC.236. Department of Chemical Engineering and Fuel Technology, University of Sheffield
9. Gupta A.K., Tippetts J.R., Swithenbank J., 1975, 'Modulated Swirl Combustor', proc 2nd European Combustion Symp. The Combustion Institute (European Section)
10. Fletcher R.S., Adkins R.C., 1974, 'The Variable Geometry Combustor', Report ARC 35779, Comb 161, Aeronautical Research Council, Dec 1974
11. Tippetts J.R., 1997, 'Multi-Switched Vortex Valves', Proc Symp FLUCOME 97, (Ed. T Kobayashi) Vol 2, Soc Instrument and Control Engineers of Japan, Tokyo, pp 523-528
12. Brundish K.D., Nash S., Wilson C.W., Tippetts J.R. and Woolhouse R.J., 1998, 'The Initial Design of a Fluidic Variable Geometry Fuel Injector for Gas Turbine Combustion Systems', Paper AIAA-98-3908, Proc Joint propulsion Conf and Exhibit AIAA Reston VA20191 (joint organiser with ASME,SAE and ASEE) July 1998
13. Lefebvre A.H., 1993, 'Gas Turbine Combustion', Hemisphere Publishing

14. Whiteman M., Swithenbank J., 1995, 'Towards Zero Pressure Combustors for Ramjets and Gas Turbines', XII ISABE,
15. Fricker N., R.H. O'Brien, K., Sutton J.A., 1986, 'Coanda Ejectors Fact and Fallacy', International Gas Research Conference: 989-1003
16. Whiteman M., Swithenbank S., 1996, 'Increasing the Efficiency of a Gas Turbine Engine by Reducing the Combustion Pressure Drop', Proceedings of the IChemE Jubilee Research Event, ISBN 0-85295-389-5
17. Whiteman M., 1997, 'Reducing the Pressure Loss in a Gas Turbine Combustor'. PhD thesis, University of Sheffield
18. ESDU, 1984. 'Ejectors and Jet Pumps- Design and Performance for Compressible Air Flow' Data Item No. 84029, ESDU International Ltd
19. Ameri M., Dybbs A., 1993, 'Theoretical Modelling of Coanda Ejectors', FED-Vol. 163, Fluid Machinery-1993, ASME
20. Priestman G H, Tippetts J R and Dick D R: The Application of Power Fluidics to Level Control in Multiphase Separators, Proc Symp "Multiphase Technology" ISBN 1 86058 139 0, BHR Group Cranfield, June 1998, pp 119-129

PAPER No. 33
Young, Woolhouse, Beck, Tippetts & Whiteman
(presenter: R.J. Woolhouse)

Question 1: T. Rosfjord, UTRC, U.S.

You discussed use of the TuVA with liquid fuel. Was the experimental effective area data obtained with a liquid-phase control flow? Is there an experience base for two-phase fluidic devices like the TuVA?

Answer:

These results are based on air as the control flow, and no liquid flow was used in these experiments. Liquid phase control is a central feature of the Phase 2 work now underway. Prior generic work on multiphase flow in vortex valves showed that very strong modulation of gas by a liquid was possible, and gave confidence to promote the current project. Some of this work is described in "effects of Multiphase Flow in Fluidic Devices," by Y.R. Goh, G.H. Priestman and J.R. Tippetts, Proc. *FLUCOME Conference*, ONERA/CERT, Toulouse, September 1994.

Question 2: G.J. Sturgess, ISSI, U.S.

A comment: A very similar device has been rig and engine tested; see U.S. Patents - Thomas DuBell and others, 1969, 1970, 1971 and thereabouts. It was found with this device that as fuel flow was increased, the swirl decreased, as the authors have noted. This created a flame-holding problem, and was solved by adding a swirler package around the device to maintain spray angle and flame stability. However, in order to maintain the overall equivalence ratio range the air entering the device had to be reduced. Air modulation was achieved, and the direction (increase or decrease with increasing fuel flow) of the modulation depended on how the fuel was introduced into the device; if fuel was not introduced carefully fuel spillage from the air inlet could result. An additional problem was that, being fuel-rich, in the high temperature conditions of engine operation, a stick of coke grew downstream from the open base of the device. This latter problem was solved by use of a dished base-plate (similar to that described by the authors), and an air-wash provision on the baseplate. Unfortunately, under sustained engine operation carbon formed in the swirl chamber, and built up to eventually block the air swirl generator within the device. Catastrophic engine failures then followed extremely rapidly. This thermal decomposition is a fundamental danger of mixed-phase fuel/air systems under high temperature operating conditions. Apart from these fatal flaws, a highly successful combustion device was produced, having exceptionally good lean blowout and ignition characteristics, and good combustion efficiency over a wide range of operating conditions. It gave low exhaust smoke and a low luminosity flame. In addition, through the use of precision castings, it was an inexpensive device. A restricting factor on how the fuel can be introduced into the device is the connection of the combustor-mounted device to the engine fuel system, with accommodation of working tolerances and thermal growth allowances. There is no doubt that fuel in the DuBell device was not introduced optimally from a modulation point of view. However, it did satisfy the engine requirements of that time, which were somewhat limited perhaps in comparison to today's requirements.

Hopefully, these experiences will be helpful in identifying some of the "gates" that a device such as you are developing might have to go through for successful engine application.

Answer:

We were not aware of the DuBell patents, or the associated work, so we will certainly take note of this information. It is disappointing that the scheme came to nothing, but the experience may actually forewarn and help us in our efforts. Our paper gives some background material and describes only the early stages of new R&D based on the TuVA. Regarding the additional swirlers, combustor design trends over the last 30 years have taken injector airflows from around 10 % to 30 - 40 % of the combustion air; thus, a lesser change in the effective area is required to suitably alter the flowfield. The unoptimized device has a turn-up of around 4.5:1 (versus a predicted requirement of approximately 2.6:1). Thus, swirl will exist at high power, making the additional swirler unnecessary. In fact, the present device is just the precursor to a much more sophisticated embodiment of the idea that (since May of 1998) is being researched as the second phase of the project. This "Phase 2" design includes extra design freedom and controllability which should give scope to avoid the problems which afflicted the DuBell device. We had our own reasons for this extra degree of controllability; Dr. Sturgess' comments add extra weight to this necessity. The potential problems of fuel spillage in the event of compressor surge is noted. In our view, the risk is not thought to be greater than for other, say LPP, designs.

Possibilities of sooting exist, and the authors agree with this point, but associated with the increase in injector airflow, the burner AFR over 30 years has increased from around 3 - 4 to over 12, making this less likely. CFD is also now available allowing prediction of stagnation and particulate impact zones, and therefore flows can be altered to reduce this.

Finally, the change in gas turbine cycles require new (potentially risky) solutions - i.e. fluidics, LPP, etc., - which would have been discarded 30 years ago as an unnecessary complication, but may now be required to meet current and future legislation.

FUEL/AIR PREPARATION IN THE DESIGN OF LOW EMISSIONS GAS TURBINE COMBUSTION SYSTEMS

Mohan K. Razdan
Rolls-Royce Allison
P.O. Box 420, SC T-14
Indianapolis, Indiana 46206, U.S.A.

ABSTRACT

This paper discusses issues related to practical fuel injection methods, and the key factors affecting the fuel/air mixing process in low emission gas turbine combustors. The mixing of fuel and air has to be accomplished in the shortest possible residence time both for current retrofit applications as well as for future high performance engines that operate at substantially higher inlet temperatures and pressures, where flashback and autoignition are serious concerns. The choice of a fuel injection method is strongly influenced not only by the selected geometry and size of a fuel/air preparation module but also by its interaction with the module air flow. Combining pressure swirl and prefilming airblast atomization concepts in a single hybrid design presents an attractive approach for achieving satisfactory atomization over a wide operating range of the combustor. Internally mixed atomization concepts show beneficial effects on fuel atomization. A fuel concentration profile tailored to the local velocity profile at the mixing module exit minimizes the flashback propensity. Autoignition concerns will limit the application of fully prevaporized lean premixed low emission approach to operating pressures up to 40 to 50 atmospheres.

1. INTRODUCTION

The low emissions gas turbine combustor design approaches [1], such as lean premixed prevaporized, lean direct injection, etc., need detailed characterization of the fuel/air mixing process. Fuel spray, evaporation, and the fuel/air ratio (FAR) distributions are the key characteristics in a fuel/air mixer that impact primary design concerns including autoignition, flashback, flame stability, and combustion generated instabilities.

The fuel/air mixer is truly the key component in the low emissions combustor. One of the important requirements for the mixer is to have fine atomization that results in small fuel droplets and good dispersion, both of which are essential in the formation of a uniform fuel vapor-air mixture in a short distance. The finer the drop size, the closer the combustion of liquid fuel approaches the combustion of premixed gaseous fuel. The effect can even be more significant for a lean fuel/air mixture. When the overall equivalence ratio is near stoichiometric, the difference between oxides of nitrogen (NO_x) produced by sprays having small droplets (20-30 μm) or large droplets (>50 μm) is small due to the fact that the flame temperature is nearly the same for both the premixed fuel-vapor or droplet combustion. But for leaner mixtures, if the spray is very fine, a significant portion of the liquid fuel will burn after the liquid has been vaporized and mixed with

air. On the other hand, if the spray is coarse, the evaporation is slow, thus a major portion of the liquid fuel will burn in droplet combustion or fuel rich pockets where the flame temperature is much higher than the flame temperature of the lean gaseous mixture. That results in a higher NO_x level for coarse spray. Droplet size distribution and dispersion that directly impact the FAR distribution will also affect NO_x emissions. While good spray dispersion is desirable for achieving FAR uniformity, it is limited by the requirement that the impingement, mainly of large fuel droplets, be minimized on the pre-mixer walls to minimize the potential for carbon formation. More non-uniform spray with more large droplets will also lead to a higher NO_x level. The design of a liquid fuel injector should be such that it will produce a fine drop size with a minimum of large droplets, and a droplet distribution that when combined with air flow field, will produce a uniform fuel vapor-air ratio distribution across the combustor.

The extent of fuel evaporation achieved before the combustion zone not only impacts NO_x production but also is essential in the combustor design. Experimental results [2] have shown that for lean fuel/air mixtures, lower evaporation fraction leads to higher NO_x with a nearly linear relationship. The knowledge of spray evaporation history is also critical in estimating autoignition time when designing a fuel/air mixer for a low emissions application. In this paper, we first discuss practical fuel injection methods and the key factors affecting the fuel/air mixing process in low emission combustors. The aerodynamic influences on flashback characteristics are discussed next. Finally, the key factors to consider in assessing the autoignition potential in the design of the fuel/air mixers are reviewed in the paper.

2. FUEL INJECTION METHODS

One of the key differences between a conventional gas turbine combustor and a low emissions combustor is the fraction of air that enters through the combustor dome. Typically, for a conventional combustor, only a quarter to a third of the total combustion liner air flow enters through the combustor dome. The aerodynamics of the primary combustion zone are not solely determined by the dome air flow. However, for a low emissions combustor, 60 to 80% of the combustor air flow may enter through the dome and the aerodynamics of the primary combustion zone are mostly determined by the dome air. A major portion of the dome air of a low emissions combustor will typically enter through fuel/air mixers or modules while a small fraction may be used for dome cooling. The air entering the module has several key functions: 1) it

helps fuel spray atomization and evaporation inside the module; 2) it helps achieve proper fuel dispersion for a given module geometry; 3) it provides a heat source for fuel spray evaporation; 4) it maintains acceptable module exit velocity and boundary layer thickness for a given module to avoid flame flashback; and 5) it provides proper air flow velocity distribution and swirl angle at the module exit to stabilize combustion and to control the position and size of the combustion zone.

For low emissions combustors, the choice of a fuel injection method is strongly influenced not only by the selected geometry and size of the fuel/air mixing module but also by its interaction with the module air flow. There are three basic and practical types of liquid fuel injection methods that can be considered for fuel/air mixing module designs: pressure swirl, plain-jet and prefilming airblast atomization. In a simple so-called simplex pressure-swirl atomizer, a swirling motion is imparted to the fuel so that it spreads out in the form of a hollow cone as soon as it leaves the fuel injector orifice. Typically, however, the fuel distribution in a pressure-swirl atomizer is centrally peaked. As pressure and temperature are increased, the spray becomes finer and the fuel/air distribution becomes more centrally peaked. Finer spray, however, reduces spray dispersion which impacts FAR uniformity.

In a plain-jet airblast atomization concept, the fuel is injected through small orifices strategically located within the mixing module to achieve maximum contact with atomizing air. A rapid evaporation rate of fuel droplets can be achieved by arranging for high relative velocity between the injected fuel and combustion air. Key parameters affecting the performance of a plain-jet atomizer are fuel injection location, swirling air configuration and fuel injection orifice size and inclination. Spatial fuel distribution in a module can be more accurately controlled than in conventional fuel injection methods. However, design of fuel delivery system with appropriate thermal shielding in the plain-jet atomizers can be a challenging task.

Typical prefilming airblast atomizers have limitations for their use in a low emissions combustor application due to their inability to spread fuel radially outward under high combustor pressures because of low fuel injection pressure. In addition, the performance of the airblast atomizer rapidly deteriorates as the air pressure drop across the atomizer is reduced. On the other hand, conventional pressure swirl atomization concepts have demonstrated the capability to produce fine sprays under high fuel injection pressure. Thus, combining both atomization concepts in a single hybrid design presents an attractive approach for achieving satisfactory atomization over the entire combustor operating range.

2.1 Hybrid Fuel Injection

Hybrid atomization can generally be achieved by either utilizing airblast forces in a pressure swirl atomizer or using a high fuel injection pressure in an airblast atomizer. The performance of an airblast atomizer with high fuel injection

pressure typically follows an almost flat mean fuel drop size profile over a wide range of fuel flow rates. Such a profile is desirable in many applications. High fuel injection pressure in prefilming airblast atomizer is beneficial in producing a more uniform liquid film even under low fuel flow rates, or for short prefilming devices that are needed to minimize fuel deposition in the atomizer. Moreover, for a low emissions combustor, high initial velocity of the fuel spray resulting from high fuel injection pressure, is an important parameter in achieving enhanced fuel/air mixing within a short distance, in particular when cross-stream penetration is used in the design. Although several studies have been conducted on the atomization process [3-6], there are few studies that actually address the combined effect of air momentum and fuel pressure utilized in the hybrid atomizer.

Several key factors affect the droplet size, characterized by Sauter Mean Diameter (SMD), in hybrid atomization. These include liquid exit velocity, air/liquid relative velocity, air/liquid ratio (ALR), and liquid film thickness. It is, however, often difficult to evaluate the effects of these parameters separately because changing one parameter usually affects the other parameters involved in the atomization process. For instance, increasing fuel injection pressure at a fixed value of air pressure drop results in simultaneous changes in the aforementioned parameters, as well as the spray angle. In order to better understand the effects of each variable with less interference from the effects of other parameters, an investigation of a research atomizer, illustrated in Fig. 1, has been conducted [7]. In this design, the fuel is injected through a number of tangential ports onto a prefilmer. The exit lip of the filming device is located at some distance upstream of the exit plane for the internally mixed atomizer (Fig. 1) or at the exit plane for the externally mixed atomizer [8].

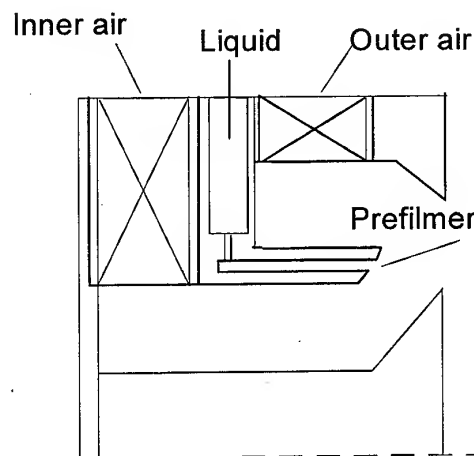


Figure 1. Internal mixing hybrid atomizer

The air swirling direction could be reversed in the design by simply installing the swirler in a backward position within the atomizer assembly. To actually separate the effects of ALR on SMD, the effective flow areas of the inner and outer air passages were simultaneously reduced with the exit section component to achieve the same reduction in the corresponding exit area. Effective areas were reduced from 100% to 62% and 38%. By this means, both air pressure drop and liquid injection pressure could be kept constant while changing the air flow rate and, consequently, the ALR. A Malvern particle analyzer was employed to measure drop size distribution.

The results obtained under constant air pressure drop and liquid injection pressure, but with different air flow areas, are plotted in Fig. 2. The results demonstrate the effect of increasing the ALR on the spray SMD at an air pressure drop of 4.0% for two levels of liquid injection pressure. The results are presented for two atomizer configurations. In one configuration, both air streams were co-rotating with the liquid, and in the other, inner air was co-rotating and outer air was counter-rotating with respect to liquid rotation. The superior performance of the atomizer when employing a counter rotating outer air passage over the one using both air streams co-rotating with the liquid is evident in the figure, in particular under higher air/liquid ratios. For example, nearly 50% reduction in SMD at ALR of 3.5 could be achieved by reversing the outer air swirler direction.

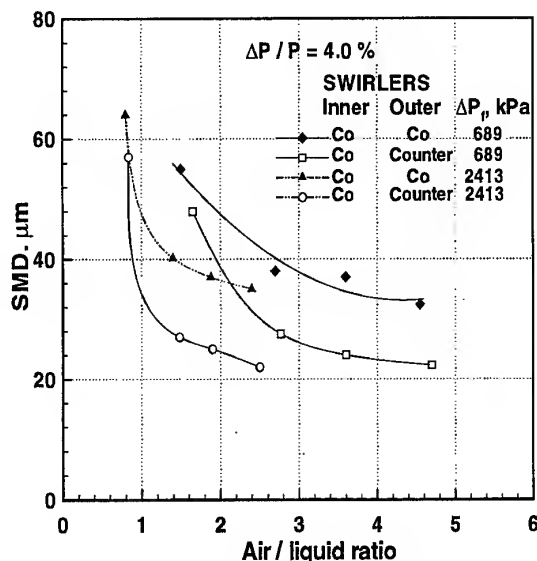


Figure 2. Effect of air/liquid ratio and fuel pressure drop on SMD

Figure 3 shows the measured SMD values at three levels of air/liquid ratio at a fixed air pressure drop of 7.9%. These results represent the true effect of ALR on atomization. Shown also in the figure is the effect of changing the air/liquid ratio through the conventional method of changing the liquid flow rate. The results show a significantly stronger

effect of air/liquid ratio on SMD when the effects of liquid velocity and relative velocity are separated from those of the ALR. In fact, while increasing the air/liquid ratio by increasing the swirler flow area (solid curve in Fig. 3) enhances the atomization, the same increase in the air/liquid ratio by reducing the liquid flow rate (dashed curve in Fig. 3) may have little effect on SMD or even result in an increase in

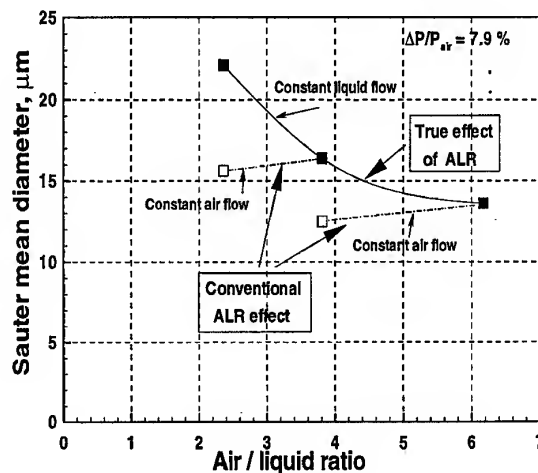


Figure 3. True effect of air/liquid ratio on SMD

its value. Increase in the already high air/liquid ratios by a significant reduction in liquid pressure adversely affects the filming process, resulting in an increase in SMD.

The results obtained for the hybrid atomizer using the 100,

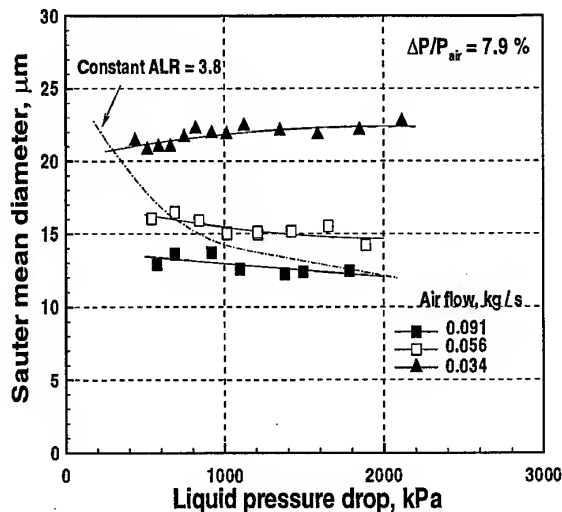


Figure 4. Variation of SMD with liquid pressure using different swirler flow area

62, and 38% swirler flow area configurations are presented in Fig. 4 in terms of SMD versus liquid injection pressure. Constant air/liquid ratio curve is also plotted in this figure. It can be seen that, at a constant air/liquid ratio, the finest sprays are produced by the largest swirler flow area (largest air flow rate) used in the tests. This indicates that a combination of higher air flow rate and liquid flow rate is more beneficial to the atomization than a combination of low flow rates having the same air/liquid ratio. The conclusion that may be drawn from these data is that using the air/liquid ratio parameter to characterize the performance of a hybrid atomizer is inadequate. Certainly, the actual roles played by the air flow rate, air passage height, liquid pressure, and liquid film thickness are all influential in the atomization process. In other words, in conventional correlations of airblast atomizers, a single value of SMD is calculated for a given ALR and air velocity levels, while the actual SMD value produced under the same two parameters may vary over a wide range based on the other aforementioned factors.

Figure 5 shows the variation of the spray specific area with air pressure drop for a constant liquid pressure drop of 1500 kPa. The specific surface area (SSA) of the spray is defined as the total surface area of the droplets per unit volume. According to this definition, the numerical value of the SSA parameter is simply the inverse of the SMD multiplied by 6. The SSA parameter is useful in assessing the parametric sensitivity of fine sprays. Changes in spray quality for fine sprays can be detected more easily by using SSA than from conventional SMD presentation. The results in Fig. 5 demonstrate a near straight line trend, with a continuous improvement in atomization quality as the air pressure drop increases. In typical airblast atomizers [5], the rate of increase in SSA with air pressure drop starts to decline once the air pressure drop exceeds a value of about 4.0 or 5.0%. This indicates that the atomizer can no longer fully utilize the kinetic energy available in the high velocity air. In other words, the results demonstrate the beneficial effects of using such an internally

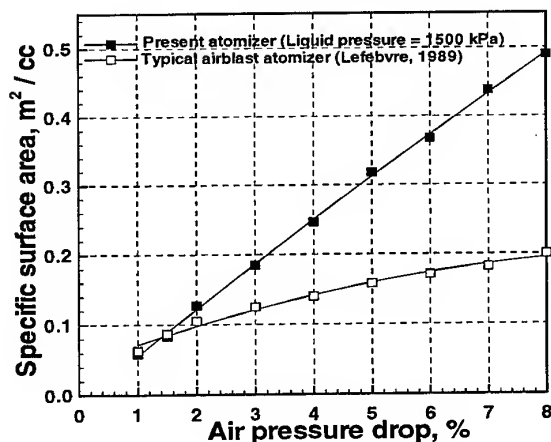


Figure 5. Variation of atomizer performance with air pressure drop

mixed atomization concept under much higher air pressure drop over conventional atomizers.

2.2 Spray Interaction

A method has been proposed in Ref. [9] to evaluate the effect of spray interaction when the two sprays at the prefilming device and pilot pressure nozzle of the hybrid atomizer exist simultaneously in the atomizer flow field. This method is intended to provide a useful tool for recommending modifications to the details of the fuel injection devices to further enhance the atomizer spray characteristics.

Figure 6 includes the data obtained for the pilot and main, each operating separately, in addition to the measured data of the combined spray of a fuel injector. To more clearly illustrate the effect of the spray interaction, the points representing the overall SMD based on the weight average of the two sprays assuming no interaction occurring, are also plotted in the figure. Comparison of the curve joining these points with the actual measured data of the combined spray indicates that for Fig. 6 the reduction in SMD due to the spray interaction increases with the increase in the pilot flow rate. Further increase in the pilot flow will eventually produce sprays with SMDs that are even less than those produced by either the pilot or the main devices operating separately. This supports the conclusion that the presence of the two sprays simultaneously causes the two sprays to help each other, with the main spray acting as a confinement to the pilot spray. The utilization of higher pilot liquid pressure to achieve the increase in the pilot flow rate helps to direct the air between the two sprays to participate more in the atomization of the main spray. The momentum transfer between the high velocity pilot spray and the surrounding air will help the air maintain a relatively high velocity in the vicinity of the main atomizer exit over a longer period resulting in an improved atomization.

Figure 7 illustrates the impact of using an air swirler around

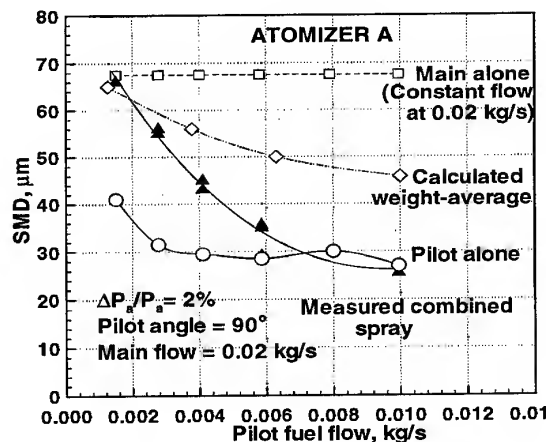


Figure 6. Reduction of SMD due to interaction of two sprays

the hybrid atomizer on the interaction between the pilot and main sprays. The figure contains the measurements obtained for the combined sprays and the calculated weight-average values. It can be seen that at the highest pilot flow rate used in this test, the measured SMD for the combined spray was $42.0\mu\text{m}$ compared to a value of $19.8\mu\text{m}$ based on the calculated average of the two sprays. In an effort to shed more light on the adverse effects of the spray interaction observed in testing of the swirler/atomizer geometry, the air flow characteristics were evaluated at various levels of pilot and main flow rates in a series of tests. Provisions were made to measure the air pressure drop across the air swirler in addition to the overall pressure drop across the combined configuration. It was observed that when both nozzles were turned on and air pressure drop was kept constant, the air flow rate through the configuration was significantly reduced. The direct impact on the atomization process was a less efficient utilization of the airblast effect. It was also noticed that the effective air pressure drop across the swirlers was about 30% of the total pressure drop of the entire configuration. Further reduction in the swirler air pressure drop at the critical region of atomization occurs as the flow rates of pilot or main devices increase. The result of all these factors is the increase in the SMD of the combined spray over the calculated weight-average value, implying a negative interaction effect on the spray characteristics. The significant impact of the interaction between multiple sprays on the fuel injector performance demonstrates that the practical utilization of a fuel/air mixer in a gas turbine combustor requires careful optimization.

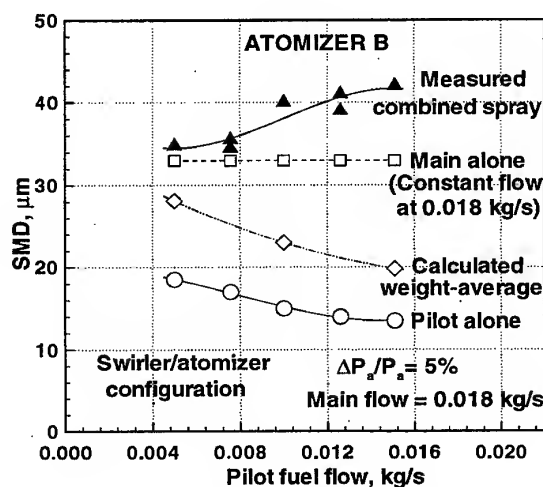


Figure 7. Effect of air swirler on spray interaction

2.3 Effect of Air Admission

The fuel injector depicted in Fig. 8 includes a liquid prefiling device and four air passages. The liquid is injected through four tangential ports, in an anti-clockwise direction onto the prefiling surface.

The results obtained for the baseline injector and two modified configurations at an air pressure drop of 4% are

plotted in Fig. 9 against the liquid injection pressure. It is observed that the SMD values measured for the baseline configuration are nearly constant over a wide range of liquid pressure. The results indicate that the performance of this atomizer is quite different from those commonly observed for either airblast or liquid pressure atomizers. The increase in liquid pressure, resulting in an increase in liquid flow rate, typically produces sprays with larger SMD for the airblast type due to the reduction in the effective air/liquid ratio under these conditions. On the other hand, significant improvement in the quality of the sprays produced by pressure atomizer is achieved due to the increase in liquid injection pressure. Thus, the results obtained for the baseline hybrid atomizer

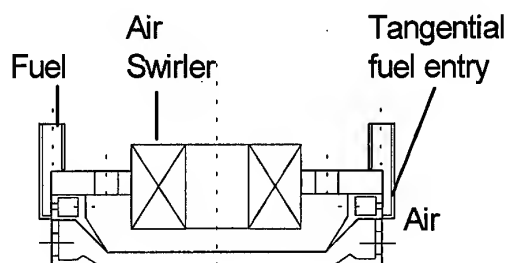


Figure 8. Fuel injector configuration with multiple air passages

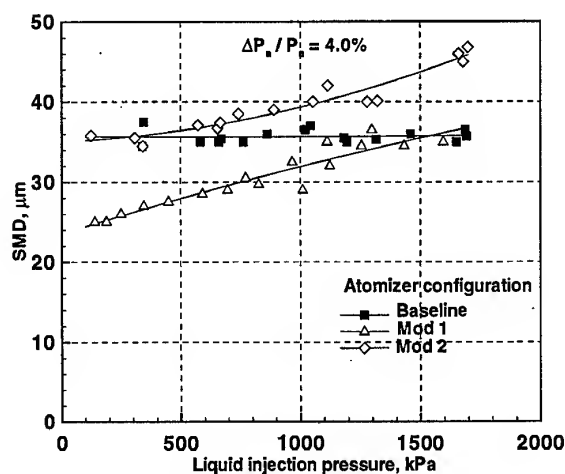


Figure 9. Effect of outer and inner air streams on atomization

indicate that the opposite effects of increasing the liquid pressure on the atomization process on both airblast and liquid pressure atomization almost cancel each other yielding the flat SMD profile observed in Fig. 9.

Figure 9 also shows that when the outer passage of the baseline atomizer is fully blocked (Mod1), an improvement in

the atomization characteristics is achieved over the baseline atomizer performance. It is noticed that the airblast function in the modified atomizer is dominating as the increase in liquid pressure and flow rate results in increase in SMD. The results imply that no real benefit is gained by using the outer air stream in the atomization process. In fact, the outer air in this particular design is hindering the atomization process as shown in the figure. On the other hand, the importance of designing the inner air passage properly is demonstrated in the results obtained for the modified atomizer (Mod 2). In this design, the air flowing through the passages on the inner side of the liquid prefilmer is reduced by 50%. This air is mainly used to support the filming of the liquid and the atomization of the liquid sheet as it exits the prefilmer. The results show that a reduction in the inner atomizing air has a negative effect on the spray quality produced by this atomizer.

Although the atomization results of the baseline atomizer and its modifications have shown less dependency on outer air configurations, the radial patternation measurements indicated that the outer air could strongly affect the radial spreading of liquid in the spray. Examples of the results are plotted in Fig. 10 for the baseline atomizer and Mod 1, where the outer air passage was fully blocked. The figure demonstrates that the utilization of the outer, non-swirling, air passage caused most of the liquid droplets to stay within a narrow region at and around the atomizer centerline. On the other hand, the elimination of the outer air in the Mod 1 atomizer resulted in a wider spread of liquid with less concentration near the atomizer centerline.

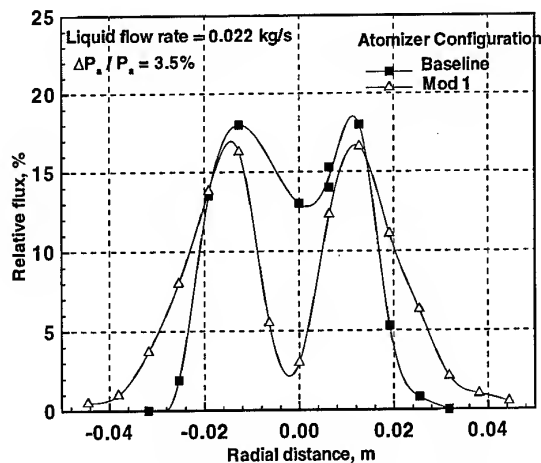


Figure 10. Effect of outer air stream on fuel distribution

3. FLASHBACK CHARACTERISTICS

The classical flashback theory of Lewis and von Elbe [10] is far from useful to predict the onset of flashback in practical combustors. Instead, flame propagation through reversed flow field, pre-ignition of the fuel/air mixtures in separated flow regions, and autoignition of the fuel/air stream can cause flashbacks. Careful design of the premixer flow path to avoid any flow separation or flow reversal is necessary to reduce the

risk for flashback. Even with a clean flow in the mixing tube, the classical flashback theory does not provide an adequate basis for defining regions of unstable operation in premixing/prevaporizing combustors [11]. Small changes in flow velocity can produce combustion instability which can lead to flashback at velocities very much higher than would be expected on the basis of classical flashback theory.

Figure 11 is a schematic representation of the basic lean premixing (LPM) module that was developed for the Rolls-Royce Allison Model 501-K gas turbine engine [12]. The combination of radial swirler plus nozzle is denoted as RSPN. Air enters into the premixer through a radial swirler positioned directly aft of a gaseous fuel distribution manifold. A fuel distribution tube, with a series of holes along its length, is positioned in the center of the passage formed between the swirler vanes. The nozzle throat functions to separate the premixing section from the combustor zone. As the premixed reactants exit the throat, they enter a

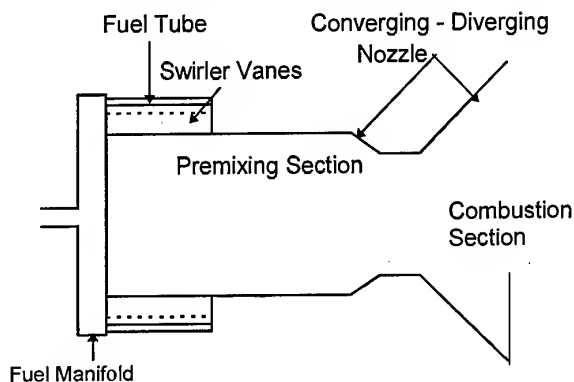


Figure 11. Lean premixed module RSPN

divergent section which produces a controlled central recirculating flow that stabilizes a flame at the discharge of the LPM module. Work at Rolls-Royce Allison [12] on radial swirler lean premixing modules has shown that a uniform fuel concentration profile at the module throat is not necessarily optimal from a flashback perspective. The central recirculation zone generated by the RSPN module produces a lower centerline velocity. To decrease flashback propensity, it is best to generate a FAR profile that is slightly lean at the core, thereby reducing the flame propagation speed at that location. In effect, for flashback resistance it is optimal to tailor the FAR profile to match the velocity profile at the throat. Figure 12 shows typical measured lean core and uniform average fuel concentration distributions at the LPM throat. To have a better control of the centerline flow field, a double radial swirler plus nozzle (DRSPN), which added straight radial (i.e. zero swirl) vanes to the facility's maximum upstream section of the basic RSPN design, shown in Fig. 13, was designed. The optimal length ratio between the swirled and non-swirled vanes was determined through a parametric study to produce an optimum flow field and fuel-air mixture at the throat exit. Figure 14 illustrates typical results predicted by the CFD analysis. The increased centerline

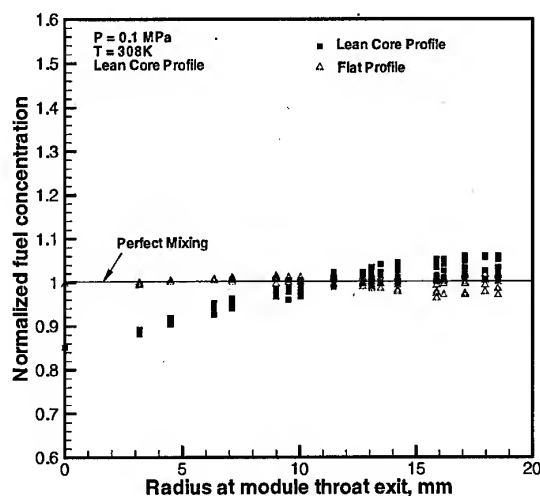


Figure 12. Fuel-air ratio profiles at DRSPN throat

velocity shown in Fig. 14 is achieved by having the primary "swirler" with a length of 15% of the overall swirler length. For primary swirler lengths greater than 15%, the centerline velocity began to decrease. The two LPM module configurations were tested extensively under atmospheric conditions to determine airflow capacity, flashback propensity, lean blowout fuel-air ratios, and fuel concentration profiles at the throat of the modules. Details of the test setup can be found in Razdan et al. [13].

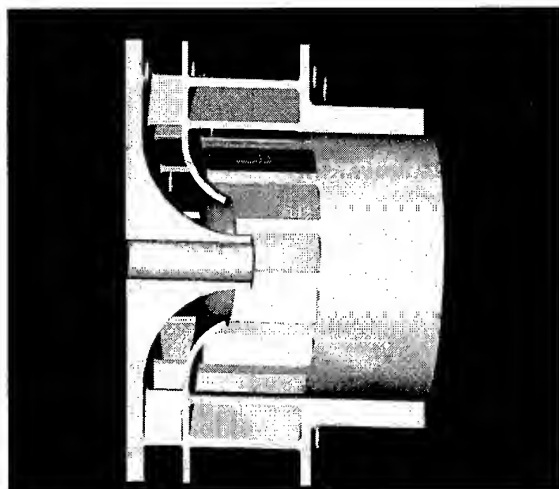


Figure 13. DRSPN LPM swirler section

The DRSPN module proved to be very flashback resistant as shown in Table 1. Flashback was not observed at the FAR limit of approximately 0.085 even with conditions much greater than stoichiometric with fully premixed ethane. A flat

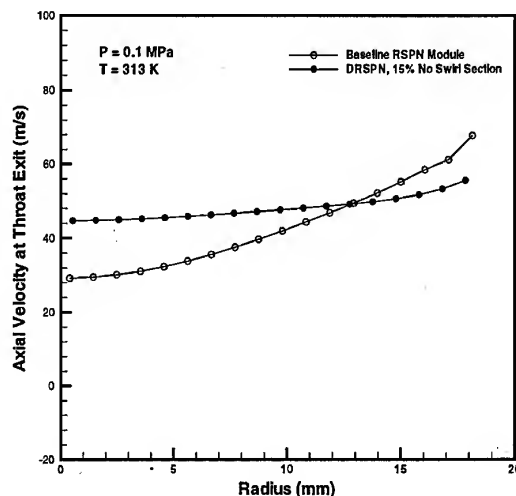


Figure 14. Centerline velocity at throat exit of DRSPN and RSPN designs

or uniform fuel concentration profile with a normalized centerline fuel concentration of 0.99, or a lean core fuel-air profile with a normalized centerline fuel concentration of 0.85 had similar flashback resistance. With ethane, the baseline RSPN demonstrated flashback at a FAR of 0.042. The addition of the second swirler passage resulted in at least a 90% increase in flashback resistance. It should also be noted that in addition to greater resistance to flashback, lean stability of the DRSPN module has not been affected. Each module has a similar FAR at LBO of approximately 0.031 which is comparable to the baseline RSPN design.

Table 1. Fuel Concentration, Flashback, and Lean Stability Effects for LPM Modules Tested with Ethane Fuel

Module	Centerline Fuel Concen.	Flashback Observed	FAR @ Flashback
RSPN	1.00	Yes	0.042
DRSPN (lean core)	0.85	No	>.085
DRSPN (flat profile)	0.99	No	>.081

4. AUTOIGNITION

One of the key design requirements of low emissions combustors is to avoid autoignition. The designer of a mixing module must ensure that not only is the module design aerodynamically clean, but it is designed such that the residence time required for fuel/air premixing in the module is less than the autoignition delay time of the fuel/air mixture. The experimental results of autoignition for liquid fuels are reported in References [14-19]. Autoignition studies on gaseous fuels have been reported in Refs. [20-21]. The data from Ref. [14] are more suitable for fuel rich mixtures. The data from Refs. [15-17] have been widely quoted but the

pressure range is low (0.68 to 1.63 MPa), and the data have shown too strong a dependence of autoignition delay time on pressure ($\sim p^{-2}$). The data from Ref. [18] have a higher pressure range (0.54 to 2.5 MPa) but a limited temperature range (550 to 700K). The test data of Ref. [19] are suitable for high pressures (3 to 6 MPa) and high inlet temperatures (770 to 980K).

The autoignition process for a liquid fuel spray and air mixture can be represented by the following steps: 1) fuel atomization, 2) spray evaporation, 3) formation of vapor-air flammable mixture, 4) gaseous phase pre-ignition chemical reaction, and 5) spontaneous ignition. The autoignition time, t_{ign} , for the mixture consists of two major portions: (1) fuel evaporation time, t_{evap} , and (2) chemical reaction time, t_{chem} , which leads to explosion (ignition). The fuel evaporation time is predominant in the liquid fuel atomization, spray evaporation and fuel-vapor/air mixing processes leading to a fuel/air mixture with enough mixture strength to start the chemical reaction. The chemical reaction time is the elapsed time between the formation of a flammable fuel/air mixture and the appearance of the first flame kernel. To prevent autoignition, t_{chem} should be greater than the residence time of the fuel/air mixture from the instance of forming the flammable mixture to the instance when the mixture exits a mixing module. The time needed to form a flammable mixture includes time for atomization, time for evaporation, etc. as mentioned above. When FAR is leaner than the flammability limit, autoignition is not possible.

Usually the chemical portion of the autoignition delay time only depends on pressure, temperature, and fuel. But the evaporation portion will vary, not only with fuel, pressure, and temperature but also with drop size distribution, air velocity, droplet velocity, total FAR, etc., particularly when temperature is high and the evaporation time is a large portion of the autoignition delay time. When chemical time is predominant, it is a function of $\exp(E/RT)$. However, at higher temperatures, the evaporation time is important, and it decreases with temperature much slower than $\exp(E/RT)$. The dependence of evaporation time on pressure is much more complicated than chemical time [22].

The autoignition characteristics of a fuel/air mixture and the minimum residence time required for mixing will set limits on combustor inlet temperature and operating pressure levels beyond which it will be practically impossible to fully operate in the lean premixed prevaporized mode. Indeed the operating pressure and temperature levels, and the overall FAR will dictate the extent of prevaporization of fuel that should be considered in the design of a mixing module. As an example, let us consider diesel fuel injection into a mixer with an overall FAR of 0.034. Global chemical time for diesel fuel can be approximated as $t_{chem} = 0.04 p^{-1.75} \exp(1600/T)$, where p is pressure in atmospheres, T is temperature in K, and R has a value of 1.987K. This equation has been deduced from the data in Ref. [19]. The lean flammability limit for hydrocarbon fuels is a function of temperature, and it can be approximated by $L_t = L[1 - 0.75(T - 298)/(L \cdot Q_c)]$ [23], where L is the lean limit in % volume at atmospheric conditions, and Q_c is the lower heat of combustion in kcal/mole.

The droplet evaporation history has been calculated for various drop sizes ranging from 10 to 140 μm using the convective spray evaporation model developed at Rolls-Royce Allison [20] for commercial multi-component fuels. We have assumed that there is no secondary droplet breakup, simple cross-sectional area for the flow field, fuel is injected in a radial direction into the mixer. Based on the calculated evaporation time, estimates were made of the elapsed time to form flammable mixtures at different pressures. Then estimates were made of the time from the formation of the flammable mixture to various levels of evaporation ranging from 50 to 99% at various operating pressure ratios. Figure 15 shows the changes in the chemical and evaporation times resulting from changes in the engine pressure ratio. At a pressure ratio of 25, 100% evaporation can take place within the mixing module without autoignition. But for a pressure ratio of 40, evaporation fraction is limited to 73%, and for a pressure ratio 50, it is limited to 55%.

Figure 16 shows the effect of fuel droplet size on the total autoignition delay time t_{ign} [22]. Coarse spray needs higher autoignition delay time. Figure 16 also shows chemical delay time portion of the autoignition time both with mixture temperature correction for evaporation and without this correction. Because of evaporation when a spray is injected into hot air, the bulk gaseous temperature is decreasing as the evaporation fraction is increased. If the spray is totally evaporated, then the temperature decrease is a function of initial air temperature and FAR [22]. The results indicate that

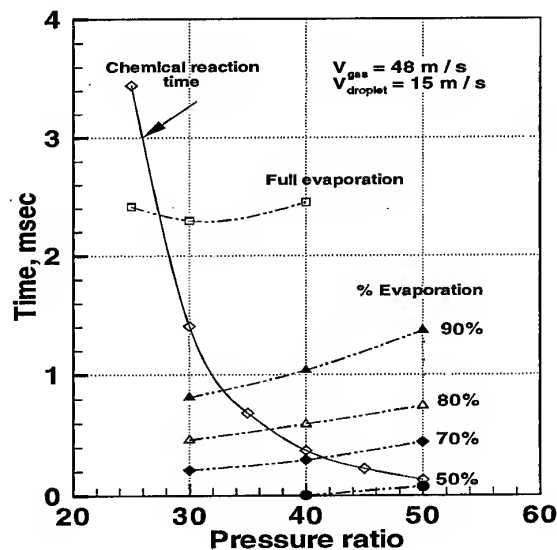


Figure 15. Effect of pressure ratio on chemical and evaporation time

at an initial hot air temperature less than 800K ($1/T > 1.25$), evaporation time is not very significant, but at an initial temperature of 900K ($1/T = 1.11$), it is significant. As the mixture temperature is decreasing, the flammability limit is also changing, thus the required evaporation fraction

increases, and the evaporation time also increases.

Assessment of the effect of initial droplet relative velocity and total equivalence ratio on autoignition delay time has indicated [22] that a higher initial droplet relative velocity accelerates spray evaporation and leads to lower autoignition time. Increased equivalence ratio leads to a decrease in the autoignition delay time at high inlet temperature.

With smaller SMD, the spray evaporates faster and evaporation curves in Fig. 15 will move down, thus the full evaporation is allowable at a higher pressure ratio. When overall FAR is higher, lean flammability limit will be reached at lower evaporation fraction, but chemical time delay will not change, and, therefore, the pressure ratio allowable for full evaporation will move to a lower value. The spray will evaporate faster if air velocity or droplet velocity is higher, and therefore, pressure ratio allowed for full evaporation will move to higher value in Fig. 15. Even with all the aforementioned potential parametric influences of changes in droplet size, air and droplet velocities, and fuel/air ratio, the conclusion from the results from Fig. 15 is that for pressure ratios beyond 40 to 50, potential of having full evaporation at module exit without autoignition is small. Therefore, autoignition concerns will limit the application of fully prevaporized lean premixed low emission approach to operating pressures up to 40 to 50 atmospheres. A practical solution at very high pressures is to consider partially prevaporized premixing low emissions designs.

From the preceding results, it is clear that consideration of autoignition characteristics in the design of low emissions

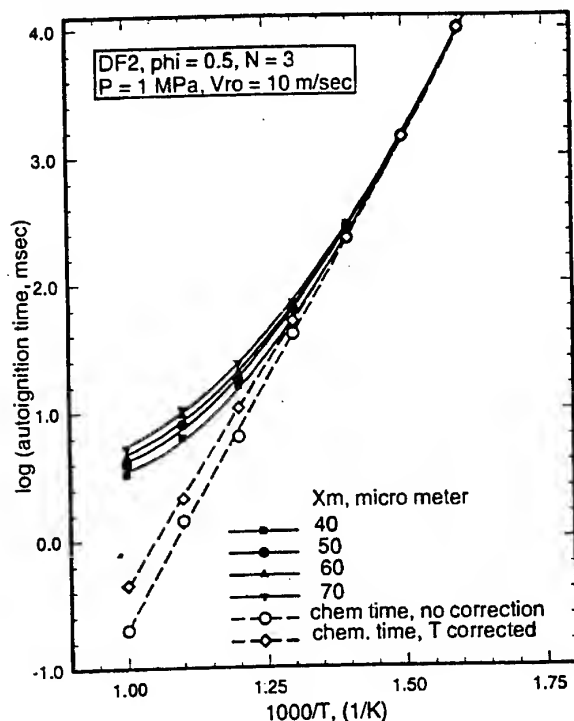


Figure 16. Effect of mean droplet size on ignition delay time

combustor requires accurate description of fuel evaporation history. The extent of fuel evaporation influences not only the local FAR and its temperature but also impacts its flammability limit.

5. SUMMARY AND CONCLUSIONS

The fuel atomizer/mixer is truly the key component in the low emissions combustor. The fuel spray characteristics have significant impact on fuel evaporation and fuel/air premixing. One of the important requirements for the mixer is to have fine atomization that results in small droplets and good dispersion that is essential in the formation of uniform fuel vapor-air mixture in a short distance. In a low emissions combustor, 60 to 80% of the liner air flow may enter through these modules. The choice of a fuel injection method is strongly influenced not only by the selected geometry and size of a fuel/air mixing module but also by its interaction with the module air flow. Combining pressure swirl and prefilming airblast atomization concepts in a hybrid design presents an attractive approach for achieving satisfactory atomization over a wide operating range of the combustor. Several conclusions may be drawn from the results presented in the paper:

1. Airblast and fuel pressure atomization concepts can be optimized to achieve an acceptable fuel spray drop size and the spray dispersion that is required for low emissions combustors. The results demonstrate a near straight line trend, with a continuous improvement in atomization quality as the airblast pressure drops increases.
2. Mixers employing counter rotating outer air swirler passage indicate better mixing performance over the one using inner and outer air streams co-rotating with liquid, in particular under higher air/liquid ratios.
3. The spray interactions in multiple fuel injector designs can produce a positive effect on atomization. This interaction can be significantly influenced by optimizing the fraction of module air used for airblast.
4. The air/liquid ratio show a significantly stronger effect on SMD, when the effects of liquid velocity and relative velocity are separated from those of the ALR.
5. A uniform fuel concentration profile at the exit of a fuel/air mixing module is not necessarily optimal from a flashback perspective. To decrease flashback propensity, it is best to generate a FAR that is slightly lean at the core, thereby reducing the flame propagation speed at that location.
6. The knowledge of spray evaporation history is critical in estimating autoignition time when designing a fuel/air mixer for low emissions applications. Autoignition concerns will limit the application of fully prevaporized lean premixed low emission approach to operating pressures up to 40 to 50 atmospheres.

6. ACKNOWLEDGMENTS

The author wishes to acknowledge Drs. Nader Rizk and J. S. Chin who have contributed significantly to the bulk of the work reported here.

7. REFERENCES

1. Razdan, M.K., and Chin, J.S., "Marine Gas Turbine Engine Emissions: Current State of the Art and Future Needs," AIAA Paper No. 94-2728, 1994.
2. Cooper, L.P., "Effect of Degree of Fuel Vaporization upon Emissions for a Premixed Partially Vaporized Combustion System," NASA Technical Paper No. 1582, 1980.
3. Jasuja, A.K., "Atomization of Crude and Residual Fuel Oils," Trans. ASME, Journal of Engineering for Power, Vol. 101, No. 2, pp. 250-258, 1979.
4. Rizk, N.K., and Lefebvre, A.H., "Influence of Atomizer Design Features on Mean Drop Size," AIAA Journal, Vol. 21, No. 8, pp. 1139-1142, 1983.
5. Lefebvre, A.H., *Atomization and Spray*, Hemisphere Publishing Corporation, 1989.
6. Suyari, M., and Lefebvre, A.H., "Drop-Size Measurements in Air-Assist Swirl Atomizer Sprays," Central States Combustion Institute, Spring Meeting, NASA LeRc, Ohio, 1986.
7. Chin, J.S., Rizk, N.K., and Razdan, M.K., "Study on High Liquid Pressure Internal Mixing Prefilming Airblast Atomization," ASME Paper 98-GT-442, 1998.
8. Chin, J.S., Rizk, N.K., and Razdan, M.K., "Effect of Inner and Outer Air Flow Characteristics on High Liquid Pressure Prefilming Airblast Atomization," Proceedings of the Thirteen International Symposium on Airbreathing Engines (ISABE) of AIAA, Chattanooga, Tennessee, 1997.
9. Chin, J.S., Rizk, N.K., and Razdan, M.K., "Experimental Investigation of Hybrid Airblast Atomization," ASME Paper 96-GT-464, 1996.
10. Lewis, B., and von Elbe, G., *Combustion, Flames and Explosions of Gases*, Academic Press, New York, 1951.
11. Coats, C.M., "Comment on 'Review of Flashed Report in Pre-vaporizing/Premixing Combustors'," *Combustion and Flame*, Vol. 37, pp. 331-333, 1980.
12. Puri, R., Stansel, D.M., Smith D.A., and Razdan, M.K., "Dry Ultra-Low NO_x 'Green Thumb' Combustor for Allison's 501-K Series Industrial Engines," Journal of Engineering for Gas Turbine and Power, Vol. 119, pp. 1-9, 1997.
13. Razdan, M.K., McLeroy, J.T., and Weaver, W.E., 1994, "Retrofittable Dry Low Emissions Combustor for 501-K Industrial Gas Turbine Engines," ASME Paper 94-GT-439.
14. Mestre, A., and Ducourneau, F., "Recent Studies of the Spontaneous Ignition of Rich Air-Kerosene Mixtures," Combustion Institute European Symposium, Academic Press, Inc., London, 1973, pp. 225-229.
15. Spadaccini, L.J., "Autoignition Characteristics of Hydrocarbon Fuels at Elevated Temperatures and Pressures," *Transactions of The ASME, J. of Engineering for Gas Turbine and Power*, Vol. 99, Series A, January 1971.
16. Spadaccini, L.J., and TeVelde, J.A., "Autoignition Characteristics of Aircraft Type Fuels," NASA CR-159886, June 1980.
17. TeVelde, J.A., and Spadaccini, L.J., "Autoignition Characteristics of No. 2 Diesel Fuel," NASA CR-165315, June 1981.
18. Marek, C.J., Papathakos, L.C., and Verbulecz, P.W., NASA Paper No. TMX-3526.
19. Stringer, F.W., Clarke, A.E., and Clarke, J.S., "The Spontaneous Ignition of Hydrocarbon Fuels in a Flowing System," Proc. Inst. Mech. Grp., London, Vol. 184, 1969-70, pp. 221-225.
20. Lefebvre, A., Freeman, W., and Cowell, L., "Spontaneous Ignition Delay Characteristics of Hydrocarbon Fuel/Air Mixtures," NASA Contract Report 175064, February 1986.
21. Spadaccini, L.J., "Ignition Delay Characteristics of Methane Fuels," Progress in Energy and Combustion Sciences, Vol. 20, pp. 431-460, 1994.
22. Chin, J. S., "An Engineering Calculation Method for Multi-Component Stagnant Droplet Evaporation With Finite Diffusivity," ASME Paper No. 94-GT-440.
23. Lefebvre, A.H., *Gas Turbine Combustion*, Taylor & Francis, 1983.

PAPER No. 34
Razdan
(presenter: M. Razdan)

Question 1 (unknown)

For liquid fuels, what happens with respect to autoignition if a spray SMD of 10 μm is achieved in a premixer?

Answer:

With such fine atomization, fuel/air premixing becomes possible without autoignition, to much higher pressures.

Question 2: N. Brehm, BMW-RR, Germany

Have you any experience with non-fully premixed modules, and what is the role of fuel droplet and airflow interaction on NO_x formation?

Answer:

Yes, we have such experience, but at lower pressures and temperatures. You do not get the best NO_x. However, partial premixing helps to reduce pilot NO_x because you get better stability in the main stage, and therefore, do not need as much pilot flow.

Experiments in a small gas-turbine combustor with gas and liquid fuels

A L Heyes, D Jelerčič and J H Whitelaw

Thermofluids Section,
Mechanical Engineering Department,
Imperial College of Science, Technology and Medicine,
London SW7 2BX
ENGLAND

ABSTRACT

Measurements of velocity, temperature, emissions and droplet diameters are reported for combustion of kerosene in a sector of a gas-turbine combustor at atmospheric pressure and air-fuel ratios and preheat temperatures corresponding to cruise and take-off conditions. The results allow comparison of flows with fuelling devices which include gas jets, a T-vaporiser and two arrangements of fan sprays, and show the extent to which droplet diameters and velocities were affected by the rate of fuel flow and by the air preheat in the main vortex of the primary zone. A single fan spray led to a central core of combustion with cold flow on either side so that the pattern factor had no practical value and subsequent experiments made use of two sprays. The droplet number density fell rapidly with distance from the injectors and with increasing air-fuel ratio and preheat temperature, and the arithmetic and Sauter mean diameters tended to decrease as droplets evaporated and burned. The exit-plane profiles of temperature were more uniform with the higher preheat temperature and lower air-fuel ratio which resulted in a combustion efficiency of 98.3 %. The lower preheat temperature led to a three-fold increase in concentrations of unburned hydrocarbon and efficiency of 91.6 %. Emissions were similar with the fan spray and the vaporiser arrangements, with NO_x concentrations larger by 10 % in the rich flows and smaller by 25 % with the higher air-fuel ratio and lower preheat temperature.

NOTATION

A/F	air fuel ratio
AMD	arithmetic mean diameter
EI	emissions index, grams pollutant/ kg fuel burned
NO_x	mixture of NO and NO_2
ppm	parts per million by volume
SMD	Sauter mean diameter
T	temperature
UHC	unburned hydrocarbons
η_c	combustion efficiency

Subscripts

max	maximum value
mean	spatially averaged mean value
pre	preheat
rms	root mean square value

1. INTRODUCTION

This paper reports a further step in the characterisation of performance of a small gas turbine combustor similar to that used in helicopter engines. It extends the information provided in previous papers, for example those of Bicen *et al* (1989), Liu *et al* (1992) and Poppe *et al* (1998), to include new results with fan sprays which were selected because it proved difficult to devise alternative injectors to provide the low fuelling rates required by the small volume of the combustor and its operation at atmospheric pressure.

The operational form of the combustor has made use of a T-vaporiser with results described by Chow *et al* (1989), Liu *et al* (1992) and Perez Ortiz (1998) and generally led to good mixing with a tendency for high temperature streaks in the plane of the exits from the vaporiser. Information of droplet characteristics was provided by Liu *et al* as part of an investigation to determine reasons for the deterioration of the combustor and were confined to the region close to the exits. Measurements with gaseous fuel made use of cones in the head end of the combustor, each with ten 0.64 mm diameter fuelling holes and located in line with the exits of the T-vaporiser of the previous arrangement. The results showed that mixing was less satisfactory, so that the pattern factor was larger than with liquid fuelling, and a small number of similar results are presented to compare with those from the fan sprays and previous results with the vaporiser.

Previous investigations with liquid fuel include that of Nicholls *et al* (1980) who studied the influence of fuel spray characteristics on emission species concentrations within the primary zone flame of a combustor with near-unidirectional flow and showed that larger droplets led to increase in unburned hydrocarbons and a decrease in the flame temperature gradients. Odgers *et al* (1993) reported experiments with two combustors over a wide range of steady state operating conditions with three different Simplex atomisers and three fuels, and found little influence of droplet size upon combustion efficiency. The different conclusions of these authors stem, in part, from the greater residence time within the recirculation region of the combustors of Odgers *et al* and on the precision of measurement.

Cameron *et al* (1988) attempted to link isothermal and combusting sprays from twin-fluid air assist atomisers and found direct comparisons difficult to make. In the isothermal case, increase in air-fuel ratio from 1.5 to 3.0 produced a more uniform and finer spray and, with combustion, more symmetric temperature profiles. Similar and more thorough comparisons were made possible by the two investigations of

Aftel *et al* (1996) who investigated the effect of atomising gases, air, nitrogen, argon and carbon monoxide in an air-assist atomiser and showed that the lighter gases (e.g. nitrogen) atomised the fuel more effectively. Denser gases led to larger droplet sizes, smaller number densities and lower velocities.

There are many more investigations of combustor performance with liquid fuels, for example those of Shisler *et al* (1975), Vranos *et al* (1976), Bhangu *et al* (1983), Winter *et al* (1986), Joos *et al* (1988) but they do not include measurements of droplet characteristics particularly within the combustor flow so that the emphasis was on performance and without ability to link to information of droplets. The results in the present investigation help to bridge this gap.

The paper has been prepared in five sections including this introduction, and corresponding respectively to a description of the flow arrangement and instrumentation, presentation of results, discussion and conclusions.

2. FLOW ARRANGEMENT AND INSTRUMENTATION

The combustor and flow circuit are shown on figures 1 and 2 together with the fuelling devices which included two ten-hole gas nozzles for the combustion of methane gas and a T-vaporiser and air-assist fan sprays for the combustion of liquid kerosene. Most results were obtained with a single and two fan sprays. In all cases, the combustor was operated with overall air-fuel ratios of 70 and 42, corresponding to cruise and take off conditions, and with preheat air temperatures of 150° and 250° C. The fuel flow rates were 0.58 and 0.97 g/s for the single atomiser and 0.29 and 0.485 g/s for each of the two atomisers and, since the droplet diameters were almost independent of flow rate, the emphasis of the results of the next section is on the results of the higher flow rate. The air flow rate through the atomiser shroud was around 35 l/min and constant so that the fuel flow rate was adjusted to modify the air-fuel ratio.

The combustor operated with a single recirculation zone driven by the splash air from the film cooling slots 1, 2 and 12, and separated from the dilution zone by five primary air jets (11). Dilution was achieved with four jets from the outer diameter and two from the inner diameter and directly opposite to two of the outer jets (4 holes no. 9 and 2 holes no. 4). The remainder of the dilution air was used for film-cooling in the lower part of the combustor (3, 5, 6, 7 and 10). The turn-around duct required 8.5 % of the total air mass flow of 41 g/s as cooling air (items 6 and 7) and was readily removed, as shown. The arrangement of the dilution holes is represented in figure 3, as viewed from the inner liner wall, together with the position of the three different fuelling arrangements under consideration.

A single fan spray atomiser was fitted centrally to the outer liner wall, 38 mm below the dome and at an angle of 45 degrees towards the dome. This arrangement allowed the fuel to travel some 270° within the recirculation vortex and provided time for mixing with air and combustion. Atomisation within the atomiser was accomplished by the impingement of opposing fuel jets, resulting in more acceptable droplet characteristics for low fuel-pressure differentials than simple pressure jets. The resulting spray was flat, elliptical in shape with relatively low drop discharge velocities, and was suitable for the narrow width of the GEM 60, Carr (1979).

The single fan spray resulted in a flame in the central portion of the combustion chamber with an uneven temperature distribution at the exit of the curtailed combustor and unsatisfactory pattern factors. The combustor was subsequently modified to accommodate two spray atomisers, 56 mm apart and corresponding to the distance between the two legs of the T-vaporiser used by Liu *et al* (1992) and Chow *et al* (1989). A small number of measurements of droplet characteristics were obtained without combustion and emphasised the recirculation zone.

Optical access was achieved through two flat optical-quality quartz windows of 5 mm thickness, located on either side of the combustion chamber and were removed for isothermal flows to avoid problems of wetting with measurements limited to the region close to the spray atomiser. Wetting of the windows was not important with combustion but sustained operation led to soot deposits so that regular but infrequent cleaning was required.

The fan sprays were examined separately in atmospheric flow prior to incorporation into the combustor. The atomiser was mounted in a specially designed plenum chamber and oriented so as to spray vertically downwards into the atmosphere. Droplet velocity, number density and size distributions were measured at a temperature of 293 K and with pressure drops and flow rates similar to those in the combustor. The plenum chamber and atomiser were arranged on a mechanism which allowed translation in two orthogonal planes with precision better than 0.2 mm and vertical translation with precision better than 0.5 mm. Velocity and size characteristics of droplets were measured across five planes with axial distances of 20, 30, 40, 60 and 80 mm from the nozzle and at 2 mm spacing in each plane. High concentrations of liquid made measurements impossible within 20 mm of the atomiser.

The phase-Doppler analyser (Acrometrics model RCV 2100 with signal processor model PDP 3100) had a transmitting optical system based on a rotating grating and the main optical characteristics are shown in table 1. A 30 degree collection angle ensured that refraction dominated the scattered light for measurements outside the combustor and a 20 degree angle was used for measurements inside the combustor due to geometric constraints. In both cases, the scattered light was focused onto a 50 µm slit to limit the effective size of the control volume and reduce the probability of more than one particle occupying the control volume simultaneously. A total of 10,000 validated samples were collected at most measurement locations with exceptions in some regions of the combustor flows where 5000 samples were collected. The validation rate varied with measurement location from 60 to 90 % of all signals and the dynamic range was limited to 35 so that with the smallest diameter set to 2.7 µm, an upper limit of 94.5 µm was imposed.

The experimental uncertainty in the measurements arose from two main sources, statistical uncertainties due to the use of a finite sample and systematic errors introduced by signal conditioning and processing. The maximum uncertainties in velocities were estimated as 2 % of the mean values and the statistical uncertainty in the cumulative droplet size distribution was estimated to be around 2 %, Tate (1982), the sizing accuracy better than 2 µm for droplets larger than 20 µm.

Additional uncertainties are possible, for example from the variation of the refractive index of the fuel droplets, as

discussed by Pitcher *et al* (1990), and were examined and considered to be small. The lack of consideration of droplets larger than $94.5 \mu\text{m}$ will undoubtedly have led to some biasing of the AMD and SMD results but examination of the probability density distribution of diameter confirmed that the number of droplets above this diameter was very small, even if they did carry proportionally larger quantities of fuel.

Photographs of the sprays in the quiescent atmosphere were obtained with a sheet of laser light to provide illumination through the axis and images were recorded on black-and-white film (Kodak T-Max 400) with a Nikon (F-801 S) camera. Flame images inside the combustor were recorded with the same camera and colour film (Kodakcolor ASA 800) with an exposure time of $1/8000 \text{ s}$ and an aperture of $f2.8$.

Temperatures were measured in the exit plane of the curtailed combustor and of the turn-around duct with platinum and platinum/13 % rhodium thermocouples fabricated from $50 \mu\text{m}$ wire. Where the $50 \mu\text{m}$ thermocouples did not survive, they were replaced by more robust thermocouple fabricated from $250 \mu\text{m}$ wire which were more likely to measure density-weighted values. The measuring grid at the exit of the curtailed combustor and at the exit of the turn-around duct encompassed the central 80 % of the total area and the pattern factors were based on this area and on the definition

$$\text{pattern factor} = \frac{T_{\text{max}} - T_{\text{mean}}}{T_{\text{mean}} - T_{\text{inlet}}}$$

Species concentrations were measured with the help of a stainless steel water cooled suction probe of 6 mm outside and 0.5 mm inside diameters. A flame ionisation detector (Analysis Automation Model 523 Series II flame ionisation detector) measured the concentrations of unburned hydrocarbons and a chemiluminescence detector (Thermo Environmental Instruments Inc. Model 42H) provided concentrations of NO_x . The concentrations of CO and CO_2 were measured by infrared analysers (Analytical Development Company Ltd) and oxygen concentrations by paramagnetic cell oxygen analyser (Analytical Development Company Ltd ADC 7000 Series). The probe was introduced from downstream of the flow and aligned to the direction of the bulk flow to limit interference effects. The frontal cross-sectional area of the probe was smaller than the recommended 0.5 % of the combustor exit area, Goulard *et al.* (1976), leading to a sampling volume of approximately 1 cm^3 . The suction velocity was maintained within a range between 6 and 20 m/s which implied, according to Toral and Whitelaw (1982), that measured concentrations were not affected. Present tests showed that the influence of suction velocity and probe inclination (for angles less than 30 degrees) on gas concentrations was less than 5 % of maximum concentrations, in accordance with the results of Heitor and Moreira (1993). The overall uncertainty associated with the species concentration measurements was estimated to be less than 10 %.

3. RESULTS

3.1 Fan spray characterisation

Experiments with the two fan spray atomisers showed similar performances and only minor differences in droplet diameters and velocities which can be attributed to small differences in the rectangular injection slot, $20 \mu\text{m}$ wide and $30 \mu\text{m}$ long, as confirmed with an electron microscope. Figure 4 a) shows that

the spray produced by the atomiser operating without air and a kerosene flow rate of 0.97 g/s , had a cone angle of 120 degrees with most of the fuel occupying the narrow central portion of the spray. Figure 4 b) shows the finer spray achieved at the same fuel flow rate and 35 l/min of air assist and a cone angle of almost 180 degrees, the edges of which are not clearly identifiable due to the additional mist produced by the added air. With fuel flow rates of 0.97 , 0.58 and 0.29 g/s , the spray maintained a constant width downstream of the atomiser as shown in figure 4 c) and d) which were software enhanced to show the spray structure.

The visual observations were supported and quantified by local measurements with the phase-Doppler anemometer and figure 5, corresponding to 0.97 g/s fuel with air assist, has two maxima in each measurement plane at around 20 mm from the centre line. With lower fuel flow rates, the maxima in droplet number density were smaller and occurred some 14 mm on either side of the centre of the spray, consistent with photograph 4 (c) on which one profile of droplet number density has been superimposed. The mean axial velocity profile of the droplets has a maxima in the centre of the spray and fuel flow rates of 0.58 and 0.29 g/s led to mean droplet velocities 25 % and 75 % less than those with the highest flow rate. Profiles of the Sauter (SMD) and arithmetic mean diameters (AMD) measured at various axial distances show symmetry with small droplets in the central region and larger ones at the edges due to the greater penetration of these along their initial trajectory. The AMDs ranged from 9 to $18 \mu\text{m}$ and the SMDs from 19 to $38 \mu\text{m}$ for all fuel flow rates. A small increase in SMD was also observed with axial distance as the smaller droplets dispersed possibly with some coalescence.

3.2 Single and twin fan spray fuelling arrangement

Tests in the GEM 60 combustor were conducted first with a single air-assist atomiser located centrally on the outer liner wall, 38 mm below the dome, pointing at an angle of 45 degrees towards the dome and spraying directly into the primary-zone vortex. The interaction of the vortex and the injected fuel droplets imparted a circulatory motion with enhanced mixing with film cooling and primary dilution air. The spray remained confined to the central section of the combustion chamber with an inadequate spread of fuel so that the sides were flame free. The flame was confined to the upper part of the combustor and almost completely extinguished before it reached the secondary dilution holes. The air delivered through the primary holes limited the extent of the vortex and pushed the flame towards the outer wall. The region of maximum flame intensity, characterised by a bright yellow flame, was concentrated in the near region of the spray where the fuel-air mixture was very rich.

Figure 6 shows the temperature distribution in the exit plane of the curtailed combustor with the single fan spray, an AFR of 70 and preheat temperature of 150°C . It is characterised by low temperatures in line with the opposed dilution holes and this separated the two areas of high temperature, and a wide region of low temperatures in the proximity of the outer walls. This pronounced non-uniformity led to high pattern factors, unsuitable for real combustors (0.86 for an air fuel ratio of 70 with the lower preheat and 0.77 for the higher preheat), and further investigations were directed to flows with two sprays.

The twin spray arrangement had atomisers 56 mm apart, to match the distance between the two legs of the T-vaporiser, and the photographs of figure 7 show that here the flame

occupied the width of the combustion chamber. In this case, the flame length increased with decreasing air fuel ratio and extended below the primary zone. The primary jets directed the flame towards the outer wall, so that a structure similar to a secondary vortex was created. Downstream, secondary dilution jets transported the hot combustion products back towards the inner wall of the annulus, leading to generally higher temperatures in this region.

Temperature distributions at the exit of the curtailed combustor with air-fuel ratios of 42 and 70 and with preheat temperatures of 423 K and 523 K are shown in figure 8. The three high temperature regions are common to all profiles, on the left ($x = 25$ mm), in the centre ($x = 80$ mm) and on the right ($x = 125$ mm). The in-between cold regions are a consequence of the opposed dilution jets at locations $x = 51$ mm and $x = 107$ mm, and the asymmetry about the centre plane is the result of the non-symmetrical arrangement of the dilution holes with a more pronounced effect in the right plane due to larger proportion of dilution air on that side. A 100 K increase in the preheat temperature led to a similar increase in the overall temperature for both equivalence ratios. The increase in the temperature maxima was, however, only a third that, resulting in lower pattern factors at higher preheat (0.34 and 0.29 for an AFR of 42 and preheat temperatures of 423 K and 523 K respectively and 0.55 and 0.47 for an AFR of 70). With increasing preheat, the temperature distributions became more uniform as the penetration of the dilution jets reduced, suggesting that better mixing was responsible for the lower pattern factors. Further mixing between the combustion products and dilution air inside the turn-around duct led to reduction in pattern factors for all flows although the two asymmetric high temperature regions remained and were more pronounced with the lower air fuel ratio.

Figure 9 shows that the distributions of concentrations of CO_2 and O_2 at exit of the curtailed combustor for an air fuel ratio of 70 and preheat of 523 K have trends consistent with those of temperature with regions of high CO concentrations coincident with those of high CO_2 , implying that the CO -to- CO_2 reaction was not quenched by the additional dilution air. The temperature was above 1500 K, the minimum value required for the combustion of CO to CO_2 (Schoenung *et al.*, 1981) and CO concentrations were lower at the exit from the turn-around-duct with some residual unburned hydrocarbon. Quenching by the dilution air occurred only in the corners of the combustor and close to the side walls.

It is expected that most of the NO_x was thermally produced and the highest concentrations were consistent with formation in high temperature regions. The spatial average NO_x concentration increased with preheat temperature and decreased with air-fuel ratio, resulting in values of 16.2 and 28.2 ppm at an air-fuel ratio of 70, and 32.3 and 46.4 ppm at an air-fuel ratio of 42 for preheat temperatures of 423 and 523 K, respectively.

3.3 Combusting spray characterisation

Droplet measurements were concentrated in the flow field near the nozzle exit since the droplet number densities were small in other regions and this made measurements difficult and of doubtful accuracy. Droplet size and vertical velocity component measurements were taken in the shaded area of figure 1 a), in the half of the primary zone vortex adjacent to the injector, in an orthogonal grid of points, spaced at 5 mm, traversing in the direction along the axis of the primary zone

vortex, 30 mm either side of the injector. The exit of the injector was selected as the origin of the three dimensional grid, and all the figures presented in this section follow this convention.

The effect of preheat and air-fuel ratio on the spray characteristics were investigated in detail. The increase in preheat temperature for the lower air fuel ratio of 42 was found to have only minor effect on the droplet characteristics of the spray, a reduction in the SMD of no more than 5% at most measurement points (15 % maximum) and a reduction in the AMDs of up to 20 %. The vertical component of the average droplet velocity increased by up to 20 % with the higher preheat.

Similar changes were observed in the high air fuel ratio case of 70, where the preheat temperature increase was accompanied by a decrease in AMDs of up to 10% at most points (15% maximum), variation in the SMD limited to about 10 % and a velocity increase of up to 20 %. Additional preheat also reduced the number density as higher temperatures enhanced evaporation with the consequent change in the diameters outlined before.

For the low preheat case of 423 K, the lower air-fuel ratio led to higher fuel droplet velocities, with increases of around 15%, but in some cases of as much as 30 %. SMDs were 20% lower, but this effect diminished with distance from the atomiser. The AMDs showed localised variations, both increases and reductions, of within 30%. For a preheat temperature of 523 K and an air-fuel ratio of 42, the SMDs were around 15% smaller than for the higher air-fuel ratio value, the AMDs were subject to a reduction of up to 30% and the velocity increased by up to 25%.

Figure 10 shows that the distributions of SMD and AMD across the injection plane of the atomiser retained the main features observed in the isothermal spray, with the smallest average diameter in the centre-region close to the axis of the atomiser, where the spray contained a high percentage of small droplets. The droplet size distributions increased radially outwards from the axis, reaching a maximum values at the spray boundary due to a higher proportion of larger drops. This is clearly seen in figure 11, which shows the droplet size distributions in the isothermal flow outside the combustor and the burning case. The measurement locations inside the combustor at 15 mm above the atomiser exit corresponded to points close to the nominal centreline of the atomiser and hence nominally in the centre of the spray. From the droplet distributions and the mean fuel velocity profiles in figure 10 it can be inferred that the primary vortex has shifted the symmetry plane of the spray along the axis of the primary vortex, inwards towards the region between the two sprays, by between 5 and 10 mm.

The SMD ranged from 36 to 72 μm and from 31 to 92 μm with the air-fuel ratio of 42 with higher preheat temperature and with the air-fuel ratio of 70 and the lower preheat temperature, respectively; the corresponding AMDs were from 19 to 63 μm and from 24 to 85 μm . The number density distribution for the burning spray was more than two orders of magnitude smaller than with the non-burning spray with the evaporation of small droplets.

4. DISCUSSION

The emission indices and performance data for the three fuelling arrangements are summarised in table 3 which shows that the fan spray led to the lowest pattern factors. The more uniform temperature distribution attained with fan sprays was the result of a more efficient distribution of the spray across the combustor width and improved mixing with the surrounding air. Figure 12 shows temperature profiles at the same operating conditions for all three injector arrangements and that the T-vaporiser and fan spray led to three regions of high temperature, separated by the opposing dilution jets, and with the latter giving rise to the more uniform temperature distribution. The performance of the vaporiser had a tendency to deteriorate with time and the fan sprays showed no loss of performance or carbon deposits after prolonged operation. Emissions of NO_x were similar. Gas injection led to two regions of high temperature, in line with the position of the gas cones in the combustor dome, and with greater penetration of fuel into the dilution region. Increase in inlet air temperature improved the completeness of the chemical reaction, and the CO and UHC emission indices decreased. Comparable combustion efficiencies were found with the T-vaporiser and the fan sprays, but the latter was more efficient at the lower air-fuel ratio. The higher air-fuel ratio led to an increase in CO emissions which lowered the combustion efficiency to 91.6 % and the higher air preheat temperature helped the evaporation rate to yield a combustion efficiency of 96.1%

The flowfield survey within the primary zone of the combustor indicates that the core of the spray injected at 45 degrees tends to follow the original injection trajectory. Evidence of this is presented in figure 10 where the maximum droplet number density is seen to occur at $z = 15$ mm corresponding to the axis of the undisturbed spray. As a result, some droplet impaction was visually observed on the combustor dome on the side opposite to the injector. After 90-hour operation carbon deposits were found on the combustor dome, in the area between the two atomisers, indicating the edges of the thin film of fuel formed by the impacted droplets. However, it should also be noted that in the measurement plane at $z = 20$ mm, droplets were found further from the spray axis (above the spray) than was the case for the isothermal conditions. This suggests that some droplets are affected by the recirculation vortex inside the primary zone leading to an asymmetric spreading of the spray to the lee of the cross flow provided by the primary vortex recirculation. The Stokes numbers of the droplets (which indicates the responsiveness to the mean air motion inside the primary zone) also helps to corroborate this assumption since high values ($\gg 1$) were calculated for droplets with diameters less than $30 \mu\text{m}$ indicating that these are more likely to follow the vortex.

Further evidence is provided by the graphs in figures 13 and 14. Figure 13 shows the vertical velocity components of 15 and $70 \mu\text{m}$ droplets along a vertical traverse through the spray and indicates the tendency of the smaller droplets to respond more rapidly to the cross-flow. Furthermore the droplet size distribution at the edge of the spray on the leeward side (figure 14) shows a high proportion of smaller droplets below $30 \mu\text{m}$. Allowing for reduction in particle diameter due to evaporation and burning is not sufficient to explain the change in droplet size distribution. No droplets were detected below the injector's plane and it can therefore be assumed that there was no droplet recirculation into the primary zone.

5. CONCLUSIONS

Measurements of velocity, temperature, emissions and droplet sizes were obtained for the fan sprays in a sector of a gas-turbine combustor at atmospheric pressure and air-fuel ratios and preheat temperatures corresponding to cruise and take-off conditions. The following is a summary of the most important conclusions:

1. The performance of fan sprays outside the combustor was characterised by a velocity profile with a maximum in the centre of the spray, corresponding to the minimum in the AMD and SMD profiles.
2. Single fan spray arrangement produced a narrow flame leading to unacceptable pattern factors. Double fan spray arrangement produced a uniform temperature profile with two hot streaks, with pattern factors less than 0.28 except for the A/F of 70 and preheat of 523 K, where the pattern factor was 0.41.
3. Comparable combustion efficiencies were found with the T-vaporiser and the fan sprays, but the latter was more efficient at the lower air-fuel ratio. The performance of the vaporiser had a tendency to deteriorate with time.
4. The arithmetic and Sauter mean diameters inside the combustor were affected by the A/F ratio and preheat temperature. A decrease in the A/F ratio and an increase in preheat temperature produced similar effects causing a reduction in the AMD and SMD and an increase in the vertical component of droplet velocity. The number density distributions indicated that a large proportion of the droplets were unaffected by the primary vortex and impinged on the combustor dome although there was also some asymmetric spreading of the spray commensurate with the high Stokes numbers of the smaller droplets.

ACKNOWLEDGEMENTS

Financial support was provided by the EPSRC under Grant GR/K 60985. We are grateful to Drs R Perez Ortiz and C Poppe for helpful suggestions and to the technicians of the Department for maintaining a flagging combustor.

REFERENCES

- Aftel, R., Gupta, A.K., Cook, C. and Presser, C. (1996) Gas property effects on droplet atomization and combustion in an air-assist atomizer. 26th Symposium on Combustion, 1645-1651
- Aftel, R., Gupta, A.K., Cook, C. and Presser, C. (1996) Control of droplet atomization in an air-assist atomizer. In Proc. 8 Intl Symp. on Appl. of Laser Techniques to Fluid Mechanics, paper 20.5
- Bachalo, W.D. and Kramer, G. (1986) Evaluation of a phase Doppler particle analyzer for measuring dense sprays from a gas turbine fuel injector. AIAA paper 86-1532
- Bhangu, J.K., Snape, D.M. and Earley, B.R. (1983) The design and development of a low emissions transpary combustor for the civil Spey engine. AGARD-CP353, Paper 23

- Bicen, A. F., Senda, M. and Whitelaw, J. H. (1989)** Scalar characteristics of combustng flow in a model annular combustor. *J. Eng. for Gas Turbines and Power*, **111**, 90.
- Cameron, C.D., Brouwer, J. and Samuelsen, G. S. (1988)** A comparison of spray characterization in an isothermal chamber and in a model gas turbine combustor. *Proc. 4th International Conference on Liquid Atomization and Spray Systems (ICLASS)*, Sendai, Japan 145
- Carr, E. (1979)** The combustion of a range of distillate fuels in small gas turbine engines. *ASME Paper 79-GT-175*.
- Chow S.K., Senda, M. and Whitelaw, J. H. (1989)** Combustion characteristics of a liquid-fuelled model annular combustor. *Proc. 7th Air-Breathing Engines Symposium*, Athens
- Goulard, R., Mellor, A. M., and Bilger, R. W. (1976)** Combustion measurements in air breathing propulsion engines. Survey and research needs. *Combust. Sci. and Tech.* **14**, 195-219.
- Heitor, M. V. and Moreira, A. L. N. (1993)** Thermocouples and sample probes for combustion studies. *Prog. Energy Combust Sci.* **19**, 259-278.
- Joos, F. and Simon, B. (1988)** Comparison of the performance of a reverse flow annular combustion chamber under low and high pressure conditions. *AGARD-CP-422*, paper 13
- Liu, C. H., Perez-Ortiz, R. M., Whitelaw, J. H. (1992)** Vaporiser performance. *Proc. I. Mech. E.* **206**, 265-273.
- Mao C.-P., Wang, C., Chigier, N. (1986)** An experimental study of air-assist atomizer spray flames. *Proc. 21st Int. Symp. on Comb.*, The Combustion Institute, 665-673.
- Nicholls, A., Kaufmann, C.W., Pelaccio, D.G., Glass, D.R. and Driscoll, J.F., (1980)** The effect of fuel sprays on emissions from a research gas turbine combustion. *Comb. Sci. and Tech.*, **23**, 203-213.
- Odgers, J., Kretschmer, D., Pearce, G.F. (1993)** The combustion of droplets within gas turbine combustors: some recent observations on combustion efficiency. *Journal of Engineering for Gas Turbines and Power*, **115**, 522-232.
- Perez Ortiz, R. (1998)** Combustion characteristics of kerosene flames in gas turbines and ducts. PhD Thesis, University of London.
- Pitcher, G, Wigley, G. and Saffmann M. (1990)** Sensitivity of droptime measurements by phase Doppler anemometry to refractive index changes in combustng fuel sprays, In *Proc. 5 Int'l Symp. on Appl. of Laser Techniques to Fluid Mechanics*, Lisbon, paper 14.4.
- Poppe C, S Sivasegaram and J H Whitelaw (1998)** Control of NO_x emissions in confined flames by oscillations, *Combustion and Flame* **113**, 13-26.
- Schoenung, S.M., and Hanson, R. K., (1981)** CO and temperature measurements in a flat flame by laser absorption. Spectroscopy and probe techniques. *Comb. Sci. and Tech.* **24**, 227-237
- Shisler, R A., Tuttle, J.H. and Mellor, A.M. (1975)** Emission from and within a film-cooled combustor. *Comb. Sci. and Tech.*, **11**, 153
- Tate, R.W. (1982)** Some problems associated with the accurate representation of particle size distribution. *Proc. 2nd Int. Conf. on Liquid Atomization and Spray Systems (ICLASS82)*.
- Toral, H. and Whitelaw, J. H. (1982)** Velocity and scalar characteristics of the isothermal and combustng flow in a combustor sector rig. *Comb. and Flame*, **45**, 251-272.
- Vranos, A. and Taback, E. F. (1976)** Combustion product distribution in the primary zone of a gas turbine combustor. *Com. Sci. and Tech.*, **14**, 229.
- Winter, J. and Maden, K.H. (1986)** The performance of a reverse flow combustor using JP10 fuel. *ASME paper 86-GT-146*.

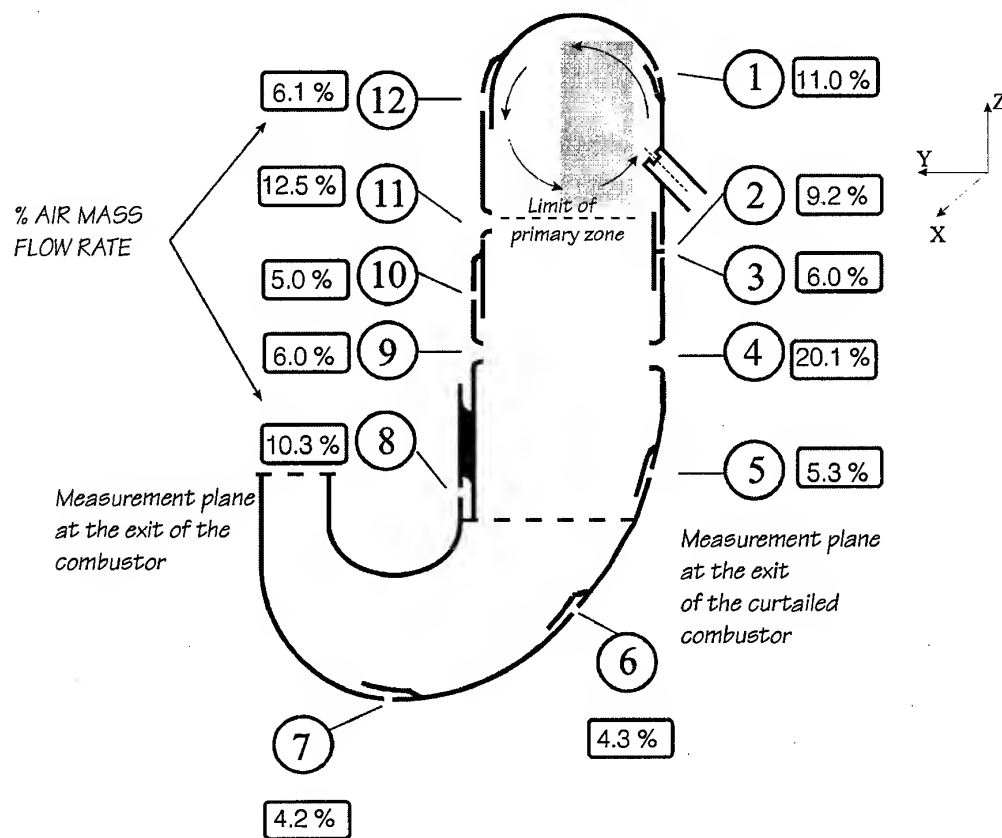


Fig. 1 a) Cross-sectional view of the GEM 60 combustor showing the air distribution and the numbered air inlets

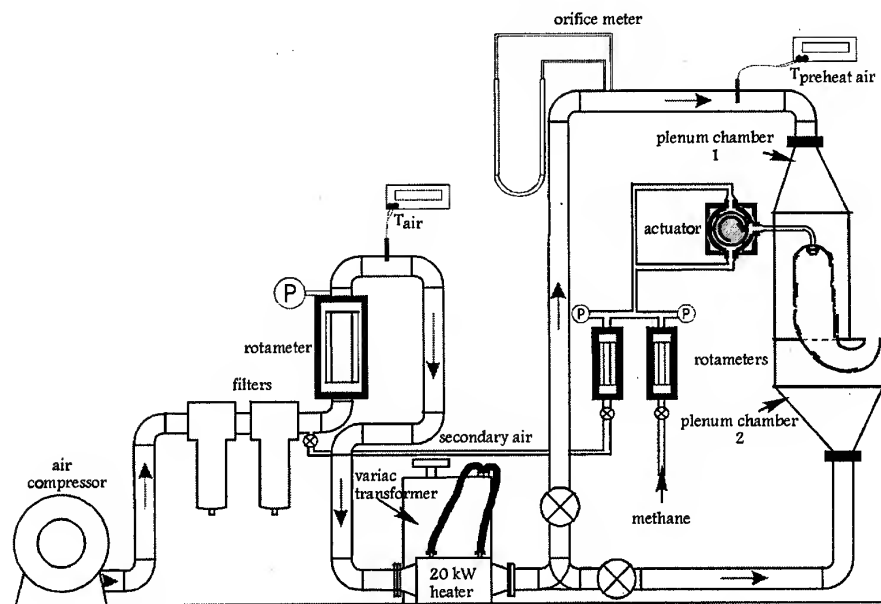


Fig. 1 b) Schematic of the flow rig with the GEM 60 combustor shown with gaseous fuelling arrangement

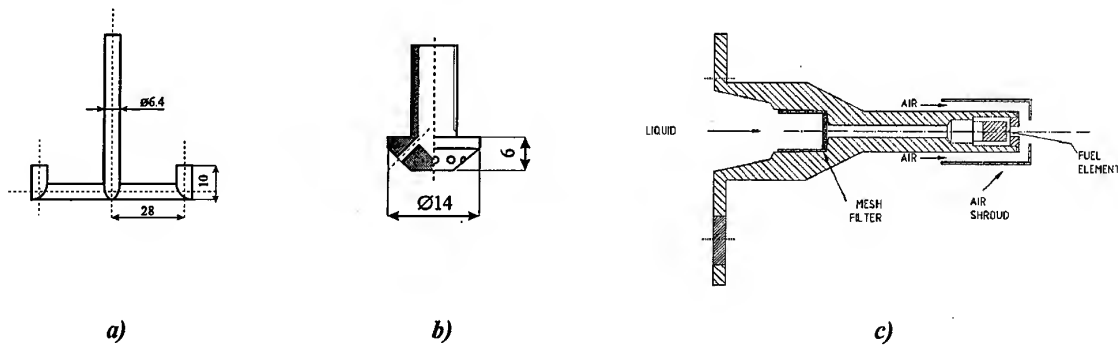


Fig. 2 *Fuelling devices*
 a) *T-vaporiser for liquid fuel (kerosene)*
 b) *Injection cones for gaseous fuel*
 c) *Fan spray atomiser*

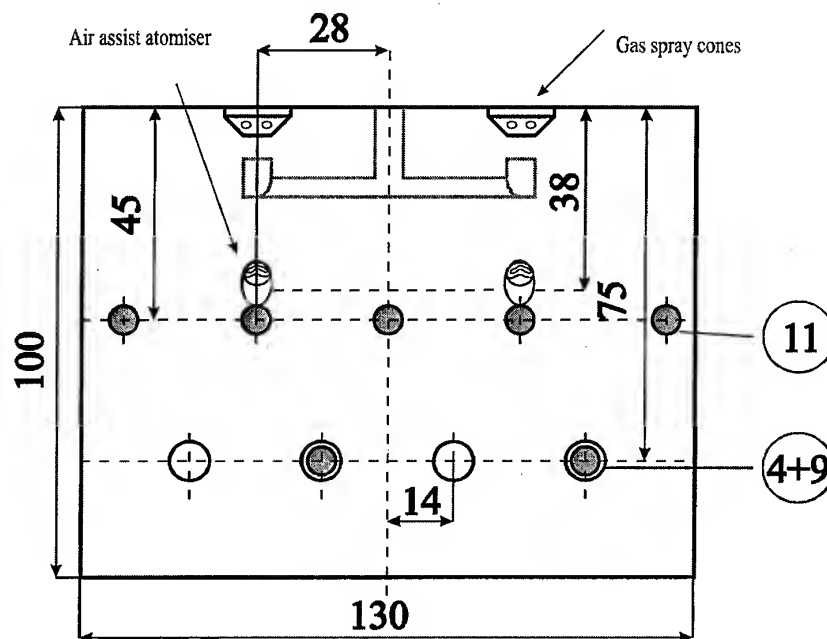


Fig. 3 *Arrangement and location of the dilution holes in the model GEM combustor with the location of the different fuelling devices*

<i>Transmitting optics</i>	I	II	
Laser: Ar ⁺	1.4 W	1.4 W	
Operating power	400	500	mW
Laser wavelength	514.5	514.5	nm
Focal length of transmitting lens	600	600	Mm
Line pairs of diffraction grating	16384	16384	
Nominal frequency shift	4	4	MHz
Beam intersection half angle	4.83	4.83	deg.
Fringe spacing	6.10	6.10	μm
Number of fringes	14	14	
Probe volume length at e ⁻² intensity	1.99	1.99	mm
Probe volume diameter at e ⁻² intensity	83.93	83.93	μm
<i>Receiving optics</i>			
Focal length of collimating lens	495	495	mm
Location of receiving optics from forward scatter angle	20	30	deg.
Spatial filter slit width	50	50	μm
Sizing range, up to	94.8	94.8	μm

I - inside the combustor

II - non-burning spray in atmosphere

Table 1 *Optical characteristics of the phase Doppler instrument*

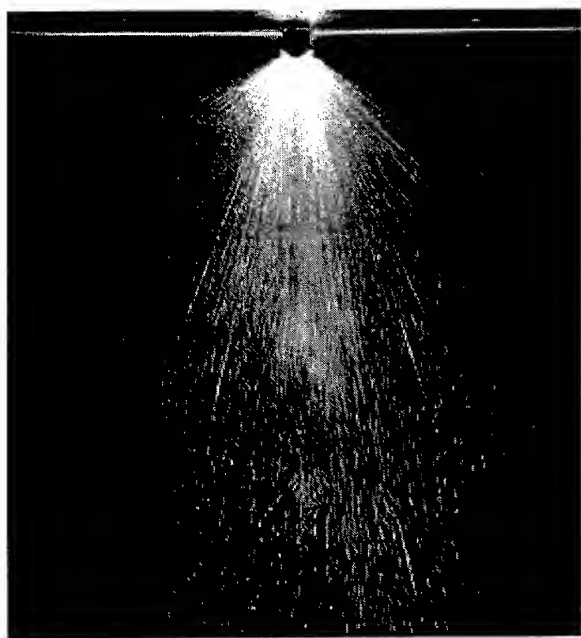
T _{pre} /K	A/F	Pattern factor	EI _{CO}	EI _{UHC}	EI _{NOx}	η _c
423	42	0.28	53	18	1.8	96.9
523	42	0.27	38	8	1.9	98.3
423	70	0.27	132	53	1.2	91.6
523	70	0.41	105	15	1.65	96.1

Table 2 *Exit plane characteristics*

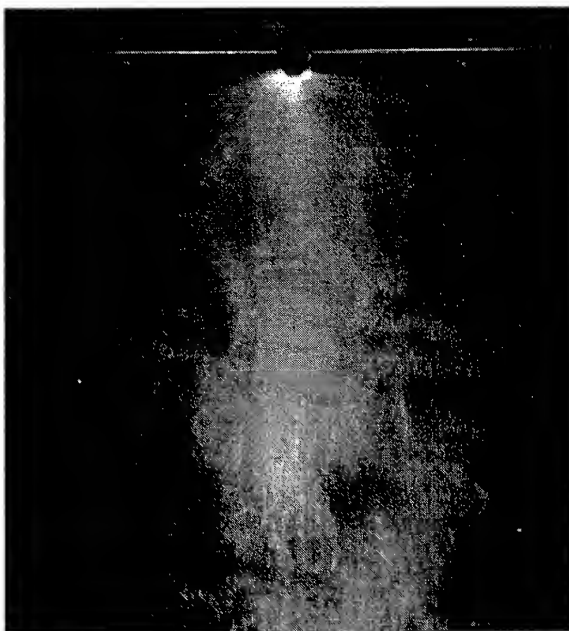
	T-vaporiser*				Gas cones				Fan spray atomisers			
T _{pre}	423 K	523 K	423 K	523 K	423 K	523 K	423 K	523 K	423 K	523 K	423 K	523 K
A/F	42	42	70	70	48	48	80	80	42	42	70	70
Pattern factor	0.42	0.38	0.28	0.22	0.63	0.61	0.5	0.48	0.28	0.27	0.27	0.41
EI _{CO}	299	91.4	27	12	71	66	133	96	53	38	132	105
EI _{UHC}	2.69	0.065	0.04	0.03	4	1.8	71	32	18	8	53	15
EI _{NOx}	-	-	-	-	0	1.75	1.1	1.57	1.8	1.9	1.2	1.65
η _c	97.9	92.7	99.3	99.7	97.0	97.5	88.2	93.4	96.9	98.3	91.6	96.1

* From Perez-Ortiz (1998)

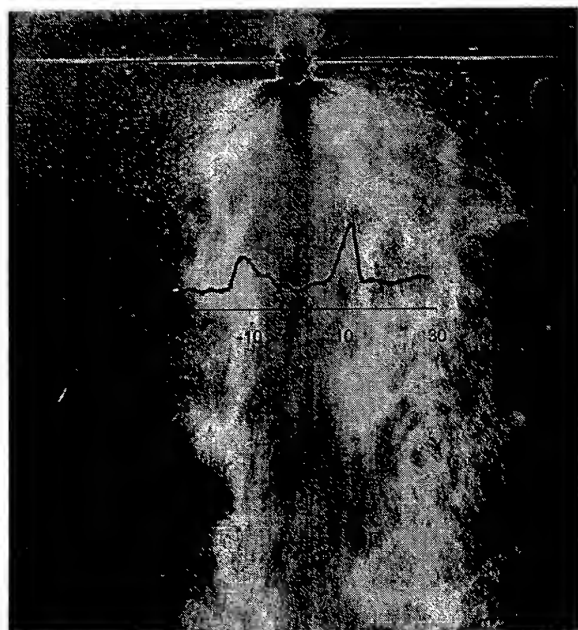
Table 3 *Emissions indices and combustion efficiency of the three different injection arrangements for the GEM model combustor*



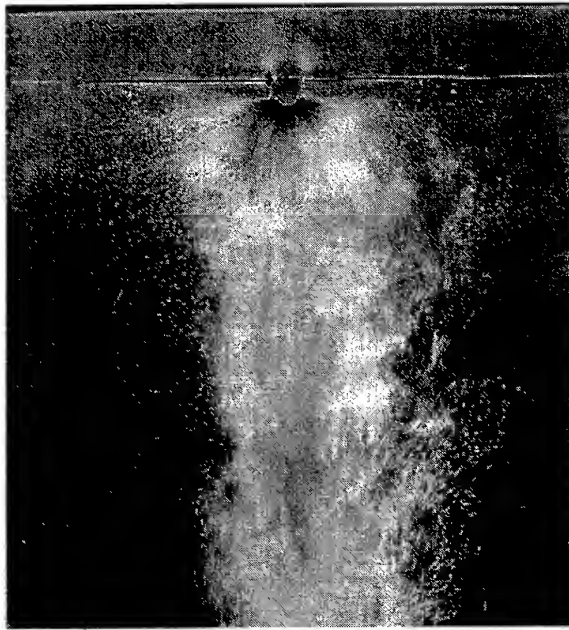
a) No air, fuel flow rate of 0.97 g/s



b) With air, fuel flow rate of 0.97 g/s



c) With air, fuel flow rate of 0.58 g/s



d) With air, fuel flow rate of 0.29 g/s

Fig. 4 *Photographs of the spray at different fuel flow rates*

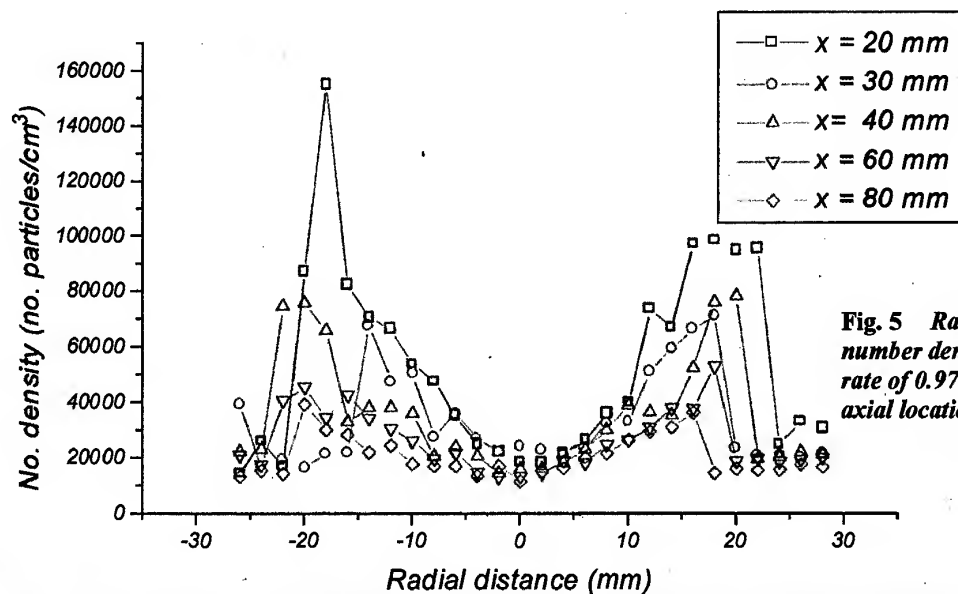


Fig. 5 Radial profile of the number density for a fuel flow rate of 0.97 g/s at different axial locations

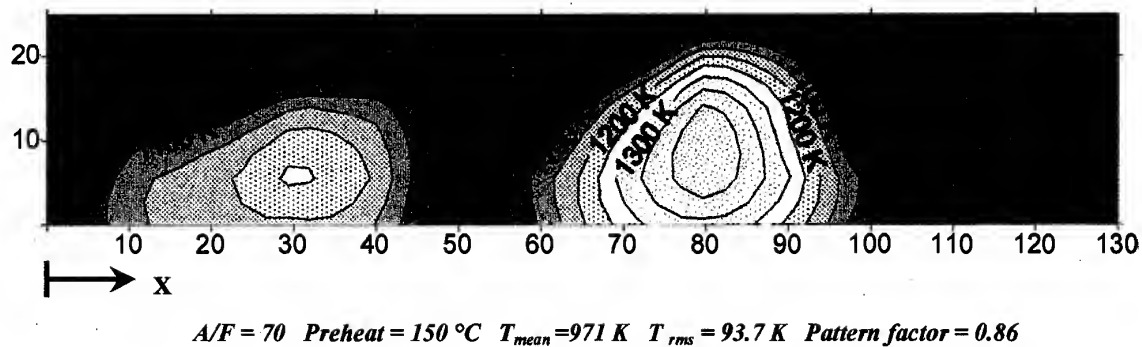


Fig. 6 Temperature profile at the exit plane of the curtailed combustor for a single atomiser for an A/F of 70 and preheat temperature of 150 °C

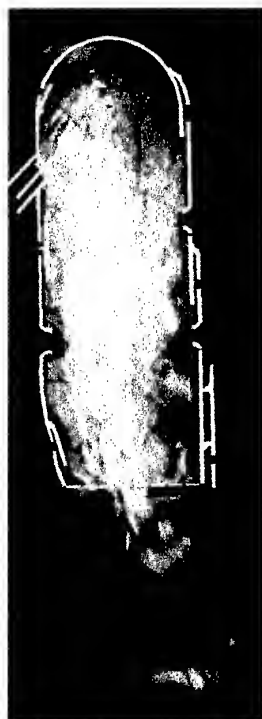


Fig. 7 Photograph of combustor flow at A/F = 42 without the turn around duct with preheat temperature of 523 K

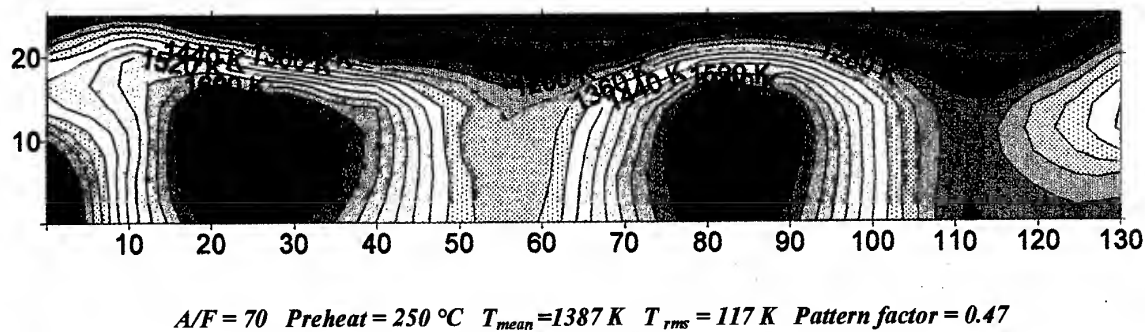
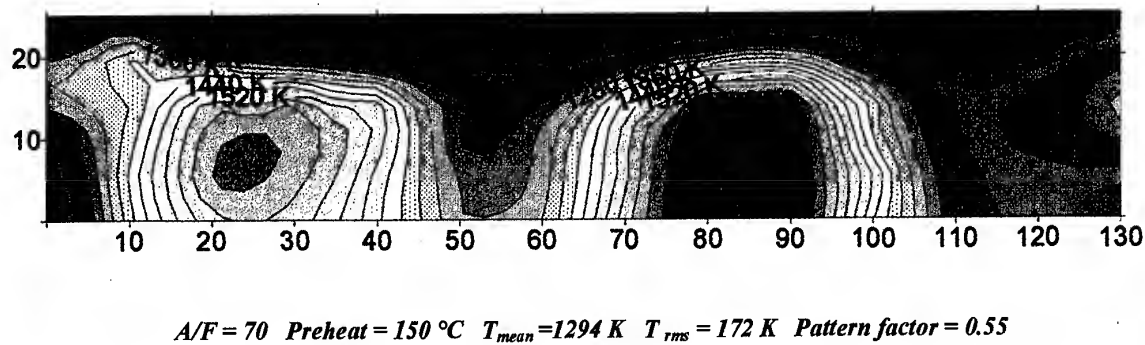
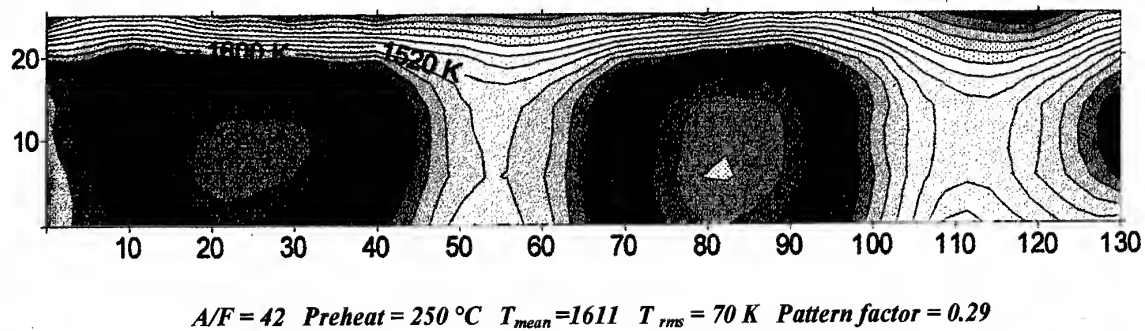
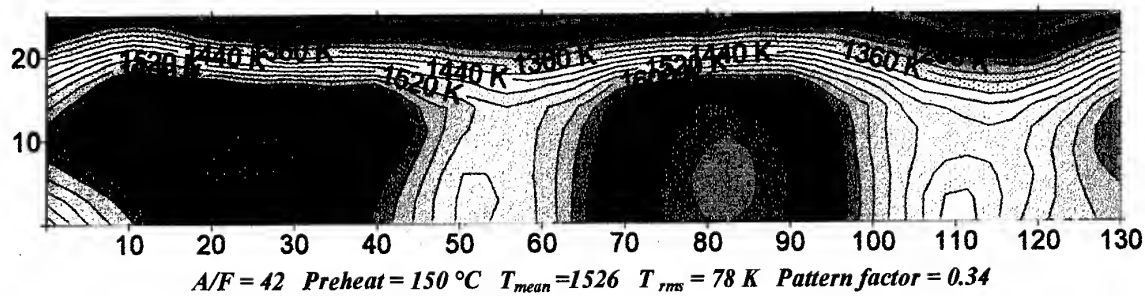


Fig. 8 Temperature distribution in the exit plane of the curtailed combustor

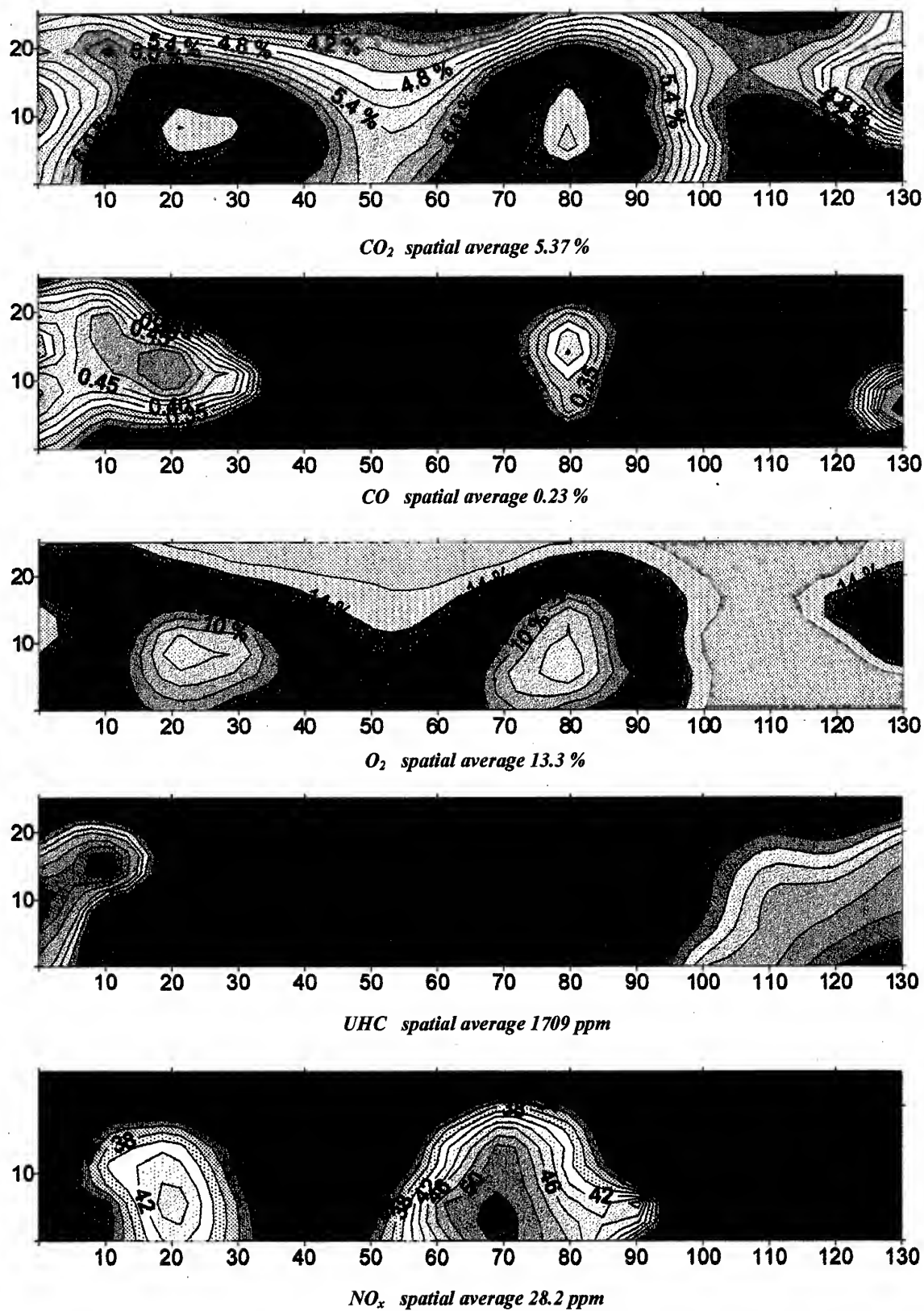


Fig. 9 Distribution of mean species concentrations at the exit of the curtailed combustor for A/F 70 and preheat of 250 °C

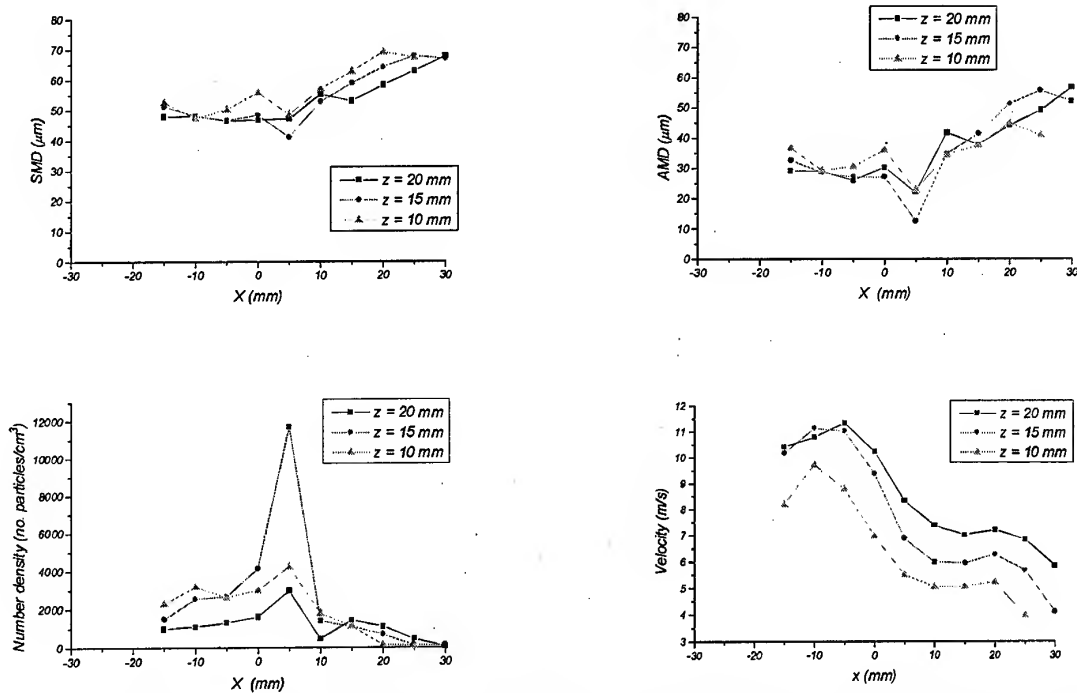


Fig. 10 Droplet size, velocity and number density characteristics inside the combustor for an A/F of 42 and preheat temperature of 523 K

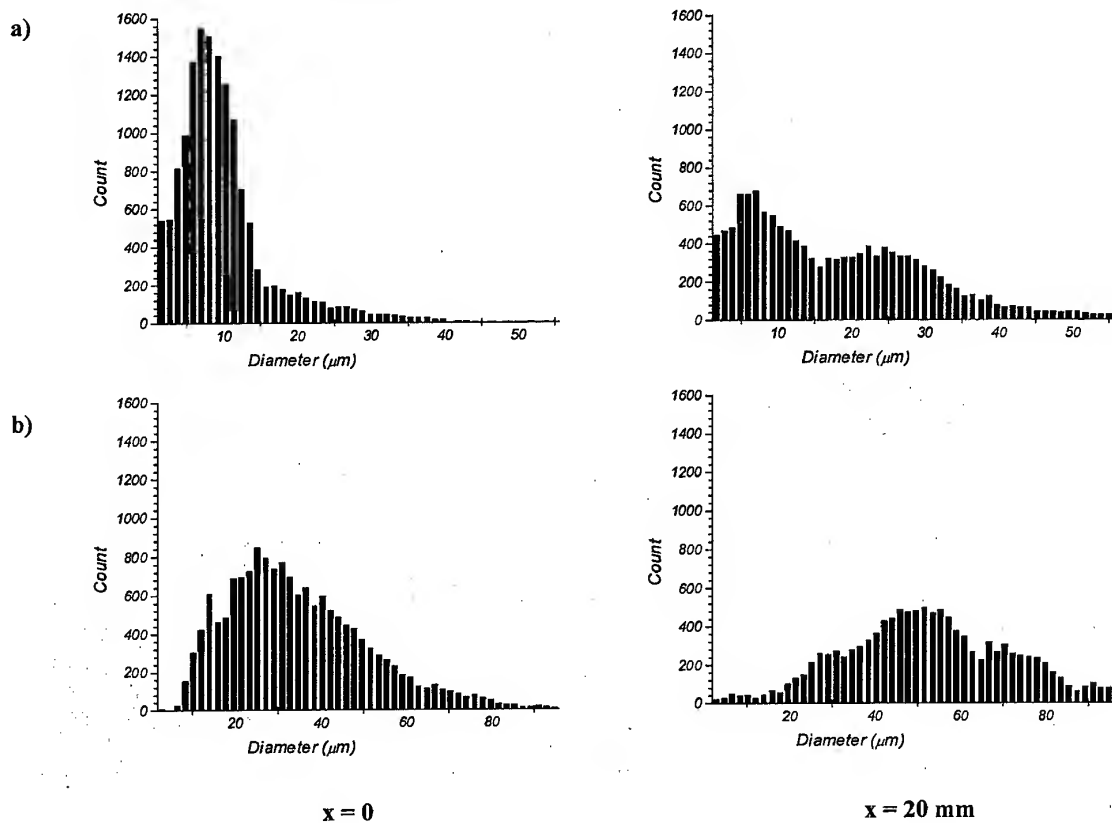
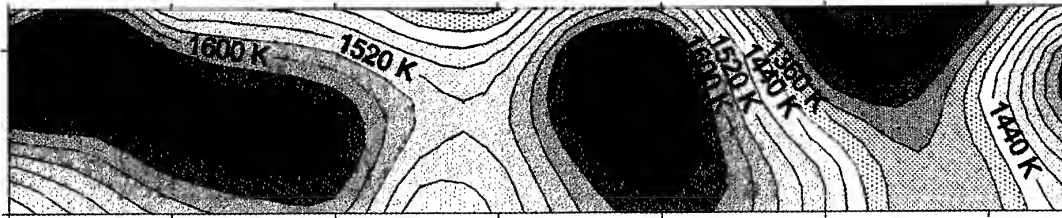


Fig. 11 Comparison of droplet size distributions for the non-combusting free spray at 20 mm from exit of the atomiser (a) and the burning case inside the combustor at a similar location (b)

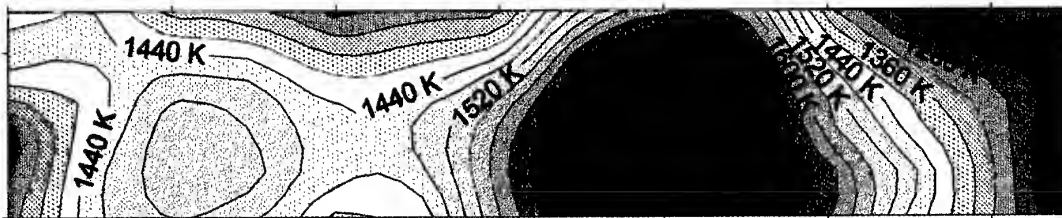
a) Kerosene fuelled, T-vaporiser

$$T_{\text{mean}} = 1539 \text{ K}$$



b) Gas fuelled, gas cones

$$T_{\text{mean}} = 1472 \text{ K}$$



c) Kerosene fuelled, two fan spray atomisers

$$T_{\text{mean}} = 1611 \text{ K}$$

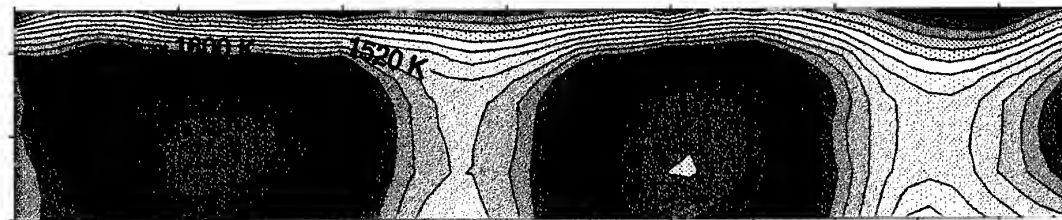


Fig. 12 Temperature profiles for the three fuelling arrangements for an A/F of 42 (equivalent to 48 for methane) and preheat temperature of 250 °C

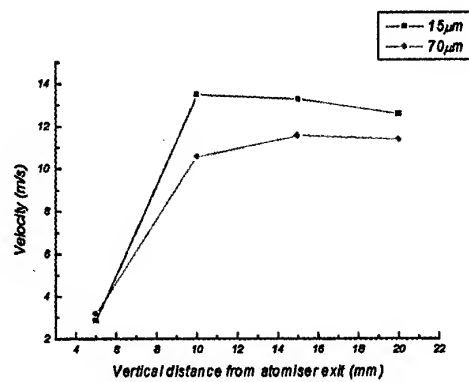


Fig. 13 Vertical component of mean velocity for droplet sizes of 15 and 70 μm as a function of vertical distance from the atomiser

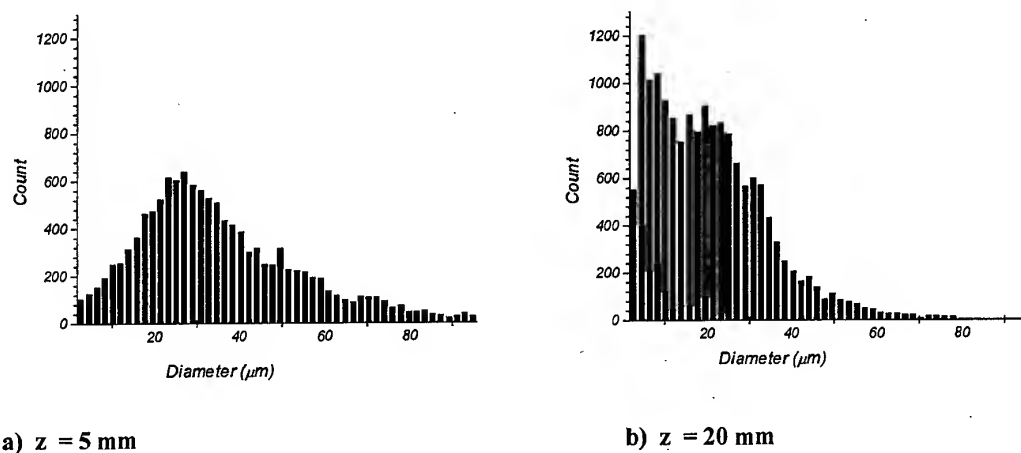


Fig. 14 *Droplet size distribution for the A/F of 42, preheat 523 K at the centre of atomiser ($x = 0$, $y = 6.5 \text{ mm}$) close to the combustor wall as a function of vertical distance from atomiser*

PAPER No. 35
Heyes, Jeleric, & Whitelaw
(presenter: A.L. Heyes)

Question 1: (unknown)

What do you think the effects of combustion pressure would be for the two main types of atomizer that you investigated?

Answer:

The unburned hydrocarbons produce would be reduced due to better fuel atomization, and the NOx would be worsened.

Question 2: V. McDonnell, University of California, Irvine, U.S.

Was it correct that you could not stabilize the combustor with the gas-fueled tee-vaporizer? Can you consider running gas in the tee-vaporizer at a condition more representative of actual engine conditions? The tee-vaporizer was run well at low temperature and atmospheric pressure.

Answer:

Yes, but that was part of a different experiment. The flame could not be stabilized because of the addition of air to the prevaporizer flow caused flame blowoff. Interesting though it may be, we cannot simulate the power condition with gaseous fuel due to the high volumetric flow rate required.

Question 3: C. Berat, Turbomeca, France

Can you explain the asymmetry of the flow at the combustor exit? Was it due to the dilution holes?

Answer:

Yes, there was a flow asymmetry; and yes, it was due to the asymmetric dilution hole array in the combustor liners. Dilution air in the GEM 60 is introduced through two sets of opposed holes; for the sector there are four in the outer liner and two in the inner liner. The non-symmetric arrangement results in the flow asymmetry, as recorded by the temperature and specie concentration measurements.

Question 4: (unknown)

How did you measure fuel droplet sizes during combustion?

Answer:

Droplet sizes during combustion were measured by a PDPA through optical windows provided in the combustor.

Question 5: (unknown)

Did you experience any difficulties with the laser probe volume in the combustor with reaction?

Answer:

We did not observe any beam steering due to gas density effects, and we did not experience any optical interference due to the windows.

AGARD Workshops on Active Combustion Control for Propulsion Systems*

Vigor Yang

Department of Mechanical Engineering
The Pennsylvania State University
111 Research Building East
University Park, PA 16802, U.S.A.

Klaus C. Schadow

Research and Technology Division
Naval Air Warfare Center
China Lake, CA 93555, U.S.A.

1. Introduction

This report summarizes the findings and conclusions of two AGARD workshops on "Active Combustion Control for Propulsion Systems" that were held during May 6-9, 1996, in Athens, Greece,** and during Oct. 16-18, 1997 in Brussels, Belgium, respectively. The workshops, organized in response to increased interest in application of active control in combustion systems, were attended by representatives from industry, government and universities in Europe and the United States. The objectives of the workshops were to: (1) define the requirements of future combustors and combustion processes, (2) determine the status of active combustion control (ACC) systems, (3) assess the potential of ACC to meet goals of the future combustors performance, and (4) determine near- and long-term ACC research and development needs. A special concern of the workshops was the confirmation of international collaborations between organizations working in this field.

Although the earliest proposals for active feedback control of combustors, and the initial experiments, were motivated by the intention to control combustion instabilities in rockets, ramjets and afterburners, subsequent work demonstrated other possible applications. Thus one can now conceive of situations in which the purpose of introducing ACC may be one or a combination of two or more of the following: (1) improve the performance of a combustor (e.g., reduce pollutant and/or noise emissions, reduce specific fuel consumption, increase combustion efficiency, improve pattern factors in gas turbine combustors, etc.); (2) permit modification of combustor design (e.g., reduce its length); (3) damp combustion instabilities; (4) increase combustor reliability; (5) extend operational limits of combustors (e.g., permit stable operation at lower equivalence ratios); and (6) improve performance of other military combustion processes such as shipboard incineration, and power and heat generation in the field. Because the practical problem of suppressing

combustion instabilities has been the chief motivation for investigating the use of active control, it is useful to explain some broad aspects of the subject by considering feedback control of unsteady motions in a combustor. The essential reason for the presence of instabilities in a combustion system is the existence of internal feedback such that energy may be transferred to a fluctuation at a rate dependent on the fluctuation itself. Passive control involves changes of design, either in the composition or types of reactants or in the geometry of the injection system and injector to either 1) reduce the rate of transfer of energy to the motions or 2) to increase losses of energy, for example by the use of suitable resonators to introduce a dissipative process. Use of active control may be effective by causing either 1) or 2) to occur. What may be possible, or what actually happens in a particular case, can be established only by understanding the system in question.

Typically in the experimental work reported to date, relatively simple laboratory burners are used, having relatively large length/diameter ratios. The undesirable oscillations often have motions largely in the axial direction. Control has been exercised, or at least the levels of oscillations have been reduced, by applying several methods of actuation, the most common being: forcing the motion of a portion of the boundary, for example of the inlet; injecting acoustic waves with a loudspeaker; modulating the primary or a secondary fuel supply. The actual performance of the system is monitored by some sort of sensor, in this case a pressure sensor. In general several sensors could be used, distributed in space and measuring several properties of the motions, for example velocity and radiation as well as pressure.

The information acquired by the sensors must be processed and used within the feedback loop to activate a controller whose output drives the actuator according to a control law. Most demonstrations to date have used simple control laws which cause oscillatory actuation to take place at some phase relative to the sensed response of the system and at some amplitude found to give best results, i.e., lowest amplitude of oscillations. That approach is a special form of classical PID (proportional/integral/derivative) in which the control signal is proportional to the error itself, its time-integral, or its derivative. The conditions for most successful operation of combustion systems have always

* Presented at the NATO-RTO Symposium on "Gas Turbine Engine Combustion, Emissions and Alternative Fuels, Lisbon, Portugal, Oct. 12-16, 1998.

** The report on the first AGARD workshop was prepared by K. Schadow, V. Yang, F. Culick, T. Rosfjord, G. Sturgess, and B. Zinn, and was published as AGARD-R-820, September 1997.

been obtained experimentally with little preparatory design work, a consequence of the lack of knowledge of the systems under investigation.

According to the preceding remarks, there are broadly four areas in which research and development must proceed to form a firm basis for practical applications of active control of combustion systems: sensing, actuation, formulation of control laws; and understanding of the systems to be controlled. As part of the progress required, it is essential to acquire understanding of the scaling laws, particularly with respect to the power density of a combustor. This report covers a broad range of issues ranging from future requirements of combustion systems to topics of basic research that must be addressed to realize the promise of active control of combustion.

2. Background

Although active feedback control had been posed and investigated for a restricted class of problems in the early 1950s for reasons cited in the preceding section, the idea was not pursued experimentally until the 1980s. It seems fair to recognize that the work at Cambridge University, supported by Rolls Royce with a view to application to afterburners, marked the beginning of the recent considerable activity in this area. Indeed, the sequence of increasingly more elaborate experimental projects within that program introduced almost all of the novel ideas which subsequently have been vigorously pursued by a large number of research groups throughout the world. In particular, almost all of the types of sensing and activation now being investigated were first used at Cambridge.

The general notion of active feedback control of the dynamics of a combustion chamber has recently attracted intense interest by customers and manufacturers, mainly those producing systems for propulsion and stationary power generation. The chief reasons for this attention include: the trend toward higher combustor pressure (particularly in the past twenty years or so) not only for higher performance in some sense, but also for smaller size, improved efficiency, and reduced emissions of pollutants. While overall efficiency of a system has in the past been largely a matter of gaining a competitive advantage, independent of any regulatory practices, that is no longer the case. Increasingly stringent specifications on pollutant generation will likely be met not only by reducing the amount of pollution produced in combustion of a unit mass of fuel, but also by requiring less fuel to generate a unit of power output or thrust. Those requirements and the traditional methods of achieving desired improvement are discussed in Section 3. An implication of that discussion is that the customary methods of design changes (a strategy of 'passive' control) seem to be approaching their limits. Hence the interest in active control is a direct consequence of widespread practical motivations.

On the other hand, the subject of active control of combustion remains primarily a matter of research. Apart from a small number of relatively recent observations of emission levels, practically all work on ACC has been concerned with control of coherent pressure oscillations, i.e. combustion instabilities. Moreover, there are no available reports of successful application of active control to suppression of combustion instabilities in full-scale systems of any sort. In fact it appears that the available demonstrations of control of combustion instabilities span a small range of scales, both of geometry and power density. Consequently, almost nothing is known about the appropriate scaling laws.

The general reasons why research on active control of combustion dynamics has concentrated on control of combustion instabilities are easy to understand. First, it is generally true that as designs of combustors are pressed to give higher performance – normally a matter of raising power density – the likelihood is also raised that combustion instabilities will occur. Many examples exist for rockets, ramjets, and afterburners. Second, in the past several years, instabilities have become a serious problem in gas turbine combustors under quite different circumstances. In order to reduce production of nitrogen oxides, it is desirable to consume much of the fuel with lean burning to reduce the temperature. That implies operating a combustor as close to lean blow-out as possible. But then the global combustion process – the flame – tends to become unstable. The consequent unsteady motions can couple to global motions in the chamber, producing combustion instabilities.

Finally, there is a class of practical applications including heaters and incineration of waste, for which intentionally pulsed combustion is effective for improved efficiency. Active control of pulsed combustion is attractive to ensure optimum operating conditions, avoiding, for example, inadvertent operation when the pulsations can cause unacceptable rates of surface heat transfer or reduced efficiency.

Several reviews or summaries of the various works on active control have been published, but no extended discussion of the subject has been given in the context of practical needs. Moreover, prior to this workshop there has been no opportunity for the international community of researchers to meet together and discuss the central issues. It became clear in early 1995 that both the research community and the potential users of active control methods for combustion systems would benefit significantly by joining to exchange information and ideas. The state of the field was such that merely presenting and publishing papers would not serve the purpose. A more informal situation was desirable, to allow extended discussions.

Work on ACC is applied research which if successful seems to have virtually immediate application to real systems. However, that view has not been proven. Despite the enthusiasm of all concerned there has been a substantial

gap between the appreciation of researchers for the actual situations in which ACC would be used – the requirements of industry – on the one hand; and on the other hand, users seem not to have a thorough understanding of what really has been accomplished in research on ACC and therefore what one can reasonably expect to accomplish with applications in the near future. A major intention of the workshop was to clarify that situation. Due to the international nature of the communities involved, AGARD offered the best opportunities for achieving that goal. Moreover, it was a hope of the organizers that a workshop would initiate plans for collaboration with international partners.

3. Requirements for Future Combustors

3.1 Introduction

Active combustion control is a technology that has been demonstrated in the laboratory but has not been scaled up to the conditions and size of operational devices. As discussed in Section 6 of this report, research and development needs exist for all components of an active control system – sensor, actuator and controller. It is therefore appropriate to identify the projected needs and challenges for future combustors when determining the application opportunities for active control. This section provides a brief assessment of the requirements for future combustors as used in aeroengine and surface gas turbines, ramjets, and rockets. Section 5 combines these future combustor requirements with the current status of active combustion control technology (Section 4) to identify near and long term applications.

3.2 Aeroengine and Surface Power/Propulsion Gas Turbines

Gas turbine engines have been developed for either aeroengine propulsion or surface power/propulsion. The aeroengine device, which is used for both military and commercial aircraft, always uses direct fuel injection in the combustor. That is, the liquid fuel is injected into the combustor, often by means of an airblast fuel nozzle, where the physical processes of atomization, vaporization and fuel-air mixing occur. In contrast, surface power/propulsion devices, which can be used for ground power generation or ship propulsion, may utilize either direct-fuel-injection or fuel-air premixing. The former is identical to aeroengine combustors, but in the premixed arrangement, the aforementioned physical processes are essentially completed prior to entering the combustor. One consequence of fuel-air premixing is that the heat release is more concentrated. Because of the differences in fuel preparation, the requirements for aeroengines and premixed surface power/propulsion gas turbine combustors may be different.

3.2.1 Aeroengine Gas Turbines

Aeroengine gas turbines provide propulsion for aircraft, both military and commercial. In addition to

requirements on performance and emissions that accompany any powerplant, there is a premium on achieving them in a compact, light-weight device that is very fuel efficient and highly reliable. These demands are projected to become increasingly severe for future aeroengine gas turbines. It is important to determine enabling technologies that might mitigate these challenges.

The basic performance trends for aeroengine gas turbines have been toward increasing thrust-to-weight ratio for military devices, and lower specific fuel consumption (i.e. fuel flow rate per pound of thrust) for commercial devices. The former is sought to increase maneuverability, while the latter supports reduced operating costs. Among the consequences common to both goals is the trend toward higher pressure ratio, with higher temperatures at both the combustor inlet and exit.

Based on these performance trends and mission-driven engine configuration studies, it is concluded that operating conditions for combustion systems will continue their historical trends toward increasing stringency. With long-term goals of doubling thrust-to-weight ratio and reducing specific fuel consumption by 25 to 50 pct, overall pressure ratios in the range of 50 to 75 are virtually certain, and values up to 100 are possible. For commercial applications, bypass ratios could increase to as high as 25 using gear-driven fans. For military applications bypass ratios will be more modest, but turbine inlet temperatures will increase significantly to values associated with combustor equivalence ratios of 0.5 - 0.7. These targets reflect the range of set-point operation over the power curve. The desire for military systems with shorter acceleration/deceleration response times imposes additional demands for more rapid transients between the set-point conditions. At times, the static stability of the combustor, and its adjacent components, will be exceeded.

These projected performance trends will impact the combustor design. Burning-length-to-dome-height ratios will approach 1.5, with a mean radius in the range of 216 to 250 mm (8.5 to 10 in.), regardless of engine airflow; dome heights will be in the range of 50 - 150 mm (2 to 6 in.) depending on the core engine airflow. Combustion intensities will range from 100 to 160 MW / m³ / bar (10 to 16 MBtu / hr / ft³ / atm). While the general combustor configuration will likely remain annular, the combustor inlet section diffuser may be changed for overall engine pressure ratios above 70. Specifically, passage heights in axial-flow compressors at very high pressures can become so small (depending on core engine airflow) that losses due to secondary flow begin to dominate, preventing final high efficiencies from being achieved. Under such circumstances, the final stages of compression might necessarily be done through one or more centrifugal-flow stages. This could have severe impacts on combustor configuration. At high pressures, secondary flow losses might also present difficulties for feeding shower-head cooling schemes in the leading edges of turbine inlet guide vanes. Therefore,

shower-head cooling requirements might preclude the use of ultra-low pressure loss combustors in engines with very high overall pressure ratios. Also the high fuel turn-down ratio associated with high temperature turbines will make fuel-staged combustion systems common.

In order to cope with the requirements for future combustors, enabling technologies must be identified. For the demands discussed above, advances in high pressure fuel pumps, high temperature combustor liner materials, and a fuel system capable of handling super-critical fuels are required. Furthermore, in order to preserve and improve the combustor performance at these severe conditions, means are required for promoting the mixing of fuel, air, and combustion products in the burner, and for preserving stable operation under both steady-state and transient conditions. That is, the critical requirement for achieving the high combustion intensities associated with high pressure conditions, in reduced-size devices, is improved mixing of fuel and air inside the burner. Fuel-air premixing, such as used in some surface power/propulsion gas turbines, is precluded because of the very short autoignition time associated with very high pressure ratio cycles. While adequate mixing and an extremely high combustion efficiency is readily achieved for very fuel-lean operation, efficiency could become mixing-limited for higher equivalence ratios. Improved mixing is also necessary to minimize undesirable emissions of NO_x, CO, and smoke at higher equivalence ratios. Further, the increased combustion intensity at any set-point may increase the likelihood of coupling with acoustic waves and promote combustor dynamics problems. Such problems may also be exacerbated by faster transient responses.

The chemical reactions that determine energy release and pollutant formation occur on the molecular scale. However, the flow in a combustor is turbulent, and the mixing process must cascade down to the smallest eddy before molecular processes can become significant. The minimum turbulent length scale (Kolmogorov), determines the smallest mixing length scale. At atmospheric conditions, the scale is approximately 0.4 mm (0.015 in.) and decreases by three-orders-of-magnitude at 100 atm. In contrast, the dimension of the flow field structures are of the same order as the combustor geometry, which are on the order of 100 mm (4 in.). Hence, the mixing process must progress through an enormous dynamic range before molecular reactions can occur in significant amounts. While a wide range of eddies always exist in the combustor, achieving the stringent standards for efficiency and emission control requires that this mixing cascade occurs quickly and efficiently. That is, to achieve worthwhile improvements in mixing at fixed pressure loss will demand dramatic reduction in the characteristic "integral" turbulent length-scale associated with combustors. Radical geometric changes, such as reducing the combustor characteristic length scale by an order of magnitude, or greatly increasing the number of active shear layers to promote many length scales, appear to be essential.

3.2.2 Premixed Surface Power/Propulsion Gas Turbines

Surface power/propulsion gas turbines provide either ground power or propulsion for ships. Among the critical requirements for these gas turbines is high power density (power per occupied volume), high durability, and extremely low emissions. The latter is distinctively different than for aeroengine gas turbines, with allowed emission levels more than an order-of-magnitude lower. While this standard may not be required of all surface gas turbines (e.g. emission goals for ship propulsion are currently less strict than for ground power gas turbines), economics should drive manufactures to develop only one surface gas turbine design. Since the lowest levels of emissions are obtained through the flame temperature control achieved with premixed combustion, and ground power gas turbines must strive for the lowest emissions levels to be competitive, the industry standard for new surface gas turbines is premixed combustion. The trend in development of surface gas turbines is toward lower emissions levels and higher cycle efficiencies. The former is driven by (real and anticipated) air quality regulations while the latter affects operating cost (i.e. "cost of electricity"). Currently, many ground power gas turbines guarantee NO_x and CO exhaust concentrations limited to 25 ppm @ 15 pct O₂ (i.e. parts per million at a standard exhaust flow dilution to achieve 15 mole pct oxygen). Future products will strive for "single digit" (e.g. 9 ppm) guarantees. Depending on the application, such emission goals may result in engine cycles other than the "simple (Brayton) cycle" – cycles which, for example, extract heat of compression (i.e. "intercool") between two compressors.

The lowest level of emissions is achieved by employing a premixed combustion strategy. Generally, a fixed distribution of effective flow area divides the combustor airflow and delivers the greatest fraction to the set of premixing fuel nozzles. The maximum airflow fraction, or leanest fuel-air mixture, is limited by the lean blowout (LBO) mixture, which is the leanest mixture which will sustain combustion. Starting from a high fuel-air ratio, as the premixing airflow fraction increases, this ratio decreases, as does both the flame temperature and the formation rate of NO_x. However, as the fuel-air ratio approaches the LBO level, the flame temperature will not support sufficiently fast CO oxidation rates and its concentration in the combustor exhaust increases. That is, CO acts as a precursor to marginal stability, reflecting either globally reduced oxidation or the presence of sub-LBO fuel-air pockets which have extinguished. Hence, as depicted in Fig 3-2, there is a "window" of fuel-air ratio, and of corresponding flame temperature, that will simultaneously result in low NO_x and CO. The width of the window will depend on both the inherent combustor stability characteristics and the level of desired emissions control. The figure shows the window width for sub-25 ppm levels; the window is clearly narrower for lower limits. Generally, homogeneous (i.e. non-catalytic) combustion systems do not provide a width covering the full mixture (or temperature) range experienced from low to baseload gas turbine power. Hence, to preserve

ultra-low emissions over a wide power range will require shifting the premixing airflow fraction as the overall fuel-air ratio changes to remain within the desired flame temperature window. It is also true that as the fuel-air mixture approaches the LBO limit, thermoacoustic instabilities become more prevalent. Indeed, premixed combustion, and its intense heat release gradients, provides greater opportunities for coupling with the acoustics and fluid mechanics, and remedies to combustion instabilities are a common development challenge.

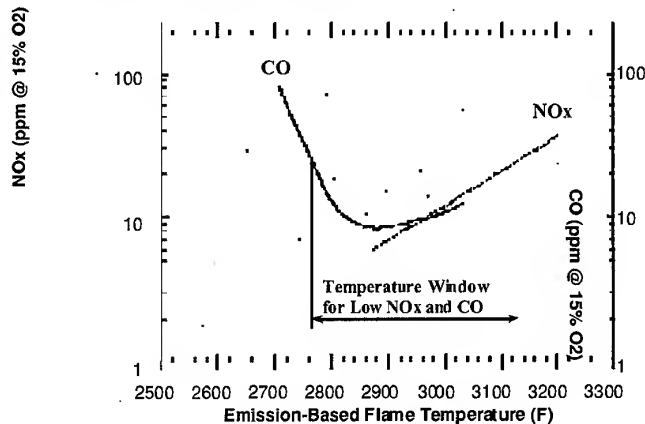


Fig 3-1 Flame temperature window for both low NOx and CO from Premixed Combustion

3.2 Tactical Airbreathing Missile Propulsion

Airbreathing propulsion will receive increasing emphasis to meet future requirements for tactical missiles, with several different types of airbreathing propulsion systems being considered. Most attention is given to the liquid fuel ramjet and gas generator ramjet (ducted rocket). Liquid fuel ramjets are operational in France (ASMP), Russia (Mosquito), and China (Silkworm), and advanced developments/demonstrations are currently being conducted in France (ASLP/ASMP) and USA (Low Drag Ramjet). Advanced development programs for ducted rocket propulsion are being conducted in fewer countries, such as France (MPSR2) and USA (VFDR). Other potential systems are the solid fuel ramjet, scramjet, expendable turbine, and pulsed detonation engine (PDE). The PDE is a device that can increase thermodynamic cycle efficiency by more than 30 pct compared to the constant pressure burn cycle (Brayton cycle) of the other systems, and has self-boost capability. Based on its advanced level of maturity, emphasis will be placed on discerning future combustor requirements for liquid fuel ramjets based on mission demands.

Airbreathing propulsion has the potential for the highest performance per unit volume and weight and is considered for several different missions, including:

- (a) Precision Strike over long range with high sustained velocity and high warhead weight,
- (b) Air Superiority with increased range and maneuverability, and reduced time to target,

- (c) Naval Surface Fire Support with increased range of gun-launched missiles,
- (d) Ship based defense with high velocities and reduced time to target, and
- (e) Surface Air Warfare (Anti-Air) with mission flexibility and log duration.

Surface Air Warfare (Anti-Air) with mission flexibility and long duration.

Generally, modern tactical weapons systems are being driven to longer ranges at minimum volume and weight. These general guidelines translate into specific requirements of: (1) increased kinetic performance to provide increased range and higher sustained and average velocity; (2) increased energy per volume and per weight to reduce weapons size and increase warhead weight; (3) increased propulsion energy management to enhance maneuverability and mission flexibility, (4) increased survivability through longer range launches, increased propulsion duration, higher velocities, and reduced plume signature, and (5) reduced cost.

As indicated in (2), the application of airbreathing propulsion to tactical missions drives the design to ever smaller combustors, which increases both the challenge to achieve high performance over a broad range of operational conditions, and the risk of combustion instabilities. The performance challenge derives from meeting the same high standards for combustion efficiency in higher through-put devices, over broader operational conditions, but with no increase in pressure loss. The risk of instability is a product of both broader operational conditions which drive the burner closer to blow-out, and increased energy release density which enhances the potential for its coupling with fluid dynamic and acoustic features of the burner.

A number of specific requirements can be identified for the liquid fuel ramjet. Future missions will require operation between sea level and 30 km (100,000 ft) altitude with a potential variation of the equivalence ratio between 0.05 and 1.0. Highly efficient and stable combustion must be achieved over the entire operation envelope. For current combustors, efficiency is high at the high Mach number design point but falls off as the mission moves the fuel-air ratio toward either the lean or rich blow-off limits. Combustion instability is often encountered at either a medium frequency range (300 Hz corresponding to a longitudinal mode) or a high frequency range (3000 Hz corresponding to a tangential mode). Currently, the pressure oscillations and mechanical vibration arising from the instabilities (which also impose adverse fluid mechanical effects on the inlet margin) are solved by baffles, aerogrids, and tailored fuel distributions, but at the expense of combustion efficiency and pressure loss penalties. An enabling technology for current and future ramjet propulsion systems is a methodology to sustain stable operation, through either passive design or active control, over a wide range of operational conditions.

Alternative tactical missile propulsion systems include the solid fuel ramjet, scramjet, expendable turbine, and pulsed detonation engine. Specific combustor requirements for a ducted rocket propulsion system are similar to those for the liquid fuel ramjet, while efficient ignition and combustion of liquid hydrocarbon fuels in dual-mode operation of compact designs are technical challenges for the scramjet. Expendable turbine systems require increased performance per volume, possibly through the use of short L/D afterburners, highly energetic fuels, and shorter inlets. The liquid fuel pulse detonation engine must enhance many features including fine-scale and large-scale mixing, fuel vaporization, two-phase detonation and shock-wave propagation, and continuous thrust generation. Clearly, these systems are not as mature as the liquid fuel ramjet.

3.4 Rocket Propulsion

Rocket propulsion systems have been developed for two applications – missile propulsion and space launchers. Each of these may be powered by either solid or liquid fuel. In all of these cases, the propulsion system is designed to deliver the maximum thrust with the minimal volume or weight. Hence the energy release densities are extremely high, and frequently this intensity causes coupling with the combustor acoustic modes to produce combustion instabilities. As a consequence, the global requirement for future rocket propulsion systems is to achieve stable, high power density systems. While both solid fuel and liquid fuel systems have this common need, the controlling processes are not the same, suggesting that the means to achieve stable operation will be different.

3.4.1 Solid-Fuel Rockets

Solid-fuel rocket propulsion systems can be divided in three main applications – tactical missiles, strategic missiles and solid rocket motors (SRM) for large space launchers. This variety results in wide ranges of size and operational conditions, and hence in a wide range of conditions for instabilities. Potentially unstable frequencies can be well predicted from acoustic mode analyses, but identifying which frequencies become amplified, and the resulting oscillatory levels, is beyond current capabilities. Such predictions depend on non-linear influences on various flow phenomena which often depend on frequency (e.g. propellant response, nozzle damping, particle damping, flow turning loss, vortex shedding driving). As a consequence, scaling rules are non-linear, and the extrapolation of results from smaller scale to larger scale devices can be uncertain. Recent CFD analyses of vortex shedding processes in solid fuel rockets have increased an understanding of some of the influences.

Large segmented motors for space launchers (e.g. Space shuttle SRB, Titan SRB and SRMU, Ariane 5 MPS P230) also display acoustic instabilities characterized by low level pressure and thrust oscillations at the first acoustic modes. Such modes are experienced despite being

predicted stable by conventional means. Attempts to expand classical acoustic balance computer codes to include the vortex shedding effects (Flandro's method) have shown some limitations that preclude their everyday use. Ongoing work in France, carried out under the ASSM program supported by CNES, is attempting to validate a full numerical approach for instability prediction at conditions with vortex shedding. Moderate success has been achieved for axisymmetric conditions in a small scale research motor. However, the quality of these results is not sufficiently accurate for industrial purposes, especially considering the required extrapolation to larger scale where both under-predictions and incorrect trends have been obtained.

3.4.2 Liquid-Fuel Rockets

Liquid rocket motors are mainly used in space launchers. They use a variety of propellants, from storable propellants to cryogenic or semi-cryogenic propellants, and can be used for all stages of the launcher. The main challenges for the liquid fuel rocket include increasing performance and reliability, particularly of the turbopumps, while decreasing costs and overall weight. Issues to be mastered include turbopump reliability, wall cooling, combustion efficiency and combustion instability. Techniques to eliminate liquid fuel rocket instabilities are critical since their occurrence can be quickly catastrophic to the system. Modifications to the injection technique and/or propellant formulation have been proposed as potential means to suppress the instabilities by altering the heat release distribution. Baffles have been used to shift the motor acoustic frequencies and avoid heat release coupling. At best, both of these approaches to eliminate the instabilities are highly empirical. While CFD approaches to predict the modes and coupling mechanisms are being developed, their physical basis is immature.

4. Status of Active Combustion Control

4.1 Overview

The concept of active combustion control has appeared in several forms over the past four decades. The first attempt was made by Tsien¹¹ in an effort to apply control theories to suppress the chugging instability in a liquid-propellant rocket engine. His analysis was based on a combustion model which considered a pressure-dependent time lag between the instants of propellant injection and burning. Stabilization of the combustion conditions was achieved by modulating the propellant injection rate through a capacitor controlled by a servomechanism with pressure feedback. The problem of intrinsic stability was studied using the Nyquist plot to determine the suitable servo coefficients. Similar approaches were used by Marble and Cox¹² and Lee et al.¹³ to control the low-frequency instabilities in bipropellant liquid rocket engines. However, no experimental results based on this "servo-stabilization" concept have been published, primarily because of the limitations of instrumentation at that time.

With recent developments in fast-response sensors and actuators, some interesting studies on the active control of various problems have been reported. Pfwowes-Williams¹⁴ described the concept of "anti-sound" ? the elimination of unwanted oscillations in an acoustic field by means of acoustic interference. The basic idea is to first determine the characteristics of a given acoustic field, and then to use that information to manipulate a secondary source of sound which serves as an acoustic actuator. Control is achieved by producing waves out of phase with the unwanted oscillations. In principle, this wave-cancellation technique is applicable to combustion systems; however, implementation to a full-scale combustor is quite unlikely because the energy density of the oscillatory flow field may well exceed that which can be matched by such acoustic actuators as loudspeakers. Furthermore, as a result of the intrinsic richness of the thermo-acoustic interactions, implementation of a control system in a combustion chamber is much more complicated than for normal temperature and pressure environments.

Practical applications of the active control of combustion instabilities have been demonstrated in several research experiments. At Cambridge University, Dine¹⁵ showed that the instabilities of a flame burning on a gauze in a Rijke tube can be eliminated as follows. First, the light emitted from CH free radicals was monitored as a measure of the unsteady heat-release rate from the flame. This information was then processed and fed back to a loudspeaker placed near one end of the tube to increase the acoustic energy dissipation from the boundary. The same problem was studied by Heckl.^{16,17} However, instead of a photo-multiplier, a microphone was used as the sensor to excite the loudspeaker. Results indicated that instabilities can be suppressed over a wide range of phase difference between unsteady oscillations and actuating pressure waves, provided the control gain is sufficiently large. This observation clearly demonstrated that the control of combustion instabilities can not be explained simply by the principle of anti-sound, which requires that the control excitation be precisely out of phase with existing oscillations.

More recently, Bloxsidge et al.^{18,19} reported the control of low-frequency combustion instabilities in a laboratory jet-engine afterburner. The mass flow into the combustion chamber was varied by oscillating a center body inserted in the choked inlet nozzle, thereby exerting the necessary modifications on the unsteady flow fields. The system was partially successful in suppressing the instabilities, with the amplitude of the fundamental mode reduced by fifty percent.

Lang et al.²⁰ and Poinot et al.^{21,22} explored the active control of instabilities in a small laboratory burner, using a loudspeaker as the control actuator. Both experiments used the same gaseous reactants, but with two different types of flame holders: a multiple orifice plate with

80 holes placed in a premixed propane-air stream; and an array of three rearward-facing steps through which fuel was injected into the air flow. Acoustic pressure was measured by a microphone located upstream of the chamber. The signal was then filtered, phased-shifted, amplified, and sent to a loudspeaker plugged to the burner. In addition to the demonstration of instability control, their work showed that the active control technique can be used effectively to study the initial transient behavior of instabilities.

One feature common to the above approaches is that they all used mechanical means, such as loudspeakers or moving bodies, to suppress instabilities. For practical systems containing high energy density, implementation of these means may not be feasible due to the relatively large amount of power required to drive control actuators. It appears that the most direct method of control should be based on the manipulation of energy sources of oscillatory flow fields. Langhorne et al.²³ reported that pressure oscillations in a laboratory afterburner can be reduced significantly by a controlled secondary supply of fuel which is effective in generating the energy necessary for instability control. This method offers a promising solution to problems of low-frequency oscillations in full-scale combustors. Sivasegaram et al.,²⁴ Billoud et al.,²⁵ Wilson et al.,²⁶ and Schadow et al.²⁷ have all demonstrated experimentally the effectiveness of this technique. The theoretical study of Yang et al.²⁸ and Fung et al.²⁹ and the numerical simulation of Menon,³⁰ Shyy et al.,³¹ and Neumeier and Zinn³² have also demonstrated the viability of controlled fuel injection. For detailed reviews of active control of combustion instabilities, see Culick,³³ Candel,² and McManus et al.¹

In addition to its applications for propulsion systems, active control technology has been used to enhance mixing in incinerator afterburners and to increase the DRE (destruction and removal efficiency) for waste materials. Parr et al.⁹ have conducted a detailed study of the concept of utilizing vortex combustion for incineration in a small-scale gaseous fuel system and an extension to a more practical system using liquid fuels. Acoustic excitation was used to stabilize coherent vortices in the air flow, with the fuel modulated and introduced into the air vortex exactly at the instant of vortex formation. This concept has demonstrated its effectiveness in improving waste destruction. The DRE for liquid benzene exceeded 99.999% for a afterburner/incinerator of 56 kW energy release, even when the waste surrogate constituted 17% of the total fuel content. The controller also reduced emissions: CO dropped from 2900 ppm to as low as 2 ppm and NO_x was reduced to 12 ppm. Parameters critical to the controller performance were the forcing level of the fuel injection, the fraction of the circumferentially entrained air, and the phase angle of the fuel injection with respect to the air vortex roll-ups.

The most common sensor used in ACC is the pressure transducer. For controlling combustion instability this is a

natural choice, as the instability is characterized by the chamber pressure oscillations. Experimentally, photomultipliers have also been successfully used, since their signals can give a measure of the unsteady heat release which is at the root of the instability. The placement of either type of sensor is important. For example, the shapes of the chamber acoustic modes should be sufficiently well-known to avoid placing a pressure sensor at a pressure node point. Also, a photomultiplier's signal could be misleading if the sensor is positioned so that its field of view does not completely cover the entire range of motion of a spatially varying reaction zone. Recent advances in machine vision applied to an array of optical sensors may offer a solution, and also provide the controller with information regarding the global distribution of unsteady heat release. Of course, optical access (including interference by sooty flames) is another problem. Other optical sensors, such as laser-induced fluorescence for species measurement and LDV for velocity sensing are probably unfeasible for practical applications, but may be useful in experimental control systems. Optical sensors may be key in pattern factor control, since the temperature distribution throughout the cross section of a chamber is desired.

For combustion instability control, most ACC actuators attack either the acoustics (directly with mechanical acoustic actuation or indirectly through controlled fuel flow), or the hydrodynamics of a reacting shear layer in a dump combustor (by fluid dynamic forcing near the origin of the shear layer). The former approach is sensible in that chamber acoustics play a defining role in the energy feedback loop which causes high-frequency instabilities. The latter approach also has intuitive merit since the spatial and temporal unsteadiness of the heat release (source of energy for the instability) is strongly tied to the turbulent hydrodynamics of the shear layer. Both actuators have demonstrated varying degrees of success in closed-loop control, and shear layer actuation has exhibited positive influence in open-loop mode. Perhaps tandem acoustic and hydrodynamic actuation could accomplish more than either one alone.

In regard to controller design, most studies have used either fixed-parameter or adaptive approaches:

(1) In a fixed parameter controller, the parameters which define the behavior of the controller do not change with time or with the state of the system. If a reliable model is available, the design of this type of controller can take advantage of well-developed and powerful control and optimization theories. The robustness issue is also most easily addressed for such control design. Unfortunately, no complete model for practical combustors exists, and the closest approaches (i.e. CFD simulations) are far too complex for direct incorporation into viable controllers. Reduced-order models may be used to develop the controller,^{28,29,34,35} but these models usually contain unknown parameters. System identification can help to

define these unknowns by effectively matching the behavior of the model to that of the actual system. Fundamental empirical studies may also aid in this way. Fixed-parameter controllers do not need to be model-based. For example, intuitive gain/phase relationships between the sensor measurements and required actuator signals have been assumed in many successful experiments. Although the controller gain and phase are adjusted for optimal damping of the combustion instability ("manual adaptation"), the controller would be essentially fixed-parameter in application. This approach was apparently also taken in Ref. 30, where a CFD-simulated "virtual combustor" was used to adjust the controller. This underscores the emerging value of CFD as a means of developing and testing controllers, as well as for increasing physical insight and understanding.

(2) An adaptive controller automatically adjusts its own parameters to achieve desired performance of the controller. In direct adaptation, the control parameters are changed based only on a measured performance function. This approach is demonstrated in Padmanabhan et al.,³⁶ where the Downhill Simplex method was used to seek control parameters which minimized the instability through shear layer actuation. In indirect adaptation, on-line system identification is performed continuously to maintain a locally accurate, updated model of the system; then the controller uses the model's parameters to adjust the control parameters and generate the actuator signal. The model in this case can be a generalized one detached from the physics of the problem (such as an FIR filter used by Billoud²⁵), or it can incorporate physical understanding. Although adaptive controllers are more complicated, their flexibility may be crucial for combustion instability control in the face of changing operating conditions, imperfect knowledge of the system, and changing or multiple modes of instability. Adaptive approaches have demonstrated practical success in the related field of noise control, and appear feasible in combustion control as well. More advanced control involving artificial intelligence techniques such as fuzzy logic and neural networks may eventually offer new solutions to the ACC problem. Although such schemes have been practically demonstrated in noise control, their ill-understood nature makes them unlikely candidates for systematic application in reliable ACC systems, at least in the near future.

Physical modeling can enhance the control design, and is a necessary component of some controllers. Many modeling efforts have concentrated on a specific process, such as acoustics or shear layer hydrodynamics. However, studies such as Cohen and Anderson³⁸ suggest that both acoustics and shear layer hydrodynamics are important in some instabilities. Instances of hysteresis in combustion chambers and significant changes in the nature of the unsteady heat release (such as the "pinching-off" of burning lumps of fuel²¹) also suggest acoustic/hydrodynamic interaction. The consideration of entropy modes may also be appropriate in systems. Although liquid fuel feed

systems typically respond only to low-frequency (<100 Hz) chamber oscillations, the gas-filled volume of a premixer may respond to chamber acoustic modes, causing unsteady flow of fuel-air premixture into the chamber and feed-system like instabilities. In addition to the combustor itself, modeling of the actuator can be an important issue, especially for injection of controlled fuel.³⁴

Finally, in any controller, it is important to squeeze the maximum amount of (accurate) information from the available sensor data to determine the state of the system being controlled. This issue of observer design has been explicitly addressed in Ref. 32. The presence of noise in a combustor, system uncertainties, and what information must be known a priori about the system are important considerations in observer design.

4.2 Recent Results

The status of the various ACC programs currently being conducted within the AGARD community was summarized at the workshop. These programs cover a broad spectrum of problems related to combustion instability and pollutant emissions. Schadow and his coworkers at the US Naval Air Warfare Center have been working on the detailed understanding of fluid dynamic/acoustics/combustion interactions. In particular the effects of large-scale structures and their transition to fine-scale mixing are being considered. The ACC is applied to a variety of combustion devices, including ramjet dump combustors and incinerator afterburners. Both systems have similar combustion characteristics with flame stabilization at a backward facing step or dump region. For these flow conditions the development of jet shear layers is critical for the combustion processes, including flammability limits, combustion efficiency, and flame stability (combustion instability). The ACC work is therefore based on controlling jet shear-flow dynamics, which are characterized by flow instability frequencies associated with initial vortex shedding and subsequent vortex merging, as well as the jet preferred mode at the end of the jet core. The physical understanding of the relationship of these flow instability frequencies and acoustic driving frequencies is critical for the control process.

The application of ACC to suppression of combustion instability was also discovered by Zinn of the Georgia Institute of Technology. The system consists of an observer that uses an iterative, Fourier-like approach to determine the amplitudes, frequencies and phases of unstable combustor modes in real time. This information is sent to a controller where open-loop test data are used to determine the gain and phase shift that are added to each unstable mode. The modified modes are combined into a control signal that is delivered to a fast response fuel injector actuator that varies the length of a magneto-strictive material and, thus, modulates the injection rate of a secondary fuel stream into the combustor. The latter damps the unstable combustor modes by generating secondary heat addition oscillations out of phase with the pressure oscillations. To date, open

loop tests has been performed to determine the frequency response of the fuel injector actuator, which was subsequently used in the closed-loop control tests. These tests showed that the developed system effectively damps large amplitude instabilities. For example, the amplitude of the most unstable combustor mode was damped by 26 dB within 40 milliseconds after activating the control.

In a research project sponsored by the US Navy, Yang and his colleagues of the Pennsylvania State University have been working on the development of integrated control methodologies for gas-turbine combustors in order to enhance performance in terms of lean blowout and combustion stability characteristics, while maintaining pollutant emissions within permissible limits.⁵⁶ A variety of active control techniques are systematically evaluated and implemented in a hierarchical approach. The control strategies are established at two levels. High-level control is carried out using modulated secondary fuel injection directly into the flame stabilization zone. Their process is appropriately synchronized with local heat release and pressure oscillations in order to stabilize the combustion flowfield and consequently extended the operating range. Low-level control is carried out using variable air swirl. This is used to change the degree of fuel-air mixing at the

combustor inlet in order to achieve minimum NO_x emissions over the entire operating range of the combustor. The two-level strategy, together with appropriate combustion transient sensors, will be part of an ACC system which will extend the stable operating range of the NO_x combustor and reduce emissions. In addition, innovative concepts for diagnostic and prognostic decision-making will be incorporated into the control system to enhance engine reliability. Optimization of combustor operations will be conducted based on requirements for flame stability and pollutant emissions. When coupled with a global engine control system, this combustor control system will allow for the development of fuel-efficient and clean gas turbine engines.

Several research groups have discovered the presence of hysteretic behavior in the vicinity of the stability boundary for oscillations in a dump combustor. The phenomenon is observed as the fuel air ratio is changed with all other parameters fixed. The existence of the hysteresis loop is the basis for a strategy of nonlinear control recently demonstrated by Culick⁵⁷ of the California Institute of Technology. When the system is operating on the upper branch of the hysteresis loop, the system can be forced to make the transition to the lower branch by injecting a single pulse of secondary fuel at the dump plane. Thus, by applying active control, the region of stable operation can be extended. Perhaps the most significant aspect of these results is that successful control has been achieved because the dynamics of the system are understood, and the control law was suitably constructed.

It is particularly important to notice that the behavior treated with this method is intrinsically nonlinear. Application of linear control ideas would be inappropriate and much less successful. A fundamental matter is the extent to which truly nonlinear control can be extended outside the region of hysteresis.

The ACC research conducted by Whitelaw and his associates at the Imperial College attempts to suppress combustion instabilities, extend flammability limits, and minimize emissions in a variety of geometric conditions. These include ducted premixed flames behind one or more bluff-body stabilizer; a model of an industrial burner; a model of an annular gas turbine combustor; and an opposed jet flame. Discrete-frequency oscillations are imposed on the flows using actuators such as acoustic drivers, periodic spark ignition of part of the fuel, and devices to oscillate liquid and gaseous fuel flows and a spray of water. The frequency limitation of the injectors was overcome by fuel injection at half the dominant frequency and the sequential operation of injectors. Control of the oscillations also led to a reduction in NO_x emissions by 5% with oscillations of liquid fuel and by 50% with a spray of water. The latter is due to heat removal. The rich flammability limits of a model industrial burner was extended from an equivalence ratio of 1 to greater than 3 by the addition of oscillations by a loudspeaker. At the same time the flame was more stable and more compact. Imposed oscillations had an adverse effect on the lean flammability limits which was partly overcome by the dilution of the fuel with air.

Burkhardt of Technical University in Hamburg-Harburg studied active combustion control of a bunsen burner flame using image processing sensors which can be superior to point sensors⁵⁸. Using a CCD camera with 250000 diodes, it is possible to carefully characterize the state of the combustion process, for example, by analyzing turbulent and non-homogeneous reaction zones. In his experiments non-optimal burning states are recognized and corrected/optimized by closed-loop active control. Two different approaches, namely optimization techniques, and fuzzy logic and neural networks, were used to analyze changes in the image sequences. Both control strategies are able to "learn" an optimal state which is set up by a human expert and determine necessary actions for active control to optimize the reaction process. For the optimization technique, the image of a non-sooting flame was selected as the optimal burning state. By proper application of image processing techniques they continuously extract image features from the combustion process to compare with a feature which is the optimum state obtained by a learning procedure. They use a quadratic, multispectral performance criterion to optimize on-line using the modified Newton-Raphson algorithm. For the fuzzy logic technique⁵⁹, a small number of features (such as flame height and brightness) which are closely related to the state variables, are extracted. These features were compared with those obtained in the optimum combustion state, and the deviations are sent to the neural-network-based controller. The implementation of

the fuzzy controller in the form of a neural network provides the possibility that the system can learn from the environment and improve the robustness against the environmental disturbances through updating of the network's weights. The system determines a control action by using a neural network which implements fuzzy inference. In this way, prior experts' knowledge can be incorporated easily.

ACC research is being conducted at UTRC under internal and DARPA funding on lean premix burners using both gaseous and liquid fuels. The focus of the research is on the control of combustion instabilities. The research is experimentally based, using a small scale atmospheric pressure rig for screening of actuation and control concepts, and a single nozzle rig running engine scale hardware at combustor operating pressures and temperatures. Actuation concepts involving fuel flow control are being evaluated. Methodology and hardware have been developed that have sufficient bandwidth to control instability frequencies up to about 200 Hz. Significant reductions in instability pressure levels have been demonstrated. For example, during screening tests on the atmospheric pressure rig operating on gas fuel, up to 8 dB reduction in combustion instability pressure oscillations were achieved using a pilot for control.

Active control has been investigated at Ecole Centrale de Paris as a means for reducing the level of nitric oxides emitted by liquid fuel combustors.^{60,61,62} Experiments carried out on a 25kW domestic boilers and a 850 kW furnace indicate that reductions of up to 30% may be obtained by open loop control techniques. This demonstrates that active control principles may be used to improve combustion in practical systems.

Work on ACC has been carried out at IST, Lisboa, Portugal, aimed at suppressing oscillations and reducing NO and CO emissions. The technique used was the sinusoidal forcing of the gaseous fuel stream with phase shift control. A wall static pressure probe was used to detect the pressure in a tube and disc burner. It was shown that different disc sizes and geometries were effective to reduce NO and CO production. This ACC work is related to earlier passive control work where pressure oscillations were reduced using different bluff body geometries.⁶³

ACC research has been conducted at the Munich University of Technology, Germany, for more than 10 years. The main aspect of this research, which was started with a joint project with Ecole Centrale de Paris,^{20,21} is the active suppression of self-excited combustion instabilities and actuators.^{65,66} The research is the basis for an industrial application of ACC to a full-size stationary gas turbine with an electric power output of 170 MW. This project is producing very encouraging results, which will be published at the ASME ASIA 97 Conference and the "18 Deutsch-Niederlaendische Flammentag."

5. Active Combustion Control Applications

5.1 Introduction

The review of future needs presented in Section 3 described several challenges which may limit the growth potential of combustion systems. For example, the evolution of aeroengine gas turbine combustors with very high pressure ratios may depend on achieving greatly accelerated mixing rates to preserve highly efficient operation at such high combustion intensity conditions. Some of the challenges may be mitigated by successful application of active combustion control methodologies. The following table depicts, for the major combustion systems, such challenges and the relative priority determined at the AGARD Workshop, based on a composite consideration of basic understanding, risk, and benefit. As indicated, a common combustion system challenge believed addressable by active combustion control was instability control; it was identified for all systems. The reason for "low" relative priorities assigned to aeroengine systems was because other systems had a more immediate need. A "low" relative priority for liquid fuel rockets was assigned because the perceived risk was very high in order to achieve a successful active control application. The reason for "high" relative priority for surface power gas turbine instability control was because it is an acknowledged developmental challenge for all manufacturers, and also laboratory demonstrations have shown the potential for active control to mitigate it. The "medium" relative priority for airbreathing missile and solid fuel rockets instability control reflected developmental needs and a belief that the key physical phenomena were known.

Relative Priority for Active Combustion Control

Combustion System	Operational Challenge Addressable by Active Control	Relative Priority
Aeroengine gas turbine	Enhanced mixing	Low
	Instability control	Low
Surface power gas turbine	Instability control	High
	Flame temperature control	Medium
Airbreathing missile	Instability control	Medium
Solid fuel rockets	Instability control	Medium
Liquid fuel rockets	Instability control	Low

Together, instability controls in surface power gas turbines, airbreathing missiles, and solid fuel rockets were judged to be high impact applications for active combustion control. Successful application of active control methodology will expand the operational capabilities of

each system to broader conditions while preserving attributes of high efficiency, stability, low emissions, etc. In pursuit of these applications, developments in sensor and actuator technology will be required to provide highly responsive, precise, and reliable devices. Further, it is important to expand the experience base for the applications from laboratory scale and conditions to realistic hardware and conditions. For example, actuator capacity which may be suitable for atmospheric operating conditions may not function at elevated pressures and flowrates. Moreover, neither the identification of the key physical instability coupling phenomena, nor their scaling to other conditions, are known. Hence, the potential demonstrated at reduced conditions does not guarantee any payoff at real conditions. The logical development of all elements of the active control system, and their use in more realistic devices, will result in new options to the combustion system designer, and permit growth of the system's potential. In the following sections, active combustion control applications specific to surface power gas turbines, airbreathing missiles, and solid fuel rockets are discussed.

5.2 Surface Power Gas Turbines

Increasingly stringent emissions standards will raise the challenge for surface power gas turbines to operate stably. That is, in order to meet lower emissions goals for NO_x and CO, premixed combustion systems will be used and operated at very lean fuel-air ratios. As previously discussed, the leanest mixture will be set by the stability characteristics of the combustor – both the static stability characterized by lean blowout and the dynamic stability characterized by lean-limit, acoustic-coupled instabilities. Both of these narrow the operational flame temperature window, and are currently encountered by most manufacturers of industrial gas turbines. Active combustion control is a technique believed capable of mitigating the lean-limit instabilities.

Subscale demonstrations of suppressed combustion instability have been performed at reduced pressure and temperature operating conditions. Such tests, performed for premixed and direct-injection systems, have shown that significant reductions in the combustor pressure oscillation can be achieved for instabilities experienced at frequencies up to approximately 300 Hz. While the coupling driving the instabilities is often termed thermo-acoustic, a detailed understanding of the key processes is not available; successful demonstrations have not relied upon this knowledge. Generally the approach is to modulate a secondary fuel injection (or pilot) in a manner to either interfere with the coupling mechanism or cancel the pressure perturbations. Control algorithms often adapt to the instability because of the wide range over which stable operation must be preserved, and both electro-mechanical and advanced material- (e.g. magnetostrictive) based actuators have displayed sufficient capacity and responsiveness for these demonstrations. While such subscale tests have shown the promise of achieving instability control of premixed combustion, these studies

must be extended to realistic operating conditions. Both reliable, durable actuators with capacities consistent with real operating conditions, and control strategies capable of breaking the coupling mechanism, must be achieved. Further, the actuator authority must be sufficient such that any fuel perturbation does not compromise the combustor emissions goals. Ongoing studies suggest that the desired attributes of active stability control are achievable.

5.3 Airbreathing Missiles

Future requirements for tactical missiles will drive the design to even smaller combustors that must maintain high-level and stable combustion over even broader ranges of operation. Active combustion control has the potential to meet these challenges. In the near term, suppression of low-frequency combustion instabilities by active control should be achievable, while in the long term, the extension of lean blow-out limits may also be realized. This promising outlook is based on the fact that the critical role of shear-flow dynamics (or the development of large-scale structures and their break-down into fine-scale turbulence) for the combustion characteristics in ramjets, the airbreathing missile combustor, is well understood. While this is particularly the case for the center-dump combustors, an understanding of the underlying unsteady fluid dynamics found in annular and side dump combustors needs further research.

Methodology to suppress low-frequency combustion instabilities in center-dump combustors has been successfully demonstrated in laboratory tests suggesting that its application to full-scale combustors is a realistic goal. The suppression of these oscillations are critical, because they can reduce the inlet margin, resulting in inlet unstart. While scale-up and transition to realistic operational conditions remain a technical challenge, current physical understanding and control strategies for vortex-driven combustion instabilities makes near-term success likely. The demand on missile system actuators and sensors to control instabilities in the frequency range of 100 to 300 Hz is reasonably within capabilities. Higher frequency-response pressure and emission sensors and liquid fuel actuators for periodic fuel modulation are being explored in the current laboratory experiments. Simple fixed parameter controllers will be used for initial experiments to determine their adequacy, with neural net and model-based adaptive controllers being considered as future alternatives.

The role of shear-flow dynamics in influencing flame blow-out limits is less understood than for combustion instabilities. Therefore, the application of active control to extend blow-out remains a longer term goal. In limited experimental experiences, flammability limits were extended by increasing fine-scale turbulence, and hence molecular mixing, by high-frequency acoustic excitation. However, practical actuators would require a higher bandwidth performance than for the combustion instability control.

5.4 Solid-Propellant Rocket Motors

Combustion instabilities remain a major concern in the development of solid-propellant rocket motors. This is particularly true for large motors including strategic missiles (about two meters in diameter) and space launchers (about three to four meters in diameter with large aspect ratio) loaded with metallized composite propellants, where modifications are more expensive and time-consuming. Active control may play an important role in curing the instability problems for this type of motor, since the pressure oscillations are dominated by low-frequency longitudinal modes, which are more accessible to control than higher-frequency oscillations associated with smaller motors. A concerted program for active control of combustion instabilities in large motors is currently being prepared by French laboratories with possible participation of a United States company or laboratory. The control strategy is based on modulated injection of liquid monopropellant at the head-end in a closed-loop system.

5.5 Military Burners and Incinerators

Successful application of ACC to military burners and incinerators will provide a promising opportunity to meet emerging emission standards. In particular, real-time monitoring of selected species should be included as an integral part of the control system. As demonstrated in a compact incinerator program, ACC implementation into burners with high energy densities can yield environmentally sound combustion processes which are not possible based on presently available technologies. Since the control strategy was established through detailed understanding of the combustion dynamics involved, the ACC approaches for incinerators can be readily applied to other burners for minimizing hazardous emissions.

6. Research and Development Needs

6.1 Introduction

Since the potential benefits of ACC are still uncertain, one of the main objectives of near term ACC research should be to demonstrate and quantify the advantages of ACC relative to other approaches. Subsequent efforts should develop know-how to guide the development and optimization of practical ACC systems. Such information must be obtained from research and development programs which investigate problems unique to the systems at hand (e.g. rocket, gas turbine, and ramjet combustors and military incinerators), and from active control studies in related engineering applications (e.g., active noise and vibrations control). Combustor-related ACC studies may, for example, investigate fundamental processes in uncontrolled and controlled combustors, develop sensors and actuators that satisfactorily perform in the harsh combustor environment, and develop models of controlled combustors. Parallel studies will have to address more general issues such as development capabilities for real time data acquisition and analysis, microelectronics, computers, software, and

nonlinear control. These research needs are discussed in the remainder of this section.

6.2 Understanding Fundamental ACC Processes

To effectively implement ACC, it is desirable to understand the fundamental aerothermochemical processes that must be controlled. For example, it is well known that combustion instabilities in dump combustors are driven by a feedback process involving periodic vortex formation and combustion processes.³⁹⁻⁴¹ During an instability, a decrease in the combustor pressure increases the velocity of the reactants flow into the combustor. This is followed by the formation of coherent vortical structures that are ignited, after a time delay, as they entrain hot gases and/or burning gas pockets. Ignition is followed by a "sudden" vortex breakdown and nearly instantaneous heat release in phase with the local pressure oscillations, which provides the energy needed to drive the pressure oscillations, according to Rayleigh's criterion. The cycle repeats itself when a subsequent combustor pressure drop near the dump plane produces another increase in the reactant flow rate into the combustor and vortex formation. This understanding of the driving process could be used to guide the development of ACC approaches for controlling such instabilities. Candidate schemes include: developing a process that prevents periodic formation of vortices; generating a secondary, periodic, combustion process within the combustor (e.g., by periodic fuel injection^{1,2,8}) that damps the instability by releasing energy 180 degrees out of phase with respect to the unstable pressure oscillations; or using mechanical drivers (e.g., oscillating valves, speakers) to excite pressure oscillations out of phase with respect to the combustor pressure oscillations (i.e., anti-sound³). Research must be performed to determine which of these proposed (or other) approaches will provide the most effective ACC.

The importance of understanding the fundamental processes in a controlled combustor is further illustrated in the case of secondary fuel injection^{1,2,8} to control combustion instabilities. Here, the ACC modulates the injection rate of a secondary fuel stream into the combustor, generally at the frequency of the unstable oscillation, to generate a secondary heat release process that damps the instability. Practical applications of this ACC technique will seek maximum damping with a minimum secondary (control) fuel flow rate. Therefore, the following questions must be addressed: (1) Does the secondary fuel injection modify the nonlinear combustion process that drives the instability and/or does it generate "another" (independent) combustion process that excites "separate" heat release oscillations out of phase with respect to the unstable pressure oscillations? (2) What is the optimum location(s) for secondary fuel injection? (3) What is the optimum secondary fuel flow rate? (4) If a liquid fuel is used to damp the instability, what should be the characteristics of its spray to optimize damping? (5) What is the optimum number, diameter, orientation and velocity of the secondary fuel jets?

To realistically evaluate a proposed ACC approach, it should be initially investigated in a small scale experiment that closely simulates the full scale system design and operating conditions. Ideally, this could be accomplished by requiring that the following parameters be the same (or close) in the experimental and full scale setup: (1) the Mach, Reynolds and Strouhal numbers of the flows, (2) the reactants and injectors, (3) the Damkohler number of the combustion process, (4) the combustor's temperature, pressure, velocity and concentration fields distributions, and (5) the boundary conditions. The small scale studies should obtain complete information about the spatial and temporal variations of, for example, the fuel spray, reaction rate, and velocity, temperature, pressure and composition fields under controlled and uncontrolled operating conditions. This information together with results of visualization studies should then be used to identify specific characteristics of the combustor that could be controlled by ACC to improve its performance. Such characteristics may include the large and small scale vortical structures that drive combustion instabilities or enhance combustion, regions of slow mixing that impede combustion, and hot spots that enhance NO_x emissions and/or distort the pattern factor causing damage to turbine blades.

Examples of additional ACC applications whose development requires further investigation of their controlling mechanisms include: (1) control of mixing, combustion, liner heating and ignition (i.e., relight)⁴² processes in gas turbines, which could result in safer operation, longer life time, reduction of combustor length and weight, emissions and liner heating, and improved pattern factor, (2) control of vortex formation in solid rockets to reduce the onset of combustion instabilities, (3) control of reactant feed processes, sprays and combustion processes in liquid rockets operating at sub- or super-critical conditions to increase combustion efficiency, reduce combustion instabilities and prevent damage to the injector face and combustor walls, and (4) control of combustion processes in various propulsive devices to reduce signature. Investigations of these control processes will elucidate the fundamental processes in both the uncontrolled system, to help identify appropriate control approaches, and in the controlled system, to help in the optimization of ACC. The results of such studies will determine, for example, processes that must be excited or "canceled" within the combustor to attain the ACC goals, the time response of the ACC, and the types, number and locations of the actuators and sensors that will optimize the ACC performance. These studies will also indicate whether available sensors, controllers and actuators could be used in proposed ACC applications or whether new components must be developed.

6.3 ACC Models

There is also a need to develop models of actively controlled combustors. Such models, together with experimental data should be used to: (1) identify the

fundamental processes that determine the performance of controlled combustors, (2) optimize the performance of ACC systems by, for example, predicting the optimal distributions and performance requirements of ACC sensors and actuators, (3) improve the design of ACC systems, and (4) develop ACC control approaches.

To pursue the above objectives, ACC models of various complexity will have to be developed. It is desirable to develop numerical simulations that fully account for all processes in controlled combustors; e.g., fast time variations, three dimensionality of the flow, vortex dynamics, acoustics, turbulence, kinetics, nonlinearities, flow-actuators interactions and effects of boundary conditions. Numerical predictions could be compared with experimental data to identify the mechanisms that determine the performance of controlled combustors. They could also serve as bench marks for the development of simplified (e.g., low order) models of controlled combustors that will be needed for ACC applications. The development of numerical simulations that can fully describe the behavior of controlled combustors will require additional research on such topics as efficient numerical solution techniques and efficient computational approaches (e.g., parallel computing).

Simplified ACC models capable of predicting the behavior of controlled combustors to within some specified level of accuracy are required to reduce the computational cost of developing ACC applications, and for possible incorporation into ACC controllers. Simplifications may include: neglecting physical and chemical processes of lesser importance, using conventional turbulence closure schemes, assuming global kinetics, spatial integration of the original conservation equations to obtain a system of simplified ODEs (e.g., Galerkin methods^{43,44}), or the use of Large Eddy Simulations⁴⁵ (LES) in which large features of the flow are computed and models are used to describe phenomena whose scales are smaller than the numerical grid size.

6.4 ACC Sensors

ACC sensors continuously measure specific system properties that are subsequently used to determine the state of the system. Fast response pressure transducers and/or photomultipliers have been used to measure pressure and radiation from radicals (e.g., CH or CC), respectively, in small-scale ACC experiments on combustion instability control. The measured data was used to determine the characteristics of the instability. It is expected, that as interest in ACC applications grows, the performance of existing sensors will have to be upgraded and new sensors will have to be developed to measure the temporal and/or spatial dependence of combustor properties (e.g., temperature, pressure, equivalence ratio, species and radical concentrations, and magnitudes of electric currents and magnetic fields). Any sensor must have a time response that is consistent with the goals of the ACC. For instance, fast response pressure transducers are required for active control

of combustion instabilities, while slow response sensors are adequate for ACC systems that control pattern factor and emissions in gas turbines. ACC applications which require spatial resolution of combustor properties along with adequate time response may possibly employ proper distribution of sensors or MEMS (micro-electronic mechanical systems) sensor arrays. In all ACC applications, sensors will have to satisfy all or some of the following requirements: simple design, reliability, high robustness, high sensitivity, low weight, low cost, high frequency response, ability to continuously operate in harsh engine environments over long periods of time, and no or minimal need for optical windows.

Future developments of ACC will critically depend upon the availability of suitable sensors. Short term research should adapt existing sensors to practical ACC applications while long term research should develop novel sensors in response to evolving ACC needs. Examples of short term ACC sensors research include: (1) development of robust sensors for measuring various combustor properties (e.g., distributions of equivalence ratio, temperature and various species), (2) sensor miniaturization, (3) optical sensors⁴⁶ that use cooled optical fiber, (4) sensors materials, (5) sensors cooling methods, and (6) sensor arrays for measuring spatial distributions of properties. Long term research should address issues such as: (1) novel sensors and measurement techniques, (2) identification of optimum sensors for different ACC applications, and (3) development of approaches for combining sensor measurements with an appropriate model to determine spatial distributions of required properties (e.g., radial temperature distribution at the combustor exit for control).

6.5 ACC Actuators

The role of an ACC actuator is to "actively force" the combustor to bring about desired performance. ACC actuators that have been used to date include: (1) injectors that rapidly modulate the flow rate of a secondary fuel stream into the combustor for control of combustion instabilities,^{1,2,8} (2) valves that modulate the air flow rate into an unstable combustor to modify its acoustics and/or increase its damping,⁴⁷ (3) speakers that excite sound within the combustor or near its boundary^{1,2} to cause destructive interference with unstable pressure oscillations, modify the instability driving process, or increase system damping,^{*} (4) valves that vary the air flow rate in a blast atomizer to control the fuel spray characteristics,⁴⁸ (5) acoustic drivers that excite sound waves to control mixing processes,⁴⁹ (6) piezoelectric actuators that control boundary layer flow,⁵⁰ and (7) valves that produce phased, periodic air and/or waste injection to improve waste incineration.^{9,10}

* In many instances, the mechanisms through the actuator attains its objectives is not fully understood.

In contrast to existing ACC sensors, which are generally based upon available combustion diagnostic techniques, the development of ACC actuators was stimulated by evolving needs of ACC. Future research in this area will have to determine the type of actuation needed for different ACC applications (e.g., piezoelectric, magnetostrictive, electric, magnetic, radicals injection, flow rate control). Such studies would help answer such questions as: should we use piezoelectric actuators or acoustic drivers to control mixing and, thus, emissions and the pattern factor in gas turbine combustors? Can we use electric or magnetic fields to control the combustion processes, or should we use air flow rate modulation or ultrasonic forcing to control the characteristics of the spray in air blast atomizers? Research is also needed to determine whether or not a MEMS-type array of actuators is required for a specific application, and if so, what its configuration would be to optimize ACC performance. For applications with individual actuators, the number and locations of the actuators should also be optimal.

Once developed, the performance of actuators will have to be evaluated in open and closed loop control experiments. The former will determine whether the actuators can force the system with adequate amplitude and time response; this will be an indication of the system's controllability.⁵¹ The latter will assess the actuators' capabilities and limitations for closed loop ACC. Once the actuators for a specific application have been chosen, their application will require additional efforts to address the actuators' scale-up, time response, reliability, robustness, weight, size, survivability in the harsh combustor environment, packaging and cost.

6.6 ACC Controller

The controller is the "brains" of an ACC system whose task is to determine the characteristics of the control signal to the actuator. These characteristics depend on whether the ACC operates in an open or closed loop control mode, and on the type of control. As stated earlier, the control signal in open loop ACC is independent of the state of the combustor and is determined a priori. In contrast, the control signal to the actuator in closed loop ACC depends upon the state of the system, which is determined from the sensor measurements.

Since open loop control is considerably simpler than closed loop control, the development of viable open loop ACC should be pursued. Such efforts will have to develop an understanding of the basic mechanisms involved in the process that needs to be controlled, and the manner in which it can be optimally "forced" to attain the ACC objectives. For example, there is evidence suggesting that combustion instabilities can be damped by open loop ACC that excites pulsations within the combustor at a frequency not equal to any of the unstable combustor mode frequencies; the period of the forced oscillation need only be of the same order as either the periods of the unstable modes, or a multiple of the period of the most unstable mode.

Research is needed to determine the feasibility of such control approaches and the optimum frequency and magnitude of the required forcing. It is also necessary to determine whether such approaches can satisfactorily stabilize combustors over wide ranges of operating conditions without producing adverse effects (e.g., undesirable signature).

Closed loop control generally consists of several steps. First, the signal measured by the sensors is used by the observer to determine the state of the system⁴⁹. Next, the observed state of the system is used to determine an "error" signal, representing the deviation from the desired state. The error signal is then used to determine the actuator's control signal, in a way determined by the controller design.

To attain effective closed loop control, the following two tasks must be accomplished: (1) the observer must determine the state of the system within a "relevant" time period that depends upon the controller's objective and characteristics of the controlled system, and (2) the controller must determine an appropriate control signal. Since the performance of practical combustors is generally described by a system of nonlinear partial differential equations (PDEs), the timely "observation" of its state would require the development of analytical/numerical approaches that can swiftly interpret the measured data in terms of the governing equations to determine the state of the system. The development of effective "observation" methods for ACC is urgently needed. These methods should account for multiple sensors in arbitrary number and locations, noise (e.g., turbulence), and the effects of process nonlinearities upon the accuracy of the "observed" state of the system. There is also a need for alternate "observation" approaches, which will not require solution of complex PDEs. Such approaches may use reduced order models or take advantage of qualitative understanding of the physics of the system. The latter approach was applied in Ref. 8 where a wavelet type analysis is used to "observe" the amplitudes, frequencies and phases of the unstable combustor modes in real time.

Improved algorithms for the determination of the control signal are also needed. Such studies should develop control approaches that take into account the effects of such phenomena as system nonlinearities and noise. There is also a need to investigate whether the controller should have constant parameters or adaptively varying parameters. The developed controllers will have to meet the ACC objectives within a specified time period and with limited resource expenditures (e.g., actuator power input).

Finally, possible application of newer control approaches such as neural network, fuzzy and chaotic control in ACC should be investigated.

6.7 ACC System Integration

Practical aspects of integrating an ACC with the engine and flight vehicle must also be studied. Specific issues that should be addressed include: (1) the packaging of the ACC and space available for its installation in the engine, (2) protection (e.g., cooling) of the ACC in the harsh engine environment, (3) added weight of the ACC and its effect upon the system's overall performance, (4) integration of the ACC with the engine's and flight vehicle's control systems, and (5) the effect of the ACC upon the system's operation and maintenance.

Acceptance of ACC by the engineering community will require demonstration of its effectiveness under practical operating conditions. The performance of full scale ACC systems will have to be demonstrated on practical combustors in their real environments (e.g., shipboard incinerators, jet engines, rocket motors). Such tests will have to quantify the benefits of the ACC and demonstrate that it can survive in the harsh engine environment over periods of time comparable to the duration of the mission or life time of the combustor.

7. Road Map for ACC Implementation

The establishment of a road map for implementation of ACC technology on practical systems was discussed at the second workshop. The roadblocks, destination, R&D needs, and technological requirements were carefully examined. The discussion outline is given in Fig.7-1. As a specific example, the development of an ACC program for aeroengine main combustors was considered, giving the result shown in Fig. 7-2. Major conclusions obtained from the discussions are briefly summarized below.

- (1) More emphasis should be given to detailed understanding of combustion dynamics under open- and closed-loop control actions. Combustion chambers should never be treated as a black box when implementing ACC techniques.
- (2) Development of sensors and actuators with acceptable durability, maintainability, and cost deserves high-priority support.
- (3) Demonstration of ACC techniques on practical systems with less complexities, such as ramjet engines and lean-premixed industrial gas turbines, merits serious consideration.

Road Blocks

- need to guarantee controller will not make thing much worse
- adaptive (look up table not sufficient?)
- demonstrated across broad operating range

- experimental
- theoretical
 - low order models
 - CFD
- with realistic noise levels
- with component interaction (including interaction/integration with engine controller)
- need to guarantee control system failure is recoverable
- need to demonstrate advantages
 - reduction in cost in development times
- durability
 - sensors
 - actuators

Road Map for Implementation of ACC

Destination

Where is there a real need?

- industrial gas turbines - driven by LPP burners
- Other applications will await successful implementation in industrial LPP systems, include:
 - unmanned aircraft
 - missiles
 - afterburners
 - solid rockets
 - aeroengine gas turbines

What should ACC deliver?

- short term fix for a particular installation while passive systems are developed
- long term installation
 - operational only occasionally
 - abnormal ambient conditions
 - in transients
 - continuous operation
 - allowing steady-state running at operating conditions not achievable otherwise
- closed loop control at frequencies $\sim 500\text{Hz}$
 - otherwise passive means are easier and preferable

How are we working to remove these road blocks?

What should be done?

Fig. 7-1 Road Map for ACC Implementation

Objectives/Goals

1. Expand UAC operating envelope by extending LBO.
2. Enhance gaseous emissions reductions for commercial applications by reducing unmixedness.
3. Enable high-rate combustion for high thrust/weight military applications by eliminating acoustic coupling at off-design conditions.

Technical Issues

1. What is the physics of LBO?
2. What are the roles of liquid fuel sprays (drop size, size distribution, placement) in driving/suppressing dynamic instabilities?
3. What are the pertinent mechanisms originating dynamic instabilities?
4. How can combustion/acoustic coupling be moderated?

Approaches

Sensors	Actuators	Control Strategies
◊ appropriate to the originating instabilities	◊ appropriate to shear layer excitation	◊ modeling based
	◊ secondary fuel injection	◊ hybrid model/neuralnet
	◊ electrical (plasmas)	
	◊ laser	

Programs

1. Model program studies (c.f.d, exptl., ROM) to address

Sensors	Technical Issues Actuators	Control Strategies
◊ opt. Nos., placement redundancy	◊ application capability	◊ flexibility demo. With
◊ application capability (signal/noise, bandwidth)	◊ minimization of required modulation	◊ appropriate speed
◊ environmental capability (temp., pressure, vibration)	◊ application capability	◊ fail safe design
◊ reliability demo.	◊ minimization of required modulation	◊ integration with engine controller
◊ signal organization	◊ fail safe design	
	◊ environmental capability	
	◊ reliability demo.	

-
- system integration studies
 - integration studies with engine systems (e.g. secondary fuel injection compatible with engine fuel system)
 - Technology Readiness Demo
(e.g. design, build and test complete combustor/ACC system, evaluate separate components, evaluate complete system operating with correct b.c's.) [rig tests only]
 - Core Engine Demonstrator
(e.g. couple technology readiness hardware with high compressor and high turbine)
[as in IHPTET program]

Fig. 7-2 ACC for Application to Main Combustors of Aeroengines

8. Concluding Remarks

The two workshops were concerned broadly with four topics:

- (1) Possible applications of active combustion control and future requirements of combustors;
- (2) Current status of active control of combustor dynamics;
- (3) Needs of research and development in order to close the gap between (1) and (2); and
- (4) Implementation of ACC techniques on practical systems.

Participants came from all NATO countries and provided broad representation of the industry, research community, and government defense agencies. All three topics were addressed thoroughly by a group comprising most of the world's leading researchers and responsible officials from the user community.

With respect to the three topics, the participants agreed upon the following broad conclusions:

- (1) The demands to be placed upon the performance and behavior of future combustors are such that they likely cannot be met within the traditional design methods. All combustion systems offer problems or characteristics that seem to be candidates for application of active control.
- (2) To the present time, no full-scale applications of active control of combustion dynamics have been publicly reported, but several are planned. Consequently, forecasts of the future of ACC rest entirely on results of laboratory demonstrations; essentially nothing is understood about scaling laws.
- (3) The needs of research and development can reasonably be divided into near-term and long-term. The former must be based primarily on existing knowledge and resources, and consist mainly in well-defined demonstrations with specific types of systems, investigating feasibility and scaling laws, for example. In the long-term, there is a wide array of research needs comprising investigations of fundamental processes (both theoretically and experimentally) and development of sensors, actuators, and control laws.

For reasons which are clear from the discussion in Section 3, "Requirements for Future Combustors," and Section 5, "Applications," there is considerable enthusiasm for introducing methods of active control in virtually the entire spectrum of combustion systems. Moreover, that aggressive view by some potential users is encouraged by optimism flowing from a growing number of successful laboratory demonstrations, the majority of which have shown that active control can be used to reduce the amplitudes of oscillations in combustion instabilities. The emphasis on combustion instabilities is partly historical and partly because of pressing practical needs but should

not be allowed to obscure the fact that other applications may be equally important. For example, some success has been achieved in using ACC to maintain an incineration process at optimum conditions.

There are some, however, who caution against full-scale tests too soon. Their reason is that, as stated several times in this report, the scaling laws are not known and any tests must be designed on the basis of results obtained in laboratory devices that have far smaller combustion energy densities than those in combustors intended for full-scale use. The primary and extremely important point to realize is that under these conditions, while success with a full-scale test would be an obvious advance, failure would not signify that ACC cannot be used – only that the particular instance was unsuccessful. Thus the financial and strategic costs must be carefully weighed.

It is quite clear that the matter of scaling is a central issue. Construction of the scaling laws can be done expensively by testing only, but practical considerations, and experience, demand that the most productive approach combine testing and theory. At the present time, theory and analysis lag far behind experimental work. And, as it happens, so also does understanding. There is, for example, no framework for interpreting quantitatively any of the experimental results reported to date. In particular, ACC has been used to reduce the amplitudes of various combustion instabilities, but no serious attempts have been made to predict the amplitudes before or after control is applied. That fact is symptomatic of the difficulties that must be recognized when full-scale tests are contemplated.

The field of active control of combustor dynamics has enormous potential. Sufficient favorable laboratory results have been generated to consider possible applications to full-scale systems. However, the state of progress in general is such that considerable research and development, both in theory and of hardware, will likely be required to achieve practical success. The workshop has shown that international collaborations promise to be highly effective to produce that success.

9. References

1. McManus, K. R., Poinso, T. and Candel, S. M., "A Review of Active Control of Combustion Instabilities", *Progress in Energy and Combust. Sci.* 1993, Vol. 19, pp. 1-29.
2. Candel, S. M., "Combustion Instabilities Coupled by Pressure Waves and Their Active Control," 24th Symposium (International) on Combustion, Sydney, July 1992.
3. Nelson, P. A. and Elliott, S. J., "Active Control of Sound", Academic Press, 1990.
4. Wang, K. W., von Flotow, A. H., Shoureshi, R., Hendricks, E. W. and Farabee, T. M., "Active Control of Vibration and Noise," ASME DE-Vol. 75, 1994.
5. Badmus, O. O., Chowdhury, S., Eveker, K. M., Nett, C. N. and Rivera, C. J., "A Simplified Approach for Control of

- Rotating Stall Part 1: Theoretical Development," AIAA 93-2229, 1993.
6. Epstein, A. H., Williams, J. E. Ffowcs and Greitzer, E. M., "Active Suppression of Compressor Instabilities," AIAA 86-1994, 1986.
 7. Harje, D. T. and Reardon, F. H., "Liquid Propellant Rocket Combustion Instability," NASA SP-194, 1972.
 8. Neumeier, Y. and Zinn, B. T., "Experimental Demonstration of Active Control of Combustion Instabilities Using Real Time Modes Observation and Secondary Fuel Injections," 26th International Symposium on Combustion, Naples, Italy, July 28, 1996.
 9. Parr, T. P., Gutmark, E. J., Wilson, K. J., Yu, K., Smith, R. A., Hanson-Parr, D. M. and Schadow, K. C., "Compact Incinerator Afterburner Concept Based on Vortex Combustion," 26th International Symposium on Combustion, Naples, Italy, July 28, 1996.
 10. Yu, K., Wilson, K. J., Parr, T. P. and Schadow, K. C., "Active Combustion Control Using Multiple Vortex Shedding," AIAA 96-2760, 1996.
 11. Tsien, H. S., "Servo-Stabilization of Combustion in Rocket Motors," *ARS Journal*, Vol. 22, 1952, pp. 256-263.
 12. Marble, F. E., and Cox, D. W. JR., "Servo-Stabilization of Low-Frequency Oscillations in a Liquid Bipropellant Rocket Motor," *ARS Journal*, Vol. 23, 1953, pp. 63-74.
 13. Lee, Y. C., Gore, M. R., and Ross, C. C., "Stability and Control of Liquid Propellant Rocket Systems," *ARS Journal*, vol. 23, 1953, pp. 75-81.
 14. Ffowcs-Williams, J. E., "Anti-Sound," *Proceedings of Royal Society of London*, Vol. A395, 1984, pp. 63-88.
 15. Dine, P. J., "Active Control of Flame Noises," Ph.D. Thesis, Cambridge University, Cambridge, England, 1983.
 16. Heckl, M. A., "Heat Sources in Acoustic Resonators," Ph.D. Thesis, Cambridge University, Cambridge, England, 1985.
 17. Heckl, M. A., "Active Control of the Noise from a Rijke Tube," *IUTAM Symposium on Aero- and Hydro-Acoustics, Lyon 1985*, Springer-Verlag, 1986, pp. 211-216.
 18. Bloxsidge, G. J., Dowling, A. P., Hooper, N., and Langhorne, P. J., "Active Control of Reheat Buzz," AIAA Paper 87-0433, 1987.
 19. Bloxsidge, G. J., Dowling, A. P., Hooper, N., and Langhorne, P. J., "Active Control of an Acoustically Driven Combustion Instability," *Journal of Theoretical and Applied Mechanics*, Vol. 6, 1987, pp. 161-175.
 20. Lang, W., Poinot, T., and Candel, S., "Active Control of Combustion Instability," *Combustion and Flame*, Vol. 70, 1987, pp. 281-289.
 21. Poinot, T., Bourienne, F., Candel, S., Esposito, E., and Lang, W., "Suppression of Combustion Instabilities by Active Control," *Journal of Propulsion and Power*, Vol. 5, No. 1, 1987, pp. 14-20.
 22. Poinot, T., Veynante, D., Bourienne, F., Candel, S., Esposito, E., and Surget, J., "Initiation and Suppression of Combustion Instabilities by Active Control," *Proceedings of the 22nd Symposium (International) on Combustion*, 1988, pp. 1363-1370.
 23. Langhorne, P. J., Dowling, A. P., and Hooper, N., "Practical Active Control System for Combustion Oscillations," *Journal of Propulsion and Power*, Vol. 6, No. 3, 1990, pp. 324-333.
 24. Sivasegaram, S., Tsai, R. F., and Whitelaw, J. H., "Control of Combustion Oscillations by Forced Oscillation of Part of the Fuel Supply," *Combustion Science and Technology*, Vol. 105, 1995, pp. 67-83.
 25. Billoud, G., Galland, M. a., Huynh, C., and Candel, S., "Adaptive Active Control of Combustion Instabilities," *Combustion Science and Technology*, Vol. 81, 1992, pp. 257-283.
 26. Wilson, K. J., Gutmark, E., Schadow, K. C., and Smith, R. A., "Feedback Control of a Dump Combustor with Fuel Modulation," *Journal of Propulsion and Power*, Vol. 11, 1995, pp. 268-274.
 27. Schadow, K. C., Gutmark, E., and Wilson, K. J., "Active Combustion Control in a Coaxial Dump Combustor," *Combustion Science and Technology*, Vol. 81, 1992, pp. 285-300.
 28. Yang, V., Shinha, A., and Fung, Y. T., "State-Feedback Control of Longitudinal Combustion Instabilities," *Journal of Propulsion and Power*, Vol. 8, 1992, pp. 66-73.
 29. Fung, Y. T., Yang, V., and Shinha, A., "Active Control of Combustion Instabilities with Distributed Actuators," *Combustion Science and Technology*, Vol. 78, 1991, pp. 217-245.
 30. Menon, S., "Active Combustion Control in a Ramjet Using Large-Eddy Simulations," *Combustion Science and Technology*, Vol. 84, 1992, pp. 51-79.
 31. Shyy, W., Thakur, S., and Udaykumar, H. S., "A High Accuracy Sequential Solver for Simulation and Active Control of a Longitudinal Combustion Instability," *Computing Systems in Engineering*, Vol. 4, 1993, pp. 27-41.
 32. Neumeier, Y., and Zinn, B. T., *Active Control of Combustion Instabilities with Real Time Observation of Unstable Combustor Modes*, AIAA 96-0758, 1996.
 33. Culick, F. E. C., *Combustion Instabilities in Liquid-Fueled Propulsion Systems*, AGARD-CP-450, Vol. 1, 1989, pp. 1-73.
 34. Fung, Y. T., "Active Control of Linear and Nonlinear Pressure Oscillations in Combustion Chambers," Ph.D. Thesis, Dept. of Mechanical Engineering, Pennsylvania State University, University Park, PA, 1991.
 35. Fung, T. T., and Yang, V., "Active Control of Nonlinear Pressure Oscillations in Combustion Chambers," *J. Propulsion & Power*, Vol. 8, 1992, pp. 1282-1289.
 36. Padmanabhan, K.T., Bowman, C.T., and Powell, J.D., "An Adaptive Optimal Combustion Control Strategy," *Combustion and Flame*, Vol. 100, 1995, pp. 101-110.
 37. Koshigoe, S., Komatsuzaki, T., and Yang, V., "Active Control of Combustion Instability with On-line System Identification," AIAA Paper 96-0759, 1996.
 38. Cohen, J.M., and Anderson, T.J., "Experimental Investigation of Near-Blowout Instabilities in a Lean, Premixed Step Combustor," AIAA Paper 96-0819, 1996.
 39. Gutmark, E., Parr, T. P., Hanson-Parr, D. M. and Schadow, K. C., "Synchronized Acoustic Excitation of Fuel

and Oxidizer for Efficient Combustion," AIAA Aeroacoustics Conference, 1995.

40. Reuter, D., Hegde, U. G., Daniel, B. R. and Zinn, B. T., "Flame Driving of Longitudinal Instabilities in Dump Type Ramjet Combustors" *Combust. Sci. and Tech.*, Vol. 55, pp. 125-138, July 1987.

41. Poinot, T. J., Trouve, A. C., Veynante, D. P., Candel, S. M. and Esposito, E. J., "Vortex-driven Acoustically Coupled Combustion Instabilities," *JFM* 177, pp. 265-292, 1987.

42. Low, H. C., Wilson, C. W., Abdel-Gayed and Bradley, D., "Evaluation of Novel Igniters in a Turbulent Bomb Facility and a Turbo-Annular Gas Turbine Combustor," AIAA-89-2944, 1989.

43. Powell, E. A. and Zinn, B. T., "Nonlinear Combustion Instability in Liquid Propellant Rocket Engines," Proceedings of the 13th Symposium (International) on Combustion. The Combustion Institute, pp. 491-503, 1971.

44. Culick, F. E. C. and Yang, V., "Overview of Combustion Instabilities in Liquid-Propellant Rocket Engines," in *Liquid Rocket Engine Combustion Instability*, Progress in Astronautics and Aeronautics, Vol. 169, 1995.

45. Menon, S., "A Numerical Study of Secondary Fuel Injection Techniques for Active Control of Combustion Instability in a Ramjet," AIAA 92-0777, 1992.

46. Furlong, E. R., Baer, D. S. and Hanson, R. K., "Combustion Control Using a Multiplexed Diode-Laser Sensor System."

47. Langhorne, P. J., "Reheat Buzz: An Acoustically Coupled Combustion Instability. Part 1. Experiment," *J. Fluid Mechanics*, Vol. 193, pp. 417-443, 1988.

48. Brouwer, J., Ault, B. A., Bobrow, J. E. and Samuelson, G. S., "Active Control Application to a Model Gas Turbine Combustor," ASME 90-GT-326, 1990.

49. Matta, L. M., Zhu, C. and Jagoda, J. I., "Mixing by Resonant Acoustic Driving in a Closed Chamber," *J. Propulsion & Power*, Vol. 12, No. 2, pp. 366-370, March-April 1996.

50. Wiltse, J. M. and Glezer, A., "Manipulation of Free Shear Flows Using Piezoelectric Actuators," *J. Fluid Mech.*, Vol. 249, pp. 261-285, 1993.

51. Ogata, K., *Modern Control Engineering*, 2nd Edition, Prentice-Hall Pub., 1990.

52. Gutmark, E., Parr, T.P., Hanson-Parr, D.M., and Schadow, K.C., "Active Control of a Premixed Flame", presented at AIAA/SAE/ASME/ASME 26th Joint Propulsion Conference, July 16-18, 1990, Orlando, FL (AIAA-90-2448)

53. Schadow, K.C., Gutmark, E.J., Parr, T.P., Wilson, K.J., and Yu, K., "Vortex Combustion with Synchronized Fuel Injection", presented at Twelfth International Symposium on Airbreathing Engines, September 10-15, 1995, Melbourne, Australia

54. Yu, K., Wilson, K.J., Parr, T.P., Smith, R.A., and Schadow, K.C., "Characterization of Pulsating Spray Droplets and Their Interaction with Vortical Structures", presented at 34th Aerospace Sciences Meeting and Exhibit, January 15-18, 1996, Reno, NV.

55. Parr, T.P., Gutmark, E.J., Wilson, K.J., Hanson-Parr, D.M., K. Yu, Smith, R.A., and Schadow, K.C., "Compact Incinerator Afterburner Concept Based on Vortex Combustion", presented at Twenty-Sixth International Symposium on Combustion, July 28-August 2, 1996, Naples, Italy.

56. Yang, V., Santavicca, D.A., and Ray, A., "Intelligent Control of Gas Turbine Combustion Dynamics for Performance and Emission Improvement," Proceedings of the Ninth ONR Propulsion Meeting, 1996, pp. 286-292.

57. Knoop, P., Culick, F.E.C., and Zukoski, E.E., "Extension of the Stability of Motions in a Combustion Chamber by Nonlinear Active Control Based on Hysteresis," submitted to *Combustion Science and Technology*.

58. Burkhardt, H. and Strubenhoff, V., "Multispectral Vision-Guided Flame Control", presented at ECAPT '93: Karlsruhe 25-27 March 1993, Second Meeting of BRITE-EURAM Concerted Action on Process Tomography, Workshop on "Process Monitoring & Control".

59. Tao, W. and Burkhardt, H., "Application of Fuzzy Logic and Neural Networks to the Control of a Flame Process". In Proceedings of the 2nd IEE Conference on "Intelligent Systems Engineering", Hamburg, September 1994.

60. Delabroy, O., Haile, E., Veynante, D., Lacas, F. and Candel, S., "Reduction de la Production des Oxydes d'azote (Nox) Dans Une Flamme de Diffusion a Fioul Par Excitation," *Revue Generale de Thermique*, Vol. 35, 1996, pp. 475-489.

61. Delabroy, O., Lacas, F., Poinot, T., Candel, S., Hoffmann, T., Hermann, J., Gleis, S., and Vortmeyer, D., "A Study of Nox reduction by Acoustic Excitation in a Liquid Fueled Burner," *Combustion Science and Technology*, Vol. 119, pp. 397-408.

62. Haile, E., Delabroy, Lacas, F., Veynante, D., and Cander, S., Structure of Acoustically Forced Spray Flame," 26th Symposium (International) on Combustion, The Combustion Institute, Pittsburgh, 1996.

63. Gutmark, E.J., Schadow, K.C., Nina, M.N.R., and Pita, G.P., "Suppression of Combustion Instability by Geometrical Design of the Bluff-Body Stabilizer," *Journal of Propulsion and Power*, Vol. 11, No. 3, pp. 456-463, 1995.

64. Gleiss, S., Vortmeter, D., and Rau, W., "Experimental Investigations on the Transition from Stable to Unstable Combustion by Means of Active Instability Control," AGARD CP 479, pp. 22.1-22.7, 1990.

65. Hermann, J., Gleis, S., and Vortmeyer, D., "Active Instability Control (AIC) of Spray Combustors by Modulation of the Liquid Fuel Flow Rate," *Combustion Science and Technology*, Vol. 118, pp. 125, 1996.

66. Hantschk, C., Hermann, J., and Vortmeyer, D., "Active Instability Control with Direct Drive Servo Valves in Liquid-Fueled Combustion Systems," 26th International Symposium on Combustion, Naples, Italy, 1996.

PAPER No. 36
Yang & Schadow
(presenter: K. Schadow)

Question 1: C. Van Erp, NAWCAD, U.S.

This is a comment: Any new technology must provide system benefits to be considered these days. For the U.S. future military, this means the IHPTET goals in particular. An example might be using active combustion control for screech control in an augmentor so that the screech liner might be eliminated, thereby reducing weight and improving thrust/weight ratio. The USAF in conjunction with Pratt & Whitney are investigating this.

Answer:

None

Question 2: H. Mongia, General Electric Aircraft Engines, U.S.

A comment and a question: I agree with the previous comment. Any new technology must buy its way on-board an engine. Could the use of active combustion control contribute to meeting the 5 ppmV NO_x goal for catalytic combustion?

Answer:

I do not know.

COMBUSTION INSTABILITIES IN LOW NO_x GAS TURBINES AND THEIR ACTIVE CONTROL

Ben T. Zinn^{*}, Tim Lieuwen^{*}, and Yedidia Neumeier[^]
Schools of Aerospace and Mechanical Engineering
Georgia Institute of Technology
Atlanta, GA 30332-0150

Key Words: Combustion Instability, Lean Premixed Combustion, Active Control

Abstract

This paper presents an investigation of the mechanisms and control of combustion instabilities in low NO_x gas turbines (LNGT) that burn fuel in a lean, premixed (LP) mode of combustion. Physical considerations show that these instabilities may be caused by interactions of combustor pressure oscillations with the reactants supply rates, producing equivalence ratio (ϕ) perturbations in the inlet duct. These perturbations are convected by the mean flow to the combustor where they produce large amplitude heat release oscillations that drive combustor pressure oscillations. The regions of instability can be approximately described in terms of a ratio of the reactants' convective time from the fuel injector to the combustor and the period of the oscillations (with some modifications that account for the structure of the combustion region). Significantly, these predictions are in good agreement with available experimental data, strongly suggesting that the proposed mechanism properly accounts for the essential physics of the problem. The predictions of this study indicate that passive control strategies may not, in general, provide a viable means for controlling these instabilities, due to the multiple number of modes that may be excited by the combustion process. The paper closes with a discussion of a recently developed, observer based, active control system and its control of combustion instabilities in a small scale Georgia Tech combustor and a sub scale Westinghouse gas turbine are presented. These results demonstrate that active control is a promising means for controlling combustion instabilities.

1. Introduction

Increasingly stringent emissions legislation has increased the demand for LNGT that employ a lean, premixed mode of combustion. However, LNGT are prone to detrimental combustion instabilities in various operating ranges, especially under the lean conditions where they are designed to operate [1]. To develop rational approaches for preventing or controlling these instabilities, an understanding of the controlling mechanism and capabilities for predicting the conditions under which these instabilities occur must be developed. This paper describes results of studies that were undertaken to meet these needs and to develop practical solutions for controlling LNGT instabilities. Specifically, this paper describes a mechanism that is likely responsible for driving LNGT instabilities, and passive and active approaches for their control.

2. Mechanism of LNGT Instability

Several different mechanisms may be responsible for instabilities in various combustion systems. These include, for example, unsteady burning rates, and a time varying flame area. A challenge in combustion instability studies is to determine which of the plethora of potential mechanisms is actually responsible for the instability in a given system. At present, there is a great deal of evidence, based on theoretical and experimental work at Georgia Tech [2-4] and the U.S. Dept. of Energy [5], that the dominant mechanism for instability in LNGT is due to ϕ oscillations formed in the inlet of the combustor that are driven by the

^{*} David S. Lewis Jr. Chair and Regents' Professor, Schools of Mechanical and Aerospace Engineering
[^] Graduate Research Assistant, School of Mechanical Engineering
^{*} Senior Research Engineer, School of Aerospace Engineering

unsteady combustion process. The objective of this section is to discuss this mechanism, and demonstrate why LNGT operating under lean conditions would be vulnerable to this instability mechanism.

There are two key components to this mechanism; first the generation of heat release oscillations by periodic variation in ϕ of the reactive mixture, and second, the formation of ϕ oscillations in the inlet section by velocity and pressure oscillations in the vicinity of the fuel injector. These are described in the following sub sections.

2.1 Sensitivity of LP systems to ϕ oscillations

This study was partially motivated by observations that properties of premixed combustion systems, such as flame thickness, flame speed, and reaction rate, are increasingly sensitive to variations in ϕ as the combustion process stoichiometry becomes leaner [2]. Moreover, systems operating near the lean limit are acutely sensitive to ϕ perturbations, because they may cause periodic (or total) extinction of the combustion process. To further examine these observations, an unsteady well stirred reactor (WSR) model was developed and subjected to ϕ perturbations in the inlet [2]. This study revealed, see Fig. 1, that the response of the WSR's reaction rate to perturbations in the inlet ϕ drastically increases (up to a factor of 200) as the mean value of ϕ decreases. Assuming that the unsteady heat release rate is proportional to the local unsteady reaction rate, this result strongly suggests that ϕ oscillations could drive substantial heat release oscillations under lean operating conditions. It also suggests that ϕ oscillations are unlikely to drive instabilities near stoichiometric conditions, because of the negligible response of the reaction rate. Observations that LNGT appear to be relatively quiet under stoichiometric conditions and become progressively louder as ϕ is reduced [1], appears to support this assertion and the trends depicted in Fig. 1.

2.2 Formation of ϕ oscillations

Section 2.1 suggested that the sensitivity of LP systems to ϕ oscillations could be responsible for the observed LNGT instabilities. While random ϕ fluctuations undoubtedly occur in LNGT due to, for example, turbulent mixing, ϕ fluctuations can play a role in an instability mechanism only if they are driven by the combustion process and pressure oscillations, thus closing the feedback loop needed to maintain an instability. Consequently, it is necessary to consider how ϕ fluctuations can arise, and to elucidate the feedback mechanism between the ϕ and heat release

oscillations that drive the instability. The following equation, derived from the definition of ϕ , suggests a mechanism for the formation of ϕ oscillations in the inlet section due to velocity and pressure perturbations:

$$\frac{\phi'}{\phi} = \frac{\frac{\dot{m}'_f}{\dot{m}_f} - \frac{\dot{m}'_o}{\dot{m}_o}}{1 + \frac{\dot{m}'_o}{\dot{m}_o}} \quad (1)$$

Here the subscripts f and o denote fuel and air, respectively, and m the mass flow rate. This equation shows that ϕ oscillations can form when air flow oscillations occur in the vicinity of the fuel injector, as well as by fuel flow oscillations due to pressure oscillations (depending on the acoustic sensitivity of the fuel injection system). Furthermore, for the low Mach number flows typical of LNGT systems, this equation implies that small acoustic fluctuations can generate significant ϕ fluctuations; for example, for $M=0.05$ and a choked fuel injector (i.e., $\dot{m}'_f=0$), acoustic oscillations of 1% of the mean will generate ϕ oscillations of 20%! The substantial oscillations in ϕ formed from such modest flow perturbations suggests that even when diffusive and turbulent mixing processes that tend to homogenize the mixture are accounted for, ϕ fluctuations may still persist at the flame.

It can be seen that a critical component of this mechanism of instability is the presence of " ϕ waves", (that is, coherent fluctuations in ϕ of the reactive mixture) in the inlet section. It is interesting to note that measurements of oscillations in the fuel mole fraction, with frequencies corresponding to the instability, have been recently reported [6].

2.3 Conditions for Instability

The discussions in section 2.1 and 2.2 have outlined the framework for a combustion instability mechanism potentially responsible for those observed in LNGT. This mechanism and its controlling steps/parameters can be better understood by considering the time evolution of the various processes that sustain it, see Fig. 2. Figure 2-a shows the time dependence of the acoustic pressure at the flame of an unstable mode with a period T (for now, the length of the combustion region is assumed to be very small relative to any relevant length scale, relaxation of this assumption may produce significant changes; see discussion in the Appendix). This disturbance propagates upstream into the inlet duct and produces standing oscillations at the fuel injector that lag those in the flame by a phase Φ , see Fig. 2-b (where $2\pi f\tau_i = \Phi$). Under most conditions,

the fuel mass flow rate and inlet duct pressure oscillations are out of phase [3, 4], see Fig. 2-c. Assuming that the ϕ oscillations are primarily due to fuel flow rate oscillations, Eq. (1) shows that m_f' and ϕ' are in phase, see Fig. 2-d. This leads to the formation of a reactive mixture with a periodically varying ϕ that is convected by the flow and reaches the flame after a convective time $\tau_{\text{convect}} = L_{\text{convect}} / \bar{u}$, see Fig. 2-e.

The combustion process responds to the ϕ perturbation after a chemical time delay, τ_{chem} , see Fig. 2-f. It follows from Rayleigh's criterion that an instability can occur if the heat release oscillations in Fig. 2-f are in phase with the pressure oscillations at the flame in Fig. 2-a; that is, if $(\tau_1 + \tau_{\text{convect}} + \tau_{\text{chem}}) / T = n - 1/2$. However, as long as the inlet duct is not too long and the Mach number is small, the pressure oscillations at the flame and fuel injector will be nearly in phase, indicating that τ_1 / T is negligible (for a discussion of cases where this may not be true, see [3]). Furthermore, for the low frequency instabilities of interest, τ_{chem} / T is also negligible. Consequently, the dominant time delay is due to convective processes and the condition for instability becomes:

$$\frac{\tau_{\text{convect}}}{T} = n - 1/2 \quad n=1, 2, \dots \quad (2)$$

This suggests that the distance from the fuel injector to the flame, the mean velocity in the inlet duct, and the frequency of oscillations are the dominant parameters that control the combustor stability. Using similar arguments, it can be shown that if the fuel supply is choked, the inlet duct is short, and the inlet duct upstream boundary condition is approximated as either a pressure or a velocity node, the corresponding conditions for instability become [3]:

$$\begin{aligned} \text{Pressure node:} \quad & \frac{\tau_{\text{convect}}}{T} = n - 1/4 \\ \text{Velocity node:} \quad & \frac{\tau_{\text{convect}}}{T} = n - 3/4 \end{aligned} \quad (3)$$

This discussion shows that, given the previously stated assumptions, the instability regions are primarily a function of $\tau_{\text{convect}} / T$. Specifically, Eqs. (2-3) indicate that the regions of instability approximately center about regions where $\tau_{\text{convect}} / T = C_n$, where C_n is a constant that depends on the combustor configuration. In a combustion system without damping, these

instability regions will lay in bands where $C_n - 1/4 < \tau_{\text{convect}} / T < C_n + 1/4$.

When damping is accounted for, it is possible that a region where instability can occur will remain stable if the energy addition due to the unsteady heat release can not overcome damping processes. However, this is unlikely due to the low levels of damping in LNGT combustors [7]. However, the presence of damping will narrow the "width" of the instability regions, causing the edges of otherwise unstable regions to become stable.

In order to better quantify regions of instability, a linear stability model has been developed at Georgia Tech. Besides accounting for damping effects, allowing it to predict stability boundaries, the model also incorporates additional effects due to mean flow and area discontinuities that slightly alter the predictions in Eqs. (2-3). A detailed description of the model and a number of results can be found in Refs. [3] and [4]. However, for the purposes of this paper, the criteria developed in Eqs. (2-3) will suffice.

2.4 Experimental Results

Predictions that the regions of instability are primarily a function of $\tau_{\text{convect}} / T$ are in agreement with data obtained at Georgia Tech and the U.S. Dept. of Energy. Figure 3 shows pressure data obtained by Straub and Richards [5] and the instability regions predicted by Eq. (3). It can be seen that their data collapses into bands when normalized by $\tau_{\text{convect}} / T$, as predicted by the preceding discussion. Furthermore, since the inlet section of the combustor was connected to a plenum (see [5]), if the upstream boundary condition is approximated as a pressure node, Eq. (3) predicts that instabilities should occur in the vicinity of $\tau_{\text{convect}} / T = 0.75, 1.75, \dots$. Figure 4 shows this result is in good qualitative agreement with the measured data.

The slight discrepancy between the predicted and measured data in Fig. 4 can be explained by noting that the mixture is not instantly consumed upon reaching the base of the flame, as assumed in the analysis in Section 2.3. Rather, it will not be completely consumed until it reaches the end of the flame region. Thus, the "effective" convective time, $\tau_{\text{conv,eff}}$, is actually longer than the time for the mixture to convect from the fuel injector to the base of the flame (the exact amount depends on the length and structure of the flame region). Consequently, since the data is plotted versus τ_{convect} and not $\tau_{\text{conv,eff}}$, this discussion suggests that the measured instability region should lay to the left of the predicted region, as it does. This is discussed further in the Appendix.

Figure 4 presents the dependence of the unstable pressure oscillation amplitudes, measured on the Georgia Tech combustor, upon $\tau_{convect}/T$ (a description of the experimental setup and additional results can be found in [8]). Since the upstream boundary of the inlet section is essentially a rigid wall, Eq. 3 predicts that instabilities should occur when $\tau_{convect}/T = 0.25, 1.25, \dots$. Figure 4 shows that the measured data is in excellent agreement with this prediction. Again, note that the measured instability region is located slightly to the left of the predicted region (due to the data being plotted versus $\tau_{convect}$ and not $\tau_{conv,eff}$).

The excellent agreement of the theory in, first, predicting the significance of the parameter $\tau_{convect}/T$, and second, predicting the unstable value of this parameter for different geometric conditions, strongly suggests that the mechanism discussed in this paper is responsible for the instabilities observed in LNGT.

2.5 Passive Control Considerations

An understanding of the mechanism responsible for LNGT instabilities gives combustor designers a powerful tool for combating these instabilities in the design stage. For example, Solar Turbines, using these ideas, has sized the diameter of the inlet section of their combustor and altered the fuel injection location so that the convective time lies outside of the unstable range [9]. However, we would suggest that, in general, such passive control approaches will not be successful in stabilizing LNGT combustors. That is, it may not be possible to have the flexibility to design a combustor whose region of operation lies outside of the unstable $\tau_{convect}/T$ ranges. The reason is that many combustor modes that may be excited, and stabilizing one may destabilize another. For example, Fig. 5 presents the instability data of Fig. 4, plotted versus the inlet velocity. It can be seen that at lower velocities, the 430 Hz. mode is excited, and that its amplitude decreases with increasing velocity. Opposite behavior is exhibited by the 630 Hz. mode, which is excited only at the higher velocities. The reason for the preferential switching of unstable modes can be understood from Fig. 4, where it is shown that both modes become unstable within the region predicted by Eq. (3). Figure 5 shows that the combustor is "quiet" only within a very narrow window in the velocity. It is possible that the designer may have some flexibility in setting this velocity, but not enough to move it into a stable range.

This discussion illustrates the potential weakness of a passive control scheme and suggests that, in general, LNGT combustors may require an active control scheme to maintain stability, especially if they must operate over a wide range of conditions. The next

section discusses active control as an alternative means of suppressing these instabilities.

3 Active Control of LNGT Instabilities

A block diagram of the Georgia Tech active control system (ACS) is shown in Fig. 6. The instability is sensed with a pressure transducer located near the upstream end of the combustor where the amplitudes of all axial modes are significant. The measured pressure is sent to an observer that determines the characteristics of the unstable mode(s) in practically real time. The observer's output is sent to the controller where each observed unstable mode is provided with a gain and phase shift. The control signal is then sent to a fuel injector actuator that modulates the injection rate of a secondary fuel stream into the combustor. The oscillatory fuel supply creates heat addition oscillations out of phase with the combustor pressure oscillations, thus rapidly damping the instability.

The performance of this control system has been extensively studied and has been shown to attenuate instabilities in combustors that burn gaseous fuels on time scales of the order of 40 ms [10]. A multi-pronged approach to apply this control strategy is being pursued for control of combustion instabilities in LNGT. First, fundamental control experiments are being performed on the LNGT combustor facility at Georgia Tech that is also being used to characterize the instabilities. Secondly, through collaboration with Westinghouse, control experiments are being performed on larger scale systems.

3.1 Control Experiments at GT

A fundamental problem hindering the optimization of ACS is lack of understanding of the precise mechanisms whereby the unsteady heat addition process is created. Furthermore, its interaction with the main combustion process is poorly understood. Fundamental control experiments are being planned on this facility to take advantage of the high degree of optical access of the combustor. It is anticipated that these investigations will provide insight into these questions, as well as providing a test bed for promising control methodologies. Results from these control experiments will be discussed in the final version of this paper.

3.2 Control Experiments at Westinghouse

The effectiveness of the ACS developed at Georgia Tech has been demonstrated on a small scale, high pressure combustor [10-12]. In order to expedite the scale up of this ACS, experiments on a larger scale

facility (1/10th full size) have been performed in collaboration with Westinghouse [13].

Results showing the performance of the ACS on this combustor are shown in Figs. 7 and 8. Figure 7 shows the time dependence of the combustor pressure before and after control was turned on. It can be seen that actuation of the ACS resulted in a very rapid and effective damping of the instability amplitude (by a factor of 4). Figure 8 shows the Fourier transformed pressure data, taken before and after the ACS was activated. The figure clearly shows the effective attenuation of the unstable mode as well as its harmonics.

4. Summary and Conclusions

This paper has shown that LNGT instabilities are likely due to a complex feedback process between the heat release, acoustic pressure, and ϕ oscillations. Furthermore, it has been shown that regions of instability are predominantly a function of $\tau_{convect}/T$, implying that the frequency of oscillation, the mean velocity, and the combustor inlet length will be key parameters affecting combustor stability. It has also been suggested that, in general, these instabilities can not be controlled by passive means, since such measures are essentially capable of controlling only a single mode, while in a real combustor a number of possible modes may be excited. Finally, performance of a recently developed ACS suggest that active control offers a viable approach for controlling LNGT instabilities.

5. Appendix

In the paper, it was shown that when (1) the inlet section was short relative to a wavelength, (2) the Mach number was low, (3) the flame region was "very short", and (4) the acoustic period was small relative to chemical time scales, then the instability regions were only a function of the ratio $\tau_{convect}/T$. In typical LNGT, conditions 1, 2 and 4 are usually met; however, it is very possible that condition 3 will not be satisfied. The reason can be understood from Fig. A-1. Here it is shown that while the length scale of the acoustic quantities is the acoustic wavelength, λ , the ϕ fluctuations occur over a much shorter convective wavelength, $M\lambda$. Thus, even though the flame may be very short relative to an acoustic wavelength, its length may be of the order of a convective wavelength (stated alternatively, the Strouhal number, fL_{flame}/U , is $O(1)$).

This implies that ϕ fluctuations may occur over the surface of the flame, potentially causing cancellation as the heat release fluctuations in one portion of the flame

will occur out of phase with those in other part. This cancellation can cause the amount of unsteady energy release to be significantly reduced. Also significant, in terms of predicting instability regions, is that the reactive mixture will not be instantly consumed when it reaches the flame base; rather each part of a given cross section of mixture will react when it reaches the flame surface, not being finally consumed until it reaches the end of the flame region. This effect is especially important if the flame region is not significantly shorter than the distance between the fuel injector and the flame base. This will introduce a phase between the ϕ fluctuation at the base of the flame and the resultant heat release oscillation of the flame. The exact value of this phase will depend upon when each portion of the reactive mixture is consumed (thus on the structure of the flame region), and on the phase of the ϕ oscillation of that portion (and thus on the Strouhal number).

In the spirit of the prior analysis, these effects can be accounted for by defining an "effective" convective time, $\tau_{conv,eff}$, the sum of the convective time from the fuel injector to the flame base and the time lag between the ϕ oscillation at the flame base and the heat release oscillation. When $St \ll 1$, this new time is a constant, independent of St . For example, it has been shown in [4] that for a conically shaped flame and $St \ll 1$, that $\tau_{conv,eff} = \tau_{convect} (1 + L_{flame}/(3 * L_{convect}))$. However, when $St \sim O(1)$, $\tau_{conv,eff}/T$ is no longer a constant, but is also a function of St .

If $\tau_{conv,eff}$ is significantly different than $\tau_{convect}$, it must be included when the instability criteria developed in Eqs. (2-3) are used. However, determining this quantity is not as straightforward as the convective time. In fact, the effective convective time can become a very complicated function of St , and also quite sensitive to the assumed shape of the flame region. For example, Fig. A-2 shows a plot of $\tau_{conv,eff}/T$ as a function of St when $L_{flame} = L_{convect}$. The figure readily shows the difference between $\tau_{conv,eff}$ and $\tau_{convect}$, depending upon the assumed shape of the flame, and the dependance of $\tau_{conv,eff}$ upon St when $St \sim O(1)$.

The implication of this is that for a fixed St , instability regions can be well described by a constant, although the value of this constant may be a complicated function of the structure of the flame region. However, for conditions where $St \sim O(1)$, and where St is changing significantly, the regions of instability can no longer be determined from the simple considerations discussed in this paper. This discussion may explain recent results at DOE where it was shown that data taken for a variety of swirl vane locations did not appear to correlate well with $\tau_{convect}/T$ [14].

It is conceivable that by incorporating the St number effects discussed in this Appendix, corrections can be

made. However, given the sensitivity of these corrections to the structure of the flame region, such a procedure may not be practical.

6. Acknowledgments

This research was supported by AGTSR and AFOSR; Dr. Daniel B. Fant, and Dr. Mitat Birkan, Contract Monitors.

7. References

- 1.) Cohen, Jeffrey, Anderson, Torger, AIAA paper # 96-0819 (1996).
- 2.) Lieuwen, T., Neumeier, Y., Zinn, B. T., *Comb. Sci. Tech.* V. 135, 1-6, (1998).
- 3.) Lieuwen, T., Zinn, B. T., AIAA paper # 98-0641 (1998).
- 4.) Lieuwen, T., Zinn, B.T., to appear in *Twenty Seventh Symposium (International) on Combustion*, The Combustion Institute, Pittsburgh, PA, (1998).
- 5.) Straub, D.L., Richards, G.A. ASME # paper 98-GT-492, (1998).
- 6.) Mongia, R., Dibble, R., Lovett, J., ASME Paper # 98-GT-304, (1998).
- 7.) Keller, J.J., *AIAA Journal*, Vol. 33 (12), (1995), pp. 2280-2287.
- 8.) Lieuwen, T., Torres, H., Johnson, C., Daniel, B.R., Zinn, B.T., to be presented at AIAA annual meeting, Reno, NV, (1999).
- 9.) Steele, Rob, *1998 AGTSR Combustion Workshop*, Berkeley, CA, Mar. 25-27, (1998).
- 10.) Neumeier, Y., Zinn, B.T., *Twenty Sixth Symposium (International) on Combustion*, The Combustion Institute, Pittsburgh, PA, (1996).
- 11.) Zinn, B.T., Neumeier, Y., *Archivum Combustionis*, Vol. 15 (3-4), (1995).
- 12.) Zinn, B.T., Neumeier, Y., AIAA paper # 97-0461, (1997).
- 13.) Sattinger, Stan, Neumeier, Y., Nabi, A., Zinn, B.T., Amos, D.J., Darling, D.D., ASME paper # 98-GT-258 (1998).
- 14.) Richards, G. Straub, D., Yip, J. Woodruff, S., *Proc. 1998 AGTSR Combustion Workshop*, Berkeley, CA, Mar. 25-27, (1998).

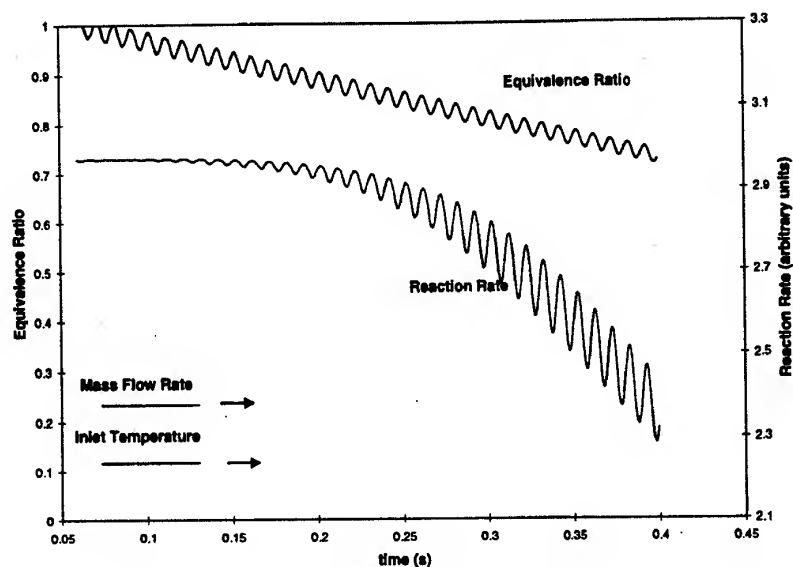


Figure 1 – Dependence of the response of the reaction rate to ϕ fluctuations upon the mean ϕ .

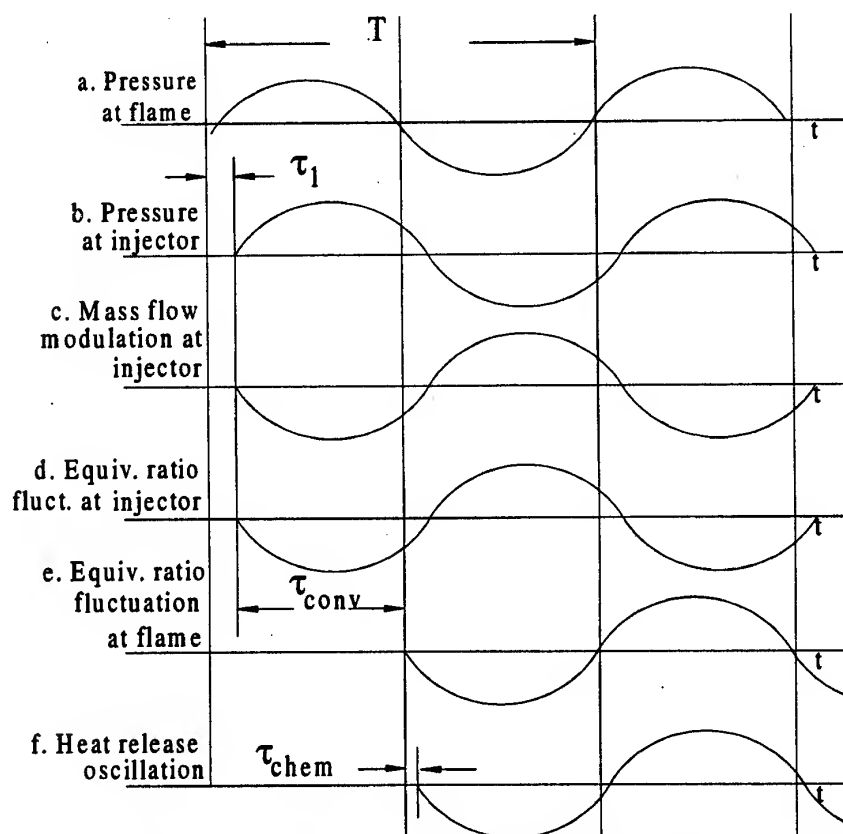


Figure 2 – A qualitative description of the manner in which ϕ perturbations drive an instability in LNGT.

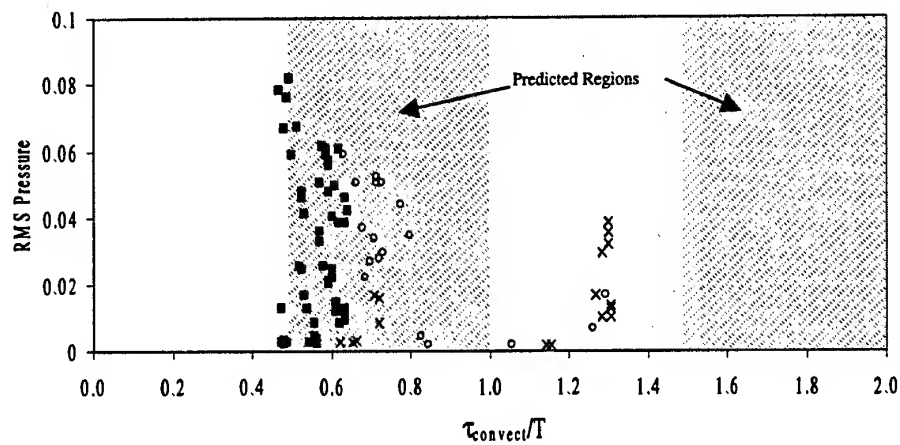


Figure 3 – Comparison of predicted stability regions (hatched regions) with data from DOE [5].

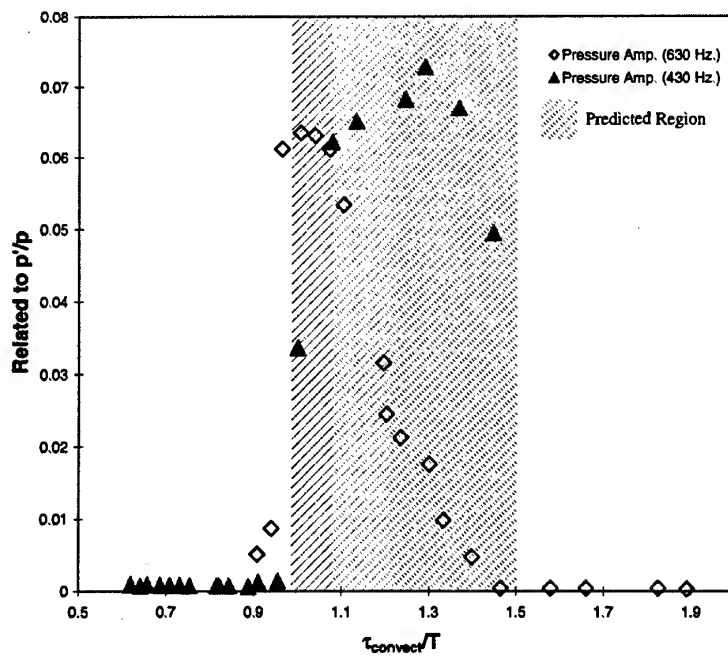


Figure 4- Dependence of normalized fluctuating pressure on parameter τ_{convect}/T , compared with predicted instability regions (hatched region).

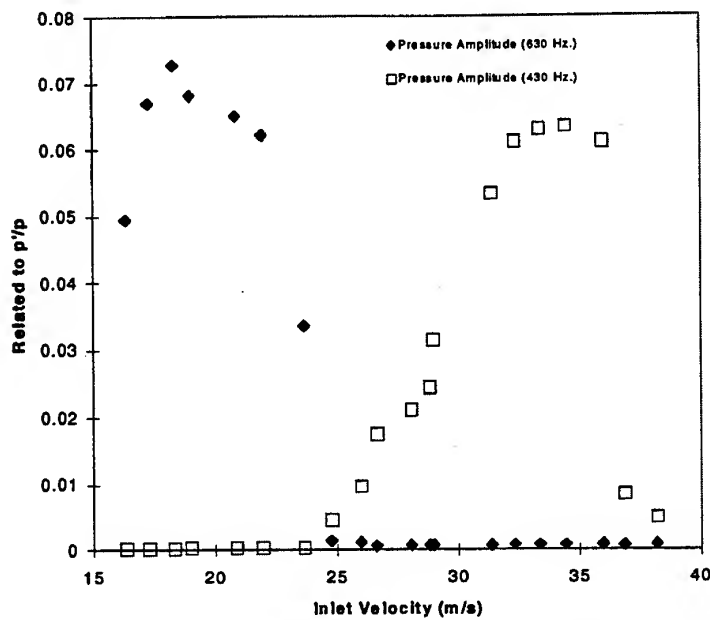


Figure 5 – Experimental data from Georgia Tech showing variation of normalized pressure with velocity in the inlet section.

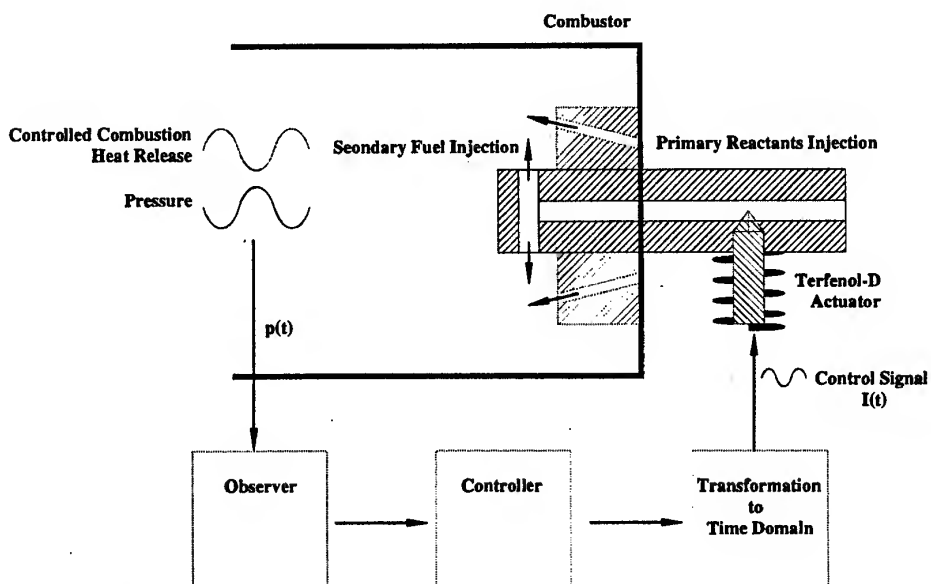


Figure 6 – Schematic of Georgia Tech's ACS.

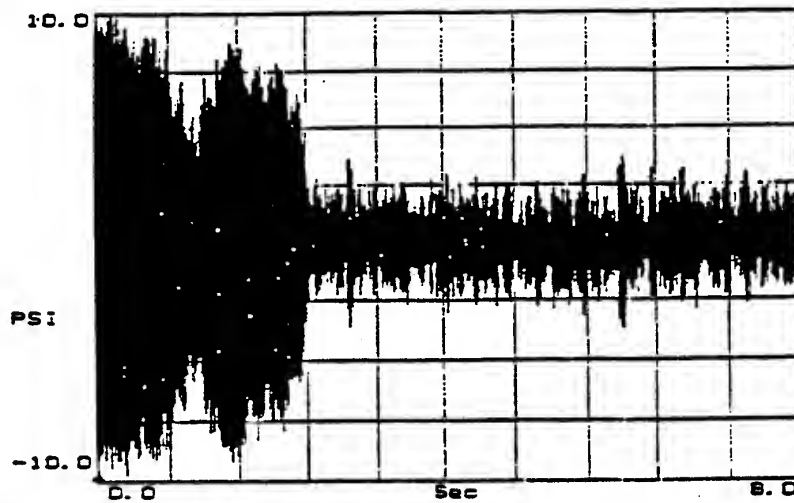


Figure 7- Time trace of combustor pressure before and after engagement of ACS.

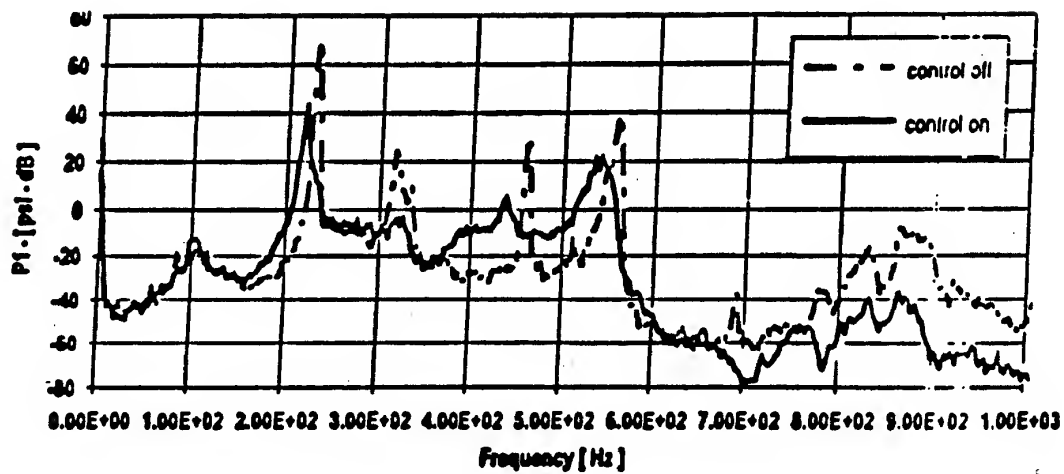


Figure 8 - Fourier Transform of combustor pressure before and after engagement of ACS.

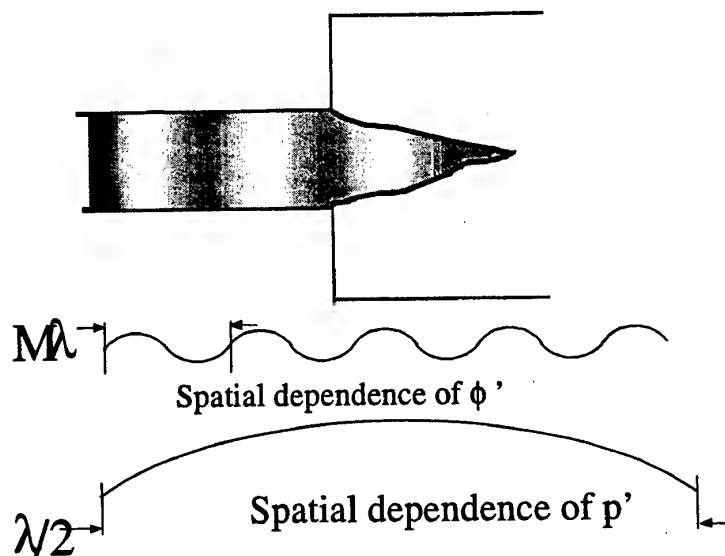


Figure A -1 - Distribution of ϕ of the reactive mixture in the inlet section and flame region.

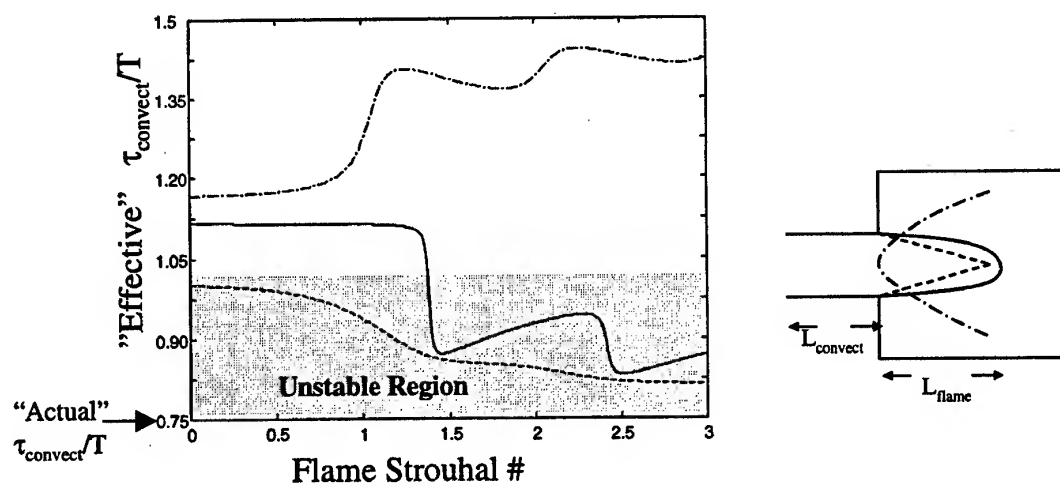


Figure A -2 - Variation of "effective" τ_{convect}/T with flame Strouhal number when $L_{\text{flame}} = L_{\text{convect}}$.

PAPER No. 37
Zinn, Liewen & Neumeier
(presenter: B.T. Zinn)

Question 1: D. Santavicca, Penn. State University, U.S.

When you encounter multiple frequencies in a combustion instability, do you trigger the actuator under these circumstances?

Answer:

No, but in the multiple frequency case the controller automatically identifies the first dominant frequency and fixes it; it could then be told to find the next dominant frequency and fix it, and so on. So, in principle, there is not a difficulty in addressing multiple frequencies.

Question 2: M. Razdan, RR-Allison, U.S.

You mention that a good control of secondary fuel is required, and showed that the method you described works well for gaseous fuels. What is the situation with respect to an actuator that has adequate response rates when using liquid fuels; also, how do you achieve successful modulation when spray atomization, secondary droplet breakup, droplet clustering, fuel evaporation and other non-linear behaviors have significant impacts on fuel/air mixing?

Answer:

We have tested a liquid fuel version of our magneto restrictive fuel actuator to excite needed pulsations of fuel, to frequencies of 5,000 hertz with successful excitation of heat release and pressure oscillation in a combustor. This indicates suitability for controlling combustion instabilities. We also find that the fuel modulation improves the liquid atomization. Obviously however, modulation of liquid fuel at higher frequencies becomes difficult. The liquid fuel actuator has three controllers, a slow response controller that controls the mean fuel flow rate through the injector, an intermediate response rate controller that modulates the fuel flow rate at the frequency of the unstable mode which needs to be damped, e.g. 500 hertz, say, and a high response controller that excites very high frequency oscillations which atomize the liquid fuel jet. We have shown that the presence of these high frequency oscillations produces good liquid fuel atomization under adverse operating conditions, e.g. at fuel pressure drops where atomization normally does not occur with conventional pressure atomizers. Also, we are now investigating the additional time delays that are introduced into the control loop by the use of a liquid fuel in active control, e.g. atomization and evaporation, as mentioned by Dr. Razdan. In summary, based upon results that we have obtained to date, we are confident that it would be possible to use liquid fuels in active control of combustion instabilities.

Active Control of Combustion Instability in a Liquid-Fueled, Low-NO_x Combustor

Jeffrey M. Cohen, Nancy M. Rey,
Clas A. Jacobson, Torger J. Anderson, and Thomas J. Rosfjord
United Technologies Research Center
411 Silver Lane
East Hartford, Connecticut USA 06108

1. ABSTRACT

A practical active control system for the mitigation of combustion instability has been designed and demonstrated in a lean, premixed, single-nozzle combustor at realistic engine operating conditions. A full-scale engine fuel nozzle was modified to incorporate a simple fuel flow actuator. Results indicate that the system was capable of reducing pressure fluctuations by 82% (15 dB or 5.6X) while maintaining or reducing NO_x and CO emissions levels.

2. INTRODUCTION

Emphasis on reducing the levels of pollutants created by gas turbine combustors has led to the development of lean, premixed combustor designs, especially for industrial applications. Premixing large amounts of air with the fuel prior to its injection into the combustor greatly reduces peak temperatures within the combustor and leads to lower NO_x emissions. Premixed combustors are often susceptible to thermoacoustic combustion instabilities, which can lead to large pressure oscillations in the combustor. These pressure oscillations result in increased noise and decreased durability due to vibration and flame motion.

In a DARPA (Defense Advanced Research Projects Agency) - funded program, United Technologies Research Center (UTRC) investigated the feasibility of attenuating combustion instability using active control techniques. Because of DARPA's interest in marine applications (which typically use liquid fuel), the initial focus of this research was on a liquid-fueled, low-NO_x combustor. This combustor exhibited a large-amplitude ($p'/p \sim 10\%$) instability at a frequency of approximately 200 Hz. The goal of the research was to develop a practical active control system which would reduce the magnitude of the pressure fluctuations caused by the instability without adversely affecting NO_x levels. The

effort stressed the practicality of the system and its ability to work with full-scale engine hardware at realistic operating conditions.

3. EXPERIMENT AND INSTRUMENTATION

Experiments were conducted in a single-nozzle, flametube combustor (see Fig. 1). The nominal energy conversion rate of the single-nozzle combustor was 4 MW. The combustor used fuel nozzles designed for engine use and ran at engine operating conditions (pressure, temperature and flow rate per injector). The fuel nozzles were designed to provide a high degree of fuel-air mixing and have been discussed thoroughly in previous papers (Snyder, et. al, 1994). Figure 2 shows a schematic of the fuel nozzle. Liquid fuel (No. 2 Diesel fuel) was injected through six axially-oriented "spokes" protruding from the nozzle centerbody. High-pressure-drop spray tips were installed at the end of each spoke. The 15.2 cm diameter combustor test section was water-cooled with a thermal barrier coating on the inner wall. A pilot fuel injector was located 2.5 cm downstream of the combustor dump plane. A water-cooled orifice plate provided a choke point to simulate the acoustic boundary of the engine's turbine inlet guide vanes. Upstream of the combustor, the air flow rate was metered using a choked venturi.

After passing through the venturi, the air flow was split between the fuel nozzle and a bypass leg. The air that flowed through the bypass leg was injected at the downstream end of the combustor (upstream of the orifice plate), representing combustor dilution air.

The volumes and lengths of the combustor, diffuser region upstream of the fuel nozzle and bypass leg were set in order to reproduce the instability observed in a full-annular engine combustor.

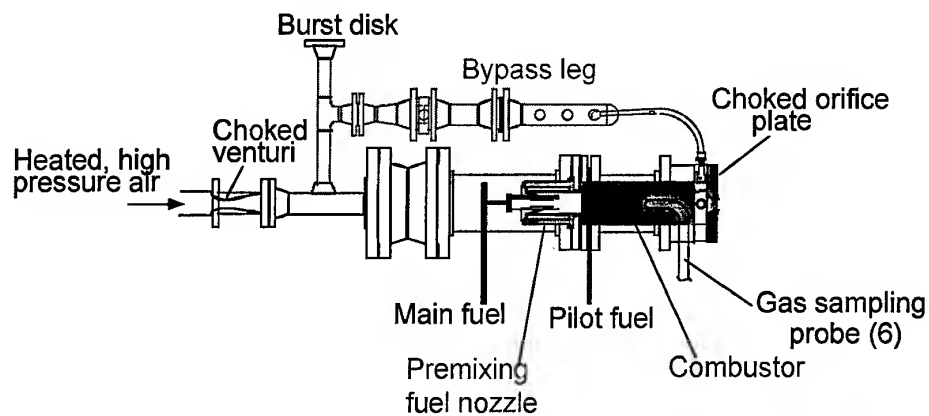


Figure 1. Schematic of single-nozzle combustor rig. Test section diameter = 15.2 cm. For clarity, only one of the 6 sampling probes is shown.

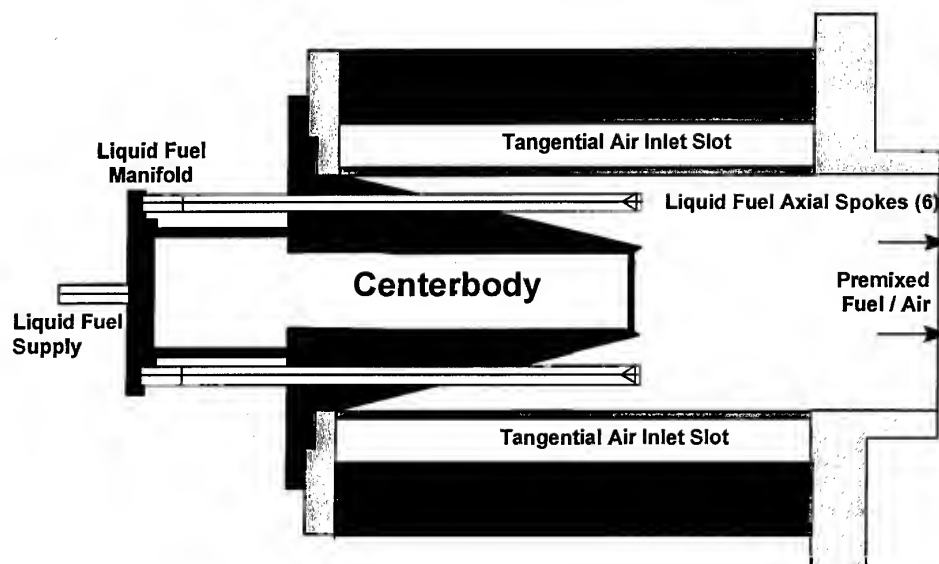


Figure 2. Schematic of tangential-entry fuel nozzle, showing liquid fuel injection spokes.

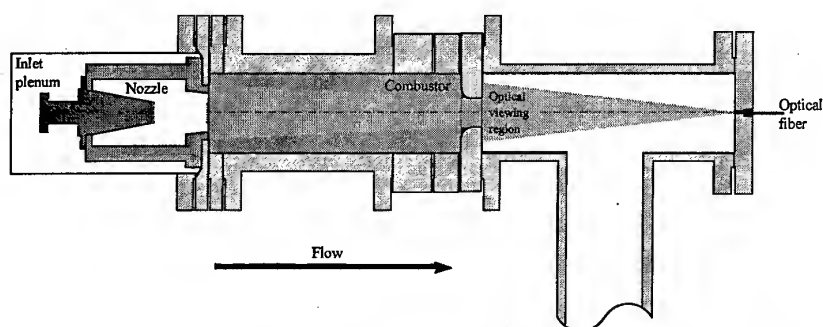


Figure 3. Layout of fiber-optic viewing region for measurement of combustor heat release rate.

An array of six gas-sampling probes, located upstream of the bypass air injection was used to measure NO_x and CO concentrations as well as combustor fuel/air ratio and combustion efficiency. Species concentrations are reported here in ppm on a 15% Oxygen basis for a ganged probe arrangement. High-response data were collected at a rate of 5 kHz on a simultaneous sample-and-hold data acquisition system. The analog signals were low-pass filtered at 2 kHz to prevent aliasing. Fluctuating pressures were measured at two locations in the combustor using high-response pressure transducers. A photomultiplier tube (PMT) was used to measure the intensity of CH and CO radical emissions in the combustor. Light was collected using a fiber optic probe "looking" upstream through the orifice plate at the fuel nozzle (see Fig. 3). This orientation allowed the PMT to "see" the majority of the combustor. A 200 μm diameter quartz fiber with a numerical aperture of 0.37 viewed through a flange in the exit plenum and was directly coupled to the PMT. With a small amount of air purge, this probe required minimal access to the combustor and provided sufficient signal to monitor the emissions from the flame. A bandpass optical filter was installed to selectively admit only those wavelengths associated with CH and CO emissions (430 nm). The intensity of these emissions has been shown to linearly track the rate of heat release in premixed systems (John and Summerfield, 1957, and Samaniego et. al, 1995). As such, this measurement yields a time-responsive, volume-averaged measurement of the combustor heat release rate. Control signals, indicating the commands sent to the actuation system, were also recorded.

4. CHARACTERIZATION OF THE INSTABILITY

The frequency of the primary mode of instability varied from 180 Hz to 220 Hz, depending on the test conditions. Secondary modes are present at higher frequencies, but are smaller in magnitude and of less interest here. Figure 4 shows power-spectral density (PSD) plots of the combustor pressure and the heat release rate during instability. These data are presented on a decibel scale, where the fluctuations are normalized by a reference value and represented on a logarithmic scale:

$$dB = 20 \log_{10} \left(\frac{P'}{P_{ref}} \right)$$

A similar expression was employed for the heat release values.

For fixed inlet pressure and temperature, the magnitude of the instability grew with decreasing fuel/air ratio, as shown in Fig. 5. This feature of the instability limited the lean-ness of the usable mixture, and therefore the level to which the NO_x emissions could be reduced. Application of a steady, sidewall diffusion flame pilot reduced the magnitude of the instability, but resulted in increased NO_x emissions.

The instability mode of interest (~200 Hz) was a bulk mode, characterized as a Helmholtz resonator/spring-mass system in

which the combustor volume represented the spring and the masses of gas in the fuel nozzle and the exit orifice represented the masses. Pressure fluctuations were coupled with the heat release process through their effect on the flow rate of air delivered through the fuel nozzle. Time-varying air flow rate led to time-varying equivalence ratio and, therefore, time-varying heat release rate. This conceptual model of the instability is discussed in more detail in Peracchio and Proscia (1998). Additional control-oriented modeling is currently being performed at UTRC using describing function analyses.

5. DESCRIPTION OF THE CONTROL SYSTEM

The control system consisted of three parts: a sensor to measure the state of the system, a control algorithm to determine the required action, and an actuator to achieve that action. The high-response measurements of combustor pressure and heat release rate had illustrated their capability for tracking the instability with high signal/noise ratio and were both available as control sensors. A variety of control algorithms, ranging from simple phase-shifting algorithms to more complex adaptive algorithms were available for implementation, depending on the need. It was apparent that the critical component was the actuator.

The initial requirements for the actuator were two-fold: it had to be able to affect the dynamics of the combustor system at the 200 Hz frequency and it had to be able to endure the operating environment in which it was placed. In addition, it was preferable that the device be simple and easy to control. Previous applications of active control to combustors have been in lab-scale devices operating at capacities, pressures and temperatures significantly lower than those considered in this study (see Yu 1997; Billoud, 1992; McManus, 1997; Richards, 1995; Zinn, 1997; Hantschk, 1996).

The high power output (4 MW per nozzle), inlet operating pressure (1.7 MPa) and temperature (730K) of this application eliminated many of the actuation concepts used in these studies from consideration. Actuation of the combustor air flow rate was considered, but it was determined that the durability of this scheme would be inadequate, again due to the high operating temperature. Other, more sophisticated actuators were discarded due to the level of complexity they introduced into the problem. Actuation of the fuel flow remained as a viable candidate. Several configurations of fuel actuation were designed and tested. Only one will be discussed in this paper.

One of the six spokes delivering fuel into the premixing fuel nozzle was disconnected from the main fuel system and was connected to a separately-metered fuel system (see Fig. 6). A high-speed solenoid valve was installed in this system external to the combustor rig, so as to isolate it from the high operating temperature. The volume of tubing between the valve and the fuel injection location was minimized in order to reduce attenuation and time lag due to capacitive effects.

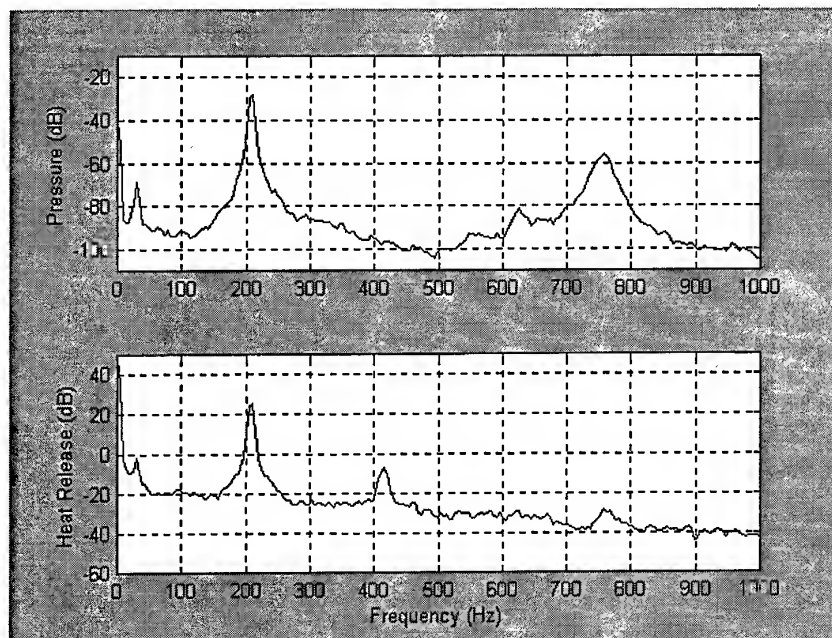


Figure 4. Combustor pressure and heat release spectra for uncontrolled combustion at an equivalence ratio $\phi=0.51$.

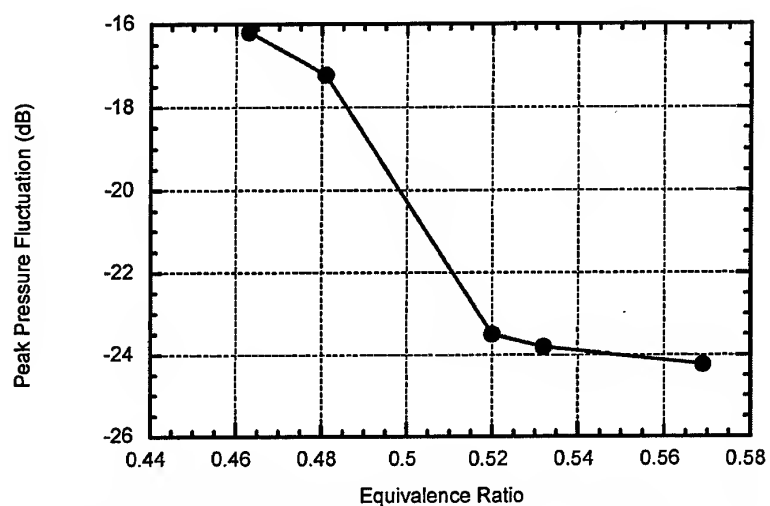


Figure 5. Effect of equivalence ratio on level of combustor pressure fluctuation in the 200 Hz mode.

An accumulator was installed immediately upstream of the solenoid valve to minimize supply pressure variations. No direct measurement of the time-varying fuel flow rate was made. Open-loop testing of the flow system indicated that the valve responded at frequencies up to approximately 250 Hz, which determined the maximum operating frequency.

Open-loop actuator authority tests were conducted under reacting conditions. In these tests 1/6 of the total fuel flow rate (time-averaged) was delivered through the control fuel system. The remainder of the fuel was delivered through the other five spokes. The solenoid valve was driven at different frequencies, independently of the combustor behavior, using a signal generator. The on/off duty cycle was maintained at 50%. The response of the combustor pressure and heat release rate were then measured. Figure 7 shows the results of open-loop forcing at 100 Hz. Note that the 200 Hz instability was still present. It was not possible to obtain a non-resonant situation under reacting conditions, although these tests were conducted at the highest practical fuel/air ratio in order to reduce the magnitude of the 200 Hz instability.

For diagnostic purposes, a simple threshold control algorithm was designed. The principle of its operation is shown in Fig. 8. Whenever the control sensor signal crossed an established threshold level, a command was sent to the solenoid valve. On positive-direction crossings, the valve was opened and on negative-direction crossings, it was closed. A time delay between the moment of crossing and the valve command was also imposed. The same delay was used for both opening and closing commands. The threshold level and time delay were manipulated via a user interface to the control algorithm. Because the opening and closing of the valve was tied to the pressure signal, the algorithm was self-tuning over the frequency range of interest (100-300 Hz).

6. RESULTS OF CONTROLLED COMBUSTION

Tests with the threshold controller and spoke actuation were conducted using the bandpass-filtered (100-300 Hz) combustor pressure as the control signal. In all the cases discussed here, the threshold level was set at zero, nominally yielding a 50% duty cycle. These tests were conducted at a combustor pressure of 1.56 MPa and a combustor inlet temperature of 730K. The nominal power output of the test combustor was 4 MW. The fuel/air equivalence ratio was varied over a wide range of values, down to near-blowout conditions.

Figure 9 shows the behavior of the controlled combustor as the delay time was varied. Proper choice of the time delay yielded significant reductions in the level of pressure oscillations. (Note that the control system was capable of increasing the magnitude of the instability as well as attenuating it.) This exercise was conducted at five equivalence ratios between 0.47 and 0.56 (based on nozzle air flow). The optimum time delay was constant at 0 ms across

this range, and also across a range of air flow rates. This value has no physical significance, in that it represents only a control system time delay and not the acoustic, convective or kinetic time delays involved in the mixing and combustion of the actuated fuel flow. These parameters were not directly measured.

Figure 10 shows PSDs of the uncontrolled and controlled combustor pressure and heat release rate at an equivalence ratio of 0.51. The magnitude of the 200 Hz mode was attenuated by 15 dB (5.6X or 82%) using the optimum time delay. The overall RMS pressure level was reduced from 29.2 kPa to 11.5 kPa.

The control system's effectiveness will ultimately be judged by its ability to suppress the level of pressure oscillations and enable low-NO_x operation simultaneously. It is desirable, then, to minimize both parameters. Figure 11 is a cross plot of the pressure fluctuation level of the 200 Hz mode versus the NO_x emissions for both uncontrolled and controlled operation over a range of equivalence ratios. The shaded regions represent the limits of acceptable operation with respect to pressure fluctuation and NO_x emissions. The reduction obtained by the control system is relatively constant at approximately 15 dB across the range of equivalence ratios. For the majority of the points (all acquired in back-to-back tests) the controlled combustor actually created less NO_x than the uncontrolled combustor. It is believed that this is because temporal "hot spots" created by the fuel/air fluctuations have been removed by the control system.

Also shown in Fig. 11 is a comparison of the controlled system to piloted operation. Piloted data were collected at an overall equivalence ratio of 0.49. While diffusion flame piloting reduced the level of pressure fluctuations, it increased the NO_x emissions. Only the actively controlled system was capable of delivering simultaneous low NO_x and low pressure fluctuations. Low CO emissions were also maintained and, especially at low equivalence ratios, lowered using control.

7. SUMMARY

A practical active combustion control system for application to liquid-fueled, lean, premixed combustion systems has been designed and demonstrated in a single-nozzle combustor at realistic engine operating conditions. A full-scale engine fuel nozzle was minimally modified to incorporate a simple actuation system using an off-the-shelf high-speed solenoid valve. Investigation of the controlled system behavior indicated that a fixed time delay between the input signal and the control signal to the valve yielded optimum effectiveness over a wide range of combustor equivalence ratios. Suppression of the instability by as much as 15 dB was typical. The control system was self-tuning over the 100-300 Hz frequency range, enabling it to track changes in frequency with changing operating conditions. The system demonstrated simultaneous achievement of both NO_x and

pressure fluctuation goals and demonstrated its superiority to diffusion-flame piloting.

8. ACKNOWLEDGEMENTS

The authors wish to thank DARPA for their sponsorship of this work. The contract monitor is Dr. William Scheuren. The contributions of Drs. Thomas Rosfjord, Aldo Peracchio, John McVey and Gonzalo Rey, Messrs. William Proscia, Jeffrey Walker, Timothy Snyder and Frederick Padget and Ms. Luu Vu were key to the success of this demonstration.

9. BIBLIOGRAPHY

Billoud, G., M.A. Galland, C. Huynh Huu and S. Candel, "Adaptive Active Control of Combustion Instabilities," *Combustion Science and Technology*, 1992, Vol. 81, pp. 257-283.

Hantschk, C., J. Hermann, and D. Vortmeyer, "Active Instability Control with Direct Drive Servo Valves in Liquid-Fuelled Combustion Systems," presented at the 26th International Symposium on Combustion, Naples, Italy, 1996.

John, R. R. and Summerfield, M., 1957, "Effect of Turbulence on Radiation Intensity from Propane Air Flames," *Jet Propulsion*, Vol. 27, pp. 169-179.

McManus, K.R., J.C. Magill, M.F. Miller and M.G. Allen, "Closed-Loop System for Stability Control in Gas Turbine Combustors," AIAA-97-0463.

Peracchio, A.A. and W. Proscia, "Nonlinear Heat-Release/Acoustic Model for Thermoacoustic Instability in Lean Premixed Combustors," presented at the ASME IGTI Turbo Expo, June 1998.

Richards, G.A., M.J. Yip, E. Robey, L. Cowell and D. Rawlins, "Combustion Oscillation Control By Cyclic Fuel Injection," ASME paper 95-GT-224, June 1995.

Samaniego, J.-M., Egolfopoulos, F. N. and Bowman, C. T., 1995, "CO₂* Chemiluminescence in Premixed Flames," *Combustion Science and Technology*, Vol. 109, pp. 183-203.

Snyder, T.S., T.J. Rosfjord, J.B. McVey and L.M. Chiappetta, "Comparison of Liquid Fuel/Air Mixing and NO_x Emissions for a Tangential Entry Nozzle," ASME paper 94-GT-283, June 1994.

Yu, K., K.J. Wilson, and K.C. Schadow, "Active Combustion Control in a Liquid-Fueled Dump Combustor," AIAA-97-0462, January 1997.

Zinn, B.T., and Y. Neumeier, "An Overview of Active Control of Combustion Instabilities," AIAA-97-0461, January 1997.

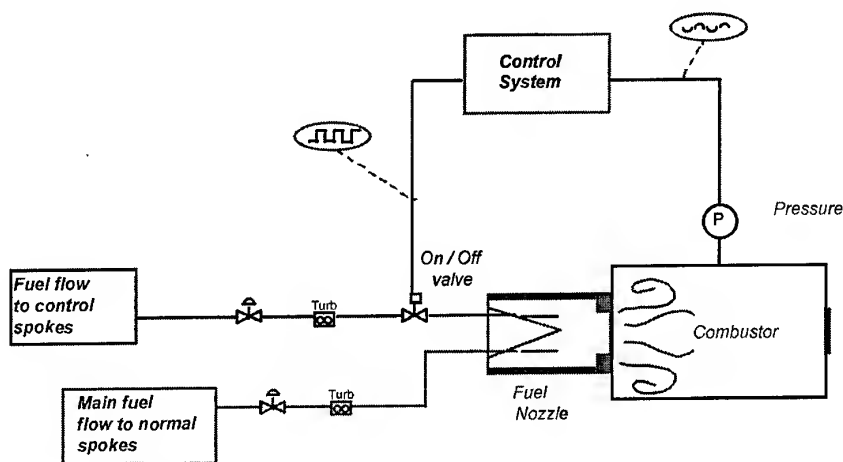


Figure 6. Schematic of fuel control system with block diagram of controller.

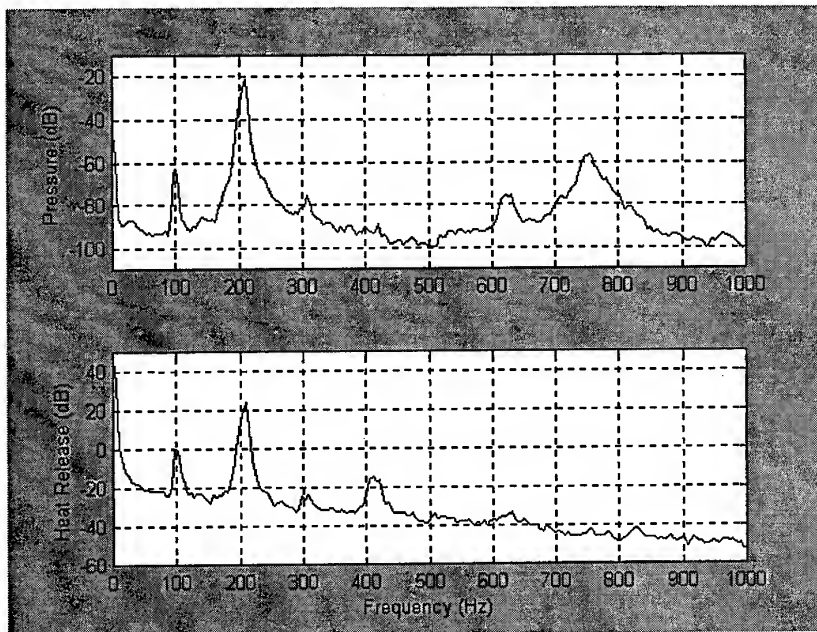


Figure 7. Pressure and heat release spectra at an equivalence ratio of 0.56 with open-loop forcing at 100 Hz.

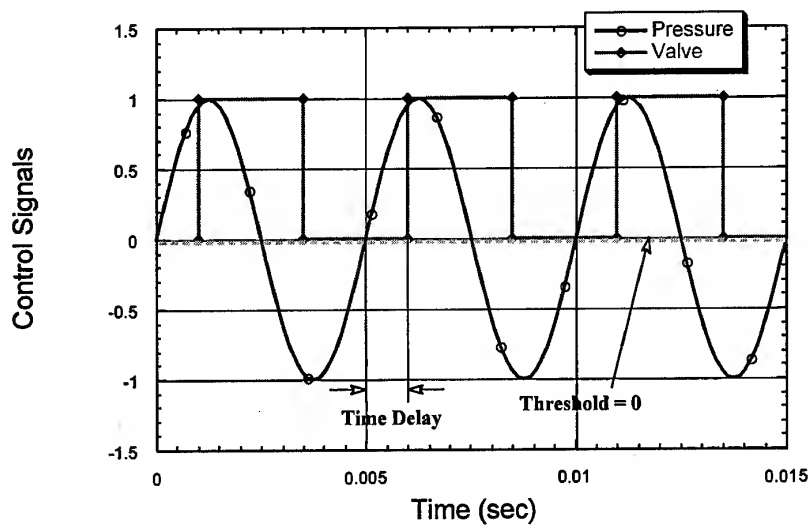


Figure 8. Threshold control algorithm schematic with illustration of delay and threshold settings.

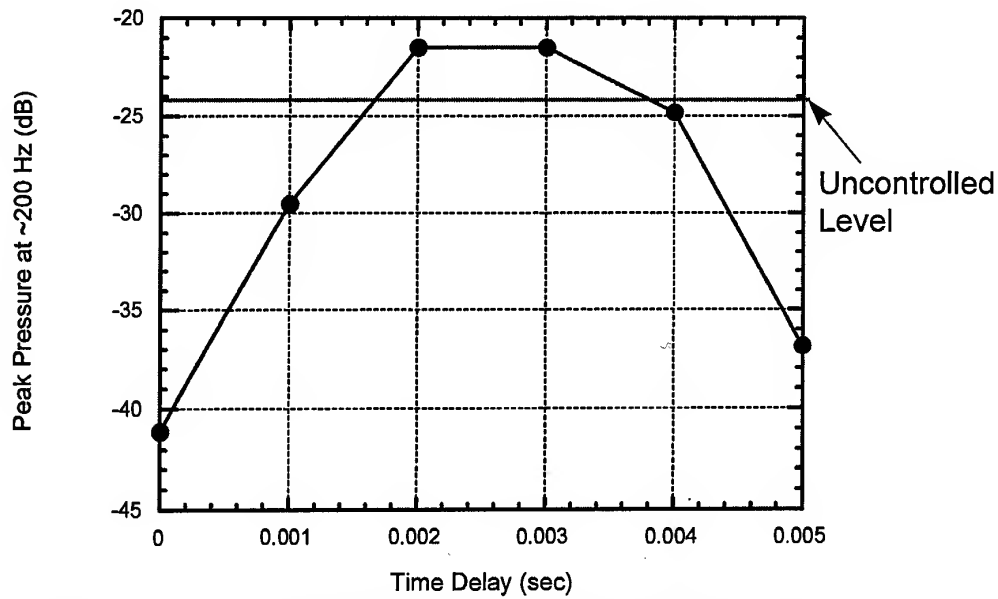


Figure 9. Effect of control delay time on attenuation of pressure fluctuations of 200 Hz mode at an equivalence ratio of 0.56.

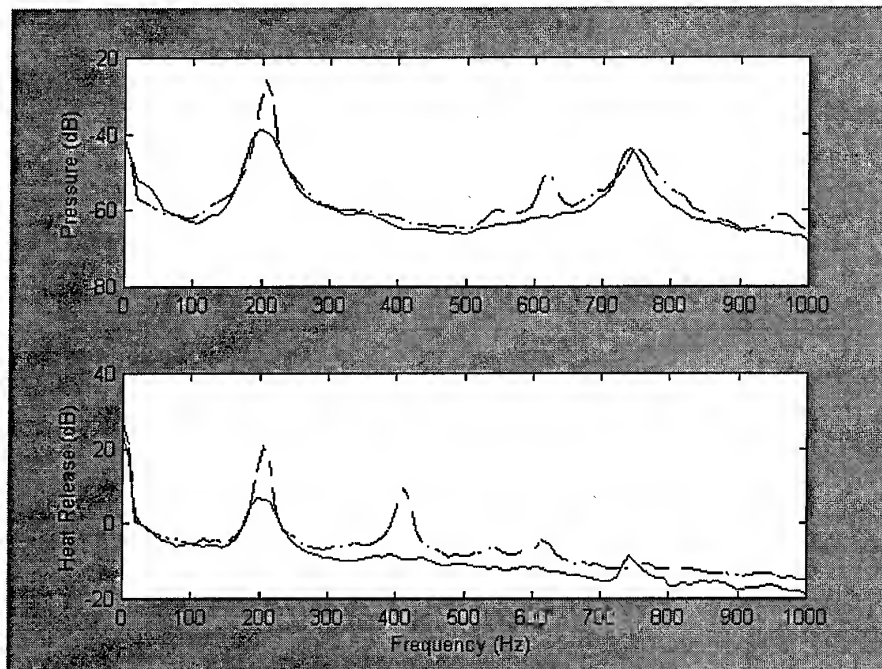


Figure 10. Spectra of pressure and heat release during controlled (solid lines) and uncontrolled (dashed lines) at an equivalence ratio of 0.51 with optimum delay.

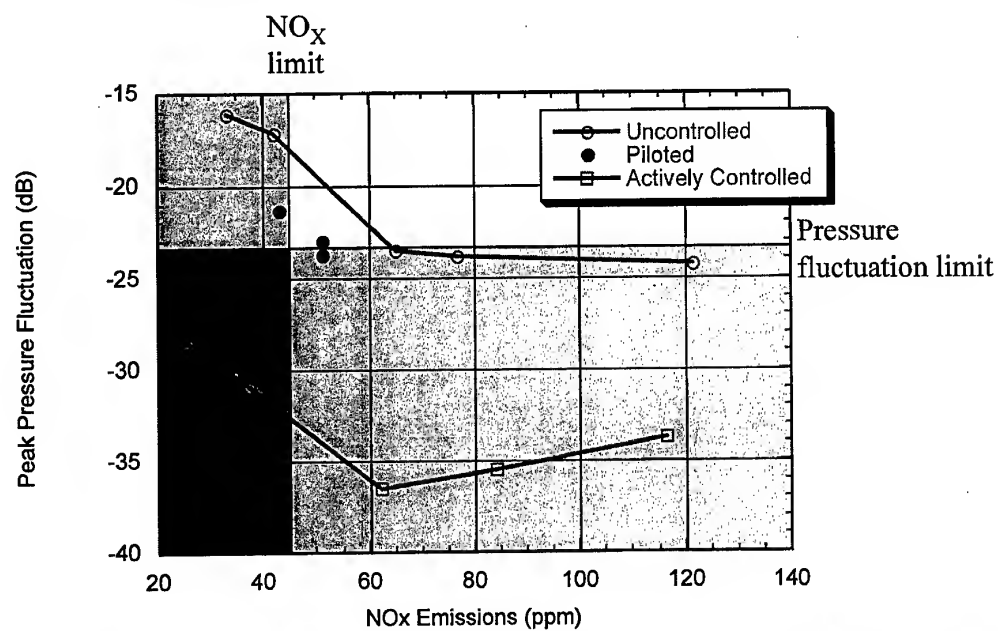


Figure 11. Cross-plot of pressure fluctuation level vs. NO_x emissions. Points represent equivalence ratios of 0.47, 0.49, 0.51, 0.53 and 0.56 from left to right on each curve. Piloted points are for operation at 0.49 with 2.5, 5.0 and 6.5% sidewall pilot, top to bottom (percentage of total fuel flow rate).

PAPER No. 38
Cohen, Rey, Jacobson & Anderson
(presenter: T. Rosfjord)

Question No. 1: C. Priddin, RR, U.K.

You mentioned that you had done some testing on a multiple fuel injector rig. Do you control these injectors independently, or do you try to integrate the control in some way?

Answer:

Open-loop tests on each fuel injector alone were performed to determine their individual response and authority. Closed-loop tests were performed using one, two or all three fuel injectors of the sector, together, with diminishing returns being achieved on use of more injectors. However, this result may be system-specific, and it might have to be used in some instances.

Question 2: G.J. Sturgess, ISSI, U.S.

Plots were shown of NO_x and CO as a function of equivalence ratio with control "on" and control "off." The lower CO achieved with control "on" at low equivalence ratios was explained as being due to "better burning." How would the lower NO_x also obtained with control "on" be explained in light of this "better burning?"

Answer:

NO_x formation is a non-linear process. I expect that the reduction in fuel/air temperal fluctuations with the control "on" reduced the time spent at NO_x-adverse combustion conditions, but we do not really know yet. This should be looked at.

Question 3: S.N.B. Murthy, Purdue University, U.S.

It was good to hear the speaker drawing attention to the basically three-dimensional, time-dependent character of gas turbine combustors! In that light, in the three-injector sector configuration used, has any attempt been made to introduce a periodic fuel supply in a 1/6 th. fuel strut?

Answer:

Aperiodic forcing was not attempted. Open-loop tests were performed at determine the response of each fuel injector so that they could be synchronized.

Adaptive control of aeroacoustic instabilities with application to propulsion systems

M. Mettenleiter, E. Haile and S. Candel

*Laboratoire E.M2.C, CNRS, Ecole Centrale Paris,
92295 Châtenay-Malabry Cedex, France*

Abstract

This paper describes an experimental investigation of adaptive control algorithms applied to aeroacoustic instabilities. The study is carried out on a cold flow experimental rig, designed to reproduce the essential features of acoustically coupled vortex shedding. This mechanism is responsible for thrust oscillations in large segmented solid rocket motors. It is also found in a wide variety of combustion instabilities. An adaptive control strategy is presented, with selected experimental results. These results show the feasibility of control. We then analyze the effect of the controller on the instability mechanism, and propose improvements to the control strategy.

1 Introduction

Propulsion systems often feature large-amplitude oscillations, or instabilities, which are generally related to acoustically coupled unsteady combustion. The problem may be particularly serious in the case of large volumetric heat release devices. It is also encountered in many practical combustors operating in the lean premixed prevaporised mode. Low frequency thrust oscillations are observed in segmented solid rocket motors and they may damage the device and its payload. There exist many possible instability mechanisms which achieve the unstable feedback between heat release and acoustic pressure. One such mechanism, very often encountered in practical applications, is unsteady vortex shedding behind dump planes or flow restrictors. In dump combustors, it has been shown that the periodic shedding of vortices, entraining reactants, leads to unsteady heat release when the reactants in the vortex core ignite or when the vortex breaks down through interactions with neighboring vortices or the combustion chamber walls. Even in the absence of unsteady heat release in the vortices, their periodic interaction with choked exhaust nozzles generates

strong acoustic pressure oscillations which may then excite unsteady reactant burning. Such a mechanism may be responsible for the thrust oscillations observed in large segmented solid rocket motors.

Among the possible solutions to such problems, active control has great potential but requires further research efforts before practical application. This paper addresses the issue of control algorithms, a key point in these efforts. Adaptive techniques are specifically investigated to examine their operational applicability. Using a cold-flow experiment simulating the vortex shedding instabilities of solid rocket motors, we study the dynamics of the controller and the controlled system. The experimental configuration is sufficiently generic so that conclusions reached in this case may be extended to other studies of technological interest, where coupling through acoustically triggered vortex shedding plays a role.

The following paragraphs briefly summarize current understanding in the area of solid rocket motor instabilities and identify some of the major questions raised by application of active control. We then describe the experimental configuration, the response of the device, and the adaptive control strategy. Selected experimental results are then discussed.

2 Aeroacoustic instabilities in solid rocket motors

Among the different mechanisms which may drive pressure oscillations in segmented solid rockets, one of the possible sources for the instabilities is the coupling between the longitudinal chamber acoustic modes and vortex shedding from inhibitors protruding into the internal flow (see for example Vuillot [1] or Dotson [2]).

Experiments with a simplified geometry, where

cold gas flows in a duct and passes through a pair of baffles (see Nomoto [3]) or a pair of diaphragms (see Culick [4] and Dunlap [5]) support this theory: peaks in pressure transducer spectra close to the acoustic modes are measured in this case. It is believed that combustion plays a minor role and that the driving source is essentially aeroacoustical. One may then try to attenuate pressure oscillations by actively controlling vortex shedding. This may be investigated in a simple laboratory experiment.

Leaving aside many technological aspects (sensors, actuators, ...) it is important to examine the central issue of control. We specifically consider adaptive methods and wish to see if they are applicable to aeroacoustic instabilities. The following questions deserve attention:

- Is it possible to control aeroacoustic coupling?
- What is the optimal actuator/sensor combination?
- How much energy is needed to suppress the instability?
- What kind of control algorithms need be used?

The aim of this article is to answer some of these questions and to gain insight into the complex problem of active control of instabilities.

In the area of fluid mechanics, active feedback control of flow instabilities is now extensively investigated. However, a review of literature indicates that:

- Few studies deal with unstable flows coupled by acoustic (see, for example Huang [6] and Billoud [7]) or mechanical (see Huang [8]) resonances.
- A limited number of studies consider adaptive control algorithms in the area of unstable flows (see, for example Billoud [7] or Ziada [9]). The inconvenience with non-adaptive algorithms in this context is the necessity to change the controller gain and phase with changing flow speed (see, for example Ziada [9], Huang [6] and [8], Ffowcs Williams [10], Welsh [11] among others).

This work treats adaptive control algorithms applied to unstable flows, coupled with system acoustics.

3 Experimental setup and phenomena

3.1 Experimental device

The experimental setup consists of 11 cylindrical segments each 10 cm long and one 2.5 cm element, forming one long tube with an internal diameter of 5 cm (Figure 1).

The first segment has eight small tubes injecting air radially into the main tube. The flow rate varies during the experiments between 5 and 20 m³/h (corresponding to an average flow speed of 4.4 – 17.6 m/s at the diaphragms). A pair of diaphragms separated by the small segment creates a cavity, where periodic vortex shedding takes place. The cavity is placed above the second segment. This geometry (ratio of cavity length and depth, length of the tube) was inspired by previous studies of Nomoto [3], Culick [4] and Dunlap [5]. As will be shown below, it guarantees relatively "clean" acoustics.

For control purposes, a flush-mounted microphone is placed 22.5 cm above the second diaphragm. The measured pressure oscillations are amplified, filtered and converted into a digital signal. In addition to that, a hot film anemometer is placed in the cavity to detect the velocity fluctuations. The acoustic component of this signal is in general smaller than the fluctuations caused by turbulence or coherent vortical structures and therefore the main part of the signal detected is assumed to be due to aerodynamic phenomena. This signal is filtered, amplified and converted into a digital signal.

These signals serve as input to the control algorithms, programmed on a TMS320C31 processor (A/D converter, processor and D/A converter hosted on a DS1102 dSPACE board). The controller output then passes through a D/A converter, filter and amplifier and finally drives a 13 cm diameter loudspeaker fixed at the base of the tube.

The transfer function between the output of the control algorithm and its input will be denoted as "secondary path" (delimited by the dashed line in Figure 1). Later on, this transfer function will play an important role in the different control algorithms.

3.2 Aeroacoustic phenomena

It is first useful to determine the acoustic modes of the system. We use a band limited white noise signal,

Experiment	Theory	Error %
140 Hz	139 Hz	-
300 Hz	280 Hz	7 %
440 Hz	417 Hz	5 %
545 Hz	548 Hz	-
665 Hz	677 Hz	2 %
820 Hz	791 Hz	3 %
975 Hz	902 Hz	7 %
1080 Hz	1035 Hz	4 %
-	1170 Hz	-
1340 Hz	1300 Hz	3 %

Table 1: Comparison of acoustic modes, experiment and theory. The error is calculated with respect to the experimental values

generated on the processor, to excite the system. The system response is measured with the microphone. The complex transfer function between the system response and the white noise signal is calculated by

$$T_{xy} = \frac{P_{xy}}{P_{xx}},$$

where P_{xy} is the cross spectral density from the input of the secondary path to its output and P_{xx} is the power spectral density of the input of the secondary path.

The amplitude and phase of the transfer function is shown in Figure 2. Peaks in the spectrum correspond to higher gain and may be attributed to resonant acoustic modes. This introduces poles in the transfer function and additional phase lag (see the lower plot in Figure 2). On the other hand, nodes in the amplitude plot correspond to zeros in the transfer function. The phase lead generated in these cases can as well be seen in the lower plot in Figure 2.

The peaks appearing in the spectra are compared in Table 1 to calculated values. The method for calculating the longitudinal acoustic modes in our installation is described in [12]. Experimental and theoretical values are in good agreement. The acoustic boundary conditions were chosen as open without end correction for the lower extremity and open with end correction for the upper section. The error shown in the table is calculated with respect to the experimental values. The resonant frequencies determined experimentally are represented by horizontal lines in Figure 3.

Air is now injected into the system. The flow rate varies from 5 to 20 m³/h, in steps of 0.5 m³/h.

Different frequencies appear in the spectrum, depending on the flow speed. The two most energetic modes for each flow rate together with their amplitudes are represented in Figure 3. It can be clearly seen that these frequencies are close to the acoustic modes identified previously. It is interesting to note that, as the flow speed increases, the excited frequency increases slightly until it "jumps" to another acoustic mode.

This phenomenon is typical of coupling between convective and acoustic modes and is reported in different publications treating the instabilities in large segmented solid motors.

As shown by Dotson [2], Dunlap [5] and Brown [13], for example, the fundamental and the second harmonic are amplified by placing the restrictor pair at a pressure node (or velocity anti-node) for the fundamental longitudinal acoustic mode. The first harmonic could be amplified by placing the cavity at a pressure anti-node for the fundamental, which corresponds to a pressure node for the first harmonic (see Dunlap [5]). In our case, only the second and fifth harmonic are not present in Figure 3 (they appear only weakly in the spectra). Using "open" boundary conditions at the inlet and exhaust, the cavity is neither at a pressure node nor at a pressure anti-node for the fundamental. But one can show that the cavity is placed at or close to a pressure node for the two most energetic frequencies, the 550 Hz and the 1100 Hz peaks. Placing the cavity somewhere else changes the amplified frequencies and their relative power.

3.3 Control Algorithm

To control the aeroacoustic oscillations described in the previous section, one may choose to design

- an anti-noise controller and
- a controller acting at the source of the noise.

In the first case, the controller will not act on the primary noise source (denoted d in Figure 4). The controller imposes a signal on the system, which is equal to the primary noise, but 180° out of phase. The remaining noise detected by the microphone is reduced and disappears in the optimal case, as the two acoustic signals interfere destructively. There are many applications of anti-noise control described in the acoustics literature, see, for example, the books of Nelson and Elliott [14] or Kuo and Morgan [15]. The anti-noise controller for our configuration works well, but the convergence of the controller

is slow. Although the controller was designed for anti-noise control, it acts as well on the noise source. This makes it possible to design a noise source controller which features improved performance and is presented below.

The control scheme associated with the noise source controller is shown in Figure 4. In comparison to the anti-noise controller, the noise source controller is assumed to act upon the noise source and therefore on the primary noise d .

For the noise source controller the microphone signal is assumed to be proportional to the noise source. Therefore, if $e = 0$, there is no primary noise (or d is sufficiently small). This assumption is contrary to the anti-noise case, where $e = 0$ means that $y_r = d$ (refer to Figure 4). If this assumption is made, then the microphone signal can be used directly as input for the controller.

It is also possible to use other sensors to generate an input signal to the control algorithm. If the sensor signal is correlated with the phenomenon to be controlled, the algorithm can diminish the instability by acting in an appropriate way. It is important to note that the secondary path information needed by the controller has to be available for these cases. Also, for controllers with a fixed secondary path (as in the examples discussed here), it is important to choose a sensor such that this path does not change too much during operation of the device. If this is not the case, the control algorithm will diverge. Therefore, a convective secondary path (corresponding to a hot wire probe, for example) cannot be used.

A combination of different sensors can also be used for the control. Taking the microphone as error sensor (the acoustic secondary path does not change much during operation) in combination with the hot wire at the input of the controller yields good results (apart from different sensor signals, the controller scheme for this configuration does not change with respect to Figure 4). As the hot film is also sensitive to the flow turbulence, the input of the controller, even in the controlled case, is much noisier than the microphone signal. This leads to problems for the algorithm which finally result in a reduced performance compared to the combination with one microphone presented in Figure 4.

The idea of using an acoustic signal for acting at the source of flow instabilities has already been

used by Ziada [9], for example. In contrast to his work, in our experiments the loudspeaker is not placed close to the noise source, nor directed towards it. Nevertheless, using a feedback controller, one may reduce the noise level significantly by acting on the noise source.

The controller consists of an adaptive FIR (finite impulse response) filter. Its coefficients are updated using the well known filtered-x LMS algorithm: in order to compensate for the secondary path, the controller input has to be filtered by an estimation of the secondary path \hat{S} before this signal can be used to update the controller coefficients \mathbf{W} . The secondary path transfer function is obtained by identification before control.

4 Experimental results

4.1 Identification of the secondary path

To identify the secondary path, a white noise signal excites the system. The response is measured by a microphone and compared to the response of an adaptive FIR filter \hat{S} . The sampling frequency in all cases is 5 kHz.

The left hand side of Figure 5 shows the effect of adaptive identification in the time domain. The difference between the microphone signal and the output of the adaptive filter becomes significantly smaller and its squared error, averaged over 50 samples, approaches zero after adaption. Good agreement is also reached in the frequency domain for the frequency range of interest (see on the right hand side of Figure 5).

Now, the coefficients of \hat{S} are fixed and the controller can be switched from identification to control mode.

4.2 Influence of the leak on controller filter coefficients

The proper convergence of the LMS algorithm depends on the properties of the input to the adaptive filter. Insufficient spectral excitation of the filter due to the input signal may result in divergence of the filter coefficients. In this case, the solution for the minimisation procedure of the algorithm is not unique and finite precision effects in real-time implementations lead to unconstrained growth of the weights (see

Kuo and Morgan [15]). The introduction of a leakage factor into the update law can prevent this effect. One may show that this corresponds to the addition of low-level white noise, which leads to sufficient spectral excitation of the algorithm. The modified update algorithm for the controller shown in Figure 4 is given by:

$$\mathbf{w}_{k+1} = \nu \mathbf{w}_k + \mu \mathbf{e}'_k \mathbf{e}_k$$

with $0 < \nu \leq 1$. If $\nu = 1$, the original update law without leak is obtained. The vector containing the filter coefficients of \mathbf{W} is denoted as \mathbf{w} , \mathbf{e} is the error signal from the microphone and \mathbf{e}' denotes the filtered error signal in vector form. The index k indicates the discrete time instants.

The cost function to be minimized by the LMS algorithm without leak is given by

$$\hat{\xi}_k = e_k^2,$$

which corresponds to a minimization of the squared instantaneous error signal. It can be shown that the leak also has an influence on this function, which can be rewritten for the modified algorithm as:

$$\hat{\xi}_k = e_k^2 + \gamma \mathbf{w}_k^T \mathbf{w}_k \quad \text{with} \quad \gamma = \frac{1 - \nu}{\mu}.$$

Again, setting $\nu = 1$ gives the original cost function without leakage factor. This function can be interpreted as follows: the uncontrolled growth of the filter weights (which corresponds to an uncontrolled growth of the controller output) is penalized. Hence, the introduction of a leak also prevents the output signal from being overdriven. This can be useful if overdriving leads to nonlinear behaviour of the secondary path which is not taken into account by the linear model $\hat{\mathbf{S}}$.

The influence of the leak during the experiment is clearly shown in Figure 6. In this case an air flow of $16 \text{ m}^3/\text{h}$ was used. The first 50 coefficients of \mathbf{W} (the sampling frequency was 5 kHz) for different times measured with respect to the controller switch on for the case without leak can be seen on the left of Figure 6. The coefficients diverge. The evolution of the filter coefficients with leak is represented on the right of Figure 6. The coefficients stay nearly constant during the whole experiment.

4.3 Control of aeroacoustic phenomena

One may analyze the results using several parameters:

- the microphone signal without and with control

- the controller output
- an estimation of the acoustic signal injected into the system by the controller (denoted srd). This enables us to estimate the acoustic power necessary to control the phenomenon. It is obtained by filtering the controller output by the identified secondary path. We suppose in this case that the real secondary path does not differ from $\hat{\mathbf{S}}$ during control.

Having fixed the coefficients of the secondary path, air is injected into the tube. The power spectral density of the pressure oscillations is calculated for the uncontrolled case. The controller is then switched on. After convergence, the pressure oscillations are again acquired at the fixed sampling frequency of 5 kHz.

In Figure 7 the spectra without control (dashed lines) are compared to the spectra with control (solid lines) for $\dot{V} = 8$ (left plot) and $14 \text{ m}^3/\text{h}$ (right plot). For $\dot{V} = 8 \text{ m}^3/\text{h}$, the peaks in the spectrum are not very strong, and are covered by the large-band noise. Nevertheless, the controller manages to reduce the two main peaks by about 7 dB. The estimation of the acoustic signal introduced by the controller (named srd in all plots) shows frequency components at the modes excited by the air flow. The level of these peaks is, in general, about the same as the noise level after control. This suggests that the controller acts on the source of noise, as was assumed for the design of this algorithm. For $\dot{V} = 14 \text{ m}^3/\text{h}$, there is one main peak at 500 Hz, 10 dB above the broad-band components. The controller reduces this peak to the level of the broad-band noise.

Figure 8 shows the results for higher flow rates ($\dot{V} = 16 \text{ m}^3/\text{h}$ on the left and $\dot{V} = 18 \text{ m}^3/\text{h}$ on the right). For $\dot{V} = 16 \text{ m}^3/\text{h}$, the uncontrolled spectrum is dominated by two peaks: the first at 550 Hz and its first harmonic at 1100 Hz. With control, these peaks disappear completely. The reductions obtained are between 30 and 40 dB. It is interesting to note that the reduction of the second peak at 1100 Hz is obtained with little effort at this frequency by the controller. This suggests that the origin of this peak is controlled by acting on the 550 Hz component.

Comparing the estimation of srd for the 550 Hz peak with the measured remaining noise, it can be seen that srd is clearly larger than the peak with control. There are two possible explanations for this:

- srd is overestimated. Tests with a true anti-noise configuration disprove this hypothesis. For fre-

quencies corresponding to acoustic modes, the amplitude was generally underestimated. For other frequencies the overestimation was much less than 10 dB.

- One part of this frequency component is used as anti-noise. Then, the primary noise interferes with the control signal and the remaining amplitude is smaller than each of the components.

An additional peak at about 820 Hz appears during control. This is not due to improper controller action at this frequency. Tests where the controller could not act on the 820 Hz peak showed that, even in this case, the peak increased during control. This effect seems to be due to mechanisms inside the experimental device, which require further analysis.

For $18 \text{ m}^3/\text{h}$, multiple peaks appear in the uncontrolled spectrum (see Figure 8). Although *srd* does not contain all of these frequencies (e.g., the components above 1100 Hz), they disappear with control. This can be explained by saturation or by the fact that "monochromatic" vortices in the cavity excite multiple acoustic modes.

The influence of the controller on the pressure signal is shown in Figure 9. Having switched on the controller, it acts immediately on the error signal. The time required to obtain a very strong reduction in the error signal is of the order of the controller length divided by the sampling frequency (see upper plot in Figure 9). The transient behavior of the controller output can also be seen: at the control onset the amplitude grows rapidly above the level which, later on, is necessary to maintain a small error signal. After this first phase, the output amplitude reduces to a more regular and small level. This behavior seems typical for controllers acting at the source of the instability. Once the phenomena at the origin of the noise are controlled, only a relatively small amount of energy is needed to maintain control.

The influence of the controller on the system dynamics can also be analyzed by looking at the hot film signal. The hot film, placed in the cavity, detects velocity fluctuations in the flow. Strong frequency components recorded in this way (see Figure 10, the upper plots, left: time domain, right: frequency domain) are associated with the vortices in the cavity. These structures are at the origin of the pressure oscillations. The hot film signal becomes less coherent during control, although its amplitude does not change (see the lower plots in Figure 10, left: time domain, right: frequency domain). This

suggests that the controller decorrelates the vortices. The energy of these structures is now distributed in the turbulence of the flow.

The present results are coherent with observations made by others (see, for example Ziada [9], Ffowcs Williams [10] or Welsh [11]). Ffowcs Williams proposes the following explanation: initially, the shear layer perturbations are linear and receptive to infinitesimal acoustic waves. A weak stimulus can thus amplify or attenuate the vortex shedding. In this way, the acoustic feedback from the second diaphragm helps to correlate the vortical structures. In the same way, an acoustic signal can also decorrelate the vortices. Active control can therefore be used to break the acoustic feedback (see Ziada [9] and Welsh [11]). The ability of an acoustic signal to correlate the vortex shedding is, for example, demonstrated by Blevins [16].

Finally, the acoustic power detected by the microphone with and without control can be calculated and compared, and one may simultaneously obtain an estimate of the acoustic power needed to achieve control (using *srd*). This is shown in Figure 11. Although the efficiency of the control varies with the air flow, the noise with control is always smaller than without. The reduction is between 5% and more than 65% (see the middle plot in Figure 11). The power needed for control is generally smaller than 50% of the power in the system in the uncontrolled case. For high air flow rates ($\geq 19 \text{ m}^3/\text{h}$) the invested power exceeds the uncontrolled noise power (see the lower plot in Figure 11). This is due to a large overestimation of the control signal power needed for the suppression of high-frequency components (above 1 kHz). In this situation, the controller creates a large peak which dominates the controlled spectrum. Nevertheless, the acoustic power in the controlled case is still lower than without control.

5 Conclusion

Results described in this article show the possibility for controlling aeroacoustic instabilities in a cold gas experimental setup. The adaptive controller is able to reduce the pressure oscillations by up to 40 dB. A stable state is reached after a short transition phase. In addition, the controller is able to take into account changes in the air flow rate: it adapts automatically to reduce the microphone signal.

The controller is less effective for frequency components of lower amplitude and broad-band

components of the spectrum. This is due to the feedback structure of the controller, which has to predict the primary noise at future sampling intervals. For broad-band signals this is impossible.

The controller is also less effective for high mass flow rates. Although it manages to reduce the main peak by about 30 dB, a new high-frequency peak appears during control. This may be due to insufficient accuracy in the secondary path for high mass flow rates or to hydrodynamic phenomena. Further analysis is required to understand this effect.

Results indicate that the algorithm acts simultaneously on the noise and on the source of the noise. The acoustic power needed for control is estimated to be generally less than 50% of the acoustic power in the system before control.

The choice of the sensors which can be used is restricted by two properties: first, the sensor which builds one part of the secondary path should be such that its transfer function does not change too much during operation. Otherwise, algorithms with on-line identification of the secondary path will have to be used (in this respect, recent results obtained in our laboratory for the same experimental device are quite promising). Second, the signal used as input for the controller should be as deterministic and as correlated to the phenomenon to control as possible. Uncorrelated noise in the sensor signal degrades the controller performance.

Acknowledgment

This work was supported in part by the French CNES (Centre National d'Etudes Spatiales). It is part of a research programme coordinated by the CNES and ONERA (Office National d'Etudes et de Recherches Aéronautiques).

References

- [1] F. Vuillot. Point sur les recherches relatives à la stabilité de fonctionnement du MPS P230 d'Ariane 5. In 3^{ème} Colloque R&T: Ecoulement interne en propulsion solide. CNES, 1998.
- [2] K. W. Dotson, S. Koshigoe, and K. K. Pace. Vortex shedding in a large solid rocket motor without inhibitors at the segmented interfaces. *J. Prop. and Power*, 13(2):197-206, 1997.
- [3] H. Nomoto and F. E. C. Culick. An experimental investigation of pure tone generation by vortex shedding in a duct. *J. Sound Vib.*, 84(2):247-252, 1982.
- [4] F. E. C. Culick and K. Magiawala. Excitation of acoustic modes in a chamber by vortex shedding. *J. Sound Vib.*, 64(3):455-457, 1979.
- [5] R. Dunlap and R. S. Brown. Exploratory experiments on acoustic oscillation driven by periodic vortex shedding. *AIAA J*, 19(3):408-409, 1981.
- [6] X. Y. Huang and D. S. Weaver. On the active control of shear layer oscillations across a cavity in the presence of pipeline acoustic resonance. *J. Fluids and Structures*, 5:207-219, 1991.
- [7] G. Billoud, M. A. Galland, H. H. Can, and S. Candel. Adaptive active control of instabilities. *J. of Intelligent Material Systems and Structure*, 2:457-471, 1991.
- [8] X. Y. Huang and D. S. Weaver. Control of flow-induced fin vibrations by anti-sound. *J. Sound Vib.*, 169(3):428-432, 1994.
- [9] S. Ziada. Feedback control of globally unstable flows: Impinging flows. In P. W. Bearman, editor, *Flow-Induced Vibration*, pages 579-591. A. A. Balkema, Rotterdam, 1995.
- [10] J. E. Ffowcs Williams and B. C. Zhao. The active control of vortex shedding. *J. Fluids and Structures*, 3:115-122, 1989.
- [11] M. C. Welsh, K. Hourigan, R. J. Alfredson, and Pan Di Lin. Active control of flow-excited acoustic resonance: higher order acoustic modes. In *International Conference on Flow Induced Vibrations*. IMechE, May 1991.
- [12] T. Poinso, A. Trounev, D. Veynante, S. Candel, and E. Esposito. Vortex driven acoustically coupled combustion instabilities. *J. Fluid Mech.*, 177:265-292, 1987.
- [13] R. S. Brown, R. Dunlap, S. W. Young, and R. C. Waugh. Vortex shedding as a source of acoustic energy in segmented solid rockets. *J. Spacecraft*, 18(4):312-319, 1980.
- [14] P. A. Nelson and S. J. Elliot. *Active Control of Sound*. Academic Press, 1992.
- [15] Sen M. Kuo and Dennis R. Morgan. *Active Noise Control Systems*. John Wiley & Sons, 1996.
- [16] R. D. Blevins. The effect of sound on vortex shedding from cylinders. *J. Fluid Mech.*, 161:217-237, 1985.

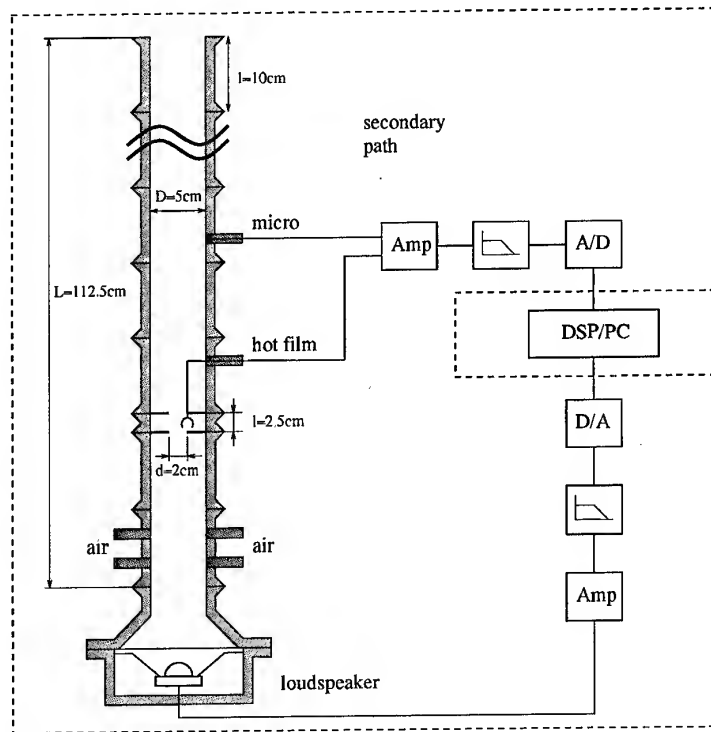


Figure 1: Experimental setup. The pressure signal is measured by a microphone, the flow velocity by a hot film anemometer. The loudspeaker serves as actuator during control. The secondary path is given by the transfer function between the output of the DSP and its input (inside the dashed lines).

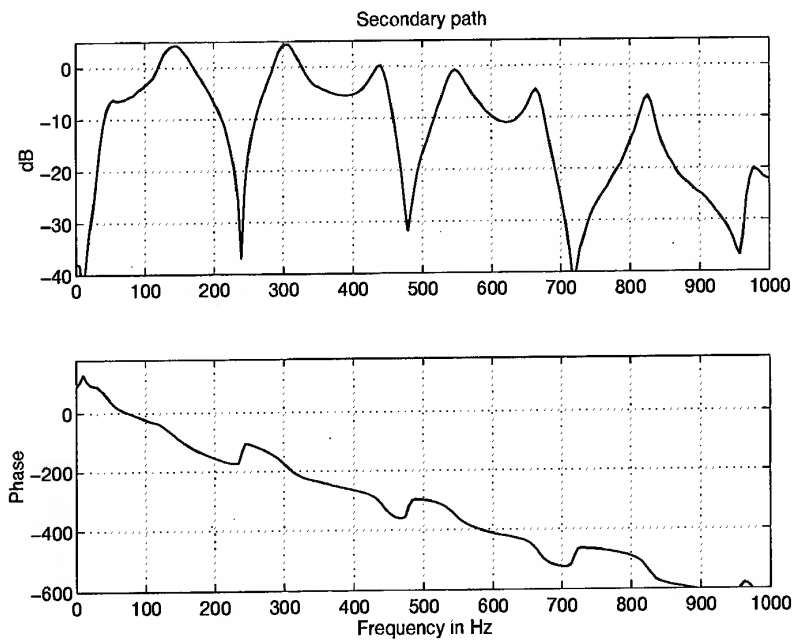


Figure 2: Identification of acoustic modes. Amplitude (upper plot) and phase (lower plot).

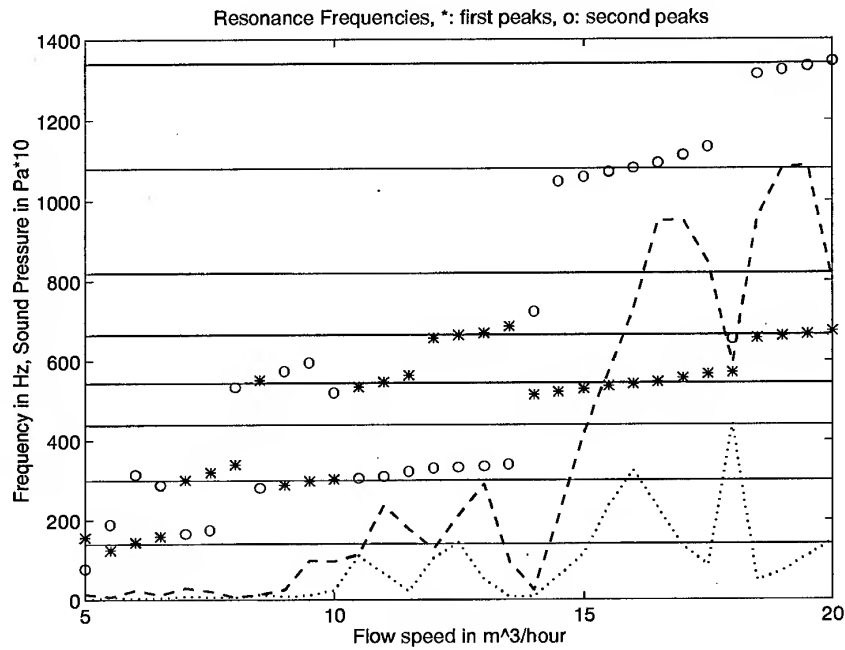


Figure 3: Coupling of convective modes with acoustics. Horizontal lines: acoustic modes. Frequencies (*) and corresponding amplitudes (----) of the most energetic modes. Frequencies (o) and corresponding amplitudes (.....) for the second-most energetic modes.

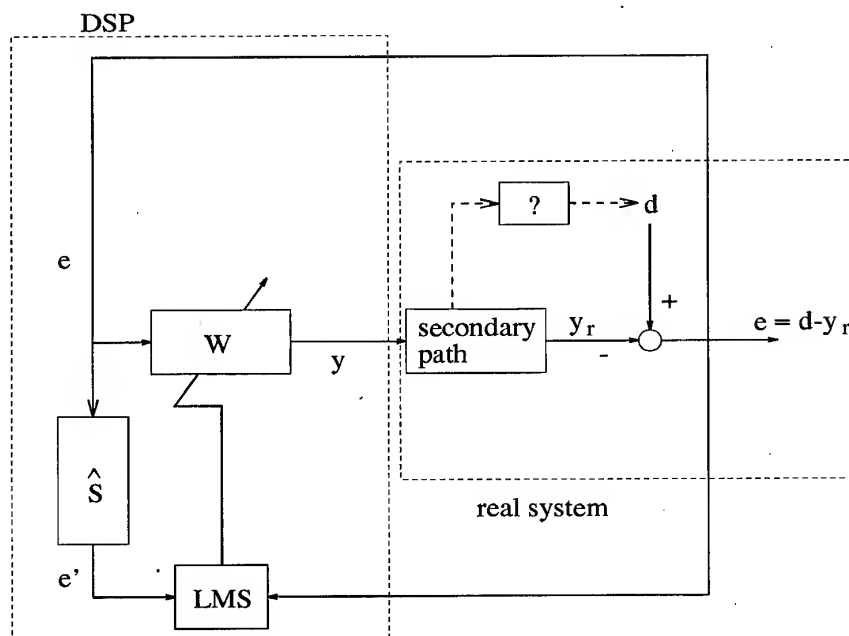


Figure 4: Noise source control scheme with single microphone input: \hat{S} is the estimation of the secondary path; W , the controller.

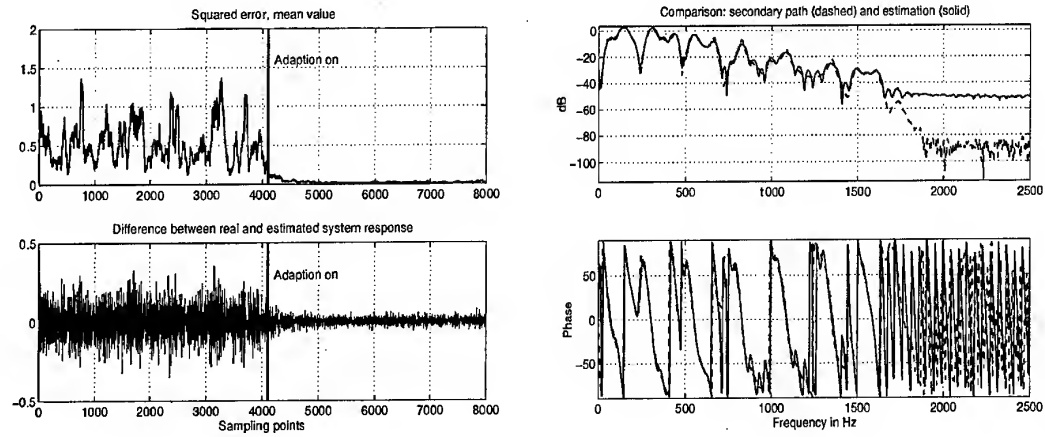


Figure 5: Identification of the secondary path. Left: time domain, e^2 in the upper, e in the lower plot. Right: frequency domain, amplitudes of S (----) and \hat{S} (—) in the upper, phases in the lower plot.

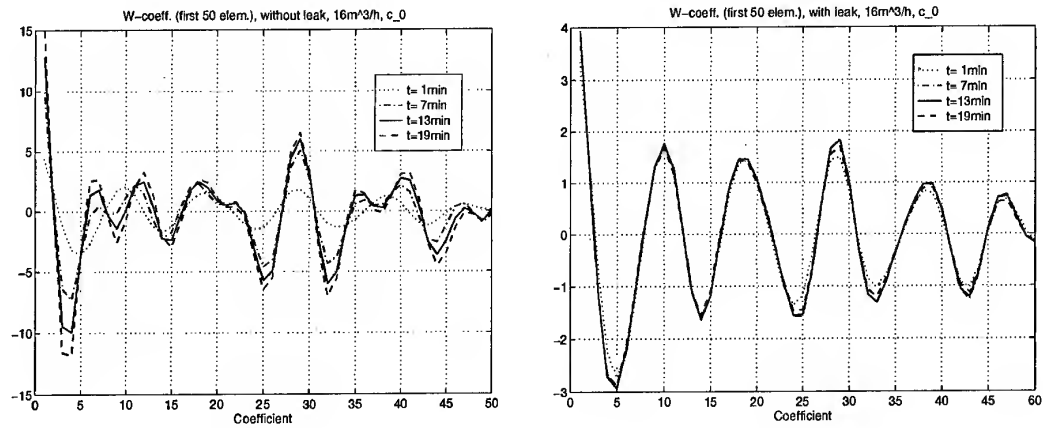


Figure 6: Left: Filter coefficients W for different times without leak. Right: Filter coefficients W for different times with leak.

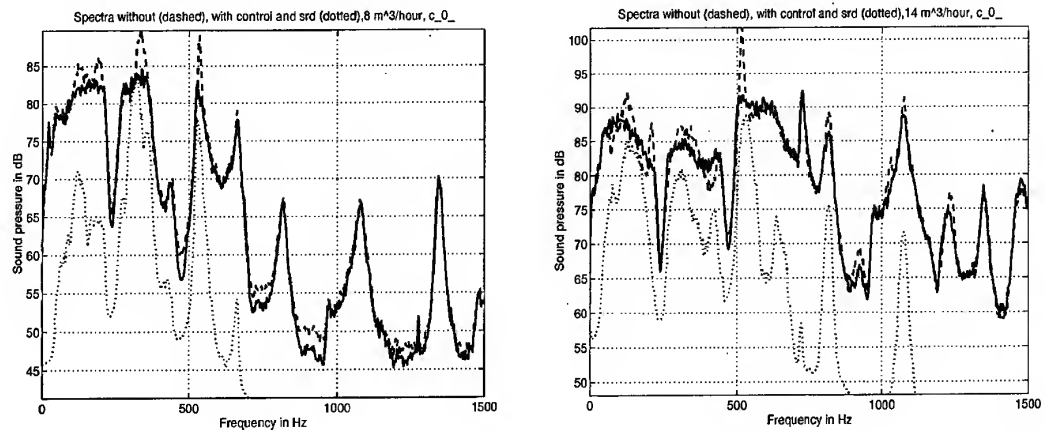


Figure 7: Spectra without (----) and with control (—), and estimation of acoustics introduced by the controller (·····). Air flow rate $V = 8$ (left) and $14\text{ m}^3/\text{h}$ (right).

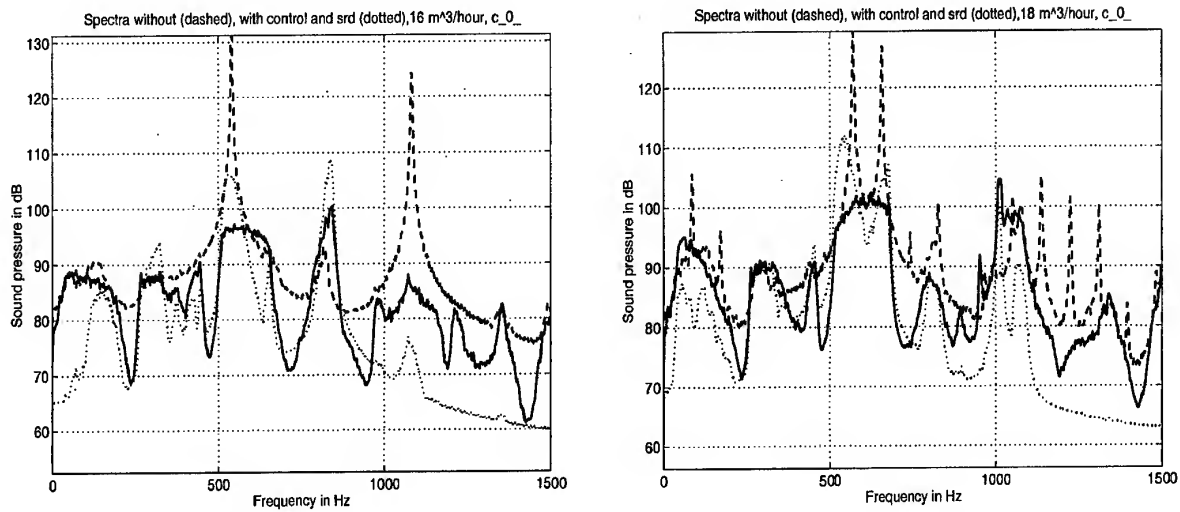


Figure 8: Spectra without (----) and with control (—), and estimation of acoustics introduced by the controller (.....). Air flow rate $\dot{V} = 16$ (left) and $18 \text{ m}^3/\text{h}$ (right).

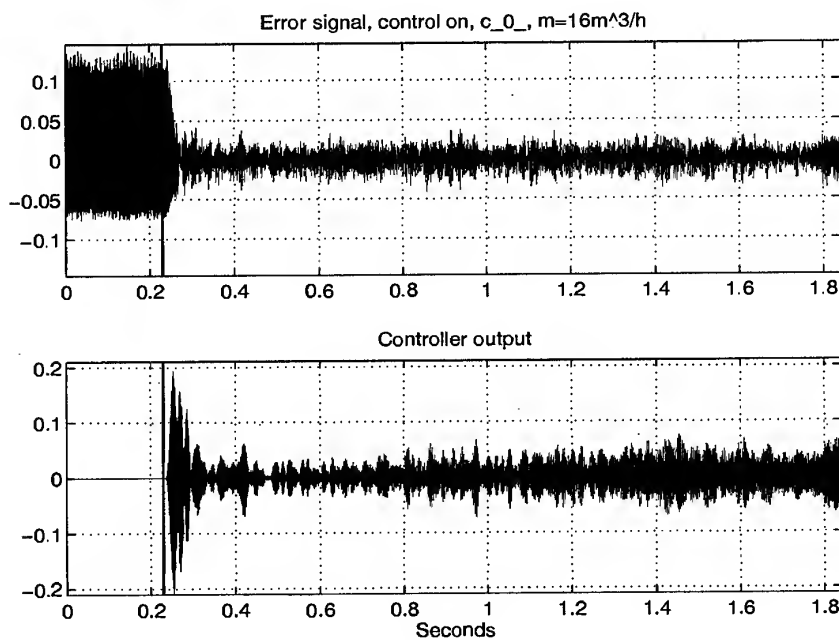


Figure 9: Error signal (upper plot) and controller action (lower plot). Air flow rate $\dot{V} = 16 \text{ m}^3/\text{h}$. Vertical line: the controller is switched on.

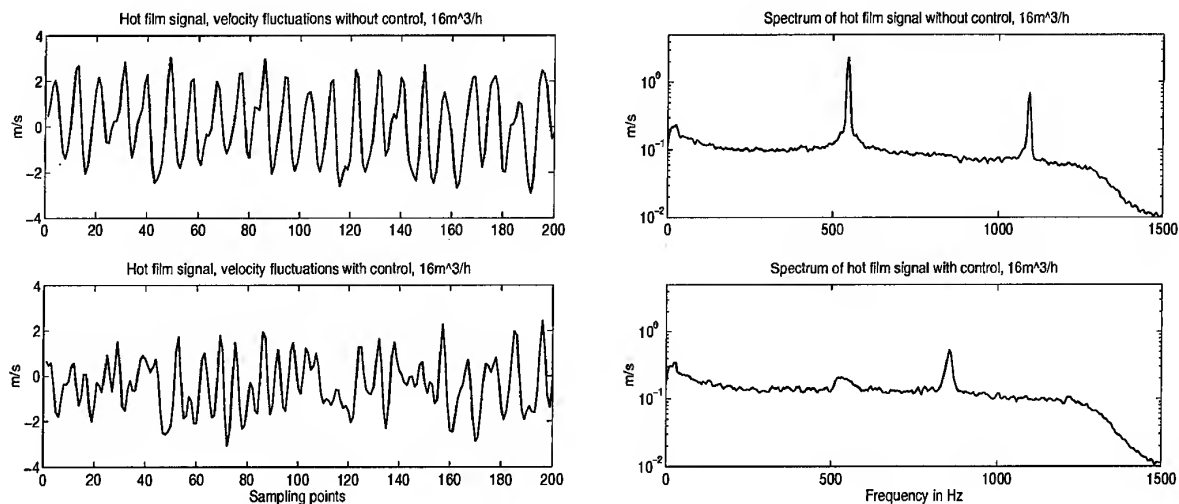


Figure 10: Left: hot film signal, without control (upper plot) and with control (lower plot). Right: Power spectral density of hot film signal without control (upper plot) and with control (lower plot). Air flow rate $V = 16 \text{ m}^3/\text{h}$.

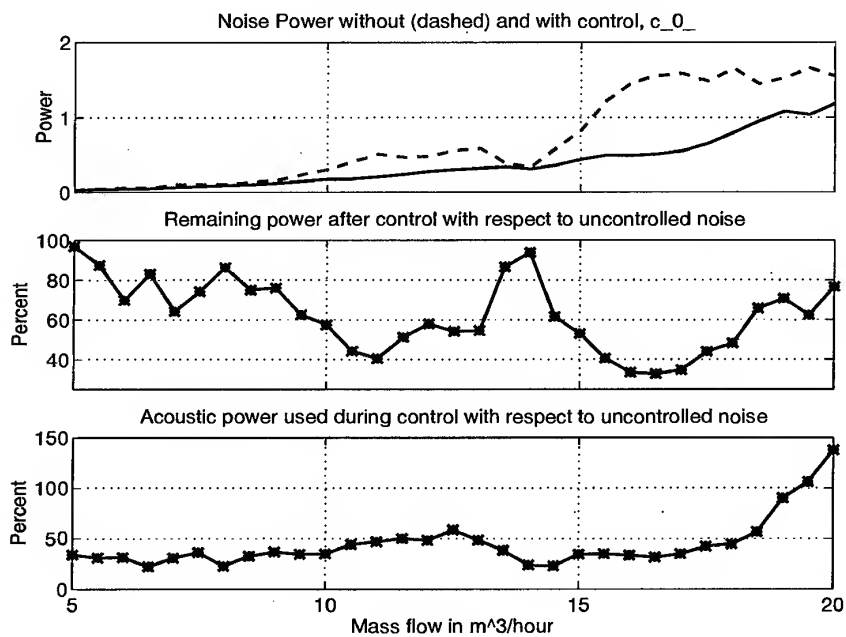


Figure 11: Comparison of the noise power with (—) and without control (----), absolute values, arbitrary units (top), in percent (middle) and comparison $srd/\text{without control}$, in percent (bottom).

PAPER No. 39
Mettenleiter, Haile & Candel
(presenter: M. Mettenleiter)

Question 1: F. Culick, Caltech., U.S.

Please identify the mechanism that you believe is the basis for control by injecting acoustic waves with a loudspeaker? How do you make the connection between the demonstration of active control and the proposed use of a modulated injected (oxidizer rich) fluid in an operating solid rocket?

Answer:

The hot film signal, amongst other, shows that the well-correlated vortical structures existing without control, become less coherent with control. As these structures are assumed to be at the origin of the pressure oscillations, we act on the noise source during control. The modulated injected propellant leads to an oscillating combustion that creates corresponding pressure oscillations. These pressure oscillations could act in the same manner as the acoustic loudspeaker signal in the cold flow experiment. Thus, the injection could prevent coherent vortical structures from organizing, and consequently, reduce pressure fluctuations.

Question 2: (unknown)

Would increased physical understanding of the problem and proposed solution help for improving control?

Answer:

For anti-noise control, no; for noise-source control, a model would definitely help.

APPLICATION OF ACTIVE COMBUSTION CONTROL TO SIEMENS HEAVY DUTY GAS TURBINES

S. Hoffmann, G. Weber and H. Judith

Siemens AG KWU

Abt. WB TVF

D-45466 Muelheim an der Ruhr

Germany

J. Hermann, A. Orthmann

IfTA, Ingenieurbuero fuer Thermoakustik GmbH, Haar-Salmdorf / Germany

Abstract

Modern gas turbines are usually featuring lean premixed combustion in order to keep the emissions at an acceptable level. Ever increasing reaction densities, however, result in an increased tendency to exhibit dynamic flame instabilities.

Active Instability Control (AIC) is a very powerful and flexible tool for the suppression of these instabilities. Due to the high fuel massflow and high system pressures, the application of AIC to heavy duty gas turbines, however, is a difficult task.

This paper reports on several applications of an AIC system to the Siemens Model V84.3A¹ and V94.3A² heavy duty gas turbines featuring annular combustion chambers. Depending on the burner configuration used, the AIC successfully solved four different tasks:

- Damping of combustion oscillations by up to 17 dB (86%)
- Complete suppression of combustion oscillations at intermediate load levels and during switchover processes
- Suppression of combustion oscillations at low pilotgas massflow during lean premixed operation, allowing for a substantial reduction of the NO_x emissions
- Suppression of combustion oscillations at baseload level, allowing for a 5%-point load increase

Several tests showed the long-term reliability of the hardware components and the failure tolerance of the AIC system.

1. Introduction

In the gas turbine industry, lean premixed combustion is a state-of-the-art technique for NO_x emissions reduction. Due to the high reaction densities in modern stationary gas turbines, combustors using lean premixed flames reveal a high tendency to form dynamic combustion instabilities also known as "humming".

In closed combustion systems, a feedback between the heat release rate of the flame and the acoustics in the combustion chamber can occur. Fluctuations in the combustion heat release excite an acoustic pressure field in the combustion chamber which in turn causes new fluctuations of the heat release rate. If the fluctuations of the pressure are nearly in phase with those of the energy release rate, i.e. if the Rayleigh criterion (Rayleigh 1878) is fulfilled, a self-amplification of the oscillations occurs.

Combustion instabilities often cause high pressure amplitudes and are accompanied by an increased heat transfer to the combustion chamber walls posing high mechanical and

¹ Rotor frequency = 60 Hz, Baseload power output = 170 MW

² Rotor frequency = 50 Hz, Baseload power output = 250 MW

thermal loads on the system. Consequently, their suppression or elimination is an important task in gas turbine combustion engineering.

Actually, there is no method of predicting self-excited combustion oscillations in complex systems and thus to take countermeasures in the developing stage of a combustion system. If oscillations occur in systems in use, two approaches are available to deal with the problem:

Passive methods using changes in the operating parameters (e.g. the equivalence ratio), the design, or the acoustics of the combustion system to hinder the self-excitation mechanism. They may reduce the prevailing sound pressure amplitudes to a tolerable level by dissipative measures, e.g. by mufflers or baffles (Culick 1988). Unfortunately, it is not possible to predict their effect on the combustion oscillations completely, so that their use entails a lot of testing. Experience reported by Scalzo, Sharkey and Emmerling (1990) for gas turbines, Vortmeyer et al. (1996) for coal gasification applications and by Konrad et al. (1996) in an aero-engine show the successful application of passive measures.

Active methods, by contrast, either use a feed-back control loop and fast actuators to counteract the oscillating heat release (Active Instability Control-AIC) or adapt the combustion process to the operating conditions by active elements like slow valves in order to increase the operation envelope of the combustion system (Active Combustion Control). Two excellent reviews on AIC have been given recently by Candel (1992) and McManus et al. (1993). The use of AIC in a 170MW heavy duty gas turbine is reported in Seume et al. (1997).

Typically, combustion oscillations are strongly depending on the hardware configuration used. Even slight modifications of the flow- and reaction field as well as the system acoustics may result in completely different combustion dynamics. During the test bed runs and in the early commissioning phase of the Siemens Model VX4.3A gas turbines, the build-up of dynamic flame instabilities could be suppressed by burner and fuel system modifications alone. A summary of the thermoacoustic phenomena existing in our ring combustors, like standing and travelling circumferential pressure waves, is given in Seume et al. (1997).

This paper reports on an active method for the suppression of dynamic instabilities in Siemens gas turbines with annular combustion chambers: An active instability control (AIC) which counteracts the heat release fluctuations during the oscillation by fast modulation of the fuel flow. This system was applied to several different burner configurations which were imposing completely different tasks to the control system, thus proving its flexibility.

2. Technical Setup

2.1. The actuator and its location

The Siemens Hybrid burner (Figure 1) can be operated in three different operation modes: The diffusion mode, (all the fuel is introduced through the central axial swirler), the premix mode (most of the fuel is mixed into the outer so called "diagonal" swirler, a small rest through the nonpremixed central pilot burner) and the mixed mode (both the premix and the diffusion burner are active, pilotgas can be introduced optionally). Similar to the AIC setup on the Siemens V84.3A gas turbine described by Seume et al. (1997) the pilot gas system was used to influence the combustion instability by the active control system. In the mixed and premixed gas modes, each of the 24 burners of the Vx4.3A operates with a small additional diffusion flame which contributes approx. 10% of the total thermal power of the burner. This pilot flame stabilizes the premixed flame and has a significant effect on the dynamic behavior of the main flame.

By modulating the heat released by the pilot flames – e.g. by modulating the fuel flow rate – the heat release in the main flame can be influenced accordingly. Therefore the AIC can modulate the larger main flame by controlling only a small fraction of the fuel instead of the

entire gas flow. To do this, each of the 24 burners of the gas turbine was equipped with a special high-speed valve, the Direct Drive Valve (DDV) manufactured by Moog, Germany.

The 2nd generation of this valve can be used with frequencies of up to 450 Hz with a loss in amplitude of only about 4 dB. By using a high temperature coil, an external driver and an external valve monitoring electronic module the valve itself can work in a hot environment with temperatures reaching up to 120°C. A longtime test over a 6 months period in an environment of 80°C showed that the valve is very robust. Only very little abrasion of the piston was observed. For the test, the valve was excited at a frequency of 400 Hz and with the maximum amplitude.

During the gas turbine tests, valve failures were simulated in order to test their impact on the overall AIC performance. A maximum of two valves was switched off during the AIC tests resulting in no noticeable degradation of the system performance, regardless of the valve position. Further tests with more inactive valves could not be performed due to time constraints.

The success of the AIC strongly depends on a sufficiently high modulation of the mass flow in the pilot gas system by the actuator. Because the mass flow modulation is determined by the acoustic field or rather the resonant behavior of the pilot gas system, this system was tuned as described by Hantschk et al. (1996), Hermann (1996) and Hermann et al. (1996).

2.2. The sensor and its location

As described by Seume et al. (1997), the fluctuating pressure measured upstream of the combustion chamber is a suitable signal for the controller input of the AIC. In case of the V94.3A, 12 high temperature piezo transducers without extra cooling were installed to measure the pressure signal along the circumference of the ring combustion chamber.

2.3. Use of symmetry to reduce feed-back loops

Due to the nature of the excited circumferential (azimuthal) modes in the ring combustion chamber, the 24 valves at each burner are located in different regions of the acoustic field where different phases and amplitudes of the combustion oscillation must be controlled. To cope with this problem, each burner could be supplied with an independent control unit together with the corresponding sensor and actuator. In this case, the input signal for a certain DDV valve could be obtained from the pressure signal measured at the same location, thus ensuring that the induced modulation of the heat release rate would indeed be anti-cyclical to the self-excited heat release oscillation at this at the corresponding location. This approach would require 24 feed-back control loops.

The number of necessary sensors and control units may be reduced by using the symmetry of the azimuthal modes. This symmetry is marked by a characteristic distribution of nodes and antinodes, i.e. of regions of high and low amplitudes which are related to each other by a constant phase shift. It is therefore possible - as described by Seume et al. 1997 - to use a signal measured at a certain circumferential location of the azimuthal mode - or the ring combustor - to determine not only the actuator input signal for this particular location but also those for several other locations. This can be done by one control unit and thus not only reduces the number of sensors needed but also the number of controllers.

This principle was applied to the AIC of both gas turbine types, the V84.3A and the V94.3A. In case of the V84.3A where only the second and fourth harmonic exhibited high amplitudes, the number of independent control loops and sensors was reduced to 6, each equipped with 4 valves as actuators. In the V94.3A the number of independent control loops was increased from 6 to 12 (see Figure 2) to cope with the fact that also the first harmonic could be observed in this engine. Altogether the AIC system for the V94.3A consisted of 12 independent control loops, each comprising a pressure sensor and a control unit as well as 2 valves as actuators. Thus a total of 24 valves was needed.

2.4. The controller

The main control work is done by 6 digital signal processors, with each processor handling two control loops. The control algorithm itself works in the frequency domain. Compared to the algorithm used for the AIC system of the V84.3A, the control algorithm for the V94.3A includes several additional features:

- suppression of two dominant frequencies (owing to the use of the symmetry for reducing the feedback loops, this suppression is only possible for 2 even or 2 odd harmonics)
- automatic determination of the control parameters
- automatic adjustment of the control parameters depending on the operating condition of the gas turbine
- identification of the frequency response of the system

For the V94.3A, the AIC hardware formerly used on the V84.3A was completely redesigned to a full industrial application. The following new hard- and software features have been included:

- modular architecture (easy to extend)
- hardware monitoring for error diagnostic
- actuator monitoring (valve seizing, deviation from the desired set point, marginal check)
- sensor monitoring (cable and sensor defect)
- redundant power supply (interchangeability during operation)
- integrated LCD-displays and keyboard for monitoring and user access
- data and control interface to the gas turbine control system
- failure and data recording system
- special tools for fast commissioning

The hard- and software setup is optimized with respect to short implementation and commissioning time scales.

3. Application in Heavy Duty Gas Turbines

This pilotgas AIC system was introduced in our V84.3A and V94.3A gas turbines and tested with several burner configurations. The results obtained in the V84.3A will only be briefly summarized in this paper. A detailed description of these test runs is given in Seume et al. (1997).

3.1. AIC results of the V84.3A

During the prototype shop tests of the 170 MW Model V84.3A gas turbine, self-excited combustion oscillations were observed in the premixed-gas mode at base load. Besides passive suppression methods, which finally solved the problem, the AIC system described above was developed to suppress these instabilities.

3.1.1. Typical AIC performance

Figure 3 shows a time plot of the relevant AIC parameters during a representative test, i.e. the control parameters (gain and phase shift between the actuator input signal and the combustor pressure which is the input to the controller), the average RMS-value of the sound pressure and the maximum amplitude (among the 6 transducers) for the two dominant harmonics (217 Hz and 433 Hz) of the fluctuating pressure. The measurements were taken at base load with constant working conditions including the time mean pilot gas massflow.

During the first 32 seconds of the shown period the gain is set to zero and the pressure amplitudes in the combustion chamber are high due to combustion oscillations. After

adjusting the phase shift to its optimum with low actuator amplitudes (reduced gain), the gain is drastically increased and consequently the dynamic pressure in the combustion chamber strongly decreases. Switching the AIC off results in an immediate increase of the dynamic pressure signal, which is decreasing immediately after the AIC is switched on again.

During the test bed runs, the dynamic pressure could be reduced by up to 17 dB or 86%.

3.1.2. Conclusions

Even in this early phase of the AIC development with a very simple version of the controller, the System prove, that by the use of AIC

- combustion oscillations could be drastically reduced (- 17 dB)
- the operation envelope could be increased and
- NO_x emissions could be minimized

in a 170MW gas turbine. These positive results lead to a continuation of the AIC development program.

3.2. AIC results of the V94.3A

The performance of the AIC was tested with two different burner designs, both being slight modifications of the Standard Hybrid burners. The modifications had a strong influence on the dynamic behavior of the combustor and the sensitivity of the flame for pilotgas variations.

With the first modification, burner A, self-excited combustion oscillations were observed at low load levels (30 to 50% of the baseload level) in the mixed operation mode. An additional instability region showed up close to base load in premixed operation. In both cases, the self-excited combustion oscillation was characterized by the second harmonic at 175 Hz and the fourth harmonic at 350 Hz.

With the second modification, burner B, no self-excited combustion instability was observed at loads below 97 % of the base load level. Further load increase resulted in the formation of combustion instabilities with two frequency peaks near the first harmonic at 110 Hz and at the second harmonic at 175 Hz.

3.2.1. AIC performance at intermediate load – mixed operation

Figure 4 shows the relevant quantities versus time during the test operation without AIC – on the left - and with AIC - on the right - at low load. The following quantities are presented:

- the RMS-value of the sound pressure (average of the 12 AIC-sensors),
- the electric power output in percent of the base load,
- the corrected turbine outlet temperature (OTC) relative to the baseload value and
- the position of the diffusion and premix gas valves.

During the tests the main pilot gas valve was opened by 60% and the compressor inlet guide vane (IGV) was constantly closed.

As is seen on the left side of Figure 4, self-excited combustion instabilities occurred during mixed operation with a diffusion fuel fraction of 30% and active pilot gas system. The partially non-premixed combustion is necessary in order to stabilize the premixed flame at low loads or low OTCs respectively. As an advantage over a pure non-premixed combustion which is very stable even at low loads the mixed operation offers significantly lower NO_x levels. Further tests showed that self-excited combustion oscillations occurred over the complete range of mixed operation and could only be avoided by completely switching to pure premixed operation which however is only possible at higher loads or OTCs respectively.

To suppress the self-excited combustion oscillation during mixed operation, the AIC-System was adjusted to the second harmonic at 175 Hz. The active control was started some seconds before the gas turbine was switched into mixed operation. In contrast to the switch-

over without AIC where very high pressure amplitudes occur immediately (left side of Figure 4) the active AIC system even decreases the dynamic pressure level from 18 to 13 mbar (top and right side of Figure 4). Figure 4 shows that with operating AIC no oscillations arise during in mixed operation as well as during the switch-over process to premix operation. The system also performs well for load decreases.

In this application, the AIC serves the purpose to suppress dynamic instabilities in the intermediate load range, making "soft" switch-over processes and load following possible.

3.2.2. AIC performance near base load – premixed operation (NO_x reduction)

The results of the AIC tests under premixed operation near base load are shown in Figure 5. The following quantities are presented:

- the RMS-value of the sound pressure (average of the 12 AIC-sensors),
- the electric power in percent of the base load,
- the corrected turbine outlet temperature relative to the baseload value and
- the opening position of the IGV.

During the tests the main pilot gas valve was open and the premix valve was partially closed in order to achieve the guaranteed NO_x emissions.

With burner A, the gas turbine showed self-excited combustion oscillations at loads above 88% of the base load (left side of Figure 5). Similar to the mixed operation, the second harmonic at 175 Hz and the fourth harmonic at 350 Hz were the dominant frequencies. With the AIC system adjusted to the second harmonic, the machine could be operated up to 98% without excessive dynamic pressures (right side of Figure 5) and well below the maximum NO_x level of 25 ppm. With maximum pilot gas massflow, achieved by opening the actuator valves statically to 100%, and, consequently, very high NO_x emissions, this load level could also be achieved. In this case, the NO_x emissions were well above 60ppm. Using the AIC, however, the time mean pilot gas massflow could be reduced to an extend that resulted in significantly lower NO_x emissions.

In this application, the AIC is not used to increase the operation envelope of the machine but to decrease the emission level by more than 60%, showing its high flexibility.

3.2.3. AIC performance at base load – premixed operation (load increase)

As described above, burner B led to a significant improvement of the operation of the gas turbine concerning self-excited combustion instabilities. Problems only occurred at loads above 97 % of the base load, with a low frequency peak at 110 Hz and a higher peak at 175 Hz. With the AIC system activated and adapted to the 175 Hz oscillation, the load could be increased to 102% of the base load without any combustion instabilities. At even higher loads, a strong resurgence of the humming took place, which could not be successfully suppressed by the AIC system due to the limited hydraulic cross-sections of the pilotgas system and the actuator.

In this case, the AIC served the purpose to increase the operation envelope by approximately 5%.

4. Summary and Conclusions

An AIC system developed for the use in heavy duty gas turbines was applied successfully to Siemens Model V84.3A and V94.3A Gas turbines. Depending on the burner configuration used, the AIC system served the following purposes:

- increase of the maximum achievable load level by suppression of pressure amplitudes by approximately 5% points

- decrease of the emission level by more than 60% (due to the possibility to reduce the pilotgas massflow)
- suppress pressure amplitudes at intermediate load levels and during switchover processes

These results illustrate the high flexibility of the presented AIC system.

Component tests and failure simulations at the real engine show the high failure tolerance as well as the failsafe design of the actuators and controllers.

The performance of the AIC system is highly dependant on the achievable massflow modulation. Thus, the acoustics of the fuel system have to be tuned to the respective case. The modulation needed to suppress a certain amplitude can be minimized decisively by optimizing the injection position of the modulated fuel portion. In the Siemens Hybrid burner, the pilot gas system was used, giving a very good flame response even to quite small flow modulations.

Due to economic evaluations, AIC is not the preferred method for the suppression of combustion oscillations. Nevertheless, it offers the capability to overcome problems related to flame oscillations on a short notice and consequently gain time for the search for passive suppression methods. In some applications, however, that use AIC to enhance the peakload capabilities of existing engines to a higher level or to reduce the NOx emissions, economic evaluations can make the use of AIC attractive even for machines without thermoacoustic problems within the usual operation envelope.

5. References

- Candel, S. M., 1992**, "Combustion Instability Coupled by Pressure Waves and their Active Control", Invited general lecture, 25. Int. Symp. on Combustion, Sydney.
- Culick, F. E. C., 1988**, "Combustion Instabilities in Liquid-Fuelled Propulsion Systems - An Overview", AGARD Conference on Combustion Instabilities in Liquid-Fuelled Propulsion Systems, Bath, AGARD-CP-450, pp. 1-1 - 1-73.
- Hantschk, C., Hermann, J., and Vortmeyer, D., 1996**, "Active Instability Control with Direct Drive Servo Valves in Liquid-Fuelled Combustion Systems," 26. Int. Symp. on Combustion, Naples.
- Hermann, J., Gleis, S., and Vortmeyer, D., 1996**, "Active Instability Control (AIC) of Spray Combustors by Modulation of the Liquid Fuel Flow Rate," Combust. Sci. and Tech., Vol. 118, pp. 1-25.
- Hermann, J., 1996**, "Anregungsmechanismen und aktive Dämpfung (AIC) selbsterregter Verbrennungsschwingungen in Flüssigkraftstoffsystemen", Dissertation, TU München.
- Konrad, W., Brehm, B., Kameier, F., Freeman, C., Day, I. J., 1996**, "Combustion Instability Investigations On The BR710 Jet Engine", ASME-Paper No. 96-TA-36, presented November 5-7, 1996 at the ASME Turbo Asia Conference, Jakarta, Indonesia.
- McManus, K. R., Poinso, T., Candel, S. M., 1993**, "A Review of Active Control of Combustion Instabilities", Prog. Energy Combust. Sci., Vol. 19, pp. 1-29.
- Rayleigh, Lord J. W. S., 1878**, "The Explanation of Certain Acoustical Phenomena", Nature, July 18, pp. 319-321.
- Scalzo, A.J., Sharkey, W.T., Emmerling, W. C., 1996**, "Solution of Combustor Noise in a Coal Gasification Cogeneration Application of 100-MW-Class Combustion Turbines", Transactions of the ASME Journal of Engineering for Gas Turbines and Power, Vol. 112/39.
- Seume, J. R., Vortmeyer, N., Krause, W., Hermann, J., Hantschk, C.-C., Zangl, P., Gleis, S., Vortmeyer, D., Orthmann, A., 1997**, "Application of Active Combustion Instability

Control to a Heavy Duty Gas Turbine", ASME Paper No. 97-AA-119, presented September 30 – October 2, 1997 at the ASME ASIA '97 Congress & Exhibition, Singapore.

Vortmeyer, N., Huth, M., Becker, B., Karg, J., Emsperger, W., 1996, "Experience in the Design and Operation of Syngas Gas Turbines", presented October 2-4, at the EPRI 1996 Gasification Technologies Conference, San Francisco, California.

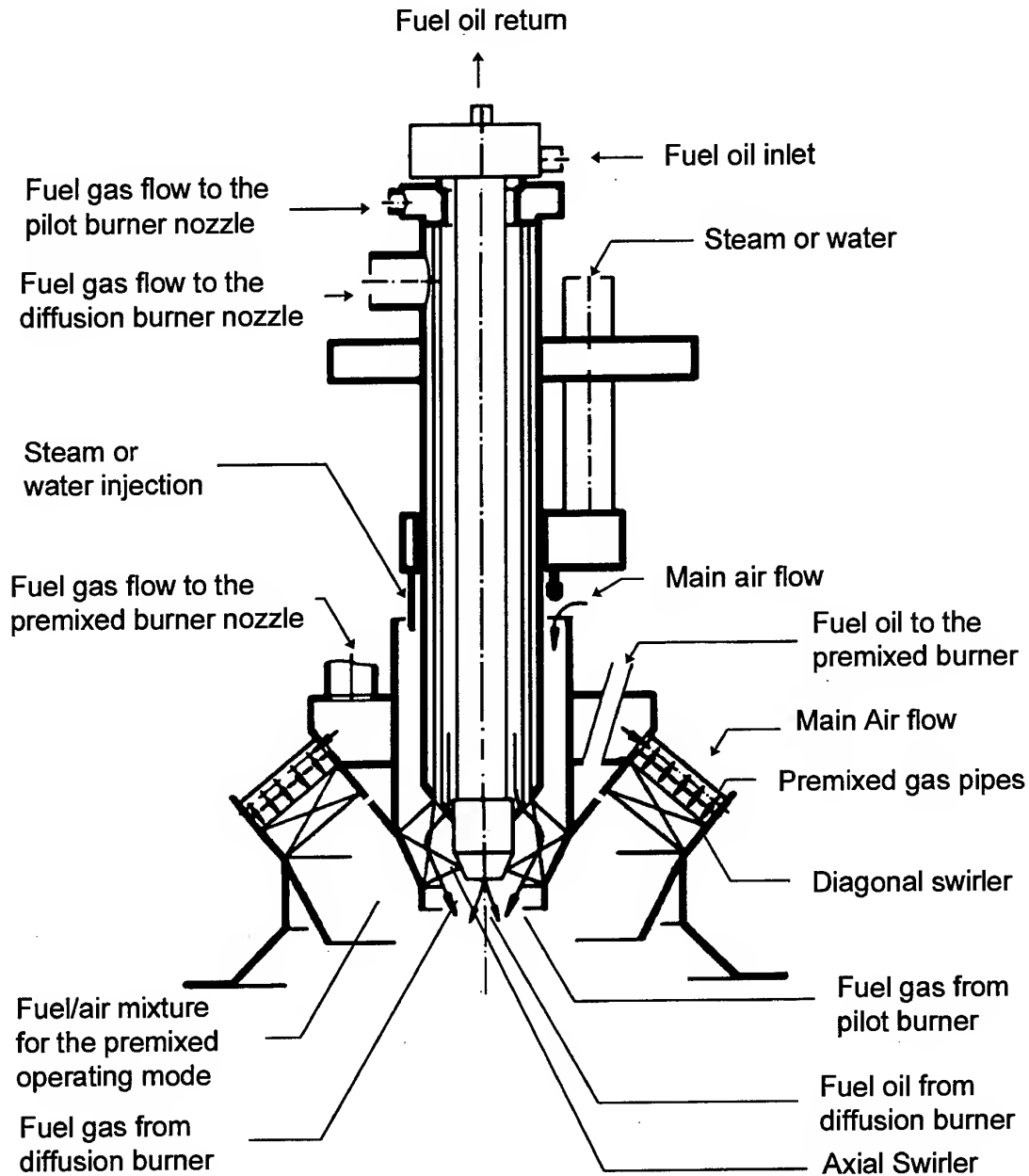


Figure 1: The Siemens Hybrid Burner

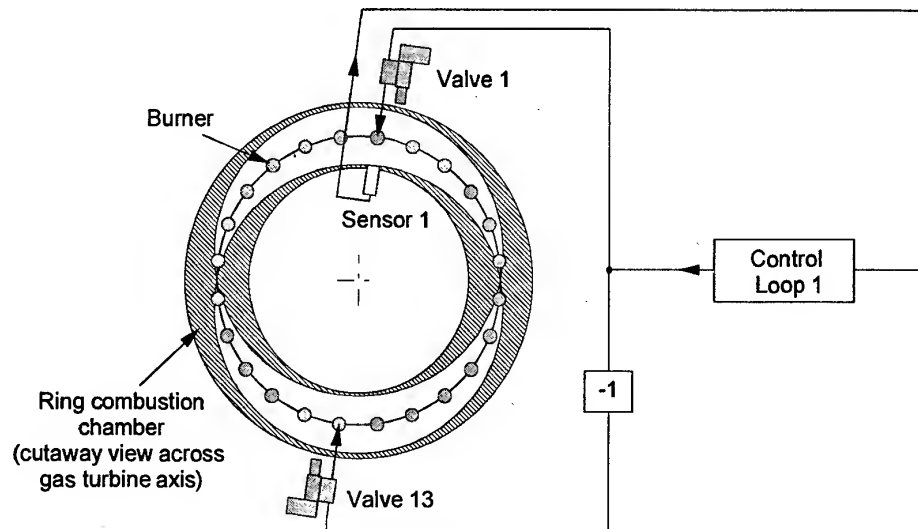


Figure 2: Use of the symmetry of azimuthal modes, here shown for the first harmonic. Here, one sensor and one controller provide input signals for two DDVs.

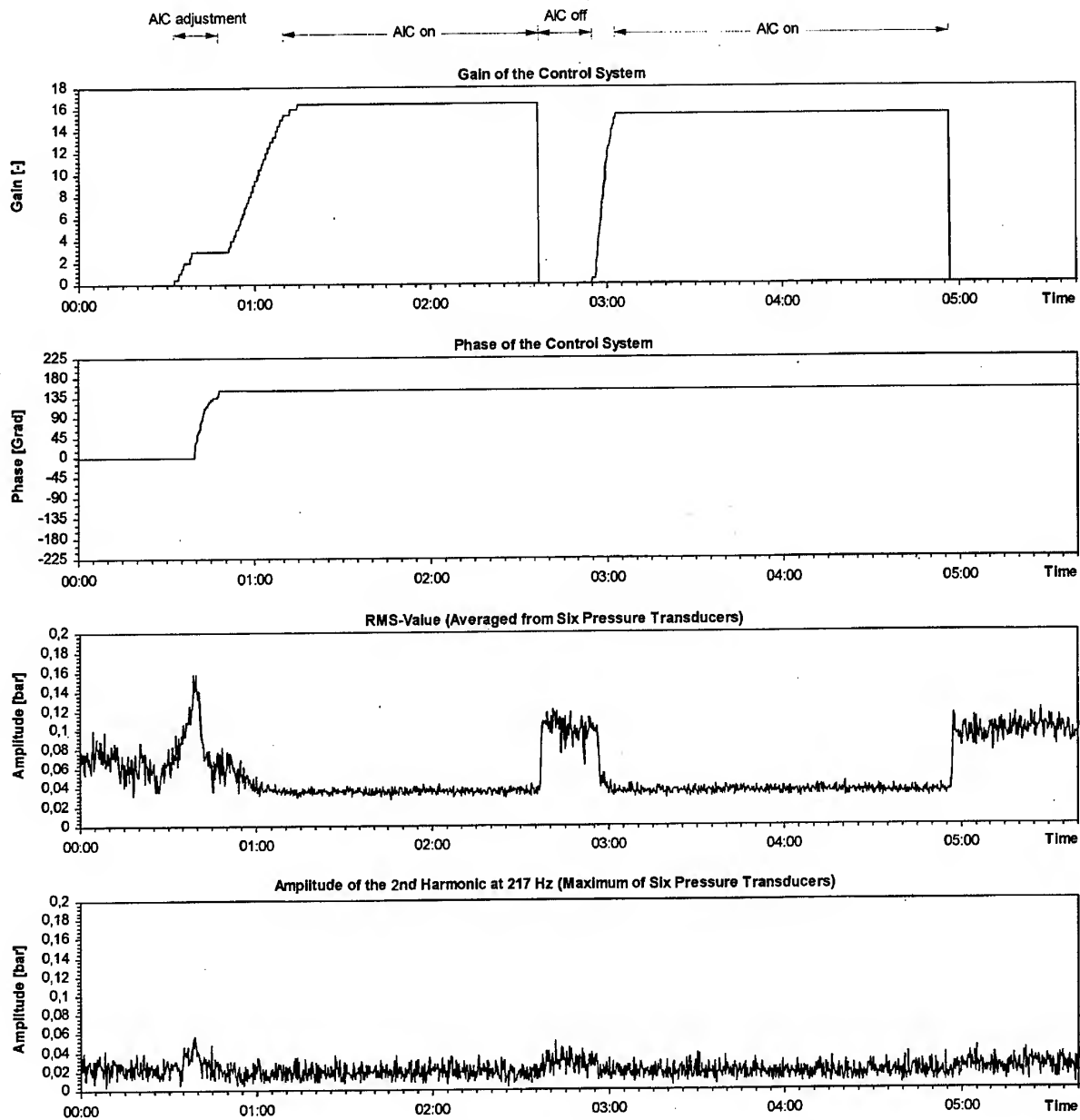


Figure 3: Test operation of the AIC at base load

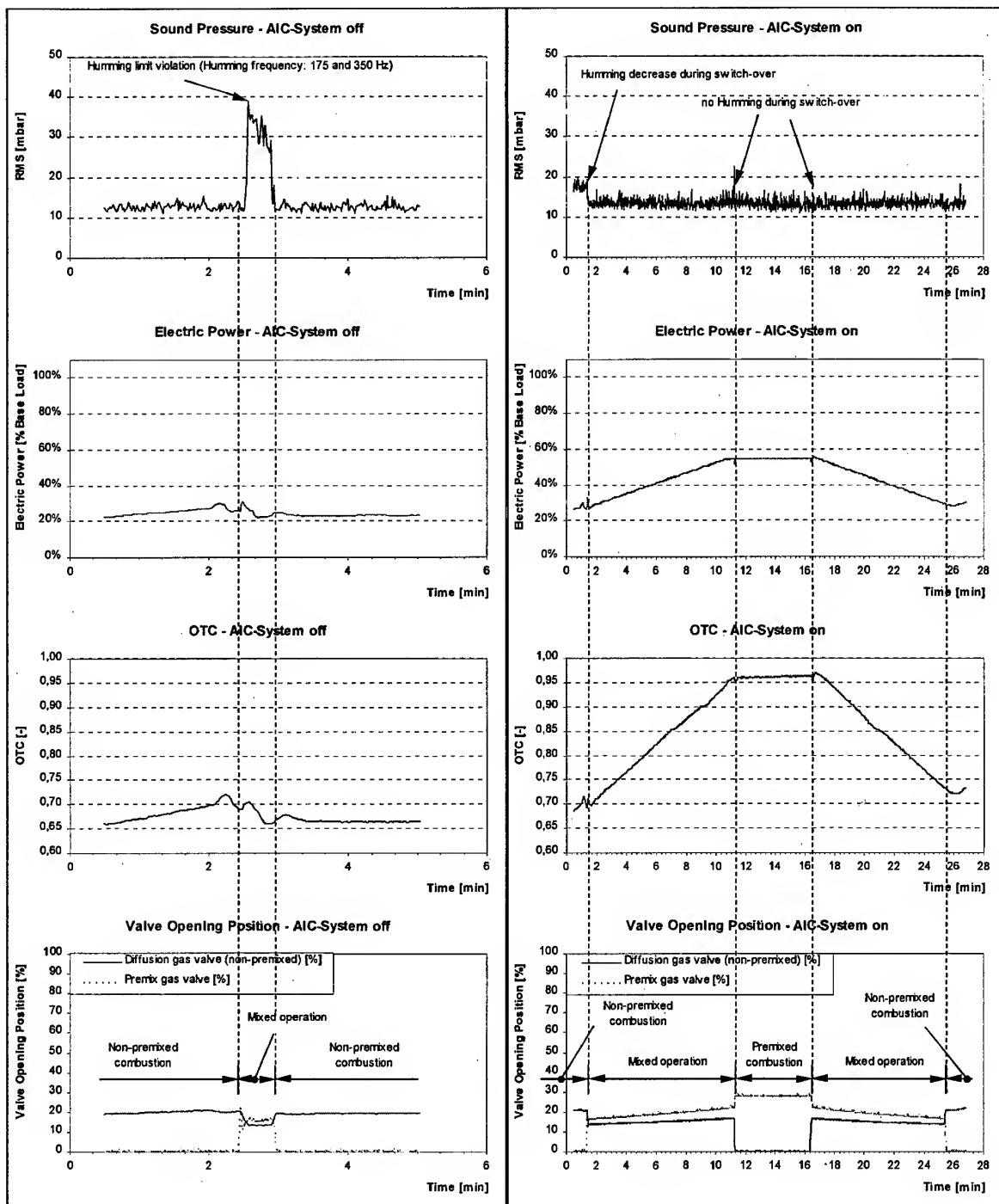


Figure 4: Test operation of the AIC at low load with burner configuration A. The inlet guide vane was constantly closed and the main pilot gas valve was open 60%.

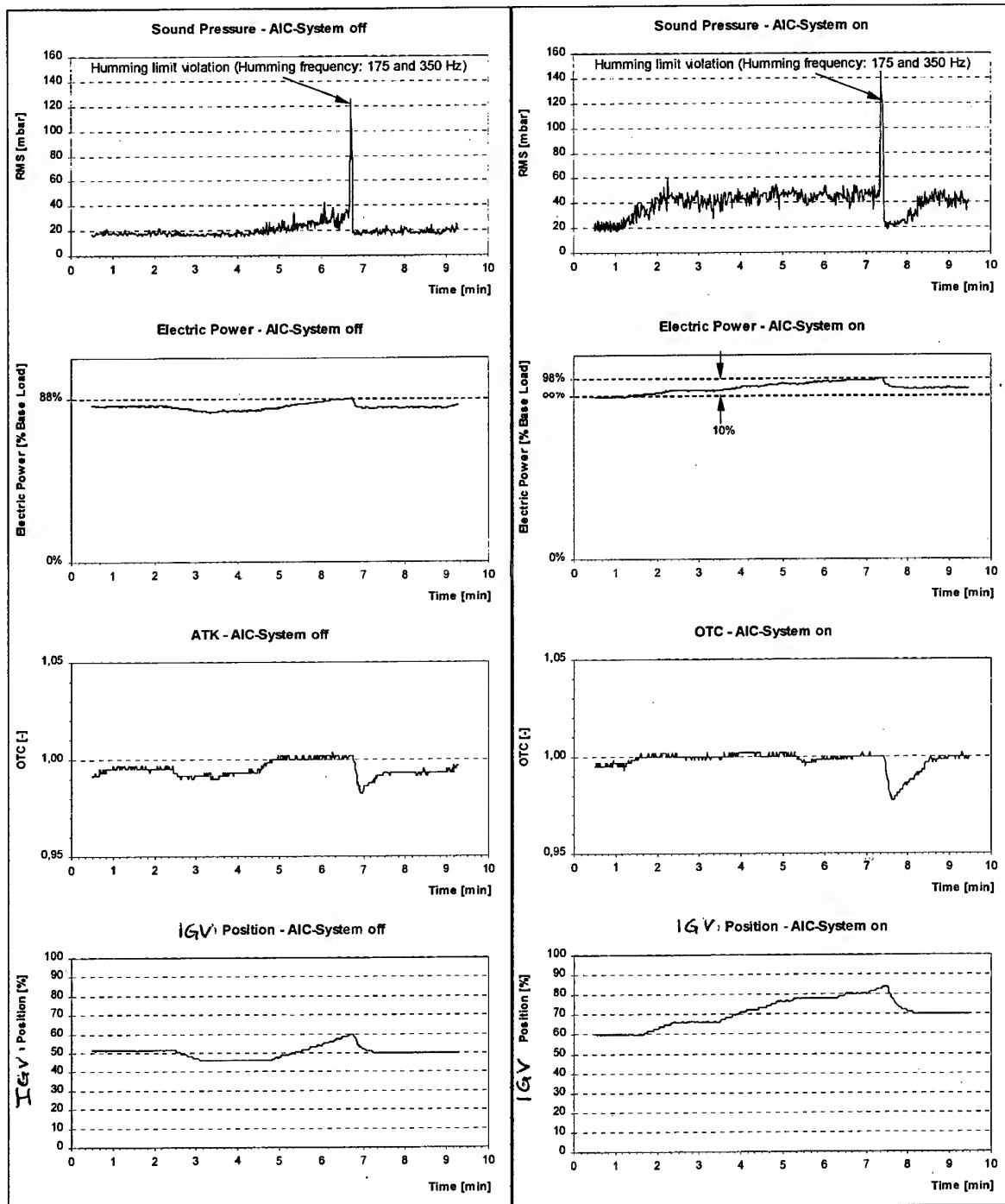


Figure 5: Test operation of the AIC near base load with burner configuration A. The pilot gas valve was completely open and the premix gas control valve was positioned according to the respective electric power.

PAPER No. 40
Hoffmann, Weber, Judith, Herman & Orthmann
(presenter: S. Hoffmann)

Question 1: D. Santavicca, Penn. State University, U.S.

What are the active combustion control (ACC) issues, solution of which would make ACC economically viable in the industrial gas turbine world?

Answer:

The reliability in long term operations of actuators and controllers. Also, good answers to the question: How does the ACC system react if the operating envelope of the machine shifts?

Question 2: (unknown), Pratt & Whitney, U.S.

What does your ACC system cost, or what is the fraction of the total machine cost that is attributable to the ACC?

Answer:

The cost hurts! A single pressure transducer for example, in this application is around US\$5,000. Since the ratio of the ACC cost to machine cost depends so strongly on the machine in question and the instability problem addressed, it is difficult to comment on this.

Question 3: F. Culick, CalTech., U.S.

The amount of energy involved in an oscillation is proportionally small for large machines. Therefore, how do you reconcile this with your need for larger actuators? How is this related to the efficiency of the ACC system?

Answer:

Flow visualizations by various authors of combustion oscillation studies show that with a fully-developed oscillation, large portions of the combustible mixture are affected. Sometimes, local flame extinctions may even occur. Thus, a major portion of the total energy release may be temporally and/or spatially, shifted during the oscillation. The fluctuations can be as high as ± 1 bar at 16 bars mean pressure; this does represent a lot of energy. In order to ensure a safe operation, ACC systems have to be able to suppress the fully-developed combustion oscillation. As our actuators only act on the fuel flow rate rather than on the air mass flow, that in fact, shows larger fluctuations during the cycle, we need to "over compensate" on the heat release fluctuations to some extent. Also, all of the energy put in by the ACC does not reach the flame as some is dissipated and lost between introduction and the flame. Experience shows that big actuators never hurt! Typically, at least 10 % of the total fuel needs to be modulated. Of course, the size of the fuel actuator can be reduced if the location of the modulated fuel injection is optimized for the combustion system under consideration.

Question 4: J. Tilston, DERA, U.K.

Have you ever cured an oscillation only to have another one pop up?

Answer:

Yes, in some configurations an additional frequency showed up after the previously dominant mode was suppressed. This can compromise the ACC effectiveness, especially if both frequencies are in a narrow bandwidth.

Optimization of Active Control Systems for Suppressing Combustion Instability

Jong Guen Lee, Boe-Shong Hong, Kwanwoo Kim,
Vigor Yang and Domenic Santavicca
111 Research Building East
The Pennsylvania State University
University Park, PA 16802, USA

1. INTRODUCTION

Combustion instabilities have proven to be a major factor limiting the development of high performance, low emissions gas turbine engines. This is a result of the fact that our current understanding of the underlying phenomenology of unstable combustion is incomplete, making it difficult to design high performance, low emissions combustors which are stable over their entire operating range. This problem is further aggravated by the fact that achieving stable combustion in a single-nozzle test of the actual combustor hardware is not a guarantee that the full-scale engine will not exhibit instabilities. Active combustion control provides an alternate approach to the successful development of high performance, low emissions gas turbine combustion systems. In theory, an active control system can be designed without *a priori* understanding of the nature or phenomenology of the instability. In practice, however, the optimization of a successful active control system requires a fundamental understanding of the phenomenology of unstable combustion, particularly in the specific engine of interest and over the complete range of desired engine operating conditions.

This paper presents results from a research program aimed at the development and optimization of an active control system for use in a low emissions gas turbine combustor. An overview of the control methodology is presented first. Then the theoretical model, which forms the basis of the model-based controller, is presented and preliminary results discussed. And lastly, experimental measurements of the stability characteristics of the lean premixed, dump combustor used in this study and of the response of the secondary fuel injector and the combustor to various control parameters are presented and the use of this type of information to optimize the control system is discussed.

2. Control Methodology

The schematic diagram in Fig. 1 illustrates the basic features of the combustor control system. This system consists of two interacting modules: a *slow-time supervisory* controller and a *fast-time flame* controller. The purpose of the *slow-time supervisory* controller in the outer loop is (1) to optimize the overall combustor performance and NOx emissions based on the measurements of quasi-steady variables and (2) to identify the flame control parameters that determine the operating points of the fast dynamic phenomena such as pressure oscillations. This controller generates signals to modulate the main fuel flow and the inlet air swirl in order to maintain near-optimum performance of the combustor for varying inlet flow over a wide operating range. The *fast-time flame* controller in the inner loop is responsible for suppression of combustion instabilities and for prevention of lean blowout of the flame.

Since combustion is a distributed parameter process, the controller relies on spatially distributed sensors and actuators. The prime objectives of this control system are reduction of pollutant emissions and enhancement of engine performance by avoiding a variety of off-normal operating conditions.

3.1 Model

The models are established at three different levels of detail in terms of controller design and implementation: (1) a low-level model for determining the overall control structure; (2) a medium-level model for synthesizing robust control laws; and (3) a high-level model for simulating the transient performance of the entire combustor and for evaluating various control methodologies. The formulation of the baseline high-level model is based on the complete, time-dependent, conservation equations with finite-rate chemical kinetics for two-phase reacting flows in three dimensions. Medium-level models represent the transient behavior within specified ranges of operation and have a multi-input, multi-output finite-dimensional structure. These models are formulated via system identification based on the input-output data generated from the respective high-level models. A low-level model which serves as the backbone for control synthesis is derived as an approximation of the respective medium-level model via model reduction. For robust control synthesis, a low-level model is treated as the nominal plant model and the modeling uncertainties are represented by the deviation of the low-level model from the medium-level model.

3.2 Formulation of Combustion Dynamics

The combustion system considered in the present work is shown in Fig. 2, representing a generic model for several types of air-breathing combustors. To control combustion instabilities, the strategy described in Fung *et al.* (1991) is followed with several steps involved in a closed loop. First, the instantaneous chamber conditions are monitored by sensors at rates sufficient to resolve the characteristics of unsteady motions. The measured signals are then processed through a controller to modulate the mass flow rate of a secondary supply of fuel. Finally, the injected fuel reacts with combustor flow as it travels downstream, exerting a distribution of external influences on the oscillatory flowfield for instability control.

The formulation of combustion dynamics can be constructed using the same approach as that employed in the previous work for state-feedback control with distributed actuators (Fung *et al.*, 1991; Fung and Yang, 1992). In brief, the medium in the chamber is treated as a two-phase mixture. The gas phase contains inert species, reactants, and combustion products. The liquid phase is comprised of fuel and/or oxidizer droplets, and its unsteady behavior can be correctly modeled as a distribution of time-varying mass, momentum, and energy perturbations to the gas-phase flowfield. If the droplets are taken to be dispersed, the

conservation equations for a two-phase mixture can be written in the following form, involving the mass-averaged properties of the flow.

$$\text{mass} \quad \frac{\partial \rho}{\partial t} + \nabla \cdot \rho \mathbf{v}_g = W \quad (1)$$

$$\text{momentum} \quad \rho \frac{\partial \mathbf{v}_g}{\partial t} + \rho \mathbf{v}_g \cdot \nabla \mathbf{v}_g = -\nabla p + F \quad (2)$$

$$\text{energy} \quad \frac{\partial p}{\partial t} + \bar{\rho} \mathbf{p} \cdot \nabla \mathbf{v}_g = -\mathbf{v}_g \cdot \nabla p + P \quad (3)$$

The subscripts g and l stands for the mass-averaged quantities for gas and liquid phases, respectively, and ρ is the density of the mixture.

Whatever physical means are devised, control inputs must be theoretically treated as sources in the above conservation equations. Therefore, Eqs. (1)-(3) are modified by adding control inputs W_c , F_c , and P_c on the right-hand sides. The subscript c represents the effects arising from the control inputs. If we consider only the influence associated with heat released from the injected fuel, P_c takes the form

$$P_c = \frac{\bar{R}}{C_v} Q_c = \frac{\bar{R}}{C_v} \dot{w}_c \Delta H_c, \quad (4)$$

where Q_c stands for the rate of energy release in the gas phase, \dot{w}_c for the burning rate of the control fuel (mass/time-volume), and ΔH_c for the heat of combustion per unit fuel mass.

A wave equation governing the unsteady motions is then derived by decomposition of all dependent variables as sums of the mean and fluctuation parts. Thus

$$\rho = \bar{\rho} + \rho'(r, t); \quad \mathbf{v}_g = \bar{\mathbf{v}}_g(r) + \mathbf{v}'_g(r, t);$$

$$p = \bar{p} + p'(r, t) \quad (5)$$

Now substitute Eq. (5) into Eqs. (1)-(3), collect coefficients of like powers, and rearrange the results to obtain the following wave equation in terms of pressure fluctuation.

$$\nabla^2 p' - \frac{1}{\bar{a}^2} \frac{\partial^2 p'}{\partial t^2} = h + h_c \quad (6)$$

where h contains all physical processes of acoustic motions, mean flow, and combustion under conditions with no external forcing. Its explicit expression is given in the thesis by Fung *et al.* (1991).

The control source h_c arising from combustion of the injected fuel can be treated as a distributed actuator, with its spatial distribution approximated by an array of M discrete sources (Fung *et al.*, 1991). If a generalized time-lag theory of Crocco and Cheng is used to model the process of the control fuel from injection to complete combustion, then h_c can be written as

$$h_c = -\frac{\bar{R} \Delta H_c}{\bar{a}^2 C_v} \sum_{k=1}^M \frac{\partial \dot{m}_{in}(t - \tau_k)}{\partial t} b_k \delta(r - r_k) \quad (7)$$

where \dot{m}_{in} stands for the mass flow rate of the injected fuel. The time delay, τ_k , is the time at which an element of fuel burns at the k th combustion source, measured from the moment

of its injection. The spatial distribution parameter, b_k , measures the fraction of the control fuel currently burning within the volume represented by the k th combustion source, located at r_k .

Conservation of mass requires that $\sum_{k=1}^M b_k = 1$.

Since the source terms in the wave equation (6) and its associated boundary conditions are treated as small perturbations to the acoustic field, within second order accuracy, the solution can be legitimately approximated by a synthesis of the normal modes of the chamber with time-varying amplitudes $\eta_n(t)$.

$$p'(r, t) = \bar{p} \sum_{n=1}^{\infty} \eta_n(t) \phi_n(r) \quad (8)$$

where ϕ_n is the normal mode function. After substituting Eq. (8) into Eq. (6), and applying a spatial-averaging technique equivalent to the Galerkin method, the following system of equations is obtained for the temporal evolution of each mode.

$$\ddot{\eta}_n + \omega_n^2 \eta_n + \sum_{i=1}^N [D_{ni} \dot{\eta}_i + E_{ni} \eta_i] + F_n^{NL}(\eta_1, \eta_2, \dots, \dot{\eta}_1, \dot{\eta}_2, \dots) = U_n(t) + d_n(t), \quad n = 1, 2, \dots, N \quad (9)$$

where $d_n(t)$ denotes plant disturbances. The coefficients D_{ni} and E_{ni} represent all linear processes. The function F_n^{NL} accommodates all nonlinear effects of gasdynamic coupling and combustion response. The control input to the n th mode takes the form

$$U_n(t) = \frac{\bar{R} \Delta H_c}{C_v \bar{p} V} \sum_{k=1}^M b_k \phi_n(r_k) \frac{\partial \dot{m}_{in}(t - \tau_k)}{\partial t} \quad (10)$$

The state of the acoustic field must be determined to complete the formulation. In the present study, the instantaneous pressure oscillation is monitored by a finite number of point sensors, located at positions r_{si} 's. The output signal of each sensor becomes

$$y_i(t) = \bar{p} \sum_{n=1}^N \eta_n(t) \phi_n(r_{si}) + \theta_i \quad (11)$$

where θ_i is the measurement noise with respect to the i th sensor.

The formulation described above provides a useful framework for treating feedback control of combustion instability. However, direct application of the model to practical problems must be exercised with caution due to uncertainties associated with system parameters such as D_{ni} and E_{ni} in Eq. (9), and time delays τ_k 's and spatial distribution b_k 's in Eq. (10). The intrinsic complexities in combustor flows prohibit precise estimates of those parameters without considerable errors, except for some simple well-defined configurations. Furthermore, the model may not accommodate all the essential processes involved because of the physical assumptions and mathematical approximations employed. These model and parameter uncertainties must be carefully treated in the development of a robust controller. To this end, the system dynamics equations, Eqs. (9)-(11), are extended to include uncertainties, and can be represented with the following state-space model.

$$\begin{aligned} \dot{x}_p &= (A_p + \Delta)x_p + Gv + Ld \\ y &= Cx_p + \theta \end{aligned} \quad (12)$$

where $x_p = (\zeta \quad \dot{\zeta})^T$ with $\zeta = \eta$, and

$\eta \equiv [\eta_1, \eta_2, \dots, \eta_N]^T$. The nominal linear system matrices are:

$$A_p = \begin{bmatrix} 0 & I \\ -\Omega - E & -D \end{bmatrix} \text{ with } \Omega \equiv \text{diag}(\omega_1^2, \omega_2^2, \dots, \omega_N^2).$$

The input vector $v(t)$ is related to the mass injection rate of the secondary fuel, \dot{m}_{in} , as

$$v(t) = \begin{bmatrix} (b_1 + \delta b_1)\dot{m}_{in}(t - \tau_1 - \delta\tau_1) \\ (b_2 + \delta b_2)\dot{m}_{in}(t - \tau_2 - \delta\tau_2) \\ \vdots \\ (b_M + \delta b_M)\dot{m}_{in}(t - \tau_M - \delta\tau_M) \end{bmatrix} \quad (13)$$

The model and parametric uncertainties are represented by a differential operator Δ and can be properly treated as a disturbance to the plant, $w_s = \Delta(x_p)$, which physically represents the energy amplification from input to output. Its global behavior is characterized by the L_2 gain as follows.

$$\begin{aligned} \|\Delta\|_\infty &< \frac{1}{\gamma}, \text{ i.e.,} \\ \int_0^T \|w_s(t)\|^2 dt &\leq \frac{1}{\gamma^2} \int_0^T \|x_p(t)\|^2 dt \quad \forall T \in [0, \infty) \end{aligned} \quad (14)$$

3.3 Robust Control

With an appropriate specification of the system performance weighting and objective function, a generalized plant dynamics is established, as shown in Fig. 3. The feedback controller processes the measured signal y to determine the injection rate of the control fuel \dot{m}_{in} based on a regulated relationship between variables w and z , where w is associated with disturbance and uncertainty, and z with the objectives of system performance and stability.

The system dynamics uncertainty $\Delta(s)$ contains parametric and model uncertainties, and its L_2 gain bounded as $\|\Delta(s)\|_\infty < 1/\gamma$. Based on the L_2 -gain control theory, the first task of a robust controller for stabilizing perturbed plants is to endow the closed-loop system with the following property:

$$\int_0^T \|z_s\|^2 dt \leq \int_0^T \|w_s\|^2 dt \quad \forall T > 0 \quad \forall w_1 \in L_2(0, T) \quad (15)$$

for the zero-state initial condition, with z_s being x_p/γ .

Another source of uncertainty arises from actuators, mainly due to the time delay and spatial distribution from injection to complete combustion of the secondary fuel. A non-rational transfer function of time delay $e^{-\delta\tau s}$ is used to treat the multiplicative uncertainty by embedding it in the family

$$\{(1 + \Delta_\tau(j\omega)W_\tau(j\omega)) : \|\Delta_\tau(j\omega)\| \leq 1\} \quad (16)$$

where $\Delta_\tau(j\omega)$ accounts for the phase uncertainty and acts as a scaling factor for the magnitude of the perturbation specified by the weighting function $W_\tau(j\omega)$. It is chosen in such a manner that the normalized perturbation satisfies

$$|e^{-\delta\tau j\omega} - 1| \leq |W_\tau(j\omega)|, \forall \omega \quad (17)$$

where $\delta\tau = \max_k \tau_k$. For robust stability, a closed-loop system must fulfill the requirement,

$$\int_0^T \|z_\tau\|^2 dt \leq \int_0^T \|w_\tau\|^2 dt \quad \forall T > 0 \quad \forall w_\tau \in L_2(0, T) \quad (18)$$

where w_τ and z_τ are shown in Fig. 3.

In addition, the control system must feature a desired performance in terms of its ability to suppress flow oscillations, measured by a positive quadratic energy-like function as follows.

$$\|z_p\|^2 = \frac{1}{V} \iiint_V \left(\frac{p'(r, t)}{\bar{p}} \right)^2 dV \quad (19)$$

The system is free of oscillations when z_p approaches zero. Since the acoustic mode satisfies the orthonormal property, Eq. (22) can be simplified as

$$\|z_p\|^2 = \frac{1}{V} \langle \sum \varphi_n \eta_n, \sum \varphi_m \eta_m \rangle = \sum \eta_n^2 = \|\eta\|^2 \quad (20)$$

In order to regulate the dynamics of the secondary fuel injector according to prescribed system performance and stability requirements, the controller needs to modulate the frequency response of the control fuel injection rate, instead of $\dot{m}_{in}(t)$ directly. A performance variable $z_u(t)$ is thus defined by incorporating a performance weighting $W_u(s)$ into control action as

$$\hat{z}_u(s) = W_u(s)u(s) \quad (21)$$

where $u(s)$ and $\hat{z}_u(s)$ are the Laplace transforms of $\dot{m}_{in}(t)$ and $z_u(t)$, respectively. The performance weighting W_u can be properly chosen by considering the bandwidth of the control system and the steady operation of the injector.

Based on the above performance concerns, Eqs. (19) and (21), an L_2 -gain robust controller is designed such that the plant disturbance d and sensor noise θ have minimum effect on the plant dynamics and control actions. In an energy sense, this can be specified by

$$\begin{aligned} \int_0^T \|qz_p\|^2 + \|rz_u\|^2 dt &\leq \int_0^T (\alpha d)^2 \\ &+ (\beta\theta)^2 dt \quad \forall T > 0 \quad \forall d, \theta \in L_2(0, T) \end{aligned} \quad (22)$$

where r , q , α and β are positive scalars, representing the weightings of plant dynamics, control action, plant disturbance, and sensor noise, respectively. Increasing q (or r), or decreasing α (or β), implies better performance is desired. When α (or β) is set smaller, a more stringent requirement of rejecting plant disturbance (or sensor noise) is specified. When q (or r) is set larger, the response of acoustic motions (or control action) is emphasized. If exogenous inputs (i.e., plant disturbance and sensor noise) are absent, the L_2 gain control optimizes the performance objective function

$$J = \int_0^\infty \left(\frac{q}{V} \iiint_V \left(\frac{p'(r, t)}{\bar{p}} \right)^2 dV + \|rz_u\|^2 \right) dt \quad (23)$$

Based on Eqs. (15), (18) and (22), a sufficient condition for the existence of a robust controller which stabilizes all perturbed

plants with desired performance, subject to some uncertainty bound, can be obtained as follows.

$$\begin{aligned} & \int_0^T \|z_s\|^2 + \|qz_p\|^2 + \|rz_u\|^2 + \|z_\tau\|^2 dt \\ & \leq \int_0^T \|w_s\|^2 + \|\alpha d\|^2 + \|\beta \theta\|^2 \\ & + \|w_\tau\|^2 dt \quad \forall T > 0 \quad \forall w \in L_2(0, T) \end{aligned} \quad (24)$$

or succinctly,

$$\int_0^T \|z\|^2 dt \leq \int_0^T \|w\|^2 dt \quad \forall T > 0 \quad \forall w \in L_2(0, T);$$

with

$$z = \begin{bmatrix} z_s \\ qz_p \\ rz_u \\ z_\tau \end{bmatrix}; w = \begin{bmatrix} w_s \\ \alpha d \\ \beta \theta \\ w_\tau \end{bmatrix} \quad (25)$$

The generalized plant shown in Fig. 3 can be expressed as a state space realization as

$$\begin{aligned} \dot{x} &= Ax + B_1 w + B_2 u \\ z &= C_1 x + D_{12} u \\ y &= C_2 x + D_{21} w \end{aligned} \quad (26)$$

where the state of the generalized plant x contains the plant state x_p and states induced from actuator dynamics and stability and performance weighting.

The robust controller consists of two main components: the first is an observer, which estimates the states of the generalized plant described by Eq. (26), and consequently the dynamics in the combustion chamber. It is capable of treating exogenous inputs and uncertainty-induced disturbances. The second is a state-feedback control gain, which determines the control action based on the estimated states \hat{x} .

The remaining task lies in the determination of the control matrix X and observer matrix Z such that the sufficient condition for robust performance, Eq. (25), holds. A Lyapunov-based approach is employed to obtain these two matrices. After some lengthy and complicated manipulations of Eq. (26) and the control structure, the following two Riccati equations are derived, whose positive-definite solutions correspond to the control and observer matrices, X and Z .

$$A^T X + XA + C_1^T C_1 - XB_2 B_2^T X + XB_1 B_1^T X = 0 \quad (27)$$

$$\begin{aligned} & Z^{-1}(A + B_1 F_1) + (A + B_1 F_1)^T Z^{-1} \\ & - C_2^T C_2 + F_2^T F_2 + Z^{-1} B_1 B_1^T Z^{-1} = 0 \end{aligned} \quad (28)$$

where $F_1 = B_1^T X$, $F_2 = -B_2^T X$, and $w_{\max} = F_1 \hat{x}$.

An optimization procedure based on the D-K iteration scheme may be employed to further improve the controller design by relaxing its conservativeness (Zhou *et al.*, 1996).

3.4 Parametric Study

As a specific example to study the characteristics of the controller, we consider herein the problem involving four modes of longitudinal oscillations. The natural radian frequency of the fundamental mode, normalized with respect to $\pi \bar{a}/L$, is taken to be unity. The nominal linear parameters D_{ni} and E_{ni} in Eq. (12) are taken from Fung *et al.* (1991), representing a typical situation encountered in several practical combustion chambers. An integrated research project comprising laser-based experimental diagnostics and comprehensive numerical simulation is currently conducted to provide direct insight into the combustion dynamics in a laboratory dump combustor, as described in detail in the following. Included as part of the results are the system and actuator parameters under feedback actions, which can be directly incorporated into the controller design established in the present work.

An extensive series of studies is conducted to investigate the effects of various weighting factors associated with the mechanical energy of the oscillatory field (q), actuation energy (r), plant disturbance (α), and sensor noise (β) on the robustness and performance of the controller. Also included in the parametric investigation are the affordable bound of system dynamics uncertainty ($1/\gamma$) and the maximum time delay of the distributed combustion of control fuel ($\delta\tau$). Results indicate that

- (1) The trade-off between oscillation energy and control fuel is similar to that based on the linear quadratic regulator (LQR) control.
- (2) The ability of rejecting exogenous inputs depends strongly on the values of α and β .
- (3) A significant trade-off exists between performance requirements (q , r) and allowable disturbances (α , β).
- (4) The affordable uncertainty bound $1/\gamma$ is insensitive to the disturbance weightings α and β .
- (5) The affordable uncertainty bound $1/\gamma$ is sensitive to q and r .
- (6) There is a trade-off between the affordable model uncertainty bound $1/\gamma$ and the maximum time delay $\delta\tau$.

The time responses of pressure oscillation and control-fuel injection rate are simulated for two cases: one for the nominal system and the other for a perturbed system with 50% parameter uncertainties from the nominal values. The following data are used in both cases.

Figures 4 and 5 present the result. The control scheme developed in the present work indeed guarantees robust performance for a wide variety of perturbed systems with significant model uncertainties.

Maximum perturbed value of time delays	$\delta\tau = 0.8$
Weighting parameters	$(\gamma, q, r, \alpha, \beta) = (20, 0.1, 0.1, 10, 0.2)$
White plant disturbance intensity	10^{-3}
White sensor noise intensity	10^{-5}
Initial conditions	an impulse of intensity 0.01/s.

4.0 Description of Experiment

The coaxial dump combustor illustrated in Fig. 6 is used in this study. The flame is stabilized on a bluff center body located at the exit of the mixing section. The centerbody is centered in the mixing section using vanes that also serve as axial swirlers. Flat vaned axial swirlers with vane angles of 0°, 30° or 60° can be used. The fuel is natural gas (96% methane) and is introduced into the mixing section, well upstream (~30 mixing section diameters) of the dump plane, resulting in a uniform, premixed fuel-air distribution at the combustor inlet. A 20kW electric heater is used to heat the air-flow and a thermocouple, located 10mm upstream of the dump plane, is used in conjunction with a temperature controller to regulate the inlet temperature of the mixture. High frequency response pressure transducers, flush mounted at the locations shown in Figure 2, are used to measure the pressure oscillations in the combustor and mixing section. An aerodynamically-quenched quartz gas sampling probe is used to extract gas samples from the exhaust and NO_x concentrations in the exhaust gases are measured using a chemiluminescence analyzer. A pulsed Nd-YAG laser and an intensified CCD camera are used to make laser induced fluorescence measurements to characterize the fuel distribution at the dump plane. The ICCD camera is also used to record CH chemiluminescence images of the flame zone which define the heat release structure in the combustor.

An active control strategy has been implemented based on the use of secondary fuel injection in the combustor for the purpose of disrupting the periodic heat release that is driving the instability. The advantage of using secondary fuel injection for this purpose is that relatively small amounts of fuel can produce a significant perturbation to the combustion process. The combustor used in this study provides for secondary fuel injection at three different locations, as shown in Fig. 7. One fuel is injected through a single 1.18 mm-diameter hole. The second location is around the outer circumference of the centerbody, where the fuel is injected through twelve 0.34 mm-diameter holes that are oriented at 45 degrees with respect to the combustor axis. The third location is on the inner circumference of the dump plane, where the fuel can be injected through twelve 0.34 mm-diameter holes. Modulation of the secondary fuel flow is accomplished using a fast-acting solenoid valve (General Valve Co., Series 9) and high voltage valve driver (General Valve Co., Iota One). This valve is capable of operating at frequencies as high as 250 Hz with open times as short as 250 micro-seconds. The volumes of the fuel line and manifold downstream of the solenoid valve are 10 mm³ and 12 mm³, respectively, for the single-hole and the multi-hole injection locations on the centerbody, and 15 mm³ for the multi-hole injection location on the dump plane.

5.0 Experimental Approach

The optimization of an active control system for suppressing unstable combustion requires an understanding of the

phenomenology of the instability, as well as, an understanding the response of the combustor to the control system.

A first step in understanding the phenomenology of the instability is the determination of the stability characteristics of the combustor and their dependence on combustor geometry and operating conditions. The stability characteristics are determined from the high frequency response pressure transducer measurements and are expressed in terms of the peak-to-peak amplitude of the pressure fluctuations, the frequency distribution of the pressure fluctuations and the mode of the instability. In this study, the stability characteristics of the combustor illustrated in Fig. 6 were determined over the range of operating conditions and combustor configurations listed in Table 1.

Table 1

Pressure	1 atm
Temperature	350, 400, 450°C
Inlet Velocity	2 to 6 m/sec
Equivalence Ratio	LBO to 1.0
Swirl	0, 30, and 60 degree
Centerbody Recess	0, 1/4, 1/2, and 1 L/D
Fuel	natural gas

In addition to determining the stability characteristics of the combustor, phase-synchronized CO_2^* -CH chemiluminescence imaging is used to determine the spatial and temporal evolution of the heat release distribution (Samaniego, *et al.*, 1995; Shih *et al.*, 1996) during unstable combustion. These images are acquired by viewing the flame at 90 degrees to the combustor axis through a bandpass filter (BG-40). An intensified CCD camera, which is phase-synchronized with the pressure fluctuations, is used to record the images. Since the chemiluminescence images are line-of-sight images, a tomographic deconvolution procedure (Dasch, 1992) is used to extract the two-dimension heat release distribution from the original line-of-sight images. These measurements are important since they provide information on the role of flame-flowfield interactions in the observed instabilities and can be used to calculate the Rayleigh index (Rayleigh, 1945), and thereby identify the regions where the instability is being driven.

In addition to understanding the phenomenology of the instability, it is essential to understand the response of the combustor to the control system in terms of the various control system parameters. The response of the combustor can be expressed in terms of the fuel transfer and global response functions discussed below. The control parameters include the frequency, duration, pressure, phase and location of secondary fuel injection, as well as whether to use open- or closed-loop control.

The fuel transfer function is the relationship between the input signal to the valve driver and the actual time-history of the fuel

that is injected into the combustor. This includes a determination of the penetration and mixing of the injected secondary fuel, which can be expected to be important factors in terms of the effectiveness of the control system. After the fuel transfer function is determined, the response of the combustion process to the periodic fuel injection, i.e., the global response function, is determined.

In order to determine the fuel transfer function, the secondary fuel is seeded with acetone and laser induced acetone fluorescence (Lozano *et al.*, 1992) is used to measure the resultant fuel distribution in the combustor. Acetone is excited using the 266nm output of a frequency quadrupled Nd:YAG laser, and the two-dimensional fluorescence image is recorded using an intensified CCD camera. The measurements are phase-synchronized with the fuel injection cycle, giving a sequence of images showing the fuel distribution in the combustor during the secondary injection cycle. Note that these measurements are made without combustion.

In order to determine the global response function, CO_2 -CH chemiluminescence imaging is used. The intensified CCD camera is phase-synchronized with the fuel injection cycle and records chemiluminescence images which describe the spatial and temporal evolution of the flame's response to the modulated secondary fuel flow. The chemiluminescence image of the flame without secondary fuel injection is then subtracted from these images to obtain a sequence of images which represent the modulation of the heat release distribution in the combustor due to the modulated secondary fuel injection. Note that these measurements, i.e., both with and without secondary fuel injection, must be made under conditions where combustion is stable. This is typically accomplished by changing the length of the combustor.

Together, the fuel transfer function and the global response function represent the overall system's response to a given input signal. Combining this information with that obtained from the chemiluminescence images, one can assess the potential effectiveness of a given injection configuration for preventing unstable combustion. The fuel transfer and global response functions and the chemiluminescence images are also necessary for the development of the model-based controller.

6.0 Experimental Results

All observed instabilities were determined to be longitudinal mode instabilities with dominant frequencies near 480 Hz. A number of trends were observed regarding the effects of operating condition and combustor configuration on the stability characteristics, including:

- i) when instabilities occurred, they were found to increase in strength as the inlet velocity increased;
- ii) a minimum inlet temperature was required for unstable combustion;
- iii) recessing the centerbody was found to significantly reduce the tendency for unstable combustion;
- iv) with swirl, instabilities were only observed at equivalence ratios near the lean blowout limit;
- v) without swirl, instabilities were not observed near the lean blowout limit, but were only observed at higher (fuel lean) equivalence ratios.

These results are reported in detail in Venkataraman *et al.* (1998), but of particular note is the effect of swirl. Fig. 8 shows a plot of the peak-to-peak pressure fluctuations versus equivalence ratio at a fixed operating condition (combustor inlet

velocity of 6 m/s; combustor inlet temperature of 400°C; no center body recess), both without and with swirl. There appear to be two distinct regimes of unstable combustion, i.e., near lean blowout with swirl and away from lean blowout without swirl. Further insight can be gained from the phase-synchronized two-dimensional chemiluminescence images, which are shown in Figures 9 and 10 for unstable combustion conditions without and with swirl, respectively. These images reveal that there is a significant difference between the fluctuations in the heat release that occurs during unstable combustion without and with swirl. In the case without swirl it appears that flame-vortex interaction is responsible for the fluctuations in the heat release; whereas in the case with swirl it appears as though the heat release fluctuations are associated with a periodic separation of the flame from the centerbody. The difference between these two instabilities is more apparent when the Rayleigh index distributions are compared. Figures 11 and 12 show the Rayleigh index distributions for the instability without and with swirl, respectively. These results show that the location in the flow field where the instability is most strongly driven is different in instabilities without and with swirl. In the case without swirl, the location of maximum Rayleigh index coincides with the location where the flame-vortex interaction occurs. In the case with swirl, however, the location of maximum Rayleigh index occurs near the outer wall of the combustor and not in the location where the flame separation is observed in the two-dimensional chemiluminescence images. An important question is, what do these results imply about the optimum location for secondary fuel injection.

In a previous study (Lee *et al.*, 1996) using a smaller combustor without swirl, it was found that the location of maximum Rayleigh index was a good indication of the location where secondary fuel injection was most effective. It was also found that effective control could be achieved with only a small amount (i.e., less than 5% of the primary fuel flow) of secondary fuel even with open-loop control, as long as the secondary fuel was injected at this "optimum" location. Based on these results, one might expect that for the instabilities encountered with swirl that the secondary injection holes located on the dump plane in this combustor would provide the most effective control. To further test this hypothesis, tests were run in this combustor using an open-loop controller with each of the three secondary fuel injection locations. The results are summarized in Fig. 13 which shows the amount of secondary fuel flow (in percent of the primary fuel flow) required to achieve a 12 dB reduction in combustion generated noise plotted versus the frequency of injection. Note that the frequency of secondary fuel injection was varied from 150Hz down to 50Hz, while the frequency of the instability was approximately 480 Hz, and that the case of continuous injection is also shown. The first, and perhaps most significant, observation is that results are shown only for the two injection locations in the centerbody, since contrary to what was expected, it was not possible to suppress the instability with secondary injection from the dump plane. The second important observation is that the amount of secondary fuel was only slightly dependent on the frequency of injection, in fact effective control was achieved with continuous injection. Note that the NO_x penalty associated with the addition of secondary fuel was less than 4 ppm for all of the conditions shown in this figure.

These results are important in that they suggest that the most effect approach to preventing unstable combustion is not to attempt to add heat in a manner which is out of phase with the instability, as implied by Rayleigh's criterion (Rayleigh, 1945), but rather to alter or disrupt the underlying mechanism which is causing the heat release fluctuations. This reasoning is further

supported by the fuel transfer function and global response function results which are presented below.

The phase-synchronized two-dimensional acetone fluorescence images of the secondary fuel injection at the three injection locations are shown in Fig. 14. For all three injection locations the supply pressure was 100psi, the injection frequency was 150 Hz and the duration of the control signal to the solenoid valve was 750 microseconds. These images show that the three injection locations do, as intended, produce significantly different fuel distributions, i.e., in the centerbody recirculation zone, in the region where the flame is attached to the centerbody, and in the dump plane recirculation zone. It also appears in these images that the fuel pulse is significantly broadened compared to the duration of the control pulse to the solenoid valve. This is to be expected to some extent due to the relatively large volume between the solenoid valve and the injection holes. As an approximation of the amount of secondary fuel injected as a function of time, one can plot the total fluorescence intensity of the images shown in Figure 10 at the various time intervals. These results are shown in Fig. 15 for the three injection locations and the same conditions shown in Fig. 14. These results show that the rise time for the start of injection is one millisecond or less (the minimum resolution of the image sequence is one millisecond). The time for the fluorescence signal to go to zero in the images is about 4 milliseconds, however, it can not be said to what extent this is the time required for the flow to stop, the time required for the injected fuel to mix with the surrounding air or some combination of both effects.

Phase-synchronized images, which characterize the global response function for the three injection locations, are shown in Fig. 16. These images, which are synchronized with the control signal to the solenoid valve, actually show the difference between the chemiluminescence image with secondary fuel flow and that without secondary fuel flow, and therefore represent the modulation in the heat release distribution that is caused by the secondary fuel. (Note that the length of the combustor has been changed to insure that combustion is stable and that the resonant frequencies of the combustor are significantly different from the fuel modulation frequencies.) These results show that the additional heat release caused by the secondary fuel occurs in approximately the same location as the injected fuel was observed in Fig. 14.

It is clear then that in the case with swirl that the instability is suppressed when the secondary fuel is injected into the region where flame separation occurs rather than the location of maximum Rayleigh index. In other words, by preventing the periodic flame separation which occurs in the annular region between the centerbody and the mixing tube, i.e., where the velocity gradients are greatest, the large heat release fluctuations which drive the pressure fluctuations are inhibited.

7.0 SUMMARY

- The control scheme developed in the present work guarantees robust performance for a wide variety of perturbed systems with significant model uncertainties.
- An understanding of the phenomenology of unstable combustion can be used to optimize an active control system employing secondary fuel injection.
- CO_2^* -CH chemiluminescence imaging has been used to show that the phenomenology of unstable combustion is different with swirl than it is without swirl; both in terms of the mechanism which drives the instability and the location

where the pressure and heat release fluctuations are most strongly coupled.

- Secondary fuel injection appears to be more effective at suppressing combustion dynamics if it is used to perturb the instability mechanism rather than attempting to directly counteract the heat release fluctuations.

ACKNOWLEDGEMENTS

This research has been supported by the Office of Naval Research under Contract #N00014-96-1-0405 with Dr. Gabriel D. Roy as the contract monitor.

REFERENCES

- Dasch, C.J., "One Dimensional Tomography: a Comparison of Abel, Onion-peeling and Filtered Back Projection Methods," *Applied Optics*, 31(6), 1992.
- Fung, Y.T., Yang, V. and Sinha, A., "Active Control of Combustion Instabilities with Distributed Actuators," *Comb. Sci. Tech.*, 78, pp. 217-245, 1991.
- Fung, Y.T. and Yang, V., "Active Control of Nonlinear Pressure Oscillations in Combustion Chambers," *Journal of Propulsion and Power*, 8, pp. 1282-1289, 1992.
- Lee, J.G., Jeon, C.H. and Santavicca, D.A., "Flame Evolution Imaging and its Application to Control of Combustion Instability in a Coaxial Dump Combustor," Fall Meeting of the Eastern States Section of the Combustion Institute, 1996.
- Lozano, A., Yip, B. and Hanson, R.K., "Acetone : Tracer for Concentration Measurements in Gaseous Flows by Planar Laser Induced Fluorescence," *Experiments in Fluids*, 13, pp.369-376, 1992.
- Rayleigh, J., *The Theory of Sound*, Vol. 2, Dover, New York, p. 226, 1945.
- Samaniego, J.M., Egolfopoulos, F.N. and Bowman, C.T., " CO^* Chemiluminescence in Premixed Flames," *Combust. Sci. Tech.*, 109, pp. 183-203, 1995.
- Shih, W.P., Lee, J.G. and Santavicca, D.A., "Stability and Emission Characteristics of a Lean Premixed Gas Turbine Combustor," *Proceedings of the Twenty-sixth International Symposium on Combustion*, The Combustion Institute, Pittsburgh, pp.2771-2778, 1996.
- Venkataraman, K.K., Preston, L.H., Simons, D.W., Lee, B.J., Lee, J.G. and Santavicca, D.A., "A Study of the Mechanism of Combustion Instability in a Lean Premixed Dump Combustor," submitted to AIAA J. of Propulsion and Power, 1998.
- Yang, V., Sinha, A. and Fung, Y.T., "State Feedback Control of Longitudinal Combustion Instabilities," *Journal of Propulsion and Power*, 8, pp. 66-73, 1992.
- Yang, V., Santavicca, D.A. and Ray, A., "Intelligent Control of Gas Turbine Combustion Dynamics for Performance and Emission Improvement," *Proceedings of Tenth ONR Propulsion Meeting*, US Office of Naval Research, Arlington, VA, 1997, pp. 32-37.
- Zhou, K., Doyle, J.C. and Glover, K., *Robust and Optimal Control*, Prentice-Hall, New Jersey, 1996.

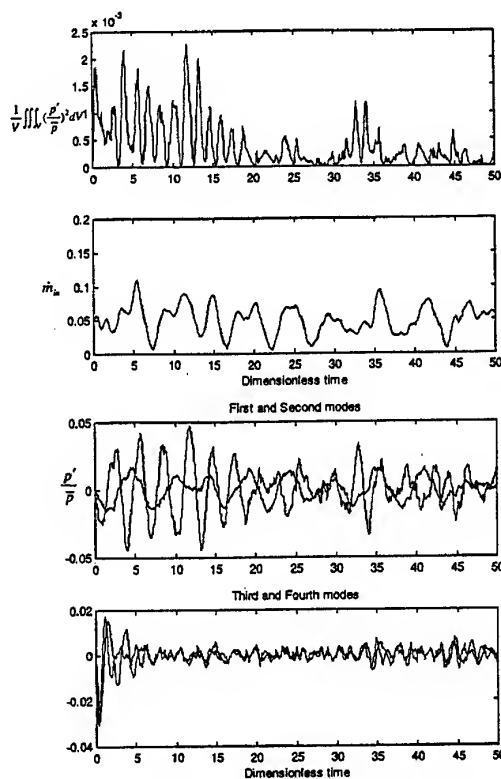


Figure 4. Time history of pressure oscillation in nominal case.

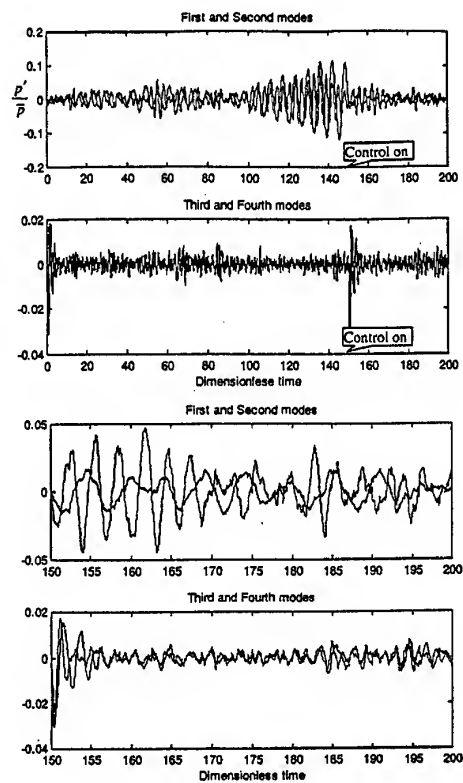


Figure 5. Time response of perturbed system with 50% model uncertainty.

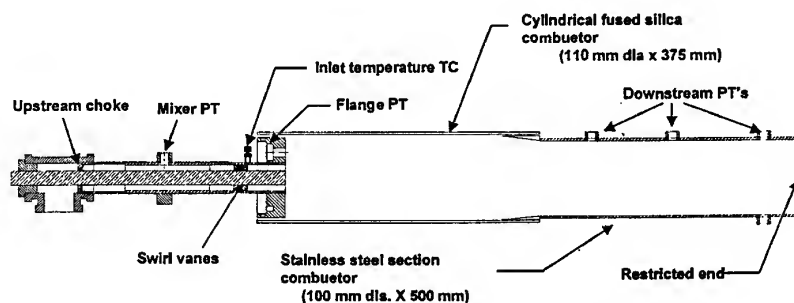


Figure 6. Schematic drawing of the optically-accessible combustor.

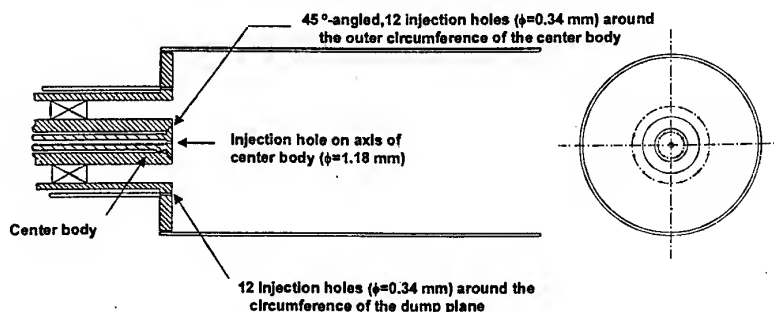


Figure 7. Secondary fuel injection locations.

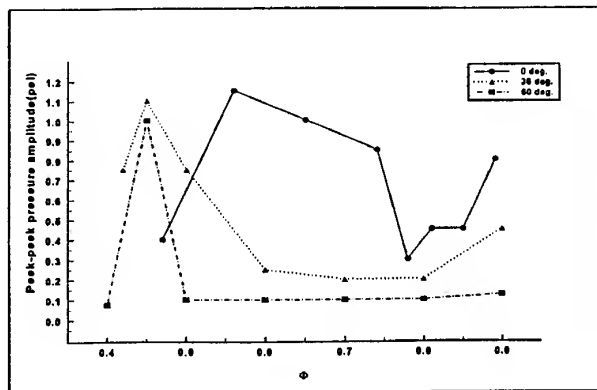


Figure 8. Stability maps with and without swirl.

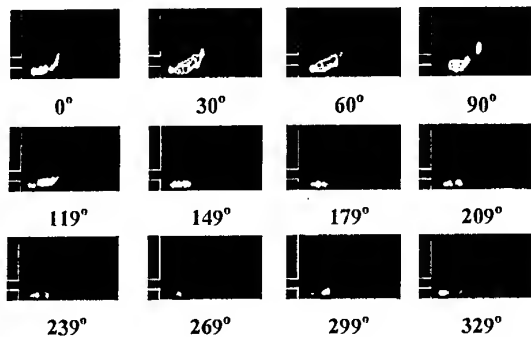
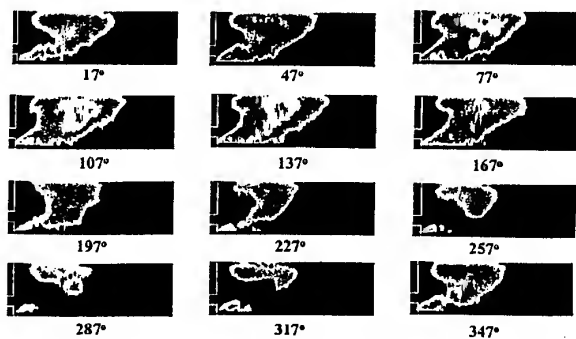
Figure 9. Two-dimensional CO_2^* -CH chemiluminescence images without swirl at 6 m/s, 400°C, $\Phi=0.6$, 100% premixed conditions.Figure 10. Two-dimensional CO_2^* -CH chemiluminescence images with swirl at 4 m/s, 400°C, $\Phi=0.45$, 100% premixed conditions.

Figure 11. Rayleigh index distribution for no-swirl case shown in Figure 9.



Figure 12. Rayleigh index distribution for swirl case shown in Figure 10.

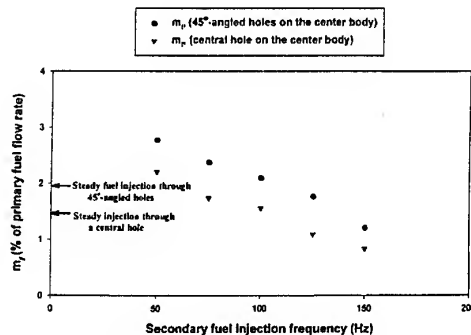


Figure 13. Effect of injection frequency and injection location on the minimum amount of secondary fuel required for a 12dB noise reduction.

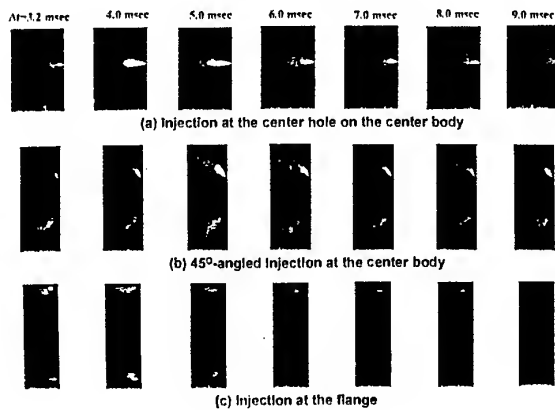


Figure 14. Fuel transfer function measurements showing the spatial and temporal evolution of the injected fuel for the three injection locations (injection frequency=150Hz, valve control signal duration=750 μ sec).

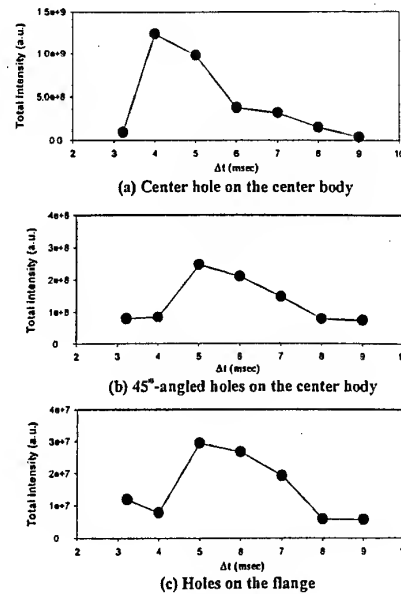


Figure 15. Total acetone LIF intensity versus time for three different injection locations (injection frequency=150Hz, valve control signal duration=600 μ sec, $t=0$ marks the beginning of the valve control signal pulse).

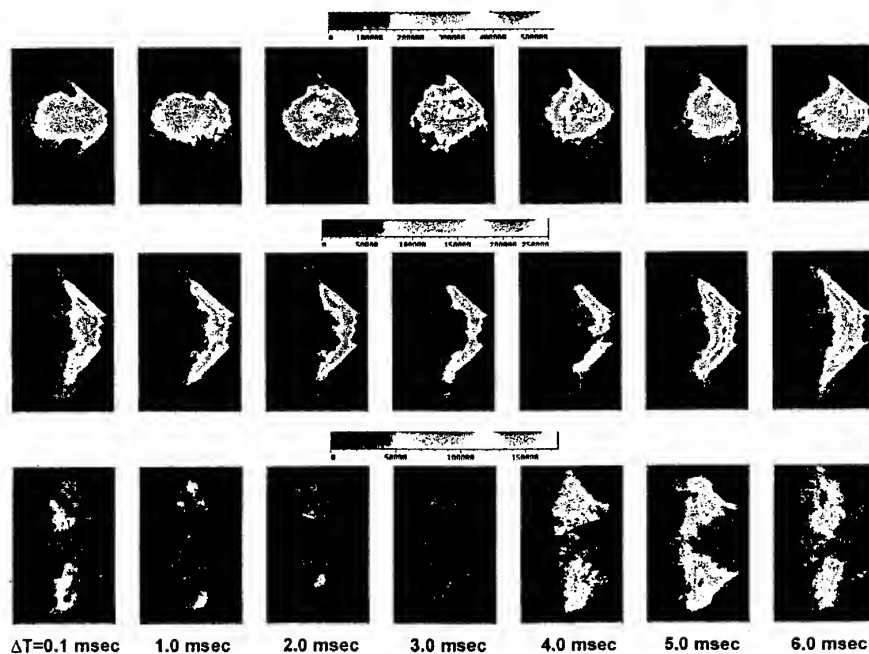


Figure 16. Global response function for the three injection location (top-center hole; middle-45° angled holes on centerbody; bottom-holes on flange) at an injection frequency of 150Hz and a valve control signal duration of 750 μ sec.

PAPER No. 41
Lee, Hong, Kim, Yang & Santavicca
(presenter: D. Santavicca)

Question 1: (unknown)

When attempting ACC with liquid fuel, the control fuel has to pass through the highly non-linear filters introduced by spray atomization, droplet evaporation and fuel vapor/air mixing before a modulated heat release is achieved. How does this filtering cloud the understanding of the control process?

Answer:

Liquid fuel is incompressible, and this is helpful. However, it will be necessary to directly measure these functions to ascertain their exact role.

Question 2: V. McDonnell, University of California, Irvine, U.S.

Have you observed any effects of active controll on lean blowout?

Answer:

No.

Optical Measurements of Jet-Mixing in a Swirling Crossflow of a Combustion Chamber

B.H. Krautkremer, M.M. Blomeyer, D.K. Hennecke

Darmstadt University of Technology

Petersenstr. 30

64287 Darmstadt, Germany

e-mail: krautkremer@gfa.tu-darmstadt.de

1 SUMMARY

An experimental investigation of isothermal jet-mixing in a swirling crossflow has been conducted using a planar Mie-scattering technique. The mixing process has been studied in a plane model of an annular combustor segment. Aiming at a lean combustion concept, emphasis was put on both the process of homogenizing in the dilution zone and the transport of secondary air into the primary zone, driven by the recirculating flow of the airblast type atomizers which have been used as swirl generating devices without fuel addition. As consequence of the observed dependence of jet penetration on the swirling flow pattern a variation of swirler type and rotation direction under retention of the swirl number has been conducted. For a quantitative study of the mixing process also temperature measurements using the analogy between heat and mass transfer have been employed.

The principal observations were:

- Mixing and homogenizing in the dilution zone is improved by the addition of swirl to the mainstream.
- Due to the three-dimensional flow field of the swirling mainstream the global momentum flux ratio has to be replaced by a local momentum flux ratio considering it as an indicator for jet penetration depth.
- This effect is very distinctive for the wall attached swirlers and weak for the wall detached ones.
- Mixing quality is better using wall attached swirlers.
- The tendency of all swirler configurations to pulsation causes also a time dependence of jet penetration.
- The pulsation caused an aerodynamic instability with effects on flow-split and mixing of the secondary air.
- Orifice diameter and spacing determine the mass-split of secondary air into main and dilution zone.

T_j	jet temperature
T_∞	mainstream temperature
I	pixel value (intensity)
c_D	discharge coefficient
d	jet diameter
f	primary zone length
h	height of the mixing zone
p	static pressure
s	spacing between adjacent jets
t	distance between swirler axis
\dot{m}_j	jet mass flow
\dot{m}_∞	mainstream mass flow, before mixing
n	number of data points in y-z-planes
v_j	jet velocity
v_x	velocity in x-direction
v_y	velocity in y-direction
v_z	velocity in z-direction
v_∞	mainstream velocity
w	width of the duct
x	downstream location from jet centerline
y	lateral distance from middle of channel
z	vertical distance from middle of channel
γ	concentration distribution, dimensionless
θ_{adb}	equilibrium temperature, dimensionless
ρ_j	jet flow density
ρ_∞	mainstream flow density
σ_{adb}	standard deviation from equilibrium temperature
σ	standard deviation from mean temperature
U	degree of unmixedness

Subscripts

eff	effective
i	local value
m	mean value
max	maximum
norm	normalized by relating to the maximum

2 NOMENCLATURE

J	momentum-flux ratio	$\frac{\rho_j v_j^2}{\rho_\infty v_\infty^2}$
S_N	swirl number	
T_{adb}	equilibrium temperature	

3 INTRODUCTION

Due to the demand of lower fuel consumption and a higher combustion efficiency of gas turbine engines the compressor pressure ratio and turbine inlet temperature have been continuously increased during the last years. As a consequence the emissions of nitrogen oxides increased because of the higher combustion temperature. In addition to the effect of strongly growing air traffic the importance of reducing this pollutant is an important topic in combustor design, even if the mechanism of environmental impact at high altitudes isn't yet sufficiently explored.

One important nitric-oxide reducing strategy is the reduction of the combustion temperature by means of a lean primary zone [8]. This strategy requires an excellent control of fuel/air ratio because of the narrow stability range of lean flames.

To determine the desired fuel air ratio in the primary zone already in the design phase, the interaction between the main-flow and the injected secondary air has to be understood. For reasons of flame stabilisation usually swirl is added to the mainstream. The swirl has to produce a toroidal flow reversal to recirculate hot combustion products. The injected secondary air can now enter this recirculation zone and reach upstream regions. This is the reason why the inspection of the primary zone is essential for understanding the mixing process of secondary air.

Due to the three dimensional flow field in the primary zone with regions of reverse flows an examination with conventional probes is not possible without any impact on the flow. Hence a laser light sheet technique was used to achieve information about the mixing process by a non intrusive method.

4 Experimental setup

The experiments were conducted in a model of a plane annular combustor segment using airblast atomizers as swirl generators. Measurements were made using both a planar Mie-scattering technique and a temperature measurement technique, based on the heat-mass-transfer analogy.

4.1 Mixing chamber

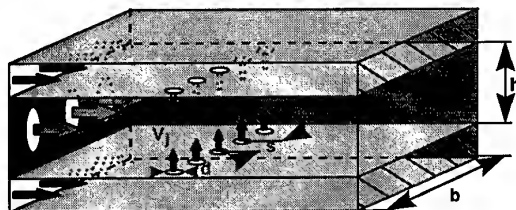


Figure 4.1 Schematic of the mixing chamber

Figure 4.1 shows schematically the atmospheric mixing chamber. It consists of three parallel ducts of rectangular cross sections. The inner duct is 300 mm in width and 100 mm in height. The outer flow channels are of the same width and 60

mm in height. The upper and lower jet streams and the mainstream pass settling chambers, flow straighteners with nozzles and enter the mixing section. Two exchangeable flat plates of 2 mm thickness separate the inner channel from the outer ones (liner walls). The jet streams were injected through a single stage of opposed rows of circular sharp edged orifices which were machined into these plates. Figure 4.2 shows a schematic side view of the mixing chamber with the main flow patterns with the toroidal recirculating mainflow, the jet flows with mass split up- and downstream as well as the mixed mainflow.

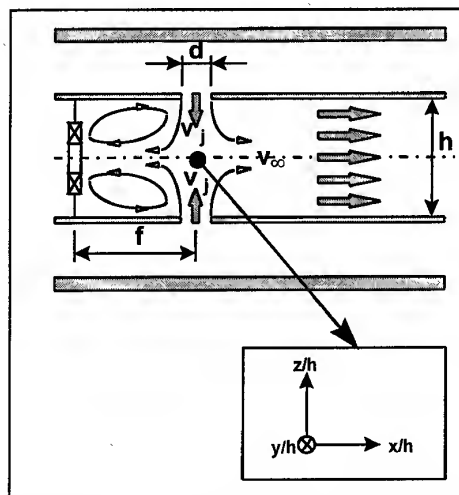


Figure 4.2 Side view of the mixing chamber with the employed co-ordinate system

The origin of the coordinate system for all configurations is placed as follows:

- x-axis, origin in the centre of the jet orifices
- y-axis, origin in the centre of the middle burner
- z-axis, origin in the centre of the middle burner

This system is also valid for the tested configurations with different primary zone length, so that the relative length for the mixing process path starts always in the centre of the injecting orifices.

The mass flow of each stream is determined by orifice flow meters. A 16-channel PSI pressure scanner provides the pressure acquisition. A 32-channel temperature-scanner equipped with thermocouples type J and K delivered the necessary temperatures. At the inlet the mainstream temperature is $T_{\infty} \approx 300\text{K}$. The jet stream enters the mixing chamber with the same temperature $T_j \approx 300\text{K}$. In case of using the heat-mass-transfer measurement technique the mainstream is slightly heated to $T_{\infty} \approx 325\text{K}$. In contrast to real combustors the density ratio ($\rho_j/\rho_{\infty} = T_{\infty}/T_j$) was about 1.1 (real gas turbine approx. 3). Keeping the momentum-flux ratio constant, the influence of the density ratio on the mixing process and on jet penetration is of second order [6,5]. A 3-axis traversing mechanism, the data acquisition and the operation of the test rig is controlled by a Personal Computer. The momentum-flux ratio J and the geometric conditions of the jet injection (s/d , h/d) have been parametrically varied for one configuration. When varying J the mainstream conditions have been kept constant.

4.2 Swirl generating devices

The effect of burner induced swirl on the mixing process was investigated by using a 3-swirler bulkhead placed 0.75h upstream of the injection plane. The employed swirler were of a two flow radial air-blast type. Due to their swirl number of 1.0 the vortex could break down and generate a recirculation zone [4,5,12]. The basis type produced a wall attached flow pattern with an approximately 100mm long recirculation zone. During this work another swirler providing a wall detached flow with the same swirl number $S_n=1.0$ has also been applied as swirl generator. Both types were applied in an ensemble with three corotating swirlers and also in an ensemble with a counterrotating middle swirler. The following picture shows a visualization of the non confined wall attached flowfield.

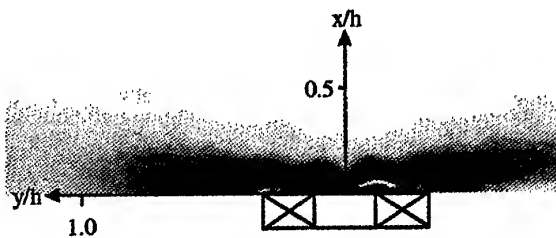


Figure 4.3 Flow visualisation of the non confined wall attached swirler flow

For this visualisation the non confined flow of the swirler has been seeded with particles. The flow has been illuminated with a uniform laser light sheet and captured with the CCD-camera.

The wall attached flow which is shown above is only about 20mm in height. The recirculation zone reaches up into the nozzle which cannot be seen in this picture. Only the M-shape of the image indicates the recirculating flow pattern. This type of swirler has been the basic swirler of this investigation. Only with this type a quantitative determination of mixing quality has been conducted over a wide range of varied parameters. The second investigated swirler type produced a wall detached flow but with the same swirl number as the first type. The following picture shows the visualization of the non confined flow in a light sheet.

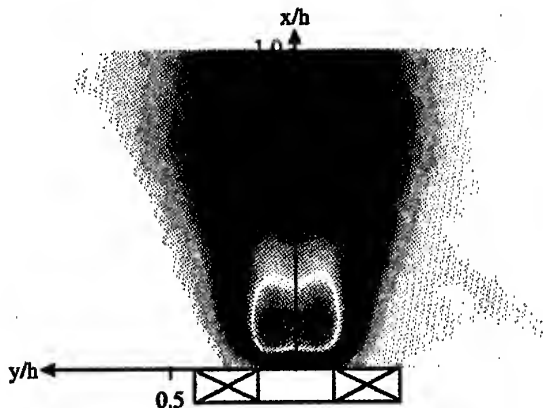


Figure 4.4 Flow visualization of the free wall detached swirler flow

On this picture the toroidal recirculation flow is clearly visible. The outer boundary of this flowfield resembles that of a free jet. The mapped flowfield was 100mm in height.

To achieve an impression of the flowfield in the injection plane by simple means, measurements using a five-hole probe have been conducted. The following graph shows the result for the wall attached configuration.

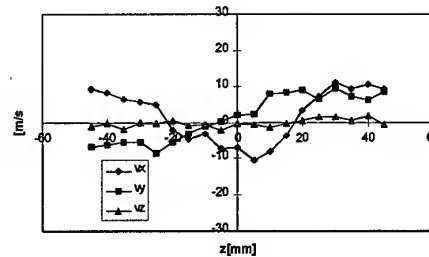


Figure 4.5 Five-hole probe measurements (tracked) in the injection plane of the wall attached configuration

Despite the fact that the measurements were time averaged the graph shows erratic fluctuations. Tracking the five-hole probe during the measurements was very difficult due to strong fluctuations in the flow. Nevertheless the graph shows that the velocity profile of a recirculating swirl flow still exists in the injection plane and is so able to suck secondary air into the primary zone. These measurements were also made with the wall detached swirler type. The following picture shows the results.

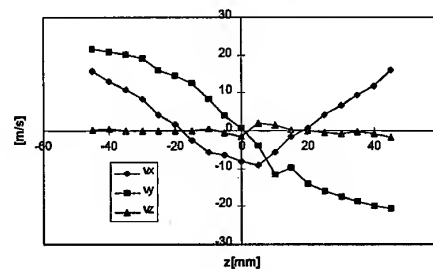


Figure 4.6 Five-hole probe measurements (tracked) in the injection plane of the wall detached configuration

This picture shows a much more balanced result. The swirl flow is very clear identifiable. In case of the wall attached swirlers the interaction of the swirl flow among each other and the wall damages this flow pattern. This is to say that the wall attached flow is much more wall depending than the detached one.

For a better understanding of swirlflow interaction the direction of rotation of the middle swirler has been reversed for both configurations to achieve an alternating swirl direction. The results of this configuration should be discussed later.

4.3 Measurement technique

4.3.1 Analogy between heat and mass transfer (HMT)

Measuring the concentration distribution and using the analogy of heat and mass transfer is a well established measurement technique [1,2,3,6]. It is used as a calibration tool for the optical measurement technique. Also a large databasis exists for different mixing investigations using the HMT [2]. Using this technique the mainstream was slightly heated to provide a thermal mark. The temperature distribution is measured by traversing a probe in the y-z-planes up to $x/h=1$ downstream of the injection plane. An iron-constantan thermocouple is used with a bent design (90°) to reduce the impact on the flowfield.

To determine the mixing quality a simplified normalized standard deviation is used [2].

$$\sigma_{\text{norm}} = \frac{\sigma}{\sigma_{\text{max}}}$$

$$\text{Where } \sigma = \sqrt{\frac{1}{n} \sum_{i=1}^n (\theta_i - \theta_m)^2} \text{ and}$$

$$\sigma_{\text{max}} = \sqrt{\theta_m \cdot (1 - \theta_m)}$$

using dimensionless temperatures

$$\theta_i = \frac{T_i - T_j}{T_\infty - T_j}$$

Using the HMT only the mixing process downstream of the injection plane using the wall attached swirlers has been examined. The aim of the examinations was to find geometric configurations (d/h ; s/t ; f/h) with good mixing properties. The following picture shows the influence of orifice geometry on mixing quality.

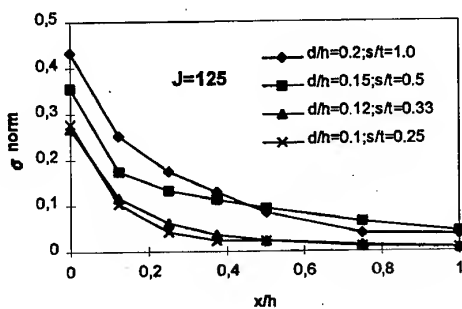


Figure 4.7 Trend of the mixing process by changing orifice geometry.

The examination showed that many small holes lead to a better homogenisation than few big ones. It was also found, that the global momentum flux ratio J (in combustion chamber relevant limits) has only little influence on mixing performance. Finally the primary zone length f/h has been varied. The results of these measurements are shown in the following graph.

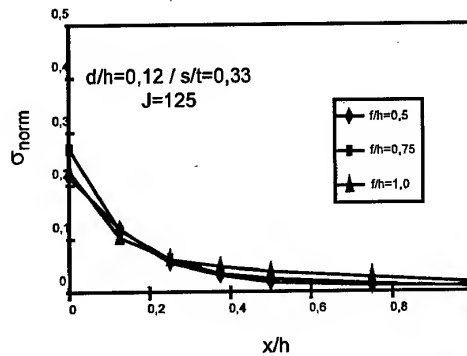


Figure 4.8 Trend of the mixing process by changing the primary zone length.

Obviously the mixing quality is little influenced by changing the primary zone length.

On the basis of this result the following investigations concerning basic phenomena of jet mixing in a swirling crossflow were done using the parameter $f/h=0.75$; $d/h=0.12$; $s/t=0.33$; $J=125$. This is also conform with common combustion chamber design.

4.3.2 The laser light-sheet technique

Using this technique the Mie-scattering of small particles (diameter of about 1micron) in a narrow intensive and parallel light sheet is photographed. The captured intensity distribution is an indication for concentration distribution of the particles. To analyse mixing processes one of at least two separate components has to be marked by a tracer with the capability to follow the considered flow. Basis for this technique is the linear dependance of the intensity of scattered light on the concentration of scattering particles, presuming the subsequently specified but not discussed circumstances.

- Particle concentration not too low to achieve sufficient contrast
- Particle concentration not too high to avoid multiple scattering
- Sufficient scattering efficiency in combination with a good capability to follow the flow
- Homogenous intensity distribution of light sheet
- No wall reflections

In case of an inhomogeneous mass flow distribution normal to the light sheet, this distribution has to be known to provide a mass flow weighting. For further information regarding optimization and correction of this measurement technique see [15].

Subsequently the realized experimental setup is described, including some remarks concerning the above mentioned demands. Figure 4.9 shows the schematic of the experimental setup.

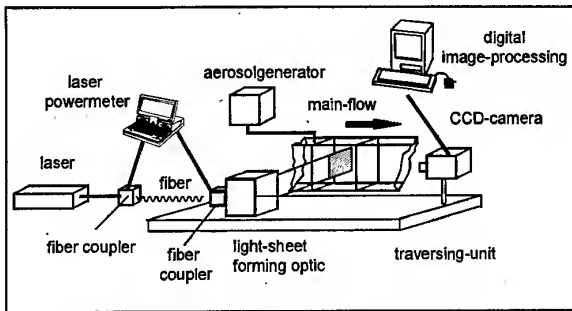


Figure 4.9 Schematic of the light sheet technique

The multiline beam of a 6W Ar-Ion Laser is coupled into a 10 μ m multimode fiber via a fiber-coupler device with a piezo adjustment. Coupling efficiency is monitored by a two-head laser powermeter to assure a constant power of outgoing light. The light which passed the fiber is coupled into the light-sheet forming optic which consists of a rotating polygonal mirror in combination with an off-axis parabolic mirror to form a uniform light sheet of 100mm height and 0.8mm width. The light sheet illuminates a plane of the mainstream which is perpendicular to the main flow direction (x-axis). An aerosolgenerator provides the seeding for the secondary flow. The mean diameter of the produced liquid particles is about 1 μ m. The illuminated mixing process is captured by a thermoelectrically cooled slow scan CCD camera, which is placed downstream of the mixing chamber. The camera has a 768x512 pixel chip providing a 220mm x 145mm spatial resolution with a 12bit resolution of the ADC. For data reduction reasons only a region of 200mm width and 100mm height was observed with the middle swirler in the centre. The captured frame is stored in a PC for digital image processing purposes.

Due to the low dark current which is produced by this camera, image acquisition with long exposure time (10 seconds) are possible to obtain time averaged data. In some cases time resolved data is desirable. Unfortunately the shutter of the camera is only able to provide exposure times longer than 20msec. Despite this shortest exposure time being relative long for the observed flow it was sufficient to discover some interesting effects which couldn't have been observed with means of the technique using the analogy between heat and mass transfer.

5 Experimental

The major strength of the laser light sheet technique is that it is relatively easy to achieve a qualitative impression of the flow patterns. Taking this characteristic into account, most of the experiments for this work were made only performing a qualitative analysis of the captured pictures. A quantitative analysis for planar concentration measurements needs much more effort in both hardware and data analysis. Looking for complex airflows like the ones in a combustion chamber also the inhomogeneous velocity distribution normal to the measurement plane has to be taken into account for the reasons of mass flow weighting. This implies the knowledge of at least the velocity distribution normal to the measurement plane, which has to be obtained via a non intrusive technique like LDV. Since these techniques need, due to their zero dimen-

sional nature, long time for measuring sufficient points, only some selected configurations may be examined.

5.1 Mixing Quality

Regardless of the above mentioned problems of quantitative measurements a first analysis of raw pictures was made to achieve an impression of the exposure quality.

For a rapid determination of the quality of the mixing process the degree of unmixedness U , which is defined as:

$$U = \frac{\sigma}{\bar{I}} \quad \text{where}$$

$$\sigma = \sqrt{\frac{1}{n} \sum_{i=1}^n (I_i - \bar{I})^2}$$

is the standard deviation from mean intensity, and

$$\bar{I} = \frac{1}{n} \sum_{i=1}^n I_i$$

the mean intensity of an image.

This allows the comparison of the mixing quality of different configurations with the same jet-to-mainstream mass flow ratio \dot{m}_j/\dot{m}_e which has been fulfilled for this work due to a

constant momentum flux ratio and constant orifice areas.

During this work four different swirler configurations with equal swirl numbers were examined.

The following picture shows the effect of different swirler types on mixing efficiency.

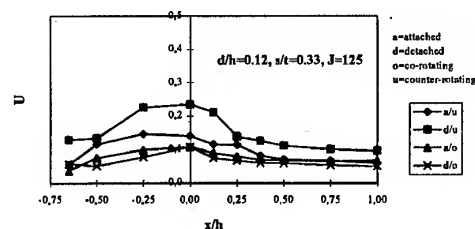


Figure 5.1 Degree of unmixedness for different swirler configurations

Taking into account, that the absolute value might be incorrect, this diagram shows one of the main reasons of the mixing enhancing effect of swirl. The mixing process also takes place in the primary zone due to the recirculated secondary air. Another important detail is that the mixing quality obviously varies for the different swirler types. The counter-rotating configurations seem to have a lower mixing efficiency than the corotating configuration. The differences between the two corotating configurations is surely smaller than measurement accuracy. The apparent demixing process which is normally an effect of missing mass-flow-weighting must here be caused by fluctuations in seeding concentration because inhomogeneities in the velocity field at a position $x/h=0.55$ are negligible.

5.2 Examination of the mixing process

The following investigations concentrated on the qualitative analysis of the mixing process in order to evaluate the mixing influencing phenomena.

The mixing process of jets in a crossflow mainly depends on jet penetration [6,7,9,10,11,13]. For this reason the injection plane has been thoroughly examined to observe the process of jet penetration.

The mixing process of jets in a crossflow is significantly influenced by mainstream swirl [11]. This effect which is mainly caused through providing large surfaces with strong shear. Commonly the strength of this effect is thought only to be related with the swirl number of the flow. But also different flow patterns with a constant swirl number may influence jet penetration. Thus during the present work the influence of a different swirler flowfield with constant swirl number was investigated.

5.2.1 Influence of swirling flow pattern on jet penetration

The first swirlers which were used were the two-flow airblast atomizers with a wall attached flowfield. (See Figure 4.3). This type had a great influence on jet penetration. The following picture illustrates this effect.



Figure 5.2 Jet penetration in injection plane

Despite the equal relative hole diameter $d/h=0.12$ and the global momentum flux ratio of $J=125$ jet penetration depth varies strongly, depending on injection location. For a better understanding of this effect the pressure distribution on the liner wall has to be known. With this information a local momentum flux ratio can be calculated. For this reason both injection plates were replaced on one side by a plate without holes and on the opposite site by a plate with 150 wall pressure taps. The following picture illustrates the situation at the mixing chamber.

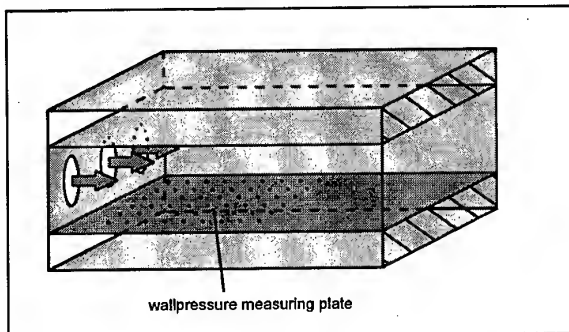


Figure 5.3 Setup for measuring wall pressures

The next picture shows the measured wall pressure distribution scaled to 1bar. The injection plane is normally situated at $x/h=0$. This was also given for the measurement shown in Figure 5.2.

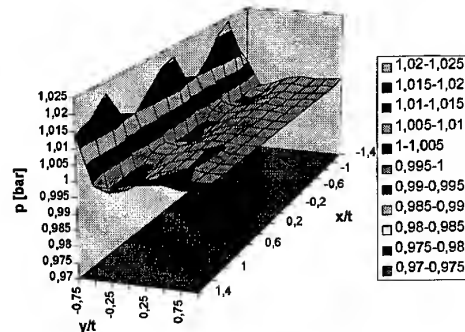


Figure 5.4 Wall pressures on injection wall; wall attached swirler

The measurements taken without secondary air-injection could not be directly used to calculate the momentum flux ratio via the pressure difference between main- and co-flow because of the missing influence of jets on the mainflow. Nevertheless they give a good idea about the effect of a swirling mainflow on jet injection. That is to say the global momentum flux ratio J which is in case of a uniform mainflow an indicator for jet penetration behaviour has to be replaced by a local momentum flux ratio $J=f(y/t)$. But obtaining this data may be expendable.

These pressure data were taken with a conventional pressure transducer and a scanivalve mechanical multiplexing device. As consequence they represent time averaged data. Inspecting the mixing process by eye leads to the presumption, that the flow is not stable. To reveal this effect images were made with the minimum possible exposure time the camera offers.

5.2.2 Instabilities caused by the swirling mainflow

The time resolved pictures showed another important aspect of the swirling mainflow. Different from the time averaged exposures jet penetration depth isn't only a function of location but also of time $J=f(y/t, t)$. The following picture shows a series of exposures which were made in the injection plane.

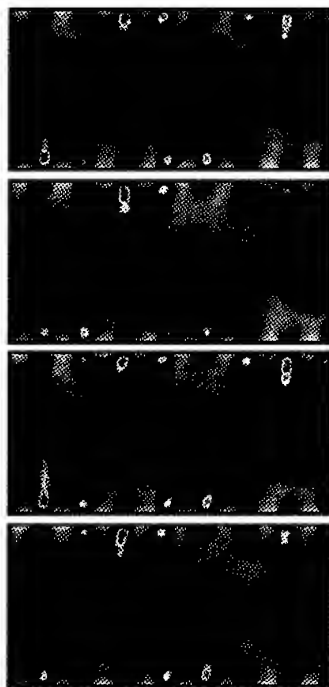


Figure 5.5 Time resolved exposures of the injection plane.

All exposures show different jet penetration at different locations. It is notable, that the global flow pattern of deeply and slightly penetrating jets seems to be little changed but large scale lateral jet movement occurs along with a varying penetration depth.

5.3 Variation of the swirler shape

In further experiments the wall attached swirlers were replaced by wall detached swirlers with approximately the same swirl number. The following figure shows the effect on jet penetration.



Figure 5.6 Injection zone time averaged; wall detached swirler type.

First obvious detail of the foregoing picture is the accumulation of secondary air in front of the middle swirler. Notable is also the penetration depth which is nearly equal for all jets. This indicates an uniform pressure distribution on the liner wall. Confirmation is given by measuring the pressure distribution with the wall pressure measuring plate. The results are shown in the following picture.

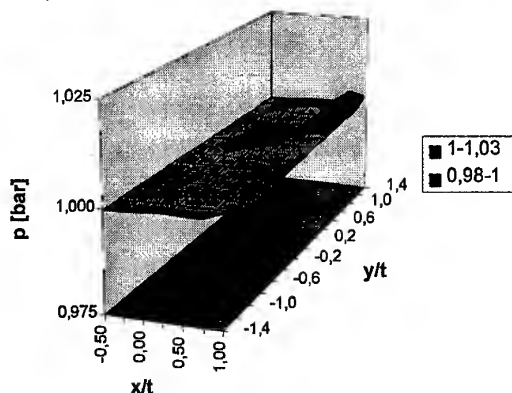


Figure 5.7 Wall pressure on injection wall; wall detached swirler

The graph shows a relatively uniform pressure distribution. This indicates also an equal momentum flux ratio for the jets. The accumulation of secondary air in front of the middle swirler could only be secondary air, which has been sucked into the recirculation zone. The following picture shows a time averaged image of the primary zone.

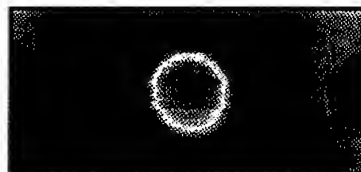


Figure 5.8 Time averaged exposure of the primary zone; wall detached swirler

Despite the relatively high swirl number of $S_N=1.0$ the outer swirlers are obviously not able to get primary air into the recirculation zone. It has to be mentioned, that this could also be an effect caused by the walls. Unfortunately during this work investigations using 5 or more swirlers in order to reduce this wall effect couldn't be made.

Regarding the mixing phenomena by eye in this case also leads to the presumption of an instable flow. Capturing some frames with the minimal possible exposure time provided the confirmation as the following pictures will show.

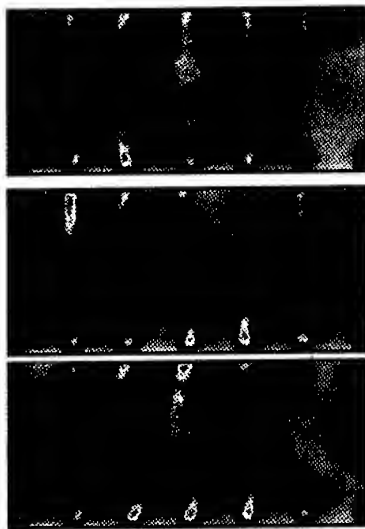


Figure 5.9 Time resolved measurements of the injection plane; wall detached swirler

Although the time averaged exposure shows an accumulation of secondary air in front of the middle swirler, the time resolved exposures indicate that an accumulation of secondary air also can take place in front of the outer swirlers. This is to say, that also the outer swirlers are able to suck secondary air into the primary zone. The process of vortex breakdown seems to be influenced by the interaction of the swirler ensemble and/or the secondary air injection despite the relatively high swirl number. This effect is also clearly visible in the time averaged captures of the primary zone which are shown in the following pictures.

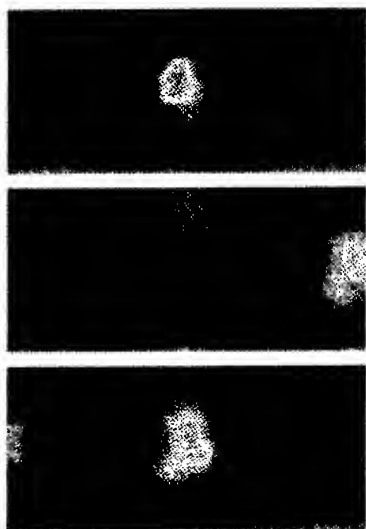


Figure 5.10 Time averaged exposures of the primary zone; wall detached swirlers.

The accumulation of secondary air takes place at every swirler but is time dependant. The frequency of this instance could not be determined by means of the optical measurement technique, but appeared to be in the order of a few Hertz.

5.4 Counterrotating swirler

Because of the fact, that corotating swirlflows produce strong shear by getting in contact and also create a rotating global flow in case of an annular combustor [2], it is consistent to examine a counterrotating configuration. For this purpose the middle swirler has been replaced by a counterrotating one. The situation in the mixing chamber is illustrated by the following picture.

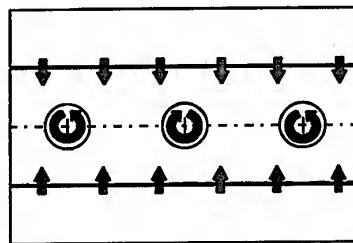


Figure 5.11 Counter rotating middle swirler

This configuration impedes the formation of shear between the swirlers and stops a rotating global flow.

Considering the injection plane both swirler types, the attached and the detached one showed unsatisfying behaviour as it is shown with the following pictures.



Figure 5.12 Time averaged exposure of the injection plane; counterrotating wall attached swirlers.



Figure 5.13 Time averaged exposure of the injection plane; counterrotating wall detached swirlers.

Both configurations showed a tendency of accumulating secondary air slightly out of the axis of the middle swirler. No preferred side could be observed. This effect seems to be related to the formation of a vortex pair which sticks together. The formation of the vortex pair happens incidentally just after the flow has been started and changes during the experiment.

Comparing the corotating wall detached version (Figure 5.6) with the counterrotating one the latter seems to force the jet mixing over a wider area. Nevertheless both configurations show regions in front of the outer swirlers with negligible recirculation of secondary air. A prediction of this effect for an annular combustor would only be possible by verifying this

examination with a greater number of swirlers in order to minimize wall effects.

5.5 Examination of the primary zone

Due to the non intrusive nature of the light sheet technique the examination of the sensitive flowfield of the primary zone is possible. Because of the recirculated secondary air these measurements were also carried out by adding particles to the secondary flow. To reveal the impact of the primary flowfield onto the jet penetration, planes near the injection zone were examined. These exposures give a good information of the flow patterns which will interact with the secondary air. Considering the problem of a stable combustion under lean conditions, the amount of recirculating secondary air has to be known to predict the local fuel air ratio. But irrespective of the combustion concept the question of homogeneity has always to be taken into account.

The laser light sheet technique offers a good means in regard to the homogeneity of the concentration field in dependance of time and location.

The following pictures will show the time averaged exposures of the primary zone plane at a location of $x/h = -0.25$ for the four examined swirler configurations.

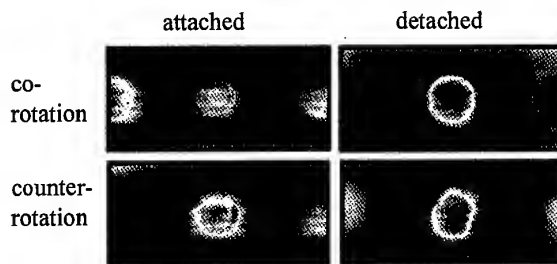


Figure 5.14 Time averaged exposures of the primary zone

The configurations with the wall attached swirlers show a more or less good homogeneity already in the primary zone, whereas the wall detached configurations are featured by a domination of the middle swirler. This is caused on one side by the taller recirculation zone of the wall detached swirlers but on the other hand by the interaction between the swirling flows. This is to say that all the wall attached swirlers have strong, stable recirculation zones whereas the wall detached swirler operate at an unstable condition. If the vortex of the middle swirler breaks down, the swirling jet gets wider and inhibits the adjacent swirlers also to break down and recirculate. These experiments have to be repeated with a greater number of swirlers to eliminate the effects of the wall on the outer swirlers and to come closer to the situation in an annular combustion chamber.

Most of the examinations were made using time averaged exposures aiming on the average of secondary flow which recirculates into the main zone. The following pictures show the basic effects which have been observed for the wall attached swirlers.

The various swirler configurations differ also in the time resolved concentration fields they produce. The following pictures show some exposures which reveal the occurring extreme of concentration distributions in the primary zone.

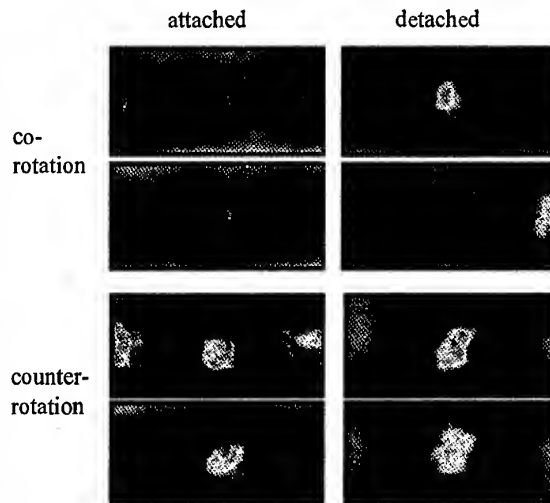


Figure 5.15 Time resolved exposures of the primary zone

Here also the wall attached configurations show a better homogeneity. The affinity to pulsation is much stronger in case of the wall detached swirlers but transparent by all configurations. The wall detached version with equal rotation is strongly pulsing. The process of vortex breakdown and recirculation alternates from the middle to the outer swirlers, whereas the total amount of recirculation time of the middle swirler is greater than for the outer swirlers which leads to the domination of the middle one considering the time averaged exposures. Regarding this flow by eye a stable combustion under these aerodynamic conditions is hard to imagine.

6 Conclusions

A laser light sheet technique for the investigation of jet mixing under the condition of the swirling mainflow of a combustion chamber has been established for isothermal experiments. This work leads to the following cognitions:

The laser light sheet technique is an excellent tool for providing qualitative information including the sensitive primary zone. It delivers measurements with a high local resolution. Time resolved measurements are also possible. Obtaining quantitative data needs much more effort both in optical setup and data analysis. However first evaluations of the raw data showed that one mixing promoting effect of swirl is the shift of the mixing process into the primary zone.

Concerning the mixing process the following statements could be made:

The flow pattern of the swirling main flow influences jet penetration.

Wall attached swirler types cause strong pressure gradients on the liner walls which leads to a variation of local momentum flux ratio.

All investigated swirler types and configurations caused aerodynamic instabilities with the result of pulsations.

The counterrotating configurations lead to very disadvantageous flowfields by enabling the formation of counter rotating vortex pairs which lead to an inhomogeneous mass distribution.

The application of swirl generating devices like airblast atomizers in combustion chambers is a commonly used technique for flame stabilisation. Nevertheless its impact on the mixing process of secondary air has to be well considered. Depending on varying geometric configurations of swirlers with the same swirl number different jet-mainflow interactions have been observed.

7 Acknowledgement

The authors gratefully acknowledge the support of the German Ministry of Science and Technology (BMBF) within the joint research program KEROMIX contract 20T9607F.

8 References

1. Blomeyer, M.M.; Krautkremer, B.H.; Hennecke, D.K.: Optimum Mixing for a Two-Sided Injection From Opposing Rows of Staggered Jets Into a Confined Crossflow, Proc. ASME Turbo Expo, Birmingham 1996, ASME 96-GT-453
2. Blomeyer, M.M.; Krautkremer, B.H.; Hennecke, D.K.: Optimization of the Mixing Process in the Mixing Zone of an RQL-Combustor, Proc. 13th ISABE, Chattanooga TN, USA 1997, ISABE 97-7208
3. Dörr, T.: Ein Beitrag zur Reduzierung des Stickoxydausstoßes von Gasturbinenbrennkammern, Dissertation TH-Darmstadt 1995.
4. Gupta, A. K.; Lilley, D. G.; Syred, N.: Swirl Flows, Cambridge, Massachusetts, USA (ABACUS Press) 1984.
5. Hillemanns, R.: Das Strömungs- und Reaktionsfeld sowie Stabilisierungseigenschaften von Drallflammen unter dem Einfluß der inneren Rezirkulationszone, Dissertation Universität Karlsruhe 1988.
6. Holdeman, J.D.; Walker, R.E.: Mixing of a Row of Jets With a Confined Crossflow, AIAA Journal, Vol. 15 No.2, p.243-249 1977
7. Holdemann, J. D.: Mixing of Multiple Jets With a Confined Subsonic Crossflow Part II-Opposed Rows of Orifices in Rectangular Ducts, Orlando 1997, ASME 97-GT-439
8. Lefebvre A.H.: Gas Turbine Combustion, Hemisphere Publishing Corporation New York 1983.
9. Liscinsky, D. S.; True, B.; Holdemann J.D.: Experimental Investigation of Crossflow Jet Mixing in a Rectangular Duct, AIAA-93-3037, 29th Joint Propulsion Conference Monterey 1993.
10. Liscinsky, D. S.; Vranos, A.; Lohmann, R.P.: Experimental Study of Cross Flow Mixing in Cylindrical and Rectangular Ducts, Report Number E-7708, United Technology Research Center, East Hartford, Connecticut 1993.
11. Liscinsky, D.S.; True B.: Effects of Inlet Flow Conditions on Crossflow Jet Mixing, AIAA-96-2881, 32nd AIAA Joint Propulsion Conference, Lake Buena Vista, FL 1996.
12. Mundus, B.: Über den Einfluß der Drallerzeugerkonstruktion auf das Strömungs- und Reaktionsfeld turbulenter Diffusionsflammen, Dissertation Ruhr Universität Bochum 1990.
13. Mungal, M. G.; Lozano, A.; van Cruyningen, I.: Large Scale Dynamics in High Reynolds Number Jets and Jet Flames, Experiments in Fluids 12, 141-150, 1992
14. Schmitt, F.; Ruck, B.: Laserlichtschnittverfahren zur qualitativen Strömungsanalyse, Laser und Optoelektronik Nr.2 1986
15. Voigt, P.; Schodl, R.: Using the Laser Light Sheet Technique in Combustion Research, Proc. RTO Symposium Toulouse, 1997.

PAPER No. 42
Krautkremer, Blomeyer & Hennecke
(presenter: B.H. Krautkremer)

Question 1: C. Wilson, DERA, U.K.

How did you measure the swirl numbers for the swirler?

Answer:

We measured the momentum of the swirler. The angular momentum effects on the swirler were obtained directly rather than by using the more conventional flow-straightener approach, because of concern over the impact of the straighteners on the flowfield. For further detailed information, please contact me.

Question 2: C. Priddin, R.R., U.K.

Did you seed all of your flowfield? Are you sure that the flow from the "wall-attached" swirler is still attached to the dome of the combustor during the combustion tests? Such flows can be stable in both modes (bistable).

Answer:

For the single swirler tests the whole flow through the swirler was seeded; in the mixing chamber, only the secondary air was seeded. Yes, the flow remained attached during combustion. We also measured the pressure distributions on the mixing chamber walls. These distributions indicated that the stagnation streamlines from the swirler immediately attached to the liner walls. Flow visualization confirmed the attachment. Confinement of the swirling jet by the chamber walls helped this flow attachment.

Question 3: C. Pridden, R.R., U.K.

Bi-modal attachment can occur with any swirler. How did you control the bimodal state of the swirling flow? Using the same geometry, the same flow conditions and the same swirler, it is possible to have either one of **both** modes (attached and detached), depending on the start-up conditions, or to have switching between modes, depending on flow disturbances.

Answer:

The operating mode of the swirler was controlled by the shape of the nozzle to a single condition. Using flow visualization and the wall static pressure measurements, the operating mode of the swirler was confirmed, and during the period of the all subsequent measurements, this swirl mode remained unchanged.

Question 4: M. Nina, Instituto Superior Tecnico, Portugal

Bimodal attachment can occur at any time with any swirler. Did you encounter any bimodal behavior?

Answer:

No, the swirler only had the one operating condition.

Optical Measurements of Spray Combustion in a Single Sector Combustor from a Practical Fuel Injector at Higher Pressures

T. Behrendt, M. Frodermann, C. Hassa, J. Heinze, B. Lehmann*, K. Stursberg
DLR, Institute for Propulsion Technology
Linder Höhe
D-51170 Köln

*DLR, Institute for Propulsion Technology, Turbulence Research
Müller-Breslau-Str.8, D-10623 Berlin
Germany

SUMMARY

A research combustor for the investigation of spray combustion of practical aeroengine fuel injectors has been built. It approximates a single sector of an annular combustor. It allows optical access for laser based measuring techniques with point- and planar measuring volumes and can be operated up to 20 bar with preheat temperatures of up to 850 K.

For this contribution, the combustor has been operated at 3, 6 and 9 bar and at preheat temperatures of 473 K and 673 K with a technology injector supplied by BMW-RR. The isothermal flowfield was investigated by Laser Doppler Anemometry and the combusting flow by Phase Doppler Anemometry, Laser Induced Fluorescence of Kerosene and OH and imaging of the spontaneous OH emission.

The injector showed a large central recirculation with an almost radial expansion of the gas flow without outer recirculation. At 6 bar, 473 K preheat and AFR 20, the bulk of the spray is evaporated before the reaction rate as signalled by OH* emission intensity reaches high values, which confirms earlier estimates postulating external group combustion for aeroengines. The investigated atomizer shows a marked influence of temperature and almost no influence of pressure on the measured dropsizes which was attributed to the design of the internal airflow promoting prompt atomization as the dominant atomization mode.

1. INTRODUCTION

„When faced with new and challenging problems, the combustion engineer has traditionally looked to the fuel injector to provide a solution“. This statement, taken from a recent review by Lefebvre [1], illustrates the motivation for the research undertaken towards understanding the physical phenomena connected with the process of fuel preparation in aeroengine combustors. Conceptually, the task has often been divided into two steps, cf. e.g. [2]:

1. Understanding the combustion aerodynamics of the primary zone including the mixing of gaseous fuel and air, which might open the way to modify the stability and emission characteristics
2. Understanding the changes introduced by the need for atomization of liquid fuel

Whereas the first task can be tackled to a large extent with research configurations singling out significant flow features or

research combustors incorporating generic designs, it is hard to find true generic configurations for liquid fuel preparation, because minor changes in atomizer design will often go hand in hand with severe performance losses. Two further important arguments in favour of research on gaseous fuelled combustors are cost and access: The effects of pressure can be more successfully abstracted because they enter „only“ through chemistry with faster reaction rates leading to higher emissions and to a smaller although less clear effect on flame stability. Hence a substantial part of the work can be done with cheaper, atmospheric experiments. Access to the desired experimental quantities is also easier since perturbations are less severe for probe and optical measurements alike. Last but not least, modelling of spray combustion loses elegance because of the lasting inability to model atomization from first principles. Hence in the first instance, the combustion scientist might look upon the presence of liquid fuels mainly as an unpleasant perturbation.

As logical as it would seem then to solve the task sequentially, there are reasons to begin with liquid fuel injectors early on: designers cannot wait until gaseous fuel injection is understood, because solving the problem thoroughly would encompass the accurate description of the turbulence chemistry interaction, which is still some time away. Moreover for the airblast atomizers used in aeroengines, the liquid fuel starts to influence the air flow right from the start of the atomization and it is not trivial to abstract a gaseous fuel injection from an airblast nozzle. Having decided then to deal with combustion characteristics of liquid fuel injectors, it is inevitable to include the investigation at higher pressure, as pressure influences spray combustion to a wide extent by its influence on the quality of atomization.

Hence, the present contribution describes a part of a larger, collaborative research effort centred around the questions of stability and emission characteristics of aeroengine fuel injectors, which deals with some effects of pressure on the combustion of a technology atomizer provided by BMW-RR. In the research co-operative KEROMIX consisting of engine manufacturers, universities and a research centre, DLR has taken up the task to investigate the influence of pressure on the lean blow out of liquid fuel injectors. Beside establishing the LBO envelopes for the agreed injectors with respect to preheat temperature and pressure, phenomenological studies are undertaken to describe the modifications forced upon the combustion by the presence of the liquid fuel. Here, some preliminary results of the latter part of the work will be presented preceded by a brief review of some earlier work, a description of the test facility which has been built and the utilised diagnostics.

Attempts to categorise spray combustion have been made by Chiu and co-workers [3] with the introduction of the group combustion number G . They distinguished between external sheath-, external group-, internal group- and single droplet combustion. With typical numbers for gasturbines given in [4], external group combustion results. That would abridge the influence of the liquid phase to the different kinetics of the liquid fuel, the local heat loss of the gas flow field by the heat of vaporisation and the difference in mixing with the delayed addition of gaseous fuel according to the evaporation history and eventual spray feedback to the gas flow. Unfortunately, the theory has to assume monodisperse, round droplets without slip and is based on the flamesheet model. Real sprays are polydisperse, move with appreciable slip velocities and flammability limits are extended into richer mixtures with higher pressure, all of which tends to blur the clean separation of flame and droplet cloud.

tribution consists in coupling planar, qualitative techniques with quantitative techniques measuring at a point in the flow-field to create the chance of relating globally observed flow features to the local changes in the two phase flow.

2. OPTICALLY ACCESSIBLE COMBUSTOR

The optically accessible single sector combustor was designed for visual and laser-based analysis of spray generation, mixing and flame stability at higher pressures.

The requirements on the design of the test rig can be summarised by the following data set of maximum conditions:

flame tube pressure	20 bar
combustion air preheat	850 K
air flow at max preheat	1.3 kg/s
cooling air flow rate	3 kg/s

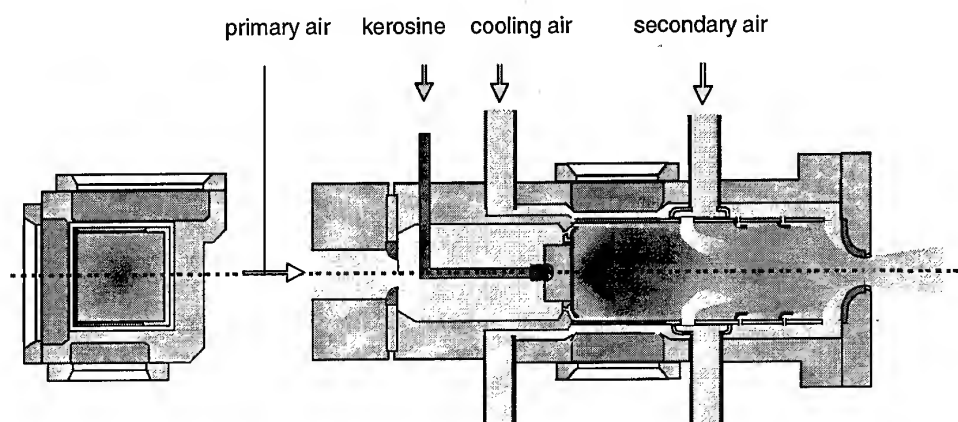


Figure 1: Single sector combustor

The test rig is schematically displayed in Figure 1. The most important design features are listed below:

- flame tube cross-section quadratic, $102 \times 102 \text{ mm}^2$
- flame tube length 286 mm
- optical access to primary zone by quartz windows in 3 side-walls
- primary air: seeding feasible for velocity measurements
- secondary air: ambient or preheated, here preheated, mass flow separately adjustable
- kerosene supply is water-cooled
- film cooling of the inner windows with preheated air, adjustable film cooling of the flame tube by cold air

Another approach taking into account turbulent mixing was proposed by Bolado & Yule [5]. They characterised spray combustion with the ratio of the length scales for vaporisation V and entrainment E in a stationary, turbulent spray jet, the vaporisation length being given by the distance needed to evaporate all fuel and the entrainment length as the distance needed to entrain enough air into the spray boundary to fully burn the fuel. For low values of V/E , the diffusion flame limit is reached, at the other extreme is the „brush flame“ or „cloud burning“. Again, the flamesheet is used as combustion model. Since in reality, there is competition between ignition delay and turbulent diffusion depending on the temperature level, for primary zone flows with lower V/E 's brush flames are possible at higher pressures and strong recirculation of hot products as well as premixed LBO characteristics in case of lifted flames at high preheat.

Investigations of two phase flows at higher pressure in the open literature are sparse, with [6] being one example done isothermally at pressures up to 12 bar. One of the conclusions was, that up to a distance of 70 mm from the injector, the spray density was too high for the used Phase Doppler Anemometer. Since evaporation and hence spray feedback on the gas phase would be well finished before that distance in the combustor, it follows that the spray densities produced by good atomizers at higher pressures prevent useful application of the applied diagnostics, such that investigation of the two phase flow aerodynamics and the spray combustion can no longer be separated at higher pressure. Recently, Planar Laser Induced Fluorescence was applied to a combustor sector at 3 bar and mean and fluctuating spray distributions were successfully imaged [7]. The diagnostic approach taken in the present con-

The design was guided by the requirement to be as close to real combustor conditions as possible and to provide sufficient optical access for laser diagnostics. The test rig dimensions, test objects, and operating conditions were agreed with the industrial and university partners of the KEROMIX research initiative.

The flow path is described with reference to Figure 1. Electrically preheated, compressed air - marked as primary air - is supplied to the plenum in front of the combustion chamber by a critical nozzle to keep the mass flow rate constant at varying combustion pressures. The primary air is splitted into the combustion air passing the airblast atomizer and into a smaller part for inside cooling of the inner windows. The primary air flow rate is controlled by the chosen pressure loss of the investigated

airblast atomizer, which amounts to 3 % in most of the conducted tests.

Preheated, compressed secondary air, metered by critical nozzles, is injected into the flame tube about 100 mm downstream by two rows of holes with 13 mm diameter in opposite side-walls to limit the recirculation of the primary zone. The mass flow is chosen such that the jets don't collide and no secondary air is recirculated by the mean motion of the flow. The combustor pressure is controlled by the cooling air flow rate, which is mixed with the combustion gas before leaving the combustor through a throttling (choking) nozzle. As the figure shows, the main function of this air flow is to cool the flame tube convectively at the outer surface and inside by film cooling fed into the secondary zone.

The liquid fuel - kerosene Jet A-1 - is fed to the atomizer by a water cooled tube; its flow rate is adjusted to the fuel/air-ratio to be examined. The spray is ignited by a hydrogen pilot flame, which is produced by a pneumatically driven spear, inserted into the combustor from the backside. The ignition of the hydrogen is done by a high voltage spark. After lighting up the kerosene, the torch is stopped and the spear ejected.

The combustor is again shown in the photograph of Figure 2 with the exhaust tube leading to the silencer. As to be seen from Figure 3, the flow direction is vertical. This was done to facilitate optical measurements more easy by keeping the adjusted diagnostic equipment fixed and by moving the much smaller combustor in 3 co-ordinates by means of a precise adjustment device. The photo shows the combustor in operation with the ignition spear in the parking position.

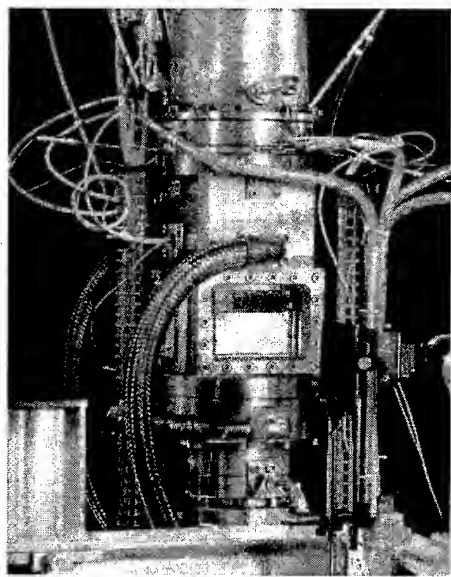


Figure 2: Photograph of combustor

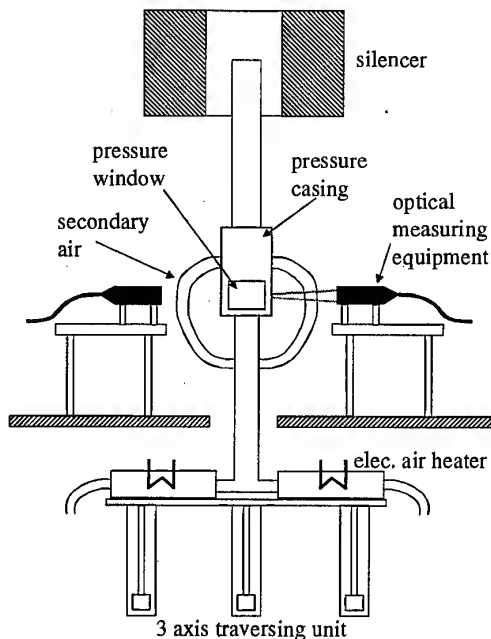


Figure 3: Test facility

The conventional measurement techniques include steady and unsteady pressure measurements, temperature measurements by thermocouples, flow rate measurements, and exhaust gas analysis. The following species can be measured: H_2 , O_2 , CO , CO_2 , UHC , NO , NO_2 . For the measurement of H_2 , O_2 , CO , and CO_2 , the gas sample, taken by a suction probe, has to be cooled down to about $-30^\circ C$ to avoid condensation. For measurements of NO_x and UHC 's, the gas sample is kept on a constant temperature of $180^\circ C$, which is achieved by a thermostated electrical heating system.

Beside logging the mass flows, temperature and pressure data, the experiments are documented by Hi 8 Video with 50 Hz. rep. Rate. The videos can help to identify instationary behaviour as well as the region of the flame position.

The airblast atomizer used in this investigation is shown in Figure 4. It was supplied by BMW-RR as a technology atomizer. It consists of three co-rotating axial swirlers. The fuel is fed through a circular gap onto the prefilming lip.

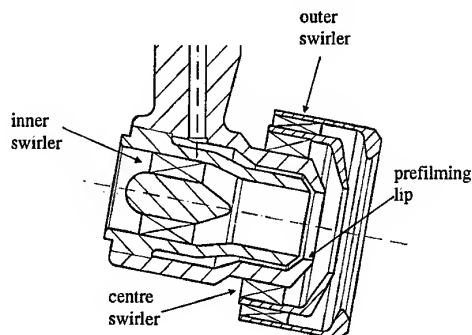


Figure 4: Schematic drawing of airblast nozzle (not to scale), courtesy of Fuel Systems TEXTRON

3. DIAGNOSTICS

3.1 Doppler Anemometry

The velocity distribution of the isothermal gasflow and the velocity and droplet diameter distribution in the reacting flow-field were mapped using Laser Doppler techniques. Laser Doppler Anemometry (LDA) measures the velocity of particles in the flowfield and Phase Doppler Anemometry (PDA) additionally gives the diameter of a spherical droplet. The intersection volume of two laser beams forms the measuring volume. The scattered light of a particle passing through this volume is frequency shifted due to the Doppler effect. The scattered light is detected by a photomultiplier (PM) and transformed into an electrical signal (burst), which can be processed. The frequency shift is proportional to the particle velocity and the conversion factor depends on geometrical properties of the optical setup and on the wavelength of the laser beams. The measurement is valid if only one particle is present in the measuring volume.

For the measurement of the diameter of a spherical particle another PM is used. The different paths of the scattered light to these two PMs cause a phase shift of the signals to each other. This phase shift is proportional to the diameter of a spherical particle and the conversion factor depends on geometrical properties of the optical setup, the wavelength of the laser beams and, in case of refracted light used for sizing, on the refractive index of the droplet. Laser and Phase Doppler Anemometry use a point-like measuring volume giving a high spatial resolution.

3.1.1 3D Laser Doppler Anemometer

A three-component laser-Doppler measurement system was used in order to measure the velocity field together with the complete Reynolds-stress tensor of the flow behind the nozzle exit. The optical setup consisted of a two component and a one component system with a rectangular angle between the respective optical axis. Both systems work in forward scatter. The two-component optics used the green and blue light of an argon laser, the single-component system the green light of the same laser in order to measure the third component. The two different green Doppler signals were optically separated by the intensity discrimination occurring between the 0° and 90° scattering angle. The transmitting optics were placed in a way that the main velocities of the swirling flowfield were measured without the necessity of transformation. The bursts were analysed by Fast Fourier Transformation (FFT) processors built by DANTEC [8], which were operated in hardware triple-coincidence mode. It applies a two-microseconds wide coincidence window. The measuring errors for the velocity is about 1%. The signals were processed if the signal to noise ratio of every burst of a particle was -6dB or better. Seeding particles were used consisting of SiO_2 with $0.8 \mu\text{m}$ mean diameter which scattered by $\pm 20\%$ around this value. About 10000 particles were collected at each measuring position. The Gaussian beam diameter of the measuring volume was $150 \mu\text{m}$. The optical set up and the triple coincidence mode lead to an approximately spherical measuring volume.

The complete optics together with the 5 Watt argon laser were fixed on a mechanical frame to be shifted in vertical direction. The flow-model apparatus could be horizontally shifted with a second frame into two directions.

Figure 5 describes the model of the combustion chamber which served for the isothermal flow measurements under atmospheric conditions. It is a simple cube-shaped chamber with a free cross-section of 102 mm by 102 mm and consists of 2

mm thick glass walls. Its bottom plate was identical with the nozzle exit plane and formed a 0.7 mm wide slit along the chamber walls in order to introduce a secondary wall flow into the chamber. The mass-flow amounted about 60% of the primary nozzle's mass flow. Both flows were fed from the common plenum volume under the nozzle plate.

The flow-chamber's exit cross-section was reduced by using four parallel rods with a diameter of 9 mm positioned with their centre lines at $x=106$ mm away from the nozzle exit. A rough approximation of the side jets' influence should be obtained in this way.

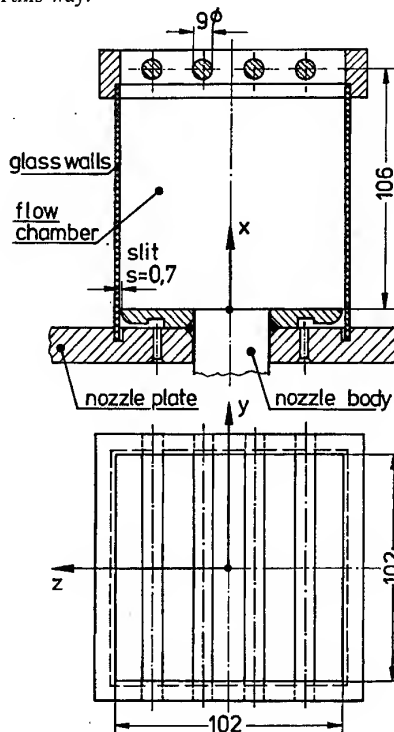


Figure 5: Combustion Chamber model for flow measurements under atmospheric isothermal conditions

3.1.2 3D Phase Doppler Anemometer

The PDA measurements were made with a three component PDA powered by an Argon Ion Laser running at about 2.5W. The specific instrument used was a DUAL PDA built by DANTEC [9]. The dual mode concept is an extension of the conventional (standard) PDA with the capability of rejecting incorrect size measurements caused by effects, which are probable to occur if the particle diameter is not small against the diameter of the measuring volume. Furthermore, the DUAL PDA is better capable in detecting non-spherical droplets than a standard PDA [10]. This benefits the accuracy of the determination of volume undersize diameter and mass flux. The Doppler-frequencies and the phase-shift were determined with a covariance - processor. The measuring errors for the velocity is about 1% and 4% for the particle diameter. The signals were processed if the signal to noise ratio of every burst of a particle was +1dB or better. At each measuring location 40000 droplets were collected or the measurement was aborted after 150 seconds. This restriction in measuring time was necessary because the combustor windows became blind within a few hours. The windows were cleaned and polished after each test condition. Where the data rate was below 5Hz, no measurement was made. The velocities and the diameter of every particle were

stored in files, so that mean and fluctuating velocities, mean diameters and mass flux distribution for all particle size classes could be calculated. As three velocity components are measured not only the mass flux in axial direction but the mass flux vector in any arbitrary direction can be calculated. The algorithm of the mass flux calculation, the accuracy and the specific problems in conducting PDA measurements in a dense spray is explained in [11]. The Gaussian beam diameter of the measuring volume was $160\mu\text{m}$ and the length was limited by a slit aperture in the receiver to about $600\mu\text{m}$. In Figure 6 the optical setup of the 3D PDA is shown in top view. The position of the airblast atomizer is indicated.

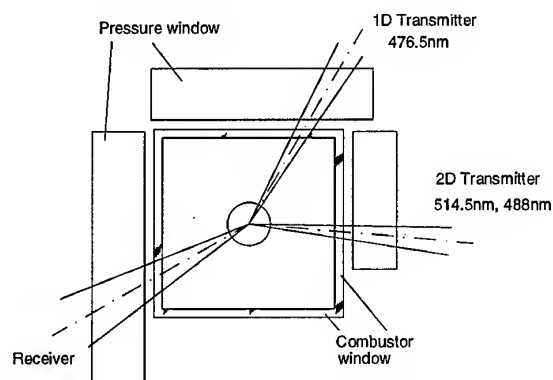


Figure 6: Top view of optical setup for 3D PDA

The measuring plane closest to the combustor dome was $x=8\text{mm}$. The limiting factor is the axial extension of the heat shield near the exit of the window cooling film, see Figure 1, which must not interfere with the envelope of the scattered light path to the receiver. Even a partial blockage of the receiver front lens will cause erroneous measurements of the particle diameter.

The axial velocity was measured directly and the tangential and radial velocities were obtained by a velocity transformation. The 2D transmitting probe was rotated by 5° to increase the scattering angle of the receiving probe. By this measure the sensitivity of the phase conversion factor against changes of the refractive index of kerosene due to droplet heat-up was reduced.

3.2 PLIF Diagnostics

The results consist of Planar Laser Induced Fluorescence (PLIF) images of the hydroxyl- ($\text{OH}\cdot$) radical and of liquid kerosene. Additionally the spontaneous fluorescence of OH (OH chemiluminescence) was detected by the same camera system.

• Generation of laser light for PLIF diagnostics

a) 283nm: The laser system used for the PLIF measurements consists of a Nd:YAG pumped dye laser whose output was frequency doubled to provide appropriate UV radiation. The dye laser was operated on Rhodamine 6G and produced 60mJ pulses at 565nm. The pulses were frequency doubled to 283nm using an BBO crystal. The pulse energy was typically 10mJ. For the excitation of OH the 283nm light was tuned to specific rovibronic transitions of the (1,0) band of the $\text{A}^2\Sigma - \text{X}^2\Pi$ system of OH. The UV beam was formed into a sheet using a combination of three lenses. A 1m spherical lens focused the beam over the spray nozzle. These optics produced a laser sheet having dimensions of 44mm x 0.2mm at the spray nozzle.

b) 355nm: The fundamental wavelength of the Nd:YAG laser was frequency tripled by mixing light of the fundamental wavelength of 1064nm with the light of the second harmonic generation (SHG) in a non-linear mixing crystal. This UV beam was coupled into the same sheet forming optic as it was done with the 283nm light produced by the Nd:YAG pumped dye laser. Thus, at every Nd:YAG laser pulse, two overlapping light sheets with different wavelength are almost at the same time present over the nozzle. The intrinsic delay of the dye laser together with a 5m optical delayline in the dye laser beam provide a time lag around 18ns between both laser pulses. This delay was sufficient to separate the gate times of both cameras with the consequence that each camera detected its appropriate light sheet.

• Signal detection and filter selection

Laser induced fluorescence images as well as the spontaneous OH fluorescence images were obtained by collecting the fluorescence at 90 degree from the laser beam. The fluorescence was detected by two UV-grade photo lenses attached to intensified and cooled CCD-cameras having an image format of 384 x 286 pixels. One of this cameras was aligned directly to the single nozzle sector. The second camera was aligned perpendicular to the first one and observed the sector via a beam splitter with a high reflection coating for $305\pm 25\text{nm}$ light. Both cameras were aligned in such a way that they detect the same field-of-view over the nozzle. The intensifier of each camera was triggered synchronously with its appropriate laser pulse and was opened with a 20ns gate. This gate time was sufficiently short to eliminate any background soot luminosity or gas emission from the laser induced emission images.

For each individual detection application a separate set of spectral filters was selected. Two different combinations of filters were attached to the front of the telephoto lenses. A combination of 3mm GG385, 3mm BG3 and 3mm KG5 Schott glass filters transmitted light between 380nm to 430nm (transmission $\tau_i = 0.5$) and so effectively collected kerosene fluorescence while discriminating against the elastically scattered light in the short wave spectral region and against the soot luminosity in the long wave spectral region.

On the other hand a 307nm interference filter (25nm FWHM) and a 3mm WG305 Schott glass filter were installed for the effective collection of OH fluorescence. The WG305 glass filter serves as a shield against the elastically scattered laser light.

• Planar laser induced fluorescence of liquid kerosene

The volume concentration of liquid kerosene is an important factor for a better understanding of processes like air-fuel-mixing or fuel vaporisation. In contrast to the Mie scattering intensity which is dominated by the droplet surface, the laser induced fluorescence (LIF) intensity is proportional to the droplet volume. This was our motivation to use the laser induced fluorescence instead of the Mie-scattering from liquid kerosene to determinate volume concentrations. Up to now this measurement technique is quantified only for isothermal kerosene sprays comparing the LIF measurements with the results of PDA measurements. Previous investigations have shown that there was only a slight absorption of 355nm light by the kerosene so that this is an appropriate wavelength for PLIF measurements in dense kerosene sprays. The subsequent kerosene fluorescence is shifted to the red with a maximum at $410 \pm 20\text{nm}$.

- Planar laser induced fluorescence of OH radical

The laser induced fluorescence of OH located in a combustion is essentially an indicator for the hot exhaust gas. In the majority of cases the OH-signal distribution appears in the shape of clouds. The main interest should be focused to the border of this clouds. In some cases the border encloses one or more liquid fuel droplets. This is an evidence for the existence of a flame front between the liquid fuel and the OH clouds. Thus, a careful analysis of combined single pulse images from the distribution of OH and kerosene fluorescence yields the trace of the flame front within the laser sheet volume.

On the other hand, directed air jets e.g. from dilution air holes image themselves within the hot exhaust gas by a sharp bounded area without OH fluorescence signal. If the OH fluorescence intensity is very strong in a close range to the sharp border, this is an evidence for a reaction of fuel rich exhaust with the dilution air.

- OH* chemiluminescence

The radiation of the electronically excited OH* radical (310 nm) has been used as a marker for the flame reaction zone in space and time. The excited OH* radical is most likely due to the reaction $\text{CH} + \text{O}_2 \rightarrow \text{CO} + \text{OH}^*$, that directly forms OH* and, in contrast to ground state OH, is present only near the reaction zone [12]. In our experiment, the chemiluminescence is spectrally filtered using an interference filter centred at 310nm (FWHM: 10 nm) and detected by the intensified CCD camera. The exposure time of the CCD camera is 10 μ s for a single image and 0.5 ms for an averaged image. Due to the camera position perpendicular to the flame tube the detected OH* fluorescence is integrated over the entire width of the flame tube.

- Postprocessing of images

The LIF signals are normalised to the intensity distribution of the particular laser light sheets. The UV light of 284 nm which is used to excite the OH radical, is partly attenuated by broadband absorption of polycyclic aromatic hydrocarbon compounds (PAH's) within the kerosene droplets and the gas phase. Additionally the LIF signal of the PAH's spectrally interferes with the OH LIF. To eliminate the contribution to the OH LIF signal, the wavelength of the dye laser was detuned from the OH absorption line. This off-resonance LIF image is subtracted from the on-resonance image to determine the OH LIF contribution. The kerosene LIF distribution of optical thin sprays induced by 284 nm light looks similarly to that induced by 355 nm light. But due to the strong absorption of the 284 nm light within dense kerosene sprays, the additional use of a 355 nm light is necessary to monitor the kerosene spray.

4. RESULTS

The operating conditions for the measurements are given in Table 1. The pressure drop across the airblast atomizer was always 3%. The primary zone air to fuel ratio was set to 20 for all test cases.

Combustor pressure	3 bar	6 bar	6 bar	9 bar
Preheat temperature	473 K	473 K	673 K	473 K

Table 1: Operating conditions

- Isothermal flow

The velocity measurements of the isothermal non-reacting gasflow were made at ambient temperature and pressure. The pressure drop across the airblast nozzle was 3%.

For a general overview over the flowfield the streamtraces are shown in Figure 7. Axis symmetry is assumed in the nearfield of the nozzle and only one half of the flowfield is shown to increase the resolution of this and the following figures.

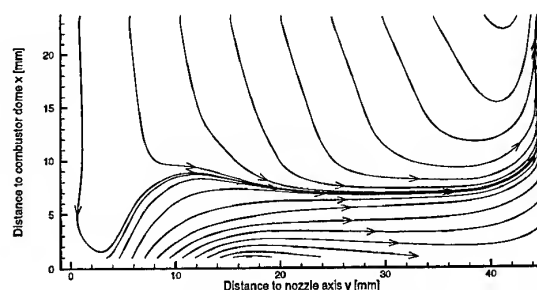


Figure 7: Streamtraces of isothermal non-reacting gas flowfield behind the airblast nozzle

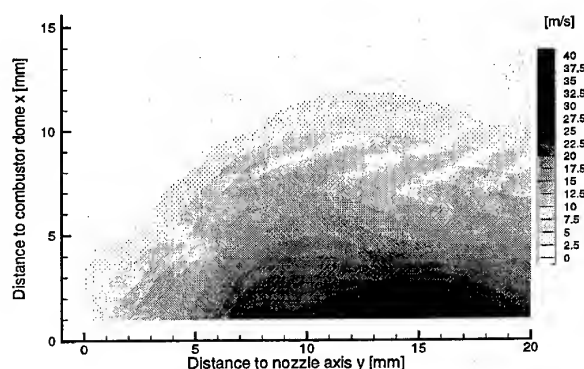


Figure 8: Tangential gas velocity for the atmospheric isothermal gasflow

The flowfield has a large expansion angle and most of the air flows radially outward between 3mm and 8mm behind the nozzle exit. No outer recirculation zone is observed. There is a large central recirculation zone beginning at about $x=10$ mm filling nearly the whole combustor cross section. Near the nozzle axis the recirculation zone reaches close up to the nozzle exit. The large recirculation zone is caused by the large swirl number S of the airblast nozzle. Despite the radial acceleration of the airflows inside the nozzle, see Figure 4, the swirl number increases from the trailing edges of the swirlers to the nozzle exit, when the turbulent stresses and the pressure term are neglected, because of the deceleration in the axial direction due to the increase in cross sectional area of the outer swirl channel. The swirl number can be estimated from the nozzle and swirler geometry according to [13] giving a swirl number of $S=1.23$ in the nozzle exit plane and $S=1.08$ in the swirler exit planes. According to [14], the injector swirl number calculated with the velocities only should be used to estimate the effect of the swirl strength on the recirculation in the combustor. Figure 8 complements the streamtraces of Figure 7 with a contour plot of the tangential velocity in the nozzle nearfield.

- Reacting flow

The next three images show some of the characteristics of the reacting flowfield. The images are integrated over 50 laser pulses to get a representative impression for the test case of 6bar and a preheat temperature of 473 K. The planar LIF imaging technique provides a correlated two-dimensional information of the kerosene and flame front distribution. The OH-LIF and kerosene-LIF images are light sheet images and the OH-fluorescence image is a volumetric mean image over the whole combustor.

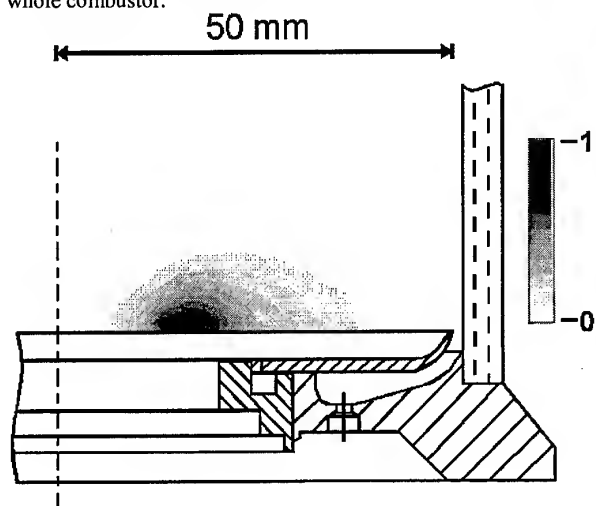


Figure 9: Kerosene-LIF at 6bar and 473K

The image of the kerosene-LIF in Figure 9 shows the qualitative distribution of the liquid fuel concentration in the combustion chamber. The spray has a large expansion angle which corresponds to the isothermal flow field in Figure 7. The fuel is almost completely evaporated at a radial position of about $r=30\text{mm}$. This is confirmed by the quantitative distribution of the liquid kerosene mass flux measured with PDA in Figure 10. The mass flux is the liquid mass flow per unit area into a specific direction. The mass flux in radial direction was chosen, as it is better capable in representing the evaporation of a fuel spray with such a large expansion angle. Currently efforts are made to achieve a coupling between qualitative PLIF and quantitative PDA at elevated pressures to gain detailed insight into the evaporation process at real engine condition.

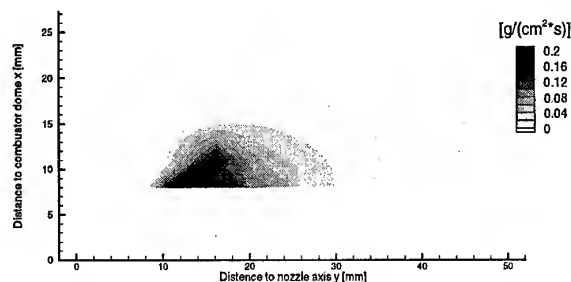


Figure 10: Mass flux distribution in radial direction at 6bar and 473K

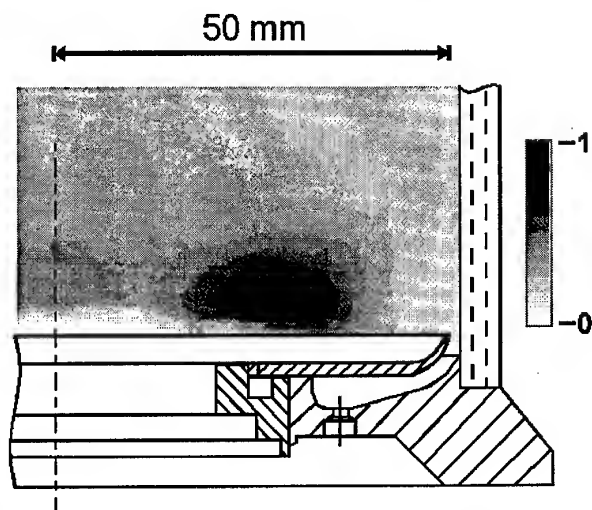


Figure 11: OH-chemiluminescence at 6bar and 473K

The OH-chemiluminescence in Figure 11 is an indicator for the area where the heat release takes place. Although the image represents the chemiluminescence along the line of sight, it is a good approximation of a sectional image if a toroidal form of the reaction volume is assumed. The peak of the chemiluminescence is located in the area where the evaporation of the kerosene is nearly completed, $r=28\text{mm}$ see Figure 9 and Figure 10. There is only a small overlap between the area with appreciable liquid fuel concentration and the combustion zone as shown in Figure 11. The images in Figure 9 and Figure 11 reveal the flame running predominantly in the external group combustion mode. However there is no such clear separation between the evaporating droplet cloud and the flame, as it is to be expected for a real case. For a correct interpretation of the overlap region, analysis of the turbulent fluctuations in the simultaneous kerosene- and OH-LIF pictures is necessary. The same behaviour was observed for the other test conditions.

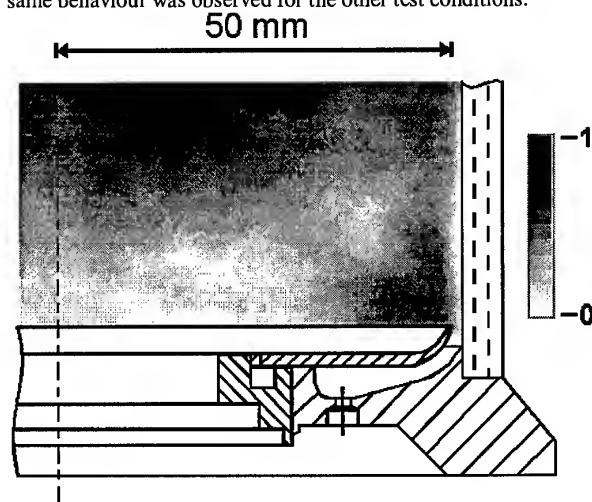


Figure 12: OH-fluorescence at 6bar and 473K

In Figure 12 the qualitative OH distribution is visualised. The complementary character of the kerosene distribution indicated by the kerosene LIF, the reaction zone (OH* chemiluminescence) and the hot exhaust gas (OH LIF) can be seen in Figure 9 through Figure 11. A low concentration of OH means a fuel rich mixture and/or low temperature. A high concentration indicates a fuel lean mixture with a high temperature. In the region of the evaporating spray, see Figure 9 and Figure 12, no

OH is present. Although the chemiluminescence shows most of the reaction taking place before higher amounts of OH as imaged by LIF persist, it cannot be decided if this reaction is taking place under rich conditions or below 1600K or both. Calculation of the mixture fraction on the base of the experimental results for evaporation could provide an answer to this question. The OH concentration rises considerably not before the end of the actual combustion zone, see Figure 11 and Figure 12. Here the temperature is high and the gas is mixing with the window cooling air providing enough oxygen for a lean mixture. Further downstream the oxidation is completed and the combustion products are mixed with a part of the secondary air leading to high OH concentrations.

- Pressure effects on the spray

These effects are felt on the droplet and the gas phase. The kerosene is driven faster radially outward with increasing pressure. A comparison of the kerosene LIF images for 3, 6 and 9bar and 473K and PDA mass flux measurements for 3 and 6bar shows as a consequence a decrease of the axial penetration of the spray from 20mm to 15mm and 13mm at 3, 6 and 9bar respectively. The effect can be discussed largely in terms of the pressure influence on the mean Stokes number. The Stokes number St is a measure for the capability of a particle to follow the gas flow [15].

$$St = \frac{T_{rel}}{T_{flow}} \quad (1)$$

T_{rel} is the particle relaxation time and T_{flow} a relevant time scale of the gas flow. A particle with a Stokes number $St \ll 1$ follows the gas flow without appreciable slip. At $x=10\text{mm}$, $y=20\text{mm}$, a point with high streamline curvature and not too high spray concentration, c.f. Figure 15 and Figure 9, local Stokes numbers have been calculated for $50\mu\text{m}$ droplets at 9 and 3bar. Approximately 90% of the spray volume resides in droplets smaller than $50\mu\text{m}$ for that preheat temperature. The relaxation time was calculated with the relative velocity between $50\mu\text{m}$ and $<5\mu\text{m}$ droplets and the preheat temperature for a first approximation of the gas density, the fluid mechanical time from $\Delta L/\Delta U$, ΔU being the gas velocity difference to the neighbouring measurement points. The mean Stokes number decreases from 3.5 at 3bar to 1.5 at 9bar. These values show, that the spray indeed changes its behaviour from rather inert to almost following the gas flow in the considered pressure range. The modification of the flowfield of the particles with $48\mu\text{m} < d < 52\mu\text{m}$ is shown in Figure 13 and Figure 14. For the 3bar condition in Figure 13 these particles move parallel to the axis of symmetry in the central region of the spray cone. Under 9bar pressure they move nearly radially towards the axis in an area of appreciable size, shown in Figure 14.

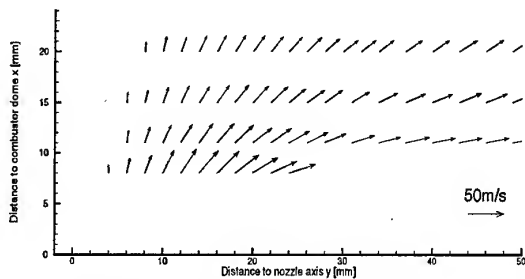


Figure 13: Velocity field of droplets with $48\mu\text{m} < d < 52\mu\text{m}$ at 3bar and 473K

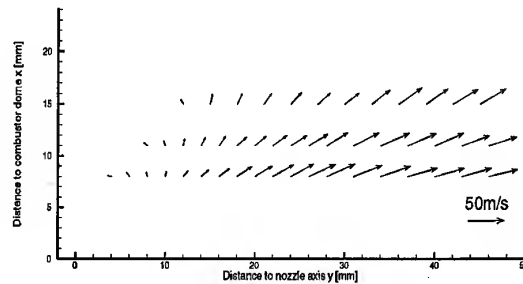


Figure 14: Velocity field of droplets with $48\mu\text{m} < d < 52\mu\text{m}$ at 9bar and 473K

- Pressure effects on the gas flow

The flowfield of the gasphase for the 3bar and 9bar test cases is shown in Figure 15 and Figure 16. The particles with a diameter smaller than $5\mu\text{m}$ were assumed to follow the gasphase without any slip.

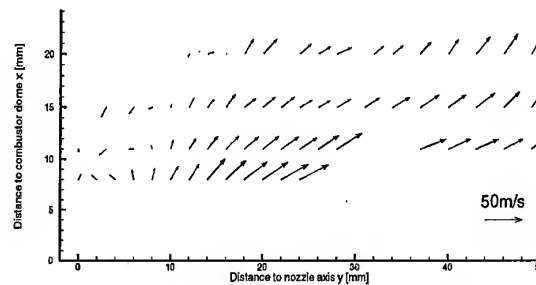


Figure 15: Velocity field of the gas phase at 3bar and 473K

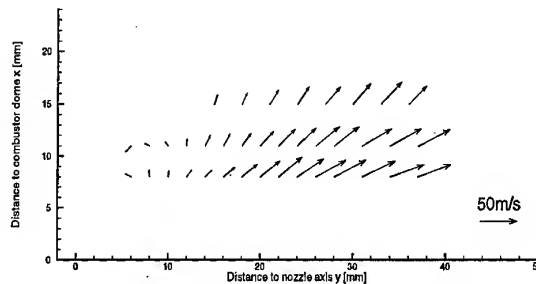


Figure 16: Velocity field of the gas phase at 9bar and 473K

The drop-outs especially in Figure 15 are caused by poor statistics. The smallest droplets evaporate very fast, causing an appreciable change in phase-shift during the residence time of the particle in the PDA measuring volume. This change reduces the signal to noise ratio for the phase determination and hence leads to more reject small particles than under non-combusting conditions [18]. Nevertheless it was possible to measure the velocity field of the gas phase in the combusting spray under realistic operating conditions. Again it can be seen, that the air pressure has a strong influence on the flow field near the nozzle. The radial location of the velocity maximum is shifted outwards and the opening angle of the diverging flow-field expands. The size of the central recirculation zone has increased considerably. On the nozzle axis no measurements could be made under 9bar as virtually no fuel droplets were present.

The increase in flow angle and recirculation zone size with the spray density is in contrast to the observations reported in [11] and [16] on confined injector flows with large recirculation and predominantly axial spray movement. They found, that the level of the tangential velocity and hence the swirl and the intensity of the recirculation decreased with the particle loading. This effect was attributed to the influence of the fuel film on the interaction of the two swirling airstreams for the particular design of the fuel nozzle. Here the opposite effect is observed. Two reasons can be forwarded for explanation: The droplets turn slower from the axial to the radial flow direction than the gas in the single gas flow, c.f. Figure 7, because of their inertia. For the dense spray and behind it, the gas phase will also feel that influence. The faster expansion of the spray at higher pressure is then also seen in the gas flow field.

The second reason is the radial movement of the combustion zone with pressure. The kerosene LIF images reveal that the evaporation lengths or droplet lifetimes are approximately the same for the three test conditions. The reason for that is discussed in the section on the spray droplets. The images of the OH-chemiluminescence indicate that the main part of the reaction always takes place in the same position relative to the end of the liquid spray, see Figure 9 and Figure 11. In consequence, the radial location of the main heat release is shifted downwards and outwards with increasing pressure. It is $14\text{mm} < y < 33\text{mm}$ and $17\text{mm} < y < 38\text{mm}$ for 3bar and 9bar respectively. The high temperature zone as indicated by the OH-LIF, c.f. Figure 12, consequently moves in the same direction. With the ensuing decrease of density the flow is radially decelerated, c.f. [17]. Hence the turn in the axial direction, marking the outer boundary of the recirculation, comes later for the higher pressure condition.

For a closer look into this change, the gas velocity in the measuring plane $x=8\text{mm}$ for the same test cases and for the isothermal case is shown. Figure 17 and Figure 18 contain the axial and tangential gas velocity respectively. For ease of comparison the velocities for the isothermal condition are scaled to the same air preheat temperature as the pressure conditions. Again the velocities of particles with $d < 5\mu\text{m}$ were assumed to represent the velocity of the gas phase.

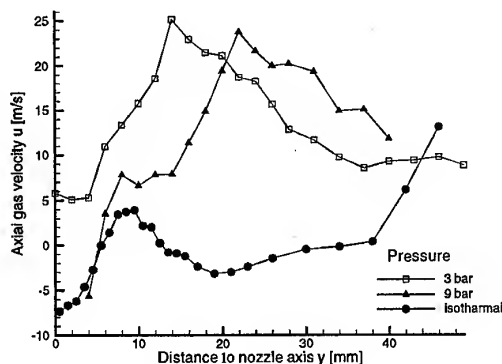


Figure 17: Axial gas velocity at $x=8\text{mm}$ under 3bar and 9bar and isothermal

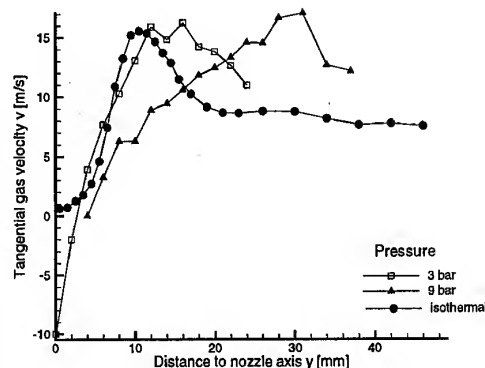


Figure 18: Tangential gas velocity at $x=8\text{mm}$ under 3bar and 9bar and isothermal

The magnitude of the velocity maxima under pressure condition did not change. For the tangential velocity the magnitude remained unchanged by combustion. However the magnitude of the axial velocity is higher with combustion at $x=8\text{mm}$. Weber and Duguè investigated in [14] the influence of the location of the heat release on the size and strength of the recirculation zone and interpreted the effects with the help of the *effective swirl number* as a modification of the swirl number in [13].

$$S_{\text{eff}} = S \frac{T_0}{T_m} \quad (2)$$

Here T_0 is the air preheat temperature and T_m is the mass mean temperature at the position of maximum reverse flow. As combustion takes place, the density decrease forces an axial acceleration which reduces the swirl number formed without the pressure term in the way described in eq. 2. This selective increase of the axial velocity following combustion can be seen in Figure 17. For a final explanation of the effects of heat release on the swirling flow it is necessary to make LDA measurements in the combustor flow to get more information of the recirculation zone and to make temperature measurements.

For the present injector, the changes seen in the gas flow might also be driven to some extent by an increase in swirl following a repartition of the flows from the different swirlers in the injector with the higher fuel loading accompanying higher gas pressures. The effective area of the outer swirler is more than 40% of the total effective area. The airstream through the third swirler undergoes a rapid expansion behind the trailing edge of the vanes, see Figure 4. This leads to a very strong swirl of the outer air flow, as described in the section on the isothermal flow.

The kerosene flows through a circular gap and is placed on the inner side of the prefilming lip, see Figure 4. The centre air stream is directed in an obtuse angle onto the fuel film and may be obstructed by the film. The outer air flow is not influenced by the fuel film at this stage. So the effective area of the nozzle is may be reduced slightly and the relative contribution of the swirlers is shifted in favour for the outer swirler leading to a small increase in swirl for the whole flowfield with increasing pressure. The influence of the fuel mass flow on the effective area of the nozzle was observed at similar nozzles supplied by BMW-RR built under the same design philosophy. The measurements were made at a different test facility especially build for the investigation of fuel injectors [19]. The change in effective area was small, only a few percent, but evident and

reproducible. The effect was much stronger for a two swirler configuration than for a three swirler configuration, indicating a modification of the relative contribution of the three air-streams. Unfortunately this effect could not be observed here as the measurement uncertainty for the pressure drop was larger than the expected reduction of the effective area. By now the pressure sensor equipment was changed to get more accurate measurements in future investigations.

The reduction of turbulence by the increasing particle number concentration in a dense spray is an effect reported by several authors [11], [16], [20] and [21]. The effect was ascribed to the dampening by the large particle concentration of small particles. This phenomenon is confirmed by the plots of the turbulent energy k of the gas phase for the 3bar and 9bar condition in Figure 19 and Figure 20 respectively. Again the velocities of particles with $d < 5\mu\text{m}$ were assumed to represent the velocity of the gas phase.

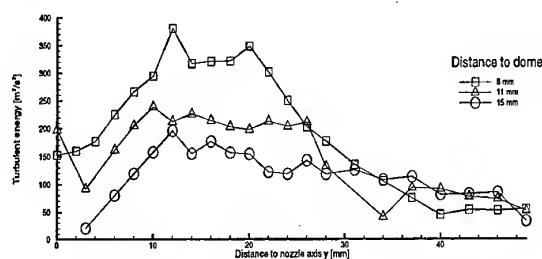


Figure 19: Turbulent energy of the gas phase at 3bar and 473K

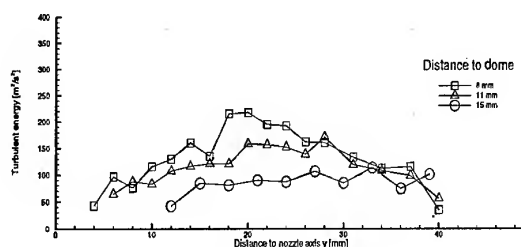


Figure 20: Turbulent energy of the gas phase at 9bar and 473K

The reduction in turbulent energy is evident. Especially between $x=8$ and $x=11$ mm the turbulent energy under 3bar is up to 50% higher than at 9bar. The 6bar 473K condition not shown fits right between the 3 and 9bar pictures. The rms values of the three main velocities all display the same tendency, but the axial rms velocity has the largest contribution. In [11] a scaling was introduced to estimate the particle number concentration in dependence of the operating conditions. The attempt was made to simulate the dense spray at engine idle condition at atmospheric pressure and ambient temperature by increasing the pressure drop across the airblast atomizer and by reducing the air to fuel ratio in order to identify changes in the gas phase caused by the dense liquid phase. The estimated particle number concentration for the pressure simulation in [11] lies between the 3bar and 6bar condition used here. A maximum decrease for k of 50% was observed for the simulation, which is the same order of magnitude as in Figure 19 and Figure 20.

Another result, that becomes evident with those figures is the apparent ability of the $5\mu\text{m}$ drops to follow the fluctuations of the gas phase. The frequency resulting from the relaxation time

of the $5\mu\text{m}$ drops calculated for creeping flow of 3bar and 473K gives about 20kHz, hence fluctuations up to a few kHz should be tracked well.

• Influence of operating conditions on drop size

Table 2 shows the global Sauter mean diameter (SMD) for several operating conditions in the measuring planes at different axial positions close to the nozzle exit. The global SMD is the mean value of the mass flux weighted local SMD of each radial position in a plane.

	3bar 473K	6bar 473K	6bar 673K	9bar 473K
8mm	28.5 μm	28.8 μm	20.9 μm	31.2 μm
11mm	29.4 μm	29.9 μm	20.9 μm	30.0 μm
15mm	33.1 μm	29.4 μm	21.9 μm	30.1 μm
20mm	36.8 μm	32.3 μm		
25mm	39.3 μm			

Table 2: Global SMD for all test conditions

Looking at the operating conditions with the same air preheat temperature does not reveal a significant influence of the air pressure on the mean diameter. This result is confirmed by an analysis of the images of kerosene LIF for 3, 6 and 9bar in Figure 21, Figure 9 and Figure 22 respectively. All three show about the same evaporation length of the spray along the flow-path. According to [5] the evaporation length or droplet lifetime depends predominantly on the initial droplet diameter for the same AFR and gas mixing as it is the case here. Taking into account that all three conditions have the same air preheat temperature and hence the same air velocity, the LIF images are a confirmation of the results in Table 2. They show qualitatively that the air pressure has no significant influence on the atomization.

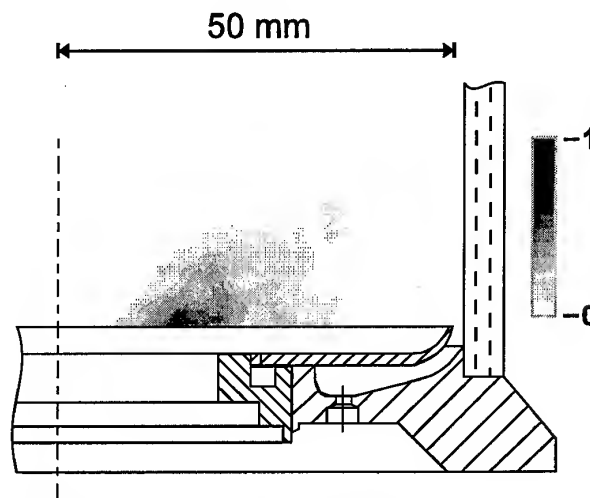


Figure 21: Kerosene LIF at 3bar and 473K

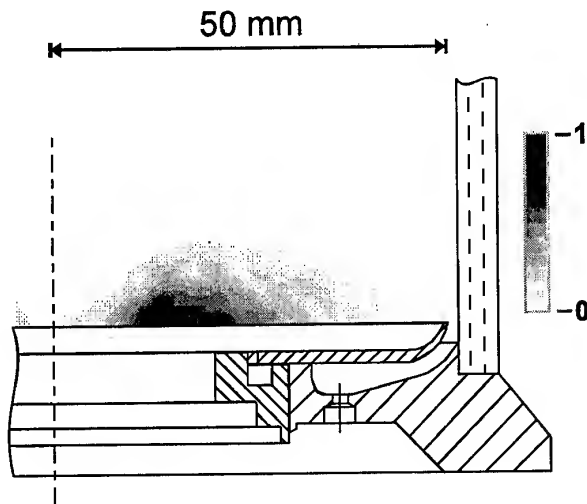


Figure 22: Kerosene LIF at 9bar and 473K

In [22] several correlations for the performance of prefilming airblast atomizers are given. They predict the influence of the air density for liquids with low viscosity with an exponent in the range of -0.5 to -1.0 , e.g. see eq. 3 and hence contradict the trend shown in Table 2. These correlations are applicable, if the liquid is atomized by a mechanism described as *wavy-sheet disintegration* [22]. A wave motion is generated by the relative velocity between air and liquid in the sheet. As the oscillation is amplified, parts of the fluid are torn away and further disintegrated by the action of the surface tension. Wavy-sheet disintegration is likely to occur if the flow direction of air and liquid is almost parallel.

$$SMD \propto \left(\frac{\sigma}{\rho_A U_A^2 D_P} \right)^{0.5} \left(1 + \frac{1}{AFR} \right) \quad (\text{eq. 3})$$

Here σ is the surface tension, ρ_A is the air density, U_A is the air velocity and D_P is a characteristic length of the atomizer. In Table 2 the diameters only change with preheat temperature. The design of the airblast atomizer used for this investigation, see Figure 4, does not allow a parallel flow of fuel and air. The air of the centre swirler has a large normal velocity component relative to the fuel film. Hence the wavy-sheet disintegration probably does not apply here. In [23] a different process called *prompt atomization* is proposed. This process is assumed to occur if the air flow impacts the film at an appreciable angle. The film oscillation cannot build up and the film is shattered almost immediately by the high impact of the air. The dependency of the air and liquid properties on the SMD derived in [23] is given in eq. 4.

$$SMD = \frac{3}{\frac{1}{t} + \frac{C \rho_L U_A^2}{4\sigma(1+1/AFR)}} \quad (\text{eq. 4})$$

Here ρ_L is the liquid density and t is the thickness of the liquid film. Depending on the geometry of the atomizer almost all of the air takes part in the atomization. Based on these assumptions an energy balance between the kinetic energy of the air flow and the energy necessary to increase the surface area of the liquid from a thin film to small droplets. The air mass and hence the pressure enters the balance in the atomizer AFR only. This energy balance leads to eq. 4. Hence we believe that eq. 4 is the right correlation for this injector.

A comparison of the SMD for 673K and 473K under 6bar in Table 2 shows a very good agreement with the influence of the air properties according to eq. 4. The higher air preheat temperature raises the air velocity and leads to a smaller SMD. The ratio of the SMD for 473K and 673K is very close to the reciprocal ratio of both temperatures. Furthermore the temperature rise probably increases the initial fuel temperature at the prefilming lip. The surface tension σ of kerosene is reduced with increasing liquid temperature, see [24]. As the initial fuel temperature is unknown in this investigation, the change in surface tension is not taken into consideration, however if it can be supposed, that the difference of the air preheat is only felt by the fuel when in direct contact with the air and not by a temperature difference of the injector itself, the heat-up is bound to be small, because with reference to Figure 4, the prefilming length is short. The film thickness t is estimated from [25] to about $55\mu\text{m}$ and $60\mu\text{m}$ for 3bar and 9bar respectively. Calculating the SMD according to eq. 4 with $C=0.007$ [23] and these values for t leads to a $SMD=7\mu\text{m}$. C representing the efficiency of the atomization process is strongly influenced by the geometry of the atomizer. Fitting C to the measured SMD gives a value of about $C=1.31 \cdot 10^{-3}$. An increase in film thickness from $55\mu\text{m}$ to $60\mu\text{m}$ rises the SMD according to this equation from $28\mu\text{m}$ to $29\mu\text{m}$. So the influence of the film thickness can be neglected. The slight increase of the SMD with the air pressure in Table 2 and hence the fuel mass flow can also be attributed to the reduced accuracy of the determination of the kerosene mass flux distribution in a dense spray, see [11]. In a very dense spray as in the 9bar condition small droplets are more likely to remain undetected by the PDA due to the scattering and extinction along the beam path of the laser light "in front of" the measuring volume. So the SMD for $x=8\text{mm}$ and $x=1\text{mm}$ under 9bar are the most uncertain values in Table 2.

The results in Table 2 reveal an often observed feature of combusting or evaporating sprays: The SMD increases with the axial distance to the nozzle exit. This is caused by the fast evaporation and hence vanishing of the smallest particles, which can not be made up for by the slower evaporation of the larger particles. The effect has been observed in [17] and [26] as well. But it does not occur necessarily as described in [27] for a prevaporizer duct.

Unfortunately the discussion above lacks the information of the initial drop size distribution just behind the prefilming lip. Beside the difficult optical access the spray density there is much too high for PDA measurements. It can be assumed, that the initial SMDs are lower, as the small drops are not yet evaporated. Since the fraction of those drops on the overall liquid volume is small, a reversal of the discussed trends in SMD is not probable. As the SMD development for 3bar and 6bar shows the same trend an extrapolation of the SMD to the prefilming lip appears admissible.

5. CONCLUSIONS AND FUTURE WORK

The application of planar and point measuring techniques on the optically accessible single sector combustor has been successful in the acquisition of experimental data on a practical injector nozzle. As the utilized injector demands minimum fuel mass flows defined by the operating envelope of the engine application, a meaningful investigation also requires higher than atmospheric air pressures. The resulting spray excludes the use of the PDA in the dense spray region, where for the investigated injector a significant portion of the spray dynamics occur. Hence both, planar qualitative and quantitative point measuring techniques are needed. Coupling the techniques to allow some quantification of the qualitative results is one of the

future tasks. Also, the role of the fluctuations in evaporation and heat release can be further investigated by the correlation of single shot OH and kerosene fluorescence. The most demanding diagnostic is however the measurement of temperature in the flow. Having done that, the experimental program can progress to the investigation of lean blow out.

For the chosen operating conditions, the spray is evaporated quickly, such that external group combustion results. Although the spray moves almost radially outward, the strong recirculation evaporates the spray well before reaching the wall, such that the observed flow pattern effectively minimizes the combustor length needed for evaporation.

The observed pressure effects on the spray underline the importance of understanding the atomizer internal flow. If the prompt atomization persists also for higher pressures, the spray flame won't exhibit a tendency to approximate the behavior of a gaseous diffusion flame as it eventually would if the droplet size continuously diminishes with pressure. That would give some motivation to look into the spray combustion even at full load conditions.

ACKNOWLEDGEMENT

The project underlying to this report was supported with means of the German Federal Minister for Research and Technology (BMBF) under supporting sign LFT9607A. The supply of the injector by BMW-RR and the useful discussions with Dr. Doerr and Dr. Bauer are gratefully acknowledged.

REFERENCES

- [1] Lefebvre, A. H., "The Role of Fuel Preparation in Low-Emission Combustion", ASME J. Eng. Gas Turbines and Power, V 117, pp. 617-654, 1995
- [2] Sturgess, G. J. et al., Flame Stability and Lean Blow-out, A Research Program Progress Report, ISABE 91-7037, pp 372-384, 1991
- [3] Chiu, H. H., Kim, H. Y., Croke, E. J., "Internal Group Combustion of Liquid Droplets", 19th Symposium (International) on Combustion / The Combustion Institute, 1982, pp. 971-980
- [4] Chigier, N., "Group Combustion Models and Laser Diagnostic Methods in Sprays: A Review", Comb. & Flame, V51, pp. 127-139, 1983
- [5] Bolado, R., Yule, A., "The Relationship between Atomization Characteristics and Spray Flame Structure", Paper 9-1, pp. 221-227, ICLASS-82
- [6] Jasuja, A. K., Lefebvre, A. H., "Influence of Ambient Pressure on Drop-Size and Velocity Distributions in Dense Sprays", 25th Int. Comb. Symp., pp. 345-352, 1994
- [7] Farrugia, N., Lockett, R. D., Harding, S., C., Greenhalgh, D. A., "LIF Imaging of Fuel Distribution In Gas Turbine Combustors", Annual European ILASS Conference, pp. 299-305, 1997
- [8] BSA enhanced user's guide, DANTEC/invent measurement technology, 1994
- [9] DUAL PDA manual, DANTEC/invent measurement technology, 1996
- [10] Damaschke, N., Gouesbet, G., Gréhan, G., Mignon, H., Tropea, C., "Response of PDA Systems to Non-spherical Droplets", ILASS 1997, pp. 382-388
- [11] Behrendt, T., Hassa, C., "Investigation of the spray dynamics of aeroengine fuel injectors under atmospheric and simulated pressure conditions", 1997, AGARD CP-598, Paper 5
- [12] Crosley, D. R., Dyer, M. J., "Two-Dimensional Imaging of Laser-Induced Fluorescence in OH in a Flame", Proceedings of the International Conference on Lasers, 1982
- [13] Gupta, A. K., Lilley, D. G., Syred, N., "Swirl Flows", Abacus Press, 1984, ISBN 0-85626-175-0
- [14] Weber, R., Dugué, J., "Combustion Accelerated Swirling Flows in High Confinements", Prog. Energy Combustion Science, Vol. 18, 1992, pp. 349 - 367
- [15] Crowe, C. T., Gore, R. A., Troutt, T. R., "Particle mixing in free shear flows", Prog. Energy Combustion Science, Vol. 14, 1988
- [16] Brandt, M., Hassa, C., Eickhoff, H., "An Experimental Study of Spray - Gasphase Interaction for a Co-Swirling Airblast Atomizer", ILASS-Europe, October 1992, pp. 115-122
- [17] Hassa, C., Deick, A., Eickhoff, H., "Investigation of the Flow in a Research Combustor under Reacting and Non-Reacting Conditions", AGARD CP 536, Paper 41, 1993
- [18] Ikeda, Y., Hirohata, T., Nakajima, T., "Measurement Uncertainties of the Phase Doppler Technique due to Effects of Slit Location, Control Volume Size and Flame Front Presence", 8th Int. Symp. On Appl. of Laser Techniques to Fluid Mechanics, 1996, Lisbon, Paper 2.6
- [19] Behrendt, T., Hassa, C., "Ein Prüfstand zur Untersuchung von Zerstäuberdüsen für Gasturbinen", Spray 96, Bremen, Germany, 1996
- [20] Wang, H. Y., Sowa, W., McDonell, V. G., Samuelsen, G. S., "Spray Gas-Phase Interaction Downstream of a Co-Axial Counter-Swirling Dome Swirl Cup", ICLASS-91, Paper 76
- [21] McVey, J. B., Kennedy, J. B., Russell, S., "Application of Advanced Diagnostics to Airblast Injector Flows", ASME 88-GT-12
- [22] Lefebvre, A. H., "Atomization and Sprays", New York, Hemisphere Publishing Corp., 1989
- [23] Lefebvre, A. H., "Energy Considerations in Twin-Fluid Atomization", ASME 90-GT-3
- [24] Rachner, M., "Die Stoffeigenschaften von Kerosin Jet A-1", DLR Mitteilung 98-01, ISSN 1434-8462, 1998
- [25] Rizk, N. K., Lefebvre, A. H., "The Influence of Liquid Film Thickness on Airblast Atomization", Transactions of ASME, Journal of Engineering for Power, Vol. 102, July 1980, pp. 706 - 710
- [26] Hassa, C., Carl, M., Frodermann, M., Behrendt, T., Heinze, J., Röhle, I., Brehm, N., Schilling, T., Doerr, T., "Experimental Investigation of an Axially Staged Combustor Sector with Optical Diagnostics at Realistic Operating Conditions", AGARD AVT-Symposium October 1998, Paper 18
- [27] Brandt, M., Gugel, K. O., Hassa, C., "Experimental Investigation of the Liquid Fuel Evaporation in a Premix Duct for Lean Premixed and Prevaporized Combustion", Jour. Eng. Gas Turbines and Power, Vol. 119, 1997, pp. 815-821

PAPER No. 43
Behrendt, Froderman, Heinze, Hassa, Rohle & Stursberg
(presenter: T. Behrendt)

Question 1: J. Salva Monfort, Termofluidodinamica ETSIA, Spain

Why was secondary air recirculation avoided?

Answer:

For reasons of lean blowout; we wanted to look only at the fuel injector effects. Our next experiments will include jet air.

Question 2: M. Razdan, R.R.- Allison, U.S.

The equation used for spray SMD includes an air velocity term. However, your tests were run for fixed 3 % pressure drop at constant temperature, but with varying pressure levels; therefore, there was no effect of velocity on SMD.

Answer:

Yes, in general there is an effect of air velocity on spray atomization with this type of fuel injector, but our tests were run at a constant $\Delta P/P$, so this parameter was not explored here.

COMBUSTION CHARACTERISTICS OF A TRAPPED VORTEX COMBUSTOR

G.J. Sturgess
K-Y Hsu

*Innovative Scientific Solutions, Inc.,
2786, Indian Ripple Road,
Beavercreek, Ohio 45440-3638, U.S.A.*

Abstract

The lean blowout stability of a laboratory-scale version of a trapped-vortex combustor is described. Three cavity axial lengths were tested at atmospheric pressure and ambient temperature over a range of mainstream velocities from 15 to 95 m/s. For each geometry and mainstream velocity, three values of cavity jet airflow were used; 5, 10 and 15 percent of the mainstream mass flow rate respectively. Pressure transducer and microphone measurements were used to assess noise levels and acoustic coupling of heat release with cavity dynamics. Planar laser-induced fluorescence of OH was used to obtain qualitative understanding of the flame structures. It was found that at very low cavity air-jet momentum, the flow in the cavity is poorly organized and is highly subject to mainstream influences. A range of operating conditions exists where the flame at blowout is contained within the cavity, and blowout stability is high. At higher cavity mass loadings burning in the cavity is not contained and is supplemented by burning in the interfacial shear layer between mainstream and cavity flows. Blowout then is from this shear layer, and depends on the ratio of mainstream to cavity momentum and the cavity axial length, as well as cavity loading. Comparison of lean blowouts with those for a swirl-stabilized combustor indicates that a well-designed trapped vortex combustor can have superior operability characteristics.

Introduction

In an introductory paper¹ a laboratory-scale combustor of unique form was described. The combustor uses a vortex mechanically trapped in a cavity (TV) for flame stabilization. The arrangement was such as to expose an axisymmetric annular cavity formed in a centerbody, to a by-passing co-axial mainflow of air that was confined by an enclosing circular cross-section duct. Primary air was injected into the cavity to strengthen the naturally occurring vortex.

In addition, a gaseous propane fuel supply was directly injected into the cavity, in close association with the primary air. A quantity of mainstream air is entrained into the cavity by the action of the cavity vortex and by the additional pumping action of the primary air and the fuel jets. This was determined indirectly by empirical means². Combustion took place within the cavity, to a degree determined by the cavity mass loading and equivalence ratio. The combustion efficiency achieved and the gaseous emissions generated both depended strongly on these quantities.

Subsequent computational fluid dynamic (CFD) studies were made of the stationary-state and time-dependent flow behavior^{3,4}. These studies revealed the important general flow structures, and provided insights into the complex dynamic behavior of the cavity and its interactions with the mainstream.

Background

Performance trends for future advanced aircraft gas turbine engines such as are being developed for the commercial market place, and especially for the IHPTET (*Integrated High Performance Turbine Engine Technology*) technology demonstrator program of the United States Air Force⁵, will demand the design and use of lightweight combustion systems that are also compact and which have high combustion intensities of the order³ of $(10-16) \times 10^6 \text{ BTU/hr.ft}^3 \text{ atm.}$ [$(10-16) \times 10^4 \text{ kW/m}^3 \text{ bar}$]. Furthermore, engines for military application will be expected to have much-expanded operating envelopes. Therefore, combustion stability, always important, will become a key design concern.

The trapped vortex combustor concept, with its great potential for enhanced stability, appears to be a natural choice for providing the stabilization capability of such future combustion systems. A TV combustor module arranged in parallel with a main combustion

module could form the pilot for a fuel-staged combustor, the main stage of which could be operated lean and with short residence time in order to minimize the formation of thermal nitric oxide, an atmospheric pollutant.

Present Contribution

Additional lean blowout (LBO) studies have been made using the original, axisymmetric centerbody combustor, over an extended range of mainstream velocities and for three cavity axial lengths. The blowout data have been analyzed to determine stable operating conditions for a vortex to be trapped within the cavity. Planar imaging of the hydroxyl radical at near-blowout conditions, together with combustor noise measurements, have been used to assist with interpreting the analyses. By comparison with LBO data for a swirl-stabilized combustor, it is demonstrated that the TV combustor does have superior flame stability.

Combustor Arrangement

The original laboratory-scale TV combustor was described in Reference 1. The combustor consists of two major portions: a centerbody assembly and, a housing assembly.

The centerbody assembly is formed from a long central shaft of stainless steel that is made up of an inner fuel tube surrounded by a concentric air passage with outer diameter d_o , of 12.7mm, and which passes with a sliding fit through a solid disk of 70mm diameter, d_f , that forms a forebody. On the downstream end of the shaft is permanently mounted a short, hollow drum of 50.8 mm diameter, d_a , that forms an afterbody.

The drum contains two inner compartments that form respectively, primary air and fuel manifolds. These manifolds are supplied through the supporting double-tube shaft. The adjustable spacing H , between the forebody, the afterbody and the shaft forms an annular cavity within which a vortex may be trapped.

Fuel is discharged upstream into the vortex cavity from the upstream face of the drum via a ring of 8 circular jets each of 1.75mm diameter; tubes from the fuel manifold pass through the air manifold to feed these into the vortex cavity from the upstream face of the

drum via two concentric rings of circular jets each of 2.286mm diameter. There are 8 air jets in the inner ring and 16 air jets in the outer. The ring of fuel jets is concentric with and between, the rings of air jets. The fuel jets are circumferentially oriented to place a fuel jet midway between adjacent pairs of inner and outer air jets.

The forebody is supported concentric in a duct of 80 mm internal diameter, d_c , that supplies main air to the combustor from an air conditioning unit similar to that described in Reference 6. The combustor main body is a length of 80mm internal diameter Pyrex tubing. The length of the combustor in the original experiment was 910mm; for an earlier set of LBO experiments reported here as a repeatability check, a replacement (due to breakage) length was 780mm. For the LBO data of the present experiments the combustor body was a metal cylinder of 80 mm internal diameter and length of 305 mm. The change in material was due to continuing breakages; no effect of main combustor length or material on cavity blowout was discernible. For the optical measurements the Pyrex tube was used.

The complete centerbody assembly is cooled by the flows of air and fuel internally through it. The combustor main wall is protected initially from direct exposure to flame temperatures by the cool annular jet of main air that is in contact with it. No downstream external cooling of the main wall was provided. The forebody has no direct cooling, other than that provided by the annular flow of main air passing its outer edge.

The combustor and its conditioning unit for main air were mounted vertically in a test cell at the Air Force Research Laboratory, Wright-Patterson Air Force Base. The main air and cavity air originated from two air supplies, and were metered and controlled separately. The gaseous propane fuel was supplied from bottles. Exhaust from the combustor was collected and removed through a conventional exhaust hood.

A horizontal schematic view of the combustor is given in Figure 1. The sketch shows fuel and air paths, and suggests the modes of burning; the combustor tunnel is not present.

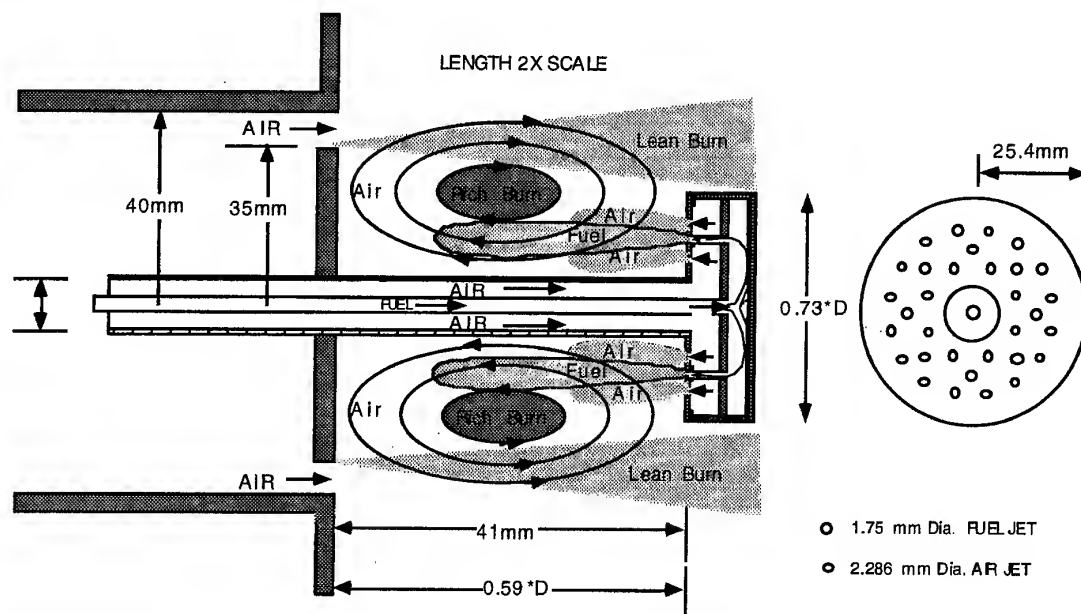


Figure 1: Schematic of Combustor Centerbody Assembly, Showing Operation

Test Conditions

The cavity axial length, H , was successively changed from 25.4 mm, to 38.1 mm, and finally, to 44.5 mm, giving variation in the cavity length to depth ratio H/d_f of 0.36, 0.54 and 0.635. The forebody diameter d_f is 70 mm. This form of geometric variation is extremely convenient. It would also have been useful to preserve the cavity aspect ratio as H was changed. However, this would have necessitated new centerbody assemblies, and would have been rather costly.

Lean blowouts were performed at atmospheric pressure and ambient temperature. Each cavity geometry was tested over a range of mainstream velocities from 15 m/s to 95 m/s. Over the range of mainstream velocities, the cavity jet air mass flow rate was set at 5 percent, 10 percent and 15 percent of the mainstream air mass flow rate.

LBO Tests

LBO's were performed by establishing burning at the desired airflows. Fuel flow was progressively reduced in a series of steps with pauses between steps to allow for thermal equilibrium to be established in the rig components. Airflows were checked and adjusted as necessary. As the blowout condition was approached,

the fuel decrements of the steps was progressively reduced to avoid overshooting the true blowout value.

OH Imaging

Planar laser-induced fluorescence (PLIF) was used to obtain a feel for the flame behavior at near-blowout conditions. A pulsed Nd:YAG - pumped dye laser was used to excite OH radicals in the cavity region. Although OH is long-lived and is therefore subject to convection effects, it does provide a simple qualitative way to capture impressions of the instantaneous flame structures.

Acoustic Measurements

The acoustic signature of the combustor was assessed by a dynamic pressure transducer that was mounted in the air duct feeding the mainstream past the combustor forebody. In addition, a microphone was mounted outside of the combustor, close to the exit from the main body duct.

Entrainment Estimates

The total mass flow rate in the cavity on a stationary state basis is the sum of the injected fuel, cavity jet air, and air entrained from the mainstream.

Entrainment measurements were not made in the present testing; information contained in Reference 2 was used for this purpose. Direct measurements of entrainment are exceedingly difficult. Therefore, the technique used was to infer entrainment from three other measurements made for cavity-contained flames. Figure 2 presents an example of correlated inferred entrainment data, taken from the reference; note both positive and negative values.

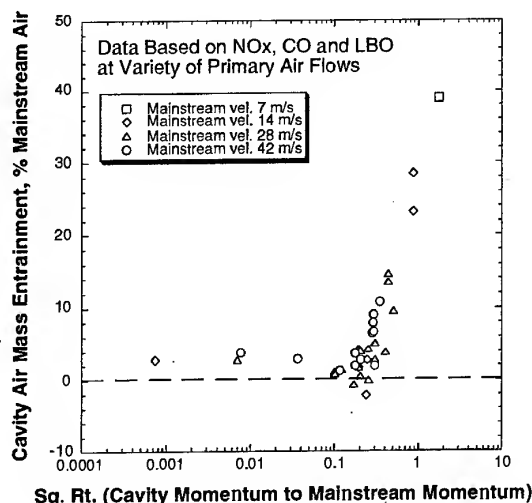


Figure 2: Example of Estimated Entrainment for the 0.54 H/d_f Cavity

Basic Blowout Data

An example of the basic blowout data is presented in Figure 3, in terms of the LBO fuel mass flow rate versus main air flow rate for the 38.1 mm cavity length, as a function of cavity air jet flow, which is expressed as a percent of mainstream mass flow rate.

The blowout fuel flow rate increases as main air flow is increased for each cavity jet air flow rate; it also increases as cavity jet air flow is increased at fixed main air flow. For the 5 percent jet flow, the blowout fuel flow appears to increase smoothly with main air flowrate, following a concave-upwards curve. However, for the 10 and 15 percent jet flows there are sharp gradient changes at a main air flow rate of about 0.0635 kg/s, with subsequent behavior following a concave-downwards characteristic. The discontinuous nature of the curves for the higher jet flows at high main air flows is indicative of a change in the blowout behavior.

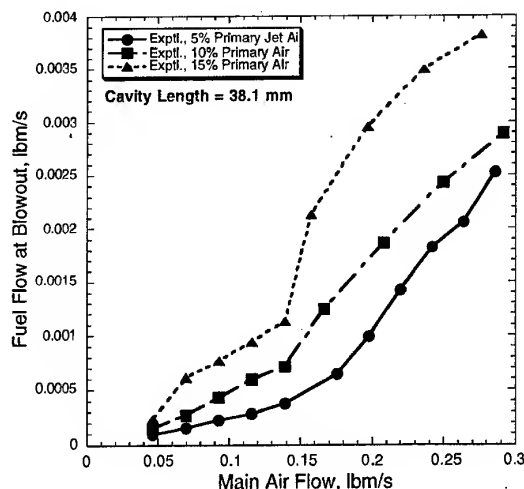


Figure 3: Basic LBO Data for the 0.54 H/d_f Cavity

Correlation of Blowout Data

Finite rate chemistry is important at LBO conditions. Reaction rate theory then leads to the loading parameter group LP, together with equivalence ratio, as controlling blowout, and experimental data can be correlated on this basis. LP is defined as follows:

$$LP = \frac{\dot{m}}{VP^n F} \quad (1.)$$

where, in the context of the cavity,

$$\dot{m} = \dot{m}_f + (\dot{m}_a)_{jets} + (\dot{m}_a)_{ent} \quad (2.)$$

$$V = V_{cav} \quad (3.)$$

$$F = \frac{10^{0.00154T_m}}{3.72} \quad (4.)$$

\dot{m} signifies mass flow rate and subscripts f and a denote fuel and air respectively; subscript 'jets' refers to the cavity air jets and subscript 'ent' indicates entrainment. The fuel is included here because, being gaseous propane, it occupies significant volume. P is the combustion pressure; exponent 'n' an apparent reaction order, and is a constant if combustion proceeds in a single step reaction, with a value of 2.0 if this reaction is second-order. In reality 'n' is a variable less than 2.0, and its actual value is determined empirically. Since the present tests were made at atmospheric pressure and P is in atmospheres, 'n' does not have to

be determined. F is an exponential temperature correction factor⁷ that corrects to an inlet temperature of 400°K.

The loading parameter has been successfully in use for correlating LBO's and combustion efficiency for many years, e.g. Kretschmer & Odgers⁸.

Figure 4 shows the data from Figure 3 plotted in loading parameter form, using Equation (1.). Also shown on the plot are some data obtained

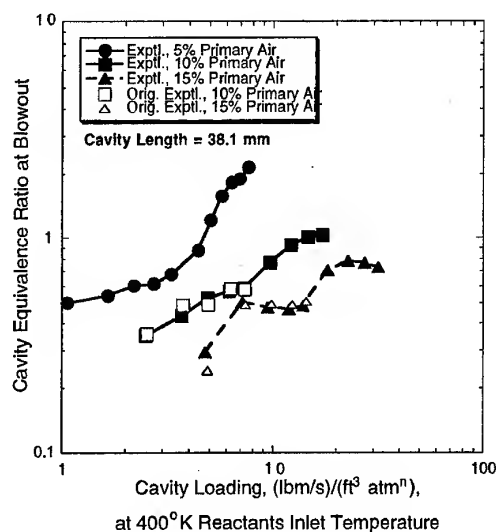


Figure 4: LBO Data for 0.54 H/d_r Cavity

earlier using the same combustor in a different test facility. The cavity equivalence ratio is defined as,

$$(\phi_{cavity})_{LBO} = \frac{(\dot{m}_f)_{LBO}}{0.06377(\dot{m}_a)_{cav}} \quad (5.)$$

where,

$$(\dot{m}_a)_{cav} = (\dot{m}_a)_{jets} + (\dot{m}_a)_{ent} \quad (6.)$$

and 0.06377 is the stoichiometric fuel/air mass ratio for propane.

The most obvious feature of Figure 4 is that, despite containing all necessary flow information, the LP group does **not** correlate this data. The plot shows that increasing cavity jet air flow improves the stability. This apparent failure of loading parameter is because cavity jet air not only affects cavity equivalence ratio and cavity loading, it also drives and strengthens

the large natural vortex that is trapped in the cavity. Therefore, change in cavity jet air may also be considered as a geometry change, analogous to a swirler vane angle change in a conventional swirl-stabilized combustor.

The earlier data at 10 and 15 percent cavity jet air flow rates agrees extremely well with the present LBO data. This confirms the repeatability of the observed behavior.

Note that the shapes of the curves change dramatically as cavity jet air flow is increased. At 15 percent jet air flow the observed behavior is that normally associated with blowout from multiple flame positions, i.e. the overall characteristic is apparently composed of components from several individual blowout characteristics; e.g. Reference 9.

A more appropriate comparison of data would be on a constant cavity jet air flow basis for all of the cavity lengths. All of the features and flows present should then be accounted for in the LP group and cavity equivalence ratio. Figures 5 and 6 show such plots at the 5 percent and 10 percent cavity jet flows respectively, and in each case for all three of the cavity lengths.

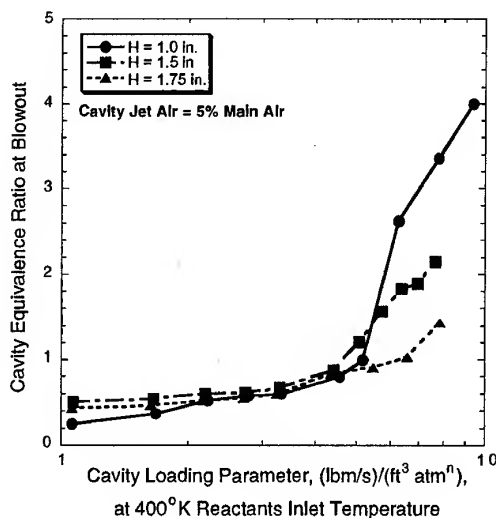


Figure 5: LBO's for All Cavities at 5% Jet Air

It can be seen that for each cavity jet airflow, a satisfactory correlation of data is obtained for a limited range of cavity loading parameter. Once a critical value

of cavity loading is exceeded, the correlation fails. After this critical loading, blowouts for all of the cavities exhibit a sharp change in slope, with the smallest cavity having the worst stability

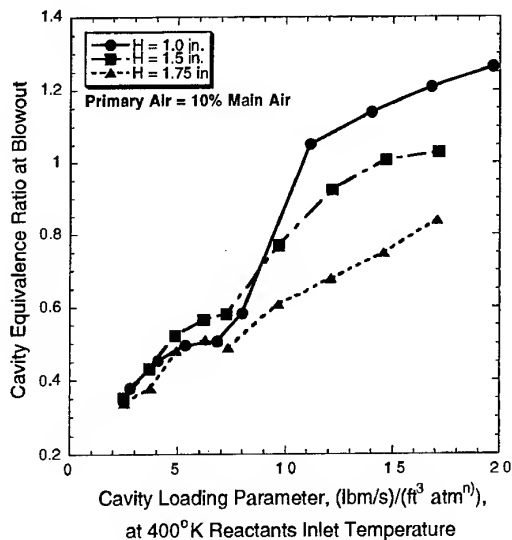


Figure 6: LBO's for All Cavities at 10% Jet Air

The cavity loading at correlation breakdown for all cavity lengths is plotted against cavity jet air mass flow rate, expressed as a percentage of main air flow, in Figure 7.

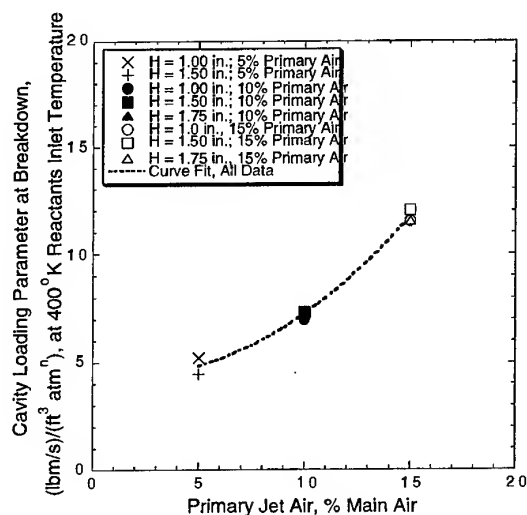


Figure 7: Cavity Loadings at Burning Mode Change

The correlation breakdown data for all three cavities agree well in this form, and the cavity loading at breakdown increases with cavity jet air. This behavior would be expected if the cavity jet air does indeed drive and strengthen the trapped vortex. The jet air, at higher flow rates, also increases the entrainment of mainstream air into the cavity, as Figure 2 indicates. Together, these increase the cavity loading. Eventually, the cavity becomes overloaded, and burning at blowout can no longer be contained within the cavity.

Figure 8 records the cavity equivalence ratio at correlation breakdown, also as a function of cavity jet air. Again, there is good agreement for all of the cavities at all of the jet flows. Note that the bulk equivalence ratios where breakdown occurs are all below unity. If burning at blowout is not contained in the cavity, then it is not due to there being insufficient air in the cavity to complete combustion.

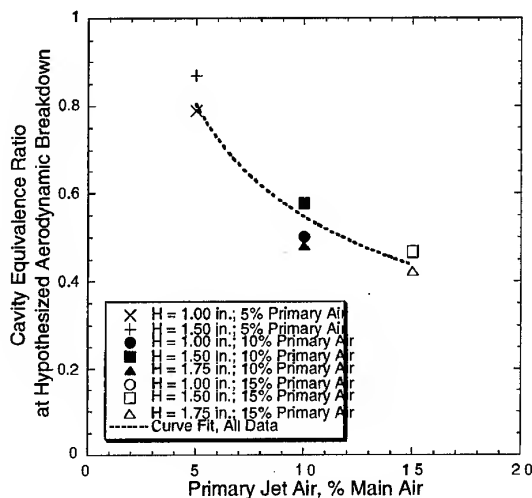


Figure 8: Equivalence Ratio at Mode Change

Cavity equivalence ratios at LBO are plotted in Figure 9 against cavity loading parameter for all flows that are contained clearly within the cavity at blowout; data falling at higher loadings than the correlation breakdown are excluded. The data correlate well and fall into two distinct groups; one group for all cavities at cavity jet flows of 5 percent of mainstream air mass flow rate, and another group for all cavities at 10 and 15 percent of mainstream air flow rate. All the cavities at 5 percent cavity jet flow have worse stability than all the cavities at 10 and 15 percent jet flows.

Referring back to Figure 4 and the discussion of it, the explanation of the two groupings of correlated data in Figure 9 would appear to be that a 5 percent cavity jet flow has insufficient momentum to organize and adequately stabilize, a lazy and inherently unstable naturally-trapped vortex.

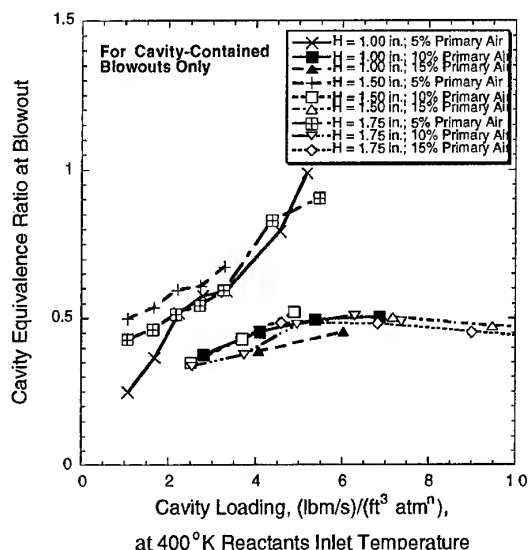


Figure 9: Blowout Correlation for Cavity-Contained Flames Only

Noise Measurements

The observed noise under non-reacting flow conditions is broad-band, and the level increases with increase in mainstream flow velocity. The presence of combustion increases the noise level at given flow conditions. Under certain reacting flow conditions for the different cavity lengths, a strong increase in combustion noise was observed. Blowout would occur abruptly with such noisy operation.

To illustrate the noise measurements, two test conditions for the 38.1 mm cavity length are presented; these are delineated as Cases A and B. The test conditions for Case A are as follows: mainstream velocity 38 m/s, cavity equivalence ratio 1.05, cavity air jet mass flow rate 1.9 percent mainstream mass flow rate, and, cavity loading of 1.31 (lbm/s)/(ft³ atmⁿ) at 400°K. For Case B: mainstream velocity 38 m/s, cavity equivalence ratio 0.7282, cavity air jet mass flow rate 3.15 percent mainstream mass flow rate, and, cavity

loading of 1.83 (lbm/s)/(ft³ atmⁿ) at 400°K. The fuel flow rate was constant for both cases. The major variable therefore, was cavity jet air flow, with mainstream entrainment following.

With respect to Figure 9, the cavity loadings place both cases in the category of cavity-contained blowouts, but following the poorer stability grouping. Of course, the equivalence ratios for both cases are considerably above LBO.

Figure 10 shows noise time traces, as a signal voltage from the microphone, for non-reacting flow at Case A conditions, and for reacting flow at Cases A and B conditions.

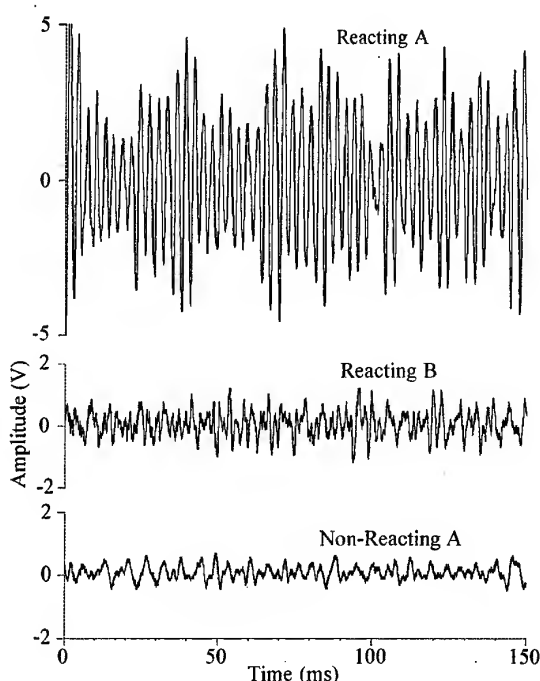


Figure 10: Noise Time Traces From Microphone

The noise level for Case A with a near-stoichiometric equivalence ratio, was considerably above that for Case B, which is fuel-lean. The corresponding power spectra for the three traces are given in Figure 11. For Case A there is a distinct peak frequency at 280 Hz. No distinct frequency was observed for Case B at the lower equivalence ratio.

It appears as though coupling exists between heat release and flow structure for the higher equivalence ratio. The apparent absence of such coupling for the

lower equivalence ratio might be due to damping effects arising from higher viscosities associated with the lower cavity temperatures at this condition.

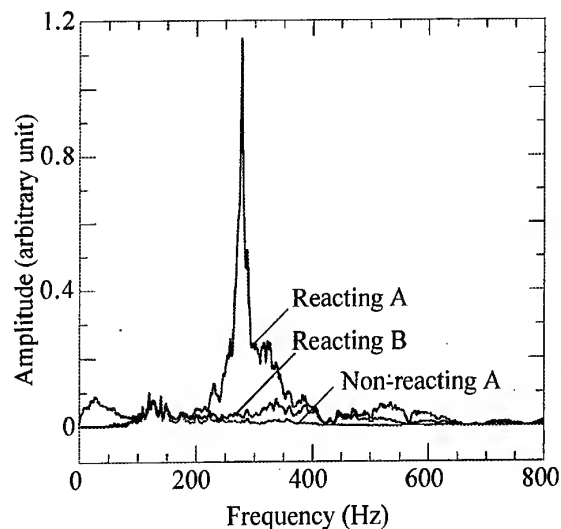


Figure 11: Noise Averaged Power Spectra

OH Imaging

The flame structures in the cavity are highly three-dimensional and the mean flow field is extremely non-stationary. Therefore, the individual, near-instantaneous, planar images of OH captured are rather difficult to interpret. Phase-locking was not attempted in this initial investigation, and structure detail was lost in ensemble-averaging many images. Careful review, sorting and sequence-animation of a large number of randomly-collected images was necessary in order to gather reasonable qualitative interpretations of the flame behavior at near-blowout conditions. Based on this process the following general observations were possible.

In general, at low mainstream and low cavity air jet mass flow rate combinations, flame is fully contained within the cavity and LBO occurs from the shear layers associated with the fuel jet. This is consistent with Figure 9 where the two sets of correlated LBO data for cavity-contained converge for small cavity loadings. For no cavity length H , is the whole cavity volume effectively utilized at LBO. As the mainstream velocity is increased while cavity air jet mass flow rate remains low, (for example, Case B conditions above), the mainstream momentum

influences the cavity flow and results in unburned fuel getting into the shear layer formed between the mainstream and the cavity flows at the outer diameter of the combustor forebody (see Figure 1). This is also consistent with Reference 2, see Figure 2, where negative entrainment was found. The fuel reacts in this shear layer, as is illustrated by two images in Figure 12 for Case B conditions with the 38.1 mm cavity length. Figure 13 shows an example of jet shear burning contained within the cavity at 0.50 cavity equivalence ratio.

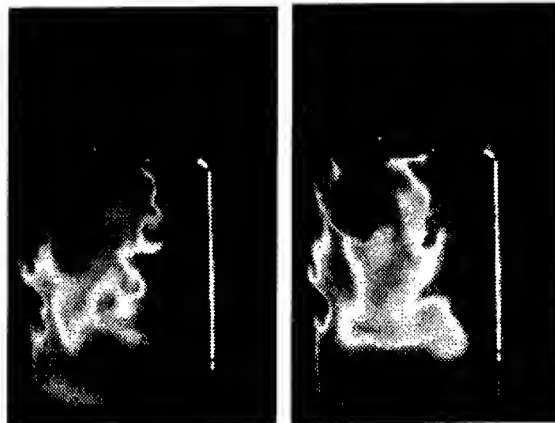


Figure 12: OH Images for Case B

In Figure 12 the combustor is mounted vertically, with mainstream flow from bottom to top and cavity jet and fuel flows from top to bottom. The central shaft that supports, and supplies fuel and cavity jet air to, the drum, is visible to the right of each image. Mainstream air is flowing to the left of each image. The origin of the fuel entering the cavity from the drum is visible as the origin of the OH emission. Jet shear layer burning in the cavity can be seen, and these jet shears oscillate left to right about the fuel origin, rather like a pendulum. Fuel enters the mainstream/cavity interfacial shear layer to the left of the images, and burns there; classical shear layer vortex roll-up is visible. The direction of the visible roll-up in this shear layer indicates that the mainstream velocity is greater than that of the cavity flow. This observation is consistent with the conditions stated above for Case B, where mainstream velocity was 38 m/s and cavity jet injection velocity was 15 m/s. Due to the high mainstream momentum, the interfacial shear layer seldom interacts with the cavity rear wall to be recirculated back into the cavity.

In Figure 13 a fuel jet is visible as a dark region of quasi-potential core, with bright OH emission

indicating burning in the jet shear layers around the fuel potential core. Flame impinges on the support shaft to the right of each image. It also is picked up by the outer layers of the large vortex trapped within the cavity and recirculated around the cavity. The indicated vortex center is not fixed in space but moves both axially and radially. In the lower left region of the left-hand image, a darker grey region is evident. This is convected OH, and does not represent a flame.

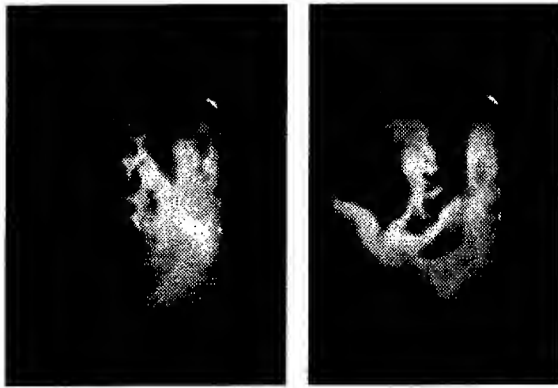


Figure 13: Example of Cavity-Burning with 0.50 Cavity Equivalence Ratio

As cavity jet flow is increased for fixed mainstream conditions in this cavity length, mixing in the cavity appears to improve, OH generation is pushed towards the cavity front wall formed by the forebody, and more, but not all, of the cavity volume is utilized by the large trapped vortex; OH is largely concentrated in the surface layers of this vortex, and there is no burning of significance taking place in the interfacial shear layer.

For increases in cavity jet air in the 25.4 mm cavity length, the jet flow reaches, and is turned radially-outwards by, the cavity front wall. The turned flow can impact the interfacial shear layer off the outer diameter of the forebody, moving it radially outwards to prevent recirculation of this layer back into the cavity by interaction with the cavity rear wall formed by the drum. Some flame spillage is observed prior to the cavity jet flow reaching the cavity forward wall, even when the cavity equivalence ratio is low. Blowout occurs suddenly from the interfacial shear layer.

For the 44.5 mm cavity length the whole cavity flow is relatively disorganized and there is a notable increase in noise level compared to the other

cavities. The large trapped vortex remains at almost the same size as that for the 25.4 mm cavity length because the fuel/air jet system is turned radially outwards before it reaches the cavity front wall by the excess mainstream momentum.

Blowouts From Shear Layer Burning

From the OH imaging, it is obvious that the LBO correlation breakdown noted in Figures 5 and 6 can be associated with the excess of mainstream momentum over cavity flow momentum entraining unburned fuel from the cavity into the interfacial shear layer off the forebody outer diameter. If this occurs when the cavity jet system itself also has high momentum, the enhanced radial outflow from the cavity moves radially and prevents the interfacial shear layer from being recirculated into the cavity by the cavity rear wall. Blowouts would then be controlled by the interfacial shear and not solely by the cavity. Cavity loading alone would not be sufficient to correlate all of the blowout data, as was noted.

For the situations with LBO from significant shear layer burning, the total fuel burned at blowout is split in undetermined fashion between cavity burning and shear layer burning. Also undetermined is the amount of air involved in the shear layer. The shear layer air can be written,

$$(\dot{m}_a)_{\text{shear layer}} = (\dot{m}_a'')_{\text{ent}} \times A_{\text{layer}} \quad (7.)$$

where,

A_{layer} = interfacial area between cavity flow and mainstream flow

$(\dot{m}_a'')_{\text{ent}}$ = entrainment mass flux across A_{layer}

For the fixed diameters forming cavity forward and rearward walls, A_{layer} will be proportional to the cavity length H . Neglecting density differences across the shear layer, which can modify entrainment rates but are presently unknown, the entrainment mass flux will be proportional to the mainstream to cavity flow momentum ratio.

These additional controlling LBO parameters were incorporated as follows: First, the volume term in the cavity loading parameter was increased to allow for the shear layer presence. For this purpose the increase in shear layer radial width over cavity length was estimated from the OH images. This gave $(LP)_{\text{SLB}}$. Second, the resulting loadings were multiplied by the mainstream to cavity flow momentum ratios. Finally, the cavity

equivalence ratios at blowout were multiplied by the cavity length, H .

The modified terms were applied to the blowout data for blowouts just from shear layer burning, i.e. the data beyond the cavity breakdown loading. Figure 14 shows that these additional terms correlate the shear layer blowout data for all cavity jet mass flow rates and for all of the cavity lengths.

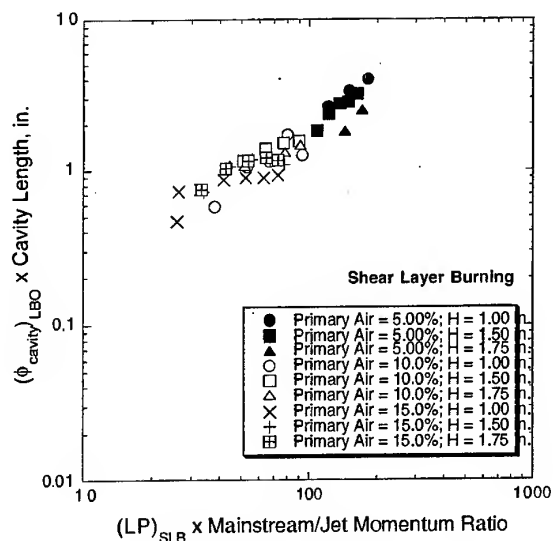


Figure 14: Correlation of LBO Data for Shear Layer Burning

Comparison with Swirl-Stabilized Combustors

The trapped vortex combustor has been promoted as a means towards achieving enhanced lean blowout stability for high altitude operations because the recirculation zone is mechanically held in place. By being trapped in a cavity it is not subject to, or is less sensitive to, variations in flow due to engine operating conditions or inlet flow distortions. To substantiate these claims the present LBO data can be compared to LBO data from a conventional swirl-stabilized combustor. A comparison of the present data is therefore made against the LBO data contained in Reference 10.

The data in Reference 10 were for a four-injector, planar sector combustor, modeled extremely closely on a full annular combustor from a real aircraft

gas turbine engine. The engine had demonstrated good LBO stability (and windmilling relights) with liquid Jet-A fuel to flight altitudes in excess of 10,700 m. The sector combustor, like the engine combustor, utilized swirling air in an airblast atomizer and a dome-swirler, together with sudden expansion into the combustor dome, to generate a recirculation zone; however, gaseous propane, as with the TV combustor tests, was used as a fuel. The dome and atomizer air swirlers generated toroidal recirculation zones around the axial centerline of each fuel injector. The sector tests were made at atmospheric pressure with ambient temperature inlet air; low pressures were simulated using an excess gaseous nitrogen dilution technique¹¹. With this approach, LBO's down to 0.25 atm. equivalent pressure were measured.

Comparisons have been made for the TV combustor operating with cavity-controlled LBO's since these operational conditions fulfill the design intent. For consistency with the swirl-stabilized combustor results the equivalence ratio used was an overall one based on the total mass flow rate exiting the combustor.

Figure 15 shows the sensitivities of the two recirculations to the amount of air directly injected into the vortices, expressed as a percentage of the total airflow to follow conventional practice.

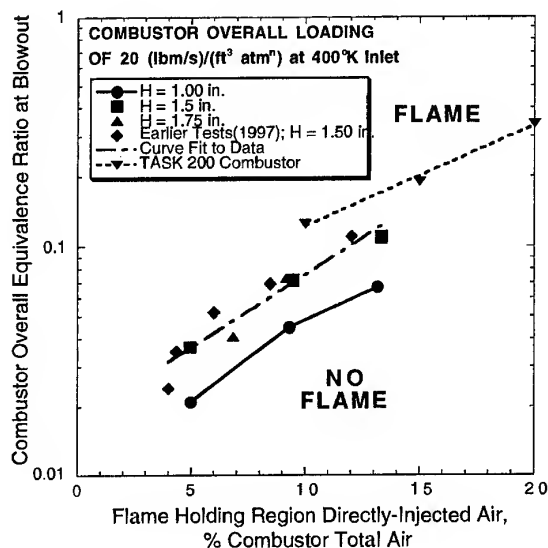


Figure 15: Comparison of TV Combustor With Swirl Combustor - Sensitivity to Directly-Injected Air

For the TV combustor the directly-injected air corresponds to the cavity jet air; for the swirl-stabilized combustor it corresponds to the air introduced through the combustor dome. The sensitivity is indicated by the overall equivalence ratio at blowout. For both combustors the combustor loading was constant at 20 (lbm/s)/(ft³ atmⁿ) at 400°K.

Setting aside the 25.4 mm length cavity, the data for the 38.1 and 44.5 mm cavities correlate well for all cavity flows. The sensitivity of the TV combustor to directly injected air **for cavity-contained blowouts** is about the same as that generated by swirl (gradients virtually the same). This is not surprising since a recirculation is a recirculation, regardless of how it is generated. The TV combustor over the range 5 to 15 percent directly-injected air has better stability than does the swirl-stabilized combustor; however, because of the slight gradient difference, this advantage is lost at higher airflows.

In Figure 16 LBO's for a "well-designed", i.e. the right amount of cavity jet air to drive the vortex but to avoid interfacial shear layer burning, are compared with the LBO's from the swirl-stabilized combustor¹⁰.

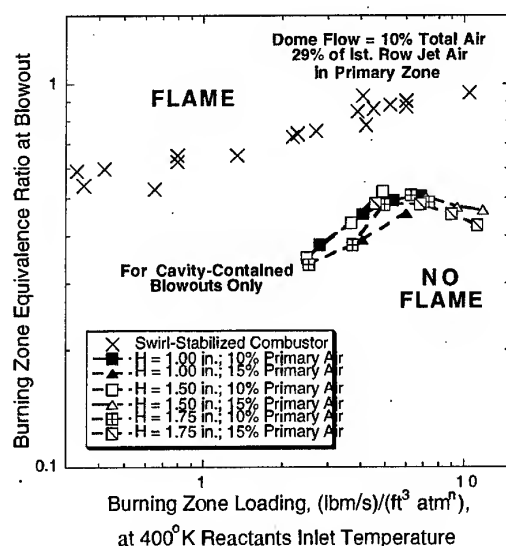


Figure 16: Comparison of Cavity-Contained TV Combustor with Swirl-Stabilized Combustor

The trapped vortex combustor data are taken directly from Figure 9. The data for the swirl-stabilized combustor were selected for a dome flow equal to 10

percent of the combustor total so that it is directly comparable to the TV combustor data. The "Burning Zone" is the cavity for the TV combustor, and the primary zone for the swirl-stabilized combustor. The primary zone length was taken as the downstream distance from the dome to the first row of transverse primary air jets in the liners. The amount of first row jet air recirculated back into the primary zone was taken as 29 percent of the jet total¹¹. This amounts to less than 2.0 percent of the combustor total.

It can be seen that within its constraints, the TV combustor has a significantly better LBO stability than does the example of swirl-stabilized combustors.

Discussion

The trapped vortex combustor is a complex device. However, it generates a recirculation zone, and that recirculation zone in general, appears to behave just like any other recirculation zone. Without direct injection of air into the cavity the natural trapped vortex generated by flow over the cavity is very lazy and is poorly organized for combustion purposes. There has to be sufficient cavity air injected in jet form, to drive the natural vortex. Present indications are that this amount is greater than 5 percent of the mainstream air. Cavity jet air equal to 10 percent of the mainstream is more than adequate, and, as Figure 9 shows, increasing the cavity jet air to 15 percent of the mainstream results in no further improvement in stability with this method of introduction.

Cavity jet air acts in three ways: 1.) it changes the cavity equivalence ratio; 2.) it drives the vortex by determining the circulation developed, and has a similar result to swirler vanes, and, 3.) it influences the cavity residence time through mass loading.

A cavity mass loading can be reached where flame is not contained within the cavity, but is supplemented by shear burning in the interface between the cavity flow and the mainstream moving by the cavity. Burning in the interfacial shear layer is very sensitive to the mainstream, and a blowout in the shear layer also results in a simultaneous blowout in the cavity. Cavity axial length only plays a role in influencing the cavity loading, and in determining the shear layer extent.

Flow behavior in the cavity, the interfacial shear layer and, in the interactions of the interfacial shear layer with the mainstream and with the cavity, is

highly dynamic. This dynamic behavior depends, in general, on cavity geometry beyond the simple axial length variation examined presently. Like many other combustion systems, despite its good LBO performance, the TV combustor can be subject to acoustic coupling of heat release with flow structure dynamic behavior, (Figure 11).

Conclusions

1. A trapped-vortex combustor requires greater than 5 percent mainstream air to be directly-injected into the cavity in order to drive the vortex, for successful combustion.
2. A critical cavity loading exists beyond which flame is not contained within the cavity at lean blowout.
3. When the critical cavity loading is exceeded, cavity burning is supplemented by classical shear layer burning at the interface between cavity and mainstream flows. Blowout occurs from the interfacial shear layer.
4. Dynamic flow interactions, involving capture or not of the interfacial shear layer by the cavity, are extremely important to cavity flame stability, and the trapped vortex can also be subject to acoustic coupling of heat release and flow structures.
5. Compared to a generic, conventional, swirl-stabilized combustor, the trapped vortex combustor exhibits superior lean blowout capability when burning is maintained within the cavity..

Acknowledgements

The enthusiasm, motivation and support of Dr. W.M. Roquemore of AFRL are greatly appreciated. Dr. Roquemore conceived applying the TV combustor to gas turbine engines. This on-going research is sponsored by the U.S. Air Force Research Laboratory, Propulsion Directorate, Wright-Patterson Air Force Base, through Contract No. F33615-95-C-2507.

References

1. Hsu, K-Y, Goss, L.P. and Roquemore, W.M., "Performance of a Trapped-Vortex Combustor," *Journal of Propulsion & Power*, Vol. 14, No.1, 1998
2. Sturgess, G.J. and Hsu, K-Y., "Entrainment of Mainstream Flow in a Trapped-Vortex Combustor," Paper No. 97-0261, *AIAA 35th. Aerospace Sciences*

Meeting & Exhibit, Reno, Nevada, January 6-10, 1997.

3. Katta, V.R. and Roquemore, W.M., "Numerical Studies on Trapped-Vortex Concepts for Stable Combustion," *Trans. ASME, J. Engineering for Gas Turbines and Power*, Vol. 20, January 1998, pp. 60-68.
4. Katta, V. R. and Roquemore, W.M., "Simulation of Unsteady Flows in an Axisymmetric Research Combustor Using Detailed Chemical Kinetics,": Paper No. 98-3766, *34th. AIAA/ASME/SAE/ASEE Joint Propulsion Conference & Exhibit*, Cleveland, Ohio, July 13-15, 1998.
5. Valenti, M., "Upgrading Jet Turbine Technology," *Mechanical Engineering*, Vol. 117, No.12, December 1995, pp. 56-60.
6. Heneghan, S.P., Vangsness, M.D., Ballal, D.R., Lesmerises, A.L., and Sturgess, G.J., "Acoustic Characteristics of a Research Step Combustor, *AIAA Paper No. 90-1851, AIAA/SAE/ASME/ASEE 26th. Joint Propulsion Conference, Orlando, Florida, July 16-18, 1990.*
7. Parnell, E.C. and Williams, M.R., "A Survey of Annular Vaporizing Combustion Chambers," *proc. Intl. Symp. Combustion and Heat Transfer in Gas Turbine Systems*, Vol. II, Pergamon Press, 1971, pp. 91-103.
8. Kretschmer, D. and Odgers, J., "Modeling of Gas Turbine Combustors - A Convenient Reaction Rate Expression," *Trans. ASME, J. Energy & Power*, 1972, pp. 173-180.
9. Sturgess, G.J., Gogineni, S. and Shouse, D.T., "Influences of Airblast-Atomizing Fuel Injector Design on Primary Zone Characteristics at Blowout," Paper No. 97-0269, *AIAA 35th. Aerospace Sciences Meeting & Exhibit*, Reno, Nevada, January 6-10, 1997.
10. Sturgess, G.J. and Shouse, D., "Lean Blowout Research in a Gaseous Gas Turbine Combustor with High Optical Access," *Trans. ASME, J. Engineering Gas Turbines & Power*, Vol. 119, January 1997, pp. 108-118.
11. Sturgess, G.J., Heneghan, S.P., Vangsness, M.D., Ballal, D.R. and Lesmerises, A.L., "Lean Blowout in a Research Combustor at Simulated Low Pressures," *Trans. ASME, J. Engineering Gas Turbines & Power*, Vol. 119(4), October 1996, pp.773-781.

12. Sturgess, G.J., McKinney, R. and Morford, S.,
 "Modification of Combustor Stoichiometry
 Distribution for Reduced NO_x Emissions from Aircraft
 Engines," Trans. ASME, *J. Engineering Gas Turbines
 & Power*, Vol. 115, No. 3, July 1993, pp. 570-580.

PAPER No. 44
Sturgess
 (presenter: G.J. Sturgess)

Question 1: N. Selcuk, Middle East Technical University, Turkey

Could you please elaborate a little bit on the CFD code that you have used.

Answer:

Although detailed reference to the CFD code and work is not given in the paper, which concentrated on the experimental results, I used some of the calculations obtained with it in the presentation to illustrate the flowfield in the trapped vortex combustor. The code is called UNICORN (Unsteady Ignition and Combustion with Reactions), and it was developed by my colleague at ISSI, Dr. Vish Katta; it is the same code that was referred to in Paper 17 by Grish et. al, presented at this meeting. The code is two-dimensional, and offers time-accurate direct numerical simulations (DNS) or time-averaged simulations with turbulence models. Global, reduced and detailed chemical reaction mechanisms are available for combustion in air of hydrogen, methane, propane, methanol, ethylene and acetylene as fuels; the fuel can be in gaseous or liquid phase if appropriate, for droplet burning and spray flames calculations. Detailed simultaneous calculations for NO_x are also provided. Post-processing software called IGAS (Integrated Graphics and Animation Software) also developed by ISSI allows for complex data presentation.

Question 2: M. Razdan, RR-Allison, U.S.

Concerning the estimation of mainstream mass entrainment into the cavity, how big an impact does such entrainment have on the cavity loading parameter, and hence, on the lean blowout in an engine situation?

Answer:

Mainstream entrainment into the cavity can vary widely, depending for a given cavity on the momentum ratio of the cavity directly-injected flow to that of the mainstream, and can be either positive or negative according to this ratio. It also depends on the cavity dimensions; the curve shown was for a near-optimum, i.e. maximum vortex stability with minimum entrainment, cavity size. Non-optimum cavities can have quite different entrainment characteristics while still showing, in general, both positive and negative entrainment (see Sturgess & Hsu, Paper No. AIAA-97-0261). Entrainment, of course, is extremely difficult to measure directly. In general, including the entrainment into the cavity loading parameter becomes particularly important at high values of cavity loading, where the "nose" of the blowout stability loop is approached.

European Evaluation Of JP8+100 Fuel And Its Impact On Engine/Fuel System Design.

S P Bullock, A Hobday, C Lewis.
Rolls-Royce plc.

PO BOX31,
Derby, DE24 8BJ
England

Abstract:

High performance aircraft use fuel as the primary heat sink for airframe power and engine lubrication system cooling. Air cooling incurs severe cost, weight and performance penalties. Current engines therefore use all the heat sink capability of the fuel and consequently stress the fuel throughout the system. The resulting high temperatures cause fuel to form deposits reducing system performance and blocking injectors. Advanced engine design calculations indicate that fuel stability will soon become an engine performance limit. The USAF are therefore coordinating the development of additives that enhance thermal/oxidative stability to overcome this limit. These are designated as "+100" signifying the target of improving operating temperature capability by 100°F.

Evaluation of these additives has been carried out at RR plc under MOD/DERA funding. Testing so far has evaluated thermal stability enhancement using the Aviation Fuel Thermal Stability Test Unit. This test unit simulates the thermal stresses found in actual fuel system components and injectors. Test modules mimic the responses to fuel deposition found in actual systems to provide prediction of long term performance.

Effectiveness of the additive tested was evaluated in blends based on two European fuels of contrasting stability. Testing the additive demonstrated additives provided a significant reduction in deposition compared to base fuel in a variety of regimes. However, blends still had definite stability limits. Results also identified novel operational aspects including additive cleaning effects during transition from normal to additised fuel. Future tests are planned to evaluate alternative additive formulations and expand testing conditions to include mission cycling, reheat system and simulated flow recirculating conditions.

Introduction

Jet fuel is used as the primary heat sink in high performance military and civil aircraft to cool engine and airframe components in addition to providing the propulsive energy for flight. The heat dissipated into the fuel can cause thermal degradation of the fuel causing fouling of key components. Thermal stability limit controls are applied to current fuels in order to avoid incidences of

such problems. However, the thermal stability limitations of current fuels will ultimately represent a whole engine and airframe performance limit for future designs.

In recognition of this the Airforce Wright Patterson Laboratory (WPAFB) is sponsoring research programmes to address this problem. The programme involves the co-operation of industry, private laboratories and universities. Technical effort is directed at increasing the design limit of current JP-8 fuel from 325°F(163°C) to 425°F (218°C) at the fuel nozzle, hence the designation +100 as the increase in °F. The final solution adopted to achieve this improvement is through the use of an additive package added to conventionally produced JP8. In the UK contributions to this programme are being sponsored and co-ordinated by the MOD/DERA.

Evaluation of these additives has been carried out at RR plc under MOD/DERA funding. Testing so far has evaluated the the capability of a candidate +100 additive to enhance the thermal stability performance of two European produced JP8 type fuels using the Aviation Fuel Thermal Stability Test Unit (AFTSTU). The AFTSTU simulates the thermal stresses in airframe and engine fuel delivery systems and measures the impact of fuel breakdown products on system operation. Results from this work relate closely to in-engine performance and therefore compliment the bench scale testing that has so far been used in the additive development programme.

JP8+100 Development

Future military aircraft need to be highly manoeuvrable and have expanded operating envelopes which is achieved using high performance engines and airframe systems. These require increased levels of cooling. The prime heat sink is fuel, but against this increase in heat load is the simultaneous reduction in fuel flow which is driving bulk fuel and fuel wetted wall temperatures upwards and beyond current stability limits. Excessive thermal stressing causes fuel to break down producing gums, lacquers and deposits. These can cause degradation of system performance by stiction of sliding components, blockage of filters, orifices, burner feed arms and afterburner manifolds. Exceeding the heat load capability of the fuel therefore leads to loss of performance, reduced system reliability and incurs high maintenance costs (ref. 1). The alternative to fuel cooling is

the use of air or fuel recirculation. These approaches incur significant cost, weight and performance penalties.

Standard JP8 and equivalent kerosine type fuels have reasonably well defined temperature limits. It is generally accepted that maximum bulk temperatures of around 163°C in fuel management units and 204°C wetted wall temperatures in injectors cannot be exceeded without inducing unacceptable deposition rates. High stability fuels which extend these temperatures are available currently e.g. JP7 and JPTS. However, their high cost and limited volume yield precludes the use of these fuels except for special applications for which they were designed.

The issue of fuel becoming a design limiting factor was originally addressed by the USAF in 1990. An Aircraft Thermal Management Working Group of Wright Research and Development Centre (WRDC) investigated the cooling requirements for current, next generation and future aircraft (ref. 2). The conclusions reached revealed three-fold heat -load increase and massive metal temperature increases for future engines.

To resolve these tremendous heat sink requirement problems the group recommended the development of high thermal stability fuels but in two stages:-

- JP8+100 to providing 50% increase in heat sink capability over conventional JP8 by allowing fuel system temperatures to increase to 218°C. In addition to thermal stability targets this fuel was required to be based on the use of fuel meeting the current JP8 specification and that achieving the +100 stability should not compromise cost or any other operational performance parameters.
- A new JP900 fuel with 482°C (900°F) thermal stability designed for projected advanced aircraft and engine designs.

Recent work (ref. 3) has shown that significant development work is still required to meet the ambitious JP900 stability targets and that an intermediate stability fuel, JP8+225, is now being developed.

Fuel Type	Max. Wetted Wall Temp. (°C)	Max. Bulk Temp. (°C)	Heat Sink (Btu/lb)	Rel. Cost (\$/gall)
JP8	204	163	125	~ 0.8
JP-TS		220	220	~ 2.0
JP7		290	330	~ 3.0
JP8+100	260	218	190	~ 0.8
JP8+225		290	330	~ 0.8+5%*
JP900		480	625	

* This would exclude the use of additional fuel processing options.

Table No 1 - Summary Of Advanced Fuel Property Targets

Technical and cost targets for JP8+100, JP8+225 and JP900 are summarised in Table No.1 with existing JP8 as baseline (refs. 1,2 and 3). Data given in this Table are approximate and provided for comparison purposes only.

In the early stage of the USAF coordinated programme additive manufacturers were surveyed and solicited for candidate additives that had potential for improving fuel thermal oxidative stability of nominal JP8. Also, bench test methodologies were developed for screening additives. The additives screened included antioxidants, dispersants, detergents, metal deactivators, antifoulants and proprietary thermal stability improvers or combinations thereof.

Laboratory tests, while having significant advantages in assessing the development of an additive package, all have some inherent disadvantages. Static tests are simple to operate and can yield results in less than a day allowing many additives to be tested. However these tests are usually operated under highly accelerated test conditions and do not replicate system conditions. Small scale flowing tests can more closely approach reality but relating to performance in real systems and therefore predicting long term impact is still difficult. Scaled rigs, the AFTSTU being one example, are closest to reality in terms of temperature, flow regimes and contain test modules which mimic in-service operation. The results they produce therefore allow accurate prediction of performance in-service. The AFTSTU has been used in this programme to validate results derived from bench scale tests on those additives that show most potential by testing one of the prime USAF additives in selected European produced Hydrotreated JP8 (selected to represent a higher stability fuel) and Merox JP8 (selected to represent a marginal stability fuel).

Note that other aspects of additive performance including compatibility and impact on operation of ground handling, airframe, engine fuel delivery and aerothermal systems and materials are also being evaluated in parallel with the thermal stability work (refs. 4 and 5).

Aviation Fuel Thermal Stability Test Unit (AFTSTU) Description

The Aviation Fuel Thermal Stability Test Unit (AFTSTU) is a proven development tool which has evolved from many years of successful fuels technology research at Rolls-Royce plc. This device incorporates third generation hardware and software which follows on from a similar unit designed, developed and commissioned for the United States Navy in 1993.

The AFTSTU is a unit capable of thermally conditioning fuels in a variety of regimes that closely simulate aircraft and engine environments and exposing the fuel to representative component modules under closely controlled dynamic and accelerated conditions. The device represents a scaled fuel system from supply tank (aircraft wing) to

nozzle module outlet (injector exit). Test modules mimic critical fuel system components known to be affected by thermal degradation products in service. Their functionality is monitored in real-time throughout testing in addition to post test analysis. Results produced on the AFTSTU relate directly to in-service performance by providing prediction of filter blockage rates, nozzle fouling rates etc.

The unit is capable of providing precise, quantitative data at relatively low cost with low fuel consumption (5 gph) and short timescales (typically 200 hours) compared to full scale rig or engine tests. It therefore provides the essential bridge between laboratory testing and full scale experience. It is the ideal vehicle to both validate candidate +100 additive data based on laboratory testing and provides prediction of performance of these additives in the field.

In a typical aircraft system three major regimes can be identified as low, intermediate and high temperature regimes (see fig. 1).

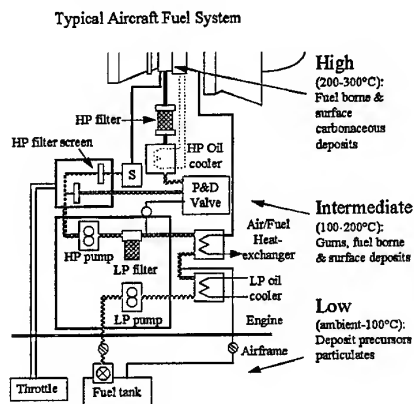


Figure 1 Typical Aircraft System Thermal Regimes

Low Temperature (Ambient to 100°C) This area includes the fuel tanks up to the engine high pressure (HP) pump. The deposits in this section are generally loosely adhered fine particulates. Deposit precursors can form in this regime resulting in further deposition downstream.

Intermediate Temperature (100°C to 250°) This regime is found within the aircraft engine after the HP pump and engine oil cooler but before the fuel nozzles. Deposits in this section tend to be gums, fuel borne and surface adhered particulate.

High Temperature (Wetted wall Temperatures 200°C to 400 °) This regime represents the fuel injector nozzles. It is characterised by the hot walls found within these parts due to the high temperature compressor exit air (see fig. 2). The deposition occurs so rapidly that deposits form at the site of heat input as opposed to the other regimes where deposits form downstream of where the heat input zone. Deposits

tend to be carbonaceous in nature and are fuel borne as well as surface deposited.

In all these regimes deposition is dependent on many factors. These include fuel type/composition including dissolved gases, water, additives etc., temperature, flow regime (residence time), surface material, surface roughness, fluid dynamics, surface temperature and previous thermal stressing.

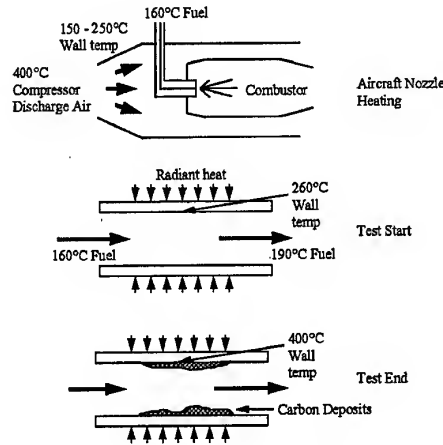


Figure 2 Aircraft Nozzle Heating And AFTSTU Simulation

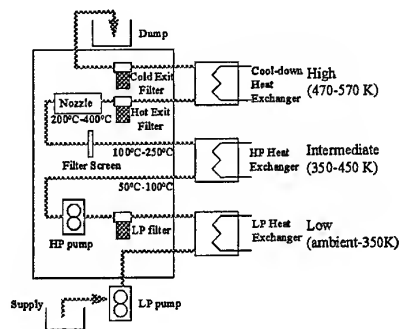


Figure 3 AFTSTU Thermal Regimes And Test Modules

The AFTSTU facility is modular in construction and as such contains a number of discrete test sections that represent the simulation of these regimes and examples of the components that operate in them. The overall flow schematic is shown in fig. 3. A brief description of each test module and its mode of operation is given below:

LP and HP filter test modules: The AFTSTU contains simulated LP (10µm rated) and HP (75µm rated) engine fuel filters, correctly scaled with respect to flow per unit area. The filter media type and ratings are identical to those

used in aircraft parts. These units are used to evaluate fuel borne particulate formation and filter blockage propensity. Filter blockage is measured throughout the test as a function of element differential pressure drop. Qualitative and quantitative analysis of entrapped debris is also carried out post-test when relevant. Test times of at least 200 hours are required to accrue measurable deposits on these units on typical stability JP8 type fuels.

Fuel Injector Test Module: A key component of the AFTSTU facility is the scaled fuel injector nozzle which simulates an engine fuel injector within the combustor. The component used takes the form of a length of thermocouple instrumented stainless steel tubing, the dimensions and surface finish of which are carefully chosen such that representative fluid dynamics conditions are achieved. The 2.3 mm inner bore of the tube ensures representative turbulent flow (Re No 10,000) at normal flow rates (Table 2).

The nozzle tube is heated via a radio frequency (RF) system. During initialisation the RF heater power is controlled to achieve the desired inner wall temperature (usually in the range 250-400°C). The system then holds that power constant for the duration of the test. Using a constant power has 2 key benefits. Firstly, it ensures a constant heat flux simulating the conditions the injector experiences in the engine. Secondly, it allows the real time monitoring of deposit build up as follows: During testing the inner metal wall temperature rises due to the insulation effect of thermally generated carbon deposition. This process is illustrated in fig 2. This temperature rise at any point during the test can be translated into carbon deposit levels from a derived correlation since the heat flux is constant. Following test, a carbon analysis technique is used to determine quantitatively the final weight of carbon in the tube.

By running a number of simulated injector nozzles at different initial inner wall temperatures, a performance "map" can be generated such as in the test programme described. All this information provides significant insight into the deposit rates and deposition mechanisms which assists in accurately characterising the fuel or fuel/additive combination under test. At the inner wall temperatures used to map the performance of a fuel/additive combination, test times can vary from 25 to 100 hours.

Hot and Cold fuel exit filters: The AFTSTU facility contains two 60µm rated sintered metal element filters downstream of the heated nozzle test section. These are the hot filter, immediately after the nozzle exit, and the cold filter, sited after the water cooled heat exchanger. They have no direct equivalent in the engine but provide qualitative and quantitative information on deposits generated by the thermal stressing within the nozzle section. These units are changed at the same time as the nozzle tube.

Test Programme

The test programme and conditions were targeted with a view to satisfying the following objectives :

- Compare and contrast the thermal stability performance with/without +100 additive of two European JP8 fuels produced via different processing routes, namely Merox and Hydrotreated.
- Determine the ultimate performance and stability of a +100 additised fuel.
- Evaluate the performance of +100 additised conventional fuels against the USAF reference, JPTS.
- Relate the benefits of +100 operation to in-service system performance and component life.

To allow these direct comparisons of fuel thermal stability behaviour, each test was carried out at the same conditions. These conditions are summarised below :

Fuel Flow	23 lthr ⁻¹
LP System Temp	50°C
HP System Temp	160°C
LP/HP System Test Duration	200 hrs minimum
Nozzle Initial Inner Wall Temp	250°C to 400°C
Nozzle Test Duration	25 hrs to 100 hrs

Table 2 Summary Of AFTSTU Test Conditions

Note that the nozzle system initial inner wall temperatures and durations were adjusted to achieve appropriate deposit levels.

The test programme comprised 5 separate tests with identical conditions but different fuel and fuel/additive combinations.

Test No	Test Fuel	Base Fuel	JP8 Mandatory Additives	+ 100 Add.
1	Merox JP8	Merox JP8	AL48, Type 6 (FSII+Nalco CI)	None
2	Merox JP8 +100	Merox JP8	AL48, Type 6 (FSII+Nalco CI)	Yes
3	JPTS	JPTS Blend Inc.Antiox. + DuPont JFA	FSII+CI	None
4	Hydro-treated JP8	Hydrotreated	AL48, Type 6 (FSII+Nalco CI)	None
5	Hydro-treated JP8+100	Hydrotreated	AL48, Type 6 (FSII+Nalco CI)	Yes

Table 3 Test Matrix and Fuel/Additive Summary

Table 3 provides a summary of the fuel types and additive details. All fuels met the requirements of MIL-83133 (JP8) apart from JPTS which was procured to MIL-T-25524. The candidate +100 additive was added at the manufacturers recommended concentration.

Results and Discussion

Test Fuel Analysis

All the fuels met the requirements of their respective specifications.

The results of breakpoint analysis (see Note 1) of the fuels are shown in table 4. The higher breakpoint of the Hydrotreated base fuel reflects the expected higher stability of fuels produced by this process compared by those produced by the Merox process. This data therefore confirms the desired contrast in stability of the two candidate base fuels. The increase in breakpoint for each of the fuel types on addition of the +100 additive confirms that, under these test conditions, the stability of the fuels is increased by the additive. The JPTS fuel is shown as >380°C reflecting the very high stability of this fuel.

Note1: This analysis was carried out to ASTM Method D3241, Determination of Thermal Stability by Jet Fuel Thermal Oxidation Tester (JFTOT). The JFTOT unit consists of a small scale flowing system with a heated tube and filter and is the standard thermal stability specification test applied to all batches of jet fuel. For specification testing the heated tube is run at 260°C. Tube colour rating and filter pressure drop criteria determine whether the fuel passes or fails the JP8 requirement. Breakpoint analysis is an extension of this method where the fuel is tested at progressively higher heated tube temperatures until a fail rating is obtained. The highest temperature at which a pass rating is achieved is termed the breakpoint. The breakpoint therefore provides a quantitative measure of stability under JFTOT test conditions which is more informative than the normal specification pass/fail rating.

Test Fuel	Breakpoint (°C)
1. Merox JP8	275
2. Merox JP8+100	285
3. JPTS	>380
4. Hydrotreated JP8	295
5. Hydrotreated JP8 +100	>320

Table 4 Test Fuel Breakpoint Data

HP and LP Filter Data

HP and LP filter pressure differentials showed only minor

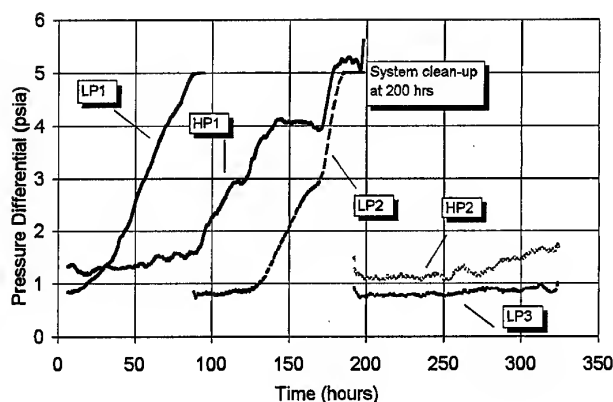


Figure 4 LP And HP Pressure Differential Data For Merox JP8+ 100

increases during base Merox testing i.e. 0.5 psia and 0.2 psia increase respectively over the 200 hours of testing. Contrary to expectations, during the Merox +100 test, significant blockage of both LP and HP filter units occurred. Figure 4 illustrates these results. The first LP filter (LP1) blocked within 80 hours and was replaced. This new filter (LP2) also blocked within 100 hours. During this same period the HP filter (HP1) also blocked. This unexpected set of results was therefore investigated further. The candidate +100 additive package present during this test contains surfactant/dispersant compounds. Such compounds have a known tendency to lift loosely adherent material off surfaces into suspension and they can also breakdown agglomerated particles producing very fine particles which can subsequently pass through filter media. Such particulate is likely to be present in ground handling equipment as well as aircraft tanks and low temperature regimes in the engine. It was therefore postulated that blockage of the LP and HP filters was due to high levels of particulate being generated from AFTSTU supply hardware and filtration units being "cleaned-up" by the +100 additive. Analysis of the filter deposits showed them to be primarily inorganic material and not thermally generated organic material thus confirming the hypothesis. This effect masked any beneficial effect the additive may have had on deposit rates in the system. Subsequent to this discovery, a special system cleaning procedure and replacement of filter elements was instigated prior to each run. Figure 4 shows the result of further testing on Merox +100 following this revised procedure with virtually no pressure differential build up in either the LP (LP3) or HP (HP3) filter units.

The pressure differential rise and deposition attributable to thermal deposition on the HP filter screen and LP filter element during the Hydrotreated JP8 and JP8+100 testing was extremely low in both cases and at the limit that can be reliably measured. These results confirmed the high stability of both the base and additised fuels. This is also

true of the JPTS which accrued over 300 hours without measurable pressure differential rise or mass increase.

HP and LP filters from these tests were retained to provide "dirty" units for future planned clean-up testing. Thus the amount of post test analysis that could be carried out on these units was limited.

Whilst the clean up effect was to some extent expected, the increase in filter blockage highlighted the potential risk associated with +100 additive cleaning up systems and filters and passing the fine particulate down stream. This is particularly relevant during the roll-over of ground based handling equipment and aircraft from JP8 to JP8+100. Thus the operational risks associated with this effect have been highlighted by this work.

This risk and problems associated with disarming of water separator systems means that at the current time +100 additives are being injected close to the skin of the aircraft for USAF operational field trials. Also, based on these results it is generally recommended that new LP and HP filters are fitted when transitioning onto +100 additive use. In field trials filter blockage has therefore not been a problem.

Supplemental tests following this work involving operation of test modules in JP8+100 that had previously been operated in normal JP8, and evidence from other sources indicate that the additive will not remove adherent particles, gums etc in intermediate regimes or carbonaceous deposits from injectors to any significant degree. Whilst the potential of this additive to reduce deposition in engine fuel systems and injectors has been clearly demonstrated by this work, the ability of the additive to clean-up systems with established deposits is still in need of investigation.

As in previous work on the AFTSTU, deposits on these units were similar in terms of morphology and chemical composition to those found in equivalent engine run units.

Nozzle Data

Figure 5 shows an example of 2 contrasting nozzle tube tests to illustrate the build up of deposit over time as determined by inner wall temperature profiles. The effect of the +100 additive can be seen as the drastic reduction of deposit despite both runs being at the same initial inner wall temperature.

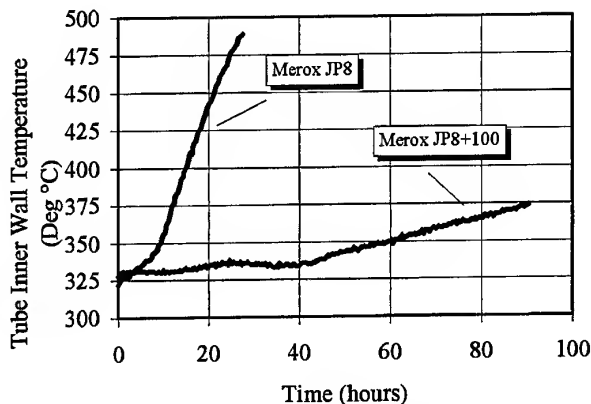


Figure 5 Inner Wall Temperature Rise Profiles For Merox JP8 And Merox JP8+100

Figure 6A and 6B show average deposit rate over nozzle test tube duration expressed as mg hr^{-1} based on carbon burn-off data for the Merox and hydrotreated fuels respectively. The JPTS results are included on both for comparison. Although deposit rate is not always linear this graphical representation clearly illustrates the contrast in deposit rates of the different test fuels under simulated injector nozzle conditions.

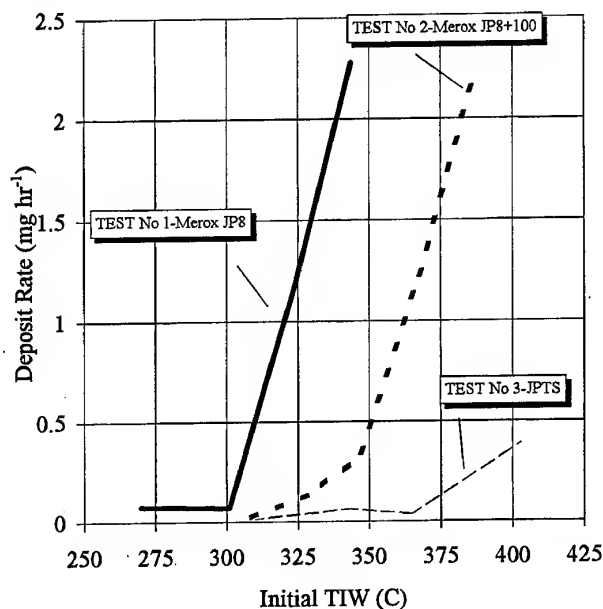


Figure 6A Average Deposit Rates The Merox JP8 And JP8+100

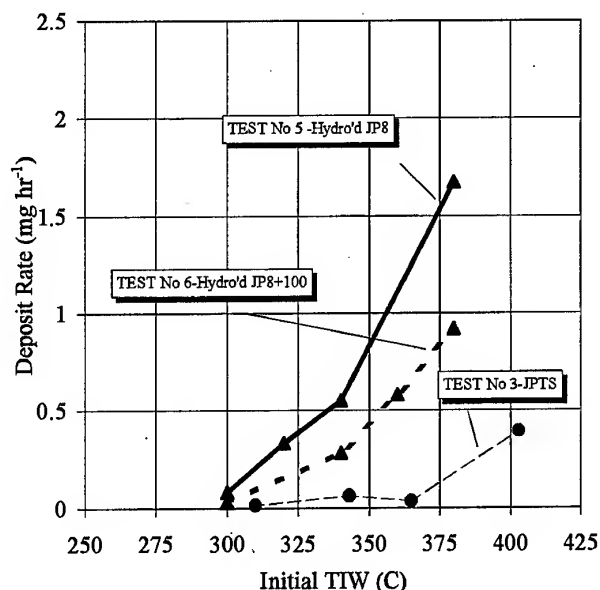


Figure 6B Average Deposit Rates For Hydrotreated JP8 And JP8+100

The base Merox and Merox+100 deposit rate vs initial inner wall (TIW) temperature data shows the characteristic of relatively modest increases with increasing wall temperature at the lower TIW range (see fig 6A). At a given temperature (known to be highly dependent the inherent stability of the fuel) an inflexion in the graph occurred above which deposit rates increased significantly with only small increases in wall temperature. This characteristic inflexion is regularly observed in such testing. The primary action of the additive on Merox fuel was to improve the stability such that this inflexion moved up by approximately 40°C.

Testing on the base Hydrotreated fuel showed lower overall deposit rates for the base fuel compared to the Merox fuel, again reflecting the expected higher inherent stability (see fig. 6B). However, the inflexion appears not as sharp. In the range 300°C to 380°C initial TIW the Hydrotreated base fuel exhibited deposit rates only slightly above those for Merox +100.

Testing on the Hydrotreated +100 showed a similarly broad inflexion as noted for the base fuel. Whilst the presence of the +100 additive improved the thermal stability and reduced deposition rates for each test temperature, this improvement was not as significant as seen with the Merox fuel. In general terms the addition of the candidate +100 additive to the Hydrotreated fuel reduced deposit rates by a factor of 2 over the range of inner wall temperatures evaluated, compared to a factor of 10 reduction for Merox fuel. It is also relevant to note that between 300°C and 350°C the Hydrotreated +100 fuel gave almost identical rates to the Merox +100. Above this the additised

Hydrotreated fuel did offer some advantage. The significant differences in response to the presence of the additive for the two fuel types tested provides clear evidence that additive effectiveness is dependent on the base fuel stability characteristics. This could have ramifications to how JP8+100 is controlled by specifications. For instance, if ultimate stability is required, consideration could be given to controlling the break point of the base fuel to more stringent levels than specified at present. In any case the thermal stability of the base fuel still needs to be controlled to at least current levels.

It is notable that whilst deposit rates are significantly reduced by the candidate additive on test, none of the +100 fuels approach the stability and the associated very low deposit rates of the JPTS reference fuel. This indicates that there is a fundamental limit to how much the stability of conventionally produced kerosine type fuels can be enhanced with this additive technology.

These results indicate that for design purposes the maximum allowable fuel system and injector wall temperatures could be increased for engines operated solely on JP8+100. The key benefits of this include

- Avoiding the need to use air cooling with its associated cost, weight and performance penalties.
- Reducing the need for injector heat shielding and thermal management currently used in more complex designs. This would both reduce cost and weight and also improve integrity by simplicity of construction. Removing the need for external heat shields can also improve aerodynamic performance.

The data also indicates that at lower (< 270°C), more realistic temperatures for current injector designs, deposit rates will be reduced. This provides benefit for existing injectors and reheat systems that currently have service life limits due to carbon build up causing blockage. The use of JP8+100 will extend the period before cleaning is required. Testing so far has been with TIWs in the range 270°C to 360°C to map additive performance whilst keeping test duration manageable. Future testing will be focussed on lower temperature testing to demonstrate and quantify this benefit of +100 additives for more typical injector wall temperatures i.e. circa 200°C.

Conclusions

Testing of a candidate JP8+100 additive in European produced fuels on the RR plc AFTSTU has provided significant insight to its thermal enhancing performance and identified important operational impacts on aircraft and fuel system performance.

The test protocol developed for this programme has enabled direct comparison of thermal stability performance between

two European produced JP8 fuels of contrasting stability both without and with a candidate +100 additive present.

The AFTSTU has demonstrated, in quantitative operational terms, the superior stability of the base Hydrotreated JP8 fuel compared to the Merox JP8.

The presence of the additive improved thermal stability of both fuels. This was demonstrated in several ways:

- Reduction in build up of deposits in HP filter units.
- General decreases in deposit rates in the injector module.
- An increase in the injector inner wall temperature above which deposition rates increased rapidly (inflection).

Stability improvement was more significant with the Merox fuel as measured in the injector module. Specifically, addition of the candidate +100 additive to the Hydrotreated fuel reduced deposit rates by a factor of 2 compared to a factor of 10 reduction for Merox fuel.

This indicates that additive effectiveness is highly dependent on the inherent stability characteristics of the base fuel.

Neither of +100 fuels achieved the performance of JPTS benchmark in terms of nozzle deposition rates indicating that there is fundamental stability limit achievable using this additive technology with conventionally produced kerosene type fuels.

Testing identified the potential risks associated with the detergent/surfactant action of the additive cleaning ground based equipment and subsequently presenting high levels of particulate to the engine inlet. This is particularly relevant during the roll-over of equipment from JP8 to JP8+100.

Test results also demonstrated that future systems designed and operated exclusively on JP8+100 fuels could operate with higher bulk fuel and wetted wall temperatures without undue deposition occurring providing key benefits in terms of cost weight and performance.

Deposit rates are also reduced at lower temperatures, more representative of current systems and injectors. This has the potential to reduce maintenance of injectors and other high temperature components that have service limits due to effects of fuel thermal deposition.

Future Studies

Further work is planned both to develop the AFTSTU capability and to evaluate alternative candidate+100 additives.

Specifically, additional modules have been designed (in some cases fitted and operating) to enable the AFTSTU to evaluate fuel and fuel/additive combinations under a wider range of test conditions and in alternative modules representing other key fuel system components. These include:

- Stiction Module (stiction and hysteresis in close tolerance sliding components).
- Reheat Module which simulates and measures deposition rates in the intermittent flow and high temperature regime in reheat manifolds, reheat igniter systems (hot shot injectors) and also low/zero flow phases of staged injector systems.
- Dry Low Emissions Injector Module that will model the environment present in proposed injector designs.
- AFTSTU development to simulate mission cycling and fuel recirculation with the fuel system.

With respect to JP8+100 work further testing is planned to encompass the following

- Evaluation of the current candidate additives under a wider range of conditions and extended durations.
- Evaluate the stability enhancing performance of other additives including a European produced version.

Acknowledgements

This work was conducted under UK MOD/DERA funding. The authors wish to acknowledge that with out this funding and the support and assistance of Mr P Brook (DERA) the work would not be possible.

References

1. Research and Development of High Thermal Stability Fuels. T Edwards, W M Roquemore, W E Harrison S D Anderson (USAF Wright Laboratory). Paper presented at an AGARD meeting on "Fuels and Combustion Technology for Advanced Aircraft Engines", May 1993.
2. Advanced Jet Fuels - JP4 Through JP8 And Beyond. W E Harrison III (USAF Wright Laboratory), S P Heneghan, D R Ballal University of Dayton, H C Mongia GE Aircraft Engines. Paper presented at the International Gas Turbine and Aeroengine Congress, June 5-8 1995. ASME No 95-GT-223.
3. Prospects for JP8+225, A Stepping Stone to JP900. T Edwards AFRL/PRSF. Extended Abstract for 98 AIAA Joint Propulsion Conference kindly supplied to RR Plc by the author on 6 Nov. 1997.

4. The Effect of Detergent / Dispersant on Aircraft Materials, Program Overview of Fuel and Fuel System Material Compatibility Studies, JP-8+100 Thermal Stability Additives, D H Kalt, presented to SAE/AE-5 Committee, 9/10 April '98.

5. 'F119 Combustor Tests at ETAL and X-960 Test Facilities using JP-8 +100 Fuel', Ted Biddle, United Technologies Corporation, Pratt & Whitney, West Palm Beach, Florida, prepared under contract no. F33615-93-C-2301 for Air Force Wright Laboratory, 8.5.95.

Bibliography

The Thermal Stability Of Fuels At 480°C (900°F). Effect Of Test Time, Flow Rate And Additives. T Edwards (Wright Laboratory) and J Krieger (University of Iowa) Paper presented at the International Gas Turbine and Aeroengine Congress, June 5-8 1995. ASME No 95-GT-68.

'Development of an Advanced JP-8 Fuel', Ted B Biddle, United Technologies Corporation, Pratt and Whitney, West Palm Beach, Florida, WL-TR-94-2033, December 1993.

'JP-8+100, The Development of High-Thermal-Stability Jet Fuel', S P Hennegan, S Zabarnick, D R Ballal, University of Dayton, W E Harrison III, WPAFB, Trans ASME, Vol.118, pps170-179, September 1996.

'JP-8+100 Development', Charles L Delaney, WPAFB, presentation to SAE, New Orleans, April 1998.

PAPER No. 45
Bullock, Hobday & Lewis
(presenter: C. Lewis)

Question 1: Capt. G. Adamopoulos, Royal Hellenic Air Force, Greece

With respect to JP-8+100 loosening deposits in a dirty fuel supply system and the downstream engine filters then catching these loosened deposits and becoming blocked, would it not be enough just to change these filters?

Answer:

The current practice is to inject the additive as close to the aircraft skin as possible, and therefore, the clean-up effect of the addition is largely not relevant. The reason that the additive package is injected where it is is because it contains surfactants that disarm the fuel system water separators.

Question 2: Prof. Dr. H. Weyer, DLR, Germany

Do the radicals produced in the fuel during the clean-up action of the additive package have any effect on fuel quality? Also, does the additive have any effect on the engine emissions?

Answer:

There is not direct impact on emissions. However, clean-up of the fuel system, and coke deposit removal from fuel injectors, for example, allows the system to operate as it was designed to do. This restores "as new" performance, and can result in less exhaust smoke, which normally tends to increase if the fuel spray becomes distorted by coke.

Question 3: P. Kotsiopoulos, Hellenic Air Force Academy, Greece

In your rig, did you investigate potential problems likely to be encountered in transients, during engine start-up and shut-down, where hot-soak might be involved? In our experience, it is here where deposits form.

Answer:

We have not done such testing. However, the USAF has conducted laboratory and rig tests, together with some service experience, on augmentor fuel manifold blockage due to hot-soak following afterburner shut-down. This has been a major service problem. JP-8+100 cures this, and this has been a major triumph for the additive package.

Question 4: P. Kotisopoulos, Hellenic Air Force Academy, Greece

Does JP-8+100 clean up engines that have dirtied by previous operation for a long time on JP-8?

Answer:

Engine fuel systems can be roughly divided into lower pressure (LP) component systems and high pressure (HP) component systems. The additive has a clean-up effect on the LP part of the system. This is because the deposits formed in the fuel are soft and result from loosely attached particles. Any detergent would tend to remove them, and the additive

package does contain detergents. In the HP part of the system the deposits are hard, and the detergents in the additive package are not strong enough to remove them. JP-8+100 is not a cleaning fluid! Carbon deposits in the combustor and coke deposits on the fuel injectors tend to be removed since they are produced from the flame.

Question 5: P. Kotisopoulos, Hellenic Air Force Academy, Greece

Some users insist that after about 50 hours operation on JP-8+100, dirty engines are cleaned.

Answer:

Yes, combustion-generated coke and carbon deposits are removed, sometimes, and there is a general improvement on engine operation.

Catalytic Combustion Concepts for Industrial Gas Turbines

From microWatt to MegaWatt

J.M. der Kinderen and R. van Yperen

GASTEC N.V.

P.O. Box 137

7300 AC APELDOORN

The Netherlands

1. SUMMARY

The desire to reduce pollutants, e.g. oxides of nitrogen (NO_x), carbon monoxide and unburned hydrocarbons, from gas turbine exhausts has stimulated the research into the use of catalytic combustion systems. These systems have the potential to minimise emissions of the above pollutants and have the added advantage of greatly reducing combustion induced vibrations, to which conventional low emission combustion systems are prone.

The development of a catalytic combustion system for gas turbines was one of the goals in the Brite EuRam project BRE2-CT92-0309 (Catalytic Combustion Systems for Pollutant Suppression in Industrial Gas Turbines, Reformers and Radiant Heaters). Durable high temperature catalytic combustion systems, which were optimised for the combustion of natural gas in the temperature range of 700 to 1500 K, and suitable for incorporation into ultra low emissions combustion systems for high pressure ratio, high efficiency industrial gas turbines were researched. In order to meet typical combustion requirements, a multi-stage catalytic combustion system incorporating a pre-burner, one or more catalysts and a homogeneous reaction zone was envisaged. A catalytic high pressure test rig was built, which was capable of testing at a maximum of 20 - 25 bar and an outlet temperature of 1600 K. Tests showed that it was possible to reach a 100% conversion of methane with hardly any CO and NO_x in the outlet stream. However, further research is required to investigate new or improved high temperature catalyst

systems with high activity and excellent thermal stability and integrity.

2. INTRODUCTION

World-wide environmental awareness has led to more stringent legislation restricting the discharge of exhaust pollutants, such as, oxides of nitrogen, carbon monoxide and unburned hydrocarbons. The basic problem with conventional combustors is that they contain flames of various types, in which the pollutants, especially oxides of nitrogen, are formed. In conventional combustors only limited improvements are possible, e.g., by lean burn or steam injection techniques. The ultimate way ahead is therefore to eliminate the flames in combustors, which is theoretically possible by using catalytic surface combustors, which use fundamentally different chemistry.

Catalytic combustion systems have the potential to minimise the above mentioned emissions. Furthermore, they have the added advantage of greatly reducing combustion induced vibrations, to which conventional low emission combustion systems are prone.

Traditional catalytic combustion systems, however, have operated at conditions very remote from those required for industrial gas turbine application. The operational boundaries need to be expanded in the areas of space velocity, thermal stress and durability of materials, operating temperatures and pressures. In addition, the light-off temperatures need to be lowered.

Therefore, durable high temperature catalytic combustion systems have to be researched, which have to be optimised for the combustion of natural gas in the temperature range of 700 to 1500 K and suitable for eventual incorporation into ultra low emissions combustion systems for high pressure ratio, high efficiency industrial gas turbines.

In the framework of the Brite EuRam project BRE2-CT92-0309 (Catalytic Combustion Systems for Pollutant Suppression in Industrial Gas Turbines, Reformers and Radiant Heaters) the possibility to use catalysis in industrial gas turbines was investigated. The aim of this four year project, which started in November 1992, was to research novel catalytic combustion systems, focused on gas turbines (used for power generation and mechanical drive) in order to achieve ultra low exhaust emissions when operating on natural gas fuel.

The targets regarding the emissions for the gas turbine concepts were:

Oxides of Nitrogen: < 5 vppm
Carbon Monoxide: < 5 vppm
Unburned Hydrocarbons: < 5 vppm

To achieve these objectives, the research was divided into three major tasks [1], including one covering management (GASTEC, co-ordinator). These technical tasks were:

- Task A Supply, Characterisation and Optimisation of Catalysts and Materials
- Task B Process Technology
- Task C Reactor Concept Testing and Quantification of Catalytic and Homogeneous Combustion Reactions

A block scheme of these tasks including their mutual interaction is given in figure 1.

The objectives of Task A were to produce and deliver the agreed catalyst samples for the concept tests using the state-of-the-art technology and to start with new developments. The most promising samples were characterised in detail to obtain the necessary information for Tasks B and C (e.g. kinetic data for Task B and light-off temperatures for Task C). New developments were especially focused on the improvement of

low temperate catalysts (precious metal based catalysts) and also on the research on new materials for the high temperature catalysts (transition metal catalysts). The low temperature catalyst has to operate in the temperature range of 700 to 1050 K and the high temperature catalyst in the range of 1050 to 1200 K. Above 1200 K it is assumed that the remaining gas/air mixture will ignite itself and a catalyst is not needed.

The objectives of Task B were to deliver validated computer models as a tool for the evaluation of different concepts for the gas turbine. The models had also the capability to evaluate whether it is worthwhile to scale up new catalyst formulations for further testing in the time consuming and expensive to operate large test rigs. In future these models are to be used as a reliable tool to design different commercial applications.

To compile these reliable models, extra information on physical parameters and correlations was required of the catalytic as well as of the homogeneous gas phase combustion process. This information was supplied by the different partners. To validate these models, the results of the concepts tested in Task C were used.

The choice of the catalyst and materials used in the different concepts were those selected in Task A. During the test programmes in Task C, results from the models were also used to modify and improve the initial concepts.

The first objective of Task C was to design and build different test rigs, which were capable of simulating typical operation conditions of commercial gas turbines in which the catalysts and new materials have to operate.

The second objective was to design, build and test different concepts, which had the potential to be successful in achieving the desired emission levels as described above for the commercial applications. The starting point of these objectives was the knowledge obtained in Tasks A and B. Finally, the results obtained with the different concepts were also used to validate the different computer models developed in Task B.

During the project approximately 300 different catalyst samples were produced and pre-tested by the different laboratories. In this paper only a few samples are discussed to

show the route from producing small amount of catalysts, pre-test (microWatt) followed by computer modelling, upscaling and finally tests in a large test rig (MegaWatt), capable of creating realistic gas turbine atmospheres (pressures, temperatures and velocities).

The project was successfully concluded with the following results:

- New catalyst formulations
- Qualification of optimised catalyst/carrier/support combinations
- Quantification of the effects of pressure and temperature on catalytic combustion processes
- Establishment of the links between catalytic and homogeneous combustion
- Computer models, validated by test rig results, describing the catalytic and homogeneous combustion processes for the chosen concepts

These different items resulted in an improved technology based on catalytic combustion and its introduction into the development for different applications involving the catalytic combustion of gaseous fuels.

The total project was undertaken with eleven organisations that are located in five different countries of the European Community. These organisations are:

GASTEC (the Netherlands)

Krebsöge (Germany)

RRIMGT (United Kingdom)

Bettini (Italy)

Degussa (Germany)

AEA Technology (United Kingdom)

Gaz de France (France)

University of Bath, Prof. S.T. Kolaczowski (United Kingdom)

Nederlandse Gasunie (the Netherlands)

LACE, Prof. M. Primet (France)

University of Utrecht, Prof. J.W. Geus (the Netherlands)

3. CATALYTIC COMBUSTION FOR GAS TURBINES

3.1 Conventional combustion systems versus catalytic combustion systems

Conventional natural gas combustion systems are characterised by high reaction temperatures. As an example, the build-up of a conventional gas turbine and the temperature levels at different axial positions are illustrated in figure 2a and 2b [2].

The temperature of the air is raised due to the compression step (C) to a level of 573 to 673 K. The compressed air is, subsequently, fed to the combustion chamber. After injection of the fuel, the combustion reaction ignites and the temperature increases up to 1773-2273 K, depending on the fuel content. At these temperatures, large amounts of nitrogen oxides can be formed. The inlet temperature of the turbine section (T) cannot be higher than 1373 to 1573 K without avoiding damage to the turbine wheels. Fresh, relatively cold air is bypassed to the outlet of the combustion chamber to decrease the temperature of the combusted gas to a sufficiently low temperature.

To abate air pollution by emission of exhaust gases without using catalysts, two procedures have been proposed [3,4]. The first procedure involves the ignition of a rich mixture, a quick quench with air and a subsequent lean burn. During the ignition of the initial rich mixture, no nitrogen oxides are formed, while during the following lean burn combustion the temperature remains thus low that nitrogen oxides are not produced either. The problem associated with this approach is the transition from rich to lean conditions through the stoichiometric point. The transition should be sufficiently rapid to prevent high temperatures, which favour the formation of thermal NO_x .

The other procedure for minimising NO_x emissions uses a thus lean premix burner that the temperature remains sufficiently low to avoid the formation of large amounts of thermal nitrogen oxides. In order to prevent locally high temperatures, extremely well mixing of the fuel and air is required. With lean premix burners, however, the stability of the combustion process is not sufficient.

A problem associated with lean combustion systems is that, although NO_x emissions can be minimised by lowering the combustion temperatures, complete burn-out of carbon monoxide calls for high reaction temperatures. At low temperatures, high CO emissions result due to flame instability. Although the levels of CO and NO_x emissions can be minimised by adjusting the combustion temperature, zero emissions of both compounds is impossible.

The problems encountered in conventional combustion systems can be solved by means of the utilisation of a catalytic combustion system. Figure 3a shows a schematic representation of a catalytic combustor for gas turbines and figure 3b the corresponding temperature levels at different axial positions.

With catalytic combustion complete conversion of methane can be achieved at fairly low temperatures, viz., 1373-1573 K, thus avoiding formation of thermal NO_x . In contrast to conventional combustion processes, furthermore, only carbon dioxide is formed when the reaction is performed catalytically. Another advantage of catalytic combustion is that the combustion process is highly stable for a wide range of fuel/air ratios, resulting in significant noise reduction with respect to homogeneous combustion processes. Noise reduction is attractive not only for environmental reasons, but also in order to minimise the attrition of combustor rigs due to vibrations occurring as a result of combustion instability in conventional combustion processes.

3.2 Catalytic combustor design for gas turbines

Figure 4 [5,6,7,8] shows a schematic representation of a staged catalytic combustor for application in gas turbines. This "hybrid" combustor has been proposed in many of the studies dealing with catalytic combustion in gas turbines. Catalytic combustion in gas turbines is characterised by extremely high linear velocities, high pressures (up to about 30 bar), and a very broad temperature range (523-1773 K). Owing to the high linear velocities, the light-off temperature of catalysts for gas turbines is much higher than that exhibited within other applications, typically 773 K and 473 K, respectively. Although the temperature of the gas is raised during the compression stage, the temperature of the gas flow is not sufficiently high to light-off the catalytic reaction,

especially when the turbine runs at low power (idle: 40% power). Therefore, a pre-burner is required to heat the fuel/air mixture by burning a part of the total fuel.

In order to prevent locally high temperatures in the catalyst zone, the catalyst feed is passed through a set of static mixers. Highly inhomogeneous radial temperature distributions in the catalyst sections are observed if the methane and air are not thoroughly mixed.

The catalytic zone has to operate over a wide range of conditions and, especially, at an extensive range of temperatures. If a low temperature at the inlet of the catalyst structure is aimed at, a highly active catalyst is required. Since the ignition of the homogeneous gas-phase reaction may occur only at high temperatures, the section at the end of the catalyst structure must be highly thermostable. Moreover, poor transport of thermal energy from the catalytic surface to the gas stream, resulting in high temperatures of the catalyst surface, has been observed. As a result, the final catalyst temperature may be far above 1200 K.

The final stage of the combustor is the homogeneous gas phase combustion zone, in which the remaining part of the fuel is combusted. Although the ignition temperature of the homogeneous reaction is well known for atmospheric conditions, the temperature of ignition under actual gas turbine conditions is still unclear. A more thorough knowledge of the ignition of the gas phase reaction after the catalyst section is highly important for the establishment of the catalyst temperatures which are required for efficient ignition of the homogeneous gas phase reaction.

3.3 Structure of the catalyst systems

There are different geometric structures possible in which a catalytic system can be produced. For catalytic combustion in gas turbines there is a general agreement that monolithic structures exhibit superior properties due to the combination of a low pressure drop and a relatively high geometric surface area (see figure 5a and 5b) [9,10,11]. Inside these honeycomb-like structures, a thin layer of a high surface area material is applied. The catalytic activity is created by impregnation of this thin layer with a catalytically active metallic material, such as, palladium and or platinum. After drying and high temperature treatments one obtains a very thin porous layer

inside the monolith, exhibiting a high internal surface area (approximately 50-100 m²/gr): This results for a one litre monolith size in an internal surface area of about 20.000 m² (three times a football field). Approximately 10-20% of this surface is covered with the catalytically active metallic compound. For the high temperature catalytic systems the washcoat layer itself exhibits the catalytic activity.

Application of metallic as well as ceramic monoliths are possible. The metallic monoliths have the advantage of a high thermal shock resistance and mechanical strength. The disadvantage is the weak adhesion of the washcoat layer which results in blowing off this layer at high gas velocities and temperatures. Another disadvantage of the metallic monoliths is that they are difficult to handle for further characterisation and tests in small laboratory equipment. Especially this last reason gave the preference to focus the research on ceramic structures.

4. APPROACH OF THE PROJECT

The question is whether catalyst washcoat materials developed on a small scale in a laboratory are suitable to be placed inside a turbine of approximately 100 MegaWatt (gas input).

4.1 Approach

To solve this question there are different possible routes.

The shortest route is going directly to expensive testing in a large and expensive test rig to simulate real gas turbine conditions.

This can be done by simply upscaling and coating the catalyst washcoat material on a monolith by a catalyst manufacturer, followed by testing in the large test rig in which one tries to create conditions similar to a gas turbine. This expensive and time consuming route will only give you the answer yes it will, or no it will not. This trial and error method will hardly give insight into the reasons why. Even before placing the monolith structure inside the test rig typical questions have to be solved such as:

- Which active material should be used?
- How much washcoat material must be present inside the monolith?
- What is the maximum allowable layer thickness?
- What must be the diameter of the monolith?

- What must be the length of the monolith?
 - What is the ignition temperature of the catalyst under these circumstances?
 - Is an extra low temperature catalyst or pre-burner needed?
- Finally every (small) improvement of this catalyst must be checked by this trial and error route.

Another route is to define precisely the activity of the catalytic washcoat material using relatively cheap microflow reactors, followed by a pre-selection using modelling before upscaling and finally to perform tests in the expensive test rig under realistic engine conditions.

Besides this activity expression obtained from the microflow reactor, the computer models must also be fed with realistic physical data, such as, diffusion limitations inside the catalytic washcoat layer and proper heat and mass transfer correlations describing the transport of heat and gaseous components from and to the catalytic walls inside the monolith channels. Validation and fine tuning of the models is done by further detailed experiments inside the microflow laboratory reactor as well as a few realistic tests in the pilot plant test rig.

4.2 Pre-tests and characterisation of the washcoat

The washcoat materials including the active components were intensively examined after severe conditions, such as, exposure to high temperatures, velocities and methane concentrations. The structure changes and the adhesion of the washcoat to the monolith walls were examined by, among other things, electron microscope techniques. After every test (treatment) the catalytic activity of the material was measured using microflow reactors under defined standard conditions.

A typical example of a standard activity test of an iron based catalyst is given in figure 6 [12].

This catalyst was produced in small quantities by the University of Utrecht and all the tests were performed in a microflow reactor at their own laboratory. The activity is determined by measuring the methane conversion at different temperatures under standard conditions. This for high temperature purpose developed iron based catalyst, shows after a high temperature heat treatment, a slight decrease in activity. This decrease in activity can be explained by the so-

called sintering of the washcoat layer resulting in a decrease of the surface area. Using a special technique this surface area can be determined. The results are given in figure 7.

A closer look at these two figures shows that the decrease in surface area is of the same order of magnitude as the decrease in activity. The activity has decreased about 25% while the surface area decreased about 30% (so one football field less).

4.3 Microflow reactor (500 microWatt)

The microflow reactor [12,13] consists of a small quartz reactor tube placed in an electrical furnace (see figure 8). A sample of 0.25 gram of the catalytic active washcoat material is placed between two beds of inert material of a length of about 0.5 cm (quartz, 0.15-0.50 mm). The function of the quartz bed on top is to heat the gas efficiently to the required temperature. The inert material downstream the catalyst section minimises the contribution of gas phase reactions taking place in the post-catalytic space.

The standard activity was tested by heating the catalyst in a total flow of 100 ml/min containing 1 vol.% methane and 4 vol.% of oxygen in nitrogen from 623 to 1223 K and back downwards to 623 K.

Besides this standard activity test, a complete kinetic rate expression can be obtained, which is needed to incorporate into the computer models.

The kinetic rate expression describes the dependence of the activity (defined as the amount of methane converted per gram of active washcoat material) on the concentration of different components in the gas phase, on the temperature and finally on the total velocity and pressure inside the system.

To determine this kinetic rate expression of a specified catalyst sample, special requirements on the isothermal behaviour of the microflow reactor are needed. Isothermal behaviour means that temperature rise caused by catalytic combustion of methane must be eliminated. This can only be reached by very small amounts of catalysts and low concentrations of methane in combination with low gas velocities. This results in a maximum heat production caused by the catalytic reaction of approximately 500 microWatt, which does not affect the temperature inside the microflow reactor.

4.4 Megaflow reactor (pilot plant test rig)

As already mentioned before, the intention of the project is to predict whether a certain catalyst sample is of interest for a 100 MegaWatt gas turbine. To check the outcome of the microflow reactor in combination with the models, an extra reference point in the scale of 500 microWatt to 100 MegaWatt is needed. This reference point is measured in a large pilot plant test rig of approximately 15 meters length and an external diameter of 0.5 meters. A detailed scheme of the external pressure casing is given in figure 9 [14].

The total test rig was built in two stages. The first test rig, in which only the catalyst samples could be tested at lower pressures and velocities, was built by Gasunie. Later, the test rig was upgraded by RRIMGT to fulfil all requirements to simulate a complete engine.

The test rig comprises a 42 kW electric heater in the inlet, a working section to accommodate a pre-burner, static mixers and up to three, one inch diameter by three inch long monolithic catalysts, an exhaust gas phase reaction duct and a closed circuit water cooled heat exchanger, to cool the exhaust gases to below 400 K. The maximum exhaust temperature is limited to 1600 K.

Also introduced was an axially traversal probe to enable more detailed quantification of the homogeneous gas phase reactions downstream of the catalysts.

Great care was taken, at the design stage, to minimise heat losses from the catalysts and prevent any gases bypassing them. Each catalyst monolith was sealed in a low density (Mullite) cylinder surrounded by a similar loosely fitting second cylinder to minimise heat losses. Eight thermocouples were fitted to each catalyst; two to measure catalyst inlet and outlet gas temperatures and six to measure monolith passage wall temperature. Figure 10 shows how these subassemblies were supported inside the test rig. It also shows how the gas samples were extracted with the option of water cooling.

The use of sonic orifices to control and measure the inlet air, ensured very stable rig inlet conditions.

Experiments were carried out at pressures up to 30 bar and gas outlet temperatures up to 1600 K. The air flow rate varied between 30 and 145 m³/hr.

In the electrical heater (42 kWe) the air was heated to the desired inlet temperatures (< 950 K). Higher inlet

temperatures up to 1100 K could be reached by using the combination of an electrical heater and a pre-burner. Natural gas or pure methane was injected behind the pre-burner just in front of the static mixers.

The first experiments inside the first test rig were performed using only one static mixer. However, the initial experiments at very lean combustion mixtures (less than 1 vol.% methane in air) resulted in a very fast deactivation (seconds) of the catalyst system even at low conversions. Visual examination after the tests showed local holes surrounded by melted ceramic material. Very high temperatures are needed to create such damage. As these temperatures cannot be reached using these air/fuel ratio's, the only explanation left is unmixed air/fuel. After placing a second mixer the problem was solved. Using this test rig, virtually all possible combinations of air/fuel ratio's, pressures, temperatures and mass flows could be chosen, representing operating conditions similar to a 100 MegaWatt gas turbine in the idle, 40% power till 100% full power range.

The pre-burner was used to create higher inlet temperatures up till 1100 K to test the performance of the high temperature catalyst systems.

4.5 Models

At the beginning of the project a more simple model [15,16] was developed, which was later, when more experimental data became available, continuously updated. In this model both heterogeneous (catalytic) and homogeneous (non catalytic) reactions were modelled.

Since the bulk flow of the gas mixture is extremely high in the channels of the monolith, heat transfer by convection is the principal method of heat transfer. Radiation and conduction were therefore neglected in this model. The catalyst support was made from ceramic with square shaped channels. The equations for the model were derived from heat, mole and momentum balances describing the heat flow and mass flow of the gas mixture in the monolith channels. The kinetic rate expression describing the specific catalytic reaction rate of a certain catalytic washcoat material was obtained by experiments performed in the microflow reactors.

5. RESULTS AND CONCLUSIONS

Different configurations and combinations of catalyst materials were examined. Two configurations, one to validate the model for a low temperature catalyst system and the second to validate the model for a high temperature catalyst system are discussed in further detail.

5.1 Low temperature catalyst system

These highly active precious metal based catalysts have a maximum allowable operating temperature of approximately 1000 K. Higher temperatures cause severe deactivation of the material.

The ignition temperature of these materials lies in the range of 750 to 850 K.

A schematic illustration of the experimental set-up in the pilot plant test rig is given in figure 11 [17].

Air is preheated by the electrical heater up to 357 K and behind the heater part of the fuel ($fr = 0.625$) is added to serve the pre-burner. The pre-burner causes a temperature rise of the gas mixture up to 896 K and the remaining fuel is added. This temperature is sufficient to ignite the catalyst system. The catalyst system consists of two monoliths placed in series, both with a length of 0.07 m and an open space of 0.005 m in between. Inside the monoliths several thermocouples are placed to measure the temperature of the washcoat layer. Two thermocouples are placed to measure the gas temperature leaving the first and second monolith.

The results are given in figure 12. In this figure the temperatures inside the catalytic system are given as a function of the axial length of the catalytic system. As can be observed, the wall temperature (washcoat material) of monolith number one increases from 877 at the heart of the monolith to 950 K at the end. The gas temperature increases only with 27 to 904 K. Inside the second monolith, the gas temperature increases with an extra 50 to 953 K. The wall temperature of the second monolith at the end is approximately 1000 K which is the maximum allowable temperature of this catalyst material. The two lines given in the figure present the outcome of the computer model containing the proper kinetic rate expression obtained by the microflow reactor. As can be observed, almost a perfect match

of the temperatures is obtained for both the washcoat material and for the gas mixture. The figure also illustrates a remarkable effect at the entrance of the monoliths, which is also predicted by the model. At the inlet of the monoliths there is a higher rate of heat transfer from the washcoat layer to the gas mixture. By modelling circular channels this effect is relatively neglectable. However, as the shape of the channels is square (which will create flow instabilities) and neither the heat flux nor the wall temperature were constant, the thermal boundary layer is never completely developed. The model simulates this effect by varying the heat transfer coefficient asymptotic from a high value at the entrance to a lower value at the outlet (that corresponds to the value of a fully developed flow).

As the outlet gas temperature is not higher than 960 K, no homogeneous gas phase reaction was predicted nor observed. So, 100% methane conversion could not be reached with this system.

5.2 High temperature catalyst system

To obtain 100% methane conversion the gas temperature must be raised further. This can be done by using a high temperature catalyst material. The advantage of this material is that it can stand higher temperatures to a maximum of 1400 K. The problem is that these catalysts require high temperatures for light-off.

To create a stable gas inlet temperature and gas composition, it was decided to raise the temperature during the test experiments only by using the pre-burner without the low temperature catalyst system. The high temperature catalytic system consists again of two monoliths in series. The results are given in figure 13 [17]. As can be seen from the figure, again a close match of the model with the experimental data is obtained.

Using this system, the gas mixture temperature could be raised from 1020 K to 1120 K which is sufficiently high to start the homogeneous gas phase reaction. This is illustrated in figure 14. In this figure the methane conversion in the gas phase zone is given as a function of the distance downstream of the second monolith exit.

By a catalyst fuel air ratio of 0.0055 and a catalyst exit temperature of 1103 K the homogeneous gas phase reaction

starts to run and at a distance of 450 mm from the second monolith a methane conversion of 35% is measured.

Using this experimental configuration (pre-burner plus two high temperature catalysts in series and a homogeneous combustion zone of 450 mm), the whole range of operation conditions of a real 100 MegaWatt engine from 40% to 100% power were experimentally simulated. The results of these experiments are summarised in figure 15.

As is evident from this figure, only 100% conversion could be reached at the condition corresponding to 100% power of the engine, but the contribution made by the high temperature catalysts was very small at only 5%. A maximum temperature at the outlet of 1540 K was reached. At this condition no CO and only NO_x produced by the pre-burner was measured. So, the catalytic combustion process as well as the homogeneous combustion process are clean from CO and NO_x . Unfortunately this condition could not be reproduced as the catalyst system deactivated during experiments. This deactivation was mainly caused by a loss of the washcoat material from the monolith walls.

At the other operation conditions of the engine, the contribution of the high temperature catalytic system to the total combustion process must be raised to higher percentages (e.g. 20% at the idle 40% power case) to obtain 100% methane conversion. This can be achieved by increasing the length (amount) of the catalyst system. As the weight of the total catalyst system is approximately 100-150 gram/MegaWatt, no problems are expected by increasing the amount of the catalyst which is negligible in comparison with the total weight of the engine. But it might give problems concerning the total pressure drop across the catalytic system. The configurations tested resulted in an increase of the pressure drop of approximately 1% in relation to the total pressure drop of a conventional engine. As no more than 3-4% is acceptable, an increase of the pressure drop of the catalytic system might cause problems.

The other solution is to improve the activity, mechanical and thermal stability of the catalytic washcoat layer. Because of time constraints of the project, this item remains a future challenge for the universities and catalyst manufacturers.

6. GENERAL CONCLUSIONS

With the tools (small and large test equipment and models) developed, knowledge obtained and the created international network during this project, it is now possible to search more efficiently for new catalyst materials and predict whether these materials are of interest for further upscaling and testing for gas turbine applications. Also knowing the kinetic rate expressions and maximum allowable temperatures of already existing catalytic washcoat materials in combination with the available models, gives us the possibility to design different concepts for different gas turbine applications.

Literature

- [1] Work Programme Brite EuRam II project no. 5846
- [2] Zwinkels, M., Ph.D. Thesis, Royal Institute of Technology, Stockholm, Sweden
- [3] Mijnaerends, H., Polytechnisch Tijdschrift, September 1994, 54
- [4] Koopmans, J.J.M., TVVL Magazine, August 1996, 12
- [5] Furuya, T., et al., ASME Paper 87-GT-99 (1987)
- [6] Sadamori, H., et al., Catalysis Today 26 (1995) 337
- [7] Dalla Betta, R.A., et al., Catalysis Today 26 (1995) 339
- [8] Griffin, T., et al., Combust. Flame 101 (1995) 81
- [9] Geus, J.W., and Van Giezen, J.C., Catalysis Today, to be published
- [10] Irandoust, S., and Andersson, B., Catal. Rev. Sci. Eng. 30 (1988) 341
- [11] Cybulski, A., and Moulijn, J.A., Catal. Rev. Sci. Eng. 36 (1994) 179
- [12] Van Giezen, J.C., The Catalytic Combustion of Methane, Thesis, Utrecht University, The Netherlands, 1997
- [13] Artizzu, P., Garbowski, E., and Primet, M., Thesis, LACE, France, 1996
- [14] Der Kinderen, J.M., Mulder, A., Final Technical Report, Gastec, Brite EuRam II project no. 5846, 1997
- [15] Kolaczowski, S.T., Awdry, S., Technical Reports: RST11, RST17, RST21 and RST28, Brite EuRam II project no. 5846, 1992-1996
- [16] Hayes, R.E., Kolaczowski, S.T., Introduction to Catalytic Combustion, 1997
- [17] Wood, B., RRIMGT RST28: Final Report on Task C, Brite EuRam II project no. 5846, February 1997

Acknowledgement

The authors wish to thank for the fruitful co-operation and contribution of each member of the project team consisting of approximately 30 persons representing 11 organisations of different disciplines located in five different countries of the European Community.

The members of the project wish to thank Dr. Campogrande for his valuable advice and guidance throughout the project and the European Commission for the financial support.

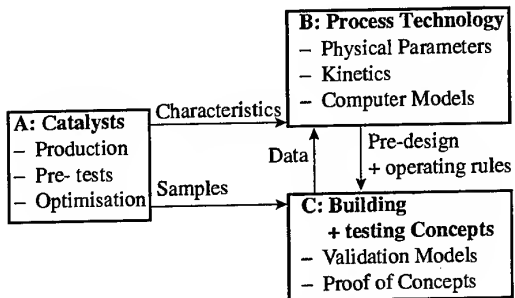


Figure 1: Block scheme of the different technical tasks

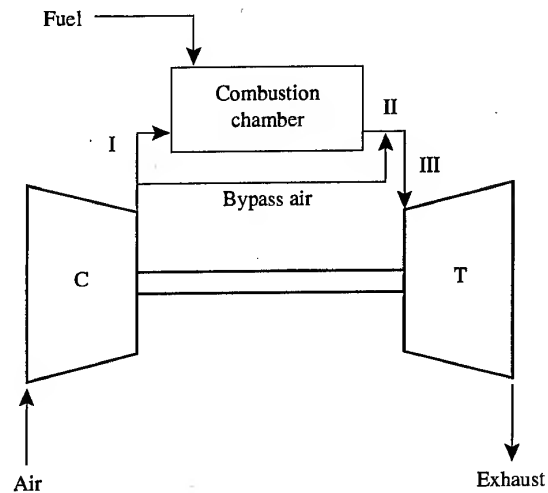


Figure 2a: Schematic representation of a conventional gas turbine

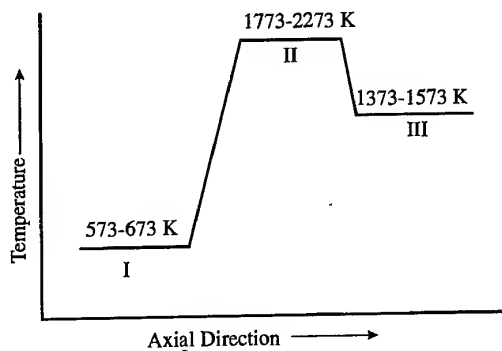


Figure 2b: The temperature levels in the axial direction

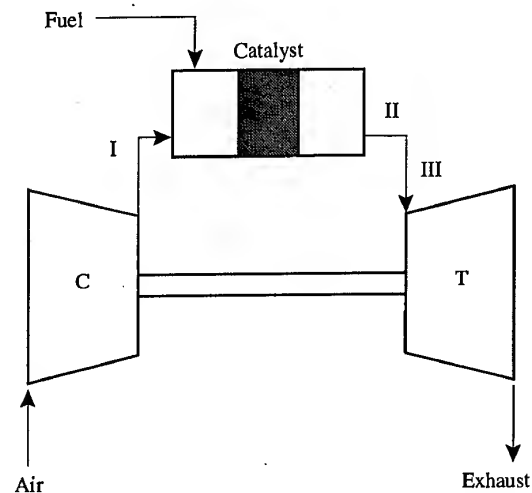


Figure 3a: Schematic representation of a catalytic gas turbine

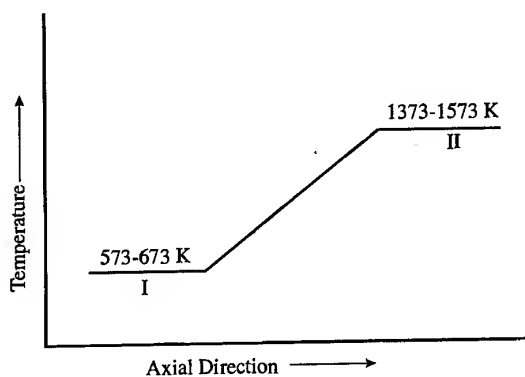


Figure 3b: The temperature levels in the axial direction

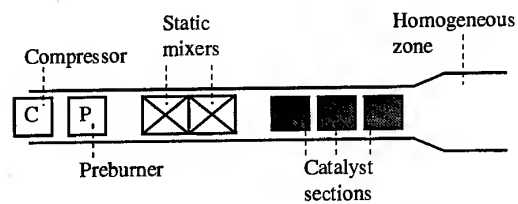


Figure 4: A schematic representation of a catalytic combustor for gas turbines

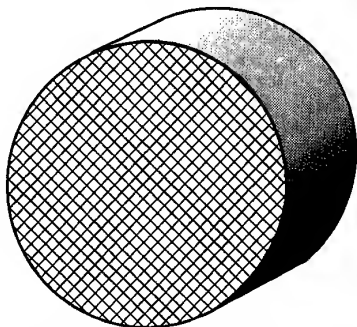


Figure 5a: End view of a 177mm diameter section, channel size approximately 1.1mm x 1.1mm.

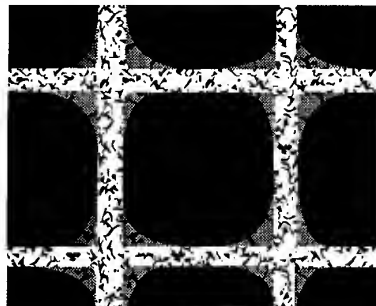


Figure 5b: Scanning electron micrograph of the face of a monolith coated channel, Photograph GASTEC

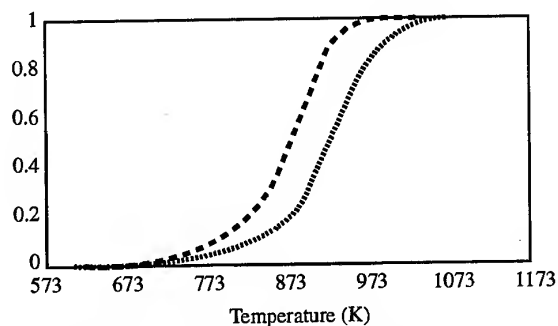


Figure 6: Conversion plots of the 16.5 wt% $\text{Fe}_2\text{O}_3/\text{La-Al}_2\text{O}_3$ catalyst prepared by impregnation with iron nitrate after calcination at 873 K (---) and after 16 hours at 1373 K (.....). The feed consisted of 1% CH_4 and 4% O_2 in N_2 .

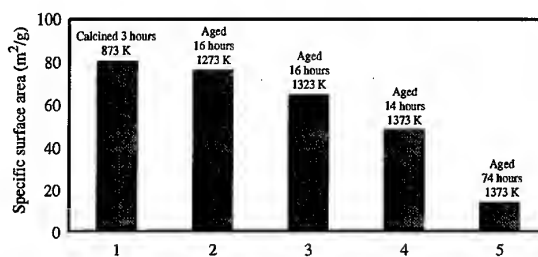


Figure 7: Surface area of the 4.6 wt% $\text{Fe}_2\text{O}_3/\text{La-Al}_2\text{O}_3$ catalyst after calcination (1) and subsequent ageing at 1273 (2), 1323 (3) and 1373 K (4 and 5).

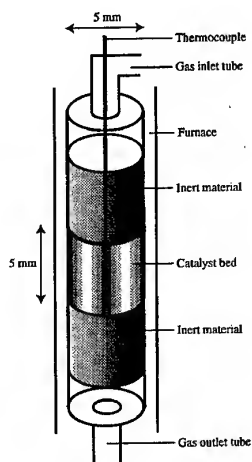


Figure 8: Microflow reactor

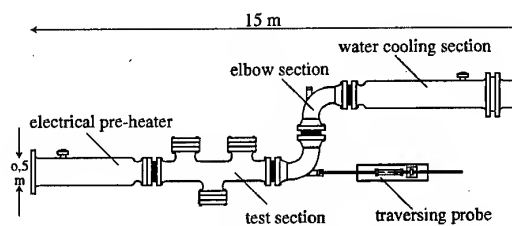


Figure 9: Catalytic combustion rig [17]

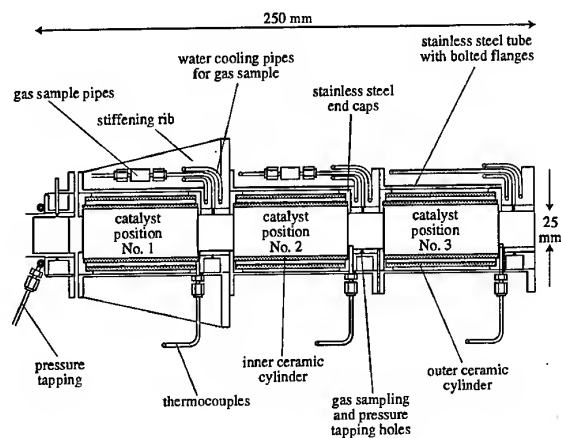


Figure 10: Sub-assembly of catalysts and ceramic support/insulation [17].

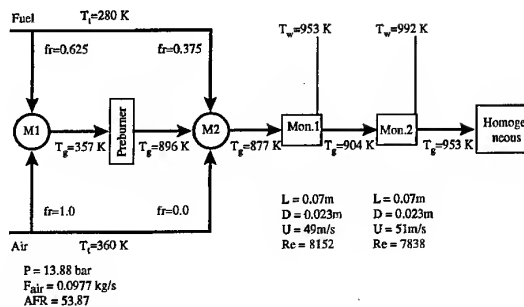


Figure 11: Gas turbine experimental setup plus results

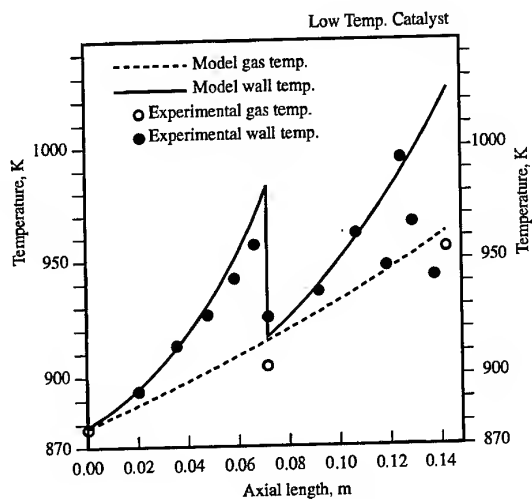


Figure 12: Comparison of the experimental data and the simulated data making use of new heat and mass transfer with $k_0 = 1.3 \times 10^8 \text{ mol s}^{-1} \text{ m}^{-2} \text{ Pa}^{-0.21}$, and $E = 153 \text{ kJ/mol}$

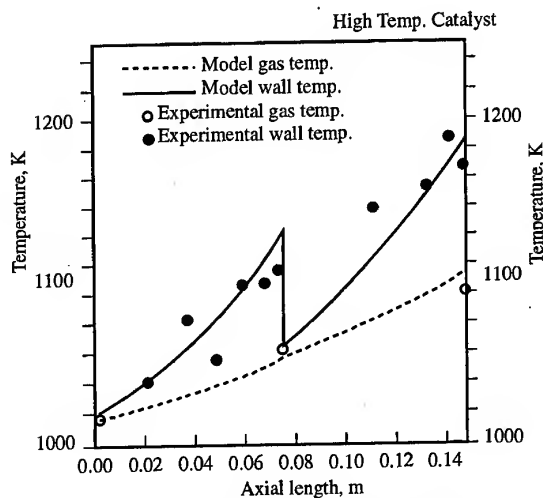


Figure 13: Comparison of the high temperature experimental data with the simulated data with $k_0 = 2.3 \text{ mol s}^{-1} \text{ Pa}^{-0.79}$, and $E = 119 \text{ kJ/mol}$

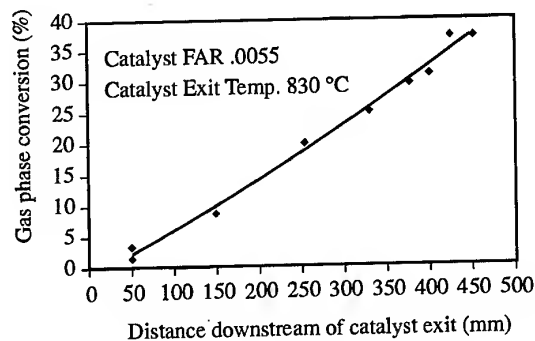


Figure 14: Gas phase conversion vs downstream of catalyst exit

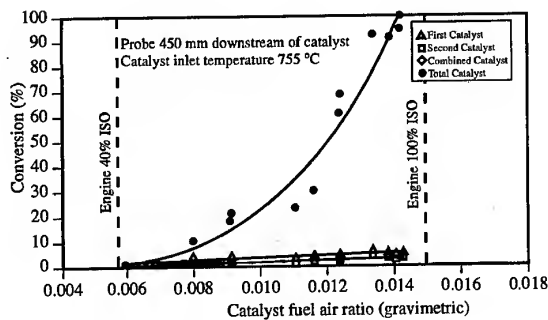


Figure 15: Conversion vs catalyst fuel air ratio

PAPER No. 47
der Kinderen & van Yperem
(presenter: R. van Yperen)

Question 1: W.P.J. Visser, National Aerospace Laboratory, Netherlands

How was your model improved by using the experimental results?

Answer:

The experimental results were used to conduct some "tuning" of the model.

Question 2: M. Razdan, R.R.-Allison, U.S.

How can you prevent the catalyst bed material from experiencing a runaway temperature?

Answer:

You must always ensure that the heat is removed from the bed by convection.

Question 3: G.J. Sturgess, ISSI, U.S.

Are not catalytic combustors always single operating point designs?

Answer:

Yes, they are; the ideal situation is a catalyst bed that always has a constant temperature while operating.

MODIFICATION OF THE FUEL CONTROL SYSTEM OF A GAS TURBINE ENGINE FROM KEROSENE TO HYDROGEN

Dino Dini

Dipartimento di Energetica dell'Università di Pisa
Via Diotisalvi n. 2 - 56126 Pisa (Italy)

ABSTRACT

Fuels for engines of road vehicles, as well of boats or aircraft, based on oil derivatives, are well known as essential factors for the air pollution. In order to adapt a gas turbine engine for the lowest emission operation, its fuel control system has to be modified from the use of a hydromechanical kerosene controller (not able to control gaseous hydrogen) into a digital system for gaseous hydrogen, consisting of an electronic control box which will modulate an electrical/pneumatical valve as a function of engine speed. This is described in the paper, as it has been tested in our laboratory, especially regarding experimental arrangements and measurements. Problems with the ignition of the oxyhydrogen gas have been solved, and the gain factors for the digital control laws were calculated using measured performance data of the kerosene driven engine. Finally, a safe 202 kW gas turbine engine is now running with gaseous hydrogen. Details of the combustion tests of the gaseous hydrogen at the operating performance are given. The data were taken upon pressure losses of the fuel nozzles, ignition performance, temperature distributions at the combustor outlet, combustion efficiency, liner wall temperature distributions, NO_x emission level, noise level, operating performance, etc.

1. INTRODUCTION

An ecologically responsible energy system must include a carbon share that is drastically reduced compared to today. The trend towards a larger hydrogen share will take the place of reduced carbon shares. Dust containment and

removal, NO_x removal and desulphurization of power plants have achieved great progress. But containment of carbon dioxide and methane, two very critical greenhouse gases with dwelling time of between 10 and 100 years in the atmosphere, have not been mandated for any fossil energy converter so far. The attendant costs are not calculated and included in a plant's operating balance sheet, they are not being internalized, and therefore they are not reflected in the final price. Solar hydrogen by water electrolysis, is unburdened by any of these because the operational fossil primary energy raw material is absent. At the most, fossil primary energy needed for the initial investment phase may result in costs that should be internalized, but experience shows that these are marginal. It is a different story when hydrogen is generated from fossil energy raw materials. The needed internalization of all external costs obviously applies to hydrogen system as well. Only at the user end are the external costs once again reduced to zero because of the absence of carbon.

Hydrogen has excellent prospects to economically defeat its competitors, if two conditions are met:

- hydrogen must be produced and consumed in a global economy in really significant amounts. Today, the total is about $500 \cdot 10^9 \text{ Nm}^3/\text{year}$; really significant would be an increase by a factor of 10;
- hydrogen's fossil competitors must be made to bear their respective external cost burdens, including the costs of carbon dioxide, of which hydrogen is free.

The recent energy crisis made our interest turned to use hydrogen as one

of the useful alternative energy sources. In the field of the gas turbine engine, hydrogen fuel is considered to be the easiest energy source for the utilization. The objective of this experiment is to study the unknown technological problems associated with hydrogen use for the gas turbine engine, in order to investigate the degree of difficulty for the hydrogen conversion.

Among others, hydrogen has the advantage of zero pollutant emission, with the exception of the oxides of nitrogen when burning in air breathing engines. One of the early studies, Ref. 1, was conducted by Pratt & Whitney Aircraft, U.S.A., using a J57 engine modified to operate on liquid hydrogen, and this led to construction and testing of a demonstration engine, known as Model 304, designed to operate supersonically on a hydrogen expander cycle. A program by U.S. Navy, Ref. 2, tested a Pratt & Whitney Canada ST6B-68 engine modified to burn hydrogen for naval applications. Both programs have successfully demonstrated that gas turbine engines, designed for liquid fuels, can be easily modified to run on hydrogen fuel. A more recent study by Nomura and co-workers (1981), Ref. 3, on combustion of gaseous hydrogen in a can type combustor and a small gas turbine engine has provided some insight into hydrogen combustion performance, but there are several short-comings. The tests with the can combustor were conducted at low pressure (atmospheric), whereas flame radiation and liner durability are known to be strong function of pressure. Thermo-sensitive paint was used to measure burner wall temperatures and these gave only approximate indications of liner durability. No correlation of combustion performance with operating parameters such as pressure, loading or fuel-air ratio, was attempted.

Detailed descriptions of the hydrogen test program are contained in Ref. 4 and in the final report of Pratt & Whitney, Ref. 5.

2. FUEL CONTROL MODIFICATION

Modification of a kerosene, or jet fuel, driven engine into one using hydrogen is to get an engine with a very similar behaviour, as in Ref. 6.

According to Ref.s 7 and 8, properties of hydrogen and jet A1, are respectively: molecular weight 2.016 and 170; liquid density (kg/m^3) 70.8 and 827; heat of combustion (kJ/kg) 122.8 and 42.8; heat of vaporization (kJ/kg) 446 and 295; flammage range, equivalence ratio 0.1 to 6.8 and 1 to 5; maximum flame temperature (K) 2,400 and 2,300; detonation velocity (m/s) 1,900 and 1,800; specific heat (kJ/kg) 9.663 and 1.966; specific gravity of gas at 0°C and 1 atm., (air = 1) 0.0685.

Because a hydromechanical kerosene controller is not able to control gaseous hydrogen, a digital one was adopted, Ref. 6, consisting of an electronic control box and of an electrical/pneumactical valve for the hydrogen. For a safe ignition of the oxyhydrogen gas and for the design of control laws of the digital hydrogen controller, the steady state and the dynamic performance of the engine have to be known, especially the relation between speed and fuel flow, as a function of the time during engine acceleration from zero to idle speed and for the uncontrolled engine.

The hydromechanical controller has closed loop speed control and overspeed and overtemperature limiter. Controller, fuel pump, and oil cooler are one single unit. The digital electronic controller modulate an electrical valve as a function of engine speed; and the fuel nozzles were changed into hydrogen ones. Driving the engine with hydrogen, the kerosene is led into the external pot.

The control of the engine using hydrogen as fuel consists, as all others, of two parts, namely: the acceleration from zero to idle speed (open loop); the normal engine control (closed loop).

Firstly, the digital controller metes out the hydrogen into the burning chamber as a function of speed similar to the function of the hydromechanical system specially at the first moment when mass flow is only a few percent of that of the corresponding kerosene mass flow to keep the gas volume at the ignition point as small as possible. This has done as an open loop control.

Secondly, at a special given speed below idle speed, the normal engine control as closed loop is activated.

3. HYDROGEN CAN COMBUSTOR

The can combustor system provides a relatively rapid means of investigating performance over a wide range of operating parameters. Comparison of combustion performance between hydrogen and kerosene fuels was made using this system, to get a hydrogen fueled engine with a very similar behaviour. It was decided to use a digital control, consisting of an electronic control box and an electrical/pneumatically valve for the hydrogen. Making the assumption that the differences in the engine behaviour are not too big using Jet A1 fuel in respect to hydrogen, the design of the controller was made referring to data of the Jet A1 fuel driven engine. To achieve these data, the engine has to be started and stabilized at idle speed with open loop control, and then idle-fuel-control has to be changed by a certain amount.

The adopted can combustor, figure 1, has primary, intermediate and diluted, zones and cooling louvres. A single fuel injector is mounted at the combustor head where tangential entry holes provide swirling air to primary zone. A standard simple nozzle is used with Jet A1 fuel, while a multiple nozzle, figure 2, is tested with hydrogen. The nozzle has eight holes injecting the fuel, at 45° to the combustor axis, into the recirculating flow. The hydrogen supply is taken from 200 bar commercial bottles. Hydrogen flow is measured using a standard Venturi, and flow control is provided by a precision valve and pressure regulators. As part of the safety precautions, a flash-back arrestor is installed upstream of the test section to isolate any flash-back of the flame and a nitrogen purge system provided for flushing the fuel line before and after each test.

The single can-type combustor is simulating the combustion performance of conventional 40-200kW small turbine, which will be mentioned here later. A low tension igniter is mounted at the outside of the recirculation zone in the combustion liner.

Pressure sensors and Pt-Ph thermocouples are fixed in the combustor to measure pressure and temperature distributions. To reduce errors due to radiation from/to the wall, the hot junctions are shielded.

Combustion efficiency and gaseous emissions are monitored with a multi-point sampling probe in the exit plane of the combustor. Hydrogen content in the exhaust is measured using a thermal conductivity analyser, and NO_x concentration using a chemiluminescent analyser. The quartz window at the back of the rig allows direct observation of flame behaviour.

Steady state performance tests are performed simulating conditions from ground idle to the maximum rating of the chosen turboshaft cycles.

At each condition gaseous emissions and liner skin temperatures are measured.

Combustion efficiency is determined from measured concentrations of unburnt hydrogen.

Additional parametric tests are performed to evaluate the effects of inlet pressure, temperature and fuel-air ratio on NO_x emissions and liner skin temperatures.

4. TESTS ON CAN COMBUSTOR

Firstly, experiments are conducted to determine the behaviour of the chosen nozzle on such a can combustor. To establish the supply pressure of hydrogen to the combustor, pressure losses across the fuel nozzle are needed. Figure 3 shows the pressure loss coefficient $\beta = \Delta p \cdot 2g / \rho_H V_H^2$, where V_H is the hydrogen velocity at the nozzle orifice (given by using the hydrogen mass flow rate), ρ_H is the specific weight. Nozzle Reynolds number Re is calculated from V_H and the hydraulic diameter obtained from the whole area of the nozzle orifice. As it can be seen on figure 3, the pressure loss coefficient of such multi-hole type is approximately constant in the covered range of Re number.

When the hydrogen operation starts, it is necessary to light immediately at the lower concentration of the hydrogen-air mixtures. Ignition limits are

established by recording the minimum fuel flow required to obtain stable combustion. The flow factors that can be expected to affect ignition limits include air pressure, temperature and velocity. Figure 4 shows the ignition fuel-air ratio versus air flow rate at ambient condition. The minimum fuel-air ratio for ignition with hydrogen is much lower (<40%) than that with Jet A1 fuel even after correcting for the difference in heating values between the two fuels. The multi-hole nozzle, with locally strong concentrations of hydrogen in the primary zone, provides better conditions for diffusion. Increasing air pressure improves ignition characteristics, figure 4. Then, the ignition tests is made to obtain the ignition limits of the combustor. The hydrogen mass flow rate is then increased slowly until the ignition occurs. When hydrogen is ignited, a "pop" sound similar to explosion is accompanied with initialization of combustion. This becomes stronger at excess hydrogen flow even at lower air flow rate, or at larger amount of fuel-air mixtures. Once the ignition is attained, the combustion can be hold even at considerably small amount of hydrogen flow.

The combustion efficiencies of hydrogen is around 100%, calculating from the entalpy differences. The hydrogen concentration in the combustion gases at the outlet of the combustor is checked by a chromatograph. The ignition performance and operating efficiency of the can combustor points to excellent mixing and combustion characteristics of hydrogen. The results once again indicate possibility of using much smaller combustors for hydrogen fuel while achieving adequate performance.

5. PERFORMANCE OF H₂ TURBINE

Two conventional small gas turbines are used for the operation test with hydrogen fuel. The can-type combustor is a simulation of these kinds of engines. In order to accomodate geometrical differences, can combustor and real flow in the turbine combustion chamber, modelling parameters are used to define the can combustor rig air

flows which simulate actual conditions on the full engine. An air loading parameter simulates reaction rate and residence time at low power, and an air velocity parameter simulates flow characteristics at high power. Thus, the air mass flows for the can combustor rig tests are determined from such modelling parameters, while inlet pressures, temperatures, and overall fuel-air ratios are kept the same as in the engines. Fuel flows are adjusted according to the net heating value of the test fuel relative to that of Jet A1.

The hydro-mechanical controller is not able to control gaseous hydrogen. Therefore a digital electronic controller is used, which is modulating an electrical valve as a function of engine speed. Driving the turboshaft (figure 5) with hydrogen, there are different metering and shut off valves, which are important for the safety point of view; it is necessary to rinse the fuel pipes before and after each engine run.

The control of the turboshaft using hydrogen as fuel consists of two parts: acceleration from zero to idle speed (open loop); normal engine control (closed cycle).

In fact here, the digital controller measures the hydrogen into the combustion chamber as a function of speed, whereas, specially at the first moment, the mass flow is only a few percent of that of the corresponding Jet A1 mass flow to keep the gas volume at the ignition point as small as possible. This acceleration from zero to idle speed is done as open loop control.

At about the idle speed, the normal engine control as closed loop is activated. The increase of fuel as function of speed (or time) is slightly smoother.

The NO_x emission rates in hydrogen use are relatively greater than those of Jet A1 combustion, in the entire range of the loading operation of the power spectrum; this is probably associated with higher flame temperature, evidenced as well by higher liner temperatures.

Combustion with the multiple nozzle may be influenced more by diffusion of individual jets of hydrogen, which can

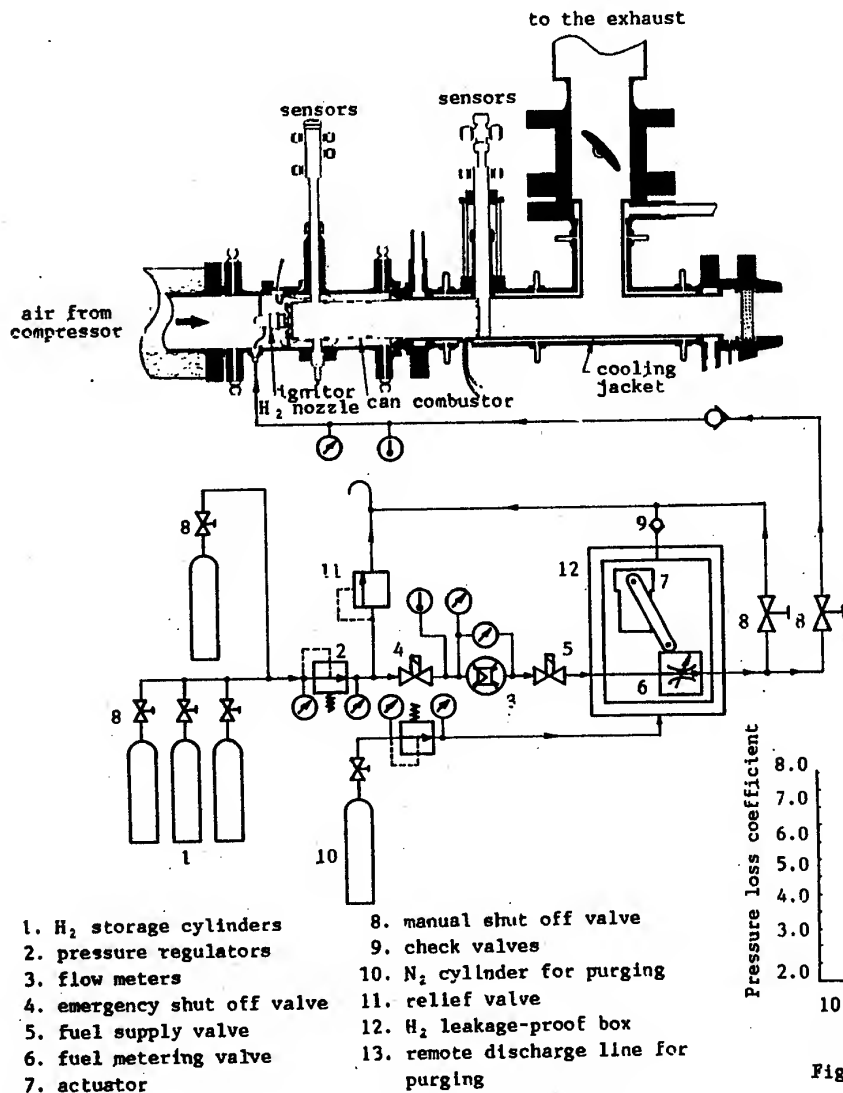
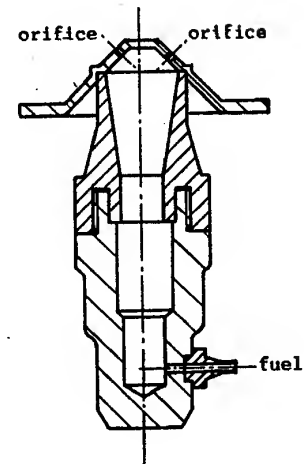
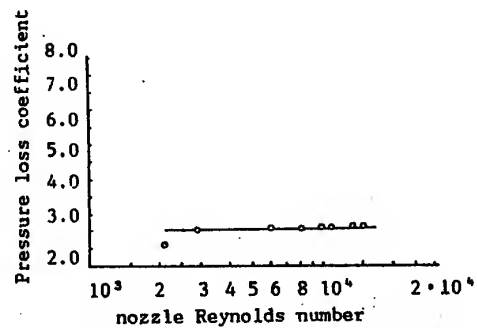
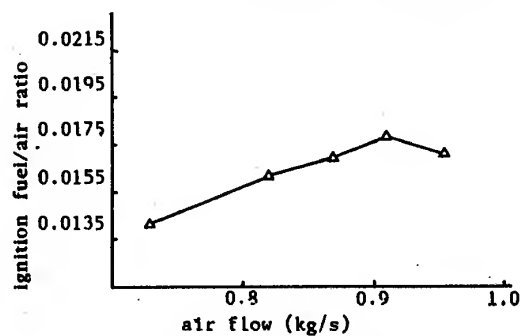
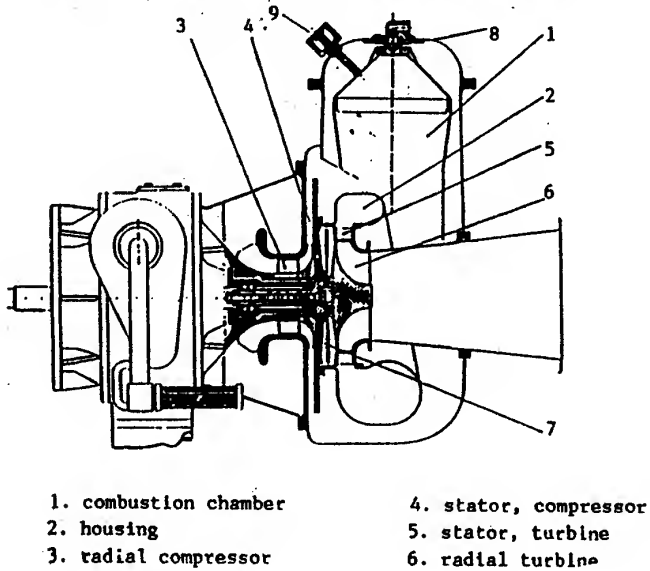
Fig. 1 - Combustor test rig and H₂ supply systemFig. 2
H₂ multi-hole nozzleFig. 3 - Pressure loss coefficient of the H₂ fuel nozzleFig. 4 - Ignition H₂ flow versus air flow

Fig. 5 - 42 kW turboshaft

result in higher local temperatures and hence higher rates of NO_x formation. While the can combustor data with kerosene fuel shows NO_x emission lower than in current production engines, corresponding data for hydrogen show considerably higher NO_x emissions. Reducing these emission can likely be achieved by leaning out the front end of the liner, or reducing primary zone residence time by moving up the location of dilution orifices. In this combustion system, such changes are not likely to result in much penalty in other performance parameters such as ignition, stability or combustion efficiency.

The temperature distributions on the liner wall of the combustor were observed by using thermocouples. The wall temperatures with hydrogen were much higher than with Jet A1, especially in the primary zone where temperatures in excess of 1,100 K were indicated for hydrogen, compared to 800-1000 K for Jet A1.

Based on the work here presented, the following conclusions are obtained:

- conventional gas turbine operated with Jet A1 fuel can be converted, with a minimum effort, to use hydrogen as an alternative fuel;
- perfect combustion of hydrogen is obtained in the operation tests of the gas turbines. Thermal efficiency in hydrogen operation agreed with the value in Jet A1 operation;
- NO_x emission level in hydrogen combustion is greater than that with Jet A1 fuel.

Conversion to hythane combustion is next experiment, to be made with turboshafts, as already made in our laboratory, Ref. 15, with alternative combustion engines.

Mixing a bit of hydrogen with compressed natural gas (C.N.G.) could yield the cleanest-burning alternative fuel yet.

A feasibility test of hythane - 5 percent hydrogen by energy content, 15 percent by volume - has produced hydrocarbon emissions less than half of those from C.N.G., and nitrogen oxide level 24 percent of those from C.N.G.

Taking suggestion from automobile application, pure hydrogen in gaseous form asks up 12.9 times as much space as gasoline, required to travel an equivalent distance, and 3.8 times as much space as natural gas. Enough hythane to make a trip of about 200 miles can be packed into a tank 3.4 times the size of an equivalent gas tank - if it is compressed to about 3,000 pounds per square inch.

It is theorized that natural gas and hydrogen can act symbiotically - one complimenting the other - to produce a more efficient burning fuel. Natural gas plays a positive role in the fuel partnership by contributing cost advantage, domestic availability, and existing infrastructure to the scenario. Another potential benefit of hythane use - extending the supply of natural gas - can be accomplished if hydrogen is formed from renewable energy sources rather than natural gas reformation. Although natural gas is clean-burning, there is still a need to lower the carbon monoxide (CO), hydrocarbon (HC) and nitrogen oxide (NO_x) levels to accommodate the projected emission standards.

Current emission standards in U.S.A. are, for automobiles, less than the following grams per mile:

0.97 (THC), 0.8 (NMHC), 10.0 (CO), 1.2 (NO_x). Proposed California "ULEV" (Ultra Low Emission Vehicle) are: 0.05 (THC), 0.04 (NMHC), 1.7 (CO), 0.2 (NO_x).

At present, hythane used in automobiles has reached: 0.01 (NMH), 0.7 (CO), 0.2 (NO_x).

In advanced turbo-engines, hythane combustion with air has to be considered an up to date procedure, even though storing aboard of hydrogen and natural gas must be separately or both in cryogenic liquid form.

6. CONCLUSIONS

Investigation of performance of gaseous hydrogen in a can type combustor has demonstrated the excellent combustion characteristics of hydrogen fuel. These include extremely good combustion efficiency, as well as ignition-stability performance. However, NO_x emissions with hydrogen are considerably higher than with the state of the art of liquid

fuel combustor; liner modifications to reduce reaction zone temperatures and residence times should help to reduce NO_x emissions without significant penalties of combustion efficiency or stability at low end. It appears that combustion of hydrogen in a liner designed for liquid fuel can result in localized regions of high combustor wall temperatures, which may require optimization of liner cooling flows, or internal air flow pattern or both. The relative ease of hydrogen combustion, and its good performance characteristics, should enable use of highly loaded combustion systems with relatively simple fuel injection devices.

Experiments were conducted to determine the desirable configuration of the hydrogen fuel nozzles. The operation tests of two (42 and 202 kW) small gas turbines were made by using the selected nozzle (figure 2). In the gas turbine operation with hydrogen fuel, other elements of the engine, except the kerosene supply line, were used without any modification of the original configuration and dimension. Based on the work here presented, the following conclusions are obtained:

- conventional gas turbine operated with fossil fuel oil could be converted with the minimum effort to use hydrogen as an alternative fuel;
- hydrogen fuel supply system has to be newly designed to avoid the explosive ignition, particularly to ensure ignition at a given air-hydrogen mixture ratio;
- the combustion results of the swirl type fuel nozzle seem to be best for the combustor of the gas turbines here used, except for the higher pressure loss coefficient. The multi-hole type also showed better results, but its metal seemed to sustain unacceptable heating, because of protrusion into the primary combustion zone;
- perfect combustion of hydrogen was obtained in these operation tests of the gas turbines;
- NO_x emission level in hydrogen combustion was greater than that in kerosene combustion. Therefore, it is necessary to reduce NO_x emission levels when hydrogen combustors and fuel nozzles are developed;
- overall noise level showed no difference existed between hydrogen

and kerosene combustion in the full load operation of the gas turbine.

The digital electronic controller is essential to modulate the electrical valve as function of engine speed. Driving the engine with hydrogen, the kerosene is led into the external pot. Besides the fuel metering valve and the shut off valve there are different other valves, which are important for the safety point of view.

The combustion engine laboratory of the Energetics Department of the University of Pisa is experimentally working since thirty years in the field of hydrogen-burning-engines, with very low nitric oxide emission, Ref.s from 10 to 28.

REFERENCES

- 1 | R.C. Mulready (1964) - "Liquid Hydrogen Engines". Technology and Uses of Liquid Hydrogen, R.G. Scott, Chapter 5, pp. 149-180.
- 2 | A.E. Ford (1977) - "Hydrogen-Fuelled Turbine Boat Demonstration" - Society of Automotive Engineers, Passenger Car Meeting, Detroit.
- 3 | M. Nomura, H. Tomaki, T. Morishita, H. Ikeda, and K. Hatori (1981) - "Hydrogen Combustion Test in a Small Gas Turbine" - International Journal of Hydrogen Energy, Vol. 6, No. 4, pp. 397-412.
- 4 | P. Sampath and M. Gratton (1983) - "Fuel Character Effects on Performance of Small Gas Turbine Combustion Systems" - AGARD Conference on Combustion Problems in Turbine Engines, Cesme, Turkey.
- 5 | F. Shum and P. Sampath (1984) - "Hydrogen Combustion Research-Final Report", Pratt & Whitney Canada.
- 6 | G.W. Dahl and R. Bizing - "Modification of the Fuel System of a Turbo shaft Engine from Kerosene to Hydrogen" - Fachhochschule Aachen, Germany - 9th World Hydrogen Energy Conference, Paris, 22-25 June 1992.
- 7 | E.M. Goodger (1975) - "Alternative Fuels for Aviation" - Aeronautical Journal, May 1975, pp. 212-224.
- 8 | F.J. Edeskuty (1979) - "Safety of Liquid Hydrogen in Air Transportation", Symposium of Hydrogen in Air Transport

tation, Germany 1979.

| 9 | D. Dini - "Computational and Experimental Results in High Pressure Combustion of H₂-Air and H₂-O₂-H₂O" - AGARD Conference Proceedings No. 536 on "Fuels and Combustion Technology for Advanced Aircraft Engines" - Colleferro, May 10-14, 1993.

| 10 | L. Martorano and D. Dini - "High Temperature H₂-Air Variable Geometry Combustor and Turbine: Test Facility and Measurements" - AGARD Conference Proceedings n. 229 - Ankara, 19-23 September 1977.

| 11 | L. Martorano and D. Dini - "Trasformazione di un motore automobilistico per il funzionamento a idrogeno" - Atti del XXXII° Congresso Nazionale della Associazione Termotecnica Italiana - Roma, Marzo 1977.

| 12 | D. Dini - "L. Martorano and D. Dini - "Hydrogen Injection in Two Stroke Reciprocating Gas Engines" - 4° W.H.E.C. - Pasadena, 13-17 June 1982.

| 13 | D. Dini and L. Martorano - "Cryogenic Fuel Storage in Cars Using Hydrogen as Power Source in Road Transport" - XV° International Congress of Refrigeration - Venezia, 23-29 September 1979.

| 14 | D. Dini - "Pipe Network and Equipment for Delivering Hydrogen Fuel in a Generalized Domestic, Industrial and Automotive Usage" - XV° International Congress of Refrigeration - Venezia, 23-29 September 1979.

| 15 | D. Dini - "Prospects of Hydrogen Production through Solar Energy for a Generalized Domestic, Industrial and Automotive Usage" - 18° International Complex Conference: "Solar Energy, New Prospects" - Milano, 23-27 September 1979.

| 16 | D. Dini - "Prospects of Hydrogen Production for a Generalized Domestic, Industrial and Automotive Usage" - 3rd World Hydrogen Energy Conference - Tokyo, 23-26 June 1980.

| 17 | D. Dini and L. Martorano - "Design of Optimized Large and Small Size Hydrogen Liquefaction Plants" - 3rd World Hydrogen Energy Conference - Tokyo, 23-26 June 1980.

| 18 | D. Dini - "Hydrogen Fuelled Engines for Low and High Supersonic Airplanes" - 7° W.H.E.C. - Moscow, 25-29 September 1988.

19 | D. Dini - "Energy-Environment Potential Impact of Hydrogen Fuelled Engines Operating on Road Vehicles" - XXIII° FISITA Congress - Torino, 7-11 May 1990.

| 20 | D. Dini - "Nitrogen-Hydrogen Automotive Engine to Avoid Atmospheric Pollution" 8° W.H.E.C. Honolulu and Waikoloa, 22-27 June 1990.

| 21 | D. Dini - "Feasible Non-Polluting Car Engine Using Air-Water Components" - A.I.E.C. and S.A.E. International Meeting - Buenos Aires, 3-6 September 1991.

| 22 | D. Dini - "Design of a Hybrid Non-Polluting Car Engine Operating through Hydrogen Combustion and Electrical Batteries" - First International Conference on "New Energy System and Conversion" - Yokohama, 27-30 June 1993.

| 23 | D. Dini and Others - "Conversion to Hydrogen of an Electronically Controlled Gasoline Supply System" - 10° World Hydrogen Energy Conference - Cape Canaveral, 20-24 June 1994.

| 24 | D. Dini and G. Nardi - "Feasibility of a Reciprocating Engine Operating with Hydrogen / Air External Combustion" - 10° W.H.E.C. - Cape Canaveral, 20-24 June 1994.

| 26 | D. Dini and G. Nardi - "Test Installation for an Already Built 20 Bar Hydrogen-Oxygen-Water Combustion Chamber" - Hypothesis International Congress - Gaeta-Cassino, 26-29 June 1995.

| 26 | D. Dini - "Ultra Low and Zero Noxious Emissions Gas Engines for Road Vehicles: Their Design / Test Installation in Italy" - 3° Convegno Internazionale "Energia e Ambiente verso il 2000" - Capri, 6-8 June 1996.

| 27 | D. Dini - "Hybrid Car Propulsion through Hydrogen Fuelled Thermal Engine and Lead-Acid Batteries Electrical Motor" - 11° World Hydrogen Energy Conference - Stuttgart, 23-28 June 1996.

| 28 | D. Dini - "Design of a Car Engine with an External Hydrogen-Air Mixture Formation" - 12° World Hydrogen Energy Conference - Buenos Aires, 21-26 June 1998.

PAPER No. 48
Dini
(presenter: D. Dini)

Question 1: G.J. Sturgess, ISSI, U.S.

You have shown that using pure hydrogen as a fuel gives much increased emissions of nitric oxide, that are produced because of the higher flame temperatures produced by this fuel. Do you think that a better way to use hydrogen might be to introduce a small amount of it into methane, that would enhance the lean stability limit to permit stable operation at much lower equivalence ratios than are normally possible with pure methane? Operation at such ultra-low equivalence ratios should then result in much less nitric oxide production.

Answer:

Yes, in fact, I tested (see Reference 26 of the paper) in our laboratory, a reciprocating car engine fueled with a combination of hydrogen with natural gas (the mixture being known as hythane). Hythanes with hydrogen contents of 15 - 30 % by volume and 5 - 10 % by energy, have been used, with most recent work being focussed on the more dilute hydrogen concentrations. The dilute hydrogen concentration has strong effects on the combustion.; NO_x and unburned hydrocarbon emissions are reduced with lean burning at part-load conditions when compared to pure methane. The effects are due to the reduced burning times that are possible through the higher flame speed of hydrogen.

NUMERICAL PREDICTIONS AND EXPERIMENTAL MEASUREMENTS OF RADIATIVE HEAT TRANSFER IN GAS TURBINE COMBUSTORS

P. Di Martino, G. Cinque
Alfa Romeo Avio S.A.P.A.
Research and Development Department
Viale Impero, 80038 Pomigliano d'Arco
Napoli, ITALY

1. SUMMARY

The present paper is concerned with the calculation of the flowfield, heat transfer and turbulent combustion processes inside a single annular reverse-flow gas turbine combustor for aircraft engines. Numerical analysis has been carried out by using a CFD home computer code based on finite-volume method and body-conforming non-orthogonal structured grids. Emphasis has been put on the evaluation of wall temperatures distribution, which was assumed in previous works. A comparison with experimental measurements obtained by means of thermal paints has also been performed. A method to evaluate wall temperatures and radiative heat fluxes is described. No attempt has been made to account for the presence of soot.

First results obtained seem encouraging in that the trend of calculations is in good agreement with experiments.

While an amount of work remains to be done in improving physical models, this study shows that CFD can be used as a tool in studying the main features of a gas turbine combustor and in correlating important design parameters.

2. INTRODUCTION

The design of a gas turbine combustor aims at the optimization of several performance parameters. High priority is usually given to expansion of the range of stable operating conditions, improvement of exit temperature traverses and, more recently, reduced pollutant emissions. All of these features are crucially dependent on internal flow patterns and the associated rates of mixing. For many years a combustor design has depended on the use of empirical correlations and "cut-and-try" approach. This approach has been reasonably successful but the time and cost involved in the development of gas turbine components in this traditional way is considerable.

The future aircraft engines will have requirements that present formidable technical challenges to the combustor designer. Reduced fuel consumption and improved durability and reliability as well as higher temperatures and pressures are forecast. Coupled with these performance requirements is the demand world wide for control of pollutant emissions from aircraft engines, especially oxides of nitrogen. These technical and environmental challenges have made the design of combustion systems a very hard task. Empirically based design methods are insufficient by themselves. Computational fluid dynamic (CFD) is showing great potential as a design tool for combustion systems in parallel to experimentation. Advances in computers allow the use of detailed numerical algorithms and physical models for more accurate predictions of complex flows.

Due to the great deal of phenomena involved, little attention has been paid to radiative heat transfer, as it was thought to be a small percentage of the total heat released by chemical reactions and there was no means by which it could be reliably evaluated. However a complete aerothermal design includes the calculation

of liner wall temperatures, thermal stresses and liner durability. Consequently an accurate means of prediction of the radiant heat fluxes is needed. Further accurate predictions of pollutant emissions necessitate a fairly precise knowledge of radiant heat transfer rates as the models for predicting the emissions of UHC, CO and NO_x require an accurate description of gas temperature distributions.

Some authors did not calculate thermal radiation based on the argument that it is very small compared with the heat released by combustion. They assumed adiabatic conditions and did not solve for the enthalpy equation. Others use some radiation prediction procedures a posteriori. The radiative heat fluxes to the walls were calculated with the hypothesis of uniform wall temperature equal to the inlet air temperature. In this condition the effects of radiative heat transfer on the flow, temperature field and chemical reaction were not accounted for.

In this paper the "discrete ordinate" radiation model has been used to predict wall temperatures in conjunction with the solution of the flowfield. The enthalpy equation is solved as well and a source term accounting for radiative heat transfer is included.

A single annular reverse-flow combustor at full load conditions has been studied. Experimental measurements of wall temperatures obtained by means of thermal paints are available for this chamber. Even if the model is approximate and there are a lot of uncertainties, the comparison with experiments is useful to test the code and to verify several hypotheses used in the calculations.

3. GAS-PHASE GOVERNING EQUATIONS

Steady fully elliptic density-weighted Navier-Stokes equations describing gas phase, under low Mach number approximation, coupled to the energy and momentum balance equations for the liquid phase, are considered [1]. Turbulence is simulated by way of the standard k-ε model along with the wall function treatment for the near-wall regions. The conservation equations solved for the gas phase are those for momentum, mass, kinetic energy of turbulence and its dissipation, energy and chemical species. The general form of these equations in cartesian coordinates, is:

$$\begin{aligned} \frac{\partial}{\partial x}(\rho u \phi) + \frac{\partial}{\partial y}(\rho v \phi) + \frac{\partial}{\partial z}(\rho w \phi) = \\ \frac{\partial}{\partial x} \left(\Gamma_{\phi} \frac{\partial \phi}{\partial x} \right) + \frac{\partial}{\partial y} \left(\Gamma_{\phi} \frac{\partial \phi}{\partial y} \right) + \frac{\partial}{\partial z} \left(\Gamma_{\phi} \frac{\partial \phi}{\partial z} \right) + S_g + S_d \end{aligned} \quad (1)$$

All terms which arise in addition to convection and diffusion are grouped in the source-term S_e for the gas-phase, while S_d accounts for liquid droplets.

In order to fit the very complex geometries encountered in industrial applications, a body conforming system of coordinates is used. Hence the equation (1) is transformed from

Cartesian coordinates (x, y, z) to curvilinear non-orthogonal coordinates (ξ, η, ζ) . The final equations to be solved are [2]:

$$\begin{aligned} \frac{\partial}{\partial \xi}(\rho U \phi) + \frac{\partial}{\partial \eta}(\rho V \phi) + \frac{\partial}{\partial \zeta}(\rho W \phi) = \\ \frac{\partial}{\partial \xi} \left(\frac{\Gamma_\phi}{J} q_{11} \frac{\partial \phi}{\partial \xi} \right) + \frac{\partial}{\partial \eta} \left(\frac{\Gamma_\phi}{J} q_{22} \frac{\partial \phi}{\partial \eta} \right) + \frac{\partial}{\partial \zeta} \left(\frac{\Gamma_\phi}{J} q_{33} \frac{\partial \phi}{\partial \zeta} \right) + \\ \frac{\partial}{\partial \xi} \left[\frac{\Gamma_\phi}{J} \left(q_{12} \frac{\partial \phi}{\partial \eta} + q_{13} \frac{\partial \phi}{\partial \zeta} \right) \right] + \frac{\partial}{\partial \eta} \left[\frac{\Gamma_\phi}{J} \left(q_{21} \frac{\partial \phi}{\partial \xi} + q_{23} \frac{\partial \phi}{\partial \zeta} \right) \right] + \\ \frac{\partial}{\partial \zeta} \left[\frac{\Gamma_\phi}{J} \left(q_{31} \frac{\partial \phi}{\partial \xi} + q_{32} \frac{\partial \phi}{\partial \eta} \right) \right] + J \cdot S(\xi, \eta, \zeta) \end{aligned} \quad (2)$$

In the foregoing mathematical expression U, V, W are the so-called contravariant velocity components, J is the Jacobian of the coordinate transformation, q_{ij} are metric quantities; terms with $i \neq j$ account for grid distortion.

Turbulence is simulated by way of the standard $k-\epsilon$ model along with the wall function treatment for the near-wall regions.

The turbulent viscosity is related to k and ϵ by dimensional arguments in the following way:

$$\mu_t = C_\mu \rho \left(\frac{k^2}{\epsilon} \right) \quad (3)$$

There are several approaches for modelling the combustion in turbulent flows. In this study we have chosen the model based on Arrhenius and Eddy Break Up concepts [3]. The density is provided by the law of perfect gases while temperature is updated from stagnation enthalpy [1].

4. LIQUID-PHASE MODEL

Two-phase effects also require to be modeled, because in combustion systems fuel is often injected in the form of a spray of small liquid droplets. Among the numerous spray models available in literature [4] we have chosen the deterministic separated flow model (DSF).

This model assumes that the fuel is injected into the combustion chamber as a fully atomized spray which consists of spherical droplets. Finite interphase transport rates are considered, but the effects of turbulent fluctuations on particle motion are neglected. Droplets are assumed to interact only with the mean gas motion. Particles follow deterministic trajectories found by solving their Lagrangian equations of motion. The model takes into account drop heat-up, including the effect of forced convections. The evaporated mass flux is based on the vapor concentration gradient concept that estimates the gas properties at reference temperature using the one-third rule.

The liquid-phase equations are coupled to the equations describing gas-phase through the droplet source terms, which are obtained by calculating what is lost or gained in terms of mass, momentum and energy as the droplets enter and leave volume elements. The set of simultaneous ordinary equations for liquid phase are solved by the fourth order Runge-Kutta method at suitable intervals within the iterative procedure. The time step is dynamically adjusted based on droplet velocity and grid cell size.

5. RADIATIVE HEAT TRANSFER MODEL

The effects of radiation transport appear in the energy conservation equation as the divergence of the radiative heat flux [5], $(-\nabla \cdot \mathbf{q}_r)$. For a grey medium, $(-\nabla \cdot \mathbf{q}_r)$ is evaluated from:

$$-\nabla \cdot \mathbf{q}_r = \kappa \left[\int_{4\pi} I(r, \Omega) d\Omega - 4\pi I_b \right] \quad (4)$$

where κ is the absorption coefficient, $I(r, \Omega)$ is the directional intensity, Ω is the direction of radiation, and I_b represents the

blackbody intensity. For an optically thin medium, the integral term in Eq. (4) is negligible, and the divergence of the radiative heat flux may be calculated without having to solve the integro-differential radiative transfer equation (RTE) [5]. However for strongly radiating flames which are not necessarily optically thin, one cannot neglect the integral term. To find $I(r, \Omega)$, we solve the RTE for grey gases:

$$\begin{aligned} (\Omega \cdot \nabla) I(r, \Omega) = -(\kappa + s) I(r, \Omega) + \kappa I_b(r) + \\ \frac{s}{4\pi} \int_{\Omega' \in 4\pi} I(r, \Omega') \Phi(\Omega' \rightarrow \Omega) d\Omega' \end{aligned} \quad (5)$$

where s is the scattering coefficient and $\Phi(\Omega' \rightarrow \Omega)$ is the scattering phase function. This says that the rate of change of intensity in the direction of propagation, Ω , is attenuated by absorption and out-scattering (from direction Ω), and is enhanced by emission and scattering (from direction Ω' to Ω). In this analysis we did not consider the effects of soot particles (i.e. $s=0$). In any case the scattering of the radiation by soot is negligible as the radiation wavelength is generally greater than the soot particle diameter when we are talking about infrared radiation from flames.

The equation for intensity, $I(r, \Omega)$, is written in a body-conforming system of coordinates according equation (2) and is solved using the discrete-ordinate approximation (DOM) to RTE. This is obtained by discretizing the entire solid angle (4π steradians) using a finite number of ordinate directions and corresponding weight factors. The RTE is written for each ordinate and the integral terms are replaced by a quadrature summed over each ordinate and this provide the source term in the enthalpy equation. This method is sometimes referred to as the S_N approximation [6], where the order of approximation is N (i.e. the number of discrete values of direction cosines to be considered). In general the total number of ordinate directions, M , is related to the order of approximation, N , through the relationship $M=N(N+2)$ given in [6]. For the work presented in this paper, we used the S_4 method, which is a good compromise between accuracy and CPU time.

The gas absorption coefficient κ_g is calculated from the total emissivity of a grey gas ϵ_g , as described in [7]:

$$\epsilon_g = 1 - \exp(-\kappa_g L) \quad (6)$$

The total emissivity is obtained by the "two grey plus one clear gas" model of Truelove [8]. Water vapor and carbon dioxide are the prime contributors to the gaseous radiation. Owing to the lack of appropriate data, the contribution of carbon oxide and fuel was not considered. Therefore the expression of ϵ_g is:

$$\epsilon_g = \sum_{n=1}^N a_{g,n}(T_g) \left[1 - \exp(-\kappa_{g,n}(P_{H_2O} + P_{CO_2})L) \right] \quad (7)$$

where the summation n is over the three gases of the assumed mixture, the $\kappa_{g,n}$ are presumed constants with the temperature dependence of emissivity being accommodated in the weighting coefficients $a_{g,n}$. P_{H_2O} and P_{CO_2} are the partial pressures of water vapor and CO_2 respectively, and L is the mean beam length of the system, approximated by $L=3.5V/A$ [9]. The values of $\kappa_{g,n}$ and $a_{g,n}$ are tabulated in [8].

If the surface bounding the medium is assumed grey and emits and reflects diffusely, then the radiative boundary condition for equation (5) is:

$$I(r, \Omega) = \epsilon_w I_b + \frac{1 - \epsilon_w}{\pi} \int_{n \cdot \Omega' < 0} |n \cdot \Omega'| I(r, \Omega') d\Omega' \quad (8)$$

where $I(r, \Omega)$ is the intensity of a radiant energy leaving a surface at a boundary location, ϵ_w is the wall emissivity (assumed constant) and n is the unit normal vector at the boundary location. The terms on the right-hand side of equation (8) represent contributions to the outgoing intensity due to emission from the surface and reflection of incoming radiation.

The effects of turbulence on radiation are not easy to be modeled and so have been neglected.

6. CALCULATION OF WALL TEMPERATURE

The boundary condition necessary to evaluate radiative heat transfer is obtained from an energy balance across the liner. The heat transfer mechanisms to be accounted for are the following: the liner is heated by radiation and convection from the hot gaseous products inside it; it is cooled by radiation to the outer casing and by convection to the annulus air. Under equilibrium conditions the liner temperature is such that the internal and external heat fluxes at any point are just equal. Heat losses by conduction along the liner wall are comparatively small and have been neglected in this analysis. Since the liner wall is usually very thin we also neglected the difference between inner and outer wall temperatures. Therefore, under steady state conditions, the energy balance across the liner can be cast as:

$$R1 + C1 = R2 + C2 \quad (9)$$

Internal radiation $R1$ is calculated from the discrete ordinate model while Reynolds analogy is used for internal convection $C1$. External radiation $R2$ and external convection $C2$ are evaluated using the correlations presented by Lefevbre [9]. The calculation procedure consists of:

- 1) First guess of wall temperature.
- 2) $R1$, $C1$, $R2$, $C2$ are calculated using wall temperature of step 1)
- 3) Using the relationship (9) the liner wall temperature is updated. A non-linear equation has to be solved, as $R1$ and $R2$ are proportional to T^4 , and the Newton-Raphson's method has been selected for the solution of this equation.
- 4) The new value of wall liner temperature is obtained and compared with the value used in step 2.
- 5) Steps 2-4 are repeated according to a convergence criterium.

7. NUMERICAL SOLUTION

The partial differential equations previously described have been transformed into difference equations by integrating over each control volume with the aid of Gauss theorem. The Fickian diffusive terms were replaced by their central difference analogues, while a higher order upwind scheme (QUICK) was used for convective terms along with a boundedness criterion to avoid numerical oscillations. Finally the well established SIMPLE algorithm [10] with the SIMPLER [11] modification was used to handle the velocity-pressure coupling and the solution of the individual equations sets was obtained by the strongly implicit procedure described by Stone [12].

The number of iterations required for convergent solution was around 1000, which corresponds to a CPU time of about 5 hours on a DEC ALPHA machine. Convergence was achieved when the normalized residuals for all equations were less than 10^{-5} .

8. ANALYTICAL TEST CASES

In order to check that the DOM algorithm for radiation had been implemented correctly it was applied to two simple test cases for which analytical solution is available.

9. TEST CASE 1

As a first test case we considered two black infinite parallel plates that are separated by a grey gas with constant absorption coefficient. The gas is in radiative equilibrium. As

shown in Fig. 1, the lower plate is at temperature T_1 , and the upper plate is at T_2 . The plates are separated by a distance D .

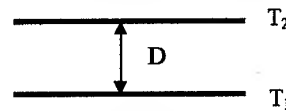


Fig. 1 Plane layer geometry

The region shown in Fig. 1 was resolved using 10 grid points with $D=0.005$ m. Dimensionless energy flux distribution obtained with SN4 model is compared with analytical solution [13] for different optical thicknesses in Fig. 2. The level of agreement is very good.

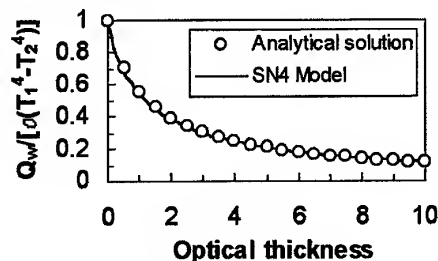


Fig. 2 Dimensionless energy flux distribution in grey gas contained between infinite black parallel plates.

10. TEST CASE 2

The second test case involves the same geometry of the previous one but we considered different wall emissivities. Again numerical results obtained with SN4 model match well the analytical solution [13], as shown in Fig. 3.

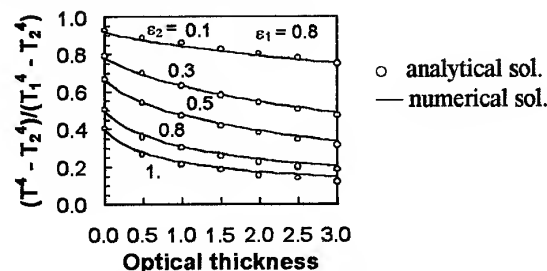


Fig. 3 Dimensionless temperature distribution in grey gas contained between infinite parallel plates with different wall emissivities.

11. TEST CASE 3

The last test case is concerned with a square cavity with cold black walls and absorbing-emitting grey gas at uniform temperature. The optical thickness $\kappa L=1$. The geometry was resolved using a 20×20 grid, with $L=0.05$ m. The agreement with analytical solution [14] is good (see Fig. 4).

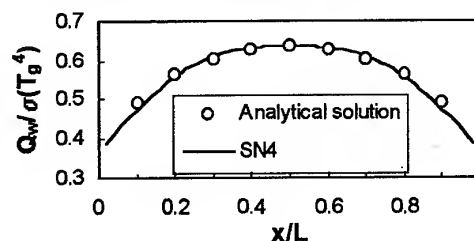


Fig. 4 Dimensionless wall heat flux profile at optical thickness $\kappa L=1$ for square enclosure.

The above results indicate that the DOM model has been implemented correctly.

12. RESULTS FOR REVERSE-FLOW COMBUSTOR

A turboprop engine reverse-flow combustor chamber (Fig. 5) is analyzed in this study. Test measurements taken from [15] were available. The fuel injection system of the annular combustor comprises 9 T-shaped vaporizers equally spaced along the circumferential direction and three torches, each having a flow number of 0.2 (gal. imp/psid^{0.5}) and a cone angle of 120 degrees. The test unit was supplied with unvitiated air from an existing plant facility, at correct air inlet temperature and pressure. The air was passed through a swirl generator to give the correct inlet air swirl of 5 degree (clockwise when viewed looking into the flame tube primary zone). The fuel used was Jet-A. The calculations are conducted for a flow in a 120 degree sector of the combustor with periodic boundary conditions being imposed on the two side planes. Within this sector there are 12 primary holes (inner liner), 8 dilution holes (4 inner and 4 outer liner), 36 dilution, 54 primary holes (between the T-shaped vaporizer) 60 primary holes and 9 film cooling slots. The geometry was represented by a body-fitted mesh (fig. 6) of 110x23x51 grid points. This grid resolution, while somewhat coarse, has been found from modelling application experience to be adequate for providing reasonably accurate predictions of combustor exit gas temperature average radial profile and traverse quality. Calculations were performed at high power conditions of operation. A one-dimensional code was used to determine air flow distribution through the rows of holes across the liner as well as pressure drops and injection angles.

Figures 7 and 8 show the predicted velocity vectors in two side view planes. The primary vortex is well defined and it is located close to the outer liner. The opposing dilution jets impinge on each other (Fig. 7) resulting in a multiple core structure of the hot gas closer to the inner liner. The primary jets (Fig. 8) penetrates across the flow domain and splashes onto the outer liner. The contours of temperature in same side view planes are reported in Figures 9 and 10. The feature of dilution air intrusion is clearly identified where cooler air penetration follows the pattern expected from the hole geometry with one cool region close to the inner wall and one near the upper wall. Figure 11 shows the enthalpy source term (divided by σT_{air}^4) in the mid side view plane. There are regions where energy is lost (negative values) and regions where energy is gained (positive values). The enthalpy source term includes only radiative contribution. The peak is located in the dilution jet. Upstream and downstream of this jet we find regions of energy loss where high temperatures are calculated. In almost all the zones close to the walls there is energy reabsorption, that is positive source terms.

Of most interest to designers is the temperature distribution in the exit plane. Figure 12 shows contours of calculated and measured temperature. The influence of the swirl angle (5 degree) is clearly evident as the high temperature region is shifted clockwise with respect the position in the middle of the section. The agreement between calculations and experiments is considered good. In making a comparison, it should be remembered that there are uncertainties associated with both the experimental and numerical results. The errors in numerical results are due to the uncertainty of the velocity and mass flows specified at various inlets, the assumption of fast chemistry, the assumption of a standard k- ϵ turbulence model and neglect of radiation effects. The experimental errors are due to sector to sector non uniformity, radiation losses from the thermocouples and those caused by the intrusion of the probes into the flow. A fairer method of comparing results is to average the temperature distribution in the circumferential direction and obtain an average profile of the temperature field between the inner and outer end of the annulus.

This is what has been done to make the comparison homogeneous. The four experimental points (corresponding to the position of four thermocouples along the radius) represented in the radial profile were also obtained by this mean sector plot. The hot region is larger in the model, but globally the agreement is reasonable.

Table 1 shows the radiative, convective and total heat fluxes to the walls divided by the energy supplied to the combustor. As it can be seen, radiative and convective fluxes are small in comparison with the energy released by combustion. In any case convective fluxes are greater than radiative ones. Small values of convective fluxes can be justified by the stream of cooling air close to the walls. Even if this air deteriorates pattern factor, reduces combustion efficiency and contributes to the presence of pollutants in the exhaust, it is necessary to reduce wall temperature. The values of convective and radiative fluxes increase going from combustor dome to inner walls and outer walls. This means that air and wall temperatures increase accordingly. In any case the ratio of total energy loss to energy supplied is around 1-2%. One of the main problem encountered in the method used for heat transfer calculation is the lack of suitable correlation for external convection and radiation. We used a distribution of convective heat transfer coefficients on the cold side which seemed reasonable based on our experience in thermal analysis. Further work is needed in this area.

Table 2 shows the combustor inlet conditions, which are typical of take off. In Table 3 we compare the experimental values of parameters at combustor exit with numerical predictions. As it can be seen the larger discrepancies are in the prediction of radial quality.

Figures 13 and 14 show the temperature distribution to the inner and dome combustor walls. The presence of cooling holes is clearly identified. Higher temperature regions are located around dilution holes (larger black circles in Fig. 14) and between the two rows of cooling holes. The temperature profile is quite flat in the dome region (Fig. 13) with a low temperature line in the middle of the section due to the cooling slots. The three equispaced regions correspond to the torch positions.

Finally in Fig. 15 there is a comparison between calculated and measured wall temperatures in the combustor outer wall. The two scales are different: for numerical results we have an equispaced temperature scale, while for the experiments it is not, due to the properties of thermal paints used. These paints have the capability of changing color according to the temperature range, which is hardly equispaced. The D region of experiments corresponds practically to C+D+E of numerical calculations, as it can be seen. The main feature is represented by hot spots located around the dilution holes. Even if the values are not exactly the same, this trend is matched well by numerical model. We can note also a quite uniform, large and relatively cold region on the right side. Even in this case the agreement with experiments is not too bad. Another hot zone is between the two rows of cooling holes on the left side. In our analysis this zone is larger than that of experiments. This may be caused by the fact that we estimated a lower velocity for the cooling flow.

In general these first results are encouraging in that the qualitative trend of wall temperatures is almost well predicted and in some cases there is also a quantitative agreement with experiments.

13. CONCLUSIONS

In this paper we described a prediction procedure for the calculation of the flow, heat transfer and combustion processes inside a gas turbine combustor for aircraft engine. We pointed out the computational scheme of a technique for evaluating wall temperatures. This fact is not very common at moment, as wall temperature was assumed in previous works or it was calculated a-posteriori with the radiative heat fluxes evaluated at uniform

wall temperature equal to the inlet air. We solved the radiative heat transfer equations in conjunction with the solution of the mass, momentum and energy equations. A source term accounting for radiative heat transfer is included in the enthalpy equation and a boundary condition based on the energy balance of the combustor liner is used to calculate wall temperatures.

We tested the discrete ordinate radiation model solving some test cases for which analytical solution was available.

Following that an aircraft gas turbine combustor has been analyzed using a combustion model based on Arrhenius and Eddy Break-up concepts, coupled with a liquid droplet spray model within a three dimensional, body-fitted CFD code. The results of these analyses suggest that the modelling techniques employed have practical application for prediction of main combustion characteristics. The agreement with experimental data used to validate code ranged from fair to good. Additional study of this model will be performed against other data bases to further assess its usefulness in the preliminary design of combustion chambers for aircraft engines.

A cause of concern is the lack of reliable data for carbon monoxide to the gas absorption coefficient. We also found that wall temperatures calculation is sensitive to convective heat transfer coefficients on the cold side. This fact implies more studies to find reliable correlations that could be used in our model. Finally some reliable methods of predicting the soot concentration and then the emissivities of luminous flames are needed. We started to do something in this direction in another paper presented in this Symposium [16]

REFERENCES

- [1] Gupta, A. K., and Lilley, D. G., Flowfield Modeling and Diagnostic, Abacus Press, 1985.
- [2] Burns, A. D., Wilkes, N. S., A Finite Difference Method for the Computation of Fluid Flows on Complex Geometries, AERE-R 12342, Harwell Laboratory, Oxfordshire, U.K., 1987.
- [3] Jones, W. P., Whitelaw, J. H., Calculation Methods for Turbulent Reacting Flows: a Review, Comb. Flame, Vol. 48, 1982, pp. 1-26.
- [4] Faeth, G. M., Evaporation and Combustion of Sprays, Prog. Energy and Comb. Sci., Vol. 9, No. 1-2, pp 1-76, 1983.
- [5] Viskanta, R., Mengüç, M. P., Radiation Heat Transfer in Combustion Systems, Prog. Energy Combust. Sci., Vol. 13, pp.97-160, 1987.
- [6] Carlson, B. G., Lathrop, K. D., Transport Theory -The Method of Discrete-Ordinates in Computing Methods in Reactor Physics, eds. H. Greenspan, C. Kelber and D. Okrent, Gordon and Breach, New York, 1968
- [7] Carvalho, M., G., Durao, D. F. G., and Lockwood, F. C., Computation of Thermal Radiation for Gas Turbine Conditions, Proceedings of 65th AGARD/PEP Symposium, CP-390, pp 201-207, 1985.
- [8] Truelove, J. S., A Mixed Grey Gas Model for Flame Radiation, United Kingdom Atomic Energy Authority Report AERE-R-8494, Harwell, 1976.
- [9] Lefebvre, A. H., Gas Turbine Combustion, Hemisphere Publishing Corporation, New York, 1983.
- [10] Patankar, S. V., Numerical Heat Transfer and Fluid Flow, Hemisphere Publishing Corporation, New York, 1980.
- [11] Van Doormal, J. P., and Raithby, G. D., Enhancements of the SIMPLE Method for Predicting Incompressible Fluid Flows, Numerical Heat Transfer, Vol. 7, pp. 147-163, 1984.
- [12] Stone, H. L., Iterative Solution of Implicit Approximations of Multidimensional Partial Differential Equations, SIAM Journal on Numerical Analysis, Vol. 5, pp. 530-558, 1968.
- [13] Heaslet, A., and Warming, R. F., Radiative Transport and Wall Temperature Slip in an Absorbing Planar Medium, Int. J. Heat Mass Transfer, Vol. 8, pp.979-994, 1965.
- [14] Fiveland, W. A., Discrete-Ordinates Solutions of the Radiative Transport Equation for Rectangular Enclosures, ASME Journal of Heat Transfer, Vol. 106, pp. 699-706.
- [15] Lucas Aerospace Fabrications Division, Report No. B49397 (commercially in confidence).
- [16] Di Martino, P. and Cinque, G., Soot Formation Modelling in Turbulent Diffusion Flames, Symposium on Gas Turbine Engine Combustion, Emissions and Alternative Fuels, Lisbon, 1998.

Table 1 Heat fluxes to combustor walls

Wall considered	Radiative heat transfer/ Energy supplied to combustor	Convective heat transfer/ energy supplied to combustor	Total heat transfer/ energy supplied to combustor
Combustore dome	0.014%	0.0264%	0.0404%
Inner annulus wall	0.39%	1.04%	1.43%
Outer annulus wall	0.63%	1.45%	2.08%

Table 2 High power condition (take off)

Air mass flow (kg/s)	2.85
Fuel mass flow (g/s)	54.6
Air/Fuel ratio	48.3
Inlet temperature (K)	568
Inlet pressure (kPa)	701
Fuel type	Aviation kerosine

Table 3 Combustor exit parameters

Take off	Experiments	Model
Specified mean exhaust T (K)	1300.	1329.
Max exhaust temperature (K)	1447	1463.
O.T.D.F. %	20.1	17.6
Radial quality %	5.7	10.12
Fuel emission index	0.0	1.9E-2

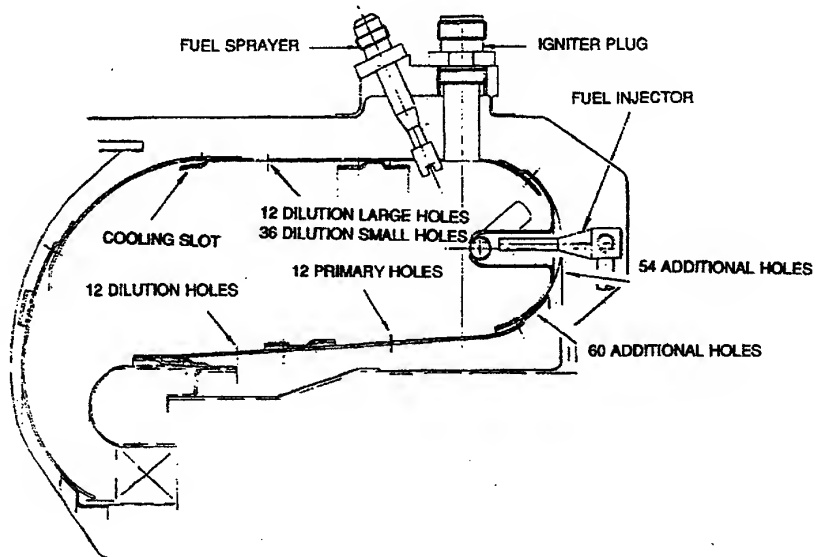


Fig. 5 Schematic drawing of single annular turboprop engine reverse-flow combustor.

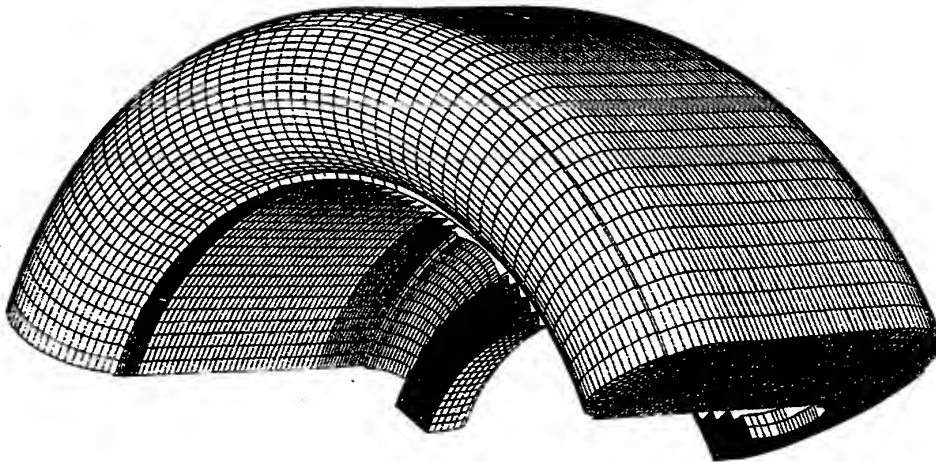


Fig. 6 Three dimensional view of computational grid for a 120° sector of single annular reverse-flow combustor.

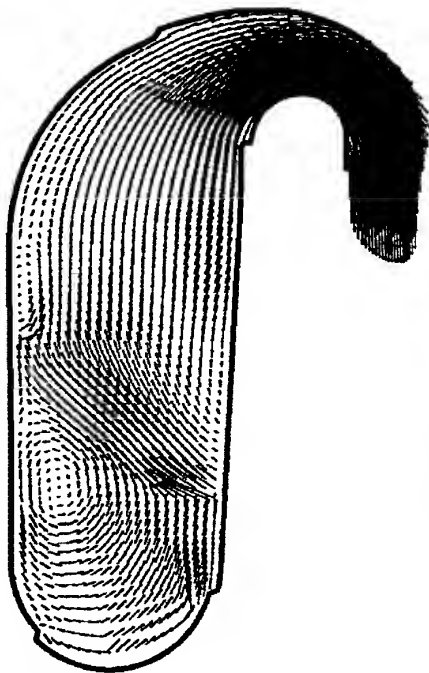


Fig 7 Velocity vectors in the side view plane with primary holes.

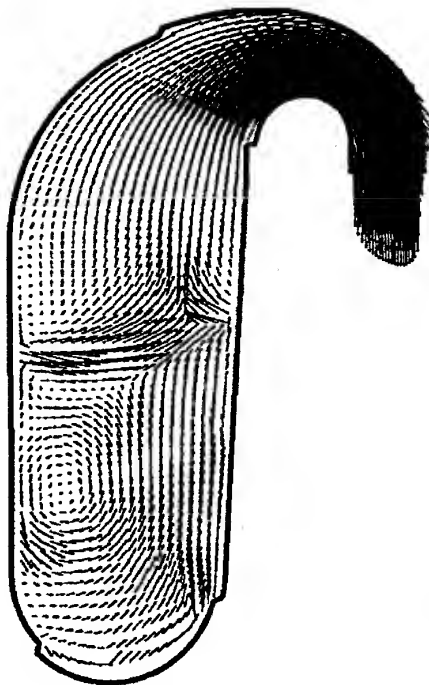


Fig 8 Velocity vectors in the side view mid plane.

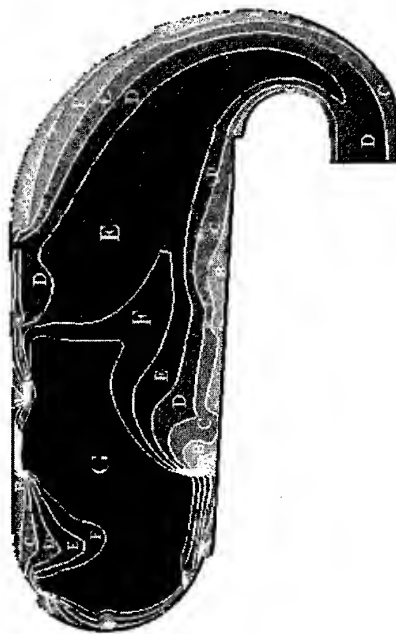


Fig 9 Temperature contours in the side view plane with primary holes.

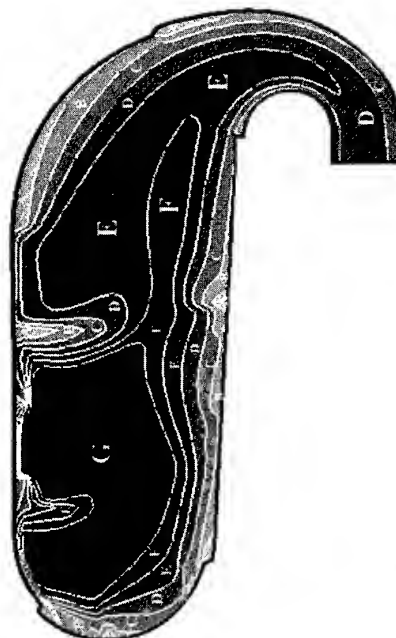


Fig 10 Temperature contours in the side view mid plane.

G
 F
 E
 D
 C
 B
 A

above 1900 K
 1700 - 1900 K
 1500 - 1700 K
 1300 - 1500 K
 1100 - 1300 K
 900 - 1100 K
 below 900 K

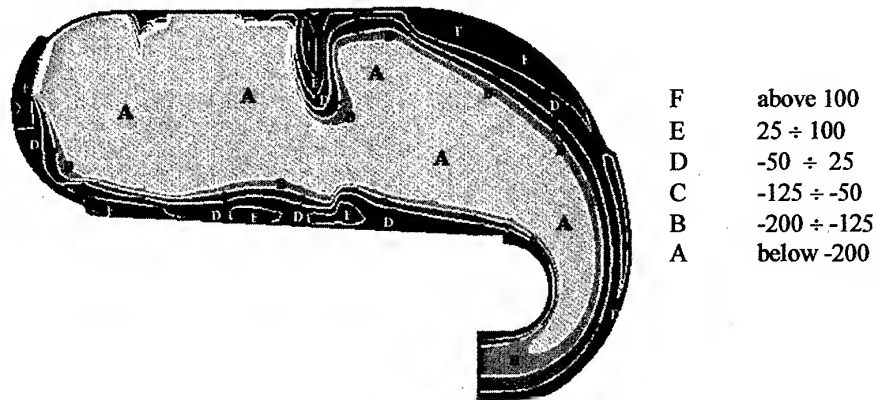


Fig. 11 Dimensionless enthalpy source term in the side view mid plane.

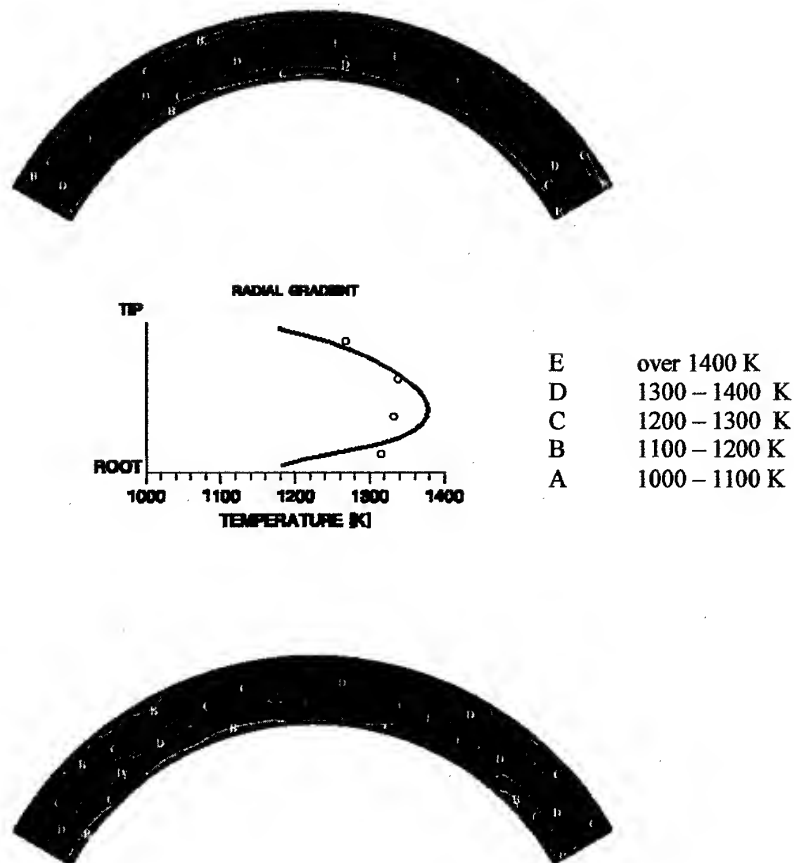


Fig. 12 Temperature contours in the exit plane and radial gradient: (o) experiments, (—) model.

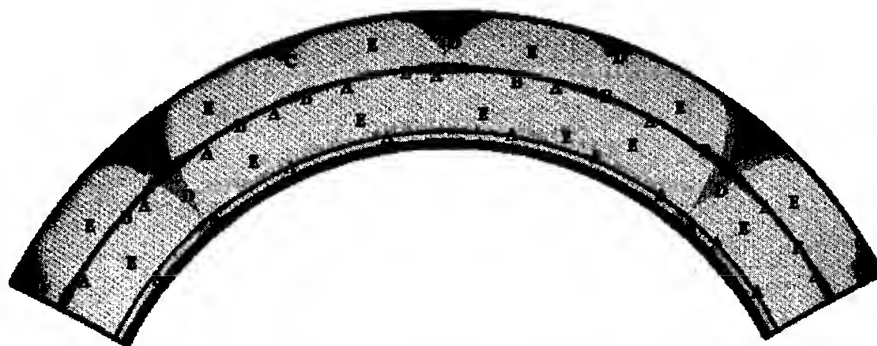


Fig. 13 Wall temperatures in the dome region.

E	above 1000 K
D	900 - 1000 K
C	800 - 900 K
B	700 - 800 K
A	600 - 700 K

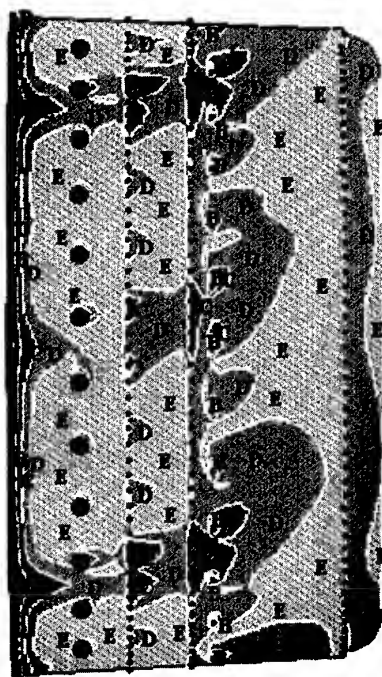


Fig. 14 Wall temperatures in the inner liner.

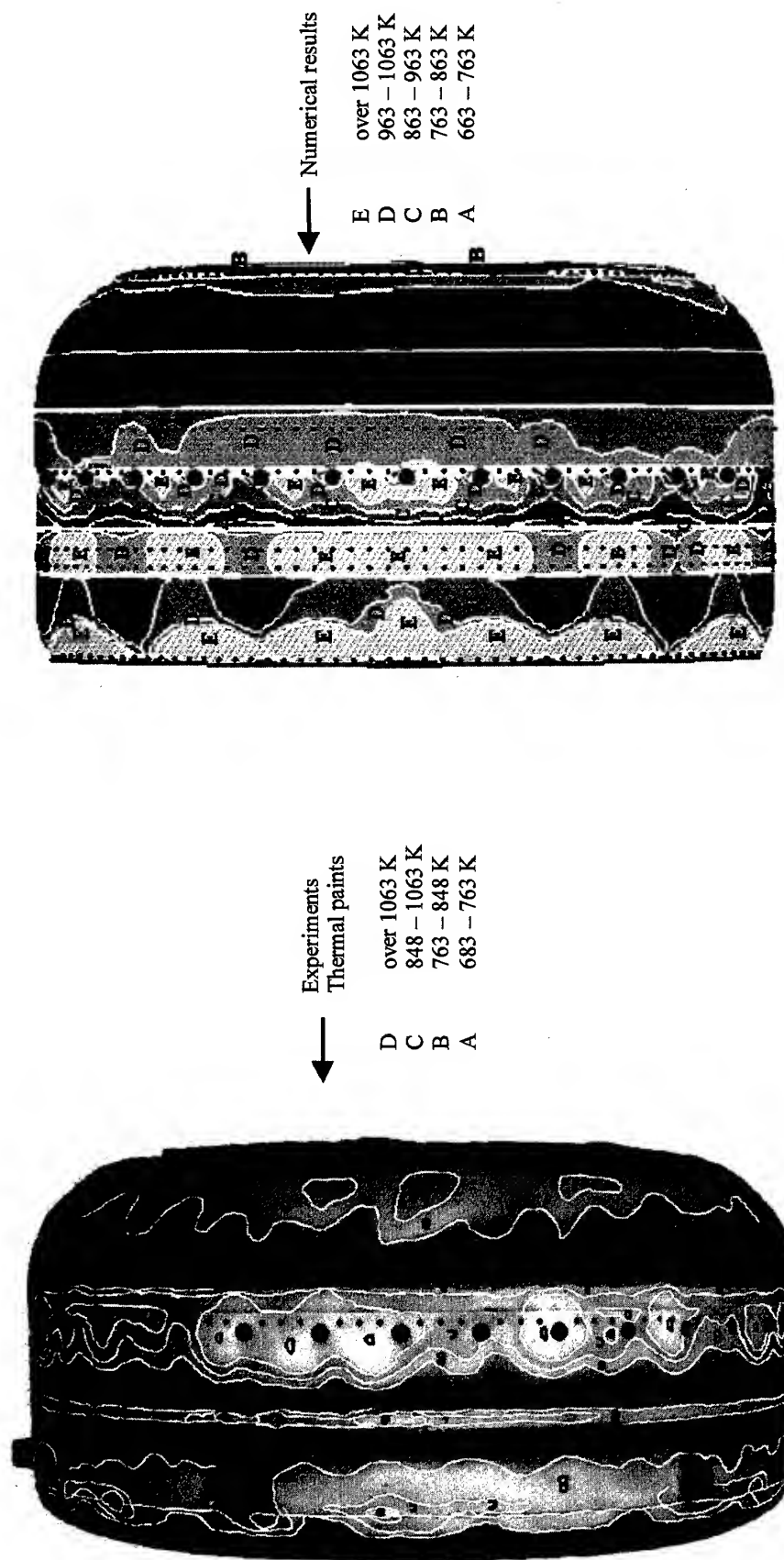


Fig. 15 Wall temperatures in the outer liner: thermal paints on the left side, numerical results on the right side.

PAPER No. 49
Martino & Cinque
(presenter: G. Cinque)

Question 1: N. Selcuk, Middle East Technical University, Turkey

I have two comments and a question. First, I think that testing of the discrete ordinate method S4 in one-dimensional, plane, parallel media is totally unnecessary as the verification has been done for 2, 4 and 6 approximations in one-dimensional, two-dimensional and even three-dimensional situations in cylindrical and rectangular enclosures, and with steep temperature gradients, all of which are appropriate for the gas turbine combustor. Second, this is the first application of the method to the gas turbine combustor that I have seen. However, you used a mean beam length based on the total volume of gas and its bounding area. This is the crudest way possible. You use quite a lot of grids by basing absorption coefficients on one value in a little combustor where there are very high gradients of concentration and temperature. The disagreements between experimental results and the calculations might be due to this coarse radiation property. Have you tried to calculate local absorption coefficients?

Answer:

Thank you for your comments, and I accept your observations. Absorption coefficients are calculated locally as a function of grid (i,j,k), so local gas concentration variations are accounted for. But, the mean beam length is an average one, and therefore, there is some crudeness.

Question 2: N. Selcuk, Middle East Technical University, Turkey

Use of local absorption coefficients together with a mean beam length gives control volumes that are far too small, and the calculation of the radiation properties is therefore wrong.

Answer:

This was just a first attempt to try to include all the effects that we felt that we had to.

Question 3: N. Brehm, BMW-RR, Germany

I apologise for missing the first part of your talk. My question concerns soot radiation; how was this calculated? Secondly, the local hot-spots on a combustor liner usually arise from convective heat fluxes, while radiation is just an even heat load for the wall. Is not the convective part of the total wall heat transfer the more important? The local flow details giving rise to the convective heat fluxes must be resolved much better than they are.

Answer:

Yes, I agree. Soot was not taken into account here, although I refer you to the second of our papers (Paper No. 50) for some details on soot. Frankly, there were just too many parameters for everything to be taken into account in this first attempt.

Question 4: G.J. Sturgess, ISSI, U.S.

This paper illustrates very nicely, the difficulties of applying CFD to practical combustors with incorporation in the calculation of comprehensive physical modeling when subject to the constraint of a reasonable computational time. I agree with Dr. Brehm that the convective contribution to wall heat load must be done much better; the use of conventional wall functions in the presence of liner film cooling for example, is totally inappropriate. Referring to my experience based on actual measurements in real combustors, the balance between radiative and convective heat fluxes in your calculations appears to be way off. This may be due to neglect of soot or may be tied up with the beam length and absorption coefficient problems discussed above by Dr. Selcuk; I personally feel that it is more to do with the former than the latter, however. Your computational domain was the inside of the combustor, which means that you had to specify many inlet boundary conditions; as part of which you mentioned the compressor exit guide vanes and residual swirl. Where did you obtain your boundary conditions? Incidentally, I do applaud the effort to do this work; it is important to attempt calculations of this kind.

Answer:

I agree with the observation concerning the use of wall functions. As is common practice in the industry, we used a one-dimensional flow code, called AIRFLOW, for the flows around the combustor, to provide the boundary conditions for flow into the combustor. There was a measured 5 degree residual swirl from the compressor exit guide vanes, and this was input to this one-dimensional code.

SOOT FORMATION MODELLING IN TURBULENT DIFFUSION FLAMES

P. Di Martino, G. Cinque
Alfa Romeo Avio S.A.P.A.
Research and Development Department
Viale Impero
80038 Pomigliano d'Arco
Napoli, ITALY

1. SUMMARY

The formation of soot and its emission from practical combustion devices is of interest to engineers and designers of gas turbines, diesel engines and power plants.

Although advances have been made, soot formation models must still be regarded as being far from complete because qualitative understanding of the physical processes remains uncertain.

The purpose of this paper was twofold: the first step was to choose the best soot formation models in the calculation of kerosine turbulent diffusion flame, more appropriate to gas turbine combustors for aircraft engines. The next step has been the optimization of the kinetic constants of soot models by comparing the computed results with available experimental measurements. Finally these constants have been used to couple soot and radiation in order to study the impact on local chemistry, temperature and heat transfer to the combustor walls. Comparisons with experiments concerning wall temperatures have also been performed.

2. INTRODUCTION

Carbon particulate that forms from gas phase combustion processes is generally referred to as soot or smoke. It consists mostly of carbon (96%) and a mixture of hydrogen, oxygen and other elements and compounds that may have been present in the original hydrocarbon fuel [1]

The formation of soot and its emission from practical combustion devices has long concerned engineers and scientists alike. Soot formation results from incomplete combustion and if produced in sufficient quantities can appear as an unsightly stack plume. Consequently the atmospheric visibility is reduced and the particle fallout is increased. Besides smoke emissions are often associated with carcinogenic polycyclic aromatic hydrocarbons and have adverse effects on health. Within the flame environment, the presence of particulate can play both a beneficial and a detrimental role in an overall industrial process. The condensed phase particles have a very high emissivity compared to the gaseous products formed and thus appreciably increase the radiant heat transfer. In certain applications, for instance in some boilers and furnaces, the aim is to produce soot in large quantities to enhance heat transfer and furnace productivity. On the other hand soot is undesirable in gas turbines for several reasons. The increased radiative heat transfer to the liner in soot forming regions affects the structural integrity of the liner and cooling requirements to remove the excess heat. Besides the impact of solid particles on liner wall and nozzle guide vanes or turbine blades in a gas turbine engine could have detrimental effects which would result in reduced service life or increased maintenance requirements of such components. Finally exhaust smoke is an indication of reduced efficiency of gas turbine combustors and therefore not acceptable.

The chemistry of soot formation is highly complex and remains relatively poorly understood. While significant progress has been reported in relation to sooting processes in simpler hydrocarbon fuels [2], even here the detailed chemical kinetic mechanisms offer little prospect of incorporation into engineering calculations. In such applications a compromise is necessary between the computational demands of the turbulent flowfield and the number of chemical species which may be incorporated in the sooting formation mechanism.

The purpose of this paper is twofold: the first step is to choose the best soot formation model available in literature to calculate kerosine turbulent diffusion flame, more appropriate to gas turbine combustors for aircraft engines. The next step is to optimize the kinetic constants of this soot model by comparing the computed results with available experimental measurements. Finally these constants will be used to couple soot and radiation models in order to study the impact on wall temperatures and radiative heat fluxes.

3. MATHEMATICAL MODEL

A model describing the formation/oxidation of soot has been incorporated in the Alfa Romeo Avio CFD code BODY3D. The code solves the steady, three dimensional, Favre-averaged partial differential equations for the conservation of mass, momentum, energy and chemical species using curvilinear non orthogonal coordinates. Turbulence is simulated by way of the k- ϵ model along with the wall function treatment for the near wall regions. Different combustion models are available. Arrhenius and Eddy Break-up model takes into account finite rate effects, flamelet approach assumes infinitely fast chemistry and links chemistry with turbulence by means of a statistical approach. Gas phase equations are coupled to momentum and energy balance equations for the liquid phase. As far as radiative heat transfer model is concerned, we used the discrete ordinate approximation, which is described in [3]. In order to optimize the soot kinetic constants we used the laminar flamelet model. Predictions of soot levels were incorporated through the solutions of transport equations for soot mass fraction and particle number density. The laminar flamelet approach has been the basis of recently developed soot formation models. This approach allows the decoupling of complex multi-component flame chemistry from the statistical uncertainties of turbulent flowfield. The decoupling is based on the assumption that the chemistry is fast and largely confined to thin reaction zones having the structure of essentially laminar flames, which are transported and distributed by mixing process in the turbulent flowfield. Scalar mixing is characterized by the mean and variance of mixture fraction (ξ , ξ'^2) and therefore the probability density function $P(\xi)$, a standard statistical distribution controlled by these two moments. Under the fast chemistry assumption, the instantaneous local scalar relationships $\phi = \phi(\xi)$ are those appropriate to the laminar flamelet and, together with the pdf

$P(\xi)$, the mean scalar properties in the turbulent flowfield may be determined simply by quadrature [4]. The above relationships are valid for an adiabatic flame but do not hold for a sooting flame due to the radiative heat loss. Therefore, a method has to be devised to relate temperature to mixture fraction accounting for heat losses. It is possible to use a model to calculate soot concentration and to estimate the radiative heat transfer. Then, an energy equation may be solved and a relationship between enthalpy and mixture fraction assumed to compute flame temperature taking into account the radiative heat loss. However this procedure is not recommended when the soot formation or oxidation models are evaluated by comparing predicted soot concentration with available measurements. Infact, soot formation and oxidation are strongly dependent on temperature. Therefore, temperature and soot distributions both depend one on the other. Soot concentration influences radiation which influences enthalpy and, therefore, temperature and soot concentration. Supposing that soot formation and oxidation models are accurate enough to provide a correct distribution of soot concentration, it may happen that turbulence/radiation or enthalpy/mixture fraction relationship yield an inaccurate temperature field. In such a case, soot concentration would be poorly predicted because the temperature field was not correct. Consequently, it is better to decouple soot from temperature predictions if attention is focused on evaluation of soot formation models. A simple method [4] can be used to adjust flamelet temperatures as a function of mixture fraction. This is based on matching the experimental temperature profile by the introduction of a heat loss factor, as illustrated in [4]. A good analysis of different soot models has been carried out in [4]. The soot formation model of Stewart, Syed and Moss [5] seems to give the best results. So we focused our attention on that. As far as soot oxidation model is concerned, we chose that of ref. [6].

4. RESULTS OF OPTIMIZATION CONSTANTS

Two burners have been taken into account. The first configuration is illustrated in Fig. 1. The flame is contained within a borosilicate glass tube of 155 mm diameter and mounted in a pressure vessel [7]. The kerosene fuel is prevaporized in a small resistively-heated pre-chamber into which the liquid fuel is sprayed through a single orifice of 100 mm. The chamber is maintained at a temperature of 900 K and the kerosene appears to flash vaporise on contact with the walls. The kerosine vapour emerges from the burner exit at a temperature of 593 K.

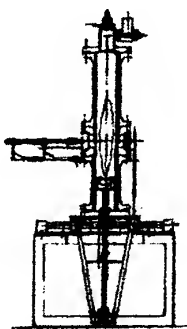


Fig. 1 Schematic of experimental apparatus [7].

Given the significant radiative loss from sooting turbulent flames, there is a complex non-linear coupling between local flame temperature and soot formation rates. For detailed combustor predictions, this may require to solve an energy

balance equation which takes into account radiative heat transfer. As previously quoted, our present objective is to establish a satisfactory model for the soot production process. Consequently it is better to decouple soot from temperature predictions. The method described earlier has been used to incorporate radiative heat loss. Soot balance equations can now be solved as a post-process.

The second configuration is illustrated in Fig. 2. It is a three-slot, Wolfhard-Parker burner [8]. It incorporates an inner fuel slot of width 6 mm and two outer air slots each of width 9 mm. The slots are 48 mm long. The kerosene fuel is prevaporised at a temperature of 700 K.

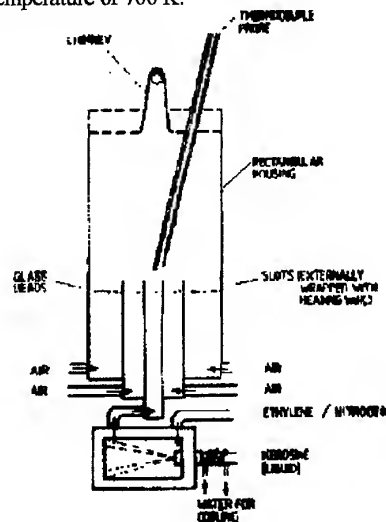


Fig. 2 Schematic of second experimental apparatus [8].

Figure 3a illustrates the temperature fitting obtained using the axial temperature measurements. Note that the adiabatic temperature is very high compared to experiments, thus indicating large radiative heat loss. We would like to point out that the standard turbulence model constants have been utilized in this study. Some authors [4] prefer to vary these constants, particularly the constant C_2 , to adjust the turbulent viscosity and therefore the temperature gradients. The optimization of the kinetic constants has led to the results shown in Fig. 3b. This work has never been carried out before. The experimental peak soot volume fraction increases very rapidly with height. The maximum value, $f_v = 9.3 \cdot 10^{-6}$, occurs at a height of 300 mm. Beyond this station in the turbulent flame f_v declines rapidly in the burnout region where turbulent mixing now promotes oxidation. Figure 3c shows the peak soot volume fraction profile relative to the second burner. Numerical predictions have been performed by using the same set of optimized constants coming from the first burner. The agreement with experiments is quite good. The optimization process can be continued if other kerosene-flame experiments are available.

5. RADIATIVE HEAT TRANSFER MODEL

The effects of radiation transport appear in the energy conservation equation as the divergence of the radiative heat flux [9], $(-\nabla \cdot \mathbf{q}_r)$. For a grey medium, $(-\nabla \cdot \mathbf{q}_r)$ is evaluated from:

$$-\nabla \cdot \mathbf{q}_r = \kappa \left[\int_{4\pi} I(\mathbf{r}, \Omega) d\Omega - 4\pi I_b \right] \quad (1)$$

where κ is the absorption coefficient, $I(\mathbf{r}, \Omega)$ is the directional intensity, Ω is the direction of radiation, and I_b represents the blackbody intensity. To find $I(\mathbf{r}, \Omega)$, we solve the radiative transfer equation RTE for grey gases [9].

The scattering of the radiation by soot is negligible as the radiation wavelength is generally greater than the soot particle diameter when we are talking about infrared radiation from flames [10]. So we set the scattering coefficient to zero.

The equation for intensity, $I(r, \Omega)$, is written in a body-conforming system of coordinates and is solved using the discrete-ordinate approximation to RTE. This is obtained by discretizing the entire solid angle (4π steradians) using a finite number of ordinate directions and corresponding weight factors. The RTE is written for each ordinate and the integral terms are replaced by a quadrature summed over each ordinate and this provide the source term in the enthalpy equation. This method is sometimes referred to as the S_N approximation [9], where the order of approximation is N (i.e. the number of discrete values of direction cosines to be considered). In general the total number of ordinate directions, M , is related to the order of approximation, N , through the relationship $M=N(N+2)$ given in [9]. For the work presented in this paper, we used the S_4 method, which is a good compromise between accuracy and CPU time. The gas absorption coefficient κ_g is calculated from the total emissivity of a grey gas ϵ_g , as described in [11]:

$$\epsilon_g = 1 - \exp(-\kappa_g L) \quad (3)$$

The total emissivity is obtained by the "two grey plus one clear gas" model of Truelove [12]. Water vapor and carbon dioxide are the prime contributors to the gaseous radiation. Owing to the lack of appropriate data, the contribution of carbon oxide and fuel was not considered. Therefore the expression of ϵ_g is:

$$\epsilon_g = \sum_{n=1}^N a_{g,n}(T_g) \left[1 - \exp\left(-\kappa_{g,n}(P_{H_2O} + P_{CO_2})L\right) \right] \quad (4)$$

Where the summation n is over the three gases of the assumed mixture, the $\kappa_{g,n}$ are presumed constants with the temperature dependence of emissivity being accommodated in the weighting coefficients $a_{g,n}$. P_{H_2O} and P_{CO_2} are the partial pressures of water vapor and CO_2 respectively, and L is the mean beam length of the system, approximated by $L=3.5V/A$ [13]. The values of $\kappa_{g,n}$ and $a_{g,n}$ are tabulated in [12]. The emissivity ϵ_s of the soot cloud is calculated from:

$$\epsilon_s = 1 - \exp(-\kappa_s C_s L) \quad (5)$$

where C_s is the soot concentration given as $kg\ m^{-3}$ and κ_s is the specific soot absorption coefficient which depends on soot temperature. Within a luminous flame, the soot emissivity can dominate. In this case the total emissivity of the combustion products-soot mixture ϵ_m can be represented by a single grey gas expression:

$$\epsilon_m = \epsilon_g + \epsilon_s - \epsilon_g \epsilon_s \quad (6)$$

Strictly speaking soot particles temperature may be different from gas temperature. In our analysis we assumed for simplicity thermal equilibrium between soot particles and gas. The boundary conditions for the RTE equation are illustrated in [9]. The effects of turbulence on radiation are not easy to be modeled and so have been neglected. The wall temperature calculation has been carried out using the procedure described in [13].

6. RESULTS FOR REVERSE-FLOW COMBUSTOR

Having obtained a reasonable set of soot kinetics constants, we solved the soot equations in conjunction with the solution of the flowfield and radiative heat transfer model, to study the impact

on gas temperature, chemistry and heat transfer to the combustor walls.

A turboprop engine reverse-flow combustor chamber (Fig. 4) has been analyzed in this study. Test measurements taken from [14] were available. The fuel injection system of the annular combustor comprises 9 T-shaped vaporizers equally spaced along the circumferential direction and three torches. The fuel used was Jet-A. The calculations are conducted for a flow in a 120 degree sector of the combustor with periodic boundary conditions being imposed on the two side planes. Within this sector there are 12 primary holes (inner liner), 8 dilution holes (4 inner and 4 outer liner), 36 dilution, 54 primary holes (between the T-shaped vaporizer) 60 primary holes and 9 film cooling slots. The geometry was represented by a body-fitted mesh (Fig. 5) of $110 \times 23 \times 51$ grid points. This grid resolution, while somewhat coarse, has been found from modelling application experience to be adequate for providing reasonably accurate predictions of combustor exit gas temperature average radial profile and traverse quality. Calculations were performed at high power conditions of operation. A one-dimensional code was used to determine air flow distribution through the rows of holes across the liner as well as pressure drops and injection angles.

The temperature field in the combustor mid plane is shown in Figures 6-7. The cool region in the primary zone is due to the fuel injection. This zone is surrounded by high temperature where the mixture fraction approaches stoichiometric value. The cold air entering through the secondary jets is clearly identified. Downstream of these jets there are further high temperature regions. The comparison between Fig. 6 (no soot) and Fig. 7 (with soot) show that the temperature pattern is almost the same. A reduction can be found downstream of the secondary jets.

Figures 8 and 9 show the dimensionless enthalpy source term in the combustor midplane. In Fig. 8 (no soot) the enthalpy source term assumes positive values (i.e. heat is gained) through the secondary jets and just close to the upper bend. The presence of soot strongly modifies this pattern. Another peak enthalpy source term is found in the region of peak soot and unburned fuel (Figures 10-11). The interesting feature is also that the values of Fig. 9 are much higher than those of Fig. 8 (note that the scale is different to the source term plot of Fig. 8). As just quoted above, the peak soot volume fraction is found in the primary zone (Fig. 11) where unburned fuel attains maximum values (Fig. 10) and temperature is high.

Figures 12 and 13 illustrate the dimensionless wall radiative fluxes to the combustor dome, without and with soot respectively. The distribution is almost uniform in both figures. Three equispaced regions in line with the torches can be seen. The most important characteristic is that soot has strongly increased the wall heat fluxes (a factor of three at least). This fact confirms that soot concentration needs to be predicted to a good degree of accuracy if the wall heat fluxes and wall temperatures are to be evaluated for stress and lifing calculation. The effects of soot are also evident in the gas temperature at combustor exit (Fig. 14). The high temperature region is reduced and also the radial gradient match better the experiments.

Finally Fig. 15 show the wall temperature of the outer liner compared with experimental results (thermal paints). As expected the temperature level is higher when soot is present. This is true in particular just between the two rows of cooling holes (a little bit left starting from the centre of figure). Hot spots around the primary holes are quite well predicted. Note that temperature distribution on the right is practically unchanged, thus revealing that no significant amounts of soot are present in that regions. In any case there are a lot of uncertainties in the wall temperature predictions. The results

presented in this paper are the first attempt, to our knowledge, to solve soot and radiation in conjunction with the flowfield. The main indication is that it is necessary to improve the calculation of soot concentration. The optimized set of constants needs to be tested on other kerosine fuelled combustors. It is also important to improve the correlations that give the soot emissivity as a function of soot temperature and concentration. Finally an assessment of convective heat transfer correlations is to be made, in order to reduce the degree of approximation in the wall temperature prediction.

Table 1 shows the radiative, convective and total heat fluxes to the walls divided by the energy supplied to the combustor. As it can be seen, radiative and convective fluxes are small in comparison with the energy released by combustion. In any case convective fluxes are greater than radiative ones. Small values of convective fluxes can be justified by the stream of cooling air close to the walls. Even if this air deteriorates pattern factor, reduces combustion efficiency and contributes to the presence of pollutants in the exhaust, it is necessary to reduce wall temperature. The values of convective and radiative fluxes increase going from combustor dome to inner and outer walls. This means that air and wall temperatures increase accordingly. In any case the ratio of total energy loss to energy supplied is around 1-2%. As expected the values of radiative heat fluxes are increased when soot is considered. One of the main problem encountered in the method used for heat transfer calculation is the lack of suitable correlation for external convection and radiation. We used a distribution of convective heat transfer coefficients on the cold side which seemed reasonable based on our experience in thermal analysis. Further work is needed in this area.

Table 2 shows the combustor inlet conditions, which are typical of take off. In Table 3 we compare the experimental values of parameters at combustor exit with numerical predictions. As it can be seen the larger discrepancies are in the prediction of radial quality. From the well established SAE standard [15], a reasonable estimate of soot present in the exhaust can be made in terms of Smoke Number. This number represents the amount of soot collected on a white paper filter of a given size and contained in a known volume of exhaust gases circulated through the filter. By shining a light on this stained paper, the reflected light intensity can be compared to a clean paper. The result of this comparison graduated from 1 to 100 is the Smoke Number (SN). So this is a value regularly and easily measured in experimental tests. Even if the measuring technique is not perfect, it is widely used in the aeroengine industry for soot measurements. In Table 3 we have a measured SN. We used a correlation given in [16] to evaluate SN from the mean soot concentration in the exit plane. We have calculated $SN=17.7$ while SN measure is 22.5. If we consider that the errors on SN measurements range from -15% to +10% [16], we can conclude that the result of our analysis is very good, or at least it has the same uncertainty of experiments.

In general these first results are encouraging in that the qualitative trend of wall temperatures is almost well predicted and in some cases there is also a quantitative agreement with experiments.

7. CONCLUSIONS

In this paper we described the work that has been carried out to optimize the kinetics constant of soot formation/oxidation model for a turbulent diffusion kerosine flame. The next step has been the coupling of soot balance equation with radiative heat transfer equations, in order to evaluate the impact on local chemistry, gas temperatures and wall temperatures. We believe that for the first time the flowfield, soot levels and wall temperatures in a real combustor have been calculated by a

CFD code. Further work needs to be done in order to improve the calculation of soot concentration. However these first results are to be considered encouraging in that wall temperatures and Smoke Number have been numerically solved for a single annular reverse-flow combustor and the agreement with measurements is globally not too bad.

The comparison between the two sets of numerical analysis (with and without the presence of soot) has shown that soot affects not only the peak value of wall heat flux, but also the distribution.

REFERENCES

- [1] I. Glassman, "Combustion", Academic Press, 1977.
- [2] I. Glassman, "Soot Formation in Combustion Processes", 22nd Symposium (International) on Combustion, p. 295, 1988.
- [3] Carlson, B. G., Lathrop, K. D., Transport Theory -The Method of Discrete-Ordinates in Computing Methods in Reactor Physics, eds. H. Greenspan, C. Kelber and D. Okrent, Gordon and Breach, New York, 1968.
- [4] AGARD CP-436, 1993.
- [5] K. J. Syed, "Soot and Radiation Modelling in Buoyant Fires", PhD Thesis, Cranfield Institute of Technology, School of Mechanical Engineering, 1990.
- [6] J. Nagle, R. F. Strickland-Constable, "Oxidation of Carbon between 1000E-2000E C", Proc. 5th Conference on Carbon, Pergamon, 1, 1961, p. 154.
- [7] C. D. Stewart, K. J. Syed and J. B. Moss, "Modelling Soot Formation in Non-Premixed Kerosene-Air Flames", Comb. Sci. and Tech., 75, 1991, pp. 211-226.
- [8] K. B. Lee, M. W. Thring, J. M. Beer, "On the Rate of Combustion of Soot in a Laminar Soot Flame, Comb. and Flame, 6, 1962, pp. 137-145.
- [9] Viskanta, R., Mengüç, M. P., Radiation Heat Transfer in Combustion Systems, Prog. Energy Combust. Sci., Vol. 13, pp.97-160, 1987.
- [10] De Ris, J., Fire Radiation - A Review, 17th Symposium (Internationale) on Combustion, pp 1003-1016, 1979.
- [11] Carvalho, M., G., Durao, D. F. G., and Lockwood, F. C., Computation of Thermal Radiation for Gas Turbine Conditions, Proceedings of 65th AGARD/PEP Symposium, CP-390, pp 201-207, 1985.
- [12] Truelove, J. S., A Mixed Grey Gas Model for Flame Radiation, United Kingdom Atomic Energy Authority Report AERE-R-8494, Harwell, 1976.
- [13] Lefebvre, A. H., Gas Turbine Combustion, Hemisphere Publishing Corporation, New York, 1983.
- [14] Lucas Aerospace Fabrications Division, Report No. B49397 (commercially in confidence), 1983.

- [15] SAE Committee E-31, Aircraft Gas Turbine Smoke Measurement, SAE ARP 1179 Rev. B, 1991.
- [16] De Champlain, A., Kretchmer, D., Tsogo, J., Prediction of Soot Emissions in Gas Turbine Combustors, ISABE 1995.

Table 1 Heat fluxes to combustor walls

Wall considered	Radiative heat transfer/ Energy supplied to combustor		Convective heat transfer/ energy supplied to combustor		Total heat transfer/ energy supplied to combustor	
	No soot	With soot	No soot	With soot	No soot	With soot
Combustor dome	0.014%	0.0342%	0.0264%	0.0132%	0.0404%	0.0474%
Inner liner wall	0.39%	0.63%	1.04%	0.88%	1.43%	1.51%
Outer liner wall	0.63%	1.05%	1.45 %	1.16%	2.08%	2.21%

Table 2 High power condition (take off)

Air mass flow (kg/s)	2.85
Fuel mass flow (g/s)	54.6
Air/Fuel ratio	48.3
Inlet temperature (K)	568
Inlet pressure (kPa)	701
Fuel type	Aviation kerosine

Table 3 Combustor exit parameters

Take off	Experiments	Model	
		No soot	With soot
Specified mean exhaust T (K)	1300.	1329.	1295.
Max exhaust temperature (K)	1447	1463.	1420.
O.T.D.F. %	20.1	17.6	17.3
Radial quality %	5.7	10.12	9.9
Fuel emission index (g/kg)	0.0	1.9E-2	1.9E-2
SAE Smoke Number (SN)	22.5	-	17.7

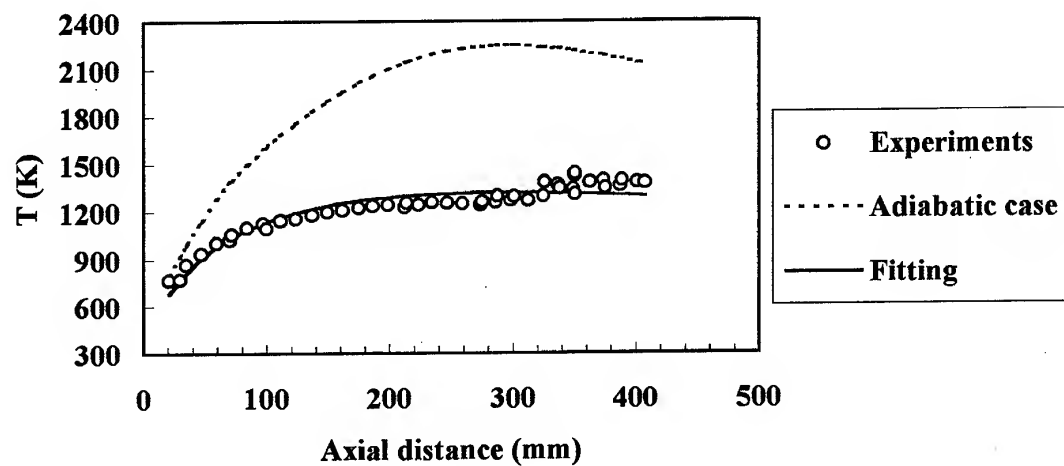


Fig. 3a Axial temperature distribution: optimization of radiative heat loss factor.

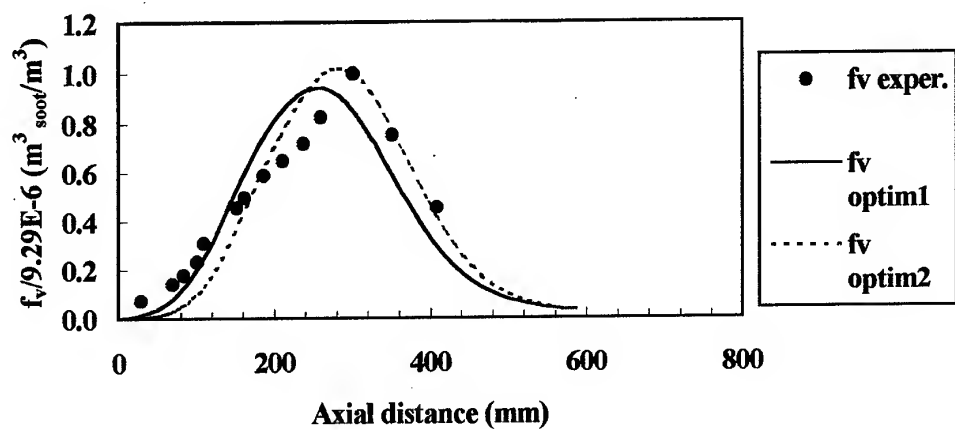


Fig. 3b Axial soot volume fraction: optimization of kinetics constants.

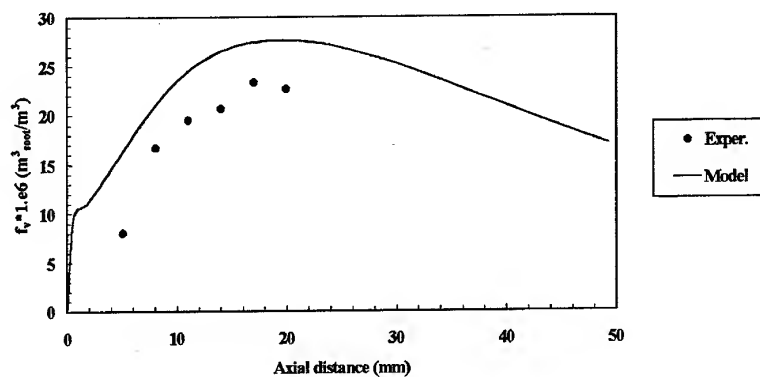


Fig. 3c Axial soot volume fraction: comparison between model and experiments.

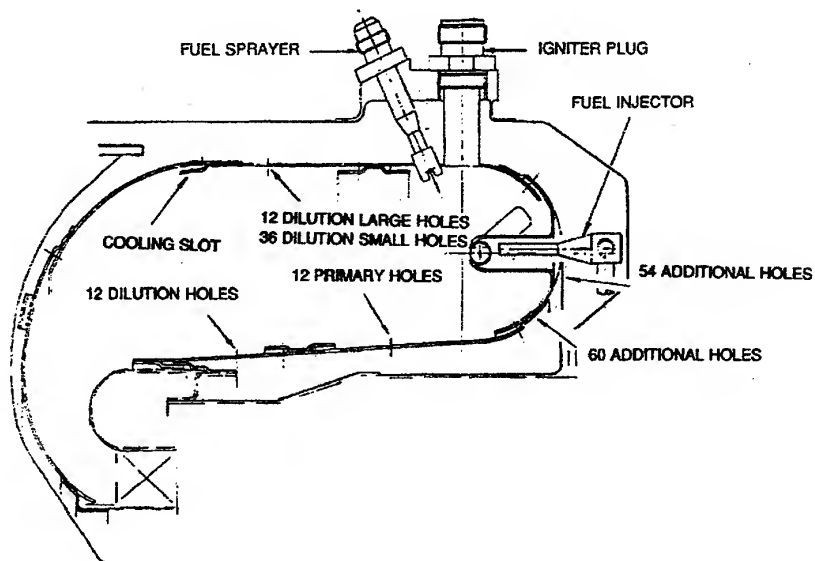


Fig. 4 Schematic drawing of single annular turboprop engine reverse flow combustor.

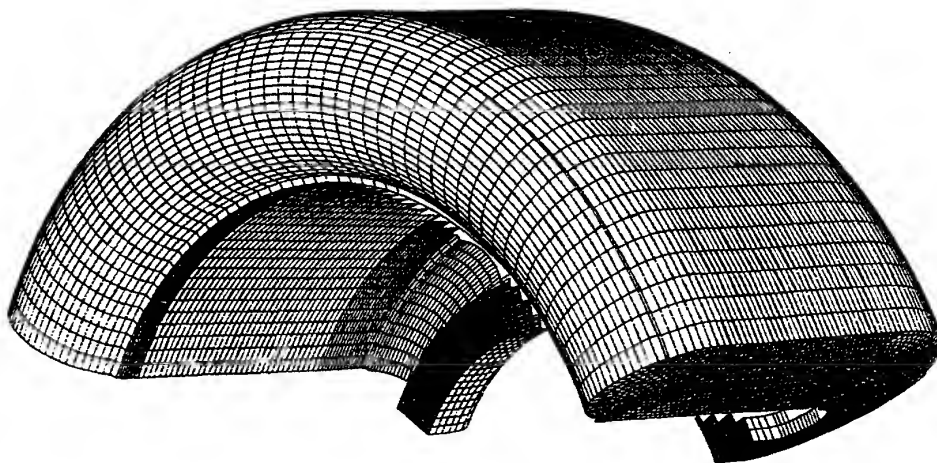


Fig. 5 Three dimensional view of computational grid for a 120° sector of single annular reverse-flow combustor.

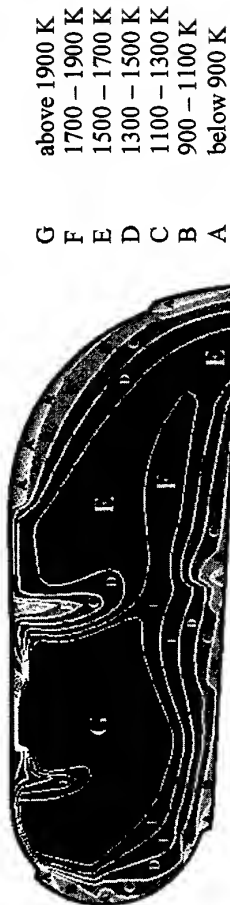


Fig. 6 Temperature contours in the side view mid plane (no soot) .

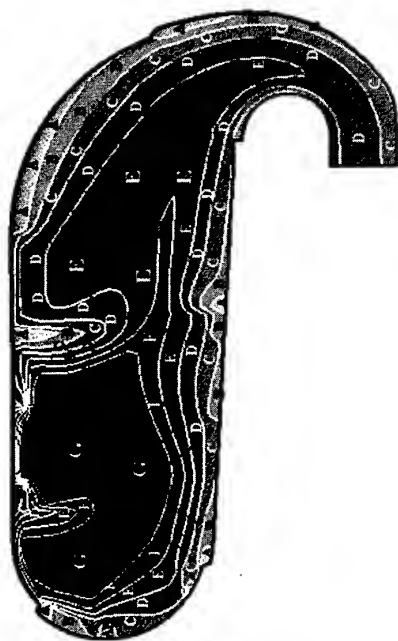


Fig. 7 Temperature contours in the side view mid plane (with soot) .



Fig. 8 Dimensionless enthalpy source term in the side view mid plane (no soot).



Fig. 9 Dimensionless enthalpy source term in the side view mid plane (with soot)

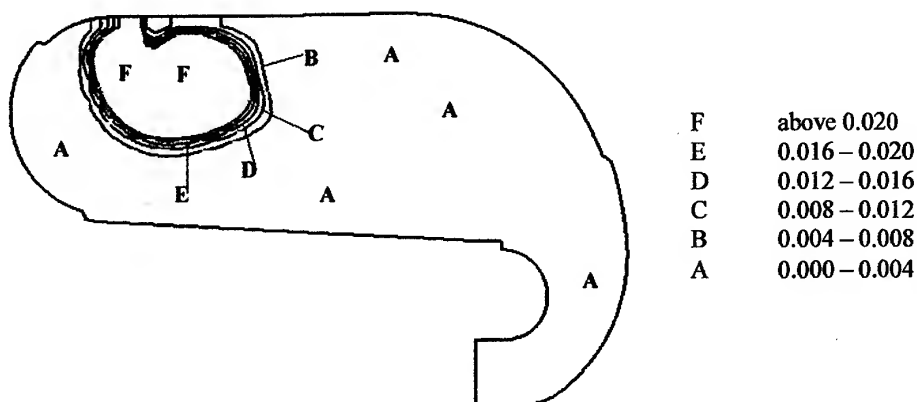


Fig. 10 Fuel mass fraction in the side view mid plane.

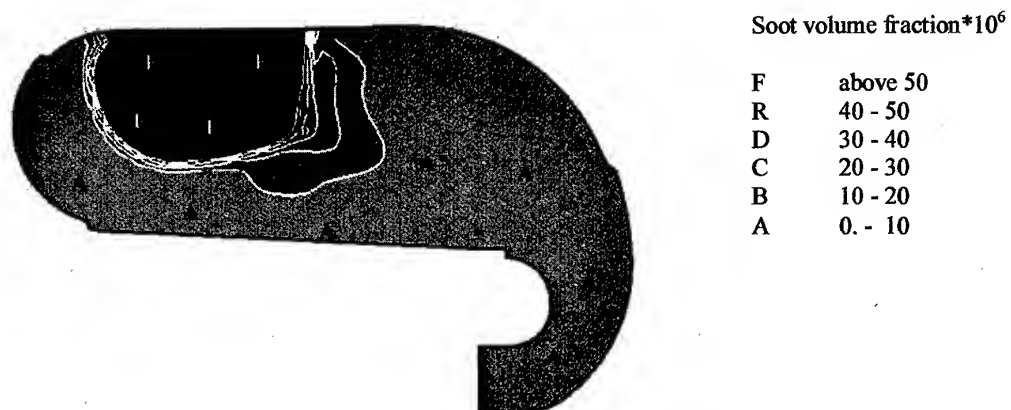
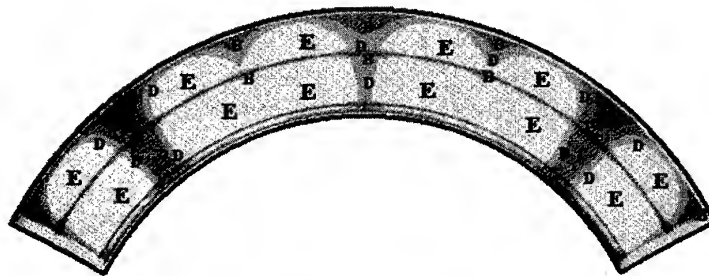


Fig. 11 Soot volume fraction in the side view mid plane.



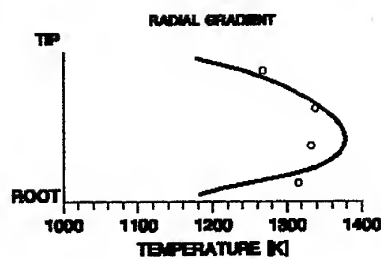
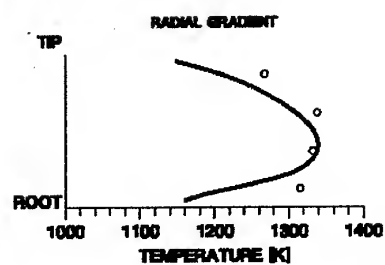
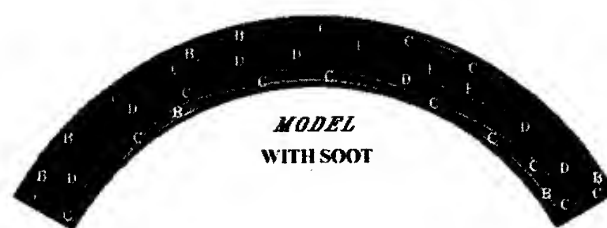
E	above 60
D	45 - 60
C	30 - 45
B	15 - 30
A	0 - 15

Fig. 12 Dimensionless radiative heat fluxes in the dome region (no soot).



E	above 200
D	150 - 200
C	100 - 150
B	50 - 100
A	0 - 50

Fig. 13 Dimensionless radiative heat fluxes in the dome region (with soot).



E	over 1400 K
D	1300 – 1400 K
C	1200 – 1300 K
B	1100 – 1200 K
A	1000 – 1100 K



Fig. 14 Temperature contours in the exit plane and radial gradient.

PAPER No. 50
Martino & Cinque
(presenter: G. Cinque)

Question 1: N. Selcuk, Middle East Technical University, Turkey

Where did your soot formation and oxidation information come from? Are you aware that Magnussen's data is applicable to gaseous propane and not liquid kerosene? Perhaps this is the reason for the differences seen between your calculations and the actual combustor.

Answer:

Yes, there are a number of constants associated with which there are uncertainties. We found that constants for propane are frequently used for kerosene, and not just in soot modeling, but also in normal combustion models.

Question 2: A. Doepelheuer, DLR, Cologne, Germany

You correlated soot formation and oxidation rates mainly to local gas temperatures. However, fuel/air ratio and local O/C atom ratios have a big effect on soot rate constants. How did you take this into account?

Answer:

We tried available soot formation and oxidation models from the literature and tailored them for kerosene. I forgot about the chemistry and concentrated on just the kinetic parameters, and then used a parametric study since it was impossible to actually measure the constants.

Question 3: C. Priddin, R.R., U.K.

In our paper on Tuesday (Paper No. 10) we used the same basic Cranfield data for soot that you did; we used the laminar constants while it appears that you used the turbulent constants. Did you actually simulate the details of this experimental flow and back out the inherent constants, or did you take whatever turbulent field was built into the original experiment and use the net results?

Answer:

We just the turbulent case. We are trying various models, and we are learning what is the best approach to use.

Efficient Numerical Calculation of Evaporating Sprays in Combustion Chamber Flows

R. Schmehl, G. Klose, G. Maier and S. Wittig

Lehrstuhl und Institut für Thermische Strömungsmaschinen
Universität Karlsruhe (T.H.)
Kaiserstr. 12, Postfach 6980
76128 Karlsruhe, Germany

Summary

Representing two different conceptual approaches, either Eulerian continuum models or Lagrangian particle models are commonly applied for the numerical description of dispersed two phase flows. Taking advantage of the positive features inherent to each model, a combination approach is presented in this study for the efficient computation of liquid fuel sprays in combustor flows. In the preconditioning stage, Eulerian transport equations for gas phase and droplet phase are solved simultaneously in a block-iterative scheme based on a coarse discretization of spray boundary conditions at the nozzle. Due to the close coupling of both phases, the time expense of this approximate flow field computation is not much higher as for single phase flows. In the refinement stage, Lagrangian droplet tracking is applied with a detailed discretization of initial conditions. To account for complete interaction between gas phase and droplets, gas flow solution and droplet tracking are concatenated by an iterative procedure. In this stage, the numerical description of the spray is enhanced by additional modeling of droplet breakup. Results of numerical simulations are compared with measurements of the two phase flow in a premix duct of a LPP research combustor.

tially requires sophisticated combustion concepts in order to meet today's strict limitations on pollutant emissions. Fundamental to these low emissions concepts is a characteristic strategy to inject and mix the liquid fuel with the compressed air flow, avoiding local stoichiometric combustion conditions as far as possible. Two promising approaches in this context are the concepts of Lean-Premix-Prevaporize (LPP) and Rich-Quench-Lean (RQL) combustion. In order to develop advanced combustor designs with the required flow characteristics, a better understanding of the two phase flow physics is necessary. Two phase flow effects typical for premix ducts of LPP combustors or prefilming air blast atomizers are summarized in Fig. 1.

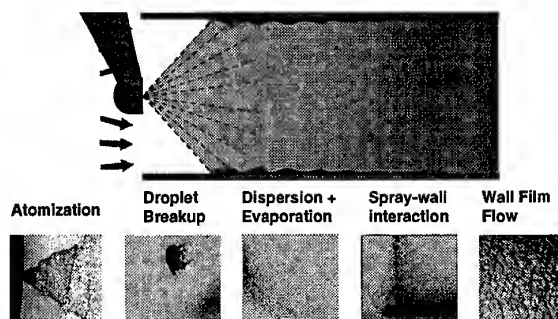


Figure 1: Two phase flow effects in a LPP premix duct

1 Notation

c_p	specific heat capacity	U	velocity component
D	droplet diameter	We	Weber number
$D_{0.5}$	mass median diameter	Y	mass fraction
D_{32}	Sauter mean diameter		
$D_{0.632}$	characteristic diameter	Greek Symbols	
f	body force	α	heat transfer coefficient
h	enthalpy	α_k	liquid volume fraction
\dot{H}	enthalpy flux	β	off axis angle
H	energy transfer rate	ε	dissipation rate of k
I	momentum transfer rate	Γ	diffusion coefficient
k	turbulent kinetic energy	μ	dynamic viscosity
\dot{m}	mass flux	ν	kinematic viscosity
\dot{M}	mass transfer rate	ρ	density
On	Ohnesorge number	τ	shear stress
P	pressure		
Pr	Prandtl number	Subscripts	
\dot{Q}	conductive heat flux	0	initial state
Re	Reynolds number	g, d	gas, droplet
S	source term	int	interface
Sc	Schmidt number	t	turbulent
T	temperature	vap	vapor
Tu	degree of turbulence		

2 Introduction

Improving modern gas turbine efficiencies by increasing pressure and temperature levels of the combustion process, essen-

Due to the enormous increase in computing performance, Computational Fluid Dynamics (CFD) offers a promising potential for efficient combustor design and optimization. In particular when compared to experimental studies at elevated pressures, CFD analysis may be employed to reduce turn-around times and costs of combustor design significantly. On the other hand, complex flow phenomena such as turbulence, atomization or chemical reaction still represent some of the most challenging topics for CFD tools.

Basically, two different conceptual approaches may be employed for the numerical description of dispersed two phase flows [3]. In analogy to single phase gas flow, the Eulerian approach is based on a continuum model of the spray, resulting in transport equations describing the propagation and evaporation of this droplet phase [28], [6]. In the Lagrangian approach, the spray is modeled by superposition of trajectories calculated for large numbers of representative droplets. Each of the two basic approaches is characterized by specific advantages and restrictions.

In the Eulerian method, the transport equations of the droplet phase are appended to the gas phase transport equations, resulting in a compact description of the interacting two phase flow system. The essential advantage is a simultaneous solution of the interacting flow fields of gas phase and spray by a single numerical method. Applying a standard block-iterative solver for systems of linearized equations, the information exchange

between phases is realized on the level of the non-linear iterations. As a consequence, computation times are generally small compared to the Lagrangian approach. However, each droplet initial condition to be simulated requires the solution of an individual set of 5 transport equations. This conceptual feature is a severe limitation for the discretization of complex sprays with wide ranges of initial droplet size, injection angles and velocities. Furthermore, Eulerian methods are generally not suited for the modeling of complex two phase phenomena like secondary atomization or spray-wall interaction.

In the Lagrangian method, a large number of droplet trajectories has to be tracked to achieve a continuous distribution of the liquid phase. Due to the stochastic simulation of turbulent spray dispersion by random sampling of gas velocity fluctuations, identical droplet initial conditions lead to different trajectories. As a consequence, the liquid phase flow field is a statistical quantity. To limit the maximum field deviations, the number of simulated droplet trajectories has to be increased to values up to $10^4 - 10^6$ for typical combustor flows. Effects of the spray back on the gas flow such as aerodynamic dragging or evaporation cooling are recorded in droplet source terms, describing the local interfacial transfer of mass, momentum and energy. Including these source terms in the gas flow transport equations, complete phase interaction is taken into account by an iterative concatenation of gas flow computation and Lagrangian droplet tracking. Besides increased computation times, this iterative procedure entails an artificial decoupling of gas flow and spray. In particular for flows with intense phase interaction, this may cause severe convergence problems, requiring strong relaxation of source term fields. Nevertheless, Lagrangian methods are commonly preferred for practical CFD analysis due to significant advantages regarding complex spray discretization and modeling of flow phenomena such as secondary droplet breakup or droplet-wall interaction.

In this study, a new hybrid approach is presented combining Eulerian and Lagrangian methods to take advantage of the capabilities inherent to both methods. In the first stage of this procedure, the Eulerian method is used for an efficient computation of an approximate two phase flow field. A coarse discretization of spray boundary conditions at the nozzle limits the size of the system of transport equations to a practical dimension. Good convergence rates are achieved due to the close coupling between gas flow and spray. In the refinement stage, iterative cycles of single phase gas flow computation and subsequent droplet tracking are employed to improve the quality of the preconditioned two phase flow field. Taking advantage of the stochastic nature of the tracking approach, a fine discretization of polydisperse sprays is achieved by random sampling of droplet initial conditions at the nozzle. The numerical description of the spray is enhanced by optional modeling of secondary droplet breakup and spray-wall interaction. Since modeling of spray-wall interaction has been described in detail in Ref. [24], only secondary atomization of droplets is considered in this study.

To demonstrate the performance and accuracy of the numerical methods discussed in this paper, the evaporating spray in the premix duct of a LPP research combustor is simulated and assessed by measured droplet data. The experimental investigation of this premix section has been a focus of various studies [15], [16], [13] and represents a valuable source of experimental data.

3 Eulerian approach

The Eulerian approach for the numerical description of dispersed two phase flows is based on the assumption that the liq-

uid phase represents an additional continuum penetrating the gas phase. In analogy to the continuum approach of single phase flows, each phase is described by a set of transport equations for mass, momentum and energy extended by interfacial exchange terms. This set of transport equations can be recasted into a universal formulation which is discretized by a conservative Finite Volume method and solved by a block-iterative scheme for systems of linearized equations.

3.1 Transport equations of the two phase flow

3.1.1 Basic equations

Except for the near region of the atomizer, the volume fraction of fuel in the flow field is low. In this dilute two phase flow regime, interactions between fuel fragments can be neglected. Starting from the basic Navier-Stokes equations, the instantaneous transport equations for gas and droplet phase are derived either by spatial, temporal [9] or ensemble phase averaging

Gas phase:

$$\frac{\partial}{\partial t} \alpha_g \rho_g + \frac{\partial}{\partial x_j} \alpha_g \rho_g U_{g,j} = M_{int,g} \quad (1)$$

$$\frac{\partial}{\partial t} \alpha_g \rho_g U_{g,i} + \frac{\partial}{\partial x_j} \alpha_g \rho_g U_{g,j} U_{g,i} =$$

$$e u - \alpha_g \frac{\partial}{\partial x_i} P_g + \frac{\partial \tau_{i,j}}{\partial x_j} + \alpha_g \rho_g f_i + I_{int,g,i} \quad (2)$$

$$\frac{\partial}{\partial t} \alpha_g \rho_g h_g + \frac{\partial}{\partial x_j} \alpha_g \rho_g U_{g,j} h_g =$$

$$- \frac{\partial \dot{q}_j}{\partial x_j} + S_{h,g} + H_{int,g} \quad (3)$$

Droplet phase:

$$\frac{\partial}{\partial t} \alpha_d \rho_d + \frac{\partial}{\partial x_j} \alpha_d \rho_d U_{d,j} = M_{int,d} \quad (4)$$

$$\frac{\partial}{\partial t} \alpha_d \rho_d U_{d,i} + \frac{\partial}{\partial x_j} \alpha_d \rho_d U_{d,j} U_{d,i} =$$

$$- \alpha_d \frac{\partial}{\partial x_i} P_g + \alpha_d \rho_d f_i + I_{int,d,i} \quad (5)$$

$$\frac{\partial}{\partial t} \alpha_d \rho_d h_d + \frac{\partial}{\partial x_j} \alpha_d \rho_d U_{d,j} h_d = H_{int,d} \quad (6)$$

The weighting factors α_g and α_d are a result of the averaging process and represent the local volume fractions of gas and liquid phases related by the following equation

$$\alpha_g + \alpha_d = 1 \quad (7)$$

Dilute two phase flows are characterized by the conditions

$$\alpha_d \ll 1 ; \quad \alpha_g \approx 1 \quad (8)$$

In this flow regime, the transport equations of the gas phase approach the standard single phase transport equations extended by additional interfacial exchange terms $M_{int,g}$, $I_{int,g}$ and $H_{int,g}$.

3.1.2 Interfacial exchange terms

The interfacial exchange terms describe the local rates of mass, momentum and energy transfer across the liquid-gas interface. Assuming a spherical shape of the droplets and a uniform internal temperature distribution, the transfer rates may be estimated from Lagrangian single droplet physics. The following model expressions are derived from Eq. (23) and the heat and mass

fluxes (28), (29) and (30) of an isolated droplet

$$M_{int,d} = -M_{int,g} = \frac{6\alpha_d}{\pi D^3} \dot{m}_{vap}^* \quad (9)$$

$$I_{int,d,i} = -I_{int,g,i} = \frac{6\alpha_d}{\pi D^3} \left(\frac{\pi}{8} D^2 \rho_g C_D |U_g - U_d| (U_{g,i} - U_{d,i}) + \dot{m}_{vap}^* U_{d,i} \right) \quad (10)$$

$$H_{int,d} = -H_{int,g} = \frac{6\alpha_d}{\pi D^3} \left(\dot{H}_{vap,s} + \dot{Q}_{cond,s}^* \right) \quad (11)$$

3.1.3 Transport equation of the droplet diameter

According to Ref. [6], a transport equation of the mean droplet diameter can be established by combining transport equations of droplet number and droplet mass (4), giving

$$\frac{\partial}{\partial t} \alpha_d \rho_d D + \frac{\partial}{\partial x_j} \alpha_d \rho_d U_{d,j} D = \frac{8\alpha_d}{\pi D^2} \dot{m}_{vap} \quad (12)$$

For non evaporating sprays this equation is identical to the continuity equation.

3.1.4 Turbulence modeling

The transport equations derived so far are suited for the numerical description of sprays in laminar gas flows. Since combustors generally operate in the turbulent flow regime, the system of transport equations (1) - (6), (12) is extended by introducing turbulent fluctuations of the transport quantities followed by Reynolds averaging of the equations. With respect to the gas phase, the standard $k-\epsilon$ model is employed to model the transport terms resulting from correlations of fluctuating quantities. This procedure has been described in detail by several authors [12], [21]. The turbulence terms in the droplet phase transport equations are approximated by an algebraic model which is based on a Boussinesq approach.

$$\frac{\partial}{\partial t} \alpha_d \rho_d + \frac{\partial}{\partial x_j} \alpha_d \rho_d U_{d,j} = \frac{\partial}{\partial x_j} \left(\frac{\mu_{t,d}}{Sc_{t,d}} \frac{\alpha_d}{\partial x_j} \right) + M_{int,d} \quad (13)$$

$$\begin{aligned} \frac{\partial}{\partial t} \alpha_d \rho_d U_{d,i} + \frac{\partial}{\partial x_j} \alpha_d \rho_d U_{d,j} U_{d,i} = \\ \frac{\partial}{\partial x_j} \left[\alpha_d \mu_{t,d} \left(\frac{\partial U_{d,i}}{\partial x_j} + \frac{\partial U_{d,j}}{\partial x_i} \right) \right] + \\ \alpha_d \rho_d f_i - \alpha_d \frac{\partial}{\partial x_i} P_g + I_{int,d,i} \end{aligned} \quad (14)$$

$$\begin{aligned} \frac{\partial}{\partial t} \alpha_d \rho_d h_d + \frac{\partial}{\partial x_j} \alpha_d \rho_d U_{d,j} h_d = \\ \frac{\partial}{\partial x_j} \left(\alpha_d \frac{\mu_{t,d}}{Pr_{t,d}} \frac{\partial h_d}{\partial x_j} \right) + H_{int,d} \end{aligned} \quad (15)$$

$$\begin{aligned} \frac{\partial}{\partial t} \alpha_d \rho_d D + \frac{\partial}{\partial x_j} \alpha_d \rho_d U_{d,j} D = \frac{8\alpha_d}{\pi D^2} \dot{m}_{vap} + \\ \frac{\partial}{\partial x_j} \left(\alpha_d \frac{\mu_{t,d}}{Pr_{t,d}} \frac{\partial D}{\partial x_j} \right) \end{aligned} \quad (16)$$

Double and triple correlations involving fluctuations of α_d are neglected on the right hand side of Eq. (14). A value of 0.9 for the turbulent Schmidt and Prandtl numbers, $Sc_{t,d}$, $Pr_{t,d}$ is chosen for the present calculations. Using this value, Eq. (13) effectively is a transport equation of a scalar in the asymptotical case of a vanishing droplet diameter. A fundamental assumption of this approach is the dependence of the turbulent viscosity of the droplet phase $\mu_{t,d}$ on local mean flow properties [17], [10]

$$\frac{\nu_{t,d}}{\nu_{t,g}} = \frac{\mu_{t,d}}{\mu_{t,g}} \frac{\rho_g}{\rho_d} = \frac{1}{1 + \left(\frac{\tau_d}{\tau_g} \right)^{2n}} \quad (17)$$

Thus, the ratio of the kinematic viscosities of droplet and gas phase is postulated to be a function of the characteristic time scales of both phases. In Ref. [10], a value of 0.25 for the empirical parameter n is suggested. The time scale τ_d which is denoted as droplet relaxation time characterizes the ability of a droplet to follow turbulent gas velocity fluctuations:

$$\tau_d = \frac{4}{3} \frac{\rho_d}{\rho_g} \frac{D^2}{C_D Re_d \nu_g} \quad (18)$$

Originally, the characteristic time of the gas flow turbulence τ_g is taken to be the dissipation time scale given by Eq. 25. In this formulation, the droplet phase turbulence model fails to describe the crossing trajectory effect which has a significant influence on turbulent droplet dispersion [27]. According to the turbulence modeling of the Lagrangian approach, the extended version of the model considers a second characteristic time scale. This crossing time t_c is the time required by a droplet to cross the current coherent turbulence structure which is estimated from Eq. 26. Combining both time scales, the gas phase time scale is now defined as

$$t_g = \min[t_e, t_c] \quad (19)$$

The validation of this enhanced turbulence model is based on the basic experiment described in Ref. [27].

3.2 Discretization of polydisperse sprays

To complete the numerical description of the spray, boundary conditions of the droplet phase have to be specified at the atomizer nozzle. However, most sprays of technical importance are characterized by a broad variety of initial droplet diameters and velocities. Since each individual droplet phase boundary condition theoretically requires the numerical solution of a separate set of transport equations (13) - (16), a polydisperse spray has to be discretized by a limited number of representative droplet classes. In practice, the computational effort increases at least linearly with the number of droplet classes employed. As a consequence, the maximum number of classes is restricted by the CPU time and memory capacity available.

For dilute sprays, direct interaction between droplet classes can be neglected although each class is coupled to the gas phase by the closure equation

$$M_{int,g} = - \sum_{k=1}^{nc} M_{int,d,k} \quad (20)$$

$$I_{int,g} = - \sum_{k=1}^{nc} I_{int,d,k} \quad (21)$$

$$H_{int,g} = - \sum_{k=1}^{nc} H_{int,d,k} \quad (22)$$

4 Lagrangian approach

4.1 Spray dispersion

The Lagrangian simulation of dispersed two phase flow is based on the tracking of statistically significant droplet parcels in the gas flow. Each parcel is represented by one droplet and is determined by discretization of the continuous spectra of droplet initial conditions in the near field of the atomizer. The tracking is based on the integration of the droplets equation of motion combined with an empirical correlation for the aerodynamic drag coefficient C_D ,

$$\frac{d\vec{u}_d}{dt} = - \frac{3}{4} \frac{\rho_g}{\rho_d} \frac{C_D}{D} |\vec{u}_d - \vec{u}_g| (\vec{u}_d - \vec{u}_g) \quad (23)$$

$$C_D = 0.36 + 5.48 Re_d^{-0.573} + \frac{24}{Re_d} \quad (24)$$

In order to simulate the effect of turbulent spray dispersion, the turbulence structure of the gas flow field is modeled by a random process along the droplet trajectories [5], [18]. In this concept, the local turbulence structure is characterized by the length scale l_e and dissipation time scale t_e of eddies representing the coherent flow structures

$$l_e = C_\mu^{\frac{1}{2}} \frac{k^{\frac{3}{2}}}{\varepsilon}, \quad t_e = \frac{l_e}{|\bar{u}_g'|}. \quad (25)$$

In addition to the life time scale t_e , a crossing time scale t_c is calculated from

$$\left\| \int_{t_0}^{t_c} (\bar{u}_g - \bar{u}_d) dt \right\| = l_e, \quad (26)$$

taking into account the droplet dynamics. Each time the smaller one of both time scales is elapsed, the droplet enters a new eddy. Consequently, the random process generates a new velocity fluctuation \bar{u}_g' from a Gaussian distribution which is determined by

$$\mu = 0, \quad \sigma = \sqrt{\frac{2}{3}k}. \quad (27)$$

This velocity fluctuation remains constant for the period of droplet-eddy interaction and is added to the local value of the gas flow velocity.

4.2 Spray evaporation

In this study, droplet evaporation is simulated by means of the Uniform Temperature model [4], [26], [2]. This computationally effective droplet model is based on the assumption of a homogeneous internal temperature distribution in the droplet and phase equilibrium conditions at the surface. The analytical derivation of this model does not consider contributions to heat and mass transport by forced convection by the gas flow around the droplet. Since diffusive time scales in the surrounding gas phase are much smaller than in the droplet fluid, a quasi stationary description of the gas phase is applied. Using reference values for variable fluid properties (1/3-rule), an integration of the radially symmetric differential equations yields analytical expressions for the transport fluxes \dot{m}_{vap} , $\dot{Q}_{cond,s}$ and $\dot{H}_{vap,s}$. At this point, convective transport is taken into account by two empirical factors [1] resulting in the corrected fluxes \dot{m}_{vap}^* , $\dot{Q}_{cond,s}^*$ and $\dot{H}_{vap,s}^*$ [23]

$$\dot{m}_{vap}^* = cfm \dot{m}_{vap}, \quad (28)$$

$$\dot{Q}_{cond,s}^* = \pi D^2 \alpha^* (T_d - T_g), \quad (29)$$

$$\dot{H}_{vap,s}^* = \dot{m}_{vap}^* c_{p,vap,ref} (T_d - T_g). \quad (30)$$

Vapor mass flux and heat transfer coefficient are calculated as follows

$$\dot{m}_{vap} = 2\pi D \rho_{g,ref} \Gamma_{im,ref} \ln \frac{1 - Y_{vap,g}}{1 - Y_{vap,s}}, \quad (31)$$

$$\alpha^* = cfh \frac{\dot{m}_{vap} c_{p,vap,ref}}{\pi D^2} \frac{\exp\left(\frac{\dot{m}_{vap} c_{p,vap,ref}}{2\pi D \lambda_{g,ref}}\right) - 1}{\exp\left(\frac{\dot{m}_{vap} c_{p,vap,ref}}{2\pi D \lambda_{g,ref}}\right) - 1}, \quad (32)$$

$$cfm = 1 + 0.276 \text{Re}^{\frac{1}{2}} \text{Sc}^{\frac{1}{3}}, \quad (33)$$

$$cfh = 1 + 0.276 \text{Re}^{\frac{1}{2}} \text{Pr}^{\frac{1}{3}}. \quad (34)$$

The balance equations of the droplet reduce to ordinary differential equations,

$$\frac{d}{dt} m_d = -\dot{m}_{vap}^*, \quad (35)$$

$$\frac{d}{dt} (m_d h_d) = -\dot{Q}_{cond,s}^* - \dot{H}_{vap,s}^*, \quad (36)$$

which can be appended to the differential equations describing the droplet motion, Eq. 23.

4.3 Secondary droplet breakup

At low relative velocities, the spherical shape of the droplets is preserved by the dominating effects of surface tension and viscous forces in the liquid. With increasing velocities, the destabilizing aerodynamic forces on the droplet surface are intensifying, resulting in deformation, oscillations and disintegration of the droplets.

4.3.1 Classification of breakup mechanisms

A common practice to classify secondary droplet atomization processes is based on two characteristic groups of parameters,

$$\text{We} = \frac{\rho_g u_{rel}^2 D}{\sigma_d}, \quad \text{On} = \frac{\mu_d}{\sqrt{\rho_d D \sigma_d}}. \quad (37)$$

The Weber number is a measure of the strength of aerodynamic forces relative to surface tension forces, whereas the Ohnesorge number assesses the damping effect of viscous friction in the droplet against surface tension. In the Weber number range from $\text{We} = 1$ up to a critical value $\text{We} = \text{We}_c$, non-destructive droplet deformation and oscillation is observed. As illustrated in Fig. 2, three different mechanisms govern the breakup of droplets for increased Weber numbers typical for flows in gas turbine combustors. From these visualizations it is obvious that

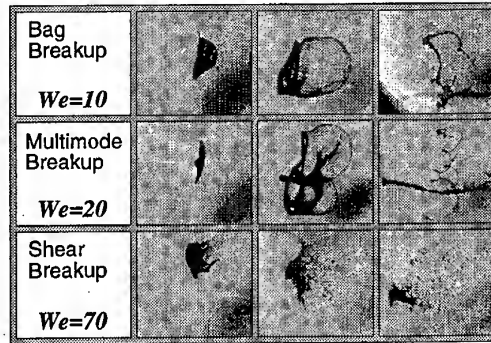


Figure 2: Breakup mechanisms of water droplets (Ref. [22])

a common feature of all three mechanisms is an initial deformation of the droplet into a disc shape. After this deformation period, various complex flow phenomena lead to the final droplet breakup depending on the intensity of the aerodynamic forces. Exceeding the critical Weber number, the first mechanism observed is bag breakup. This process is characterized by the formation of a thin hollow bag of droplet fluid stretching from a toroidal rim. The thin film of this bag is eventually bursting into a cloud of tiny droplets, followed by a disintegration of the toroidal rim into significantly larger fragments. With increasing aerodynamic forces, a transition to more complex bag structures is observed. In this multimode or stamen breakup regime the aerodynamic flow interaction is forming an additional fluid filament in the center of the bag structures which is aligned with the relative flow velocity. For even higher Weber numbers, shear breakup is observed. This mechanism is fundamentally different to the preceding mechanisms and is characterized by a rapidly disintegrating film of fluid continuously stripped off the rim of the disc shaped droplet by shear forces.

Fig. 3 summarizes the results of various experimental studies [11], [19] in a breakup regime map, indicating the relevant mechanism corresponding to a specific combination of Ohnesorge and Weber number. For $\text{On} > 0.1$ a significant influence of viscosity is observed. The transitions between the different mechanisms are given by the following functions

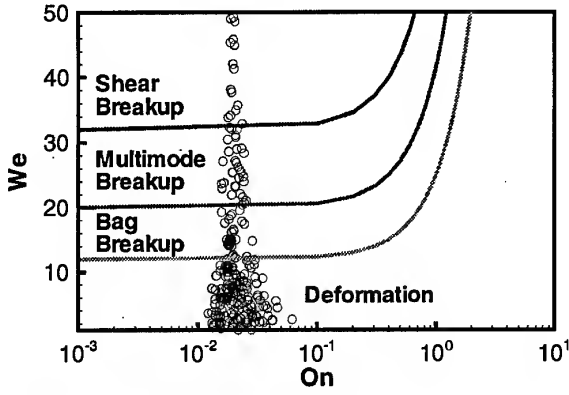


Figure 3: Breakup regime map (○ : Present flow simulation)

- Critical Weber number (Transition to bag breakup):

$$We_c = 12 (1 + 1.077 On^{1.6}) \quad (38)$$

- Transition to multimode breakup:

$$We = 20 (1 + 1.200 On^{1.5}) \quad (39)$$

- Transition to shear breakup:

$$We = 40 (1 + 1.500 On^{1.4}) \quad (40)$$

4.3.2 Deformation and breakup times

Basically, the breakup process can be subdivided in two stages: Initial deformation and further deformation with disintegration. It is convenient to express the relevant times of the breakup process in terms of the characteristic time of shear breakup

$$t^* = \frac{u_{rel}}{D_0} \sqrt{\frac{\rho_g}{\rho_d}} \quad (41)$$

As stated in Ref. [8], the time of initial droplet deformation t_{def} has a constant value independent of the specific breakup mechanism

$$\frac{t_{def}}{t^*} = 1.6. \quad (42)$$

However, the breakup time t_b measured from begin of deformation until final destruction strongly depends on the specific mechanism. A fit to a large number of experimental data is given in Ref. [19]

$$\frac{t_b}{t^*} = \begin{cases} 6 (We - 12)^{-0.25} & 12 < We < 18 \\ 2.45 (We - 12)^{0.25} & 18 < We < 45 \\ 14.1 (We - 12)^{-0.25} & 45 < We < 351 \\ 0.766 (We - 12)^{0.25} & 351 < We < 2670 \\ 5.5 & 2670 < We. \end{cases} \quad (43)$$

For $On > 1$, liquid viscosity is the dominating parameter of the breakup process resulting in the following correlation

$$\frac{t_b}{t^*} = 4.5 (1 + 1.2 On^{0.74}). \quad (44)$$

4.3.3 Droplet drag

Deformation of the droplet prior to breakup leads to a significant increase of aerodynamic drag. Due to the resulting acceleration, the droplet generally experiences substantial displacement from initial deformation until final breakup. With respect to the deformation period, several authors [8] report a linear increase

of the droplet size from D_0 up to a maximum value given by ($On < 0.1$, $We < 100$)

$$\frac{D_{max}}{D_0} = 1 + 0.19 \sqrt{We}, \quad \text{for} \quad (45)$$

The effect of higher Ohnesorge numbers is taken into account by using a corrected Weber number in the above and following equations.

$$We_{corr} = \frac{We}{1 + 1.077 On^{1.6}}. \quad (46)$$

As suggested in Ref. [8], a linear transition of the drag coefficient from the sphere shape value to the disc shape value is used in the present study to model the aerodynamic properties of the flattening droplet.

In the following period of disintegration, droplet drag depends on the specific breakup mechanism. As illustrated in Fig. 3, the bag and filament structures observed prior to breakup are very complex. According to Refs. [11], [22] the toroidal rim evolving in bag breakup is expanding to seven times the initial droplet diameter, whereas in multimode breakup a maximum diameter of six times the initial diameter is reached (see Fig. 6). At this time however, a major part of the droplet cross section consists of a thin fluid film accelerated in direction of the relative velocity thus decreasing the aerodynamic drag. To bypass the difficulties of describing these opposing effects, the drag of the disintegrating droplet is calculated from the constant disc state reached at the end of the deformation period. In shear breakup, the size of the disc shaped droplet is continuously decreasing to its final value at t_b .

4.3.4 Secondary droplet sizes

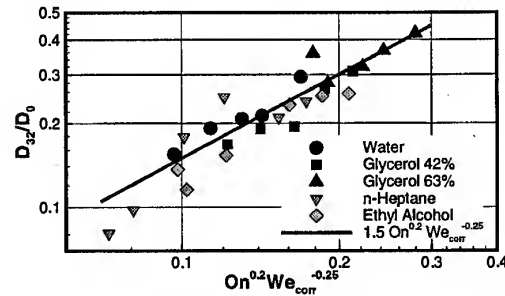
Based on an extended experimental study covering the complete range of breakup mechanisms, a single correlation for the Sauter mean diameter D_{32} has been derived in Ref. [8] for all three mechanisms ($On < 0.1$, $We < 1000$)

$$\frac{D_{32}}{D_0} = 6.2 On^{0.5} We^{-0.25} \quad (47)$$

The exponents in this correlation have been determined by the authors from an approximate analysis of the droplet internal flow during shear breakup, leaving only a constant factor as a parameter for the fitting to experimental data. Using the Weber number given by Eq. 46 to account for viscosity effects, additional fitting of the exponents leads to an improved correlation

$$\frac{D_{32}}{D_0} = 1.5 On^{0.2} We_{corr}^{-0.25}. \quad (48)$$

This correlation which is used for the flow simulations in the present study and the experimental data is shown in Fig. 4. Although the above correlation is valid for the complete range

Figure 4: Improved correlation for D_{32} (Data from Ref. [8])

of breakup conditions, the distribution function of the droplet

diameter is substantially different for the various mechanisms of secondary breakup.

Bag and multimode breakup

Considering bag or multimode breakup, the volume distribution of the droplet fragments is approximated by a root normal distribution [25], given by the following density function

$$f(D) = \frac{x}{2\sqrt{2\pi}\sigma D} \exp\left\{-\frac{1}{2}\left[\frac{x-\mu}{\sigma}\right]^2\right\}, \quad (49)$$

and the parameters

$$x = \sqrt{\frac{D}{D_{0.5}}}, \quad \mu = 1, \quad \sigma = 0.238 \quad (50)$$

For a volume distribution with this distribution function, the mass median diameter $D_{0.5}$ is related to the Sauter mean diameter D_{32} by

$$\frac{D_{0.5}}{D_{32}} = 1.2 \quad (51)$$

Shear breakup

According to Ref. [8], the volume distribution resulting from shear breakup is characterized by a bimodal density function with a maximum at small diameters and a second maximum at large diameters. From the experimental data illustrated in Fig. 5, it is concluded that the fine fraction of the droplet fragments corresponds to approximately 80% of the total cumulated volume. These droplets result from film fragments stripped off the

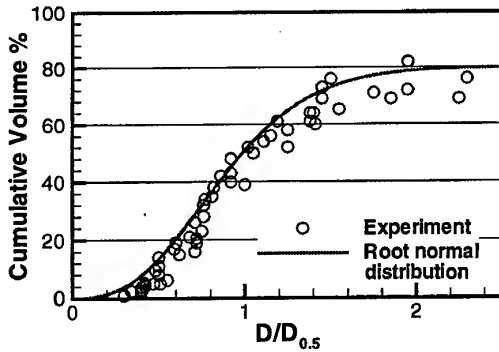


Figure 5: Cumulative droplet volume (Data from Ref. [8])

disc-shaped droplet by shear forces. The 20% in the large diameter range not specified in Fig. 5 represent the contribution of the core droplet fragment left by the stripping process. The diameter D_c of this core droplet is estimated from the critical Weber number, evaluating Eq. (38) at flow conditions at the instant of breakup. As illustrated by the curve in Fig. 5, the volume distribution of the fine fraction of the droplet spectrum after shear breakup can be approximated by a root normal distribution based on a reduced Sauter mean diameter

$$D_{32,red} = \frac{4 D_{32} D_c}{5 D_c - D_{32}} \quad (52)$$

In this equation, the Sauter mean diameter of the complete droplet spectrum is evaluated from Eq. 48.

4.3.5 Secondary droplet velocities

Due to the dominating influence of aerodynamic forces on small droplets, tiny breakup products are immediately dragged with the gas flow. So, an accurate modeling of initial velocities is not necessary in general. These considerations apply in particular to the tiny droplet fragments generated by bursting of film bags or by shear induced film stripping. The motion of large droplets

in turn is dominated by inertia forces. As a consequence, the modeling of initial velocities of large droplet fragments has a significant influence on the dispersion behavior of the spray.

As a first approximation, the fragments generated by droplet breakup inherit the velocity of the parent droplet due to momentum conservation. In bag or multimode breakup, a transverse velocity component of droplet fragments is observed induced by the transverse spreading motion of droplet fluid during the expansion of the toroidal rim. This transverse velocity component is responsible for increased dispersion of sprays with secondary atomization. For an approximate estimation, the growth velocity of the rim is determined from time-resolved visualizations of breakup processes. Fig. 6 indicates that the ring has

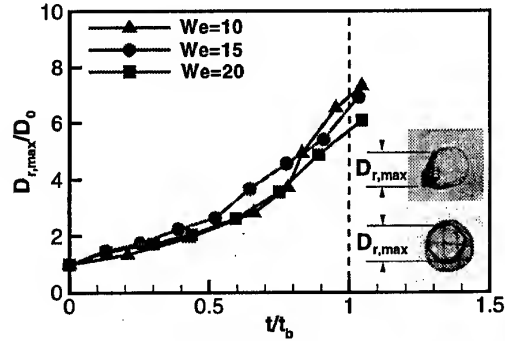


Figure 6: Growth of the toroidal rim (Water droplet, [22])

an extension of about seven times the original droplet diameter in bag breakup against six times in multimode breakup. These observations agree with the values reported in Ref. [11]. Based on these results, the transverse velocity component is estimated as

$$v_t = \frac{D_{r,max} - D_0}{2(t_b - t_{def})} \quad (53)$$

With respect to multimode breakup, a fraction of the droplet fluid is concentrating on the axis of the disintegrating droplet (see Fig. 2, $We = 20$). Due to the alignment of this prolate filament with the flow, the fragments of this structure have no transverse velocity component. The volume fraction of the filament is estimated from a Weber number based interpolation between the limiting values of 0% for bag breakup and 20% (core droplet) for shear breakup.

4.3.6 Stochastic simulation of droplet breakup

The period of droplet disintegration is specified by the characteristic times t_{def} , and t_b of the breakup process. In shear breakup mode, the secondary droplets are continuously generated in the time from t_{def} to t_b , whereas in bag or multimode breakup mode significant generation of fragments is observed during the second half of this time period [22]. Instead of focusing on a realistic simulation of each individual breakup event, the computational implementation makes use of the Lagrangian trajectory superposition approach involving large numbers of droplet parcels.

During droplet deformation, the cross sectional area of the droplet and the drag coefficient are continuously increased up to their maximum values at t_{def} . A certain time later, the parent droplet trajectory is terminated and a fixed number of child droplets is generated by random sampling of initial conditions. Each secondary trajectory is assigned an equal fraction of the volume flux. To limit the number of secondary droplets to be tracked, only 3 child droplets have been modeled per breakup event in the present flow simulation in which 10000 parent droplets are injected per Lagrangian step. In analogy

to the stochastic modeling of fuel atomization and gas flow turbulence effects, the superposition of large numbers of trajectories leads to continuous and thus realistic representation of secondary atomization.

Modeling a single shear breakup event, the time of droplet disintegration is determined as a random number with uniform distribution between t_{def} and t_b . To model bag and multimode breakup events, the time of disintegration is sampled in the second half of this interval. The initial size of the child droplets is determined as a random number with a root normal distribution or from stability criteria (core droplet in shear breakup). Droplets generated by rim fragmentation are provided with an additional transverse velocity component. In bag breakup mode, virtually all larger fragments possess a transverse velocity component whereas in multimode breakup a volume fraction of up to 20% of the largest fragments is starting without dispersive transverse momentum. The limiting value of 20% represents the transition to shear breakup and corresponds to the volume fraction of the core droplet. In this breakup regime all secondary droplets inherit the velocity of the parent droplet since no significant spreading motion is observed.

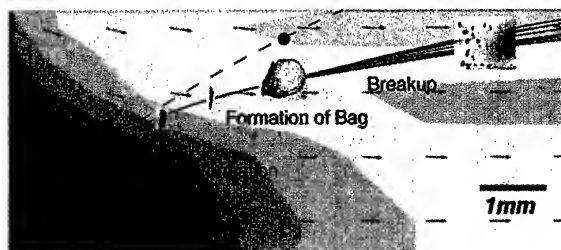


Figure 7: Breakup of a 60 μm droplet

Fig. 7 illustrates the computation of a deforming and disintegrating droplet in the near field of the nozzle. Compared to the trajectory of a rigid spherical droplet (dashed line), a significant deflection of the deforming droplet due to increased aerodynamic forces is observed. This single droplet computation clearly demonstrates that advanced modeling of secondary breakup has to take into account the time scales of the breakup process since the droplets experience considerable displacements before their final disintegration.

4.4 Iterative solution procedure

Tracking of a statistically significant number of droplet parcels and superposition of their trajectories yields a flow field approximation of the dispersed liquid phase. However, a simple Lagrangian two step calculation consisting of a gas flow computation and subsequent droplet tracking does not take account of spray effects on the gas flow such as aerodynamic dragging or evaporation cooling. In particular for evaporating sprays in combustor flows, these effects have a significant influence on the overall two phase flow field. To establish mutual information exchange between both phases, Lagrangian two step cycles are concatenated in an iterative procedure with droplet source terms being updated during each tracking step. Representing local transfer rates of mass, momentum and energy from spray to gas flow, droplet source terms are included in the gas flow computation of the following iteration cycle. This iterative approach is illustrated in the lower part of Fig. 8.

The separated computation of gas and liquid phase flow fields and the iterative exchange of interfacial transfer data entails an artificial decoupling of both phases. In particular for two phase flows with intense phase interaction, this effect leads to a critical overestimation of droplet source terms in the first iteration

cycles. To achieve convergence of the iterative procedure, a relaxation of the droplet source term fields is employed. Recursive damping of the source terms on the level of the iteration cycles is realized by the following equation

$$\bar{S}_{d,\phi}^{i+1} = \alpha_\phi S_{d,\phi}^i + (1 - \alpha_\phi) \bar{S}_{d,\phi}^i. \quad (54)$$

According to Eq. 54, only a fraction of the source terms recorded during the previous droplet tracking, $S_{d,\phi}^i$, is contributing to the source term $\bar{S}_{d,\phi}^{i+1}$ included in the current gas flow solution. The second contribution is calculated from the source term included in the previous gas flow computation. For gas flows which are substantially influenced by the fuel spray, strong relaxation of droplet source terms may be necessary to enforce convergence of the iterative procedure. In these cases an increased number of two stage iterations may be necessary for complete consideration of phase interaction [24]. In the present flow simulation, only weak relaxation ($\alpha_\phi > 0.5$) is required to achieve a convergent solution for the two phase flow field within 10 two stage iterations.

5 The Hybrid procedure

As indicated in the preceding sections, the continuum description of the Eulerian method has the advantage of close coupling of gas and liquid phase in a single numerical scheme. Thus, computation times are rather short as long as the number of droplet classes used for the discretization of the spray is small. Consequently, Eulerian methods are particularly suited for an approximate but efficient computation of polydisperse two phase flows in combustors. Lagrangian methods in turn achieve a high resolution discretization of complex spray structures by tracking large numbers of droplet parcels of various initial sizes and velocities. However, the price to be paid for

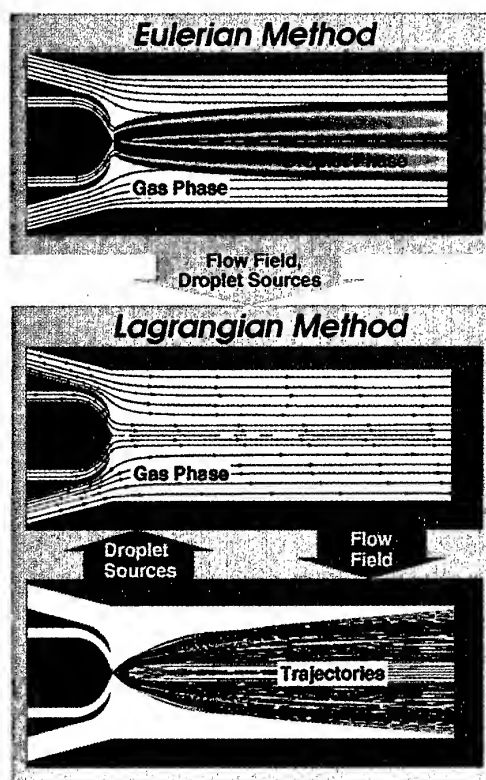


Figure 8: Structure of the Hybrid procedure

a realistic spray representation is high. Due to the artificial de-

coupling of the two phase flow computation by separate solution schemes for each phase and iterative realization of phase interaction, total computation times are rather large [24]. For flow cases where strong relaxation of droplet source terms is required, time expenses can grow to practically unmanageable extents.

For such two phase flows, a reduction of computational effort is achieved by preconditioning the two phase flow field by means of an Eulerian method based on a coarse discretization of the spray. This is in fact the basic idea of the Hybrid procedure: A two stage combination of both methods in order to reduce total computation times by Eulerian preconditioning yet maintaining the detailed modeling of spray physics in a Lagrangian refinement stage. This approach is schematically illustrated in Fig. 8. Following an approximate computation of the two phase flow, the flow field and the droplet source terms are passed to the refinement stage. Here, Lagrangian iteration cycles are based on a fine discretization of droplet injection conditions and an advanced modeling of secondary droplet breakup. Since the two phase flow field calculated by the Eulerian method already accounts for spray effects on the gas flow, the droplet source terms recorded during subsequent tracking steps are the final flow result. Consequently, the number of iterations is significantly reduced compared to a standard Lagrangian simulation.

6 Simulation of a LPP premix duct flow

The performance and accuracy of the numerical methods presented is demonstrated by a simulation of the two phase flow in the premix duct of a LPP combustor. The experimental investigation of this combustor has been part of an extended research project on low emission combustion concepts [15], [16], [13]. A detailed description of the test rig and the measurement techniques is presented in a parallel study [20]. The combustor section of interest for the present flow simulation is illustrated in Fig. 9. Compressed air is supplied to the cylindrical duct

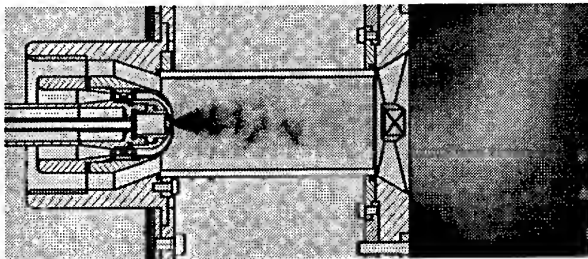


Figure 9: Premix zone of the LPP research combustor

($l = 124\text{mm}$, $d_i = 44.6\text{mm}$) by two coaxial annular ducts. The fuel is injected into the gas flow by a pressure swirl atomizer aligned with the duct axis. The nozzle diameter is about 1 mm . In order to perform PDPA measurements, optical access to the flow is given by circumferential slits in the duct liner at various axial positions. For spray visualizations, the metallic liner is substituted by a quartz glass cylinder. Premix and reaction zones are separated by an arrangement of swirler vanes acting as a flame stabilizer. The complete configuration illustrated in Fig. 9 is enclosed in a pressure casing with water cooled window ports. The outer coaxial annular air flow (bypass air) is shielding the duct liner from droplet impact and film formation. The highly accelerated inner flow (atomization air) is focused directly onto the conical fuel sheet generated by the pressure swirl atomizer. The fundamental idea of this atomization concept is a further reduction of droplet sizes by high

velocity aerodynamic interaction between spray and gas flow. The operating point of the premix duct investigated in this study is specified by the flow parameters summarized in Table 1. The

Gas Flow (Air)		Fuel (Diesel)	
\dot{m}_g	213 g/s	\dot{m}_{fuel}	6 g/s
T_g	753 K	T_{fuel}	350 K
p_g	4 bar	v_{sheet}	30 m/s
Tu_g	15 %	β_{sheet}	40°

Table 1: Parameters at the inlet of the premix duct ($z = 0\text{mm}$) computational domain of the flow simulation is illustrated in Fig. 10 including (from left to right) intake section, coaxial annular ducts, premix zone, swirler vanes, reaction zone, dilution holes and burnout zone. The axial coordinate is measured from

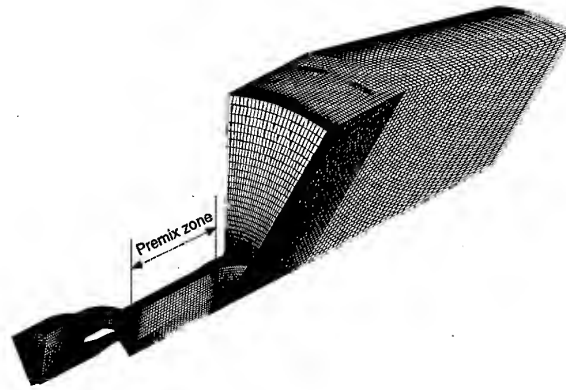


Figure 10: Computational domain (30°-Segment)

the atomizer nozzle. To model the evaporation behavior of the diesel spray, tetradecane is used as a single component diesel substitute in the present flow simulation. A detailed description of the calculated non-reacting single phase gas flow in the intake and premix zone is given in Ref. [20].

6.1 Discretization of the spray

In order to derive droplet phase boundary conditions for the Eulerian method and droplet initial conditions for the Lagrangian method, the spray is visualized in the near field of the atomizer ($0 < z < 10\text{ mm}$). A side view on the three dimensional spray cone is given by the flashlight shadowgraph in Fig. 11(a). The picture was taken under atmospheric, cold conditions without bypass air flow, using water as a fuel substitute. It is evident that the outer region of the spray is dominated by larger fuel fragments. To get an impression of the spray structure inside

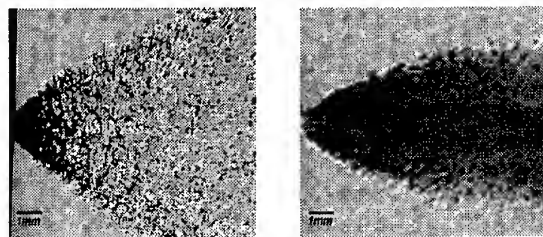


Figure 11: (a) Flashlight shadowgraphy, (b) Laser light sheet

the cone, a laser light sheet photograph is shown in Fig. 11(b), which was taken under real operation conditions of the combustor. In contrast to the coarse structure of the outer spray region, this cross view reveals a very fine droplet distribution in the spray cone.

The spray visualizations indicate two basic processes that govern the atomization of the liquid fuel [15]. Due to its high swirl, the fuel is leaving the nozzle as a conical sheet. According to Fig. 11(a), this sheet is completely disintegrating along a distance of 1 to 2 mm. In this immediate near zone of the nozzle, prompt atomization is the governing process. This mechanism is controlled mainly by the internal sheet dynamics [14]. Further disintegration of sheet fragments is induced by aerodynamic interaction with the high velocity gas flow which penetrates the spray. The resulting small secondary fragments are dragged by the gas flow into the core flow as indicated in Fig. 11(b).

With respect to the numerical simulation, it is obvious that a representation of the complex two phase flow in the nozzle near field by non-interacting droplets is a rather crude approximation of the physical reality. But despite of this simplified modeling of fuel atomization, the simulation of spray dispersion and evaporation in the premix duct agrees well with the experimental data. In the following sections, two strategies are presented to derive droplet injection conditions at the nozzle. The Eulerian calculation is essentially based on droplet data measured at a downstream position of the atomizer. It is important, that secondary atomization has ceased completely and droplets are spherical at this position. Basically, the procedure starts from an assumed discretization of the injection conditions of the droplet phase. In subsequent optimization iterations, the computed droplet data is fitted to the corresponding measured data. In contrast to this approach, the Lagrangian calculation is based on a rather crude approximation of the fuel sheet disintegration in the nozzle near field. Here, a far more physical description of the spray in the secondary atomization region is achieved by modeling droplet deformation and breakup. A similar strategy is described in Ref. [7] where pressure swirl fuel injection into a diesel engine combustion chamber is discussed.

6.1.1 Eulerian method, droplet phase boundary conditions

Since secondary droplet breakup is observed in a spray region up to 50 mm downstream of the atomizer, measured droplet data at $z = 55$ mm is used for an optimization of droplet phase boundary conditions. The droplet size distribution of the spray is discretized by means of 3 diameter classes. The volume flux fraction (or normalized volume flux) of each class is described by a Rosin-Rammler distribution evaluated at the representative class diameter D_i

$$\frac{\dot{V}_i}{\dot{V}} = 1 - \exp \left[- \left(\frac{D_i}{D_{0.632}} \right)^n \right], D_{0.632} = \frac{D_{0.5}}{0.693^{\frac{1}{n}}} \quad (55)$$

Values of $D_{0.5} = 46 \mu\text{m}$ for the mass median diameter and $n = 4.8$ for the spreading parameter are determined as a good fit to the reference droplet data at $z = 55$ mm. The mean injection velocity of the droplet phase of 30 m/s is derived from the mean velocity of the liquid sheet. The remaining parameters with significant influence on the spray structure are the injection angles of the droplet phases. Introducing 3 angle classes per diameter class leads to a final discretization of the spray by means of 9 droplet phases with different boundary conditions at the nozzle. Table 2 summarizes the correlations between droplet phase diameter, normalized volume flux and injection angle employed for the Eulerian two phase flow simulation in the present study.

6.1.2 Lagrangian method, droplet initial conditions

In the Eulerian calculation, the boundary conditions of the droplet phase at the nozzle have to account implicitly for secondary atomization in an extended downstream flow region.

$D_i [\mu\text{m}]$	\dot{V}_i/\dot{V} [1]	$\beta_i [^\circ]$
0 - 41.2	4/15	34
	1/30	7
	1/30	21
41.2-50.7	4/15	30
	1/30	10
	1/30	20
50.7- ∞	4/15	27
	1/30	13.5
	1/30	20.5

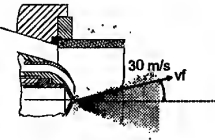


Table 2: Droplet phase boundary conditions

It is evident that small secondary droplets originating from breakup of larger sheet fragments in outer flow regions may not be reproduced by a spray representation as described in the previous section. The approximation by rigid spherical particles of different size injected into the contracting, high velocity gas flow leads to a separation of droplet sizes. As a consequence, tiny and small droplets are captured in the axis region of the core flow unless they are injected with unphysically large radial velocity components.

In the Lagrangian calculation, secondary breakup of droplets is taken into account during trajectory integration. Thus, only prompt atomization of the conical sheet has to be considered for the formulation of droplet initial conditions. The basic idea is to inject most of the fuel in form of large droplets with sizes similar to the characteristic sheet thickness of about 100 to 200 μm . Due to this coarse primary spray structure and the high relative velocities in the nozzle near zone, the critical conditions of droplet breakup are significantly exceeded as indicated by the data points mapped Fig. 3. Modeling of delayed droplet deformation, drag increase and breakup results in a fine secondary spray contribution to the core flow region in the premix duct. Very good agreement to the experimental droplet data is

Droplet diameter:

- 10 size classes equally spaced from 0 to 200 μm
- Rosin-Rammler distribution of \dot{V}_i/\dot{V}
- $D_{0.5} = 88.5 \mu\text{m}$, $n = 3$

Droplet velocities:

- Sampled, Gaussian distribution
- $\bar{v} = 30 \text{ m/s}$, $\sigma_v = 5 \text{ m/s}$

Injection angle:

- Sampled, Gaussian distribution
- $\bar{\beta} = 40^\circ$, $\sigma_{\beta,i} = 30^\circ, \dots, 5^\circ$
- $\beta_{max} = 45^\circ$ (clipping value)

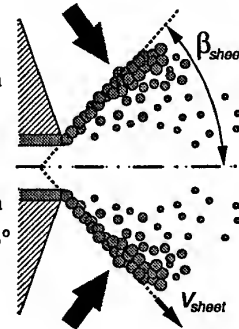


Table 3: Droplet initial conditions

achieved by using the spray discretization summarized in Table 3. Droplet velocity and injection angle are sampled as random numbers with Gaussian distributions. From Fig. 11(b) it is obvious that the disintegration of the conical sheet is responsible for a fine primary contribution to the spray in the core flow. To model this effect approximately, the variance $\sigma_{\beta,i}$ of the injection angle β is correlated with droplet size resulting in values of 30° for the smallest droplets (D from 0 to $20 \mu\text{m}$) up to 5° for the largest droplets (D from $180 \mu\text{m}$ to $200 \mu\text{m}$)

6.2 Results

To illustrate the calculated two phase flow in the premix duct, contour plots of the Eulerian flow simulation are discussed first. Comparing the axial gas velocities of the single phase and the two phase flow calculations from Fig. 12 indicates that spray-induced deceleration of the gas flow is limited to the core flow of the duct. In particular in the nozzle near zone, the axial gas velocity is decreased by up to 40 m/s due to the aerodynamic acceleration of the droplet phase.

The influence of fuel evaporation is indicated by the gas flow temperature and fuel vapor concentration in Figs. 13 and 14. Although the gas phase experiences a substantial temperature drop across the whole core flow region, significant concentrations of fuel vapor are not calculated in the first half of the duct. This delay in vapor generation is a consequence of low evaporation rates in the transient heating phase of the droplets. This conclusion is confirmed by an analysis of Lagrangian single droplet computations, which indicate that heatup and propagation time scales of typical droplets are of the same order. In total, 28% of the injected fuel is evaporated in the Eulerian simulation, in contrast to a value of 42% in the Lagrangian simulation. The difference is caused by the secondary atomization modeling in the tracking algorithm, resulting in considerable numbers of small, rapidly evaporating droplet fragments. At this point it should be noted that the total fraction of evaporated fuel substantially depends on the D_{32} -correlation used for the secondary breakup modeling. Summarized over all calculated breakup events, Eq. 47, which is actually not used, leads to a fragment mass median diameter of $D_{0.5} = 53 \mu\text{m}$, whereas Eq. 48 results in a value of $D_{0.5} = 38 \mu\text{m}$.

To compare the calculated axial volume flux density $\alpha_d U_d$ with PDPA measurements, it is weighted by the annular area and normalized by the total axial volume flux,

$$\frac{\dot{V}_r}{\dot{V}} = \frac{2\pi \int_{r=0.5\text{mm}}^{r+0.5\text{mm}} \alpha_d U_d r dr}{2\pi \int_0^{24\text{mm}} \alpha_d U_d r dr} \quad (56)$$

This normalized volume flux is illustrated in Fig. 15 and represents the fraction of the total liquid volume flux which passes an annular fraction of the duct cross section. The contour plot includes mean trajectories determined by integration of the mean axial velocity of the droplet phase. The trajectories are evaluated for the two limiting size classes and clearly demonstrate the influence of initial droplet momentum on the propagation of the droplet phase.

The second point of discussion is concerning the comparison of experimental droplet data with Eulerian and Lagrangian two phase flow simulations. In this context, the Hybrid procedure is used as a computational tool to accelerate the Lagrangian calculation. The overall reduction of computation time achieved is about 30% of the time required for a standard Lagrangian flow simulation without Eulerian preconditioning. Radial profiles of number averaged two phase flow variables are presented at axial positions $z = 20, 55$ and 90 mm . With respect to the mean axial velocities of the droplets shown in Figs. 16 and 17, both numerical methods predict a maximum in the core flow ($r < 6 \text{ mm}$) which is not observed in experiment. In particular at $z = 55$ and 90 mm the axial droplet velocities in the core flow region are overestimated by the Lagrangian calculation. Basically, this effect is a result of an insufficient spray-induced flow deceleration. This conclusion is supported by the underestimated liquid volume flux in the core flow region at the corresponding axial positions as shown in Fig. 19. With respect to the Eulerian result shown in Fig. 18, it is evident that

the unavailability of secondary breakup models requires small injection angles of the droplet phase to meet the radial volume flux profile in the second half of the duct flow. Consequently, substantial deviations are observed in the upstream flow region where secondary atomization occurs. As illustrated by Figs. 20 and 21, Eulerian and Lagrangian flow simulations predict rather similar radial profiles of the Sauter mean diameter. Although the calculated values are deviating from experimental data by up to $20 \mu\text{m}$, both flow simulations reproduce the trend in the evolution of the droplet size spectrum.

7 Conclusions

Evaporating fuel sprays in combustor flows are characterized by high rates of mass, momentum and enthalpy transfer between spray and gas flow. Fuel atomization, spray dispersion and evaporation are often complicated by additional physical effects such as droplet-wall interaction, shear driven evaporating wall films or secondary breakup of droplets.

The primary objective in this study is the design of a computational tool for an efficient numerical simulation of combustor two phase flows including advanced modeling of secondary atomization physics. Compared to state of the art Lagrangian spray simulations, a significant reduction of computation time is achieved by the presented Hybrid procedure. Basically, this computational strategy is a two stage combination of an Eulerian and a Lagrangian method. The Eulerian method is used as an efficient preconditioner for the interacting two phase flow field, in order to reduce the number of subsequent Lagrangian gas flow computation - droplet tracking iterations. In this refinement stage, advanced modeling of secondary breakup of droplets including bag, multimode and shear mechanisms is used to improve the physical description of the spray.

To assess the accuracy of the two fundamental numerical approaches, Eulerian and Lagrangian flow simulations are compared with droplet data measured in the two phase flow of a LPP combustor premix duct. The atomization concept employed in this premix duct achieves a substantial improvement of fuel atomization by aerodynamic breakup of droplets in an extended flow region downstream of the nozzle. With respect to the Eulerian flow simulation, extrapolation of measured droplet data to the point of injection with implicit consideration of secondary atomization effects results in a rather crude approximation of the spray structure. Since secondary breakup of droplets is modeled in detail by the tracking algorithm, the numerical description of the spray structure in the Lagrangian flow simulation is significantly improved.

It is evident that the computational acceleration achieved by the Hybrid procedure significantly depends on the structure of the two phase flow. With respect to the rather uncritical premix duct flow presented in this study, it is certainly questionable whether the moderate time savings are worth the additional complexity of the CFD program. However, technical practice offers a sufficient number of critical two phase flow applications, where strong relaxation of droplet source terms requires an excessive number of Lagrangian coupling iterations [24]. In these flow cases, the Hybrid procedure has an increased potential for substantial speedup of flow simulations.

Acknowledgement

This work has been founded by the Department of Education, Science, Research and Technology of Germany under contract No. 50-807642. The support is gratefully acknowledged. The authors would like to thank Mr. Michael Willmann, BMW Rolls-Royce, Germany, for his support concerning the develop-

ment of droplet breakup models.

References

- [1] B. Abramzon and W.A. Sirignano. Droplet Vaporisation Models for Spray Combustion Calculations. *International Journal of Heat and Mass Transfer*, 32:1605–1618, 1989.
- [2] S.K. Aggarwal and F. Peng. A Review of Droplet Dynamics and Vaporization Modeling for Engineering Calculations. *ASME-Journal of Engineering for Gas Turbines and Power*, 117:453–461, 1995.
- [3] C. T. Crowe. Review - Numerical Models for Dilute Gas-Particle Flows. *Journal of Fluids Engineering*, 104:297–303, 1982.
- [4] G.M. Faeth. Evaporation and Combustion of Sprays. *Progress in energy and combustion science*, Pergamon Press, 9:1–76, 1983.
- [5] A.D. Gosman, E. Ioannides. Aspects of Computer Simulation of Liquid-Fueled Combustors. *Journal of Energy*, 7(6):482–490, 1983.
- [6] M. Hallmann, M. Scheurlen, and S. Wittig. Computation of Turbulent Evaporating Sprays: Eulerian Versus Lagrangian Approach. *Transactions of the ASME*, 117:112–119, 1995.
- [7] Z. Han, S. Parrish, P.V. Farrell, and R.D. Reitz. Modeling Atomization Processes of Pressure-Swirl Hollow-Cone Fuel Sprays. *Atomization and Sprays*, 7:663–684, 1997.
- [8] L.-P. Hsiang and G.M. Faeth. Near-Limit Drop Deformation and Secondary Breakup. *Int. J. Multiphase Flow*, 18(5):635–652, 1992.
- [9] M. Ishii. *Thermo-Fluid Dynamic Theory of Two Phase Flow*. Eyrolles, 1975.
- [10] M. Krämer. *Untersuchungen zum Bewegungsverhalten von Tropfen in turbulenter Strömung in Hinblick auf Verbrennungsvorgänge*. PhD thesis, Institut für Feuerungstechnik, Universität Karlsruhe, 1988.
- [11] S.A. Krzeczkowski. Measurements of Liquid Droplet Disintegration Mechanisms. *Int. J. Multiphase Flow*, 6:227–239, 1980.
- [12] B. E. Launder and D. B. Spalding. The Numerical Computation of Turbulent Flows. *Computer Methods in Applied Mechanics and Engineering*, 3, 1974.
- [13] W. Layher, G. Maier, and Wittig. Schadstoffemissionen und Betriebsverhalten einer LPP-Brennkammer. In *DGLR Jahrestagung in Bremen, Germany*, 1998.
- [14] A.H. Lefebvre. *Atomization and Sprays*. Hemisphere Publications, New York, 1998.
- [15] G. Maier, M. Willmann, and S. Wittig. Development and Optimization of Advanced Atomizers for Application in Premix Ducts. In *97-GT-56*. ASME, 1997.
- [16] G. Maier and S. Wittig. Effects of Liquid Properties on the Operating Performance of Air-Assisted Pressure Swirl Atomizers. In *ILASS Europe*, pages 193–199, 1998.
- [17] W. K. Mellville and K. N. C. Bray. A Model of the Two-Phase Turbulent Jet. *International Journal of Heat and Mass Transfer*, 22:647–656, 1979.
- [18] D. Milojević. Lagrangian Stochastic-Deterministic (LSD) Predictions of Particle Dispersion in Turbulence. *Particle and Particle Systems Characterization*, 7:181–190, 1990.
- [19] M. Pilch and C.A. Erdman. Use of Breakup Time Data and Velocity History Data to Predict the Maximum Size of Stable Fragments for Acceleration-Induced Breakup of a Liquid Drop. *Int. J. Multiphase Flow*, 13(6):741–757, 1987.
- [20] K. Prommersberger, G. Maier, and S. Wittig. Validation and Application of a Droplet Evaporation Model for Real Aviation Fuel. To be presented at the 92nd Symp. on Gas Turbine Engine Combustion, Emissions and Alternative Fuels, Lisbon, Portugal, 1998.
- [21] W. Rodi. Turbulence Models and their Application in Hydraulics - A State of the Art Review. *IAHR*, 1984.
- [22] W. Samenfink. Sekundärzerfall von Tropfen. In *Atomization and Sprays, Short Course 1995*. Institut für Thermische Strömungsmaschinen, Universität Karlsruhe, 1995.
- [23] R. Schmehl. Theory and Application of Single Component Evaporation Models. Technical report, Institut für Thermische Strömungsmaschinen, Universität Karlsruhe, <http://itsnova.mach.uni-karlsruhe.de/~schmehl>, 1998.
- [24] R. Schmehl, H. Roskamp, M. Willmann, and S. Wittig. CFD Analysis of Spray Propagation and Evaporation Including Wall Film Formation and Spray/Film Interactions. In *ILASS Europe*, pages 546–555, 1998.
- [25] H.C. Simmons. The Correlation of Drop-Size Distributions in Fuel Nozzle Sprays; Part I: The Drop-Size/Volume-Fraction Distribution. *ASME-Journal of Engineering for Power*, 99:309–314, 1977.
- [26] W.A. Sirignano. Fuel Droplet Vaporization and Spray Combustion Theory. *Progress in energy and combustion science*, Pergamon Press, 9:291–322, 1984.
- [27] W. Snyder and J. L. Lumley. Some Measurements of Particle Velocity Autocorrelation Functions in a Turbulent Flow. *Journal of Fluid Mechanics*, 48:41–71, 1971.
- [28] S. Wittig, M. Hallmann, M. Scheurlen, and S. Schmehl. A New Eulerian Model for Turbulent Evaporating Sprays in Recirculating Flows. *AGARD-CP-536*, 1993.

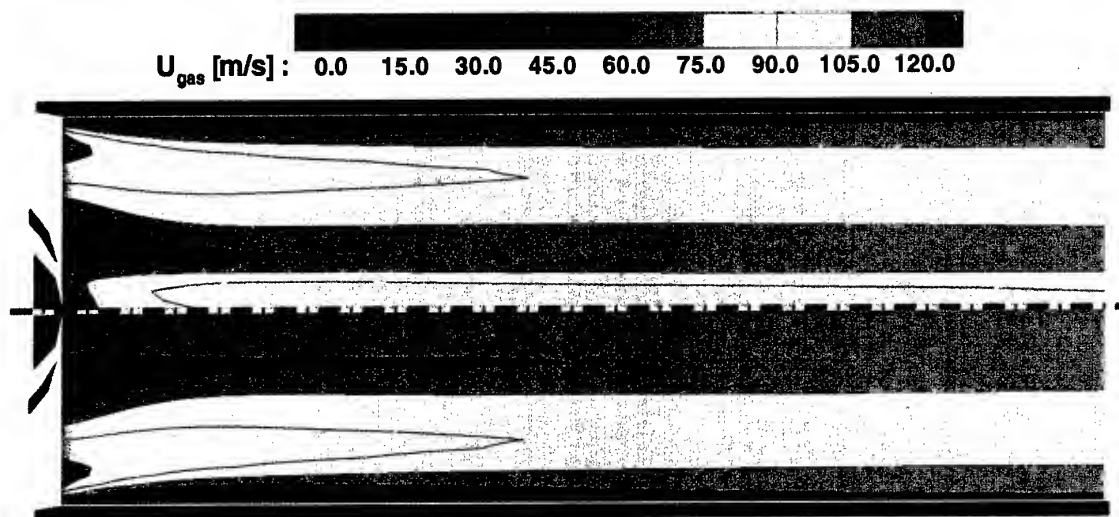


Figure 12: Axial gas velocity: Single phase calculation (top half) and two phase calculation (bottom half)

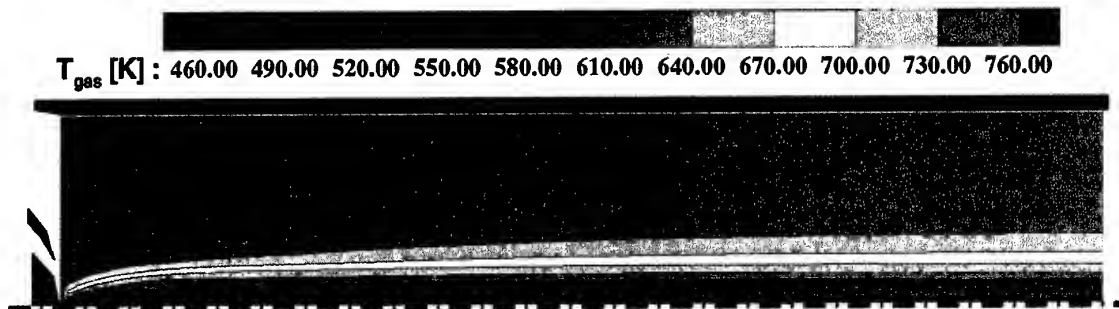


Figure 13: Calculated gas temperature

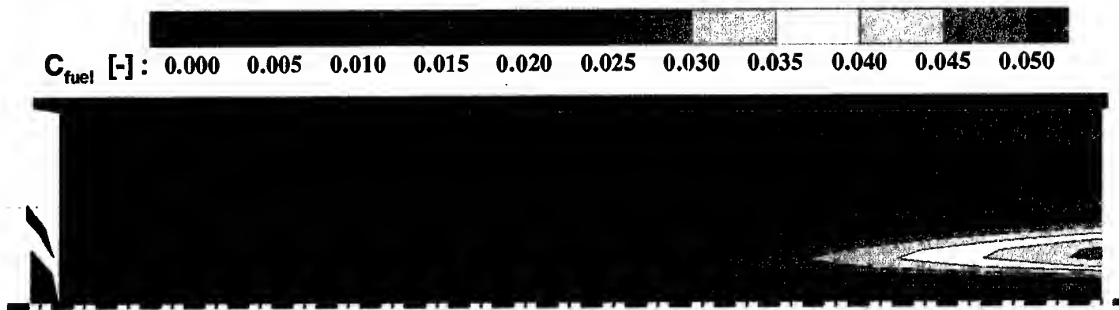


Figure 14: Calculated vapor concentration

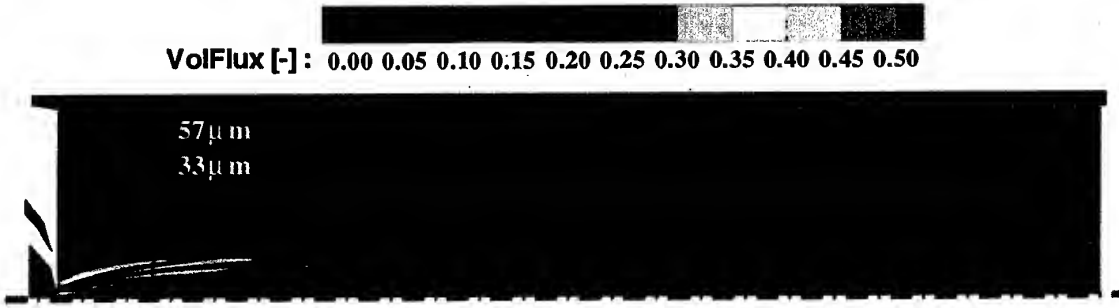


Figure 15: Normalized volume flux and mean trajectories

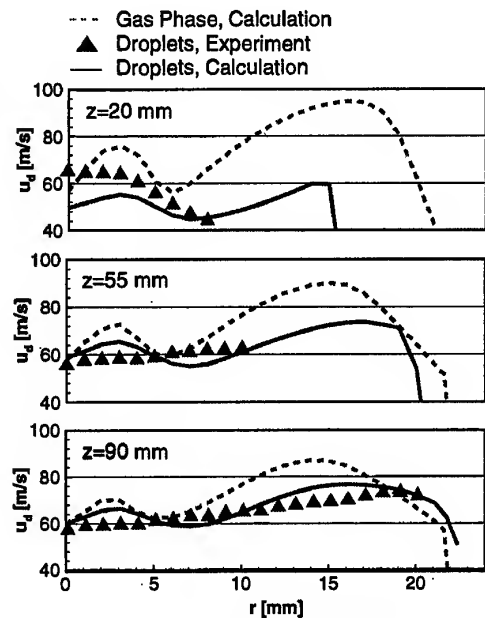


Figure 16: Mean axial velocities (Euler)

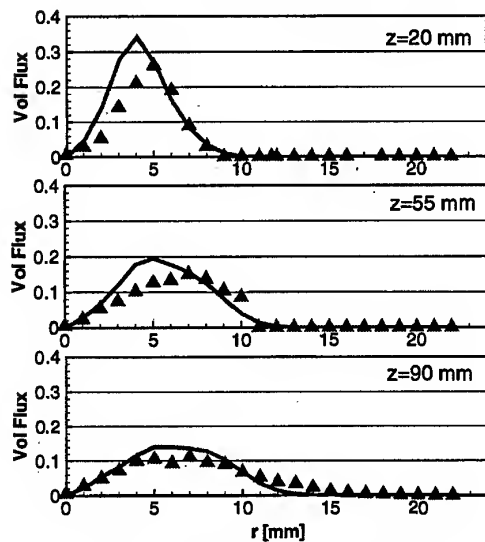


Figure 18: Normalized volume flux (Euler)

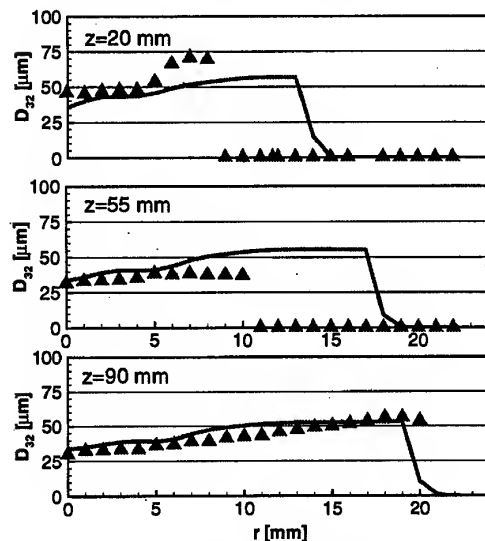


Figure 20: Sauter mean diameter (Euler)

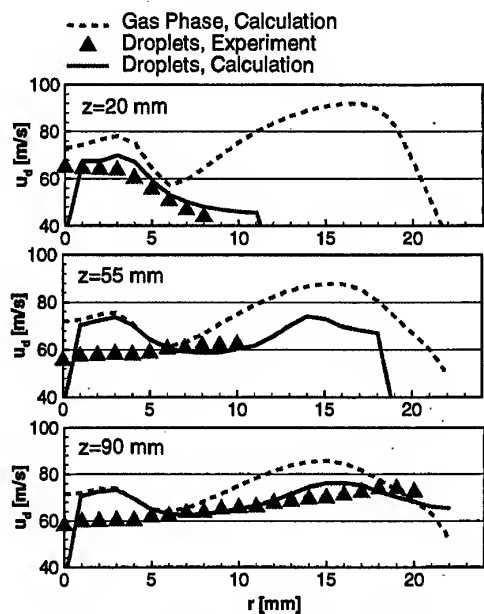


Figure 17: Mean axial velocities (Lagrange)

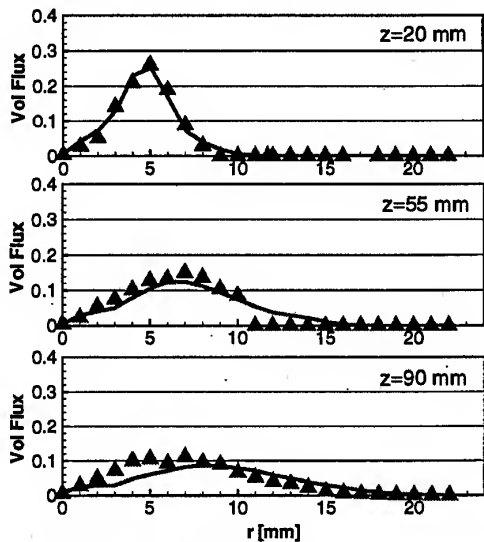


Figure 19: Normalized volume flux (Lagrange)

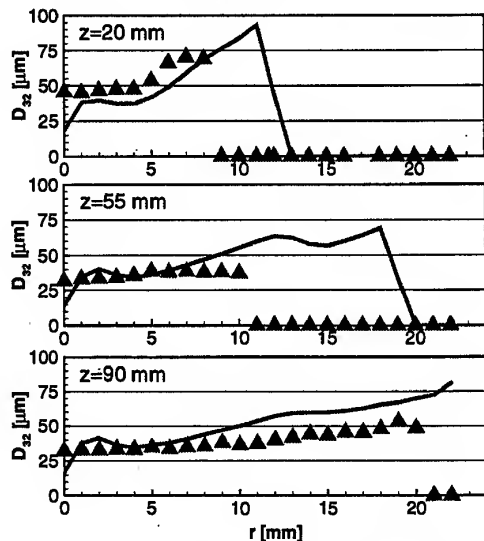


Figure 21: Sauter mean diameter (Lagrange)

PAPER No. 51
Schmehl, Klose, Prommersberger, Willmann & Wittig
 (presenter: R. Schmehl)

Question 1: V. McDonell, University of California, Irvine, U.S.

Your computations and approach are very interesting and thorough. I am wondering if you can comment on the uncertainties introduced by assuming two-dimensional flow, and also on the measurement uncertainties. The agreements between the PDPA measurements and the predictions appear to be very good - these agreements would perhaps be within the measurement uncertainty.

Answer:

Yes, we are assuming cylindrical symmetry. With respect to the PDPA measurements of droplet sizes and velocities, the measurements at $z = 20$ mm and $Z = 55$ mm are critical since fuel fragments from **primary atomization** and **secondary droplet breakup** are, of course, not spherical. Since the measurements of droplet size by the PDPA technique requires assumption of spherical droplets, this for sure, introduces substantial measurement errors. However, I do not know the exact uncertainty on these measurements.

Question 2: C. Hassa, DLR, Cologne, Germany

First, can you tell down to what particle size the secondary droplet breakup occurred? Second, have you seen incidents when secondary droplet breakup was not achieved due to changing gas surroundings?

Answer:

In answer to the first question, I cannot tell exactly, but estimate 30 - 40 μm . For the second question, **all** droplets are subjected to the **high relative velocities** in the atomizer near-field, and all (see answer to first question) large droplets are disintegrating. Of course, along with the acceleration of the droplets during breakup, local Weber Numbers are decreasing. But in our breakup model, droplet breakup is determined by the local flow conditions around the droplet at the beginning of breakup.

Question 3: C. Hassa, DLR, Cologne, Germany

Let me ask again. Have you ever observed numerically, termination of the secondary breakup process due to convection of the droplet, during the process, into local regions of low gas-phase velocities and gradients?

Answer:

Yes, there are some limitations on the breakup models. A major deficiency of the whole process is that it does not take into account any except local initial conditions, and does not take into account local changes during the breakup process. There is currently nothing available in the literature to provide guidance in this case.

Pollutants Emission Prediction in Combustion in Inert Porous Media

I. Malico, X. Y. Zhou and J. C. F. Pereira

Mechanical Engineering Department

Instituto Superior Técnico

Av. Rovisco Pais,

1096 Lisboa Codex

Portugal

1. SUMMARY

Two-dimensional predictions of flow, temperature, major species mass fractions and emissions were obtained for a porous burner. Combustion was described by the skeletal mechanism of Glarborg et al. (1992), which consists of 77 reactions and 26 species. Thermal non-equilibrium between the gas and solid phases was considered and two energy equations were solved. The discrete ordinates method was used to calculate radiation in an emitting, absorbing and isotropically scattering medium. For the two-dimensional calculations, predicted CO and NO emissions are compared with experimental values for a 7 KW thermal power and several excess air ratios. The model underpredicts the CO emissions and overpredicts the NO emissions, especially for close to stoichiometric conditions. The influence of pressure on combustion in porous media was examined using a one-dimensional model for a very simple burner configuration. It may be concluded that, as the pressure is increased, the flame speed is reduced, CO emissions are decreased and NO emissions are increased.

2. INTRODUCTION

In recent years more attention has been focused on porous materials to enhance the efficiency of the combustion systems and to reduce the emissions of pollutants. These two characteristics, allied with the possibility to have very compact geometries, are very interesting and promising to burners, in general, and combustors of gas turbines, in particular. However, there is still a long research work to be done prior to the application of combustion in inert porous media in propulsion systems. Before the high-pressure conditions or the material mechanical properties being investigated, it is of fundamental importance to understand and to be able to predict the heat transfer and premixed combustion characteristics in inert porous media at atmospheric pressure.

In porous medium combustion the flame stabilises inside a solid matrix, which enhances the heat transfer. The enthalpy released in the combustion, convectively heats the solid, which, in turn, radiates and conducts heat against the flow direction. Consequently, after the premixed fuel and air having entered the porous matrix, it is convectively heated as it passes through the interstitial voids in the matrix.

Mathematical and physical modelling is required to develop and optimise the design of such advanced combustion systems. A large number of different models with several degrees of sophistication have been developed (e. g. Baek, 1989, Sathe et al., 1989, Hsu et al., 1993, Bouma et al. 1995, Zhou and Pereira, 1997). However, the majority of the previous studies on porous medium combustion assume one-dimensional flow conditions and no radial heat losses. These two common assumptions may become inaccurate if the burner investigated has a complex geometry. In that case, two or three-dimensional models may be needed.

The main objective of this work is to investigate the performance of a skeletal reaction mechanism in describing the combustion, heat transfer and emissions in axisymmetric porous burners with integrated heat exchangers. The burner studied was developed at LSTM-Erlangen for household applications (Trimis and Durst, 1996), however, apart from the heat exchanger region, it has an identical geometrical configuration to the geometry a porous burner used in gas turbines combustion chambers would have.

Since the burner studied in this paper, is axisymmetric, the two-dimensional flow, temperature and mass fraction fields were calculated by solving the mass, momentum, energy and species conservation equations. Combustion was described by the skeletal mechanism of Glarborg et al. (1992), which consists of 77 reactions and 26 species. An operator-splitting technique was used in order to be able to solve the system of species conservation equations. Gas and solid energy equations were solved separately to account for thermal non-equilibrium between the two phases. Radiation was accounted for, isotropic scattering was assumed and the discrete ordinates method used. Predicted NO and CO emissions are compared with the experimental data of Durst et al. (1996). Two-dimensional temperature and chemical species concentration fields are presented.

Even though, the main objective of this study is to validate a two-dimensional model for combustion in porous media at atmospheric pressures, due to possible application of such kind of combustion in propulsion systems, the authors also present a parallel study on the influence of pressure in porous media combustion. For this study a one-dimensional model was used for a simpler burner configuration.

3. PROBLEM FORMULATION

The two-dimensional calculations were performed in a 10 KW porous burner prototype developed and tested at LSTM – Erlangen (Trimis and Durst, 1996). A sketch of this prototype can be seen in figure 1. Premixed methane enters the burner through the preheating zone (region A), then combustion occurs in the combustion zone (region B) and afterwards the hot combustion products flow through a heat exchanger zone (region C) and heat cold water that flows inside the heat exchanger. The preheating and heat exchanger zones are composed of 5 and 3 mm alumina spheres and the combustion region of a 10 ppi SiC ceramic foam. The maximum internal diameter of this burner is 74 mm, the minimum 40 mm and the total length of the porous matrixes is 260 mm (region A has 35 mm, region B 105 mm and region C 120 mm). The burner walls are water cooled, but the combustion region is insulated from the cold walls by a ceramic cylinder, in order to enable a steady combustion.

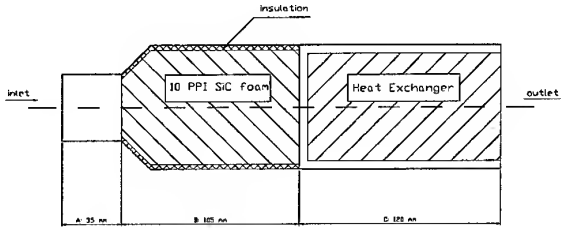


Figure 1 – Porous burner prototype under study.

4. MATHEMATICAL MODELLING

Steady, laminar, axisymmetric and Newtonian flow in inert, noncatalytic, isotropic and homogeneous media is assumed. The combustion is described by multistep kinetics and the skeletal mechanism of Glarborg et al. (1992), which consists of 77 reactions and 26 chemical species, is used. This mechanism is listed in table I and was driven from the full mechanism of Miller and Bowman (1989) through sensitivity analysis and rate-of-production analysis for perfectly stirred reactor calculations. Compared to the full mechanism the most important simplification of this skeletal model is that the C-2 chain has been excluded, however, the most important reaction steps for methane oxidation and nitrogen chemistry are retained. The latter reaction paths may be important for fuel rich mixtures but only lean mixtures are considered in this work. The flame front location is not assigned *a priori*, but is a result of the calculations.

The two-dimensional conservative form of the governing equations used is presented:

Continuity Equation

$$\nabla \cdot (\rho \mathbf{v}) = 0 \quad (1)$$

Axial Momentum Equation

$$\nabla \cdot (\rho u \mathbf{v}) = -\frac{\partial p}{\partial z} + \nabla \cdot (\mu \nabla u) - \frac{\Delta P}{\Delta L} \quad (2)$$

Radial Momentum Equation

$$\nabla \cdot (\rho v \mathbf{v}) = -\frac{\partial p}{\partial r} + \nabla \cdot (\mu \nabla v) - \frac{\Delta P}{\Delta L} \quad (3)$$

Gas Phase Energy Equation

$$\nabla \cdot (\rho c_p T_f) = \nabla \cdot (\epsilon \lambda_f \nabla T_f) + H(T_s - T_f) - \sum_{k=1}^K \dot{\omega}_k h_k W_k \quad (4)$$

Solid Phase Energy Equation

$$0 = \nabla \cdot ((1 - \epsilon) \lambda_s \nabla T_s) + H(T_f - T_s) - \nabla \cdot \mathbf{q} \quad (5)$$

Species Conservation Equation

$$\nabla \cdot (\rho \mathbf{v} Y_k) = \nabla \cdot (\rho D_{AB} \nabla Y_k) + \dot{\omega}_k W_k, \text{ with } k \in [1, K] \quad (6)$$

where ρ is the density, u and v the components of the velocity vector, p the pressure, μ the viscosity, r and z the radial and axial coordinates, respectively, c_p the specific heat of the fluid, T the temperature, ϵ the porosity, λ the thermal conductivity, H the convective heat transfer coefficient, $\dot{\omega}$ the molar reaction rate, h_k the specific enthalpy of species k , W_k the

molecular weight of the k^{th} species, \mathbf{q} the radiative flux, D_{AB} the diffusion coefficient and Y_k the k^{th} species mass fraction. The subscripts f and s mean gas and solid phase, respectively.

The energy transport due to the diffusion of the species is neglected, since, for lean methane-air flames, the Lewis numbers of the participating species do not deviate much from one (Somers, 1994).

The Ergun model (1952) modified by Macdonald et al. (1979) is used to account for the pressure loss due to the porous matrix, $\Delta P / \Delta L$.

$$\frac{\Delta P}{\Delta L} = 180 \frac{(1 - \epsilon)^2}{\epsilon^3} \frac{\mu u_i}{d_p^2} + 1.8 \frac{1 - \epsilon}{\epsilon^3} \frac{\rho |\mathbf{v}| u_i}{d_p} \quad (7)$$

where d_p is the particle diameter.

Since, locally, the solid and gas temperature may not be equal, separate energy equations for the solid and the gas phases were considered. These two equations were coupled through a convective heat transfer coefficient that accounts for the convective heat transfer between the two phases. The correlations adopted in this study for this coefficient were the one of Wakao and Kagueli (1982) for packed beds and the one of Younis and Viskanta (1996) for ceramic foams.

Gas radiation was not considered since the solid has a high emissivity when compared to the gas. Emission, absorption and isotropic scattering by the porous media were considered. To determine the radiative heat flux, the solid and fluid phases were treated as a single continuum homogeneous phase and the radiative heat transfer equation was solved. This equation can be derived by making an energy balance on the radiative energy travelling in a given direction within an infinitesimal control volume. (Siegel and Howell (1992) present the fundamental mathematical development of the radiative transfer equation for a homogeneous medium).

$$\frac{dI_\eta}{ds} = \hat{s} \cdot \nabla I_\eta = \kappa_\eta I_{b\eta} - \beta_\eta I_\eta + \frac{\sigma_{s\eta}}{4\pi} \int_{4\pi} I_\eta(\hat{s}) \Phi_\eta(\hat{s}_i, \hat{s}) d\Omega_i \quad (8)$$

The first term accounts for the change of intensity, I , in a given direction, \hat{s} , and is equal to the summation of the contributions from emission (first term on the right hand side), absorption and scattering away from the direction \hat{s} (second term on the right hand side), and scattering into the direction \hat{s} (third term on the right hand side). κ_η is the linear absorption coefficient, $\sigma_{s\eta}$ the scattering coefficient, $\beta_\eta = \kappa_\eta + \sigma_{s\eta}$ the extinction coefficient and Φ_η the scattering phase function. The medium is considered grey, homogeneous and the scattering isotropic ($\Phi=1$). The values for the radiative properties are taken from Mital et al. (1996) for the ceramic foams and calculated considering large independent specularly reflecting spheres (Siegel and Howell, 1992) for the packed beds of spheres.

The chemical reaction rates and thermophysical properties are obtained using CHEMKIN II and its database (Kee et al., 1996a). The binary diffusion coefficients are evaluated using the package of Kee et al. (1996b).

5. BOUNDARY CONDITIONS

The following boundary conditions were considered:

At the inlet:

$$u=u_{in}; v=0; T_f=T_{f,in}; Y_i=Y_{i,in} \text{ and } I=\sigma T_0^4 \quad (9)$$

where the subscript *in* means inlet and σ is the Stefan-Boltzmann constant. T_0 was set equal to 300 K, to simulate a cold environment. The solid temperature at the inlet can be given by:

$$(1-\varepsilon)\lambda_s \frac{\partial T_s}{\partial z} = -\varepsilon_r \sigma (T_s^4 - T_0^4) \quad (10)$$

where ε_r , the surface emissivity, was assumed equal to the absorptivity.

At the outlet:

$$\frac{\partial u}{\partial z} = \frac{\partial v}{\partial z} = \frac{\partial T_f}{\partial z} = \frac{\partial Y_i}{\partial z} = 0 \text{ and } I=\sigma T_0^4 \quad (11)$$

the solid temperature at the outlet was given by:

$$(1-\varepsilon)\lambda_s \frac{\partial T_s}{\partial z} = -\varepsilon_r \sigma (T_s^4 - T_0^4) \quad (12)$$

At the axis symmetry conditions were imposed:

$$\frac{\partial u}{\partial r} = v = \frac{\partial T_s}{\partial r} = \frac{\partial T_f}{\partial r} = \frac{\partial Y_i}{\partial r} = 0 \quad (13)$$

At the heat exchanger surfaces and burner walls no-slip and impenetrability conditions were imposed on the momentum equations. These walls were considered opaque, diffusely emitting and reflecting. The heat flux to the cooled walls was given by:

$$q' = -\left(\lambda_s \frac{\partial T_s}{\partial n} + \lambda_f \frac{\partial T_f}{\partial n} \right) = \frac{T - T_c}{R_t} \quad (14)$$

where n is the outward normal to the surface, T_c is the coolant temperature, T the medium temperature and R_t the thermal resistance between the bed and the coolant.

6. NUMERICAL MODEL

The finite-difference/control volume approach was used and the SIMPLE algorithm applied to staggered grids (Patankar and Spalding, 1972). Diffusion terms were discretised by central differences and the convection terms by hybrid central/upwind scheme. Since, when the finite rate chemical kinetics model is employed, the mass fraction conservation equations are stiff, other technique is required to solve them. When the characteristic time scales for the chemical reactions are much smaller than the convective and diffusive transport ones, operator splitting methods are an effective way of dealing with such combustion problems. Yanenko (1971) has presented the theoretical basis of this method and, for example, Coelho and Pereira (1993) used it to calculate a confined axisymmetric laminar diffusion flame.

Table I – Skeletal reaction mechanism of methane/air (The reaction rate is given by $\kappa_{fi} = A_i T^{\beta_i} \exp\left(-\frac{E_i}{RT}\right)$, the units are mole, cm, s, K and the units of E are cal/mole).

Reaction	A	β	E
1. $H+O_2=O+OH$	3.47E+16	-0.7	17070.0
2. $O+H_2=H+OH$	5.00E+04	2.7	6290.0
3. $OH+H_2=H_2O+H$	5.90E+08	1.4	3520.0
4. $OH+OH=H_2O+O$	2.10E+08	1.4	-400.0
5. $H+OH+M \rightarrow H_2O+M$ CO ₂ /4.0/ H ₂ O/15/ N ₂ /2/	7.60E+21	-2.0	0.0
6. $H+O_2+M \rightarrow HO_2+M$ CO/2.11/ H ₂ /3.3/ CO ₂ /4.2/ H ₂ O/18.6/ N ₂ /1.26/	7.08E+17	-0.8	0.0
7. $HO_2+H \rightarrow OH+OH$	2.50E+14	0.0	19000.0
8. $HO_2+OH \rightarrow H_2O+O_2$	3.90E+13	0.0	-50.0
9. $CO+OH=CO_2+H$	1.50E+07	1.3	-760.0
10. $CH_4+H=CH_3+H_2$	2.20E+04	3.0	8750.0
11. $CH_4+O \rightarrow CH_3+OH$	3.70E+07	1.9	7690.0
12. $CH_4+OH=CH_3+H_2O$	1.29E+06	2.2	2530.0
13. $CH_3+H \rightarrow CH_4$	2.63E+28	-5.1	-2630.0
14. $CH_3+H=CH_2+H_2$	8.90E+13	0.0	15100.0
15. $CH_3+H=CH_2(S)+H_2$	1.29E+17	-0.8	15900.0
16. $CH_3+O \rightarrow CH_2O+H$	8.32E+13	0.0	0.0
17. $CH_3+OH=CH_2+H_2O$	3.80E+06	2.0	5000.0
18. $CH_3+OH=CH_2(S)+H_2O$	2.30E+17	-1.5	-70.0
19. $CH_3+OH=CH_2OH+H$	1.70E+10	1.0	3140.0
20. $CH_3+O_2 \rightarrow CH_2OH+O$	1.29E+13	0.0	26900.0
21. $CH_3+HO_2 \rightarrow CH_2OH+OH$	2.00E+13	0.0	0.0
22. $CH_3+HCO \rightarrow CH_4+CO$	3.02E+13	0.0	0.0

23. $\text{CH}_2\text{OH}+\text{M}\rightarrow\text{CH}_2\text{O}+\text{H}+\text{M}$	4.09E+31	-8.0	43000.0
24. $\text{CH}_2\text{OH}+\text{O}_2\rightarrow\text{CH}_2\text{O}+\text{HO}_2$	1.51E+13	0.0	690.0
25. $\text{CH}_2\text{O}+\text{H}\rightarrow\text{HCO}+\text{H}_2$	2.19E+08	1.8	3000.0
26. $\text{CH}_2\text{O}+\text{OH}\rightarrow\text{HCO}+\text{H}_2\text{O}$	3.39E+09	1.2	-450.0
27. $\text{HCO}+\text{M}\rightarrow\text{CO}+\text{H}+\text{M}$ CO/1.9/ CO ₂ /3/ H ₂ O/5/ CH ₄ /2.8/ H ₂ /1.9/	1.95E+17	-1.0	17020.0
28. $\text{HCO}+\text{H}\rightarrow\text{CO}+\text{H}_2$	7.24E+13	0.0	0.0
29. $\text{HCO}+\text{OH}\rightarrow\text{CO}+\text{H}_2\text{O}$	1.10E+14	0.0	0.0
30. $\text{HCO}+\text{O}_2\rightarrow\text{CO}+\text{HO}_2$	7.59E+12	0.0	400.0
31. $\text{CH}_2+\text{H}+\text{M}\rightarrow\text{CH}_3+\text{M}$	2.39E+31	-4.4	0.0
32. $\text{CH}_2+\text{H}=\text{CH}+\text{H}_2$	2.40E+17	-1.4	0.0
33. $\text{CH}_2+\text{O}\rightarrow\text{CO}+\text{H}+\text{H}$	5.00E+13	0.0	0.0
34. $\text{CH}_2+\text{O}\rightarrow\text{CO}+\text{H}_2$	3.02E+13	0.0	0.0
35. $\text{CH}_2+\text{OH}\rightarrow\text{CH}_2\text{O}+\text{H}$.02E+13	0.0	0.0
36. $\text{CH}_2+\text{OH}=\text{CH}+\text{H}_2\text{O}$	1.10E+07	2.0	3000.0
37. $\text{CH}_2+\text{O}_2\rightarrow\text{CH}_2\text{O}+\text{O}$	5.00E+13	0.0	9000.0
38. $\text{CH}_2+\text{O}_2\rightarrow\text{CO}_2+\text{H}_2$	2.29E+12	0.0	600.0
39. $\text{CH}_2(\text{S})+\text{M}=\text{CH}_2+\text{M}$ CO/9.0/ H/55/ CO ₂ /6/ H ₂ O/18/ N ₂ /1.7/	3.63E+12	0.0	0.0
40. $\text{CH}_2(\text{S})+\text{O}_2\rightarrow\text{CO}+\text{OH}+\text{H}$	3.10E+13	0.0	0.0
41. $\text{CH}_2(\text{S})+\text{CO}_2\rightarrow\text{CH}_2\text{O}+\text{CO}$	6.60E+12	0.0	0.0
42. $\text{CH}+\text{H}=\text{C}+\text{H}_2$	1.09E+14	0.0	0.0
43. $\text{CH}+\text{O}\rightarrow\text{CO}+\text{H}$	6.03E+13	0.0	0.0
44. $\text{CH}+\text{OH}\rightarrow\text{HCO}+\text{H}$	3.20E+13	0.0	0.0
45. $\text{CH}+\text{OH}=\text{C}+\text{H}_2\text{O}$	4.00E+07	2.0	3000.0
46. $\text{CH}+\text{O}_2\rightarrow\text{HCO}+\text{O}$	3.30E+13	0.0	0.0
47. $\text{CH}+\text{H}_2\text{O}\rightarrow\text{CH}_2\text{O}+\text{H}$	1.29E+15	-0.8	0.0
48. $\text{CH}+\text{CO}_2\rightarrow\text{HCO}+\text{CO}$	3.39E+12	0.0	690.0
49. $\text{C}+\text{OH}\rightarrow\text{CO}+\text{H}$	5.00E+13	0.0	0.0
50. $\text{C}+\text{O}_2\rightarrow\text{CO}+\text{O}$	6.17E+13	0.0	650.0
51. $\text{NH}+\text{H}\rightarrow\text{N}+\text{H}_2$	3.00E+13	0.0	0.0
52. $\text{NH}+\text{O}\rightarrow\text{NO}+\text{H}$	5.50E+13	0.0	0.0
53. $\text{NH}+\text{O}\rightarrow\text{N}+\text{OH}$	7.00E+11	0.5	0.0
54. $\text{NH}+\text{NO}=\text{N}_2\text{O}+\text{H}$	1.20E+14	-0.3	0.0
55. $\text{N}+\text{OH}\rightarrow\text{NO}+\text{H}$	3.80E+13	0.0	0.0
56. $\text{N}+\text{O}_2\rightarrow\text{NO}+\text{O}$	6.46E+09	1.0	6280.0
57. $\text{N}+\text{NO}=\text{N}_2+\text{O}$	3.31E+12	0.3	0.0
58. $\text{O}+\text{N}_2+\text{M}\rightarrow\text{N}_2\text{O}+\text{M}$ O ₂ /1.5/ H ₂ O/5.0/ N ₂ /1.5/	3.25E+08	1.4	15340.0
59. $\text{N}_2\text{O}+\text{H}\rightarrow\text{N}_2+\text{OH}$	7.60E+13	0.0	15200.0
60. $\text{HCN}+\text{O}\rightarrow\text{NCO}+\text{H}$	1.41E+04	2.6	4980.0
61. $\text{HCN}+\text{O}\rightarrow\text{NH}+\text{CO}$	3.47E+03	2.6	4980.0
62. $\text{HCN}+\text{OH}\rightarrow\text{CN}+\text{H}_2\text{O}$	1.50E+15	-0.7	12380.0
63. $\text{HCN}+\text{OH}\rightarrow\text{NCO}+\text{H}_2$	5.50E+03	2.7	10800.0
64. $\text{CN}+\text{OH}\rightarrow\text{NCO}+\text{H}$	6.00E+13	0.0	0.0
65. $\text{CN}+\text{O}_2\rightarrow\text{NCO}+\text{O}$	1.00E+13	0.0	0.0
66. $\text{NCO}+\text{H}\rightarrow\text{NH}+\text{CO}$	5.01E+13	0.0	0.0
67. $\text{NCO}+\text{OH}\rightarrow\text{NO}+\text{CO}+\text{H}$	1.00E+13	0.0	0.0
68. $\text{NCO}+\text{NO}\rightarrow\text{N}_2\text{O}+\text{CO}$	3.02E+17	-1.5	260.0
69. $\text{CH}+\text{N}_2\rightarrow\text{HCN}+\text{N}$	4.37E+12	0.0	22000.0
70. $\text{C}+\text{N}_2\rightarrow\text{CN}+\text{N}$	6.31E+13	0.0	46000.0
71. $\text{CH}_2+\text{NO}\rightarrow\text{NCO}+\text{H}_2$	2.30E+12	0.0	-1100.0
72. $\text{CH}_2(\text{S})+\text{NO}\rightarrow\text{OH}+\text{HCN}$	1.00E+14	0.0	0.0
73. $\text{CH}+\text{NO}\rightarrow\text{HCN}+\text{O}$	1.10E+14	0.0	0.0
74. $\text{C}+\text{NO}\rightarrow\text{CN}+\text{O}$	1.90E+13	0.0	0.0
75. $\text{C}+\text{NO}\rightarrow\text{N}+\text{CO}$	2.88E+13	0.0	0.0
76. $\text{N}+\text{CO}_2=\text{NO}+\text{CO}$	1.29E+12	0.0	4950.0
77. $\text{N}+\text{CH}_3\rightarrow\text{HCN}+2\text{H}$	7.08E+13	0.0	0.0

Calculations start using a 1-step global kinetics mechanism to describe combustion. When the normalised residuals reach 6×10^{-2} the multistep mechanism is switched on and the following procedure is performed:

1. The velocity and pressure correction equations are solved.
2. Transient convection and diffusion of the species and of the gas energy equation (equations 15 and 16) are accounted for using an explicit procedure.

$$\frac{\partial \rho Y_k}{\partial t} + \nabla \cdot (\rho \mathbf{v} Y_k) = \nabla \cdot (\rho D_{AB} \nabla Y_k) \quad (15)$$

$$\frac{\partial \rho c_p T_f}{\partial t} + \nabla \cdot (\rho c_p \mathbf{v} T_f) = \nabla \cdot (\epsilon \lambda_f \nabla T_f) + H(T_s - T_f) \quad (16)$$

3. Then, the chemical reactions are dealt with by solving simultaneously the following set of equations for each control volume:

$$\frac{\partial}{\partial t} (\rho Y_k) = \omega_k W_k \quad (17)$$

$$\frac{\partial}{\partial t} (\rho c_p T_f) = - \sum_{k=1}^K \omega_k h_k W_k \quad (18)$$

The integration time is the minimum residence time of the gas in the control volumes. The above equations are solved using a subroutine of CHEMKIN II (Kee et al, 1996b) based on the Hindmarsh-Gear algorithm.

4. The updated mass fractions and temperatures $[Y_i]^{new}$ and $[T_f]^{new}$ are calculated by:

$$[Y_i]^{new} = [Y_i]^{old} + [\Delta Y_i]^{transport} + [\Delta Y_i]^{source} \quad (19)$$

$$[T_f]^{new} = [T_f]^{old} + [\Delta T_f]^{transport} + [\Delta T_f]^{source} \quad (20)$$

where $[Y_i]^{old}$ and $[T_f]^{old}$ are the mass fractions and temperatures of the previous iteration, $[\Delta Y_i]^{transport}$ and $[\Delta T_f]^{transport}$, respectively, the mass fractions and temperature differences before and after calculating equations 15 and 16 and $[\Delta Y_i]^{source}$ and $[\Delta T_f]^{source}$, respectively, the mass fractions and temperature difference before and after calculating equations 17 and 18.

5. The radiative transfer equation and the solid energy equation are calculated and the thermophysical properties updated.
6. The normalised residuals are checked and if the convergence criterion was not achieved the procedure would be repeated.

The calculations were performed on an Alpha station 500/400 MHz. A total number of 2640 grid nodes were used. Typical runtimes were about 15-28 CPU hours, depending on the operating conditions specified. A relative convergence of 2×10^{-2} was specified.

7. RESULTS AND DISCUSSION

7.1 Two-dimensional Calculations

In figure 2, predicted centreline temperatures for 7 KW and an excess air ratio of 1.4 are presented.

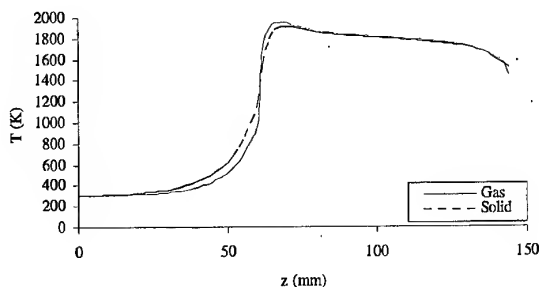


Figure 2 – Predicted centreline temperatures for 7 KW and an excess air ratio of 1.4.

For the thermal power and excess air ratio presented in figure 2, no experimental data was available. However, in a previous work (Malico et al., 1998) a comparison of the experimental and predicted temperature profile was performed. In that paper, it was shown that the centreline temperature predictions generally agreed well with the experimental data obtained. The peak temperature and the flame front location were well predicted. However, the centreline temperatures near the heat exchanger were overpredicted. The simplified numerical description of the complex heat exchanger is responsible for this difference between the experimental and predicted values.

In Figure 3 a) and b) two-dimensional temperature contours are presented.

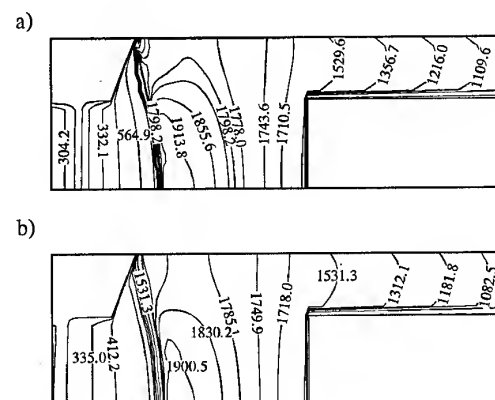
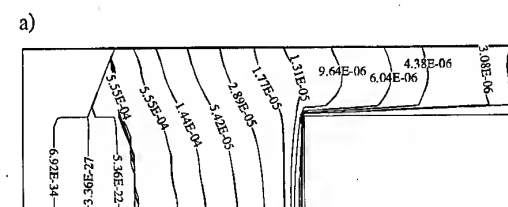


Figure 3 a) Gas b) solid temperature contours for 7 KW and an excess air ratio of 1.4.

In figure 4, two-dimensional major species mass fractions are presented.



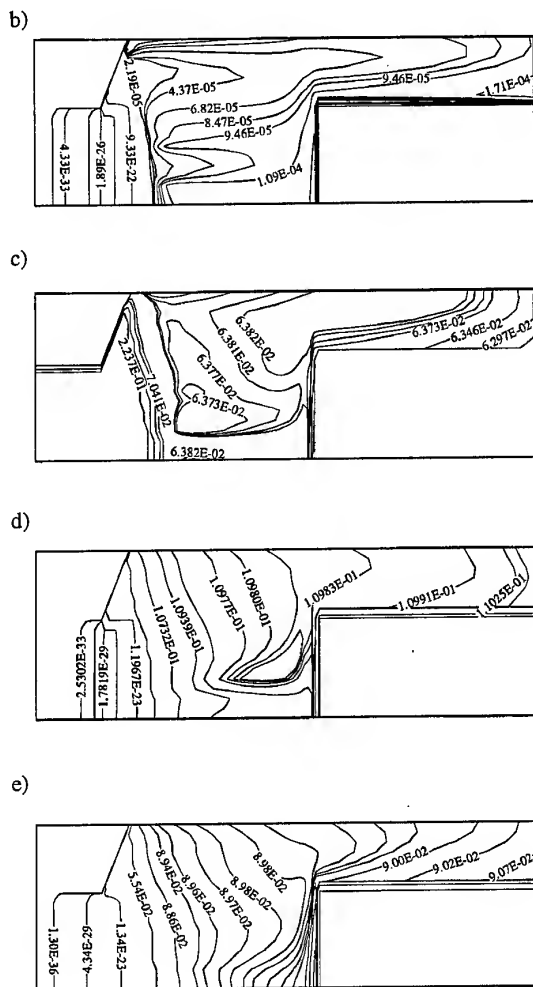


Figure 4 a) CO, b) NO, c) O₂, d) CO₂ and e) H₂O mass fractions for 7 KW and an excess air ratio of 1.5.

In figure 5 predicted NO emissions are compared with experiments (Durst and Trimis, 1996) for the cases of 7 KW and several excess air ratios. The trend was well predicted, but qualitatively the predictions are not good. The prediction of NO emissions is rather complicated since the NO formation and destruction mechanisms are very complex. In addition to this factor, the predicted emissions greatly depend on the accuracy of the temperature profiles. Leung et al. (1997) performed a sensitivity analysis that indicated large sensitivities to peak temperature and temperature profile for richer flames. In fact, it is for richer mixtures that the NO emission predictions departure more from experiments. As already mentioned, the temperatures near the heat exchanger are overpredicted, which will lead to an overprediction of the NO emissions.

In figure 6 CO emissions are compared with experiments for the cases of 7 KW and several excess air ratios. The CO predictions are not so sensitive to the temperatures profile and, therefore, are more accurate than the NO predictions. Nevertheless, the predictions underpredict the measurements of Durst and Trimis (1996). If the experimental error is taken into account (± 3 ppm) the predictions may be considered satisfactory.

7.2 Pressure Influence on Porous Media Combustion

The influence of pressure in combustion in inert porous media was studied. A one-dimensional free premixed flame of methane and air in a 101.6 mm long burner made of 10 ppi PSZ was simulated (Zhou and Pereira, 1998). The pressure was increased from 1.0 to 16.0 bar. Tables II and III show that increasing the pressure, caused the flame speed to lower, CO emissions to decrease and NO emissions to increase. This is due to an increase of the total flow rate with an increase of pressure and the consequent increase of the maximum flame temperature.

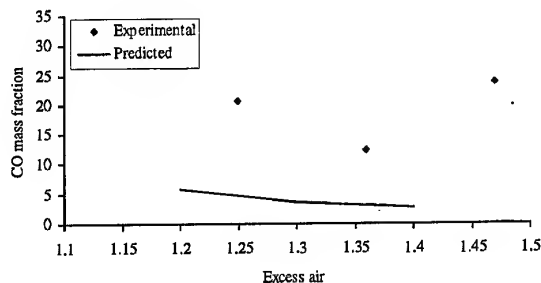


Figure 5 Predicted and experimental NO emissions for 7KW.

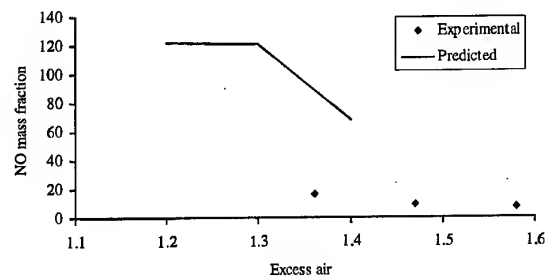


Figure 6 Predicted and experimental CO emissions for 7KW.

Table II – Predicted flame speed and CO and NO emissions for an excess air ratio of 1.0 and several pressures.

Pressure (bar)	Flame speed (cm/s)	CO emissions (%)	NO emissions (ppm)
1.0	107.3	1.033	168.7
1.5	93.3	0.838	220.8
2.0	83.9	0.748	265.0
2.5	76.9	0.697	299.4
3.0	70.9	0.668	340.9
3.5	66.12	0.644	377.2
4.0	62.12	0.624	412.5
8.0	43.4	0.527	611.6
16.0	29.8	0.448	884.1

Table III- Predicted flame speed and CO and NO emissions for an excess air ratio of 1.4 and several pressures.

Pressure (bar)	Flame speed (cm/s)	CO emissions (%)	NO emissions (ppm)
1.0	76.2	200.8	14.9
1.5	63.4	103.0	15.8
2.0	55.3	83.49	16.4
2.5	49.2	74.2	16.9
3.0	44.7	67.6	17.4
3.5	41.2	63.3	18.3
4.0	28.2	59.3	19.0
8.0	25.3	42.3	26.5
16.0	16.6	30.0	43.2

8. CONCLUSIONS

A two-dimensional model for the study of combustion, heat transfer and pollutant emission was developed and applied to the particular case of a porous burner with an integrated heat exchanger for household applications. Combustion was modelled as the skeletal mechanism of Glarborg et al. (1992), which comprises 77 reactions and 26 species. Thermal non-equilibrium was considered and two energy equations were solved, one for the gas and the other for the solid phase. Radiation was accounted for and the discrete ordinates method applied. Since, when the finite rate chemical kinetics model is employed, the mass fraction conservation equations are stiff, other technique is required to solve them. In this study an operator-splitting method was used. Calculations start using a 1-step global kinetics mechanism to describe combustion and when the normalised residuals reach 6×10^{-2} the multistep mechanism is switched on. Centreline temperature profiles are presented as well as two-dimensional temperature and mass fraction contours. The CO and NO emissions are compared with experimental data. The CO emissions are underpredicted, but taking into account the experimental error, the predictions are considered satisfactory for engineering applications. The NO emissions are overpredicted and for close to stoichiometric conditions cannot be considered satisfactory. Therefore, a better description of the nitrogen chemistry is needed, as well as more correct temperature profiles.

A one-dimensional model was used to evaluate the influence of pressure on combustion in inert porous media. An increase in the pressure loss causes the flame speed to lower, the CO emissions to decrease and the NO emissions to increase.

9. ACKNOWLEDGEMENTS

The first and second authors would like to thank the grants conceded by *Fundação para a Ciência e a Tecnologia* (reference no. PRAXIS XI/BD/5885/95 and PRAXIS XXI/BPD/11846/97, respectively).

10. REFERENCES

Baek, S. W. (1989) The premixed flame in a radiatively active porous medium *Combust. Sci. and Tech.*, 64: 277-287.

Bouma, P. H., Eggels, R. L. G. M., Goey, L. P. H., Nieuwenhuizen, J. K. and Van Der Drift, A. (1995). A numerical and experimental study of the NO-emission of ceramic foam surface burners. *Combust. Sci. and Tech.*, 108: 193-203.

Bouma, P. H. (1997). Methane-air combustion on ceramic foam surface burners. Ph.D. Dissertation, Eindhoven University of Technology.

Coelho, P. J. and Pereira, J. C. F. (1993). Calculation of a confined axisymmetric laminar diffusion flame using a local grid refinement technique. *Combust. Sci. and Tech.*, 92: 243-264.

Durst, F. and Trimis, D. (1996). Compact porous medium burner and heat exchanger for household applications. EC project report (contract no. JOE3-CT95-0019).

Ergun, S. (1952). Fluid flow through packed columns. *Chem. Eng. Progress*, 48: 89-94.

Glarborg, P., Lilleheie, N., Byggstøl, S., Magnussen, B. F., Kilpinen P. and Hupa, M. (1992) A reduced mechanism for nitrogen chemistry in methane combustion, Twenty-fourth Symposium (International) on Combustion, pp. 121-145.

Hsu, P.-F. and Matthews, R. D. (1993). The necessity of using detailed kinetics in models for premixed combustion within porous media. *Combustion and Flame* 93: 457-466

Kee, R. J., Dixon-Lewis, G., Warnatz, J., Coltrin, M. E. and Miller, J. A. (1996a). A Fortran computer code package for the evaluation of gas phase multicomponent transport properties. Sandia National Lab. Report SAND86-8246.

Kee, R. J., Miller, J. A. and Jefferson, T. H. (1996b). CHEMKIN: A general purpose problem independent, transportable, Fortran, chemical kinetic program package. Sandia National Lab. Report SAN80-8003.

Leung, K. M., Lindstedt, R. P., McCann, H., Skevis, G. and Vaos, E. (1997). Compact porous medium burner and heat exchanger for household applications. E-C project (contract no. JOE3-CT95-0019) final report.

Macdonald, I. F., El-Sayed, M. S., Mow, K. and Dullien, F. A. L. (1979). Flow through porous media - Ergun equation revisited, *Ind. Eng. Chem. Fund.*, 18: 199-208.

Malico, I., Zhou, X.-Y. and Pereira, J. C. F. (1998). Two-dimensional numerical study of combustion and pollutants formation in porous burners. Submitted to *Combust. Sci. and Techn.*

Miller, J. A. and Bowman, C. T. (1989). Mechanism and modelling of nitrogen chemistry in combustion. *Prog. Energy Combust. Sci.*, 15: 287-338

Mital, R., Gore, J. P. and Viskanta, R. (1996). Measurements of radiative properties of cellular ceramics at high temperatures. *J. of Thermophysics and Heat Transfer*, 10: 33-38.

Patankar, S. V. and Spalding, D. B. (1972). A calculation procedure for heat, mass and momentum transfer in three-dimensional parabolic flows, *Int. J. Heat Mass Transfer*, 15: 1787-1806.

Sathe, S.B, Peck, R. E and Tong, T. W. (1990). Flame stabilization and multimode heat transfer in inert porous media: A numerical study. *Combust. Sci. Technol.*, 70:93-109.

Siegel, R. and Howell, J. R. (1992). *Thermal radiation heat transfer*, 3rd Ed., Taylor and Francis, Washington, D. C.

Somers, L. M. T. (1994). The simulation of flat flames with detailed and reduced chemical models. Ph.D. Dissertation, Eindhoven University of Technology.

Trimis, D. and Durst, F. (1996). Combustion in a Porous Medium - Advances and applications, *Combust. Sci. and Tech.*, 121: 153-168.

Wakao, N. and Kaguei, S. (1982). *Heat and mass Transfer in packed beds*. Gordon and Breach, London.

Yanenko, N. N. (1971). *The method of fractional time steps: the solution of problems of mathematical physics in several variables*, M. Holt (Editor), Springer-Verlag, New York.

Younis, L. B. and Viskanta, R. (1996). Experimental determination of the volumetric heat transfer coefficient between stream of air and ceramic foam, *Int. J. Heat Mass Transfer*, 36:1425-1434.

Zhou, X. Y. and Pereira, J. C. P. (1997). Numerical study of combustion and pollutants formation in inert nonhomogeneous porous media. *Combust. Sci. and Tech.*, 130: 335-364.

Zhou, X. Y. and Pereira, J. C. P. (1998). Comparison of four combustion models for simulating the premixed combustion in inert porous media. *Fire and Materials* (to appear).

PAPER No. 53
Malico, Zhou & Pereira
(presenter: I. Malico)

Question 1: M. Cathonnet, LCSR-CNRS, Orleans, France

How do you explain the over-prediction of NO?

Answer:

We do not have adequate NO-chemistry for porous media. The mechanisms were developed for free flames, and therefore, some things are not taken into account for porous media. NO is very sensitive to the temperature profiles. Our profiles calculated near the heat exchanger are not very good, and overpredict the temperature. This gives higher NO.

Return Comment from M. Cathonnet

Yes, but the temperature explanation is only for thermal NO. You may have formation of N₂O, especially at your low temperatures, as in fluidized-bed coal combustion. Also, there may be heterogeneous reactions taking place on the surfaces of the porous media. It might be useful to look at coal combustion for NO formation, where these effects are taken into account.

Question 2: M. Nina, Instituto Superior Tecnico, Portugal

What was the dynamic range of your burner compared to conventional burners, and is this affected by the pressure?

Answer:

The range was 1- 20 kW; we did not look at the effect of pressure.

REPORT DOCUMENTATION PAGE

1. Recipient's Reference	2. Originator's References RTO-MP-14 AC/323(AVT)TP/10	3. Further Reference ISBN 92-837-0009-0	4. Security Classification of Document UNCLASSIFIED/ UNLIMITED																				
5. Originator	Research and Technology Organization North Atlantic Treaty Organization BP 25, 7 rue Ancelle, F-92201 Neuilly-sur-Seine Cedex, France																						
6. Title	Gas Turbine Engine Combustion, Emissions and Alternative Fuels																						
7. Presented at/sponsored by	the Applied Vehicle Technology Panel (AVT) Symposium (organized by the former AGARD Propulsion and Energetics Panel (PEP)), held in Lisbon, Portugal, 12-16 October 1998.																						
8. Author(s)/Editor(s) Multiple	9. Date June 1999																						
10. Author's/Editor's Address Multiple	11. Pages 616																						
12. Distribution Statement	There are no restrictions on the distribution of this document. Information about the availability of this and other RTO unclassified publications is given on the back cover.																						
13. Keywords/Descriptors	<table><tbody><tr><td>Gas turbine engines</td><td>Performance evaluation</td></tr><tr><td>Combustion</td><td>Research projects</td></tr><tr><td>Combustion chambers</td><td>Combustion efficiency</td></tr><tr><td>Fuel consumption</td><td>Combustion control</td></tr><tr><td>Exhaust emissions</td><td>Mathematical models</td></tr><tr><td>Jet engine fuels</td><td>Computerized simulation</td></tr><tr><td>Aviation fuels</td><td>Optical measurement</td></tr><tr><td>Availability</td><td>Emission control</td></tr><tr><td>Alternative fuels</td><td>Design</td></tr><tr><td>Aircraft engines</td><td>Ignition</td></tr></tbody></table>			Gas turbine engines	Performance evaluation	Combustion	Research projects	Combustion chambers	Combustion efficiency	Fuel consumption	Combustion control	Exhaust emissions	Mathematical models	Jet engine fuels	Computerized simulation	Aviation fuels	Optical measurement	Availability	Emission control	Alternative fuels	Design	Aircraft engines	Ignition
Gas turbine engines	Performance evaluation																						
Combustion	Research projects																						
Combustion chambers	Combustion efficiency																						
Fuel consumption	Combustion control																						
Exhaust emissions	Mathematical models																						
Jet engine fuels	Computerized simulation																						
Aviation fuels	Optical measurement																						
Availability	Emission control																						
Alternative fuels	Design																						
Aircraft engines	Ignition																						
14. Abstract	<p>The symposium dealt with Gas Turbine Engine Combustion, Emissions and Alternative Fuels. Forty-six papers and a Keynote Address elucidated the role of the combustion process as a crucial factor of engine performance and operability under various conditions including non-standard, new fuels and environmental effects of civil and military interest.</p> <p>There were 12 Sessions covering the following topics (some in 2 sessions):</p> <ul style="list-style-type: none">- Gas Turbines in Land, Sea and Air Applications- Low-Emission Combustors- Combustion Modelling- Optical Measurements- Emissions- Combustor Design- Ignition Processes- Active Combustion Control- Alternative Fuels																						



RESEARCH AND TECHNOLOGY ORGANIZATION

BP 25 • 7 RUE ANCELLE

F-92201 NEUILLY-SUR-SEINE CEDEX • FRANCE

Télécopie 0(1)55.61.22.99 • E-mail mailbox@rta.nato.int

DIFFUSION DES PUBLICATIONS

RTO NON CLASSIFIEES

L'Organisation pour la recherche et la technologie de l'OTAN (RTO), détient un stock limité de certaines de ses publications récentes, ainsi que de celles de l'ancien AGARD (Groupe consultatif pour la recherche et les réalisations aérospatiales de l'OTAN). Celles-ci pourront éventuellement être obtenues sous forme de copie papier. Pour de plus amples renseignements concernant l'achat de ces ouvrages, adressez-vous par lettre ou par télécopie à l'adresse indiquée ci-dessus. Veuillez ne pas téléphoner.

Des exemplaires supplémentaires peuvent parfois être obtenus auprès des centres nationaux de distribution indiqués ci-dessous. Si vous souhaitez recevoir toutes les publications de la RTO, ou simplement celles qui concernent certains Panels, vous pouvez demander d'être inclus sur la liste d'envoi de l'un de ces centres.

Les publications de la RTO et de l'AGARD sont en vente auprès des agences de vente indiquées ci-dessous, sous forme de photocopie ou de microfiche. Certains originaux peuvent également être obtenus auprès de CASI.

CENTRES DE DIFFUSION NATIONAUX

ALLEMAGNE

Fachinformationszentrum Karlsruhe
D-76344 Eggenstein-Leopoldshafen 2

BELGIQUE

Coordinateur RTO - VSL/RTO
Etat-Major de la Force Aérienne
Quartier Reine Elisabeth
Rue d'Evère, B-1140 Bruxelles

CANADA

Directeur - Recherche et développement -
Communications et gestion de l'information -
DRDCGI 3
Ministère de la Défense nationale
Ottawa, Ontario K1A 0K2

DANEMARK

Danish Defence Research Establishment
Ryvangs Allé 1, P.O. Box 2715
DK-2100 Copenhagen Ø

ESPAGNE

INTA (RTO/AGARD Publications)
Carretera de Torrejón a Ajalvir, Pk.4
28850 Torrejón de Ardoz - Madrid

ETATS-UNIS

NASA Center for AeroSpace Information (CASI)
Parkway Center, 7121 Standard Drive
Hanover, MD 21076-1320

FRANCE

O.N.E.R.A. (Direction)
29, Avenue de la Division Leclerc
92322 Châtillon Cedex

GRECE

Hellenic Air Force
Air War College
Scientific and Technical Library
Dekelia Air Force Base
Dekelia, Athens TGA 1010

ISLANDE

Director of Aviation
c/o Flugrad
Reykjavik

ITALIE

Aeronautica Militare
Ufficio Stralcio RTO/AGARD
Aeroporto Pratica di Mare
00040 Pomezia (Roma)

LUXEMBOURG

Voir Belgique

NORVEGE

Norwegian Defence Research Establishment
Attn: Biblioteket
P.O. Box 25
N-2007 Kjeller

PAYS-BAS

NDRCC
DGM/DWOO
P.O. Box 20701
2500 ES Den Haag

PORTUGAL

Estado Maior da Força Aérea
SDFA - Centro de Documentação
Alfragide
P-2720 Amadora

ROYAUME-UNI

Defence Research Information Centre
Kentigern House
65 Brown Street
Glasgow G2 8EX

TURQUIE

Millî Savunma Başkanlığı (MSB)
ARGE Dairesi Başkanlığı (MSB)
06650 Bakanlıklar - Ankara

AGENCES DE VENTE

NASA Center for AeroSpace

Information (CASI)
Parkway Center
7121 Standard Drive
Hanover, MD 21076-1320
Etats-Unis

The British Library Document

Supply Centre
Boston Spa, Wetherby
West Yorkshire LS23 7BQ
Royaume-Uni

Canada Institute for Scientific and

Technical Information (CISTI)
National Research Council
Document Delivery,
Montreal Road, Building M-55
Ottawa K1A 0S2
Canada

Les demandes de documents RTO ou AGARD doivent comporter la dénomination "RTO" ou "AGARD" selon le cas, suivie du numéro de série (par exemple AGARD-AG-315). Des informations analogues, telles que le titre et la date de publication sont souhaitables. Des références bibliographiques complètes ainsi que des résumés des publications RTO et AGARD figurent dans les journaux suivants:

Scientific and Technical Aerospace Reports (STAR)

STAR peut être consulté en ligne au localisateur de ressources uniformes (URL) suivant:
<http://www.sti.nasa.gov/Pubs/star/Star.html>
STAR est édité par CASI dans le cadre du programme NASA d'information scientifique et technique (STI)
STI Program Office, MS 157A
NASA Langley Research Center
Hampton, Virginia 23681-0001
Etats-Unis

Government Reports Announcements & Index (GRA&I)

publié par le National Technical Information Service
Springfield
Virginia 2216
Etats-Unis
(accessible également en mode interactif dans la base de données bibliographiques en ligne du NTIS, et sur CD-ROM)



Imprimé par le Groupe Communication Canada Inc.

(membre de la Corporation St-Joseph)

45, boul. Sacré-Cœur, Hull (Québec), Canada K1A 0S7



RESEARCH AND TECHNOLOGY ORGANIZATION

BP 25 • 7 RUE ANCELLE

F-92201 NEUILLY-SUR-SEINE CEDEX • FRANCE

Telefax 0(1)55.61.22.99 • E-mail mailbox@rta.nato.int

DISTRIBUTION OF UNCLASSIFIED

RTO PUBLICATIONS

NATO's Research and Technology Organization (RTO) holds limited quantities of some of its recent publications and those of the former AGARD (Advisory Group for Aerospace Research & Development of NATO), and these may be available for purchase in hard copy form. For more information, write or send a telefax to the address given above. **Please do not telephone.**

Further copies are sometimes available from the National Distribution Centres listed below. If you wish to receive all RTO publications, or just those relating to one or more specific RTO Panels, they may be willing to include you (or your organisation) in their distribution.

RTO and AGARD publications may be purchased from the Sales Agencies listed below, in photocopy or microfiche form. Original copies of some publications may be available from CASI.

NATIONAL DISTRIBUTION CENTRES

BELGIUM

Coordonateur RTO - VSL/RTO
Etat-Major de la Force Aérienne
Quartier Reine Elisabeth
Rue d'Evère, B-1140 Bruxelles

CANADA

Director Research & Development
Communications & Information
Management - DRDCIM 3
Dept of National Defence
Ottawa, Ontario K1A 0K2

DENMARK

Danish Defence Research Establishment
Ryvangs Allé 1, P.O. Box 2715
DK-2100 Copenhagen Ø

FRANCE

O.N.E.R.A. (Direction)
29 Avenue de la Division Leclerc
92322 Châtillon Cedex

GERMANY

Fachinformationszentrum Karlsruhe
D-76344 Eggenstein-Leopoldshafen 2

GREECE

Hellenic Air Force
Air War College
Scientific and Technical Library
Dekelia Air Force Base
Dekelia, Athens TGA 1010

ICELAND

Director of Aviation
c/o Flugrad
Reykjavik

ITALY

Aeronautica Militare
Ufficio Stralcio RTO/AGARD
Aeroporto Pratica di Mare
00040 Pomezia (Roma)

LUXEMBOURG

See Belgium

NETHERLANDS

NDRCC
DGM/DWOO
P.O. Box 20701
2500 ES Den Haag

NORWAY

Norwegian Defence Research Establishment
Attn: Biblioteket
P.O. Box 25
N-2007 Kjeller

PORTUGAL

Estado Maior da Força Aérea
SDFA - Centro de Documentação
Alfragide
P-2720 Amadora

SPAIN

INTA (RTO/AGARD Publications)
Carretera de Torrejón a Ajalvir, Pk.4
28850 Torrejón de Ardoz - Madrid

TURKEY

Millî Savunma Başkanlığı (MSB)
ARGE Dairesi Başkanlığı (MSB)
06650 Bakanlıklar - Ankara

UNITED KINGDOM

Defence Research Information Centre
Kentigern House
65 Brown Street
Glasgow G2 8EX

UNITED STATES

NASA Center for AeroSpace Information (CASI)
Parkway Center, 7121 Standard Drive
Hanover, MD 21076-1320

SALES AGENCIES

NASA Center for AeroSpace Information (CASI)

Parkway Center
7121 Standard Drive
Hanover, MD 21076-1320
United States

The British Library Document Supply Centre

Boston Spa, Wetherby
West Yorkshire LS23 7BQ
United Kingdom

Canada Institute for Scientific and Technical Information (CISTI)

National Research Council
Document Delivery,
Montreal Road, Building M-55
Ottawa K1A 0S2
Canada

Requests for RTO or AGARD documents should include the word 'RTO' or 'AGARD', as appropriate, followed by the serial number (for example AGARD-AG-315). Collateral information such as title and publication date is desirable. Full bibliographical references and abstracts of RTO and AGARD publications are given in the following journals:

Scientific and Technical Aerospace Reports (STAR)

STAR is available on-line at the following uniform resource locator:

<http://www.sti.nasa.gov/Pubs/star/Star.html>

STAR is published by CASI for the NASA Scientific and Technical Information (STI) Program

STI Program Office, MS 157A
NASA Langley Research Center
Hampton, Virginia 23681-0001
United States

Government Reports Announcements & Index (GRA&I)

published by the National Technical Information Service

Springfield
Virginia 22161

United States

(also available online in the NTIS Bibliographic Database or on CD-ROM)



Printed by Canada Communication Group Inc.

(A St. Joseph Corporation Company)

45 Sacré-Cœur Blvd., Hull (Québec), Canada K1A 0S7

ISBN 92-837-0009-0